

**UNIVERSIDAD NACIONAL DE COLOMBIA**  
**PROGRAMA DE DOCTORADO EN INGENIERÍA –**  
**SISTEMAS ENERGÉTICOS**  
**Departamento de Procesos y Energía**

**UNIVERSIDAD DE GRANADA**  
**PROGRAMA DE DOCTORADO EN QUÍMICA**  
**Departamento de Química Inorgánica**



**TESIS DOCTORAL**

**Development of Multifunctional Nanomaterials for the  
co-Production of Upgraded Heavy Crude Oil and  
Hydrogen at Different Pressures and Temperatures**

**Oscar Enrique Medina Erazo**  
**Granada, Junio 2023.**





# **Development of Multifunctional Nanomaterials for the co-Production of Upgraded Heavy Crude Oil and Hydrogen at Different Pressures and Temperatures**

Por  
**Oscar Enrique Medina Erazo**

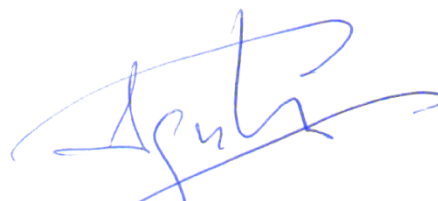
Memoria presentada para aspirar al grado de Doctor por la  
Universidad Nacional de Colombia y la Universidad de  
Granada

Fdo: Oscar Enrique Medina Erazo  
Ingeniero de Petróleos.

## **Los directores de la Tesis**



**Prof. Dr. Camilo A. Franco Ariza**  
Prof. Asociado del Departamento de  
Procesos y Energía, Universidad  
Nacional de Colombia



**Prof. Dr. Agustín F. Pérez Cadenas**  
Prof. Catedrático del Departamento de  
Química Inorgánica, Universidad de  
Granada



Camilo Andrés Franco Ariza y Agustín Francisco Pérez Cadenas como directores de la presente Tesis Doctoral y el doctorando Oscar Enrique Medina Erazo

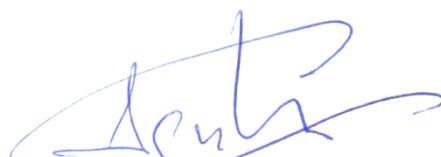
### **GARANTIZAN QUE**

El trabajo ha sido realizado por el doctorando respetando los derechos de otros autores a ser citados cuando se han utilizado sus resultados o publicaciones

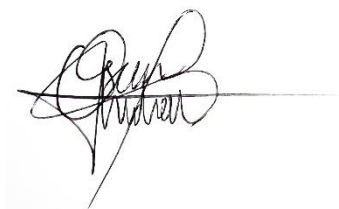
Y para que conste a los efectos oportunos, en el cumplimiento de la legislación vigente, firmamos el presente certificado en Granada, Junio del 2023.



Fdo: Camilo A. Franco Ariza  
Prof. Asociado del Departamento de  
Procesos y Energía, Universidad  
Nacional de Colombia



Fdo: Agustín F. Pérez Cadenas  
Catedrático del Departamento de Química  
Inorgánica, Universidad de Granada



Fdo: Doctorando Oscar Enrique Medina Erazo  
Ingeniero de Petróleos.



**DEVELOPMENT OF MULTIFUNCTIONAL NANOMATERIALS  
FOR THE CO-PRODUCTION OF UPGRADED HEAVY CRUDE  
OIL AND HYDROGEN AT DIFFERENT PRESSURES AND  
TEMPERATURES**

**DESARROLLO DE NANOMATERIALES MULTIFUNCIONALES  
PARA LA COPRODUCCIÓN DE CRUDO PESADO MEJORADO  
E HIDRÓGENO A DIFERENTES PRESIONES Y  
TEMPERATURAS**

Tesis presentada para aspirar al grado de Doctor por

**OSCAR ENRIQUE MEDINA ERAZO**

Realizada bajo la dirección y co-tutela del Dr. Camilo A. Franco Ariza, Prof. Asociado del Departamento de Procesos y Energía, Universidad Nacional de Colombia, y del Dr. Agustín F. Pérez Cadenas, Catedrático de Química Inorgánica de la Universidad de Granada, y juzgada el día 7 de junio de 2023, en la Facultad de Ciencias de la Universidad de Granada, por el siguiente Tribunal:

PRESIDENTE:

Prof. Dra. María de los Ángeles Ferro, Departamento de Química Inorgánica, Universidad de Granada.

VOCAL 1:

Prof. Dr. Pedro Nel Benjumea, Departamento de Procesos y Energía, Universidad Nacional de Colombia.

VOCAL 2:

Prof. Dr. Miguel Ángel Álvarez Merino, Departamento de Química Inorgánica y Química Orgánica, Universidad de Jaén.

VOCAL 3:

Dr. Julio Llorca Porcel, Responsable Laboratorio de Cromatografía, Cepsa Centro de Investigación, CEPISA.

SECRETARIA:

Dra. Esther Bailón García, Investigadora Ramón y Cajal, Departamento de Química Inorgánica, Universidad de Granada.



*“Those who can imagine anything, can create the impossible.”*

*— Alan Turing.*





# Acknowledgments

I would like to express my sincere thanks to my advisors Prof. Ph.D. Camilo Andrés Franco Ariza and Prof. Ph.D. Agustín Francisco Pérez Cadenas, for their shared time and knowledge which encouraged me with the necessary competencies for developing this study and all my academic achievements in the last years.

Exceptional thanks to Prof. Ph.D. Farid Cortés Correa for always being there for me when I needed him and for his unfailing generosity. His life story has always motivated me to pursue this dream.

I am infinitely grateful to Prof. Ph.D. Francisco Carrasco Marín for his unceasing guidance, his encouragement words, for receiving me in Granada and making me feel at home.

I want to express my gratitude to Prof. Ph.D. Jaime Gallego, for extending his helping hand and disposition in my learning. Thanks for teaching me how to be a better researcher and person. Especially, thanks for being a friend.

A huge thanks to the wonderful people I met in the Michael Polanyi Surface Phenomena and Carbon Materials research groups. Saray Pérez, Johanna Vargas, Eliana Gonzales, Cristina Caro, Yurany Villada, Iván Moncayo, Daniela Arias, Luciana Cardona, Daniel López, Karol Zapata, Santiago Cespedes, Jessica Castelo, Yira Hurtado, Lady Giraldo, Juan Guzmán, Andrea Muños, Leonardo Parra, Samira Heidari, Alejandra Muños, Camilo Mazo. Thank you for these incredible years and unforgettable experiences.

I also want to thank to Prof. Nashaat N. Nassar, Prof. Ph.D. Arno De Klerk, Prof. Ph.D. Masoud Riazi, Prof. Ph.D. Raul Ocampo Perez, and Prof. Ph.D. Socrates Acevedo for their contribution to my research. It was an honor to learn from all of them during this journey.

I acknowledge Ph.D. Bergit Brattekas and Prof. Ph.D. Martin Fernø for welcoming me into the research group for Reservoir Physics, Energy Technology, and CO<sub>2</sub> storage (CCUS) during my doctoral stay, as well as the valuable people and co-workers I met there. Weekly meetings with talented people like Ph.D. Nicole Dopffel, Ph.D.(c) Maksim Lysyy, Ph.D. Na Liu, Ph.D.(c) Raymond Mushabe, and Prof. Ph.D. Geir Ersland were very enriching in my learning process. A special thanks to Prof. Ph.D. Pedro Nel Benjumea, for making this dream possible.

To the Norad project “CO<sub>2</sub>-EOR for CCUS in Colombia and Ecuador: Norwegian energy initiative” for the support with a grant equivalent to the State Education Loan Fund (Lånekassen) during my stay at the University of Bergen. I will never forget this magic city and the wonderful people I met: Ine Si Stalheim, Stephanie Dilini Steffensen, Aleksandra Magdalena Sæle, Rebecca, Jorge Rodriguez, Marco Antonio, and Daria. Thanks to my partner in crime in this adventure, Isabel Giraldo. Only you and I know everything we lived through and how special our friendship made.

Thanks to the Forskerskolene HySchool og NFiP and the University of Bergen for allowing me to attend courses and conferences around Norway, USA, and UK. These experiences definitely had a positive impact on my academic training.

To my friends, thank you for always being there to take care of me. You've been a constant pillar in these trying times. To my most special friends, Banesa Garces, Dahiana Galeano, Brenda Benítez, Nathaly Garzón, Valentín Hernández, Paulina Quintero, Laura Valentina, Mateo Arango, Alejandra Chávez, Camila Ramírez, Alejandra Martínez, María José V, Sindy Ojeda, Luisa Fernanda Bravo, Valentina Gómez, and Felipe Arroyave, I'm thankful for your unwavering company.

Thanks to the love, thank you for coming into my life and filling it with happiness, magic, colors, and flavors.

Finally, to the most important people in my life, “Mis Viejos”. Thank you for helping me to shape my life with positivity and passion. Without you, I'd never be the person I am today. Thank you is a very small word to convey my gratitude towards you, but I am still using it to say how fortunate I am to be raised by you. The sacrifices you've made for me are beyond any description. My beloveds. I hope to make you proud someday. To my another love, Hermanita, I cannot say enough thanks for your contribution to my life. Love you.

*A la memoria de quien más he extrañado en este mundo, Héctor Jesús Erazo, que tantas veces metió baza en mi vida, con su palabra aguda y redicha como una campanita de convento, que, a despecho del mundo, todavía me sonaba a amanecer.*

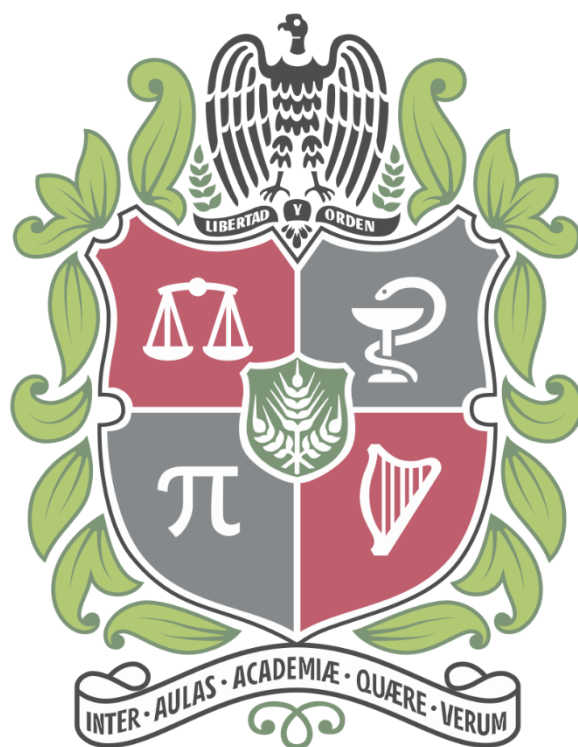
*A Concepción Zambrano, por ser tú, la mejor abuela que he podido tener.*

*A Tommy, mi Little brother, por toda la felicidad que le diste a mi vida.*





## Índice





# Índice

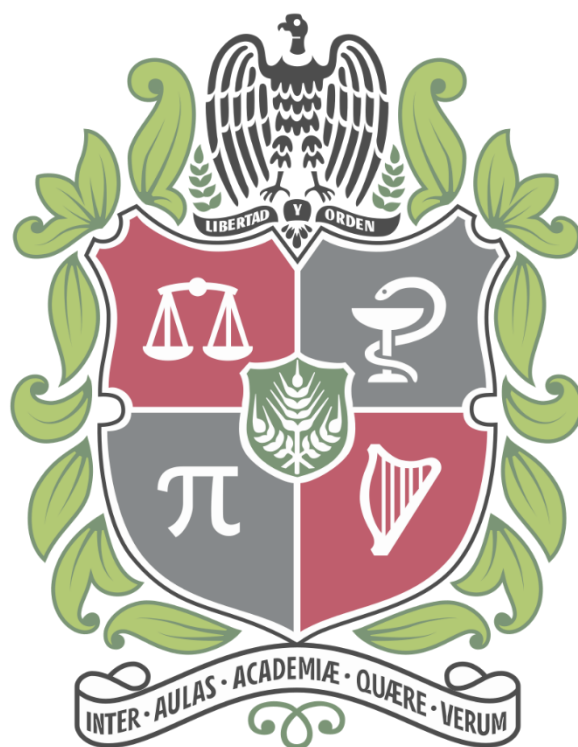
<b>Abstract and Keywords:</b> .....	21
<b>Resumen y Palabras Clave:</b> .....	28
<b>Apartado 1:</b> .....	48
<b>Introducción.</b> .....	50
<b>Objetivos.</b> .....	64
<b>Apartado 2:</b> Materiales y métodos .....	66
<b>Apartado 3:</b> .....	88
<b>Capítulo 1.</b> Effect of pressure on the oxidation kinetics of Asphaltenes. 90	
<b>Capítulo 2.</b> Thermo-oxidative decomposition behaviors of different sources of <i>n</i> -C <sub>7</sub> Asphaltenes under high-pressure conditions. ....	120
<b>Capítulo 3.</b> Experimental and theoretical study of the influence of solvent on asphaltene-aggregates thermo-oxidation through high-pressure thermogravimetric analysis.....	172
<b>Capítulo 4.</b> Chemical and Structural Changes of Asphaltenes During Oxygen Chemisorption at Low and High-Pressure. ....	210
<b>Capítulo 5.</b> Effect of pressure on thermo-oxidative reactions of saturates, aromatics, and resins (S-Ar-R) from extra-heavy crude oil.....	246
<b>Capítulo 6.</b> Effect of pressure on the thermo-oxidative behavior of saturates, aromatics, and resins (S-Ar-R) mixtures.....	290
<b>Apartado 4:</b> .....	326
<b>Capítulo 7.</b> Optimization of the load of transition metal oxides (Fe <sub>2</sub> O <sub>3</sub> , Co <sub>3</sub> O <sub>4</sub> , NiO and/or PdO) onto CeO <sub>2</sub> nanoparticles in catalytic steam decomposition of <i>n</i> -C <sub>7</sub> asphaltenes at low temperatures.....	328
<b>Capítulo 8.</b> Redox-couple on the cyclic regeneration for adsorptive and catalytic performance of NiO-PdO/CeO <sub>2+δ</sub> nanoparticles for <i>n</i> -C <sub>7</sub> asphaltene steam gasification.....	366
<b>Capítulo 9.</b> Insights into the morphology effect of ceria on the catalytic performance of NiO-PdO/CeO <sub>2</sub> nanoparticles for thermo-oxidation of <i>n</i> -C <sub>7</sub> asphaltenes under isothermal heating at different pressures. ....	408
<b>Capítulo 10.</b> Theoretical and Experimental Study of Adsorption and Catalytic Reactivity of Asphaltene Fractions A1 and A2 over Cubic NiO-PdO/CeO <sub>2</sub> Nanoparticles. ....	446
<b>Capítulo 11.</b> Molecular Dynamic Simulation and Experimental Study on <i>n</i> -C <sub>7</sub> Asphaltene Pyrolysis under High-Pressure Conditions using Ceria-Based Nanocatalysts.....	472

<b>Capítulo 12.</b> Catalytic Conversion of <i>n</i> -C <sub>7</sub> Asphaltenes and Resins II into Hydrogen Using CeO <sub>2</sub> -Based Nanocatalysts.....	510
<b>Apartado 5.</b> .....	548
<b>Capítulo 13.</b> Upgrading of extra-heavy crude oils by dispersed injection of NiO–PdO/CeO <sub>2+δ</sub> nanocatalyst-based nanofluids in the steam. ....	550
<b>Capítulo 14.</b> A Theoretical and Experimental Approach to the Analysis of Hydrogen Generation and Thermodynamic Behavior in an In Situ Heavy Oil Upgrading Process Using Oil-Based Nanofluids. ....	586
<b>Capítulo 15.</b> Simultaneous CO <sub>2</sub> adsorption and conversion over Ni-Pd supported CeO <sub>2</sub> nanoparticles during catalytic <i>n</i> -C <sub>7</sub> asphaltene gasification. ....	624
<b>Capítulo 16.</b> Upscaling Process for Nanofluids Deployment in Wells Affected by Steam Injection Processes: Experimental Design and Field Trial Application. ....	664
<b>Apartado 6</b> .....	696
<b>Capítulo 17.</b> Sulfur Removal from Heavy Crude Oils based on the Adsorption Process using Nanomaterials: Experimental and Theoretical Study.....	698
<b>Capítulo 18.</b> Sulfur removal using nanomaterials as a potential upgrading mechanism of heavy-crude oils: Cyclic reuse and thermal regeneration. ....	738
<b>Capítulo 19.</b> Monolithic carbon xerogels-metal composites for crude oil removal from oil in-saltwater emulsions and subsequent regeneration through oxidation process: Composites synthesis, adsorption studies, and oil decomposition experiments.....	766
<b>Capítulo 20.</b> Development of a monolithic carbon xerogel-metal composite for crude oil removal from oil in-saltwater emulsions: Evaluation of reuse cycles.....	814
<b>Conclusiones generales</b> .....	842





## Contenidos y estructura de la Tesis





# Development of Multifunctional Nanomaterials for the co-Production of Upgraded Heavy Crude Oil and Hydrogen at Different Pressures and Temperatures

## Abstract

This Thesis includes the synthesis of various nanomaterials based on oxides of lanthanide elements, transition, aluminosilicates, carbon, and composite materials. Some evaluated composite materials contain metal oxides-lanthanide oxides, metal oxides-lanthanide oxides-carbon xerogels. The performance of the materials was evaluated in their ability to produce hydrogen and improve the quality of the crude oil from the catalytic degradation of hydrocarbon macromolecules, heteroatoms, and crude in oxidation, gasification, and pyrolysis atmospheres.

The experimental results obtained and their discussion are presented in this report divided into six main sections, in which 20 chapters have been distributed that include the different activities carried out for the development of nanomaterials with catalytic properties tailored for the re-evaluation and use of heavy and extra-heavy crudes and the obtaining of H<sub>2</sub> as a transient and complementary energy source, promoted during the accumulation of the heavy fractions plus crude oil and the use of different by-products to help the intermediate reactions that increase the production of H<sub>2</sub>.

The **first section** presents the approach to the problem around energy consumption, the deterioration of conventional crude oil reserves, and the need humanity faces to migrate to clean energy, as well as the state of the art of nanomaterials capable of improving specific crude oil properties, proposed as possible strategies to promote energy transition processes.

The **second section** describes the materials and methods used. The methods of characterization of the crude fractions and the synthesized nanomaterials are exposed. In addition, the techniques for evaluating the adsorptive and catalytic performance of nanomaterials are shown.

The **third section** contains Chapters 1-6 that present the studies carried out on the different crude oil fractions at low and high-pressure conditions in the absence of nanomaterials to understand their reactivity and propose

nanomaterials capable of assisting chemical reactions that potentiate the production of hydrogen.

Chapter 1 is dedicated to evaluating the effect of pressure on the oxidation kinetics of asphaltenes. The chapter also includes the basic principles of different high-pressure variables, such as temperature and heating rate. In addition to a diffusional study to analyze the problems of mass and heat transfer during the tests. Chapter 2 collects information on the oxidation of *n*-C<sub>7</sub> asphaltenes extracted from different heavy and extra-heavy crudes at different pressures. The amount of oxygen chemisorbed was affected by the type of oxygen species in the asphaltenes, such as COO<sup>-</sup>. Furthermore, as the degree of aromatization increases and the degree of alkylation decreases, so does the number of chemisorbed oxygen atoms. Chapter 3 focuses on understanding the oxidative behavior of *n*-C<sub>7</sub> asphaltene aggregates under high-pressure conditions. This chapter evaluates different asphaltene model solutions using three xylene isomers to represent asphaltene-asphaltene interactions in a heavy crude matrix. The evaluation is carried out through experimental analysis and molecular dynamics simulations. The -CH<sub>3</sub> location in xylene substantially impacted the aggregation state. The oxidative experiments of the aggregates showed that oxygen chemisorption decreased as the size of the asphaltene aggregate increased, reducing its reactivity. This study improves our understanding of the relationship between aggregation and thermal oxidation of crude oils, characterizing the physical behavior to propose alternatives that reduce asphaltene aggregation and improve oxidative kinetics. Chapter 4 aims to investigate the change in the chemical properties of asphaltenes during the OC region from an experimental and theoretical perspective. The results validate that the chemisorption sites are strongly related to molecular characteristics. Carboxyl or COO<sup>-</sup> groups were formed for one class of asphaltene, whereas for asphaltene E, oxygen bonds are expected to form phenolic and etheric oxygen. MD also suggests the size of the aromatic nucleus as the most relevant characteristic. In Chapter 5, the thermo-oxidative behavior is investigated as a function of the pressure of the other fractions of the crude, that is, saturates, aromatic, and resin compounds. The main findings were that, for pressures above 3.0 MPa, aromatics and resins were described in all four stages (OC, DCO, FC, and SC), while saturates were only described in FC and SC regions at all pressures. At 6.0 MPa, the aromatics show rapid decomposition in the FC region, while the resins show a slower decomposition spread across all three decomposition regions. This

result suggests that aromatics have a greater impact on oxidation reactions at high temperatures as pressure increases. The pyrolysis curves revealed that, for all applied pressures, the amount of coke produced increases in the following order: saturates < aromatics < resins. Chapter 6 seeks to understand the effect of pressure on the interactions between the saturates, aromatics, and resins (S-Ar-R) fractions during thermo-oxidation reactions. For this, the simultaneous oxidation between saturates:aromatics (S:Ar), saturates:resins (S:R) and resins:aromatics (Ar:R) is evaluated. The results demonstrate the role of pressure in the simultaneous oxidation of S:Ar, S:R and Ar:R mixtures. First, FC and SC describe the thermo-oxidative profiles of S:Ar at 0.084 MPa, regardless of the S:Ar ratio. When oxidation is evaluated at 3.0 and 6.0 MPa, OC, and DCO zones are observed, and the amount of chemisorbed oxygen increases with increasing pressure. The same trend was observed for the S:R and Ar:R systems. Among the S:Ar mixtures, oxygen chemisorption increased as aromatics increased at 3.0 and 6.0 MPa. Structures formatted at high pressure present greater reactivity; therefore, the total consumption of the samples ends at lower temperatures. During S:R oxidation, the higher the resin content, the higher the chemisorption of oxygen, and the lower the temperature required to decompose the samples. Finally, the mixture between aromatics and resins shows slower kinetic speeds than the other systems.

In the **fourth section**, Chapters 7-12 are collected, in which the design and evaluation of nanomaterials with catalytic properties tailored for the decomposition of the heaviest fraction of crude oil is presented, which will allow the re-evaluation and use of heavy and extra-heavy crudes by improving their quality and the co-production of H<sub>2</sub>. Chapter 7 covers the development of amorphous CeO<sub>2</sub> nanoparticles and surface doping with pairs of transition element oxides (Fe<sub>2</sub>O<sub>3</sub>, Co<sub>3</sub>O<sub>4</sub>, and/or NiO) and noble elements (PdO) to determine their adsorption capacity and catalytic activity to capture and decompose asphaltenes. The results showed that by incorporating monoelemental and bielemental oxides into CeO<sub>2</sub> nanoparticles, the adsorption and isothermal conversion of asphaltenes increase. It is worth mentioning that bielemental nanoparticles reduced the gasification temperature of asphaltenes to a greater extent than monoelemental nanoparticles. In addition, the optimized nanoparticles with the best match (Ni-Pd) have the best performance, obtaining 100% asphaltene conversion in less than 90 min at 220 °C while reducing the activation energy by 80%. In Chapter 8, once the nanoparticle with the best

couple of TEOs has been selected and the load optimized, the evaluation of its regenerative capacity during the adsorption and subsequent decomposition of asphaltenes *n*-C<sub>7</sub> in steam gasification processes is addressed. The evaluation has considered the influence of the redox cycle (Ce<sup>3+</sup>/Ce<sup>4+</sup>) on the self-regeneration of CeO<sub>2±δ</sub>, as well as the thermodynamic and potential properties of the adsorption process, the kinetic parameters of the catalytic process, and the change in the surface chemistry of the material. Among the main results, it was obtained that the asphaltenes showed a high affinity for being adsorbed on the surface of the nanoparticles during nine evaluated regeneration cycles. Furthermore, the catalytic activity of the nanoparticles did not change significantly, showing that they decomposed 100% of the *n*-C<sub>7</sub> asphaltenes in all cycles. In Chapter 9 it is considered to change the morphology of CeO<sub>2</sub> nanoparticles, between (C) cubic; (O) orthorhombic; and (S) spherical, for the thermo-oxidation of asphaltenes *n*-C<sub>7</sub> to potentiate some limitations of the support without defined morphology, evaluated in Chapters 7 and 8. This study considered previous advances in phase doping, for which Ni and Pd oxides in 1% mass fractions were selected. The catalytic activity of the systems was evaluated by non-isothermal and isothermal thermogravimetric analyses at different pressures. The non-isothermal thermogravimetric results showed an increase in the mass of asphaltenes *n*-C<sub>7</sub> as the temperature increases between 100 and 230 °C for all systems and operating conditions. The Ni and Pd phases increase the amount of chemisorbed oxygen in all systems in the order S-NiPdCe < O-NiPdCe < C-NiPdCe, and reduce the temperature required for the total decomposition of *n*-C<sub>7</sub> asphaltenes at temperatures below 200 °C to 6.0 MPa in the same order. Chapter 10 evaluates the nanomaterial with the morphology that presents the highest performance during the catalytic oxidation of asphaltenes for a subsequent evaluation in pyrolysis reactions, which are fundamental in oil thermal recovery processes. In this chapter, our knowledge about low and high-pressure pyrolysis processes is expanded through experimental and simulation approaches under the scope that the presence of oxygen vacancies that cause the coexistence and exchange of Ce<sup>4+</sup> and Ce<sup>3+</sup> in its lattice structure is one of the main reasons for its catalytic activity. Chapter 11 considers the fractionation of asphaltene molecules into A1 and A2. Analyzing the adsorbent and catalytic behavior of nanoparticles with both fractions is of vital help to developing catalysts that can improve the reaction pathway of asphaltene aggregates. The MD simulations reveal that the size of the aggregates increases in the order A1 < A2, which is explained by the higher density of the A1 fraction. The adsorption affinity of A1-CeO<sub>2</sub> nanoparticles was

higher than that of A2-CeO<sub>2</sub> nanoparticles, resulting in more adsorbed A1 asphaltenes. Oxidative experiments show that oxygen chemisorption occurs in asphaltenes due to the A1 subfraction; no oxygen chemisorption was observed in A2. Finally, the non-catalytic pyrolysis of A2 exhibited better thermogravimetric characteristics, including a higher mass loss at lower temperatures and less coke at the end of heating due to the different densities between A1 and A2 aggregates. Chapter 12 summarizes the results of the volumetric production of hydrogen in the gas mixture released from the catalytic steam gasification of *n*-C<sub>7</sub> asphaltenes and resins II at low temperatures (< 230 °C). Hydrogen production agrees with the catalytic activity of each material to decompose both fractions under the evaluated conditions. CeNi1Pd1 showed the highest yield among the other three samples, leading to the highest hydrogen production in the effluent gas with values of ~44 vol%. When samples were heated to higher temperatures (i.e., 230 °C), H<sub>2</sub> production increased by up to 55% by volume during the conversion of resin, and *n*-C<sub>7</sub> catalyzed asphaltenes, indicating an increase of up to 70% compared to uncatalyzed systems under the same temperature conditions.

The **fifth section** contains Chapters 13-16, which include the necessary activities to determine the potential of nanomaterials for improving the quality of crude oil and the production of H<sub>2</sub> and other valuable products with low CO<sub>2</sub> emissions under thermal enhanced oil recovery processes. In Chapter 13, a nanofluid is designed from one of the nanocatalysts with the best performance in decomposing the heavy fractions of crude oil and producing hydrogen from these reactions. This study proposes a novel injection method of nanofluid in the porous medium, dispersed in the steam stream, to improve the mobility conditions of crude oil at reservoir pressure and temperature and the oil recovery factor. For the different steps of the dynamic test, increases of 25 and 42% in oil recovery were obtained for the dispersed injection of the nanofluid in the steam stream and after a soaking time of 12 h, compared to the base curve with only steam injection, respectively. The upgraded crude reached an API gravity level of 15.9°, an increase of 9.0° units compared to the untreated extra-heavy crude, representing an increase of 130%. In Chapter 14, a thermodynamic analysis of the fugacity of hydrogen is presented to obtain a clearer picture of its behavior in situ. The H<sub>2</sub> fugacity was determined between the reservoir pressure and overburden and different temperatures, which were determined by the thermal profiles in the displacement test. Hydrogen acquired a higher chemical potential

through the presence of nanoparticles. However, the difference in H<sub>2</sub> fugacity between the two points is much greater with nanoparticles, which means that hydrogen has a lower tendency to migrate by diffusion to the high-pressure point. Based on this analysis, it was possible to determine the tendency of hydrogen to be trapped in the reservoir and its dissipation in the porous medium. In Chapter 15, the feasibility of using geological formations subjected to thermal recovery processes as reactors is investigated: where both the adsorption and conversion of CO<sub>2</sub> and the production of other high-quality by-products occur. CO<sub>2</sub> adsorption increased in the order S-CeO<sub>2</sub> < O-CeO<sub>2</sub> < C-CeO<sub>2</sub> < C-CeNiPd, regardless of temperature. Nanoparticles with adsorbed asphaltenes also showed a high tendency to adsorb CO<sub>2</sub>. Finally, for the conversion of CO<sub>2</sub>, a mixture of gases composed of CO, CH<sub>4</sub>, H<sub>2</sub>, and light hydrocarbons (LHC) is obtained. The hydrogen production content follows a trend that agrees well with the adsorption capacity and catalytic activity of each material. This study demonstrates that using nanocatalyst-assisted combined CO<sub>2</sub> and steam injection technologies can potentially increase the volume of crude oil produced and its quality based on in situ upgrading and simultaneously improve CO<sub>2</sub> capture and conversion. Chapter 16 exposes the methodology applied to carry out an increase from a technological readiness level (TRL) of 3 to a TRL -8 for implementing nanotechnology in a field application, going through the experimental design and the initial field test results. The application was conducted as a field test application in a Colombian field through a cyclic steam stimulation process.

In the **sixth section**, Chapters 17-20 are presented, where two technologies are proposed, including i) the use of heteroatoms present in the heaviest fractions of crude oil, such as sulfur, to improve the quality of crude oil and the co-production of hydrogen through adsorption/catalysis processes with custom-designed nanomaterials, and ii) the removal of oil from emulsions of crude oil in water for the production of gases with high calorific value through adsorption and catalysis processes. In the next two Chapters (17 and 18), desulfurization processes are proposed as mechanisms to produce hydrogen and improve crude oil quality. The efficiency of the adsorption process of nanomaterials is validated by estimating their adsorption/removal capacity and affinity for sulfur species through batch and continuous adsorption experiments. The second part focused on discovering the influence of the regeneration atmosphere on sulfur adsorption, sulfur conversion, and hydrogen production. These studies made it possible to enhance the chemical properties of a nanomaterial to extend its half-



life with high selectivity, adsorption, and catalytic capacity. This generates valuable information on adsorbent reuse processes while removing sulfur compounds from heavy crudes. On the other hand, the information presented in Chapters 19 and 20 corresponds to a new application focused on the development of carbon-metal xerogel monolithic compounds for oil removal by adsorption and regeneration processes from oil-in-salt-water emulsions. The adsorption results show that crude removal increased with increasing metal content in the composite for all experimental setups. The catalytic activity of three monolithic carbon xerogels was corroborated with calculations of effective activation energy, which decreased by 24.9, 32.5, and 52.4 % from virgin crude decomposition to adsorbed decomposition on samples X, XCe, and XCeNi, respectively. The gaseous analysis of the products involved in the oxidation of crude oil in each cycle was considered, finding an increase in the production of light hydrocarbons and reducing the emissions of gases such as CO<sub>2</sub>, NO<sub>x</sub>, and SO<sub>x</sub> in all reuses.

**Keywords:** Energy transition; Oil and gas industry; Nanotechnology.; Hydrogen production

## Resumen

En la presente Tesis Doctoral se recoge la síntesis de diversos nanomateriales basados en óxidos de elementos lantánidos, transición, aluminosilicatos, carbono y materiales compuestos. Algunos materiales compuestos evaluados contienen óxidos metálicos-óxidos lantánidos, óxidos metálicos-óxidos lantánidos-xerogeles de carbono. El rendimiento de los materiales fue evaluado en su capacidad para producir hidrogeno y mejorar la calidad del crudo a partir de la descomposición catalítica de macromoléculas de hidrocarburo, heteroátomos y crudos en atmosferas de oxidación, gasificación y pirolisis.

El uso de petróleo crudo como fuente de carbono para la producción de  $H_2$  en presencia de nanomateriales aún no se ha examinado a fondo. Por lo tanto, quedan tareas importantes para identificar la participación de las fracciones de crudo en la producción de  $H_2$  a diferentes presiones y temperaturas. En este contexto, es indispensable evaluar la respuesta térmica de las fracciones de crudo en ausencia de nanomateriales y bajo diferentes escenarios (cambios de presión y temperatura). Su entendimiento eventualmente conducirá a una comprensión más profunda del comportamiento térmico del petróleo, y cuyo conocimiento será la base para el correcto diseño de nanomateriales con propiedades catalíticas para ayudar a reacciones que dejen una mayor liberación de hidrógeno durante el craqueo térmico de los crudos.

Los resultados experimentales obtenidos y su discusión se presentan en esta Memoria divididos en 6 apartados principales, en los cuales se han distribuido 20 capítulos que recogen las diferentes actividades realizadas para el desarrollo de nanomateriales con propiedades catalíticas a la medida para la reevaluación y aprovechamiento de crudos pesados y extrapesados y la obtención de  $H_2$  como fuente de energía transitoria y complementaria, promovida durante la descomposición de las fracciones más pesada del petróleo crudo y el uso de diferentes subproductos para ayudar a las reacciones intermedias que aumentan la producción de  $H_2$ .

El **primer Apartado** presenta el planteamiento del problema alrededor del consumo energético, el deterioro de las reservas de crudo convencional y la

necesidad que enfrenta la humanidad a migrar a energías limpias, así como el estado del arte de los nanomateriales capaces de mejorar propiedades específicas del crudo, planteados como posibles estrategias para fomentar procesos de transición energética. El apartado también recoge los objetivos generales y específicos.

El **segundo Apartado** describe los materiales y métodos utilizados. Se exponen los métodos de caracterización de las fracciones del crudo, así como de los nanomateriales sintetizados. Además, se muestran las técnicas de evaluación del rendimiento adsorptivo y catalítico de los nanomateriales.

En el **tercer Apartado** se recogen los **Capítulos 1-6** que presentan los estudios realizados a las diferentes fracciones del crudo a condiciones de baja y alta presión en ausencia de nanomateriales, con el fin de comprender su reactividad y proponer nanomateriales capaces de asistir reacciones químicas que potencialicen la producción de hidrógeno.

El **Capítulo 1** está dedicado a evaluar el efecto de la presión sobre la cinética de oxidación de asfaltenos insolubles en *n*-heptano derivados de un crudo extrapesado a través de análisis termogravimétricos (TGA). Las evaluaciones se realizaron bajo una atmósfera de aire a presiones que oscilan entre 0.084 MPa y 7 MPa, temperaturas que oscilan entre 100 y 600 °C y rampas de calentamiento de 5, 10 y 15 °C·min<sup>-1</sup>, usando un modelo cinético de primer orden para calcular los parámetros cinéticos. De acuerdo con el perfil TGA, el rango de temperatura se dividió en cuatro regiones principales para una mejor comprensión de la oxidación de asfaltenos en condiciones de alta presión: i) quimisorción de oxígeno (OC), ii) descomposición del oxígeno quimisorbido (DCO), iii) primera región de combustión (FC), y iv) segunda región de combustión (SC). Se encontró que aumentos de presión favorecen la descomposición de asfaltenos a bajas temperaturas. El capítulo recoge, además, los principios básicos de diferentes variables a alta presión, tales como la temperatura y la tasa de calentamiento. Además de un estudio difusional para analizar los problemas de transferencia de masa y calor durante las pruebas.

En el **Capítulo 2** se recoge información sobre la oxidación de asfaltenos *n*-C<sub>7</sub> extraídos de diferentes crudos pesados y extrapesados a diferentes presiones entre 0.084 y 6.0 MPa. Los asfaltenos *n*-C<sub>7</sub> se caracterizaron minuciosamente

mediante análisis elemental, osmometría de presión de vapor, espectroscopia de fotoelectrones de rayos X, espectroscopia infrarroja transformada de Fourier, difracción de rayos X y técnicas de resonancia magnética nuclear, con el fin de esclarecer su comportamiento térmico ante cambios de presión y temperatura en función de su naturaleza química. Se descubrió que la cantidad de oxígeno quimisorbido se ve afectada por el tipo de especie de oxígeno en los asfaltenos, como COO-. Además, a medida que aumenta el grado de aromatización y disminuye el grado de alquilación, también lo hace la cantidad de átomos de oxígeno quimisorbidos. El capítulo recoge, además, un análisis cinético comparativo considerando la reactividad del asfalteno como múltiples pasos usando una aproximación del método isoconversional de Ozawa, Flynn y Wall basado en tendencias en el factor pre-exponencial y energías de activación efectivas.

El **Capítulo 3** se centra en comprender el comportamiento oxidativo de los agregados de asfaltenos  $n$ -C<sub>7</sub> en condiciones de alta presión. En este capítulo se evalúan diferentes soluciones modelo de asfaltenos utilizando tres isómeros de xileno con el fin de representar las interacciones asfalteno-asfalteno en una matriz de crudo pesado. La evaluación se realiza a través de análisis experimental y simulaciones de dinámica molecular. Se encontró que la ubicación -CH<sub>3</sub> en el xileno impacta sustancialmente en el estado de agregación. Las moléculas de *o*-xileno que rodeaban los agregados de asfaltenos orientaron los grupos -CH<sub>3</sub> hacia los agregados, aumentando su energía de interacción y reduciendo el tamaño de los agregados. Además, los experimentos oxidativos de los agregados mostraron que la quimisorción de oxígeno disminuyó a medida que aumentaba el tamaño del agregado de asfaltenos, reduciendo su reactividad. El capítulo correlaciona propiedades como energías de interacción y tamaños de agregado, con la reactividad del asfalteno y su respuesta térmica a condiciones de alta presión. Este estudio mejora nuestra comprensión de la relación entre la agregación y la oxidación térmica de los crudos, caracterizando el comportamiento físico para proponer alternativas que reduzcan la agregación de asfaltenos y mejoren la cinética oxidativa.

Se encontró que, si bien la presión fue un factor de control en las cuatro regiones de oxidación, hubo un comportamiento extraño en la gráfica termogravimétrica para temperaturas inferiores a 250 °C, donde se presenta la OC. Curiosamente, la región OC ganó mucha atención porque la respuesta de las

muestras en el resto de los eventos térmicos parece depender de cómo interactúa el oxígeno con los asfaltenos en esa región. La respuesta térmica en OC de cada asfalteno fue diferente según la naturaleza química de los asfaltenos. En algunos casos, el comportamiento térmico de los asfaltenos no dependió de la cantidad de masa ganada en OC para completar la descomposición a temperaturas más altas. Esto nos hace pensar que dependiendo de los grupos oxigenados que se formen en el OC, la reactividad de los asfaltenos puede cambiar en mayor o menor grado. En **Capítulo 4** tiene como objetivo investigar el cambio en las propiedades químicas de los asfaltenos durante la región OC desde una perspectiva experimental y teórica. Para lograr esto, se seleccionaron dos muestras de asfaltenos *n*-C<sub>7</sub> obtenidos de diferentes fuentes de crudo pesado (anteriormente denominados B y E) con diferentes naturalezas químicas para examinar su oxidación a baja (0.084 MPa) y alta presión (6.0 MPa). Además, se llevaron a cabo simulaciones MD para proporcionar más información sobre el efecto de las características moleculares de los asfaltenos en el proceso de quimisorción de oxígeno y estimar la masa teórica de oxígeno quimisorbida y la configuración de quimisorción por función de distribución radial (RDF). Los resultados validan que los sitios de quimisorción están fuertemente relacionados con las características moleculares. Los resultados sugieren que para el asfalteno B se obtuvo un primer pico de coordinación bien definido para la interacción entre el oxígeno, el nitrógeno y el carbono. Para el asfalteno E, el primer pico de coordinación corresponde a las interacciones con oxígeno, hidrógeno y nitrógeno. Por lo tanto, para el asfalteno B se pueden formar los grupos carboxilo o COO-, mientras que para el asfalteno E se puede esperar que se formen enlaces oxígeno-oxígeno formando oxígeno fenólico y oxígeno etérico. MD también sugiere el tamaño del núcleo aromático como la característica más relevante. Comprender el comportamiento térmico de las moléculas de asfalteno en los procesos de oxidación-conversión permite a los investigadores seleccionar el mejor diseño de mejora para las muestras de crudo pesado y extrapesado durante los procesos tEOR.

En el **Capítulo 5** se investiga el comportamiento termo oxidativo en función de la presión de las demás fracciones del crudo, es decir, los compuestos saturados, aromáticos y resinas. Este capítulo busca discretizar los aportes adicionales por evaporación, pirólisis y oxidación durante las reacciones termo-oxidativas, incluyendo la presión como factor clave de los experimentos. Simulando la destilación, se evaluó la evaporación atmosférica de S, Ar y R. Por

el contrario, se utilizaron la ecuación de Clapeyron y la ecuación de estado de Redlich-Kwong para calcular las curvas de destilación a alta presión. Para determinar las respuestas de pirólisis y oxidación, se evaluaron los perfiles de cambio de masa y tasa de cambio de masa en un analizador termogravimétrico de alta presión (HP-TGA). Se utilizó un modelo cinético de primer orden que discretiza los perfiles de oxidación térmica en cuatro regiones distintas. Los principales hallazgos fueron que, para presiones superiores a 3,0 MPa, los aromáticos y las resinas se describieron en las cuatro etapas (OC, DCO, FC y SC), mientras que los saturados solo se describieron en las regiones FC y SC en todas las presiones. A 6,0 MPa, los aromáticos muestran una descomposición rápida en la región FC, mientras que las resinas muestran una descomposición más lenta distribuida en las tres regiones de descomposición. Esto sugiere que los aromáticos tienen un mayor impacto en las reacciones de oxidación a altas temperaturas a medida que aumenta la presión. Las curvas de pirólisis revelaron que, para todas las presiones aplicadas, la cantidad de coque producido aumenta en el siguiente orden: saturados < aromáticos < resinas.

El **Capítulo 6** busca comprender el efecto de la presión en las interacciones entre las fracciones de saturados, aromáticos y resinas (S-Ar-R) durante las reacciones de termo oxidación. Para esto, se evalúa la oxidación simultánea entre saturados:aromáticos (S:Ar), saturados:resinas (S:R) y resinas:aromáticos (Ar:R). Este estudio este trabajo ofrece una comprensión mecánica y cinética del proceso de descomposición por oxidación de mezclas de fracciones de petróleo crudo a alta presión y temperatura. Los resultados demuestran el papel de la presión en la oxidación simultánea de las mezclas S:Ar, S:R y Ar:R. En primer lugar, FC y SC describen los perfiles termooxidativos de S:Ar a 0.084 MPa, independientemente de la relación S:Ar. Cuando la oxidación se evalúa a 3.0 y 6.0 MPa, se observan zonas OC y DCO, y la cantidad de oxígeno quimisorbido aumenta a medida que aumenta la presión. Se observó la misma tendencia para los sistemas S:R y Ar:R. Entre las mezclas de S:Ar, la quimisorción de oxígeno aumentó a medida que aumentaba la cantidad de compuestos aromáticos a 3.0 y 6.0 MPa. Las estructuras formateadas a alta presión presentan mayor reactividad; por lo tanto, el consumo total de las muestras termina a temperaturas más bajas. Durante la oxidación S:R, cuanto mayor sea el contenido de resinas, mayor será la quimisorción de oxígeno y menor la temperatura requerida para descomponer las muestras. Finalmente, la mezcla entre aromáticos y resinas muestra velocidades cinéticas más lentas que los otros sistemas.

En el **cuarto Apartado** se recogen los **Capítulos 7-12** en los cuales se presenta el diseño y evaluación de nanomateriales con propiedades catalíticas a la medida para la descomposición de la fracción más pesada del petróleo crudo que permitirá la reevaluación y aprovechamiento de crudos pesados y extrapesados mediante el mejoramiento de su calidad y la coproducción de H<sub>2</sub>.

El **Capítulo 7** recoge el desarrollo de nanopartículas de CeO<sub>2</sub> amorfa y dopaje superficial con parejas de óxidos elementos de transición (Fe<sub>2</sub>O<sub>3</sub>, Co<sub>3</sub>O<sub>4</sub>, y/o NiO) y elementos nobles (PdO), con el fin de determinar su capacidad de adsorción y actividad catalítica para capturar y descomponer asfaltenos. La naturaleza química de las nanopartículas es propuesta basado en las interacciones asfaleno-asfaleno y los conocimientos adquiridos durante los primeros seis capítulos de la presente tesis doctoral. Se utilizaron experimentos de adsorción por lotes y análisis termogravimétricos combinados con espectroscopía infrarroja transformada de Fourier (FTIR) para medir las isothermas de adsorción y el proceso de descomposición de vapor posterior de los asfaltenos, respectivamente, para evaluar la catálisis. Las isothermas de adsorción y el comportamiento catalítico fueron descritos por el modelo de equilibrio sólido-líquido (SLE) y el modelo isotérmico, respectivamente. Posteriormente, un diseño de experimentos de mezcla simplex-centroide (SCMD) de tres componentes para optimizar la concentración de óxidos metálicos (Ni y Pd) sobre la superficie de CeO<sub>2</sub> variando la concentración de TEO entre fracciones de masa de 0.0% y 2.0% para maximizar la conversión de asfaltenos a bajas temperaturas. Los resultados mostraron que al incorporar óxidos monoelementales y bielementales en nanopartículas de CeO<sub>2</sub>, tanto la adsorción como la conversión isotérmica de los asfaltenos aumentan. Cabe mencionar que las nanopartículas bielementales redujeron la temperatura de gasificación de los asfaltenos en mayor medida que las nanopartículas monoelementales. Además, las nanopartículas optimizadas con la mejor pareja (Ni-Pd) tienen el mejor rendimiento al obtener el 100% de conversión de asfaltenos en menos de 90 min a 220 °C mientras reducen un 80 % la energía de activación

En el **Capítulo 8**, una vez seleccionada la nanopartícula con la mejor pareja de TEOs, y optimizada la carga, se aborda la evaluación de su capacidad regenerativa durante la adsorción y posterior descomposición de asfaltenos *n*-C<sub>7</sub> en procesos de gasificación con vapor. La evaluación ha considerado la influencia del ciclo redox (Ce<sup>3+</sup>/Ce<sup>4+</sup>) en la auto regeneración de CeO<sub>2±δ</sub>, así como las

propiedades termodinámicas y potencial del proceso de adsorción, los parámetros cinéticos del proceso catalítico, y el cambio en la química superficial del material. Dentro de los principales resultados, se obtuvo que los asfaltenos mostraron una alta afinidad por ser adsorbidos sobre la superficie de las nanopartículas durante nueve ciclos de regeneración evaluados como se observa en la constante de Henry que aumentó ligeramente, con cambios de 21, 26 y 31% a 25, 55 y 75°C, respectivamente. El potencial de adsorción de Polanyi disminuye un 2.6% para la misma cantidad adsorbida desde el primer ciclo hasta el noveno. Además, la actividad catalítica de las nanopartículas no cambió significativamente, demostrando que descomponen el 100% de los asfaltenos  $n$ -C<sub>7</sub> en todos los ciclos. Sin embargo, la ligera disminución en la capacidad de adsorción y la actividad catalítica de las nanopartículas se debe principalmente a la presencia y el cambio en la concentración y proporción de ciertos elementos como oxígeno, hierro u otros en la superficie de la nanopartícula, como lo muestra la espectroscopia de fotoelectrones de rayos X.

En el **Capítulo 9** se considera cambiar la morfología de las nanopartículas de CeO<sub>2</sub>, entre (C)cúbica; (O) ortorrómbica; y (S) esférica, para la termo-oxidación de asfaltenos  $n$ -C<sub>7</sub> con el fin de potenciar algunas limitaciones del soporte sin morfología definida, evaluado en los Capítulos 7 y 8. En este estudio se consideraron los avances previos en términos de fase dopante, para lo cual se seleccionaron óxidos de Ni y Pd en fracciones de masa de 1%. La actividad catalítica de los sistemas se evaluó mediante análisis termogravimétricos no isotérmicos e isotérmicos a diferentes presiones. El capítulo recoge información sobre el impacto del ciclo redox, las vacantes de oxígeno, el tamaño del cristal y la química de la superficie en las propiedades catalíticas de la ceria para la aplicación mencionada. Además, se evaluó el efecto de SMSI en los sistemas dopados. Los resultados termogravimétricos no isotérmicos evidenciaron un aumento en la masa de asfaltenos  $n$ -C<sub>7</sub> a medida que la temperatura aumenta entre 100 y 230 °C para todos los sistemas y condiciones de operación. A 3.0 MPa, el asfalteno  $n$ -C<sub>7</sub> gana 3.6, 5.8 y 3.2 % para O-CeO<sub>2</sub>, C-CeO<sub>2</sub> y S-CeO<sub>2</sub>, respectivamente, mientras que a 6.0 MPa hay un aumento de 7.3, 10.4 y 5.9 % para los mismos sistemas, respectivamente. Las fases Ni y Pd aumentan la cantidad de oxígeno quimisorbido en todos los sistemas en el orden S-NiPdCe < O-NiPdCe < C-NiPdCe, y reducen la temperatura requerida para la descomposición total de asfaltenos  $n$ -C<sub>7</sub> a temperaturas inferiores a 200 °C a 6.0 MPa en el mismo orden. Además, el análisis termogravimétrico isotérmico



demuestra que la conversión de asfaltenos aumentó con nanocatalizadores a base de ceria en orden creciente S- CeO<sub>2</sub> < O- CeO<sub>2</sub> < C- CeO<sub>2</sub>. El CeO<sub>2</sub> cúbico dopado con Ni y Pd presenta el mayor rendimiento, alcanzando el 100 % de conversión a 170 °C y 6,0 MPa a los 60 min. Los datos confirman que la presencia de Ni y Pd facilita la transferencia de vacantes de oxígeno entre la masa y la superficie del nanocatalizador y, por lo tanto, se potencia la actividad catalítica. La actividad catalítica, a su vez, se ve mejorada por la presencia de faces {110}, {100} y {111}, vacantes de oxígeno y especies de Ce<sup>3+</sup> y NiO-Ce.

El **Capítulo 10** evalúa el nanomaterial con la morfología que presenta un mayor rendimiento durante la oxidación catalítica de asfaltenos para una subsecuente evaluación en reacciones de pirólisis, las cuales son fundamentales en los procesos de recobro térmico de petróleo. En este capítulo se amplía nuestro conocimiento sobre los procesos de pirólisis a baja y alta presión a través de enfoques experimentales y de simulación bajo la premisa que la presencia de vacantes de oxígeno que provocan la coexistencia y el intercambio oportuno de Ce<sup>4+</sup> y Ce<sup>3+</sup> en su estructura reticular es una de las principales razones de su actividad catalítica. Además, el control sobre algunos factores como las interacciones de soporte de metal fuerte (SMSI) con elementos nobles y de transición, así como los parámetros de morfología y tamaño, demostraron influir en el rendimiento catalítico.

En el **Capítulo 11** se considera el fraccionamiento de las moléculas de asfalteno en A1 y A2. Analizar el comportamiento adsorbente y catalítico de las nanopartículas con ambas fracciones es de vital ayuda para desarrollar catalizadores que puedan mejorar la vía de reacción de los agregados de asfaltenos. Este estudio intentó por primera vez investigar la adsorción y la reacción catalítica de los asfaltenos *n*-C<sub>7</sub> con énfasis en los subgrupos A1 y A2 utilizando nanopartículas cúbicas basadas en CeO<sub>2</sub> en condiciones de baja y alta presión. La principal diferencia entre estas estructuras es la cadena lateral (n-octilo) en A2 y dos ciclos de alquilo en A1. De esta forma, se relacionaron las propiedades químicas de las moléculas de asfaltenos con los subgrupos propuestos (A1 y A2), y se obtuvo una mejor comprensión del proceso de adsorción y oxidación de los asfaltenos. Las simulaciones MD revelan que el tamaño de los agregados aumenta en el orden A1 < A2, lo que se explica por la mayor densidad de la fracción A1. La afinidad de adsorción de las nanopartículas A1-CeO<sub>2</sub> fue mayor que la de las nanopartículas A2-CeO<sub>2</sub>, lo que resultó en una

mayor cantidad de asfaltenos A1 adsorbidos. Los experimentos oxidativos muestran que la quimisorción de oxígeno ocurre en los asfaltenos debido a la subfracción A1; ya que no se observó quimisorción de oxígeno en A2. Finalmente, la pirólisis no catalítica de A2 exhibió mejores características termogravimétricas, incluyendo mayor pérdida de masa a temperaturas más bajas y menos coque al finalizar el calentamiento como resultado de las diferentes densidades entre los agregados A1 y A2. Los estados de agregación alterados de las muestras en tolueno para experimentos de adsorción conducen al resultado opuesto cuando las nanopartículas catalizan la reacción de pirolisis.

El **Capítulo 12** resume los resultados de producción volumétrica de hidrógeno en la mezcla gaseosa liberada de la gasificación catalítica con vapor de asfaltenos *n*-C<sub>7</sub> y resinas II a bajas temperaturas (< 230 °C). Para ello se seleccionaron cuatro nanocatalizadores: CeO<sub>2</sub>, CeO<sub>2</sub> dopados con Ni-Pd, Fe-Pd y Co-Pd. Para cumplir con este objetivo se evalúa la adsorción de ambas fracciones y una mezcla de las mismas en los nanocatalizadores. Luego, se calculó la liberación de hidrógeno durante el proceso de gasificación isotérmica. Se analizaron algunas variables como la temperatura, la relación resinas:asfaltenos (R:A) y la naturaleza del nanocatalizador. La producción de hidrógeno concuerda con la actividad catalítica de cada material para descomponer ambas fracciones en las condiciones evaluadas. CeNi1Pd1 mostró el rendimiento más alto entre las otras tres muestras, lo que llevó a la mayor producción de hidrógeno en el gas efluente con valores de ~44 % en volumen. Cuando las muestras se calentaron a temperaturas más altas (es decir, 230 °C), la producción de H<sub>2</sub> aumentó hasta un 55% en volumen durante la conversión de resina y asfaltenos *n*-C<sub>7</sub> catalizados, lo que indica un aumento de hasta un 70% en comparación con los sistemas no catalizados en las mismas condiciones de temperatura. Se espera que este estudio amplíe el uso de combustibles fósiles para producir un gas rico en hidrógeno con bajo contenido de CO<sub>2</sub> (< 5%*vol*) a partir de la gasificación de las fracciones más complejas del crudo.

El **quinto Apartado** contiene los **Capítulos 13-16**, los cuales recogen las actividades necesarias para determinar el potencial de los nanomateriales para el mejoramiento de la calidad del crudo, así como la producción de H<sub>2</sub> y otros productos valiosos con bajas emisiones de CO<sub>2</sub>, bajo procesos de recobro térmico mejorado de petróleo.

En el **Capítulo 13** se diseña un nanofluido a partir de uno de los nanocatalizadores con mejor rendimiento en la descomposición de las fracciones pesadas del crudo y la producción de hidrogeno a partir de estas reacciones. Este estudio propone un método de inyección novedoso de nanofluido en el medio poroso, disperso en la corriente de vapor, con el fin de mejorar las condiciones de movilidad del crudo a presión y temperatura de yacimiento, y a su vez mejorar el facto de recobro de aceite. Para los diferentes pasos de la prueba dinámica se obtuvieron incrementos de 25 y 42% en la recuperación de aceite para la inyección dispersa del nanofluido en la corriente de vapor y luego de un tiempo de remojo de 12 h, en comparación con la curva base con solo inyección de vapor, respectivamente. El crudo mejorado alcanzó un nivel de gravedad API de 15.9°, es decir, un incremento de 9.0° unidades en comparación con el crudo extrapesado sin tratar, lo que representa un incremento del 130%. Asimismo, se observaron reducciones de hasta 71 y 85% en el contenido de asfaltenos y viscosidad del crudo. Con el desarrollo de este trabajo se propone un nuevo enfoque para la aplicación de nanofluidos dispersos en la corriente de vapor y, en general, para futuras aplicaciones en procesos de recuperación mejorada de aceite térmico.

Aunque hasta el momento se han desarrollado muchos nanomateriales para mejorar la recuperación de HO, aún queda trabajo por hacer para mejorar la calidad de los productos obtenidos durante el craqueo de fracciones de petróleo pesado. Nanopartículas bien diseñadas pueden lograr este objetivo, las cuales deben presentar una alta afinidad por las fracciones de petróleo pesado (asfaltenos), que posteriormente pueden descomponerse en hidrocarburos de menor peso molecular y gases de alto poder calorífico (como el hidrógeno y otros) por las interacciones entre el vapor y los sitios catalíticos activos de las nanopartículas. Sin embargo, las propiedades particulares del hidrógeno, como el pequeño tamaño de la molécula, le confieren una gran capacidad de transporte en un medio poroso, incluso con propiedades casi impermeables. Por lo tanto, es imperativo analizar las características termodinámicas del H<sub>2</sub> producido en el yacimiento durante la implementación de la inyección de vapor asistida por nanotecnología. En el **Capítulo 14** se presenta un análisis termodinámico de la fugacidad del hidrógeno para obtener un panorama más claro de su comportamiento in situ. La fugacidad de H<sub>2</sub> se determinó entre la presión del yacimiento y sobrecarga y diferentes temperaturas, las cuales fueron determinadas por los perfiles térmicos en la prueba de desplazamiento. La

fugacidad se calculó mediante la aplicación de ecuaciones de estado viriales con reglas de mezcla basadas en las posibles interacciones intermoleculares entre los componentes. El hidrógeno adquirió un mayor potencial químico a través de la presencia de nanopartículas. Sin embargo, la diferencia de fugacidad del H<sub>2</sub> entre ambos puntos es mucho mayor con las nanopartículas, lo que significa que el hidrógeno presenta una menor tendencia a migrar por difusión al punto de alta presión. Con base en este análisis, fue posible determinar la tendencia del hidrógeno a quedar atrapado en el reservorio y su disipación en el medio poroso.

En el **Capítulo 15** se investiga la factibilidad de utilizar formaciones geológicas sometidas a procesos de recobro térmico como reactores: donde ocurre tanto la adsorción y conversión de CO<sub>2</sub> como la producción de otros subproductos de alta calidad. Las nanopartículas de CeO<sub>2</sub> con diferente morfología son usadas para la adsorción de CO<sub>2</sub> y su posterior transformación en subproductos valiosos durante la descomposición catalítica de asfaltenos en una atmósfera de gasificación de vapor. La adsorción de CO<sub>2</sub> aumentó en el orden S-CeO<sub>2</sub> < O-CeO<sub>2</sub> < C-CeO<sub>2</sub> < C-CeNiPd, independientemente de la temperatura. Cuando se inyecta vapor, la adsorción de CO<sub>2</sub> se reduce en todos los sistemas. A 200 °C, la adsorción disminuyó un 3.0, 2.7, 2.5 y 2.0 % en los procesos asistidos por S-CeO<sub>2</sub>, O-CeO<sub>2</sub>, C-CeO<sub>2</sub> y C-CeNiPd, respectivamente. Las nanopartículas con asfaltenos adsorbidos también presentaron una alta tendencia a la adsorción de CO<sub>2</sub>. La nanopartícula con mejor morfología (C-CeO<sub>2</sub>) adsorbió alrededor del 24.3 % (3.92 mmol) de CO<sub>2</sub> a 200 °C, y el rendimiento aumentó tras dopar con Ni y Pd, obteniendo una adsorción de CO<sub>2</sub> del 34 %. Finalmente, para la conversión de CO<sub>2</sub> se obtiene una mezcla de gases compuesta por CO, CH<sub>4</sub>, H<sub>2</sub> e hidrocarburos ligeros (LHC). El contenido de producción de hidrógeno sigue una tendencia que concuerda bien con la capacidad de adsorción y la actividad catalítica de cada material. El %vol máximo de H<sub>2</sub> producido a 200 °C durante la gasificación de asfaltenos fue 31, 29, 24 y 23 % para C-CeNiPd, C-CeO<sub>2</sub>, O-CeO<sub>2</sub> y S-CeO<sub>2</sub>, respectivamente. Este estudio demuestra que el uso de tecnologías combinadas de inyección de CO<sub>2</sub> y vapor asistidas por nanocatalizadores puede resultar en un camino potencial para aumentar el volumen de petróleo crudo producido, su calidad basada en la mejora in situ y, al mismo tiempo, mejorar la captura de CO<sub>2</sub> y su conversión.

El **Capítulo 16** expone la metodología aplicada para llevar a cabo un escalamiento desde un nivel de preparación tecnológica (TRL) de 3 hasta un

TRL-8 para la implementación de nanotecnología en una aplicación de campo en pozos afectados por procesos de inyección de vapor, a través del diseño experimental y los resultados iniciales del ensayo de campo. Los nanofluidos se diseñaron para mejorar la productividad de un yacimiento de petróleo pesado con inyección en frío (sin vapor) y con inyección de vapor. Las pruebas estáticas mostraron la capacidad de los nanofluidos para reducir la viscosidad del petróleo crudo, la alta afinidad de las nanopartículas por la adsorción de moléculas de petróleo pesado y la alteración de la humectabilidad del sistema a un estado fuertemente mojado por agua. En consecuencia, se realizaron pruebas de desplazamiento para escenarios fríos y calientes, que mostraron una mejora en la movilidad y recuperación del petróleo en presencia de los nanofluidos en comparación con el sistema en ausencia de nanotecnología.

Finalmente, se realizó una aplicación de prueba de campo en cuatro pozos en un campo de interés colombiano. Dos pozos consistían en una inyección de nanofluidos fríos y dos incluían inyección de vapor junto con los nanofluidos. El objetivo principal de la prueba de campo fue lograr un aumento en la movilidad del petróleo y reducir la cantidad de gas de combustión requerida para desarrollar el campo. De acuerdo con los resultados de las pruebas de campo, los beneficios se asocian principalmente a la producción incremental luego de la ejecución de las 2 primeras pruebas con nanofluidos, una en frío y otra con vapor (pozos A y B) entre junio y julio de 2022. La producción incremental percibida durante 2022 corresponde a 8603 bbl relacionados con 3231 bbl (pozo A) y 5372 bbl (pozo B). De igual forma, con la ejecución de 2 pruebas adicionales, una con vapor y otra con frío (pozos C y D), entre noviembre y diciembre de 2022, se reportan beneficios asociados a la implementación tecnológica en 430 bbl (pozo C) para los procesos en frío, y 980 bbl (pozo D) en el caso de inyección de vapor en presencia de nanofluidos.

En el **sexto Apartado** se presentan los **Capítulos 17-20** donde se proponen dos tecnologías que incluyen: *i*) el uso de heteroátomos presentes en las fracciones más pesadas del crudo, tales como el azufre, para el mejoramiento de la calidad del crudo y la co-producción de hidrogeno a través de procesos de adsorción/catálisis con nanomateriales diseñados a la medida, y *ii*) la remoción de aceite proveniente de emulsiones de crudo en agua para la producción de gases con alto poder calorífico a través de procesos de adsorción y catálisis.

En los dos **Capítulos** siguientes (**17** y **18**), se propone los procesos de desulfuración como mecanismos para producir hidrogeno y mejorar la calidad del crudo. En la primera parte se desarrollan diferentes nanopartículas de óxido de elementos de transición de  $\text{Fe}_3\text{O}_4$ ,  $\text{NiO}$ ,  $\text{ZnO}$ ,  $\text{MoO}_3$ ,  $\text{CuO}$  y  $\text{AgO}$  y se probaron para la adsorción de azufre en modo discontinuo en diferentes proporciones de adsorbente: petróleo crudo, y luego se usaron para modificar la superficie del soporte de sílice. La eficiencia del proceso de adsorción de los nanomateriales se valida mediante la estimación de su capacidad de adsorción/eliminación y afinidad por las especies de azufre mediante experimentos de adsorción por lotes y continuos. El software de adsorción Aspen se utilizó para simular el proceso de adsorción de azufre del petróleo crudo. Para ello se resolvieron las ecuaciones de continuidad en conjunto con modelos de isotermas de adsorción (isoterma de Freundlich). Los parámetros necesarios para resolver el conjunto de ecuaciones se obtuvieron mediante experimentación. La segunda parte se centró en descubrir la influencia de la atmósfera de regeneración en la adsorción de azufre, la conversión de azufre y la producción de hidrógeno. Estos estudios permitieron potenciar las propiedades químicas de un nanomaterial para extender su vida media útil con alta selectividad, adsorción y capacidad catalítica. Esto genera información valiosa sobre los procesos de reutilización de adsorbentes mientras se eliminan los compuestos de azufre de los crudos pesados.

Por otro lado, la información presentada en los **Capítulos 19** y **20** corresponde a una nueva aplicación, centrado en el desarrollo de compuestos monolíticos de xerogeles de carbono-metal para la eliminación de aceite mediante procesos de adsorción y regeneración a partir de emulsiones de aceite en agua salada. Este trabajo presenta la síntesis de tres materiales de carbono con y sin contenido de metal (Ni y/o Ce) mediante un método sol-gel: XCe (xerogel de carbono con 18 % en peso de cerio), XCeNi (xerogel de carbono con 18 y 4% en peso de cerio y níquel, respectivamente) y X (xerogel de metal-carbono libre). El mejor material es regenerado constantemente en ciclos de adsorción y descomposición de crudo, ciclos en los cuales la química superficial y la generación de gases con alto poder calorífico fue evaluada. Los resultados de adsorción muestran que la eliminación de crudo aumentó con el aumento del contenido de metal en el material compuesto para todas las configuraciones experimentales. Además, se evaluó con éxito la descomposición del crudo, obteniendo el pico de descomposición principal a 150 °C durante los ensayos no isotérmicos. Para los experimentos isotérmicos, los tres xerogeles de carbono

monolítico lograron una conversión del 100 % del crudo adsorbido para todas las temperaturas, mientras que el crudo solo se descompuso en un 60 %. La actividad catalítica de tres xerogeles de carbono monolítico se corroboró con cálculos de energía de activación efectiva, que se redujo en un 24.9, 32.5 y 52.4 % desde la descomposición del crudo virgen hasta la descomposición adsorbida en las muestras X, XCe y XCeNi, respectivamente. Se consideró el análisis gaseoso de los productos involucrados en la oxidación del crudo en cada ciclo, encontrando un incremento en la producción de hidrocarburos livianos, y reduciendo las emisiones de gases como CO<sub>2</sub>, NO<sub>x</sub> y SO<sub>x</sub> en todos los reúsos.

**Palabras Clave:** Transición energética; Industria del petróleo y gas; Nanotecnología; Producción de hidrogeno.

Parte de los resultados del trabajo de investigación realizado durante el desarrollo de esta Tesis se recogen en los siguientes artículos de difusión internacional:

- ❖ **Medina, O. E.**, Olmos, C., Lopera, S. H., Cortés, F. B., & Franco, C. A. (2019). Nanotechnology applied to thermal enhanced oil recovery processes: A review. *Energies*, 12(24), 4671.
- ❖ **Medina, O. E.**, Gallego, J., Rodríguez, E., Franco, C. A., & Cortés, F. B. (2019). Effect of pressure on the oxidation kinetics of Asphaltenes. *Energy & Fuels*, 33(11), 10734-10744.
- ❖ **Medina, O. E.**, Gallego, J., Nassar, N. N., Acevedo, S. A., Cortés, F. B., & Franco, C. A. (2020). Thermo-oxidative decomposition behaviors of different sources of *n*-C<sub>7</sub> Asphaltenes under high-pressure conditions. *Energy & Fuels*, 34(7), 8740-8758.
- ❖ **Medina, O. E.**, Moncayo-Riascos, I., Pérez-Cadenas, A. F., Carrasco-Marín, F., Franco, C. A., & Cortes, F. B. (2023). Experimental and theoretical study of the influence of solvent on asphaltene-aggregates thermo-oxidation through high-pressure thermogravimetric analysis. *Fuel*, 333, 126491.
- ❖ Moncayo-Riascos, I., **Medina, O. E.**, Cortés, F. B., & Franco, C. A. (2023). Structural-Compositional Effect of Polycyclic Aromatic Hydrocarbons on

Thermal-Oxidative Decomposition at High-Pressure: A MolecularDynamics and Machine Learning Approach. *Energy & Fuels*, 37(4), 2702-2712.

- ❖ **Medina, O. E.**, Gallego, J., Cespedes, S., Nassar, N. N., Montoya, T., Cortés, F. B., & Franco, C. A. (2022). Effect of pressure on thermo-oxidative reactions of saturates, aromatics, and resins (S-Ar-R) from extra-heavy crude oil. *Fuel*, 311, 122596.
- ❖ **Medina, O. E.**, Gallego, J., Redondo, J. D., Cortés, F. B., & Franco, C. A. (2022). Effect of pressure on the thermo-oxidative behavior of saturates, aromatics, and resins (S-Ar-R) mixtures. *Fuel*, 314, 122787.
- ❖ **Medina, O. E.**, Gallego, J., Arias-Madrid, D., Cortés, F. B., & Franco, C. A. (2019). Optimization of the load of transition metal oxides (Fe<sub>2</sub>O<sub>3</sub>, Co<sub>3</sub>O<sub>4</sub>, NiO and/or PdO) onto CeO<sub>2</sub> nanoparticles in catalytic steam decomposition of *n*-C<sub>7</sub> asphaltenes at low temperatures. *Nanomaterials*, 9(3), 401.
- ❖ **Medina, O. E.**, Gallego, J., Restrepo, L. G., Cortés, F. B., & Franco, C. A. (2019). Influence of the Ce<sup>4+</sup>/Ce<sup>3+</sup> Redox-couple on the cyclic regeneration for adsorptive and catalytic performance of NiO-PdO/CeO<sub>2+δ</sub> nanoparticles for *n*-C<sub>7</sub> asphaltene steam gasification. *Nanomaterials*, 9(5), 734.
- ❖ **Medina, O. E.**, Gallego, J., Olmos, C. M., Chen, X., Cortés, F. B., & Franco, C. A. (2020). Effect of multifunctional nanocatalysts on *n*-C<sub>7</sub> asphaltene adsorption and subsequent oxidation under high-pressure conditions. *Energy & Fuels*, 34(5), 6261-6278.
- ❖ **Medina, O. E.**, Gallego, J., Perez-Cadenas, A. F., Carrasco-Marin, F., Cortés, F. B., & Franco, C. A. (2021). Insights into the morphology effect of ceria on the catalytic performance of NiO-PdO/CeO<sub>2</sub> nanoparticles for thermo-oxidation of *n*-C<sub>7</sub> asphaltenes under isothermal heating at different pressures. *Energy & Fuels*, 35(22), 18170-18184.
- ❖ **Medina, O. E.**, Gallego, J., Acevedo, S., Riazi, M., Ocampo-Pérez, R., Cortés, F. B., & Franco, C. A. (2021). Catalytic Conversion of *n*-C<sub>7</sub> Asphaltenes and Resins II into Hydrogen Using CeO<sub>2</sub>-Based Nanocatalysts. *Nanomaterials*, 11(5), 1301.



- ❖ Mateus, L., Moreno-Castilla, C., López-Ramón, M. V., Cortés, F. B., Álvarez, M. Á., **Medina, O. E.**, ... & Yebra-Rodríguez, Á. (2021). Physicochemical characteristics of calcined MnFe<sub>2</sub>O<sub>4</sub> solid nanospheres and their catalytic activity to oxidize para-nitrophenol with peroxymonosulfate and n-C<sub>7</sub> asphaltenes with air. *Journal of Environmental Management*, 281, 111871.
- ❖ Cerón, K. M., Arias-Madrid, D., Gallego, J., **Medina, O. E.**, Chinchilla, L. E., Cortés, F. B., & Franco, C. A. (2022). Catalytic Decomposition of n-C<sub>7</sub> asphaltenes using tungsten oxides–functionalized SiO<sub>2</sub> nanoparticles in steam/air atmospheres. *Processes*, 10(2), 349.
- ❖ Arias-Madrid, D., **Medina, O. E.**, Gallego, J., Acevedo, S., Correa-Espinal, A. A., Cortés, F. B., & Franco, C. A. (2020). NiO, Fe<sub>2</sub>O<sub>3</sub>, and MoO<sub>3</sub> supported over SiO<sub>2</sub> nanocatalysts for asphaltene adsorption and catalytic decomposition: optimization through a simplex–centroid mixture design of experiments. *Catalysts*, 10(5), 569.
- ❖ **Medina, O. E.**, Caro-Vélez, C., Gallego, J., Cortés, F. B., Lopera, S. H., & Franco, C. A. (2019). Upgrading of extra-heavy crude oils by dispersed injection of NiO–PdO/CeO<sub>2+δ</sub> nanocatalyst-based nanofluids in the steam. *Nanomaterials*, 9(12), 1755.
- ❖ **Medina, O. E.**, Hurtado, Y., Caro-Velez, C., Cortés, F. B., Riazi, M., Lopera, S. H., & Franco, C. A. (2019). Improvement of steam injection processes through nanotechnology: An approach through in situ upgrading and foam injection. *Energies*, 12(24), 4633.
- ❖ **Medina, O. E.**, Céspedes, S., Zabala, R. D., Franco, C. A., Pérez-Cadenas, A. F., Carrasco-Marín, F., ... & Franco, C. A. (2022). A Theoretical and Experimental Approach to the Analysis of Hydrogen Generation and Thermodynamic Behavior in an In Situ Heavy Oil Upgrading Process Using Oil-Based Nanofluids. *Catalysts*, 12(11), 1349.
- ❖ **Medina, O. E.**, Galeano-Caro, D., Brattekkås, B., Pérez-Cadenas, A. F., Carrasco-Marín, F., Cortés, F. B., & Franco, C. A. (2023). Simultaneous CO<sub>2</sub>

adsorption and conversion over Ni-Pd supported CeO<sub>2</sub> nanoparticles during catalytic *n*-C<sub>7</sub> asphaltene gasification. *Fuel*, 342, 127733.

- ❖ Giraldo, L. J., **Medina, O. E.**, Ortiz-Pérez, V., Franco, C. A., & Cortés, F. B. (2023). Enhanced Carbon Storage Process from Flue Gas Streams Using Rice Husk Silica Nanoparticles: An Approach in Shallow Coal Bed Methane Reservoirs. *Energy & Fuels*, 37(4), 2945-2959.
- ❖ **Medina, O. E.**, Galeano-Caro, D., Castelo-Quibén, J., Ocampo-Pérez, R., Perez-Cadenas, A. F., Carrasco-Marín, F., ... & Cortés, F. B. (2021). Monolithic carbon xerogels-metal composites for crude oil removal from oil in-saltwater emulsions and subsequent regeneration through oxidation process: Composites synthesis, adsorption studies, and oil decomposition experiments. *Microporous and Mesoporous Materials*, 319, 111039.
- ❖ **Medina, O. E.**, Galeano-Caro, D., Ocampo-Pérez, R., Pérez-Cadenas, A. F., Carrasco-Marín, F., Franco, C. A., & Cortés, F. B. (2021). Development of a monolithic carbon xerogel-metal composite for crude oil removal from oil in-saltwater emulsions: Evaluation of reuse cycles. *Microporous and Mesoporous Materials*, 327, 111424.
- ❖ **Medina, O. E.**, Moncayo-Riascos, I., Heidari, S., Nassar, N. N., Pérez-Cadenas, A. F., Franco, C. A., & Cortes, F. B. (2023). Chemical and Structural Changes of Asphaltenes During Oxygen Chemisorption at Low and High-Pressure. Submitted to Journal of Petroleum Science and Engineering.
- ❖ **Medina, O. E.**, Franco, C. A., & Cortes, F. B. (2023). Molecular Dynamic Simulation and Experimental Study on *n*-C<sub>7</sub> Asphaltene Pyrolysis under High-Pressure Conditions using Ceria-Based Nanocatalysts. Submitted to ACS Applied Nano Materials.
- ❖ **Medina, O. E.**, Moncayo-Riascos, Franco, C. A., & Cortes, F. B. (2023). Theoretical and Experimental Study of Adsorption and Catalytic Reactivity of Asphaltene Fractions A1 and A2 over Cubic NiO-PdO/CeO<sub>2</sub> Nanoparticles. Submitted to Journal of Petroleum Science and Engineering.

- ❖ **Medina, O. E.**, Franco, C. A., & Cortés, F. B. Upscaling Process for Nanofluids Deployment in Wells Affected by Steam Injection Processes: Experimental Design and Field Trial Application. In progress.
- ❖ **Medina, O. E.**, Pérez-Cadenas, A. F., Carrasco-Marín, F., Franco, C. A., & Cortés, F. B. Sulfur Removal from Heavy Crude Oils based on the Adsorption Process using Nanomaterials: Experimental and Theoretical Study. In progress.
- ❖ **Medina, O. E.**, Pérez-Cadenas, A. F., Carrasco-Marín, F., Franco, C. A., & Cortés, F. B. Sulfur removal using nanomaterials as a potential upgrading mechanism of heavy-crude oils: Cyclic reuse and thermal regeneration. In progress.

Además, algunos de los resultados recogidos en la presente Tesis han dado lugar a la solicitud de la siguiente patente:

- ❖ **Medina, O. E.**, Gallego, J., Franco, C. A., & Cortés, F. B. (2023). NC2020/0002593 NANOCATALIZADOR A PARTIR DE ÓXIDOS DE LANTÁNIDOS Y ÓXIDOS DE ELEMENTOS DE TRANSICIÓN PARA MEJORAMIENTO IN-SITU DE CRUDOS PESADOS Y EXTRAPESADOS.

La publicación de los capítulos de libro:

- ❖ **Medina, O. E.**, Gallego, J., Cortés, F. B., & Franco, C. A. (2022). Effect of Pressure on Thermo-oxidation and Thermocatalytic Oxidation of *n*-C<sub>7</sub> Asphaltenes. In *Nanoparticles: An Emerging Technology for Oil Production and Processing Applications* (pp. 165-200). Cham: Springer International Publishing.
- ❖ **Medina, O. E.**, Galeano-Caro, D., Villada-Villada, Y., Perez-Cadenas, A. F., Carrasco-Marín, F., Franco, C. A., & Cortés, F. B. (2023). Regeneration/reuse Capability of Monolithic Carbon Xerogels-Metal Nanocomposites for Crude Oil Removal from Oil in-Saltwater Emulsions. In *Nanotechnology for Oil-Water Separation*. Cham: Elsevier.

Los resultados más relevantes de esta Tesis se han presentado, además, en los siguientes congresos tanto nacionales como internacionales:

- ❖ National Student Paper Contest, Bucaramanga, Colombia, 2019.
- ❖ Regional Student Paper Contest, Santa Cruz de la Sierra, Bolivia, 2019.
- ❖ VII SUMMER SCHOOL 2019: New Technologies in Productivity and Improved Recovery of Petroleum and Gas. Medellín, Colombia, 2019.
- ❖ Nanotechnology Applied to the Recovery and Productivity of Hydrocarbon Facilities, Bogota, Colombia, 2019.
- ❖ 40<sup>th</sup> World Recovery Forum IEA EOR TCP 2019, Cartagena, Colombia, 2019.
- ❖ Nanoscience & Materials World, Barcelona, Spain, 2019.
- ❖ Virtual-Regional Student Paper Contest, 2020.
- ❖ MSc Ph.D. Latin America and the Caribbean Student paper contest, 2021.
- ❖ VIII SUMMER SCHOOL: THE ROLE OF CONVENTIONAL AND NON-CONVENTIONAL RESOURCES IN ENERGY TRANSITION. Medellín, Colombia, 2021.
- ❖ In-Situ Reactions, Technical Collaboration Program in Enhanced Oil Recovery of the International Energy Agency - IEA EOR TCP, 2021.
- ❖ SPE Colombia Heavy Oil Annual Meeting, 2021.
- ❖ SPE Annual Technical Conference and Exhibition (ATCE), International Student Paper Contest, Dubai, UAE, 2021.
- ❖ 1<sup>er</sup>. Foro de Adsorción en México, Asociación Mexicana de Adsorción. México, 2021.
- ❖ THERMAL METHODS FOR ENHANCED OIL RECOVERY WORKSHOP, Virtual, 2021.
- ❖ APLICACIÓN DE NANOTECNOLOGÍA EN PROCESOS DE RECOBRO TÉRMICO MEJORADO, Perú, 2021.
- ❖ LatinXChem, 2021.
- ❖ International Adsorption Society, 2<sup>nd</sup> Annual Twitter Poster Conference, 2021.
- ❖ Competencia Académica Científica Ingeniería Química y Petróleos - Innovación y Desarrollo, Colombia, 2022.
- ❖ Petrophase, Bucaramanga, Colombia, 2022.
- ❖ Congreso Colombiano del Petróleo, Gas y Energía, Colombia, 2022.
- ❖ SPE Regional Student Paper Contest, Ciudad de Panamá, Panamá, 2022.
- ❖ SPE Annual Technical Conference and Exhibition (ATCE), International Student Paper Contest, Texas, USA, 2022.
- ❖ RCS Posters, 2022.

Algunos de los premios recibidos con los resultados de la Tesis se presentan a continuación:

- ❖ First Place in Poster Presentation, VII SUMMER SCHOOL 2019: New Technologies in Productivity and Improved Recovery of Petroleum and Gas. Medellín, Colombia, 2019.
- ❖ First Place in Oral Presentation, Ph.D. Latin America and the Caribbean Student paper contest, 2021.
- ❖ Second place in Oral presentation, VIII SUMMER SCHOOL 2021. Medellín, Colombia, 2021.
- ❖ Honorable mention in the #LXChemEnv category. LatinXChem, 2021.
- ❖ First Place in Doctoral Category, Competencia Académica Científica Ingeniería Química y Petróleos - Innovación y Desarrollo, Medellín, Colombia, 2022.
- ❖ First Place in Oral Presentation, Ph.D. Latin America and the Caribbean Student paper contest, 2022.
- ❖ First place, Category: Non-Renewable Energy and Hydrocarbons Area – Non-Conventional Deposits, Congreso Colombiano del Petróleo, Gas y Energía, 2022.



## Apartado 1.







## Introduction





## Introduction

Energy plays a vital role in global economic growth. All our work, leisure, economic, social, and physical welfare depend on the sufficient, uninterrupted supply of energy.<sup>1</sup> The global population's growth, economic expansion, and increased energy-based living standards have drawn higher energy demand. In 2020, the total global energy consumption was in the range of 550-530 EJ (1 Exajoules= 1018J).<sup>2</sup> The total world energy requirement is increasing due to population growth, estimated to reach 8.5 billion by 2035. Consequently, the whole world's energy consumption is still expected to increase in absolute terms to 700-810 EJ by 2035, double of 1990's consumption.<sup>2,3</sup>

The global oil demand projected by the Organization of the Petroleum Exporting Countries (OPEC) will reach 111.1 million barrels per day by 2040, with a 23.1% increment compared to current data.<sup>4</sup> Meanwhile, the consumption of conventional oils has resulted in declining reserves of such resources.<sup>5</sup> As fossil fuel will remain the primary energy source for the coming decades, there is a pressing need to exploit alternative fossil resources. Substantial efforts, therefore, have been devoted to the effective utilization of the unconventional heavy and extra-heavy (i.e., natural bitumen or oil sands) oils, which account for 70% of total world oil reserves.<sup>6</sup> However, the combustion of fossil fuels for energy production, electricity generation, transportation, or other industrial process releases carbon dioxide and other greenhouse gases into the atmosphere, thereby negatively impacting the environment.

Energy environmentally friendly technologies are critical inputs to today's society and economy.<sup>7,8</sup> As mentioned, our society highly demands a sufficient and uninterrupted supply of energy. This high demand is impossible to satisfy through traditional fossil energy sources.<sup>9</sup> Thus, utilizing heavy and extra-heavy oils reasonably, efficiently, and cleaner becomes a subject worth studying in-depth.

Nowadays, the gap between supply and growing demand for energy needs an alternative renewable energy source. Hydrogen has been recognized globally as an energy carrier that complies with environmental quality, energy security, and economic competitiveness demands.<sup>10,11</sup> Hydrogen (H<sub>2</sub>) is the most abundant element in the universe and the third most abundant element on Earth.<sup>12</sup> The

energy content of H<sub>2</sub> (285.9 KJ·mol<sup>-1</sup>) is 2.7 times higher than the energy content of gasoline and, when used in fuel cells, the combination of H<sub>2</sub> and oxygen (O<sub>2</sub>) generates electricity, heat and water.<sup>13</sup>

In this context, renewable energy sources should incorporate traditional energy sources to be more sustainable.<sup>13</sup> Development of technologies/nanomaterials for the revaluation and use of HO and EHO, in parallel, will entail obtaining H<sub>2</sub> from HO and EHO as a transitory and complementary source of energy that will help the implementation of this fuel on a large scale until it is achieved the development of 100% “eco” technologies that allow a sufficient supply of green H<sub>2</sub>.

In response to the proposed technology, some conventional processes could be considered for H<sub>2</sub> production from fossil fuels. Most used methods include fossil-fuel steam gasification and partial oxidation.<sup>14-16</sup> Both ways require thermal energy to favor the advance of chemical reactions, providing hydrogen as a direct product. Until now, both processes have been widely used for natural gas, light hydrocarbons, and coal, obtaining efficiencies between 50-75% and a large amount of CO<sub>2</sub> is released to the atmosphere.<sup>14-16</sup>

Due to the complexity of heavy crude oils, high calorific value, and carbon content,<sup>17</sup> it is expected that the efficiencies will not exceed 75% and that large amounts of CO<sub>2</sub> will also be produced.<sup>18</sup> Thus, the conversion advance aimed at directly obtaining high hydrogen yield can be further improved by adding nanomaterials based on tailor catalytic properties.<sup>19-21</sup>

The use of nanomaterials has been extensively studied in the oil and gas industry. Generally, reported nanomaterials for catalytic treatments of heavy oil and bitumen could be roughly classified as (1) water-soluble catalysts, (2) oil-soluble catalysts, (3) amphiphilic catalysts, (4) minerals, zeolites, and solid superacids, and (5) metallic nanoparticles (NPs).

Nanomaterials could change the reaction rate of crude oil by stimulating different mechanisms for its thermal reaction.<sup>22</sup> This substance makes it feasible to obtain products with a lower energy barrier affecting either the yield and the selectivity and remain unaltered at the end of the reaction. In other words, accelerate or slow the reaction or appearance of a particular product species, using less energy without affecting the equilibrium. It is homogeneous if the catalyst is soluble in the reactant phase and heterogeneous if it is distinct from the reactant or medium.<sup>23</sup>

Activation energy is the minimum total kinetic energy that molecules must bring to their collisions for a chemical reaction to occur.<sup>24</sup> The reduction of

activation energy is accomplished by providing active sites for adsorption and reaction, where the products are created. In crude oil upgrading, nanomaterials have three main objectives: hydrogenation of aromatics and olefins (avoiding coke formation), removing metals (Vanadium and nickel) and removing heteroatoms (sulfur, nitrogen, and oxygen).<sup>6, 25, 26</sup>

There are many mechanisms proposed that explain the catalyst behavior with a reactant. The most accepted for a unimolecular reaction consists of *i*) the diffusion of the reactant from the whole fluid to the surface of the nanomaterial, *ii*) adsorption of reactant into the surface, *iii*) reaction on the surface, *iv*) desorption of the product, *v*) diffusion of the product from the surface of nanomaterial to the fluid.<sup>26, 27</sup>

The adsorption can be physical and chemical. During physical adsorption, the forces of attraction are weak and are Van der Waals forces. This interaction is exothermic in the range of 1-15 kcal·mol<sup>-1</sup>.<sup>28</sup> In chemical adsorption, the reactants are held to the nanomaterial surface by valence forces of the same type of the atom's bonds in molecules, causing a very reactive attachment.<sup>29</sup>

In this sense, several authors have investigated the adsorption capacity of nanomaterials for the heaviest crude oil macromolecules like asphaltenes, resins and heteroatoms like sulfur and nitrogen. Among the most widely studied materials, carbon-based materials, silica,<sup>30, 31</sup> alumina,<sup>32-34</sup> rare earths,<sup>35-37</sup> and metal oxides,<sup>32</sup> among others are found. They are usually found as supported or unsupported materials. The first one usually refers to a minute particle of an active material dispersed over a less active one called support. Once high adsorption is ensured, it is imperative to decompose the adsorbed compounds to promote crude oil upgrading. The active phase of the supported materials functions as a promoter to increase the selectivity and activity of the support, resulting in significant reductions in the decomposition temperatures of heavy crude oil fractions under different atmospheres (air, steam, inert).<sup>30, 38-40</sup>

To evaluate the catalytic capacity of nanomaterials, low-pressure thermogravimetric analysis and differential scanning calorimetry (DSC) are commonly used. Among the first applications of nanoparticles for the oxidation of asphaltenes, Nassar et al.<sup>41</sup> investigated the adsorption and subsequent oxidation of Athabasca asphaltenes in different metal nanoparticles (NiO, Co<sub>3</sub>O<sub>4</sub>, and Fe<sub>3</sub>O<sub>4</sub>).<sup>41</sup> The authors found reductions of more than 100 °C in the asphaltene decomposition temperature in all cases, obtaining a better result for NiO nanoparticles. Furthermore, the surface acidity of the nanoparticles was evaluated in another study.<sup>42</sup> Basic, acid, and neutral alumina were assessed for

the oxidation of Athabasca asphaltenes. The results show affinity increases as the acidic surface increases. On the contrary, catalytic activity is higher for basic alumina.

Besides, Fe<sub>3</sub>O<sub>4</sub> nanoparticles were used for catalytic oxidation of different visbroken asphaltenes from a cracked vacuum residue. Results show a significant reduction in the oxidation temperature and average activation energy.<sup>43</sup> Also, TiO<sub>2</sub>, ZrO<sub>2</sub>, and CeO<sub>2</sub> nanoparticles' catalytic activity have been investigated.<sup>44</sup> CeO<sub>2</sub> nanoparticles showed the highest performance for asphaltene catalytic oxidation, confirmed by the lowest effective activation energy trends and lowest values of Gibbs free energy and enthalpy changes.

On the other hand, fumed silica nanoparticles were doped with transition element oxides of Ni and Pd at different dosages for the oxidation of Colombian asphaltenes.<sup>30</sup> This study presents essential conclusions on the application of doped materials. First, a higher dosage of each metal in the mono-elemental nanoparticles increases the catalytic capacity of the material. Also, bi-elemental nanoparticles show better performance than mono-elemental nanoparticles. The application of transition elements can significantly improve the performance of the supports. Further, the design of experiments can lead to the development of an optimal material (0.29 wt.% Ni and 1.32 wt.% Pd) to reduce the activation energy for the catalytic oxidation of asphaltenes.

The influence of resins on the adsorption of asphaltenes on nanoparticles has also been studied. The results present different adsorption isotherm types according to the resin/asphaltene ratio. However, it was concluded that resins I do not significantly influence asphaltenes' adsorption on nanoparticles and help to solubilize them in the medium.<sup>45</sup> Other works have focused on the effect of resins I on the catalytic decomposition of asphaltenes adsorbed on nanoparticles. Combined thermogravimetric analysis and softening point measurements were used to evaluate the adsorption of asphaltenes and resins I in heavy oil model solutions. The results of the catalytic behavior show that the presence of resins I do not significantly change the decomposition temperature of the asphaltenes adsorbed on the nanoparticles.<sup>46</sup>

Evaluating this technology under different pressure and temperature conditions will guarantee the upscaling and application in field conditions. Yuan et al.<sup>47</sup> employed nickel nanoparticles to promote aquathermolysis reactions under a gasifying atmosphere at high pressure (~3.0 MPa).<sup>47</sup> The authors evaluated the effect of Ni nanoparticles' presence, concentration, and penetration depth at low temperatures between 150-220 °C in crude oil upgrading using a

silica-containing reactor for oil displacement and determining the recovery factor.<sup>47</sup> They found that the highest recovery factor was generated with a mass fraction of 0.02 % of nickel nanoparticles at 220 °C, associated with the breakdown of C-S bonds.<sup>47</sup> However, the effect of nanoparticles tends to decrease significantly with the passage of cycles.

Additionally, the authors reveal that the increase in recovery factor (RF) is mainly due to the nanoparticles distributed near the injection port, showing that distribution along the reservoir with greater depth penetration could increase the oil recovery and oil quality. In another study, Afzal et al.<sup>48</sup> evaluated the effect of different concentrations of Fe<sub>2</sub>O<sub>3</sub> nanoparticles to varying temperatures during steam injection. They demonstrated that Fe<sub>2</sub>O<sub>3</sub>-based materials could activate some gasification reactions, which mainly attack C-S, C=C and C≡C bonds, causing a significant decrease in the recovered oil viscosity, increasing crude oil quality.<sup>48</sup> The optimum concentration of Fe<sub>2</sub>O<sub>3</sub> nanoparticles was found between a mass fraction of 0.2 and 0.5%, and high temperatures favor their performance. Regarding the composite materials, only Cardona et al.<sup>49</sup> evaluated the efficiency of SiO<sub>2</sub>-based nanoparticles, with active phases of NiO and PdO in mass fractions of 1% dispersed on the support surface. The authors demonstrated that adding these nanoparticles together with a hydrogen donor increases the recovery factor by 56% for the steam injection with nanoparticles compared with the scenario without the catalytic agents. Also, an improvement in oil quality in terms of API from 7.2 to 12.1° was found.

Nevertheless, most of them have been studied for crude oil upgrading without considering the gaseous mixture released during heating. In the same context, the few studies evaluating the gases produced during the catalytic crude oil upgrading report contents of CO<sub>2</sub> higher than 15%*vol* and no significant contribution of H<sub>2</sub>. These results are a consequence of the fact that the materials are synthesized thinking of a single application and not resolving multiple issues that include the enhanced hydrogen production.

These facts suggest that the H<sub>2</sub> production from heavy and extra heavy crude oil remains challenging, and further efforts are required. Hence, integrating thermochemical and nanotechnological processes to advance the development of H<sub>2</sub> production technologies from crude oil provides an encouraging outlook on energy sectors and global impact. Also, the understanding and determination of the operational conditions in which the multifunctionality of the nanomaterial is optimized propose an alternative

method to avoid the increased risk of supply disruptions, price volatility, air pollution, and global impact.

The overall goal of this research is to develop multifunctional nanomaterials based on tailor-made catalytic properties for the co-production of upgraded crude oil and hydrogen at different pressures and temperatures. The tasks and specific objectives assumed for this thesis are listed below:

- ❖ To evaluate the reactivity of crude oil fractions at different pressures and temperatures without nanomaterials.
- ❖ To synthesize and characterize multifunctional nanomaterials for crude oil upgrading and H<sub>2</sub> production.
- ❖ To evaluate the adsorption capacity and catalytic activity of the nanomaterials for crude oil fractions adsorption/decomposition and hydrogen production.
- ❖ To determine the potential of nanomaterials for crude oil upgrading at different conditions of pressure and temperature.
- ❖ To evaluate H<sub>2</sub> production and other valued products from crude oil upgrading at different pressures and temperatures using nanomaterials.

## References

1. Stout, B.; Best, G., Effective energy use and climate change: needs of rural areas in developing countries. **2001**.
2. Outlook, A. E., Energy information administration. *Department of Energy* **2010**, 92010, (9), 1-15.
3. Chow, J.; Kopp, R. J.; Portney, P. R., Energy resources and global development. *Science* **2003**, 302, (5650), 1528-1531.
4. OUTLOOKS, O., FIFTH IEA IEF OPEC SYMPOSIUM ON ENERGY OUTLOOKS.
5. Klass, D. L., A critical assessment of renewable energy usage in the USA. *Energy Policy* **2003**, 31, (4), 353-367.
6. Medina, O. E.; Olmos, C.; Lopera, S. H.; Cortés, F. B.; Franco, C. A., Nanotechnology applied to thermal enhanced oil recovery processes: a review. *Energies* **2019**, 12, (24), 4671.

7. Dave, C. D.; Pant, K., Renewable hydrogen generation by steam reforming of glycerol over zirconia promoted ceria supported catalyst. *Renewable energy* **2011**, *36*, (11), 3195-3202.
8. Lund, H., Renewable energy strategies for sustainable development. *Energy* **2007**, *32*, (6), 912-919.
9. Gielen, D.; Boshell, F.; Saygin, D.; Bazilian, M. D.; Wagner, N.; Gorini, R., The role of renewable energy in the global energy transformation. *Energy Strategy Reviews* **2019**, *24*, 38-50.
10. Christopher, K.; Dimitrios, R., A review on exergy comparison of hydrogen production methods from renewable energy sources. *Energy & Environmental Science* **2012**, *5*, (5), 6640-6651.
11. Turner, J.; Sverdrup, G.; Mann, M. K.; Maness, P. C.; Kroposki, B.; Ghirardi, M.; Evans, R. J.; Blake, D., Renewable hydrogen production. *International journal of energy research* **2008**, *32*, (5), 379-407.
12. Coughlin, R. W.; Farooque, M., Hydrogen production from coal, water and electrons. *Nature* **1979**, *279*, (5711), 301-303.
13. Muradov, N., How to produce hydrogen from fossil fuels without CO<sub>2</sub> emission. *International Journal of Hydrogen Energy* **1993**, *18*, (3), 211-215.
14. Seyitoglu, S.; Dincer, I.; Kilicarslan, A., Energy and exergy analyses of hydrogen production by coal gasification. *International Journal of Hydrogen Energy* **2017**, *42*, (4), 2592-2600.
15. Lutz, A. E.; Bradshaw, R. W.; Bromberg, L.; Rabinovich, A., Thermodynamic analysis of hydrogen production by partial oxidation reforming. *International Journal of Hydrogen Energy* **2004**, *29*, (8), 809-816.
16. Freni, S.; Calogero, G.; Cavallaro, S., Hydrogen production from methane through catalytic partial oxidation reactions. *Journal of Power Sources* **2000**, *87*, (1-2), 28-38.
17. Wei, B.; Zou, P.; Shang, J.; Gao, K.; Li, Y.; Sun, L.; Pu, W., Integrative determination of the interactions between SARA fractions of an extra-heavy crude oil during combustion. *Fuel* **2018**, *234*, 850-857.
18. Rahimi, P. M.; Gentzis, T., The chemistry of bitumen and heavy oil processing. In *Practical advances in petroleum processing*, Springer: 2006; pp 597-634.
19. Zhang, X.; Liu, Q.; Fan, Z., Enhanced in situ combustion of heavy crude oil by nickel oxide nanoparticles. *International Journal of Energy Research* **2019**, *43*, (8), 3399-3412.

20. Franco, C.; Cardona, L.; Lopera, S.; Mejía, J.; Cortés, F. In *Heavy oil upgrading and enhanced recovery in a continuous steam injection process assisted by nanoparticulated catalysts*, SPE improved oil recovery conference, 2016; Society of Petroleum Engineers: 2016.
21. Masudi, A.; Muraza, O., Zirconia-based nanocatalysts in heavy oil upgrading: a mini review. *Energy & Fuels* **2018**, *32*, (3), 2840-2854.
22. Elahi, S. M.; Scott, C. E.; Chen, Z.; Pereira-Almao, P., In-situ upgrading and enhanced recovery of heavy oil from carbonate reservoirs using nano-catalysts: Upgrading reactions analysis. *Fuel* **2019**, *252*, 262-271.
23. Boreskov, G. K., *Heterogeneous catalysis*. Nova Publishers: 2003.
24. Kaufman, M., *Principles of thermodynamics*. CRC Press: 2002.
25. Xie, K.; Karan, K., Kinetics and thermodynamics of asphaltene adsorption on metal surfaces: A preliminary study. *Energy & fuels* **2005**, *19*, (4), 1252-1260.
26. De Lasa, H.; Salaices, E.; Mazumder, J.; Lucky, R., Catalytic steam gasification of biomass: catalysts, thermodynamics and kinetics. *Chemical reviews* **2011**, *111*, (9), 5404-5433.
27. Alvarado, V.; Manrique, E., Enhanced oil recovery: an update review. *Energies* **2010**, *3*, (9), 1529-1575.
28. Vidali, G.; Ihm, G.; Kim, H.-Y.; Cole, M. W., Potentials of physical adsorption. *Surface Science Reports* **1991**, *12*, (4), 135-181.
29. Webb, P. A., Introduction to chemical adsorption analytical techniques and their applications to catalysis. *Micromeritics Instrument Corp. Technical Publications* **2003**.
30. Franco, C. A.; Montoya, T.; Nassar, N. N.; Pereira-Almao, P.; Cortés, F. B., Adsorption and subsequent oxidation of colombian asphaltenes onto nickel and/or palladium oxide supported on fumed silica nanoparticles. *Energy & Fuels* **2013**, *27*, (12), 7336-7347.
31. Montoya, T.; Argel, B. L.; Nassar, N. N.; Franco, C. A.; Cortés, F. B., Kinetics and mechanisms of the catalytic thermal cracking of asphaltenes adsorbed on supported nanoparticles. *Petroleum Science* **2016**, *13*, (3), 561-571.
32. Nassar, N. N.; Franco, C. A.; Montoya, T.; Cortés, F. B.; Hassan, A., Effect of oxide support on Ni-Pd bimetallic nanocatalysts for steam gasification of n-C7 asphaltenes. *Fuel* **2015**, *156*, 110-120.
33. Franco, C.; Patiño, E.; Benjumea, P.; Ruiz, M. A.; Cortés, F. B., Kinetic and thermodynamic equilibrium of asphaltenes sorption onto nanoparticles of nickel oxide supported on nanoparticulated alumina. *Fuel* **2013**, *105*, 408-414.



34. Cardona Rojas, L. Efecto de nanopartículas en procesos con inyección de vapor a diferentes calidades. Magister Thesis, Universidad Nacional de Colombia-Sede Medellín, Online, 2018.
35. Medina, O. E.; Gallego, J.; Arias-Madrid, D.; Cortés, F. B.; Franco, C. A., Optimization of the load of transition metal oxides (Fe<sub>2</sub>O<sub>3</sub>, Co<sub>3</sub>O<sub>4</sub>, NiO and/or PdO) onto CeO<sub>2</sub> nanoparticles in catalytic steam decomposition of n-C<sub>7</sub> asphaltenes at low temperatures. *Nanomaterials* **2019**, 9, (3), 401.
36. Medina, O. E.; Gallego, J.; Restrepo, L. G.; Cortés, F. B.; Franco, C. A., Influence of the Ce<sup>4+</sup>/Ce<sup>3+</sup> Redox-couple on the cyclic regeneration for adsorptive and catalytic performance of NiO-PdO/CeO<sub>2</sub>± $\delta$  nanoparticles for n-C<sub>7</sub> asphaltene steam gasification. *Nanomaterials* **2019**, 9, (5), 734.
37. Medina, O. E.; Hurtado, Y.; Caro-Velez, C.; Cortés, F. B.; Riazi, M.; Lopera, S. H.; Franco, C. A., Improvement of steam injection processes through nanotechnology: An approach through in situ upgrading and foam injection. *Energies* **2019**, 12, (24), 4633.
38. Villegas, J. P.; Arcila, N.; Ortega, D.; Franco, C. A.; Cortés, F. B., Crude oil removal from production water using nano-intermediates of a SiO<sub>2</sub> support functionalized with magnetic nanoparticles. *Dyna* **2017**, 84, (202), 65-74.
39. Cardona, L.; Arias-Madrid, D.; Cortés, F. B.; Lopera, S. H.; Franco, C. A., Heavy oil upgrading and enhanced recovery in a steam injection process assisted by NiO- and PdO-Functionalized SiO<sub>2</sub> nanoparticulated catalysts. *Catalysts* **2018**, 8, (4), 132.
40. Franco, C. A.; Nassar, N. N.; Cortés, F. B., Removal of oil from oil-in-saltwater emulsions by adsorption onto nano-alumina functionalized with petroleum vacuum residue. *Journal of colloid and interface science* **2014**, 433, 58-67.
41. Nassar, N. N.; Hassan, A.; Pereira-Almao, P., Comparative oxidation of adsorbed asphaltenes onto transition metal oxide nanoparticles. *Colloids and surfaces A: Physicochemical and Engineering aspects* **2011**, 384, (1-3), 145-149.
42. Nassar, N. N.; Hassan, A.; Pereira-Almao, P., Effect of surface acidity and basicity of aluminas on asphaltene adsorption and oxidation. *Journal of colloid and interface science* **2011**, 360, (1), 233-238.
43. Nassar, N. N.; Hassan, A.; Carbognani, L.; Lopez-Linares, F.; Pereira-Almao, P., Iron oxide nanoparticles for rapid adsorption and enhanced catalytic oxidation of thermally cracked asphaltenes. *Fuel* **2012**, 95, 257-262.
44. Nassar, N. N.; Hassan, A.; Vitale, G., Comparing kinetics and mechanism of adsorption and thermo-oxidative decomposition of Athabasca asphaltenes

onto TiO<sub>2</sub>, ZrO<sub>2</sub>, and CeO<sub>2</sub> nanoparticles. *Applied Catalysis A: General* **2014**, 484, 161-171.

45. Franco, C. A.; Lozano, M. M.; Acevedo, S.; Nassar, N. N.; Cortés, F. B., Effects of resin I on Asphaltene adsorption onto nanoparticles: a novel method for obtaining asphaltenes/resin isotherms. *Energy & Fuels* **2015**, 30, (1), 264-272.

46. Lozano, M. M.; Franco, C. A.; Acevedo, S. A.; Nassar, N. N.; Cortés, F. B., Effects of resin I on the catalytic oxidation of n-C 7 asphaltenes in the presence of silica-based nanoparticles. *RSC advances* **2016**, 6, (78), 74630-74642.

47. Yi, S.; Babadagli, T.; Li, H. A., Use of nickel nanoparticles for promoting aquathermolysis reaction during cyclic steam stimulation. *SPE Journal* **2018**, 23, (01), 145-156.

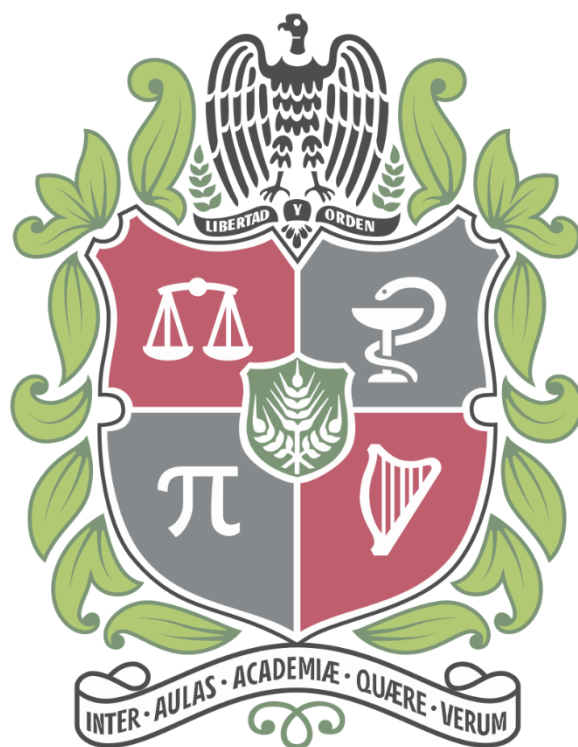
48. Afzal, S.; Nikookar, M.; Ehsani, M. R.; Roayaei, E., An experimental investigation of the catalytic effect of Fe<sub>2</sub>O<sub>3</sub> nanoparticle on steam injection process of an Iranian reservoir. *Iranian Journal of Oil & Gas Science and Technology* **2014**, 3, (2), 27-36.

49. Cardona, L.; Arias-Madrid, D.; Cortés, F.; Lopera, S.; Franco, C., Heavy oil upgrading and enhanced recovery in a steam injection process assisted by NiO- and PdO-Functionalized SiO<sub>2</sub> nanoparticulated catalysts. *Catalysts* **2018**, 8, (4), 132.





## Objetivos



## **Objetivo general**

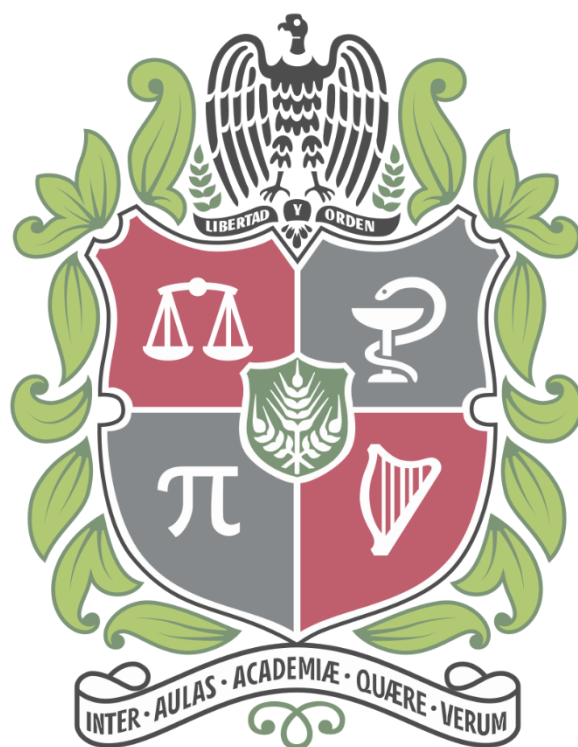
Desarrollar nanomateriales multifuncionales para la coproducción de crudo mejorado e hidrógeno a diferentes condiciones de presión y temperatura.

## **Objetivos específicos**

- I. Evaluar la reactividad de fracciones de crudo a diferentes presiones y temperaturas sin nanomateriales.
- II. Sintetizar y caracterizar nanomateriales multifuncionales para la mejora del crudo y la producción de H<sub>2</sub>.
- III. Evaluar la capacidad de adsorción y actividad catalítica de los nanomateriales sintetizados para la adsorción/descomposición de fracciones de petróleo crudo y la producción de hidrógeno.
- IV. Determinar el potencial de los nanomateriales para la mejora del petróleo crudo en diferentes condiciones de presión y temperatura.
- V. Evaluar la producción de H<sub>2</sub> y otros productos valiosos de la mejora del petróleo crudo a diferentes presiones y temperaturas utilizando nanomateriales.



## Apartado 2.







## Materials and Methods





## Materials and methods

### 1. Synthesis of nanoparticles

#### 1.1. Synthesis of ceria nanoparticles with different morphologies

Three different routes were selected for the synthesis of nanoparticles and thus obtained three shapes, which were used to clear the controlling factors of adsorption capacity and catalytic activity of CeO<sub>2</sub> for *n*-C<sub>7</sub> asphaltene uptake and oxidative decomposition, respectively. First, spherical CeO<sub>2</sub> (S-CeO<sub>2</sub>) was obtained by the hydrothermal method. Then, some variations of the operating conditions reported in the literature were executed to obtain nanometric particles.<sup>1</sup> Initially, 4 mmol of Ce(NO<sub>3</sub>)<sub>3</sub>·6H<sub>2</sub>O and PVP were diluted in 40 mL of deionized water. The solution was stirred for 4 h and transferred to a 50 mL Teflon-lined stainless-steel autoclave heated at 200 °C for 4 h. Next, orthorhombic CeO<sub>2</sub> (O-CeO<sub>2</sub>) was synthesized by a modified version of the previous method. For this, 8 mmol of the precursor cerium salt with 10 mmol of PVP were dissolved in an ethanol and deionized water solution (1:3 volume ratio) and stirred for 30 min. The autoclave was heated at 200 °C for 24 h. Finally, cubic CeO<sub>2</sub> (C-CeO<sub>2</sub>) was obtained by dissolving 1 mmol of Ce(NO<sub>3</sub>)<sub>3</sub>·6H<sub>2</sub>O in 35 mL of water. Once the solution was homogeneous, 0.35 mL of water containing 0.1 mol·L<sup>-1</sup> of KOH was added dropwise. The system was introduced in the autoclave and heated at 230 °C for 36 h. All the samples were slowly cooled at room temperature and washed several times with ethanol and water.

#### 1.2. Synthesis of monolithic carbon xerogels

Resorcinol (R), formaldehyde (F), and cesium carbonate (CsCO<sub>3</sub>) were provided from Sigma-Aldrich (St. Louis, MO, USA) and were used for carbon xerogels synthesis. Active phases of cerium and nickel were formed using Ce(NO<sub>3</sub>)<sub>3</sub>·6H<sub>2</sub>O and Ni(C<sub>2</sub>H<sub>3</sub>O<sub>2</sub>)<sub>2</sub>·4H<sub>2</sub>O, respectively.

The synthesis of the monolithic carbon xerogels was done by sol-gel polymerization of R with F in water (W), following a modification of Pekala's method<sup>2</sup> using CsCO<sub>3</sub> as polymerization catalyst (C). The molar ratios were F/R=2, W/R=20, and R/C=500. The mixture was stirred and cast into glass molds to prevent the evaporation of the solvent. The mixture was cured as follows: 24

hours at 20 °C, then 24 h at 50 °C, and ends heating at 80 °C for 120 h. Once obtained the organic gel, monoliths were cut into 5-cm length 2-mm diameter pellets, removed from the glass molds, and immersed into acetone for five days for a solvent exchange, refreshing the acetone daily. Afterward, the organic gel was dried by microwave heating using a Saivod MS-287W microwave oven (Spain), through argon injection for periods of 1 minute at 20 Watts until a constant weight was achieved. Finally, the organic gel was carbonized under pure nitrogen flow at 900 °C with a heating rate of 2 °C min<sup>-1</sup> for a soft removal of the pyrolysis gases and a dwell time of 2 h at the target temperature. The sample obtained was labeled as X.

The monolithic carbon xerogels-metal composites were obtained by following the same procedure with the exception of the precursors mixing step, where the corresponding amount of Ce(NO<sub>3</sub>)<sub>3</sub>·6H<sub>2</sub>O and Ni(C<sub>2</sub>H<sub>3</sub>O<sub>2</sub>)<sub>2</sub>·4H<sub>2</sub>O were added into the R/F/W mixture. The amount of the metal precursor, to obtain a Ce and Ni content of 20 and 5 wt.%, respectively, was calculated assuming a mass loss of 50.0% during the carbonization, which was corroborated posteriorly by Inductively Coupled Plasma Mass-Spectrometry (ICP-MS). Monolithic carbon xerogels are designated XCe (carbon xerogel with 18 wt.% of cerium), XCeNi (carbon xerogel with 18 wt.% of cerium and 4 wt.% of nickel). These values are computed theoretically and experimentally.

### 1.3. Commercial nanoparticles

Some commercial nanoparticles were evaluated in this thesis including Ceria (CeO<sub>2</sub>) nanoparticles, purchased from Nanostructured & Amorphous Materials (Houston, TX, USA) and silica gel provided by (Evonik, Essen, Germany), using NiCl<sub>2</sub>·6H<sub>2</sub>O, and Pd(NO<sub>3</sub>)<sub>2</sub>·2H<sub>2</sub>O as salt precursors.

### 1.4. Doping of morphological ceria nanoparticles

Cubic (C-CeO<sub>2</sub>), orthorhombic (O-CeO<sub>2</sub>), and spherical (S-CeO<sub>2</sub>) ceria nanoparticles were synthesized using the hydrothermal method and doped with 1.0% in mass fraction of Ni and Pd oxides by the incipient wetness impregnation. The obtained nanoparticles were dried at 120 °C for 6 h and calcined at 450 °C for 6 h.<sup>3</sup>

### 1.5. Doping of commercial ceria nanoparticles

For obtaining the optimum concentration of the best doping couple on the cerium oxide nanoparticles, the following systems were considered: (i) initially, three pairs of nanoparticles were evaluated with different TEO at a fixed concentration of a mass fraction of 1% over the ceria surface (CeNi1Pd1,

CeCo1Pd1, and CeFe1Pd1) to choose the best TEO couple, and posteriorly (ii) a three-component simplex centroid mixture design (SCMD) of experiments was carried out for different TEO dosages up to mass fractions of 2%. The support of CeO<sub>2</sub> nanoparticles was previously dried at 120 °C for 2 h to remove any humidity. For TEOs doping, aqueous solutions of iron chloride, nickel chloride, cobalt chloride, and/or palladium nitrate are employed using the incipient wetness technique as reported in previous studies.<sup>4-6</sup> Then, the obtained composite nanoparticles were dried at 120 °C for 6 h, and finally, the solid obtained was calcined at 450 °C for 6 h.<sup>3</sup> The nomenclature, as well as the mass fraction and mole fraction of the synthesized samples according to the design of experiments, are shown in Table 1.

**Table 1.** Nomenclature, mass fraction, and molar fraction of the prepared nanoparticles composed of ceria support (CeO<sub>2</sub>) functionalized with transition metal oxides (Fe<sub>2</sub>O<sub>3</sub>, Co<sub>3</sub>O<sub>4</sub>, NiO and/or PdO).

Sample	Nominal Oxides	Nominal Mass Fraction (%)	Nominal Molar Fraction (%)
CeO <sub>2</sub>	CeO <sub>2</sub>	100.0	100.0
CeNi1Pd1	CeO <sub>2</sub>	98.0	98.8
	NiO	1.0	0.4
	PdO	1.0	0.7
CeFe1Pd1	CeO <sub>2</sub>	98.0	98.4
	Fe <sub>2</sub> O <sub>3</sub>	1.0	0.9
	PdO	1.0	0.7
CeCo1Pd1	CeO <sub>2</sub>	98.0	97.9
	Co <sub>3</sub> O <sub>4</sub>	1.0	1.4
	PdO	1.0	0.7
CeNi2	CeO <sub>2</sub>	98.0	99.1
	NiO	2.0	0.9
CePd2	CeO <sub>2</sub>	98.0	98.6
	PdO	2.0	1.4
CeNi1	CeO <sub>2</sub>	99.0	99.6
	NiO	1.0	0.4
CePd1	CeO <sub>2</sub>	99.0	99.3
	PdO	1.0	0.7
CeNi0.66Pd0.66	CeO <sub>2</sub>	98.7	99.2
	NiO	0.7	0.3
	PdO	0.7	0.5

#### 1.6. Doping of commercial silica nanoparticles

The silica gel used as support was provided by (Evonik, Essen, Germany) and doped with Ag(NO<sub>3</sub>) and CuCl<sub>2</sub>·2H<sub>2</sub>O (Merck KGaA, Darmstadt, Germany).

The doped nanomaterials were robustly characterized. Seven nanomaterials, including SiCu<sub>2</sub>, SiAg<sub>2</sub>, SiCu<sub>4</sub>, SiAg<sub>4</sub>, SiAg<sub>2</sub>Cu<sub>2</sub>, SiAg<sub>1.32</sub>Cu<sub>1.32</sub>, SiAg<sub>1.5</sub>Cu<sub>1.4</sub>, were prepared through incipient wetness impregnation. The samples were labeled using the first two letters of the support (Si), the periodic symbol of the active phase (Ag or Cu), and the mmol of the TEO (2, 4, 1.32, 1.5, and 1.4).

## 2. Characterization of nanoparticles

The nanomaterials were characterized by different experimental techniques in order to study their morphology, porous structure, surface area, and surface chemical characteristics, as well as the nature and dispersion of the active phases.

### 2.1. Characterization of ceria nanoparticles

N<sub>2</sub> adsorption-desorption at -196 °C was done using a Micromeritics ASAP2020 (Micromeritics, Norcross, GA, USA) to determine the specific surface area ( $S_{\text{BET}}$ ). BET equation was used for the calculation.<sup>7</sup> The morphology of the nanoparticles was analyzed by high-resolution transmission electron microscopy (HR-TEM) in an FEI Titan G2 microscope (HR-TEM) (Eindhoven, The Netherlands) and by scanning electron microscopy in an FEI microscope model Quanta 400 (SEM) (Eindhoven, The Netherlands) equipped for energy-dispersive X-ray analysis to obtain the Ce and O semiquantitative content. Inductively Coupled Plasma Mass Spectrometry (ICP-MS) was used to estimate the final metal loading of Ni and Pd.

The crystal size and lattice parameter were calculated from the Debye-Scherrer and Bragg equations, respectively,<sup>8</sup> using the data obtained from X-ray diffraction analysis on a Bruker D8 Venture X-ray diffractometer (BRUKER, Rivas-Vaciamadrid, Spain). The radiation was Cu K $\alpha$  in the range of  $10^\circ < 2\theta < 80^\circ$ . The data was processed from Rietveld refinement. Raman spectroscopy was realized on a Renishaw spectrometer at ambient conditions using  $\lambda = 532$  nm. X-ray photoelectron spectroscopy was executed to analyze the surface chemistry of the samples. The experimental procedure was done in a Kratos Axis Ultra-DLD spectrometer (Manchester, UK). A monochromatic Al K $\alpha$  source with step energy of 90 eV (1 eV step) and 20 eV (0.1 eV step) for general high-resolution spectra (O<sub>1s</sub>, Ce<sub>3d5/2</sub>, Ni<sub>2p</sub>, Pd<sub>3d</sub>). Calibration of the adventitious C=C peak was performed at 284.8 eV. All patterns were analyzed using the XPSpeak4.1 software. Shirley-type background correction was used for baseline correction, whereas different Gaussian-Lorentzian ratios were employed to fit the

deconvoluted peaks. H<sub>2</sub> titration was performed for measuring metal dispersion and the average size of the nanocrystal in supported nanoparticles. The tests were performed in a Chembet 3000 (Quantachrome Instruments, Boynton Beach, FL, USA) following the previous work procedure.<sup>9</sup>

## 2.2. Characterization of carbon xerogels

The porous texture was analyzed by N<sub>2</sub> adsorption-desorption and CO<sub>2</sub> adsorption at -196 °C and 0 °C, respectively, using a Micromeritic ASAP2020 instrument (Micromeritics, Norcross, GA, USA). First, samples were outgassed overnight at 110 °C under a high vacuum (10<sup>-6</sup> mbar), and then the gas adsorption isotherms were constructed. To obtain the specific surface area ( $S_{\text{BET}}$ ) through the N<sub>2</sub> adsorption data, the BET equation was used;<sup>7</sup> meanwhile, the micropore volume ( $W_0$ ) and micropore means ( $L_0$ ) were estimated by the Dubinin-Radushkevich (DR) equation.<sup>10</sup> Total pore volume ( $V_{0.95}$ ) is obtained from the N<sub>2</sub> adsorption isotherms at 0.95 relative pressure. Finally, the mesopore volume ( $V_{\text{MESO}}$ ) is calculated using the BJH method. Thermal stability was assessed by heating samples from 50 to 800 °C, using a heating ramp of 10 °C min<sup>-1</sup>, and an air flow of 100 mL min<sup>-1</sup> in a thermogravimetric analyzer Q50 (TA Instruments, Inc., New Castel, DE, USA).

The point of zero charges ( $\text{pH}_{\text{Pzc}}$ ) was estimated based on the solid addition method,<sup>11</sup> using a Nanoplus-3, Micromeritics (GA, USA). The final amount of cerium and nickel was estimated by Inductively Coupled Plasma Mass Spectrometry (ICP-MS).

The texture and morphology of samples were analyzed by scanning electron microscopy (SEM) and high-resolution transition electron microscopy (HR-TEM) using an FEI microscope model Quanta 400 (SEM) (Eindhoven, The Netherlands) and an FEI Titan G2 microscope (HR-TEM) (Eindhoven, The Netherlands).

The crystalline phases of the obtained materials were analyzed by X-ray diffraction using a Bruker D8 Venture X-ray diffractometer (BRUKER, Rivas-Vaciamadrid, Spain) with Cu K $\alpha$  radiation. The XRD patterns were recorded in the 2-theta ( $2\theta$ ) range from 6° to 77°. The Debye-Scherrer equation was used for estimating the average crystal size.<sup>8</sup> The surface chemistry was studied by X-ray photoelectron spectroscopy (XPS) by using a Kratos Axis Ultra-DLD spectrometer (Manchester, UK) equipped with a hemispherical electron analyzer connected to a detector DLD (delay-line detector). Finally, Raman spectra were

recorded using a Micro-Raman JASCO NRS-5100 (JASCO, Tokyo, Japan) dispersive spectrophotometer with a 532 nm laser line.

Finally, the samples' wettability was estimated through contact angle measurements in crude oil/monolithic carbon xerogels/air systems using the sessile drop method. For this test, an optical tensiometer (Attention Theta, Biolin Scientific, Finland) was employed. The setup included an automatic pump, a contact angle platform, a light source, and software (Attention Theta, Biolin Scientific, Ver 4.1.0) analyzer. The oil droplets were placed into the monolithic carbon surface using the automatic pump using 0.5  $\mu\text{L}$  of fluid, and the photographs were taken with a high-definition camera.

### **3. SARA extraction and characterization**

#### **3.1. Asphaltene extraction**

Asphaltenes were extracted from the heavy crude oil sample by mixing each crude oil in a 40:1 ratio with *n*-heptane following the ASTM D2892 and ASTM D5236 standards.<sup>12-14</sup> After the precipitation, the samples were centrifuged and filtered using a 3- $\mu\text{m}$  quantitative filter to remove the insoluble fraction and washed with excess *n*-heptane. More details about the extraction experiments can be found in our previous works.<sup>9, 15</sup>

#### **3.2. S-Ar-R Extraction and Quantification**

The separation process includes diluting the crude oil in *n*-heptane in a 1:40 weight ratio for asphaltene precipitation.<sup>16</sup> Maltene was collected by evaporating the *n*-heptane. The maltenes portion is further separated using a liquid chromatography column with solvents to dissolve the saturates, aromatics, and resin fractions.<sup>17</sup> The column consists of a 40 cm long glass tube, 1 cm in diameter, and packed with a 100-200 mesh silica gel, previously activated during 6 h at 600 °C. First, 10 g of maltene was dissolved in 100 mL of *n*-heptane and introduced into the glass column. Saturates, aromatic, and resins were eluted with *n*-heptane, toluene, and a mixture of toluene/ethanol (3:1), respectively. After the extraction, the samples were placed in an oven to evaporate the remaining solvents. The light components are the compounds lost during the solvent evaporation process. The mass difference between the collected SARA fractions and the original loaded crude oil in the chromatography column was counted as the lightweight components. Briefly, Figure 1 summarizes the S-Ar-R extraction process.

### 3.3. Elemental analysis

The elemental composition of C, H, S, and N of the isolated samples was measured by a Thermo Flash elemental analyzer EA 1112 (Thermo Finnigan, Milan, Italy), using the conventional combustion procedure following the ASTM D5291 standard.<sup>18</sup> The oxygen content was obtained by the difference considering its sum equals 100 %.

### 3.4. Vapor pressure osmometry

The average molecular weight ( $M_w$ ) for SARA samples was calculated by vapor pressure osmometry (VPO) using a Knauer osmometer (Knauer, Berlin-Heidelberg, West Germany) calibrated with benzyl. The hydrocarbons are dissolved in toluene using sample and standard solutions with  $1 \text{ g}\cdot\text{Kg}^{-1}$  and  $0.005 \text{ mol}\cdot\text{Kg}^{-1}$ , respectively. Considering the benzyl calibration constant  $K_{cal}$  ( $\text{mol}\cdot\text{Kg}^{-1}$ ), the sample constant  $K_s$  ( $\text{g}\cdot\text{Kg}^{-1}$ ), and the  $K_{cal} / K_s$  ratio, the  $M_w$  value was determined.<sup>19</sup> It is important to mention that, before the measurement, disaggregation was performed by an ultrasonic bath for 30 min to obtain the smallest possible molecular weight associated with a monomer.<sup>20, 21</sup> It is important to remark that the disaggregation process is reversible. After some hours of the ultrasound treatment, the molecular weight increases again, and if the measurements are not completed, the ultrasound bath must be repeated.

### 3.5. Fourier-transform infrared spectroscopy

IR spectrum was obtained in a Fourier-transform infrared spectrophotometer (IRAffinity, Shimadzu, Nakagyo-Ku, Kyoto, Japan) containing a KCl cell with 0.22 mm spacing. Solid samples were mixed in a 30:1 weight ratio with KBr and placed on a reflection diamond crystal plate. The equipment operates in the scanning range between  $4000 \text{ cm}^{-1}$  and  $400 \text{ cm}^{-1}$  in transmission mode with a resolution of  $4 \text{ cm}^{-1}$ .

### 3.6. X-ray photoelectron spectroscopy

The tests were performed on a Specs brand X-ray photoelectron spectrometer (NAP-XPS) with a PHOIBOS 150 1D-DLD analyzer, with Al-K $\alpha$  (1486.7 eV, 13 kV, 100 W) as a monochromatic source and with step energy of 90 eV for general spectra and 20 eV for high-resolution spectra. The step was 1 eV during five measurement cycles and 0.1 eV for 20 cycles for the general and high-resolution spectra, respectively. Load compensation of 3eV and 20  $\mu\text{A}$  was used. The spectra were calibrated based on the C<sub>1s</sub> peak at 284.8 eV.

### 3.7. X-Ray diffraction

The X-ray diffraction (DRX) analysis was performed with a Bruker D8 Advance X-ray diffractometer (BRUKER, Rivas-Vaciamadrid, Spain). The diffraction patterns were obtained with a Cu K $\alpha$  radiation of 40 kV and 40 mA and a wavelength ( $\lambda$ ) of 1.541 Å, contemplating a step size of 0.02° (2 $\theta$ ) and a scanning speed of 1 min<sup>-1</sup>. The recorded patterns were smoothed and deconvoluted. The position, intensity, and area of the peaks and the full width at half maximum (FWHM) were then determined. The macrostructure parameters of the different samples were calculated according to other studies<sup>22</sup> and are shown in Table 2.

**Table 2.** Calculation of macro-structure parameters using diffraction patterns information

Equation	Description
$d_m = \frac{\lambda}{2\sin(\theta)}$	Distance between the neighboring aromatic sheets
$d_\gamma = \frac{5\lambda}{8\sin(\theta)}$	Interchain layer distance
$L_a = \frac{1.84\lambda}{\omega\cos(\theta)}$	Average diameter of the aromatic sheets
$L_c = \frac{0.9\lambda}{\omega\cos(\theta)}$	Average diameter of the cluster
$M = \frac{L_c}{d_m}$	Number of aromatic sheets in a stacked cluster

$\omega$  is the peak FWHM, 2.667 Å is the width of a single aromatic nucleus, Approximate Bragg angle positions  $2\theta_{002}=26.23^\circ$   $2\theta_{010}=42.48^\circ$ , and  $\lambda=1.5406\text{Å}$ .

### 3.8. Nuclear magnetic resonance

<sup>1</sup>H and <sup>13</sup>C NMR were performed on a Bruker Ascend III HD spectrometer (Karlsruhe, Germany) operating between 600 and 125 MHz with a 5 mm TCI cryoprobe. The samples were dissolved in CDCl<sub>3</sub> (99.8%) containing traces of tetramethylsilane (TMS) and used as standard internal solvents for <sup>1</sup>H NMR measurements. As for the <sup>13</sup>C NMR, it operates at 75.45 MHz, and the values of the chemical shifts were related to the central signal at 77 ppm of CDCl<sub>3</sub>. The sample concentration was fixed at mass fractions of 15.0% and 21.0% in 0.5 mL of the solvent agent for <sup>1</sup>H and <sup>13</sup>C measurements, respectively. The settings for the <sup>1</sup>H NMR spectra were adjusted with a pulse angle of 90° (10.5  $\mu$ s), a spectral width of 12.3 kHz, and a delay time of 1 s. The quantitative <sup>13</sup>C NMR spectra were acquired with an inverse gated



decoupling, a pulse angle of 30° (2.2 μs), a spectral width of 35 kHz, and a delay time of 180 s. Then, the <sup>1</sup>H NMR spectrum was divided into four regions associated with four different protons, according to their position in the molecule, and <sup>13</sup>C NMR was split into two main intervals for aliphatic and aromatic carbon types, respectively. The chemical shift ranges of building blocks for the measurements are shown in Table 3. Finally, the spectra were integrated for each region and normalized. The average structure parameters are calculated using the equations given in Table 4.

**Table 3.** <sup>1</sup>H NMR and <sup>13</sup>C NMR chemical shift ranges of building blocks, using CDCl<sub>3</sub> as solvent TMS as reference.

Abbreviation	Building Block	Chem. Shift Ranges [ppm]
C <sub>al</sub>	Aliphatic carbon	10.0 – 70.0
C <sub>ar</sub>	Aromatic carbon	100.0 – 178.0
H <sub>a</sub>	Aromatic hydrogen	6.5 – 9.5
H <sub>α</sub>	Hydrogen on α carbons to aromatic rings	1.9 – 4.5
H <sub>β</sub>	Hydrogen on β carbons to aromatic rings, CH <sub>2</sub> or naphthenic-type carbon	1.0 – 1.9
H <sub>γ</sub>	Hydrogen on γ carbons or CH <sub>3</sub> terminal of aliphatic chains alkylating an aromatic ring	0.5 – 1.0

**Table 4.** Calculation of average structural parameters using <sup>1</sup>H-RMN and chemical elemental composition information.

Equation	Description
$f_A = \frac{\left[ \frac{C}{H} - \frac{H_\alpha}{2} - \frac{H_\beta}{2} - \frac{H_\gamma}{3} \right]}{\frac{C}{H}}$	Aromaticity Factor
$\sigma = \frac{\left[ \frac{H_\alpha}{2} \right]}{\frac{H_\alpha}{2} + H_A}$	Hydrogen periphery replacement rate in the aromatic ring system
$\frac{H_{AU}}{C_A} = \frac{\left[ \frac{H_\alpha}{2} + H_A \right]}{\frac{C}{H} - \frac{H_\alpha}{2} - \frac{H_\beta}{2} - \frac{H_\gamma}{3}}$	Condensation degree parameter of the aromatic ring system
$\frac{C}{H} = \frac{C\%}{H\% \times 12}$	Carbon/Hydrogen ratio
$H_T = M_w \times H\%$	Total hydrogen numbers
$C_T = M_w \times C\%$	Total carbon numbers
$C_A = C_T \times f_A$	Aromatic carbon numbers

$C_S = C_T - C_A$	Saturated carbon numbers
$C_\alpha = \frac{H_\alpha \times H_T}{2}$	Carbon numbers on the $\alpha$ position of an aromatic ring
$C_{ap} = C_\alpha + H_A \times H_T$	Peripheral carbon in a fused aromatic ring
$C_i = C_A - C_{ap}$	Internal carbon in a fused aromatic ring
$R_{Ar} = \frac{C_i}{2} + 1$	Aromatic rings
$R_t = C_T - \frac{H_T}{2} + 1 - \frac{C_A}{2}$	Total rings
$R_n = R_t - R_{Ar}$	Naphthenic rings
$n = \frac{H_\alpha + H_\beta + H_\gamma}{H_\alpha}$	Average alkyl chain length

---

#### 4. Adsorption experiments

##### 4.1. Asphaltene adsorption

The adsorption capacity of the nanoparticles for  $n$ -C<sub>7</sub> asphaltenes was studied by batch experiments using a colorimetric method.<sup>23-25</sup> Different model solutions containing  $n$ -C<sub>7</sub> asphaltenes in toluene were done between 100 and 1500 mg·L<sup>-1</sup>. Then, nanoparticles were added in a 10:1 ratio of adsorbent mass (mg) to solution volume (mL). The ultraviolet-visible (UV-vis) spectrophotometer Genesys 10S UV-VIS (Thermo Scientific, Waltham, MA, USA) was used to determine the change in asphaltene concentration in the supernatant. First, a calibration curve of the UV-vis absorbance versus asphaltenes concentration was constructed in which the linearity can be ensured at 298 nm wavelength. Then, nanoparticles-asphaltene mixtures are stirred for 24 h at 25 °C. Finally, the remaining solid was separated through centrifugation at 4500 rpm. The residual concentration was obtained by the absorbance measurements.<sup>9</sup> The amount of adsorbed asphaltenes  $q$  (mg·m<sup>-2</sup>) was determined by mass balance (Equation 1):

$$q = \frac{C_o - C_E}{A} V \quad (1)$$

where  $C_E$  (mg·L<sup>-1</sup>) is the equilibrium concentration of asphaltenes in the supernatant,  $C_o$  (mg·L<sup>-1</sup>) is the initial concentration of  $n$ -C<sub>7</sub> asphaltenes in solution,  $A$  (m<sup>2</sup>·g<sup>-1</sup>) is the dry surface area of nanoparticles, and  $V$  (L) is the solution volume.

#### 4.2. Adsorption of asphaltene and resin mixtures

The competitive adsorption between resins and asphaltenes was evaluated using different R:A mass ratios of 8:2, 1:1, and 2:8. The amount adsorbed of each component was obtained by combining softening point (SP) and thermogravimetric (TGA) experiments following the ASTM E28-12 standard methods <sup>26</sup>. Figure 1 shows the calibration curve of SP against *n*-C<sub>7</sub> asphaltenes percentage where an R<sup>2</sup> value close to the unity was obtained.

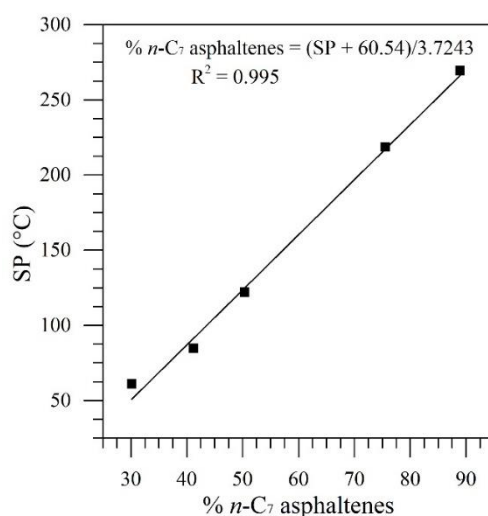


**Figure 1.** Softening point calibration curve.

#### 4.3. Adsorption of sulfur compounds

The adsorption isotherms were varying the amount of the crude oil (40, 30, 20, 10 g, 4, and 2g, that is, 1:20, 2:30, 1:10, 1:5, 1:2, and 1:1 adsorbent mass: crude oil mass ratio, respectively). The mixtures were magnetically stirred at three temperatures (25, 35, and 55°C) until equilibrium was achieved. Then, aliquot samples were collected using a syringe filter (hydrophobic polytetrafluoroethylene). After adsorption, the concentration of sulfur was determined through X-ray fluorescence spectrometry (XRF) in a Philips model 1400 wavelength-dispersive spectrometer. The instrumental conditions were fixed as 100 s irradiation time, operating at 100 mA and set at 15 kV. A Germanium crystal and a proportional flow counter were used to measure the K alpha lines of sulfur and the background next to the peaks. Sulfur standards were prepared from *n*-dibutyl sulfide diluted with mineral spirits. A fivefold dilution of the waste oil samples with mineral spirits prepared samples for the XRF measurements. The diluted samples were introduced into the spectrometer in 31

mm diameter plastic cups with polypropylene windows (Chemplex). Initially, the cups were filled to within 4 mm of the top.

#### 4.4. Adsorption of crude oil from O/W emulsions

Emulsions containing 100 mg L<sup>-1</sup>, 300 mg L<sup>-1</sup>, 500 mg L<sup>-1</sup>, and 1000 mg L<sup>-1</sup> of crude oil as a dispersed phase were employed for batch adsorption studies. Monolithic carbon xerogels were added into the glass beaker with the O/W emulsions and stirred for 24 h to ensure adsorption equilibrium. Next, each system was centrifuged at 4500 rpm for 45 min. The supernatant was removed, and the precipitate was dried at room temperature. The adsorbed amount of the crude oil ( $q$ ) was determined by thermogravimetric analysis in an air atmosphere and using the mass balance described by the Equation (2)

$$q = \frac{m_i - m_f}{m_a} \quad (2)$$

where,  $m_i$ ,  $m_f$ , and  $m_a$  are the initial, final and dry mass of the adsorbent.

Different variables were analyzed during this test. Initially, different ratios of the solution volume to the dry mass of the xerogels ( $M$ ) were evaluated (0.03, 0.1, and 0.3 g L<sup>-1</sup>) at a fixed temperature of 25 °C and pH of 7.0.  $M$  were selected according to the ratios found in the literature.<sup>27, 28</sup> Then, the effect of temperature was assessed measuring crude oil adsorption at 25, 55, and 75 °C at a fixed  $M$ . Finally, pH was varied fixing the rest of the variables.

#### 4.5. Dynamic adsorption and validation through simulation

Dynamic adsorption tests were performed on a fixed-bed column based on the experimental setup shown in Figure 2. It consists of a positive displacement pump, a crude oil-containing cylinder containing two regulating valves, and an open packed-bed system with 0.3 porosity. The adsorbent was packed inside the column (2 cm diameter - 50 cm height). Next, the crude oil was injected with a controlled flow rate of 2.0 ml·min<sup>-1</sup> at room pressure (0.1 MPa) and temperature (25 °C). The desulfurization products were collected periodically in a beaker to analyze sulfur content by XRF. The test provides information about the adsorption capacity and speed of saturation of the packed bed.

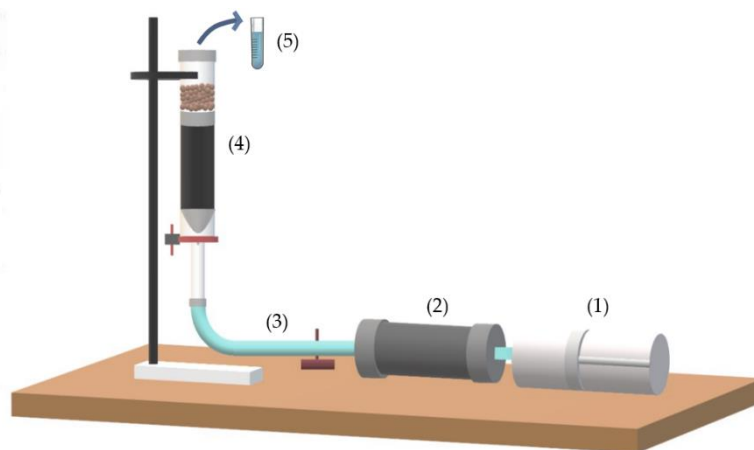


**Figure 2.** Experimental setup for dynamic adsorption tests consisting of (1) positive displacement pump, (2) crude oil containing cylinder, (3) regulating valves, (4) open packed-bed system, and (5) effluent collection.

## 5. Thermal experiments

5.1. High-pressure thermogravimetric analyses for oxidation and pyrolysis experiments.

To assess the pressure effect on SARA oxidation, thermogravimetric analyses were performed at high-pressure and high-temperature conditions using a HP-TGA 750 (TA instruments Inc., Hüllhorst, Germany), which generates a highly uniform electromagnetic field that levitates a permanent magnet attached to the suspension shaft. When a sample is placed in the crucible, the current required to keep the balance position is proportional to the sample weight, making the process extremely sensitive.<sup>30</sup> To begin, the asphaltenes surface is vacuumed to remove gases and humidity. For 10 minutes, a vacuum of 0.00025 MPa is maintained. The equipment then reaches the pressure and flow conditions before beginning to heat. To raise the pressure, the system has a set of valves that allows it to be pressurized by the working gases, in this case, the air. Due to flow effects such as buoyancy, the equipment performs two runs at the same conditions (air flow, temperature, and pressure) to automatically perform the corrections. After the first run has finished and the asphaltene has been consumed, the second test is performed on the empty sample holder. The automatic correction is performed by subtracting the measurements of the empty holder from the one containing the asphaltene sample. The gas delivery system diagram for the HP-TGA 750 is shown in Figure 3. Four measuring gas mass flow controllers (MFCs) are used to inject gases into the system. The MFC1 feeds

a constant inert gas flow through the balance tubing to protect sensitive balance parts from any harmful gas atmosphere. Thereby, gas 1 protects the levitation system; in this gas line, an  $N_2$  flow of  $5 \text{ mL}\cdot\text{min}^{-1}$  is maintained. The second line allows air entry, and lines 3-4 are closed for these tests. Each gas line has its own pressure sensor at the inlet. Additional pressure sensors are used to ensure safe gas switching conditions.

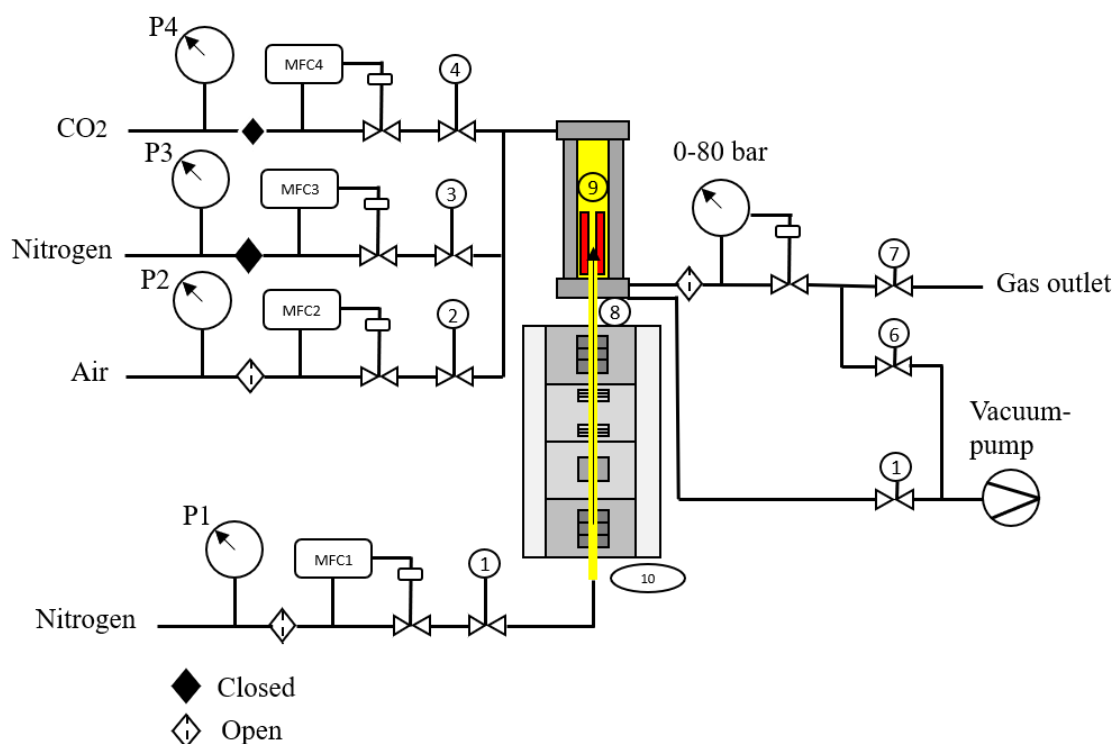


**Figure 3.** Gas delivery system diagram for the high-pressure thermogravimetric analyzer HP-TGA 750. MCF# are the mass flow controller for each gas injected into the system. P# are the manometers, 1-6 are the automatic valves, 7 is the gas outlet pressure regulator, 8 is the tube balance, 9 is the magnet-levitated balance, and 10 is the high-pressure reaction furnace.

### 5.1.1.1. Non-isothermal experiments

Non-isothermal experiments were done by differential scanning calorimetry (DSC) and high-pressure thermogravimetric analysis (HP-TGA). DSC runs were done in a Q2000 DSC (TA. Instruments, Inc., New Castel, DE, USA) at a defined heating rate between  $100 \text{ }^\circ\text{C}$  and  $700 \text{ }^\circ\text{C}$  in an alumina crucible. The catalyzed and non-catalyzed experiments were executed with  $5 \text{ mg}$  of sample. The gas flow rate was  $100 \text{ mL}\cdot\text{min}^{-1}$ . HP-TGA runs were carried out in HP-TGA 750 (TA instruments Inc., Hüllhorst, Germany) under the following procedure. Initially, a high vacuum was done at  $2.5 \times 10^{-4}$

<sup>4</sup> MPa for 10 min for cleaning the surface sample. Then, the equipment adjusts the selected pressure. Once the pressure is reached, the heating starts at a defined rate between 100 and 700 °C under a gasflow of 80 mL·min<sup>-1</sup> in an alumina crucible. The sample weight was 1 mg. The run is done by two times, for the crucible with the sample and one more empty due to buoyancy correction. All the experiments were performed at least twice for repeatability.

### 5.1.2. Isothermal experiments

Isothermal experiments were done by high-pressure thermogravimetric analysis aligned to a mass spectrometer (Shimadzu GC-MS, Tokyo, Japan). The samples were heated at a fixed temperature for 300 min to ensure the asphaltene conversion quantification. The runs were performed at different pressures between 0.084 and 6.0 MPa.

## 5.2. Thermogravimetric analyses for gasification experiments

The steam catalytic gasification of virgin and adsorbed compounds on nanocatalysts was performed using a Q50 thermogravimetric analyzer (TA Instruments, Inc., New Castel, DE, USA). Two different processes were executed. The first one, under non-isothermal heating between 100–600 °C, at a defined heating rate. The samples were subjected to isothermal heating at three different temperatures in the second one. Samples in the absence of nanocatalysts were heated at higher temperatures (> 350 °C), while the nanocatalysts with adsorbed compounds were at lower temperatures (< 250 °C). The steam atmosphere was simulated by introducing 100 mL·min<sup>-1</sup> of N<sub>2</sub> and 6.30 mL·min<sup>-1</sup> of H<sub>2</sub>O<sub>(g)</sub> using a gas saturator controlled by a thermostatic bath at atmospheric pressure.<sup>31</sup>

## 5.3. Gas monitoring

TGA was coupled with an online gas chromatography/mass spectrometer (Shimadzu GC-MS, Tokyo, Japan) to investigate the evolved gases that were emitted during the thermal experiments, using a linear scan rate of the ion trap mass analyzer of 0.03 M/Z from 0 M/Z up to 200 M/Z.

## 6. Displacement tests.

### 6.1. Oil Recovery

The displacement test was divided into four main stages to recreate the injection conditions of the steam stimulation processes and evaluate the effect of the nanoparticle in oil recovery, in situ upgrading and hydrogen production.

Figure 4 shows a schematic representation of the experimental setup. The system consists of two positive displacement pumps (DB Robinson Group, Edmonton, AB, Canada), one to control the injection of oil and water and another to control the injection of water to the steam generator and nanofluid to the porous medium. The system also includes four cylinders (Max Servicios, S.A.S., Medellín, Colombia) containing EHO, synthetic brine, deionized water, and nanofluid; a steam generator (Thermo Scientific Waltham, MA, USA), thermocouples (Termocuplas, S.A.S., Medellín, Colombia); valves (Swagelok, Cleveland, OH, USA); manometers (Rosemount, Emerson, Chesterfield, MO, USA); fraction collectors; a pressure transducer (Rosemount, Emerson, Chesterfield, MO, USA); a hydraulic pump (Enercap, Actuant Corporation, Milwaukee, WI, USA); and a pressure multiplier. A leak test was performed by pressuring the core holder with N<sub>2</sub> up to 1000 psi, where a change in 1% pressure per hour was considered the maximum pressure reduction allowed.

Before the steam injection, measurements of the absolute permeability ( $K$ ) and the effective permeabilities of water ( $k_w$ ) and oil ( $k_o$ ) were performed. For this, 10 VP of each phase was injected in the order water–oil–water until a constant pressure drop was observed during each injection.  $K$ ,  $k_w$ , and  $k_o$  values were calculated using the Darcy equation.<sup>32</sup> For this scenario, the system temperature was maintained at 80 °C, and the pore and overburden pressure were fixed at 150 and 800 psi, respectively.

To construct initial oil recovery by steam injection, 7 porous volumes of water equivalent (PVWE) were injected at 210 °C. Steam was injected between 3 and 5 mL·min<sup>-1</sup> to prevent condensation into the coil line and porous medium. Under these conditions, steam was injected at 70% quality, with a massive flow of vapor and liquid water. The steam quality was ensured through numerical simulation by calculating the mass balance between the steam generator and the entrance of the porous medium. Considering the steam injection conditions ( $T = 210$  °C,  $x = 70\%$ ), the properties of the line connecting the points for the material balance (length = 0.63 m, thermal conductivity = 16.3 W·m<sup>-1</sup>·K<sup>-1</sup>, internal radius = 0.0046 m, and external radius = 0.00635 m) and using the Antoine correlation, heat losses, and the pressure at each node necessary to ensure the quality of steam at the entrance of the porous medium were calculated. Radial heat persistence was not considered because of the liquid–vapor equilibrium conditions of the system. The heat transfer coefficient was very high; therefore, the resistance value could be neglected.<sup>33</sup>



The injection of the nanocatalyst-based nanofluid was performed through the continuous nanofluid addition to the steam current for approximately 7 PVWE. The nanofluid was injected into the steam generator outlet at a rate between 0.5 and 1 mL·min<sup>-1</sup> before entering the porous medium. The pressure profile of the system was monitored throughout the displacement test to ensure the nanofluid transport in the steam stream. The oil recovery was obtained until no more oil was produced. Then, the porous media was left to stand for 12 h, and steam in the absence of the nanofluid was injected again until there was no oil production.

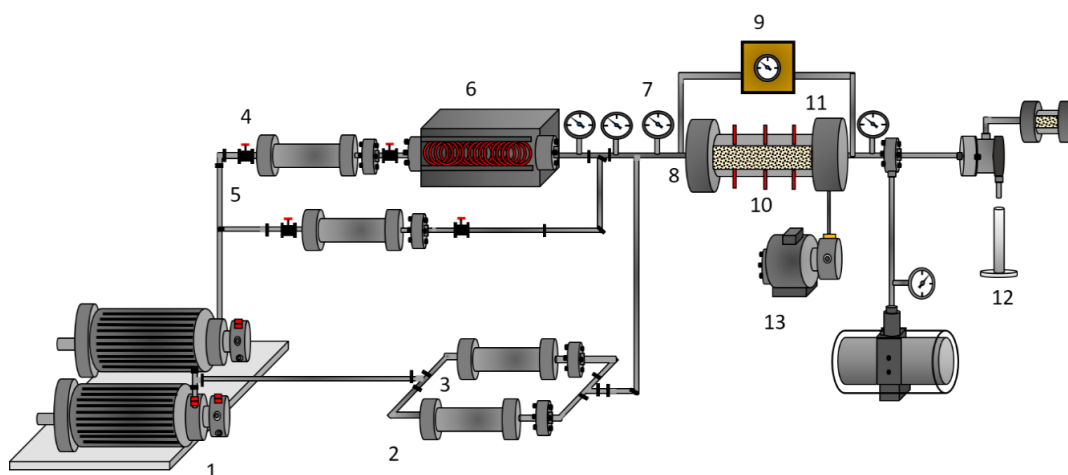


**Figure 4.** Experimental setup: (1) positive displacement pumps, (2,3,4,5) oil, brine, water, and nanofluid-containing cylinders, respectively, (6) steam generator, (7) manometers, (8) thermocouple, (9) pressure transducer, (10) core holder, (11) sand packed bed, (12) sample output and (13) hydraulic pump.

Finally, the gas outlet line was coupled with a mass spectrometer (Shimadzu MS, Tokyo, Japan). The scan rate of the linear ion trap mass analyzer was 0.03  $m/z$  from 0  $m/z$  to 200  $m/z$ . The MS instrument was equipped with a hot capillary column heated at 150 °C to prevent gas condensation. The components targeted for analysis were obtained by using a 100-eV electron impact mode to achieve sufficiently strong signals for information on the HO transformation.

## 6.2. Oil Characterization before and after Upgrading

The effectiveness of the nanoparticles in changing the physicochemical properties of the EHO was evaluated through API gravity, oil viscosity, and SARA content. The API gravity measurements were performed using an Anton Paar Stabinger SVM 3000 (Madrid, Spain). The asphaltene content was calculated

by micro de-asphalting and SARA distribution was determined following the ASTM D6560 standard.<sup>34, 35</sup> The rheological behavior of the crude oil after each stage was evaluated through a Kinexus Pro (Malvern Instruments, Worcestershire, UK) rheometer, using a parallel plate-plate geometry and 0.3 mm of GAP at 25 °C and varying the shear rate from 0 to 100 s<sup>-1</sup>. The degree of viscosity reduction (DVR) was calculated using the viscosity of the untreated EHO ( $\mu_{v,EHO}$ ) and upgraded crude oil ( $\mu_{treated}$ ) after the three stages, using the following expression:

$$DVR = \frac{(\mu_{v,EHO} - \mu_{treated})}{\mu_{v,EHO}} \times 100 \quad (3)$$

## References

1. Zhang, B.; Huyan, Y.; Wang, J.; Wang, W.; Zhang, Q.; Zhang, H., Synthesis of CeO<sub>2</sub> nanoparticles with different morphologies and their properties as peroxidase mimic. *Journal of the American Ceramic Society* **2019**, 102, (4), 2218-2227.
2. Morales-Torres, S.; Maldonado-Hódar, F. J.; Pérez-Cadenas, A. F.; Carrasco-Marín, F., Textural and mechanical characteristics of carbon aerogels synthesized by polymerization of resorcinol and formaldehyde using alkali carbonates as basification agents. *Physical Chemistry Chemical Physics* **2010**, 12, (35), 10365-10372.
3. Ariza, F.; Andrés, C. Synthesis and application of supported metallic and multi-metallic oxides nanoparticles for in-situ upgrading and inhibition of formation damage. Universidad Nacional de Colombia-Sede Medellín.
4. Nassar, N. N.; Betancur, S.; Acevedo, S. c.; Franco, C. A.; Cortés, F. B., Development of a population balance model to describe the influence of shear and nanoparticles on the aggregation and fragmentation of asphaltene aggregates. *Industrial & Engineering Chemistry Research* **2015**, 54, (33), 8201-8211.
5. Cardona, L.; Arias-Madrid, D.; Cortés, F. B.; Lopera, S. H.; Franco, C. A., Heavy Oil Upgrading and Enhanced Recovery in a Steam Injection Process Assisted by NiO-and PdO-Functionalized SiO<sub>2</sub> Nanoparticulated Catalysts. *Catalysts* **2018**, 8, (4), 132.
6. Lozano, M. M.; Franco, C. A.; Acevedo, S. A.; Nassar, N. N.; Cortés, F. B., Effects of resin I on the catalytic oxidation of n-C 7 asphaltenes in the presence of silica-based nanoparticles. *RSC Advances* **2016**, 6, (78), 74630-74642.

7. Naderi, M., Surface Area: Brunauer–Emmett–Teller (BET). In *Progress in filtration and separation*, Elsevier: 2015; pp 585-608.
8. Kroon, R., Nanoscience and the Scherrer equation versus the 'Scherrer-Gottingen equation'. *South African Journal of Science* **2013**, 109, (5-6), 01-02.
9. Medina, O. E.; Gallego, J.; Arias-Madrid, D.; Cortés, F. B.; Franco, C. A., Optimization of the load of transition metal oxides (Fe<sub>2</sub>O<sub>3</sub>, Co<sub>3</sub>O<sub>4</sub>, NiO and/or PdO) onto CeO<sub>2</sub> nanoparticles in catalytic steam decomposition of n-C<sub>7</sub> asphaltenes at low temperatures. *Nanomaterials* **2019**, 9, (3), 401.
10. Nguyen, C.; Do, D., The Dubinin–Radushkevich equation and the underlying microscopic adsorption description. *Carbon* **2001**, 39, (9), 1327-1336.
11. Nassar, N. N., Iron oxide nanoadsorbents for removal of various pollutants from wastewater: an overview. *Application of adsorbents for water pollution control* **2012**, 81-118.
12. Barre, L.; Espinat, D.; Rosenberg, E.; Scarsella, M., Colloidal structure of heavy crudes and asphaltene solutions. *Revue de l'Institut Français du Pétrole* **1997**, 52, (2), 161-175.
13. International, A., ASTM D5236-13, Standard Test Method for Distillation of Heavy Hydrocarbon Mixtures (Vacuum Potstill Method). *Annual Book of ASTM Standards* **2013**.
14. International, A., ASTM D2892, Standard Test Method for Distillation of Crude Petroleum (15-Theoretical Plate Column). *Annual Book of ASTM Standards* **2016**.
15. Medina Erao, O. E.; Gallego, J.; Olmos, C. M.; Chen, X.; Cortés, F. B.; Franco, C. A., Effect of Multifunctional Nanocatalysts on n-C<sub>7</sub> Asphaltene Adsorption and Subsequent Oxidation under High Pressure Conditions. *Energy & Fuels* **2020**.
16. Franco, C. A.; Montoya, T.; Nassar, N. N.; Cortés, F. B., NiO and PdO supported on fumed silica nanoparticles for adsorption and catalytic steam gasification of Colombian C<sub>7</sub> asphaltenes. *Handbook on Oil Production Research; Nova Science Publishers: Hauppauge, NY, USA* **2014**, 101-145.
17. Liu, D.; Song, Q.; Tang, J.; Zheng, R.; Yao, Q., Interaction between saturates, aromatics and resins during pyrolysis and oxidation of heavy oil. *Journal of Petroleum Science and Engineering* **2017**, 154, 543-550.
18. Lopes, S. M.; Geng, P., Estimation of elemental composition of diesel fuel containing biodiesel. *SAE International Journal of Fuels and Lubricants* **2013**, 6, (3), 668-676.

19. Acevedo, S.; Castillo, J.; Vargas, V.; Castro, A.; Delgado, O. Z.; Ariza, C. A. F.; Cotés, F. B.; Bouyssiere, B., Suppression of Phase Separation as a Hypothesis to Account for Nuclei or Nanoaggregate Formation by Asphaltenes in Toluene. *Energy & Fuels* **2018**.
20. Acevedo, S.; Gutierrez, L. B.; Negrin, G.; Pereira, J. C.; Mendez, B.; Delolme, F.; Dessalces, G.; Broseta, D., Molecular weight of petroleum asphaltenes: A comparison between mass spectrometry and vapor pressure osmometry. *Energy & fuels* **2005**, 19, (4), 1548-1560.
21. Yarranton, H. W.; Alboudwarej, H.; Jakher, R., Investigation of asphaltene association with vapor pressure osmometry and interfacial tension measurements. *Industrial & engineering chemistry research* **2000**, 39, (8), 2916-2924.
22. Shao, R.; Shen, Z.; Li, D.; Sun, Z.; Pei, L.; Liu, X.; Li, W.; Dan, Y., Investigation on composition and structure of asphaltenes during low-temperature coal tar hydrotreatment under various reaction pressures. *Journal of Analytical and Applied Pyrolysis* **2018**, 136, 44-52.
23. Mullins, O. C. S., E. Y., Eds.; Plenum Press: , Optical interrogation of aromatic moieties in crude oil sand asphaltenes. In Structures and dynamics of asphaltenes;. **New York, 1998**.
24. Goncalves, S.; Castillo, J.; Fernandez, A.; Hung, J., Absorbance and fluorescence spectroscopy on the aggregation behavior of asphaltene–toluene solutions. *Fuel* **2004**, 83, (13), 1823-1828.
25. Acevedo, S.; Escobar, G.; Gutiérrez, L. B.; Rivas, H.; Gutiérrez, X., Interfacial rheological studies of extra-heavy crude oils and asphaltenes: role of the dispersion effect of resins in the adsorption of asphaltenes at the interface of water-in-crude oil emulsions. *Colloids and Surfaces A: Physicochemical and Engineering Aspects* **1993**, 71, (1), 65-71.
26. D36, A., Standard Test Method for Softening Point of Bitumen (Ring-and-Ball Apparatus). *Annual Book of Standards* **2006**.
27. Pekdemir, T.; Copur, M.; Urum, K., Emulsification of crude oil–water systems using biosurfactants. *Process Safety and Environmental Protection* **2005**, 83, (1), 38-46.
28. Rajaković-Ognjanović, V.; Aleksić, G.; Rajaković, L., Governing factors for motor oil removal from water with different sorption materials. *Journal of hazardous materials* **2008**, 154, (1-3), 558-563.
29. Acosta, L. G.-C., D.; Medina, O.E.; Cortés, F.B.; Franco, C.A. , Nano-Intermediate of Magnetite Nanoparticles Supported on Activated Carbon from

Spent Coffee Grounds for Treatment of Wastewater from Oil Industry and Energy Production. *Processes* **2021**, *9*, 63.

30. Gimzewski, E., An accurate and compact high-pressure thermogravimetric analyser. *Journal of thermal analysis* **1991**, *37*, (6), 1251-1260.

31. Franco, C. A.; Montoya, T.; Nassar, N. N.; Cortés, F. B., NIOAND PDO SUPPORTED ON FUMED SILICA NANOPARTICLES FOR ADSORPTION AND CATALYTIC STEAM GASIFICATION OF COLOMBIAN C7ASPHALTENES. **2014**.

32. Whitaker, S., Flow in porous media I: A theoretical derivation of Darcy's law. *Transport in porous media* **1986**, *1*, (1), 3-25.

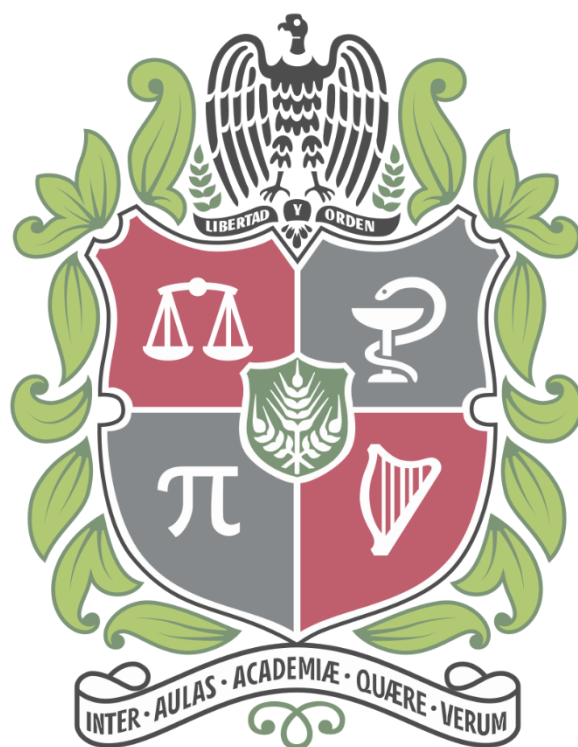
33. Incropera, F. P.; Lavine, A. S.; Bergman, T. L.; DeWitt, D. P., *Fundamentals of heat and mass transfer*. Wiley: 2007.

34. Bansal, V.; Krishna, G.; Chopra, A.; Sarpal, A., Detailed hydrocarbon characterization of RFCC feed stocks by NMR spectroscopic techniques. *Energy & fuels* **2007**, *21*, (2), 1024-1029.

35. Cardona, L.; Arias-Madrid, D.; Cortés, F.; Lopera, S.; Franco, C., Heavy oil upgrading and enhanced recovery in a steam injection process assisted by NiO- and PdO-Functionalized SiO<sub>2</sub> nanoparticulated catalysts. *Catalysts* **2018**, *8*, (4), 132.



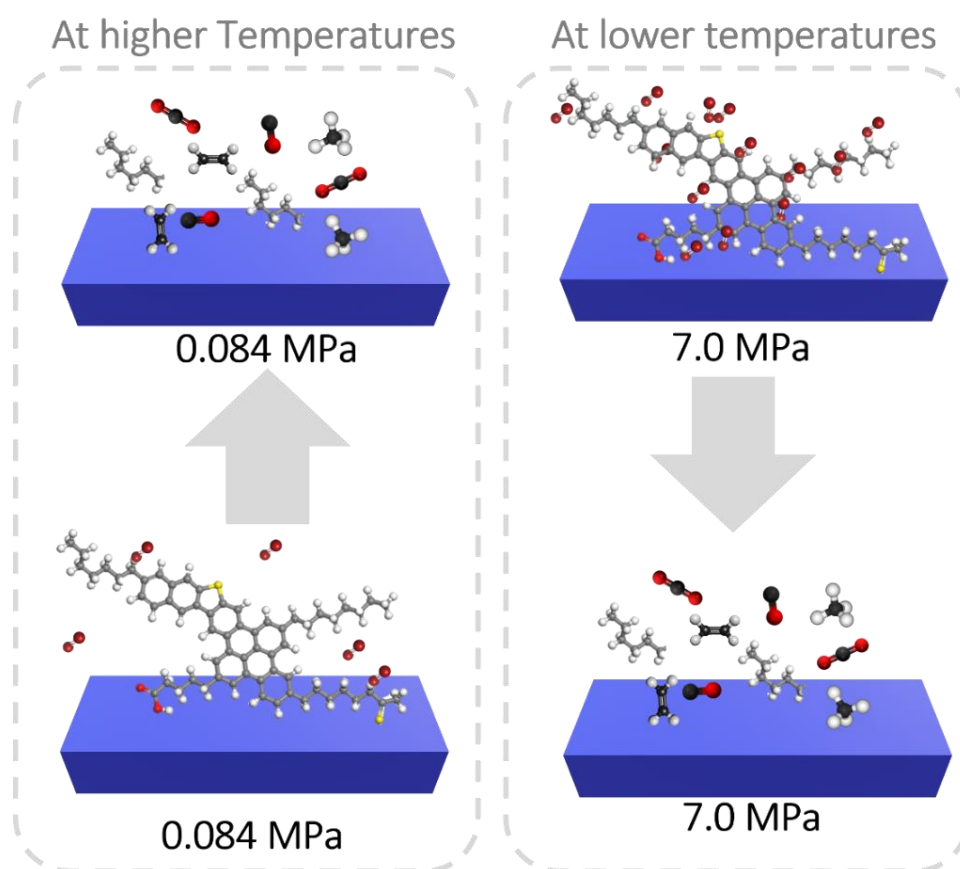
### Apartado 3.





## Chapter 1.

# Effect of Pressure on the Oxidation Kinetics of Asphaltenes.



Published Article in *Energy & Fuels*: [doi.org/10.1021/acs.energyfuels.9b02611](https://doi.org/10.1021/acs.energyfuels.9b02611).

Impact factor: 4.654



# Effect of Pressure on the Oxidation Kinetics of Asphaltenes

## Abstract

The purpose of this study was to determine the effect of pressure on the oxidation kinetics of n-heptane insoluble asphaltenes derived from extra-heavy crude oil. Thermogravimetric analyses (TGA) were carried out in an air atmosphere at pressures ranging from 0.084 MPa to 7 MPa, temperatures ranging from 100 °C to 600 °C, and heating ramps of 5, 10, and 15 °C·min<sup>-1</sup>. A first-order kinetic model was used to calculate the effective activation energy and kinetic parameters. According to the TGA profile, the temperature range was divided into four main regions for a better understanding of asphaltene oxidation under high-pressure conditions: i) oxygen chemisorption (OC), ii) decomposition of the chemisorbed oxygen (DCO), iii) first combustion region (FC), and iv) second combustion region (SC). Pressure increases favor asphaltene decomposition, with 20% mass loss in the first combustion region at 0.084 MPa and 50% at 7 MPa. Furthermore, the temperature at which each thermal event ends is reduced by approximately 35, 23, 13, and 51 °C for OC, DCO, FC, and SC, respectively, from 0.084 MPa to 7 MPa. Furthermore, increasing the heating rate increases asphaltene decomposition in the second combustion region, indicating that the decomposition follows different mechanisms depending on the exposure time. However, as the system pressure increased, the effective activation energy values for the thermal events associated with oxygen chemisorption and decomposition increased by 53.1% and 71.1%, respectively. In contrast, the activation energy decreases by 61.4 and 75.6%, respectively, for the combustion (FC and SC) stages, indicating that pressure controls the asphaltene oxidation behavior in the four regions. All these facts indicate that the chemisorption of oxygen, which is favored by pressure increase, is the kinetic limiting step for asphaltene oxidation.

## 1. Introduction

Nowadays, the supply of hydrocarbons from conventional reservoirs has decreased due to their depletion,<sup>1, 2</sup> forcing the oil industry to consider unconventional oil reserves to supply the world's energy demand.<sup>3, 4</sup> These oil deposits are usually constituted by heavy (HO) and extra heavy crude oils (EHO) which have a significant economic value as it is estimated that their reserves represent about 70% of total world oil reserves.<sup>5</sup> In the specific case of HO and EHO production, there are significant difficulties due to the low efficiency of conventional treatments and production systems related to their high viscosity and high content of heavy fractions.<sup>6-8</sup> Asphaltenes are the heaviest and the most polar molecular compounds in the crude oil matrix. These chemical compounds are found in between 2 and 30% mass fractions in HO and EHO.<sup>9-11</sup> They can be defined as a solubility class insoluble in low molecular weight paraffin (such as *n*-heptane) and soluble in aromatics (such as toluene).<sup>12-14</sup> To understand the asphaltenes' behavior, different molecular structures have been proposed, such as an island,<sup>15</sup> archipelago,<sup>16</sup> continental,<sup>17</sup> and rosary-type structures.<sup>18</sup> Currently, the Yen-Mullins theory<sup>19</sup> is the most accepted for describing the structure of asphaltene as a molecule composed mainly of a single polycyclic aromatic core of around 7-10 benzene rings mixed with peripheral substituents of cycloalkane and branched and straight alkane chains, heteroatoms of sulfur, oxygen, and nitrogen, and heavy metals such as nickel, vanadium, and iron.<sup>18, 20</sup> Nevertheless, because the Yen-Mullins model does not predict the products of thermocracking and hydrocracking processes, other models should be used to describe their physicochemical changes. Remarkably, the location and high content of the heteroatoms on the molecular structure lead to high polarity of the molecule, which provides the self-assembly characteristic to the asphaltenes.<sup>18</sup> Besides, the asphaltene-asphaltene and asphaltene-resin interactions are responsible for generating a rigid and stable viscoelastic network that prevents the flow of crude oil,<sup>21, 22</sup> making necessary the addition of energy by means of heat or the inclusion of diluents to improve production and transport operations.<sup>21, 23-25</sup>

Thermal enhanced oil recovery processes for heat injection into the reservoir include *in-situ* combustion (ISC),<sup>26-28</sup> and low-temperature oxidation

(LTO) methods,<sup>29-32</sup> which involves the injection of an oxidizing agent (air or oxygen) into the target formation for a defined period.<sup>33</sup> During the ISC, the oxidizing agent is activated by specialized tools, pyrophoric substances, steam, or by the same oil reactivity by burning a portion of the same.<sup>34, 35</sup> In this burned area, a heated front is formed that pushes the rest of the hydrocarbons through a combination of the combustion gases, steam, and water to the producing wells. In addition, the thermal cracking reduces the oil viscosity, increasing oil mobility and improving the production capacity.<sup>36</sup> During these processes, a series of chemical reactions such as oxidation, catalytic disintegration, and distillation are generated mainly with the heaviest fraction of the crude oil.<sup>26, 37, 38</sup> Asphaltenes are the main precursor of the solid part formed from thermal cracking reactions named coke; that is, they are the primary fuel to generate high-temperature oxidation reactions (HTO), also known as breaking reactions or simply combustion reactions.<sup>39</sup> As the amount of injected air that reacts with the coke increase, a flame or combustion front is generated. The highest temperature of the process is located at the front, and the viscosity of the crude oil is substantially reduced at the front.<sup>40</sup> Hence, it is necessary to understand the asphaltenes' behavior and their oxidation kinetics under high pressure and high-temperature conditions to optimize the use and productivity of heavy crude oil during thermal enhanced oil recovery processes.<sup>41-43</sup> Yoshiki and Philip et al.<sup>44</sup> evaluated the thermo-oxidative and thermal cracking reactions of Athabasca bitumen through differential thermal analysis (DTA) and found that the heating rate controls the low-temperature oxidation degree and, therefore, the availability of fuel during *in-situ* combustion.<sup>44</sup> The authors also used differential scanning calorimetry and thermogravimetric analysis to identify three main combustion regions: distillation/low-temperature oxidation (LTO), cracking/first combustion (FC), and high-temperature oxidation (HTO)/second combustion (SC). Tadema et al.<sup>45</sup> developed a study of the thermal effect of mixtures of oils and sands under an air atmosphere. The authors found two main decomposition peaks in the thermogravimetric analysis of the samples around 270 and 400 °C. For temperatures higher than 350 °C, CO and CO<sub>2</sub> are the main products, and a "clean-burnt" formation can be formed.<sup>45</sup> Philips et al.<sup>46</sup> showed with high-pressure differential scanning calorimetry (PDSC) that pressure increases the endothermicity at low and exothermicity at high temperatures.<sup>46</sup> Sonibare et al.<sup>47</sup> showed that with the increase in the heating rate, a change is generated in the reaction

regions, displacing the temperatures where the maximum decomposition is generated at higher temperatures and generating an increase in the exothermicity of the reactions, mainly in the HTO region.<sup>47</sup>

Despite the robust research done to understand the oxidation of heavy crude oils and bitumen, there is no information about the effect of pressure on thermo-oxidative reactions of asphaltenes, neither the temperature intervals nor the oxidation kinetic data. Therefore, this work aims to study the oxidation kinetics of asphaltenes to varying pressures from 0.084 to 7 MPa in a wide range of temperatures between 100 and 800 °C, and three different heating rates (5, 10, and 15 °C·min<sup>-1</sup>). The effective activation energy and pre-exponential factor of the oxidation kinetics were calculated for each reaction region. This work is expected to contribute to understanding the behavior of asphaltenes under reservoir conditions to optimize the thermal EOR techniques and provide better exploitation of heavy and extra-heavy crude oils.

## 2. Experimental.

### 2.1. Materials.

Asphaltenes were isolated from a Colombian extra-heavy crude oil, characterized by saturates, aromatics, resins, and asphaltenes (SARA) composition through a combined process of micro de-asphalting and the IP 469 method using a LATROSCAN MK6 TLC-FID/FPD equipment.<sup>48</sup> The EHO has a mass fraction of saturates, aromatics, resins, and asphaltenes of 13.0%, 16.9%, 49.9%, and 20.2%, respectively. The EHO viscosity was obtained using a rheometer Kinexus Pro+ (Malvern Instruments, Worcestershire, UK) at 25 °C and the American Petroleum Institute (API) gravity was measured using an Anton Paar Stabinger SVM 3000 (Madrid, Spain). The viscosity was  $3.1 \times 10^6$  cP at 25 °C, and the API gravity of 6.4°. The asphaltenes were extracted using *n*-heptane (99%, Sigma-Aldrich, St. Louis, MO, USA) in a 40:1 ratio at 25 °C.<sup>49</sup> The asphaltenes were separated from the solution by centrifugation and filtering processes and finally washed continuously with the *n*-heptane to obtain a bright black material. The extraction process is detailed in previous work.<sup>50</sup> The isolated asphaltenes were characterized by elemental analysis to obtain the weight percent of the polar atoms (N, S, and O) as well as hydrogen and carbon in their structure using a Thermo Flash elemental analyzer EA 1112 (Thermo Finnigan, Milan,

Italy), obtaining a mass fraction of C, H, N, S, and O of 81.7%, 7.8%, 0.3%, 6.6%, and 3.6%, respectively, and a H/C ratio of 1.15.

For the thermogravimetric analyses, the reacting gas employed consists of synthetic air NTC 2561 (CRYOGAS, Colombia) containing  $\text{H}_2\text{O} < 3 \text{ mg}\cdot\text{L}^{-1}$  and total hydrocarbons content (THC)  $< 3 \text{ mg}\cdot\text{L}^{-1}$  composed by 20.93% of balanced  $\text{O}_2$  and  $\text{N}_2$ , with high purity.

## 2.2. High-Pressure Thermogravimetric Analysis (HP-TGA)

To assess the pressure effect on asphaltene oxidation, thermogravimetric analyses were performed at high-pressure and high-temperature conditions using a HP-TGA 750 (TA instruments Inc., Hüllhorst, Germany), which generates a highly uniform electromagnetic field that levitates a permanent magnet attached to the suspension shaft. When a sample is placed in the crucible, the current required to keep the balance position is proportional to the sample weight, making the process extremely sensitive.<sup>51</sup> To begin, the asphaltene surface is vacuumed to remove gases and humidity. For 10 minutes, a vacuum of 0.00025 MPa is maintained. The equipment then reaches the pressure and flow conditions before beginning to heat. To raise the pressure, the system has a set of valves that allows it to be pressurized by the working gases, in this case, the air. Due to flow effects such as buoyancy, the equipment performs two runs at the same conditions (air flow, temperature, and pressure) to automatically perform the corrections. After the first run has finished and the asphaltene has been consumed, the second test is performed on the empty sample holder. The automatic correction is performed by subtracting the measurements of the empty holder from the one containing the asphaltene sample. The gas delivery system diagram for the HP-TGA 750 is shown in Figure 1. Four measuring gas mass flow controllers (MFCs) are used to inject gases into the system. The MFC1 in particular feeds a constant inert gas flow through the balance tubing to protect sensitive balance parts from any harmful gas atmosphere. Thereby, gas 1 protects the levitation system; in this gas line, an  $\text{N}_2$  flow of  $5 \text{ mL}\cdot\text{min}^{-1}$  is maintained. The second line allows air entry, and lines 3-4 are closed for these tests. Each gas line has its own pressure sensor at the inlet. Additional pressure sensors are used to ensure safe gas switching conditions.

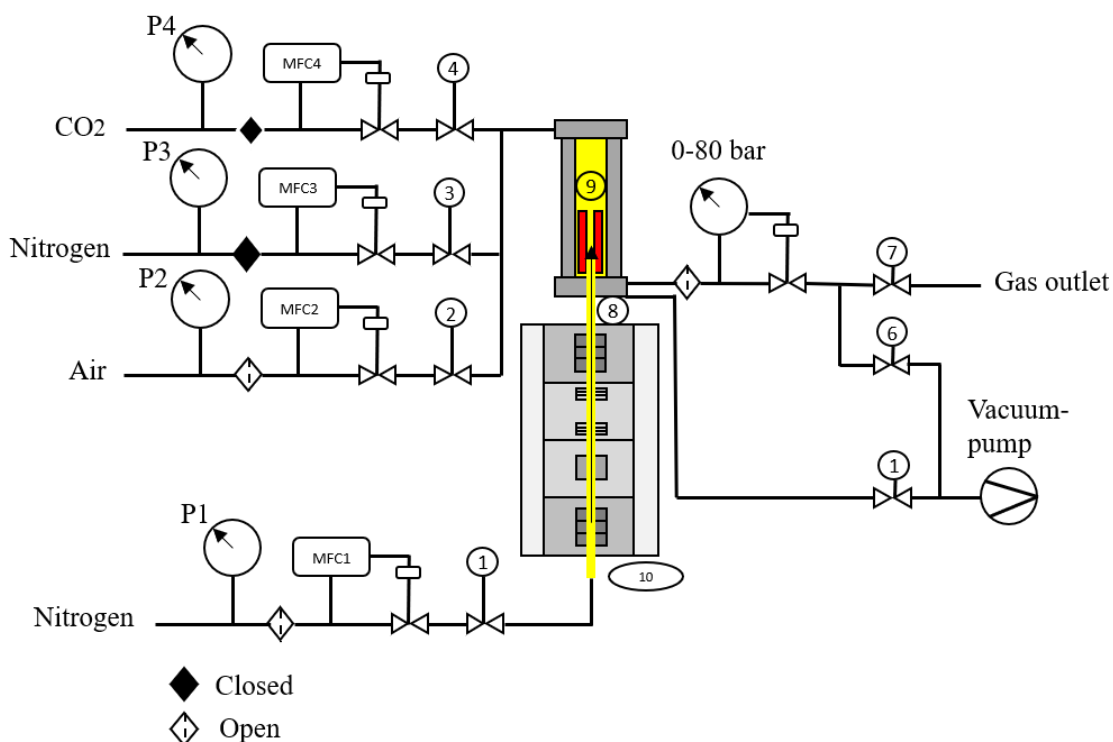


**Figure 1.** Gas delivery system diagram for the high-pressure thermogravimetric analyzer HP-TGA 750. MCF# are the mass flow controller for each gas injected into the system. P# are the manometers, 1-6 are the automatic valves, 7 is the gas outlet pressure regulator, 8 is the tube balance, 9 is the magnet-levitated balance, and 10 is the high-pressure reaction furnace.

In this section, different effects were evaluated. Initially, to avoid the diffusional effect, the decomposition of different masses of asphaltenes of 0.8, 1, 4, and 6 mg, at 6 MPa and a heating rate of  $10\text{ }^{\circ}\text{C}\cdot\text{min}^{-1}$  in a temperature range from  $100\text{ }^{\circ}\text{C}$  to  $600\text{ }^{\circ}\text{C}$  was performed. Once the mass value was obtained, the influence of pressure was evaluated by varying it between 0.084 to 7 MPa, in the same temperature range and heating rate. Finally, the effect of the heating rate was determined, evaluating the oxidative response at 5, 10, and  $15\text{ }^{\circ}\text{C}\cdot\text{min}^{-1}$  at the same pressure (6 MPa). The airflow was fixed at  $80\text{ mL}\cdot\text{min}^{-1}$  at standard pressure in all cases, and the experiments were carried out in triplicate to ensure the repeatability of the process, obtaining uncertainties for temperature and weight of  $\pm 0.01\text{ }^{\circ}\text{C}$  and  $\pm 0.0001\text{ mg}$ , respectively.

### 3. Modeling

The mathematical procedure<sup>52, 53</sup> employed to study the oxidation kinetics of asphaltenes at high-pressure conditions is based on the assumption that during the conversion process, the instantaneous reactivity  $r$  of asphaltenes can be expressed as Equation (1):<sup>54</sup>

$$r = \frac{d\theta}{dt} = f(\theta) \cdot P_{O_2}^n \cdot k \quad (1)$$

where  $\theta$  is the asphaltene conversion at time  $t$ ,  $k$  is the velocity constant, and  $P$  is the oxidizing gas partial pressure. The above equation can be re-written as Equation (2):

$$\frac{d\theta}{dt} \frac{1}{f(\theta)} = k_o \exp\left(-\frac{E_a}{RT}\right) \cdot P_{O_2}^n \quad (2)$$

where  $k_o$  ( $s^{-1} \cdot MPa^{-n}$ ) is the pre-exponential factor,  $E_a$  ( $kJ \cdot mol^{-1}$ ) the effective activation energy,  $P$  (MPa) the partial pressure of the reactant gas ( $O_2$ ),  $n$  the order of reaction and  $R$  ( $J \cdot mol^{-1} K^{-1}$ ) the gas constant. The function  $f(\theta)$  considers the evolution of the asphaltene with the conversion degree.

Substituting for the heating rate ( $\beta$ ) concerning  $dt$ , where  $dt = dT / \beta$  and using the volumetric model for the consumption of the particle  $f(\theta) = (1 - \theta)$ ,<sup>54</sup> Equation (3) is obtained:

$$\frac{d\theta}{f(\theta)} \beta = k_o P_{O_2}^n \exp\left(-\frac{E_a}{RT}\right) dT \quad (3)$$

Using the Ozawa-Wall-Flyn approximation<sup>54</sup> for the integral of the conversion regarding the temperature integral of the Arrhenius equation, and considering,  $F(\theta) = \int d\theta / f(\theta)$ , Equation (4) is obtained:

$$\ln \left[ \frac{\beta F(\theta)}{P_{O_2}^n T^2} \right] = \ln \left( \frac{k_o R}{E_a} \right) - \frac{E_a}{RT} \quad (4)$$

Further, for asphaltene conversion, it is necessary that  $F(\theta) = \int \frac{d\theta}{1-\theta} = -\ln(1-\theta)$ , considering a volumetric model in the whole temperature range, leading to the general expression (Equation 5):

$$\ln \left[ \frac{\beta(-\ln(1-\theta))}{P_{O_2}^n T^2} \right] = \ln \left( \frac{k_o R}{E_a} \right) - \frac{E_a}{RT} \quad (5)$$

The above equation is linear, and the values of the Arrhenius pre-exponential factor and the effective activation energy are obtained from the intercept and slope. It is worth mentioning that this is a correlation model based on the experimental results obtained at specific operating conditions of the HP-TGA and the asphaltenes extracted.

## 4. Results and discussion

### 4.1. Thermogravimetric analysis

Through high-pressure thermogravimetric (HP-TGA) measurements, this section investigated the effect of temperature, time, asphaltene mass, pressure, and heating rate on the oxidation rate of asphaltenes.

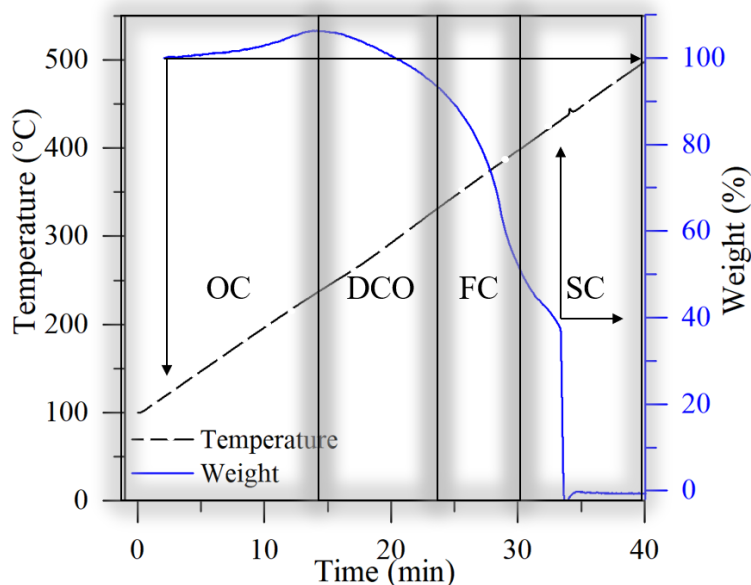
#### 4.1.1. Effect of temperature and time on the oxidation rate of asphaltenes at 6 MPa.

Figure 2 depicts the profiles of asphaltene mass in percentage and temperature during oxidation processes at 6 MPa. The temperature was divided into four regions for practical purposes: oxygen chemisorption region (OC), decomposition of chemisorbed oxygen functional groups (DCO), cracking/first combustion/oxidation (FC), and high-temperature oxidation (HTO)/second combustion (SC). Each region is limited by the atypical behavior of the mass change curve, which defines the zones where the various asphaltene oxidation and decomposition reactions occur. Each limit demonstration is shown in Figures 1-3 of the Appendix A.

The OC region is the temperature range in which oxygen is chemisorbed over the asphaltene molecular structure and aggregates. DCO, on the other hand, is the zone where the first mass loss is observed, which is primarily associated with the decomposition or loss of the oxygenated functional groups. Finally, the regions of first and second combustion are where the



increase in temperature consumes the entire amount of asphaltene. These last two regions differ after the thermal event at around 400 °C. The difference in the mass loss profile between experiments at low pressure values is due to an increase in mass in the OC zone, which has not been observed in previous reports.<sup>55-59</sup>



**Figure 2.** Mass in percentage and temperature profile for asphaltene oxidation under an air atmosphere at 6 MPa discretized in four regions called: *i*) oxygen chemisorption (OC) region, *ii*) decomposition of the chemisorbed oxygen (DCO) region, *iii*) first combustion (FC) region, and *iv*) second combustion (SC) region. Heating rate: 10 °C·min<sup>-1</sup>, air flow: 80 mL·min<sup>-1</sup> and sample mass: 6 mg.

#### 4.1.2. Effect of asphaltene mass.

To evaluate the diffusional limitations, asphaltene oxidation was performed using a high-pressure thermogravimetric analyzer and varying the mass sample. Figure 3a-c depicts the (a) mass percentage, (b) mass loss rate, and (c) temperature profiles of asphaltene oxidation in an air atmosphere with sample masses of 0.8, 1, 4, and 6 mg at a fixed pressure of 6 MPa. Figure 3a shows that at this pressure, the mass of the samples increases at low temperatures up to 250 °C. This phenomenon may be related to oxygen chemisorption (OC) on the chemical structure of asphaltenes as well as the thermal expansion of asphaltene aggregates.<sup>60, 61</sup>

The highest mass increase at  $T < 250$  °C is observed for 0.8 and 1 mg of mass sample, followed by 4 and 6 mg due to a higher distribution of asphaltenes in the sample holder at low mass samples and, thus, greater

oxygen diffusion (Figure 3a).<sup>62</sup> The samples then lose mass at temperatures greater than 250 °C. Initially, it can be attributed to the desorption and decomposition of previously absorbed oxygen functional groups, followed by a rapid fall because the material undergoes exothermic reactions, which are reflected in the change in slope around 400 °C, which is more pronounced in the sample with a lower percentage of oxygen chemisorption (6 mg).

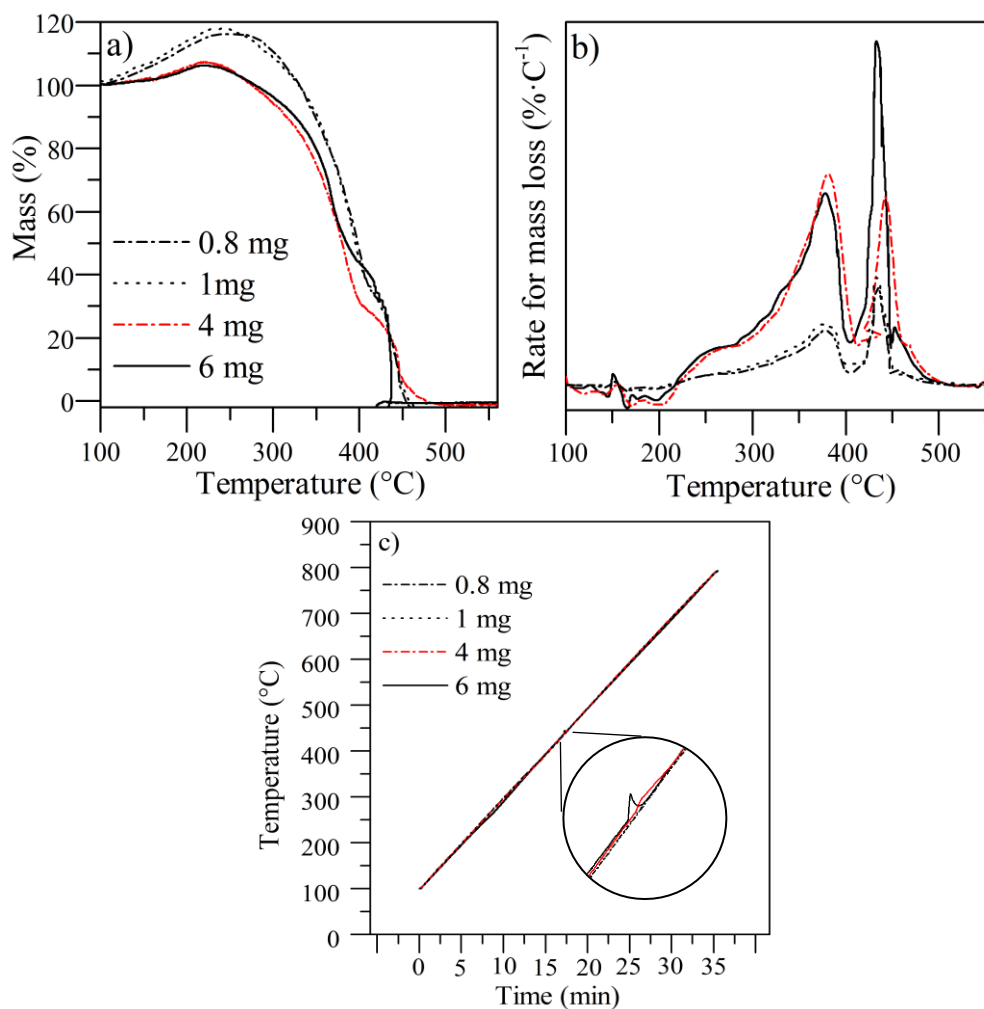


**Figure 3.** a) Percentage of mass loss, b) rate for mass loss, and c) temperature profiles for asphaltene oxidation under air atmosphere varying the sample mass in 0.84 mg, 1 mg, 4 mg, and 6 mg. Heating rate: 10 °C·min<sup>-1</sup>, pressure: 6 MPa, and airflow: 80 mL·min<sup>-1</sup>.

This is confirmed at temperatures less than 250 °C, where a smaller amount of oxygen is absorbed as the sample mass increases (Figure 3a). A change in the temperature profile is also observed around 400 °C (see Figure 3c), which may be explained by the occurrence of exothermic reactions, as the temperature generated is higher than that programmed for the test in the HP-

TGA 750 equipment. This behavior is consistent with the findings of Zhao et al.<sup>39</sup>, who found that high-pressure conditions boosted exothermic oxidative reactions of heavy oil related to the conversion of lighter chemical compounds using high-pressure differential scanning calorimetry.<sup>39</sup> Heat conduction and mass diffusion mechanisms (Figure 3c) are expected to be inhibited because there is no abnormal increase in temperature at any point for 0.8 and 1 mg.

These findings suggest that oxygen chemisorption influences other thermal events, as the number and type of oxygen structures formed in OC influence the asphaltene thermal response at higher temperatures. As a result, the different masses of asphaltenes will have different thermal reactivity, which will be reflected in the temperature interval changes of each region. Furthermore, Figure 3b depicts the rate of mass loss for asphaltenes at 6 MPa for the various initial masses considered. The decomposition of asphaltenes is influenced by the mass employed in the experiment, which is consistent with the results obtained by Trejo et al.<sup>63</sup> and Song et al.<sup>64</sup>

Furthermore, the mass change and rate for mass loss profiles for 1 and 0.8 mg show no significant differences in mass and thermal profiles (Figures 3a,c). To avoid diffusional effects, an initial mass sample of 1 mg will be used for subsequent experiments.

#### 4.1.3. Effect of pressure on asphaltene oxidation.

HP-TGA measurements were conducted using 1 mg of the sample due to the results obtained in the previous section. The profiles of the rate for mass change and mass change of asphaltenes during oxidation at different pressures are shown in Figure 4.

The asphaltene mass change curve indicates that the asphaltene oxidation phenomenon is pressure-dependent and occurs in four main stages, supporting that the asphaltenes thermal oxidation consists of multiple parallel and subsequent complex reactions.<sup>47, 65, 66</sup> Figure 4a-f shows that for  $P < 0.3$  MPa, only FC and SC regions are appreciated. This result indicates that pressure is essential in decomposing asphaltenes in an air atmosphere. These results agree with Hosseinpour et al.<sup>67</sup>, who evaluated the oxidation of asphaltenes at low-pressure conditions and found that the OC and DCO regions are insignificant, and the gaseous products appear at temperatures above 300 °C, where the first and second combustion thermal events occur. The results also agree with the easy bond scission, and the volatile content of

the asphaltenes are driven off as light hydrocarbons at similar temperatures.<sup>67</sup> Thereby, the lower temperature peak in the rate for mass loss for asphaltene oxidation seems to arise from low combustion of less-refractory moieties in the asphaltene structure.<sup>58</sup>

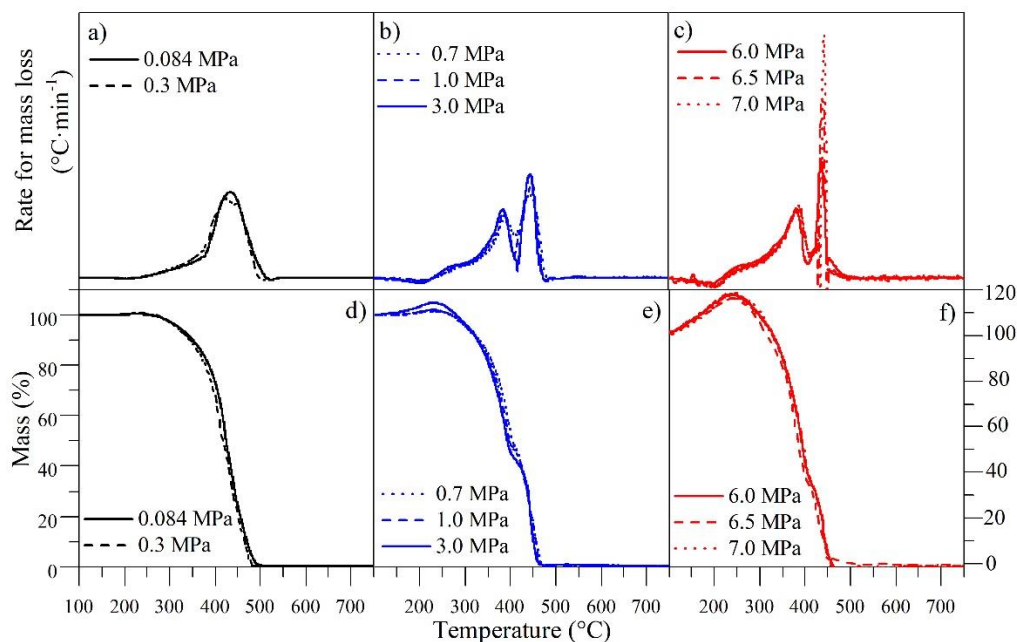


**Figure 4.** Rate for mass loss and mass percentage for asphaltene oxidation under an air atmosphere at (a, d) 0.084 MPa and 0.3 MPa, (b,e) 0.7 MPa, 1 MPa and 3 MPa, and (c, f) 6 MPa, 6.5 MPa, and 7 MPa. Heating rate: 10 °C·min<sup>-1</sup>, air flow: 80 mL·min<sup>-1</sup>, and sample mass: 1 mg.

In this context, the increase in pressure favors the oxygen chemisorption of oxygen on asphaltenes at low temperatures (<250 °C). The immediate exposure of asphaltenes can explain this result to oxygen and increase the rate of bond cleavage and the evolution of oxidation products.<sup>67,68</sup> On the other hand, the behavior of the mass percentage curves in Figure 4d-f during the transition from the first to second combustion region (approximately at 400 °C) at high-pressure conditions suggests a contribution of adding and decomposition reactions.<sup>67</sup> Additionally, high-pressure conditions increase the probability of collision events between the oxygen molecules, increasing the kinetic energy and triggering a more rapid exothermic reaction.<sup>69, 70</sup> The remaining asphaltenes are completely burned at higher temperatures (around 400 °C - 500 °C). Because the aliphatic chains of the original asphaltenes are expected to react during the first two thermal events, these structures have a low H/C and a high aromaticity. The oxidation of these

structures begins with the oxidation of the most reactive sites on the condensate structures' peripheral atoms. Finally, oxygenated groups can be formed in the basal plane of the aromatic structures, increasing the kinetics of hydrocarbon consumption.<sup>71</sup>

From the mass loss rate, it is observed that the pressure generates a positive effect over the asphaltene decomposition at lower temperatures in the DCO region, starting around 220 °C for 7 MPa (Figure 4a, c). Also, there is a significant increase in the mass loss rate at high-pressure conditions above 400 °C (during the SC event), which could be associated with the energy released by the generation of strong and significant exothermic reactions.<sup>72</sup> The pressure controls this behavior since for  $P < 0.7$  MPa, this phenomenon does not occur, while as the pressure increases, the magnitude of the decomposition peak in the SC region rises.<sup>72</sup> Table 1 shows the fractional mass loss/gain and temperature intervals for each region at different pressures; this is obtained through a DTG (derivative thermogravimetric) signal decomposition using Lorentzian-gaussian functions.<sup>73</sup>

From the data in Table 1, three main important results are observed. The first one is that for pressures higher than 0.3 MPa, the OC region finishes at lower temperatures as the pressure increases, and the amount of oxygen chemisorbed on asphaltene molecular structure follows the order  $0.7 \text{ MPa} < 1 \text{ MPa} < 3 \text{ MPa} < 6 \text{ MPa} < 6.5 \text{ MPa} < 7 \text{ MPa}$ . In the case of the first and second combustion regions, due to the positive influence of pressure on the oxidation of asphaltene, each requires less energy to carry out under high pressure than under low-pressure conditions because the process starts at lower temperatures. Therefore, the temperature at the end of each phenomenon follows the same order as the oxygen chemisorption region. Another significant result is found in the DCO region, where the mass loss is greater than the mass gain in the previous event, suggesting that in this temperature interval, the decomposition of the functional groups formed by the chemisorbed oxygen could take place in the form of  $\text{CO}_2$  and  $\text{CO}$ , as a result of competitive reactions between the decomposition of the groups included in the first thermolabile chemisorption, and the new oxidation of the structure.<sup>60, 61</sup>

**Table 1.** Thermogravimetric characteristics of asphaltene oxidation at different pressures divided into four thermal events: *i*) oxygen chemisorption (OC) region, *ii*) decomposition of the chemisorbed oxygen (DCO) region, *iii*) first combustion (FC) region, and *iv*) second combustion (SC) region. Heating rate: 10 °C·min<sup>-1</sup>, mass sample: 1 mg, and airflow: 80mL·min<sup>-1</sup>

Pressure (MPa)	OC Region		DCO Region		FC Region		SC Region	
	Temperature range (°C)	Mass gain (mass fraction in %)	Temperature range (°C)	Mass loss (mass fraction in %)	Temperature range (°C)	Mass loss (mass fraction in %)	Temperature range (°C)	Mass loss (mass fraction in %)
0.084	-	-	-	-	100-400	20.0	401-550	80.0
0.3	100-255	1.2	256-350	5.7	351-400	25.5	100-540	74.5
0.7	100-252	1.8	253-345	6.8	346-411	38.7	412-525	56.8
1.0	100-250	2.0	251-338	8.0	339-405	40.0	406-521	52.0
3.0	100-240	5.0	242-335	10.0	336-403	44.5	404-518	50.5
6.0	100-225	18.0	226-330	23.5	331-401	45.0	402-510	49.5
6.5	100-220	18.5	221-329	25.0	330-400	48.0	401-501	45.5
7.0	100-220	19.0	221-328	27.2	329-399	50.0	400-499	41.8

Finally, the mass loss obtained in each test during the first combustion increases as pressure increases; this means that despite favoring oxidation reactions, the increase in pressure also increases the rate of decomposition reactions. Hence, the rise in pressure reduced the mass loss in the second combustion event.

#### 4.1.4. Effect of the heating rate

Figure 5 depicts the effect of heating rate on asphaltene oxidation in an air atmosphere at a pressure of 6 MPa and a mass sample of 1 mg. As the heating rate increases, the temperature intervals for the thermal regions shift at higher temperatures. The second combustion region is partially inhibited at a heating rate of 5 °C·min<sup>-1</sup>, implying that the asphaltenes are mostly decomposed in the first combustion. The intensity of the second peak of the mass loss rate in Figure 5a reflects this. Furthermore, as the heating rate increases, the intensity of the second peak increases, indicating that low heating rates favor the decomposition of asphaltenes in the first combustion region.

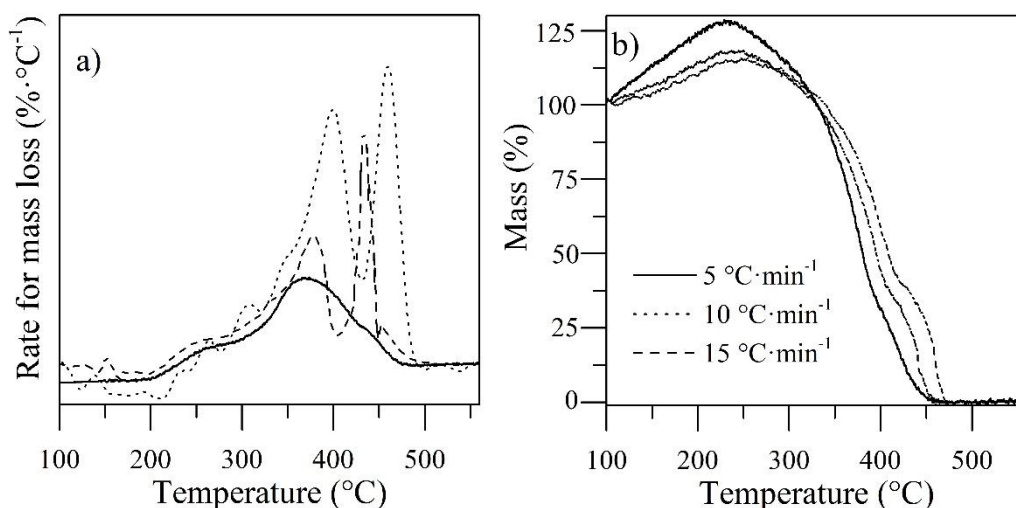


**Figure 5.** a) Rate for mass change and b) mass in percentage for asphaltene oxidation under an air atmosphere at different heating rates from  $5\text{ }^{\circ}\text{C}\cdot\text{min}^{-1}$  to  $15\text{ }^{\circ}\text{C}\cdot\text{min}^{-1}$ . Airflow:  $80\text{mL}\cdot\text{min}^{-1}$ , pressure:  $6\text{ MPa}$ , and sample mass:  $1\text{ mg}$ .

Thereby, the mass lost in the first combustion decreases as the heating rate increases, indicating that the prevalence of decomposition reactions diminishes oxygen chemisorption over the asphaltene molecular structure. In the case of asphaltene oxidation kinetics at low pressures, oxygen chemisorption is insignificant, regardless of the heating rate used.<sup>47, 55, 56, 58, 74</sup> Therefore, a direct relationship between asphaltene decomposition and heating rate changes is observed. Table 2 summarizes the temperature ranges and mass loss of asphaltenes obtained in each test.

**Table 2.** Thermogravimetric characteristics of asphaltene oxidation at different heating rates for the different thermal events: i) oxygen chemisorption (OC) region, ii) decomposition of the chemisorbed oxygen (DCO) region, iii) first combustion (FC) region, and iv) second combustion (SC) region. Pressure: 6 MPa, mass sample: 1 mg, and airflow: 80 mL·min<sup>-1</sup>.

Pressure (MPa)	Heating Rate (°C·min <sup>-1</sup> )	OC Region		OCD Region		FC Region		SC Region	
		Temperature range (°C)	Mass gain (mass fraction in %)	Temperature range (°C)	Mass loss (mass fraction in %)	Temperature range (°C)	Mass loss (mass fraction in %)	Temperature range (°C)	Mass loss (mass fraction in %)
6	5	100-220	25.5	221-305	36.0	306-390	70.0	391-470	19.5
	10	100-225	18.0	226-330	23.5	331-410	45.0	411-510	45.0
	15	100-230	16.5	231-340	21.0	341-440	44.0	451-530	51.5

#### 4.2. Estimation of kinetic parameters of asphaltene oxidation

Thermal processes are aided by numerous competing complex reactions. The mass change is caused by the simultaneous combustion of several oxidized components, which divides their decomposition into four distinct regions. Using the model described in Section 3.0, the effective activation energy required to carry out the different thermal events was calculated.<sup>52</sup> For this,  $\ln \left[ \frac{\beta(-\ln(1-x))}{P_{O_2} T^2} \right]$  vs  $1 \times T_i^{-1}$  plots were constructed and are shown in Figure 6. The value for the effective activation energy ( $E_a$ ) was estimated from the slope of the line and the Arrhenius constant ( $k_o$ ) from the intercept. A good fit ( $R^2 > 0.99$ ) was found when assuming a first-order reaction over the temperature intervals evaluated. It is worth mentioning that a good fitting of the first order is achieved because the asphaltene oxidation was discretized for different regions; this means that the reactions approach simple first-order systems for each interval in which the TGA curves are divided. This analysis, however, should not be used to examine the entire range of decomposition because the same division indicates an order greater than 3. Due to the complexity of the molecular structure and the various thermal events that occur during this process, a reaction order greater than three should be considered to perform a thorough examination of the reaction order in the decomposition/oxidation of asphaltenes at high pressures.



In general, the  $E_a$  values for the OC, DCO, FC, and SC varied from 39.12 kJ·mol<sup>-1</sup> to 83.46 kJ·mol<sup>-1</sup>, 64.47 kJ·mol<sup>-1</sup> to 223.84 kJ·mol<sup>-1</sup>, 108.97 kJ·mol<sup>-1</sup> to 42.04 kJ·mol<sup>-1</sup>, and 210.71 kJ·mol<sup>-1</sup> to 53.43 kJ·mol<sup>-1</sup>, for 0.084 MPa - 7 MPa, respectively.

Considering the mass change in each region, it is observed that for the de OC and DCO regions, the effective activation energy required to decompose the asphaltenes follows the opposite trend to that reported in the literature, because in these scenarios, a high conversion is directly related to high activation energy values, which can be associated with the oxygen chemisorbed on the active sites of the asphaltenes, i.e., aromatic core and heteroatoms, and the formation of labile oxides in the new structure. Another explanation could be that isoconversional methods for calculating activation energy do not account for different mechanisms as a function of heating rate. Thus, unlike the other regions, the activation energy of the OC and DCO increases as pressure increases due to the nature of the functional groups formed during OC, which are more reactive than those formed under low-pressure conditions.<sup>75</sup> Nevertheless, pressure generates a positive effect over asphaltene decomposition under an oxidative atmosphere since an increase of  $E_a$  during OC and DCO implies less energy to complete the total combustion of the material during FC and SC regions. This result could be explained because the reaction rate of the gas injected increases significantly with the pressure increase, which is equivalent to increasing the activity of the reactants and the gas concentration.

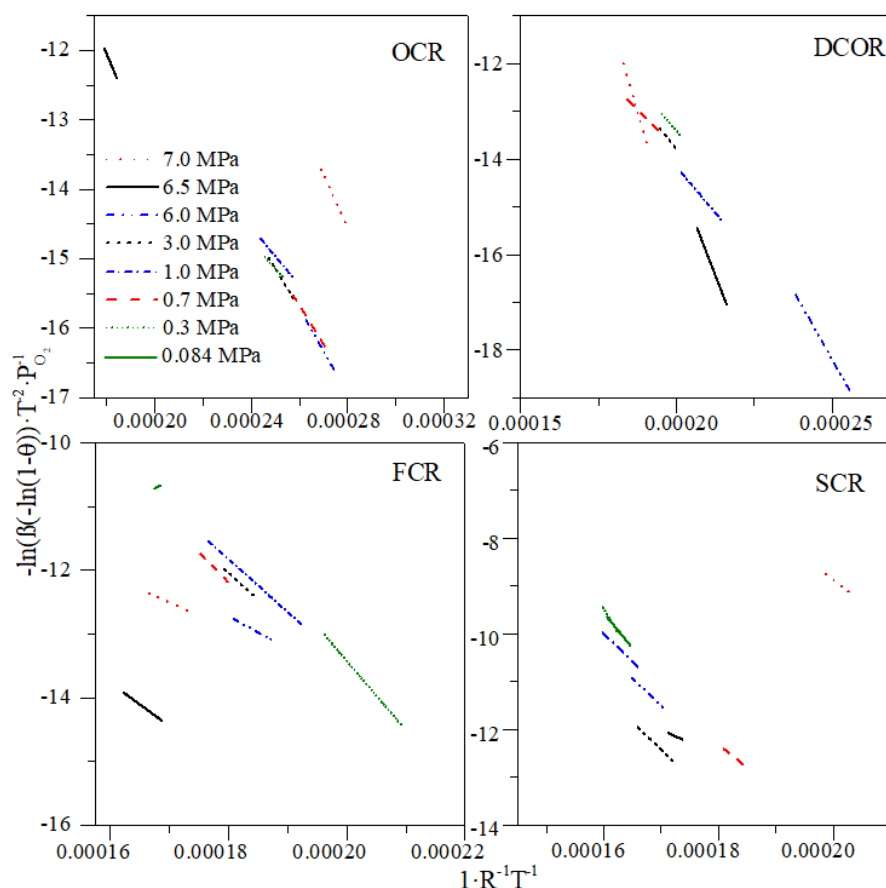


**Figure 6.** Arrhenius plot of asphaltene oxidation at different pressure for (a) oxygen chemisorption (OC) region, (b) decomposition of the chemisorbed oxygen (DCO) region, (c) first combustion (FC) region, and (d) second combustion (SC) region. Heating rate:  $10\text{ }^{\circ}\text{C}\cdot\text{min}^{-1}$ , mass sample:  $1\text{ mg}$ , and airflow:  $80\text{ mL}\cdot\text{min}^{-1}$ .

Table 3 shows the activation energy and Arrhenius constant values for the asphaltene decomposition at the different pressures evaluated in the different regions. In general, for pressures lower than  $0.3\text{ MPa}$ , the energy required increases as follows:  $\text{OC} < \text{DCO} < \text{FC} < \text{SC}$  region, corroborating that the degree of oxygen chemisorption at low pressures is not significant compared to pressures of around  $6\text{ MPa}$  or higher and showing that the oxygen chemisorption is the most thermodynamically favorable event for these conditions. On the other hand, for the systems evaluated at  $6\text{ MPa}$ ,  $6.5\text{ MPa}$ , and  $7\text{ MPa}$ , the activation energy on the DCO thermal event is greater than for the other regions due to the amount of functional groups that are decomposed in this region that depends of the OC. Also, the pressure increment shows that the energy required in the FC and SC regions is diminished, which favors its total thermal decomposition at lower

temperatures. The most important impact for its reduction is the decrease in energy consumption from 0.084 MPa to 7 MPa in the second combustion event, decreasing the value by approximately 71.19 % and alluding to the decomposition generated in the other regions under high-pressure conditions. On the other hand, the energy required to decompose the fractions in the DCO region (for pressures above 6 MPa) is greater than that for the first combustion due to the functional groups formed in the asphaltenes.

Table 3 shows that the pre-exponential factor has a significant dependency on the pressure with changes by several orders of magnitude as the pressure increases from 0.084 MPa to 7 MPa. The pre-exponential factor is linked to the activation energy, that is, to the different degrees of disorder the system will have when it goes from the reactive to the transition state.<sup>66</sup> This depends fundamentally on the number of accessible states whereby the low values obtained from the Arrhenius constant for the oxygen chemisorption region could be related to the change in entropy change that is produced due to the molecular disorganization of the system at the time of the union of reagents to give an activated complex.<sup>69, 76</sup> In this same way, the decrease of the pre-exponential factor is explained by the increase in pressure for the FC and SC regions. In all cases, the rise in pressure modifies the kinetic parameters, displaying positive effects on the reaction rate for the asphaltene oxidation process.

The kinetic parameter values were calculated for the systems evaluated at a different heating rate from the OC to SC region and are shown in Table 4. The effective activation energy values corroborate the results obtained for the mass change and rate for mass change at different heating rates at high-pressure conditions (6 MPa). For the OC and DCO regions, an increase in the heating rate implies a low decrease in the energy required to carry out the asphaltene decomposition reactions in an oxidative atmosphere. Anyhow, the FC and SC regions show that the energy decreases to a greater degree with the increase in heating rate. The most significant effect is found in the second combustion region, where the activation energy decreases around 33 kJ·mol<sup>-1</sup> because, at a heating rate of 15 °C·min<sup>-1</sup>, the adsorptive phenomenon of oxygen is drastically reduced. Hence, high molecular mass compounds are not created through bonds formed with the oxygen heteroatoms. Thus, the energy needed in the subsequent regions is only required to decompose the original molecular structure of asphaltenes.

**Table 3.** Estimated kinetic parameters at different pressures over oxidation atmosphere for the different regions a) oxygen chemisorption (OC) region, b) decomposition of the chemisorbed oxygen (DCO) region, c) first combustion (FC) region, and d) second combustion (SC) region. Heating rate: 10 °C·min<sup>-1</sup>, mass sample: 4 mg, and airflow: 80 mL·min<sup>-1</sup>.

Pressure (MPa)	OC Region			DCO Region		
	$E_a$ (kJ·mol <sup>-1</sup> )	$k_o$ (min <sup>-1</sup> ·MPa <sup>-1</sup> )	R <sup>2</sup>	$E_a$ (kJ·mol <sup>-1</sup> )	$k_o$ (min <sup>-1</sup> ·MPa <sup>-1</sup> )	R <sup>2</sup>
0.084	-	-	-	-	-	-
0.3	39.12	2.21x10 <sup>-2</sup>	0.99	64.47	3.21x10 <sup>1</sup>	0.99
0.7	42.34	6.40x10 <sup>-2</sup>	0.99	75.03	33.69x10 <sup>1</sup>	0.97
1.0	56.23	23.64x10 <sup>-1</sup>	0.98	77.25	44.31x10 <sup>1</sup>	0.98
3.0	58.09	38.01x10 <sup>-1</sup>	0.99	78.76	67.71x10 <sup>1</sup>	0.99
6.0	62.43	12.79x10 <sup>1</sup>	0.99	115.99	68.53x10 <sup>4</sup>	0.99
6.5	76.85	1.22x10 <sup>2</sup>	0.97	169.05	59.05x10 <sup>8</sup>	0.98
7.0	83.46	1.98x10 <sup>2</sup>	0.99	223.84	10.13x10 <sup>13</sup>	0.98

Pressure (MPa)	FC Region			SC Region		
	$E_a$ (kJ·mol <sup>-1</sup> )	$k_o$ (min <sup>-1</sup> ·MPa <sup>-1</sup> )	R <sup>2</sup>	$E_a$ (kJ·mol <sup>-1</sup> )	$k_o$ (min <sup>-1</sup> ·MPa <sup>-1</sup> )	R <sup>2</sup>
0.084	108.97	56.47x10 <sup>3</sup>	0.99	210.71	85.55x10 <sup>10</sup>	0.99
0.3	94.73	14.67x10 <sup>2</sup>	0.99	147.06	20.54x10 <sup>6</sup>	0.99
0.7	83.46	22.70x10 <sup>1</sup>	0.97	119.12	12.44x10 <sup>4</sup>	0.99
1.0	83.03	19.77x10 <sup>1</sup>	0.98	116.77	23.36x10 <sup>3</sup>	0.97
3.0	81.52	88.13x10 <sup>-2</sup>	0.98	114.22	22.93x10 <sup>3</sup>	0.97
6.0	68.74	52.13x10 <sup>-2</sup>	0.99	99.35	31.11x10 <sup>2</sup>	0.99
6.5	47.71	26.34x10 <sup>-2</sup>	0.97	94.56	25.91x10 <sup>2</sup>	0.98
7.0	42.04	43.05x10 <sup>-7</sup>	0.99	53.43	34.28x10 <sup>-2</sup>	0.98

Furthermore, the changes in effective activation energy and thermogravimetric characteristics shown in Table 2 suggest that the heating rate influences asphaltene oxidation/decomposition. A decrease in this variable indicates that the sample was exposed to the reaction gas for a longer period. As a result, the aromatic structure may be condensed, resulting in more thermodynamically stable species. Therefore, higher effective activation energy values are required; additionally, several reaction mechanisms are produced during the thermal events for the different heating rates. For this reason, isoconversional methods for estimating effective activation energy should be avoided when assessing asphaltene decomposition in different atmospheres.

**Table 4.** Estimated kinetic parameters at different heating rates for asphaltene oxidation during the different regions: *i*) oxygen chemisorption *ii*) decomposition of the chemisorbed oxygen (DCO) region, *iii*) first combustion (FC) region, and *iv*) second combustion (SC) region. Pressure: 6 MPa, mass sample: 1 mg, and airflow: 80 mL·min<sup>-1</sup>.

Heating rate (°Cmin <sup>-1</sup> )	OC Region			DCO Region		
	$E_a$ (kJ·mol <sup>-1</sup> )	$k_o$ (min <sup>-1</sup> ·MPa <sup>-1</sup> )	R <sup>2</sup>	$E_a$ (kJ·mol <sup>-1</sup> )	$k_o$ (min <sup>-1</sup> ·MPa <sup>-1</sup> )	R <sup>2</sup>
5	67.66	5.33x10 <sup>4</sup>	0.97	119.55	9.13x10 <sup>5</sup>	0.99
10	62.43	1.28x10 <sup>2</sup>	0.99	115.99	6.85x10 <sup>5</sup>	0.99
15	55.21	1.04x10 <sup>-2</sup>	0.99	105.01	1.33x10 <sup>2</sup>	0.98
Heating rate (°Cmin <sup>-1</sup> )	FC Region			SC Region		
	$E_a$ (kJ·mol <sup>-1</sup> )	$k_o$ (min <sup>-1</sup> ·MPa <sup>-1</sup> )	R <sup>2</sup>	$E_a$ (kJ·mol <sup>-1</sup> )	$k_o$ (min <sup>-1</sup> ·MPa <sup>-1</sup> )	R <sup>2</sup>
5	85.88	1.18x10 <sup>-3</sup>	0.98	127.19	5.25x10 <sup>4</sup>	0.98
10	68.74	5.21x10 <sup>-1</sup>	0.99	99.35	3.11x10 <sup>3</sup>	0.99
15	45.49	6.37x10 <sup>2</sup>	0.99	78.73	1.19x10 <sup>1</sup>	0.98

## 5. Conclusions.

Asphaltene oxidation tests were performed to determine the effect of pressure on its decomposition and the kinetic parameters involved. It was discovered that pressure has a positive effect on asphaltene oxidation. Above 0.3 MPa, the decomposition of asphaltenes is divided into four distinct regions, which are determined by the predominant phenomenon. Oxygen chemisorption, decomposition of the oxygen chemisorbed, and first and second combustion were the regions observed through the behavior of the mass loss of the asphaltenes at non-isothermal conditions.

Pressure increases imply an increase in activation energy for the OC and DCO regions and a decrease in activation energy for the remaining stages, primarily in the second combustion region, where the activation energy is reduced the most compared to the other events. Because of the previous breaking during the thermal event, the coke produced at the end of the first combustion region has a lower content of heavy asphaltene components. On the other hand, reduced heating rate, resulted in a significant shift in the reaction regions, such that at the heating ramp of 5 °C·min<sup>-1</sup>, the asphaltene is decomposed in its highest percentage in the first combustion region, partially inhibiting the last combustion. It is worth noting that the kinetic parameters obtained can be used to understand the kinetic behavior of the

thermal decomposition of asphaltenes as well as the effect of pressure in an oxidative environment.

## References

1. Hirsch, R. L., Mitigation of maximum world oil production: Shortage scenarios. *Energy policy* **2008**, 36, (2), 881-889.
2. De Castro, C.; Miguel, L. J.; Mediavilla, M., The role of non conventional oil in the attenuation of peak oil. *Energy Policy* **2009**, 37, (5), 1825-1833.
3. Speight, J. G., *Heavy oil production processes*. Gulf Professional Publishing: 2013.
4. Curtis, C.; Kopper, R.; Decoster, E.; Guzmán-García, A.; Huggins, C.; Knauer, L.; Minner, M.; Kupsch, N.; Linares, L. M.; Rough, H., Heavy-oil reservoirs. *Oilfield Review* **2002**, 14, (3), 30-51.
5. Elahi, S. M.; Scott, C. E.; Chen, Z.; Pereira-Almao, P., In-situ upgrading and enhanced recovery of heavy oil from carbonate reservoirs using nano-catalysts: Upgrading reactions analysis. *Fuel* **2019**, 252, 262-271.
6. Santos, R.; Loh, W.; Bannwart, A.; Trevisan, O., An overview of heavy oil properties and its recovery and transportation methods. *Brazilian Journal of Chemical Engineering* **2014**, 31, (3), 571-590.
7. Dorian, J. P.; Franssen, H. T.; Simbeck, D. R., Global challenges in energy. *Energy Policy* **2006**, 34, (15), 1984-1991.
8. Owen, N. A.; Inderwildi, O. R.; King, D. A., The status of conventional world oil reserves—Hype or cause for concern? *Energy policy* **2010**, 38, (8), 4743-4749.
9. Kokal, S.; Aramco, S., Crude Oil Emulsions: A State-Of-The-Art Review. *SPE Production & Facilities* **2005**, 20, 5-13.
10. Luo, P.; Gu, Y., Effects of asphaltene content on the heavy oil viscosity at different temperatures. *Fuel* **2007**, 86, (7-8), 1069-1078.
11. Medina, O. E.; Gallego, J.; Restrepo, L. G.; Cortés, F. B.; Franco, C. A., Influence of the Ce<sup>4+</sup>/Ce<sup>3+</sup> Redox-Couple on the Cyclic Regeneration for Adsorptive and Catalytic Performance of NiO-PdO/CeO<sub>2</sub>±δ Nanoparticles for n-C<sub>7</sub> Asphaltene Steam Gasification. *Nanomaterials* **2019**, 9, (5), 734.

12. Mullins, O. C.; Sheu, E. Y., *Structures and dynamics of asphaltenes*. Springer Science & Business Media: 2013.
13. Mansoori, G. A., Modeling of asphaltene and other heavy organic depositions. *Journal of petroleum science and engineering* **1997**, 17, (1-2), 101-111.
14. Mannistu, K.; Yarranton, H.; Masliyah, J., Solubility modeling of asphaltenes in organic solvents. *Energy & fuels* **1997**, 11, (3), 615-622.
15. Sabbah, H.; Morrow, A. L.; Pomerantz, A. E.; Zare, R. N., Evidence for island structures as the dominant architecture of asphaltenes. *Energy & Fuels* **2011**, 25, (4), 1597-1604.
16. Alshareef, A. H.; Scherer, A.; Tan, X.; Azyat, K.; Stryker, J. M.; Tykwinski, R. R.; Gray, M. R., Formation of archipelago structures during thermal cracking implicates a chemical mechanism for the formation of petroleum asphaltenes. *Energy & Fuels* **2011**, 25, (5), 2130-2136.
17. Groenzin, H.; Mullins, O. C., Molecular size and structure of asphaltenes from various sources. *Energy & Fuels* **2000**, 14, (3), 677-684.
18. Acevedo, S.; Castro, A.; Negrin, J. G.; Fernández, A.; Escobar, G.; Piscitelli, V.; Delolme, F.; Dessalces, G., Relations between asphaltene structures and their physical and chemical properties: The rosary-type structure. *Energy & fuels* **2007**, 21, (4), 2165-2175.
19. Mullins, O. C.; Sabbah, H.; Eyssautier, J.; Pomerantz, A. E.; Barré, L.; Andrews, A. B.; Ruiz-Morales, Y.; Mostowfi, F.; McFarlane, R.; Goual, L., Advances in asphaltene science and the Yen–Mullins model. *Energy & Fuels* **2012**, 26, (7), 3986-4003.
20. Acevedo, S.; Escobar, O.; Echevarria, L.; Gutiérrez, L. B.; Méndez, B., Structural analysis of soluble and insoluble fractions of asphaltenes isolated using the PNP method. Relation between asphaltene structure and solubility. *Energy & fuels* **2004**, 18, (2), 305-311.
21. Montes, D.; Orozco, W.; Tabora, E. A.; Franco, C. A.; Cortés, F. B., Development of Nanofluids for Perdurability in Viscosity Reduction of Extra-Heavy Oils. *Energies* **2019**, 12, (6), 1068.
22. Franco, C. A.; Lozano, M. M.; Acevedo, S.; Nassar, N. N.; Cortés, F. B., Effects of resin I on asphaltene adsorption onto nanoparticles: a novel method for obtaining asphaltenes/resin isotherms. *Energy & Fuels* **2015**, 30, (1), 264-272.

23. Acevedo, S.; Méndez, B.; Rojas, A.; Layrisse, I.; Rivas, H., Asphaltenes and resins from the Orinoco basin. *Fuel* **1985**, 64, (12), 1741-1747.
24. Ilyin, S.; Arinina, M.; Polyakova, M.; Bondarenko, G.; Konstantinov, I.; Kulichikhin, V.; Malkin, A., Asphaltenes in heavy crude oil: Designation, precipitation, solutions, and effects on viscosity. *Journal of Petroleum Science and Engineering* **2016**, 147, 211-217.
25. Padula, L.; Balestrin, L. B. d. S.; Rocha, N. d. O.; de Carvalho, C. H. M.; Westfahl Jr, H.; Cardoso, M. B.; Sabadini, E.; Loh, W., Role of asphaltenes and additives on the viscosity and microscopic structure of heavy crude oils. *Energy & Fuels* **2016**, 30, (5), 3644-3651.
26. Guo, K.; Li, H.; Yu, Z., In-situ heavy and extra-heavy oil recovery: A review. *Fuel* **2016**, 185, 886-902.
27. Kök, M.; Keskin, C. In *Comparative combustion kinetics for in-situ combustion process*, IOR 1999-10th European Symposium on Improved Oil Recovery, 1999; 1999.
28. Ozbas, K. E.; Hicyilmaz, C.; Kök, M. V.; Bilgen, S., Effect of cleaning process on combustion characteristics of lignite. *Fuel processing technology* **2000**, 64, (1-3), 211-220.
29. Alexander, J. D.; Dew, J. N.; Martin, W. L., Low temperature in-situ combustion. In Google Patents: 1965.
30. Dabbous, M. K.; Fulton, P. F., Low-temperature-oxidation reaction kinetics and effects on the in-situ combustion process. *Society of Petroleum Engineers Journal* **1974**, 14, (03), 253-262.
31. Greaves, M.; Xia, T. X.; Ayasse, C. In *Underground upgrading of heavy oil using THAI-'toe-to-heel air injection'*, SPE International Thermal Operations and Heavy Oil Symposium, 2005; Society of Petroleum Engineers: 2005.
32. Niu, B.; Ren, S.; Liu, Y.; Wang, D.; Tang, L.; Chen, B., Low-temperature oxidation of oil components in an air injection process for improved oil recovery. *Energy & Fuels* **2011**, 25, (10), 4299-4304.
33. Pu, W.-F.; Liu, P.-G.; Li, Y.-B.; Jin, F.-Y.; Liu, Z.-Z., Thermal characteristics and combustion kinetics analysis of heavy crude oil catalyzed by metallic additives. *Industrial & Engineering Chemistry Research* **2015**, 54, (46), 11525-11533.



34. Zhao, R.; Chen, Y.; Huan, R.; Castanier, L. M.; Kovscek, A. R., An experimental investigation of the in-situ combustion behavior of Karamay crude oil. *Journal of Petroleum Science and Engineering* **2015**, 127, 82-92.
35. Zhang, X.; Liu, Q.; Fan, Z.; Liu, Q., An in situ combustion process for recovering heavy oil using scaled physical model. *Journal of Petroleum Exploration and Production Technology* **2019**, 1-8.
36. Zhang, X.; Liu, Q.; Fan, Z.; Liu, Y., Enhanced heavy oil recovery and performance by application of catalytic in-situ combustion. *Petroleum Science and Technology* **2019**, 37, (5), 493-499.
37. Burger, J. G., Chemical aspects of in-situ combustion-heat of combustion and kinetics. *Society of Petroleum Engineers Journal* **1972**, 12, (05), 410-422.
38. Yuan, S.; Jiang, H.; Shi, Y.; Ren, Z.; Wang, J.; Zhang, Y., Study on heavy oil components transformation path based on core analysis during in-situ combustion process. *Fuel* **2019**, 253, 72-78.
39. Zhao, S.; Pu, W.; Varfolomeev, M. A.; Yuan, C.; Qin, S.; Wang, L.; Emelianov, D. A.; Khachatryan, A. A., Thermal behavior and kinetics of heavy crude oil during combustion by high pressure differential scanning calorimetry and accelerating rate calorimetry. *Journal of Petroleum Science and Engineering* **2019**, 106225.
40. Ren, Y.; Freitag, N.; Mahinpey, N. In *A Simple Kinetic Model for Coke Combustion During an In Situ Combustion (ISC) Process*, Canadian International Petroleum Conference, 2005; Petroleum Society of Canada: 2005.
41. Varfolomeev, M. A.; Nurgaliev, D. K.; Kok, M. V., Calorimetric study approach for crude oil combustion in the presence of clay as catalyst. *Petroleum Science and Technology* **2016**, 34, (19), 1624-1630.
42. Kök, M. V.; Varfolomeev, M. A.; Nurgaliev, D. K., Thermal characterization of crude oils in the presence of limestone matrix by TGA-DTG-FTIR. *Journal of Petroleum Science and Engineering* **2017**, 154, 495-501.
43. Kök, M. V.; Varfolomeev, M. A.; Nurgaliev, D. K., Crude oil characterization using tga-dta, tga-ftir and tga-ms techniques. *Journal of Petroleum Science and Engineering* **2017**, 154, 537-542.

44. Kök, M. V.; Pamir, M. R., Pyrolysis and combustion studies of fossil fuels by thermal analysis methods. *Journal of analytical and applied pyrolysis* **1995**, 35, (2), 145-156.
45. Tadema, H.; Wiejdema, J., Spontaneous ignition of oil sands. *Oil Gas J.:(United States)* **1970**, 68, (50).
46. Phillips, C. R.; Luymes, R.; Halahel, T. M., Enthalpies of pyrolysis and oxidation of Athabasca oil sands. *Fuel* **1982**, 61, (7), 639-646.
47. Sonibare, O.; Egashira, R.; Adedosu, T., Thermo-oxidative reactions of Nigerian oil sand bitumen. *Thermochimica Acta* **2003**, 405, (2), 195-205.
48. Cardona, L.; Arias-Madrid, D.; Cortés, F.; Lopera, S.; Franco, C., Heavy oil upgrading and enhanced recovery in a steam injection process assisted by NiO- and PdO-Functionalized SiO<sub>2</sub> nanoparticulated catalysts. *Catalysts* **2018**, 8, (4), 132.
49. Barre, L.; Espinat, D.; Rosenberg, E.; Scarsella, M., Colloidal structure of heavy crudes and asphaltene solutions. *Revue de l'Institut Français du Pétrole* **1997**, 52, (2), 161-175.
50. Medina, O. E.; Gallego, J.; Arias-Madrid, D.; Cortés, F. B.; Franco, C. A., Optimization of the Load of Transition Metal Oxides (Fe<sub>2</sub>O<sub>3</sub>, Co<sub>3</sub>O<sub>4</sub>, NiO and/or PdO) onto CeO<sub>2</sub> Nanoparticles in Catalytic Steam Decomposition of n-C<sub>7</sub> Asphaltenes at Low Temperatures. *Nanomaterials* **2019**, 9, (3), 401.
51. Gimzewski, E., An accurate and compact high-pressure thermogravimetric analyser. *Journal of thermal analysis* **1991**, 37, (6), 1251-1260.
52. Senneca, O.; Vorobiev, N.; Wütscher, A.; Cerciello, F.; Heuer, S.; Wedler, C.; Span, R.; Schiemann, M.; Muhler, M.; Scherer, V., Assessment of combustion rates of coal chars for oxy-combustion applications. *Fuel* **2019**, 238, 173-185.
53. Niksa, S.; Liu, G.-S.; Hurt, R. H., Coal conversion submodels for design applications at elevated pressures. Part I. devolatilization and char oxidation. *Progress in Energy and Combustion Science* **2003**, 29, (5), 425-477.
54. Liu, G.-S.; Niksa, S., Coal conversion submodels for design applications at elevated pressures. Part II. Char gasification. *Progress in energy and combustion science* **2004**, 30, (6), 679-717.
55. Franco, C. A.; Montoya, T.; Nassar, N. N.; Pereira-Almao, P.; Cortés, F. B., Adsorption and subsequent oxidation of colombian asphaltenes onto nickel

and/or palladium oxide supported on fumed silica nanoparticles. *Energy & Fuels* **2013**, 27, (12), 7336-7347.

56. Franco-Ariza, C. A.; Guzmán-Calle, J. D.; Cortés-Correa, F. B., Adsorption and catalytic oxidation of asphaltenes in fumed silica nanoparticles: Effect of the surface acidity. *Dyna* **2016**, 83, (198), 171-179.

57. Nassar, N. N.; Hassan, A.; Luna, G.; Pereira-Almao, P., Kinetics of the catalytic thermo-oxidation of asphaltenes at isothermal conditions on different metal oxide nanoparticle surfaces. *Catalysis today* **2013**, 207, 127-132.

58. Nassar, N. N.; Hassan, A.; Pereira-Almao, P., Comparative oxidation of adsorbed asphaltenes onto transition metal oxide nanoparticles. *Colloids and surfaces A: Physicochemical and Engineering aspects* **2011**, 384, (1-3), 145-149.

59. Nassar, N. N.; Hassan, A.; Pereira-Almao, P., Effect of surface acidity and basicity of aluminas on asphaltene adsorption and oxidation. *Journal of colloid and interface science* **2011**, 360, (1), 233-238.

60. Frakman, Z.; Ignasiak, T.; Lown, E.; Strausz, O., Oxygen compounds in Athabasca asphaltene. *Energy & Fuels* **1990**, 4, (3), 263-270.

61. Furimsky, E.; Duguay, D.; Houle, J., Chemisorption of oxygen by coke deposited on catalyst surface. *Fuel* **1988**, 67, (2), 182-185.

62. Ebrahimpour, O.; Chaouki, J.; Dubois, C., Diffusional effects for the oxidation of SiC powders in thermogravimetric analysis experiments. *Journal of Materials Science* **2013**, 48, (12), 4396-4407.

63. Trejo, F.; Ancheyta, J., Kinetics of asphaltenes conversion during hydrotreating of Maya crude. *Catalysis Today* **2005**, 109, (1-4), 99-103.

64. Song, Q.; He, B.; Yao, Q.; Meng, Z.; Chen, C., Influence of diffusion on thermogravimetric analysis of carbon black oxidation. *Energy & fuels* **2006**, 20, (5), 1895-1900.

65. Murugan, P.; Mahinpey, N.; Mani, T., Thermal cracking and combustion kinetics of asphaltenes derived from Fosterton oil. *Fuel Processing Technology* **2009**, 90, (10), 1286-1291.

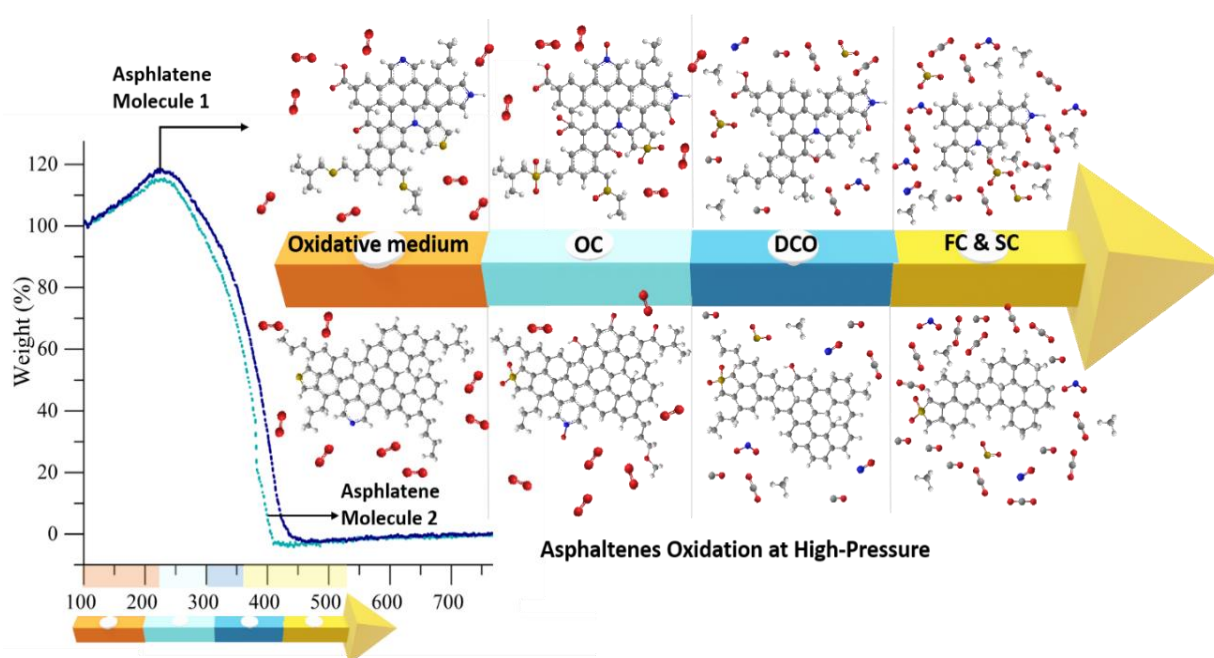
66. Herrington, P. R., Effect of concentration on the rate of reaction of asphaltenes with oxygen. *Energy & fuels* **2004**, 18, (5), 1573-1577.

67. Hosseinpour, N.; Mortazavi, Y.; Bahramian, A.; Khodatars, L.; Khodadadi, A. A., Enhanced pyrolysis and oxidation of asphaltenes adsorbed onto transition metal oxides nanoparticles towards advanced in-situ combustion EOR processes by nanotechnology. *Applied Catalysis A: General* **2014**, *477*, 159-171.
68. Volta, J.-C., Site isolation for light hydrocarbons oxidation. *Topics in Catalysis* **2001**, *15*, (2-4), 121-129.
69. Hänggi, P.; Talkner, P.; Borkovec, M., Reaction-rate theory: fifty years after Kramers. *Reviews of modern physics* **1990**, *62*, (2), 251.
70. Berne, B. J.; Borkovec, M.; Straub, J. E., Classical and modern methods in reaction rate theory. *The Journal of Physical Chemistry* **1988**, *92*, (13), 3711-3725.
71. Murugan, P.; Mani, T.; Mahinpey, N.; Asghari, K., The low temperature oxidation of Fosterton asphaltenes and its combustion kinetics. *Fuel processing technology* **2011**, *92*, (5), 1056-1061.
72. Ranzi, E.; Faravelli, T.; Gaffuri, P.; Sogaro, A., Low-temperature combustion: automatic generation of primary oxidation reactions and lumping procedures. *Combustion and flame* **1995**, *102*, (1-2), 179-192.
73. Perejón, A.; Sánchez-Jiménez, P. E.; Criado, J. M.; Pérez-Maqueda, L. A., Kinetic analysis of complex solid-state reactions. A new deconvolution procedure. *The Journal of Physical Chemistry B* **2011**, *115*, (8), 1780-1791.
74. Nassar, N. N.; Hassan, A.; Pereira-Almao, P., Metal oxide nanoparticles for asphaltene adsorption and oxidation. *Energy & Fuels* **2011**, *25*, (3), 1017-1023.
75. Canil, D.; Muehlenbachs, K., Oxygen diffusion in an Fe-rich basalt melt. *Geochimica et Cosmochimica Acta* **1990**, *54*, (11), 2947-2951.
76. Pollak, E.; Talkner, P., Reaction rate theory: What it was, where is it today, and where is it going? *Chaos: An Interdisciplinary Journal of Nonlinear Science* **2005**, *15*, (2), 026116.



## Chapter 2.

# Thermo-Oxidative Decomposition Behaviors of Different Sources of $n$ -C<sub>7</sub> Asphaltenes under High-Pressure Conditions



Published article in *Energy & Fuels*: [doi.org/10.1021/acs.energyfuels.0c01234](https://doi.org/10.1021/acs.energyfuels.0c01234)

Impact factor: 4.654

# Thermo-Oxidative Decomposition Behaviors of Different Sources of *n*-C<sub>7</sub> Asphaltenes under High-Pressure Conditions

## Abstract

The effect of pressure on the thermo-oxidative decomposition of different sources of *n*-C<sub>7</sub> asphaltenes was investigated at high pressure. The *n*-C<sub>7</sub> asphaltenes were extracted from different heavy and extra-heavy crude oils and thoroughly characterized by elemental analysis, vapor pressure osmometry, X-ray photoelectron spectroscopy, Fourier transform infrared spectroscopy, X-ray diffraction, and nuclear magnetic resonance techniques. A high-pressure thermogravimetric analyzer coupled to a mass spectrometer was employed to obtain thermograms at 0.084, 3.0, and 6.0 MPa. Kinetic analyses for thermo-oxidative multistep reactions were performed and compared using an approximation of the Ozawa, Flynn, and Wall isoconversional method based on trends in preexponential factor and effective activation energies. We discovered that the amount of chemisorbed oxygen is affected by the type of oxygen species in asphaltenes, such as COO-. Furthermore, as the aromatization degree increases and the alkylation degree decreases, so does the amount of chemisorbed oxygen atoms. Concerning the DCO region, it was confirmed that increasing the pressure from 0.084 to 6.0 MPa has a positive influence on mass loss in this region for all samples tested. The *n*-C<sub>7</sub> asphaltenes with the highest chemisorption lost the most mass during DCO. According to XPS analysis, *n*-C<sub>7</sub> asphaltenes with a higher sulfur content as thioethers decompose more easily due to the low energy required for oxidation and subsequent cracking across the pressure range studied. Furthermore, the higher hydrogen content on  $\alpha$  carbons to aromatic rings implies that some of their small alkyl side chains are cracked in this zone due to the easy decomposition of  $\alpha$ -methyl,  $\alpha$ -methylene, and  $\alpha$ -methine structures. As for the FC region, *n*-C<sub>7</sub> asphaltenes with a high content of short aliphatic chains lose more mass up to 3.0 MPa. Nonetheless, at 6.0 MPa, the mass loss percentage decreases in similar measures for all samples, indicating that under these conditions, the functional groups located both in the basal plane of the aromatic rings and on the periphery of the molecules

are more easily broken. Finally, higher aromaticity increases the percentage of mass loss during high-temperature oxidation reactions (SC). These findings imply that the sequential reaction mechanisms characterized by the four thermal events control  $n\text{-C}_7$  asphaltene mass loss, particularly under high-pressure conditions.



## 1. Introduction

Exploitations of heavy (HO) and extra heavy crude oils (EHO) are still facing several challenges due to their high density and viscosity, which cause low mobility in porous media.<sup>1, 2</sup> Hence, many thermal recovery methods were developed.<sup>3-6</sup> These methods are classified mainly into two types that are widely known as steam injection, and *in-situ* combustion (ISC).<sup>7, 8</sup> During steam injection, heavy oil extraction is accomplished by periodic or continual injection of steam that builds up heat, which is transferred to the adjacent area, reducing the viscosity of the HO and subsequently mobilizing it or generating heat, which allows the flow to the surface. This process is known to consume a lot of energy and water.<sup>9</sup> During *in-situ* combustion (ISC), or "fire flooding", heat is propagated throughout the reservoir by igniting HO and EHO by air or oxygen-enriched gas injection into the formation and subsequently reducing the unburnt oil viscosity by heat transfer, thus improving the flow.<sup>10, 11</sup> Temperatures up to 800 °C can be reached at the combustion front in a range of air injection pressure from 3.0 MPa to 6 MPa.<sup>12</sup> <sup>13</sup> However, in the current context, ISC is facing several challenges pertaining to the combustion front instability, caprock fracturing, and the increase in oil viscosity due to low-temperature reaction that hinders its large-scale deployment.<sup>14</sup> In addition, in an oxidizing atmosphere, HO and EHO are transformed into coke at low temperatures, producing more oxygen-containing compounds.<sup>15, 16</sup> As a result of the complexity of heavy hydrocarbons and their chemical reactions that take place under ISC conditions, several studies have focused on the individual fractions, namely, saturates (S), aromatics (Ar), resins (R), and asphaltenes (A). Among these, asphaltenes are the heaviest molecular weight fraction of crude oils, consisting of polyaromatic condensed rings; long aliphatic chains; alicyclic substituents; heteroatoms such as nitrogen (N), oxygen (O), and sulfur (S); and transition elements such as nickel (Ni), iron (Fe), and vanadium (V).<sup>17</sup> Most asphaltene molecules have a molecular weight in the range of 500-1000 Da, with an average molecular weight ( $M_w$ ) of ~750 Da.<sup>18, 19</sup>

To achieve an optimum design of petroleum operation, it is important to understand the chemical reactions and thermal behavior of the heaviest oil fraction. Asphaltenes are known as coke precursors during low-temperature

oxidation (LTO), which are used as a fuel to perform high-temperature oxidation (HTO) reactions.<sup>15, 16</sup> This is explained by the aggregation phenomena and development of addition reactions during oxidation processes, where alkyl side chains are lost from the asphaltenes, leading to aggregation and precipitation of polyaromatic sheets into coke.<sup>20</sup> Also, depending on the temperature range, different reactions govern the thermal decomposition of *n*-C<sub>7</sub> asphaltenes. At low temperatures (150-350 °C), oxygenated hydrocarbons and CO are the main products, while high temperatures (>350 °C) promote exothermic, and combustion reactions (CO<sub>2</sub> emissions).<sup>21, 22</sup> The oxidation mechanisms of the heavy oil fractions defined by different reaction schemes are temperature-dependent. For low temperatures, Brown and Fish et al.<sup>23</sup> proposed elementary free-radical reactions with oxygen, where RO<sub>2</sub><sup>\*</sup> and ROOH are produced by the removal of H atoms from branched and/or straight chains of carbon and hydrogen. ROOH is hydroperoxide and RO<sub>2</sub><sup>\*</sup> is an alkyl-proxy free radical.<sup>24</sup>

Moreover, several fundamental studies have been introduced to examine the kinetic behavior of different asphaltenes through thermogravimetric analysis (TGA) and differential scanning calorimetry (DSC).<sup>25-27</sup> Wei et al.<sup>25</sup> employed *Take* asphaltenes with a mass-based composition of 84.56, 13.18, 1.29, and 0.89% of carbon, hydrogen, nitrogen, and sulfur, respectively, to evaluate, through TG/DSC combustion experiments, the kinetics alterations caused by low-temperature oxidation. The authors found that LTO has the highest reaction activity, driven by hydrocarbon oxygenation. In contrast, in HTO, the most significant mass loss was evidenced due to the burning of deposited fuel. In another study, the authors investigated the combustion of SARA fractions as individual and/or binary mixtures using DSC tests at non-isothermal conditions.<sup>26</sup> The alterations in kinetic parameters and thermal variables clearly showed the influence of binary mixtures on the combustion of asphaltenes. Remarkably, the presence of saturates and aromatics increases the reactivity of LTO since asphaltenes tend to react with the products of the thermal decomposition of both components. In contrast, resins do not generate a significant change in the combustion of *n*-C<sub>7</sub> asphaltenes due to their similar chemical structures.<sup>26</sup> Finally, the asphaltene decomposition activation energy at HTO is reduced by the presence of saturates and resins because of the boosted coke formation. Goncalves et al.<sup>27</sup> used *n*-C<sub>7</sub> asphaltenes with 85.8% carbon, 8.4% hydrogen, and 1.8% nitrogen to investigate their thermal behavior through

thermogravimetric experiments using different heating rates from 2 °C·min<sup>-1</sup> to 20 °C·min<sup>-1</sup> under nitrogen and air atmospheres. The authors found in the first step an asphaltene mass loss of about 5 % below 250 °C and a decrease of 45 % between 250 °C and 550 °C, evidencing the coke formation, approximately equal to 50% of the initial mass. Murugan et al.<sup>28</sup> employed asphaltenes derived from Fosterton oil, and with the general model for the n<sup>th</sup>-order reaction, the kinetic parameters were calculated using TGA analysis. The apparent activation energy for the isothermal oxidation kinetics was found to be equal to 93.46 kJ·mol<sup>-1</sup>, by nonlinear regression, and the pre-exponential factor was 9.59 ×10<sup>5</sup> min<sup>-1</sup>.

Nevertheless, the studies above do not cover the effects of pressure and only provide a first approximation to understanding the thermal behavior of fossil fuels. Among the most recent studies, Medina et al.<sup>20</sup> reported the first study that addressed the influence of pressure on the oxidation kinetics of *n*-C<sub>7</sub> asphaltenes. In this study, the oxidation phenomenon of asphaltenes was identified as being pressure dependent. It consisted of four main well-defined stages supporting that during asphaltenes, thermal oxidation occurs in several parallel and subsequent complex-reactions. These thermal events were called (i) oxygen chemisorption, (ii) oxygen decomposition of chemisorbed oxygen functional groups, (iii) first combustion, and (iv) second combustion or high-temperature oxidation, abbreviated as OC, DCO, FC, and SC, respectively. The pressure affects, to a greater extent, the OC region behavior, favored by the increase of pressure. It is worth mentioning that a single source of asphaltenes was studied in our previous research. It is well-known that the reactivity depends directly on the chemical nature of the *n*-C<sub>7</sub> asphaltenes.

Therefore, this study continues our previous work and focuses on evaluating the effects of the chemical nature of the *n*-C<sub>7</sub> asphaltenes (isolated from different crude oil sources) on the oxidation kinetics at low and high pressures (0.084–6.0 MPa) in a temperature range from 100 to 800 °C, because *in-situ* combustion is carried out in field tests under the aforementioned pressure and temperature ranges. LTO and HTO reactions were carried out and analyzed regarding effective activation energy ( $E_a$ ) and pre-exponential factor ( $k_o$ ). Understanding the behavior of asphaltene molecules in oxidation-conversion processes based on their chemical nature will allow determining the best upgrading scheme for the heavy and extra-heavy crude oils during the thermal EOR processes.

## 2. Experimental.

### 2.1. Materials.

Six different heavy and extra-heavy crude oil samples were obtained from industrial partners from different regions worldwide and were used for *n*-C<sub>7</sub> asphaltene extraction. *n*-Heptane (99%, Sigma-Aldrich, St. Louis, MO, USA) was used to extract asphaltenes. For the thermogravimetric analyzes, the reacting gas employed consists of synthetic air NTC 2561 (CRYOGAS, Bogotá, Colombia) containing < 3 mg·L<sup>-1</sup> H<sub>2</sub>O, < 3 mg·L<sup>-1</sup> total hydrocarbon content (THC), and 20.93% of balanced O<sub>2</sub> and N<sub>2</sub>.

### 2.2. Asphaltene extraction and characterization

#### 2.2.1. Asphaltene extraction

Asphaltenes were extracted from the heavy crude oil sample by mixing each crude oil in a 40:1 ratio with *n*-heptane following the ASTM D2892 and ASTM D5236 standards.<sup>29-31</sup> After the precipitation, the samples were centrifuged and filtered using a 3- $\mu$ m quantitative filter to remove the insoluble fraction and washed with excess *n*-heptane. More details about the extraction experiments can be found in our previous works.<sup>32, 33</sup>

#### 2.2.2. Elemental analysis

The elemental composition of C, H, S, and N of the extracted *n*-C<sub>7</sub> asphaltenes samples was measured by a Thermo Flash elemental analyzer EA 1112 (Thermo Finnigan, Milan, Italy), using the conventional combustion procedure following the ASTM D5291 standard.<sup>34</sup> The oxygen content was obtained by the difference considering its sum equals 100 %.

#### 2.2.3. Vapor pressure osmometry

The average molecular weight ( $M_w$ ) for asphaltene samples was calculated by vapor pressure osmometry (VPO) using a Knauer osmometer (Knauer, Berlin-Heidelberg, West Germany) calibrated with benzyl. The hydrocarbons are dissolved in toluene using sample and standard solutions with 1 g·Kg<sup>-1</sup> and 0.005 mol·Kg<sup>-1</sup>, respectively. Considering the benzyl calibration constant  $K_{cal}$  (mol·Kg<sup>-1</sup>), the sample constant  $K_s$  (g·Kg<sup>-1</sup>), and the  $K_{cal} / K_s$  ratio, the  $M_w$  value was determined.<sup>18</sup> It is important to mention that, before the measurement, disaggregation was performed by an ultrasonic bath for 30 min to obtain the smallest possible molecular weight associated

with a monomer.<sup>35,36</sup> It is important to remark that the disaggregation process is reversible. After some hours of the ultrasound treatment, the molecular weight increases again, and if the measurements are not completed, the ultrasound bath must be repeated.

#### 2.2.4. Fourier-transform infrared spectroscopy

IR spectrum was obtained in a Fourier-transform infrared spectrophotometer (IRAffinity, Shimadzu, Nakagyo-Ku, Kyoto, Japan) containing a KCl cell with 0.22 mm spacing. Solid samples were mixed in a 30:1 weight ratio with KBr and placed on a reflection diamond crystal plate. The equipment operates in the scanning range between 4000  $\text{cm}^{-1}$  and 400  $\text{cm}^{-1}$  in transmission mode with a resolution of 4  $\text{cm}^{-1}$ .

#### 2.2.5. X-ray photoelectron spectroscopy

The tests were performed on a Specs brand X-ray photoelectron spectrometer (NAP-XPS) with a PHOIBOS 150 1D-DLD analyzer, with Al-K $\alpha$  (1486.7 eV, 13 kV, 100 W) as a monochromatic source and with step energy of 90 eV for general spectra and 20 eV for high-resolution spectra. The step was 1 eV during five measurement cycles and 0.1 eV for 20 cycles for the general and high-resolution spectra, respectively. Load compensation of 3eV and 20  $\mu\text{A}$  was used. The spectra were calibrated based on the C<sub>1s</sub> peak at 284.8 eV.

#### 2.2.6. X-Ray diffraction

The X-ray diffraction (DRX) analysis was performed with a Bruker D8 Advance X-ray diffractometer (BRUKER, Rivas-Vaciamadrid, Spain). The diffraction patterns were obtained with a Cu K $\alpha$  radiation of 40 kV and 40 mA and a wavelength ( $\lambda$ ) of 1.541 Å, contemplating a step size of 0.02° (2 $\theta$ ) and a scanning speed of 1  $\text{min}^{-1}$ . The recorded patterns were smoothed and deconvoluted. The position, intensity, and area of the peaks and the full width at half maximum (FWHM) were then determined. The macrostructure parameters of the different asphaltene samples were calculated according to other studies<sup>37</sup> and are shown in Table 1.

**Table 1.** Calculation of macro-structure parameters using diffraction patterns information

Equation	Description
$d_m = \frac{\lambda}{2\sin(\theta)}$	Distance between the neighboring aromatic sheets
$d_\gamma = \frac{5\lambda}{8\sin(\theta)}$	Interchain layer distance
$L_a = \frac{1.84\lambda}{\omega\cos(\theta)}$	Average diameter of the aromatic sheets
$L_c = \frac{0.9\lambda}{\omega\cos(\theta)}$	Average diameter of the cluster
$M = \frac{L_c}{d_m}$	Number of aromatic sheets in a stacked cluster

$\omega$  is the peak FWHM, 2.667 Å is the width of a single aromatic nucleus, Approximate Bragg angle positions  $2\theta_{002}=26.23^\circ$   $2\theta_{010}=42.48^\circ$ , and  $\lambda=1.5406\text{Å}$ .

### 2.2.7. Nuclear magnetic resonance

$^1\text{H}$  and  $^{13}\text{C}$  NMR were performed on a Bruker Ascend III HD spectrometer (Karlsruhe, Germany) operating between 600 and 125 MHz with a 5 mm TCI cryoprobe. The asphaltene samples were dissolved in  $\text{CDCl}_3$  (99.8%) containing traces of tetramethylsilane (TMS) and used as standard internal solvents for  $^1\text{H}$  NMR measurements. As for the  $^{13}\text{C}$  NMR, it operates at 75.45 MHz, and the values of the chemical shifts were related to the central signal at 77 ppm of  $\text{CDCl}_3$ . The sample concentration was fixed at mass fractions of 15.0% and 21.0% in 0.5 mL of the solvent agent for  $^1\text{H}$  and  $^{13}\text{C}$  measurements, respectively. The settings for the  $^1\text{H}$  NMR spectra were adjusted with a pulse angle of  $90^\circ$  (10.5  $\mu\text{s}$ ), a spectral width of 12.3 kHz, and a delay time of 1 s. The quantitative  $^{13}\text{C}$  NMR spectra were acquired with an inverse gated decoupling, a pulse angle of  $30^\circ$  (2.2  $\mu\text{s}$ ), a spectral width of 35 kHz, and a delay time of 180 s. Then, the  $^1\text{H}$  NMR spectrum was divided into four regions associated with four different protons, according to their position in the molecule, and  $^{13}\text{C}$  NMR was split into two main intervals for aliphatic and aromatic carbon types, respectively. The chemical shift ranges of building blocks for the measurements are shown in Table 2. Finally, the spectra were integrated for each region and normalized. The average structure parameters are calculated using the equations given in Table 3.

**Table 2.**  $^1\text{H}$  NMR and  $^{13}\text{C}$  NMR chemical shift ranges of building blocks, using  $\text{CDCl}_3$  as solvent TMS as reference.

Abbreviation	Building Block	Chem. Shift Ranges [ppm]
$C_{al}$	Aliphatic carbon	10.0 – 70.0
$C_{ar}$	Aromatic carbon	100.0 – 178.0
$H_a$	Aromatic hydrogen	6.5 – 9.5
$H_\alpha$	Hydrogen on $\alpha$ carbons to aromatic rings	1.9 – 4.5
$H_\beta$	Hydrogen on $\beta$ carbons to aromatic rings, $\text{CH}_2$ or naphthenic-type carbon	1.0 – 1.9
$H_\gamma$	Hydrogen on $\gamma$ carbons or $\text{CH}_3$ terminal of aliphatic chains alkylating an aromatic ring	0.5 – 1.0

**Table 3.** Calculation of average structural parameters using  $^1\text{H}$ -RMN and chemical elemental composition information.

Equation	Description
$f_A = \frac{\left[ \frac{C}{H} - \frac{H_\alpha}{2} - \frac{H_\beta}{2} - \frac{H_\gamma}{3} \right]}{C/H}$	Aromaticity Factor
$\sigma = \frac{\left[ \frac{H_\alpha}{2} \right]}{H_\alpha/2 + H_A}$	Hydrogen periphery replacement rate in the aromatic ring system
$\frac{H_{AU}}{C_A} = \frac{\left[ \frac{H_\alpha}{2} + H_A \right]}{C/H - \frac{H_\alpha}{2} - \frac{H_\beta}{2} - \frac{H_\gamma}{3}}$	Condensation degree parameter of the aromatic ring system
$\frac{C}{H} = \frac{C\%}{H\% \times 12}$	Carbon/Hydrogen ratio
$H_T = M_w \times H\%$	Total hydrogen numbers
$C_T = M_w \times C\%$	Total carbon numbers
$C_A = C_T \times f_A$	Aromatic carbon numbers
$C_S = C_T - C_A$	Saturated carbon numbers
$C_\alpha = \frac{H_\alpha \times H_T}{2}$	Carbon numbers on the $\alpha$ position of an aromatic ring
$C_{ap} = C_\alpha + H_A \times H_T$	Peripheral carbon in a fused aromatic ring
$C_i = C_A - C_{ap}$	Internal carbon in a fused aromatic ring
$R_{Ar} = \frac{C_i}{2} + 1$	Aromatic rings
$R_t = C_T - \frac{H_T}{2} + 1 - \frac{C_A}{2}$	Total rings
$R_n = R_t - R_{Ar}$	Naphthenic rings

$$n = \frac{H_{\alpha} + H_{\beta} + H_{\gamma}}{H_{\alpha}}$$

Average alkyl chain length

---

### 2.2.8. Average molecule construction of asphaltenes

The purpose of this section is to build an average representative molecule of asphaltenes using molecular mechanic software Materials Studio (BIOVIA, San Diego, CA, USA). The model considers carbon type (derived from the  $^{13}\text{C}$ -NMR spectrum), average molecular weight, and elemental composition. The molecules were constructed based on density functional theory (DFT). Molecular geometries are fully optimized by DFT using Becke's three-parameter and Lee–Yang–Parr functions, commonly known as B3LYP.<sup>38</sup> Clar's theory of the aromatic sextet is used to predict the stability of aromatic systems. Under this theory, it is established that the most important representation of a PAH must have the highest number of  $\pi$  sextets and the lowest number of fixed double bonds.<sup>39, 40</sup>

### 2.3. High-Pressure Thermogravimetric Analysis

High-pressure thermogravimetric analyzer HP-TGA 750 (TA instruments Inc., Hüllhorst, Germany) coupled to a mass spectrometer (Shimadzu GC-MS, Tokyo, Japan) containing a magnetically levitated balance was employed to appraise the thermal behavior of different  $n\text{-C}_7$  asphaltenes under an air atmosphere at three different pressures (0.084 MPa, 3.0 MPa, and 6.0 MPa). The magnetic system generates a uniform electromagnetic field to levitate a magnet adjusted to the suspension shaft and sample holder.<sup>41</sup> To perform the experiments, the surface of the solid samples is cleaned during a vacuum test (0.00025 MPa) for 10 minutes. Next, the equipment adjusts to the initial test conditions regarding pressure, gas flow, and temperature. To reach high pressures, there is a system of valves and manometers that automatically control the entry and exit of gases during the test. Also, for each experiment, two runs, one for the solid sample and one for the empty sample holder, are performed under the same conditions to make corrections associated with the effect of buoyancy produced by the flow of gases. The mass profile obtained for the empty sample holder is subtracted from the  $n\text{-C}_7$  asphaltenes to correct the data. The equipment is calibrated according to temperature and weight. The temperature calibration for a high-pressure instrument is complicated. This is due to the physical fact that the heat conductivity of the gas changes with temperature and pressure. Hence,



it is necessary to perform the Curie measurements over the entire pressure range of the instrument.

The tests were carried out using a heating ramp of 10 °C·min<sup>-1</sup> from 100 °C to 800 °C under an airflow of 80 mL·min<sup>-1</sup>. The pressure was varied as mentioned, while the sample mass was set at 1 mg to avoid diffusional effects of mass and heat transfer, according to the results obtained in a previous study.<sup>20</sup> In addition, to investigate the evolved gases that were emitted during *n*-C<sub>7</sub> asphaltenes oxidation, the HP-TGA was coupled with an online gas chromatography/mass spectrometer (Shimadzu GC-MS, Tokyo, Japan) using a linear scan rate of the ion trap mass analyzer of 0.03 M/Z from 0 M/Z up to 200 M/Z. Each test was performed in triplicate to ensure the repeatability of the results, obtaining uncertainties of ± 0.01 °C and 0.0001 mg.

### 3. Kinetic analysis of asphaltene thermo-oxidative decomposition

Thermal behavior analysis is performed to obtain information about the kinetic parameters of asphaltene cracking under high-pressure conditions in different temperature regions. Since the thermal decomposition of asphaltenes is a complex process that entails consecutive and parallel reactions, the kinetic variables represent the consecutive reaction history.<sup>42, 43</sup> The instantaneous reactivity *r* of a fraction is described by the following Equation (1) for an *n*-order kinetic equation,<sup>44</sup> which can be rewritten as Equation (2).

$$r = \frac{d\theta}{dt} = f(\theta) \cdot P_{O_2}^n \cdot k \quad (1)$$

$$\frac{d\theta}{dt} \frac{1}{f(\theta)} = k_o \exp\left(-\frac{E_a}{RT}\right) \cdot P_{O_2}^n \quad (2)$$

where  $P_{O_2}^n$  (bar) represents the pressure of the reactant gas (O<sub>2</sub>), *k* is the velocity constant,  $\theta$  is associated with the conversion of asphaltene at any time *t*, *n* is the order of reaction, *R* (kJ·mol<sup>-1</sup>K<sup>-1</sup>) is the universal gas constant, *E<sub>a</sub>* (kJ·mol<sup>-1</sup>) is the effective activation energy, *k<sub>o</sub>* (s<sup>-1</sup>·bar<sup>-*n*</sup>) is the pre-exponential factor and *f*( $\theta$ ) takes into account the asphaltene conversion degree during the test. Making the substitution  $\beta = dT / dt$ , employing the volumetric model for a radial consumption of the *n*-C<sub>7</sub> asphaltenes (

$f(\theta) = (1-\theta)^{44}$  and applying the Ozawa-Wall-Flynn approximation to resolve the integral of conversion, Equation (3) is obtained:

$$\ln \left[ \frac{\beta F(\theta)}{P_{O_2}^n T^2} \right] = \ln \left( \frac{k_o R}{E_a} \right) - \frac{E_a}{RT} \quad (3)$$

where,  $F(\theta) = \int d\theta / f(\theta)$ . Therefore, Equation (3) can be expressed as Equation (4).

$$\ln \left[ \frac{\beta(-\ln(1-x))}{P_{O_2}^n T^2} \right] = \ln \left( \frac{k_o R}{E_a} \right) - \frac{E_a}{RT} \quad (4)$$

Hence, the plot  $\ln \left[ \frac{\beta(-\ln(1-x))}{P_{O_2}^n T^2} \right]$  against  $\frac{1}{RT}$  for each thermal region represents a straight line. Therefore, the effective activation energy and pre-exponential factor are calculated from the slope and intercept of the best-fit-line assuming a first-order reaction, considering discretization by regions for temperature characterized by different thermal events.

## 4. Results and discussion

### 4.1. Asphaltene characterization

#### 4.1.1. Elemental analysis

The elemental composition, atomic ratios, and molecular weights of the different *n*-C<sub>7</sub> asphaltenes employed in this study are summarized in Table 4. As can be seen, the oxygen content increases following the order D < E < F ≈ A < B < C, nitrogen content in the order C < D < A < E < B < F, and sulfur content in the order C < B ≈ D < A < E < F. The content of heteroatoms in the molecular structure of asphaltenes depends on the asphaltene origin.<sup>45</sup> Carbon content was comparable between C and D samples, while hydrogen percentage was found to be identical between A and C asphaltenes. Furthermore, the H/C ratio rises as follows: B < C < A < D < E < F, indicating that B- asphaltenes have a higher aromatic degree. Meanwhile, the content of heteroatoms (N + S + O) decreases in the following order: B < A < C < F < D < E, indicating that the B, A, and C samples are more polar. The basic composition of the asphaltenes is consistent with the literature.<sup>32, 46, 47</sup> Further,

the  $M_w$  of  $n$ -C<sub>7</sub> asphaltenes decreases as the number of heteroatoms decreases too, following the increasing order E < F < D ≈ C < A < B. The  $M_w$  values obtained are in the range reported in other studies for asphaltenes isolated from HO and EHO.<sup>27, 45</sup>

**Table 4.** Analytical data of different  $n$ -C<sub>7</sub> asphaltenes

Sample	Elemental mass fraction concentration ± 0.1 %					Atomic ratio				$M_w$ ± 5.0 g·mol <sup>-1</sup>
	C	H	N	S	O	H/C	N/C	S/C	O/C	
A	82.6	7.39	1.50	5.43	3.08	1.07	0.17	1.36	0.43	950.3
B	82.4	7.25	1.88	5.32	3.15	1.06	0.22	1.06	0.44	1051.6
C	83.0	7.40	1.15	5.13	3.32	1.07	0.13	1.67	0.49	722.4
D	83.0	7.55	1.41	5.32	2.72	1.09	0.16	1.41	0.38	717.3
E	84.1	7.78	1.64	3.49	2.99	1.11	0.18	0.80	0.64	555.7
F	82.5	7.93	2.34	4.21	3.02	1.15	0.25	0.67	0.54	650.9

#### 4.1.2. FTIR structural characterization

FTIR spectra were performed to obtain information about the specific functional groups for the different asphaltenes, shown in Figure 1. As can be seen, the spectrum differed from each asphaltene according to the transmittance in different wavenumbers regions. These regions were related to aromatic (700-900 cm<sup>-1</sup> and 1400-1600 cm<sup>-1</sup>) and aliphatic (2700-3000 cm<sup>-1</sup>) compounds.<sup>48</sup> In general, all  $n$ -C<sub>7</sub> asphaltenes present a strong transmittance peak near 3000 cm<sup>-1</sup> due to the content of saturated components in the molecular structure. Besides, the peak at 3318 cm<sup>-1</sup> (between 3600 cm<sup>-1</sup> and 3100 cm<sup>-1</sup>) is predominant in asphaltenes B and C. This indicates that these samples have a high amount of N-H and O-H groups, considered one of the promoters of the asphaltene aggregation phenomena through hydrogen bonds.<sup>49</sup> Moreover, these peaks can allude to the OH-ether oxygen and self-associated OH hydrogen bonds.<sup>50</sup> The transmittance bands around 3318 cm<sup>-1</sup> are strong and well-defined due to the high amount of oxygen-containing compounds observed through elemental analysis, and are most likely related to the OH functional groups from alcoholic and phenol components.<sup>48</sup>

By contrast, saturated C-H stretch bonds present low-intensity signals between 1500 and 1300 cm<sup>-1</sup> in all samples compared with the bands near 1606 cm<sup>-1</sup>, representative of aromatic C=C stretching vibration. In addition, the weak peak at 3045 cm<sup>-1</sup> is related to its elevated substitution degree and condensed aromatic rings.<sup>50</sup> The transmittance bands around 3318 cm<sup>-1</sup> are

strong and well-defined due to the high amount of oxygen-containing compounds observed through elemental analysis, and are most likely related to the OH functional groups from alcoholic and phenol components.

These components are also characterized by transmittance bands between 700-900  $\text{cm}^{-1}$  and at 815  $\text{cm}^{-1}$  and 750  $\text{cm}^{-1}$  interpreted as aromatic out-of-plane C-H bending, two adjacent aromatic hydrogens, and ortho-substitution in the aromatic rings, respectively, which are predominant in the C asphaltenes, but present in all samples.<sup>51</sup>

Further, the transmittance percentage has no significant intensity in the peaks located at 725  $\text{cm}^{-1}$  and 720  $\text{cm}^{-1}$  for B, C, and A asphaltenes, showing a low content of long aliphatic chains over these components.<sup>51</sup>

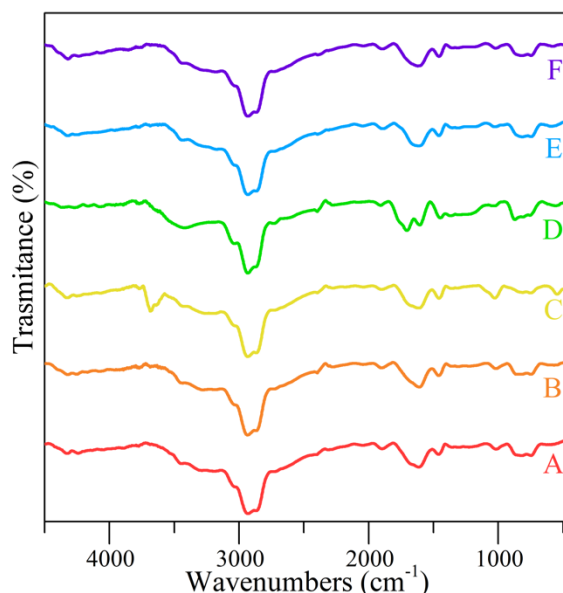


**Figure 1.** FTIR spectra for different  $n\text{-C}_7$  asphaltenes considered in this study.

Carbonyl vibrations produced by aldehyde groups and carboxylic acids show weak peaks in 1799 and 2730  $\text{cm}^{-1}$ , respectively, with the signals in B, C, and A samples having a higher intensity. In general, the C-O and C-O-H peaks are shown between 1300 and 1100  $\text{cm}^{-1}$ . These species are more defined in A and D asphaltenes, indicating that oxygen is primarily present in these samples in the form of C-O bonds rather than other single bonds, as promoted by ether, phenol, alcohol, and phenolic stretching vibrations.<sup>51</sup> According to the low-intensity peaks at 2500  $\text{cm}^{-1}$ , there is a low presence of S-H bonds in sulfur-containing functional groups. However, absorption bands at 1032  $\text{cm}^{-1}$  may be present as a result of S=O groups, particularly in

A and C samples.<sup>51</sup> Finally, nitrogenated compounds are distinguished by current stretching C-H vibrations of aromatic amines in the 1340-1250  $\text{cm}^{-1}$  range and heterocyclic skeleton vibrations in the E and F asphaltenes in the 1660-1415  $\text{cm}^{-1}$  range. It is worth mentioning that the vibrations of the aliphatic and aromatic C-H skeletons overlap the nitrogen peaks, it is difficult to provide detailed information about the present nitrogen functional groups using FTIR.<sup>50</sup>

#### 4.1.3. Surface functional group analyses

Figure 2 depicts the full-scan X-ray photoelectron spectroscopy spectrum analysis and high-resolution spectra for the main elements on the surface of E asphaltenes. In general, XPS experiments were designed to acquire additional information about the surface compositional differences between asphaltene samples. Figure 2 shows the presence of X-ray-induced Auger transitions associated with four distinct signals related to O<sub>1s</sub>, C<sub>1s</sub>, N<sub>1s</sub>, and S<sub>2p</sub> atoms, indicating the presence of oxygen, carbon, nitrogen, and sulfur functional groups on the asphaltene surface, which is confirmed by bulk (elemental analysis) tests. These elements were found in all of the asphaltenes. The high-resolution spectra of carbon and heteroatoms (O, N, and S) were investigated using casaXPS software (Casa Software Ltd., Teignmouth, UK) to obtain additional data on the form and distribution of chemical groups on the surface of the samples.

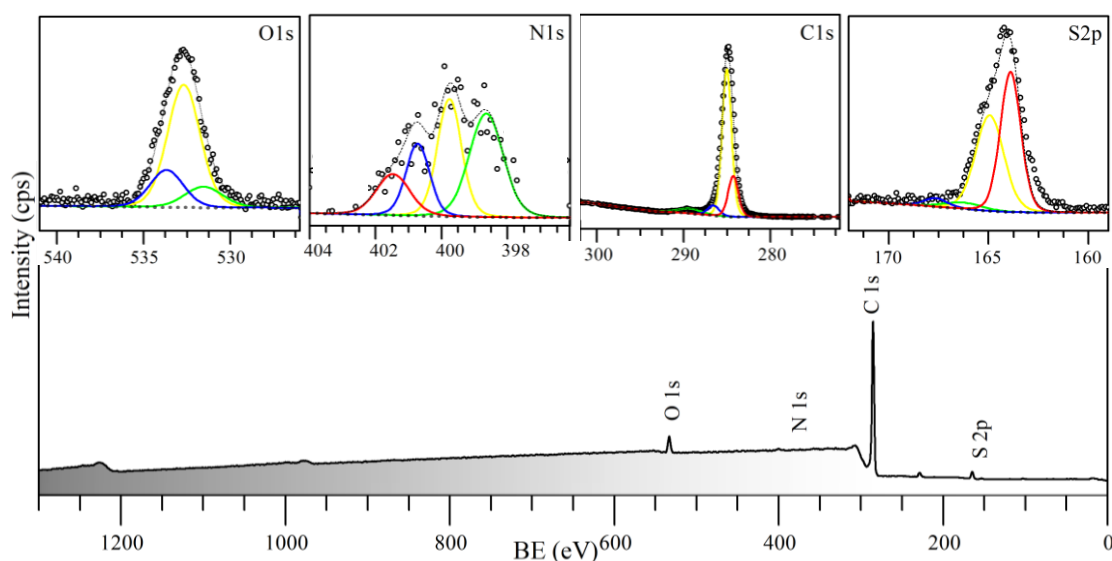


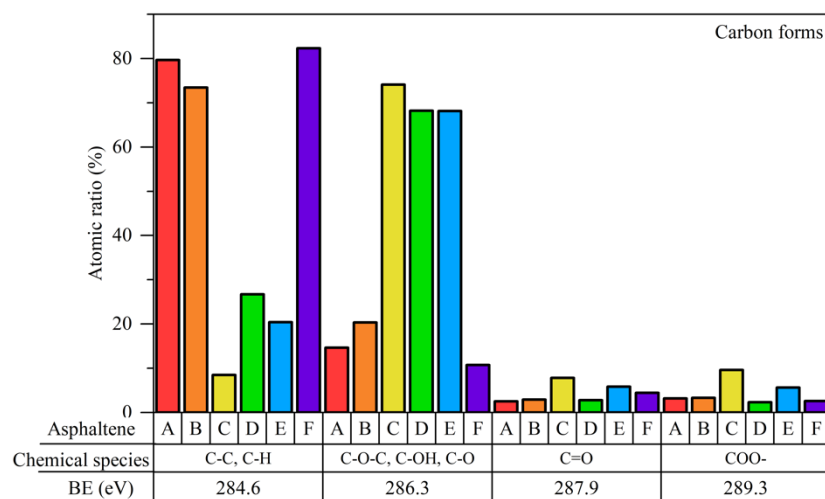
**Figure 2.** XPS analysis for E- asphaltene. Survey spectrum was principal photoelectron are shown, and high-resolution spectra for main elements.

In panels of Figure 2, the fitting peak curves for C<sub>1s</sub>, O<sub>1s</sub>, N<sub>1s</sub>, and S<sub>2p</sub> for E-asphaltenes are observed. The binding energy values obtained for each spectrum are in accordance with those reported in previous studies.<sup>51, 52</sup> For the C<sub>1s</sub> spectrum, four main peaks were found at 248.6, 286.3, 287.9, and 289.3 eV corresponding to C-C, C-H; C-O-C, C-OH, C-O; C=O; and COO- species, respectively.<sup>51</sup> The peak at 248.6 eV can be associated with carbon-heteroatoms groups, such as C-N, C-O, and C-S.

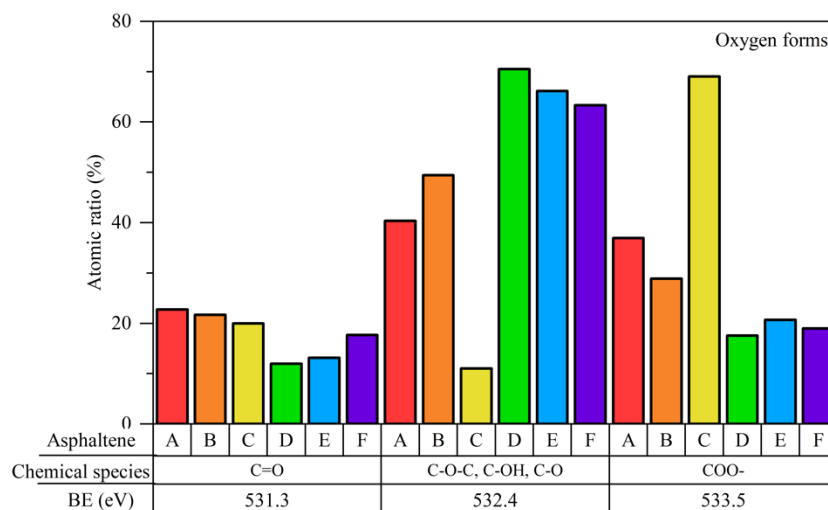
Figure 3a-d shows the configurations and atomic contents of the carbon, oxygen, nitrogen, and sulfur compounds. Panel a shows the carbon-containing compounds observed from the fitting results of the C<sub>1s</sub> spectrum for the *n*-C<sub>7</sub> asphaltenes evaluated in this study. Herein, it was found that carbon-containing compounds are mainly present as carbon-carbon and carbon-hydrogen single bonds and in the form of hydroxyl and ether groups for all samples. The single bonds C-C and C-H are dominant in asphaltenes A, B, and F, while the bonds C-O-C, C-OH, and C-O are in greater proportion in samples C, D, and E, with asphaltenes F and C being those that present the highest content of these functional groups on their surface. Instead, carbon-containing groups occur in low proportion as carbonyl and carboxyl groups, less than 11 %, except for asphaltene C, whose total content of C=O and COO-compounds is greater than 17%. The oxygen form and atomic percentage content were acquired from the 1s (K layer electron) peaks of oxygen and are shown in Panel b of Figure 3. The oxygen form is divided into three main types: carbonyl (C=O), single-bond oxygen (C-O-C, C-OH, and C-O), and carboxyl (COO-) for all samples; however, its content in each asphaltene varies considerably. In the case of D, E, and F asphaltenes, there is a smaller quantity of oxygen compounds as C=O and COO- compared to those as C-O-C, C-OH, and C-O bonds, whose content is 60% higher. By contrast, the oxygen-containing compounds present as a single bond for C, A, and B asphaltenes are below 10% and mainly as carboxyl groups. The nitrogen XPS analysis data are presented in Panel c of Figure 3. It is worth mentioning that N<sub>1s</sub> spectra had a relatively weak signal intensity for the six *n*-C<sub>7</sub> asphaltenes analyzed and hence a low signal-to-noise ratio. From Panel c of Figure 3, the signal was decomposed into four peaks. The first peak at 398.8 eV is attributed to pyridinic N species, the peak at 399.9 eV is attributed to pyrrolic-N species, the one at 400.7 eV to amino-nitrogen compounds, and the peak at 401.2 eV is attributed to quaternary-N species. The peak fitting data and the atomic ratio of nitrogen illustrated that quaternary nitrogen was still the

minor part of the nitrogen form for all asphaltenes. In the case of D and F asphaltenes, amine functional groups predominate over pyrrolic and pyridinic nitrogen. The high percentage of these two species can be attributed to the asphaltenes' high content of acidic phenolic groups, which easily form hydrogen bridges with pyridinic N compounds, converting them to quaternary nitrogen. Asphaltenes A, B, and C, on the other hand, are rich in pyrrolic and pyridinic structures.

a)



b)



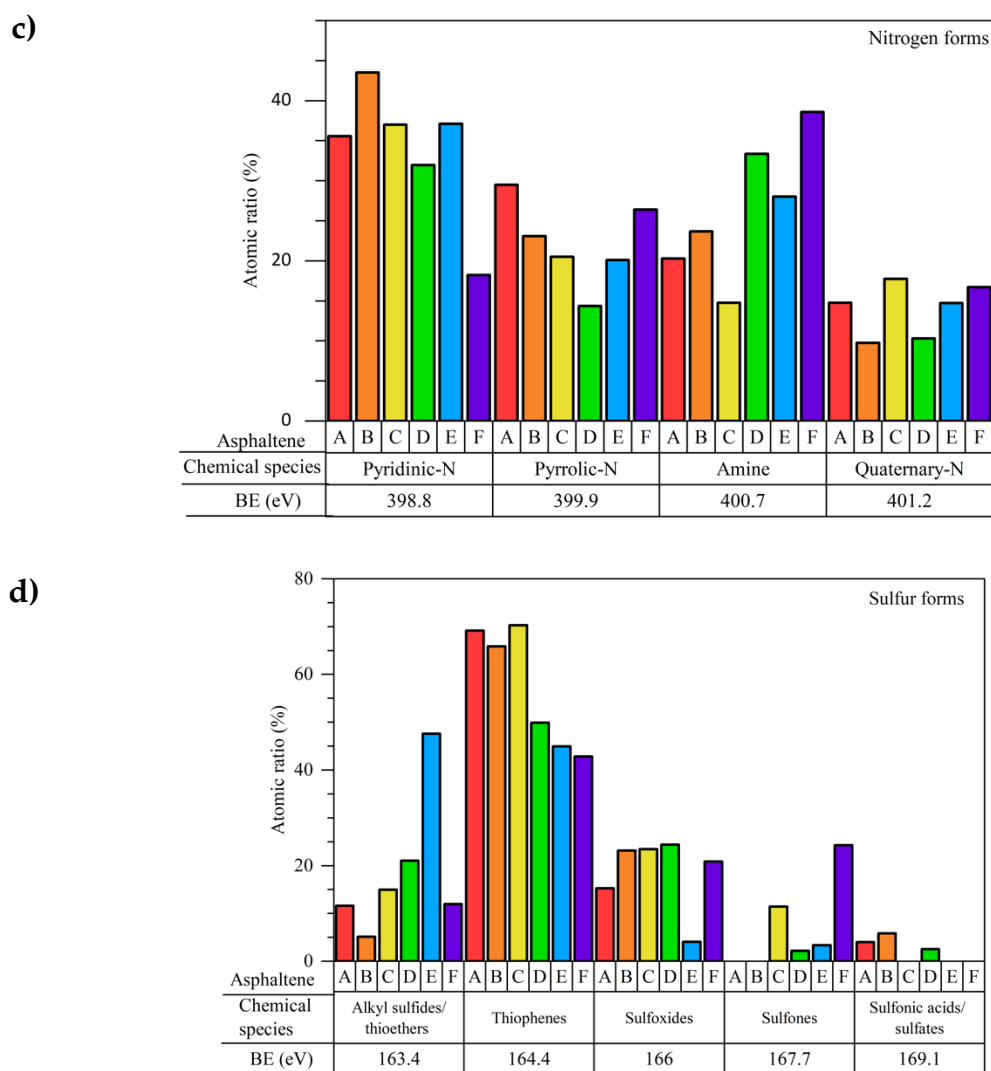


**Figure 3.** Configurations and atomic contents (%) of a) carbon-containing compounds derived from the fitting results of the  $C_{1s}$ , b) oxygen-containing compounds derived from the fitting results of the  $O_{1s}$  spectrum, c) nitrogen-containing compounds derived from the fitting results of the  $N_{1s}$  spectrum, and d) sulfur-containing compounds derived from the fitting results of the  $S_{2p}$  spectrum of different asphaltene samples.

The  $S_{2p}$  spectrum analysis reveals sulfur-containing compounds on the asphaltene aggregate surface. Panel d of Figure 3 depicts the atomic ratio and formed configurations of sulfur for the analyzed samples. The results revealed five sulfur-containing compounds at 163.4, 164.4, 166.0, 167.7, and 169.1 eV, respectively: alkyl sulfides or thioethers, thiophenes, sulfoxides, sulfones, and sulfonic acids or sulfates. As shown, thiophene sulfur (around 50% in all cases) dominates the sulfur speciation of the samples studied, followed by alkylates and sulfoxides. Thiophene sulfur is the most difficult



form to remove due to its aromatic structure, remaining in crude oils even after desulfurization treatments as dibenzothiophene family compounds.<sup>53</sup> Further, it is also a consequence of sulfides into thiophenes during crude oil maturation. These findings are in accordance with previous works.<sup>51, 53</sup> Finally, it was observed that asphaltenes A and B do not have sulfone groups on their surface and that asphaltenes C, E, and F do not have sulfur in the form of sulfates.

#### 4.1.4. XRD analysis of different *n*-C<sub>7</sub> asphaltenes

The structural parameters for the different asphaltene samples were determined from the signal decomposition of XRD patterns through the equations shown in Table 1 according to the techniques reported by Yen et al.<sup>54</sup> The XRD patterns of the asphaltenes are shown in Figure 4. As can be seen, *n*-C<sub>7</sub> asphaltenes exhibit qualitatively similar peaks that give three maxima approximately at 25° graphene (002), 20° gamma ( $\gamma$ ), and 44° (010). The  $\gamma$ -band tells about the spacing between aliphatic layers.<sup>52</sup> These broad features suggest that the ordering is widely dispersed in *n*-C<sub>7</sub> asphaltenes.<sup>55</sup> Furthermore, deconvolutions revealed that the intensity of the (002)  $\gamma$ -band decreased in the order C > A > B > E > F > D, whereas the intensity of the-band increased in the order C < A < B < E < F < D. These findings imply that asphaltenes C has a higher degree of dealkylation than the other samples, implying that the conditions for staking polyaromatic sheets are better.<sup>52</sup>

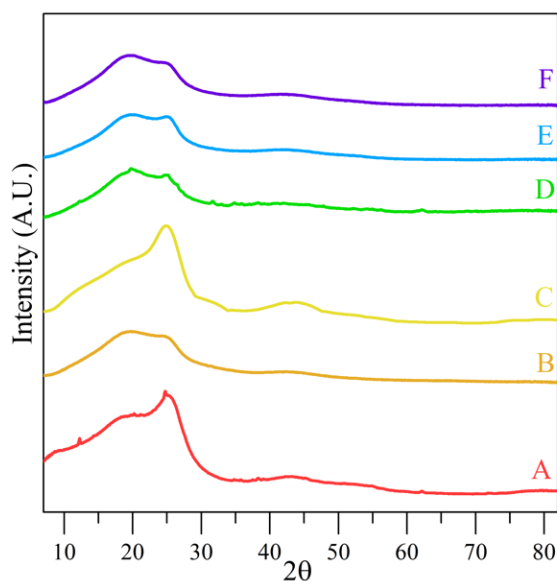


**Figure 4.** XRD patterns for different *n*-C<sub>7</sub> asphaltenes considered in this study.

The macrostructure parameter results for asphaltenes are given in Table 5. The results are similar to those obtained from other studies.<sup>54</sup> The  $d_m$  and  $d_\gamma$  are higher for C- asphaltenes (3.507 and 6.160 Å, respectively) than for the other asphaltenes. The diameter of the cluster  $L_c$  increases in the order  $A < C < F < B < E < D$ , so the value of the average number of aromatic sheets per stack ( $M$ ) followed a similar trend, where A, C, and F exhibit lower values than B, E, and D asphaltenes. This suggests that each asphaltene has approximately four aromatic sheets per cluster.

**Table 5.** Crystalline parameters derived from XRD data for different asphaltene samples.

Crystalline parameters	Asphaltenes					
	A	B	C	D	E	F
$d_m$ (Å)	3.466	3.474	3.507	3.562	3.477	3.590
$d_\gamma$ (Å)	5.838	5.995	6.160	5.690	5.690	5.838
$L_a$ (Å)	19.063	16.610	19.507	11.953	16.135	14.897
$L_c$ (Å)	12.734	13.342	12.908	14.526	13.851	13.943
$M$	3.674	3.841	3.681	4.078	3.984	3.885

#### 4.1.5. Average structural parameters analysis

The <sup>1</sup>H-NMR spectrum was normalized and integrated to get the proportional distribution relationship of the hydrogen-type protons using MestRenova software (San Diego, CA, USA) and is listed in Table 6. There is no signal between 4.5 ppm and 6.5 ppm, indicating the absence of olefinic hydrogen entities.<sup>56</sup> Moreover, the content of the aliphatic  $\beta$ -hydrogen linked to the aromatic ring ( $H_\beta$ ) is higher than the  $\alpha$ -hydrogen ( $H_\alpha$ ) and  $\gamma$ -hydrogen ( $H_\gamma$ ) in all asphaltenes and increases in the order  $B < A < C < E < D < F$ , which is associated to naphthenic or paraffinic hydrogens ( $CH_2$ ) at position  $\beta$  to aromatic and alkyl terminal system, indicating that the asphaltenes E, D, and F have a lower aromaticity degree and higher alkylation degree than asphaltenes A and B.<sup>57</sup> These results are in accordance with the elemental analysis reported in previous sections and X-ray diffraction results. Furthermore, the content of  $H_\alpha$  and  $H_\gamma$  protons increases in the orders  $D < F < C < E < A < B$  and  $C < E < A < D < B < F$ , respectively. The results show that the content of long alkyl side chains present in the aromatic structure is higher in F asphaltenes. That is a higher number of structures connected to

paraffinic hydrogens (CH<sub>3</sub>) in position  $\gamma$  or aromatic system. Also, the B asphaltenes have a high content of short alkyl side chains mainly in the form of  $\alpha$ -methyl,  $\alpha$ -methine, and  $\alpha$ -methylene linked to aromatic rings, as well as other groups such as -OH and -SH, which agrees well with the results of H/C ratio and content of heteroatoms (N+O+S).<sup>48, 58</sup> The results are consistent with the infrared analysis, which shows that B asphaltenes have the lowest intensity for the peak of  $-(CH_2)_n-$  ( $n \geq 4$ ) and the highest transmittance for F asphaltenes. The percentage of aromatic protons (H<sub>a</sub>) is lower for A asphaltenes and increases in the order A < F < B < E < D < C. On the other hand, aliphatic and aromatic carbon content increase in the orders B < A < C < D < F < E and E < F < D < C < A < B, respectively.

**Table 6.** Hydrogen and Carbon types present in whole  $n$ -C<sub>7</sub> asphaltenes and its fractions obtained by <sup>1</sup>H-NMR and <sup>13</sup>C-NMR analysis.

Hydrogen protons	Relative amount (%) in asphaltenes					
	A	B	C	D	E	F
H <sub>a</sub>	4.10	5.55	11.20	8.79	5.65	5.22
H <sub><math>\alpha</math></sub>	13.42	20.06	9.33	3.46	10.80	3.81
H <sub><math>\beta</math></sub>	61.80	50.26	62.81	65.02	62.89	66.60
H <sub><math>\gamma</math></sub>	20.68	24.13	17.07	22.72	20.66	24.37
Carbon	Relative amount (%) in asphaltenes					
	A	B	C	D	E	F
C <sub>ar</sub>	62.12	68.2	65.9	60.3	55.6	57.8
C <sub>al</sub>	37.9	31.8	34.1	39.7	44.4	42.2

Furthermore, the quantification of average structural parameters (ASP) for these complex hydrocarbon mixtures can be done considering the elemental analysis, <sup>1</sup>H-NMR, and molecular weight by vapor pressure osmometry. The structural characteristics of the hydrocarbon groups were deduced (Table 7) using the modified Brown-Ladner method.<sup>58</sup> In the first instance, it was discovered that asphaltenes B and C have a higher degree of aromaticity than the other samples, as evidenced by a higher value of the  $f_A$  parameter, which is consistent with the findings obtained from elemental analysis and hydrogen- and carbon- NMR analysis, which follows the increasing order E  $\approx$  F < A < D < B < C. In contrast, another important feature of asphaltenes A and B is their low average alkyl chain length ( $n$ ). This implies that the substituents are mostly ethyl and methyl groups.<sup>48, 59</sup> This parameter increases in the order B < A < E < C < F < D.

Also, it was observed that  $H_{AU}/C_A$  and  $\sigma$  are higher for  $n$ -C<sub>7</sub> asphaltenes with higher aromaticity factor.<sup>59</sup> The number of carbons in the  $\alpha$  position of an aromatic ring and peripheral carbons in a fused ring is in a lower amount in  $n$ -C<sub>7</sub> asphaltenes with lower  $f_A$ , while the content obtained for internal carbons is higher. This result suggests a greater aromatic ring grouping, as it has a more condensed aromatic structure, resulting in the formation of more aggregates.<sup>59, 60</sup> As for the content of naphthenic rings, there is a lower content in the B asphaltenes and a higher in the A asphaltenes.

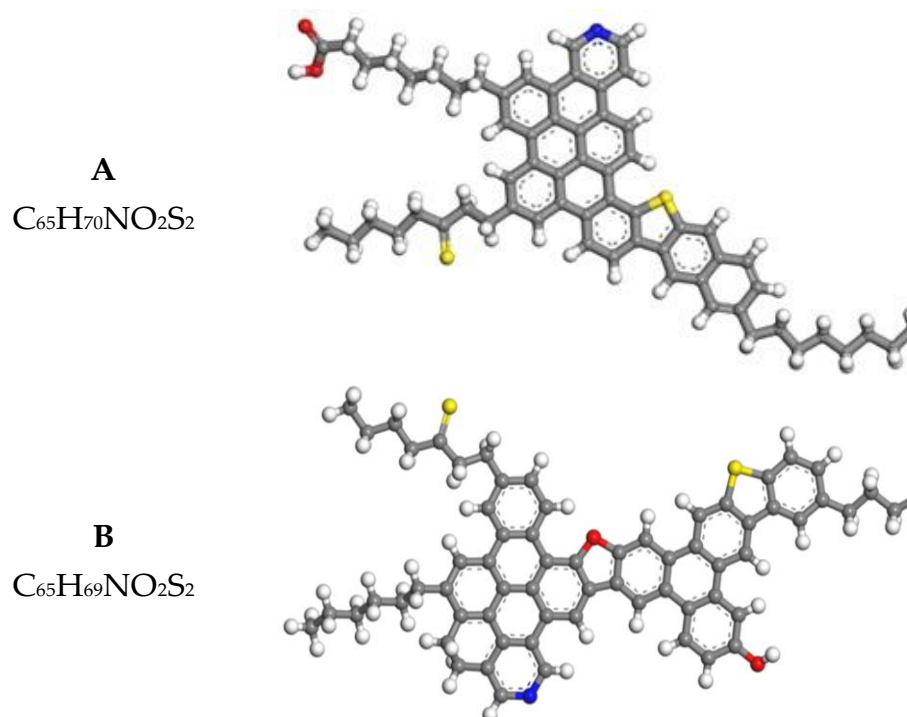
**Table 7.** Average molecular structure parameter of different  $n$ -C<sub>7</sub> asphaltenes, obtained through the chemical elemental analysis and <sup>1</sup>H-NMR spectra.

Parameter	Asphaltenes					
	A	B	C	D	E	F
$f_A$	0.570	0.608	0.616	0.588	0.561	0.561
$\sigma$	0.621	0.644	0.294	0.164	0.489	0.267
$H_{AU}/C_A$	0.183	0.233	0.235	0.176	0.197	0.129
$C/H$	1.035	1.101	1.093	1.016	0.997	0.987
$H_T$	69.372	80.973	55.625	50.926	40.010	46.214
$C_T$	80.395	88.229	61.043	60.121	48.179	56.173
$C_A$	45.827	53.608	37.602	35.378	27.046	31.513
$C_S$	34.569	34.621	23.440	24.743	21.133	24.659
$C_\alpha$	4.655	8.122	2.595	0.881	2.161	0.880
$C_{ap}$	7.499	12.616	8.825	5.362	4.421	3.293
$C_i$	38.328	40.992	28.777	30.016	22.625	28.221
$R_{Ar}$	20.164	21.496	15.389	16.008	12.313	15.110
$R_t$	23.796	21.939	15.429	17.969	15.651	18.309
$R_n$	3.632	0.442	0.040	1.961	3.338	3.199
$n$	7.146	4.708	9.562	26.358	8.736	24.877

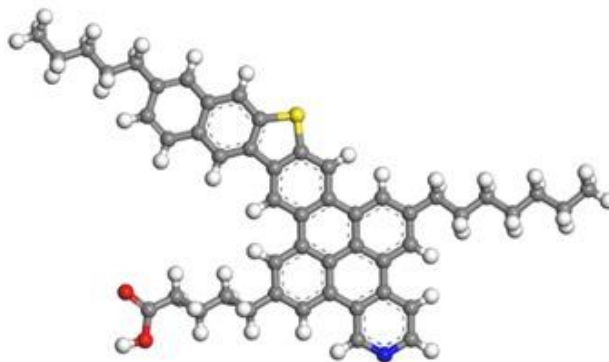
#### 4.1.6. Average molecular structure

Asphaltene molecules were experimentally resolved through NMR spectral analysis, combined with elemental content (CHNSO) and average molecular weight analysis. Overall, NMR results suggest the island-type structure for asphaltene molecules, according to the Yen–Mullins model.<sup>61</sup> In

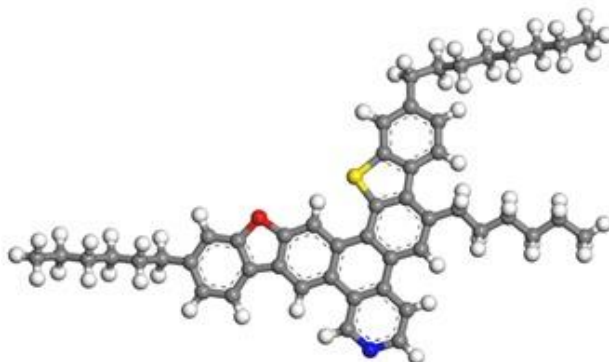
the case of the archipelago-type structure, indeed, long atomic distances between carbon and hydrogen in the aromatic cores are determined by aliphatic chains linked to the aromatic cores.<sup>17</sup> DFT calculations were performed to obtain asphaltene molecule models. The structure of these molecules is analyzed using Clar's sextet theory for optimizing the arrangement of the electron  $\pi$  sextets in the fused aromatic ring region and achieving lower-energy isomers.<sup>40</sup> Figure 5 shows the proposed chemical structure for the asphaltene molecules under consideration. It was obtained that asphaltenes A ( $C_{65}H_{67}NO_2S_2$ ), B ( $C_{77}H_{69}NO_2S_2$ ), C ( $C_{50}H_{49}NO_2S$ ), D ( $C_{49}H_{55}NOS$ ), E( $C_{39}H_{45}NOS$ ), and F( $C_{45}H_{53}NOS$ ) have molecular weights of 959, 1043, 724, 701, 570, and 660  $g \cdot mol^{-1}$ , respectively, with mean deviations of 0.9, 0.8, 0.2, 0.9, 2.6, and 1.4%, for each asphaltene, respectively, regarding experimental values. The results indicate that structural differences exist between the molecules based on the experimental parameters obtained using the characterization techniques.



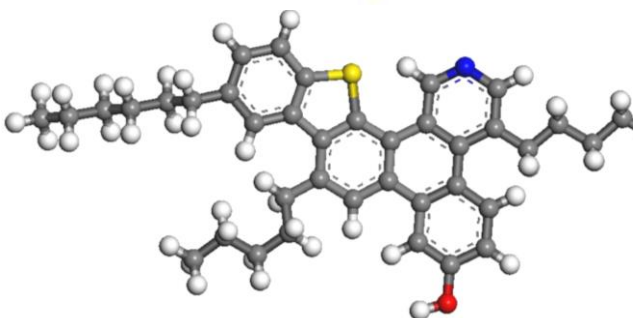
**C**  
 $C_{46}H_{49}NO_2S$



**D**  
 $C_{49}H_{54}NOS$



**E**  
 $C_{39}H_{44}NOS$



**F**  
 $C_{45}H_{52}NOS$

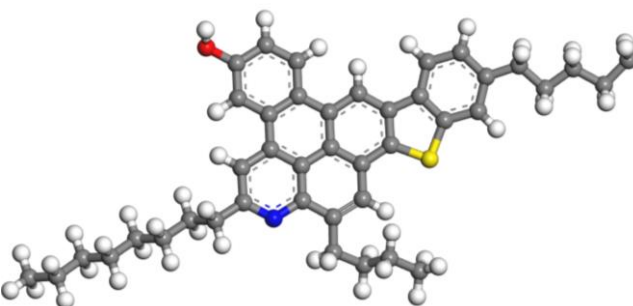


**Figure 5.** Representative chemical structures of the *n*-C<sub>7</sub> asphaltene samples of different sources based on the NMR spectral analysis, elemental composition, and average molecular weight.

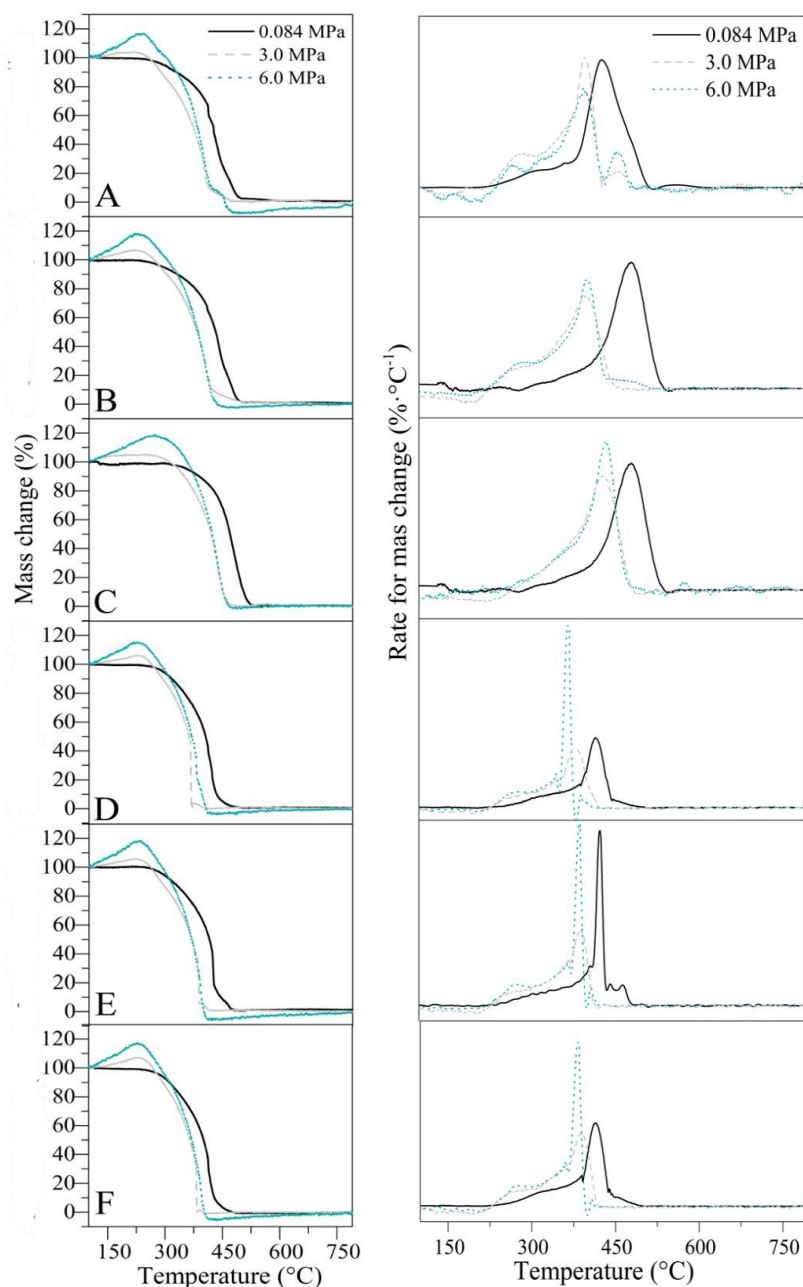
#### 4.2. High-pressure thermogravimetric analysis.

Figure 6 depicts the thermograms obtained for each *n*-C<sub>7</sub> asphaltene oxidation at three pressures (0.084, 3.0, and 6.0 MPa). The mass change

profiles are shown on the left, while the rate of mass change is shown on the right.

As seen, for all cases, the asphaltene thermo-oxidative decomposition profile is determined by four thermal events called oxygen chemisorption (OC), decomposition/desorption of chemisorbed oxygen functional groups (DCO), first (FC), and second combustion (SC). Each of them was delimited by the atypical behavior of the curves during each temperature interval. Details about these regions are found in a previous study.<sup>20</sup> It is important to clarify that during *n*-C<sub>7</sub> asphaltene oxidation, OC and DCO regions appear at pressures higher than 0.3 MPa. According to the results, the oxygen chemisorption percentage increases in the order D F E B A C for 3.0 MPa and 6.0 MPa. Asphaltenes can have up to 1018 spins·g<sup>-1</sup> free radicals, depending on their origin, which act as active sites for oxygen anchoring on the asphaltene chemical structure.<sup>62</sup> Furthermore, it is expected that increasing the pressure increases the amount of chemisorbed oxygen in the *n*-C<sub>7</sub> asphaltene structure due to the thermal expansion of the aggregates, increasing the contact area for the interaction with the oxygen atoms.<sup>27</sup>

Interesting correlations were found between thermal profiles and the physicochemical properties of asphaltenes. Although the oxygen content is in a different order, a direct relationship with oxygen in the form of carboxyl groups was discovered in the system's molecular structure. This demonstrates that the amount of chemisorbed oxygen is determined not so much by the percentage of oxygen present in the *n*-C<sub>7</sub> asphaltenes and aggregates as it is by whether it is found in a higher proportion as COO-group. The carboxyl group can be ionized by releasing a proton (hydrogen atom) from a hydroxyl group in response to the interaction of the carbon of the carboxylate group and the neighboring carbon by the presence of a carbon-associated partial density of the positively charged carboxylate group to respond to a pseudo-second-order kinetic model, which weights the interaction of two points of the organic molecule at the adsorbent.<sup>63</sup> Thus, the -OH group is considered strongly activating.<sup>64</sup> Further, *n*-C<sub>7</sub> asphaltenes B, C, and A, with a higher content of carbonyl groups, also presented a higher increase in mass in the OC zone than D, E, and F asphaltenes.

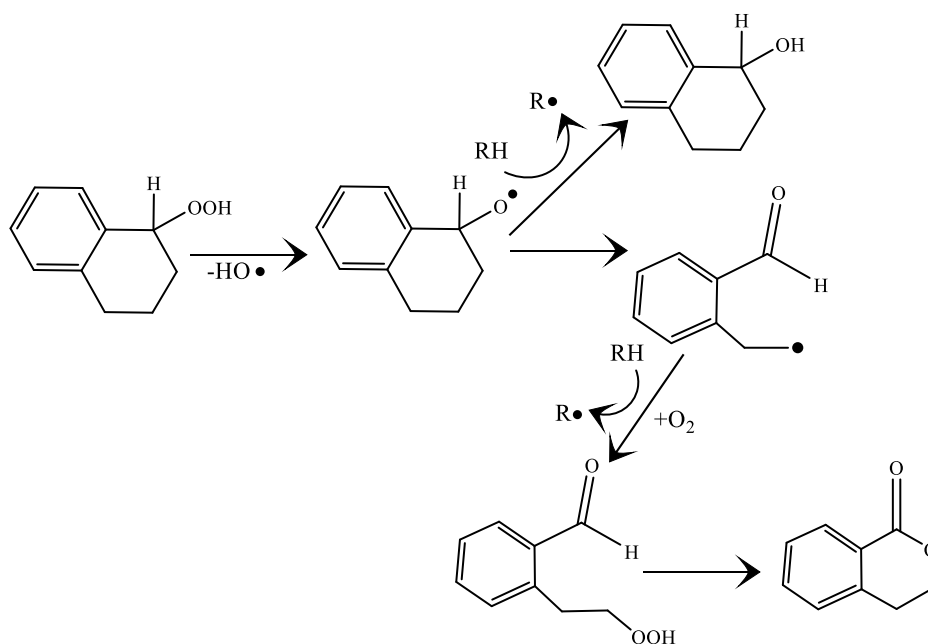


**Figure 6.** Mass percentage and rate for mass change for different *n*-C<sub>7</sub> asphaltene oxidation at different pressures from 0.084 MPa to 6.0 MPa. Sample weight: 1 mg, heating rate: 10 °C·min<sup>-1</sup>, and airflow: 80 mL·min<sup>-1</sup>.

Another significant finding was related to the  $\beta$ -hydrogen content of the alkyl chain linked to the aromatic ring ( $H_{\beta}$ ) and the H/C ratio. The amount of chemisorbed oxygen atoms increases as the aromatization degree increases and the alkylation degree decreases. One of the primary sites for intermolecular attraction with diatomic oxygen compounds are the fused aromatic rings within asphaltene molecules. The interaction grows as the number of fused rings in the polyaromatic structure grows.<sup>57</sup> This interaction



could be caused by the ability of the  $\pi$ -electron density in condensed aromatic rings to interact with an electrophile such as molecular oxygen. In this sense, increasing the system pressure during thermal heating can result in the formation of oxygenated groups in the basal aromatic plane as a result of the oxidation of the aromatic cores, resulting in groups such as acids, ketones, phenols, and alcohols.<sup>20</sup> The temperature region has the greatest influence on the nature of the oxygenated groups formed during asphaltene oxidation. Alcohols and ketones were reported to be the primary oxidation products at low temperatures. However, at temperatures close to 100 °C, the main oxygenate functional groups identified are ketones and aromatic ethers.<sup>62</sup> A possible pathway for ester formation is explained during Scheme 1, where the oxidation of cycloalkanes proposed by Krerck et al.<sup>62</sup> is shown. Because asphaltenes are rich in multicycle molecules where cycloalkane and aromatic rings are adjoining, indan hydroperoxide functions as a good representative of a substructure obtained in the complex molecules.<sup>62</sup>



**Scheme 1.** Reaction pathway explaining ester formation during oxygen chemisorption of indan hydroperoxide as a model molecule representative of asphaltene oxidation at low temperatures.

The proposed pathway starts with the formation of an oxygen-centered alkoxy radical from indan, which can then produce alcohol by removing hydrogen from another hydrocarbon. Alkoxy radicals can also undergo  $\beta$ -scission, which results in ring-opening and the formation of a carbon-

centered radical. The final radical oxidizes easily to form a hydroperoxide intermediate. Like hydroperoxide decomposition works, so does indan decomposition. Nonetheless, the fragments corresponding to the ring-opened cycloalkane can be attached to a structurally ridged unit. As a result, the likelihood of an "in-cage" reaction increase. An ester is formed during this reaction as a result of the elimination of a water molecule.<sup>62</sup>

Figure 7 summarizes the relationships between different parameters and the amount of oxygen chemisorbed.

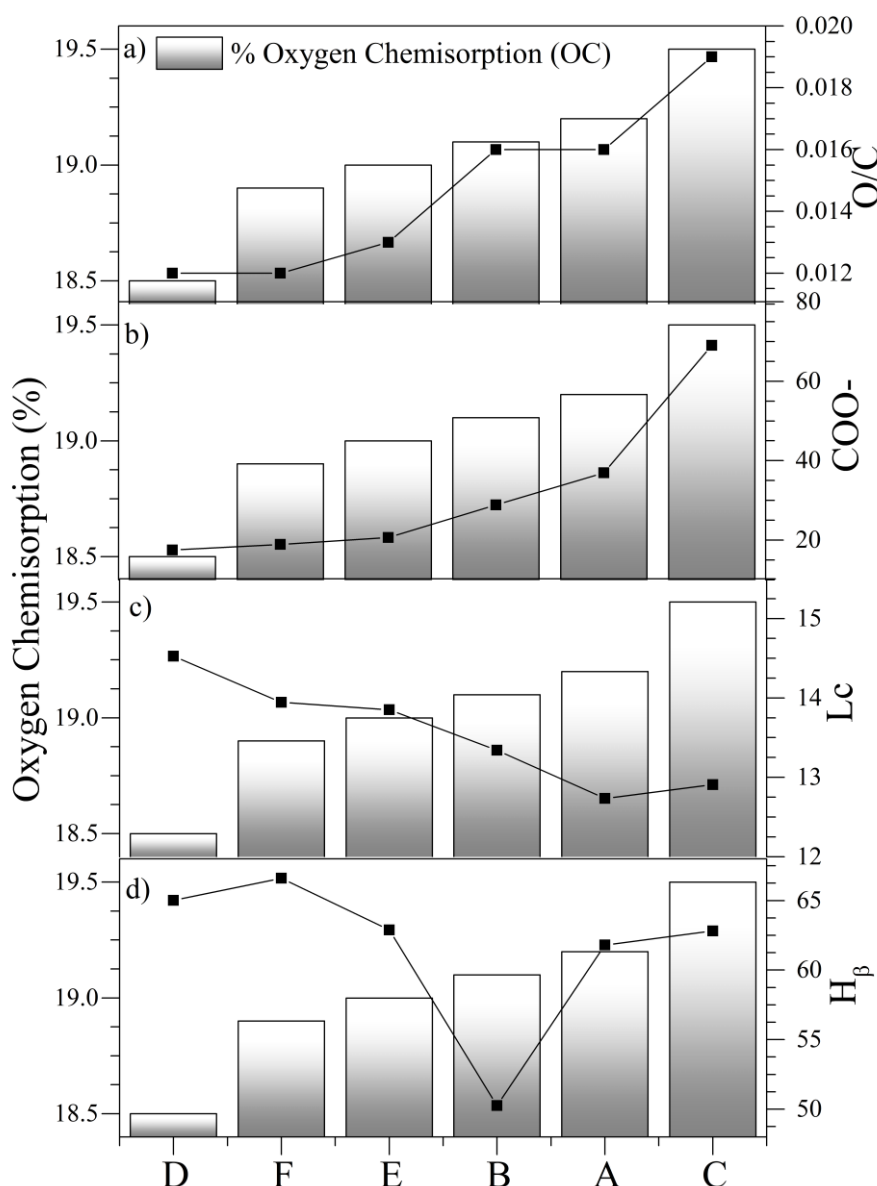


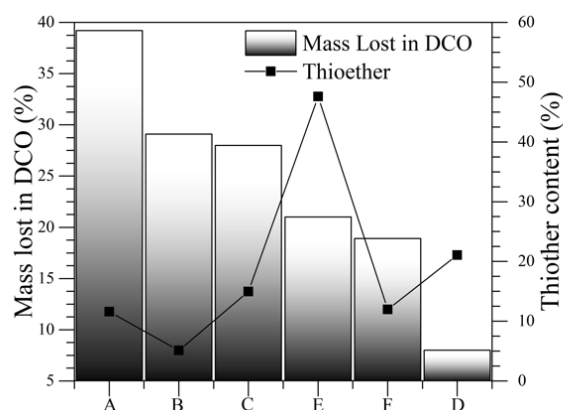
**Figure 7.** Effect of (a) oxygen/carbon ratio, (b) amount of carboxyl functional groups, (c) cluster diameter ( $L_c$ ), and (d)  $\beta$ -hydrogen of the alkyl chain linked to the aromatic ring ( $H_\beta$ ) over the amount of oxygen chemisorbed during OC zone.

The diameter of the cluster also influences the oxygen chemisorption yield.<sup>52</sup> With the decrease in  $L_c$ , the OC zone is favored because of increased the active surface area available for oxygen absorption. Similarly, as mentioned before, the rise in pressure could promote the thermal expansion of  $n$ -C<sub>7</sub> asphaltene structures, increasing the interactions with the oxygen molecules.<sup>52</sup> Furthermore, the temperature at which the OC region ends rises in the same order as the %OC increase. This is because carboxyl groups are polar molecules that can form hydrogen bonds with each other and with other types of molecules (O<sub>2</sub>). This association causes higher-than-normal organic compound boiling temperatures, delaying the beginning of the DCO region.<sup>63</sup>

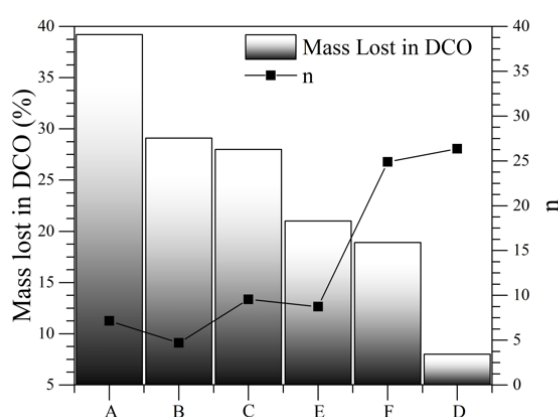
Regarding the DCO region, it was confirmed that pressure has a positive influence on mass loss in this zone for all samples tested. For both pressures of 3.0 MPa and 6.0 MPa, the amount of mass loss follows the order D < F < E < C < B < A. Because there are more oxygenated groups in the basal plane of aromatic structures as well as in aliphatic structures, the kinetic of carbonaceous material consumption is increased in the  $n$ -C<sub>7</sub> asphaltenes with higher chemisorption in the previous region. In addition, according to our previous work,<sup>20</sup> cracking of the saturated compounds could occur during this thermal event, as well as loss of related aliphatic sulfur and nitrogen. According to the XPS analysis, asphaltenes A and B have a higher content of thioethers. These species require low energy for their oxidation which facilitates their subsequent cracking.<sup>53</sup> Further, the higher content of  $H_\alpha$  in the A and B asphaltenes suggests that some of their small alkyl side chains are cracked in this zone due to the easy decomposition of  $\alpha$ -methyl,  $\alpha$ -methylene, and  $\alpha$ -methine structures.<sup>59</sup> Figure 8 summarizes the relationships among the thioether content, the average alkyl chain length, and the mass lost during the DCO thermal event.

In the FC region, pressure is extremely important. The percentage that decomposes during this region is very low for low pressures close to atmospheric pressure. For pressures greater than 3.0 MPa, however, there is a significant increase in mass loss for all samples. Because of the high content of short aliphatic chains and heteroatoms located in the ramifications of the molecular structure, A and B asphaltenes lose more mass at 3.0 MPa.<sup>16</sup> At 6.0 MPa, the mass% decreases in similar measures for all samples, indicating that under these conditions, any functional group located both in the basal plane

of the aromatic rings and on the molecule's periphery is more easily broken<sup>24</sup> Furthermore, pressure can shift the aromatic core of asphaltene molecules from peri- to cata-condensation, resulting in a higher content of double-bonded aromatic carbon than triple-bonded aromatic carbon, making it easier to break these compounds.<sup>65</sup> Peripheral substituents, such as alkanes and cycloalkanes, are cracked in greater quantities during this thermal event. Because these compounds cause steric hindrance, the attractive forces are no longer balanced, resulting in coke production.<sup>61</sup> However, if the pressure is high enough, these groups may be eliminated more quickly due to an increase in the decomposition reaction rate. As a result, at 6.0 MPa, the amount of *n*-C<sub>7</sub> asphaltenes decomposed during high-temperature oxidation reactions (SC) is lower than at the other pressures for C, D, E, and F asphaltenes.



a)



b)

**Figure 8.** Effect of (a) thioether content and (b) average alkyl chain length over the amount of mass lost during DCO zone at 6.0 MPa.

The intensity of the (002)-band increased as the intensity of the  $\gamma$ -band decreased, as determined by deconvolution of XRD peaks. The  $\gamma$ -band intensity was higher for A, B, and C asphaltenes than for the others, while the (002)-band intensity was the opposite.<sup>54</sup> This finding implies that dealkylation occurs during the oxidation of these asphaltenes, allowing polyaromatic sheets to stack together and form coke.<sup>52</sup> This is reflected in the behavior of the mass loss rate of these asphaltenes. For all pressures tested, there is a large amount of asphaltenes to decompose during the second combustion.

By contrast, the rest of the *n*-C<sub>7</sub> asphaltenes exhibit a considerable increase in the intensity of the peak at 6.0 MPa during the first combustion related to the increase in the collision probability between the oxygen molecules, triggering rapid exothermic reactions with the aliphatic chains and promoting asphaltene dealkylation. These results are corroborated by the amount of mass loss for these systems during the FC event, where the mass loss for D, E, and F asphaltenes is thrice compared to that of A, B, and C samples.

In addition, the high aromatic character of the asphaltenes A, B, and C also provides strong  $\pi$ - $\pi$  interaction between aromatic rings, corroborating their mass loss curve profile. These findings are also consistent with the total aromatic ring  $R_{Ar}$  value and with the higher thiophene content, as thiophene is an aromatic heterocyclic with six  $\pi$  electrons in a planar, cyclic, and conjugated system.<sup>66</sup> Furthermore, the high content of pyridinic structures increases the aromaticity of these samples by introducing extra polar interactions between the condensed aromatic rings (sheets). Then, high energy bond cleavage occurs during the fourth stage at higher temperatures, and the parent molecular skeletons are destroyed. Finally, larger molecules are degraded into gaseous compounds as smaller molecules. Figure 9 summarizes the relationships between these variables and the mass lost during the FC thermal event.

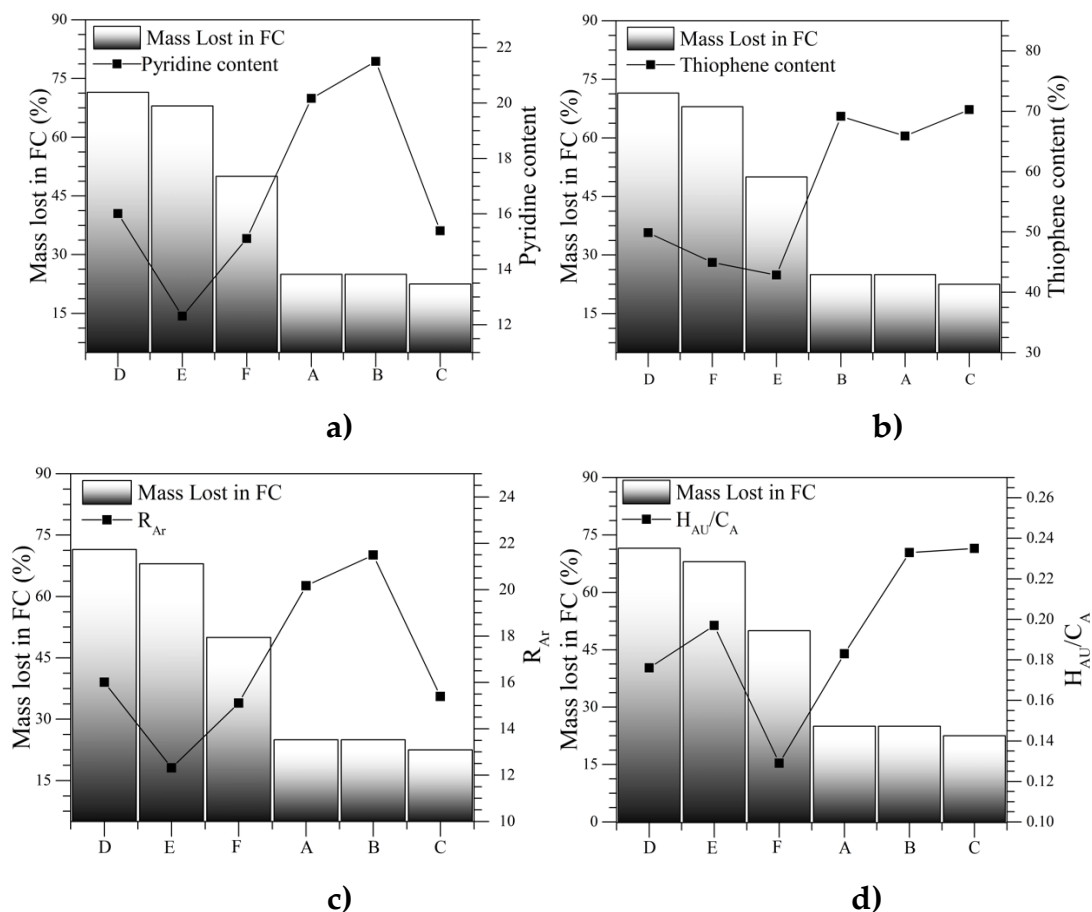


**Figure 9.** Effect of (a) pyridinic content, (b) thiophene content, (c)  $R_{Ar}$ , and (d)  $H_{AU}/C_A$  over the amount of mass lost during the FC zone at 6.0 MPa.

On the other hand, a direct relationship between the width of the mass loss rate profile in the second combustion and the  $M_w$  of  $n-C_7$  asphaltenes is observed. As the average molecular weight decreases, so does the width of the TGA profile, following the order  $E < F < D < C < B < A$ , regardless of system pressure. These results are according to the results reported in previous works.<sup>67-69</sup>

All these findings suggest that  $n-C_7$  asphaltene mass loss occurs by sequential reaction mechanisms considered to be oxygen chemisorption, decomposition of mainly chemisorbed functional groups, first combustion, and second combustion. Hence, oxidized  $n-C_7$  asphaltenes should be analyzed and modeled by a multistep reaction mechanism.<sup>20</sup> Table 6 summarizes the temperature intervals and mass change percentage of each stage at the different pressures evaluated for all samples.

**Table 6.** Thermogravimetric characteristics for the oxidation of different  $n$ -C<sub>7</sub> asphaltene discretized in the different regions: *i*) oxygen chemisorption (OC) *ii*) decomposition of the chemisorbed oxygen (DCO) region, *iii*) first combustion (FC) region and *iv*) second combustion (SC) region at 0.084, 3.0, and 6.0 MPa.

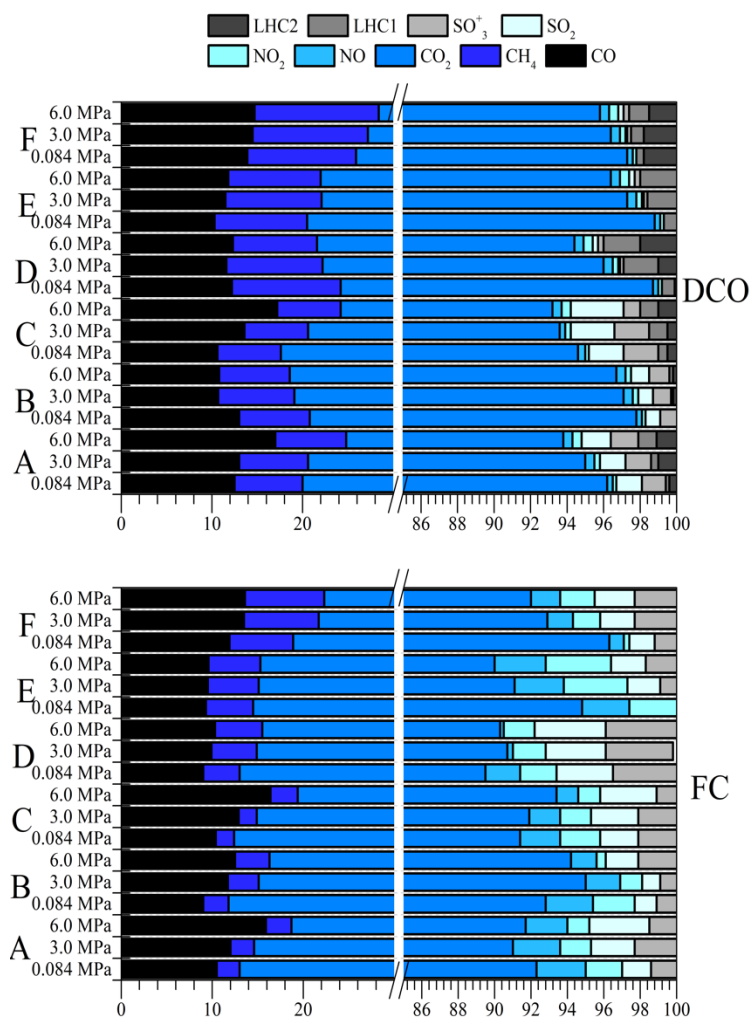
Asphalten e	Pressur e (MPa)	OC Region		DCO Region		FC Region		SC Region	
		Temperatur e range (°C)	Mass gain (mass fractio n in %)	Temperatur e range (°C)	Mass loss (mass fractio n in %)	Temperatur e range (°C)	Mass loss (mass fractio n in %)	Temperatur e range (°C)	Mass loss (mass fractio n in %)
A	0.084	-	-	-	-	100-380	15.0	381-570	85.0
	3.0	100-230	8.0	231-360	38.0	361-430	65.0	431-490	5.0
	6.0	100-245	19.2	246-350	39.2	351-385	25.0	386-500	55.0
B	0.084	-	-	-	-	100-375	15.0	376-550	85.0
	3.0	100-228	8.0	229-315	18.0	316-410	60.0	411-500	30.0
	6.0	100-240	19.1	241-310	29.1	341-380	25.0	381-450	65.0
C	0.084	-	-	-	-	100-410	10.0	411-580	90.0
	3.0	100-250	8.5	251-370	18.5	371-408	20.0	409-500	70.0
	6.0	100-270	19.5	271-380	28.0	381-405	22.5	406-500	69.0
D	0.084	-	-	-	-	100-345	15.0	346-490	85.0
	3.0	100-220	6.0	221-275	7.0	276-360	49.0	361-425	50.0
	6.0	100-235	18.5	236-270	8.0	271-350	71.5	351-410	40.0
E	0.084	-	-	-	-	100-420	40.0	41-560	60.0
	3.0	100-227	7.0	228-290	14.0	291-385	53.0	386-450	40.0
	6.0	100-240	19.0	241-280	21.0	281-375	68.0	376-430	30.0
F	0.084	-	-	-	-	100-350	20.0	351-510	80.0
	3.0	100-225	7.0	226-280	10.0	281-365	42.0	361-430	55.0
	6.0	100-240	18.9	241-278	18.9	279-355	50.0	356-415	50.0

#### 4.2.1. Gaseous analysis

The amount of gaseous products that evolved during the oxidation of the different  $n$ -C<sub>7</sub> asphaltenes was obtained for the different stages of OC, DCO, FC, and SC and are presented in Figure 10. According to our previous studies,<sup>20, 33</sup> we focus here on the thermal release profile of permanent gases (carbon monoxide (CO), and carbon dioxide (CO<sub>2</sub>)), light hydrocarbons (methane (CH<sub>4</sub>), pentane (C<sub>4</sub>H<sub>10</sub>) named LHC1, and propane (C<sub>2</sub>H<sub>6</sub>) named LHC2), nitrogen oxides (nitric oxide (NO), nitrogen dioxide (NO<sub>2</sub>)), and sulfur oxides (sulfur dioxide (SO<sub>2</sub>), and sulfur trioxide (SO<sub>3</sub>)), represented by mass spectra profiles of  $m/z = 28, 44, 16, 58, 72, 30, 43, 64,$  and  $80$  respectively. The data in Figure 10 show that NO, NO<sub>2</sub>, SO<sub>2</sub>, and SO<sub>3</sub> gases are released from  $n$ -C<sub>7</sub> asphaltenes at low temperatures during the DCO event, and that the amount of these products increases significantly across the temperature range in the FC and SC regions. When the temperature rises above the DCO region, the products change. These findings are consistent with those obtained from asphaltene decomposition under low-pressure conditions.<sup>22, 33,</sup>

Pressure increases the evolution of these gases in all regions, especially during the first combustion. This implies that at the end of FC, lower molecular weight compounds remain at high pressure. Furthermore, the different percentages found in each sample persist because *n*-C<sub>7</sub> asphaltenes with higher production of these gases contain a significant proportion of nitrogen, oxygen, and sulfur in their molecular structures.

For example, a higher concentration of thioethers promotes the production of sulfur-based gases during DCO (A, B, and C asphaltenes), while a lower concentration of pyridinic functional groups reduces the amount of nitrogen-based gases in the DCO zone. Nonetheless, at 6.0 MPa, as described, the decomposition reaction rate increases, making it easier to break the functional groups located in the aliphatic chains and the basal plane of the aromatic rings.





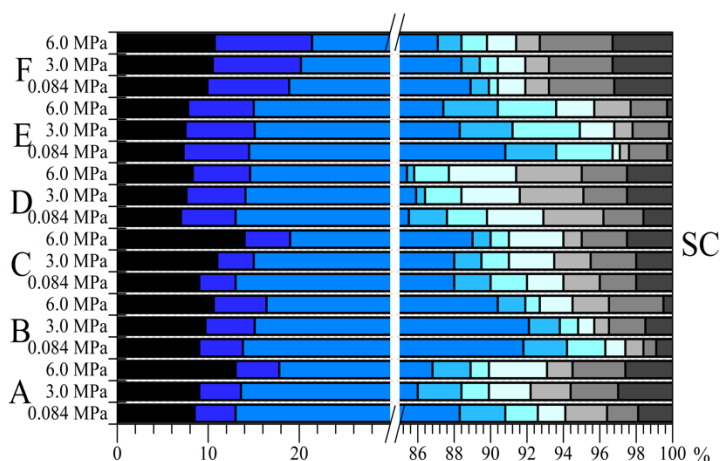
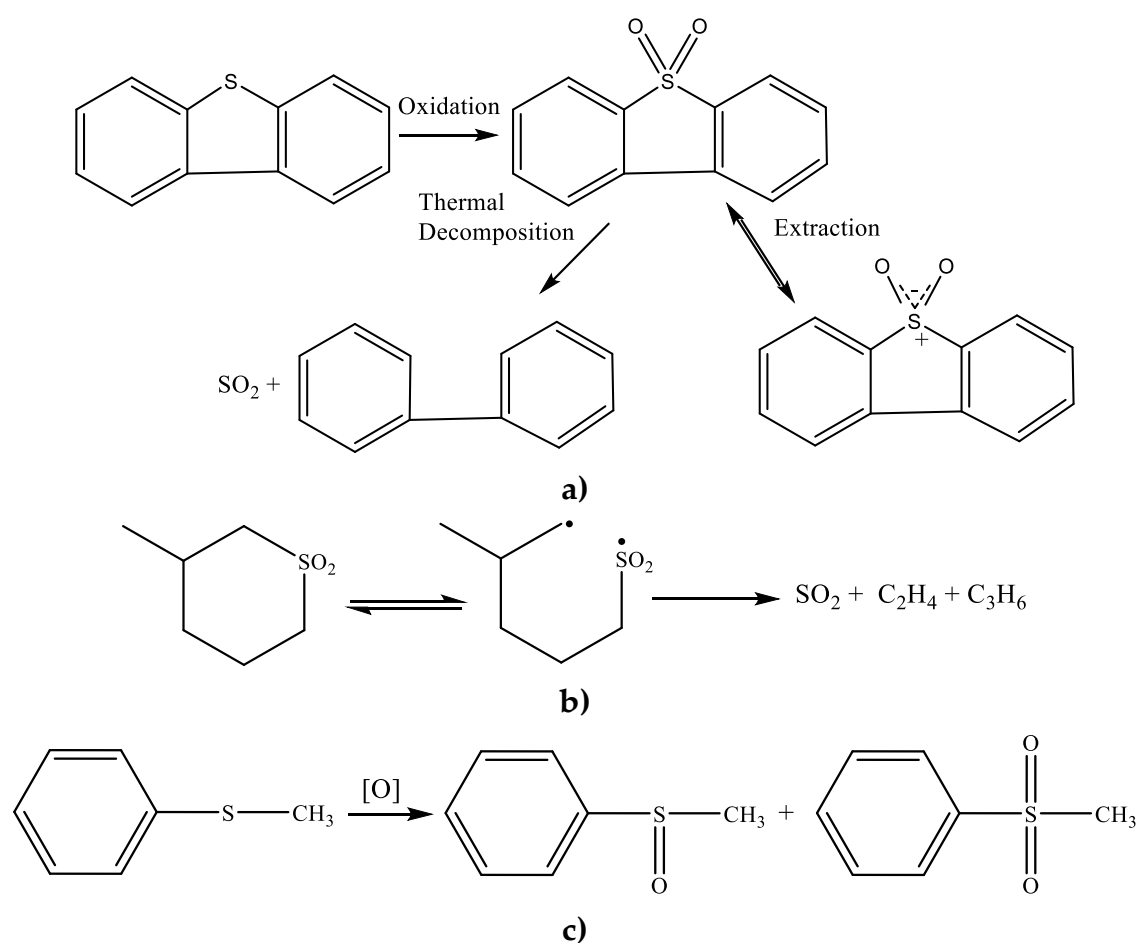


**Figure 10.** Selectivity distributions of light gases produced from the oxidation of different  $n$ -C<sub>7</sub> asphaltenes in air at different pressures discretized in different thermal events.

Furthermore, for D, E, and F asphaltenes, an increase in SO<sub>x</sub> production is observed during the first and second combustion at pressures greater than 3.0 MPa, which can be attributed to the presence of thiophene functional groups. The reactivity of thiophene is greatly increased under these conditions and in the presence of air because aromatic sulfur species oxidize by air to a greater extent in the presence of aldehydes or hydrocarbon molecules, becoming more reactive than their original forms.<sup>71</sup> Under high-pressure conditions, it is possible to reproduce oxidative desulfurization through gas-phase oxidation (GPO).<sup>72</sup> In the OC region, selective binding of oxygen to organic sulfides and thiophenes may occur, without the breakdown of C-C and C-S bonds; that is, GPO occurs. This is possible because of the strong affinity of sulfur-containing groups for oxygen. Also, throughout the formation of sulfoxides and sulfones by selective oxidation, the polarity changes sharply; therefore, these products can be separated by thermal decomposition with the formation of sulfur dioxide during the FC and SC zone. Scheme 2a represents it.

The formation of sulfoxides and sulfones places great importance on the OC thermal event because these compounds are more reactive and facilitate desulfurization than the unoxidized sulfur compounds for two important reasons. (i) oxidized sulfur compounds acquire high polarity, and (ii) the C-S bond strength decreases substantially when the sulfur is oxidized. Hence, it is easier to remove the oxidized sulfur by thermal decomposition.<sup>73</sup> Moreover, another path for the biradical is to split into C<sub>2</sub>H<sub>4</sub> + CH<sub>2</sub> = SO<sub>2</sub> from the split of sulfones by the thermal heating of the samples, showed in Scheme

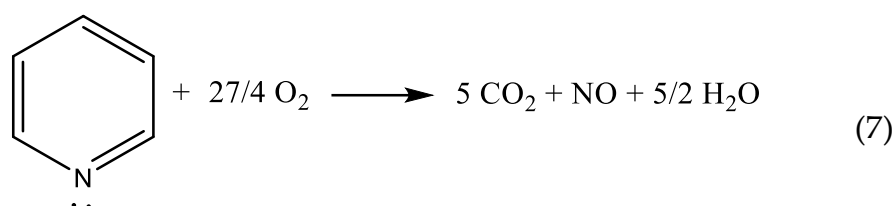
2b. The reaction is exothermic, and the activation energy does not exceed 12 kcal since the energy to detach  $\text{SO}_2$  from the biradical requires some 15 kcal.<sup>74</sup> Another important factor that promotes the production of  $\text{SO}_x$  compounds is the olefin hydrocarbon content. As it is shown in Scheme 2c, the oxidation of these compounds encourages the production of sulfones with a low amount of sulfoxides and, therefore, the production of sulfur-based gases. Finally, the  $\text{SO}_4$  is stable relative to decomposition into  $\text{SO}_3 + \text{O}$  by 38 kcal and stable relative to decomposition into  $\text{SO}_2 + \text{O}_2$  by  $2 \pm 5$  kcal.



**Scheme 2.** a) Simplified reaction scheme of sulfone compounds removal during asphaltene decomposition through GPO. b) Simplified reaction scheme of  $\text{SO}_2$  production by the split of 3-methyl thiolane and c) Scheme of oxidation reactions of model methyl phenyl sulfide and benzothiophene.

For pressures above 3.0 MPa, there is also an increase in the production of nitrogen-based gases during the FC and SC combustion events, particularly for pyrrolic- and pyridinic-ring-rich samples. As a first instance,

NO can be produced by the interaction between diatomic oxygen and pyridine, according to the following oxidation reaction (Equation 7):

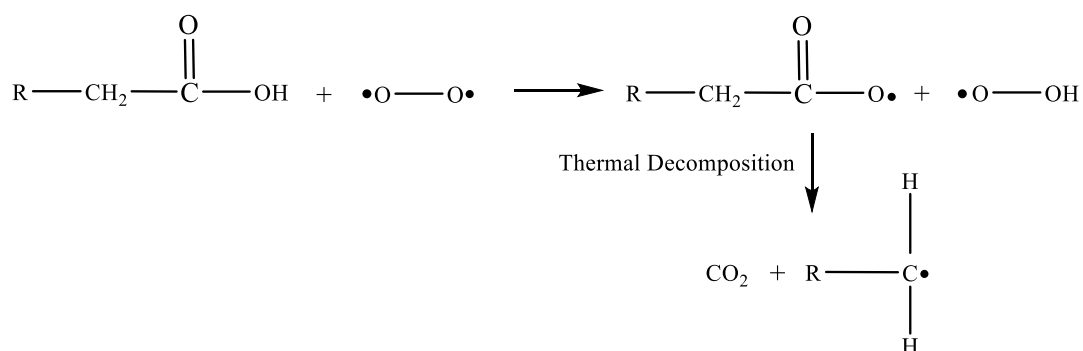


In addition, NO production involves different N-intermediate species like cyanide and amines. Its formation occurs by complex reaction pathways. In this case, NO is produced by the oxidation of nitrogen-based compounds in the asphaltene molecular structure. This conversion to nitrogen oxides varies slightly depending on the type of nitrogen-containing compound, indicating that oxidation of N-rich functional groups occurs via analogous mechanisms using analogous intermediates.<sup>75</sup> For example, both pyridine and pyrrole oxidations require the intermediate formation of nitriles. Returning to the case of NO, a key intermediate is HCN, which originated from pyridine combustion under oxygen-rich conditions or was released from pyrrole and its derivatives. Studies also have shown that under an air atmosphere in a flow reactor, the reaction of NO with HO<sub>2</sub> radicals to produce NO<sub>2</sub> is important, even though it has no appreciable effect on the results since NO<sub>2</sub> is recycled back to NO.<sup>76</sup> It is important to mention that a small amount of pyrrolic can be produced during the conversion of pyridine.

On another side, the gases (CO, CO<sub>2</sub>, CH<sub>4</sub>) produced from asphaltene oxidation during all events are the main products. As it is reported in the literature, both alkyl derivatives and condensed aromatics produce hydrocarbons gases at FC temperature interval, and the oxygen-containing gases could be produced from the easy decomposition of oxygen functional groups that are reputed to be present originally and after the OC event in all the samples evaluated.<sup>41</sup> However, the amount of carbon dioxide produced during the SC region decreases as the production of the rest of the gas remains constant. This explanation is directly associated with improving C<sub>4</sub>H<sub>10</sub> and C<sub>2</sub>H<sub>6</sub> production during the SC event. The presence of higher paraffins indicates the occurrence of more severe thermal degradation.<sup>70</sup> Nevertheless, during the DCO zone, these compounds are slightly produced. Presumably, at these temperatures, the more thermally labile groups, such as

those on peripheral sites, are eliminated, while at high temperatures (SC zone), more severe degradation of the asphaltene molecule occurs.

Pressure also promotes the increase in the production of these compounds during both thermal events. As pressure could modify the aromatic core of the *n*-C<sub>7</sub> asphaltenes, by increasing the content of double-bonded aromatic carbons and reducing the triple-bonded ones, according to their resonance, the energy required for their breaking is reduced.<sup>77</sup> Finally, the higher amount of CO<sub>2</sub> could well arise from the increased presence of carboxylic functional groups; therefore, A, B, and C asphaltenes show a higher production of this gas. Due to the  $\pi$ - $\pi$  resonance effect between the hydroxyl and carbonyl group in the carboxyl structure, the hydrogen atom is active and could be captured by oxygen.<sup>78</sup> What makes the H atom in the hydroxyl group easy to combine with O<sub>2</sub> is the transfer of some electron clouds from the hydroxyl group to the carbonyl group.<sup>78</sup> The abstraction reaction of hydrogen by oxygen is endothermic. However, this reaction does not need a large amount of heat and occurs during the OC event. In addition, the products generated from the hydrogen-oxygen extraction reaction are unstable and will react further to generate CO<sub>2</sub>, that is, the decarboxylation reaction. The main reaction pathway proposed for CO<sub>2</sub> generation during asphaltene combustion is shown in Scheme 3.<sup>78</sup>



**Scheme 3.** Oxidation sequence, including hydrogen abstraction reaction by oxygen and decarboxylation reaction. Adapted from <sup>78</sup>

#### 4.2.2. Kinetic analysis

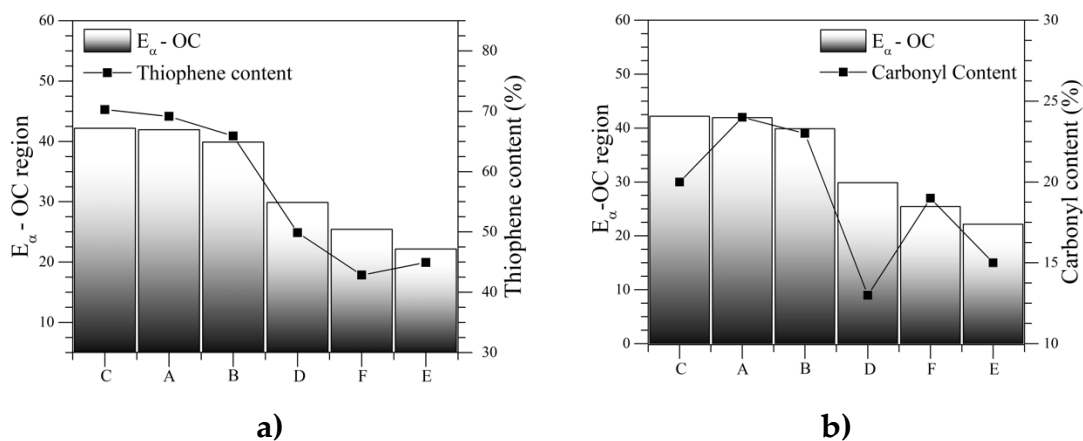
Kinetics parameters were obtained considering multistep reaction mechanisms after considering the four thermal regions described (OC, DCO, FC, and SC). Table 7 summarizes the effective activation energy and pre-exponential factor values calculated from the slope and intercept of the best-fit-line of  $\ln\left[\beta(-\ln(1-x))/P_{\text{O}_2}T^2\right]$  against  $1:T_i^{-1}$ . It is worth mentioning that, for

all cases, the first-order reaction over each thermal event was fitted with  $R^2 > 0.99$ , which is in accordance with our previous studies.<sup>20, 42, 43</sup>

From the results obtained, an increase in the effective activation energy is observed in OC and DCO regions as the pressure increases for all samples. For the first region, as the amount of oxygen chemisorbed increases, the effective activation energy increases as well, favored by high pressures. However, the DCO depends fundamentally on the functional groups formed during the OC region. This, in turn, depends on the sulfur, nitrogen, and oxygen forms present in the asphaltenes' chemical structure.

The effective activation energy values for the DCO zone are higher than those obtained for the OC zone.<sup>20, 79</sup> By contrast, the effective activation energy decreases as the pressure increases for the first and second combustion zones. Nevertheless, differences in  $E_a$  values likely reflect changes in the strength of bonds and the chemical structure of each asphaltene.<sup>45, 80</sup>

The values for the OC zone of the different samples suggest that the high content of sulfur and nitrogen anchored to aromatic rings reduces the energy required to chemisorb oxygen, as these are critical active sites for their interaction. Furthermore, the higher the degree of aromatization, the more energy is required due to the high percentage of oxygen that can chemisorb. Carbonyl and carboxyl group content, on the other hand, influences these values to the extent that their interaction with molecular oxygen increases as their content in the chemical structure of asphaltenes increases; thus, their effective activation energy increases. As a result, the aromatic carbon content has a similar effect on effective activation energy values. The relationships between some variables and the effective activation energy during the OC region are shown in Figure 11.



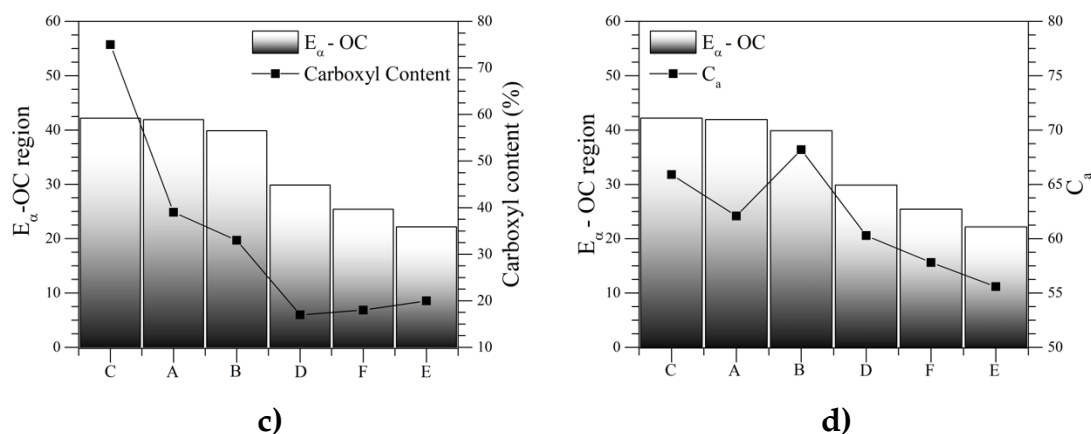


**Figure 11.** Effect of (a) thiophene content, (b) carbonyl content, (c) carboxyl content, and (d) aromatic carbon content over the amount of effective activation energy during the OC zone at 6.0 MPa.

For the case of asphaltenes A, B, and C, the  $E_{\alpha}$  values are lower in FC than the SC region, supporting the results observed in the previous sections. On the other hand, F, D, and E asphaltenes show the opposite behavior. They represent a possible decrease in the number of aromatic sheets per stack during the FC region. In addition, it is reported that at the temperatures at which F, D, and E asphaltenes end the FC region, there is a decrease in cluster diameter due to the cleavage in alkyl side chains, which suggests more refractory asphaltenes compared to the untreated molecules.<sup>63, 65</sup>

In terms of the second combustion region, results indicate that for A, B, and C, dealkylation of aliphatic side chains, cyclization of alkyl chains, polymerization of rings' radicals, aromatization of naphthenic rings, condensation and peri-condensation of aromatic rings occur during this interval, resulting in a cracking pathway that requires high energy to achieve.<sup>24, 28, 45</sup> On another side, as seen in Table 7, it is noted that the pre-exponential factor has a significant dependency on the pressure and the chemical nature of the  $n$ -C<sub>7</sub> asphaltenes. As it was reported, a change in pressure modifies  $k_0$  values by several orders of magnitude.<sup>20</sup> With the increase in the number of accessible states, the Arrhenius constant for OC is modified due to the change in entropy change by the molecular disorganization of the system and the formation of an activated complex. In all cases, asphaltene chemical nature modifies the kinetic parameters.

**Table 7.** Estimated kinetic parameters for the oxidation of different  $n$ -C<sub>7</sub> asphaltenes discretized in the different regions: *i*) oxygen chemisorption (OC) *ii*) decomposition of the chemisorbed oxygen (DCO) region, *iii*) first combustion (FC) region, and *iv*) second combustion (SC) region.

Asphaltene	Pressure (MPa)	Thermal Events					
		OC Region			DCO Region		
		$E_a$ (kJ·mol <sup>-1</sup> )	$k_o$ (min <sup>-1</sup> ·MPa <sup>-1</sup> )	R <sup>2</sup>	$E_a$ (kJ·mol <sup>-1</sup> )	$k_o$ (min <sup>-1</sup> ·MPa <sup>-1</sup> )	R <sup>2</sup>
A	0.084	-	-	-	-	-	-
	3.0	28.81	5.03 ×10 <sup>16</sup>	0.999	41.87	3.17 ×10 <sup>2</sup>	0.998
	6.0	41.93	2.74 ×10 <sup>21</sup>	0.997	98.70	1.44 ×10 <sup>8</sup>	0.999
		FC Region			SC Region		
	0.084	132.15	1.32 ×10 <sup>10</sup>	0.996	138.37	2.62 ×10 <sup>6</sup>	0.999
	3.0	71.61	1.24 ×10 <sup>5</sup>	0.998	83.14	1.18 ×10 <sup>6</sup>	0.997
	6.0	23.23	8.72 ×10 <sup>-1</sup>	0.999	79.12	4.42 ×10 <sup>5</sup>	0.996
		OC Region			DCO Region		
	0.084	-	-	-	-	-	-
3.0	26.94	3.13 ×10 <sup>19</sup>	0.999	55.74	3.29 ×10 <sup>3</sup>	0.996	
6.0	39.88	8.65 ×10 <sup>21</sup>	0.999	172.05	1.39 ×10 <sup>15</sup>	0.989	
B		FC Region			SC Region		
	0.084	76.12	3.01 ×10 <sup>6</sup>	0.999	95.43	6.90 ×10 <sup>6</sup>	0.999
	3.0	47.53	6.29 ×10 <sup>2</sup>	0.995	62.03	2.48 ×10 <sup>6</sup>	0.998
	6.0	37.80	2.17 ×10 <sup>1</sup>	0.999	52.50	1.78 ×10 <sup>4</sup>	0.999
		OC Region			DCO Region		
	0.084	-	-	-	-	-	-
	0.3	26.42	3.31 ×10 <sup>16</sup>	-	20.30	8.34 ×10 <sup>16</sup>	0.998
	6.0	42.18	1.07 ×10 <sup>22</sup>	0.998	21.37	8.40 ×10 <sup>17</sup>	0.998
		FC Region			SC Region		
0.084	80.25	9.31 ×10 <sup>4</sup>	0.996	129.59	4.83 ×10 <sup>8</sup>	0.999	
3.0	75.40	6.45 ×10 <sup>4</sup>	0.998	120.86	4.38 ×10 <sup>8</sup>	0.999	
6.0	74.49	4.52 ×10 <sup>1</sup>	0.998	107.53	2.67 ×10 <sup>8</sup>	0.999	
C		OC Region			DCO Region		
	0.084	-	-	-	-	-	-
	3.0	16.94	4.21 ×10 <sup>15</sup>	0.999	88.77	8.87 ×10 <sup>4</sup>	0.996
	6.0	29.88	8.65 ×10 <sup>21</sup>	0.999	130.02	1.30 ×10 <sup>5</sup>	0.989
		FC Region			SC Region		
	0.084	74.67	1.34 ×10 <sup>5</sup>	0.999	47.84	2.22 ×10 <sup>26</sup>	0.999
	3.0	44.54	4.42 ×10 <sup>2</sup>	0.995	31.82	2.62 ×10 <sup>8</sup>	0.998
	6.0	32.83	3.51 ×10 <sup>1</sup>	0.999	14.55	4.42 ×10 <sup>5</sup>	0.999
		OC Region			DCO Region		
0.084	-	-	-	-	-	-	
0.3	18.34	6.43 ×10 <sup>19</sup>	0.999	94.14	5.61 ×10 <sup>7</sup>	0.999	
6.0	22.18	8.12 ×10 <sup>20</sup>	0.998	146.20	2.79 ×10 <sup>11</sup>	0.998	
D		FC Region			SC Region		
	0.084	157.07	9.78 ×10 <sup>18</sup>	0.996	78.38	2.23 ×10 <sup>18</sup>	0.999
	3.0	72.92	4.71 ×10 <sup>4</sup>	0.998	57.17	1.29 ×10 <sup>9</sup>	0.999
	6.0	49.10	1.29 ×10 <sup>3</sup>	0.998	10.86	5.38 ×10 <sup>7</sup>	0.999
		OC Region			DCO Region		
	0.084	-	-	-	-	-	-
	0.3	20.14	8.67 ×10 <sup>14</sup>	0.999	41.87	3.17 ×10 <sup>2</sup>	0.999
	6.0	25.43	2.47 ×10 <sup>16</sup>	0.998	98.70	1.44 ×10 <sup>8</sup>	0.998
		FC Region			SC Region		
0.084	75.47	1.92 ×10 <sup>5</sup>	0.996	62.23	1.05 ×10 <sup>13</sup>	0.999	
3.0	54.52	3.91 ×10 <sup>3</sup>	0.998	21.20	9.11 ×10 <sup>11</sup>	0.999	
6.0	52.21	2.58 ×10 <sup>3</sup>	0.998	14.79	5.38 ×10 <sup>7</sup>	0.999	

## 5. Conclusions.

The chemical nature of the  $n$ -C<sub>7</sub> asphaltenes was found to have a direct influence on their thermo-oxidative decomposition behavior as the system pressure changed in this study. Asphaltenes with a high carboxyl structure content exhibited higher oxygen chemisorption. The thermal decomposition during DCO, FC, and SC events changes as the mass gained in the OC event increases. Furthermore, the aromaticity degree, the content of different chemical groups such as thioethers, thiophenes, pyridines, and pyrroles, the length of the alkyl side chains, and the diameter of the clusters, all affect the  $n$ -C<sub>7</sub> asphaltene oxidation process. Furthermore, increasing the  $\gamma$ -band intensity and decreasing the (002)-band intensity promotes dealkylation, allowing polyaromatic sheets to stack together and form coke. Hence, the mass loss rate of these  $n$ -C<sub>7</sub> asphaltenes is higher during the second combustion. By contrast,  $n$ -C<sub>7</sub> asphaltenes with long alkyl side chains trigger a faster exothermic reaction with oxygen, promoting asphaltene dealkylation. The effective activation energy and pre-exponential factor of the proposed multistep reactions were estimated using an approximation of the isoconversional method of Ozawa-Wall-Flynn. Higher  $E_a$  was required to carry out OC as the aromaticity factor, C=O and COO functional group contents, and total heteroatom content increased.

Furthermore, the activation energy in DCO is altered because of the oxygen structures formed in OC. This implies that thioethers, thiophenes, pyridines, and pyrroles influence DCO energy values, which are higher than those obtained for the OC region, implying that more complex molecules are broken, requiring more energy to react.

Some asphaltenes have higher  $E_a$  values in FC than in SC due to the initial chemical structure, indicating that dealkylation of aliphatic side chains, cyclization of alkyl chains, a combination of rings' radicals, aromatization of naphthenic rings, and condensation and peri-condensation of aromatic rings occur during the first combustion, resulting in a cracking pathway that requires high energy to achieve.



## References.

1. Hart, A. Advanced studies of catalytic upgrading of heavy oils. University of Birmingham, 2014.
2. Medina, O. E.; Hurtado, Y.; Caro-Velez, C.; Cortés, F. B.; Riazi, M.; Lopera, S. H.; Franco, C. A., Improvement of Steam Injection Processes Through Nanotechnology: An Approach through in Situ Upgrading and Foam Injection. *Energies* **2019**, 12, (24), 4633.
3. Liu, H.; Cheng, L.; Huang, S.; Jia, P.; Chen, M., Evolution characteristics of SAGD steam chamber and its impacts on heavy oil production and heat consumption. *International Journal of Heat and Mass Transfer* **2018**, 121, 579-596.
4. Greaves, M.; Xia, T. X.; Ayasse, C. In *Underground upgrading of heavy oil using THAI-'toe-to-heel air injection'*, SPE International Thermal Operations and Heavy Oil Symposium, 2005; Society of Petroleum Engineers: 2005.
5. McKay, A. S.; Nasr, T. N., Recovery of bitumen or heavy oil in situ by injection of hot water of low quality steam plus caustic and carbon dioxide. In Google Patents: 1991.
6. C.A., A.-M. D. M. O. E. G. J. A. S. C.-E. A. A. C. F. B. F., NiO, Fe<sub>2</sub>O<sub>3</sub>, and MoO<sub>3</sub> Supported over SiO<sub>2</sub> Nanocatalysts for Asphaltene Adsorption and Catalytic Decomposition: Optimization through a Simplex–Centroid Mixture Design of Experiments. *Catalysts* **2020**, 10, (569).
7. Guo, K.; Li, H.; Yu, Z., In-situ heavy and extra-heavy oil recovery: A review. *Fuel* **2016**, 185, 886-902.
8. Shah, A.; Fishwick, R.; Wood, J.; Leeke, G.; Rigby, S.; Greaves, M., A review of novel techniques for heavy oil and bitumen extraction and upgrading. *Energy & Environmental Science* **2010**, 3, (6), 700-714.
9. Medina, O. E.; Caro-Vélez, C.; Gallego, J.; Cortés, F. B.; Lopera, S. H.; Franco, C. A., Upgrading of Extra-Heavy Crude Oils by Dispersed Injection of NiO–PdO/CeO<sub>2±δ</sub> Nanocatalyst-Based Nanofluids in the Steam. *Nanomaterials* **2019**, 9, (12), 1755.
10. Kök, M.; Keskin, C. In *Comparative combustion kinetics for in-situ combustion process*, IOR 1999-10th European Symposium on Improved Oil Recovery, 1999; 1999.

11. Akkutlu, I. Y.; Yortsos, Y. C., The dynamics of in-situ combustion fronts in porous media. *Combustion and Flame* **2003**, 134, (3), 229-247.
12. Yuan, C.; Varfolomeev, M. A.; Emelianov, D. A.; Suwaid, M. A.; Khachatryan, A. A.; Starshinova, V. L.; Vakhitov, I. R.; Al-Muntaser, A. A., Copper stearate as a catalyst for improving the oxidation performance of heavy oil in in-situ combustion process. *Applied Catalysis A: General* **2018**, 564, 79-89.
13. Amanam, U. U.; Kavscek, A. R., Analysis of the effects of copper nanoparticles on in-situ combustion of extra heavy-crude oil. *Journal of Petroleum Science and Engineering* **2017**, 152, 406-415.
14. Melcon, S., Oil recovery by in situ combustion. In Google Patents: 1965.
15. Ranzi, E.; Faravelli, T.; Gaffuri, P.; Sogaro, A., Low-temperature combustion: automatic generation of primary oxidation reactions and lumping procedures. *Combustion and flame* **1995**, 102, (1-2), 179-192.
16. Dabbous, M. K.; Fulton, P. F., Low-temperature-oxidation reaction kinetics and effects on the in-situ combustion process. *Society of Petroleum Engineers Journal* **1974**, 14, (03), 253-262.
17. Acevedo, S.; Castro, A.; Vásquez, E.; Marcano, F.; Ranaudo, M. a. A., Investigation of physical chemistry properties of asphaltenes using solubility parameters of asphaltenes and their fractions A1 and A2. *Energy & Fuels* **2010**, 24, (11), 5921-5933.
18. Acevedo, S.; Castillo, J.; Vargas, V.; Castro, A.; Delgado, O. Z.; Ariza, C. A. F.; Cotés, F. B.; Bouyssiére, B., Suppression of Phase Separation as a Hypothesis to Account for Nuclei or Nanoaggregate Formation by Asphaltenes in Toluene. *Energy & Fuels* **2018**.
19. Acevedo, S.; Castro, A.; Negrin, J. G.; Fernández, A.; Escobar, G.; Piscitelli, V.; Delolme, F.; Dessalces, G., Relations between asphaltene structures and their physical and chemical properties: The rosary-type structure. *Energy & fuels* **2007**, 21, (4), 2165-2175.
20. Medina, O. E.; Gallego, J.; Rodriguez, E.; Franco, C. A.; Cortés, F. B., Effect of Pressure on the Oxidation Kinetics of Asphaltenes. *Energy & Fuels* **2019**.
21. Zhao, S.; Pu, W.; Varfolomeev, M. A.; Yuan, C.; Qin, S.; Wang, L.; Emelianov, D. A.; Khachatryan, A. A., Thermal behavior and kinetics of heavy crude oil during combustion by high pressure differential scanning calorimetry

and accelerating rate calorimetry. *Journal of Petroleum Science and Engineering* **2019**, 106225.

22. Murugan, P.; Mani, T.; Mahinpey, N.; Asghari, K., The low temperature oxidation of Fosterton asphaltenes and its combustion kinetics. *Fuel processing technology* **2011**, 92, (5), 1056-1061.

23. Brown, D.; Fish, A., The extension to long-chain alkanes and to high temperatures of the hydroperoxide chain mechanism of autoxidation. *Proceedings of the Royal Society of London. Series A. Mathematical and Physical Sciences* **1969**, 308, (1495), 547-568.

24. Freitag, N. P., Chemical-reaction mechanisms that govern oxidation rates during in-situ combustion and high-pressure air injection. *SPE Reservoir Evaluation & Engineering* **2016**, 19, (04), 645-654.

25. Wei, B.; Zou, P.; Zhang, X.; Xu, X.; Wood, C.; Li, Y., Investigations of structure–property–thermal degradation kinetics alterations of Tahe Asphaltenes caused by low temperature oxidation. *Energy & fuels* **2018**, 32, (2), 1506-1514.

26. Wei, B.; Zou, P.; Shang, J.; Gao, K.; Li, Y.; Sun, L.; Pu, W., Integrative determination of the interactions between SARA fractions of an extra-heavy crude oil during combustion. *Fuel* **2018**, 234, 850-857.

27. Gonçalves, M.; Teixeira, M.; Pereira, R.; Mercury, R.; Matos, J. d. R., Contribution of thermal analysis for characterization of asphaltenes from Brazilian crude oil. *Journal of thermal analysis and calorimetry* **2001**, 64, (2), 697-706.

28. Murugan, P.; Mahinpey, N.; Mani, T., Thermal cracking and combustion kinetics of asphaltenes derived from Fosterton oil. *Fuel Processing Technology* **2009**, 90, (10), 1286-1291.

29. Barre, L.; Espinat, D.; Rosenberg, E.; Scarsella, M., Colloidal structure of heavy crudes and asphaltene solutions. *Revue de l'Institut Français du Pétrole* **1997**, 52, (2), 161-175.

30. International, A., ASTM D5236-13, Standard Test Method for Distillation of Heavy Hydrocarbon Mixtures (Vacuum Potstill Method). *Annual Book of ASTM Standards* **2013**.

31. International, A., ASTM D2892, Standard Test Method for Distillation of Crude Petroleum (15-Theoretical Plate Column). *Annual Book of ASTM Standards* **2016**.
32. Medina, O. E.; Gallego, J.; Arias-Madrid, D.; Cortés, F. B.; Franco, C. A., Optimization of the Load of Transition Metal Oxides (Fe<sub>2</sub>O<sub>3</sub>, Co<sub>3</sub>O<sub>4</sub>, NiO and/or PdO) onto CeO<sub>2</sub> Nanoparticles in Catalytic Steam Decomposition of n-C<sub>7</sub> Asphaltenes at Low Temperatures. *Nanomaterials* **2019**, 9, (3), 401.
33. Medina Erao, O. E.; Gallego, J.; Olmos, C. M.; Chen, X.; Cortés, F. B.; Franco, C. A., Effect of Multifunctional Nanocatalysts on n-C<sub>7</sub> Asphaltene Adsorption and Subsequent Oxidation under High Pressure Conditions. *Energy & Fuels* **2020**.
34. Lopes, S. M.; Geng, P., Estimation of elemental composition of diesel fuel containing biodiesel. *SAE International Journal of Fuels and Lubricants* **2013**, 6, (3), 668-676.
35. Acevedo, S.; Gutierrez, L. B.; Negrin, G.; Pereira, J. C.; Mendez, B.; Delolme, F.; Dessalces, G.; Broseta, D., Molecular weight of petroleum asphaltenes: A comparison between mass spectrometry and vapor pressure osmometry. *Energy & fuels* **2005**, 19, (4), 1548-1560.
36. Yarranton, H. W.; Alboudwarej, H.; Jakher, R., Investigation of asphaltene association with vapor pressure osmometry and interfacial tension measurements. *Industrial & engineering chemistry research* **2000**, 39, (8), 2916-2924.
37. Shao, R.; Shen, Z.; Li, D.; Sun, Z.; Pei, L.; Liu, X.; Li, W.; Dan, Y., Investigation on composition and structure of asphaltenes during low-temperature coal tar hydrotreatment under various reaction pressures. *Journal of analytical and applied pyrolysis* **2018**, 136, 44-52.
38. Lee, C.; Yang, W.; Parr, R. G., Results obtained with the correlation energy density functionals. *Phys. Rev. B: Condens. Matter Mater. Phys* **1988**, 37, 785.
39. Schmider, H. L.; Becke, A. D., Optimized density functionals from the extended G2 test set. *The Journal of chemical physics* **1998**, 108, (23), 9624-9631.
40. Martín-Martínez, F. J.; Fini, E. H.; Buehler, M. J., Molecular asphaltene models based on Clar sextet theory. *RSC Advances* **2015**, 5, (1), 753-759.
41. Gimzewski, E., An accurate and compact high-pressure thermogravimetric analyser. *Journal of thermal analysis* **1991**, 37, (6), 1251-1260.

42. Senneca, O.; Vorobiev, N.; Wütscher, A.; Cerciello, F.; Heuer, S.; Wedler, C.; Span, R.; Schiemann, M.; Muhler, M.; Scherer, V., Assessment of combustion rates of coal chars for oxy-combustion applications. *Fuel* **2019**, 238, 173-185.
43. Niksa, S.; Liu, G.-S.; Hurt, R. H., Coal conversion submodels for design applications at elevated pressures. Part I. devolatilization and char oxidation. *Progress in Energy and Combustion Science* **2003**, 29, (5), 425-477.
44. Liu, G.-S.; Niksa, S., Coal conversion submodels for design applications at elevated pressures. Part II. Char gasification. *Progress in energy and combustion science* **2004**, 30, (6), 679-717.
45. Calemme, V.; Iwanski, P.; Nali, M.; Scotti, R.; Montanari, L., Structural characterization of asphaltenes of different origins. *Energy & Fuels* **1995**, 9, (2), 225-230.
46. Santos, R.; Loh, W.; Bannwart, A.; Trevisan, O., An overview of heavy oil properties and its recovery and transportation methods. *Brazilian Journal of Chemical Engineering* **2014**, 31, (3), 571-590.
47. Medina, O. E.; Gallego, J.; Restrepo, L. G.; Cortés, F. B.; Franco, C. A., Influence of the Ce<sup>4+</sup>/Ce<sup>3+</sup> Redox-couple on the cyclic regeneration for adsorptive and catalytic performance of NiO-PdO/CeO<sub>2</sub>± $\delta$  nanoparticles for n-C<sub>7</sub> asphaltene steam gasification. *Nanomaterials* **2019**, 9, (5), 734.
48. Carvalho, V. V.; Vasconcelos, G. A.; Tose, L. V.; Santos, H.; Cardoso, F. M.; Fleming, F.; Romão, W.; Vaz, B. G., Revealing the chemical characterization of asphaltenes fractions produced by N-methylpyrrolidone using FTIR, molecular fluorescence, <sup>1</sup>H NMR, and ESI (±) FT-ICR MS. *Fuel* **2017**, 210, 514-526.
49. Olvera, J. N. R.; Gutiérrez, G. J.; Serrano, J. R.; Ovando, A. M.; Febles, V. G.; Arceo, L. D. B., Use of unsupported, mechanically alloyed NiWMoC nanocatalyst to reduce the viscosity of aquathermolysis reaction of heavy oil. *Catalysis Communications* **2014**, 43, 131-135.
50. Chen, C.; Gao, J.-S.; Yan, Y.-J., Original preasphaltenes and asphaltenes in coals. *Fuel processing technology* **1998**, 55, (2), 143-151.
51. Sun, Z.-H.; Li, D.; Ma, H.-X.; Tian, P.-P.; Li, X.-K.; Li, W.-H.; Zhu, Y.-H., Characterization of asphaltene isolated from low-temperature coal tar. *Fuel Processing Technology* **2015**, 138, 413-418.

52. Nguyen, N. T.; Kang, K. H.; Lee, C. W.; Kim, G. T.; Park, S.; Park, Y.-K., Structure comparison of asphaltene aggregates from hydrothermal and catalytic hydrothermal cracking of C5-isolated asphaltene. *Fuel* **2019**, 235, 677-686.
53. Bava, Y. B.; Geronés, M.; Giovanetti, L. J.; Andrini, L.; Erben, M. F., Speciation of sulphur in asphaltenes and resins from Argentinian petroleum by using XANES spectroscopy. *Fuel* **2019**, 256, 115952.
54. Yen, T. F.; Erdman, J. G.; Pollack, S. S., Investigation of the structure of petroleum asphaltenes by X-ray diffraction. *Analytical chemistry* **1961**, 33, (11), 1587-1594.
55. Yasar, M.; Akmaz, S.; Gurkaynak, M., Investigation of the molecular structure of Turkish asphaltenes. *Petroleum Science and Technology* **2009**, 27, (10), 1044-1061.
56. Tsuji, N.; Kennemur, J. L.; Buyck, T.; Lee, S.; Prévost, S.; Kaib, P. S.; Bykov, D.; Farès, C.; List, B., Activation of olefins via asymmetric Brønsted acid catalysis. *Science* **2018**, 359, (6383), 1501-1505.
57. Ascanius, B. E.; Garcia, D. M.; Andersen, S. I., Analysis of asphaltenes subfractionated by N-methyl-2-pyrrolidone. *Energy & fuels* **2004**, 18, (6), 1827-1831.
58. Retcofsky, H.; Schweighardt, F.; Hough, M., Determination of aromaticities of coal derivatives by nuclear magnetic resonance spectrometry and the Brown-Ladner equation. *Analytical Chemistry* **1977**, 49, (4), 585-588.
59. AlHumaidan, F. S.; Hauser, A.; Rana, M. S.; Lababidi, H. M., NMR Characterization of Asphaltene Derived from Residual Oils and Their Thermal Decomposition. *Energy & Fuels* **2017**, 31, (4), 3812-3820.
60. Vukovic, J. P.; Novak, P.; Jednacak, T., NMR Spectroscopy as a Tool for Studying Asphaltene Composition. *Croatica Chemica Acta* **2019**, 92, (3), 1G-1G.
61. Mullins, O. C., The modified Yen model. *Energy & Fuels* **2010**, 24, (4), 2179-2207.
62. Sánchez, N. M.; de Klerk, A., Low-temperature oxidative asphaltenes liquefaction for petrochemicals: fact or fiction? *Applied Petrochemical Research* **2016**, 6, (2), 97-106.

63. Kuakpetoon, D.; Wang, Y.-J., Structural characteristics and physicochemical properties of oxidized corn starches varying in amylose content. *Carbohydrate Research* **2006**, 341, (11), 1896-1915.
64. Shafeeyan, M. S.; Daud, W. M. A. W.; Houshmand, A.; Shamiri, A., A review on surface modification of activated carbon for carbon dioxide adsorption. *Journal of Analytical and Applied Pyrolysis* **2010**, 89, (2), 143-151.
65. Zijun, W.; Wenjie, L.; Guohe, Q.; Jialin, Q., Structural characterization of guda asphaltene by ruthenium ion catalyzed oxidation. *Petroleum science and technology* **1997**, 15, (5-6), 559-577.
66. Fernandez, I.; Frenking, G., Direct estimate of conjugation and aromaticity in cyclic compounds with the EDA method. *Faraday discussions* **2007**, 135, 403-421.
67. Franco, C. A.; Nassar, N. N.; Montoya, T.; Ruíz, M. A.; Cortés, F. B., Influence of asphaltene aggregation on the adsorption and catalytic behavior of nanoparticles. *Energy & Fuels* **2015**, 29, (3), 1610-1621.
68. Franco, C. A.; Montoya, T.; Nassar, N. N.; Pereira-Almao, P.; Cortés, F. B., Adsorption and subsequent oxidation of colombian asphaltenes onto nickel and/or palladium oxide supported on fumed silica nanoparticles. *Energy & Fuels* **2013**, 27, (12), 7336-7347.
69. Medina, O. E.; Olmos, C.; Lopera, S. H.; Cortés, F. B.; Franco, C. A., Nanotechnology Applied to Thermal Enhanced Oil Recovery Processes: A Review. *Energies* **2019**, 12, (24), 4671.
70. Moschopedis, S. E.; Parkash, S.; Speight, J. G., Thermal decomposition of asphaltenes. *Fuel* **1978**, 57, (7), 431-434.
71. Ismagilov, Z.; Yashnik, S.; Kerzhentsev, M.; Parmon, V.; Bourane, A.; Al-Shahrani, F.; Hajji, A.; Koseoglu, O., Oxidative desulfurization of hydrocarbon fuels. *Catalysis Reviews* **2011**, 53, (3), 199-255.
72. Javadli, R.; de Klerk, A., Desulfurization of heavy oil—oxidative desulfurization (ODS) as potential upgrading pathway for oil sands derived bitumen. *Energy & fuels* **2012**, 26, (1), 594-602.
73. Javadli, R.; De Klerk, A., Desulfurization of heavy oil. *Applied Petrochemical Research* **2012**, 1, (1-4), 3-19.

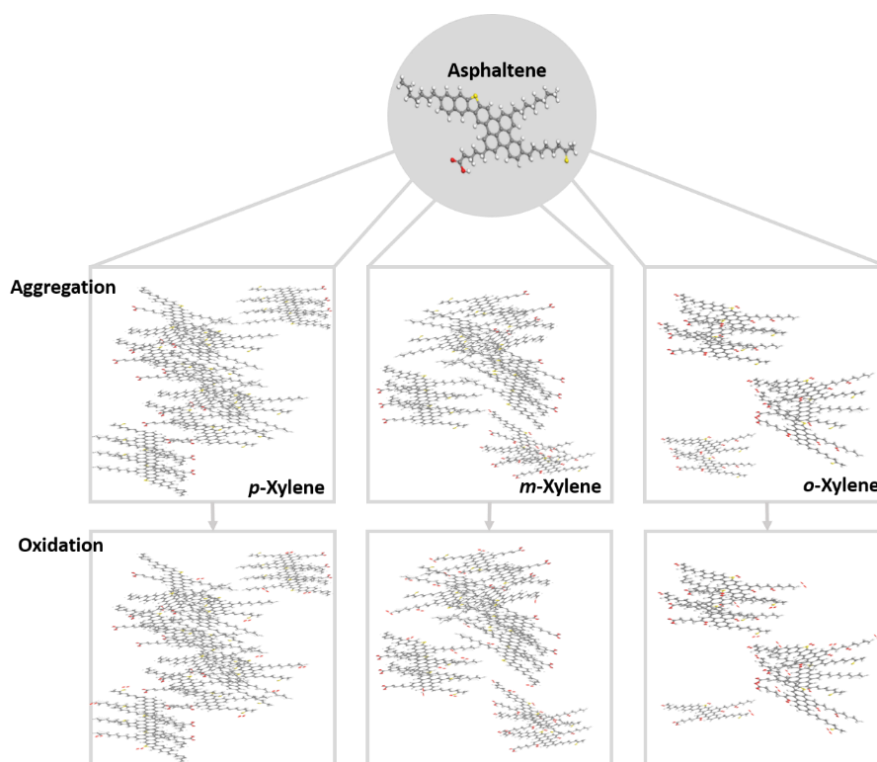
74. Benson, S. W., Thermochemistry and kinetics of sulfur-containing molecules and radicals. *Chemical Reviews* **1978**, 78, (1), 23-35.
75. Prado, G. H.; Rao, Y.; de Klerk, A., Nitrogen removal from oil: a review. *Energy & Fuels* **2017**, 31, (1), 14-36.
76. Alzueta, M.; Tena, A.; Bilbao, R., Pyridine conversion in a flow reactor and its interaction with nitric oxide. *Combustion science and technology* **2002**, 174, (10), 151-169.
77. Mortensen, P. M.; Grunwaldt, J.-D.; Jensen, P. A.; Knudsen, K.; Jensen, A. D., A review of catalytic upgrading of bio-oil to engine fuels. *Applied Catalysis A: General* **2011**, 407, (1-2), 1-19.
78. Qi, X.; Wang, D.; Xue, H.; Jin, L.; Su, B.; Xin, H., Oxidation and self-reaction of carboxyl groups during coal spontaneous combustion. *Spectroscopy Letters* **2015**, 48, (3), 173-178.
79. Zahabi, A.; Gray, M. R.; Dabros, T., Kinetics and properties of asphaltene adsorption on surfaces. *Energy & fuels* **2012**, 26, (2), 1009-1018.
80. Liu, D.; Hou, J.; Luan, H.; Pan, J.; Song, Q.; Zheng, R., Coke yield prediction model for pyrolysis and oxidation processes of low-asphaltene heavy oil. *Energy & Fuels* **2019**, 33, (7), 6205-6214.





## Chapter 3.

# Experimental and Theoretical Study of the Influence of Solvent on Asphaltene-Aggregates Thermo-oxidation through High-Pressure Thermogravimetric Analysis



Published article in Fuel: [doi.org/10.1016/j.fuel.2022.126491](https://doi.org/10.1016/j.fuel.2022.126491)

Impact factor: 8.035

# Experimental and Theoretical Study of the Influence of Solvent on Asphaltene-Aggregates Thermo-oxidation through High-Pressure Thermogravimetric Analysis

## Abstract

This study focuses on understanding *n*-C<sub>7</sub> asphaltene-aggregates oxidative behavior under high-pressure conditions. For this aim, different asphaltene model solutions were prepared using three asphaltene concentrations (0.1, 1.0, and 10 wt.%) on three xylene isomers. The experimental results revealed that the asphaltene aggregate size increased as *o*-xylene < *m*-xylene < *p*-xylene. Also, molecular dynamics (MD) simulations were carried out to explain the aggregation differences. It was found that the -CH<sub>3</sub> location in the xylene substantially impacts the aggregation state. The *o*-xylene molecules surrounding the asphaltene aggregates oriented their -CH<sub>3</sub> groups towards the aggregates, increasing their interaction energy and reducing the aggregation size. Further, the oxidative experiments of the aggregates showed that the oxygen chemisorption decreased as the asphaltene aggregate size increased, reducing their reactivity. Contrasting the xylene isomers, for concentrations > 1.0 wt.%, the mass gained by oxygen chemisorption increased in the order: *p*-xylene < *m*-xylene < *o*-xylene. This study improves our understanding of the relationship between the aggregation and thermal oxidation of crude oils, characterizing the physical behavior to propose alternatives that reduce asphaltene aggregation and improve the oxidative kinetic.

## 1. Introduction

Extra-heavy (EHO) and heavy crude oil (HO) are commonly subjected to thermal treatments from production to refining operations, involving asphaltene conversion under a wide range of operating conditions of pressure and temperature [1-3]. Depending on the crude oil's chemical nature, asphaltenes present different aggregation states that could affect the rheological behavior and subsequent thermal conversion [4-6]. Thus, studying the asphaltene fraction and aggregates is relevant to understanding their rheological properties and determining the best upgrading scheme for HO and EHO during thermal treatments [7, 8].

Most of the studies [9-12] have been focused on evaluating the thermo-oxidative behavior of asphaltene molecules at low and high pressure. The found thermograms suggested that the asphaltene thermal oxidation is pressure-dependent and occurs in four mainly thermal events, namely *i*) oxygen chemisorption (OC), *ii*) oxygen decomposition of chemisorbed oxygen functional groups (DCO), *iii*) the first combustion (FC), and *iv*) second combustion (SC) or high-temperature oxidation, for pressures higher than 0.7 MPa [11]. The OC and DCO disappear for pressures < 0.7 MPa.

Nevertheless, asphaltenes have high polarity and complex structure; they present a high self-association degree during heavy oil processing. Thus, further efforts are needed to provide more comprehensive knowledge and understand the processes of asphaltene decomposition, considering the complexity of the aggregation state of asphaltenes in the crude oil matrix [11].

Molecular dynamics (MD) simulations have become a valuable tool. Some authors have used representative asphaltene model solutions to study variables such as viscosity and asphaltene aggregate size, among others [13-16]. Moncayo et al. [13] studied the methyl substituent (-CH<sub>3</sub>) effect on the rheological behavior of model solutions of asphaltenes at different concentrations, comparing *p*-xylene and toluene. In addition, MD simulations evidence that solvent characteristics strongly influence asphaltene aggregation [17-19]. They determined an increase in the viscosity as the asphaltene concentration increases, 739 % higher in *p*-xylene than toluene. Also, Larichev et al. [16] evaluated the influence of various organic compounds on the aggregation of asphaltenes, obtaining a higher length of

13.6 nm for a consisting solution of 20 % in mass fraction of asphaltene diluted on furfural. In this current context, solvents can affect the aggregation phenomenon and rheologic behavior of asphaltene model solutions. Some authors have evaluated the relationship between asphaltene aggregation state and rheologic behaviour. D'Avila et al. [20] demonstrated that the influence of the aggregation stages on the viscosity was not linear. There was an optimal aggregation state to cause lower viscosity values. Also, Moncayo et al. [21] introduced the effect of xylene isomers on asphaltene aggregates and oil solution model viscosities. They found that as higher the asphaltene concentration, the higher the size of the aggregates and the higher the viscosity of the systems. Despite the valuable contributions found, there is still no clear study on the effect of aggregate size on asphaltene reactivity.

Solvents might differ in their maximum oxygen solubility, which might impact the oxygen transfer reaction of asphaltenes, affecting their reactivity [22]. Indeed, depending on the identity of the solvent, several mechanistic routes are possible, including hydrogen abstraction from the solvent and radical accepting capability [13].

Regarding the mechanism, several factors influence the aggregates interactions, including thermo-oxidation of labile bonds, asphaltene structure, asphaltene condensation degree, and thus, the aggregate structure [12].

Hence, this work aims to understand for the first time the thermo-oxidative behavior at high pressure of different asphaltene model solutions with varying states of aggregation. This study includes the effect of other solvents, including *o*-, *m*-, and *p*-xylene, on the asphaltene-aggregate size of asphaltene model solutions. The analysis was done experimentally through SAXS measurements and theoretically using molecular dynamic simulation. Then the reactivity was analyzed by high-pressure thermogravimetric experiments. In the first set of thermogravimetric experiments, the effect on the reactivity of the concentration of asphaltenes varied between 0.1% and 10% in a mass fraction was evaluated, using *p*-xylene as a reference solvent. Then, three aromatic solvents (*p*-xylene, *m*-xylene, and *o*-xylene) with different chemical structures and solubility parameters were used to determine their effect on asphaltene aggregation and reactivity.

This is the first work addressing the aggregation state's effect on asphaltene reactivity at high-pressure conditions. We believe that the findings of our investigations shed physical light on understanding the real

fluid. To isolate input variables and evaluate the impact on the output variable (aggregate sizes, thermal oxidation), asphaltene-xylene interactions were considered. Therefore, in the asphaltene-maltene interaction (resins or aromatics), effects such as chain length, location of the same, sizes of the aromatic nucleus, and shape of the aromatic nucleus, among others, will be seen, which will have an impact on the macroscopic behavior of the fluid according to the mechanisms reported in writing. It is hoped that a new landscape can be opened to deepen knowledge and understanding of thermo-oxidation reactions of asphaltene aggregates.

## 2. Experimental

### 2.1. Materials.

A Colombian extra-heavy crude oil was employed for *n*-C<sub>7</sub> asphaltene isolation following the ASTM standard [23]. The crude oil has 6.7 ° API, a viscosity of  $6 \times 10^6$  cP at 25 °C, and SARA content of 13.0, 16.9, 49.9, and 20.2% w·w<sup>-1</sup>, respectively. *n*-heptane (99.5%, Sigma-Aldrich, St. Louis, MO, USA) was used for asphaltene extraction. The chemical and physical properties are detailed in a previous study [24].

For the thermogravimetric analyses, the reacting gas employed consists of synthetic air NTC 2561 (CRYOGAS, Bogotá, Colombia) composed of 20.93% balanced O<sub>2</sub>. *p*-Xylene, *m*-xylene, and *o*-xylene (98%) were purchased from ITW Reagents (Chicago, USA). Xylene was chosen as the solvent based on a previous study [13], where the rheological and aggregation behavior was evaluated using the three xylene isomers. The results indicate that minor structure differences promoted changes in the aggregation state and, thus, in the viscosity of the solution models. Hence, to determine the aggregation size effect on the thermo-oxidative process, the three xylene isomers were used. The basic properties of the selected diluents provided by the supplier are summarized in Table 1. Solubility parameters were determined using inert gas chromatography using a Chromosorb P AW DMCS, 80/100 mesh, based on the ASTM D5480 [25].

**Table 1.** General properties of the diluents used for preparing asphaltene model solutions.

Diluent	Density (mg·L <sup>-1</sup> ) <sup>a</sup>	Viscosity (cp) <sup>a</sup>	Molecular weight (g·mol <sup>-1</sup> )	Purity (%)	Solubility parameter $\delta$ ( $\gamma \cdot V^{-1/3} \text{ dyn} \cdot \text{mol}^{1/3} \cdot \text{cm}^{-2}$ )
<i>p</i> -xylene	0.864	0.644	106.17	98.0	5.7
<i>m</i> -xylene	0.860	0.617	106.17	98.0	5.8
<i>o</i> -xylene	0.880	0.809	106.17	98.0	6.1

<sup>a</sup>Measured at 25 °C.

## 2.2. Asphaltene characterization

The elemental composition of C, H, S, and N for each type of the extracted *n*-C<sub>7</sub> asphaltenes samples was measured by a Thermo Flash elemental analyzer EA 1112 (Thermo Finnigan, Milan, Italy) using the conventional combustion procedure following the ASTM D5291 standard [26]. As for the oxygen content, it was obtained by the difference considering its sum equals 100 %. The average molecular weight ( $M_w$ ) for asphaltene samples was calculated by vapor pressure osmometry (VPO) using a Knauer osmometer (Knauer, Berlin-Heidelberg, West Germany) calibrated with benzyl [27, 28].

The X-ray diffraction (DRX) analysis for each asphaltene sample was performed using a Bruker D8 Advance X-ray diffractometer (BRUKER, Rivas-Vaciamadrid, Spain). Diffraction patterns were recorded at room temperature ( $2\theta = 6^\circ$ - $8^\circ$ ) using a scanning speed of  $1 \text{ min}^{-1}$  and a step size of  $0.02^\circ$  ( $2\theta$ ) with a Cu  $K\alpha$  radiation of 40 kV and 40 mA and a wavelength ( $\lambda$ ) of 1.541 Å. The recorded patterns were smoothed and deconvoluted. The position, intensity, and area of the peaks and the full width at half maximum (FWHM) were then determined. The macro-structure parameters of the different asphaltene samples were calculated according to other studies [29]. The <sup>1</sup>H and <sup>13</sup>C NMR was performed on a Bruker ASCEND III HD spectrometer (Karlsruhe, Germany) operating between 600 and 125 MHz, with a 5 mm cryoprobe TCI. The asphaltene samples were dissolved in CDCl<sub>3</sub> (99.8%) containing traces of tetramethylsilane (TMS) and used as standard internal solvents for <sup>1</sup>H NMR measurements. As for the <sup>13</sup>C NMR, it operates at 75.45 MHz, and the values of the chemical shifts were related to the central signal at 77 ppm of CDCl<sub>3</sub>. The sample concentration was fixed in a mass fraction of 15.0 % and 21.0 % in 0.5 mL of the solvent agent for <sup>1</sup>H and <sup>13</sup>C measurements, respectively. The settings for the <sup>1</sup>H NMR spectra were

adjusted with a pulse angle of 90° (10.5 μs), a spectral width of 12.3 kHz, and a delay time of 1 s. The quantitative <sup>13</sup>C NMR spectra were acquired with an inverse gated decoupling, a pulse angle of 30° (2.2 μs), a spectral width of 35 kHz, and a delay time of 180 s.

### 2.3. Solution model preparation

*n*-C<sub>7</sub> Asphaltene model solutions were prepared following the one-stage procedure described by Minale et al.[30]. The process suggests that asphaltenes should be diluted in the desired quantity of the specific pure solvent in one stage. To this aim, asphaltenes were slowly added to the respective xylene isomers (*o*-, *m*-, *p*-xylene) while the mixture was magnetically stirred at 300 rpm for 30 min. Here, it is worth mentioning that depending on the procedure applied to construct the model solution, its viscosity could be modified by the induction of clusters or shrinkage aggregates.

Different model solutions consisting of mass fractions of 0.1 %, 1.0 %, and 10.0 % of *n*-C<sub>7</sub> asphaltenes were prepared. The total dilution of the samples was confirmed under the microscope with a 40× magnification lens. The microscope used in this study was biological, model AmScope B340, coupled with an MU300 microscope digital camera. This method was used based on the steps proposed by Tavakkoli et al.[31] which can be extended to a wide range of oils, from very low to high asphaltene concentrations.

### 2.4. Aggregate size measurements

Asphaltene aggregate sizes on the different solvents were registered by Small-angle X-ray scattering (SAXS) using an S3-MICRO diffractometer (Hecus, Austria) with a Cu anode ( $\lambda_{\text{CuK}\alpha} = 1.541 \text{ \AA}$ ). The patterns were analyzed in the wave factor range ( $h$ ) between 0.01 and 0.6  $\text{\AA}^{-1}$ , which is defined by the Equation (1):

$$h = 4\pi \sin(\theta) / \lambda \quad (1)$$

where  $2\theta$  are the scattering angle and  $\lambda$  the wavelength of the applied radiation using 1.5 mm quartz capillaries. The patterns for asphaltenes were obtained by subtracting the corresponding SAXS of the initial solvents from the asphaltene solutions, considering the X-ray absorption coefficients [22, 32].



The radius of gyration ( $R_G$ ) of the particles was assessed by the slope of the small-angle curve of the graph ( $\ln(I(h))$  against  $h^2$ ), whereas the radius of gyration of the cross-section ( $R_{G(cross)}$ ) of the particles was obtained by the slope of the plot ( $\ln(I(h)) * h$  against  $h^2$ ) as long as  $R_G * h < 1.3$  [33, 34]. Finally, the fitting of the SAXS results was analyzed via the ellipsoid model (Equation (2)):

$$I(h) = \int_0^{\infty} F(h, R) \cdot D_v(R) dR \quad (2)$$

where  $F(h, R)$  is an average form factor and  $D_v(R)$  is the volume size distribution of the dispersed particles. Considering that HP-TGA measurements were performed after flash solvent evaporation, the aggregate size of the asphaltenes after the process was estimated to corroborate that the size of the asphaltene aggregate is not affected during flash evaporation of the solvent. Flash evaporation was carried out at the evaporation temperature of each solvent using a rotary evaporator with a speed of 70 rpm for 5 min. Data were processed in the ATSAS program package (version 2.4) [35].

## 2.5. High-Pressure Thermogravimetric Analysis

High-pressure thermogravimetric analyzer HP-TGA 750 (TA instruments Inc., Hüllhorst, Germany) containing a magnetically levitated balance was employed to appraise the thermal behavior of different *n*-C<sub>7</sub> asphaltenes under an air atmosphere at high pressure (6.0 MPa). Details of the system equipment are reported elsewhere [36].

Flash evaporation was realized before TGA measurements to avoid diffusional effects on thermal profiles so that the impact of the state of aggregation of asphaltene is achieved. The tests were carried out using a heating ramp of 10 °C·min<sup>-1</sup> from 100 °C to 800 °C under an airflow of 80 mL·min<sup>-1</sup>. The pressure was maintained at 6.0 MPa, while the sample mass was set at 1 mg after flash solvent evaporation to avoid the diffusional effects of mass and heat transfer. The evaporation process was done at the boiling point of the respective solvent used and at vacuum pressure to ensure that the asphaltenes did not oxidize.

Each test was performed in triplicate to ensure the repeatability of the results, obtaining a ± 0.01 °C uncertainty.

### 3. Molecular dynamics methods

To obtain some physical insights into the effect of the methyl group (-CH<sub>3</sub>) location on the aggregation behavior in xylene isomers, molecular dynamics (MD) simulations were carried out. Asphaltenes were represented by a single average structure dissolved in each xylene isomer (ortho, meta, and para). The theoretical evaluation was done for the concentration of 10% in the asphaltene fraction. To this aim, 27 molecules were used to represent the experimental model solutions computationally since this number allows for obtaining a reliable representation of the state of aggregation according to results reported in the literature and previous studies [13, 37, 38]. The number of xylene molecules required to represent a 10% asphaltene concentration was then calculated, yielding 2086 molecules. The optimized potential for liquid simulations (OPLS), which is widely used to describe organic compounds such as crude oil and asphaltenes, was used to simulate asphaltene and solvents [39, 40]. Intermolecular interactions, van der Waals type, and electrostatic interactions were described using the Lennard-Jones (12-6) and Coulombic models, respectively. In the case of bonds and angle flexions, they were represented by harmonic models, whereas the model proposed by Watkins and Jorgensen et al. [41] was used to describe the torsions.

To obtain an adequate explanation of the aggregation behavior of asphaltenes, three stages were carried out, which satisfactorily described the experimental measurements in a previous study [13]. First, the initial configuration was simulated in an NVT (i.e., at volume, temperature, and number of molecules constant) ensemble at 400 K and an initial density of 0.4 g·cm<sup>-3</sup> (simulation box expanded) for 0.5 ns with a time step of 1 fs. Then, using an NVT ensemble at 298 K, another 1.5 ns were performed at the same density. This first stage ensured that the initial configuration corresponded to minimum energy, preventing it from falling into a local minimum. The density of equilibrium was determined in the second stage. An NPT (i.e., pressure, temperature, and number of molecules constant) ensemble was used during 3 ns at 298 K and 1 atm. Finally, after the equilibrium density was reached in the third stage, an NVT ensemble was conducted to fully equilibrate the system during 25 ns of simulations with a time step of 2 fs. Hence, 30 ns were simulated for each asphaltene solution. In addition, periodic boundaries were considered in all directions.

To evaluate the effect of the -CH<sub>3</sub> location on the aggregation behavior, radial distribution function (RDF), asphaltene-asphaltene interaction energies, and root mean square displacement (RMDS) calculations were carried out. A detailed description of how these calculations were carried out can be found elsewhere.

MD simulations were performed using LAMMPS [42]. In addition, VMD [43] was used to visualize the simulations, obtain images, and calculate the radial distribution function. The Nosé-Hoover thermostat and barostat were used to fix the temperature and pressure, respectively. The cross-interaction parameters between atoms of different species were determined using geometric mixing rules. The cut-off radius was set at 16 Å for both van der Waals and electrostatic interactions. Whereas long-range electrostatic interactions were calculated using the particle-particle-particle mesh method.

#### 4. Kinetic analysis of asphaltene oxidation

Thermal behavior analysis is performed to obtain information about the kinetic parameters of thermo-oxidation of asphaltene aggregates at high-pressure conditions in different temperature regions [44, 45]. For this aim, the instantaneous reactivity was used, expressed in Equation (3).

$$r = \frac{d\theta}{dt} = f(\theta) \cdot P_{O_2}^n \cdot k \quad (3)$$

where,  $\theta$  is the conversion at a time  $t$ ,  $k$  is the velocity constant, and  $P$  is the oxidizing gas partial pressure. The above equation can be rewritten as Equation (4):

$$r = \frac{d\theta}{dt} \frac{1}{f(\theta)} = k_o \exp\left(-\frac{E_a}{RT}\right) \cdot P_{O_2}^n \quad (4)$$

where  $P_{O_2}^n$  (bar) represents the partial pressure of the reactant gas (O<sub>2</sub>),  $n$  the order of reaction,  $R$  (J×mol<sup>-1</sup>K<sup>-1</sup>) the universal gas constant,  $E_a$  (kJ×mol<sup>-1</sup>) the effective activation energy,  $k_o$  (s<sup>-1</sup>×bar<sup>-n</sup>) the pre-exponential factor. The function  $f(\theta)$  considers the evolution of the asphaltene with the conversion degree.

Substituting for the heating rate ( $\beta$ ) concerning  $dt$  where  $dt = dT / \beta$  and using the volumetric model for the consumption of the particle  $f(\theta) = (1-x)$  [46], the Equation (5) is obtained:

$$\frac{d\theta}{\beta} \frac{1}{f(\theta)} = k_o P_{O_2}^n \exp\left(-\frac{E_a}{RT}\right) dT \quad (5)$$

Then, the Ozawa-Wall-Flynn approximation [46] was used to resolve the integral of the conversion regarding the temperature integral of the Arrhenius equation, obtaining the Equation (6):

$$\ln\left[\frac{\beta f(\theta)}{P_{O_2}^n T^2}\right] = \ln\left(\frac{k_o R}{E_a}\right) - \frac{E_a}{RT} \quad (6)$$

Further, for the conversion of the asphaltene of the solid, it is expressed as the function  $f(\theta) = -\ln(1-x)$  based on a volumetric model, leading to the general expression in Equation (7):

$$\ln\left[\frac{\beta(-\ln(1-x))}{P_{O_2}^n T^2}\right] = \ln\left(\frac{k_o R}{E_a}\right) - \frac{E_a}{RT} \quad (7)$$

The effective activation energy is calculated using the slope of the  $\ln\left[\frac{\beta(-\ln(1-x))}{P_{O_2}^n T^2}\right]$  against  $\frac{1}{RT}$  obtained from Equation (7).

## 5. Results and discussion.

### 5.1. Asphaltene Characterization

Briefly, carbon, hydrogen, oxygen, sulfur, and nitrogen content were 81.7, 7.8, 3.6, 6.6, and < 0.5 % in mass fraction, respectively. The molecular weight  $M_w$  of  $n-C_7$  asphaltenes was  $907.3 \text{ g}\cdot\text{mol}^{-1}$ . Using X-ray diffraction (XRD) (Figure 1), it was obtained the inter-aromatic layer distance ( $d_m$ ) and inter-chain or inter-naphthenic layer distance ( $d_\gamma$ ) in  $n-C_7$  asphaltenes. They were found at  $3.47 \text{ \AA}$  and  $5.61 \text{ \AA}$ , respectively. The average height of the stacked aromatic sheets perpendicular to the sheet plane ( $L_c$ ) was found at

13.93 Å, and the average diameter of the aromatic sheet ( $L_a$ ) was equal to 19.06 Å. Finally, according to  $M$  value, there are approximately five aromatic sheets in the stacked cluster. The results are similar to the reported for asphaltenes isolated from EHO [12, 47, 48].

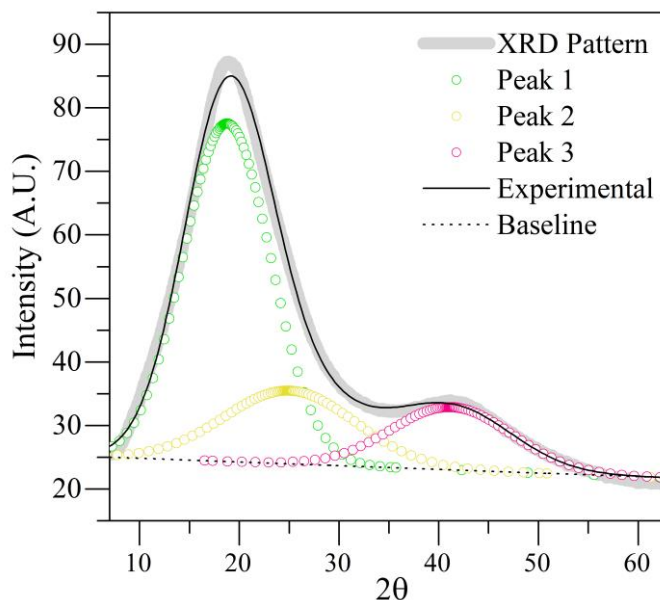


**Figure 1.** XRD Pattern with the de-convolution curves for  $n$ -C<sub>7</sub> asphaltenes

Figure 2 shows the <sup>1</sup>H-NMR and <sup>13</sup>C-NMR patterns for  $n$ -C<sub>7</sub> asphaltenes. From <sup>1</sup>H-NMR, it was obtained the proportional distribution relationship of aromatic hydrogen ( $H_a$ ), aliphatic hydrogens  $\alpha$ ,  $\beta$ , and  $\gamma$  linked to aromatic rings, named  $H_{\alpha}$ ,  $H_{\beta}$ , and  $H_{\gamma}$ , respectively. Results show a relative amount of  $H_{\alpha}$  of 23.49%, attributed to the high aromaticity degree reported by bulk tests. Aliphatic hydrogen follows the order:  $H_{\alpha}$  (4.79%) <  $H_{\gamma}$  (8.98) <  $H_{\beta}$  (62.72%). Through the <sup>13</sup>C-NMR analysis, the total content of 35.51% for aliphatic carbon ( $C_{al}$ ) and 64.48% for aromatic carbon ( $C_{ar}$ ) was identified, which agrees with the reported in the literature [12, 49-51]. The modified Brown-Ladner method [52] quantified average structural parameters (APS) using results from <sup>1</sup>H-NMR, elemental analysis, and vapor pressure osmometry. Table 2 summarizes the results obtained.

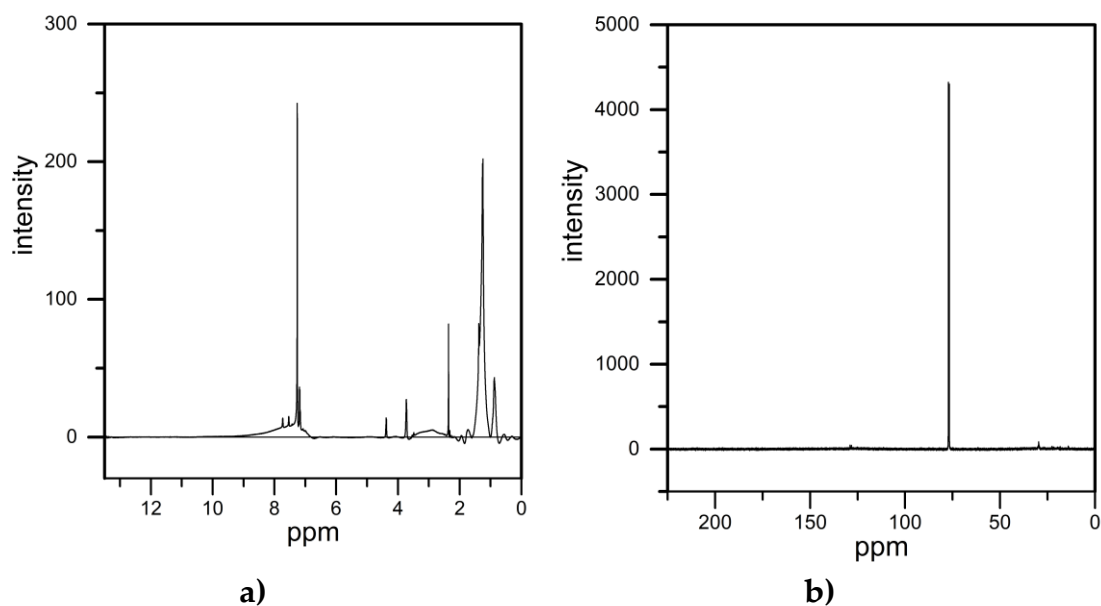


**Figure 2.** a)  $^1\text{H}$ -NMR and b)  $^{13}\text{C}$ -NMR patterns for  $n\text{-C}_7$  asphaltenes.

**Table 2.** Average molecular structure parameter of  $n\text{-C}_7$  asphaltenes, obtained through the chemical elemental analysis and  $^1\text{H}$ -NMR spectra

Parameter	Description	$n\text{-C}_7$ Asphaltenes
$f_A$	Aromaticity Factor	0.645
$\sigma$	Hydrogen periphery replacement rate in the aromatic ring system	0.093
$H_{AU}/C_A$	Condensation degree parameter of the aromatic ring system	0.388
$H_T$	Total hydrogen numbers	70.746
$C_T$	Total carbon numbers	74.102
$C_A$	Aromatic carbon numbers	47.788
$C_S$	Saturated carbon numbers	26.314
$C_\alpha$	Carbon numbers on the $\alpha$ position of an aromatic ring	1.696
$C_{ap}$	Peripheral carbon in a fused aromatic ring	18.320
$C_i$	Internal carbon in a fused aromatic ring	29.468
$R_{Ar}$	Aromatic rings	15.734
$R_t$	Total rings	15.835
$R_n$	Naphthenic rings	0.101
$n$	Average alkyl chain length	15.956

The results of asphaltene characterization are of great value in identifying the effect of different functional groups as well as the structural and chemical characteristics on its aggregation and subsequent reactivity.

Similarly, these results are used to construct the average molecular structure for the asphaltene studied. This structure is reported in a previous study [24], with a proposed molecular formula of  $C_{62}H_{70}S_2O_2$ .

## 5.2. Asphaltene aggregates characterization

Figure 3 shows the experimental results of SAXS measurements for various asphaltene concentrations dissolved in *p*-, *m*-, and *o*- xylene. As the concentration of asphaltene in the model solution increases, so does the size of the asphaltene aggregate. This result is related to asphaltenes' overlapping ability, which increases fluid elasticity [53, 54]. This result agrees with the trends reported in the literature [13, 55].

Furthermore, asphaltene aggregate size is also affected by the diluent used. For both low and high asphaltene concentrations, the aggregate size increases in the order *o*-xylene < *m*-xylene < *p*-xylene, indicating that the position of a methyl group affects the intermolecular interactions between asphaltenes.

As the concentration of asphaltene changed, some differences were discovered. The average length ( $L$ ) for all solutions was similar between 3 and 4 nm for a mass fraction of 0.1% asphaltenes.  $L$  varies from 7.5 nm (*o*-xylene) to 9.9 nm (*p*-xylene) as asphaltene concentration increases up to 1.0% in mass fraction. The average length of the systems with 10.0% asphaltene mass fraction varies by more than 18 nm between the system with the smallest aggregate size (*o*-xylene) and the system with the largest aggregate size (*p*-xylene). The aggregation mechanisms gain importance at high concentrations, increasing the interactions between the aromatic cores forming aggregates by full stacking [13, 56]. Hence, the results indicate that the asphaltene solution models behave as concentrated suspensions, considering that an increase in volumetric fraction promotes growth in asphaltene aggregate size [13].

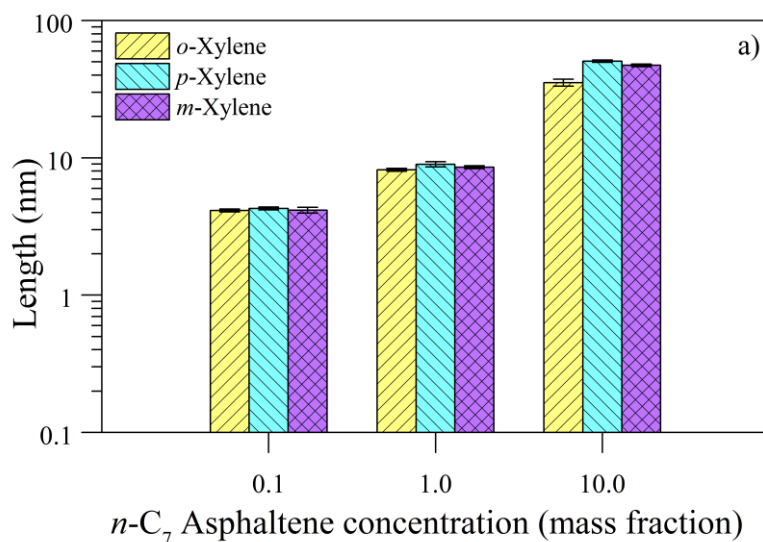


**Figure 3.** Average length ( $L$ ) of  $n$ -C<sub>7</sub> asphaltenes particles in different aromatic solvents.

The results are compared with the viscosity of the model solutions. The viscosity analysis is divided into three sections including *i*) rheological behavior analysis of the solutions, *ii*) relative viscosities determination at a fixed shear rate ( $10 \text{ s}^{-1}$ ) ( $\mu_r = \mu_{\text{solution}} / \mu_{\text{solvent}}$ ), i.e., the viscosity of the  $n$ -C<sub>7</sub> asphaltene ( $\mu_{\text{solution}}$ ) solution divided by the solvent's viscosity ( $\mu_{\text{solvent}}$ ) and *iii*) intrinsic viscosity ( $\mu_{\text{in}}$ ) calculation. These results are shown in Figures 1-3 of Appendix B.

### 5.3. Molecular dynamic simulation

MD simulations were run to determine the impact of the -CH<sub>3</sub> location on aggregation behavior. RDF, the average size of asphaltene aggregates, asphaltene-asphaltene and asphaltene-xylene interaction energies, and the root mean square displacement (RMDS) were calculated for this purpose. Figure 4 depicts the asphaltenes' final configuration after the system was fully equilibrated. The RMSD results are shown in Figure 5, indicating that the time simulations were sufficient to ensure that the aggregation state converged to an equilibrium state. Figure 6 depicts the RDF results between the center of mass of the asphaltenes molecules in each solution evaluated in MD simulations at a 10% asphaltene concentration in mass fraction. The results show that the internal structure of each asphaltene solution differs significantly. The asphaltenes dissolved in *p*-xylene have the highest coordination peak at 6.35 Å, whereas the RDF curves for *m*-xylene and *o*-



xylene are shifted to the right at 7.05 and 7.35 Å, respectively. This finding suggests that the location of the methyl substituent in the xylene molecular structure affects aggregation behavior. The average asphaltene aggregate size was calculated to back this up.

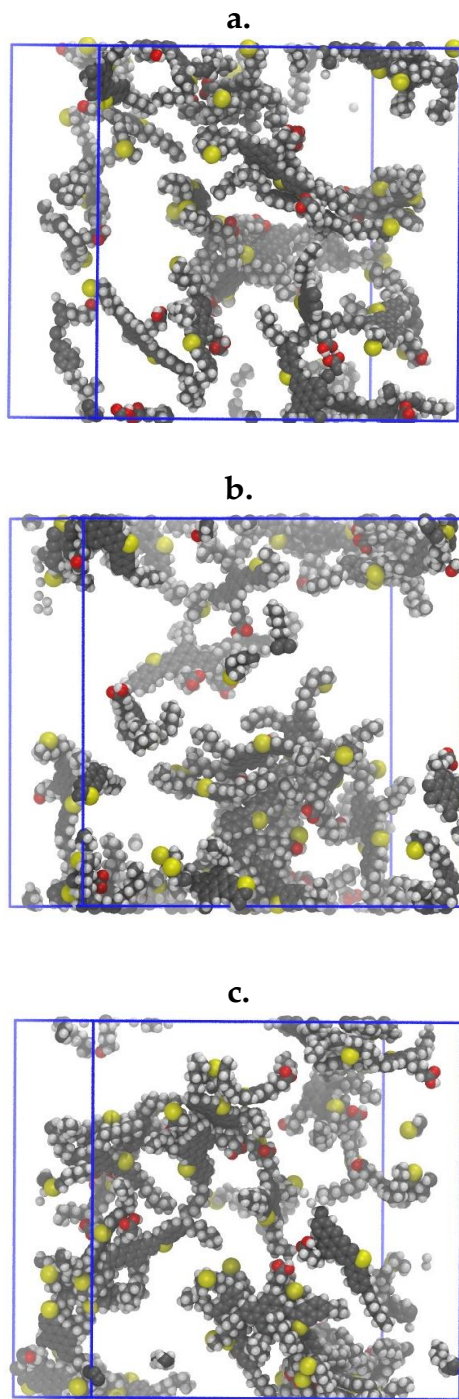


**Figure 4.** Asphaltenes aggregates at the final configuration at an asphaltene concentration of 10 wt.% dissolved in (a) *o*-xylene, (b) *m*-xylene, and (c) *p*-xylene. For clarity, solvent molecules are hidden. Carbon atoms are shown in gray, hydrogen in white, sulfur in yellow, and oxygen in red.

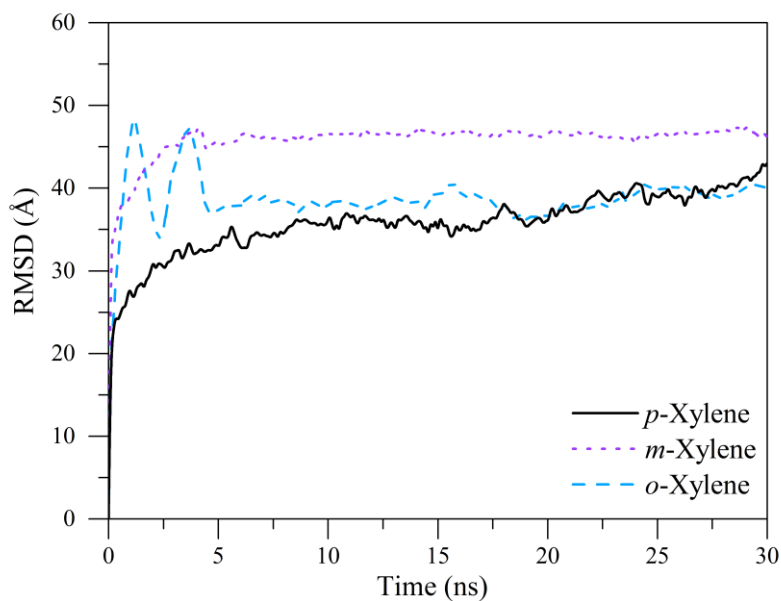


**Figure 5.** RMSD results for molecular dynamic simulation.

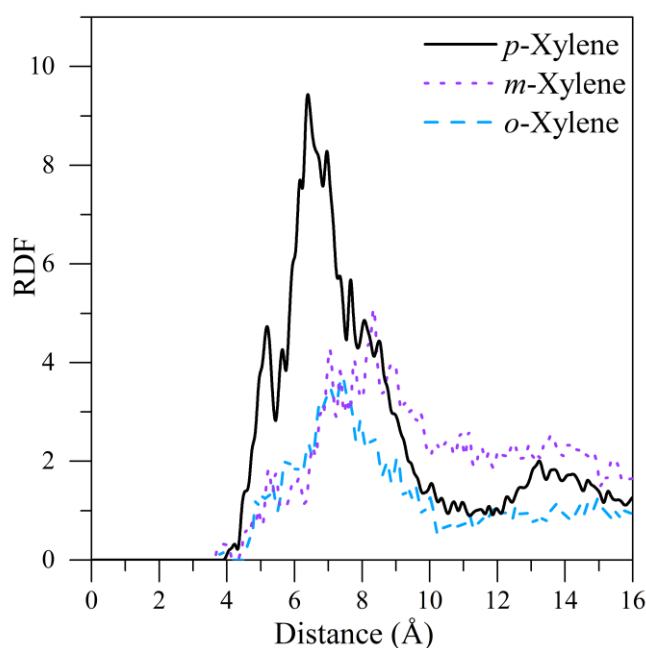


**Figure 6.** Radial distribution function (RDF) between the center of mass of the asphaltene molecules dissolved in each solvent at a concentration of 10% in mass fraction.

Figure 7 depicts the average size of the asphaltene aggregates, demonstrating that the location of the methyl in the xylene molecular structure influences aggregation behavior. The results show that asphaltenes dissolved in *o*-xylene have the lowest aggregation, followed by *m*-xylene and *p*-xylene, in that order. When comparing *m*-xylene to *o*-xylene, the average size of aggregates increases by 16%, while *p*-xylene increases by 36%. In all

cases, the aggregate size does not exceed 2.5 molecules per aggregate. When compared to the data reported in the literature, this value is significantly higher. Headen et al. [38] obtained aggregate sizes of 4.35 molecules per aggregate, evaluated in toluene at an asphaltene concentration of 7%. At the same asphaltene concentration, an average size of 4.5 molecules per aggregate was obtained in previous work. Considering that the aggregation increases as the concentration of asphaltenes increases [13], these results indicate that xylene isomers can dissolve asphaltenes more than toluene, the most widely used solvent in asphaltene solution models.

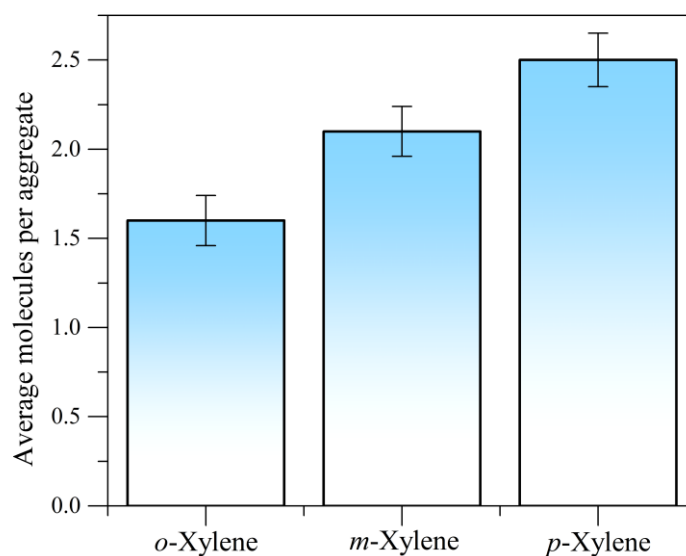


**Figure 7.** Average size of asphaltene aggregates of each solution evaluated by MD simulations at an asphaltene concentration of 10 % in mass fraction.

The asphaltene-asphaltene and asphaltene-solvent interaction energies are shown in Figure 8 for each solution model evaluated by MD simulations. Positive interaction energies indicate repulsion, whereas negative interaction energies indicate attraction. As previously stated, these calculations are performed as an average over the molecules considered pairwise. This means that it considers all contributions, and thus, while Figure 8-a shows that asphaltene-asphaltene interaction energies indicate repulsion, it does not imply that asphaltenes are not aggregated. Nonetheless, it indicates that, on average, asphaltene tends to remain dispersed when compared to aggregated molecules. Previous research discovered that these asphaltene-asphaltene interaction energies are positive at low asphaltene concentrations and turn negative as the asphaltene concentration increases [13]. For toluene, it was

found that the asphaltene-asphaltene interaction energy is  $-2.45 \text{ kcal}\cdot\text{mol}^{-1}$  at an asphaltene concentration of 7 % in mass fraction, which is due to the difference of the aggregation state shown above. The higher the aggregation state of the asphaltene, the higher their interaction energy.

The asphaltene-xylene interaction energies, on the other hand, are all negative, indicating attraction. When comparing the interaction energy results, a clear trend can be seen. As the asphaltene-asphaltene interaction energies increase, so do the asphaltene-xylene interaction energies (*o*-xylene, *m*-xylene, and *p*-xylene, in that order). The aggregation state of the asphaltenes in the solution is directly related to this behavior. Because the asphaltene molecules are dispersed, they are surrounded by a specific number of xylene molecules (coordination number). As a result, the surface area contact of an asphaltene with the solvent molecules is greater than the aggregated surface area contacts of asphaltene molecules. This suggests that *o*-xylene keeps asphaltenes more dispersed than the other two xylene isomers.

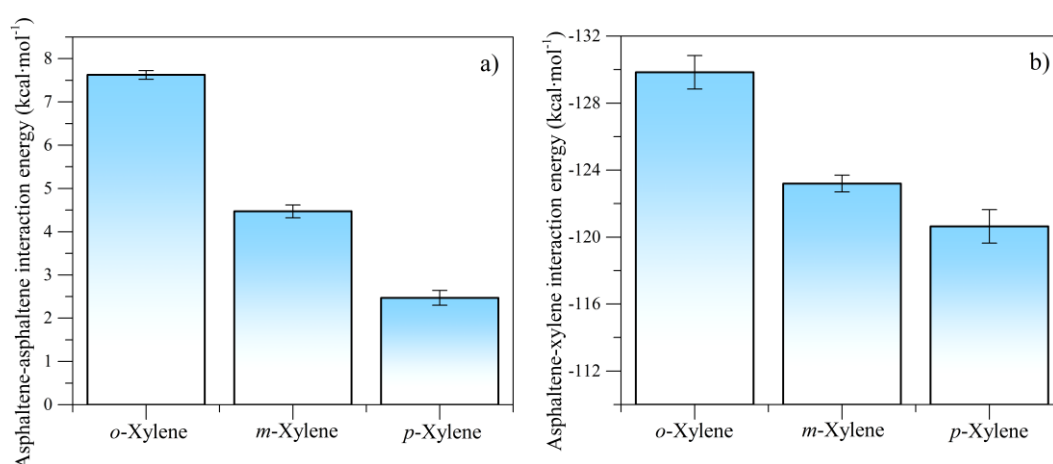


**Figure 8.** Average of the interaction energy between (a) the asphaltenes and (b) asphaltene-solvent pairwise.

Finally, the RDF between the center of mass of the asphaltene molecules and the carbon atoms of the methyl substituent of each xylene isomer were calculated to determine what structural changes are due to the location of the  $-\text{CH}_3$ . Figure 9 shows the results indicating significant differences in the xylene molecules located around the asphaltene molecules. The first coordination peak was identified at  $6 \text{ \AA}$ , indicating a higher intensity of this peak for *o*-xylene, followed by *m*-xylene and *p*-xylene, in that order. This indicates that the carbon atoms of the methyl groups are closer to the

asphaltene molecules, i.e., the methyl groups are oriented toward the asphaltene molecule. The second coordination peak was identified at 12.5 Å, obtaining a higher intensity of the peak for *o*-xylene, whereas *m*-xylene and *p*-xylene seem similar between them. Therefore, the location of the methyl group has a strong effect on the asphaltene-xylene interaction since the number of near and far neighbors depends on that

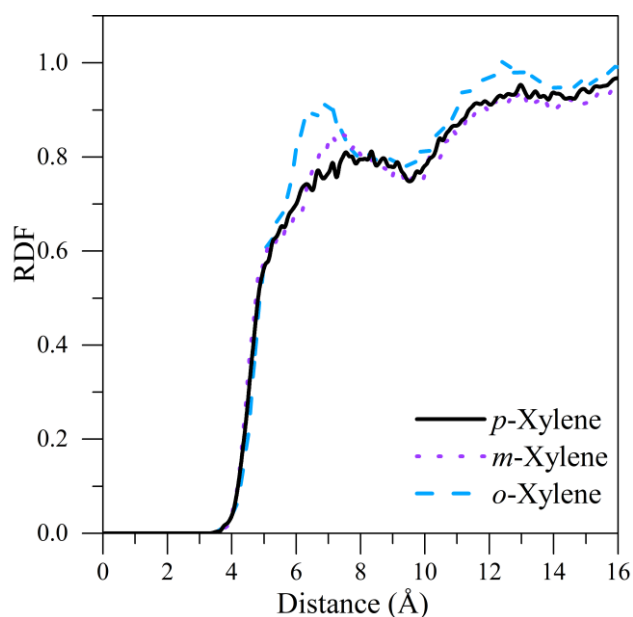


**Figure 9.** RDF between the center of mass of the asphaltene molecules and the carbon atoms of the methyl substituent of each xylene isomer.

Therefore, a strong entropic volume effect is observed due to the location of the  $-CH_3$ , which increases the asphaltene-xylene interaction energies impacting the aggregation behavior. Figure 10 shows how xylene molecules are distributed around two asphaltenes aggregated, located at 2.5 Å. This illustrates the results reported in Figure 9, indicating that the  $-CH_3$  substituents are mainly oriented toward the asphaltene molecules, increasing their interaction energy, and thus reducing the aggregation trend. For this reason, both experimentally and theoretically, it was found out that *o*-xylene reduces the aggregation compared to the other two xylene isomers.

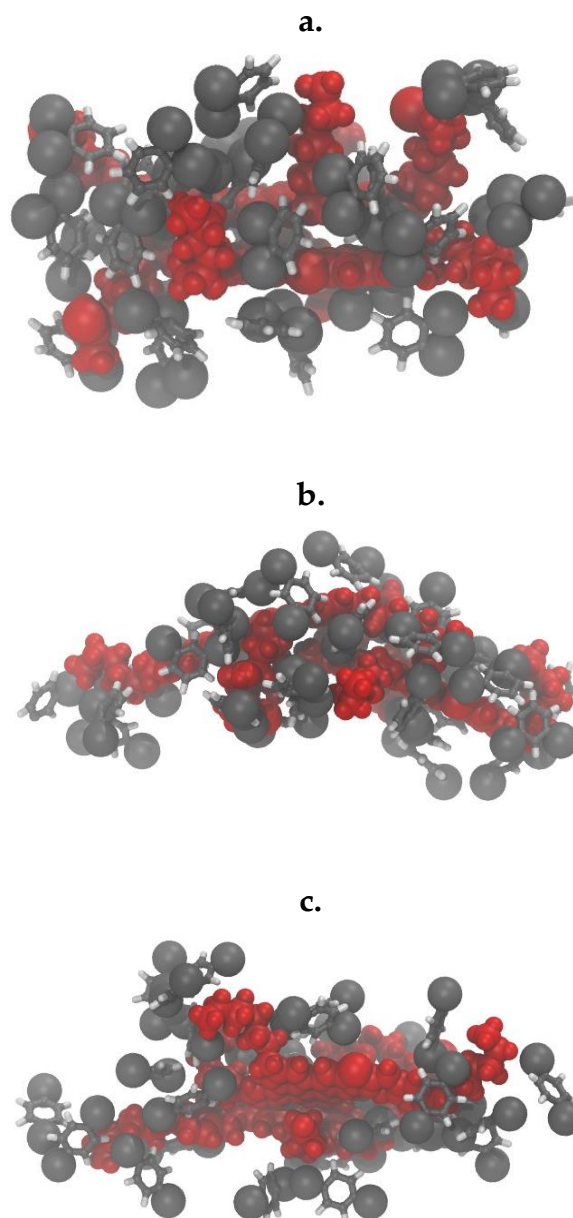


**Figure 10.** Asphaltene aggregate composed of two molecules surrounded by (a) *o*-xylene, (b) *m*-xylene, and (c) *p*-xylene. The whole asphaltene molecule is shown in red, carbon in gray, and hydrogen in white.

Finally, Figure 4 of the Appendix B shows the RDF between the heteroatoms of the asphaltene, revealing that they interact mainly by  $\pi$ - $\pi$ , hydrogen bonding, and acid-base interactions as a result of the strong intensity peaks for C-C, C-H, H-O, H-N, and O-N bonds.

#### 5.4. High-Pressure experiments

The thermo-oxidative reactivity of the different samples was evaluated in different steps, including *i*) the effect of the concentration of asphaltenes

diluted in *p*-xylene as a reference solvent and *ii*) the impact of the addition and position of a methyl group in the model solutions (*p*-, *m*-, and *o*-xylene) for different asphaltene concentrations.

#### 5.4.1. Effect of *n*-C<sub>7</sub> asphaltene content

The effect of the *n*-C<sub>7</sub> asphaltene content was assessed by estimating the oxidation profiles at a fixed pressure (6.0 MPa) to different model solutions containing mass fractions of 0.1%, 1.0%, and 10.0% of asphaltenes diluted in *p*-xylene. Figure 11 a-b shows the mass change and rate for mass change profiles obtained, while the thermogravimetric characteristics are found in Table 3. As a first instance, it is observed that regardless of the asphaltene concentration, when the system is subjected to high pressure, the thermograms are described by the four thermal events *i*) oxygen chemisorption (OC), *ii*) oxygen decomposition of chemisorbed oxygen functional groups (DCO), *iii*) first combustion (FC), and *iv*) the second combustion.

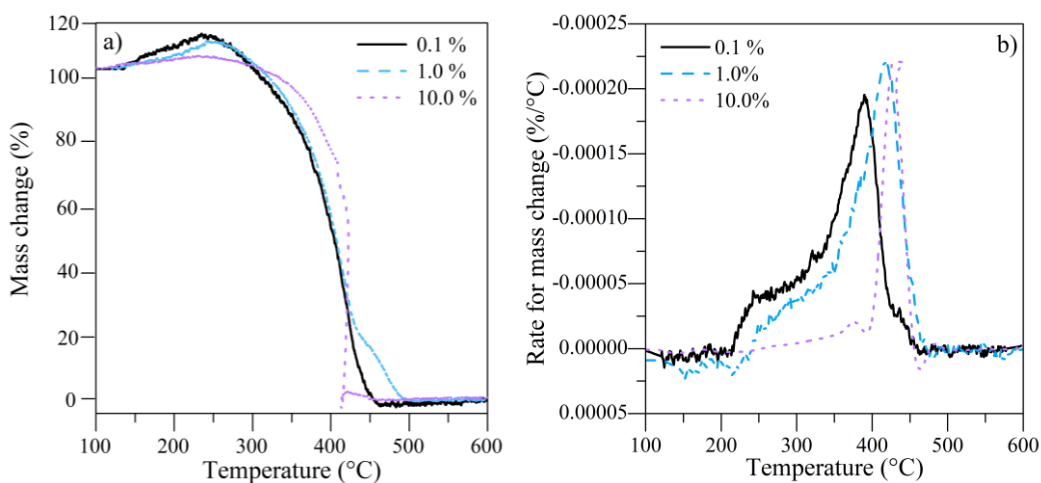


**Figure 11.** Mass percentage and rate for mass change for the thermo-oxidation of *n*-C<sub>7</sub> asphaltene model solutions in *p*-xylene for different asphaltene concentrations of 0.1, 1.0 and 10.0% at 6.0 MPa. Sample weight: 1 mg, heating rate: 10 °C·min<sup>-1</sup>, and airflow: 80 mL·min<sup>-1</sup>.

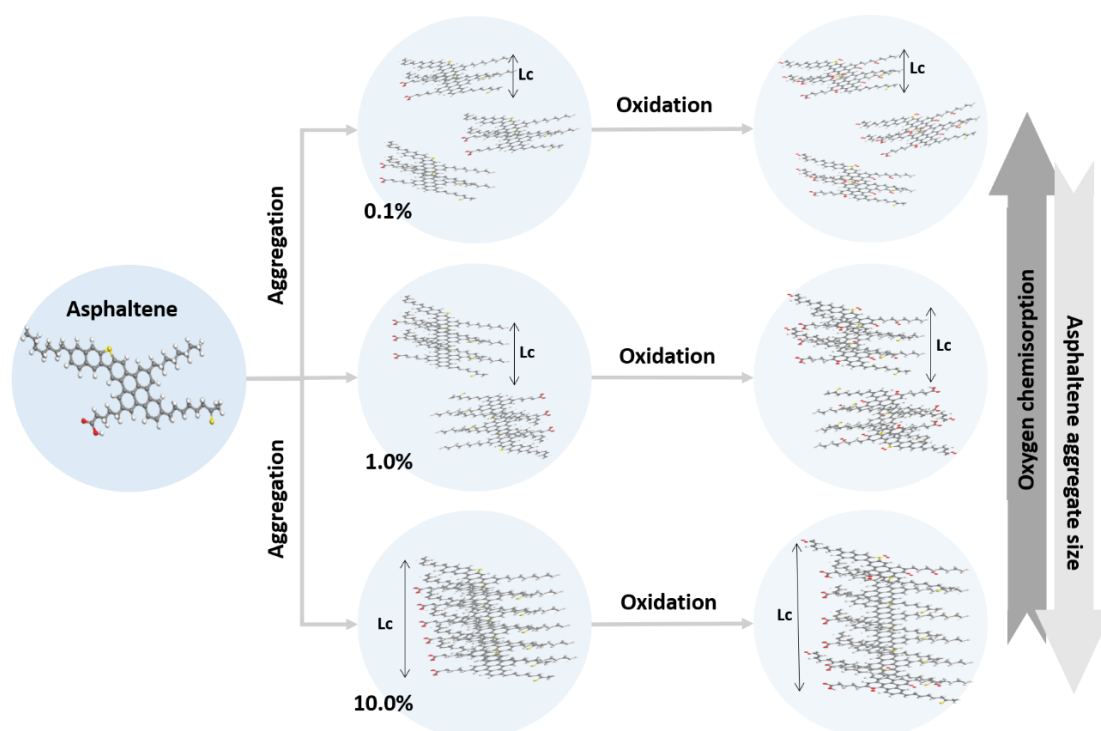
Interestingly, substantial differences were found in the different thermal stages as the asphaltene content increased in the model solutions. Notwithstanding, it is essential to mention that *p*-xylene is the solvent in which the size of the asphaltene aggregate was affected to a greater degree with the increase in asphaltene concentration than the rest of the aromatic solvents considered in this study.

**Table 3.** Thermogravimetric characteristics for the thermo-oxidation of *n*-C<sub>7</sub> asphaltene model solutions in toluene at different asphaltene concentrations of 0.1%, 1.0%, and 10.0% discretized in the different regions: *i*) oxygen chemisorption (OC) *ii*) decomposition of the chemisorbed oxygen (DCO) region, *iii*) first combustion (FC) region and *iv*) second combustion (SC) region at 6.0 MPa.

Asphaltene Concentration (% mass fraction)	OC Region		DCO Region		FC Region		SC Region	
	Temperature range (°C)	Mass gain (mass fraction in %)	Temperature range (°C)	Mass loss (mass fraction in %)	Temperature range (°C)	Mass loss (mass fraction in %)	Temperature range (°C)	Mass loss (mass fraction in %)
0.1	100-226	11.0	227-314	13.1	315-425	75.9	426-443	22.0
1.0	100-241	9.3	242-312	10.5	313-415	53.8	416-455	45.0
10.0	100-248	2.3	249-325	5.9	326-375	18.0	376-477	80.0

The thermograms show that the amount of oxygen chemisorbed increases as the asphaltene concentration decreases, which is intrinsically attributed to the size and surface area of the aggregates and the subsequent thermal expansion. The findings imply that the surface area/volume ratio of the smaller aggregates is higher. In comparison to larger agglomerates, they provide more active sites for interacting with O<sub>2</sub>, which represents a higher adsorbed mass fraction. Furthermore, because it is immediately exposed to the gas phase, thermal expansion happens naturally. Additionally, as the aggregate size increases, the number of active oxygen anchoring sites decreases [14, 57, 58]. Aromatic structures are less exposed to oxidation. For example, pyridines, pyrroles, and thiophenes, which in previous works were shown to play a fundamental role in OC, would now be clogged in the aggregate complexes [12]. Since other groups, like COO-, rely on the ionizing of carboxyl, which in turn depends on the activation of -OH groups, they might also reduce their interaction with O<sub>2</sub> [59]. Scheme 1 shows a representative scheme for OC of different asphaltene aggregate sizes.





**Scheme 1.** Mechanistic representation of asphaltene aggregation considering  $\pi$ -stacking interactions at different concentrations (0.1%, 1.0%, and 10.0% in mass fraction) diluted in *p*-xylene and subsequent oxidation at high-pressure conditions.

DCO zone is also affected by the asphaltene aggregate state because subsequent thermal events depend on the structures created in OC. In this sense, the systems that formed structures with higher reactivity spread DCO at higher temperatures than those with low oxygen chemisorption. The system with 0.1% by the mass fraction of asphaltenes in *p*-xylene ends DCO at lower temperatures, further losing more mass than the systems with 1.0 and 10.0% by a mass fraction. In this context, combustion zones also show differences between each system. According to panel b of Figure 11, the system with 0.1% presents low intensities for FC and SC zones, whereas the systems with 1.0 and 10.0% present the opposite behavior. The trend is observed; the intensity of the two last peak increases with increasing aggregate size (0.1% < 1.0% < 10.0%). It has been shown that the critical nanoaggregate concentration (CNC) of asphaltenes in *p*-xylene is between 0.1 - 3.4 g $\times$ L<sup>-1</sup>, similar to critical micelle concentration in surfactant solutions [60]. In this sense, it is evident that the systems with 1.0 and 10.0 % in mass fraction of asphaltenes are higher than CNC. Therefore, thermo-oxidative reactions require higher temperatures to completely oxidize the organic matter. This is

a consequence of the low reactivity that samples present due to the low OC and the more condensed structure resulting after DCO.

#### 5.4.2. Effect methyl position

It has been shown that the addition of methyl groups and their position in the xylene molecule affect the asphaltene aggregate size of the system. Hence, this section is focused on studying their effect on oxidative reactivity at high-pressure conditions. The tests were done for three asphaltene concentrations (0.1, 1.0, and 10.0% in mass fraction). The results are shown in panels a-f of Figure 12, and thermogravimetric characteristics are shown in Table 4. The results indicate that the thermal profiles are influenced by both properties; notwithstanding, it also depends on the asphaltene concentration used. Panels a-b shows the mass change and rate for mass change for an asphaltene concentration of 0.1% in mass fraction, from which it is observed that the thermograms can be divided into four regions: OC, DCO, FC, and SC for all cases (*o*-xylene, *m*-xylene, and *p*-xylene). Each region ends at similar temperatures for this concentration, and the mass lost in DCO, FC, and SC does not differ significantly.

The differences in thermogravimetric profiles become more noticeable as the concentration of asphaltenes in the system increases. In the case of 1.0% in a mass fraction of asphaltenes, the limits of each region and the mass change are affected. Remembering that for a concentration of 1.0% of asphaltenes, the aggregate size presents greater variations than at 0.1%; this parameter is correlated with the profiles obtained. The mass gained in OC for the three systems increases in the order: *p*-xylene < *m*-xylene < *o*-xylene. This result indicates that the larger the size of the asphaltene aggregate, the lower the interactions with O<sub>2</sub> because of a reduction in active sites of the asphaltene structure. Most of the asphaltenes in crude oil are polycyclic aromatic hydrocarbons capable of interacting with neighboring asphaltene molecules through several intermolecular forces, including London dispersion forces between aliphatic moieties,  $\pi$ -stacking of aromatic cores, hydrogen bonding between nitrogen-hydrogen and oxygen-hydrogen-containing functionalities, and acid/base interactions between carboxylic acids and pyridine rings [57]. That is, aromatic core-dominated interactions ( $\pi$ -stacking) drive asphaltene aggregation; however, it has been proven that heteroatom-based intermolecular forces also significantly affect the overall

solubility and aggregation behavior [1]. These sites, in turn, are the main sites for oxygen chemisorption.

**Table 4.** Thermogravimetric characteristics for the thermo-oxidation of *n*-C<sub>7</sub> asphaltene model solutions in *o*-xylene, *m*-xylene, and *p*-xylene at different asphaltene concentrations of 0.1%, 1.0%, and 10.0% discretized in the different regions: *i*) oxygen chemisorption (OC) *ii*) decomposition of the chemisorbed oxygen (DCO) region, *iii*) first combustion (FC) region and *iv*) second combustion (SC) region at 6.0 MPa.

Solvent	Asphaltene Concentration (% mass fraction)	OC Region		DCO Region		FC Region		SC Region	
		Temperature range (°C)	Mass gain (mass fraction in %)	Temperature range (°C)	Mass loss (mass fraction in %)	Temperature range (°C)	Mass loss (mass fraction in %)	Temperature range (°C)	Mass loss (mass fraction in %)
<i>o</i> -xylene	0.1	100-228	12.9	229-317	18.1	318-399	80.5	400-440	14.3
	1.0	100-230	10.0	231-320	17.2	321-402	76.6	403-445	15.9
	10.0	100-215	9.5	216-330	11.6	331-409	48.9	410-450	47.0
<i>m</i> -xylene	0.1	100-227	12.7	228-315	15.9	316-412	77.3	413-442	19.5
	1.0	100-232	10.1	233-314	16.5	315-410	65.9	411-450	27.7
	10.0	100-218	8.8	219-328	10.2	329-394	49.4	395-456	47.5
<i>p</i> -xylene	0.1	100-226	11.0	227-314	13.1	315-425	75.9	426-443	22.0
	1.0	100-241	9.3	242-312	10.5	313-415	53.8	416-455	45.0
	10.0	100-248	2.3	249-325	5.9	326-375	18.0	376-477	80.0

The main difference is found in the mass gain during OC for a concentration of 10.0% in mass fraction of asphaltenes, which for the systems with *o*-, and *m*-xylene, the mass growth was higher in 7.2% and 6.5%, respectively, than *p*-xylene. This generates minor differences in the other regions since the reactivity of the systems depends on the structures formed during OC. In this sense, the asphaltene model solution with a mass fraction of 10.0% in the *p*-xylene system completes the total decomposition 17 °C and 11 °C after *o*-xylene and *m*-xylene, respectively.

In this sense, depending on the solvent used, asphaltenes have greater or lesser interactions between them and the solvent. The reduction in OC as the aggregate size increases suggests a considerable increase in the interactions by alkyl-alkyl, hydrogen bonds, and acid/base.

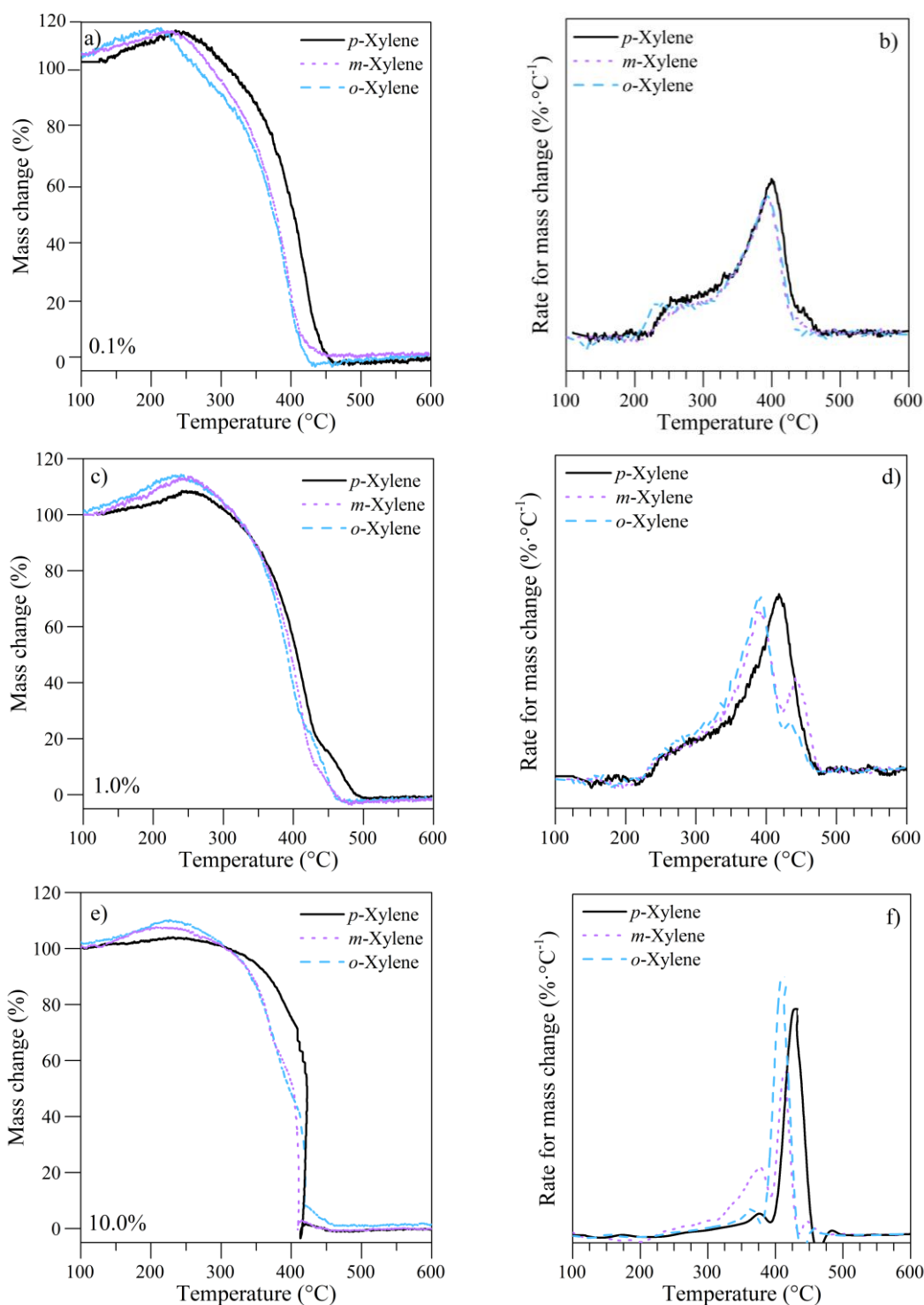


**Figure 12.** Mass percentage and rate for mass change for the thermo-oxidation of *n*-C<sub>7</sub> asphaltene model solutions in *o*-xylene, *m*-xylene, and *p*-xylene at different asphaltene concentrations of 0.1% (a-b), 1.0% (c-d), and 10.0% (e-f) at 6.0 MPa. Sample weight: 1 mg, heating rate: 10 °C·min<sup>-1</sup>, and airflow: 80 mL·min<sup>-1</sup>.

Due to the mass gained in OC, the thermal events DCO, FC, and SC change significantly. First, the DCO region in systems with 10% in a mass

fraction of asphaltenes ends at lower temperatures in *p*-xylene than *m*- and *o*-xylene due to the few oxygenated structures formed. Afterward, both FC and SC end up at higher temperatures. The main change is observed for the SC region, where the profiles for the model solutions of asphaltene with *m*- and *o*-xylene present a small peak between 400 and 500 °C, while in *p*-xylene, this is the predominant peak of the curve. Finally, a greater change is observed between the three curves for a concentration of 10.0% in mass fraction (panels e and f).

Furthermore, in previous work [12], it was demonstrated that the size of the cluster of asphaltenes directly influences the rate of mass loss during FC and SC [12]. Asphaltenes with high  $L_c$  tend to present a violent exothermic reaction resulting from the dealkylation of the structure [11]. According to the thermograms, all the systems offer a controlled loss of their mass, given that, in all cases, the size of the added system is greater than those evaluated in previous works.

## 5.5. Kinetic analysis

Previous sections corroborated that the thermo-oxidation of asphaltene aggregates occurs throughout many competing complex reactions. The thermal profiles were described mathematically under four Gaussians, representing OC, DCO, FC, and SC. Kinetic fitting was successfully done by assuming a first-order kinetic model, i.e.,  $n=1$ , obtaining  $R^2 > 0.99$  for all cases [61]. The estimated effective activation energy of each thermal event for the systems evaluated at 6.0 MPa is reported in Figure 13a-c.

As a first instance, it is observed that the effective activation energy is affected by the asphaltene aggregation state. Panel a shows the results for asphaltene aggregates formed with a content of 0.1% in mass fraction of *n*-C<sub>7</sub> asphaltenes. The values for OC region are similar in all cases following the incremental order: *o*-xylene < *m*-xylene < *p*-xylene. This behavior suggests that as the size of the asphaltene aggregate increases, the structure requires more energy for the chemical anchoring of oxygen. Notwithstanding, the difference between each system does not change greatly, as in the case of DCO, where the difference of  $E_\alpha$  between the systems is much larger and follows the opposite order of OC. The different final structures can explain this at the end of OC in each system. Apparently, in the asphaltene aggregation state in *p*-xylene, less reactive structures are formed than in *m*- and *o*-xylene, so the value of  $E_\alpha$  is much lower than the rest of the systems.

Then, during the first combustion zone,  $E_\alpha$  increases for all systems; meanwhile in SC, it is reduced in *o*-xylene. These results agree with the thermogravimetric profiles, where for the *p*-xylene aggregation state, the mass to decompose in SC is greater than for the rest of the systems. When the asphaltene concentration in the systems increases to 1.0% in mass fraction, there are similar trends to the previous systems. This is because the aggregate sizes do not differ much from each other. However, some important changes have occurred. The first is that the activation energy increases for OC in all systems while DCO decreases for all systems, except for *p*-xylene. The latter is because, in this state of aggregation, all systems lose reactivity since there is less oxygen chemisorption. Therefore, the structures predominate their decomposition into FC and SC. That is the reason for these last two regions present values of  $E_\alpha$  slightly higher than by 0.1%.

Something crucial for the systems with 0.1 and 1.0% of a mass fraction because OC is the most thermodynamically favourable event since lower  $E_\alpha$  is always obtained.

Finally, panel c shows the results for the model solutions with 10.0% in mass fraction of asphaltenes. It is observed that the values for OC increased compared to the other two concentrations for all model solutions, confirming once again that in the larger aggregate complexes, the spontaneity of the asphaltene-oxygen interactions is decreased. Interestingly, in DCO, the value of  $E_\alpha$  compared to OC, for *p*-xylene decreases, and in systems formed with *m*- and *o*-xylene,  $E_\alpha$  remains almost constant.

In the case of FC, all systems increased the  $E_\alpha$  since for these systems, there is still a high amount of mass for decomposing. The order increased as follows: *p*-xylene < *m*-xylene < *o*-xylene. *o*-Xylene presents the highest values because this model solution decomposes higher during this zone, whereas in SC, it decreases its value, while the other three systems behave differently. For all cases, it was obtained that the asphaltene aggregation state modifies the activation energy in each region, obtaining a global negative effect as the asphaltene size increases due to the rise in energy expenditure at higher temperatures.

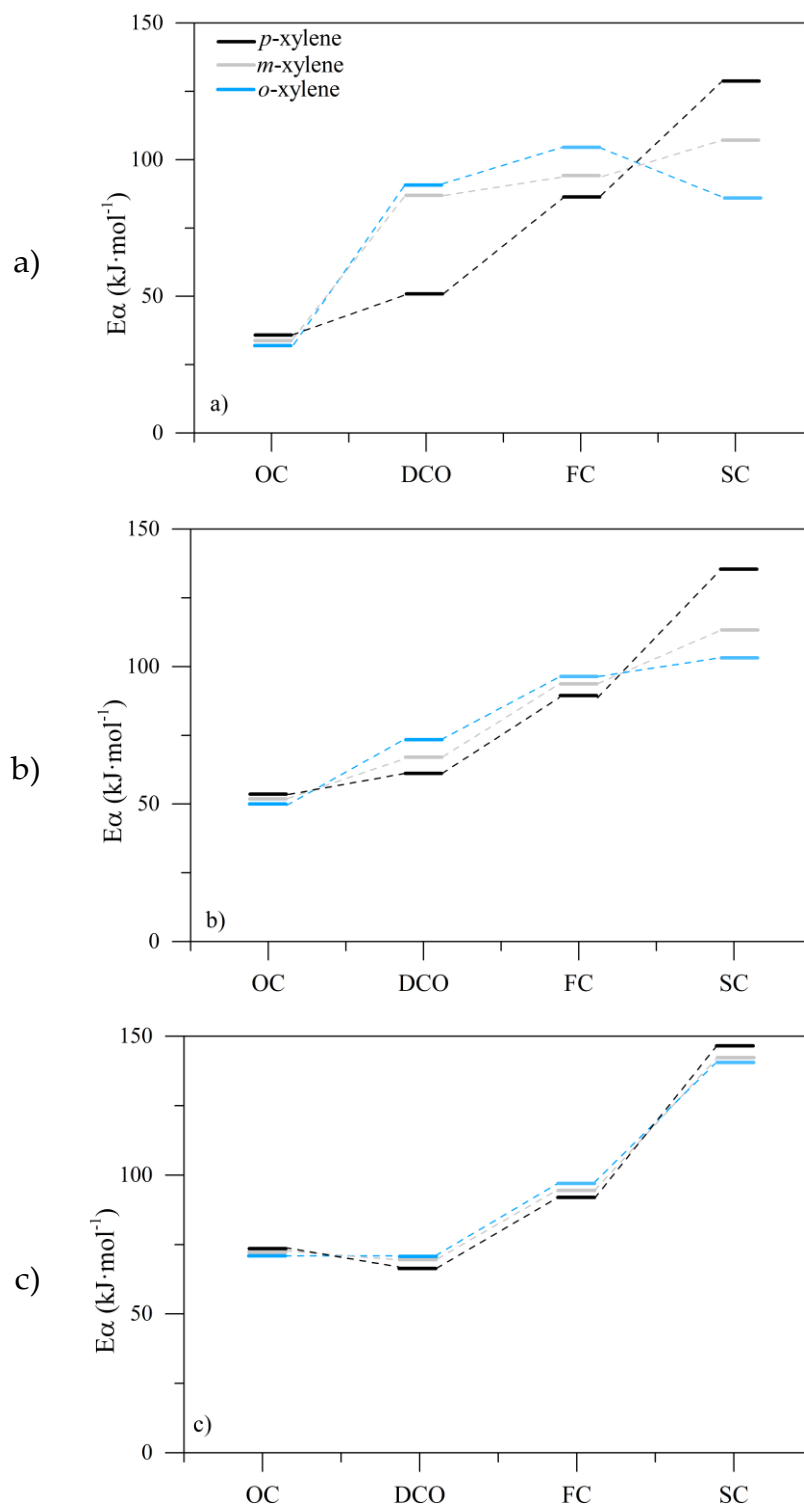


**Figure 13.** Estimated effective activation energy for the thermo-oxidation aggregates of *n*-C<sub>7</sub> asphaltenes with concentrations of a) 0.1, b) 1.0, and c) 10.0% in mass fraction, discretized in different thermal events named oxygen chemisorption (OC), desorption/decomposition of chemisorbed oxygen (DCO), first combustion (FC) and second combustion (SC) at 6.0 MPa.

## 6. Conclusions.

This research aimed to comprehend for the first time the thermo-oxidative behavior of various asphaltene model solutions with varying states of aggregation at high pressure. First, it was discovered that the size of the asphaltene aggregate increases with an increase in asphaltene concentration. The aggregate size increased in the order *o*-xylene, *m*-xylene, and *p*-xylene when the solvents were considered. To understand why the location of the methyl substituent in the xylene structure modifies the aggregation states, MD simulations were run. The asphaltene molecules are more structured (RDF peak of high intensity) for *p*-xylene than the other two xylene isomers, according to the RDF curves, which show a significant difference in the internal structure of the asphaltenes dissolved in each xylene isomer. Hence, the asphaltene molecules tend to be more aggregated in *p*-xylene. This was corroborated by the analysis of the aggregate size, the asphaltene-asphaltene, and asphaltene-xylene interaction energies, which showed that the asphaltenes are less aggregated in *o*-xylene, followed by *m*-xylene and *p*-xylene in that order. RDF between the asphaltenes and the carbon atoms of the methyl substituents demonstrated that the methyl substituents are oriented towards asphaltenes, in the case of *o*-xylene, increasing the number of near and far neighbors, compared to the other two cases. Therefore, a strong entropic volume effect is determined because of the location of the –CH<sub>3</sub>, which increases the asphaltene-xylene interaction energies impacting the aggregation state.

The high-pressure thermogravimetric analysis to evaluate the thermo-oxidative behavior of asphaltene aggregates is included in the second section. Using *p*-xylene as a reference solvent, the concentration of asphaltenes was varied in the first set of thermogravimetric experiments from 0.1 to 10% in mass fraction to assess its impact on the reactivity of the model solutions. According to the findings, the system's reactivity decreased as asphaltene concentration rose because oxygen chemisorption decreased. To examine the impact of the location of a methyl group on the solvent molecule on thermo-oxidation reactions, three aromatic solvents (*p*-xylene, *m*-xylene, and *o*-xylene) were selected. There is no significant change in the thermogravimetric profiles for a concentration of 0.1% by a mass fraction in the different solvents used. However, with increasing the concentration to 1.0 and 10.0%, the mass gained by oxygen chemisorption increased in the order:



*o*-xylene < *m*-xylene < *p*-xylene. This result indicates that the larger the size of the asphaltene aggregate, the lower the interactions with O<sub>2</sub> because of a reduction in active sites of the asphaltene structure.

## References.

- [1] Acevedo S, Castillo J, Vargas V, Castro A, Delgado OZ, Ariza CAF, et al. Suppression of Phase Separation as a Hypothesis to Account for Nuclei or Nanoaggregate Formation by Asphaltenes in Toluene. *Energy & Fuels* 2018.
- [2] Medina OE, Gallego J, Redondo JD, Cortés FB, Franco CA. Effect of pressure on the thermo-oxidative behavior of saturates, aromatics, and resins (S-Ar-R) mixtures. *Fuel* 2021:122787.
- [3] Medina OE, Gallego J, Cespedes S, Nassar NN, Montoya T, Cortés FB, et al. Effect of pressure on thermo-oxidative reactions of saturates, aromatics, and resins (S-Ar-R) from extra-heavy crude oil. *Fuel* 2021:122596.
- [4] Medina OE, Olmos C, Lopera SH, Cortés FB, Franco CA. Nanotechnology applied to thermal enhanced oil recovery processes: a review. *Energies* 2019;12(24):4671.
- [5] Dabbous MK, Fulton PF. Low-temperature-oxidation reaction kinetics and effects on the in-situ combustion process. *Society of Petroleum Engineers Journal* 1974;14(03):253-62.
- [6] Kök MV, Karacan Ö, Pamir R. Kinetic analysis of oxidation behavior of crude oil SARA constituents. *Energy & Fuels* 1998;12(3):580-8.
- [7] Liu D, Hou J, Luan H, Pan J, Song Q, Zheng R. Coke yield prediction model for pyrolysis and oxidation processes of low-asphaltene heavy oil. *Energy & Fuels* 2019;33(7):6205-14.
- [8] Amrollahi Biyouki A, Hosseinpour N, Nassar NN. Pyrolysis and Oxidation of Asphaltene-Born Coke-like Residue Formed onto in Situ Prepared NiO Nanoparticles toward Advanced in Situ Combustion Enhanced Oil Recovery Processes. *Energy & fuels* 2018;32(4):5033-44.
- [9] Zhao S, Pu W, Yuan C, Peng X, Zhang J, Wang L, et al. Thermal behavior and kinetic triplets of heavy crude oil and its SARA fractions during

- combustion by high-pressure differential scanning calorimetry. *Energy & fuels* 2019;33(4):3176-86.
- [10] Yuan C, Varfolomeev MA, Emelianov DA, Eskin AA, Nagrimanov RN, Kok MV, et al. Oxidation behavior of light crude oil and its SARA fractions characterized by TG and DSC techniques: differences and connections. *Energy & fuels* 2018;32(1):801-8.
- [11] Medina OE, Gallego J, Rodríguez E, Franco CA, Cortés FB. Effect of pressure on the oxidation kinetics of Asphaltenes. *Energy & Fuels* 2019;33(11):10734-44.
- [12] Medina OE, Gallego J, Nassar NN, Acevedo SA, Cortés FB, Franco CA. Thermo-Oxidative Decomposition Behaviors of Different Sources of n-C7 Asphaltenes at High-Pressure Conditions. *Energy & Fuels* 2020.
- [13] Moncayo-Riascos I, Taborda E, Hoyos BA, Franco CA, Cortés FB. Theoretical-experimental evaluation of rheological behavior of asphaltene solutions in toluene and p-xylene: Effect of the additional methyl group. *Journal of Molecular Liquids* 2020;303:112664.
- [14] Tanaka R, Hunt JE, Winans RE, Thiyagarajan P, Sato S, Takanohashi T. Aggregates structure analysis of petroleum asphaltenes with small-angle neutron scattering. *Energy & fuels* 2003;17(1):127-34.
- [15] Lee H, Lee Y-K. Effects of the asphaltene structure and the tetralin/heptane solvent ratio on the size and shape of asphaltene aggregates. *Physical Chemistry Chemical Physics* 2017;19(21):13931-40.
- [16] Larichev YV, Nartova A, Martyanov O. The influence of different organic solvents on the size and shape of asphaltene aggregates studied via small-angle X-ray scattering and scanning tunneling microscopy. *Adsorption Science & Technology* 2016;34(2-3):244-57.
- [17] Hu D, Gu X, Cui B, Pei J, Zhang Q. Modeling the oxidative aging kinetics and pathways of asphalt: A ReaxFF molecular dynamics study. *Energy & Fuels* 2020;34(3):3601-13.
- [18] Lan T, Zeng H, Tang T. Understanding adsorption of violanthrone-79 as a model asphaltene compound on quartz surface using molecular dynamics simulations. *The Journal of Physical Chemistry C* 2018;122(50):28787-96.

- [19] Law JC, Headen TF, Jiménez-Serratos G, Boek ES, Murgich J, Müller EA. Catalogue of Plausible Molecular Models for the Molecular Dynamics of Asphaltenes and Resins Obtained from Quantitative Molecular Representation. *Energy & Fuels* 2019;33(10):9779-95.
- [20] D'Avila F, Silva C, Steckel L, Ramos A, Lucas E. Influence of asphaltene aggregation state on the wax crystallization process and the efficiency of EVA as a wax crystal modifier: A study using model systems. *Energy & Fuels* 2020;34(4):4095-105.
- [21] Moncayo-Riascos I, Lozano MnM, Hoyos BA, Franco CA, Riazi M, Cortés FB. Physical Insights about Viscosity Differences of Asphaltene Dissolved in Benzene and Xylene Isomers: Theoretical–Experimental Approaches. *Energy & Fuels* 2021;35(22):18574-82.
- [22] Hosseini-Dastgerdi Z, Tabatabaei-Nejad S, Khodapanah E, Sahraei E. A comprehensive study on mechanism of formation and techniques to diagnose asphaltene structure; molecular and aggregates: a review. *Asia-Pacific Journal of Chemical Engineering* 2015;10(1):1-14.
- [23] Barre L, Espinat D, Rosenberg E, Scarsella M. Colloidal structure of heavy crudes and asphaltene solutions. *Revue de l'Institut Français du Pétrole* 1997;52(2):161-75.
- [24] Medina OE, Gallego J, Acevedo S, Riazi M, Ocampo-Pérez R, Cortés FB, et al. Catalytic Conversion of n-C7 Asphaltenes and Resins II into Hydrogen Using CeO<sub>2</sub>-Based Nanocatalysts. *Nanomaterials* 2021;11(5):1301.
- [25] Voelkel A, Fall J. Solubility parameter as polarity measure for high-boiling oil products. *Fuel* 2014;122:310-5.
- [26] Lopes SM, Geng P. Estimation of elemental composition of diesel fuel containing biodiesel. *SAE International Journal of Fuels and Lubricants* 2013;6(3):668-76.
- [27] Acevedo S, Gutierrez LB, Negrin G, Pereira JC, Mendez B, Delolme F, et al. Molecular weight of petroleum asphaltenes: A comparison between mass spectrometry and vapor pressure osmometry. *Energy & Fuels* 2005;19(4):1548-60.
- [28] Yarranton HW, Alboudwarej H, Jakher R. Investigation of asphaltene association with vapor pressure osmometry and interfacial tension

- measurements. *Industrial & engineering chemistry research* 2000;39(8):2916-24.
- [29] Shao R, Shen Z, Li D, Sun Z, Pei L, Liu X, et al. Investigation on composition and structure of asphaltenes during low-temperature coal tar hydrotreatment under various reaction pressures. *Journal of Analytical and Applied Pyrolysis* 2018;136:44-52.
- [30] Minale M, Merola MC, Carotenuto C. Effect of solvents on the microstructure aggregation of a heavy crude oil. *Fuel Processing Technology* 2018;177:299-308.
- [31] Tavakkoli M, Grimes MR, Liu X, Garcia CK, Correa SC, Cox QJ, et al. Indirect method: a novel technique for experimental determination of asphaltene precipitation. *Energy & Fuels* 2015;29(5):2890-900.
- [32] Tanaka R, Sato E, Hunt JE, Winans RE, Sato S, Takanohashi T. Characterization of asphaltene aggregates using X-ray diffraction and small-angle X-ray scattering. *Energy & fuels* 2004;18(4):1118-25.
- [33] Eyssautier J, Frot D, Barré L. Structure and dynamic properties of colloidal asphaltene aggregates. *Langmuir* 2012;28(33):11997-2004.
- [34] Larichev YV, Martyanov O. The dynamics of asphaltene aggregates in heavy crude oils on a nanometer scale studied via small-angle X-ray scattering in situ. *Journal of Petroleum Science and Engineering* 2018;165:575-80.
- [35] Petoukhov MV, Franke D, Shkumatov AV, Tria G, Kikhney AG, Gajda M, et al. New developments in the ATSAS program package for small-angle scattering data analysis. *Journal of applied crystallography* 2012;45(2):342-50.
- [36] Gimzewski E. An accurate and compact high-pressure thermogravimetric analyser. *Journal of thermal analysis* 1991;37(6):1251-60.
- [37] Xu Z, Wang Y, Cao J, Chai J, Cao C, Si Z, et al. Adhesion between asphalt molecules and acid aggregates under extreme temperature: A ReaxFF reactive molecular dynamics study. *Construction and Building Materials* 2021;285:122882.

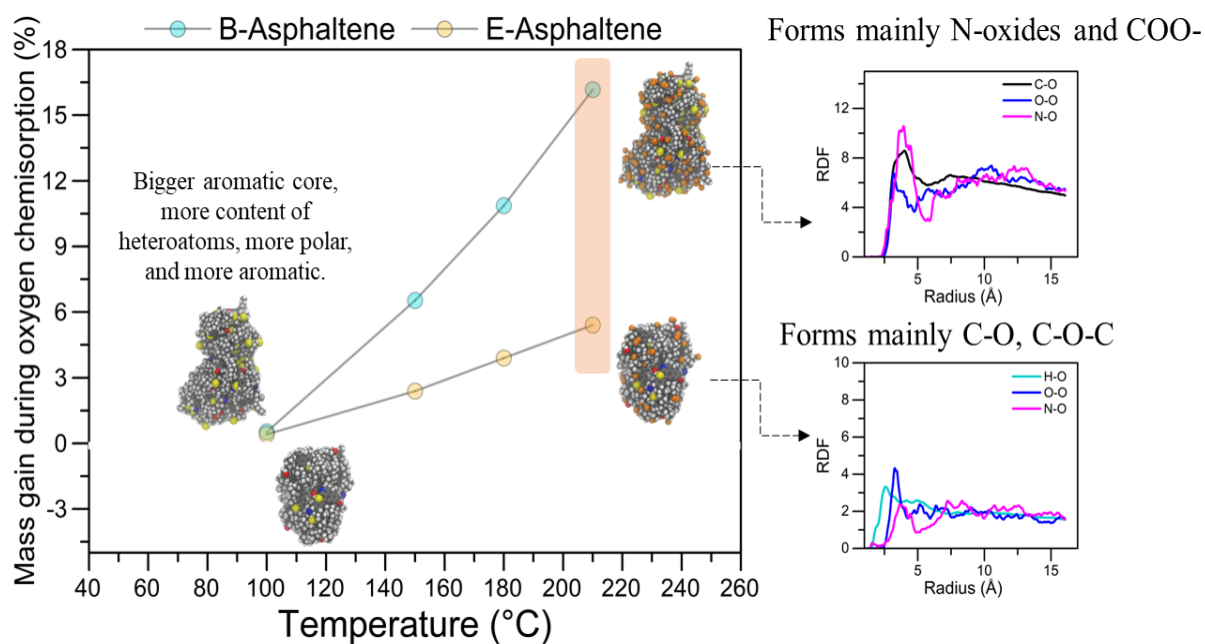
- [38] Headen T, Boek E, Jackson G, Totton T, Müller E. Simulation of asphaltene aggregation through molecular dynamics: Insights and limitations. *Energy & Fuels* 2017;31(2):1108-25.
- [39] Jorgensen W, Maxwell D, Tirado-Rives J. Optimized potential for liquid simulations. *J Am Chem Soc* 1996;118:11225-36.
- [40] Jorgensen WL, Maxwell DS, Tirado-Rives J. Development and testing of the OPLS all-atom force field on conformational energetics and properties of organic liquids. *Journal of the American Chemical Society* 1996;118(45):11225-36.
- [41] Watkins EK, Jorgensen WL. Perfluoroalkanes: Conformational analysis and liquid-state properties from ab initio and Monte Carlo calculations. *The Journal of Physical Chemistry A* 2001;105(16):4118-25.
- [42] Plimpton S. Fast parallel algorithms for short-range molecular dynamics. *Journal of computational physics* 1995;117(1):1-19.
- [43] Humphrey W, Dalke A, Schulten K. VMD: visual molecular dynamics. *Journal of molecular graphics* 1996;14(1):33-8.
- [44] Senneca O, Vorobiev N, Wütscher A, Cerciello F, Heuer S, Wedler C, et al. Assessment of combustion rates of coal chars for oxy-combustion applications. *Fuel* 2019;238:173-85.
- [45] Niksa S, Liu G-S, Hurt RH. Coal conversion submodels for design applications at elevated pressures. Part I. devolatilization and char oxidation. *Progress in Energy and Combustion Science* 2003;29(5):425-77.
- [46] Liu G-S, Niksa S. Coal conversion submodels for design applications at elevated pressures. Part II. Char gasification. *Progress in energy and combustion science* 2004;30(6):679-717.
- [47] Yen TF, Erdman JG, Pollack SS. Investigation of the structure of petroleum asphaltene by X-ray diffraction. *Analytical chemistry* 1961;33(11):1587-94.
- [48] Jennings J, Growney D, Brice H, Mykhaylyk O, Armes S. Application of scattering and diffraction techniques for the morphological characterization of asphaltene. *Fuel* 2022;327:125042.

- [49] AlHumaidan FS, Hauser A, Rana MS, Lababidi HM. NMR Characterization of Asphaltene Derived from Residual Oils and Their Thermal Decomposition. *Energy & Fuels* 2017;31(4):3812-20.
- [50] Vukovic JP, Novak P, Jednacak T. NMR Spectroscopy as a Tool for Studying Asphaltene Composition. *Croatica Chemica Acta* 2019;92(3):1G-G.
- [51] Salehzadeh M, Husein MM, Ghotbi C, Dabir B, Taghikhani V. In-depth characterization of light, medium and heavy oil asphaltenes as well as asphaltenes subfractions. *Fuel* 2022;324:124525.
- [52] Retcofsky H, Schweighardt F, Hough M. Determination of aromaticities of coal derivatives by nuclear magnetic resonance spectrometry and the Brown-Ladner equation. *Analytical Chemistry* 1977;49(4):585-8.
- [53] Taborda EA, Alvarado V, Franco CA, Cortés FB. Rheological demonstration of alteration in the heavy crude oil fluid structure upon addition of nanoparticles. *Fuel* 2017;189:322-33.
- [54] Moghaddam RK, Yarranton H, Natale G. Interfacial micro and macro rheology of fractionated asphaltenes. *Colloids and Surfaces A: Physicochemical and Engineering Aspects* 2022;651:129659.
- [55] Pierre C, Barré L, Pina A, Moan M. Composition and heavy oil rheology. *Oil & Gas Science and Technology* 2004;59(5):489-501.
- [56] Oguamah IAU, Isehunwa S, Ndubisi O, Stephen U, Jude O. Molecular Dynamics Study of Solvent Effect on the Structure and Characteristics of Asphaltene aggregates. 2022.
- [57] Johansson B, Friman R, Hakanpää-Laitinen H, Rosenholm JB. Solubility and interaction parameters as references for solution properties II: Precipitation and aggregation of asphaltene in organic solvents. *Advances in colloid and interface science* 2009;147:132-43.
- [58] Pal R. A new model for the viscosity of asphaltene solutions. *The Canadian Journal of Chemical Engineering* 2015;93(4):747-55.
- [59] Kuakpetoon D, Wang Y-J. Structural characteristics and physicochemical properties of oxidized corn starches varying in amylose content. *Carbohydrate Research* 2006;341(11):1896-915.

- [60] Andreatta G, Bostrom N, Mullins OC. High-Q ultrasonic determination of the critical nanoaggregate concentration of asphaltenes and the critical micelle concentration of standard surfactants. *Langmuir* 2005;21(7):2728-36.
- [61] Medina Erao OE, Gallego J, Olmos CM, Chen X, Cortés FB, Franco CA. Effect of Multifunctional Nanocatalysts on n-C7 Asphaltene Adsorption and Subsequent Oxidation under High Pressure Conditions. *Energy & Fuels* 2020.

## Chapter 4.

# Chemical and Structural Changes of Asphaltenes During Oxygen Chemisorption at Low and High-Pressure



Submitted article to **Journal of Petroleum Science and Engineering:**

PETROL33079

Impact factor: 5.168



# Chemical and Structural Changes of Asphaltenes During Oxygen Chemisorption at Low and High-Pressure

## Abstract

This study investigates the changes in asphaltene chemical properties during oxygen chemisorption (OC), to understand its thermal behavior at high temperatures and pressures. Two *n*-C<sub>7</sub> asphaltene samples (B and E) were subjected to non-isothermal heating up to determined temperatures at two different pressures 0.084 MPa and 6.0 MPa, in an oxygen environment. After that, the sample residues were characterized using elemental analysis, x-ray photoelectron spectroscopy, and nuclear magnetic resonance. The experimental observations suggest that oxygen chemisorption is influenced by the asphaltene chemical structure including the C, N, S, and O species and the aromatic size core. In parallel, molecular dynamics simulations (MD) were carried out using a reactive force field to obtain more insights into the chemisorption mechanism. MD results properly describe the amount of oxygen chemisorbed for both systems at high pressure (6.0 MPa). The results validate that the chemisorption sites are strongly related to the molecular characteristics, as asphaltene samples have different molecular characteristics. Using the radial distribution function (RDF), the main pairwise interactions were determined. The results suggest that for asphaltene B a well-defined first coordination peak was obtained for the interaction between the oxygen, nitrogen, and carbon. For asphaltene E, the first coordination peak corresponds to the interactions with oxygen, hydrogen, and nitrogen. Therefore, for asphaltene B the carboxyl or COO<sup>-</sup> groups can be formed, whereas for asphaltene E can be expected to obtain oxygen-oxygen bond formation by forming phenolic oxygen and ether oxygen. MD also suggests the size of the aromatic core as the most relevant feature.

## 1. Introduction

Most conventional reservoirs have lost their hydrocarbon supplies due to their depletion,<sup>1,2</sup> forcing the oil producers to rely on unconventional oil reserves to meet the world energy needs.<sup>3,4</sup> These oil deposits, which provide 70% of the world oil reserves, include heavy (HO) and extra-heavy crude oils (EHO).<sup>5</sup> Several challenges exist in conventional treatments, production methods, and refining operations of HO and EHO, resulting from their high viscosity and density.<sup>6,7</sup> It is insufficient to benefit from traditional recovery methods to extract unconventional supplies effectively.<sup>7</sup> Hitherto, many thermal-enhanced oil recovery (tEOR) methods have been developed to improve the mobility of HO and EHO in porous media,<sup>8-11</sup> classified into the in-situ combustion (ISC) of oil or gas, surface mining with hot water, and in-situ recovery by steam injection.<sup>8, 12, 13</sup> As for other surface processes, crude oils can be treated under different mechanisms that include oxy-cracking, hydrotreating, among others.<sup>14-17</sup>

In-situ combustion (ISC) or fire flooding is one of the oldest thermal oil recovery methods. During this technique an overwhelming number of oxygen-containing compounds are produced in the oxidizing atmosphere at low temperatures, changing the reactivity of HO and EHO and affecting the combustion front stability and oil viscosity.<sup>14, 18, 19</sup> On the other hand, depending on the operating conditions on surface treatments (temperature and pressure), HO and EHO can suffer different thermal behaviors since their reaction with oxygen is highly controlled by both variables.<sup>20-22</sup>

To overcome the problems involved in ISC and oxygen-based treatments and understand the reactions that occur during this process, it is essential to understand the oxidation kinetics of HO at different conditions of pressures and temperatures.<sup>23-26</sup> Hitherto, several studies have been conducted on individual fractions of HO and EHO entitled resin (R), aromatic (Ar), asphaltenes (A), and saturate (S). Among the mentioned fractions, asphaltenes in the form of asphalt or bitumen products are the heaviest-molecular-weight fraction of crude oils. Asphaltenes, which are defined as the paraffin-insoluble and aromatic-soluble component, consist of *polycyclic aromatic rings*, aliphatic long chains, alicyclic substituents, transition elements (e.g., nickel, vanadium, and iron), and heteroatomic derivatives (e.g., nitrogen, oxygen, and sulfur).<sup>27-29</sup>

To pave the way for oil producers, it is essential to clarify the chemical reactions and thermal behavior of asphaltenes under high-pressure and high-temperature conditions. In a previous study, we examined the effect of pressures (0.084 to 7 Mpa) and temperatures (100-800 °C) on the oxidation kinetics of different asphaltene samples.<sup>30</sup> First, we have demonstrated that the asphaltene oxidation reaction mechanism can be described by four main regions for pressures higher than 0.7 Mpa based on its chemical structure and composition. The regions were known as oxygen chemisorption (OC) region, decomposition of chemisorbed oxygen structures (DCO), first combustion (FC) or commonly known as low-temperature oxidation, and second combustion or high-temperature oxidation (SC) region.<sup>30</sup>

It was found that although pressure was a controlling factor in the four oxidation regions, there was a strange behavior in the thermogravimetric graph for temperatures below 250 °C, where OC takes place. Interestingly, the OC region gained high attention because the response of the samples in the rest of the thermal events appears to be dependent on how the oxygen interacts with the asphaltene in that region. This hypothesis arises from a study where different types of asphaltenes with different chemical natures were evaluated.<sup>31</sup> The thermal response in OC of each asphaltenes was different according to asphaltene chemical nature. In some cases, asphaltene thermal behavior did not depend on the amount of mass gained in OC to complete the decomposition at higher temperatures. This makes us believe that depending on the oxygenated groups that are formed in OC, asphaltene reactivity can change to a lesser or greater degree. There are several properties, such as aromaticity factor, alkylation degree, and distribution of oxygenated species (e.g., COO-, C=O, etc) can affect asphaltene reactivity. However, during that work, it was not possible to describe in detail how asphaltene thermal properties changed in the OC region, and why the subsequent thermal regions were drastically affected.<sup>31</sup>

Furthermore, molecular dynamics simulations (MD) have been widely used to obtain phenomenological information about the mechanism involved in asphaltene systems, mainly for studying the aggregation behavior using classical force fields.<sup>32-34</sup> Even though some studies have used reactive force fields or theoretical tools that describe the reactive process such as density functional theory (DFT), but mainly focusing on determining the interaction energies and aggregation behavior. Hence, studies relating to the asphaltene reactive process are less numerous. Alvarez-Ramírez et al.<sup>35</sup> calculated the asphaltene-asphaltene, asphaltene-resin, and resin-resin interaction energies using density functional

theory (DFT) and a classical force field. They found that the binding energies for the asphaltene–asphaltene, asphaltene–resin, and resin–resin dimers are ~12–15, ~12–14, and ~4–7.5 kcal·mol<sup>-1</sup>, respectively. Chen et al.<sup>36</sup> developed an MD model, using the ReaxFF force field, to describe the char oxidation processes under CO<sub>2</sub>, O<sub>2</sub>-CO<sub>2</sub>, and air environments. The authors found that O radical and CO<sub>2</sub> could adsorb and destroy the edge of representative polyaromatic hydrocarbon molecules in the char model during char oxidation and gasification. Despite the valuable contributions reported so far, the effect of the asphaltene structural characteristics on the oxygen chemisorption is not fully understood yet.

Therefore, this study aims to investigate the change in asphaltene chemical properties during the OC region from an experimental and theoretical perspectives. To achieve this, two *n*-C<sub>7</sub> asphaltene samples obtained from different heavy crude oil sources (previously named B and E) with different chemical natures were selected to examine their oxidation at low (0.084 Mpa) and high pressure (6.0 Mpa). The two samples are subjected to non-isothermal heating up to a determined temperature in the range of 100 °C – 250 °C, both at 0.084 and 6.0 Mpa. Once these conditions are reached, the samples are characterized by elemental analysis (EA), X-ray photoelectron spectroscopy (XPS), and nuclear magnetic resonance (NMR) to describe the chemical changes in the OC region. In addition, MD simulations were carried out to provide more insights on the effect of the asphaltene molecular characteristics on the oxygen chemisorption process and estimating the theoretical oxygen mass chemisorbed and the chemisorption configuration by radial distribution function (RDF). Understanding the thermal behavior of asphaltene molecules in oxidation-conversion processes allows researchers to select the best upgrading design for the heavy and extra-heavy crude oil samples during tEOR processes.

## 2. Experimental

### 2.1. Materials

Two different *n*-C<sub>7</sub> asphaltene samples, named B and E, were separately extracted from two crude oil samples provided by two different oil industrial partners. Table 1 summarizes the basic characteristics of B and E crude oils. To extract the asphaltene from the crude oils, the crude oil samples were mixed with *n*-heptane (Sigma-Aldrich, St. Louis, MO) in a 40:1 ratio according to the ASTM D2892 and ASTM D5236 standards.<sup>37-44</sup>

**Table 1.** Basic characteristics of B- and E- crude oils.

Crude Oil	Saturates (wt.%)	Aromatics (wt.%)	Resins (wt.%)	Asphaltenes (wt.%)	API gravity	Viscosity (cP) at 20 °C
B	13.90	18.58	52.48	15.0	9	30200
<sup>a</sup> E	44.42	26.11	24.72	0.75	45	2.5

<sup>a</sup>Taken from Abbas et al.<sup>45</sup>

NTC 2561 synthetic air (CRYOGAS, Bogotá, Colombia), which contains water (H<sub>2</sub>O, < 3 mg·L<sup>-1</sup>), total hydrocarbons content (THC, < 3 mg·L<sup>-1</sup>), and balanced oxygen and nitrogen (O<sub>2</sub> and N<sub>2</sub>, ~ 20.93%) was used as a reacting gas for TGA analyses.

The proposed workflow to investigate oxygen chemisorption of asphaltenes is shown schematically in Figure 1. The work was divided into three stages, in which experimental and simulation tools were used to describe and elucidate the chemical and structural differences between both molecules when they are subjected to oxidation at low and high pressures. In the first stage, the asphaltenes were extracted from the raw crude oil and their basic characteristics were obtained through elemental analysis, X-ray photoelectron spectroscopy, and nuclear magnetic resonance. In the second stage, the asphaltenes were subjected to oxidation at two pressures (0.084 and 6.0 MPa). The samples were heated until they reach a defined temperature (150, 180, and 210 °C). Next, they were characterized to describe the changes they had undergone during the heat treatment. In the third stage, molecular dynamic simulation was used to validate the oxygen chemisorption values at 6.0 MPa. Then, radial distribution functions between oxygen and each asphaltene atom (C, H, N, S, and O) were used to understand which functional groups are the closest to being generated during heat treatment. Details of each stage are described in the next sections.

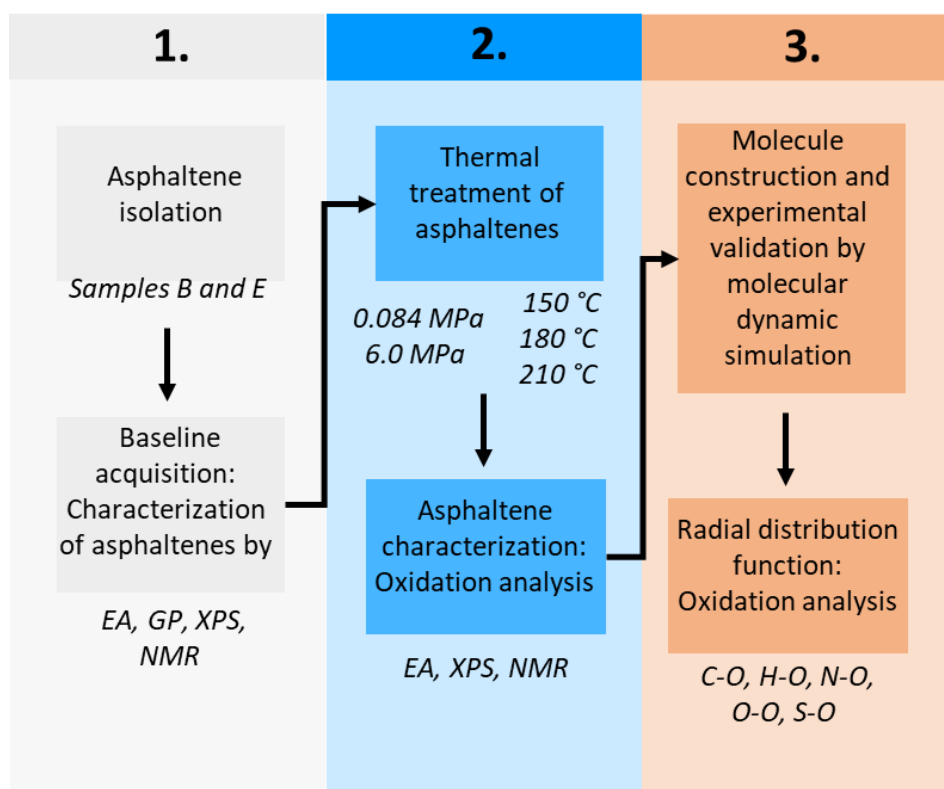


**Figure 1.** Schematic representation of the workflow conducted in this study.

## 2.2. Thermal Heating of Asphaltenes

An HP-TGA 750 analyzer (Hullhorst, Germany) was used to prepare oxidized *n*-C<sub>7</sub> asphaltenes at two different pressures (0.084 and 6.0 MPa). The system is based on a magnetic levitation technique. More details can be found in the previous studies.<sup>30, 46</sup> Samples were heated from 100 °C to 150 °C, 180 °C, or 210 °C using a heating ramp of 10 °C·min<sup>-1</sup> and an airflow of 80 mL·min<sup>-1</sup>. According to the obtained results in previous work,<sup>30</sup> the sample mass was adjusted to 1 mg to avoid mass and heat transfer limitations. Once the conditions of pressure and temperature are reached, the test ends, and the residue (i.e., unburned asphaltene fraction) are characterized by different analytical techniques. Each experiment was repeated three times to ensure the accuracy of the results.

## 2.3. Asphaltene elemental analysis

A Thermo Fisher Flash 2000 elemental analyzer using a chromatographic separation followed by a thermal conductivity detector was used to quantify the amount of C, H, and N elements in the non-treated and oxidized *n*-C<sub>7</sub> asphaltene. Five milligrams of virgin asphaltene were weighed on a precision scale and placed in the tin capsule and inserted into the carousel. The contents were burned

in a combustion chamber set at 1150 °C. The reduction chamber was set at 850 °C. The UOP 864 standard was used to determine S content. The oxygen content of the asphaltenes was measured by infrared detection of CO<sub>2</sub>, CO, COS, and SO<sub>2</sub> generated by pyrolysis of the asphaltenes up to 1150 °C in a quartz tube microreactor under 80 sccm Ar feed. Prior to being fed, the Ar flow was passed through an oxygen trap. The metal content (i.e., Ni and V) of the asphaltene samples was determined by inductively coupled plasma mass spectrometry (ICP-MS) using a Varian 820-MS instrument. The analytical test was performed in triplicates on each sample to verify the quality of the analyses.

#### 2.4. Asphaltene X-ray Photoelectron Spectroscopy (XPS)

A Near-ambient pressure X-ray photoelectron spectroscopy (Specs, Germany), equipped with a PHOIBOS 150 ID-DLD analyzer, monochromatic Al K $\alpha$  source (1486.7 eV), a step 90 eV-energy (for general spectra), and step 20 eV-energy (for high-resolution spectra), was used to measure the influence of the gases on the surface of the samples. While the period was 1 eV for the general spectra during five measurement cycles, it was 0.1 eV during 20 cycles for the high-resolution spectra. A 3 eV-20  $\mu$ A load compensation was used. The calibration of spectra was performed according to the C 1s peak at 284.8 eV.

#### 2.5. Asphaltene Nuclear Magnetic Resonance (NMR)

An NMR spectrometer (Bruker Ascend III HD, Karlsruhe, Germany), equipped with a TCI (5 mm) cryoprobe, was used to measure <sup>1</sup>H and <sup>13</sup>C nuclei through a frequency between 125 and 600 MHz. Tetramethylsilane (TMS) was used as a standard internal solvent to measure <sup>1</sup>H NMR. The asphaltene samples were dissolved in deuterated chloroform (CDCl<sub>3</sub>, 99.8 %), including tracers of TMS. The frequency of 75.45 MHz was considered for <sup>13</sup>C NMR, where the chemical shift values belonged to the central signal at 77 ppm concentration of CDCl<sub>3</sub>. The concentration of the samples was supposed to be a weight fraction of 15.0 (for <sup>1</sup>H) and 21.0 (for <sup>13</sup>C) in 0.5 mL of the solvent. To conduct <sup>1</sup>H NMR measurements, the NMR spectrometer was set at an angle of 90°, a signal width of 12.3 kHz, and a delay time of 1 s. Inverse-gated (IG) decoupling technique was used to measure <sup>13</sup>C NMR measurements at an angle, a signal width, and a delay time of 30°, 35 kHz, and 180 s, respectively. While <sup>13</sup>C NMR was detached into two major intervals related to the aromatic or aliphatic carbon types, the <sup>1</sup>H NMR spectrum was separated into four distinct regions based on the four different protons and their locations. More information about the chemical shift values and

chemical elemental compositions of the NMR building blocks is available from the previous study.<sup>31</sup> In the end, the spectra were completed and normalized for each specific region, and average structural parameters were computed based on the <sup>1</sup>H NMR equations as shown in Table 2.<sup>31</sup> Hydrogen is found in four different forms: Aromatic hydrogen (H<sub>a</sub>), and aliphatic hydrogens α, β, and γ linked to aromatic rings, (H<sub>α</sub>, H<sub>β</sub>, and H<sub>γ</sub> respectively).

**Table 2.** Calculations of average structural parameters using <sup>1</sup>H-NMR.

Equation	Description
$f_A = \frac{\left[ \frac{C}{H} - \frac{H_\alpha}{2} - \frac{H_\beta}{2} - \frac{H_\gamma}{3} \right]}{C/H}$	Aromaticity Factor
$\sigma = \frac{\left[ \frac{H_\alpha}{2} \right]}{\frac{H_\alpha}{2} + H_A}$	Hydrogen periphery replacement rate in the aromatic ring system
$\frac{H_{AU}}{C_A} = \frac{\left[ \frac{H_\alpha}{2} + H_A \right]}{\frac{C}{H} - \frac{H_\alpha}{2} - \frac{H_\beta}{2} - \frac{H_\gamma}{3}}$	Condensation degree parameter of the aromatic ring system
$C_\alpha = \frac{H_\alpha \times H_T}{2}$	Carbon numbers on the α position of an aromatic ring
$C_{ap} = C_\alpha + H_A \times H_T$	Peripheral carbon in a fused aromatic ring
$C_i = C_A - C_{ap}$	Internal carbon in a fused aromatic ring
$R_{Ar} = \frac{C_i}{2} + 1$	Aromatic rings
$n = \frac{H_\alpha + H_\beta + H_\gamma}{H_\alpha}$	Average alkyl chain length

### 3. Molecular Dynamics Methods (MD)

To describe the oxygen chemisorption process by MD, the REAX-FF was employed. To do this, the asphaltene aggregates and the air was constructed separately. Each asphaltene aggregate was formed in a vacuum condition, to allow all asphaltene molecules to be located at the minimum energy configuration, using 27 asphaltene molecules in each case (types B and E). To do this, an NVT ensemble was used with a time step of 1 fs during 2 ns. The air was represented as a mixture of 79 % mass fraction of nitrogen and 21% of oxygen at 6 MPa, using an NPT ensemble with 1 fs of time step during 5 ns. In both cases, the asphaltene aggregates and air were represented using a classical MD



simulation,<sup>47</sup> describing the bonds and angles flexion by harmonic models and the torsion by Watkins's model.<sup>48</sup> Then, these two simulation boxes were joined for describing each aggregate at 25 °C and 6 Mpa. The air molecules which overlap with the PAHs molecules were deleted, and relaxation was carried out during 5 ns at 25 °C and 3 Mpa by an NPT ensemble with a time step of 0.5 fs. Finally, after fully equilibrating the asphaltene-air system, all bonds, angles, and dihedrals were deleted to switch this configuration to a reactive force field.

The next step was to describe the oxygen chemisorption process by MD simulations using a reactive force field (REAX-FF).<sup>49</sup> This potential was initially parameterized to study hydrocarbon chemical reactions from the heat of formation and geometric data obtained from quantum chemistry calculations, correlating the bond distances, bond orders, and bond energies. Therefore, it allows to adequately dissociate of those atoms that are separated, i.e., without forming a bond. However, due to its versatility, this potential has been extended to the study of chemical reactions of other types of compounds, including solid phases.<sup>50, 51</sup> Results reported in the literature indicate comparable or better accuracy compared to computational chemistry methods (PM3 or DFT),<sup>49</sup> with computational times up to 100 times faster. More detailed description on the operation and applications of REAX-FF in the study of reactive systems can be found elsewhere.<sup>49</sup>

To study the oxygen chemisorption each system was soft heated from 25 to 100 °C using a time step of 0.001 fs, during 5 ns, and the other 5 ns were carried out at constant temperature (100 °C) to relax the system. Then, the oxygen chemisorption process was described, considering the asphaltene aggregates as a solid, i.e., their mobility was restricted. This is due to solid freedom degrees being significantly lesser compared to air molecules. An NVT ensemble was used for heating from 100 °C to the temperature used for the oxygen chemisorption experimentally (220-230 °C) for 10 ns. A distance of 2 Å was defined to determine if oxygen is chemisorbed onto the PAHs aggregate.<sup>52</sup> From this condition, the number of oxygen molecules chemisorbed can be determined for each type of PAHs evaluated, quantifying the mass fraction obtained by MD simulation and comparing it with the experimental values.

## 4. Results and discussion

### 4.1. Chemical Characterization of Non-Treated and Oxidized Asphaltenes

To better understand the chemical changes of asphaltenes during oxygen chemisorption, asphaltenes B and E were characterized by elemental analysis, gel permeation chromatography, nuclear magnetic resonance, and X-ray photoelectron spectroscopy. Previously, we identified that at high pressure, asphaltenes gain mass at temperatures below 250 °C, and the region was named oxygen chemisorption (OC) region.<sup>30</sup> The mass gained in this region at 6.0 MPa was 19.1 wt% and 19.0 wt% for B- and E-asphaltenes; respectively. Beyond this point, the behavior of the mass profile is very different at higher temperatures for both samples. These differences suggest that during OC the asphaltenes undergo important compositional changes that determine their thermal behavior at higher temperatures.

#### 4.1.1. Changes of Asphaltene Elemental Content During Oxygen Chemisorption at Low and High Pressures

The elemental mass fractions of the asphaltene samples B and E are given in Figure 2. Based on the asphaltene origin, there were different amounts of heteroatoms (N, O, and S) in the molecular structures of the asphaltene samples. For sample B, oxygen, nitrogen, and sulfur contents were more than that for sample E, revealing the high polarity of sample B. Besides, there was different C content in the asphaltene samples, and the H/C ratio of sample B (1.05) was lower than sample E (1.11), confirming the high aromatic content of sample B. The content of Ni was 153.6 ppm and 62.5 ppm for B and E asphaltenes, respectively, whereas the V content was 213.6 ppm and 81.0 ppm for B and E samples, respectively. There is a good agreement between the studied asphaltene sample elemental analyses and the literature studies using asphaltenes isolated from light and heavy crude oils.<sup>27, 47, 53</sup>

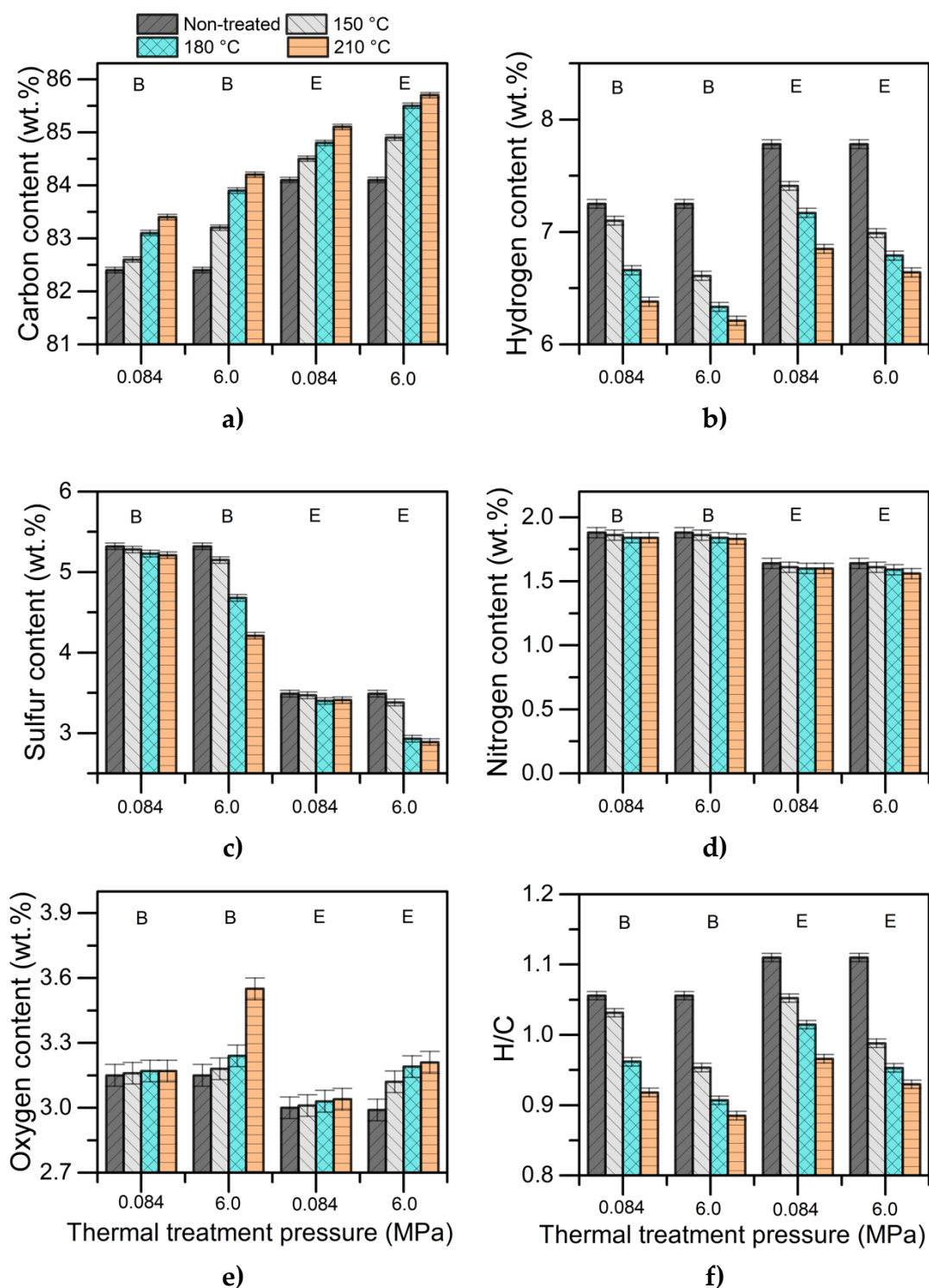


**Figure 2.** Elemental analysis for a) carbon content, b) hydrogen content, c) sulfur content, d) nitrogen content, e) oxygen content and f) H/C ratio of asphaltene samples B and E thermally treated between 150 °C and 210 °C at 0.084 MPa and 6.0 MPa.

Considering the elemental content changes of both samples as a function of the pressure and temperature, the following analysis was obtained: At low

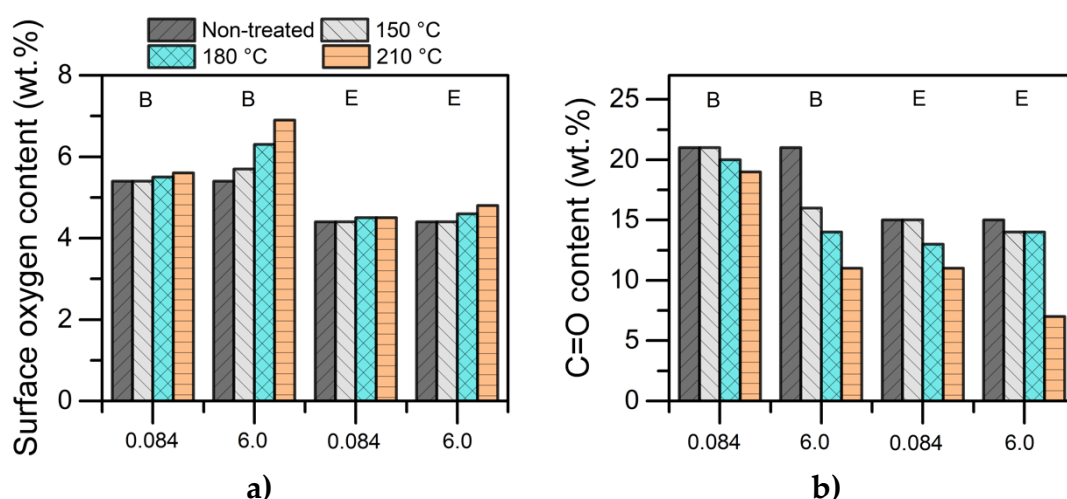
pressure (0.084MPa), increasing the temperature from 100 to 210 °C caused a 1.21% increment of carbon content in the asphaltene sample B, which was lower to that of sample E with a 1.18% carbon increment. The rising temperature at high pressure (6.0 MPa) showed a meaningful carbon increase in both asphaltene samples, which was 2.1% and 1.9% for samples B and E, respectively. For the H content of the asphaltene sample B, a falling trend occurred by increasing the temperature, reducing the content by 12.0% and 14.3% at 0.084 MPa and 6.0 MPa, respectively. Similar trends were observed for E-asphaltene, reducing hydrogen % by 11.9% and 14.6% at 0.084 MPa and 6.0 MPa, respectively. Based on H and C content, the H/C ratio was calculated at all the experimental conditions obtaining that B-asphaltene remains more aromatic than E-asphaltene with the temperature and pressure changes. At 0.084 MPa, the H/C ratio decreased from 1.05 to 0.91 (B-sample) and 1.11 to 0.96 (E-sample) between 100 and 210 °C. When pressure increases to 6.0 MPa at 210 °C the H/C ratio was 0.88 and 0.92 in B and E asphaltenes, respectively. The greater aromaticity for both samples at high pressure may result from a greater change in the asphaltene structure. At higher pressures, more active hydrogens in the carbon chains may be substituted by oxygen atoms, forming hydroperoxides. Then more partial oxides and side products (CO<sub>2</sub>, CO, and H<sub>2</sub>O) could be yielded by the isomerization and decomposition reactions of hydroperoxides formed. Furthermore, these formed partial oxides tend to encounter dehydrogenation and aromatization reactions, resulting in a lower H/C ratio.<sup>54-58</sup>

For S content, this was highly modified at high pressure, decreasing from 5.32 wt% to 4.21 wt% in B-sample, and from 3.49 wt% to 2.89 wt% in E-sample, while there was a falling trend of sulfur content by increasing pressure in both asphaltene samples, this was an inverse trend for oxygen content. At 0.084 MPa, the oxygen % is not highly modified for both samples, while at 6.0 MPa, the oxygen content increased considerably for both samples, corroborating the formation of oxygenated structures by the interactions with O<sub>2</sub> during OC. Results indicate that there was a rising trend in the O content of the asphaltene samples by increasing pressure. Because of the thermal expansion (TE) of the aggregates capable of interaction with oxygen atoms, the increase in pressure promotes the amount of chemisorbed oxygen in the asphaltene structure.<sup>59</sup> This upward trend at 210 °C was twelve times that at 150 °C in the asphaltene sample B and twice in the asphaltene sample E. Hence, the final content of oxygen in asphaltene sample B was much higher (12.6%) than in asphaltene sample E (7.3%). This is likely due to the different interactions between oxygen and the

functional groups of asphaltenes during the OC region. Finally, the rising temperature at low and high pressure showed a negligible nitrogen change in both asphaltene samples.

#### 4.1.2. Changes of Atomic Contents (%) of Oxygen-Containing Compounds During Oxygen Chemisorption of Asphaltenes at Low and High Pressure

XPS analysis was conducted to reveal the oxygen content of both asphaltene samples, B and E. Figure 3 shows XPS results and  $O_{1s}$  high-resolution spectra analysis for the asphaltene molecules of samples B and E. The presence of oxygen functional groups on the surface of the asphaltene samples B and E, which appeared in the elemental analysis, was confirmed by the existence of Auger transitions correlated to clear signals related to  $O_{1s}$  atoms. More information about the form and distribution of the oxygen groups on the surface of the asphaltene samples was provided by investigating the high-resolution spectra of O atoms using casaXPS software (Casa Software Ltd., Teignmouth, Devon, U.K.).<sup>16,31,60</sup> The oxygen bonds were divided into three different groups: carbonyl groups (C=O) at 531.1, carboxyl groups (COO<sup>-</sup>) at 533.5 eV, and single-bond oxygen groups (C-O, C-OH, C-O-C) at 532.4 eV. Generally, the oxygen content of asphaltene sample B in the form of carbonyl and carboxyl groups was more than that of sample E, in contrast to the single-bond oxygen groups. Although the oxygen content of both asphaltene samples varied at each temperature and pressure, the highest amount of oxygen was found in the form of single-bond oxygen groups at each temperature and pressure.



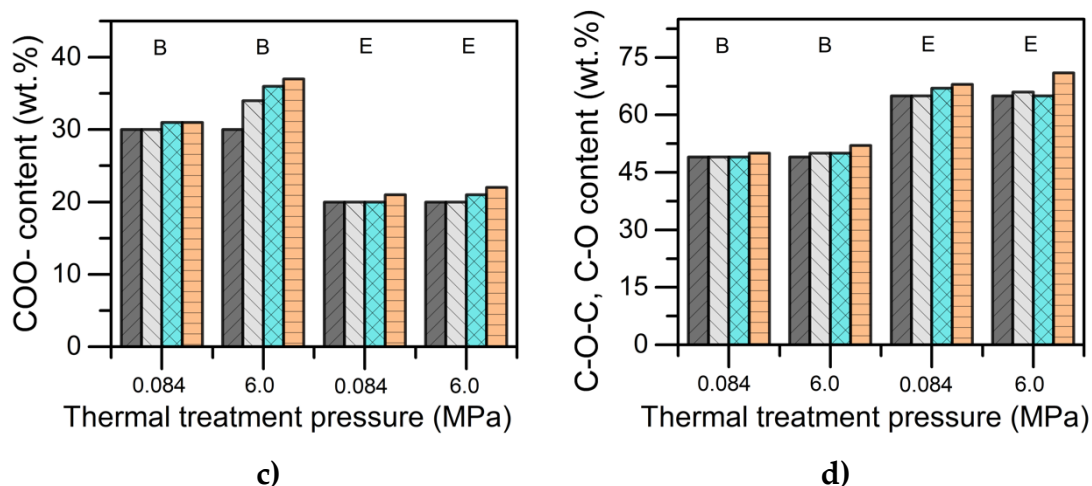


**Figure 3.** Configurations and atomic contents (%) of oxygen-containing compounds derived from the fitting results of the a) survey spectrum and high-resolution  $O_{1s}$  spectrum of b) C=O groups, c) COO- groups, and d) single-bond oxygen groups for asphaltene samples B and E thermally treated between 150 and 210 °C at 0.084 and 6.0 MPa.

The surface oxygen content of the asphaltenes B and E increased with increasing the temperature over the entire pressure range. However, the temperature had a more significant effect at high pressure compared to low pressure, in such a way that the content changes of the survey at high pressure were 5.7 and 4 times that of at low pressure in the asphaltene B and E, respectively.

For both asphaltene samples, the effect of pressure on the surface oxygen content at the high temperature was more pronounced than at medium and low temperatures. Although there was a 23.21 and 6.75% increase in surface oxygen content at 210 °C for the asphaltene samples B and E, respectively, this was 2.3 and 0% at 150 °C, in order. By increasing the temperature, the kinetic interactions between oxygen molecules from the oxidative environment and the asphaltenes become more abundant, generating more oxygenated structures.

In terms of carbonyl groups, there was a falling trend in both asphaltene samples during the whole pressure and temperature ranges. At high pressure, increasing the temperature reduced the oxygen content of the C=O group by 31.25 and 50% at the asphaltene samples B and E, respectively, which were 3.3 and 1.7 times that at low pressure, in order.

An opposite trend was seen in the carboxyl and single-bond oxygen groups (C-O-C, C-OH, C-O) in such a way that their oxygen content increased by increasing temperature and pressure. By increasing the temperature, there was a

7% increase in the oxygen content of COO<sup>-</sup> groups of the asphaltene sample B at 6.0 MPa, which was 2% in the accordance pressure in the asphaltene sample E. This reveals that the oxygen content of B-asphaltene increased by forming carboxyl structures during OC. The ionization of the carboxyl groups happens with the release of protons (hydrogen atoms) from the hydroxyl groups, proving the high activity of the -OH group.<sup>61</sup> Also, carboxyl groups are polar molecules that can form hydrogen bonds with each other and with other types of molecules (O<sub>2</sub>). Thus, the group (-OH) is considered strongly active.<sup>62</sup> Hand in hand with the increase in carboxyl groups, the polarity of the molecules increased in the same order. To calculate the polarity, the O/CHNSO ratio was estimated with the elemental analysis results. This relationship is found in Figure 4. The increase in carboxyl groups can promote an increase in the polarity of asphaltenes, which would affect their reactivity at higher temperatures. In addition, it is expected that the carboxyl groups generate a greater steric hindrance, which would help to avoid agglomerations via stacking or van der Waals.<sup>63</sup> This tendency agrees well with the thermal profile for both asphaltenes evaluated in previous work.<sup>31</sup> For example, the B asphaltenes finish each event at lower temperatures than the E asphaltenes. The mass lost in DCO was higher for B asphaltenes than E asphaltenes, and oppositely, during FC, the E asphaltenes lost more mass. A very interesting result was found during the transition between FC and SC. The E asphaltenes exhibit a predominant increase in the intensity of the rate for mass change profile which is not observed in the B asphaltenes. These important differences suggest that during OC the formation of carboxyl structures undergoes very important compositional changes that determine their thermal behavior in the following regions.

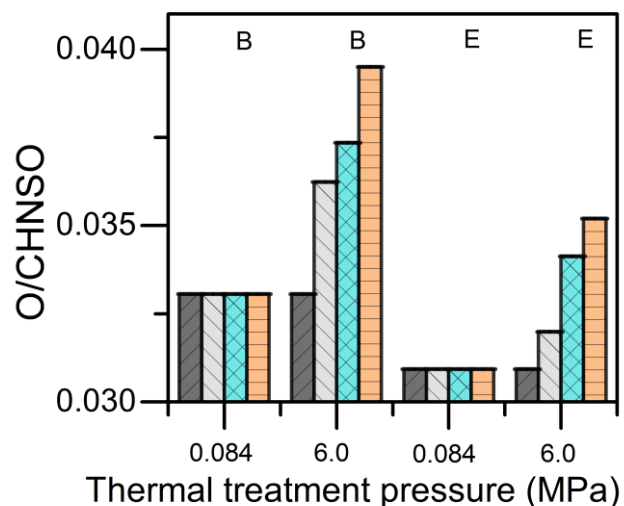
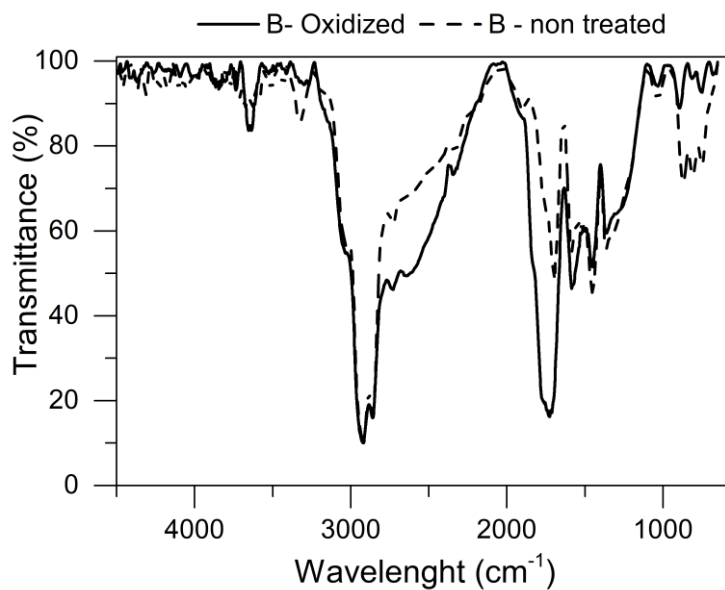


**Figure 4.** Polarity for asphaltene samples B and E thermally treated between 150 °C and 210 °C at 0.084 MPa and 6.0 MPa

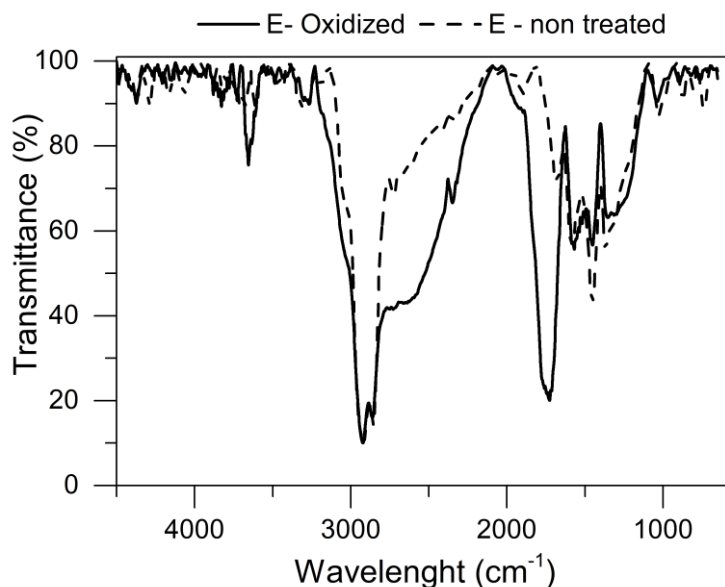
FTIR spectra were also executed to corroborate the presence of COO-groups. Figure 5 shows the results for non-treated asphaltenes, and samples oxidized at 6.0 MPa and 210 °C. After thermal treatment, the intensity bands at 3400  $\text{cm}^{-1}$  and 1600  $\text{cm}^{-1}$  increased for both asphaltenes, which correspond to the C=O group with a hydrogen-bonded molecule.<sup>64</sup>

For the single-bond oxygen groups, the increasing temperature at high pressure caused a 4% and 7.6% increase in the oxygen content of asphaltene samples B and E, respectively, which were twice and 4.4 times more than those at low pressure. It illustrates that at high pressure, the formation of COO- groups occurs easily in B-asphaltene, whereas E-asphaltene is more likely to form single bonds with oxygen. This result suggests that asphaltene E tends to form phenolic oxygen and ether oxygen during OC.<sup>65</sup> Also, in the  $\text{O}_2$  chemisorption mechanism of asphaltene molecules, the presence of oxygen-containing groups such as carbon-centered peroxy radicals, peroxides, and hydrogen peroxides was proposed.<sup>65</sup>





a)



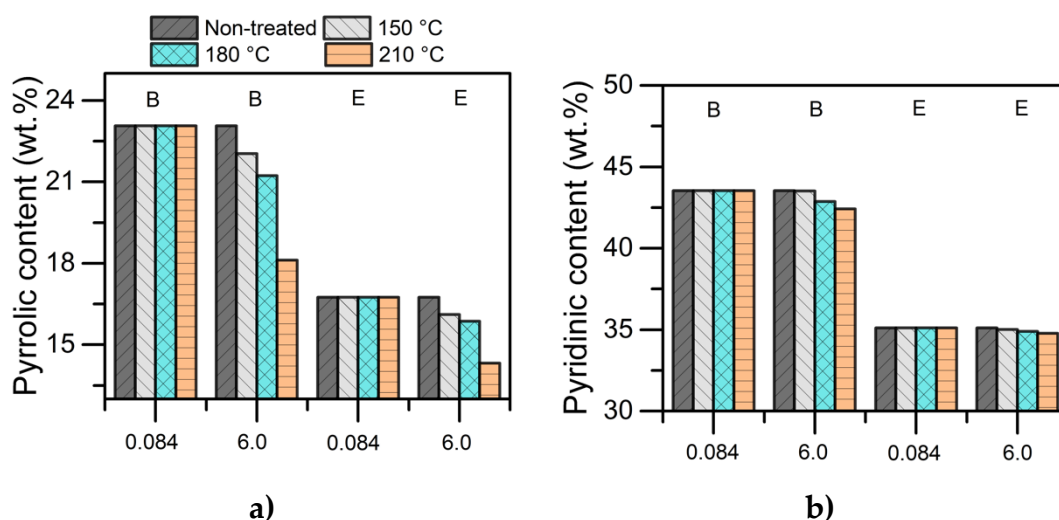
b)

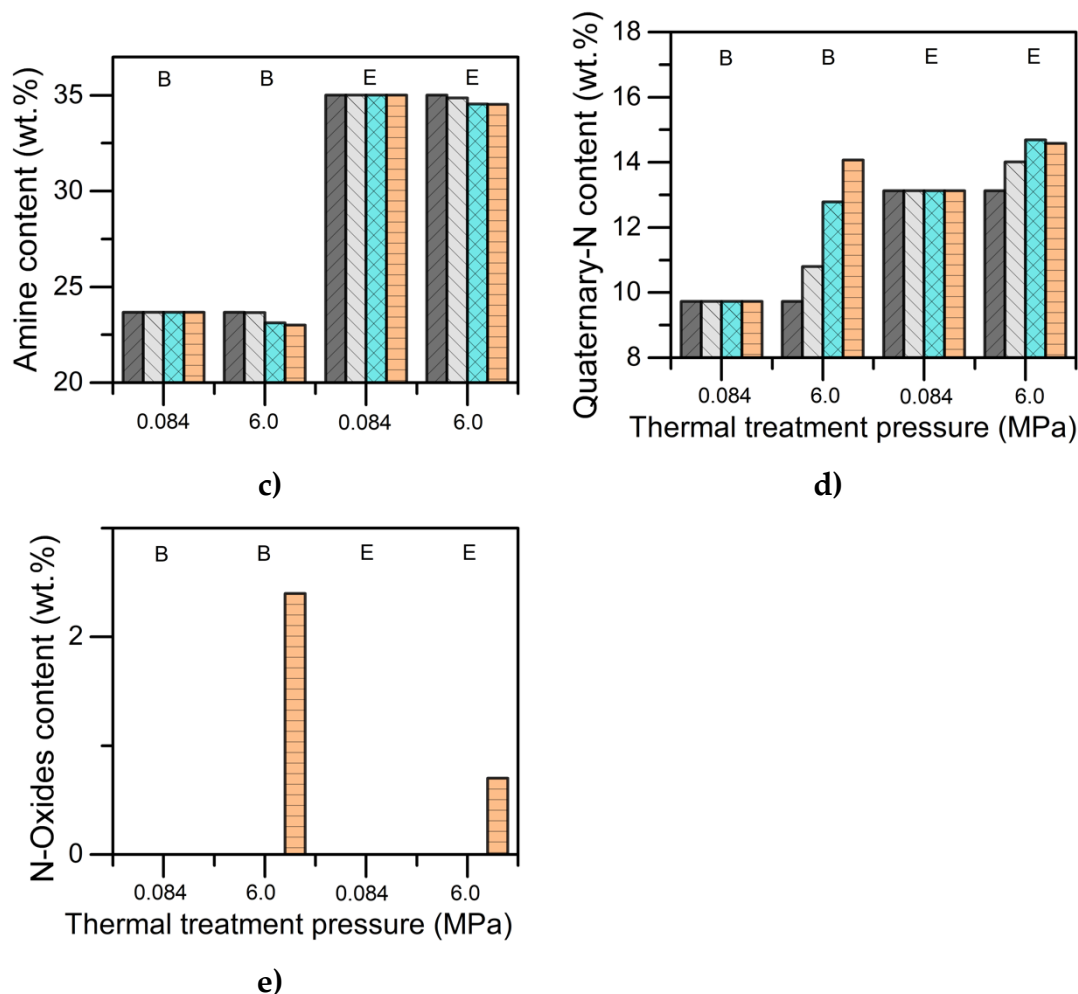
**Figure 5.** FT-IR spectra for a) B-asphaltene and b) E asphaltene non- and treated at 210 °C and 6.0 MPa under air oxidation.

In terms of the pressure effect, there was a falling trend in the oxygen content of the C=O groups of both asphaltene samples at low, medium, and high temperatures, which was more severe at higher temperatures. Conversely, the changes in oxygen content of the carboxyl groups of both asphaltene samples were upward with pressure at all investigated temperatures.<sup>61</sup> It illustrates that oxygen chemisorption is mainly controlled by the formation of carboxyl and single-bond oxygen structures.

Based on these assumptions, asphaltene B which presents the higher oxygen chemisorption percentage (TGA results) also presents the higher formation of carboxyl structures in the temperature range evaluated at high-pressure. In this sense, these structures could be an important factor that determines the thermal behavior of the asphaltene in the rest of the regions.

To further quantify the functional group evolution and the differences at 0.084 MPa and 6.0 MPa, the high-resolution  $N_{1s}$  and  $S_{2p}$  spectra were respectively analyzed, and the results are shown in Figures 6 and 7, respectively. It is worth mentioning that  $N_{1s}$  spectra had a relatively weak signal intensity for both asphaltenes and hence a low signal-to-noise ratio. The main existence forms of nitrogen components included pyrrolic, pyridinic, amine, and quaternary, corresponding to different peaks at different energy positions at 398.8, 399.0, 400.7, and 401.2 eV, respectively. For the non-treated B asphaltene, it was found a major content of pyrrolic (23.07 %) and pyridinic (43.53 %) structures than E asphaltenes (16.75% pyrrolic and 35.11% pyridinic). In contrast, non-treated E-asphaltenes presented a higher content of amine (35.01%) and quaternary-N (13.13%) than B asphaltenes (23.67% amine and 9.73% quaternary-N). Different results were found at low and high pressure. At 0.084 MPa, with the increase in temperature from 100 °C to 210 °C, no significant changes in nitrogen distribution were observed for both samples. By contrast, at 6.0 MPa the proportion of pyrrolic-N presented a decreasing trend, while the pyridinic type seems to be more stable with a smaller reduction. Part of both N-species undergoes further transformation into N-oxides, which is observed in a small percentage at 210 °C for both systems. Based on these results, the content of pyrrolic species on asphaltene structure is a determining factor during OC, controlling the thermal behavior of the asphaltenes in the rest of the regions.

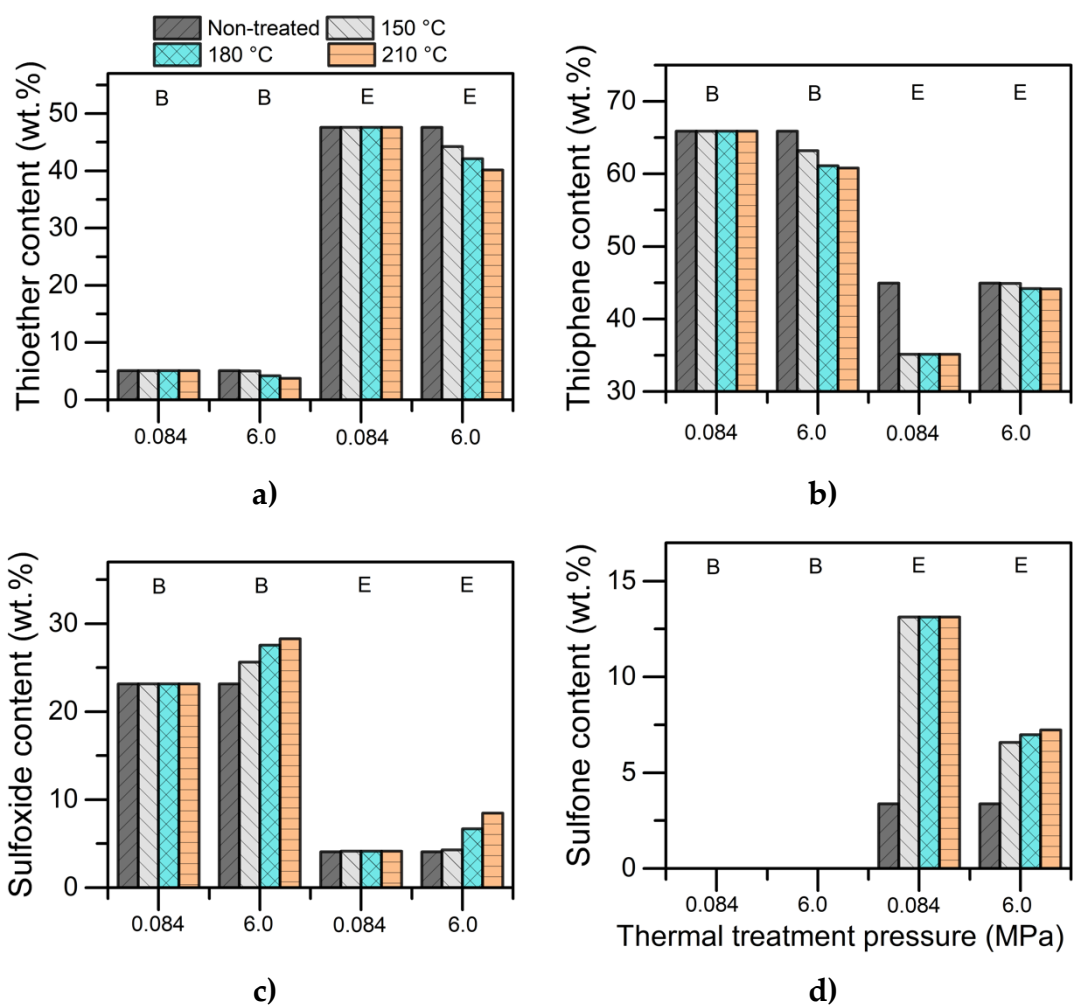


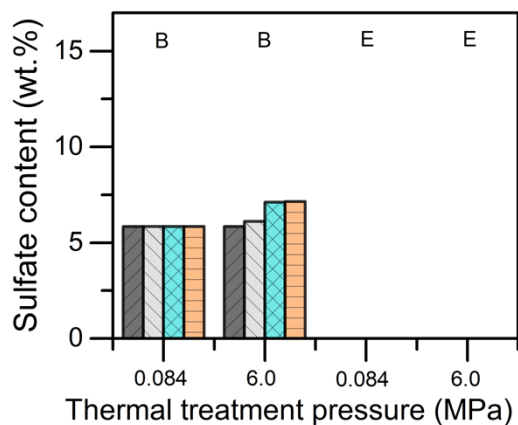


**Figure 6.** Configurations and atomic contents (%) of nitrogen-containing compounds derived from the fitting results of the high-resolution  $N_{1s}$  spectrum of a) pyrrolic-N groups, b) pyridinic-N groups, c) amine-N groups, d) Quaternary-N groups and e) N-Oxides groups for asphaltene samples B and E thermally treated between 150 °C and 210 °C at 0.084 MPa and 6.0 MPa.

The results for  $S_{2p}$  species on asphaltenes are shown in Figure 7. According to the results, B asphaltene contains four compounds including alkyl sulfides or thioethers, thiophenes, sulfoxides, and sulfonic acids or sulfates at 163.4, 164.4, 166.0, and 169.1 eV, respectively. Interestingly, sample E contains similar structures, except that it does not contain sulfates, but sulfones. The sulfur speciation of both samples is dominated by thiophene on B-asphaltene and thioethers on E-asphaltenes. When samples are subjected to oxidation at 0.084 MPa, the distribution of sulfur species is not modified. At 6.0 MPa, it is observed that with increasing temperature, the thioether content is highly reduced in sample E, while the content of sulfones and sulfoxides increases. In the case of B-asphaltenes, the content of thioethers and thiophenes is reduced, and the content

of sulfoxides and sulfates increased. The formation of sulfoxides, sulfones, and sulfates places great importance on the OC thermal event, because these compounds are more reactive and facilitate desulfurization than the unoxidized sulfur compounds, for two important reasons, (i) oxidized sulfur compounds acquire high polarity and (ii) the C-S bond strength decreased substantially when the sulfur is oxidized. Hence, it is easier to remove the oxidized sulfur by thermal decomposition.





e)

**Figure 7.** Configurations and atomic contents (%) of nitrogen-containing compounds derived from the fitting results of the high-resolution  $S_{2p}$  spectrum of a) thioether groups, b) thiophene groups, c) sulfoxide groups, d) sulfone groups, and e) sulfate groups for asphaltene samples B and E thermally treated between 150 °C and 210 °C at 0.084 MPa and 6.0 MPa.

#### 4.1.3. Changes in Structural Parameters from $^1H$ NMR During Oxygen Chemisorption of Asphaltenes at Low and High Pressure

The  $^1H$  NMR spectra of the asphaltene molecules B (Table 3) and E (Table 4) were normalized and integrated using MestRenova software (San Diego, California) to obtain their average structural parameters (ASP) using the modified Brown-Ladner (BL) method. As the first instance, it was observed that, in all the examined temperature and pressure ranges, there was a higher aromaticity ( $f_A$ ) in sample B than that in sample E, which agreed with the results of elemental analysis. At low pressure (0.084 MPa), the aromaticity factor decreased by increasing temperature for both asphaltene samples. For samples B and E, it was 0.606 and 0.547 at 150 °C and fell to 0.601 and 0.513 at 210 °C, respectively. This is a result of the breaking of the asphaltene structure as the temperature rise. Probably, the aromatic structure is affected at low pressure.

**Table 3.** <sup>1</sup>H-NMR parameters for asphaltene sample B thermally treated between 150 °C and 210 °C at 0.084 MPa and 6.0 MPa.

Parameter	Thermal treatment						
	Without treatment *	0.084 MPa			6.0 MPa		
		150°C	180°C	230°C	150°C	180°C	210°C
$f_A$	0.608	0.606	0.603	0.601	0.614	0.625	0.631
$\sigma$	0.644	0.647	0.649	0.644	0.666	0.674	0.683
$H_{AU}/C_A$	0.233	0.333	0.335	0.236	0.342	0.444	0.448
$C_\alpha$	8.122	8.122	8.122	8.018	8.018	7.913	7.831
$C_{ap}$	12.616	12.616	12.616	12.455	12.455	12.291	12.164
$C_i$	40.992	39.835	39.835	39.968	40.312	40.476	40.634
$R_{Ar}$	21.496	20.918	20.918	20.984	21.156	21.238	21.317
$n$	4.708	4.704	4.608	4.708	4.707	4.705	4.702

\*Data reproduced from Medina et al.<sup>62</sup>

**Table 4.** <sup>1</sup>H-NMR parameters for asphaltene sample E thermally treated between 150 °C and 210 °C at 0.084 MPa and 6.0 MPa.

Parameter	Thermal treatment						
	Without treatment *	0.084 MPa			6.0 MPa		
		150°C	180°C	230°C	150°C	180°C	210°C
$f_A$	0.561	0.547	0.526	0.513	0.546	0.552	0.558
$\sigma$	0.489	0.489	0.489	0.489	0.490	0.494	0.499
$H_{AU}/C_A$	0.197	0.209	0.217	0.220	0.210	0.219	0.227
$C_\alpha$	2.161	2.191	2.279	2.338	2.192	2.163	2.134
$C_{ap}$	4.421	4.483	4.663	4.784	4.485	4.425	4.366
$C_i$	22.625	21.220	19.975	19.152	21.176	21.482	21.847
$R_{Ar}$	12.313	11.610	10.988	10.576	11.588	11.741	11.923
$n$	8.736	8.731	8.725	8.655	8.735	8.732	8.729

\*Data reproduced from Medina et al.<sup>62</sup>

On the other hand, an inverse trend was observed at high pressure (6.0 MPa), and the aromaticity of the asphaltenes increased by rising temperature in both asphaltene samples. However, the increment in aromaticity was more pronounced in the B sample because of the interactions between the aromatic

sites and the oxygen. A primary site for diatomic oxygen compounds to have intermolecular attractions is the fused aromatic rings in the asphaltene structure in which the density of the  $\pi$  electron can result in interactions with the diatomic oxygen as an electrophile. Increasing the pressure increases the interactions of diatomic oxygen compounds on the fused aromatic rings in the polyaromatic molecules.<sup>61</sup> Therefore, increasing pressure within the thermal heating process could produce oxygenated groups resulting from aromatic cores oxidation in the fundamental aromatics alcohol, ketone, phenol, and acid groups,<sup>66</sup> increasing the aromaticity of the molecule.

Generally, for both asphaltene samples, the effect of pressure on the aromaticity was more significant than that of temperature. However, it was demonstrated that the temperature region affects the feature of the oxygenated groups that appeared during the oxidation of the asphaltene molecules. Alcohols and ketones arise at low temperatures, and ketones and aromatic ethers are the dominant oxygenated functional groups at temperatures close to 100 °C.<sup>67</sup> Klerk et al.<sup>67</sup> thoroughly explained ester formation due to cycloalkane oxidation. They concluded that there are many multicycle molecules in the structure of asphaltenes in which aromatic rings and cycloalkanes are joined together, where indane hydroperoxides are good representatives of the complex structures.

Similarly, there were more values for  $\sigma$  (hydrogen periphery replacement rate in the aromatic ring system) and  $H_{AU}/C_A$  (the condensation degree of the aromatic rings) in the asphaltene sample B with more aromatic factors than sample E. In both samples, the  $H_{AU}/C_A$  and  $\sigma$  increased with the increase in temperature at high pressure, indicating that the oxygenated structures formed to increase the condensation of the asphaltenes. For both B and E asphaltenes, the  $H_{AU}/C_A$  increased from 0.342 to 0.448 and 0.210 to 0.227, respectively. That is, the structures formed in the B asphaltenes condensate their structure at a higher level than E asphaltenes.

Besides,  $C_\alpha$  (the number of carbons on the  $\alpha$  position of an aromatic ring),  $C_{ap}$  (the peripheral carbon in a fused aromatic ring), and  $C_i$  (internal carbons) had fewer values in the asphaltene sample E with a low aromaticity factor. In general,  $C_i$  had more content than  $C_\alpha$  and  $C_{ap}$  in both asphaltene samples. At low pressure (0.084 MPa), the asphaltene sample B's carbons in the form of  $C_\alpha$  and  $C_{ap}$  were decreased by increasing the temperature, which was against the carbon numbers in the form of  $C_i$ . It is expected that at low pressure the asphaltene sample B expresses that some of the small alkyl side groups might be cracked because of  $\alpha$ -methyl,  $\alpha$ -methine, and  $\alpha$ -methylene decomposition.<sup>68</sup> The changes in carbon

number in the asphaltene sample E were in contrast to the asphaltene sample B, as there were two different trends in high and low pressure. Results indicated more aromatic rings ( $R_{Ar}$ ) and condensed aromatic structures in the asphaltene sample B, almost twice in sample E at each temperature and pressure. This superiority improves the stability of the asphaltene sample B and causes it to easily interact with other asphaltene molecules, leading to aggregation.<sup>30</sup> Since the average alkyl chain lengths ( $n$ ) were low in both asphaltene samples, with slight changes in the whole temperature and pressure range, the substituents were chiefly ethyl and methyl groups.<sup>68, 69</sup>

#### 4.1.4. Molecular Dynamics (MD) Simulations

The results from the characterization section were used to propose the asphaltene chemical structures of the B and E samples. Slight modifications were made concerning the structures proposed in our previous work.<sup>31</sup> Some restrictions were applied to avoid structural issues such as the pentane effect, i.e., relate to the hydrogen overlapping, and proper distribution of  $\pi$ -electrons in the aromatic core attending to the sextet rule of Clar.<sup>29</sup> The final configuration of the aggregates at the environment temperature is shown in Figure 8.

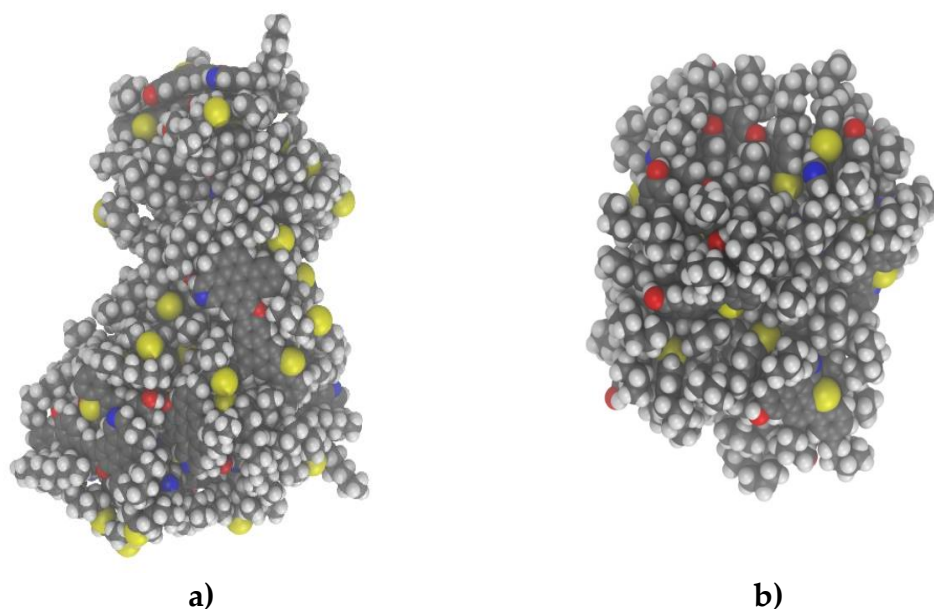


**Figure 8.** Configuration of equilibration of the aggregates formed at environment temperature for a) B-asphaltene and b) E-asphaltene. Carbon atoms are shown in gray, hydrogen in white, oxygen in red, nitrogen in blue, and sulfur in yellow.



Figure 9 shows the mass gain for each asphaltene aggregate due to the oxygen chemisorption. The results indicate that, in both cases, the experimental values were properly reproduced by the MD simulations, with deviations lesser than 29 and 6 % for asphaltene B and E, respectively.

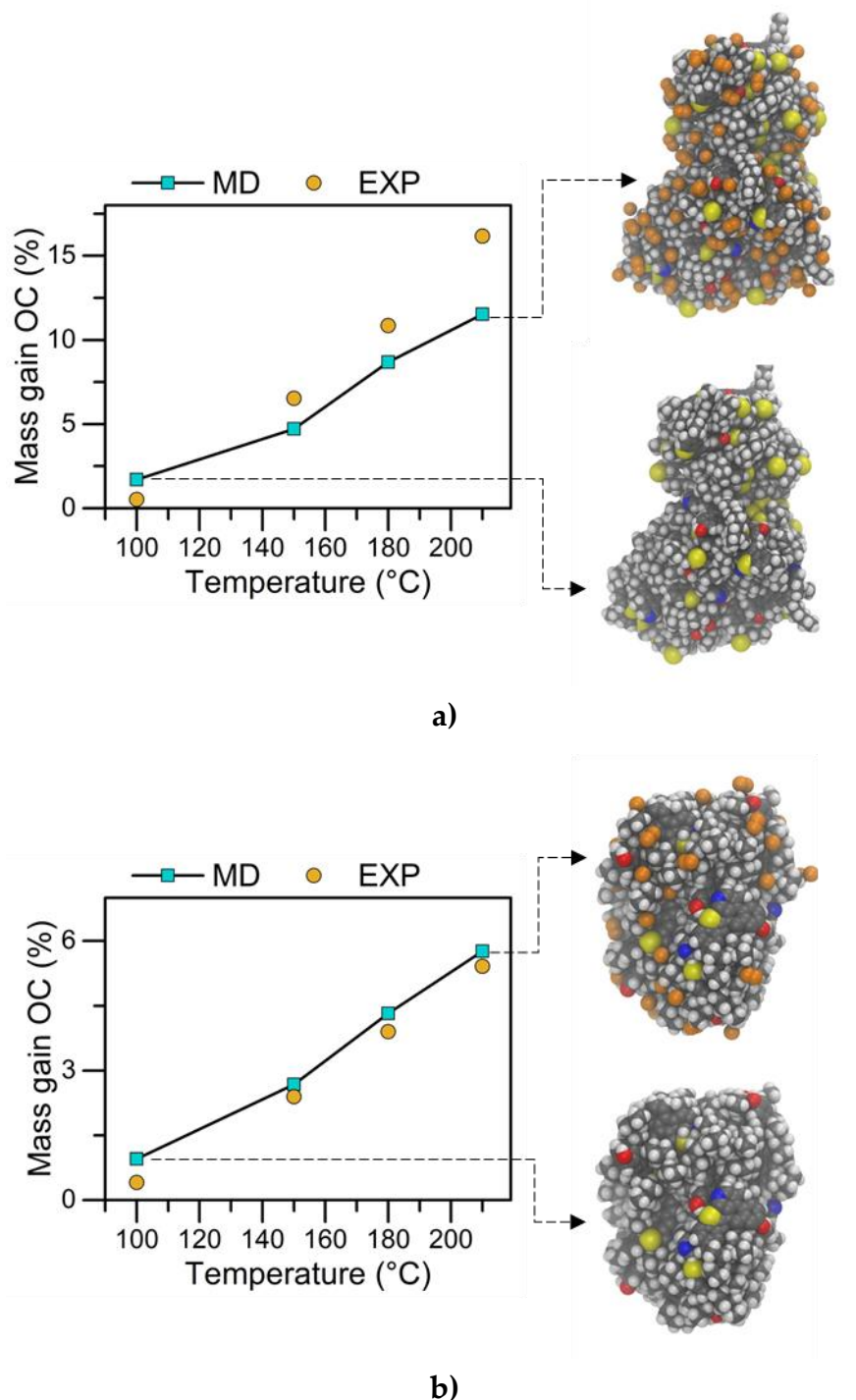


**Figure 9.** Experimental (EXP) and molecular dynamics (MD) mass gain by oxygen chemisorption for (a) asphaltene B and (b) asphaltene E. Carbon atoms are in grey, hydrogen in white, oxygen in red, nitrogen in blue, sulfur in yellow, and oxygen chemisorbed in orange.

In the case of asphaltene B, the higher deviation could be due to a high polydispersity of the asphaltene molecules,<sup>70, 71</sup> whereby the more amorphous aggregates can be obtained with the higher surface area to chemisorb oxygen molecules. As mentioned before, the two molecular structures of the considered asphaltenes are significantly different, hence, asphaltene B gains more mass and thus more quantity of oxygen molecules are chemisorbed. This can be explained by the surface available to chemisorb oxygen since the radius of gyration of asphaltene B (69.62 Å) is 3.3 times higher than the radius of gyration of asphaltene E (21.15 Å).

To identify the main configuration of the oxygen chemisorption on each asphaltene type, the radial distribution function was calculated (RDF) between the oxygen atoms of the air and each element of the asphaltene (CHONS). Figure 10 shows the results obtained, indicating that in all cases the intensity of the peaks is higher for asphaltene B than E, which is in agreement with the results reported in Figure 9 since a higher quantity of oxygen atoms are located close to asphaltene B than E. In addition, the RDF results allow for defining the main pairwise interaction by determining the main pairwise well-defined first coordination peak. In the case of asphaltene B, a well-defined first coordination peak was obtained for the interaction nitrogen-, carbon-, and oxygen-oxygen, in that order without a clear first coordination peak for the interaction sulfur-oxygen. Whereas the asphaltene E corresponds to oxygen-oxygen, hydrogen-oxygen, nitrogen-oxygen, and carbon-oxygen, in that order. Therefore, the results indicate that the molecular characteristics have a strong effect on the ability to chemisorb oxygen, for asphaltene B the carboxyl or COO<sup>-</sup> groups can be formed, whereas the asphaltene E can be expected to obtain oxygen-oxygen bonds formation. Considering that asphaltene B has a higher aromatic core size, it is possible that the oxygen can be chemisorbed onto the aromatic carbons more for asphaltene B than E. Also, the formation of N-oxides may occur more easily on B-asphaltene than on E-asphaltene, which agrees with XPS results.

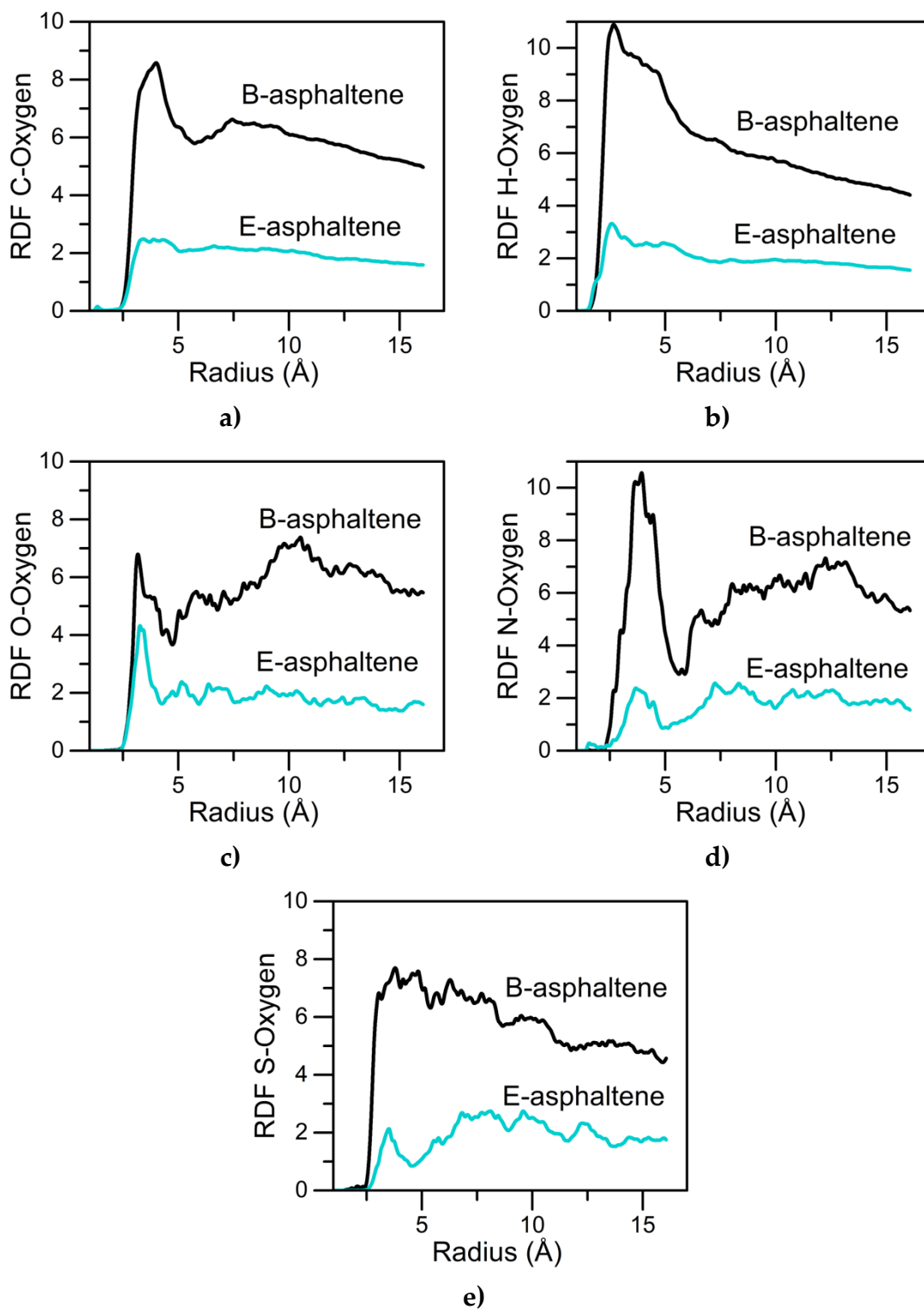


**Figure 10.** Radial distribution function (RDF) between the oxygen of the air and each element of the asphaltene molecules (CHONS), including a) carbon-oxygen, b) hydrogen-oxygen, c) oxygen-oxygen, d) nitrogen-oxygen, e) sulfur-oxygen.

## 5. Conclusions

This study successfully investigated the chemical composition changes in two different asphaltene samples during their thermal treatment at low temperatures between 150 and 210 °C, and low (0.084 MPa) and high pressures (6.0 MPa). The two *n*-C<sub>7</sub> asphaltenes were labeled as B and E. Oxygen chemisorption takes place at high-pressure (6.0 MPa). Under these conditions, it was observed that both asphaltenes undergo different reactions. The B asphaltenes which is more aromatic and polar presented a lower H/C ratio at the end of OC, indicating the formation of higher content of hydroperoxide groups through the hydrogen substitution for oxygen atoms on the aliphatic structure. This could result in higher isomerization and aromatization reactions at higher temperatures. As expected, there was an increment in oxygen content by the interactions with O<sub>2</sub> during OC. This upward trend at 210 °C was twelve times that at 150 °C in the asphaltene sample B and twice in the asphaltene sample E. Hence, the final content of oxygen in asphaltene sample B was much higher (12.6%) than in asphaltene sample E (7.3%). This is likely due to the different interactions between oxygen and the functional groups of asphaltenes during the OC region.

Specific differences occurred during the oxidation of the C, S, and N species in the asphaltenes. Asphaltene B was more susceptible to forming COO-structures during OC, whereas E-asphaltene formed mainly single-bond oxygen groups, that is, phenolic oxygen and ether oxygen. The proportion of pyrrolic-N presented a decreasing trend, while the pyridinic type seems to be more stable with a smaller reduction. Part of both N-species undergoes a further transformation into N-oxides, which is observed in a higher percentage for B-asphaltene. For sulfur content, the thioether content is highly reduced in sample E, while the content of sulfones and sulfoxides increases. In the case of B-asphaltene, the content of thioethers and thiophenes is reduced, and the content of sulfoxides and sulfates increased. Also, the aromaticity and polarity of both samples are increased, and the B sample becomes more condensed.

On the other hand, the experimental values, and the tendencies of the mass gain in the oxygen chemisorption were properly reproduced by molecular dynamics simulations, indicating that the chemical structure and CHNSO distribution as well as the aromatic core are key in this process. Through the radial distribution function (RDF) the main pairwise interactions were determined. The results indicate that for asphaltene B a well-defined first

coordination peak was obtained for the interaction between the oxygen and nitrogen and carbon, whereas the asphaltene E corresponds to the interactions with oxygen, hydrogen, and nitrogen, in that order. Therefore, for asphaltene B the carboxyl or COO<sup>-</sup> groups can be formed, whereas the asphaltene E can be expected to obtain oxygen-oxygen bond formation by forming phenolic oxygen and ether oxygen. MD suggested that another reason for higher oxygen chemisorption in asphaltene B is its higher aromatic core size (oxygen can be chemisorbed onto the aromatic carbons). Experimentally, this was corroborated by observing the increment in aromaticity which was more pronounced in the B sample because of the interactions between the aromatic sites and the oxygen.

## References

1. Zúñiga-Hinojosa, M.; Cosultchi, A.; Martinez-Martinez, M.; Cadena-Nava, R.; Ruiz-Garcia, J., Behavior comparison of films of Mexican bitumen and its asphaltene and maltenes fractions at interfaces. *Fuel* **2022**, 307, 121852.
2. Medina, O. E.; Gallego, J.; Cespedes, S.; Nassar, N. N.; Montoya, T.; Cortés, F. B.; Franco, C. A., Effect of pressure on thermo-oxidative reactions of saturates, aromatics, and resins (S-Ar-R) from extra-heavy crude oil. *Fuel* **2021**, 122596.
3. Pang, X.; Shao, X.; Li, M.; Hu, T.; Chen, Z.; Zhang, K.; Jiang, F.; Chen, J.; Chen, D.; Peng, J., Correlation and difference between conventional and unconventional reservoirs and their unified genetic classification. *Gondwana Research* **2021**, 97, 73-100.
4. Medina, O. E.; Gallego, J.; Redondo, J. D.; Cortés, F. B.; Franco, C. A., Effect of pressure on the thermo-oxidative behavior of saturates, aromatics, and resins (S-Ar-R) mixtures. *Fuel* **2021**, 122787.
5. Li, R. In *The overview of the development of future energy*, IOP Conference Series: Earth and Environmental Science, 2021; IOP Publishing: 2021; p 022044.
6. Zhao, S.; Pu, W.; Sun, B.; Gu, F.; Wang, L., Comparative evaluation on the thermal behaviors and kinetics of combustion of heavy crude oil and its SARA fractions. *Fuel* **2019**, 239, 117.
7. Huang, X.; Wang, P.; Tian, J.; Qi, Z.; Yan, W.; Qian, Y.; Li, S.; Shi, S., A novel method to assess steam injection rate in the steam-flooding process of shallow heavy oil reservoirs. *Energy Sources, Part A: Recovery, Utilization, and Environmental Effects* **2020**, 1-17.

8. Medina, O. E.; Olmos, C.; Lopera, S. H.; Cortés, F. B.; Franco, C. A., Nanotechnology applied to thermal enhanced oil recovery processes: a review. *Energies* **2019**, *12*, (24), 4671.
9. Bagci, A.; Gumrah, F. In *Effects of CO<sub>2</sub> and CH<sub>4</sub> addition to steam on recovery of West Kozluca heavy oil*, SPE international thermal operations and heavy oil symposium and western regional meeting, 2004; OnePetro: 2004.
10. Chen, Y.-f.; Pu, W.-f.; Liu, X.-l.; Li, Y.-b.; Varfolomeev, M. A.; Hui, J., A preliminary feasibility analysis of in situ combustion in a deep fractured-cave carbonate heavy oil reservoir. *Journal of Petroleum Science and Engineering* **2019**, *174*, 446-455.
11. Freitag, N. P., Chemical-reaction mechanisms that govern oxidation rates during in-situ combustion and high-pressure air injection. *SPE Reservoir Eval. Eng.* **2016**, *19*, (04), 645.
12. Yang, S.; Nie, Z.; Wu, S.; Li, Z.; Wang, B.; Wu, W.; Chen, Z., A Critical Review of Reservoir Simulation Applications in Key Thermal Recovery Processes: Lessons, Opportunities, and Challenges. *Energy & Fuels* **2021**, *35*, (9), 7387-7405.
13. Li, N.; Yan, B.; Xiao, X.-M., Kinetic and reaction pathway of upgrading asphaltene in supercritical water. *Chemical Engineering Science* **2015**, *134*, 230-237.
14. Zhao, S.; Pu, W.-F.; Su, L.; Shang, C.; Song, Y.; Li, W.; He, H.-Z.; Liu, Y.-G.; Liu, Z.-Z., Properties, combustion behavior, and kinetic triplets of coke produced by low-temperature oxidation and pyrolysis: Implications for heavy oil in-situ combustion. *Petroleum Science* **2021**, *18*, (5), 1483-1491.
15. Hauser, A.; Bahzad, D.; Stanislaus, A.; Behbahani, M., Thermogravimetric analysis studies on the thermal stability of asphaltenes: pyrolysis behavior of heavy oil asphaltenes. *Energy & fuels* **2008**, *22*, (1), 449-454.
16. Pei, L.; Li, D.; Liu, X.; Cui, W.; Shao, R.; Xue, F.; Li, W., Investigation on asphaltenes structures during low temperature coal tar hydrotreatment under various reaction temperatures. *Energy & Fuels* **2017**, *31*, (5), 4705-4713.
17. Jennings, J.; Growney, D.; Brice, H.; Mykhaylyk, O.; Armes, S., Application of scattering and diffraction techniques for the morphological characterization of asphaltenes. *Fuel* **2022**, *327*, 125042.
18. Varfolomeev, M. A.; Yuan, C.; Bolotov, A. V.; Minkhanov, I. F.; Mehrabi-Kalajahi, S.; Saifullin, E. R.; Marvanov, M. M.; Baygildin, E. R.; Sabiryanov, R. M.; Rojas, A., Effect of copper stearate as catalysts on the performance of in-situ combustion process for heavy oil recovery and upgrading. *Journal of Petroleum Science and Engineering* **2021**, *207*, 109125.

19. Sharma, J.; Dean, J.; Aljaberi, F.; Altememee, N., In-situ combustion in Bellevue field in Louisiana–History, current state and future strategies. *Fuel* **2021**, *284*, 118992.
20. Salehzadeh, M.; Husein, M. M.; Ghotbi, C.; Dabir, B.; Taghikhani, V., In-depth characterization of light, medium and heavy oil asphaltenes as well as asphaltenes subfractions. *Fuel* **2022**, *324*, 124525.
21. Al-Obaidi, S. In *Investigation of rheological properties of heavy oil deposits*, Conference of the Arabian Journal of Geosciences, 2022; Springer: 2022; pp 399-402.
22. Moghaddam, R. K.; Yarranton, H.; Natale, G., Interfacial micro and macro rheology of fractionated asphaltenes. *Colloids and Surfaces A: Physicochemical and Engineering Aspects* **2022**, *651*, 129659.
23. Hu, D.; Gu, X.; Cui, B.; Pei, J.; Zhang, Q., Modeling the oxidative aging kinetics and pathways of asphalt: A ReaxFF molecular dynamics study. *Energy & Fuels* **2020**, *34*, (3), 3601-3613.
24. Trejo, F.; Rana, M. S.; Ancheyta, J., Thermogravimetric determination of coke from asphaltenes, resins and sediments and coking kinetics of heavy crude asphaltenes. *Catalysis Today* **2010**, *150*, (3-4), 272-278.
25. Burnham, A. K.; Dinh, L., A comparison of isoconversional and model-fitting approaches to kinetic parameter estimation and application predictions. *Journal of Thermal Analysis and Calorimetry* **2007**, *89*, (2), 479-490.
26. Oguamah, I. A. U.; Isehunwa, S.; Ndubisi, O.; Stephen, U.; Jude, O., Molecular Dynamics Study of Solvent Effect on the Structure and Characteristics of Asphaltene aggregates. **2022**.
27. Groenzin, H.; Mullins, O. C., Asphaltene molecular size and structure. *The Journal of Physical Chemistry A* **1999**, *103*, (50), 11237-11245.
28. Adams, J. J., Asphaltene adsorption, a literature review. *Energy Fuels* **2014**, *28*, (5), 2831.
29. Martín-Martínez, F. J.; Fini, E. H.; Buehler, M. J., Molecular asphaltene models based on Clar sextet theory. *RSC Advances* **2015**, *5*, (1), 753-759.
30. Medina, O. E.; Gallego, J.; Rodríguez, E.; Franco, C. A.; Cortés, F. B., Effect of pressure on the oxidation kinetics of Asphaltenes. *Energy & Fuels* **2019**, *33*, (11), 10734-10744.
31. Medina, O. E.; Gallego, J.; Nassar, N. N.; Acevedo, S. c. A.; Cortés, F. B.; Franco, C. A., Thermo-Oxidative Decomposition Behaviors of Different Sources of n-C7 Asphaltenes under High-Pressure Conditions. *Energy & Fuels* **2020**, *34*, (7), 8740-8758.

32. Headen, T.; Boek, E.; Jackson, G.; Totton, T.; Müller, E., Simulation of asphaltene aggregation through molecular dynamics: Insights and limitations. *Energy & Fuels* **2017**, 31, (2), 1108-1125.
33. Moncayo-Riascos, I.; Lozano, M. n. M.; Hoyos, B. A.; Franco, C. A.; Riazi, M.; Cortés, F. B., Physical Insights about Viscosity Differences of Asphaltene Dissolved in Benzene and Xylene Isomers: Theoretical–Experimental Approaches. *Energy & Fuels* **2021**, 35, (22), 18574-18582.
34. Jian, C.; Tang, T.; Bhattacharjee, S., Molecular dynamics investigation on the aggregation of Violanthrone<sup>78</sup>-based model asphaltenes in toluene. *Energy & fuels* **2014**, 28, (6), 3604-3613.
35. Alvarez-Ramirez, F.; Ramirez-Jaramillo, E.; Ruiz-Morales, Y., Calculation of the interaction potential curve between asphaltene– asphaltene, asphaltene–resin, and resin– resin systems using density functional theory. *Energy & Fuels* **2006**, 20, (1), 195-204.
36. Chen, C.; Zhao, L.; Wu, X.; Lin, S., Theoretical understanding of coal char oxidation and gasification using reactive molecular dynamics simulation. *Fuel* **2020**, 260, 116300.
37. Barre, L.; Espinat, D.; Rosenberg, E.; Scarsella, M., Colloidal structure of heavy crudes and asphaltene solutions. *Revue de l'Institut Français du Pétrole* **1997**, 52, (2), 161-175.
38. International, A., ASTM D5236-13, Standard Test Method for Distillation of Heavy Hydrocarbon Mixtures (Vacuum Potstill Method). *Annual Book of ASTM Standards* **2013**.
39. International, A., ASTM D2892, Standard Test Method for Distillation of Crude Petroleum (15-Theoretical Plate Column). *Annual Book of ASTM Standards* **2016**.
40. Cardona, L.; Medina, O. E.; Céspedes, S.; Lopera, S. H.; Cortés, F. B.; Franco, C. A., Effect of Steam Quality on Extra-Heavy Crude Oil Upgrading and Oil Recovery Assisted with PdO and NiO-Functionalized Al<sub>2</sub>O<sub>3</sub> Nanoparticles. *Processes* **2021**, 9, (6), 1009.
41. Medina, O. E.; Gallego, J.; Arias-Madrid, D.; Cortés, F. B.; Franco, C. A., Optimization of the load of transition metal oxides (Fe<sub>2</sub>O<sub>3</sub>, Co<sub>3</sub>O<sub>4</sub>, NiO and/or PdO) onto CeO<sub>2</sub> nanoparticles in catalytic steam decomposition of n-C<sub>7</sub> asphaltenes at low temperatures. *Nanomaterials* **2019**, 9, (3), 401.
42. Arias-Madrid, D.; Medina, O. E.; Gallego, J.; Acevedo, S.; Correa-Espinal, A. A.; Cortés, F. B.; Franco, C. A., NiO, Fe<sub>2</sub>O<sub>3</sub>, and MoO<sub>3</sub> Supported over SiO<sub>2</sub> Nanocatalysts for Asphaltene Adsorption and Catalytic Decomposition:



Optimization through a Simplex–Centroid Mixture Design of Experiments. *Catalysts* **2020**, *10*, (5), 569.

43. Medina, O. E.; Caro-Vélez, C.; Gallego, J.; Cortés, F. B.; Lopera, S. H.; Franco, C. A., Upgrading of Extra-Heavy Crude Oils by Dispersed Injection of NiO–PdO/CeO<sub>2±δ</sub> Nanocatalyst-Based Nanofluids in the Steam. *Nanomaterials* **2019**, *9*, (12), 1755.

44. Medina, O. E.; Gallego, J.; Pérez-Cadenas, A. F.; Carrasco-Marín, F.; Cortés, F. B.; Franco, C. A., Insights into the Morphology Effect of Ceria on the Catalytic Performance of NiO–PdO/CeO<sub>2</sub> Nanoparticles for Thermo-oxidation of n-C<sub>7</sub> Asphaltenes under Isothermal Heating at Different Pressures. *Energy & Fuels* **2021**.

45. Abbas, H. A.; Manasrah, A. D.; Carbognani, L.; Sebakhy, K. O.; Nokab, M. E. H. E.; Hacini, M.; Nassar, N. N., A study on the characteristics of Algerian Hassi-Messaoud asphaltenes: solubility and precipitation. *Petroleum Science and Technology* **2022**, *40*, (11), 1279-1301.

46. Medina, O. E.; Gallego, J.; Olmos, C. M.; Chen, X.; Cortés, F. B.; Franco, C. A., Effect of multifunctional nanocatalysts on n-C<sub>7</sub> asphaltene adsorption and subsequent oxidation under high-pressure conditions. *Energy & Fuels* **2020**, *34*, (5), 6261-6278.

47. Moncayo-Riascos, I.; Taborda, E.; Hoyos, B. A.; Franco, C. A.; Cortés, F. B., Theoretical-experimental evaluation of rheological behavior of asphaltene solutions in toluene and p-xylene: Effect of the additional methyl group. *Journal of Molecular Liquids* **2020**, *303*, 112664.

48. Watkins, E. K.; Jorgensen, W. L., Perfluoroalkanes: Conformational analysis and liquid-state properties from ab initio and Monte Carlo calculations. *The Journal of Physical Chemistry A* **2001**, *105*, (16), 4118-4125.

49. Van Duin, A.; Dasgupta, S.; Lorant III, F., e Goddard WA III. *J. Phys. Chem. A* **2001**, *105*, 9396.

50. Hong, S.; van Duin, A. C., Molecular dynamics simulations of the oxidation of aluminum nanoparticles using the ReaxFF reactive force field. *The Journal of Physical Chemistry C* **2015**, *119*, (31), 17876-17886.

51. Rimola, A.; Costa, D.; Sodupe, M.; Lambert, J.-F.; Ugliengo, P., Silica surface features and their role in the adsorption of biomolecules: computational modeling and experiments. *Chemical reviews* **2013**, *113*, (6), 4216-4313.

52. Chan, A. E.; Hoffmann, R.; Ho, W., Theoretical aspects of photoinitiated chemisorption, dissociation, and desorption of oxygen on platinum (111). *Langmuir* **1992**, *8*, (4), 1111-1119.

53. LI, C.; WANG, J.; SUI, L.; CUI, M.; DENG, W., Study on XPS of Venezuela Heavy Oil Asphaltene. *Acta Petrolei Sinica (Petroleum Processing Section)* **2013**, 03.
54. Franco, C. A.; Montoya, T.; Nassar, N. N.; Pereira-Almao, P.; Cortés, F. B., Adsorption and subsequent oxidation of colombian asphaltenes onto nickel and/or palladium oxide supported on fumed silica nanoparticles. *Energy & Fuels* **2013**, 27, (12), 7336-7347.
55. Franco-Ariza, C. A.; Guzmán-Calle, J. D.; Cortés-Correa, F. B., Adsorption and catalytic oxidation of asphaltenes in fumed silica nanoparticles: Effect of the surface acidity. *Dyna* **2016**, 83, (198), 171-179.
56. Nassar, N. N.; Hassan, A.; Luna, G.; Pereira-Almao, P., Kinetics of the catalytic thermo-oxidation of asphaltenes at isothermal conditions on different metal oxide nanoparticle surfaces. *Catalysis today* **2013**, 207, 127-132.
57. Nassar, N. N.; Hassan, A.; Pereira-Almao, P., Comparative oxidation of adsorbed asphaltenes onto transition metal oxide nanoparticles. *Colloids and surfaces A: Physicochemical and Engineering aspects* **2011**, 384, (1-3), 145-149.
58. Nassar, N. N.; Hassan, A.; Pereira-Almao, P., Effect of surface acidity and basicity of aluminas on asphaltene adsorption and oxidation. *Journal of colloid and interface science* **2011**, 360, (1), 233-238.
59. Gonçalves, M.; Teixeira, M.; Pereira, R.; Mercury, R.; Matos, J. d. R., Contribution of thermal analysis for characterization of asphaltenes from Brazilian crude oil. *Journal of thermal analysis and calorimetry* **2001**, 64, (2), 697-706.
60. Shao, R.; Shen, Z.; Li, D.; Sun, Z.; Pei, L.; Liu, X.; Li, W.; Dan, Y., Investigation on composition and structure of asphaltenes during low-temperature coal tar hydrotreatment under various reaction pressures. *Journal of Analytical and Applied Pyrolysis* **2018**, 136, 44-52.
61. Kuakpetoon, D.; Wang, Y.-J., Structural characteristics and physicochemical properties of oxidized corn starches varying in amylose content. *Carbohydrate Research* **2006**, 341, (11), 1896-1915.
62. Shafeeyan, M. S.; Daud, W. M. A. W.; Houshmand, A.; Shamiri, A., A review on surface modification of activated carbon for carbon dioxide adsorption. *Journal of Analytical and Applied Pyrolysis* **2010**, 89, (2), 143-151.
63. Whitby, R. L.; Korobeinyk, A.; Glevatska, K. V., Morphological changes and covalent reactivity assessment of single-layer graphene oxides under carboxylic group-targeted chemistry. *Carbon* **2011**, 49, (2), 722-725.
64. Zojaji, I.; Esfandiarian, A.; Taheri-Shakib, J., Toward molecular characterization of asphaltene from different origins under different conditions

by means of FT-IR spectroscopy. *Advances in Colloid and Interface Science* **2021**, 289, 102314.

65. Furimsky, E.; Palmer, A.; Duguay, D.; McConnell, D.; Henson, D., Characterization of carbonaceous solids by oxygen chemisorption. *Fuel* **1988**, 67, (6), 798-802.

66. Medina, O. E.; Gallego, J.; Rodriguez, E.; Franco, C. A.; Cortés, F. B., Effect of Pressure on the Oxidation Kinetics of Asphaltenes. *Energy & Fuels* **2019**.

67. Sánchez, N. M.; de Klerk, A., Low-temperature oxidative asphaltenes liquefaction for petrochemicals: fact or fiction? *Applied Petrochemical Research* **2016**, 6, (2), 97-106.

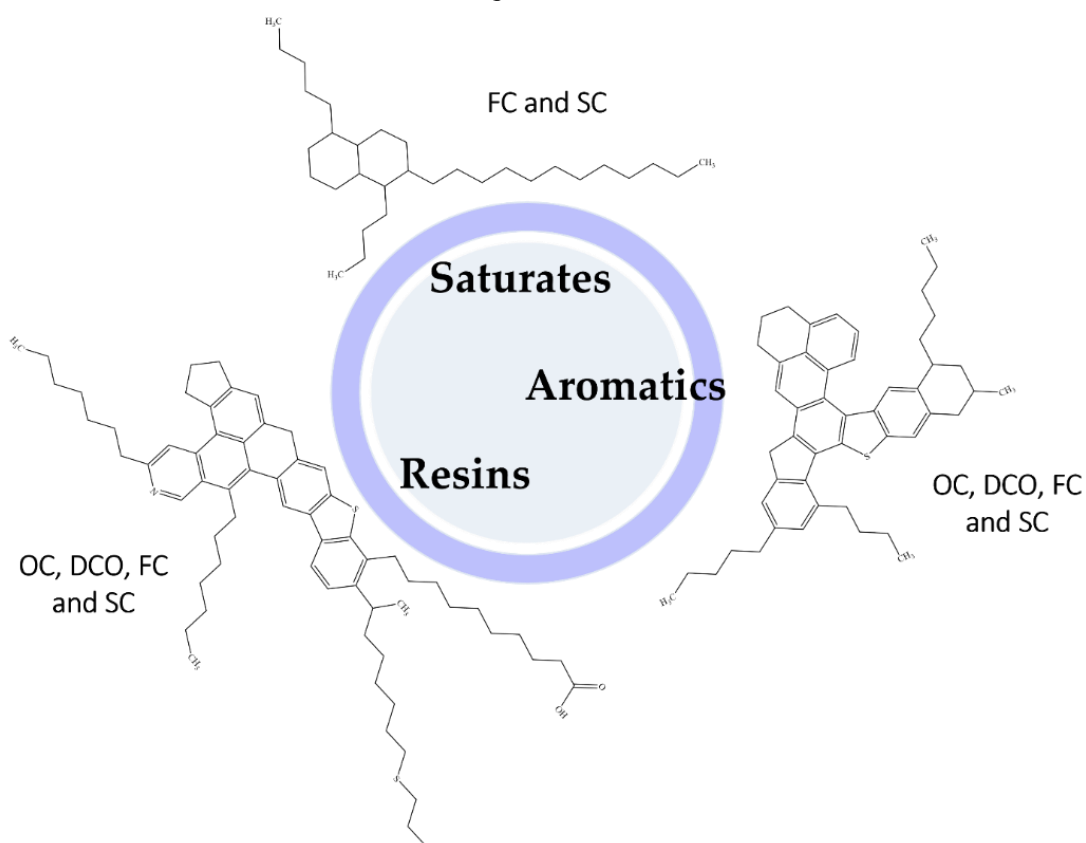
68. AlHumaidan, F. S.; Hauser, A.; Rana, M. S.; Lababidi, H. M., NMR Characterization of Asphaltene Derived from Residual Oils and Their Thermal Decomposition. *Energy & Fuels* **2017**, 31, (4), 3812-3820.

69. Carvalho, V. V.; Vasconcelos, G. A.; Tose, L. V.; Santos, H.; Cardoso, F. M.; Fleming, F.; Romão, W.; Vaz, B. G., Revealing the chemical characterization of asphaltenes fractions produced by N-methylpyrrolidone using FTIR, molecular fluorescence, <sup>1</sup>H NMR, and ESI (±) FT-ICR MS. *Fuel* **2017**, 210, 514-526.

70. Ruiz-Morales, Y.; Miranda-Olvera, A. D.; Portales-Martínez, B. n.; Domínguez, J., Experimental and theoretical approach to determine the average asphaltene structure of a crude oil from the golden lane (Faja de Oro) of Mexico. *Energy & Fuels* **2020**, 34, (7), 7985-8006.

## Chapter 5.

# Effect of Pressure on Thermo-oxidative Reactions of Saturates, Aromatics, and Resins (S-Ar-R) from Extra-Heavy Crude Oil.



Published article in *Fuels*: [doi.org/10.1016/j.fuel.2021.122787](https://doi.org/10.1016/j.fuel.2021.122787)

Impact factor: 8.035

# Effect of Pressure on Thermo-oxidative Reactions of Saturates, Aromatics, and Resins (S-Ar-R) from Extra-Heavy Crude Oil

## Abstract

In this study, saturates, aromatics, and resins are investigated for their thermo-oxidative behavior under various pressures of 0.084, 3.0, and 6.0 MPa. Elemental analysis, vapor pressure osmometry,  $^1\text{H}$ - and  $^{13}\text{C}$ -nuclear magnetic resonance, and X-ray photoelectron spectroscopy were used to characterize saturates (S), aromatics (Ar), and resins (R). By simulating distillation, the atmospheric evaporation of S, Ar, and R was assessed. In contrast, the Clapeyron equation and the Redlich-Kwong equation of state were used to calculate the high-pressure distillation curves. To determine the pyrolysis and oxidation responses, the mass change and rate of mass change profiles were evaluated in a high-pressure thermogravimetric analyzer (HP-TGA). A first-order kinetic model that discretizes the thermal oxidation profiles in four distinct regions—oxygen chemisorption (OC), decomposition of chemisorbed oxygen-based compounds (DCO), first combustion (FC), and second combustion (SC)—was used for the kinetic analysis. The main findings were that, for pressures higher than 3.0 MPa, aromatics and resins were described by the four stages (OC, DCO, FC, and SC), while saturates were only described by the FC and SC regions at all pressures. At 6.0 MPa, aromatics show a quick decomposition in the FC region, whereas resins show a slower decomposition spread out over the three decomposition regions. This suggests that aromatics have a greater impact on oxidation reactions at high temperatures as pressure rises. Pyrolysis curves revealed that for all applied pressures, the amount of coke produced increases in the following order: saturates; aromatics; resins. The kinetic parameters supported the findings. The DCO effective activation energy values and, were higher for the higher oxygen chemisorption. At the same time, the pre-exponential factor showed opposite results, given slower reaction kinetics in these stages.

## 1. Introduction

*In-situ* combustion (ISC) is an enhanced oil recovery (EOR) method with great performance on heavy and extra heavy crude oil (EHO) exploitation [1, 2]. During ISC, the air is injected into the reservoir for HO and EHO burning [3]. With the increase in temperature, the viscosity, and the chemical composition of the crude oil change, facilitating its recovery. Understanding the oxidation of heavy crude oils (HO) is fundamental for optimizing ISC [4].

The composition of heavy crude oil is complicated; therefore, it is conventionally divided into saturates, aromatics, resins, and asphaltenes (S-Ar-R-A) [5-7]. Each fraction comprises several compounds with similar chemical and physical properties [8, 9]. During heating in ISC, each fraction transforms into gases, lighter hydrocarbons, or coke precursors [8, 10, 11]. Coke formation is a process in which the products from low-temperature oxidation further polymerize and crack to form coke [8]. It is well known that aromatics, resins, and asphaltenes contribute to coke formation [12-14]. Besides, each chemical compound has different pyrolysis and oxidation reactivity depending on the pressure and temperature. Therefore, it is imperative to comprehend isolated fractions' oxidative behavior at reservoir conditions.

The oxidation of S, Ar, and R has been divided into two main stages: low-temperature oxidation or first combustion (LTO or FC) and high-temperature oxidation or second combustion (HTO or SC) [15]. Each region presents different limits depending on the chemical composition and physical properties of the specific fractions (S-Ar-R) [16-18]. Experimental tools, including thermogravimetric analysis (TGA) and differential scanning calorimetry (DSC), have been widely used in the literature to study the oxidation of heavy crude oil and its components, that is, S-Ar-R fractions [19, 20]. In their TGA experiments on Turkish crude oil, Kok and Gul et al. [20] found that resins lost the main mass during SC, while saturates decomposed less than 6.0 wt.% of their mass in the same region. In the FC, the mean activation energies varied between 60 and 70 kJ·mol<sup>-1</sup>, 80 and 90 kJ·mol<sup>-1</sup>, and 90 and 100 kJ·mol<sup>-1</sup> for saturates, aromatics, and resins, respectively. However, activation energy values increase more than 40 kJ·mol<sup>-1</sup> for all

fractions in SC. In another study [21], the authors evaluated the pyrolysis and oxidation of S-Ar-R fractions of Turkish crude oil and found that saturates mainly lost its mass by evaporation during pyrolysis, whereas approximately 15 wt.% is transformed into coke during oxidation. Aromatic pyrolysis and oxidation have two distinctive peaks in the rate for mass change profile, and its contribution to the production of coke was five times greater than that of saturated ones. Finally, resins decompose in two and three main stages during pyrolysis and oxidation; respectively, i.e., SC decomposed in two mass loss stages.

So far, the oxidation of the S, Ar, and R fractions has been carried out at low-pressure conditions. Recently, our research group pioneered the inclusion of pressure in the oxidation phenomena of asphaltenes [22]. We found that asphaltene thermal oxidation is pressure dependent. Unlike low-pressure systems above 0.3 MPa, four different thermal events are observed, namely: oxygen chemisorption region (OC), decomposition of chemisorbed oxygen region (DCO), first (FC), and second combustion (SC). Each region is defined by a particular behavior associated with its mass change and rate for mass change curves [22, 23]. Nevertheless, to our knowledge, no studies reported the effects of pressure on the rest of the S-Ar-R fractions.

Therefore, this study continues our previous work and further investigates the thermal oxidation behavior of S-Ar-R fractions at high-pressure conditions for the first time. This shall provide insights into the heavy oil thermal oxidation mechanisms at different pressures, which finds application in improving ISC process. It is important to emphasize that this work seeks to discretize the additional contributions by evaporation, pyrolysis, and oxidation during thermo-oxidative reactions, including the pressure as a key factor of the experiments. Thus, this work provides deeper mechanistic insights into the effects of pressure on thermo-oxidation reactions of saturates, aromatics, and resins.

## 2. Experimental

### 2.1 Materials

A Colombian extra-heavy crude oil was used to isolate saturates, aromatics, and resins following the Chinese national standard NBSHT 0509-2010 [21]. The standard sample has a viscosity  $3.0 \times 10^6$  cP and 6.7 °API at 25 °C. *n*-Heptane (99.5%), toluene (99.8%), and ethanol (99.8%) were purchased

from Sigma-Aldrich (St. Louis, MO, USA). The reacting gas for SAR oxidation consists of synthetic air NTC 2561 (CRYOGAS, Bogotá, Colombia) composed of 20.93% balanced O<sub>2</sub> with high purity. The pyrolysis runs were done by N<sub>2</sub> injection (CRYOGAS, Bogotá, Colombia) with high purity (99.5% N<sub>2</sub> and 0.5% O<sub>2</sub> content).

## 2.2. S-Ar-R Extraction and Quantification

The separation process includes diluting the crude oil in *n*-heptane in a 1:40 weight ratio for asphaltene precipitation [24]. Maltene was collected by evaporating the *n*-heptane. The maltenes portion is further separated using a liquid chromatography column with solvents to dissolve the saturates, aromatics, and resin fractions [21]. The column consists of a 40 cm long glass tube, 1 cm in diameter, and packed with a 100-200 mesh silica gel, previously activated during 6 h at 600 °C. First, 10 g of maltene was dissolved in 100 mL of *n*-heptane and introduced into the glass column. Saturates, aromatic, and resins were eluted with *n*-heptane, toluene, and a mixture of toluene/ethanol (3:1), respectively. After the extraction, the samples were placed in an oven to evaporate the remaining solvents. The light components are the compounds lost during the solvent evaporation process. The mass difference between the collected SARA fractions and the original loaded crude oil in the chromatography column was counted as the lightweight components. Briefly, Figure 1 summarizes the S-Ar-R extraction process.

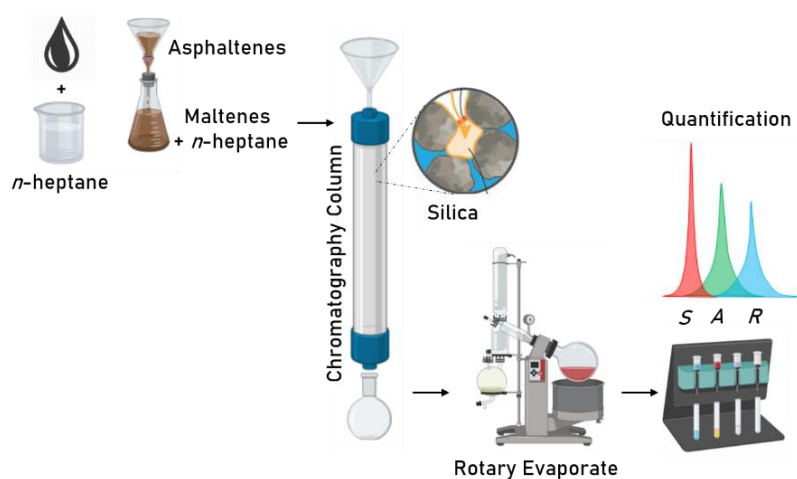


**Figure 1.** SARA separation scheme



### 2.3. S-Ar-R Characterization

S-Ar-R-A composition was obtained by combining micro de-asphalting and the IP 469 method using a IATROSCAN MK6 TLC-FID/FPD equipment [25]. The EHO has a SARA composition of 13.0%, 16.9%, 49.9%, and 20.2% in mass fraction, respectively. The quantification was corroborated after extracting each fraction on the silica chromatographic column, and similar results were found for each fraction to those obtained by the IP 469 method. The content of light compounds was 3.0%, associated with the lost compounds during the evaporation of the solvent. Saturates, aromatics and resins were characterized by elemental analysis (EA) for determining the atomic content of carbon, hydrogen, sulfur, and nitrogen of the samples using a Thermo Flash elemental analyzer EA 1112 (Thermo Finnigan, Milan, Italy) following the ASTM D5291 standard [26]. Oxygen content was calculated by the difference, considering their sum equal to 100%. Average molecular weights ( $M_w$ ) of S-Ar-R fractions were estimated by vapor pressure osmometry (VPO) in a Knauer osmometer (Knauer, Berlin-Heidelberg, West Germany). Benzyl was used for calibration. Samples were dissolved in chloroform using sample and standard solutions with  $1 \text{ g}\cdot\text{kg}^{-1}$  and  $0.005 \text{ mol}\cdot\text{kg}^{-1}$ , respectively. Then, using the constants of benzyl calibration  $K_{cal}$  ( $\text{mol}\cdot\text{kg}^{-1}$ ), sample  $K_s$  ( $\text{g}\cdot\text{kg}^{-1}$ ), and the  $K_{cal} / K_s$  ratio, the molecular weight was obtained [27].  $^1\text{H}$  NMR analysis was performed on a Bruker AMX 300 spectrometer (Karlsruhe, Germany) operating at 300 MHz, with a 5 mm inner diameter tube. The samples were dissolved in  $\text{CDCl}_3$  (99.8 %) containing traces of tetramethylsilane (TMS) used as standard internal solvents. The sample concentration was fixed in a mass fraction of 15 % in 0.5 mL of the solvent. Besides, the  $^1\text{H}$  NMR spectra settings were adjusted with a pulse angle of  $90^\circ$  ( $10.5 \mu\text{s}$ ), a spectral width of 12.3 kHz, and a delay time of 1 s. Then, each spectrum was divided into four regions that are associated with four different protons, namely aromatic hydrogen ( $\text{H}_a$ ), hydrogen on  $\alpha$  carbons to aromatic rings ( $\text{H}_\alpha$ ), hydrogen on  $\beta$  carbons to aromatic rings,  $\text{CH}_2$  or naphthenic-type carbon ( $\text{H}_\beta$ ), and hydrogen on  $\gamma$  carbons or  $\text{CH}_3$  terminal of aliphatic chains alkylating an aromatic ring ( $\text{H}_\gamma$ ), each one associated to the chemical shifts ranges: [6.5 - 9.5], [1.9 - 4.5], [1.0 - 1.9] and [0.5 - 1.0] ppm, respectively. As for  $^{13}\text{C}$  NMR, it was performed using a relaxation delay of 5 s, a spectral width covering of 3.4 kHz, the time domain was 122K, and 3000 scans were averaged for each spectrum. X-ray photoelectron spectrometry was performed on a Specs brand X-ray photoelectronic spectrometer (NAP-

XPS) with a PHOIBOS 150 1D-DLD analyzer, using a monochromatic source of Al-K $\alpha$  (1486.7 eV, 13 kV, 100 W) with step energy 90 eV and 20 eV for general and high-resolution spectra, respectively.

#### 2.4. High-Pressure Thermogravimetric Analysis

In this study, HP-TGA 750 (TA instruments Inc., Hüllhorst, Germany) thermal analysis coupled to a mass spectrometer (Shimadzu GC-MS, Tokyo, Japan) (HP-TGA-MS) was used to perform high-pressure experiments. Details of both instruments are found in previous work [3]. The experimental procedure involves placing 1 mg of the sample in a magnetically levitated balance, setting the absolute pressure at 0.084 MPa, 3.0 MPa, and 6.0 MPa, at a gas flow rate at 80 mL·min<sup>-1</sup> and the heating rate at 10 °C·min<sup>-1</sup>. Oxidation and pyrolysis experiments were done by injecting air and nitrogen, respectively. Before the warm-up procedure, samples are cleaned by vacuum test at 0.00025 MPa for 10 minutes. All experiments were carried out in two steps. First, the run is performed for the samples, and then the run is repeated for the empty sample holder due to buoyancy effects [28]. Each thermogravimetric experiment was performed in triplicate to ensure the repeatability of the results, obtaining  $\pm 1.0$  °C uncertainty and  $\pm 0.1$  mg. Finally, the evolved gases during S-Ar-R oxidation were analyzed in a mass spectrometer using a linear scan rate of ion trap of 0.03 *m/e* from 0 up to 200 *m/e*. It is worth mentioning that all analyzes are expressed in terms of the partial pressure of oxygen.

#### 2.5. Simulated Distillation at Low-Pressure

The experimental test was performed following the ASTM D2892-05 standard [29], using a SimDis Analyzer, GC, Agilent, 7890A, coupled with a chromatography column of 530  $\mu$ m of diameter having an efficiency at total reflux of at least 14, but not greater than 18, theoretical plates. For the low-pressure test (0.00067-0.00027 MPa), sample preparation was done by mixing 100 mg of individual S-Ar-R fractions and 5 mg of carbon disulfide. Hydrogen flow was fixed at 40 mL·min<sup>-1</sup>, air and nitrogen at 450 mL·min<sup>-1</sup>. Runs were made between 150 °C and 500 °C, and the injected sample volume was 0.1  $\mu$ L.

#### 2.6. Simulated Distillation at High-Pressure

Simulated distillation curves at 3.0 and 6.0 MPa were obtained using the Clapeyron equation modified with the Redlich Kwong (RK) equation of state to

consider deviations from ideality [30]. The approximation was made regarding the individual behavior of saturates, aromatics, and resins from the simulated distillation experiments. The equation was resolved as follows:

According to the fact that Gibbs free energy at equilibrium is similar for both phases, vapor ( $\alpha$ ) and liquid ( $\beta$ ), regardless of the S-Ar-R fraction evaluated [31-33]:

$$dG^\alpha = dG^\beta \quad (1)$$

Equation (1) can be rewritten as follows (Equation (2)):

$$v^\alpha dP^{sat} - S^\alpha dT = v^\beta dP^{sat} - S^\beta dT \quad (2)$$

where,  $v^\alpha$  and  $v^\beta$  represent the specific volume of the substance in vapor and liquid phases, respectively.  $S^\alpha$  and  $S^\beta$  are the entropies of both phases, respectively. Then, reorganizing, Equation (3) is obtained:

$$\frac{dP^{sat}}{dT} = \frac{S^\beta - S^\alpha}{v^\beta - v^\alpha} = \frac{\Delta S^{\alpha\beta}}{\Delta v^{\alpha\beta}} \quad (3)$$

Using the fundamental relation of thermodynamics (Equation (4)), solving the integral (Equation (5)), taking into account that the phase changes occur at constant temperatures and pressures (equilibrium temperature and pressure) and substituting in Equation (3), Equation (6) is obtained [32]:

$$\int_\alpha^\beta dH = \int_\alpha^\beta T dS + \int_\alpha^\beta v dP \quad (4)$$

$$\Delta H^{\alpha\beta} = T \Delta S^{\alpha\beta} \quad (5)$$

$$\frac{dP^{sat}}{dT} = \frac{\Delta H^{\alpha\beta}}{T \Delta v^{\alpha\beta}} = \frac{\Delta H^{vl}}{T \Delta v^{vl}} \quad (6)$$

Equation 6 is known as the Clapeyron equation. For the case of transition from the liquid phase ( $l$ ) to the vapor phase ( $v$ ), the change in specific volume is calculated through equations of state, as shown in Equation (7).

$$\Delta v^{vl} = \frac{RT}{P^{sat}} \Delta Z^{vl} \quad (7)$$

where  $\Delta Z^{vl}$  is the evaporation compressibility change. Modifying Equation (6) with Equation (7), a new expression is obtained for the Clapeyron equation (Equation (8) and Equation (9)).

$$\frac{d \ln P^{sat}}{dT} = \frac{\Delta H^{vl}}{RT^2 \Delta Z^{vl}} \quad (8)$$

$$\frac{d \ln P^{sat}}{d(1/T)} = - \frac{\Delta H^{vl}}{R \Delta Z^{vl}} \quad (9)$$

where  $\Delta H$  ( $\text{J}\cdot\text{g}^{-1}$ ) is the latent heat,  $T_{vap}$  (K) is the phase transition temperature, and  $R$  the ideal gas constant.  $\Delta Z^{vl}$  is calculated with the equation of state RK applied to each condition, as shown in the following expression [32]:

$$Z = 0.08664 \frac{P_r}{T_r} + Z \left( Z + 0.08664 \frac{P_r}{T_r} \right) \left( \frac{1 + 0.08664 \frac{P_r}{T_r} - Z}{\frac{0.42748}{T_r^{5/2}} P_r} \right) \quad (10)$$

where  $P_r$  is the reduced pressure and  $T_r$  is the reduced temperature, which are the relations between the properties in a specific state and the properties in the critical state.

The critical properties of each fraction considered are calculated based on the relations shown by Pedersen et al. [34]:

$$T_c = 0163.12\rho + 8.605 \ln(M_w) + 0.43475M_w - \frac{0.0018774}{M_w} \quad (11)$$

$$P_c = -0.13408 + 2.5019\rho + \frac{208.46}{M_w} - \frac{3987.2}{M_w^2} \quad (12)$$

where  $\rho$  is the density ( $\text{g}\cdot\text{cm}^{-3}$ ) and  $M_w$  is the molecular weight of the fraction considered. The densities for saturates, aromatics, and resins were  $0.83 \text{ g}\cdot\text{cm}^{-3}$ ,  $0.89 \text{ g}\cdot\text{cm}^{-3}$ , and  $0.93 \text{ g}\cdot\text{cm}^{-3}$ , respectively. The molecular weights were estimated as  $432 \text{ g}\cdot\text{mol}^{-1}$ ,  $690 \text{ g}\cdot\text{mol}^{-1}$ , and  $957 \text{ g}\cdot\text{mol}^{-1}$  for S, Ar, and R, respectively.

The expression  $\frac{d \ln P^{sat}}{dT}$  was solved considering a unique dependency of the chemical species studied. For the integration process, the first state is defined by the atmospheric pressure ( $P = 0.084 \text{ MPa}$ ) and the temperature data from the

simulated distillation curve. In contrast, the second state is determined by the proposed pressure ( $P = 3.0$  and  $6.0$  MPa) and the unknown temperature. Considering the reduced pressure and the estimated saturation temperature, the compressibility factors of each phase are calculated (Equation 10). With these results, the equilibrium conditions and actual equilibrium temperature are estimated (Equation 9). This procedure was realized for each pressure considered ( $P = 3.0$  and  $6.0$  MPa). Finally, differential scanning calorimetry was used to obtain the latent heat of S-Ar-R fractions for resolving the Clapeyron equation. The tests were done in a Q2000 DSC (TA. Instruments, Inc., New Castel, DE, USA). The procedures included putting a minor amount of the S-Ar-R sample ( $\sim 5$  mg) in an aluminum sample pan, setting the airflow rate ( $80 \text{ mL}\cdot\text{min}^{-1}$ ), and heating rate ( $10 \text{ }^\circ\text{C}\cdot\text{min}^{-1}$ ) between  $100 \text{ }^\circ\text{C}$  and  $600 \text{ }^\circ\text{C}$ . Each run was conducted three times to ensure the correctness and repeatability of experimental results. The error of temperature did not exceed  $\pm 1 \text{ }^\circ\text{C}$ . DSC curves are shown in Figure 2.

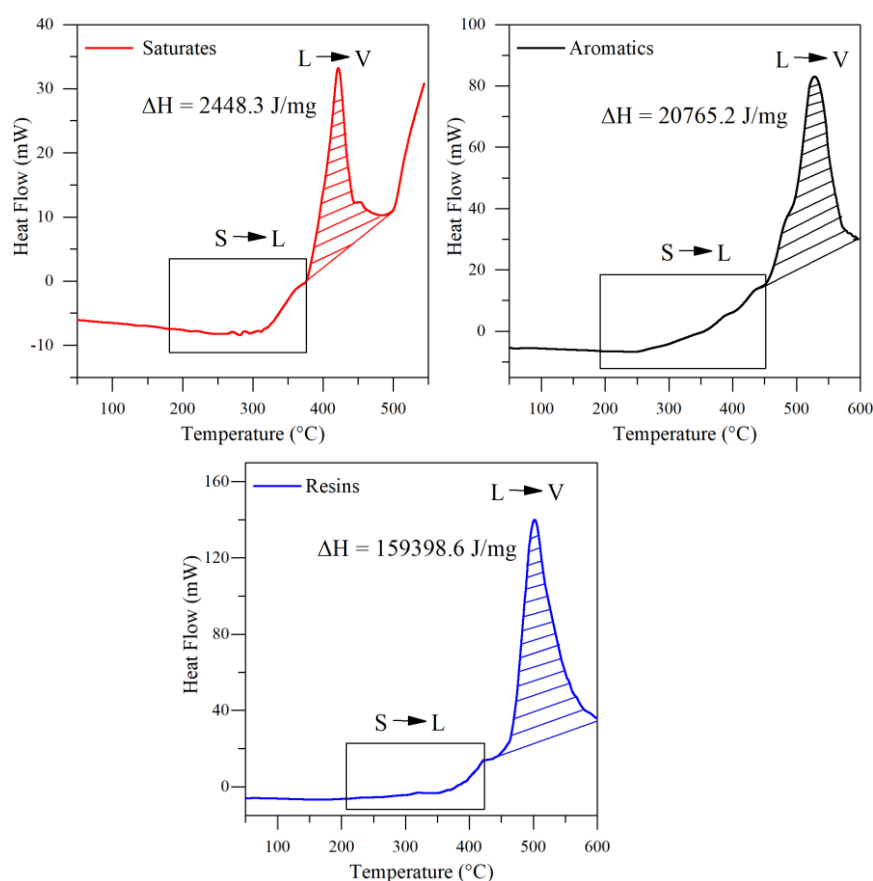


**Figure 2.** Differential scanning calorimetry for saturates aromatics and resins. The second peak refers to the latent heat of the sample. Sample weight: 10 mg, heating rate:  $10 \text{ }^\circ\text{C}\cdot\text{min}^{-1}$ , and airflow:  $80 \text{ mL}\cdot\text{min}^{-1}$ .

Finally, latent heat was obtained following the typical protocols described in the literature [35]. Saturates, aromatics, and resins present a latent heat of 2.5 kJ·g<sup>-1</sup>, 20.7 kJ·g<sup>-1</sup>, and 159.4 kJ·g<sup>-1</sup>, respectively.

### 3. Kinetic Analysis for S-Ar-R Thermo-Oxidative Decomposition

Thermal behavior analysis is performed to obtain information about the kinetic parameters of S-Ar-R oxidation at high-pressure conditions in different temperature regions. Since the thermal decomposition of crude oil fractions is a complex process that entails consecutive and parallel reactions, the kinetic variables are regarded as apparent numeric values, representing the straight reaction history [36, 37]. It is worth mentioning that an isoconversional analysis might also be worth considering because there is no need to assume a reaction order [38].

Briefly, the kinetic parameters were calculated using a single power-law equation bearing in mind the materials' immediate reactivity. Ozawa-Wall-Flynn approximation was used to resolve non-isothermal experiments considering the thermal profiles at three different heating rates, including 5 °C·min<sup>-1</sup>, 10 °C·min<sup>-1</sup>, and 20 °C·min<sup>-1</sup> [39], leading the Equation (13):

$$\ln \left[ \frac{\beta F(\theta)}{P_{O_2}^n T^2} \right] = \ln \left( \frac{k_o R}{E_a} \right) - \frac{E_a}{RT} \quad (13)$$

where,  $\beta$  (°C·min<sup>-1</sup>) is the heating rate,  $P_{O_2}$  (bar) is the oxygen partial pressure,  $n$  represents the order of oxidation reaction,  $E_a$  (kJ·mol<sup>-1</sup>) is the effective activation energy,  $k_o$  (s<sup>-1</sup>·bar<sup>-n</sup>) is the Arrhenius pre-exponential factor and  $R$  (J·mol<sup>-1</sup>·K<sup>-1</sup>) is the ideal gas constant.  $F(\theta)$  is represented by the expression ( $\int d\theta / f(\theta) = -\ln(1-x)$ ) related to the volumetric consumption model [22, 40].

## 4. Results and discussion

### 4.1. Characterization of S-Ar-R fractions

The elemental analysis, vapor pressure osmometry, and molecular mass ( $M_w$ ) for S-Ar-R fractions are presented in Table 1. Saturates do not have heteroatoms on their chemical structure, whereas the total content of N, S, and O for aromatics and resins was 5.69% and 10.92%, respectively. These findings are in accordance with their molecular mass, which increased in the order  $S < Ar < R$ . Elemental content agreed with those reported by several researchers for saturates, aromatics, and resins isolated from EHO [5, 10, 11].

The  $^1\text{H-NMR}$  and  $^{13}\text{C NMR}$  spectra were analyzed using MestRenova software (San Diego, CA, USA) to obtain the proportional distribution relationship of hydrogen proton and carbon-type structures (see Table 2). Hydrogen was divided into aromatic hydrogen ( $\text{H}_a$ ), and aliphatic hydrogens  $\alpha$ ,  $\beta$ , and  $\gamma$  linked to aromatic rings, named as  $\text{H}_\alpha$ ,  $\text{H}_\beta$ , and  $\text{H}_\gamma$ , respectively. Meanwhile, carbon was analyzed as aromatic ( $\text{C}_{ar}$ ) and aliphatic ( $\text{C}_{al}$ ).

The findings show that the three fractions have a higher content of  $\text{H}_\beta$  than  $\text{H}_\alpha$  and  $\text{H}_\gamma$ . That is, naphthenic or paraffinic hydrogens in  $\beta$ -position predominate in the aromatic or aliphatic structure. Comparing each fraction, the content of  $\text{H}_\gamma$  increased in the order  $R < Ar < S$ , while  $\text{H}_\alpha$  increased in the opposite order. This means that saturates have a higher content of long chains connected to paraffinic hydrogen ( $\text{CH}_3$ ) in  $\gamma$ -position than the other two fractions [41]. Furthermore, aromatic hydrogen is in a similar proportion in aromatics and resins. The resins have the highest  $\text{H}_a$  content and have similar distributions of long and short aliphatic chains, as shown by the percentages  $\text{H}_\alpha$  and  $\text{H}_\gamma$ . The  $^{13}\text{C NMR}$  results show that the aromatic carbon content increased in the order  $S < Ar < R$ , which agrees well with those reported in the literature [41, 42].

**Table 1.** Elemental analysis, atomic ratios, and molecular mass for saturates, aromatics, and resins.

Crude Oil Fraction	M <sub>w</sub> g·mol <sup>-1</sup>	Elemental mass fraction concentration ± 0.2 %					Atomic ratio					
		C	H	N	S	O	H/C	N/C ×10 <sup>-1</sup>	S/C ×10 <sup>-1</sup>	O/C ×10 <sup>-1</sup>		
S	432	86.63	13.28	-	-	-	1.84	-	-	-		
Ar	690	83.31	10.73	<0.1	4.6	5	9	<0.5	1.54	<0.01	0.13	<0.01
R	957	80.00	9.09	9	5	3.18	1.36	0.12	1.90	0.45		

**Table 2.** Hydrogen and carbon types present in S-Ar-R fractions obtained by <sup>1</sup>H NMR and <sup>13</sup>C NMR analyses. The hydrogen spectrum was divided into aromatic hydrogen (H<sub>a</sub>), hydrogen on α carbons to aromatic rings (H<sub>α</sub>), hydrogen on β carbons to aromatic rings (H<sub>β</sub>), and hydrogen on γ carbons to the aromatic ring (H<sub>γ</sub>). In contrast, the Carbon spectrum is presented in aliphatic carbon (C<sub>al</sub>) and aromatic carbon (C<sub>ar</sub>).

Crude Oil Fraction	<sup>1</sup> H-NMR				<sup>13</sup> C-NMR	
	H <sub>α</sub>	H <sub>β</sub>	H <sub>γ</sub>	H <sub>a</sub>	C <sub>al</sub>	C <sub>ar</sub>
S	1.62	63.77	32.03	2.58	95.45	4.55
Ar	17.03	52.82	20.93	9.22	71.06	28.94
R	18.09	53.86	17.36	10.69	60.96	39.04

Based on the Brown-Ladner method, average structural parameters (APS) were quantified [43]. Table 3 summarizes the findings obtained. As observed, aromatic factor ( $f_A$ ) increases in the order S < Ar < R, following the distribution of hydrogen and carbon obtained by <sup>1</sup>H-NMR and <sup>13</sup>C NMR spectra. Besides, it was found that aromatics have a high replacement rate of hydrogen periphery in the aromatic ring system ( $\sigma$ ), and resins present a higher condensation degree in the aromatic ring system ( $H_{AU}/C_A$ ). The parameters associated with the number of internal and peripheral carbons in a fused aromatic ring, and the number of naphthenic and aromatic rings, were higher for the resins than aromatics and saturates. These results are consistent with the high polarity and aromatic degree obtained in elemental analysis for S-Ar-R fractions.



**Table 3.** Average molecular structure parameters of saturates, aromatics, and resins obtained through the chemical elemental analysis and  $^1\text{H-NMR}$  spectra.

Parameter	S	Ar	R
$f_A$	0.22	0.40	0.42
$\sigma$	-	0.48	0.45
$H_{AU} / C_A$	-	0.63	0.63
$H_T$	55.00	67.18	87.01
$C_T$	37.24	56.83	76.57
$C_A$	8.39	22.81	32.76
$C_S$	28.84	34.02	43.80
$C_\alpha$	0.44	5.72	7.86
$C_{ap}$	1.86	11.91	17.17
$C_i$	6.53	10.89	15.59
$R_{Ar}$	4.26	6.44	8.79
$R_i$	6.53	12.83	17.68
$R_n$	2.27	6.38	8.88
$n$	-	-	4.93

From XPS results, high-resolution spectra for  $\text{C}_{1s}$ ,  $\text{O}_{1s}$ ,  $\text{S}_{2p}$ , and  $\text{N}_{1s}$  were analyzed using CasaXPS software (Casa Software Ltd., Teignmouth, UK), and results are summarized in Table 4. For aromatics and resins, three peaks fit  $\text{C}_{1s}$  spectrum at 284.6 eV, 287.9 eV, and 289.3 eV, attributed to C-C and C-H bonds, C=O, and COO-, C-containing functional groups. Carbonyl content was higher for aromatics than resins, whereas C-C, C-O, and COO- groups were higher in resins. The  $\text{O}_{1s}$  spectra for both fractions were fitted by two peaks associated with C-O-C, C-O (532.4 eV), and carboxyl groups (533.5 eV). Both aromatics and resins had a lower content of COO- groups. Three main curves fitted nitrogen spectra at binding energies characteristics of amines (400.7 eV), pyridines (398.8 eV), and pyrroles (399.9 eV) functional groups. The atomic ratio follows the order: amines (18.9%) < pyridines (36.7%) < pyrroles (44.4%) for aromatics and amines (14.2%) < pyrroles (22.6%) < pyridines (63.1%) for resins. Finally, The  $\text{S}_{2p}$  spectra for aromatics and resins were fitted by 2 and 3 peaks, respectively. Aromatics present binding energy characteristics of thiophene (80.1%) and sulfones (19.9%) functional groups; meanwhile, resins decompose in thioethers (49.5%), thiophenes (25.2%), and sulfones (25.3%).

**Table 4.** Atomic concentrations (%) of a) oxygen forms, b) nitrogen forms, c) carbon forms, and d) sulfur forms obtained by the fitting results of the O<sub>1s</sub>, N<sub>1s</sub>, C<sub>1s</sub>, and S<sub>2p</sub> spectra, respectively, for aromatics and resins.

Sample	Peak							
	C <sub>1s</sub>		O <sub>1s</sub>		S <sub>2p</sub>		N <sub>1s</sub>	
	Assignment	%	Assignment	%	Assignment	%	Assignment	%
Ar	C-C, C-H	68.3	C-O-C, C-O	78.4	Thiophene	80.1	Pyridines	36.7
	C=O	21.7	COO-	21.6	Sulfones	19.9	Pyrroles	44.4
	COO-	10.0					Amines	18.9
R	C-C, C-H	76.3	C-O-C, C-O	73.2	Thioether	49.5	Pyridines	63.1
	C=O	8.6	COO-	26.8	Thiophene	25.2	Pyrroles	22.6
	COO-	15.1			Sulfones	25.3	Amines	14.3

## 4.2. Thermal oxidation analysis of S-Ar-R fractions

### 4.2.1. Thermo-oxidation characteristics of saturates.

Thermo-oxidation response of saturates under airflow and at three different pressures (0.084, 3.0, and 6.0 MPa) are shown in Figure 3. Only two distinct regions, first (FC) and second (SC) combustion, are seen for saturates oxidation at all pressures. During the first interval, the mass loss was mainly attributed to the evaporation of light components [5, 21]. By contrast, SC is where deposited solid fuel is wholly decomposed. Unlike asphaltenes, saturates do not have a defined chemisorption process at low temperatures for high-pressure systems [22]. In a previous study [22], it was found that for pressures higher than 0.3 MPa, two new reaction regions appear in the mass change and rate for mass change curves for asphaltene oxidation, named oxygen chemisorption (OC) and decomposition of chemisorbed oxygen (DCO). In these intervals, oxygen addition reactions and isomerization/decomposition of oxygenated structures were believed to be dominant OC and DCO reaction pathways, respectively [3]. With this in mind and considering the XPS and NMR results, it is concluded that saturates are less susceptible to forming oxygenated compounds under high pressure than the rest of the crude oil fractions because they are mainly composed of branched chains without heteroatoms and low aromatic factor [10, 44].

On the other hand, pressure positively affects the overall mechanism for saturates decomposition. The second event (SC) became less pronounced with increasing pressure while the FC peak intensity rose. The temperature at which FC ends is reduced for high-pressure systems, from 330 °C at 0.084 MPa to 280 °C and 275 °C at 3.0 MPa and 6.0 MPa, respectively. The mass loss

increased by 10.0% and 12.0% for the same systems. As pressure increased, it was apparent that saturates made a dominating contribution to the FC reactions. The presence of oxygen and its interaction with the saturated chains increased the reaction rate, causing a greater sample consumption at low temperatures.

It is well known that hydrocarbons decompose mainly by evaporation, cracking, and oxidation reactions, which significantly control the entire FC region's pathway. To further support this, the distillation curves and the TGA pyrolysis experiments of saturates conducted under a nitrogen atmosphere at the three different pressures (at 0.084 MPa, 3.0 MPa, and 6.0 MPa) are obtained, and the findings are shown in Figure 4 and 5, respectively.

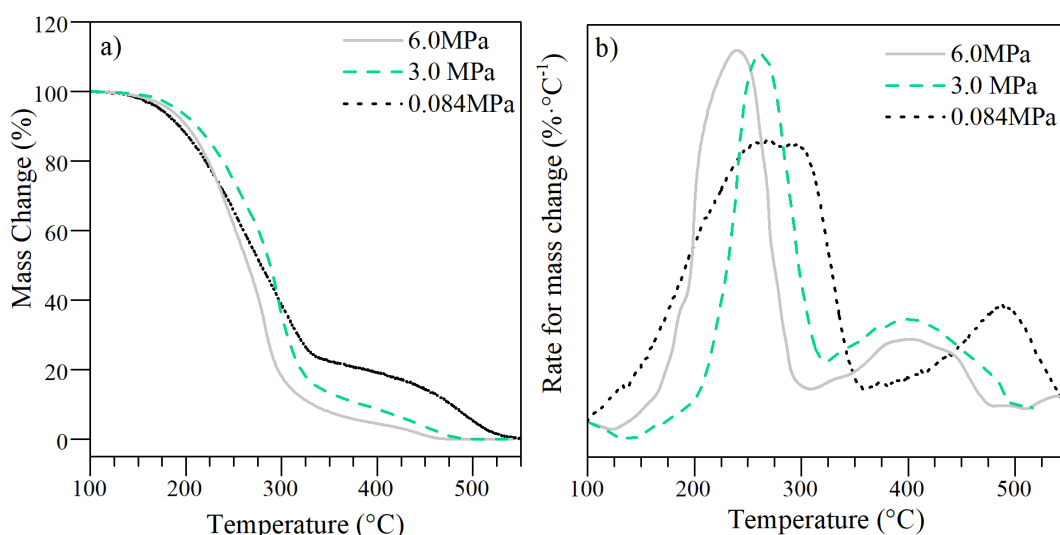


**Figure 3.** (a) Mass percentage and (b) rate for mass change for the oxidation of saturates at different pressures. Sample mass: 1 mg, heating rate: 10 °C·min<sup>-1</sup>, and airflow: 80 mL·min<sup>-1</sup>.

From Figure 4, simulated distillation curves at the three pressures reflect that as pressure increases, the boiling curve is shifted to the right; that is, the mass loss from the physical evaporation of saturates at a fixed temperature is reduced in higher pressure systems. These findings agreed with those reported in the literature, in which pressure increases caused a slight displacement of the temperature required for distillation [45-47].

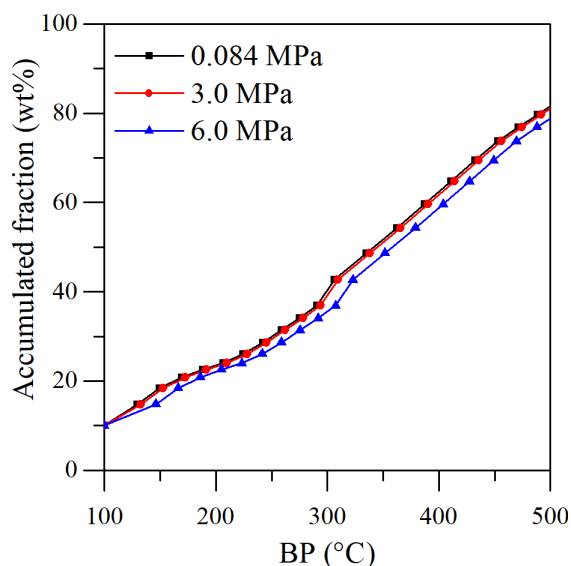


**Figure 4.** Simulated distillation curves for saturates at different pressures (0.084 MPa, 3.0 MPa, and 6.0 MPa).

To complete this analysis, light hydrocarbons (LHC) contribution in the production of carbon from the oxidation of saturates was analyzed through HP-TGA-mass-spectrometry and elemental analysis (CHNSO). The results are summarized in Table 5. The mass carbon balance found that the amount of carbon produced by LHC in the full range of temperature evaluated was 85.7%, 87.9%, and 89.3% at 0.084 MPa, 3.0 MPa, and 6.0 MPa, respectively. This indicates that as the pressure increases, there is a more significant contribution of carbon produced by LHC decomposition, as observed in the effect of temperature on saturation pressure for hydrocarbon mixtures [45-47]. Contrasting with the distillation curves, the accumulated fraction produced by physical evaporation does not exceed 80% for any pressure evaluated, indicating that approximately 5.7% at 0.084 MPa, 7.9% at 3.0 MPa, and 9.3% at 6.0 MPa, of the mass, was lost by evaporation after cracking reactions. It is worth mentioning that other reactions, such as hydrogen abstraction and polymerization, may be involved in this process.

**Table 5.** Contribution of light hydrocarbons (LHC) in the production of carbon from the oxidation of saturates, aromatics, and resins through HP-TGA- mass-spectrometry and elemental analysis (CHNSO) at different pressures.

Crude Oil Fraction	0.084 MPa	3.0 MPa	6.0 MPa
S	85.7	87.9	89.3
Ar	79.4	79.7	81.9
R	83.8	78.3	77.7

On the other hand, two stages can be observed for all pressures according to mass change and rate for mass change in the pyrolysis process (Figure 5). The first stage is related to the evaporation of hydrocarbons with low boiling points and weak chemical bonds breaking. For the three pressures evaluated, the first event ends before 350 °C, similar to FC during oxidation experiments. However, during the pyrolysis of saturates, the increase in pressure delayed the mass loss, which is the opposite of what occurred during oxidation. This could be associated with different reaction mechanisms, including the increment of addition reactions, due to the absence of oxygen atoms that could interact with free radicals avoiding the addition and polymerization reactions, and the coke deposition at the end of SC. Figure 5 shows that at 0.084 MPa, 3.0 MPa, and 6.0 MPa, approximately 4.0%, 7.0%, and 8.0% of the mass is decomposed at temperatures above 500 °C (i.e., coke deposition). Also, it can be explained by the generation of new light hydrocarbons requiring higher temperatures (independent of the evaporation process), verified in Section 4.2.4. where light hydrocarbons are the main by-products of saturates in FC. These findings imply that during the FC event of the saturates, the contribution by physical evaporation at high-pressure conditions decreased, which agrees with the distillation curves analysis for saturates. In this sense, during oxidation, the isomerization and decomposition reactions become significant pathways, producing new light hydrocarbons. These findings agree with those reported by Zhao et al. [9], who reported that saturates were vulnerable to severe mass loss during low-temperature oxidation reactions.

Unlike low-pressure systems, the temperature at which the second region ends in pyrolysis experiments was also reduced for high-pressure systems, to a greater extent to 6.0 MPa, and the mass lost was less than 10.0%, contrasting the mass lost at 0.084 MPa. Table 6 summarizes the mass loss values for these experiments in each region (first and second stages). The weak SC region during the oxidative experiment means that not enough fuel was deposited, and with decreasing pressure, the saturates react almost entirely with oxygen during the first combustion, which implies that the saturates used in this study make a small contribution to coke deposition during crude oil oxidation [7, 20].

Based on the findings above, the reactions between the atmosphere gas and the liquid saturates produced the evaporation of lightweight components and their polycondensation during FC. Then, the remaining

products during FC are decomposed by cracking reactions and oxidation, with the difference that at low pressures, the amount of sample decomposed by thermal cracking in SC is much lower than that at high pressures, as shown in Table 6. These findings agree with those reported by Yang and Sheng et al. [48], who, through accelerating rate calorimetry, showed that all saturated samples exhibited FC behavior with rapid temperature rise and that the increase in pressure results in higher exothermic reactions.

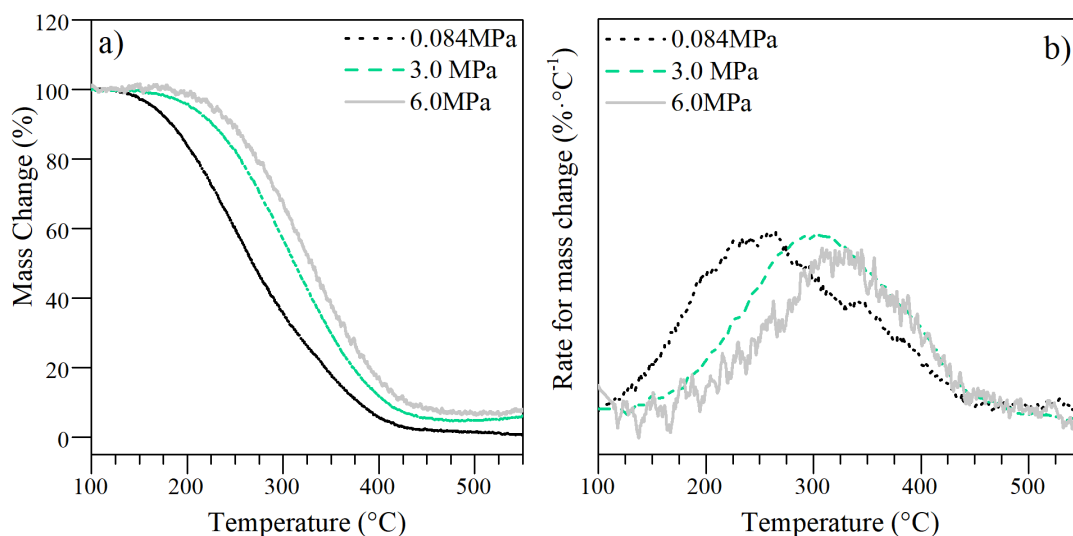


**Figure 5.** (a) Mass percentage and (b) rate for mass change for the pyrolysis of saturates at different pressures. Sample mass: 1 mg, heating rate:  $10\text{ }^{\circ}\text{C}\cdot\text{min}^{-1}$ , and nitrogen flow:  $80\text{ mL}\cdot\text{min}^{-1}$ .

**Table 6.** Thermogravimetric characteristics for the oxidation of saturates, discretized in the different regions: *i*) first combustion (FC) region, and *ii*) second combustion (SC) region at 0.084 MPa, 3.0 MPa, and 6.0 MPa.

Experiment	Pressure (MPa)	First combustion		Second combustion	
		Temperature range ( $^{\circ}\text{C}$ )	Mass loss (mass fraction in %)	Temperature range ( $^{\circ}\text{C}$ )	Mass loss (mass fraction in %)
Oxidation	0.084	100-330	78.0	331-525	22.0
	3.0	100-280	88.0	281-475	12.0
	6.0	100-275	90.0	276-470	10.0
Pyrolysis	First region		Second region		
	0.084	100-330	75.0	321-520	21.0
	3.0	100-330	65.0	331-515	28.0
	6.0	100-340	60.0	341-510	33.0

#### 4.2.2. Thermo-oxidation characteristics of aromatics

As seen in Figure 6, aromatic oxidation is defined by two regions at 0.084 MPa (FC and SC) and four areas at 3.0 MPa and 6.0 MPa (OC, DCO, FC, and SC). Unlike the oxidation of saturates, aromatics present a defined region characterized only by oxygen-adding reactions. In this region, oxygen atoms are chemisorbed in the aromatic molecular structure, which releases heat and forms numerous products such as ketones, carboxylic acids, esters, phenols, and alcohols anchored to aromatic rings [6, 8, 49]. The aromatic rings are believed to function as important sites for interactions with O<sub>2</sub> due to the easiness of its  $\pi$ -electron density to interact with electrophiles such as diatomic oxygen [3]. In this sense, increasing the pressure increases the number of oxygenated groups in the basal aromatic plane. Consequently, the mass lost in the following regions depends directly on the complexity, reactivity, and number of structures formed in this process. This result agrees well with those reported for asphaltenes with different chemical natures, in which it was found that its reactivity depends on its aromatic factor and the structures formed in the OC region [3].

As the temperature increases, the aromatics decomposition may be produced through the condensation reaction of the aromatic nuclei to form coke precursors with a much higher condensation degree [4]. The condensation degree of the structure at the end of FC is related to the pressure used [22].

As observed in Table 7, twice the mass of oxygen is chemisorbed at 6.0 MPa than at 3.0 MPa, and in DCO, 7.0% more mass is lost at 3.0 MPa than at 6.0 MPa. This indicates that the oxygenated structures formed in the aromatic nuclei directly influence the condensation degree of the structure once the cracking reactions begin. When the temperature is high enough, pressure plays a fundamental role in the aromatic decomposition, according to their FC behavior; at lower temperatures, a more significant part of the aromatic structure is decomposed in this region. This indicates that the low percentage of mass lost in DCO at 6.0 MPa does not mean that the reagents are inactive or resistant. Furthermore, this means that the physical evaporation of the aromatics used was almost negligible, and their contribution to mass loss at low temperatures is less than that of the saturates [21, 50].

Further, from panel b of Figure 6, a peculiar behavior is observed for aromatic oxidation at 6.0 MPa. At the end of FC, close to 410 °C, a high peak of mass loss is observed. This apparent mass loss can be attributed to the violent occurrence of intricate reactions such as the cleavage of C-heteroatom and C-C bonds in alkanes and alkyl side chains connected to aromatic rings and/or

naphthenes, as well as the dehydrogenation and ring-opening of the aromatic structure and/or naphthenes. This behavior was detected by different researchers [3, 4, 11], where the hydrocarbons that had shorter aliphatic chains surrounding the aromatic nuclei presented a violent and rapid consumption of mass, causing an increase in the collision probability between the oxygen molecules and, therefore a high release of heat. Also, researchers reported similar results for the thermo-oxidative decomposition asphaltenes with low content of aliphatic chains and high aromaticity degree [3, 4, 11]. Once the violent reaction of aromatics is over, a more controlled decomposition continues at high temperatures, with a peak around 460 °C. During this temperature interval, the SC region takes place, where the heavier compounds and remnants of FC progressively decompose.

On the other hand, the amount of mass lost in the SC region is higher than that of FC at all pressures. As VPO findings showed, the aromatic family evaluated in this study presents a high average molecular weight, suggesting the presence of some aromatic structures consisting of three (9,10- dimethyl anthracene ( $C_{16}H_{14}$ )), four (7,12-dimethylbenzanthracene ( $C_{20}H_{16}$ )) or more benzene rings that behave similarly to asphaltenes (i.e., SC reactions are stronger than FC reactions) [51]. However, as pressure increases, the amount of mass lost in SC is reduced, possibly associated with the change of aromatic core molecules from peri-condensed to cata-condensed during FC due to the pressure effect [52].

In Figure 6a, near 420 °C, there is a common point of intersection for the three curves. This point is close to the transition between FC and SC for systems at 3.0 MPa and 6.0 MPa, which indicates that regardless of pressure, aromatic oxidation presents the transition between the combustion regions at a similar temperature.



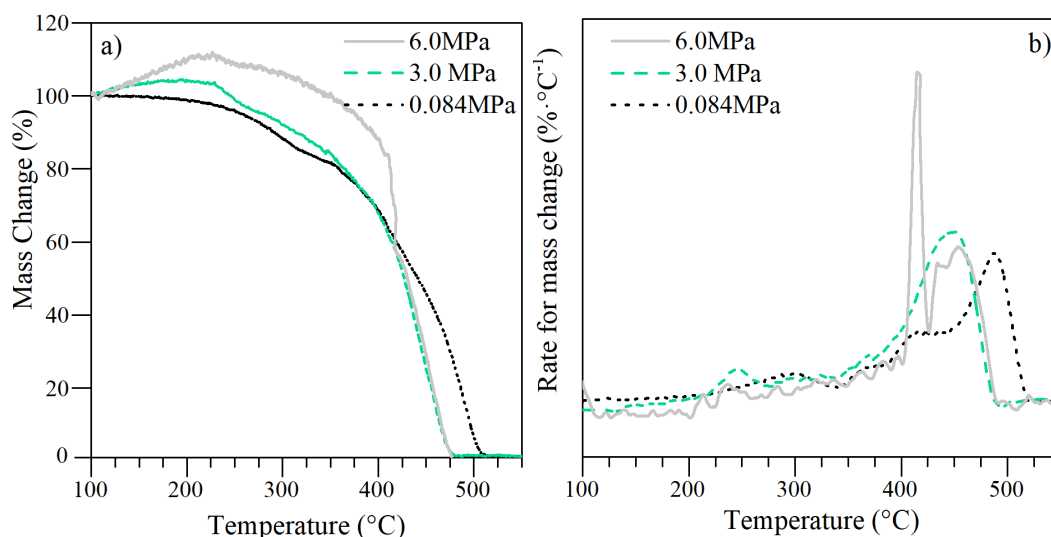


**Figure 6.** (a) Mass percentage and (b) rate for mass change for aromatics oxidation at different pressures. Sample mass: 1 mg, heating rate:  $10\text{ }^{\circ}\text{C}\cdot\text{min}^{-1}$ , and airflow:  $80\text{ mL}\cdot\text{min}^{-1}$ .

Further, the construction of simulated distillation curves and TGA pyrolysis experiments for aromatic fractions were also performed. Results are shown in Figures 7 and 8, respectively. The previous hypothesis, which explained that aromatic evaporation has a low contribution at low temperatures, is corroborated by distillation curves, which show that less than 30% of the total content was decomposed by physical evaporation during the first 300 °C at all pressures evaluated. Additionally, the accumulated fraction that evaporated decreased as pressure rose.

As for saturates, the contribution by evaporation of aromatics during their thermo-oxidative reactions was analyzed through mass balance for carbon produced by light hydrocarbon release using HP-TGA-MS results CHNSO. Results are detailed in Table 5. It was obtained that around 79.4, 79.7, and 81.9% of carbon comes from LHC decomposition at 0.084, 3.0, and 6.0 MPa, respectively. In contrast, distillation curves suggest that around 64.9, 64.5, and 64.0% were released by physical evaporation for the same pressures. Hence, approximately 14.5, 15.2, and 17.9% were produced by evaporation after cracking reactions of aromatic fractions at 0.084 MPa, 3.0 MPa, and 6.0 MPa, respectively. These results are only presented to understand the contribution of evaporation to the oxidative process; however, deeper comprehension analysis should be done because other reactions may be involved in this process.

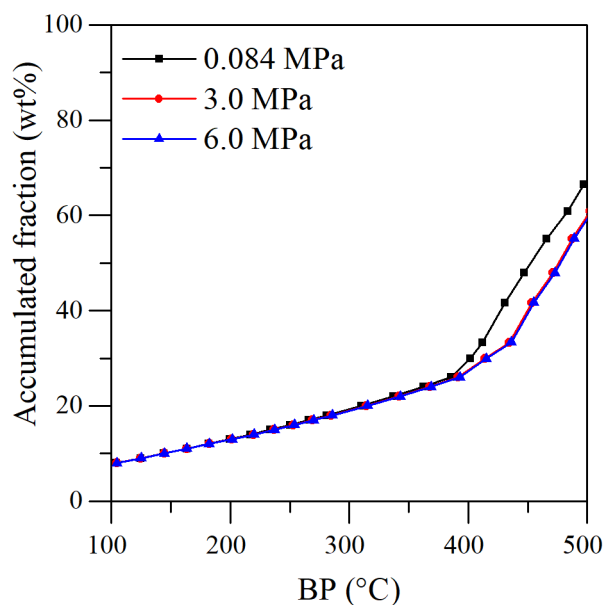


**Figure 7.** Simulated distillation curves for aromatics at different pressures (0.084 MPa, 3.0 MPa, and 6.0 MPa).

On the other hand, the mass change and rate for mass change profiles for aromatics pyrolysis (Figure 8) suggest that two distinct regions define the thermal cracking curves for all pressures evaluated. The weight loss in the first region can be attributed to the distillation of light components and the cracking of lower molecular weight compounds. The second region until 500 °C mainly involves visbreaking and the thermal cracking reaction of higher molecular weight hydrocarbons.

The results of the first region corroborated with the results of aromatic distillation and oxidation because, during this first thermal event, evaporation and thermal cracking reactions could occur. By contrast, when pressure increases, isomerization, and decomposition reactions to produce ketones, alcohols, and others by hydrogen abstraction occur at lower temperatures during oxidation experiments.

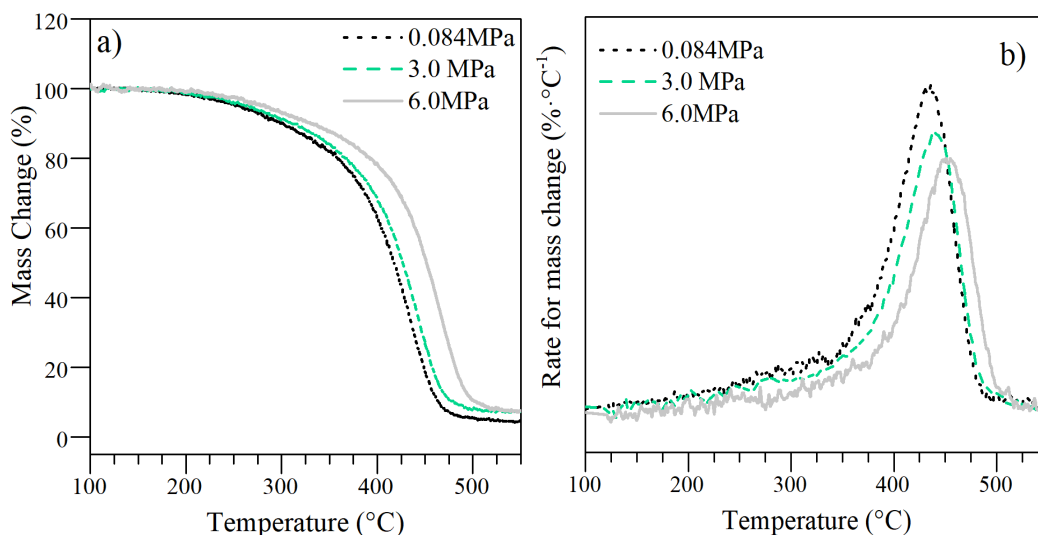


**Figure 8.** (a) Mass percentage and (b) rate for mass change for the pyrolysis of aromatics at different pressures. Sample mass: 1 mg, heating rate: 10 °C·min<sup>-1</sup>, and nitrogen flow: 80 mL·min<sup>-1</sup>.

Table 7 lists the thermogravimetric characteristics for pyrolysis. The mass lost percentage during the FC period of aromatics pyrolysis is first seen to decrease with increasing pressure, indicating that thermal cracking reactions take place at higher temperatures. As a result, the FC period of aromatics thermo-oxidation is dominated by oxygen consumption and combustion reactions.

At all pressures, the mass lost during the first stage of aromatics pyrolysis was significantly less than that of saturates. At 0.084, 3.0, and 6.0 MPa, aromatic compounds decompose to about 24.0, 22.0, and 19.0%, respectively. Then, for the same pressures, during SC, the contributions were 69.0, 70.0, and 71.0%, yielding a residual "coke" of 7.0, 8.0, and 10.0%, respectively. Regardless of resin profiles, the residue was higher in every case.

**Table 7.** Thermogravimetric characteristics for the oxidation of aromatics discretized in the different regions: *i*) oxygen chemisorption (OC) *ii*) decomposition of the chemisorbed oxygen (DCO) region, *iii*) first combustion (FC) region, and *iv*) second combustion (SC) region at 0.084 MPa, 3.0 MPa, and 6.0 MPa.

Experiment	Pressure (MPa)	OC Region		DCO Region		FC Region		SC Region	
		Temperature range (°C)	Mass gain (mass fraction in %)	Temperature range (°C)	Mass loss (mass fraction in %)	Temperature range (°C)	Mass loss (mass fraction in %)	Temperature range (°C)	Mass loss (mass fraction in %)
Oxidation	0.084	-	-	-	-	100-330	45.0	331-520	55.0
	3.0	100-220	5.0	221-260	10.0	261-430	38.0	431-470	57.0
	6.0	100-230	10.0	231-255	3.0	256-425	55.0	426-475	52.0
						First Region	Second Region		
Pyrolysis	0.084	-	-	-	-	100-360	24.0	361-510	69.0
	3.0	-	-	-	-	100-370	22.0	371-520	70.0
	6.0	-	-	-	-	100-385	19.0	386-525	71.0

#### 4.2.3. Thermo-oxidation characteristics of resins

The mass change and rate of mass change for resin oxidation are shown in Figure 9. According to the profiles, the resin oxidation mechanism is controlled by four thermal events. Oxygen chemisorption at temperatures below 215 °C, decomposition/desorption of oxygenated functional groups up to 375 °C, first combustion at temperatures lower than 450 °C and second combustion ranged between 475 °C and 530°C. As pressure increases, substantial differences in resin oxidation are observed. First, both the mass gained in OC and the mass lost during DCO increased. This resulted in a decrease in both the mass lost in SC and the temperature at which FC starts. This suggests that positive changes occur in all regions. The most structurally related substance to asphaltenes is a resin. They are composed of aromatic, aliphatic, and heteroatom structures; resins have many active sites for adding oxygen [53, 54]. Previously, heteroatoms and free radicals were identified as the main points for anchoring oxygen in the hydrocarbon molecular structure [3]. This is also corroborated by %OC, which is higher for resins than for aromatics.

It has been reported that the oxidation of structures such as thioethers, thiophenes, and sulfoxides requires shallow energy and becomes more reactive [55-57]. Therefore, the mass lost in DCO increased. Additionally, as previously mentioned, the resins contain a lot of short-sized branched chains ( $H_{\alpha}$ ), which are also capable of breaking down in this region and even cracking some long

aliphatic chains. It was widely believed that the primary reaction pathway in the OC stage consisted of oxygen addition reactions that produced hydroperoxides [6, 42, 49]. The formed hydroperoxides were transformed into oxygenated compounds (ketones, aldehydes, carboxylic acids, etc.), H<sub>2</sub>O, CO<sub>2</sub>, and CO via isomerization and decomposition reactions during DCO. Both stages were more favored for resins than for aromatics.

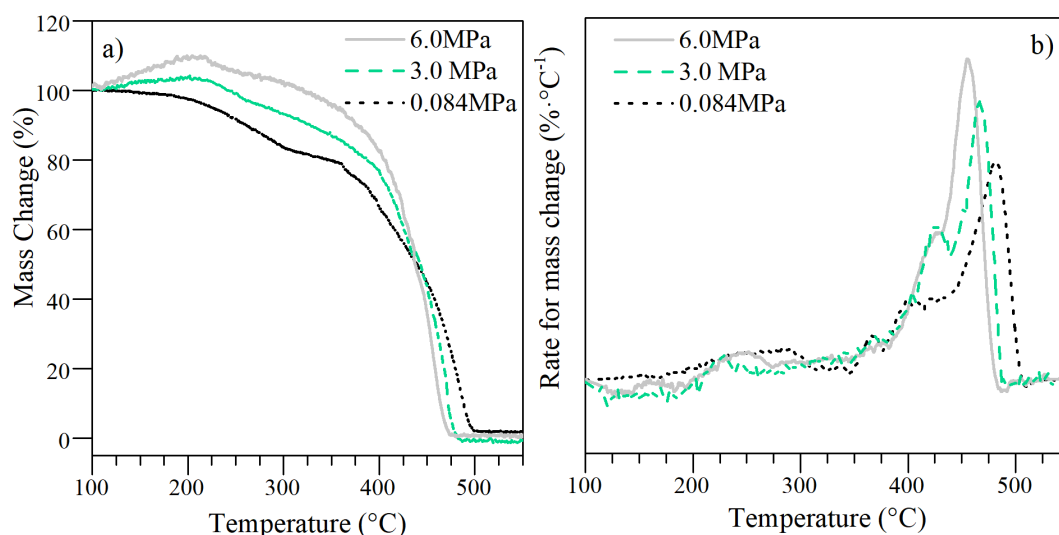


**Figure 9.** (a) Mass percentage and (b) rate for mass change for resins oxidation at different pressures. Sample mass: 1 mg, heating rate: 10 °C·min<sup>-1</sup>, and airflow: 80 mL·min<sup>-1</sup>.

Later, the thermal processes that take place in FC and SC are more complex. The C-C bonds in the remaining aliphatic chains after the long aliphatic chain cracking could be broken in the initial stage of FC. Then, the rupture of naphthenic rings attached to polycyclic aromatics could occur [6]. Meanwhile, the bridge bonds can also be broken during this event. The bridging bonds linked to the unitary resin sheets consist of two aspects: *i*) functional groups containing oxygenated heteroatoms (N, S, O), forming intermolecular forces like hydrogen or ether-type bonds, and *ii*) remaining aliphatic chains [16, 51]. In the higher temperature range of this region, dehydroaromatization of the naphthenic rings and condensation of the aromatic structure occurs, forming a remaining solid with a high condensation degree [4, 11, 12]. At low pressures, resins generate a higher coke precursor content, reflected in the higher percentage of mass lost in SC. This agrees with the low value of  $H_{AU} / C_A$  and its high degree of aromaticity ( $f_A$ ). However, with increasing pressure, the contribution of resins in SC reactions decreased while aromatics increased. This behavior could imply that

under high-pressure conditions, it is possible to reproduce desulfurization and denitrogenating processes during FC, therefore systems with heteroatoms manage to lose a greater mass in FC.

The low-pressure distillation and high-pressure pyrolysis of resins were also performed, and the results are depicted in Figures 10 and 11, respectively. As seen in Figure 10, only 25% of the resins were distilled at low temperatures (<300 °C), consistent with the characterization results, which indicate a higher molecular weight and a higher content of heavy fractions with high boiling points. Due to the complexity of the molecules, higher temperatures were required for the distillation of resins, considering the obtained for aromatics and saturates at all pressures. In this context, approximately 45.0%, 43.0%, and 40.0% of the accumulated fraction evaporated at 0.084 MPa, 3.0 MPa, and 6.0 MPa, respectively. These results are compared with the percentage of carbon produced by light hydrocarbons released in the thermo-oxidation of resins obtained by HP-TGA-MS and elemental analysis results. Unlike aromatic and saturates, the percentage of carbon produced decreased with increasing pressure: 83.8% at 0.084 MPa, 78.3% at 3.0 MPa, and 77.7% at 6.0 MPa. This is because the resins have a higher content of heteroatoms in their structure that can cause LHC production through other reaction pathways. However, despite this behavior, the distilled accumulated fraction in Figure 10 is still much smaller, indicating that, like the other systems, resins lost mass by physical evaporation and thermal cracking reactions. Resins lost around 38.8% at 0.084 MPa, 35.3% at 3.0 MPa, and 37.7% at 6.0 MPa by evaporation in the distillation curves (Figure 10).

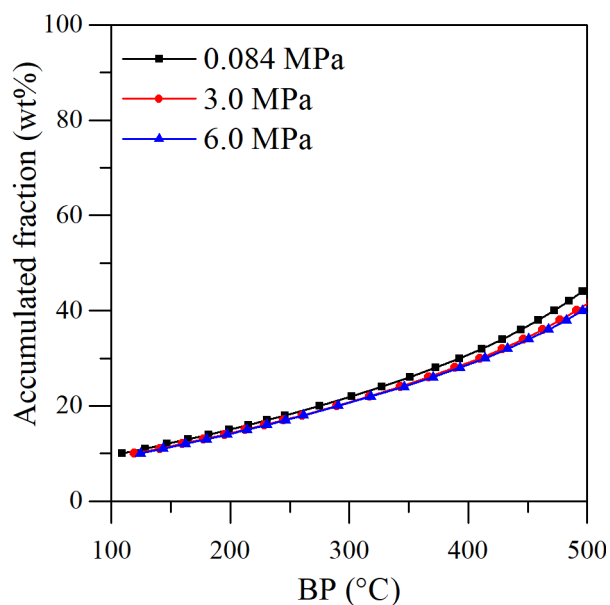


**Figure 10.** Simulated distillation curves for resins at different pressures (0.084 MPa, 3.0 MPa, and 6.0 MPa).

Like aromatics, two distinctive regions are observed in a wide range of temperatures (Figure 11) for resin thermo-oxidation. The first event ends at lower temperatures at 0.084 MPa than at 3.0 MPa, and 6.0 MPa, losing around 32.0%, 45.0%, and 40.0%, respectively. Compared with aromatics, resins have a greater mass loss by pyrolysis in this region, possibly due to short-chain aliphatic chains and heteroatoms positioned in the aliphatic structure, whose thermal cracking occurred at low temperatures.

Also, it was observed that the second stage mostly coincides with the SC intervals for the oxidation of resins for all pressures. However, after the resins' pyrolysis, the solid was around 10.0%, 11.0%, and 12.0%, respectively. The amount of coke generated follows the increasing order of saturates < aromatics < resins for all pressures used. This trend agreed well with the molecular mass and chemical composition of the S-Ar-R fractions reported in the characterization section of the samples. Also, with increasing pressure, the amount of coke deposited was higher for all systems, which corroborates the thermal characteristics of the pyrolysis profiles.

During the ISC process, coke is believed to be produced by pyrolysis of non-volatile hydrocarbons. A similar temperature range for both scenarios is reported in the literature [5, 58]. These results imply that the non-volatile hydrocarbons that remained after the FC reactions and did not oxidize under OC must be related to the coke deposition by both pyrolysis and oxidation reactions. All thermogravimetric characteristics are revealed in Table 8.

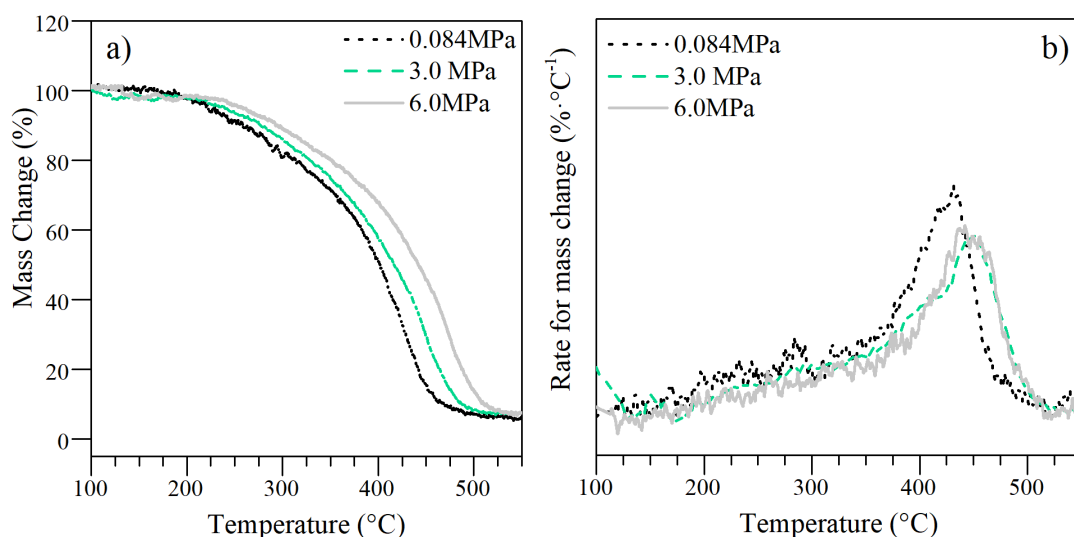


**Figure 11.** (a) Mass percentage and (b) rate for mass change for the pyrolysis of resins at different pressures. Sample mass: 1 mg, heating rate:  $10\text{ }^{\circ}\text{C}\cdot\text{min}^{-1}$ , and nitrogen flow:  $80\text{ mL}\cdot\text{min}^{-1}$ .

The differences in oxidation activity were due to the molecular structure aspect: resins are the heaviest component of crude oil (considering saturates, aromatics, and resins), which contains a large number of aromatic rings, alicyclic rings, and many kinds of short and long-chain branches, resulting in a strong polarity and can react with oxygen more efficiently than aromatics and saturate fractions [44]. Besides, resins contain many heteroatoms, such as S and N atoms. The bond energy of C–S and C–N is significantly lower than C–C, so the resin is more susceptible to oxygen attack, especially at high pressure [59-61]. The differences in oxidation activity were due to the molecular structure aspect: resins are the heaviest component of crude oil (considering saturates, aromatics, and resins), which contains a large number of aromatic rings, alicyclic rings, and many kinds of short and long-chain branches, resulting in a strong polarity and can react with oxygen more efficiently than aromatics and saturate fractions [44]. Besides, resins contain many heteroatoms, such as S and N atoms. The bond energy of C–S and C–N is significantly lower than C–C, so the resin is more susceptible to oxygen attack, especially at high pressure [59-61]. Each fraction's contribution to the different oxidation reactions of heavy and extra-heavy crude oils is limited by pressure. The oxidation reaction rate of neat S-Ar-R fractions increased with reaction temperature and pressure. This is the reason why the oxygen consumption capacity of crude oils increased at high-pressure and high-temperature systems.



**Table 8.** Thermogravimetric characteristics for the oxidation of resins discretized in the different regions: *i*) oxygen chemisorption (OC) *ii*) decomposition of the chemisorbed oxygen (DCO) region, *iii*) first combustion (FC) region, and *iv*) second combustion (SC) region at 0.084 MPa, 3.0 MPa, and 6.0 MPa.

Experiment	Pressure (MPa)	OC Region		DCO Region		FC Region		SC Region	
		Temperature range (°C)	Mass gain (mass fraction in %)	Temperature range (°C)	Mass loss (mass fraction in %)	Temperature range (°C)	Mass loss (mass fraction in %)	Temperature range (°C)	Mass loss (mass fraction in %)
Oxidation	0.084	-	-	-	-	100-325	40.0	326-530	60.0
	3.0	100-210	7.0	211-375	17.0	376-450	37.0	451-480	53.0
	6.0	100-215	11.0	216-360	20.0	361-440	41.0	406-475	50.0
						First stage	Second stage		
Pyrolysis	0.084	-	-	-	-	100-335	32.0	336-530	58.0
	3.0	-	-	-	-	100-425	45.0	426-530	44.0
	6.0	-	-	-	-	100-430	40.0	436-535	48.0

#### 4.2.4. Gaseous products

The amount of gases produced during the thermal events DCO, FC, and SC are presented in Figures 12-14 for the individual oxidation of saturates, aromatics, and resins at different pressures. The specific percentage (%vol) of the gases in the oxidation process was calculated based on their sensibility factor, following the protocol described in previous works [3, 23]. For this research, we considered the released thermal profiles of several gases, such as CO, CO<sub>2</sub>, light hydrocarbons (including CH<sub>4</sub>, C<sub>3</sub>H<sub>6</sub>, C<sub>4</sub>H<sub>8</sub>, C<sub>5</sub>H<sub>12</sub>, C<sub>2</sub>H<sub>6</sub>), nitrogen-based gases (NO, NO<sub>2</sub>), and sulfur-based gases (SO<sub>2</sub>, and SO).

##### 4.2.4.1. Gaseous analysis for saturates oxidation.

Only LHC, CO, and CO<sub>2</sub> are released from saturates during all regions and at three pressures, as shown in Figure 12. Some differences were obtained in the produced percentage of each gas. During the FC region, LHC production predominates in the system, being greater than 50% of total gas production at all pressures evaluated. Further, a high output of CO than CO<sub>2</sub> was found, associated with the incomplete combustion of these hydrocarbons. The presence of these gases during this region indicated that evaporation and oxidation co-exist in the first combustion of the saturates. Also, combustion gases increased in the SC region for all pressures. It was explained that during the lowest temperature range (FC interval), the formation of hydroperoxides through the oxygen-adding reaction is believed to be the main saturates oxidation reaction path like the following:



where RH refers to any possible aliphatic hydrocarbon and ROOH is a hydroperoxide. Reaction in Equation (14) is the sum of a series of elementary free-radical reactions, which is believed to start from the following reactions:



When the temperature was increased to the highest FC range, the formed hydroperoxides started to participate in decomposition and isomerization reactions. At this point, several products were released, such as ketones or alcohols, according to the following reactions.



where  $RO^\bullet$  is an alkoxy free radical,  $\bullet OH$  is a hydroxyl radical, ROH is an alcohol, and  $R^\bullet$  is an alkyl free radical. This is considered the most accepted pathway related to the hydrogen abstraction reactions during the oxidation of aliphatic hydrocarbons. Hence, the oxidized products' bond-scission promotes  $CO_2$  and CO during the following stage (SC), as explained below.

After FC, some oxygen-rich products formed from hydroperoxides' conversion remain, called FC residue. Therefore, the overall reaction of the isomerization and decomposition processes can be described as the following:



As seen in the case of saturates, the production of gases depends fundamentally on the number of free radicals in their structure because the active sites for oxygen chemisorption are limited. Also, pressure does not affect how each gas is produced in the thermal events, obtaining similar results at the three pressures evaluated.

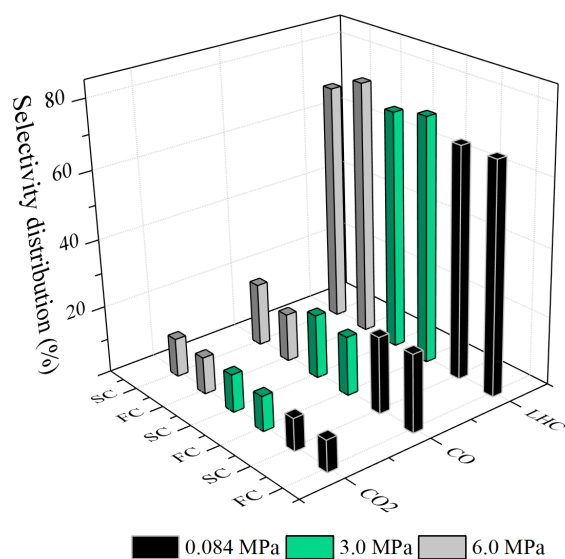


**Figure 12.** Selectivity distribution of light gases produced from saturates oxidation at different pressures.

#### 4.2.4.2. Gaseous analysis for aromatic oxidation.

The results for aromatic thermo-oxidative decomposition gases are shown in Figure 13. As a first instance, aromatics exhibit the production of nitrogen- and sulfur-based gases, which follow their elemental composition. The aromatics exhibited a high production of CO and CO<sub>2</sub> concerning the other gases for the FC and SC regions. At 0.084 MPa, higher production of CO and CO<sub>2</sub> was obtained in SC than in FC. In contrast, most of the light hydrocarbons exhibited the opposite behavior, consistent with the simulated distillation results, indicating that evaporation reactions occur during the initial heating of aromatics. As for nitrogen and sulfur gases, they were produced in similar proportions in both combustion regions. As pressure increased, CO production increased in the FC region, obtaining higher percentages than in the case of SC.

Regarding the DCO region that appears for high-pressure systems, a greater release of light hydrocarbons is observed for both fractions due to evaporation. Further, a high CO production was also observed, similar to SC at 3.0 MPa, and higher than SC at 6.0 MPa. On the other hand, the production of NO<sub>x</sub> and SO<sub>x</sub> in DCO is deficient compared to the other regions, suggesting some hydrocarbons' incomplete combustion.

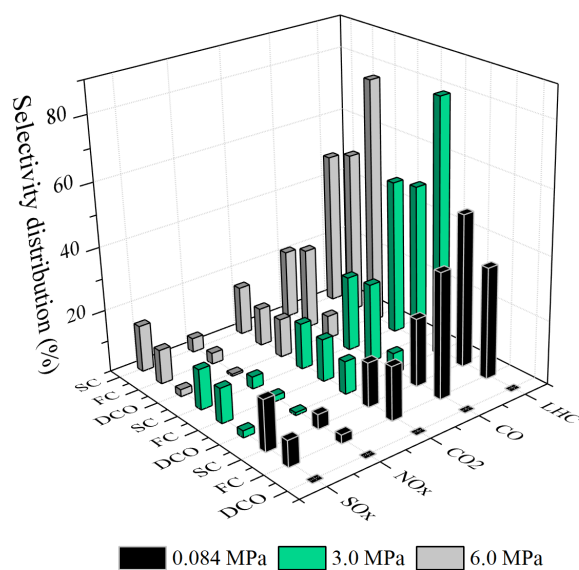


**Figure 13.** Selectivity distribution of light gases produced from aromatics oxidation at different pressures.

#### 4.2.4.3. Gaseous analysis for resin oxidation.

The results for resin thermo-oxidative decomposition gases are shown in Figure 14. First, lower production of CO and CO<sub>2</sub> is noted than in the case of aromatics, especially in the FC region. For low pressures, combustion gas production increased in SC, and the same behavior was followed by nitrogen and sulfur gases.

At 3.0 MPa, an increase is observed for CO release during FC; however, at 6.0 MPa, similar production was obtained in DCO, FC, and SC stages. Compared with aromatics, the resins showed a higher production of NO<sub>x</sub> and SO<sub>x</sub>, mainly in DCO, where resins show remarkable intensities at 6.0 MPa. This is associated with the heteroatom position in the branched structures like sulfoxides or thioethers, whose decomposition is more straightforward at lower temperatures under high pressure [3].

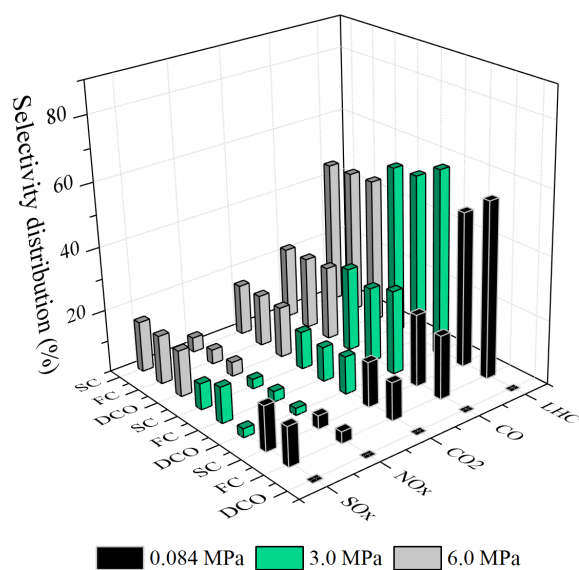


**Figure 14.** Selectivity distribution of light gases produced from resin oxidation at different pressures.

#### 4.3. Reaction Kinetic Analysis

Considering that the thermo-oxidative decomposition reactions of saturates and aromatics/resins consist of two and four different reaction stages, respectively. Kinetic parameters of OC, DCO, FC, and SC are determined by a first-order kinetic model at three different heating rates (see Figure 15), obtaining good correlation coefficients  $R^2 > 0.98$ . Figure 16 shows the effective activation energy values obtained from the best fit of straight

lines of  $\ln \left[ \frac{\beta(-\ln(1-x))}{P_{O_2}^n T^2} \right]$  as a function of  $\frac{1}{RT}$ ; meanwhile, pre-exponential

factors are summarized in Table 9. From the results, it was obtained that the effective activation energy of saturates for the FC stage was larger than the obtained for the SC stage for all evaluated pressures. The variations in  $E_a$  between combustion regions are opposite; for FC, the values present a gradually increasing trend with the rising pressure, while in SC decrease. The  $E_a$  values varied between 40 and 45  $\text{kJ}\cdot\text{mol}^{-1}$  for FC and 34 and 40  $\text{kJ}\cdot\text{mol}^{-1}$  for SC, in the range of pressures evaluated. This indicates that the best scenario for the thermo-oxidation of saturates is at 6.0 MPa, where their contribution to the second combustion reactions is the most reduced. The results obtained for this fraction corroborate with the thermal profiles obtained in thermogravimetric tests. The greatest mass loss occurred at low temperatures during FC, associated with evaporation, cracking, and

oxidation reactions. The phenomenon observed in the first combustion stage can be explained by the fact that the enhancement of instantaneous thermal energy at the higher pressure has a finite effect on accelerating the rate of reactions of saturates, mainly containing a distillation of light components and the rupture of weak chemical bonds.

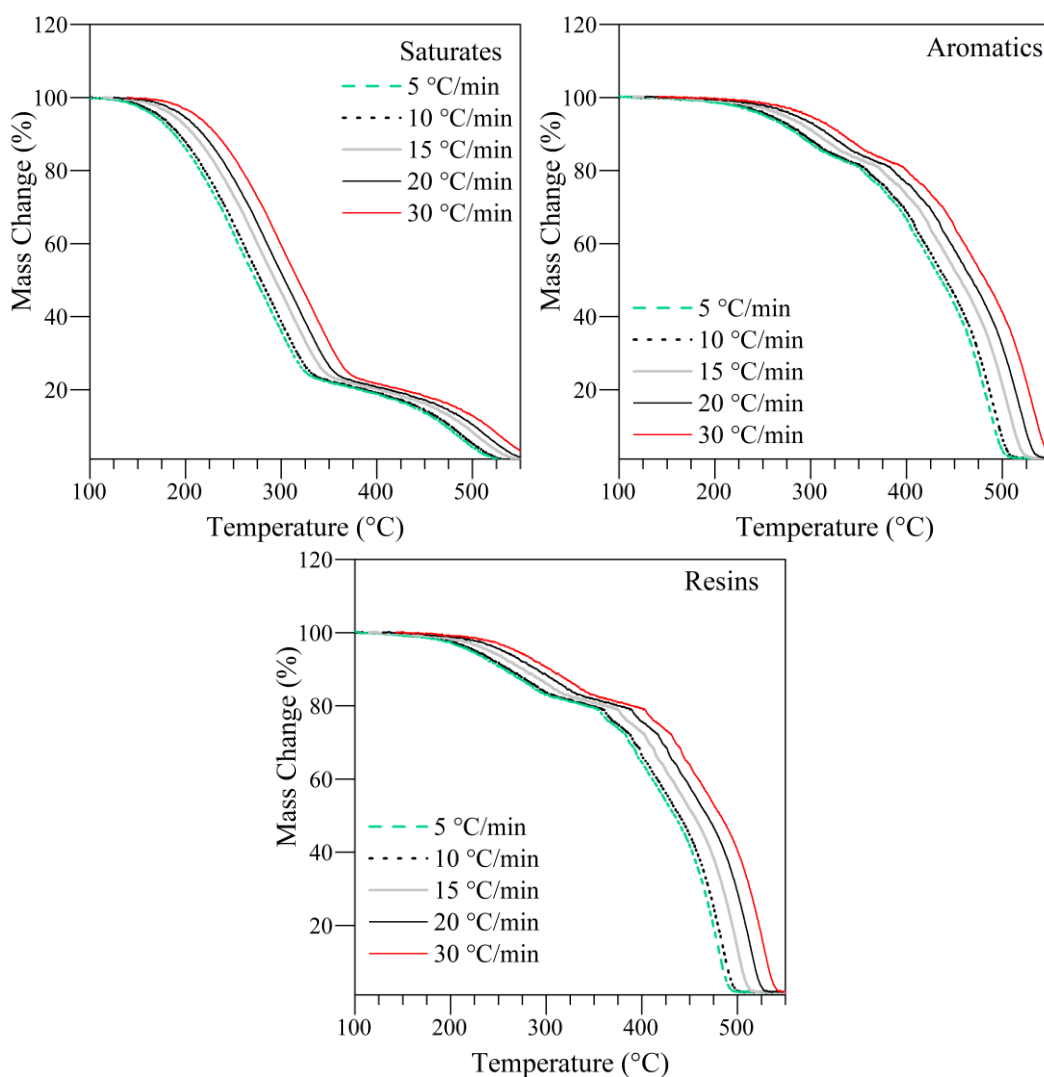


**Figure 15.** Mass percentage for the oxidation of saturates, aromatics, and resins at 0.084 MPa. Sample mass: 1 mg, heating rates: 5, 10, 15, 20, and 30 °C·min<sup>-1</sup>, and airflow: 80 mL·min<sup>-1</sup>.

For the case of aromatics thermo-oxidation, OC presents the lowest values for  $E_a$ , with a slight increase from 3.0 to 6.0 MPa, associated with the higher OC chemisorption degree in the higher-pressure system. During DCO,  $E_a$  is higher than in OC. Because a greater number of oxygenated structures are formed during OC at 6.0 MPa, in DCO, a higher energy

requirement than at 3.0 MPa is also observed. The values for the combustion regions increase compared to DCO, following the same behavior as the saturates. It is observable that its values are also higher for the thermo-oxidation of saturates at all pressures in both FC and SC regions.

The behavior of  $E_a$  for aromatics decomposition regions follows the order DCO < FC < SC. Nevertheless, at 6.0 MPa,  $E_a$  is higher for FC than SC. This trend was similar to the one obtained for asphaltenes with short aliphatic chains since, in these systems, there is a high amount of interaction between the aromatic nucleus and the oxygen atoms. During FC a decrease in the number of aromatic sheets per stack can occur; hence fewer refractory molecules are obtained, that is, more resistant to high temperature, especially at high-pressure conditions. Therefore, the effective activation energy in SC slightly decreased.

For resins, the  $E_a$  values in all regions are higher than those obtained for aromatics and saturates. For high-pressure systems, the values in OC and DCO increase with pressure increment, which varies between 11 and 15  $\text{kJ}\cdot\text{mol}^{-1}$  and 35 and 40  $\text{kJ}\cdot\text{mol}^{-1}$ , respectively. Unlike aromatics, resins at all pressures evaluated require higher energy to carry out SC reactions than FC. The behavior is similar, FC increases with increasing pressure, and SC decreases. This phenomenon observed for both regions can be explained by the fact that the high content of alkyl free radicals produced from the thermo-oxidation reactions at the highest pressure favors more severe reactions in FC, requiring more energy, further promoting the reaction rate. These results agree with the one reported by Zhao et al. [9], who found that higher energy demand was used at atmospheric pressure to touch off reactions during the first combustion stage, and the subsequent thermo-oxidative cracking in SC became easier to take place. In this work, it was shown that pressure does not alter this behavior.

Comparing SAR fractions, resins were the most resistant fraction to thermo-oxidative decomposition reactions, with the difference that, at 6.0 MPa, there is a higher contribution of aromatics in the SC stage. At this pressure, the activation energy of resins facilitated the FC processes to enhance the combustion front sustainability.

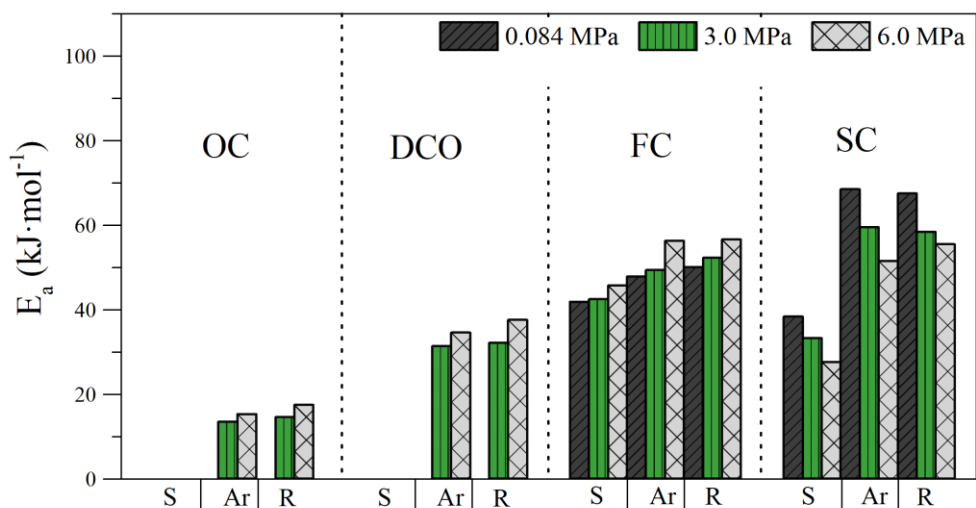


**Figure 16.** Estimated effective activation energy for *S-Ar-R* oxidation discretized in the different regions: *i*) oxygen chemisorption (OC) *ii*) decomposition of the chemisorbed oxygen (DCO) region, *iii*) first combustion (FC) region and *iv*) second combustion (SC) region.

Also, it is noted that the pre-exponential factor depends on the pressure and chemical nature of the sample. Pressure modifies  $k_o$  values by several orders of magnitude. The low values obtained for  $k_o$  in OC for aromatics and resins are related to the low entropy change produced by the molecular disorder through oxygen chemisorption [22]. The increase in pressure increases the entropy change ruled by the rise in collision frequency and therefore increases the value of  $k_o$ . In this same way, the decrease in  $k_o$  in SC with the increase in pressure for all samples can be explained due to the decomposition of *S-Ar-R* fractions at lower temperatures (DCO and FC) that reduce the amount of molecules available for the collision. Hence the values for  $k_o$  in the last combustion increased in the order  $S < Ar < R$ , at all evaluated pressures.



**Table 9.** Estimated pre-exponential factor for *S-Ar-R* oxidation discretized in the different regions: *i*) oxygen chemisorption (OC) *ii*) decomposition of the chemisorbed oxygen (DCO) region, *iii*) first combustion (FC) region, and *iv*) second combustion (SC) region.

Sample	Pressure (MPa)	Thermal Events			
		OC Region		DCO Region	
		$k_o$ (min <sup>-1</sup> ·MPa <sup>-1</sup> )	R <sup>2</sup>	$k_o$ (min <sup>-1</sup> ·MPa <sup>-1</sup> )	R <sup>2</sup>
Saturates	0.084	-	-	-	-
	3.0	-	-	-	-
	6.0	-	-	-	-
		FC Region		SC Region	
	0.084	3.33 ×10 <sup>2</sup>	0.99	1.78 ×10 <sup>1</sup>	0.99
	3.0	1.29 ×10 <sup>9</sup>	0.99	2.75 ×10 <sup>-2</sup>	0.99
	6.0	3.12 ×10 <sup>10</sup>	0.99	3.66 ×10 <sup>-5</sup>	0.99
Aromatics		OC Region		DCO Region	
	0.084	-	-	-	-
	3.0	2.21 ×10 <sup>2</sup>	0.99	4.23 ×10 <sup>12</sup>	0.99
	6.0	6.12 ×10 <sup>4</sup>	0.99	4.11 ×10 <sup>14</sup>	0.99
		FC Region		SC Region	
	0.084	7.21 ×10 <sup>4</sup>	0.99	6.32 ×10 <sup>3</sup>	0.99
	3.0	4.21 ×10 <sup>10</sup>	0.99	5.63 ×10 <sup>1</sup>	0.99
	6.0	6.01 ×10 <sup>12</sup>	0.99	8.74 ×10 <sup>-5</sup>	0.99
Resins		OC Region		DCO Region	
	0.084	-	-	-	-
	3.0	2.91 ×10 <sup>3</sup>	0.99	4.32 ×10 <sup>7</sup>	0.99
	6.0	6.02 ×10 <sup>6</sup>	0.99	9.41 ×10 <sup>8</sup>	0.99
		FC Region		SC Region	
	0.084	3.11 ×10 <sup>5</sup>	0.99	3.78 ×10 <sup>5</sup>	0.99
	3.0	4.01 ×10 <sup>11</sup>	0.99	4.92 ×10 <sup>3</sup>	0.99
	6.0	5.59 ×10 <sup>15</sup>	0.99	1.23 ×10 <sup>-2</sup>	0.99

## 5. Conclusions

This work provided mechanistic insights into the thermo-oxidative decomposition of saturates, aromatics, and resins at different pressures. The thermo-oxidative decomposition profiles were analyzed considering the contributions of evaporation, pyrolysis, oxidation, and combustion reactions. Among the most important results of this work, the following stand out:

- Saturates oxidation is described only by FC and SC between 0.084 MPa and 6.0 MPa.

- During FC of saturates, the amount of mass loss was mainly attributed to light components evaporation, whereas during SC, solid fuel is wholly decomposed.
- Saturates two stages describe pyrolysis at all pressures. The first stage is related to the evaporation of hydrocarbons with low boiling points and weak chemical bonds breaking, which ends before 350 °C, like FC during oxidation experiments.
- The pyrolysis of aromatic compounds reveals that with increasing system pressure, the mass lost decreases at lower temperatures.
- Resins present higher oxygen chemisorption than aromatics at all pressures.
- The contribution by evaporation to the resin oxidation was lower than reported for aromatics and saturates.
- Two distinctive regions are observed during pyrolysis reactions of resins that account for evaporation and cracking phenomena.

## References.

- [1] Zhang X, Liu Q, Fan Z. Enhanced in situ combustion of heavy crude oil by nickel oxide nanoparticles. *International Journal of Energy Research* 2019;43(8):3399-412.
- [2] Medina OE, Olmos C, Lopera SH, Cortés FB, Franco CA. Nanotechnology applied to thermal enhanced oil recovery processes: a review. *Energies* 2019;12(24):4671.
- [3] Medina OE, Gallego J, Nassar NN, Acevedo SA, Cortés FB, Franco CA. Thermo-Oxidative Decomposition Behaviors of Different Sources of n-C7 Asphaltenes at High-Pressure Conditions. *Energy & Fuels* 2020.
- [4] Freitag NP. Chemical-reaction mechanisms that govern oxidation rates during in-situ combustion and high-pressure air injection. *SPE Reservoir Evaluation & Engineering* 2016;19(04):645-54.
- [5] Hao J, Che Y, Tian Y, Li D, Zhang J, Qiao Y. Thermal cracking characteristics and kinetics of oil sand bitumen and its SARA fractions by TG-FTIR. *Energy & Fuels* 2017;31(2):1295-309.
- [6] Kök MV, Karacan Ö, Pamir R. Kinetic analysis of oxidation behavior of crude oil SARA constituents. *Energy & Fuels* 1998;12(3):580-8.
- [7] Yuan C, Varfolomeev MA, Emelianov DA, Eskin AA, Nagrimanov RN, Kok MV, et al. Oxidation behavior of light crude oil and its SARA fractions

- characterized by TG and DSC techniques: differences and connections. *Energy & fuels* 2018;32(1):801-8.
- [8] Wei B, Zou P, Shang J, Gao K, Li Y, Sun L, et al. Integrative determination of the interactions between SARA fractions of an extra-heavy crude oil during combustion. *Fuel* 2018;234:850-7.
- [9] Zhao S, Pu W, Sun B, Gu F, Wang L. Comparative evaluation on the thermal behaviors and kinetics of combustion of heavy crude oil and its SARA fractions. *Fuel* 2019;239:117-25.
- [10] Akmaz S, Iscan O, Gurkaynak M, Yasar M. The structural characterization of saturate, aromatic, resin, and asphaltene fractions of Batiraman crude oil. *Petroleum Science and Technology* 2011;29(2):160-71.
- [11] Zhao S, Pu W, Yuan C, Peng X, Zhang J, Wang L, et al. Thermal behavior and kinetic triplets of heavy crude oil and its SARA fractions during combustion by high-pressure differential scanning calorimetry. *Energy & fuels* 2019;33(4):3176-86.
- [12] Gonçalves M, Teixeira M, Pereira R, Mercury R, Matos JdR. Contribution of thermal analysis for characterization of asphaltenes from Brazilian crude oil. *Journal of thermal analysis and calorimetry* 2001;64(2):697-706.
- [13] Nassar NN, Hassan A, Vitale G. Comparing kinetics and mechanism of adsorption and thermo-oxidative decomposition of Athabasca asphaltenes onto TiO<sub>2</sub>, ZrO<sub>2</sub>, and CeO<sub>2</sub> nanoparticles. *Applied Catalysis A: General* 2014;484:161-71.
- [14] Wei B, Zou P, Zhang X, Xu X, Wood C, Li Y. Investigations of structure–property–thermal degradation kinetics alterations of Tahe Asphaltenes caused by low temperature oxidation. *Energy & fuels* 2018;32(2):1506-14.
- [15] Dabbous MK, Fulton PF. Low-temperature-oxidation reaction kinetics and effects on the in-situ combustion process. *Society of Petroleum Engineers Journal* 1974;14(03):253-62.
- [16] Fan C, Zan C, Zhang Q, Ma D, Chu Y, Jiang H, et al. The oxidation of heavy oil: Thermogravimetric analysis and non-isothermal kinetics using the distributed activation energy model. *Fuel processing technology* 2014;119:146-50.
- [17] Pu W-F, Yuan C-D, Jin F-Y, Wang L, Qian Z, Li Y-B, et al. Low-temperature oxidation and characterization of heavy oil via thermal analysis. *Energy & Fuels* 2015;29(2):1151-9.
- [18] Chu Y, Fan C, Zhang Q, Zan C, Ma D, Jiang H, et al. The oxidation of heavy oil to enhance oil recovery: The numerical model and the criteria to

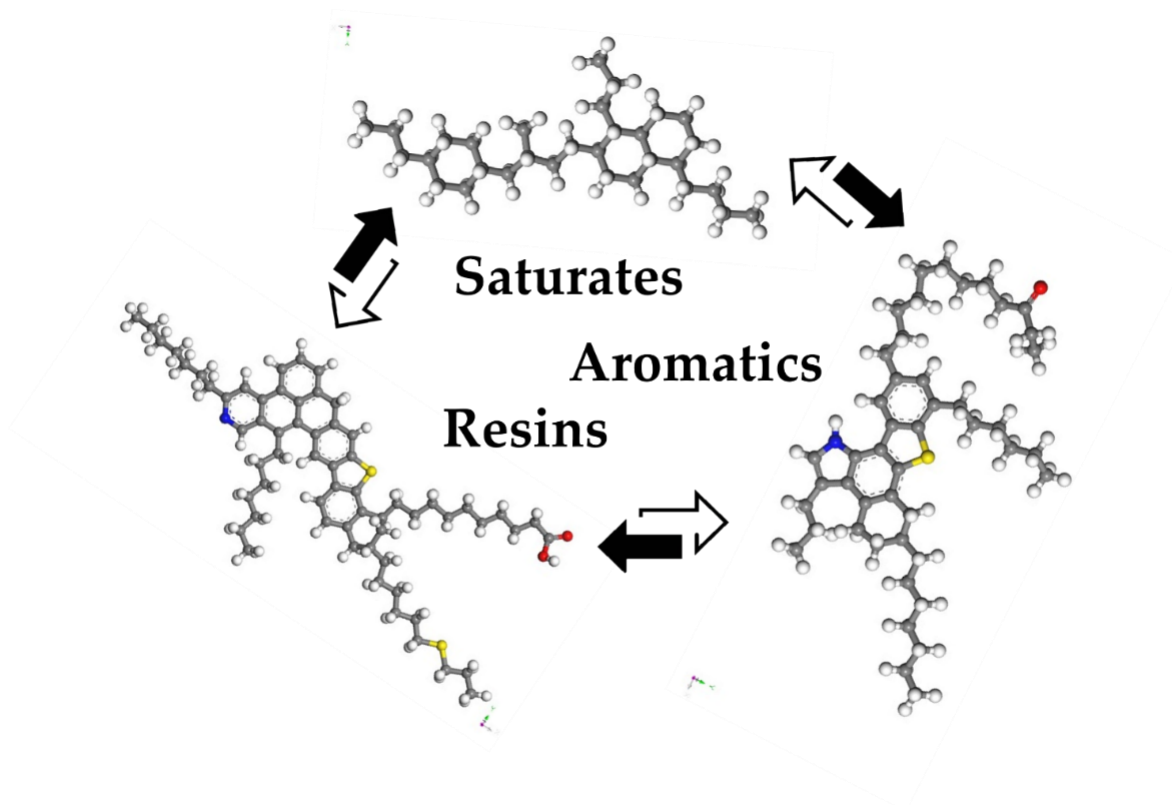
- describe the low and high temperature oxidation. *Chemical Engineering Journal* 2014;248:422-9.
- [19] Li Y-B, Chen Y-F, Pu W-F, Dong H, Gao H, Jin F-Y, et al. Low temperature oxidation characteristics analysis of ultra-heavy oil by thermal methods. *Journal of industrial and engineering chemistry* 2017;48:249-58.
- [20] Kok MV, Gul KG. Thermal characteristics and kinetics of crude oils and SARA fractions. *Thermochimica acta* 2013;569:66-70.
- [21] Liu D, Song Q, Tang J, Zheng R, Yao Q. Interaction between saturates, aromatics and resins during pyrolysis and oxidation of heavy oil. *Journal of Petroleum Science and Engineering* 2017;154:543-50.
- [22] Medina OE, Gallego J, Rodríguez E, Franco CA, Cortés FB. Effect of pressure on the oxidation kinetics of Asphaltenes. *Energy & Fuels* 2019;33(11):10734-44.
- [23] Medina OE, Gallego J, Olmos CM, Chen X, Cortés FB, Franco CA. Effect of Multifunctional Nanocatalysts on n-C7 Asphaltene Adsorption and Subsequent Oxidation under High-Pressure Conditions. *Energy & Fuels* 2020.
- [24] Franco CA, Montoya T, Nassar NN, Cortés FB. NiO and PdO supported on fumed silica nanoparticles for adsorption and catalytic steam gasification of colombian c7asphaltenes. *Handbook on Oil Production Research*; Nova Science Publishers: Hauppauge, NY, USA 2014:101-45.
- [25] Cardona L, Arias-Madrid D, Cortés F, Lopera S, Franco C. Heavy oil upgrading and enhanced recovery in a steam injection process assisted by NiO- and PdO-Functionalized SiO<sub>2</sub> nanoparticulated catalysts. *Catalysts* 2018;8(4):132.
- [26] Lopes SM, Geng P. Estimation of elemental composition of diesel fuel containing biodiesel. *SAE International Journal of Fuels and Lubricants* 2013;6(3):668-76.
- [27] Acevedo S, Castillo J, Vargas V, Castro A, Delgado OZ, Ariza CAF, et al. Suppression of Phase Separation as a Hypothesis to Account for Nuclei or Nanoaggregate Formation by Asphaltenes in Toluene. *Energy & Fuels* 2018.
- [28] Gimzewski E. An accurate and compact high-pressure thermogravimetric analyser. *Journal of thermal analysis* 1991;37(6):1251-60.
- [29] Austrich A, Buenrostro-Gonzalez E, Lira-Galeana C. ASTM D-5307 and ASTM D-7169 SIMDIS standards: a comparison and correlation of methods. *Petroleum Science and Technology* 2015;33(6):657-63.

- [30] Koutsoyiannis D. Clausius–Clapeyron equation and saturation vapour pressure: simple theory reconciled with practice. *European Journal of physics* 2012;33(2):295.
- [31] Baker LE, Pierce AC, Luks KD. Gibbs energy analysis of phase equilibria. *Society of Petroleum Engineers Journal* 1982;22(05):731-42.
- [32] Smith J, Van Ness H, Abbot M. *Introduction to Thermodynamics in Chemical Engineering*. 2005.
- [33] Pedersen KS, Christensen PL, Shaikh JA. *Phase behavior of petroleum reservoir fluids*. CRC press; 2014.
- [34] Pedersen KS, Fredenslund A, Thomassen P. *Properties of oils and natural gases*. Gulf Publishing Company; 1989.
- [35] Takahashi Y. Latent heat measurement by DSC with sapphire as standard material. *Thermochimica Acta* 1985;88(1):199-204.
- [36] Senneca O, Vorobiev N, Wütscher A, Cerciello F, Heuer S, Wedler C, et al. Assessment of combustion rates of coal chars for oxy-combustion applications. *Fuel* 2019;238:173-85.
- [37] Niksa S, Liu G-S, Hurt RH. Coal conversion submodels for design applications at elevated pressures. Part I. devolatilization and char oxidation. *Progress in Energy and Combustion Science* 2003;29(5):425-77.
- [38] Burnham AK, Dinh L. A comparison of isoconversional and model-fitting approaches to kinetic parameter estimation and application predictions. *Journal of Thermal Analysis and Calorimetry* 2007;89(2):479-90.
- [39] Liu G-S, Niksa S. Coal conversion submodels for design applications at elevated pressures. Part II. Char gasification. *Progress in energy and combustion science* 2004;30(6):679-717.
- [40] Medina Erao OE, Gallego J, Olmos CM, Chen X, Cortés FB, Franco CA. Effect of Multifunctional Nanocatalysts on n-C7 Asphaltene Adsorption and Subsequent Oxidation under High Pressure Conditions. *Energy & Fuels* 2020.
- [41] Rakhmatullin I, Efimov S, Tyurin V, Al-Muntaser A, Klimovitskii A, Varfolomeev M, et al. Application of high resolution NMR (<sup>1</sup>H and <sup>13</sup>C) and FTIR spectroscopy for characterization of light and heavy crude oils. *Journal of Petroleum Science and Engineering* 2018;168:256-62.
- [42] Molina D, Uribe UN, Murgich J. Correlations between SARA fractions and physicochemical properties with <sup>1</sup>H NMR spectra of vacuum residues from Colombian crude oils. *Fuel* 2010;89(1):185-92.

- [43] Retcofsky H, Schweighardt F, Hough M. Determination of aromaticities of coal derivatives by nuclear magnetic resonance spectrometry and the Brown-Ladner equation. *Analytical Chemistry* 1977;49(4):585-8.
- [44] Shi Q, Hou D, Chung KH, Xu C, Zhao S, Zhang Y. Characterization of heteroatom compounds in a crude oil and its saturates, aromatics, resins, and asphaltenes (SARA) and non-basic nitrogen fractions analyzed by negative-ion electrospray ionization Fourier transform ion cyclotron resonance mass spectrometry. *Energy & Fuels* 2010;24(4):2545-53.
- [45] Liu G, Fan Z, Li X, Gu D. Estimate of Saturation Pressures of Crude Oil by Using Ensemble-Smoother-Assisted Equation of State. *Industrial & Engineering Chemistry Research* 2018;57(49):17024-31.
- [46] Elsharkawy AM. An empirical model for estimating the saturation pressures of crude oils. *journal of petroleum Science and engineering* 2003;38(1-2):57-77.
- [47] Farasat A, Shokrollahi A, Arabloo M, Gharagheizi F, Mohammadi AH. Toward an intelligent approach for determination of saturation pressure of crude oil. *Fuel processing technology* 2013;115:201-14.
- [48] Yang L, Sheng JJ. Experimental study on the oxidation behaviors of Wolfcamp light crude oil and its saturate, aromatic and resin fractions using accelerated rate calorimetry tests. *Fuel* 2020;276:117927.
- [49] Freitag N, Verkoczy B. Low-temperature oxidation of oils in terms of SARA fractions: why simple reaction models don't work. *Journal of Canadian petroleum technology* 2005;44(03):54-61.
- [50] Liu D, Hou J, Luan H, Pan J, Song Q, Zheng R. Coke yield prediction model for pyrolysis and oxidation processes of low-asphaltene heavy oil. *Energy & Fuels* 2019;33(7):6205-14.
- [51] Li J, Mehta S, Moore R, Zalewski E, Ursenbach M, Van Fraassen K. Investigation of the oxidation behaviour of pure hydrocarbon components and crude oils utilizing PDSC thermal technique. *Journal of Canadian Petroleum Technology* 2006;45(01).
- [52] Zijun W, Wenjie L, Guohe Q, Jialin Q. Structural characterization of gudao asphaltene by ruthenium ion catalyzed oxidation. *Petroleum science and technology* 1997;15(5-6):559-77.
- [53] Lozano MM, Franco CA, Acevedo SA, Nassar NN, Cortés FB. Effects of resin I on the catalytic oxidation of n-C 7 asphaltenes in the presence of silica-based nanoparticles. *RSC advances* 2016;6(78):74630-42.

- [54] Moncayo-Riascos I, Taborda E, Hoyos BA, Franco CA, Cortés FB. Effect of resin/asphaltene ratio on the rheological behavior of asphaltene solutions in a de-asphalted oil and p-xylene: A theoretical–experimental approach. *Journal of Molecular Liquids* 2020;113754.
- [55] Javadli R, de Klerk A. Desulfurization of heavy oil–oxidative desulfurization (ODS) as potential upgrading pathway for oil sands derived bitumen. *Energy & fuels* 2012;26(1):594-602.
- [56] Sánchez NM, de Klerk A. Low-temperature oxidative asphaltene liquefaction for petrochemicals: fact or fiction? *Applied Petrochemical Research* 2016;6(2):97-106.
- [57] Ismagilov Z, Yashnik S, Kerzhentsev M, Parmon V, Bourane A, Al-Shahrani F, et al. Oxidative desulfurization of hydrocarbon fuels. *Catalysis Reviews* 2011;53(3):199-255.
- [58] Yuan C, Emelianov DA, Varfolomeev MA. Oxidation behavior and kinetics of light, medium, and heavy crude oils characterized by thermogravimetry coupled with fourier transform infrared spectroscopy. *Energy & fuels* 2018;32(4):5571-80.
- [59] Medina OE, Gallego J, Restrepo LG, Cortés FB, Franco CA. Influence of the Ce<sup>4+</sup>/Ce<sup>3+</sup> Redox-couple on the cyclic regeneration for adsorptive and catalytic performance of NiO-PdO/CeO<sub>2</sub>+ $\delta$  nanoparticles for n-C<sub>7</sub> asphaltene steam gasification. *Nanomaterials* 2019;9(5):734.
- [60] Arias-Madrid D, Medina OE, Gallego J, Acevedo S, Correa-Espinal AA, Cortés FB, et al. NiO, Fe<sub>2</sub>O<sub>3</sub>, and MoO<sub>3</sub> Supported over SiO<sub>2</sub> Nanocatalysts for Asphaltene Adsorption and Catalytic Decomposition: Optimization through a Simplex–Centroid Mixture Design of Experiments. *Catalysts* 2020;10(5):569.
- [61] Medina OE, Gallego J, Arias-Madrid D, Cortés FB, Franco CA. Optimization of the load of transition metal oxides (Fe<sub>2</sub>O<sub>3</sub>, Co<sub>3</sub>O<sub>4</sub>, NiO and/or PdO) onto CeO<sub>2</sub> nanoparticles in catalytic steam decomposition of n-C<sub>7</sub> asphaltene at low temperatures. *Nanomaterials* 2019;9(3):401.

# Effect of Pressure on the Thermo-Oxidative Behavior of Saturates, Aromatics, and Resins (S-Ar-R) Mixtures



Published article in *Fuel*: [doi.org/10.1016/j.fuel.2021.122787](https://doi.org/10.1016/j.fuel.2021.122787)

Impact factor: 8.035



# Effect of Pressure on the Thermo-Oxidative Behavior of Saturates, Aromatics, and Resins (S-Ar-R) Mixtures

## Abstract

To understand the effect of pressure on the interactions between saturates, aromatics, and resins (S-Ar-R) fractions during thermo-oxidation reactions, this study evaluates the oxidation behavior of saturates:resins (S:R), saturates:aromatics (S:Ar), and aromatics:resins (Ar:R) mixtures at 0.084, 3.0 and 6.0 MPa. Oxidation was analyzed by high-pressure thermogravimetric analysis of mass change and rate for mass change. Kinetic analysis was done using a first-order kinetic model discretizing thermal profiles in four regions: oxygen chemisorption (OC), decomposition of chemisorbed oxygen-based compounds (DCO), first combustion (FC), and second combustion (SC). The results demonstrate the role of pressure on the simultaneous oxidation of S:Ar, S:R, and Ar:R mixtures. First, S:Ar thermo-oxidative profiles are described by FC and SC at 0.084 MPa, regardless of the S:Ar ratio. When the oxidation is evaluated at 3.0 and 6.0 MPa, OC, and DCO zones are observed, and the amount of oxygen chemisorbed increases as pressure increases. The same trend was observed for S:R and Ar:R systems. Between the S:Ar mixtures, the oxygen chemisorption increased as the amount of aromatics increased at 3.0 and 6.0 MPa. The structures formatted at high pressure present higher reactivity; therefore, the samples' total consumption ends at lower temperatures. During S:R oxidation, the higher the content of resins, the higher the oxygen chemisorption and the lower the temperature required to decompose the samples. Finally, the mixture between aromatics and resins shows slower kinetic rates than the other systems. The products from the oxidation of the resins' aliphatic structure react in FC with the aromatics, promoting combustion reactions at higher pressures. The kinetic parameters corroborated the results obtained. For the systems with higher chemisorption, the effective activation energy values were higher, therefore, the DCO values. The pre-exponential factor showed opposite results, given slower reaction kinetics in these stages.

## 1. Introduction

Because of its high density and viscosity, heavy oil recovery is still a considerable challenge [1]. *In-situ* Combustion is a thermal-enhanced oil recovery (TEOR) technique with an outstanding performance for heavy oil exploitation [2]. During ISC, low-temperature oxidation (LTO) and addition reactions occur, responsible for increasing the reservoir temperature and producing coke [3]. The key to the success of an *in-situ* combustion process is the rapid development of the combustion front and keeping it stable from the injection well to the producing well.

However, this is influenced by operational parameters (air injection rate, injection pressure), reservoir properties (lithology, heterogeneity, porosity, permeability, reservoir pressure), fluids composition, and the efficiency of the addition and pyrolysis reactions [4-7]. Because the composition of crude oil is complicated, it has not yet been possible to understand chemical reactions fully. There are at least four kinds of chemical components named saturates (S), aromatics (Ar), resins (R), and asphaltenes (A) [8]. Each chemical family has different pyrolysis and oxidation reactivity as pressure and temperature change. Further, they can interact during the first and second combustion [9, 10]. Therefore, heavy oil's reaction mechanism during ISC is highly complex [11].

Given this complexity, many experimental studies are focused on evaluating heavy oil oxidation through thermogravimetric analysis and differential scanning calorimetry [9, 10, 12-14]. However, obtaining detailed information about the reaction pathway is difficult because of its perplexing chemical composition. In this sense, some authors have used the S-Ar-R-A fractions to describe the oxidation of crude oil. Kok et al. [9] report that most saturates decompose during LTO (around 90 wt.%); resins only lost 40 wt%. In another study, Freitag et al. [2], using pressure differential scanning calorimetry (PDSC), report a significant difference in the heat release behavior of each S-Ar-R-A component and direct influence of aromatics, resins, and asphaltenes in saturates oxidation, since, in the presence of them, the heat release of saturates during LTO shifted from 250 to 330 °C.

The interactions between S-Ar-R-A fractions during pyrolysis and oxidation were studied by Liu et al. [15] through thermogravimetric analysis.

Compared with independent pyrolysis and oxidation of each fraction, the authors found little and poor interactions during co-pyrolysis but significant interactions during simultaneous oxidation. Simultaneous oxidation of saturates with aromatics or resins increases the beginning temperatures of LTO. Besides, modifications in the rate for mass loss peaks at HTO in both mixtures were observed.

Then, Liu et al. [16] used the kinetic information of the single and mixtures of saturates, aromatics, and resins subfraction to construct a prediction model for coke yield production. As a first instance, the activation energy of coke from the coke precursor was  $177 \text{ kJ}\cdot\text{mol}^{-1}$  and  $65 \text{ kJ}\cdot\text{mol}^{-1}$  in an inert and oxidizing atmosphere, respectively. Finally, the model successfully adjusts the experimental values with an error of less than 15%.

The previous studies were developed at atmospheric pressure. In another study, Wiehe et al. [17] discovered the contribution of each fraction to coke formation during pyrolysis and combustion experiments. The research found that saturates, aromatics, and resins transformed into asphaltenes after LTO, and asphaltenes precipitated from the oil phase and formed coke. All the experiments describe the overall S-Ar-R-A oxidation into two regions (LTO and HTO). Despite all efforts to understand the kinetic oxidation of S-Ar-R compounds, there are still several empty points to overcome. As a first instance, most studies have focused on the oxidation of individual S-Ar-R compounds. In contrast, this work contemplates the oxidation of S-Ar-R mixtures, highlighting its importance and contribution to understanding global crude oil thermal description. This study surges because of the interactions between the S-Ar-R compounds in the crude oil matrix. Along the same line, the pressure is a key variable in the thermal behavior of crude oil and its respective compounds; however, until now, there are no reports that contemplate its effect on the kinetic oxidation of S-Ar-R mixtures.

In a recent study, Medina et al. [18] evaluated the independent S, Ar, and R pyrolysis and oxidation by high-pressure thermogravimetric analysis, obtaining that both phenomena are pressure-dependent. Four thermal events were observed during oxidation tests for high pressures, defined by a peculiar behavior in the mass change and rate for mass change profiles [4]. The events were named *oxygen chemisorption region* (OC), *decomposition of chemisorbed oxygen region* (DCO), *first combustion* (FC), and *second combustion* (SC). Depending on each fraction, the different regions have a greater or

lesser contribution from the main reaction pathway that occurs during their thermo-oxidation (i.e., evaporation, pyrolysis, and oxidation) [5, 19].

Briefly, according to the literature, the S-Ar-R fractions interact with each other when they are subjected to thermo-oxidation processes. As our previous study [18] demonstrated, pressure plays a crucial role in S-Ar-R individual reactivity. In this sense, this work aims to evaluate for the first time the effect of pressure on the simultaneous oxidation between saturates:aromatics, saturates:resins, and resins:aromatics. This study offers the first mechanistic and kinetic understanding of the decomposition process by oxidation of mixtures of crude oil fractions at high pressure and high temperature.

## 2. Experimental.

### 2.1. Materials.

Saturates, aromatics and resins were isolated from Colombian extra-heavy crude oil following the Chinese national standard NBSHT 0509-2010 [15]. Crude oil presents a viscosity of  $3.0 \times 10^6$  cP, a density of 6.7 °API at 25 °C, and a content of saturates, aromatics, resins, and asphaltenes of 13.0%, 16.9%, 49.9%, and 20.2%, in mass fraction.

S-Ar-R extraction was done with *n*-heptane (99.5%), toluene (99.8%), ethanol (99.8%), and chromatographic silica, all purchased from Sigma-Aldrich (St. Louis, MO, USA). Also, S-Ar-R fractions were characterized by elemental analysis (EA), vapor pressure osmometry (VPO), <sup>1</sup>H- Nuclear magnetic resonance, <sup>13</sup>C- Nuclear magnetic resonance (NMR), and X-ray photoelectron spectroscopy (XPS), following the protocols described in a previous study [5, 20, 21]. Table 1 shows the elemental composition and molecular weight (*M<sub>w</sub>*) of S-Ar-R fractions, whereas NMR and XPS results are summarized in the previous chapter.

**Table 1.** Elemental analyses and molecular weight for saturates, aromatics, and resins.

Crude Oil Fraction	Elemental mass fraction concentration ± 0.2 %					<i>M<sub>w</sub></i> g·mol <sup>-1</sup>
	C	H	N	S	O	
S	86.63	13.28	-	-	-	432.1
Ar	83.31	10.73	<0.5	4.69	<0.5	690.5
R	80.00	9.09	1.09	6.65	3.18	957.1

Mixtures between saturates:aromatics (S:Ar), saturates:resins (S:R), and aromatics:resins (Ar:R) were prepared by diluting the respective weight of each fraction to form the ratios 2:1, 1:1, and 1:2 in dichloromethane. The systems were subjected to magnetic stirring for 2 hours and subsequent evaporation at 40 °C.

## 2.2. High-pressure thermogravimetric analysis for S:Ar, S:R and Ar:R simultaneous oxidation

Simultaneous oxidation experiments between saturates:aromatics (S:Ar), saturates:resins (S:R), and aromatics:resins (Ar:R) were done in a high-pressure thermogravimetric analyzer (HP-TGA 750, TA instruments Inc., Hüllhorst, Germany) coupled to a mass spectrometer (Shimadzu GC-MS, Tokyo, Japan). The description of both instruments is summarized in our previous studies [5, 19, 22, 23]. Three pressures were used, including 0.084 MPa, 3.0 MPa, and 6.0 MPa. Thermal experiments were run by cleaning the samples during a vacuum test at 0.00025 MPa for 10 min and then heating them from 100 to 600 °C on a heating ramp of 10 °C·min<sup>-1</sup>. The equipment carries the routine twice, once for the sample holder loaded with 1 mg of each system and once for the empty sample holder, to counteract the buoyancy effects [24-28]. Later, the gases released in the thermal decomposition were collected and analyzed by a mass spectrometer programmed to analyze gases between 0 and 200 *m/z* in a linear scan rate of ion trap of 0.03 *m/z*. Each test was done in triplicate, ensuring repeatability.

## 2.3. Fitting of thermo-oxidation curves for S:Ar, S:R, and Ar:R simultaneous oxidation

The simultaneous oxidation experimental profiles were fitted by constructing theoretical curves for each system considering the concentration of the S-Ar-R species in the mixtures and the individual oxidation of each fraction, following the procedures of Liu et al. [15]. For example, the 1:1 S:R experimental profile was theoretically constructed by the sum of the observed profiles of saturates and resins with a contribution of 50% each.

### 3. Kinetic analysis for S:Ar, S:R, and Ar:R simultaneous oxidation

Kinetic analysis was done to understand kinetic insights about S-Ar-R simultaneous oxidation at high-pressure conditions in each thermal region following the methodology described in a previous study [4, 29]. The model was resolved considering the instantaneous reactivity of each fraction represented by Equation (1), which in turn can be defined based on Equation (2), using the Ozawa-Wall-Flynn approximation for non-isothermal heating [30]:

$$r = \frac{d\theta}{dt} = f(\theta) \cdot P_{O_2}^n \cdot k \quad (1)$$

$$\ln \left[ \frac{\beta F(\theta)}{P_{O_2}^n T^2} \right] = \ln \left( \frac{k_o R}{E_a} \right) - \frac{E_a}{RT} \quad (2)$$

where  $\beta$  ( $^{\circ}\text{C}\cdot\text{min}^{-1}$ ) is the heating rate,  $P_{O_2}$  (bar) is the oxygen partial pressure,  $n$  represents the order of oxidation reaction,  $E_a$  ( $\text{kJ}\cdot\text{mol}^{-1}$ ) the effective activation energy,  $k_o$  ( $\text{s}^{-1}\cdot\text{bar}^{-n}$ ) the Arrhenius pre-exponential factor and  $R$  ( $\text{J}\cdot\text{mol}^{-1}\cdot\text{K}^{-1}$ ) the ideal gas constant. Besides,  $F(\theta)$  is represented by the expression  $\int d\theta / f(\theta) = -\ln(1-x)$  related to the volumetric consumption model [4].

## 4. Results and discussion.

### 4.1. High-Pressure thermogravimetric analysis

#### 4.1.1. Effect of pressure on simultaneous oxidation characteristics between saturates and aromatics.

Figure 1 shows the simultaneous oxidation profiles for saturates and aromatics mixtures at 0.084, 3.0, and 6.0 MPa, and Table 2 summarizes their thermogravimetric characteristics. The pressure effect is noted in the thermal profiles of the S:Ar mixtures, regardless of the S:Ar ratio used. At 0.084 MPa, S:Ar oxidation profiles are deconvoluted into two main Gaussian-Lorentzian curves, associated with two characteristic thermal events named first combustion (FC), and second combustion (SC), respectively. The thermal profiles at 0.084 MPa agree with those reported in previous work for individual oxidation of crude oil

fractions [4-6]. Then, at higher pressures (3.0 and 6.0 MPa), thermal profiles present a mass gain at temperatures  $< 250\text{ }^{\circ}\text{C}$ , which is one of the main characteristics associated with the effect of pressure on thermal profiles for individual hydrocarbons oxidation that have aromatic rings or heteroatoms (i.e., aromatics and resins) [4-6]. This event, called oxygen chemisorption (OC), is associated with the formation of oxygen-rich structures on the chemical structure of the analyzed sample. Then, another important event is the desorption/decomposition of the chemisorbed and oxygenated structures formed during OC, known as (DCO). Compared with the individual oxidation of saturates and aromatics, saturates present two main regions attributed to FC and SC during the broad range of pressures evaluated between  $100 - 800\text{ }^{\circ}\text{C}$ . By contrast, aromatics individual oxidation is decomposed into four main regions (OC, DCO, FC, and SC). It indicates that as pressure rises during S:Ar simultaneous oxidation, the contribution of saturates to SC decreases. Similarly, at 3.0 and 6.0 MPa, the four thermal events are observed in the simultaneous decomposition of S and Ar, which is associated with the aromatic ring-oxygen interactions.

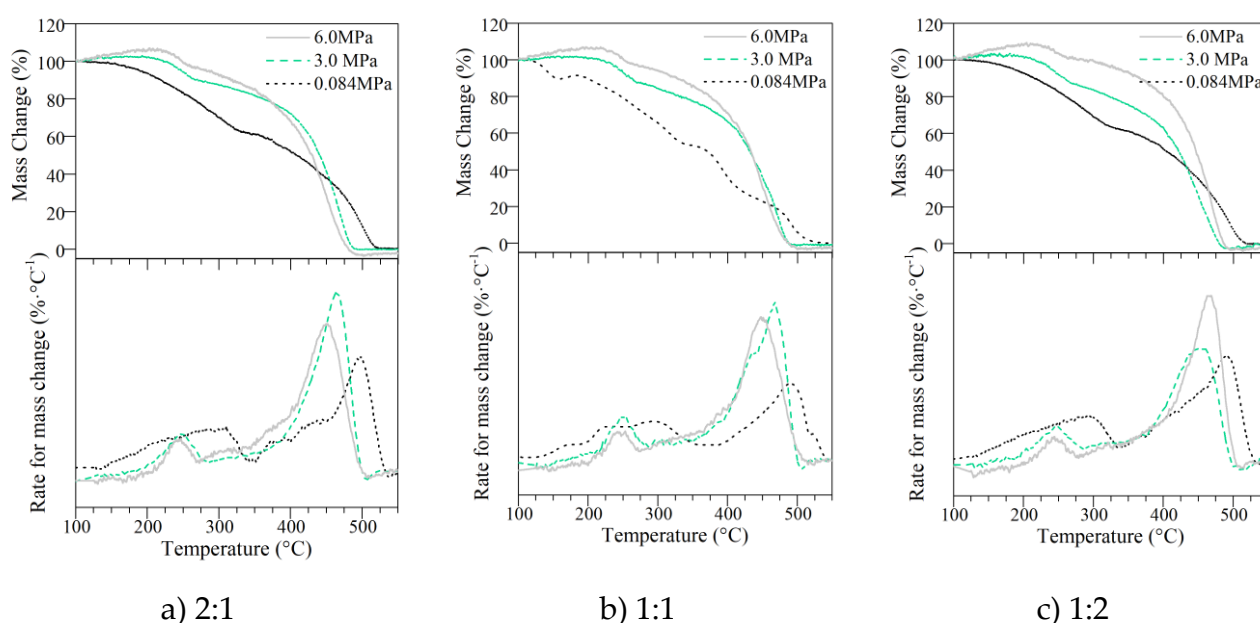


**Figure 1.** Mass percentage and rate for mass change for simultaneous oxidation of S:Ar mixtures at different S:Ar ratios of (a) 2:1, (b) 1:1, and (c) 1:2 at different pressures. Sample weight: 1 mg, heating rate:  $10\text{ }^{\circ}\text{C}\cdot\text{min}^{-1}$ , and airflow:  $80\text{ mL}\cdot\text{min}^{-1}$

Some essential characteristics observed in the thermal profiles are summarized next. During the simultaneous oxidation of saturates and aromatics,

there is less mass loss during DCO and FC than during SC, and complete decomposition ends at lower temperatures as pressure increases. It is also observed that the mixture of saturates and aromatics consumption is slower than saturates individual oxidation at low temperatures when comparing the profiles of rate for mass change. At 0.084 MPa, the main decomposition peak in FC is shifted to the right (between 50 and 100 °C) for all S:Ar systems, regarding saturates individual oxidation. As the pressure increases, the temperature shifted from the mass loss rate peak decreases. Also, the presence and amount of aromatics influence oxidative reactions at higher temperatures [31].

On the other hand, the profiles of the combustion regions in the S:Ar mixtures are similar for the individual oxidation of aromatics [3, 9, 12]. The polycondensation products from simultaneous oxidation between saturates and aromatics could have chemical and physical properties similar to aromatics, according to Barzin et al. [32]. This behavior is affected by the increase in pressure since oxygen chemisorption takes on greater importance for these systems. Therefore, aromatics change their structure to a more oxygenated one and change their interactions and reactions with saturates, forming products with greater reactivity. At 140 °C, hydrogen atoms on aromatic rings are approximately 100 times more prone to abstraction than aliphatic compounds [2, 33]. Thus, a higher content of oxygenated structures is produced, such as aromatic-based hydroperoxides. In this sense, all the S:Ar systems present higher oxygen interactions at lower temperatures than individual aromatics.

Also, it is observed that with increased saturates content, DCO ends at higher temperatures. A possible reason to explain DCO behavior for S:Ar systems is that the alkyl free radicals produce an intense cracking of alkyl chain structures, activate hydrogen atoms located at naphthenic rings to promote their opening, and break it to form small molecule products and new alkyl free radicals and the subsequent addition reactions [34]. The systems with a high aromatics content inhibit the addition reactions by H free radicals donated from naphthenic rings and aromatic rings [34].

The thermal events FC and SC are delayed to higher temperatures as the aromatic content in the system increases in the order  $6.0 < 3.0 < 0.084$  MPa. This can be explained because part of the aromatic structure acts as a natural antioxidant, especially with a high phenol content [2, 35]. Also, it is expected that phenols could be formed during OC at high pressure by oxygen added to the aromatic structure. Freitag et al. [2] suggested that phenols are highly likely to be one kind of natural antioxidant in crude oil, where only 1% by mass of phenols



will reduce the reaction speed to a large extent. Phenolic groups are functional groups that contain benzene rings with hydroxyl groups attached [36]. Adding phenolic groups to the hydrocarbons usually increases the polarity. Therefore, the chance of finding phenolic groups increases with increasing polarity [37].

The transition between FC and SC corresponds to the temperature range in which aromatic molecules become ineffective as oxidant inhibitors. This may be the main reason the 1:2 system ends the FC region at higher temperatures. Another significant result is that with saturates addition, the strong decomposition peak at 6.0 MPa for aromatics individual oxidation disappeared. This corroborates the hypothesis that aliphatic chains' presence can prevent the development of violent reactions in the aromatic nucleus at high pressures [5].

**Table 2.** Thermogravimetric characteristics for the simultaneous oxidation of saturates and aromatic mixtures at different S:A ratios of 2:1, 1:1, and 1:2. Temperature was discretized into four sub-intervals: *i*) oxygen chemisorption (OC) *ii*) decomposition of the chemisorbed oxygen (DCO) region, *iii*) first combustion (FC) region and *iv*) second combustion (SC) region at 0.084 MPa, 3.0 MPa, and 6.0 MPa.

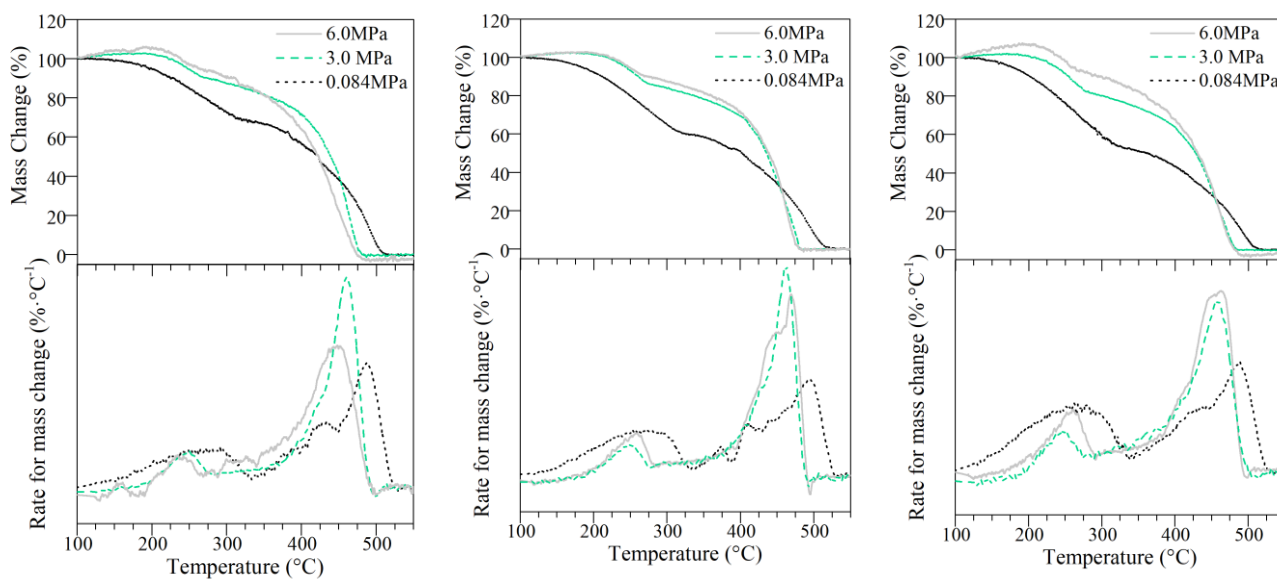
S:A ratio	Pressure (MPa)	OC Region		DCO Region		FC Region		SC Region	
		Temperature range (°C)	Mass gain (mass fraction in %)	Temperature range (°C)	Mass loss (mass fraction in %)	Temperature range (°C)	Mass loss (mass fraction in %)	Temperature range (°C)	Mass loss (mass fraction in %)
2:1	0.084	-	-	-	-	100-325	35.0	326-525	65.0
	3.0	100-220	4.0	221-280	16.0	281-430	28.0	431-495	62.0
	6.0	100-230	7.0	231-275	13.5	276-425	37.5	426-485	57.0
1:1	0.084	-	-	-	-	100-320	31.0	321-525	69.0
	3.0	100-220	6.0	221-275	17.0	276-430	26.0	431-497	63.0
	6.0	100-225	8.5	226-270	14.5	271-425	36.0	426-490	58.0
1:2	0.084	-	-	-	-	100-315	30.0	316-525	70.0
	3.0	100-210	6.2	211-270	21.2	271-408	13.0	409-495	72.0
	6.0	100-220	9.5	221-250	20.5	251-405	24.0	406-490	65.0

#### 4.1.2. Effect of pressure on simultaneous oxidation characteristics between saturates and resins

Figure. 2 shows co-oxidation thermogravimetric results for saturates and resins mixtures at different S:R ratios, and Table 3 summarizes the thermogravimetric characteristics. Results indicate that pressure has an important effect on the thermal profiles for saturates-aromatics simultaneous oxidation. From the mass change profiles in Figure 2, low-pressure S:Ar systems (0.084 MPa) do not show oxygen chemisorption, that is, an increase in the mass

at low temperatures. In contrast, high-pressure systems (3.0 MPa and 6.0 MPa) gain mass during OC; they follow individual resins' oxidation behavior. The mass gained increases as pressure increases regardless of the S:R ratio. As the amount of resins increases in the mixture, the OC% increases too. Additionally, the systems at 6.0 MPa end their conversion at lower temperatures than 3.0 and 0.084 MPa. It is noted that the pressure benefits the thermo-oxidative decomposition of the different systems. Comparing the S:R oxidation at high pressure, the S:Ar systems are decomposed at higher temperatures than S:R systems, directly associated with the percentage and type of structures formed during OC, which seem to be more reactive in saturates-resins than in saturates-aromatics.

Regarding the mixing ratios, as the resins' content increases, the oxygen chemisorption increases for the systems evaluated at 3.0 and 6.0 MPa. This agrees with individual oxidation for both fractions since saturates did not have a marked region for OC and DCO at low and high pressures, and resins had the highest chemisorption percentage. The oxygen chemisorption on the individual resins was higher than in all S:R ratios at all evaluated pressures. Resins increase their mass 7.0 and 11.0% at 3.0 and 6.0 MPa, respectively, whereas in the best of S:R systems, an increase of mass of 5.5% and 10.1% is observed for the same pressures. The relationship is clear: the greater the number of functional groups, the chemisorption of oxygen increases, and given the S:R interactions, there is a reduction in the interaction of active sites in the resins for the anchoring of O<sub>2</sub> molecules.



a) 2:1

b) 1:1

c) 1:2

**Figure. 2.** Mass percentage and rate for mass change for simultaneous oxidation of S:R mixtures at different S:R ratios of (a) 2:1, (b) 1:1, and (c) 1:2 at different pressures. Sample weight: 1 mg, heating rate: 10 °C·min<sup>-1</sup>, and airflow: 80 mL·min<sup>-1</sup>

Contrasting with individual oxidation for saturates, the intensity of the rate for mass change peaks in FC at low and high pressure of S:R mixtures are reduced considerably, even for systems with more than 50% saturated (S:R = 2:1). Additionally, compared to the oxidation of individual saturates, this same peak in the mixtures shifts approximately 20 °C and 40 °C to the right for the high and low-pressure systems, respectively. Displacement is also increased in the order 2:1 < 1:1 < 1:2 due to their higher molecular weight. It is possible that resins and saturates reacted during DCO through polycondensation reactions, retarding the reaction rate, and the interactions decreased as pressure increased.

It is reported in the literature that resins can act as potent antioxidants as they prevent rapid exothermic behavior at low temperatures once mixed with saturates [31]. Kök et al. [38] report that oxygen does not affect resins until very high temperatures. However, it is appreciated that pressure plays a significant role in changing the resins' original structure at low temperatures and modifying their interaction with saturates. According to Freitag et al. [2], when radicals of antioxidants are gradually consumed, the saturates' rapid reaction is restored. Thus, during OC, the resin radicals are activated by O<sub>2</sub> chemisorption, and the antioxidant nature of the resins is avoided.

**Table 3.** Thermogravimetric characteristics for the simultaneous oxidation of saturates and resins mixtures at different S:R ratios of 2:1, 1:1, and 1:2. The temperature was discretized into four sub-intervals: *i*) oxygen chemisorption (OC) *ii*) decomposition of the chemisorbed oxygen (DCO) region, *iii*) first combustion (FC) region and *iv*) second combustion (SC) region at 0.084 MPa, 3.0 MPa, and 6.0 MPa.

S:R ratio	Pressure (MPa)	OC Region		DCO Region		FC Region		SC Region	
		Temperature range (°C)	Mass gain (mass fraction in %)	Temperature range (°C)	Mass loss (mass fraction in %)	Temperature range (°C)	Mass loss (mass fraction in %)	Temperature range (°C)	Mass loss (mass fraction in %)
2:1	0.084	-	-	-	-	100-325	35.0	326-510	65.0
	3.0	100-210	4.0	211-260	11.0	261-425	30.0	426-475	63.0
	6.0	100-200	7.5	201-250	12.5	251-400	45.0	401-470	47.0
1:1	0.084	-	-	-	-	100-330	40.0	331-520	60.0
	3.0	100-208	4.8	209-265	13.0	266-430	33.0	431-480	58.8
	6.0	100-210	8.0	211-270	15.0	271-425	35.0	426-475	55.0
1:2	0.084	-	-	-	-	100-335	45.0	336-525	55.0
	3.0	100-210	5.5	211-270	19.0	271-408	21.5	409-480	65.0
	6.0	100-215	10.5	216-280	19.5	281-405	30.0	406-475	61.0

Comparing the S-Ar oxidation at high pressure, the S-R systems conclude the oxidative process before S-Ar systems, directly associated with the percentage and type of structures formed during OC, which seem to be more reactive in resins than in aromatics. First, it was demonstrated that the aromatic structure favors OC; however, the heteroatoms have a crucial role in oxygen anchorage; resins (with higher aromaticity factor and higher heteroatoms content) present a higher capacity for interacting with O<sub>2</sub> than aromatics.

#### 4.1.3. Effect of pressure on simultaneous oxidation characteristics between aromatics and resins

Simultaneous oxidation results for aromatics and resins at different Ar:R ratios are revealed in Figure 3, while Table 4 summarizes the thermogravimetric characteristics of each thermal event. The thermal reactivity followed by the mixtures is similar to the behavior of the individual fractions at low pressure. However, some specific differences were found in the reactivity of the mixtures as the Ar:R ratio was changed.

In the first instance, it is observed that the oxidation rate of the Ar:R mixtures is slower than individual fractions, increasing in the order Ar:R 2:1 < 1:1 < 1:2. Comparing the mass change at a fixed temperature, regardless of the

pressures used, there is a more significant mass loss in the 1:2 system followed by the 1:1 and 2:1 systems.

With the increase in pressure, it is observed the appearance of the OC and DCO regions. In comparison with the S:Ar and S:R systems, the chemisorption was higher in the Ar:R mixtures because, in the presence of saturates, the active sites for the oxygen addition were only found in the other fractions. At low temperatures during DCO, an individual aromatics' oxidation behavior is observed in the mass change rate profiles. For high pressures, systems containing at least 50% resins increase the peak intensity between 250 and 300 °C. This result suggests that the resin products in DCO react later with the aromatics, promoting the combustion reactions to a greater degree for high-pressure systems. Because resins lose more mass in DCO when aromatics are present, the SC process changes for both fractions. First, at 6.0 MPa, violent reactions in the aromatic ring are eliminated due to the lower condensation degree of the aromatic ring in the presence of aliphatic structures from resins and its reactivity with O<sub>2</sub>. Besides, one main peak is observed, described by the two combustion regions (FC and SC). During FC, the coke precursors are produced higher for Ar-R simultaneous oxidation than for the individual fractions (as Table 4 shows).

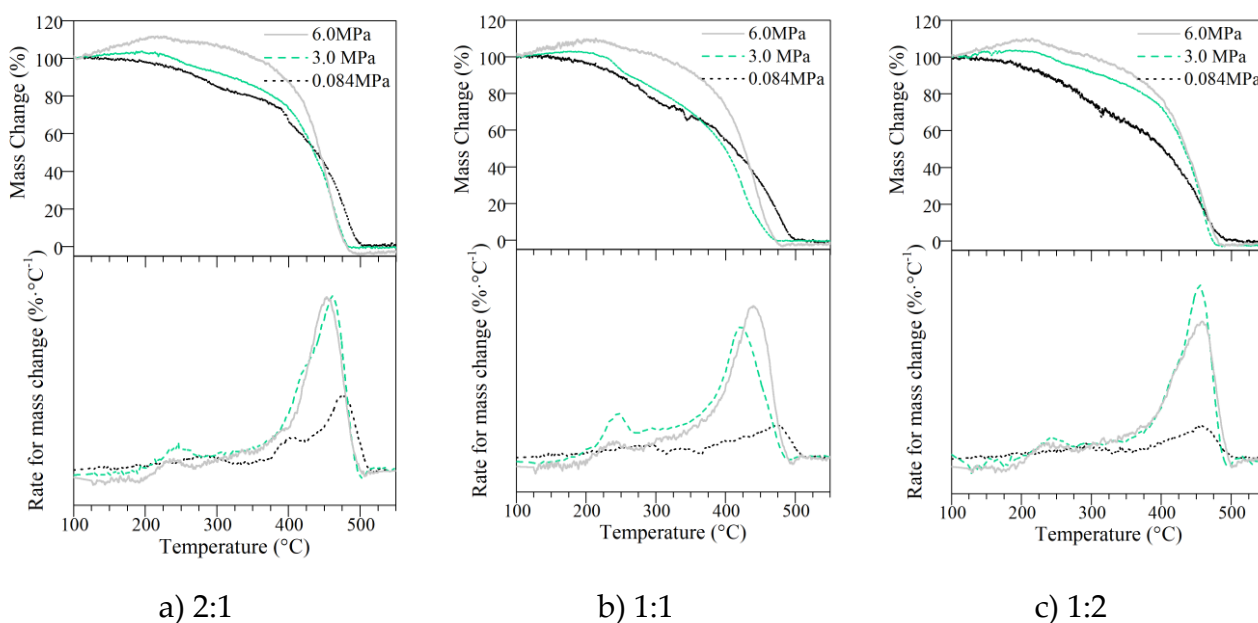


**Figure 3.** Mass percentage and rate for mass change for simultaneous oxidation of Ar:R mixtures at different Ar:R ratios of (a) 2:1, (b) 1:1, and (c) 1:2 at different pressures. Sample weight: 1 mg, heating rate: 10 °C·min<sup>-1</sup>, and airflow: 80 mL·min<sup>-1</sup>

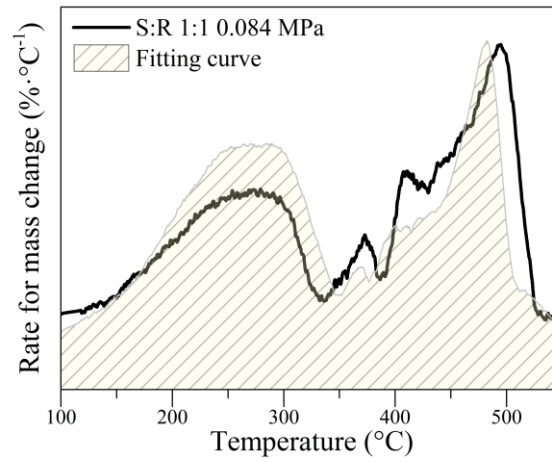
However, FC ends at lower temperatures for all systems at high pressure. Some authors report that the branching of aliphatic hydroperoxides takes place up to 350 °C, at atmospheric pressure [39]. Mixing both fractions promotes the branching of aromatic hydroperoxides at similar temperatures and subsequent isomerization. With increasing pressure, more hydroperoxides will likely form in OC; therefore, FC ends at lower temperatures. These results indicated that the interactions should be considered when using the S-Ar-R results to study the heavy oil oxidation process, especially at high-pressure conditions.

**Table 4.** Thermogravimetric characteristics for the simultaneous oxidation of aromatics and resins mixtures at different A:R ratios of 2:1, 1:1, and 1:2. Temperature was discretized into four sub-intervals: *i*) oxygen chemisorption (OC) *ii*) decomposition of the chemisorbed oxygen (DCO) region, *iii*) first combustion (FC) region, and *iv*) second combustion (SC) region at 0.084 MPa, 3.0 MPa, and 6.0 MPa.

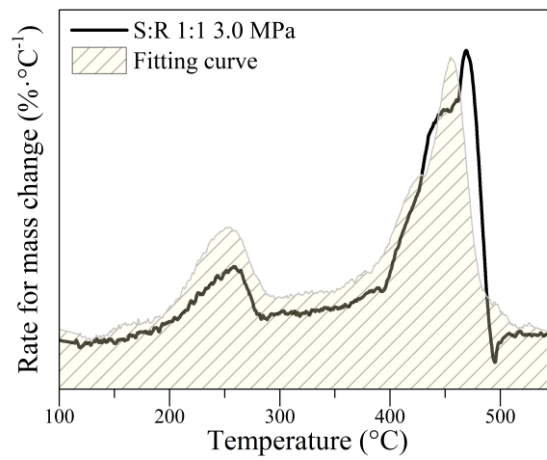
A:R ratio	Pressure (MPa)	OC Region		DCO Region		FC Region		SC Region	
		Temperature range (°C)	Mass gain (mass fraction in %)	Temperature range (°C)	Mass loss (mass fraction in %)	Temperature range (°C)	Mass loss (mass fraction in %)	Temperature range (°C)	Mass loss (mass fraction in %)
2:1	0.084	-	-	-	-	100-310	20.0	311-515	80.0
	3.0	100-220	6.0	221-280	9.0	281-425	32.0	426-495	65.0
	6.0	100-230	10.0	231-255	6.0	256-410	44.0	411-490	60.0
1:1	0.084	-	-	-	-	100-305	22.0	306-520	78.0
	3.0	100-220	7.0	221-275	13.0	276-435	59.0	436-490	35.0
	6.0	100-225	11.5	226-250	9.5	251-415	52.0	416-480	50.0
1:2	0.084	-	-	-	-	100-300	25.0	301-525	75.0
	3.0	100-210	7.5	211-270	10.0	271-450	52.5	451-485	45.0
	6.0	100-220	12.5	221-240	10.5	251-425	62.0	426-480	40.0

#### 4.2. Fitting for the S:Ar, S:R, and Ar:R simultaneous oxidation profiles

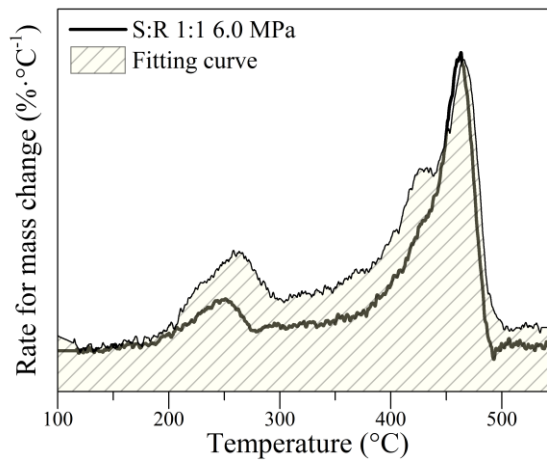
Figures 4-6 show the comparison of S:R, Ar:R, and Ar:R thermogravimetric profiles and the superposition of S-Ar-R reaction results according to mass ratio (1:1) during oxidation at different pressures. Figures 4-6 exhibits huge differences between the fitting and experimental curves for each system depending on the decomposition zone.



a)



b)



c)

**Figure 4.** Rate for mass change curves for S:R mixtures at a fixed S:R ratio (1:1) and fitting curves of S:R superposition at a) 0.084 MPa, b) 3.0 MPa, and c) 6.0 MPa.

For simultaneous oxidation of S:R (Figure 4), it is observed that for DCO and SC regions, the rate for mass change profile of the fitting curve was

higher than that of the measurement curve for all pressures evaluated. This phenomenon disclosed that the evident inhibiting effect primarily existed among saturates and resins at low temperatures, which was near related to the findings concluded by some researchers. Freitag et al. [14] stated that saturates involved a few natural oxidation inhibitors that restricted oxidation rates by rapidly consuming an essential intermediate in the low-temperature reaction chain. At high pressures, both curves' intensity difference differs to a greater degree, given the rapid consumption of the saturates and a faster reaction rate. On the other hand, for the SC region, when the pressure is less than 3.0 MPa, it is observed that the main decomposition peak runs to the left in the fitting curve, while at 6.0 MPa, an almost perfect adjustment is obtained. This suggests that pressure can influence both fractions' interactions, as explained in the previous section.

Furthermore, at 6.0 MPa in the fitting curve, appears another rate for mass change peak at 425 °C. The incorrect adjustment is probably associated with the fact that some of the products from saturates oxidation react with resins at higher temperatures, promoting fuel deposition through polycondensation reactions (exothermic effect), lengthening the FC reactions, and forming a single peak, described by both combustion stages. All these differences demonstrate the significant interactions between saturates and resins during oxidation.

Regarding the simultaneous oxidation of aromatics and saturates (Figure 5), it was found that the different regions behave differently in the adjustment curves according to the pressure. At 0.084 MPa, the FC peak of the S:A simultaneous oxidation coincided with the fitting curve, while in SC, the experimental profile is always above the adjusted one. This implies that saturates, and aromatic ones do not interact strongly in FC at low pressure, which follows what is reported in the literature [12, 15].

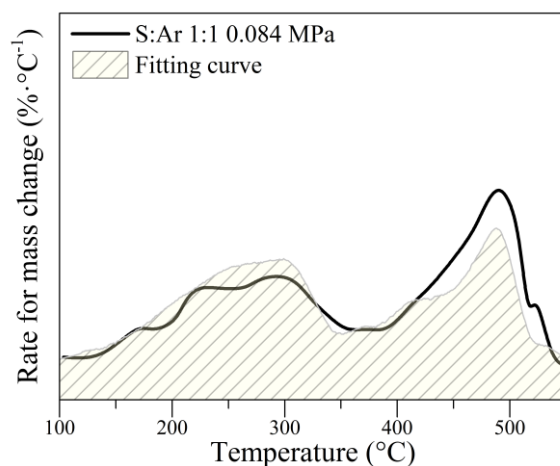
With increasing pressure, it is observed that the polycondensation products of S:Ar differ from each other since, in SC, both curves show different adjustments. For systems with a better fit (0.084 MPa), products with physical and chemical properties similar to those of aromatics are intuited at the end of FC.

For the systems evaluated at 0.084 and 3.0 MPa, a greater intensity was found in the fitting rate of mass loss than in the experimental at low temperatures. Like saturates, aromatics have natural oxidation inhibitors in their chemical structure, such as phenol derivatives, whose primary role

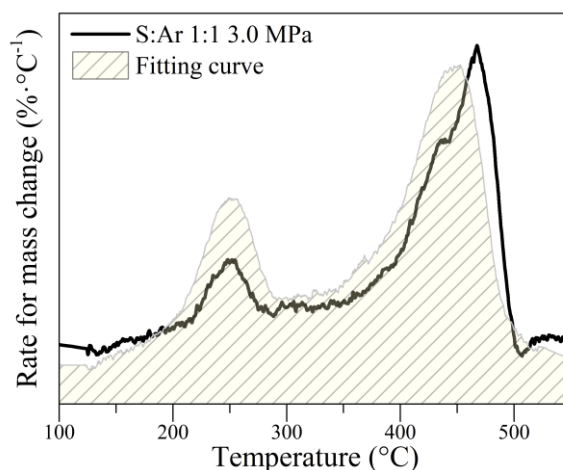


occurs in the early stages of oxidation, and oxidation reactions do not occur unless the rate of radical formation exceeds the rate of inhibition, or all inhibitors were oxidized and inert (FC end).

At 6.0 MPa, the two curves' comparison indicated that aromatics' strongest peak at 425 °C disappears when the aromatics co-oxidize saturates. This suggests that the aromatic oxygen-adding reaction products reacted with the saturates at low temperatures; therefore, the aromatic structure presents a lower condensation degree than in the absence of saturates, and, thus, violent exothermic reactions are avoided during SC.



a)



b)

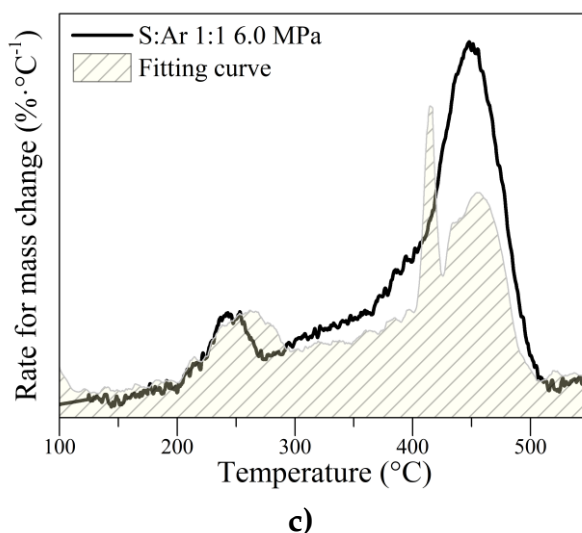
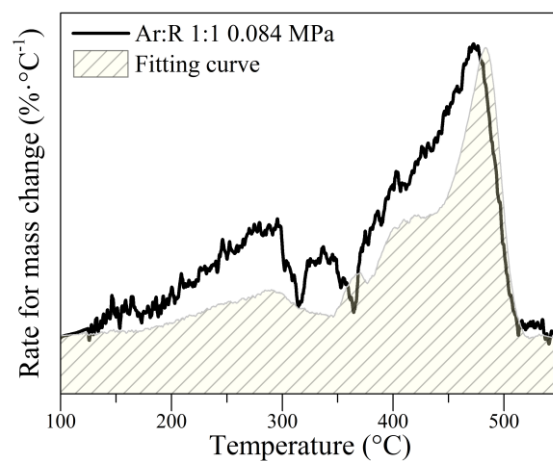


**Figure. 5.** Rate for mass change curves for saturates:aromatics mixtures at a fixed S:Ar ratio (1:1) and fitting curves of S:Ar superposition at a) 0.084 MPa, b) 3.0 MPa, and c) 6.0 MPa.

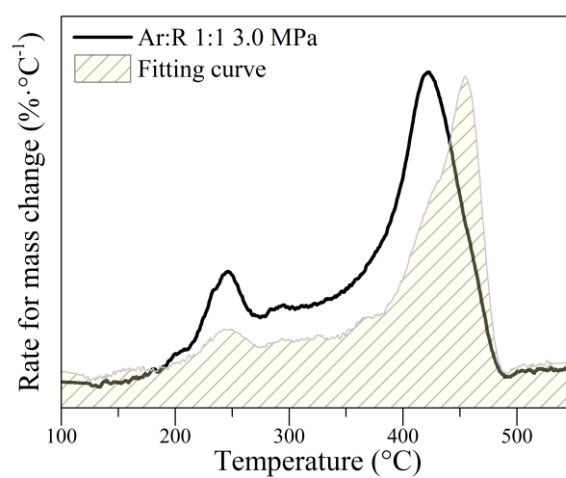
Figure 6 shows the fitting results for Ar-R simultaneous oxidation. Results show differences between the fitting and experimental curves for all regions at low and high pressures. Unlike the other systems, the experimental curve for Ar-R simultaneous oxidation remains above the fitting curve for the systems evaluated at 0.084 MPa and 3.0 MPa, indicating that the products of both reactions are reacting with each other, promoting exothermic effects. However, at 6.0 MPa, there appears to be a good fit during DCO. At the end of this region at 6.0 MPa, both curves differ significantly from those obtained at lower pressures. This means that the products obtained from DCO differ from those obtained individually by both fractions. For example, the predominant peak at high temperatures for aromatics disappears, meaning that resins' aliphatic structure prevents violent reactions that can occur in oxygenated and polycondensed structures during combustion regions. The peak mass loss rate shifts slightly to the left on the fit curve at 0.084 MPa and 3.0 MPa.

Finally, the experimental rate for mass change curves at high temperatures (FC, and SC stages) was higher than the fitting curves; thus, resins may also react with the products from DCO reactions of aromatic.

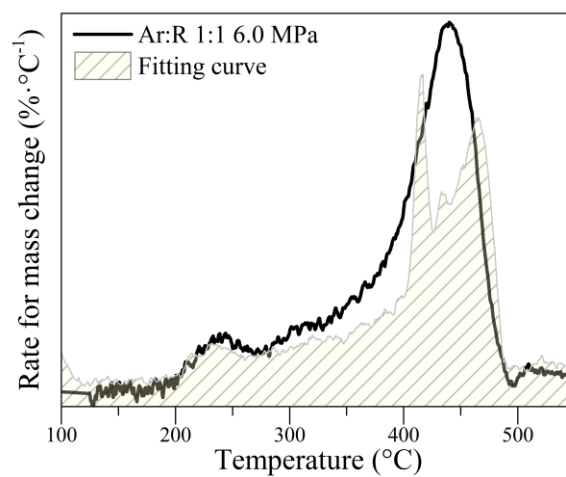
The results of saturates, aromatics, and resins simultaneous oxidation indicated that the interactions should be considered when using the S-Ar-R-A results to study the heavy oil oxidation process.



a)



b)



c)

**Figure 6.** Rate for mass change curves for aromatics:resins mixtures at a fixed Ar:R ratio (1:1) and fitting curves of Ar:R superposition at a) 0.084 MPa, b) 3.0 MPa, and c) 6.0 MPa.

### 4.3. Gaseous products

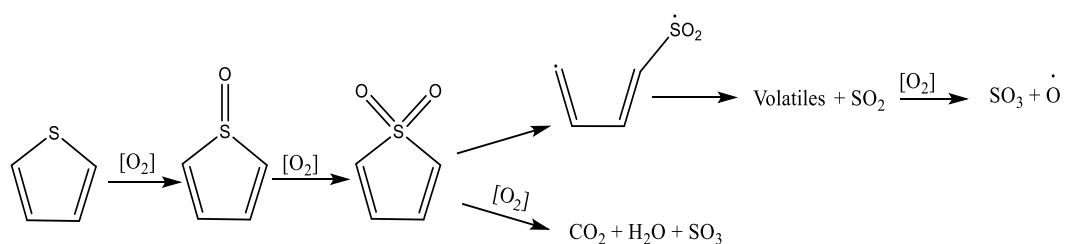
The amount of gases produced during the thermal events DCO, FC, and SC are presented in Figures 7-9 for the simultaneous oxidation of S:Ar, S:R, and Ar:R at different pressures, respectively. The specific percentage (%vol) of the gases in the oxidation process was calculated based on their sensibility factor, following the protocol described in previous studies [5, 19]. For this work were considered the thermal release profiles of several gases, including CO, CO<sub>2</sub>, light hydrocarbons (CH<sub>4</sub>, C<sub>3</sub>H<sub>6</sub>, C<sub>4</sub>H<sub>8</sub>, C<sub>5</sub>H<sub>12</sub>, C<sub>2</sub>H<sub>6</sub>), nitrogen-based gases (NO, NO<sub>2</sub>), and sulfur-based gases (SO<sub>2</sub> and SO<sub>3</sub>).

#### 4.3.1. Gaseous products released from simultaneous oxidation of S:Ar mixtures

Simultaneous oxidation between saturates and aromatics at different pressures is shown in Figures 7. In the first instance, it is observed that the production of NO<sub>x</sub> and SO<sub>x</sub> gases is similar in the three stages DCO, FC, and SC for all pressures if the aromatic content is less than 50%. For the 1-2 system, it is obtained at low pressure that there is a short evolution of these gases during FC, especially sulfur gases. In contrast, at 3.0 and 6.0 MPa, their release increases in the early stages, indicating the importance of OC thermal event, characteristic of high-pressure systems, capable of oxidizing aromatic structures that contain S and N, such as thiophenes, pyrrole, and pyridines. Further, in the literature, it has been shown that the NO<sub>x</sub> formation mechanism depends on the nitrogen source [40]. In the case of an S:Ar system, nitrogen oxides are produced due to the presence of nitrogen-based heterocyclic compounds in aromatic structure and their interaction with oxygen in combustion air; hence a similar behavior of individual aromatic oxidation was found. The reaction pathway follows the Zeldovich mechanism [41]. NO produced by this mechanism results from the interaction between nitrogen and diatomic oxygen. It can be oxidized to NO<sub>2</sub> due to oxygenated radicals such as OH or OH<sub>2</sub>, which can be formed in the oxidation of aliphatic compounds during the OC stage. Also, it is reported that NO<sub>x</sub> can be produced by the interactions between aliphatic or aromatics free radicals and oxygen based on the reaction pathway proposed by Lopatin et al. [42], where aliphatic radicals react with nitrogen in the air to produce hydrogen cyanide (for methane radicals) or nitriles (for bigger alkyl-radicals) as intermediaries to form nitrogen oxides [42]. In the case of aromatics, these compounds will break into aliphatic structures at high enough temperatures, and the reaction will be similar to those for non-cyclic compounds.

The most probable sulfur forms in S:Ar systems are heterocyclic compounds such as thiophene and its polyaromatics derivatives. The reaction pathway that involves the sulfur oxides synthesis, in general, follows a similar mechanism for all sulfur-based compounds due to the high affinity between oxygen atoms that originates the oxidation, and the sulfur atoms present in the aromatic structure. The polar attraction between oxygen and sulfur leads to the selective oxidation of sulfur-based compounds without the rupture of C-C and C-S bonds [43] to produce sulfoxides and, later, the sulfone derivative. According to Javadi et al. [44] and Benson et al. [45], the sulfonyl group (SO<sub>2</sub>) can be removed from the sulfone structure by thermal degradation or low-temperature oxidation. Because the initial sulfide group's oxidation weakens the C-S bond, it facilitates its rupture and subsequent desulfurization.

As shown, SO<sub>2</sub> and SO<sub>3</sub> release is observed from the DCO stage for all systems, including those with predominantly saturated content. Sulfur compounds normally oxidize at relatively low temperatures [44]. The earlier oxidation of saturates compounds leads to the production of alkyl peroxy radicals, which can contribute as oxidant agents for sulfoxides and sulfones formation. Furthermore, aromatic compounds substituted with aliphatic chains can increase the production and diversity of volatile compounds produced during the initial oxidation pathway. Subsequent oxidation of sulfones leads to the production of volatile compounds derived from the precursor molecule. Furthermore, this reaction produces SO<sub>2</sub>, which can also be oxygenated to produce SO<sub>3</sub>. Based on the oxidation pathway proposed by Izadifard et al. [46] for the oxidation of sulfolane, it is also possible to wait for the oxidation of sulfones to produce CO<sub>2</sub>, SO<sub>3</sub>, and water in an oxygen-rich environment, as shown the Scheme 1.

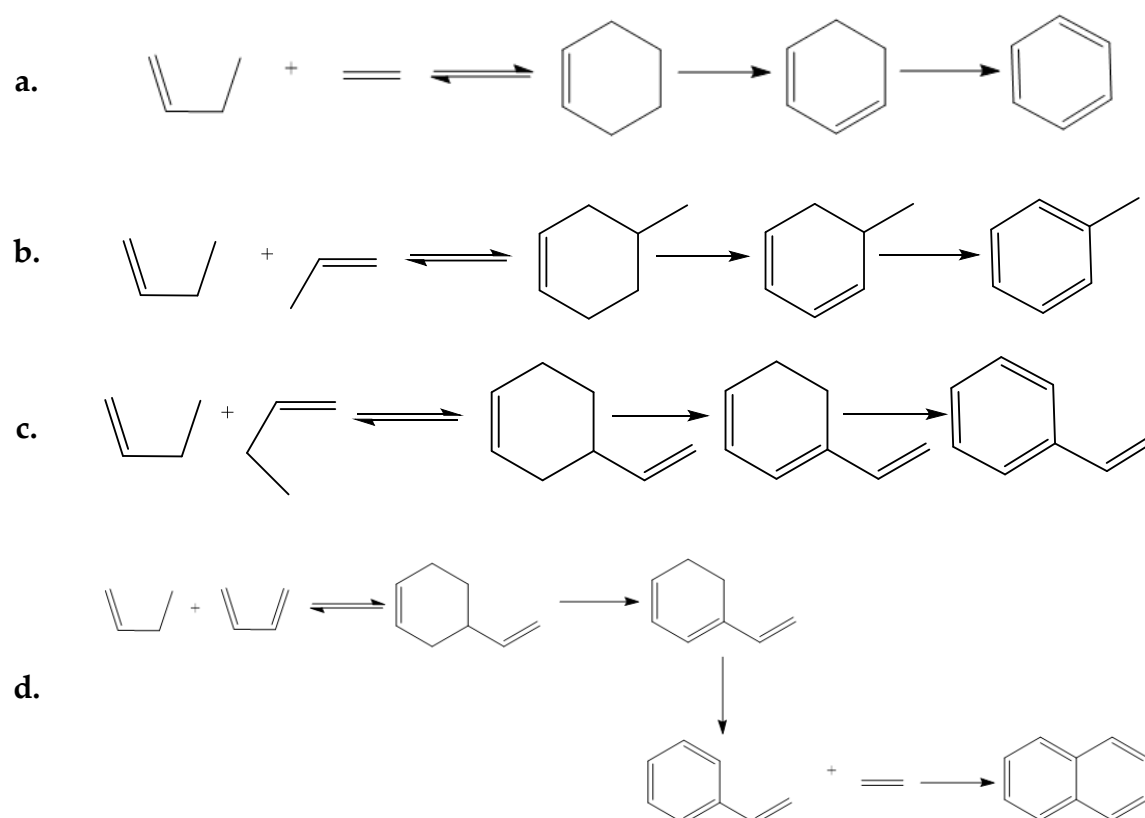


**Scheme 1.** Reaction pathway for SO<sub>3</sub>, SO<sub>2</sub>, and CO<sub>2</sub> release from thiophene structure.

The production of light hydrocarbons was higher for all pressures. It was found that during DCO, a higher amount of LHC is released compared to combustion regions. Greensfelder et al. [47] suggest that the oxidation at low

temperatures of aliphatic compounds usually has as final products alpha-olefins, ethylene ( $C_2H_4$ ), propylene ( $C_3H_6$ ), methane ( $CH_4$ ), and ethane ( $C_2H_6$ ) [47]. The olefins produced by the low-temperature oxidation and thermal degradation of alkanes and their subsequent accumulation are possible precursors of the synthesis and condensation of aromatic compounds following the Diels-Alder reaction mechanism (Scheme 2a-c) [48]. The schemas give the mechanisms for benzene, toluene, and alkyl aromatics formation by Diels-Alder reaction with the light olefins, produced by the thermal degradation of the alkanes

The continuous condensation of aromatics and its interaction with olefins following the same mechanism may also be a precursor of bigger polyaromatic compounds following the Diels-Alder mechanism (Scheme 2b) [48]. Therefore, it is possible that in the presence of saturates, aromatics increase their degree of condensation, delaying their opening and subsequent rupture until the second combustion and producing LHC in all stages. Notably, as the pressure increases, there is a greater production of LHC in FC than in SC, which suggests the decomposition of aromatic rings previously condensed at lower temperatures.



**Scheme 2.** Reaction pathway for forming a) benzene, b) toluene, and c) alkyl aromatics and condensation of d) aromatics by Diels-Alder reaction with the light olefins, produced by the thermal degradation of alkanes.

In addition, for a higher content of saturates, the production in the combustion stages decreases, given the higher degree of condensed structures that could contribute to coke formation.

The final combustion of aromatic compounds occurs at higher temperatures than in aliphatic compounds [2]. This may also allow the production of bigger polyaromatic structures, which can be considered new resins. This also agrees with the simplified reaction pathway proposed by Freitag et al. [49] for the oxidation of S-Ar-R-A fractions [49]. The thermal decomposition of saturates produces a fraction of gases, light intermediates, and aromatics. In the case of aromatics, the reaction leads to the production of gases, lightweight intermediates, aliphatic compounds, and resins produced by the condensation of polyaromatic compounds, just as Cypres et al. [48] suggested. New S-Ar-R fractions produced from the oxidized S-Ar-R fraction react similarly to the original fraction [49].

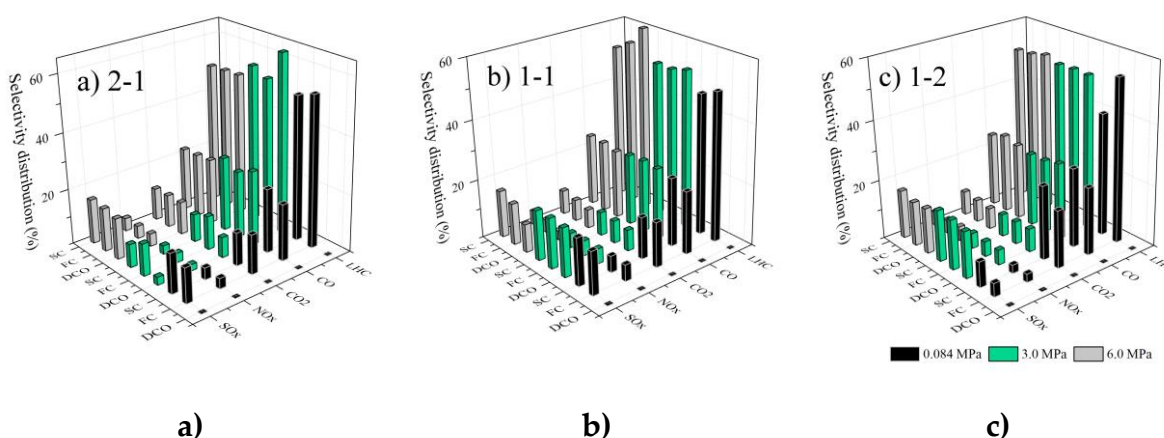


**Figure 7.** Selectivity distribution of light gases produced from simultaneous oxidation of saturates and aromatics at different S:Ar ratios a) 2:1, b) 1:1, and c) 1:2, at different pressures.

#### 4.3.2. Gaseous products released from simultaneous oxidation of S:R mixtures

The evolved gases from the simultaneous oxidation of S:R at 0.084 MPa, 3.0 Mpa, and 6.0 Mpa are shown in Figure 8. For the gaseous products from the S:R simultaneous oxidation, it is observed that there is a contribution of Nox, Sox, LHC, CO, and CO<sub>2</sub>. As the resin content in the system increases, the production of Nox and Sox increases, which is in accordance with its chemical composition. The presence of resins promotes the production of CO over other gases; however,

The presence of saturates decreases the production of CO<sub>2</sub>, stimulating LHC production because saturates are mainly composed of *n*-alkanes, isoparaffins, and cycloparaffins. The high output of CO<sub>2</sub> and CO, is due to the content of C=O bonds with stretching vibration. The C=O in saturates reacts with O<sub>2</sub> to produce -COOH.

Further, the -COOH is continuously oxidized, generating aldehydes, alcohols, and ketones in the OC stage and CO, CO<sub>2</sub>, CH<sub>4</sub> in the rest of the stages [50]. The increase in pressure changes systems with a low content of saturates to a greater degree, corroborating the previous section's results. The 1-2 S:R system shows that in SC, the production of CO increases with increasing pressure. Similarly, Nox and Sox gases increase their production in FC and DCO at high pressure due to the increased reactivity during the oxidation of nitrogen and sulfur compounds in the OC stage.

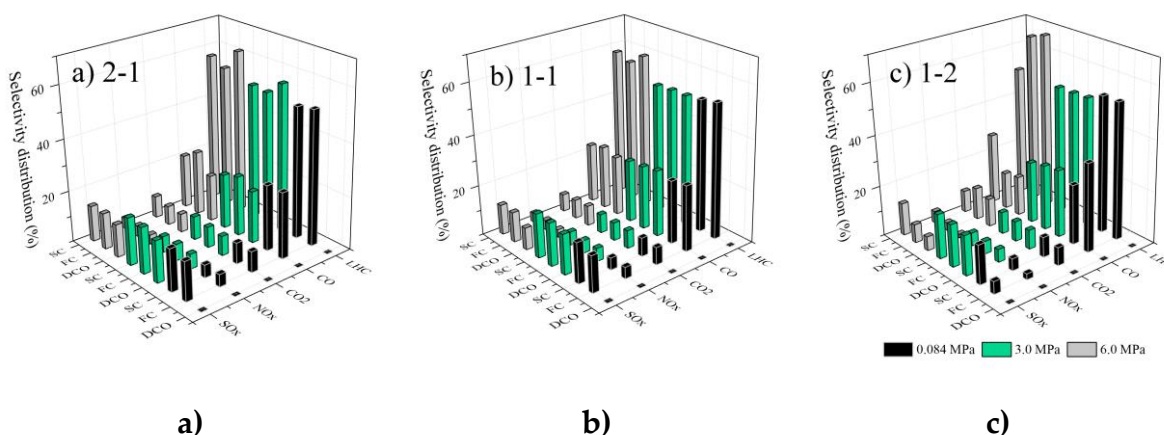


**Figure 8.** Selectivity distribution of light gases produced from simultaneous oxidation of saturates and resins at different S:R ratios a) 2:1, b) 1:1, and c) 1:2, at different pressures.

#### 4.3.3. Gaseous products released from simultaneous oxidation of Ar:R mixtures

The released products from the simultaneous oxidation between aromatics and resins at different pressures are shown in Figure 9. In these systems, a reduction in the production of some LHC (C<sub>5</sub>H<sub>12</sub>, C<sub>4</sub>H<sub>8</sub>, C<sub>2</sub>H<sub>6</sub>) concerning the S:Ar and S:R simultaneous oxidations is observed due to the reduction of aliphatic compounds. The distribution of LHC increases in the order Ar:R 2:1 < 1:1 < 1:2, for all the pressures. On the other hand, the production of Nox and Sox increases to a higher degree in the DCO region for systems where the resins' content is greater than 50%, associated with the content of heteroatoms in aliphatic chains,



whose oxidation is possible at low temperatures. Finally, it is observed that the pressure for high aromatics content increases CO production in DCO, and for high content of resins, it decreases it in the same region.

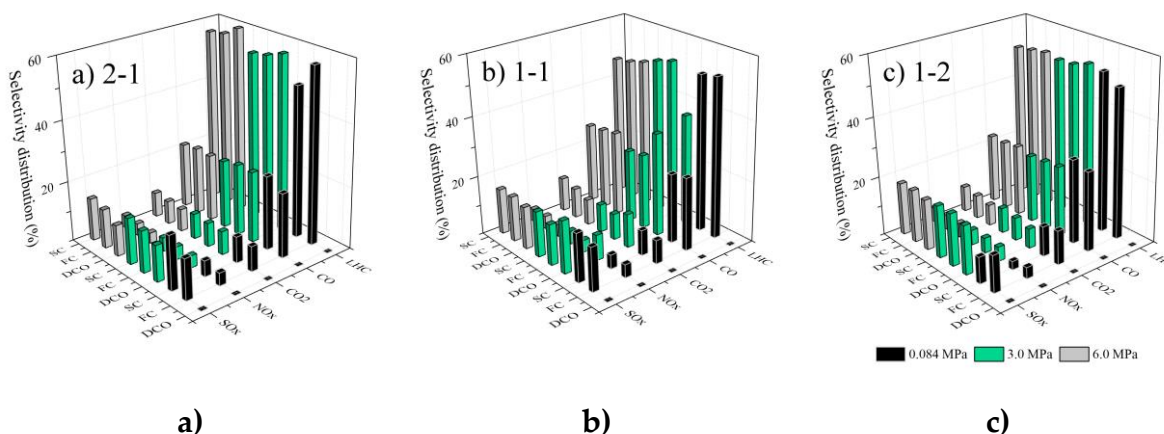


**Figure 9.** Selectivity distribution of light gases produced from simultaneous oxidation of aromatics and resins at different Ar:R ratios a) 2:1, b) 1:1, and c) 1:2, at different pressures.

#### 4.4. Kinetic analysis

Kinetic parameters for simultaneous oxidation of S-Ar-R fractions at different pressures were obtained from thermogravimetric experiments using a first-order kinetic model, considering their discretization in four different thermal events (OC, DCO, FC, and SC), obtaining a better fit for  $n = 1$  ( $R^2 > 0.98$ ). Figure 10 exhibits the activation energy values obtained from the fitting straights of  $\ln\left[\frac{\beta(-\ln(1-x))}{P_{O_2}^n T^2}\right]$  as a function of  $\frac{1}{RT}$  for S:R, S:Ar, and Ar:R simultaneous oxidation.

From panel a), it is noted that when pressure rises,  $E_a$  for simultaneous oxidation of saturates and resins increases in OC and DCO; and decreases in FC and SC stages. Compared to individual resins ( $38 \text{ kJ}\cdot\text{mol}^{-1}$  at 3.0 Mpa and  $36 \text{ kJ}\cdot\text{mol}^{-1}$  at 6.0 Mpa), oxidation of S:R systems during DCO shows a considerable increase at 3.0 Mpa and 6.0 Mpa. At high pressure, the saturates would be believed to react with the oxygenated fractions formed during OC in the resins' molecular structure. This is corroborated by the  $E_a$  increase in the order  $2:1 < 1:1 < 1:2$ .

The main difference between both fractions' simultaneous oxidation and individual oxidation systems is that the energy during FC decreases with pressure. Additionally, as the resin content increases by more than 50%, the energy required in FC exceeds that required in SC. As mentioned previously, the saturates' contribution occurs mainly in the reactions in FC, so systems with a high content of saturates, promote greater energy expenditure during that stage. On the other hand, when increasing the pressure from 3.0 Mpa to 6.0 Mpa, the energy difference between both regions increases during SC at high pressure because of the interactions between the products of the decomposition of saturates in FC and the resins increase.

For simultaneous oxidation between saturates and aromatics, similar behavior of saturates:resins simultaneous oxidation was found. For the DCO stage, it was observed that both simultaneous oxidations present similar values in the activation energy, indicating that the saturates tend to interact to a greater extent with the oxidized products in the aromatic structure. Specifically, the DCO values for  $E_a$  in S:Ar systems are slightly lower than in S:R due to the greater number of oxygenated structures formed in the resins. In this same sense, the pressure increases the values of  $E_a$  in DCO. For the combustion regions, different characteristics were found. In the first instance, during FC the  $E_a$  increased with the increase of the aromatic content in the system for all the pressures evaluated, while its value decreased as the pressure increased. In this sense, the lowest energy requirement was obtained for the S:Ar 2:1 system at 6.0 Mpa. For the second combustion region, a similar behavior was obtained, with the difference that more energy was required to carry out the decomposition reactions. The interactions of these two fractions are of great importance in DCO; however, according to the results, the decomposition of a high content of aromatic rings is still required in SC.

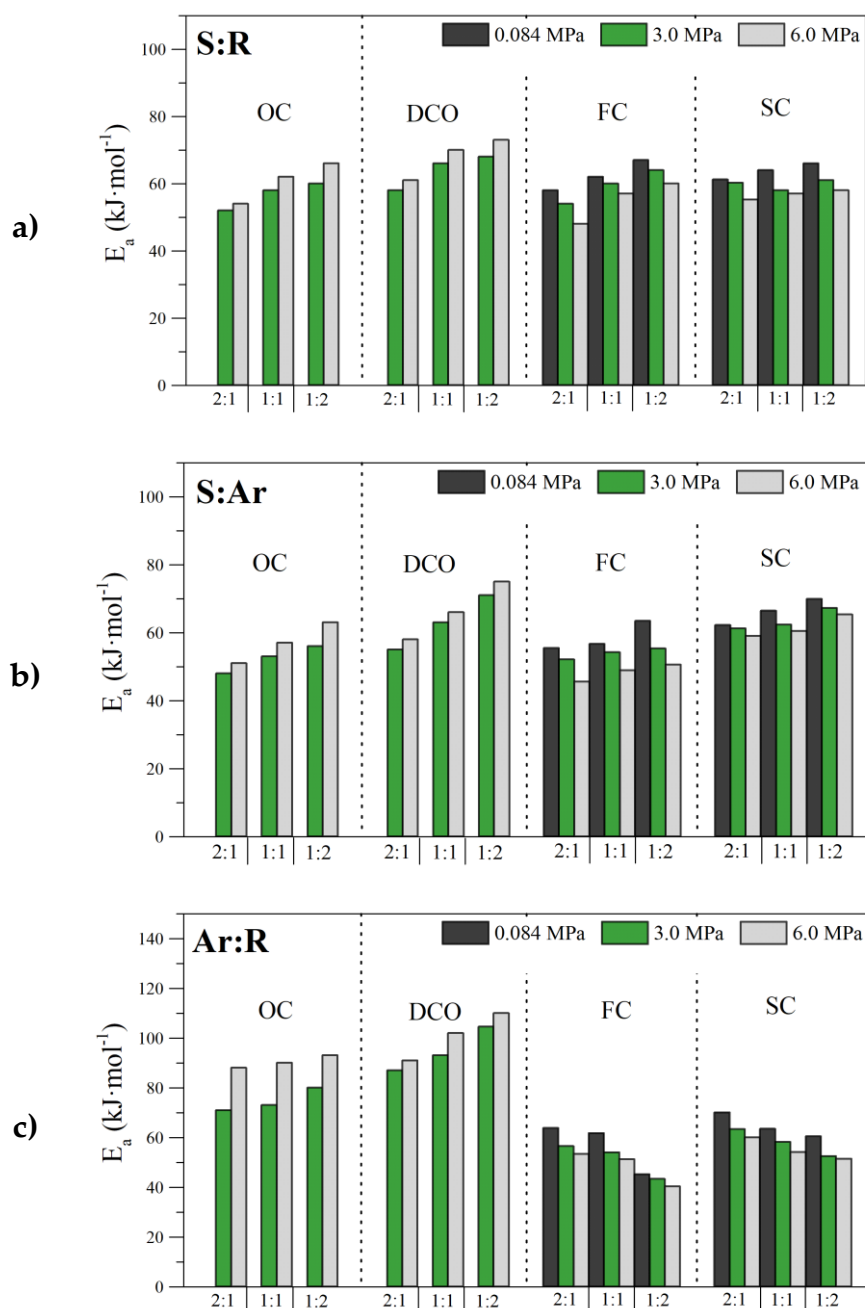


**Figure. 10.** Estimated effective activation energy for simultaneous oxidation of a) saturates and resins, b) saturates and aromatics, and c) aromatics and resins at different ratios and discretized in the four thermal events: *i*) oxygen chemisorption (OC) *ii*) decomposition of the chemisorbed oxygen (DCO) region, *iii*) first combustion (FC) region and *iv*) second combustion (SC) region.

Finally, the effective activation energy for the simultaneous oxidation of aromatics and resins is shown in panel c. These systems, unlike the simultaneous oxidations with saturates, present a considerable increase of

$E_a$  in OC and DCO. The values are like those found for asphaltenes with a high degree of aromatization, large cluster sizes, added to aliphatic chains of different sizes, and heteroatoms located in the aromatic and aliphatic structures. In other words, the presence of both fractions generates several active sites for the anchorage of oxygen in their molecular structure. There are small differences in the magnitude of the values for the simultaneous oxidation of Ar-R, which are slightly higher than those of asphaltenes, associated with a higher proportion of aromatic active sites requiring higher energy expenditure. The combustion zones for these systems need less energy than DCO to carry out; however, their magnitude depends on the aromatic content in the system. For a percentage greater than 50% of aromatics,  $E_a$  is higher for the simultaneous oxidation of Ar:R than for S:R and Ar:R. As the aromatic content decreases in the system, the effective activation energy decreases, obtaining values below S:Ar and S:R. In other words, aromatics affect the resins' reactivity in the combustion regions when their content represents more than half of the total.

The oxygen chemisorption percentage is correlated with the activation energy for the three systems evaluated (S:R, S:Ar, and Ar:R) as shown in Figure 11. Results corroborate that as higher the chemisorption percentage, the higher the effective activation energy at the same pressure. In the case of S:R and S:Ar, the 1:1 and 1:2 relationships, at 3.0 Mpa require higher energy than the 2:1 ratio at 6.0 Mpa, due to the low content of saturates in the systems.

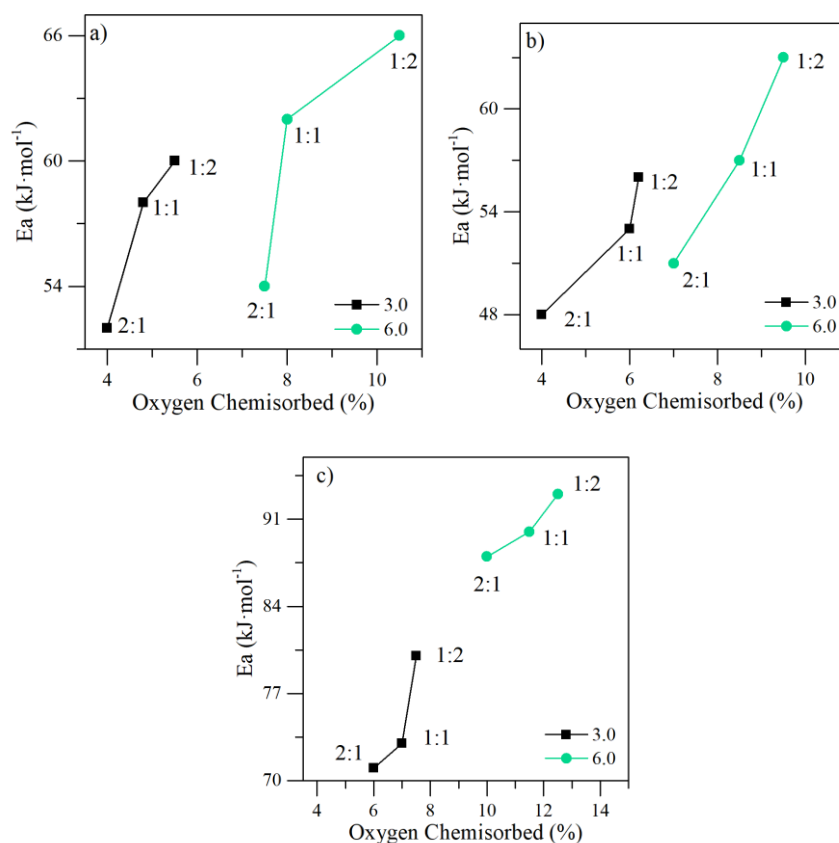


**Figure. 11.** Effective activation energy as a function of oxygen chemisorption percentage at 3.0 and 6.0 Mpa for simultaneous oxidation of S-Ar-R fractions in couples: a) S:R, S:Ar, and Ar:R at different ratios of 2:1, 1:1, and 1:2.

## 5. Conclusions

With the execution of this work, it was possible to understand the interactions between the different mixtures of S-Ar-R fractions of crude oil at different pressures. As a first instance, the S:R systems show that part of the products from saturates in DCO react with the resins during FC, increasing their contribution to coke production. These interactions decreased as the pressure increased.

On the other hand, the reactions between some olefins from saturates and aromatics can generate the condensation of naphthenic and aromatic rings. This indicates that for high saturates content in S:Ar mixtures, DCO reactions are prolonged at higher temperatures. In addition, free radical chain reactions are inhibited by the combination of aliphatic radicals with donated radicals from naphthenic and aromatic rings. This behavior predominates at 3.0 MPa over 6.0 MPa. Finally, the mixture between aromatics and resins shows slower kinetic rates than the other systems. The oxidation of the

aliphatic structure of the resins reacts in FC with the aromatics, promoting combustion reactions at higher pressures. The kinetic parameters corroborated the results obtained. For the systems with higher chemisorption, the effective activation energy values were higher and, therefore, the DCO values. Finally, FC and SC zones present lower values for the effective activation energy, considering that the products at the end of DCO were more reactive, and its consumption at higher temperatures becomes easiness.

## References.

- [1] Downie C. Strategies for Survival: The International Energy Agency's response to a new world. *Energy Policy* 2020;141:111452.
- [2] Freitag NP. Chemical-reaction mechanisms that govern oxidation rates during in-situ combustion and high-pressure air injection. *SPE Reservoir Evaluation & Engineering* 2016;19(04):645-54.
- [3] Zhao S, Pu W, Sun B, Gu F, Wang L. Comparative evaluation on the thermal behaviors and kinetics of combustion of heavy crude oil and its SARA fractions. *Fuel* 2019;239:117-25.
- [4] Medina OE, Gallego J, Rodríguez E, Franco CA, Cortés FB. Effect of pressure on the oxidation kinetics of Asphaltenes. *Energy & Fuels* 2019;33(11):10734-44.
- [5] Medina OE, Gallego J, Nassar NN, Acevedo SA, Cortés FB, Franco CA. Thermo-Oxidative Decomposition Behaviors of Different Sources of n-C7 Asphaltenes at High-Pressure Conditions. *Energy & Fuels* 2020.
- [6] Dabbous MK, Fulton PF. Low-temperature-oxidation reaction kinetics and effects on the in-situ combustion process. *Society of Petroleum Engineers Journal* 1974;14(03):253-62.
- [7] Chen Y, Pu W, Liu X, Li Y, Gong X, Hui J, et al. Specific kinetic triplet estimation of Tahe heavy oil oxidation reaction based on non-isothermal kinetic results. *Fuel* 2019;242:545-52.
- [8] Shi Q, Hou D, Chung KH, Xu C, Zhao S, Zhang Y. Characterization of heteroatom compounds in a crude oil and its saturates, aromatics, resins, and asphaltenes (SARA) and non-basic nitrogen fractions analyzed by

- negative-ion electrospray ionization Fourier transform ion cyclotron resonance mass spectrometry. *Energy & Fuels* 2010;24(4):2545-53.
- [9] Kok MV, Gul KG. Thermal characteristics and kinetics of crude oils and SARA fractions. *Thermochimica acta* 2013;569:66-70.
- [10] Hao J, Che Y, Tian Y, Li D, Zhang J, Qiao Y. Thermal cracking characteristics and kinetics of oil sand bitumen and its SARA fractions by TG-FTIR. *Energy & Fuels* 2017;31(2):1295-309.
- [11] Chen Y-f, Pu W-f, Liu X-l, Li Y-b, Varfolomeev MA, Hui J. A preliminary feasibility analysis of in situ combustion in a deep fractured-cave carbonate heavy oil reservoir. *Journal of Petroleum Science and Engineering* 2019;174:446-55.
- [12] Wei B, Zou P, Shang J, Gao K, Li Y, Sun L, et al. Integrative determination of the interactions between SARA fractions of an extra-heavy crude oil during combustion. *Fuel* 2018;234:850-7.
- [13] Yuan C, Varfolomeev MA, Emelianov DA, Eskin AA, Nagrimanov RN, Kok MV, et al. Oxidation behavior of light crude oil and its SARA fractions characterized by TG and DSC techniques: differences and connections. *Energy & fuels* 2018;32(1):801-8.
- [14] Freitag N, Verkoczy B. Low-temperature oxidation of oils in terms of SARA fractions: why simple reaction models don't work. *Journal of Canadian petroleum technology* 2005;44(03):54-61.
- [15] Liu D, Song Q, Tang J, Zheng R, Yao Q. Interaction between saturates, aromatics and resins during pyrolysis and oxidation of heavy oil. *Journal of Petroleum Science and Engineering* 2017;154:543-50.
- [16] Liu D, Hou J, Luan H, Pan J, Song Q, Zheng R. Coke yield prediction model for pyrolysis and oxidation processes of low-asphaltene heavy oil. *Energy & Fuels* 2019;33(7):6205-14.
- [17] Wiehe IA. A phase-separation kinetic model for coke formation. *Industrial & engineering chemistry research* 1993;32(11):2447-54.
- [18] Medina et al. CS, Gallego J., Cortés F.B., and Franco C.A. Effect of Pressure on Thermo-oxidation Reactions of Saturates, Aromatics, and Resins (SAR) from Extra-Heavy Crude Oil. 2021.

- [19] Medina OE, Gallego J, Olmos CM, Chen X, Cortés FB, Franco CA. Effect of Multifunctional Nanocatalysts on n-C7 Asphaltene Adsorption and Subsequent Oxidation under High-Pressure Conditions. *Energy & Fuels* 2020.
- [20] Medina OE, Galeano-Caro D, Ocampo-Pérez R, Perez-Cadenas AF, Carrasco-Marín F, Franco CA, et al. Development of a monolithic carbon xerogel-metal composite for crude oil removal from oil in-saltwater emulsions: Evaluation of reuse cycles. *Microporous and Mesoporous Materials* 2021;327:111424.
- [21] Medina OE, Gallego J, Acevedo S, Riazi M, Ocampo-Pérez R, Cortés FB, et al. Catalytic Conversion of n-C7 Asphaltenes and Resins II into Hydrogen Using CeO<sub>2</sub>-Based Nanocatalysts. *Nanomaterials* 2021;11(5):1301.
- [22] Medina OE, Galeano-Caro D, Castelo-Quibén J, Ocampo-Pérez R, Perez-Cadenas AF, Carrasco-Marín F, et al. Monolithic carbon xerogels-metal composites for crude oil removal from oil in-saltwater emulsions and subsequent regeneration through oxidation process: Composites synthesis, adsorption studies, and oil decomposition experiments. *Microporous and Mesoporous Materials* 2021;319:111039.
- [23] Mateus L, Moreno-Castilla C, López-Ramón MV, Cortés FB, Álvarez MÁ, Medina OE, et al. Physicochemical characteristics of calcined MnFe<sub>2</sub>O<sub>4</sub> solid nanospheres and their catalytic activity to oxidize para-nitrophenol with peroxymonosulfate and n-C7 asphaltenes with air. *Journal of Environmental Management* 2021;281:111871.
- [24] Gimzewski E. An accurate and compact high-pressure thermogravimetric analyser. *Journal of thermal analysis* 1991;37(6):1251-60.
- [25] Medina OE, Caro-Vélez C, Gallego J, Cortés FB, Lopera SH, Franco CA. Upgrading of Extra-Heavy Crude Oils by Dispersed Injection of NiO-PdO/CeO<sub>2+δ</sub> Nanocatalyst-Based Nanofluids in the Steam. *Nanomaterials* 2019;9(12):1755.
- [26] Medina OE, Hurtado Y, Caro-Velez C, Cortés FB, Riazi M, Lopera SH, et al. Improvement of steam injection processes through nanotechnology: An approach through in situ upgrading and foam injection. *Energies* 2019;12(24):4633.



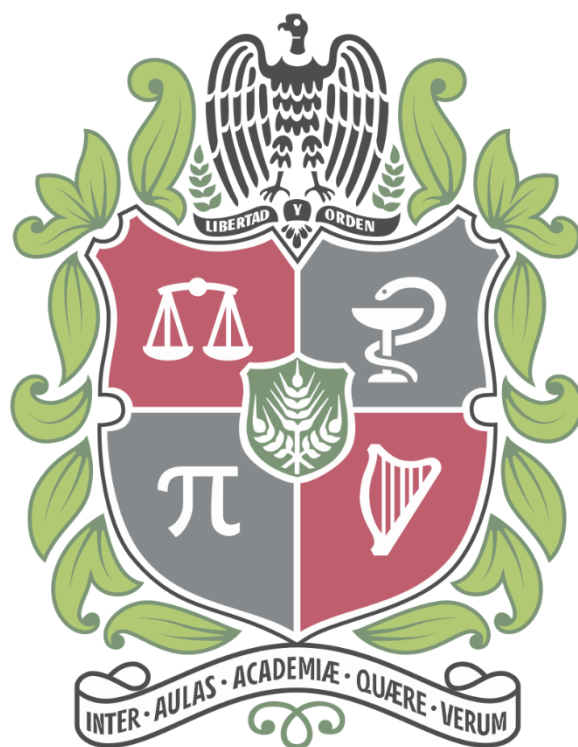
- [27] Medina OE, Gallego J, Restrepo LG, Cortés FB, Franco CA. Influence of the Ce<sup>4+</sup>/Ce<sup>3+</sup> Redox-couple on the cyclic regeneration for adsorptive and catalytic performance of NiO-PdO/CeO<sub>2±δ</sub> nanoparticles for n-C<sub>7</sub> asphaltene steam gasification. *Nanomaterials* 2019;9(5):734.
- [28] Arias-Madrid D, Medina OE, Gallego J, Acevedo S, Correa-Espinal AA, Cortés FB, et al. NiO, Fe<sub>2</sub>O<sub>3</sub>, and MoO<sub>3</sub> Supported over SiO<sub>2</sub> Nanocatalysts for Asphaltene Adsorption and Catalytic Decomposition: Optimization through a Simplex–Centroid Mixture Design of Experiments. *Catalysts* 2020;10(5):569.
- [29] Medina OE, Gallego J, Pérez-Cadenas AF, Carrasco-Marín F, Cortés FB, Franco CA. Insights into the Morphology Effect of Ceria on the Catalytic Performance of NiO–PdO/CeO<sub>2</sub> Nanoparticles for Thermo-oxidation of n-C<sub>7</sub> Asphaltenes under Isothermal Heating at Different Pressures. *Energy & Fuels* 2021.
- [30] Liu G-S, Niksa S. Coal conversion submodels for design applications at elevated pressures. Part II. Char gasification. *Progress in energy and combustion science* 2004;30(6):679-717.
- [31] Yang L, Sheng JJ. Experimental study on the oxidation behaviors of Wolfcamp light crude oil and its saturate, aromatic and resin fractions using accelerated rate calorimetry tests. *Fuel* 2020;276:117927.
- [32] Barzin Y, Moore RG, Mehta SA, Mallory DG, Ursenbach MG, Tabasinejad F. Role of vapor phase in oxidation/combustion kinetics of high-pressure air injection (HPAI). *SPE Annual Technical Conference and Exhibition. OnePetro*; 2010.
- [33] Ushakova A, Emelyanov D, Zatsepin V, Varfolomeev M. The free radical chain mechanism of the initial stages of crude oil oxidation in term of SARA fractions. *IOP Conference Series: Earth and Environmental Science*. 155. IOP Publishing; 2018:012013.
- [34] Ishii Y, Sakaguchi S, Iwahama T. Innovation of hydrocarbon oxidation with molecular oxygen and related reactions. *Advanced Synthesis & Catalysis* 2001;343(5):393-427.
- [35] Sequera Marin BM. Numerical simulation of low temperature oxidation reactions of Athabasca bitumen using sara fractions. University of Calgary; 2007.

- [36] Zabetakis MG, Furno AL, Jones GW. Minimum spontaneous ignition temperatures of combustibles in air. *Industrial & Engineering Chemistry* 1954;46(10):2173-8.
- [37] Letzel T, Pöschl U, Wissiack R, Rosenberg E, Grasserbauer M, Niessner R. Phenyl-modified reversed-phase liquid chromatography coupled to atmospheric pressure chemical ionization mass spectrometry: A universal method for the analysis of partially oxidized aromatic hydrocarbons. *Analytical chemistry* 2001;73(7):1634-45.
- [38] Kök MV, Karacan Ö, Pamir R. Kinetic analysis of oxidation behavior of crude oil SARA constituents. *Energy & Fuels* 1998;12(3):580-8.
- [39] Freitag NP. Evidence that naturally occurring inhibitors affect the low-temperature oxidation kinetics of heavy oil. *Journal of Canadian Petroleum Technology* 2010;49(07):36-41.
- [40] Deng L, Jin X, Zhang Y, Che D. Release of nitrogen oxides during combustion of model coals. *Fuel* 2016;175:217-24.
- [41] Glarborg P, Miller JA, Ruscic B, Klippenstein SJ. Modeling nitrogen chemistry in combustion. *Progress in Energy and Combustion Science* 2018;67:31-68.
- [42] Lopatin O. Chemistry of the process of formation of nitrogen oxides in the combustion chamber of gas-diesel. *Journal of Physics: Conference Series*. 1515. 2020:052004.
- [43] Ismagilov Z, Yashnik S, Kerzhentsev M, Parmon V, Bourane A, Al-Shahrani FM, et al. Oxidative Desulfurization of Hydrocarbon Fuels. *Catalysis Reviews* 2011;53(3):199-255.
- [44] Javadli R, de Klerk A. Desulfurization of Heavy Oil–Oxidative Desulfurization (ODS) As Potential Upgrading Pathway for Oil Sands Derived Bitumen. *Energy & Fuels* 2011;26(1):594-602.
- [45] Benson SW. Thermochemistry and Kinetics of Sulfur-Containing Molecules and Radicals. *Chemical Reviews* 1978;78(1):23-35.
- [46] Izadifard M. Oxidation of Sulfolane in Aqueous Systems by Chemical and Photochemical Processes. 2019.

- [47] Greensfelder B, Voge H, Good G. Catalytic and thermal cracking of pure hydrocarbons: Mechanisms of Reaction. *Industrial & Engineering Chemistry* 1949;41(11):2573-84.
- [48] Cypres R. Aromatic hydrocarbons formation during coal pyrolysis. *Fuel Processing Technology* 1987;15:1-15.
- [49] Freitag NP, Exelby D. A SARA-based model for simulating the pyrolysis reactions that occur in high-temperature EOR processes. *Journal of Canadian Petroleum Technology* 2006;45(03).



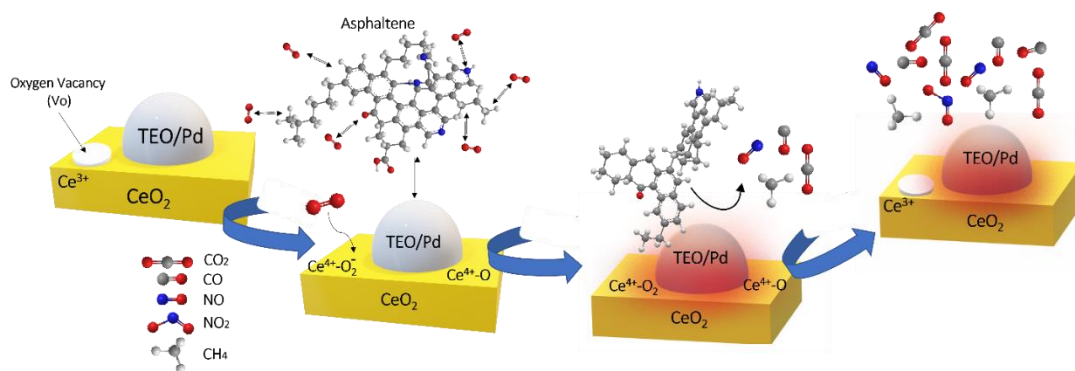
#### Apartado 4.





## Chapter 7.

# Optimization of the Load of Transition Metal Oxides ( $\text{Fe}_2\text{O}_3$ , $\text{Co}_3\text{O}_4$ , $\text{NiO}$ and/or $\text{PdO}$ ) onto $\text{CeO}_2$ Nanoparticles in Catalytic Steam Decomposition of $n\text{-C}_7$ Asphaltenes at Low Temperatures



Published article in *Nanomaterials*: [doi.org/10.3390/nano9030401](https://doi.org/10.3390/nano9030401)

Impact factor: 5.719

# Optimization of the Load of Transition Metal Oxides (Fe<sub>2</sub>O<sub>3</sub>, Co<sub>3</sub>O<sub>4</sub>, NiO and/or PdO) onto CeO<sub>2</sub> Nanoparticles in Catalytic Steam Decomposition of *n*-C<sub>7</sub> Asphaltenes at Low Temperatures

## Abstract

The main goal of this research is to maximize asphaltene conversion under isothermal conditions at low temperatures (250 °C) during steam injection processes by optimizing the catalyst of Fe<sub>2</sub>O<sub>3</sub>-, Co<sub>3</sub>O<sub>4</sub>-, NiO- and/or PdO- (transition element oxides—TEO) functionalized CeO<sub>2</sub> nanoparticles. Batch adsorption experiments and thermogravimetric analyses combined with Fourier-transform infrared spectroscopy (FTIR) were used to measure the adsorption isotherms and asphaltenes' subsequent steam decomposition process, respectively, to assess the catalysis. The adsorption isotherms and the catalytic behavior were described by the solid-liquid equilibrium (SLE) model and isothermal model, respectively. Initially, three pairs of metal oxide combinations with 1% loading of CeNi1Pd1, CeCo1Pd1, and CeFe1Pd1 nanoparticles were evaluated for adsorption and catalytic activity, with CeNi1Pd1 showing better results due to Lewis acidity changes. Posteriorly, a simplex-centroid mixture design of experiments (SCMD) of three components was employed to optimize the metal oxides concentration (Ni and Pd) onto the CeO<sub>2</sub> surface by varying the concentration of the TEO between mass fractions of 0.0 and 2.0% to maximize the asphaltene conversion at low temperatures. Results showed that by incorporating mono-elemental and bi-elemental oxides onto CeO<sub>2</sub> nanoparticles, both adsorption and isothermal conversion of asphaltenes decrease in the order CeNi1Pd1 > CePd2 > CeNi0.66Pd0.66 > CeNi2 > CePd1 > CeNi1 > CeO<sub>2</sub>. It is worth mentioning that bi-elemental nanoparticles reduced the gasification temperature of asphaltenes to a larger degree than mono-elemental nanoparticles at a fixed amount of adsorbed asphaltenes of 0.02 mg·m<sup>-2</sup>, confirming the synergistic effects between Pd and Fe, Co, and Ni. Further, optimized nanoparticles (CeNi0.89Pd1.1) have the best performance by obtaining 100% asphaltenes conversion in less than 90 min at 220 °C while reducing 80% the activation energy.

## 1. Introduction

The demand for conventional crude oils increases every day worldwide, and it is expected that in the future, these reserves will decrease substantially [1]. Consequently, the energy industries have shown great attention in recent years to using alternative techniques to supply the current energy consumption [2]. The use of fossil fuels such as heavy crude oil (HO) and extra heavy crude oil (EHO) has become an important source of the alternative energy supply [3]. This type of crude oil has a high content of heavy hydrocarbons, such as asphaltenes, which drastically increase the viscosity of crude oil and reduce the American Petroleum Institute (API) gravity [4]. Thermal methods are used to reduce viscosity to improve the mobility ratio, productivity, and recovery of HO and EHO [5–7]. However, some of these methods, such as steam injection processes, do not generate changes in crude oil quality [8–11]. Generally, the temperatures employed in steam injection processes do not exceed 240 °C [12], while the decomposition temperature of asphaltenes in the presence of steam occurs around 450–550 °C [13–15].

Nanoscale technologies have recently been used as an alternative for improving conventional techniques and enhancing oil recovery [16–19]. Several authors [20–23] have shown that highly adsorbent nanomaterials can capture the asphaltene molecules of crude oil due to their high affinity [24]. Posteriorly, these nanoparticles can be used as catalysts in processes such as steam injection [25], pyrolysis [26], and in-situ combustion [27], looking for catalytic decomposition that leads to improved HO and EHO properties. Two major lines of the research reported in the literature focused on the catalytic upgrading of HO and EHO via nanotechnology. Metal oxide nanoparticles are used in the first, while functionalized nanoparticulated supports with metal oxides are used in the second (composite materials or supporting hygroscopic salt materials—SHS). Within the first branch, many types of nanoparticles such as NiO, SiO<sub>2</sub>, TiO<sub>2</sub>, WO<sub>3</sub>, MgO, CaCO<sub>3</sub>, ZrO<sub>2</sub>, Al<sub>2</sub>O<sub>3</sub>, Fe<sub>2</sub>O<sub>3</sub>, and CO<sub>3</sub>O<sub>4</sub>, among others, have been evaluated with the final purpose of reducing the decomposition temperature and activation energy of the asphaltenes, calculated under isothermal [28] or iso-conversional models [15]. Metal oxide nanoparticles can reduce the asphaltene decomposition temperature up to 300 °C, which is still a relatively high temperature for steam injection in an oilfield [22,29–33]. In the case of



functionalized materials, such as nickel and palladium nanocrystals over nanoparticulated supports of alumina, silica, or TiO<sub>2</sub>, decompose asphaltenes at low temperatures between 200 °C and 240 °C [33–37]. However, isothermal conditions have not been used in these studies with functionalized materials to simulate steam injection processes. In the case of asphaltene decomposition under isothermal conditions, Nassar et al. [28] evaluated three metal oxides nanoparticles of Fe<sub>2</sub>O<sub>3</sub>, Co<sub>3</sub>O<sub>4</sub>, and NiO at 300 °C under an air atmosphere, obtaining that NiO decomposes 100% of asphaltene in less than 170 min. Cardona et al. [38,39] evaluated the catalytic steam decomposition of asphaltenes using a composite material of NiO and PdO nanocrystals over alumina support under isothermal conditions at 220 °C. Under these conditions, 90% of asphaltene decomposition was achieved in less than 150 min, and its effect on upgrading the physicochemical properties of an EHO was corroborated through displacement tests of steam injection [39].

Cerium dioxide (IV) has been evaluated in several catalytic studies due to its ability to absorb and release oxygen through the Ce<sup>3+</sup>/Ce<sup>4+</sup> redox cycle [40,41]. This lanthanide may promote asphaltene catalytic reactions through (a) the interactions between transition elements oxides (TEO) and ceria (CeO<sub>2</sub>) [42–44] and (b) the activity of the redox pair Ce<sup>3+</sup>/Ce<sup>4+</sup> [45–47]. Recently, it was demonstrated that Ni as a disperse phase linked to cerium as active support in the framework of Zeolite Socony Mobil-Five (MFI) presents a synergistic effect in the water-gas shift (WGS) reaction, accelerating its production at low temperatures of around 230 °C [48]. However, to our knowledge, no studies evaluate and optimize the concentration of metal oxides on the CeO<sub>2</sub> nanoparticles for the adsorption/cracking of *n*-C<sub>7</sub> asphaltenes under isothermal steam injection conditions. Therefore, the main objective of this study was to find the best combination of transition elements oxides (Pd, Ni, Co, and Fe) and their optimum concentration in the surface of a CeO<sub>2</sub> nanoparticulated support that allows for the improvement of the conversion of *n*-C<sub>7</sub> asphaltene during steam injection processes at low temperatures (<240 °C), which can further lead to the HO and EHO upgrading. Hence, three TEOs are combined with a noble element oxide in the couples Fe–Pd, Co–Pd, Ni–Pd and are functionalized over CeO<sub>2</sub> nanoparticles for further evaluation through batch adsorption experiments and thermogravimetric analyses. Finally, through a simplex-centroid mixture design (SCMD) of experiments, the optimum concentration of the best element oxide pair is determined to maximize the *n*-C<sub>7</sub> asphaltenes conversion under isothermal conditions at 220 °C. Therefore, this work will allow for a better understanding

of the catalytic effect of transition metals, noble metals, and lanthanides for the decomposition of asphaltenes in steam injection processes, as well as the variables that can affect this process.

## 2. Experimental

### 2.1. Materials

The extraction of the asphaltenes was performed by isolation with *n*-heptane (99%, Sigma-Aldrich, St. Louis, MO, USA) [49,50] from a Colombian extra heavy crude oil (EHO) of 6.4 °API, viscosity of  $3.1 \times 10^6$  cP at 25 °C, and approximate mass fractions of saturates, aromatics, resins and asphaltenes (SARA) of 13.0, 16.9, 49.9, and 20.2%, respectively. The *n*-C<sub>7</sub> asphaltenes were characterized by elemental analysis using an elemental analyzer Flash EA 1112 (Thermo Finnigan, Milan, Italy), obtaining mass fractions of C, H, O, N, and S of 81.7, 7.8, 3.6, 0.3, and 6.6%, and a H/C ratio of 1.15, which is following the values reported in the literature [51]. Ceria (CeO<sub>2</sub>) nanoparticles were purchased from Nanostructured & Amorphous Materials (Houston, TX, USA). Salt precursors of NiCl<sub>2</sub>·6H<sub>2</sub>O, CoCl<sub>2</sub>·6H<sub>2</sub>O, FeCl<sub>3</sub>·6H<sub>2</sub>O, Pd(NO<sub>3</sub>)<sub>2</sub>·2H<sub>2</sub>O (Merck KGaA, Darmstadt, Germany), and distilled water were used for the functionalization of ceria nanoparticles.

### 2.2. Methods

#### 2.2.1. Functionalization of CeO<sub>2</sub> Nanoparticles with NiO, Fe<sub>2</sub>O<sub>3</sub>, Co<sub>3</sub>O<sub>4</sub>, and PdO

For obtaining the optimum concentration of the best functionalizing couple on the cerium oxide nanoparticles, the following systems were considered: (i) initially, three pairs of nanoparticles were evaluated with different TEO at a fixed concentration of a mass fraction of 1% over the ceria surface (CeNi1Pd1, CeCo1Pd1, and CeFe1Pd1) to choose the best TEO couple, and posteriorly (ii) a three-component simplex centroid mixture design (SCMD) of experiments was carried out for different TEO dosages up to mass fractions of 2%. The support of CeO<sub>2</sub> nanoparticles was previously dried at 120 °C for 2 h to remove any humidity. For the functionalization, aqueous solutions of iron chloride, nickel chloride, cobalt chloride, and/or palladium nitrate are employed using the incipient wetness technique as reported in previous studies [23,39,52]. Then, the obtained composite nanoparticles were dried at 120 °C for 6 h, and finally, the solid obtained was calcined at 450 °C for 6 h [15]. The nomenclature, as well as

the mass fraction and mole fraction of the synthesized samples according to the design of experiments, are shown in Table 1.

**Table 1.** Nomenclature, mass fraction, and molar fraction of the prepared nanoparticles composed of ceria support ( $\text{CeO}_2$ ) functionalized with transition metal oxides ( $\text{Fe}_2\text{O}_3$ ,  $\text{Co}_3\text{O}_4$ ,  $\text{NiO}$  and/or  $\text{PdO}$ ).

Sample	Nominal Oxides	Nominal Mass Fraction (%)	Nominal Molar Fraction (%)
$\text{CeO}_2$	$\text{CeO}_2$	100.0	100.0
$\text{CeNi1Pd1}$	$\text{CeO}_2$	98.0	98.8
	$\text{NiO}$	1.0	0.4
	$\text{PdO}$	1.0	0.7
$\text{CeFe1Pd1}$	$\text{CeO}_2$	98.0	98.4
	$\text{Fe}_2\text{O}_3$	1.0	0.9
	$\text{PdO}$	1.0	0.7
$\text{CeCo1Pd1}$	$\text{CeO}_2$	98.0	97.9
	$\text{Co}_3\text{O}_4$	1.0	1.4
	$\text{PdO}$	1.0	0.7
$\text{CeNi2}$	$\text{CeO}_2$	98.0	99.1
	$\text{NiO}$	2.0	0.9
$\text{CePd2}$	$\text{CeO}_2$	98.0	98.6
	$\text{PdO}$	2.0	1.4
$\text{CeNi1}$	$\text{CeO}_2$	99.0	99.6
	$\text{NiO}$	1.0	0.4
$\text{CePd1}$	$\text{CeO}_2$	99.0	99.3
	$\text{PdO}$	1.0	0.7
$\text{CeNi0.66Pd0.66}$	$\text{CeO}_2$	98.7	99.2
	$\text{NiO}$	0.7	0.3
	$\text{PdO}$	0.7	0.5

It is important to mention that Ni, Pd, Co, and Fe precursors become oxides after calcination. The first part of this manuscript consists of three composite bielemental materials based on a load of a fixed mass fraction of 1.0% of nickel and palladium oxides supported on the  $\text{CeO}_2$  nanoparticles ( $\text{CeNi1Pd1}$ ), 1.0% of iron and palladium oxides ( $\text{CeFe1Pd1}$ ), and 1.0% of cobalt and palladium oxides ( $\text{CeCo1Pd1}$ ). In the second part, seven samples were prepared with the salt precursors according to the SCMD, varying the mass fraction between 0.0% and 2.0% of nickel and palladium oxides, according to Figure 1. The functionalized nanoparticles were labeled by the chemical symbol of the support (Ce), followed by the symbol of the transition element and its percentage. For instance, nanoparticles with loads of a mass fraction of 1.0% of  $\text{NiO}$  and  $\text{PdO}$ , are labeled as  $\text{CeNi1Pd1}$ .

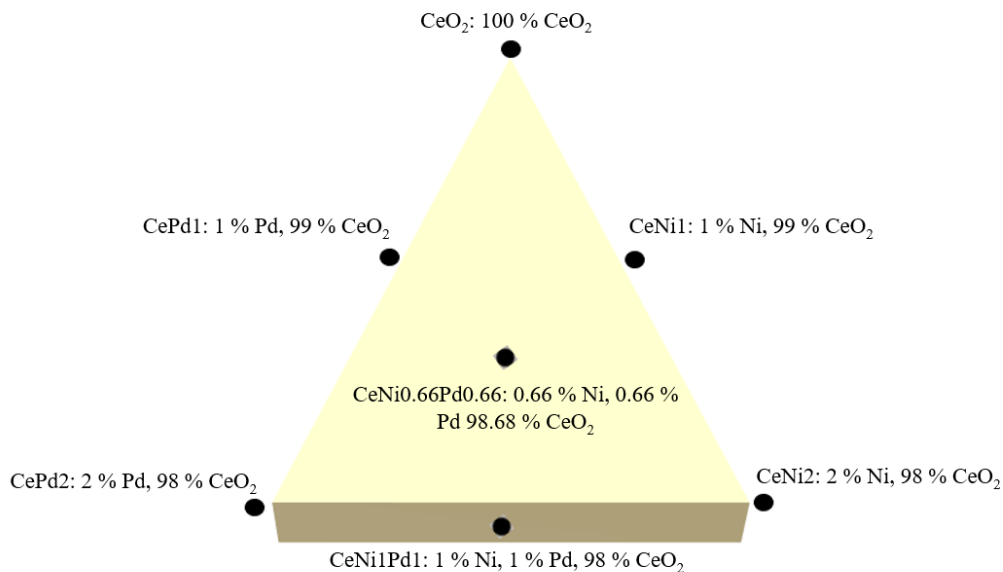


**Figure 1.** Three components simplex-centroid mixture design with ceria support ( $\text{CeO}_2$ ) functionalized with nickel oxide (NiO) and palladium oxide (PdO).

### 2.2.2. Characterization of the Nanoparticles

The size and morphology of the composite nanoparticles and the support were characterized by high-resolution transmission electron microscopy (HR-TEM) using a Tecnai G2 F20 microscope (FEI, Hillsboro, OR, USA) and dynamic light scattering (DLS) measurements using a Nanoplus-3 from Micromeritics (Norcross, GA, USA). Metal dispersion and the average diameter of the metals in the catalyst support were found by pulse chemisorption, using  $\text{H}_2$  titration with a Chembet 3000 (Quantachrome Instruments, Boynton Beach, FL, USA), where approximately 100 mg of sample was subjected to a U-shaped quartz tube dried at  $200\text{ }^\circ\text{C}$  for 1 h. Then the catalysts were subjected to  $600\text{ }^\circ\text{C}$  for 1 h in a volumetric fraction of 10% of  $\text{H}_2$  in Ar at  $80\text{ mL}\cdot\text{min}^{-1}$  and purged with flowing Ar for 1 h until the samples reached room temperature. Hydrogen pulses continued until no additional uptake of  $\text{H}_2$  was observed. The surface area ( $S_{\text{BET}}$ ) was measured using  $\text{N}_2$  physisorption at  $-196\text{ }^\circ\text{C}$  using an Auorosorb-1 Quantacrome (USA) following the method proposed by Brunauer-Emmett-Teller [41].

### 2.2.3. Equilibrium Adsorption Isotherms

The model solutions for the batch adsorption experiments were prepared by dissolving a desired amount of the obtained asphaltenes in toluene. The procedure started with a stock solution containing  $1500\text{ mg}\cdot\text{L}^{-1}$  of  $n\text{-C}_7$

asphaltenes diluted at different concentrations. The initial concentration of *n*-C<sub>7</sub> asphaltene solutions varied from 100 mg·L<sup>-1</sup> to 1500 mg·L<sup>-1</sup>. A fixed amount of nanoparticles was added in a 1:10 ratio of solution volume to the dry mass of nanoparticles. Subsequently, the mixtures were stirred at 200 rpm and allowed to equilibrate for 24 h [24]. Nanoparticles with asphaltenes adsorbed were separated by centrifugation at 5000 rpm for 45 min and dried in a vacuum oven at 60 °C for 24 h. The change in the asphaltenes concentration after adsorption was determined by UV-vis spectrophotometry using a Genesys 10S spectrophotometer (Thermo Scientific, Waltham, MA, USA). The amount of adsorbed asphaltenes *q* (mg·m<sup>-2</sup>) was determined by mass balance:

$$q = \frac{C_o - C_e}{A} V \quad (1)$$

where  $C_e$  (mg·L<sup>-1</sup>) is the equilibrium concentration of asphaltenes in the supernatant,  $C_o$  (mg·L<sup>-1</sup>) is the initial concentration of *n*-C<sub>7</sub> asphaltenes in solution,  $A$  (m<sup>2</sup>·g<sup>-1</sup>) is the dry surface area of nanoparticles, and  $V$  (L) is the solution volume.

#### 2.2.4. Thermogravimetric Analysis of Asphaltenes

Catalytic steam gasification of adsorbed *n*-C<sub>7</sub> asphaltenes over the nanoparticles was carried out using a thermogravimetric analyzer Q50 (TA Instruments, Inc., New Castel, DE, USA) coupled to an IR-Affinity-1 FTIR device (Shimadzu, Kyoto, Japan) with a gas cell to analyze produced gases during the decomposition process. For gasification experiments, N<sub>2</sub> flow was fixed at 100 mL·min<sup>-1</sup> and at the same time, H<sub>2</sub>O<sub>(g)</sub> was introduced to the system at a flow rate of 6.30 mL·min<sup>-1</sup> using a gas saturator filled with distilled water at a fixed temperature controlled by a thermostatic bath. This flow rate allows the excess steam to be present above the sample [53].

The samples were subjected to two procedures under non-isothermal and isothermal conditions. Under non-isothermal conditions, the samples were heated from 100 to 600 °C at a heating rate of 20 °C·min<sup>-1</sup>. After the gasification process, oxidation under an air flow from 100 to 600 °C at 20 °C·min<sup>-1</sup> was conducted to estimate the coke yield. Under isothermal conditions, the samples were heated at 230, 240, and 250 °C for 300 min to obtain the highest conversion of asphaltenes possible. In the case of *n*-C<sub>7</sub> asphaltenes in the absence of nanoparticles, the temperatures for isothermal decomposition were established

at 360, 370, and 380 °C due to the refractory nature of this compound. The selected nanomaterials for thermogravimetric analyses (TGA) experiments had the same loading of *n*-C<sub>7</sub> asphaltenes per unit surface area of 0.2 mg·m<sup>-2</sup>. However, for the best system regarding catalytic activity, the effect of asphaltenes loading was evaluated for asphaltenes loadings of 0.02, 0.05, and 0.2 mg·m<sup>-2</sup>. To avoid diffusion limitations, the sample mass in the analyzer was kept low (~5 mg) [54].

The gases produced by the asphaltene decomposition process were analyzed via Fourier transform infrared spectroscopy (FTIR), which operated in transmission mode at a resolution of 2 cm<sup>-1</sup> in the range of 4000–100 cm<sup>-1</sup> with ten scans per minute. The gases that were produced by the cracking of asphaltenes were CH<sub>4</sub>, CO<sub>2</sub>, CO, NO<sub>x</sub>, and light hydrocarbons (LHC). Their analysis was carried out considering the characteristic intensities of the absorption bands for each gas: 3016 cm<sup>-1</sup> (CH<sub>4</sub>), 2349 cm<sup>-1</sup> (CO<sub>2</sub>), 2149 cm<sup>-1</sup> (CO), 1615 cm<sup>-1</sup> (NO<sub>x</sub>), and 2750 cm<sup>-1</sup> (LHC), respectively [16]. Each run was repeated at least twice to confirm the reproducibility of the experiment. Finally, the catalytic activity of the samples from the SCMD was evaluated under isothermal conditions of 220 °C and for an asphaltene load of 0.02 mg·m<sup>-2</sup>.

### 3. Modeling

#### 3.1. Simplex-Centroid Mixture Design

A design of experiments was developed to find the optimal mixture of NiO or PdO and ceria nanoparticles for maximizing the conversion of the asphaltenes. A simplex-centroid mixture design (SCMD) was run using the STATGRAPHICS Centurion XVI software (StartPoint Technologies Inc., Addison, TX, USA), varying the mass fraction of palladium, cerium, and nickel. The SCMD is used to predict the response of a selected parameter according to the variability of a controlled variable. The proportion of each component must satisfy the following restriction [55]:

$$\sum_{i=1}^{\sigma} x_i = x_1 + x_2 + x_3 + \dots + x_q = 1 \quad x_i \geq 0 \quad (2)$$

where, the " $\sigma$ " parameter refers to the number of components varying in the mixture and  $x_i$  is the proportion of each component. In this study, for each mixture design  $\sigma = 3$ ,  $x_1 = Ce$ ,  $x_2 = Pd$  and  $x_3 = Ni$ . Consequently, the limits of each compound are:

$$0.98 \leq Ce \leq 1.00 \quad (3)$$

$$0 \leq Pd \leq 0.02 \quad (4)$$

$$0 \leq Ni \leq 0.02 \quad (5)$$

Specifically, for a cubic model, it is important to evaluate the maximum and minimum concentration for each compound and other points at which the three components of the mixture are related according to the rule of experiments. Using a special cubic regression, the model for the asphaltene conversion was established. The regression model equations are as follows:

$$\alpha_m = \beta_1 x'_1 + \beta_2 x'_2 + \beta_3 x'_3 + \beta_{12} x'_1 x'_2 + \beta_{13} x'_1 x'_3 + \beta_{123} x'_1 x'_2 x'_3 \quad (6)$$

$$x'_i = \frac{x_i - L_i}{1 - L} \quad (7)$$

where  $\alpha_m$  is the conversion of asphaltenes during the steam gasification,  $\beta_i$ ,  $\beta_{ij}$  and  $\beta_{ijk}$  are the coefficients of the linear terms, binary mixtures of nonadditive components, and ternary mixture of nonadditive components, respectively. In the expression (7),  $L_i$  is the lower limit of each component,  $L$  is the sum of the lower boundaries and  $x'_i$  is a pseudo-component of  $x_i$  and is used because of the restrictions mentioned in Equations (3)–(5).

### 3.2. Solid-Liquid Equilibrium (SLE) Model

From the theory of association suggested by Talu and Maunier [56] for the self-association and molecular adsorption on micropores, the solid-liquid equilibrium model (SLE) is used to evaluate the adsorption of asphaltenes onto nanoparticles [57]. The expression given by the model is as follows:

$$C = \frac{\psi H}{1 + K\psi} e^{\left(\frac{\psi}{q_m A}\right)} \quad (8)$$

where  $K$  ( $\text{g} \cdot \text{g}^{-1}$ ) indicates the degree of asphaltenes molecules self-association over the active sites of the surface of the nanoparticles,  $H$  ( $\text{mg} \cdot \text{g}^{-1}$ ) is an indicator of the adsorption affinity of asphaltenes onto a solid surface,  $A$  the surface area ( $\text{m}^2 \cdot \text{g}^{-1}$ ),  $q_m$  ( $\text{mg} \cdot \text{m}^{-2}$ ) is the maximum adsorption capacity of asphaltenes, and  $\psi$  defined by:

$$\psi = \frac{-1 + \sqrt{1 + 4K\xi}}{2K} \quad (9)$$

where  $\xi$  is given by:

$$\xi = \frac{q_m q}{(q_m - q)} A \quad (10)$$

### 3.3. Estimation of Activation Energy and Reaction Kinetic Rate

The effective activation energy ( $E_a$ ) can be calculated following the isothermal procedure [28] according to the following Equation (11):

$$\frac{d\alpha}{dt} = K_a \exp\left(-\frac{E_a}{RT}\right) f(\alpha) \quad (11)$$

where,  $\alpha$  is the conversion degree and is equal to  $(m_o - m_t) / (m_o - m_f)$ ;  $m_o$ ,  $m_t$  and  $m_f$  are the initial mass of the sample, the current mass of the sample at a determined time  $t$ , and the final mass of the sample, respectively.  $K_a$  ( $s^{-1}$ ) is the pre-exponential factor,  $E_a$  ( $\text{kJ}\cdot\text{mol}^{-1}$ ) is the effective activation energy for a constant degree of conversion,  $R$  ( $\text{J}\cdot\text{mol}^{-1}\cdot\text{K}^{-1}$ ) is the ideal gas constant,  $T$  (K) is the reaction temperature,  $f(\alpha)$  is the reaction mechanism function, and  $d\alpha/dt$  is the reaction rate. As the analysis was performed under isothermal conditions, the separation of variables and the integration of the Equation (11) is as follows:

$$g(\alpha) = \int_0^\alpha \frac{d\alpha}{f(\alpha)} = \int_0^t K_a \exp\left(-\frac{E_a}{RT}\right) dt = K_a \exp\left(-\frac{E_a}{RT}\right) t \quad (12)$$

Assuming the value of  $E_a$  constant and taking the natural logarithm for both sides, Equation (12) is written as (13):

$$\ln(t_{a,i}) = \ln\left(\frac{g(\alpha)}{K_a}\right) + \frac{E_a}{RT_i} \quad (13)$$

The  $E_a$  is calculated from the slope of the Equation (13) obtained through the plot  $\ln(t_{a,i})$  vs.  $1/T_i$ . The subscript  $i$  is introduced to indicate different isothermal temperature conditions and  $t_{a,i}$  is the time for the reaction to reach a conversion ( $\alpha$ ) at a given temperature. On the other hand, the slope of Equation (13) provides an approximation of the reaction kinetics and has the next form:



$$\ln\left(\frac{g(\alpha)}{K_\alpha}\right) = \ln\left(\frac{\int_0^\alpha \frac{d\alpha}{f(\alpha)}}{K_\alpha}\right) = \ln\left(\int_0^\alpha \frac{d\alpha}{K_\alpha(\alpha)}\right) \quad (14)$$

mathematically,

$$-\ln\left(\frac{\int_0^\alpha \frac{d\alpha}{f(\alpha)}}{K_\alpha}\right) = \ln\left(\frac{1}{\int_0^\alpha \frac{d\alpha}{K_\alpha(\alpha)}}\right) \quad (15)$$

The above equation is solved from the harmonic mean of the reaction rate. This equation is applied as follows:

$$H_x = \frac{n}{\sum_{i=1}^n \frac{1}{(x)_i}} \quad (16)$$

where,  $H_x$  is the reaction rate, and  $x = d\alpha / dt$ , being  $d\alpha / dt > 0$ . The Equation (13) can be described as the Equation (17) applying the following consideration

$$\sum_{i=1}^n \frac{1}{\left(\frac{d\alpha}{dt}\right)_i} = k' \int_0^\alpha \frac{1}{\frac{d\alpha}{dt}} d\alpha$$

$$H_{\frac{d\alpha}{dt}} = \frac{K \exp\left(-\frac{E_\alpha}{RT}\right)}{g(\alpha)} \quad (17)$$

where  $K = n / k'$ . Taking the natural logarithm of both sides

$$\left(\frac{H_{\frac{d\alpha}{dt}}}{K}\right) = -\ln\left(\frac{g(\alpha)}{K_\alpha}\right) - \frac{E}{RT} \quad (18)$$

Then, comparing the Equations (13) and (18).

$$(19)$$

$$\ln(t_{a,i}) = \ln\left(\frac{H \frac{d\alpha}{dt}}{K}\right)$$

$$H \frac{d\alpha}{dt} = \frac{K^*}{t_{a,i}} \quad (20)$$

From the estimation of the harmonic mean, the reciprocal of the reaction time and a  $K^*$  parameter that may depend on the conversion is obtained.

## 4. Results and discussion

### 4.1. Nanoparticle Characterization

The surface area of the ceria nanoparticles was estimated at  $65 \pm 2 \text{ m}^2\cdot\text{g}^{-1}$ . Once the metal oxides were added to the nanoparticle, the surface area decreased slightly as the percentage of the TEO increased. However, the surface area is not affected considerably as the support material is non-porous, and no pores can be blocked.

The DLS results showed that the mean hydrodynamic diameter of the  $\text{CeO}_2$  nanoparticles was 22 nm, confirming its nanometric nature in agreement with the value reported by the provider. Figure 2 shows the TEM micrographs of  $\text{CeNi}_1\text{Pd}_1$ ,  $\text{CeCo}_1\text{Pd}_1$ , and  $\text{CeFe}_1\text{Pd}_1$  nanoparticles, where an undefined morphology of the support material and crystallization planes in the nanocrystals of the metal oxides are observed.

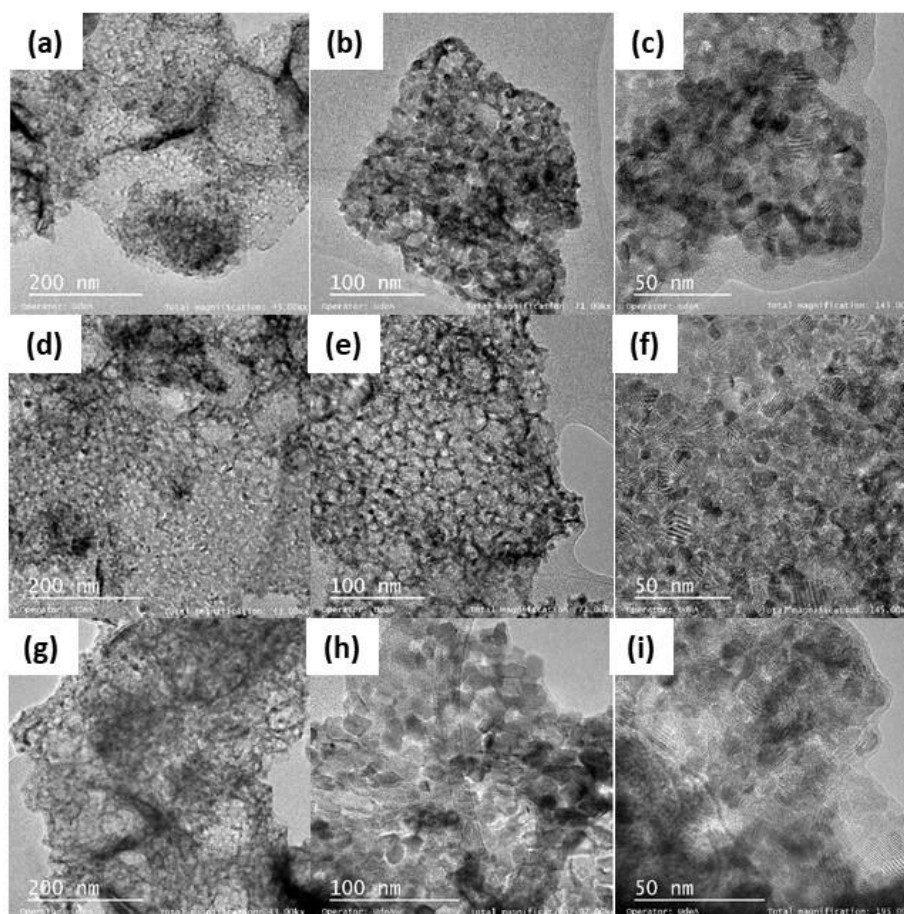


**Figure 2.** HR-TEM micrographs of (a–c) CeNi1Pd1, (d–f) CeCo1Pd1, and (g–i) CeFe1Pd1 nanoparticles at different magnifications.

The sizes of the metal oxide crystals and the dispersion thereof on the surface of the support are shown in Table 2. The dispersion of the Pd crystals increased in the order  $Fe < Co < Ni$ , while the different metals' dispersion followed the  $Fe < Ni < Co$ . In general, for all samples, a smaller crystal size implies a greater dispersion of the same on the nanoparticle's surface. These results show that the employed metals have a synergistic effect, which avoided sintering processes and generated a less heterogeneous surface due to the high dispersion of these crystals in the support. This could be due to the migration and coalescence of the crystals being significant when the material is heated above Tamman's temperature, where the oxides manage to form thermally induced vacancies called Schottky and Frenkel defects [58,59]. In this sense, the Tamman's temperatures of Ni, [60] Fe, [61], and Co [62] are approximately 690, 800, and 880 °C, respectively, indicating that the movement of the Co atoms by diffusion over the support surface required higher temperature and energy regarding Ni and Fe. Hence, it can be inferred that higher mobility of the Ni over the support

surface would inhibit the Pd mobility, resulting in an alleviated sintering characteristic of complex materials with noble metals [13].

**Table 2.** Estimated values of surface area ( $S_{\text{BET}}$ ), NiO, Fe<sub>2</sub>O<sub>3</sub>, Co<sub>3</sub>O<sub>4</sub>, and PdO mean crystal diameter (dp) and the dispersion over the CeO<sub>2</sub> support.

Sample	$S_{\text{BET}} \pm 0.1$ $\text{m}^2 \cdot \text{g}^{-1}$	dp (nm $\pm$ 0.2 nm)				Dispersion (%)	
		NiO	Co <sub>3</sub> O <sub>4</sub>	Fe <sub>2</sub> O <sub>3</sub>	PdO	Ni/Co/Fe	Pd
CeO <sub>2</sub>	67.0	-	-	-	-	-	-
CeNi1Pd1	63.8	6.4	-	-	3.9	12.7	38.6
CeFe1Pd1	64.1	-	-	5.4	6.9	11.2	12.8
CeCo1Pd1	64.4	-	1.9	-	6.1	18.1	20.4

#### 4.2. Asphaltene Adsorption onto Nanoparticles

First, the adsorption isotherms of *n*-C<sub>7</sub> asphaltenes were obtained for the CeO<sub>2</sub> support. The CeO<sub>2</sub> nanoparticles were functionalized with 1% in mass fraction of different TEO at a and PdO (CeNi1Pd1, CeCo1Pd1, and CeFe1Pd1). The best TEO-Pd functionalizing couple is selected for performing the SCMD experiments. Figure 3 shows the adsorption isotherms at 25 °C for the CeNi1Pd, CeCo1Pd1, and CeFe1Pd1 nanoparticles together with the fit of the SLE model.

According to the International Union of Pure and Applied Chemistry (IUPAC), the obtained adsorption isotherms are type Ib [63], which is consistent with earlier studies. [13,22,29–32,39,53]. In all cases, the asphaltene adsorption was higher for the bi-elemental nanoparticles than for non-doped support. In addition, the adsorption between the three bielemental systems increased in the order CeO<sub>2</sub> < CeFe1Pd1 < CeCo1Pd1 < CeNi1Pd1. This pattern might be caused by the CeNi1Pd1 sample having a higher metal dispersion than other adsorbents, which results in stronger intermolecular forces between heteroatoms (HA) and functional groups of the nanoparticle.

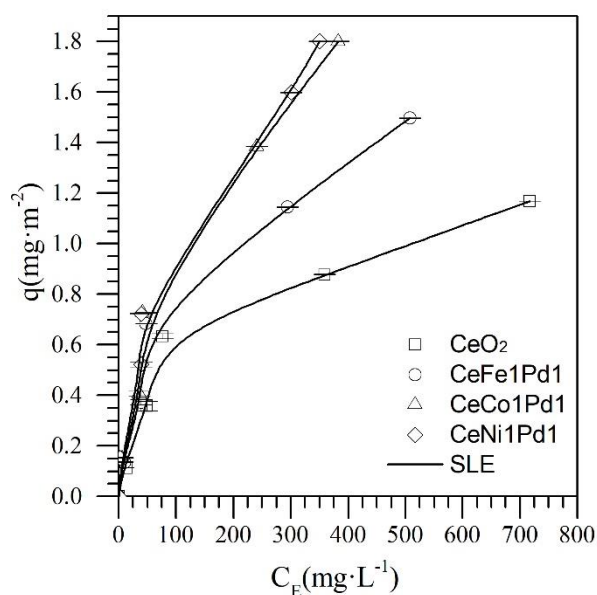


**Figure 3.** Adsorption isotherms of *n*-C<sub>7</sub> asphaltenes onto CeO<sub>2</sub> nanoparticles and CeO<sub>2</sub> nanoparticles functionalized with Ni, Fe, Co, and Pd at 25 °C. Adsorption isotherms were obtained for *n*-C<sub>7</sub> asphaltene concentrations from 100 mg·L<sup>-1</sup> to 1500 mg·L<sup>-1</sup> in toluene for a fixed dosage of nanoparticles of 100 mg per 10 mL of solution. The symbols are experimental data, and the solid lines are from the SLE model.

Additionally, these results are corroborated with the parameters obtained by the SLE model, where the value of  $H$  decreased in the order CeO<sub>2</sub> > CeFe1Pd1 > CeCo1Pd1 > CeNi1Pd1, indicating that there was a higher affinity between the asphaltenes and the bielemental nanoparticles. The TEO-based catalyst showed an excellent capability to interact with carbonaceous molecules and activate the C-C, C-O, C-N, and C-H bonds. According to the adsorption experiments and the values of  $H$  from the SLE model, the affinity for asphaltene changes due to the presence of the different TEOs, obtaining a greater affinity for Ni than for Co and Fe. Hence, it can be established that these TEO/CeO<sub>2</sub> hybrid materials interact with the asphaltene molecules via coordinated bonds (HA-TE) [64].

It is well known that the organic functional groups containing HA (O, N, and S) are Lewis bases due to the electron lone pairs located on them. Therefore, this family of molecules can form coordinate bonds by interacting with Lewis acids, such as transition elements (TE), with adequate orbitals and strength. The Lewis acidity is expected to change as the periodic group increases for the different elements. This can be explained by the rise in the effective nuclear charge (Fe < Co < Ni) [65]. On the other hand, the interaction between TE and Pd shows synergetic effects that improve catalytic performances.

Accordingly, the Ni–Pd couple was selected to optimize the metal concentrations over the CeO<sub>2</sub> support according to the simplex-centroid mixture design of experiments. Figure 4 shows the adsorption isotherms at 25 °C of *n*-C<sub>7</sub> asphaltenes on nanoparticles established in the SCMD. In general, all samples showed high adsorption affinity for *n*-C<sub>7</sub> asphaltenes. The asphaltene uptake follows the order CeNi1Pd1 > CePd2 > CeNi0.66Pd0.66 > CeNi2 > CePd1 > CeNi1 > CeO<sub>2</sub>. Table 3 summarizes the estimated SLE parameters for all nanoparticles evaluated. The values for the *H* parameter (related to the affinity for the adsorption) increase in the order CeNi1Pd1 < CePd2 < CeNi0.66Pd0.66 < CeNi2 < CePd1 < CeNi1 < CeO<sub>2</sub>, corroborating that the loading of the metal on the support surface matters insofar as *H* is smaller for the CePd2 and CeNi2 nanoparticles than for CePd1 and CeNi1 materials.

Also, the value of *H* is lower for the bielemental system (CeNi1Pd1), indicating after Ni and Pd doping, the support increases its adsorptive capacity and affinity for *n*-C<sub>7</sub> asphaltenes. On the other hand, the *K* parameter follows the same trend as *H*, indicating the highest association rate of asphaltenes molecules once the primary sites were occupied for nanoparticle support without metals on its surface. This suggests that ceria supported TEO nanoparticles are more prone to inhibit the asphaltenes' self-association over its surface than the support [14,32,53].

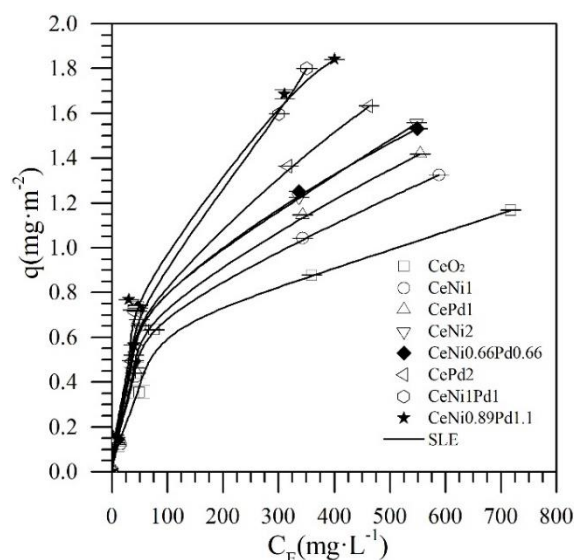


**Figure 4.** Adsorption isotherms at 25 °C of *n*-C<sub>7</sub> asphaltenes onto CeO<sub>2</sub> nanoparticles and CeO<sub>2</sub> nanoparticles functionalized with different mass fractions of Ni and/or Pd up to 2%. Adsorption isotherms were obtained for *n*-C<sub>7</sub> asphaltene concentrations from 100 mg·L<sup>-1</sup> to 1500 mg·L<sup>-1</sup> in toluene for a fixed dosage of nanoparticles of 100 mg per 10 mL of solution. The symbols are experimental data, and the solid lines are from the SLE model.

**Table 3.** Estimated values of the SLE model parameters for the adsorption isotherms of *n*-C<sub>7</sub> asphaltenes onto CeO<sub>2</sub> nanoparticles and CeO<sub>2</sub> nanoparticles functionalized with Ni, Fe, Co, and Pd at 25 °C.

<b>Material</b>	<b><math>H \pm 0.02 \text{ (mg}\cdot\text{g}^{-1}) \times 10^{-2}</math></b>	<b><math>K \pm 0.08 \text{ (g}\cdot\text{g}^{-1})</math></b>	<b><math>q_m \pm 0.01 \text{ (g}\cdot\text{g}^{-1})</math></b>	<b><i>RSM</i> (%)</b>
CeO <sub>2</sub>	10.12	0.21	0.13	0.02
CePd1	7.19	0.29	0.16	0.03
CeNi1	7.34	0.03	0.15	0.04
CePd2	6.25	0.39	0.18	0.01
CeNi2	6.70	0.04	0.16	0.01
CeNi0.66Pd0.66	6.61	0.05	0.16	0.02
CeNi1Pd1	6.02	0.06	0.22	0.01
CeFe1Pd1	6.58	0.04	0.17	0.02
CeCo1Pd	5.34	0.06	0.19	0.01
Ce Ni0.89Pd1.1	2.84	0.04	0.25	0.01

### 4.3. Catalytic Steam Gasification of *n*-C<sub>7</sub> Asphaltenes

#### 4.3.1. Mass Loss Analysis

The selected nanoparticles were tested in an atmosphere of N<sub>2</sub> saturated with H<sub>2</sub>O<sub>(g)</sub> for asphaltenes catalytic steam gasification. Figure 5 shows the rate of mass loss of *n*-C<sub>7</sub> asphaltenes in the presence and absence of CeO<sub>2</sub> nanoparticles and CeO<sub>2</sub> nanoparticles functionalized with Ni, Fe, Co, and Pd metal oxides. Figure 4 reveals that for virgin *n*-C<sub>7</sub> asphaltenes, the decomposition occurs between 400 and 550 °C. The gasification of *n*-C<sub>7</sub> asphaltenes appears to occur at much lower temperatures when are adsorbed on nanoparticles.

The temperature range under consideration will be divided into three regions, the first of which is the low-temperature region (LTR), with temperature values ranging from 200 to 250 °C. The second medium-temperature region (MTR) will be from 251 to 450 °C, and the high-temperature region (HTR) will be from 451 to 600 °C. From the rate of mass loss plot, it can be observed that CeO<sub>2</sub> nanoparticles without functionalization reduce the decomposition temperature of *n*-C<sub>7</sub> asphaltenes from approximately 455 °C to 370 °C. However, all the functionalized samples manage to reduce the *n*-C<sub>7</sub> asphaltenes decomposition temperature from HTR to LTR in the order Ni > Co > Fe. However, this decomposition is generated in several stages for the three cases, indicating a distribution of asphaltene sizes (low, medium, and high molecular weight). The components with lower molecular weight decompose at lower temperatures. These values vary for all nanoparticles due to the transferring electrons that different TEO has due to their charges on the surface of CeO<sub>2</sub>.

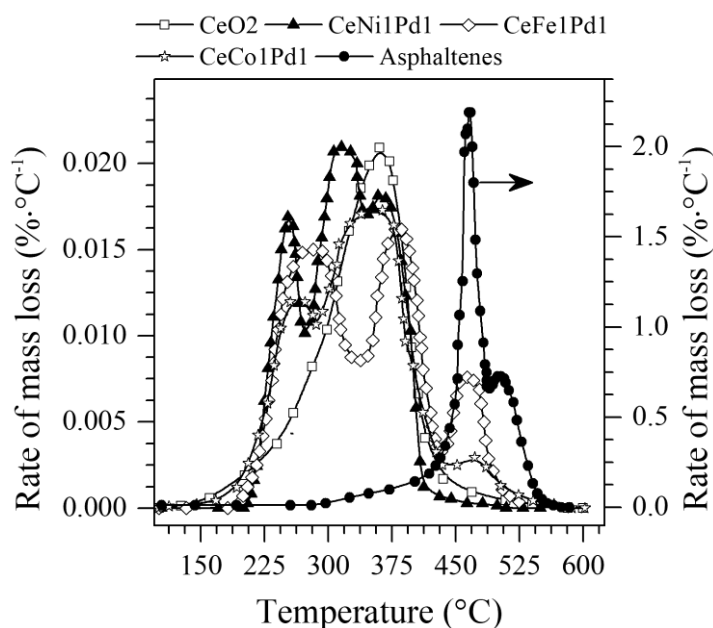


**Figure 5.** Rate of mass loss as a function of the temperature for steam gasification of *n*-C<sub>7</sub> asphaltenes in the absence and presence of CeO<sub>2</sub>, CeNi1Pd1, CeCo1Pd1, and CeFe1Pd1 nanoparticles. Nitrogen flow rate = 100 mL·min<sup>-1</sup>, H<sub>2</sub>O(g) flow rate = 6.30 mL·min<sup>-1</sup>, heating rate = 20 °C·min<sup>-1</sup> and *n*-C<sub>7</sub> asphaltene loading 0.2 mg·m<sup>-2</sup>.

The decomposition of *n*-C<sub>7</sub> asphaltenes over CeNi1Pd1 nanoparticles begins at 220 °C in the LTR region, continues at 310 °C in the MTR region, where it decomposes larger chains of hydrocarbons, and ends in this same region at 375 °C. This means that during the gasification process, the heavier compounds were cracked in lower molecular weight hydrocarbon chains either by the loss of heteroatoms in the breakage of bonds (C–S, C–N, C–O) or the breakdown of C–C and C–H bonds. For the CeCo1Pd1 and CeFe1Pd1 nanoparticles, they produce decomposition of *n*-C<sub>7</sub> asphaltenes in the three regions, at 230 °C, 350 °C, 455 °C and 250 °C, 370 °C, and 455 °C, respectively. Between these two systems, the CeCo1Pd1 system in the HTR region produces a lower mass loss compared to CeFe1Pd1. Among the three systems evaluated, the system formed by Ni and Pd had a synergistic effect reflected in its better performance for the decomposition of *n*-C<sub>7</sub> asphaltenes in the LTR region.

Additionally, differences in the intensity of the peaks in the different regions could be due to the suppression of addition reactions of the *n*-C<sub>7</sub> asphaltenes after decomposition. Samples that show peaks with lower intensities in the MTR and HTR have higher catalytic activity, as they would promote an earlier decomposition independently of the molecular weight of the asphaltene adsorbed.



Figure 6 shows the conversion or the extent of reaction ( $\alpha$ ) of  $n$ -C<sub>7</sub> asphaltenes in the presence and absence of the employed nanoparticles as a function of time at isothermal conditions of 240 °C. As can be seen in Figure 5, the presence of nanoparticles generates a catalytic effect reflected in the decomposition time or reaction velocity, which is lowest for CeNi1Pd1 nanoparticles, followed by CeCo1Pd1, CeFe1Pd1, and CeO<sub>2</sub>. However, an important change was achieved in the conversion concerning virgin asphaltenes for all samples.

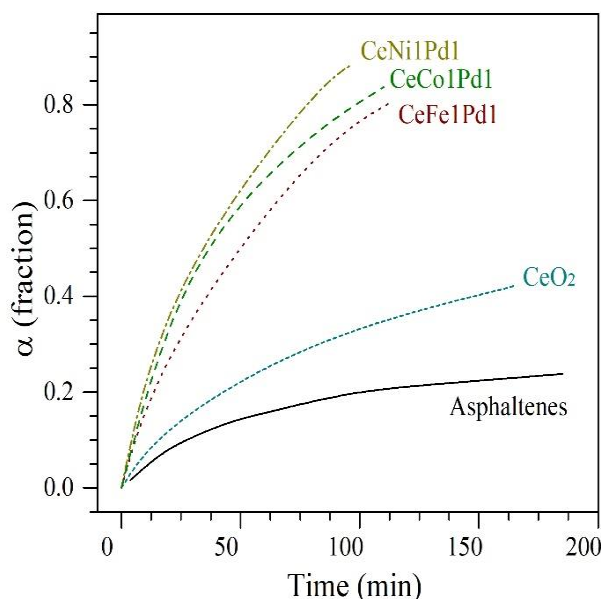
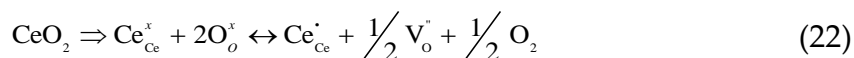


**Figure 6.** Isothermal conversion ( $\alpha$ ) for steam gasification of  $n$ -C<sub>7</sub> asphaltenes in the absence (360 °C) and presence (240 °C) of CeO<sub>2</sub>, CeNi1Pd1, CeCo1Pd1, and CeFe1Pd1 nanoparticles. Nitrogen flow rate = 100 mL·min<sup>-1</sup>, H<sub>2</sub>O<sub>(g)</sub> flow rate = 6.30 mL·min<sup>-1</sup> and  $n$ -C<sub>7</sub> asphaltene loading 0.2 mg·m<sup>-2</sup>.

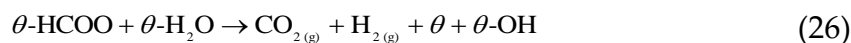
The best catalytic is obtained for the CeNi1Pd1 nanoparticles with an 89% of asphaltene conversion in less than 100 min at 240 °C. It is important to note that the differences in the catalytic activity are related to the synergistic effect of the TE on the surface of the CeO<sub>2</sub> nanoparticles and the interactions between asphaltenes-nanoparticles because the asphaltenes, being non-pure compounds, could have different selectivity for different combinations. The higher catalytic activity of the Ni-Pd couple could be due to the inhibition of the growth of the PdO nanocrystal and the enhanced dispersion over the CeO<sub>2</sub> surface.

#### 4.3.2. Analysis of the Gaseous Products Evolved during the Steam Gasification Process

The evolution of gaseous products during the gasification process of virgin asphaltenes and asphaltenes adsorbed onto CeO<sub>2</sub>, CeNi1Pd1, CeCo1Pd1, and CeFe1Pd1 nanoparticles is shown in Figure 7. The gaseous products of asphaltenes gasification were evaluated using an FTIR device coupled to the TGA under isothermal conditions of 240 °C. During the steam gasification of *n*-C<sub>7</sub> asphaltenes, a series of reactions occur, such as water-gas-shift (WGS) reaction, partial oxidation reaction, Boudouard reaction, methanation reaction, and steam reforming reaction, among others, generating as main products CO, CO<sub>2</sub>, CH<sub>4</sub>, NO<sub>x</sub>, and light hydrocarbons (LHC). Results are normalized based on the signal with the highest intensity corresponding to the gas production for CeNi1Pd1 in all cases. The gases that are being produced are initially due to the catalytic effect of CeO<sub>2</sub> and its redox cycle (Ce<sup>4+</sup> / Ce<sup>3+</sup>) that allows the oxygen adsorption under oxidation conditions and its release under reduced conditions, as is shown in Equations (21) and (22):



Bielemental systems increased gas production in the following order (Fe < Co < Ni). The high performance of the CeNi1Pd1 system is mainly due to the influence of nickel oxides as a dispersant material together with cerium as an active support material in the acceleration of the production of the WGS reaction at low temperatures (240 °C) due to the oxygen anion vacancy on the surface [48]. This reaction is generally associated with two mechanisms in which the cerium oxide generates a catalytic effect, namely, (a) associative mechanism mediated by methanoate species and (b) redox mechanism, which is widely favored by the addition of noble metals in the support. Hydroxyl groups (OH) formed by the reaction between H<sub>2</sub>O and partially reduced ceria oxygen vacancies react with CO to form methanoate species of the bridge. Above 170 °C, these species are transformed into bidentate formates to decompose into final products of CO<sub>2</sub> and H<sub>2</sub> [66]. Vignatti et al. [67] proposed a mechanism mediated by methanoate species to explain the catalytic behavior of the ceria with the addition of noble transition elements (TE) like Pd, according to Equations (23)–(26), where  $\theta$  refers to the support and  $\sigma$  represents the adsorption sites in the TE [45–47]:



According to the redox reaction mechanism, the CO is adsorbed on the active sites of the TE to react with the cerium oxide, reducing it to cerium (III) oxide (schematized as  $\text{CeO}_{2-\delta}$ , see Equations (21) and (22)). This reduction generates oxygen vacancies or defects that, in contact with water molecules, produce OH groups and eventually  $\text{H}_2$  (Equations (23)–(26)). Further, it is important to emphasize the role of TE in activating CO and forming oxygen vacancies in the TE/ceria interface [40,41], as follows:

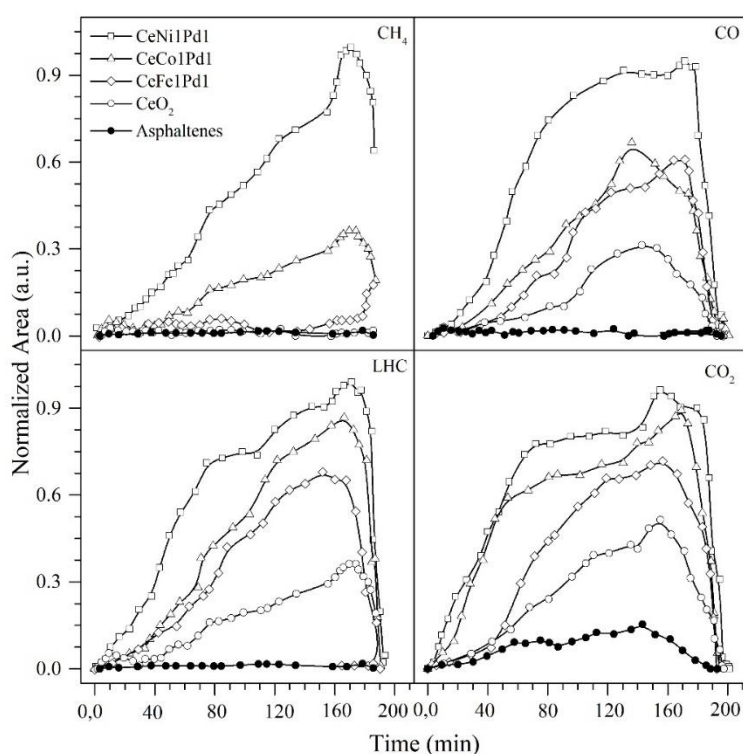
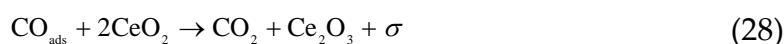


**Figure 7.** Evolution profiles of gaseous products during steam gasification under isothermal conditions at 240 °C of *n*-C<sub>7</sub> asphaltenes in the presence and absence of the selected catalysts. Nitrogen flow rate = 100 mL·min<sup>-1</sup>, H<sub>2</sub>O<sub>(g)</sub> flow rate = 6.30 mL·min<sup>-1</sup> and *n*-C<sub>7</sub> asphaltene loading 0.2 mg·m<sup>-2</sup>.

Hence, the CO is produced through the reaction of free radicals with the oxygen released from O-containing functional groups in the asphaltene structures. Further, this gas's production generates H<sub>2</sub> due to the catalytic activity of CeO<sub>2</sub> loaded with TEO on the water-gas shift reaction and CO oxidation. The CeO<sub>2</sub> role is not limited to the storage of oxygen since it allows the transfer of oxygen from ceria to the TEO interface and re-oxidation of ceria through the adsorption of CO on the active sites of the TEO, as shown in Equations (27)–(29). On the other hand, two main oxygen sources for CO<sub>2</sub> production can be attributed: (i) the oxygen content of the asphaltenes and (ii) lattice oxygen from the nanoparticles. For all cases, the evolution profile constantly increases with time.

#### 4.3.3. Coke Yield

For the asphaltenes in the presence and absence of CeO<sub>2</sub>, CeNi1Pd, CeCo1Pd1, and CeFe1Pd1, the coke yield was evaluated under an air atmosphere from 100 °C to 600 °C for 20 °C·min<sup>-1</sup>, with a flow rate of 100 mL·min<sup>-1</sup>. Figure 8 shows the results obtained for the coke yield of the samples evaluated. For virgin *n*-C<sub>7</sub> asphaltenes, the coke yield was estimated in a mass fraction of 63% ± 2%, and for *n*-C<sub>7</sub> asphaltenes adsorbed onto the CeO<sub>2</sub> nanoparticles surface, the coke yield was 8.1%. In the case of the functionalized nanoparticles, the coke yield follows the trend CeFe1Pd1 > CeCo1Pd1 ≅ CeNi1Pd1 with an inhibition of the coke production of more than 99%, regarding the CeO<sub>2</sub> support.

In general, and through the analysis performed in each of the tests, the nanoparticle with better performance regarding catalytic activity refers to CeNi1Pd1. Further, the Ni-Pd couple is selected for the following experiments. It is important to emphasize that the CeO<sub>2</sub>, CeFe1Pd1, and CeCo1Pd1 nanoparticles also have a good catalytic effect in the reactions that generate the asphaltenes decomposition.

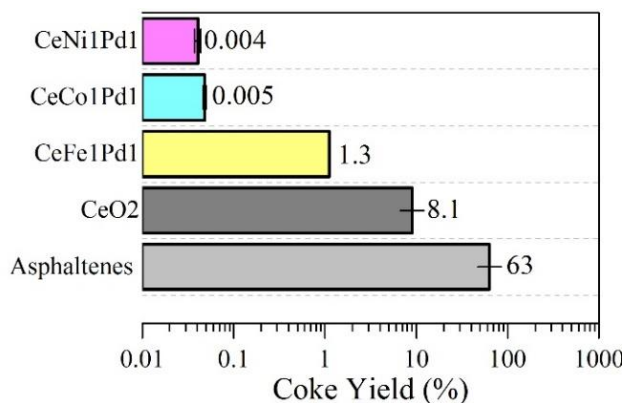


**Figure 8.** Coke yield for *n*-C<sub>7</sub> asphaltenes decomposition under steam gasification in the absence and presence of CeO<sub>2</sub>, CeNi1Pd1, CeCo1Pd1, and CeFe1Pd1 nanoparticles. Nitrogen flow rate = 100 mL·min<sup>-1</sup>, H<sub>2</sub>O<sub>(g)</sub> flow rate = 6.30 mL·min<sup>-1</sup>, heating rate = 20 °C·min<sup>-1</sup> and asphaltene loading 0.2 mg·m<sup>-2</sup>.

#### 4.4. Effect of *n*-C<sub>7</sub> Asphaltene Amount Adsorbed on the Decomposition Temperature

According to the results, the CeNi1Pd1 sample was used to evaluate the effect of the *n*-C<sub>7</sub> asphaltenes amount adsorbed on the decomposition temperature. For this analysis, three different loads of asphaltenes of 0.2 mg·m<sup>-2</sup>, 0.05 mg·m<sup>-2</sup>, and 0.02 mg·m<sup>-2</sup> were evaluated. In this case, the samples were heated at 20 °C·min<sup>-1</sup> until 220 °C (according to the first decomposition peak for this sample in Figure 4), where isothermal conditions were fixed until no significant changes in the mass loss were observed and finally heated again up to 700 °C at the same heating rate. Figure 9 shows (a) the rate of mass loss and (b) isothermal conversion at 220 °C for the CeNi1Pd1 nanoparticles with different asphaltene amounts adsorbed.

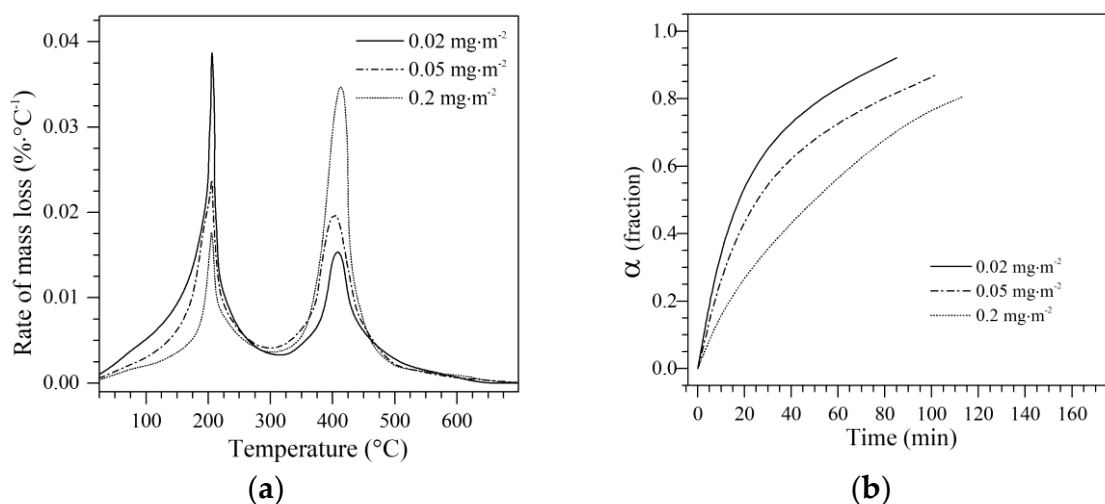


**Figure 9.** (a) Plot of the rate of mass loss and (b) isothermal conversion ( $\alpha$ ) at 220 °C for asphaltene loadings of 0.2 mg·m<sup>-2</sup>, 0.05 mg·m<sup>-2</sup>, and 0.02 mg·m<sup>-2</sup> over CeNi1Pd1 nanoparticles. Nitrogen flow rate = 100 mL·min<sup>-1</sup>, H<sub>2</sub>O<sub>(g)</sub> flow rate = 6.30 mL·min<sup>-1</sup>. The samples were heated at 20 °C·min<sup>-1</sup> until 220 °C (according to the first decomposition peak), where isothermal conditions were fixed until no significant changes in the mass loss were observed, and finally heated again up to 700 °C at the same heating rate.

The three samples exhibit two peaks of mass loss. The intensity of the first peak, however, increases while the second peak's intensity decreases as the loading of asphaltenes decreases. This effect may be brought on by the asphaltenes adhering to the TEO active sites prior to the ceria active sites. Additionally, fewer adsorbed asphaltenes can result in less self-association over the active sites, forming smaller aggregates, and therefore, less energy required for decomposition. As can be observed from Figure 9b, when the amount of asphaltenes decreases, the conversion increases since a more significant number of active sites free for the reaction are available.

#### 4.5. Maximization of Conversion of Asphaltenes during Steam Gasification through an SCMD

##### 4.5.1. Isothermal Conversion of Asphaltenes Adsorbed on Nanoparticles from SCMD

The maximum conversion of the asphaltenes adsorbed on nanoparticles was used as a response variable ( $\alpha_m$ ) when performing the maximization. The process was carried out for the best system among the three functionalizing couples evaluated (i.e., CeNi1Pd1) for an amount adsorbed of asphaltenes of 0.02

$\text{g}\cdot\text{m}^{-2}$  under isothermal conditions at 220 °C according to the results in Figure 10. The STATGRAPHICS Centurion XVI software was used to obtain the statistical outcomes, and the process was validated using the special cubic model with a  $R^2 > 0.99$ . In this way, asphaltene conversion can be predicted for any Ce, Pd, and Ni concentration in the evaluated range. The conversion model values are shown in Table 4 as functions of the pseudo-components Ce, Ni, and Pd. For dosages of mass fractions of 1.1% and 0.89% of palladium and nickel, respectively (CeNi0.89Pd1.1), the optimal point for conversion maximization is discovered. An adsorption isotherm was constructed for this sample, as shown in Figure 4. As can be seen, the CeNi0.89Pd1.1 nanoparticle has a better performance than all the samples except for CeNi1Pd1 and CePd2 for  $c_0 < 500 \text{ mg}\cdot\text{L}^{-1}$ .

Figure 11 shows the asphaltene conversion using CeNi0.89Pd1.1 nanoparticles compared to all samples evaluated from the SCMD. A reduction in the reaction time for asphaltene decomposition for the optimized sample, including the CeNi1Pd1 can be observed. Also, the results in Figure 9 indicate that a better catalytic activity is obtained for bielemental samples regarding the monoelementals. However, the SPd2 shows a better performance than the CeNi0.66Pd0.66, indicating that the PdO presence is a key controller parameter in the catalytic activity of the material. These results also corroborate that the crystallite size and dispersion of the active phase led to a more efficient decomposition. This optimization's importance lies in reducing the TEO percentage to generate a better catalytic effect and a reduction of the Pd concentration by almost 50% regarding the SPd2 sample.

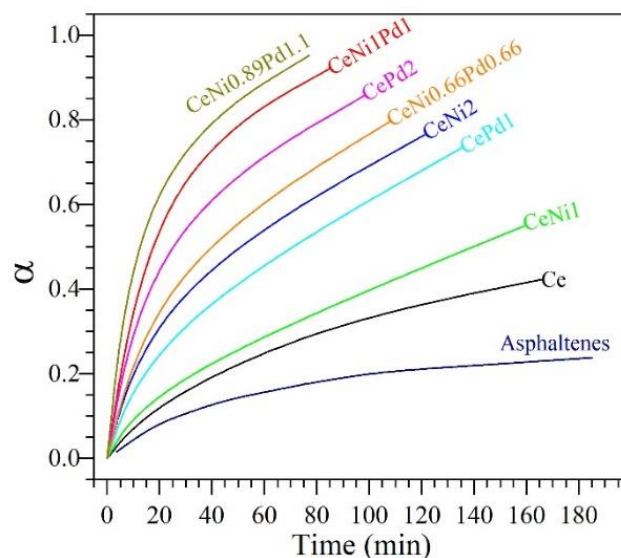


**Figure 11.** Isothermal conversion ( $\alpha$ ) for steam gasification of *n*-C<sub>7</sub> asphaltenes in the absence (360 °C) and presence (220 °C) of CeO<sub>2</sub>, CeNi1, CeNi2, CePd1, CePd2, CeNi0.66Pd0.66, CeNi1Pd1, and CeNi0.89Pd1.1 (optimized sample) nanoparticles. The nanoparticles are selected from a simplex-centroid mixture design of experiments for maximizing the asphaltene conversion. Nitrogen flow rate = 100 mL·min<sup>-1</sup>, H<sub>2</sub>O<sub>(g)</sub> flow rate = 6.30 mL·min<sup>-1</sup> and *n*-C<sub>7</sub> asphaltene loading 0.02 mg·m<sup>-2</sup>.

**Table 4.** Calculated parameters of the Special Cubic Model for the *n*-C<sub>7</sub> asphaltenes conversion time in the presence of SCMD nanoparticles.

$\beta_1$	$\beta_2$	$\beta_3$	$\beta_{12}$	$\beta_{13}$	$\beta_{23}$	$\beta_{123}$	$R^2$
0.006896	0.008264	0.008928	0.000246	0.002873	0.006017	0.003310	0.99

#### 4.5.2. Effective Activation Energy and Kinetics of the Catalytic Steam Gasification of Asphaltenes in the Presence and Absence of Nanoparticles

Thermogravimetric analyses were carried out for asphaltenes adsorbed on all nanoparticles selected from the SCMD at 230, 240, and 250 °C to obtain information about the catalytic effect of the selected TEO on effective activation energy and reaction kinetics. In the case of asphaltenes in the absence of nanoparticles, the employed temperatures were 350, 360, and 370 °C. Figure 12a–d shows the time of isothermal conversion ( $\alpha$ ) of virgin asphaltenes and adsorbed asphaltenes onto CeO<sub>2</sub>, CeNi1Pd1, and CeNi0.89Pd1.1 at the corresponding temperatures.



The effective activation energies ( $E_a$ ) were calculated from the slope of the plot  $\ln(t_{a,i})$  vs.  $1/T_i$  in Figure 13, and Table 5 summarizes the results obtained for the  $E_a$  and reaction kinetics.

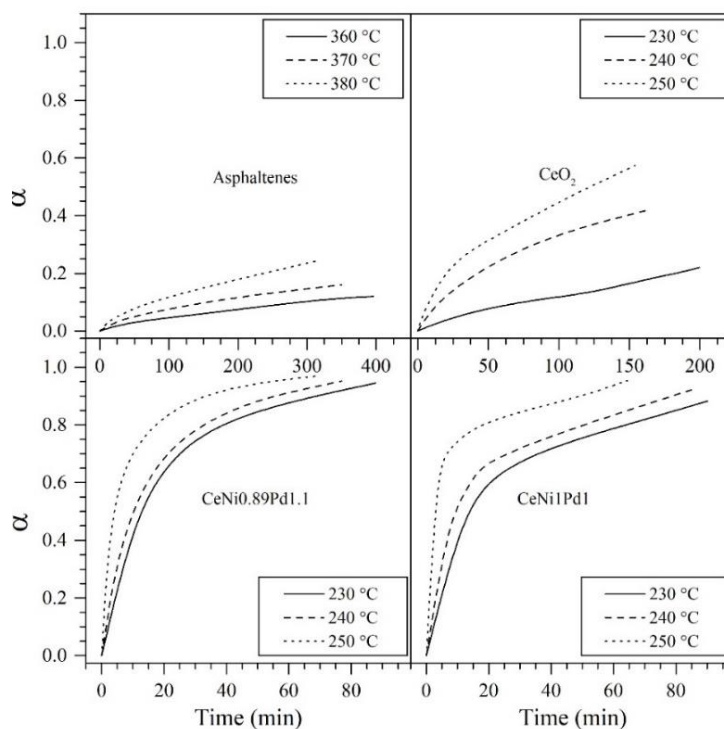


**Figure 12.** Isothermal conversion ( $\alpha$ ) at different temperatures for steam gasification of  $n$ -C<sub>7</sub> asphaltenes in the absence and presence of CeO<sub>2</sub>, CeNi1Pd1, and CeNi0.89Pd1.1 (optimized sample) nanoparticles. The nanoparticles are selected from a simplex-centroid mixture design of experiments for maximizing the asphaltene conversion. Nitrogen flow rate = 100 mL·min<sup>-1</sup>, H<sub>2</sub>O<sub>(g)</sub> flow rate = 6.30 mL·min<sup>-1</sup> and  $n$ -C<sub>7</sub> asphaltene loading 0.02 mg·m<sup>-2</sup>.

As expected, the conversion of asphaltenes increased with the increase in temperature. For the asphaltenes in the presence of CeO<sub>2</sub> nanoparticles, the asphaltene conversion was lower than 0.6 for the three temperatures evaluated. For the CeNi1Pd1 sample, the conversion was 0.9, 0.92, and 0.96 at 230, 240, and 250 °C, respectively. In the case of the optimized sample, for all temperatures evaluated,  $\alpha = 1$  was obtained, indicating that an effective decomposition of asphaltenes is achieved under typical temperatures of steam injection EOR processes.

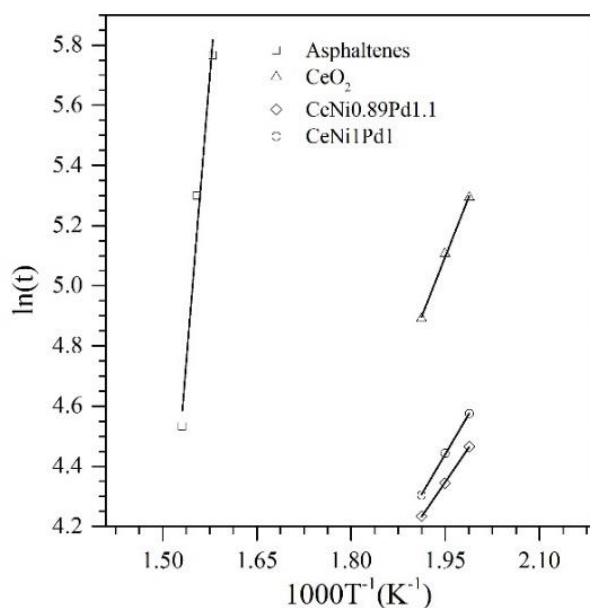


**Figure 13.** Arrhenius plot for the isothermal model of catalytic and thermal gasification of asphaltenes in the presence and absence of CeO<sub>2</sub>, CeNi1Pd1, and CeNi0.89Pd1.1 (optimized sample) nanoparticles.

In all the cases that were examined, it was discovered that the effective activation energy was lower, pointing to a change in the reaction's mechanism. The values of the kinetic rate, which indicate a faster reaction, are consistent with the values of the CeNi0.89Pd1.1 < CeNi1Pd < CeO<sub>2</sub> trend, which indicates a higher efficiency in the decomposition of the asphaltenes for the optimized sample. It is also corroborated with the values of the kinetic rate that suggest that the reaction occurs faster on CeNi0.89Pd1.1. These values serve as an effective variable when comparing the catalytic activity of the nanoparticles because they approximate the potential reaction rate that can be achieved without the reaction barrier. The gasification reaction of asphaltenes is influenced by the chemical elements used and their proportions, as shown by the kinetic reaction rate being faster for CeNi0.89Pd1.1 than CeNi1Pd1, and this last was faster than CeO<sub>2</sub>.

**Table 5.** Estimated effective activation energy ( $E_a$ ) and kinetic rate for isothermal catalytic steam gasification of asphaltenes in the absence and presence of CeO<sub>2</sub>, CeNi1Pd1, and CeNi0.89Pd1.1 nanoparticles.

Sample	Temperature °C	$E_a$ (kJ)	$d\alpha / dt$ Kinetic Rate (min <sup>-1</sup> ) at 50% Conversion
<i>n</i> -C <sub>7</sub> asphaltenes (without nanoparticles)	360	211.5	0.012
	370		0.018
	380		0.032
CeO <sub>2</sub>	230	44.0	0.013
	240		0.021
	250		0.879
CeNi1Pd1	230	29.6	0.0187
	240		0.0401
	250		0.1002
CeNi0.89Pd1.1	230	25.6	0.029
	240		0.084
	250		0.179

Figure 14 shows the relationship between the adsorptive behavior according to the SLE model parameters and the catalytic activity of the CeO<sub>2</sub>, CeNi1Pd1, and CeNi0.89Pd1.1 systems in terms of the effective activation energy. Figure 14 shows a direct relationship between Henry's law constant and the effective activation. The values of  $E_a$  increase in the order CeO<sub>2</sub> < CeNi1Pd1 < CeNi0.89Pd1.1, indicating that there is a synergistic effect between the support and functionalizing agents (NiO and PdO). These active phases also increase the affinity of the *n*-C<sub>7</sub> asphaltenes, mainly in the active sites belonging to the TEOs. Hence, the values of the  $H$  parameter (Table 3) decrease in the same order than  $E_a$ , indicating a direct relationship between the catalytic activity and the adsorption capacity of the materials. Similarly, it is observed that the effective activation energy increased as the  $K$  parameter increased, suggesting that higher asphaltene self-association over the active sites of the nanoparticles required higher energy for the decomposition. This could be due to the proximity of the asphaltene to the active phase, which is lower for systems with multilayers. Also, results indicate that the distribution of the active phase over the CeO<sub>2</sub> support is a controlling factor for the adsorption and subsequent catalytic decomposition of

the asphaltenes. These trends agree with previous studies [13] in which the effective activation energy was related to the adsorption affinity, the degree of asphaltene self-association, and the chemical nature of the support.

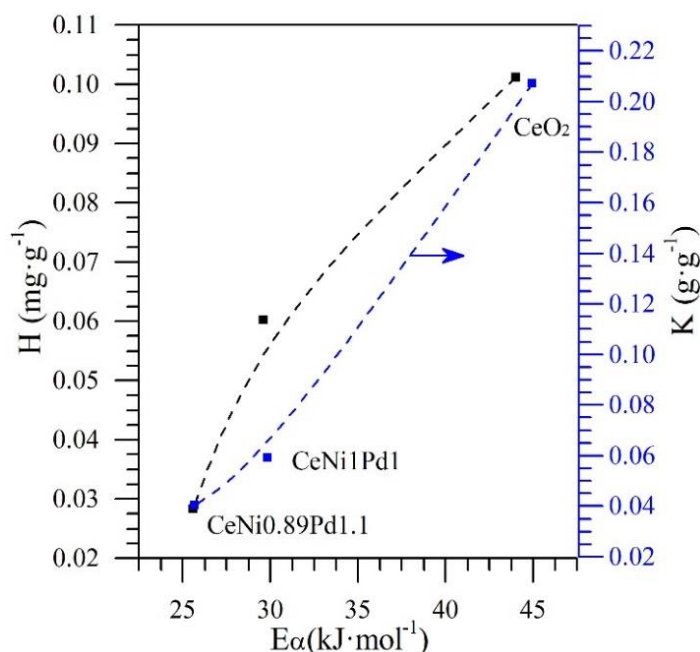


**Figure 14.** Relationship between Henry's law constant ( $H$  parameter of the SLE model), the degree of asphaltene self-association over the active sites of the catalyst ( $K$  parameter of the SLE model) and the effective activation energies ( $E_{\alpha}$ ) calculated by the isothermal model for the catalytic steam gasification of  $n$ -C<sub>7</sub> asphaltenes.

## 5. Conclusions

This study investigates the synergistic effect between PdO with NiO, Co<sub>3</sub>O<sub>4</sub>, or Fe<sub>2</sub>O<sub>3</sub> supported on ceria nanoparticles to evaluate the catalytic effect on steam decomposition of asphaltenes extracted from an extra heavy oil sample. The evaluated temperatures were lower than 250 °C under isothermal conditions, aiming at reproducing the temperatures of steam injection EOR processes. The adsorptive capacity of the nanoparticles increases with the addition of TEO on its surface. Likewise, these nanoparticles are prone to reduce the degree of self-association of asphaltenes and increase the affinity of adsorption, as confirmed by the values of the parameters  $K$  and  $H$  of the SLE model. Among the three main systems Ni–Pd, Co–Pd, and Fe–Pd over the ceria support, the CeNi1Pd1 is the one that shows the best results in terms of reducing the temperature of asphaltenes decomposition in steam injection processes and its respective

maximum conversion generated under isothermal conditions. Also, the nanoparticles induce inhibition of the coke formation and, like the other systems evaluated, increase the production of CH<sub>4</sub> and CO. These results indicate that water gas shift and other reactions are occurring. The output of H<sub>2</sub> also increased, allowing the hydrogenation of the cracked asphaltene molecules. A simplex-centroid mixture design (SCMD) was performed to optimize the concentration of transition element oxides on the surface of the nanoparticle, obtaining the optimized system CeNi<sub>0.89</sub>Pd<sub>1.1</sub> which effectively generates a conversion of 100% of asphaltenes in less than 90 min at 220 °C, whose value is within the range of temperatures in which a steam injection process is carried out. Results showed that the employed SCMD could predict the physicochemical properties in complex systems. The optimized nanoparticles can reduce the effective activation energy over CeNi<sub>1</sub>Pd<sub>1</sub>, confirming that different nanoparticles utilized different reaction mechanisms.

Further studies should include the regeneration of the proposed catalysts, the effect of other heavy hydrocarbons such as resins, high pressure (reservoir conditions), and displacement tests for heavy and extra-heavy oil upgrading in porous media. This study should open a broader landscape about the implementation of nanotechnology in the oil and gas industry and expands the range of application of nanoparticles and nanofluids in thermal enhanced oil recovery operations.

## References

1. Gill, S.; Tsolakis, A.; Dearn, K.; Rodríguez-Fernández, J. Combustion characteristics and emissions of Fischer–Tropsch diesel fuels in IC engines. *Prog. Energy Combust. Sci.* **2011**, *37*, 503–523.
2. Mitra-Kirtley, S.; Mullins, O.C. Sulfur chemical moieties in carbonaceous materials. In *Asphaltenes, Heavy Oils, and Petroleomics*; Springer: Berlin/Heidelberg, Germany, 2007; pp. 157–188.
3. Lv, Y.; Tang, D.; Xu, H.; Luo, H. Production characteristics and the key factors in high-rank coalbed methane fields: A case study on the Fanzhuang Block, Southern Qinshui Basin, China. *Int. J. Coal Geol.* **2012**, *96*, 93–108.
4. Gray, M.R.; McCaffrey, W.C. Role of chain reactions and olefin formation in cracking, hydroconversion, and coking of petroleum and bitumen fractions. *Energy Fuels* **2002**, *16*, 756–766.

5. Groenzin, H.; Mullins, O.C. Molecular size and structure of asphaltenes from various sources. *Energy Fuels* **2000**, *14*, 677–684.
6. Calemma, V.; Iwanski, P.; Nali, M.; Scotti, R.; Montanari, L. Structural characterization of asphaltenes of different origins. *Energy Fuels* **1995**, *9*, 225–230.
7. Piro, G.; Canonico, L.B.; Galbariggi, G.; Bertero, L.; Carniani, C. Asphaltene adsorption onto formation rock: An approach to asphaltene formation damage prevention. *SPE Prod. Facil.* **1996**, *11*, 156–160.
8. Yi, S.; Babadagli, T.; Li, H.A. Use of nickel nanoparticles for promoting aquathermolysis reaction during cyclic steam stimulation. *SPE J.* **2018**, *23*, 145–156.
9. Hashemi, R.; Nassar, N.N.; Pereira Almaso, P. In situ upgrading of Athabasca bitumen using multifunctional ultradispersed nanocatalysts in an oil sands packed-bed column: Part 1. Produced liquid quality enhancement. *Energy Fuels* **2013**, *28*, 1338–1350.
10. Barillas, J.; Júnior, T.D.; Mata, W. Improved oil recovery process for heavy oil: A review. *Braz. J. Petrol. Gás* **2008**, *2*, 45–54.
11. Sarathi, P.S.; Olsen, D.K. *Practical Aspects of Steam Injection Processes: A Handbook for Independent Operators*; National Inst. for Petroleum and Energy Research: Bartlesville, OK, USA, 1992.
12. Benavides Nieves, L.D.; Pinilla Najjar, L.A. *Evaluación de la Viabilidad Técnica de la Inyección de vapor en Yacimientos de Crudo pesado, Mediante un Modelo Analítico*; Fundación Universidad de América: Bogotá, Colombia, 2017.
13. Nassar, N.N.; Franco, C.A.; Montoya, T.; Cortés, F.B.; Hassan, A. Effect of oxide support on Ni–Pd bimetallic nanocatalysts for steam gasification of n-C7 asphaltenes. *Fuel* **2015**, *156*, 110–120.
14. Franco, C.; Cardona, L.; Lopera, S.; Mejía, J.; Cortés, F. Heavy oil upgrading and enhanced recovery in a continuous steam injection process assisted by nanoparticulated catalysts. In Proceedings of SPE Improved oil Recovery Conference, Tulsa, OK, USA, 11–13 April 2016.
15. Franco, C.A. Synthesis and application of supported metallic and multimetallic oxides nanoparticles for in-situ upgrading and inhibition of formation damage. Ph.D. Thesis, Universidad Nacional de Colombia-Sede Medellín, Online, 2015.
16. Nassar, N.N.; Hassan, A.; Pereira-Almaso, P. Application of nanotechnology for heavy oil upgrading: Catalytic steam gasification/cracking of asphaltenes. *Energy Fuels* **2011**, *25*, 1566–1570.

17. Franco, C.A.; Zabala, R.; Cortés, F.B. Nanotechnology applied to the enhancement of oil and gas productivity and recovery of Colombian fields. *J. Petrol. Sci. Eng.* **2017**, *157*, 39–55.
18. Guo, K.; Li, H.; Yu, Z. In-situ heavy and extra-heavy oil recovery: A review. *Fuel* **2016**, *185*, 886–902.
19. Shah, A.; Fishwick, R.; Wood, J.; Leeke, G.; Rigby, S.; Greaves, M. A review of novel techniques for heavy oil and bitumen extraction and upgrading. *Energy Environ. Sci.* **2010**, *3*, 700–714.
20. Betancur, S.; Carmona, J.C.; Nassar, N.N.; Franco, C.A.; Cortés, F.B. Role of particle size and surface acidity of silica gel nanoparticles in inhibition of formation damage by asphaltene in oil reservoirs. *Ind. Eng. Chem. Res.* **2016**, *55*, 6122–6132.
21. Cortés, F.B.; Montoya, T.; Acevedo, S.; Nassar, N.N.; Franco, C.A. Adsorption-desorption of n-c7 asphaltenes over micro-and nanoparticles of silica and its impact on wettability alteration. *CT&F-Ciencia, Tecnología y Futuro* **2016**, *6*, 89–106.
22. López, D.; Giraldo, L.J.; Salazar, J.P.; Zapata, D.M.; Ortega, D.C.; Franco, C.A.; Cortés, F.B. Metal Oxide Nanoparticles Supported on Macro-Mesoporous Aluminosilicates for Catalytic Steam Gasification of Heavy Oil Fractions for On-Site Upgrading. *Catalysts* **2017**, *7*, 319.
23. Nassar, N.N.; Betancur, S.; Acevedo, S.c.; Franco, C.A.; Cortés, F.B. Development of a population balance model to describe the influence of shear and nanoparticles on the aggregation and fragmentation of asphaltene aggregates. *Ind. Eng. Chem. Res.* **2015**, *54*, 8201–8211.
24. Adams, J.J. Asphaltene adsorption, a literature review. *Energy Fuels* **2014**, *28*, 2831–2856.
25. Hamedi Shokrlu, Y.; Babadagli, T. In-situ upgrading of heavy oil/bitumen during steam injection by use of metal nanoparticles: A study on in-situ catalysis and catalyst transportation. *SPE Reserv. Eval. Eng.* **2013**, *16*, 333–344.
26. Nassar, N.N.; Hassan, A.; Pereira-Almao, P. Thermogravimetric studies on catalytic effect of metal oxide nanoparticles on asphaltene pyrolysis under inert conditions. *J. Therm. Anal. Calorim.* **2012**, *110*, 1327–1332.
27. Amanam, U.U.; Kovscek, A.R. Analysis of the effects of copper nanoparticles on in-situ combustion of extra heavy-crude oil. *J. Petrol. Sci. Eng.* **2017**, *152*, 406–415.

28. Nassar, N.N.; Hassan, A.; Luna, G.; Pereira-Almao, P. Kinetics of the catalytic thermo-oxidation of asphaltenes at isothermal conditions on different metal oxide nanoparticle surfaces. *Catal. Today* **2013**, *207*, 127–132.
29. Franco, C.; Patiño, E.; Benjumea, P.; Ruiz, M.A.; Cortés, F.B. Kinetic and thermodynamic equilibrium of asphaltenes sorption onto nanoparticles of nickel oxide supported on nanoparticulated alumina. *Fuel* **2013**, *105*, 408–414.
30. Cortés, F.B.; Mejía, J.M.; Ruiz, M.A.; Benjumea, P.; Riffel, D.B. Sorption of asphaltenes onto nanoparticles of nickel oxide supported on nanoparticulated silica gel. *Energy Fuels* **2012**, *26*, 1725–1730.
31. Franco, C.A.; Montoya, T.; Nassar, N.N.; Pereira-Almao, P.; Cortés, F.B. Adsorption and subsequent oxidation of colombian asphaltenes onto nickel and/or palladium oxide supported on fumed silica nanoparticles. *Energy Fuels* **2013**, *27*, 7336–7347.
32. Nassar, N.N.; Hassan, A.; Pereira-Almao, P. Metal oxide nanoparticles for asphaltene adsorption and oxidation. *Energy Fuels* **2011**, *25*, 1017–1023.
33. Hashemi, R.; Nassar, N.N.; Pereira Almao, P. Enhanced heavy oil recovery by in situ prepared ultradispersed multimetallic nanoparticles: A study of hot fluid flooding for Athabasca bitumen recovery. *Energy Fuels* **2013**, *27*, 2194–2201.
34. Nassar, N.N.; Hassan, A.; Pereira-Almao, P. Comparative oxidation of adsorbed asphaltenes onto transition metal oxide nanoparticles. *Colloids Surf. A Physicochem. Eng. Asp.* **2011**, *384*, 145–149.
35. Hashemi, R.; Nassar, N.N.; Almao, P.P. Nanoparticle technology for heavy oil in-situ upgrading and recovery enhancement: Opportunities and challenges. *Appl. Energy* **2014**, *133*, 374–387.
36. Nassar, N.N. Asphaltene adsorption onto alumina nanoparticles: Kinetics and thermodynamic studies. *Energy Fuels* **2010**, *24*, 4116–4122.
37. Cardona Rojas, L. Efecto de nanopartículas en procesos con inyección de vapor a diferentes calidades. M.Sc. Thesis, Universidad Nacional de Colombia-Sede Medellín, Medellín, Colombia, March 2018.
38. Cardona, L.; Arias-Madrid, D.; Cortés, F.B.; Lopera, S.H.; Franco, C.A. Heavy Oil Upgrading and Enhanced Recovery in a Steam Injection Process Assisted by NiO- and PdO-Functionalized SiO<sub>2</sub> Nanoparticulated Catalysts. *Catalysts* **2018**, *8*, 132.
39. Jacobs, G.; Ricote, S.; Graham, U.M.; Patterson, P.M.; Davis, B.H. Low temperature water gas shift: Type and loading of metal impacts forward



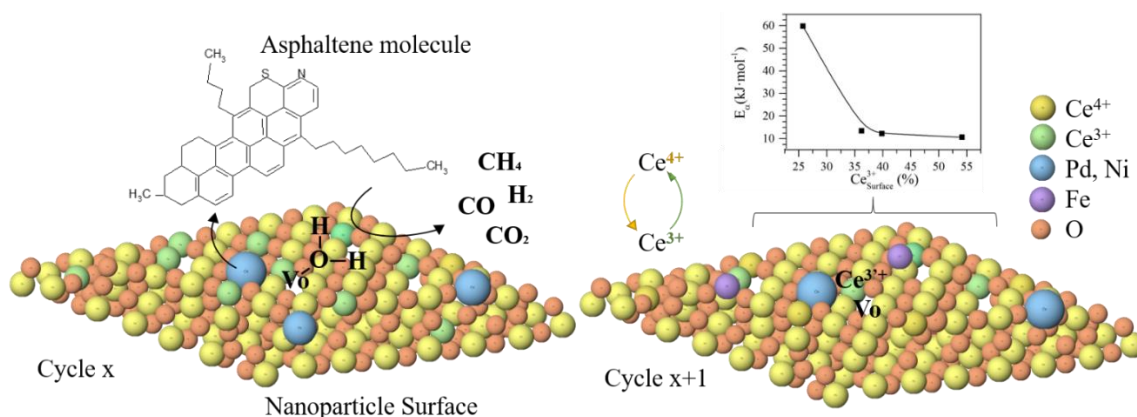
- decomposition of pseudo-stabilized formate over metal/ceria catalysts. *Catal. Today* **2005**, *106*, 259–264.
40. Brunauer, S.; Emmett, P.H.; Teller, E. Adsorption of gases in multimolecular layers. *J. Am. Chem. Soc.* **1938**, *60*, 309–319.
  41. Dejhosseini, M.; Aida, T.; Watanabe, M.; Takami, S.; Hojo, D.; Aoki, N.; Arita, T.; Kishita, A.; Adschiri, T. Catalytic cracking reaction of heavy oil in the presence of cerium oxide nanoparticles in supercritical water. *Energy Fuels* **2013**, *27*, 4624–4631.
  42. Nassar, N.N.; Hassan, A.; Vitale, G. Comparing kinetics and mechanism of adsorption and thermo-oxidative decomposition of Athabasca asphaltenes onto TiO<sub>2</sub>, ZrO<sub>2</sub>, and CeO<sub>2</sub> nanoparticles. *Appl. Catal. A Gen.* **2014**, *484*, 161–171.
  43. Sánchez Gil, J.J. Síntesis y Estudios de Catalizadores Nanoestructurados de Óxido de Cerio soportado sobre Óxido de Magnesio con baja cantidad en Lantánido. Master's Thesis, Universidad de Cádiz, Cádiz, Spanish, January 2013.
  44. Li, Y.; Fu, Q.; Flytzani-Stephanopoulos, M. Low-temperature water-gas shift reaction over Cu-and Ni-loaded cerium oxide catalysts. *Appl. Catal. B Environ.* **2000**, *27*, 179–191.
  45. Bunluesin, T.; Gorte, R.; Graham, G. Studies of the water-gas-shift reaction on ceria-supported Pt, Pd, and Rh: Implications for oxygen-storage properties. *Appl. Catal. B Environ.* **1998**, *15*, 107–114.
  46. Meunier, F.; Reid, D.; Goguet, A.; Shekhtman, S.; Hardacre, C.; Burch, R.; Deng, W.; Flytzani-Stephanopoulos, M. Quantitative analysis of the reactivity of formate species seen by DRIFTS over a Au/Ce (La) O<sub>2</sub> water–gas shift catalyst: First unambiguous evidence of the minority role of formates as reaction intermediates. *J. Catal.* **2007**, *247*, 277–287.
  47. Alamolhoda, S.; Vitale, G.; Hassan, A.; Nassar, N.N.; Almao, P.P. Synergetic effects of cerium and nickel in Ce-Ni-MFI catalysts on low-temperature water-gas shift reaction. *Fuel* **2019**, *237*, 361–372.
  48. Ancheyta, J.; Centeno, G.; Trejo, F.; Marroquin, G.; Garcia, J.; Tenorio, E.; Torres, A. Extraction and characterization of asphaltenes from different crude oils and solvents. *Energy Fuels* **2002**, *16*, 1121–1127.
  49. Franco, C.A.; Nassar, N.N.; Montoya, T.; Ruíz, M.A.; Cortés, F.B. Influence of asphaltene aggregation on the adsorption and catalytic behavior of nanoparticles. *Energy Fuels* **2015**, *29*, 1610–1621.

50. Choi, S.; Byun, D.H.; Lee, K.; Kim, J.-D.; Nho, N.S. Asphaltene precipitation with partially oxidized asphaltene from water/heavy crude oil emulsion. *J. Petrol. Sci. Eng.* **2016**, *146*, 21–29.
51. Lozano, M.M.; Franco, C.A.; Acevedo, S.A.; Nassar, N.N.; Cortés, F.B. Effects of resin I on the catalytic oxidation of n-C 7 asphaltenes in the presence of silica-based nanoparticles. *RSC Adv.* **2016**, *6*, 74630–74642.
52. Franco, C.A.; Montoya, T.; Nassar, N.N.; Cortés, F.B. Nioand pdo supported on fumed silica nanoparticles for adsorption and catalytic steam gasification of colombian c7asphaltenes. In *Handbook On Oil Production Research*, Publications, N., Ed. 2014; pp. 101–145.
53. Franco, C.A.; Zabala, R.D.; Zapata, J.; Mora, E.; Botero, O.; Candela, C.; Castillo, A. Inhibited gas stimulation to mitigate condensate banking and maximize recovery in cupiagua field. *SPE Prod. Oper.* **2013**, *28*, 154–167.
54. Chen, R.; Zhang, Z.; Feng, C.; Hu, K.; Li, M.; Li, Y.; Shimizu, K.; Chen, N.; Sugiura, N. Application of simplex-centroid mixture design in developing and optimizing ceramic adsorbent for As (V) removal from water solution. *Microporous Mesoporous Mater.* **2010**, *131*, 115–121.
55. Talu, O.; Meunier, F. Adsorption of associating molecules in micropores and application to water on carbon. *AIChE J.* **1996**, *42*, 809–819.
56. Montoya, T.; Coral, D.; Franco, C.A.; Nassar, N.N.; Cortés, F.B. A Novel Solid–Liquid Equilibrium Model for Describing the Adsorption of Associating Asphaltene Molecules onto Solid Surfaces Based on the “Chemical Theory”. *Energy Fuels* **2014**, *28*, 4963–4975, doi:10.1021/ef501020d.
57. Cao, A.; Lu, R.; Veser, G. Stabilizing metal nanoparticles for heterogeneous catalysis. *Phys. Chem. Chem. Phys.* **2010**, *12*, 13499–13510.
58. Allen, K.M.; Auyeung, N.; Rahmatian, N.; Klausner, J.F.; Coker, E.N. Cobalt ferrite in YSZ for use as reactive material in solar thermochemical water and carbon dioxide splitting, part II: Kinetic modeling. *JOM* **2013**, *65*, 1682–1693.
59. Sharma, A.; Saito, I.; Nakagawa, H.; Miura, K. Effect of carbonization temperature on the nickel crystallite size of a Ni/C catalyst for catalytic hydrothermal gasification of organic compounds. *Fuel* **2007**, *86*, 915–920.
60. Stone, H. Electrical conductivity and sintering in iron oxides at high temperatures. *J. Mater. Sci.* **1968**, *3*, 321–325.
61. Phalnikar, C.; Evans, E.; Baldwin, W. High Temperature Scaling of Cobalt-Chromium Alloys. *J. Electrochem. Soc.* **1956**, *103*, 429–438.

62. Ravikovitch, P.I.; Neimark, A.V. Characterization of nanoporous materials from adsorption and desorption isotherms. *Colloids Surf. A Physicochem. Eng. Asp.* **2001**, *187*, 11–21.
63. Headen, T.; Boek, E.; Jackson, G.; Totton, T.; Muller, E. Simulation of asphaltene aggregation through molecular dynamics: Insights and limitations. *Energy Fuels* **2017**, *31*, 1108–1125.
64. Bates, M.K.; Jia, Q.; Doan, H.; Liang, W.; Mukerjee, S. Charge-transfer effects in Ni–Fe and Ni–Fe–Co mixed-metal oxides for the alkaline oxygen evolution reaction. *ACS Catal.* **2015**, *6*, 155–161.
65. Shido, T.; Iwasawa, Y. Reactant-promoted reaction mechanism for water-gas shift reaction on Rh-doped CeO<sub>2</sub>. *J. Catal.* **1993**, *141*, 71–81.
66. Vignatti, C.I.; Avila, M.S.; Apesteguia, C.R.; Garetto, T.F. Study of the water-gas shift reaction over Pt supported on CeO<sub>2</sub>–ZrO<sub>2</sub> mixed oxides. *Catal. Today* **2011**, *171*, 297–303.

## Chapter 8.

# Influence of the $\text{Ce}^{4+}/\text{Ce}^{3+}$ Redox-Couple on the Cyclic Regeneration for Adsorptive and Catalytic Performance of $\text{NiO-PdO/CeO}_{2+\delta}$ Nanoparticles for $n\text{-C}_7$ Asphaltene Steam Gasification



Published article in *Nanomaterials*: [doi.org/10.3390/nano9050734](https://doi.org/10.3390/nano9050734)

Impact factor: 5.719

# Influence of the Ce<sup>4+</sup>/Ce<sup>3+</sup> Redox-Couple on the Cyclic Regeneration for Adsorptive and Catalytic Performance of NiO-PdO/CeO<sub>2±δ</sub> Nanoparticles for *n*-C<sub>7</sub> Asphaltene Steam Gasification

## Abstract

The main objective of this study is to evaluate the regenerative effect of functionalized CeO<sub>2±δ</sub> nanoparticles with a mass fraction of 0.89% of NiO and 1.1% of PdO in adsorption and subsequent decomposition of *n*-C<sub>7</sub> asphaltenes in steam gasification processes. During each regeneration cycle, the nanoparticles' adsorption capacity and catalytic activity were evaluated. To estimate the adsorption capacity of the nanoparticles, adsorption kinetics were studied at a fixed concentration of *n*-C<sub>7</sub> asphaltenes of 10 mg·L<sup>-1</sup> as well as adsorption isotherms at three different temperatures at 25, 55, and 75 °C. To evaluate the catalytic activity, the mass loss of the nanoparticles was assessed by isothermal conversions at 230, 240, and 250 °C, and non-isothermal conditions involving heating from 100 to 600°C at a 20 °C·min<sup>-1</sup> heating rate. The asphaltenes showed a high affinity for being adsorbed over the surface of the nanoparticles due to the nanoparticles-asphaltene interactions being stronger than those that occur between asphaltene-asphaltene, and this was maintained during nine evaluated regeneration cycles as observed in Henry's constant that increased slightly, with changes of 21, 26 and 31% at 25, 55, and 75°C, respectively. Polanyi's adsorption potential decreases by 2.6% for the same amount adsorbed from the first cycle to the ninth. In addition, the catalytic activity of the nanoparticles did not change significantly, showing that they decompose 100% of the *n*-C<sub>7</sub> asphaltenes in all cycles. However, the slight decrease in the adsorption capacity and catalytic activity of the nanoparticles is mainly due to the presence and change in concentration and ratio of certain elements such as oxygen, iron, or others at the nanoparticle's surface as shown by X-ray photoelectron spectroscopy (XPS) analyses. Thermodynamic parameters of adsorption, such as  $\Delta H_{ads}^o$ ,  $\Delta S_{ads}^o$ , and  $\Delta G_{ads}^o$  and the effective activation energy (E<sub>a</sub>) were calculated to compare adsorptive and catalytic performance during each cycle. There is an increase of

9.3 and 2.6% in the case of entropy and enthalpy, respectively, and a decrease of 0.5, 3.1, and 6.5% at 25, 55, and 75°C, respectively of  $\Delta G_{ads}^o$  from cycle 1 to cycle 9. It was found that these parameters are correlated with the Ce concentration and oxidation state ratios ( $\text{Ce}^{3+}/\text{Ce}^{4+}$  couple) at the surface.

## 1. Introduction

With the reduction of conventional oil reserves and the growth of global energy demand, it is necessary to restore or increase these reserves by encouraging the production of heavy (HO) and extra-heavy oils (EHO) [1,2]. However, these types of crude oils present difficulties in production, transport, and refinery, which implies an increase in costs. This is because they are characterized by a low American Petroleum Institute (API) gravity [3-7] and a high viscosity due mainly to the high content of asphaltenes [8,9]. For this reason, enhanced oil recovery methods (EOR) have been developed to facilitate the extraction of HO and EHO, including chemical processes such as polymer flooding and thermal processes [10-12]. Thermal EOR methods are divided into two groups: those that use hot fluid (water, steam) from the surface to transfer the energy and those that generate chemical reactions in crude oil during the injection process, such as in-situ combustion (ISC). In particular, steam injection is performed by continuous or cyclic injection [13], mainly focused on oil viscosity reduction and thermal expansion. Cyclic steam injection is the most used mechanism due to its easy implementation. It consists of a single well operation where the steam is injected over time [14]. This is followed by the soaking stage (from one to three weeks), where the energy contained in the steam is transferred to the formation and the reservoir fluids. After, the well is opened for production [15]. When production declines to such a point that it ceases to be profitable, a second cycle can be carried out to increase production. In this way, several cycles can be performed until it is not profitable for the projected production [16].

However, this method involves specific problems. As steam injection cycles are performed, the lighter components of the crude oil matrix are vaporized [17]. The produced crude oil undergoes an increase in the cracking activation energy, and the heavier residual oil is generated due to the loss of the light components [18,19]. Other problems with this technique include decreased performance as the steam is injected cyclically and the operating temperature ranges do not exceed 300 °C [16]. Hence, permanent improvement in the oil quality cannot be achieved since the asphaltene compounds start their decomposition around 450 °C in a steam atmosphere [20-22].

Consequently, some catalytic agents, such as nanoparticles, have been used for the adsorption [22-26] and subsequent transformation of the asphaltenes [27-32]. This is due to nanoparticle properties, such as size, surface area, and surface energy density, which favor their application to HO and EHO reservoirs [20-22,26,33-39]. Some nanoparticles used in steam gasification [26] are derived from transition element oxides, such as  $\text{Co}_3\text{O}_4$ ,  $\text{NiO}$ , and  $\text{Fe}_3\text{O}_4$  [22]. Also, there are functionalized materials supported on silica [20], alumina [40], ceria [41], and titania [21], among others [42-44]. In these studies, it was found that the catalytic activity is affected by the nature of the oxide and the interactions between asphaltenes and nanoparticles. Also, the nanoparticles' presence significantly reduces the activation energy [8,45,46], and the functionalization of the nanoparticles improves their catalytic behavior by enhancing the heavy oil compounds' decomposition [41].

The implementation of nanocatalysts promotes the generation of several reactions, such as  $\text{CO}_2$  reduction, water-gas shift [47], methanization [48], partial oxidation [49], Boudouard [50] and steam reforming reactions [29,35,51,52]. Maintaining the reaction rate during steam injection cycles requires catalysts capable of regenerating in-situ and having an appropriate half-life. Due to the redox behavior of  $\text{CeO}_{2\pm\delta}$ , this material has regenerative autocatalytic properties, which means that the result after any catalytic process is the same as initially, where one of the components of the reaction is the one that acts as a catalyst [53]. This will allow it to reverse the oxidation state or the loss of an electron from  $\text{Ce}^{4+}$  to  $\text{Ce}^{3+}$ , indicating that it would return to its initial conditions, enabling the nanoparticles to be reutilized and making possible better use of their properties. The catalytic character of the redox cycle ( $\text{Ce}^{3+}/\text{Ce}^{4+}$ ) has been demonstrated in reactions such as  $\text{CH}_4/\text{CO}_2$  reforming [54]. However, until now, the application of this material as a supporting agent or catalyst for its regeneration in the adsorption-decomposition cycles of heavy compounds has not been reported.

This property of  $\text{CeO}_{2\pm\delta}$  is due to the changes in oxidation state according to the stimuli to which it is subjected. This behavior allows it to participate in several chemical reactions, which in turn enable it to reverse its oxidation state [55]. Another proposed mechanism for the ceria regeneration and its return to the initial state is proposed by Das et al. (2007), who suggest that the mixture of valence states on the surface of  $\text{CeO}_{2\pm\delta}$  nanoparticles acts as an antioxidant, allowing it to release free radicals [56].

Furthermore, the addition of transition element oxides, such as  $\text{NiO}$ , and noble element oxides, such as  $\text{PdO}$ , can improve the catalytic performance of the



support through a synergetic effect known as strong metal support interaction phenomena (SMSI) [57]. Other studies show that ceria as support has a synergistic impact with nickel highly dispersed in Zeolite Socony Mobil-five (IFM) structures, reducing the start temperature of the water gas shift (WGS) reaction to low temperatures of around 230 °C [58]. As for Pd, it increases the interactions between the support and the gases produced through the production of formiate species. When ceria returns to its initial state, hydrogen release reactions and a generation of free radicals will occur again, which indicates that a cycle of regeneration or autocatalytic reaction has been developed. This could allow the conservation of its capacity of *n*-C<sub>7</sub> asphaltene adsorption and decomposition, while the heavy molecules could become smaller as each cycle occurs and could decrease the problems related to heavy and extra heavy oils. For this reason, through adsorption experiments and thermogravimetric analysis, the affinity for asphaltenes and catalytic activity of NiO and PdO nanoparticles supported on CeO<sub>2±δ</sub> were designed [41]. In the development of this study, loads of the transition element oxides (TEO) on the support were optimized to generate a greater asphaltene conversion with steam present at low temperatures (220°C), and it was found that with a mass fraction of 0.89% and 1.1% of NiO and PdO, respectively, it was possible to maximize the conversion of the asphaltenes to 100% in less than 80 min.

It is worth mentioning that, to the best of our knowledge, there has not been any scientific report on nanoparticle regeneration (adsorption/steam gasification cycles) for thermal-enhanced oil recovery processes. Therefore, the main objective of this work was to evaluate the regenerative capacity of CeO<sub>2±δ</sub> nanoparticles with the optimal loads on their surface through the evaluation of several cycles of *n*-C<sub>7</sub> asphaltene adsorption/catalysis in a steam gasification process. The assessment has considered the redox cycle's influence (Ce<sup>3+</sup>/Ce<sup>4+</sup>) on the self-regeneration of CeO<sub>2±δ</sub>. This work will open a new approach for future studies on the application of nanocatalysts in regenerative processes during EOR applications.

## 2. Experimental

### 2.1. Materials

The *n*-C<sub>7</sub> asphaltenes were extracted from an extra heavy Colombian crude oil using an excess amount of *n*-heptane (99%, Sigma-Aldrich, St. Louis, MO, USA) in a volume ratio of 40:1. Toluene (99.5%, Merk KGaA, Darmstadt,

Germany) was used to prepare asphaltene solutions for adsorption experiments. The crude oil has a viscosity of  $3.1 \times 10^6$  cP at 25 °C and 6.4°API and an approximate content of saturates, aromatics, resins, and asphaltenes of mass fraction 13.0, 16.9, 49.9, and 20.2%, respectively. Ceria (CeO<sub>2</sub>) nanoparticles of 21.6 nm and a surface area of  $65 \text{ m}^2\cdot\text{g}^{-1} \pm 2 \text{ m}^2\cdot\text{g}^{-1}$  were purchased from Nanostructured and Amorphous Materials (Houston, TX, USA) and were used as support [59,60]. Using the incipient wetness technique, the nanoparticles were functionalized with a mass fraction of 0.89 and 1.1% of NiO and PdO. These amounts of NiO and PdO have been optimized in a previous study [41]. The sample was labeled CeNi0.89Pd1.1 and had a Ni–Pd particle size of 5.53–3.61 nm with 25 and 36% dispersion, respectively. A more detailed description of the characterization of the nanoparticles used in the present study can be found in a previous study [41].

## 2.2. Methods

### 2.2.1. Selection of Catalytic Nanoparticles

For the selection of nanocatalyst, a series of tests have been carried out previously, starting from the evaluation of three bimetallic systems supported on CeO<sub>2+x</sub> nanoparticles functionalized with transition element oxides (TEO) for the pairs Ni–Pd, Co–Pd, and Fe–Pd [41]. Performance was studied according to adsorption isotherms, thermogravimetric analysis, isothermal conversions, gases produced, and coke yield. Then, a three-component simplex centroid mixture design (SCMD) was performed, varying the dosage of the TEO on the surface of the nanoparticle from a mass fraction of 0 to 2.0%. The nanoparticles were functionalized with a mass fraction of 0.89 and 1.1% of NiO and PdO, respectively.

### 2.2.2. Nanoparticles Regeneration

The nanoparticle regeneration process starts from the asphaltene adsorption and their catalytic decomposition. The nanoparticles with adsorbed asphaltenes were subjected to a steam atmosphere in a tubular furnace (Thermo Scientific Lindberg/Blue, Waltham, MA, USA) at 240 °C for 2 h. For this, N<sub>2</sub> flow was fixed at 100 mL·min<sup>-1</sup> and steam injection was performed at a flow rate of 6.3 mL·min<sup>-1</sup> using a gas saturator with a controlled temperature. In each regeneration cycle, nanoparticles were characterized by X-ray photoelectron spectroscopy analyses.

### 2.2.3. The *n*-C<sub>7</sub> Asphaltene Adsorption over Nanoparticles

A stock solution containing 15000 mg·L<sup>-1</sup> of *n*-C<sub>7</sub> asphaltenes in toluene was prepared and diluted to different concentrations for the adsorption tests. The changes in concentration after adsorption were determined by UV-vis spectrophotometer (Thermo Scientific, Waltham, MA, USA). The initial concentrations of the *n*-C<sub>7</sub> asphaltene solutions varied from 100 to 1500 mg·L<sup>-1</sup>. A fixed amount of nanoparticles (100 mg per 10 mL of model solution) was employed. Once the nanoparticles were added to the solutions, they were stirred at 300 rpm, and an aliquot was taken every 10 min to evaluate adsorption kinetics until the amount adsorbed remained constant. The nanoparticles with *n*-C<sub>7</sub> asphaltenes adsorbed were separated by centrifugation at 5000 rpm for 45 min and dried in a vacuum oven at 60°C for 24 h. The adsorption experiments were carried out at 25, 55, and 75°C. The amount adsorbed in units of mg of *n*-C<sub>7</sub> asphaltenes per gram mass of nanoparticle was estimated according to Equation (1).

$$N_{ads} = \frac{C_o - C_E}{W} V, \quad (1)$$

where  $C_o$  (mg·L<sup>-1</sup>) and  $C_E$  (mg·L<sup>-1</sup>) are the initial and equilibrium concentrations in the equilibrium, respectively;  $V$  (L) is the volume of the solution, and  $w$  (g) is the mass of nanoparticles added to the solution. The concentration of *n*-C<sub>7</sub> asphaltenes in the supernatant was measured at a wavelength of 298 nm using a Genesys 10S UV-vis spectrophotometer with an uncertainty of 0.001 a.u. in the measurement of absorbance. This implies a standard deviation of 0.05 mg·L<sup>-1</sup> in the calculation of the residual concentration.

### 2.2.4. Thermogravimetric Analyses

The catalytic activity of nanoparticles in the steam gasification of the *n*-C<sub>7</sub> asphaltenes adsorbed on the nanoparticle surface was evaluated using a thermogravimetric analyzer Q50 (TA Instruments, Inc., New Castel, DE, USA). For the development of the tests, N<sub>2</sub> flow was fixed at 100 mL·min<sup>-1</sup> and hauling steam controlled by a thermostatic bath was introduced simultaneously at a gas flow rate of 6.3 mL·min<sup>-1</sup> using a gas saturator [22]. During each catalytic regeneration cycle, the nanoparticles with adsorbed *n*-C<sub>7</sub> asphaltenes were subjected to the TGA under isothermal and non-isothermal conditions. The samples were heated to three different temperatures (230, 240, and 250°C). On

the other hand, the experiments at non-isothermal conditions were performed by heating the samples from 100 to 600°C at a heating rate of 20°C·min<sup>-1</sup> to observe the rate for mass loss of *n*-C<sub>7</sub> asphaltenes on the nanoparticle surface [61].

Finally, each run at isothermal conditions was carried out with an adsorbed amount of *n*-C<sub>7</sub> asphaltenes that remained constant at 0.02 mg·m<sup>-2</sup>, while for non-isothermal conditions, the asphaltene load was 0.2 mg·m<sup>-2</sup>.

### 2.2.5. X-ray Photoelectron Spectroscopy Analysis

During each catalytic regeneration cycle, the nanoparticles were characterized by X-ray photoelectron spectroscopy (XPS) using a Specs X-ray photoelectronic spectrometer (NAP-XPAS) using a monochromatic source of Al-Kα (1486.7 eV, 13 kV, 100 W) together with a PHOIBOS 150-1D-DLD analyzer. Energies of 100 eV (1 eV·step<sup>-1</sup>) during three measurement cycles and 20 eV (0.1 eV·step<sup>-1</sup>) in ten measurement cycles were used for general and high-resolution spectra, respectively.

## 3. Modeling

### 3.1. Double Exponential Model

In this model, the adsorption mechanism, and the transfer of the adsorbate to the adsorbent are described in two steps. The first step is a fast transfer from the bulk to the adsorbent. Then, during the second step, rate-determining is dominated by diffusion through the adsorbent surface and asphaltene self-association over the active sites until equilibrium is reached. Equation (2) describes this model.

$$N_{ads} = N_{ads,e} - \frac{D_f}{V} \exp(-k_f t) - \frac{D_s}{V} \exp(-k_s t), \quad (2)$$

where the adsorbed amount at time *t* is expressed by  $N_{ads}$  (mg·g<sup>-1</sup>), the adsorbed amount in the equilibrium, and the volume ratio of solvent/mass of material added to the adsorptive processes carried out are  $N_{ads,e}$  (mg·g<sup>-1</sup>) and  $V$  (L·g<sup>-1</sup>), respectively. Additionally, the adsorption and mass transfer coefficients for the fast stage are given by  $D_f$  (mg·L<sup>-1</sup>) and  $k_f$  (min<sup>-1</sup>), respectively. The adsorption and mass transfer coefficients for the slow stage are  $D_s$  (mg·L<sup>-1</sup>) and

$k_s$  ( $\text{min}^{-1}$ ). If  $k_f \gg k_s$ , the exponential term corresponding to the rapid process can be assumed to be negligible [62-64].

### 3.2. Solid–Liquid Equilibrium (SLE) Model

The chosen model allows the description of the adsorption isotherms using the theory of association and adsorption of molecules in micropores suggested by Talu and Meunier [65]. The model can be described by Equations (3)–(5): [66]

$$C = \frac{\psi K_H}{1 + K\psi} e^{\left(\frac{\psi}{A \cdot N_m}\right)} \quad (3)$$

$$\psi = \frac{-1 + \sqrt{1 + 4K\xi}}{2K} \quad (4)$$

$$\xi = \frac{N_m N}{(N_m - N)}, \quad (5)$$

where  $C$  ( $\text{mg} \cdot \text{g}^{-1}$ ) represents the concentration of  $n\text{-C}_7$  asphaltenes at the equilibrium and  $K_H$  ( $\text{mg} \cdot \text{g}^{-1}$ ) is the affinity of the adsorbate for the surface of the solid. A low value implies greater affinity, i.e., greater accessibility (or ease of access) of the  $n\text{-C}_7$  asphaltenes to the active sites.

Likewise,  $K$  ( $\text{g} \cdot \text{g}^{-1}$ ) is a constant related to the asphaltene self-association over the active sites on the surface of the nanoparticles,  $N_m$  ( $\text{g} \cdot \text{g}^{-1}$ ) is the maximum capacity of  $n\text{-C}_7$  asphaltene adsorption, and the adsorbed amount is expressed as  $N$  ( $\text{g} \cdot \text{g}^{-1}$ ). Finally,  $\xi$  depends on the maximum adsorption capacity ( $N_m$ ) and amount adsorbed ( $N$ ).

### 3.3. Thermodynamic Properties of Adsorption

To better understand the effect of temperature on  $n\text{-C}_7$  asphaltene adsorption, thermodynamic parameters are used. To describe the thermodynamic properties of adsorption, five temperature-independent parameters are needed, using equations of the SLE model, and replacing  $K_H$  and  $K$  with Equations (6) and (7) shown below.

$$K_H = e^{(H_0 + \frac{H_1}{T})} \quad (6)$$

$$K = e^{(K_0 + \frac{K_1}{T})} \quad (7)$$

where  $K_0$  is related to the entropy of reaction and  $K_1$ , related to enthalpy. It is possible to find the three thermodynamic parameters, change in entropy  $\Delta S_{ads}^\circ$ , change in enthalpy  $\Delta H_{ads}^\circ$  and change in Gibbs free energy  $\Delta G_{ads}^\circ$ , through Equations (8)–(10).

$$\Delta S_{ads}^\circ = K_0 R \quad (8)$$

$$\Delta H_{ads}^\circ = K_1 R \quad (9)$$

$$\Delta G_{ads}^\circ = -RT \ln K \quad (10)$$

A negative value for the Gibbs free energy change would indicate the spontaneity and thermodynamic favorability of the process. Similarly, a negative enthalpy change value would suggest that the process occurs exothermically; negative enthalpy also indicates that the adsorption would decrease as temperature increased.

Finally, a positive value of the entropy change would indicate that due to the *n*-C<sub>7</sub> asphaltene adsorption, there would be an increase in the system's randomness at the liquid-solid interface (nanoparticle *n*-C<sub>7</sub> asphaltenes) [66,67].

### 3.4. Adsorption Potential Model by Michael Polanyi

The adsorption potential is defined as the work required for an adsorbate molecule to be transferred from the bulk phase to the surface of the adsorbent. In this theory, it is considered that the adsorbed layer is a thick film whose density decreases as the distance from the surface increases. It is independent of the temperature for a fixed adsorbed amount  $N_{ads}$ . The adsorption potential or Polanyi's potential can be expressed as shown in Equation (11):

$$A = RT \ln \left( 1 + \frac{1}{C_E} \right) \quad (11)$$

where the adsorption potential is represented by  $A$ , and the concentration of  $n$ -C<sub>7</sub> asphaltenes in equilibrium is expressed as  $c_e$  (g·g<sup>-1</sup>). Additionally,  $R$  (J·mol<sup>-1</sup>·K<sup>-1</sup>) is the constant of ideal gases, and  $T$  (K) is the system's absolute temperature [68,69].

### 3.5. Estimation of Effective Activation Energy

The calculation of the activation energy was carried out with the following model given by the ICTAC Kinetics committee. Equation (12) provides a basis for differential kinetic methods and applies to any temperature [70,71].

$$\frac{d\alpha}{dt} = K_a \exp\left(-\frac{E_a}{RT}\right) f(\alpha), \quad (12)$$

where the effective activation energy is expressed by  $E_a$  (kJ·mol<sup>-1</sup>), while  $\alpha$  is the degree of conversion. The latter depends on the initial mass of the sample, the current mass at time  $t$  and the final mass.

Likewise,  $K_a$  (s<sup>-1</sup>) is the pre-exponential factor, and  $T$  (K) is reaction temperature. The reaction mechanism is given by  $f(\alpha)$  and the reaction rate is  $d\alpha/dt$ . With the analysis of isothermal conditions and integration by separation of variables, the integral reaction model shown by Equation (13) is obtained:

$$g(\alpha) = K_a e^{\frac{E_a}{RT}} \quad (13)$$

Taking constant the energy of activation and applying natural logarithm to both sides, Equation (14) is obtained,

$$\ln(t_{a,i}) = \ln\left(\frac{g(\alpha)}{K_a}\right) + \frac{E_a}{RT_i} \quad (14)$$

From the plot of  $\ln(t_{a,i})$  vs.  $1/T_i$ , it is possible to obtain the value of the activation energy from the slope.

### 3.6. Statistical Analysis

The accuracy of the parameters for each model was presented using the optimized gradient model. The root mean square error (RMS) was selected to minimize the differences between the experimental and obtained values under the theoretical considerations of the different models. The values obtained for the mean squared error were calculated under Equation (15), where  $m$  represents the amount of data or measurements made and  $\times$  the evaluated parameter for each model:

$$RMS\% = \sqrt{\sum_i^m (X_{\text{experimental},i} - X_{\text{model},i})^2 \times m^{-1}} \times 100. \quad (15)$$

## 4. Results and discussion

### 4.1. Selection of Nanocatalyst

In a previous study [41], three main systems were evaluated, the first consisting of a mass fraction of 1% of NiO and 1% of PdO (CeNi1Pd1), the second 1% of Fe<sub>2</sub>O<sub>3</sub> and 1% of PdO (CeFe1Pd1) and the third 1% Co<sub>3</sub>O<sub>4</sub> and 1% PdO (CeCo1Pd1), all supported on ceria nanoparticles. For the adsorption, the system CeNi1Pd1 showed better results than CeFe1Pd1 and CeCo1Pd1. The catalytic activity of the nanoparticles was evaluated with a series of tests, (a) rate for mass loss, (b) isothermal conversions, (c) analysis of the gaseous products, and (d) coke yield. On all four tests, CeNi1Pd1 performed better than the other systems. Finally, to optimize the concentration of the metals of the best system, a simplex-centroid mixture design (SCMD) was made using the STATGRAPHICS Centurion XVI software (StartPoint Technologies Inc. Addison, TX, USA) [72]. This new system was called CeNi0.89Pd1.1 and had a mass fraction of 0.89% and 1.1% of NiO and PdO, respectively, on the surface of the cerium oxide [41].

### 4.2. Adsorption Kinetics

Figure 1 shows the adsorption kinetics for *n*-C<sub>7</sub> asphaltenes on the CeNi0.89Pd1.1 nanoparticles through the different catalytic regeneration cycles at an initial concentration of 10 mg·L<sup>-1</sup> of *n*-C<sub>7</sub> asphaltenes. In general, two stages are observed in adsorption kinetics. The first stage is characterized by rapid adsorption due to the electrostatic and van der Waals attraction forces between the nanoparticle and the *n*-C<sub>7</sub> asphaltene molecules. In the second stage, a slow uptake is observed that involves a gradual *n*-C<sub>7</sub> asphaltene adsorption on the surface of the nanoparticles through complex reactions and the subsequent self-



association over the active sites [73]. From Figure 1, it is observed that the process of asphaltene adsorption is a fast process where a maximum time of 40 min is required for the equilibrium to be reached. This is due to the impediment for diffusion through the materials, related to the auto-associative characteristics of the asphaltenes, which generate growth in the size of the asphaltene according to the concentration in the system [74]. Additionally, in each cycle, the time to reach equilibrium does not change drastically, and the amount of  $n\text{-C}_7$  asphaltenes that adsorbs at that point decreases from 0.1740 to 0.1160  $\text{mg}\cdot\text{g}^{-1}$  from cycle one to cycle nine, respectively.

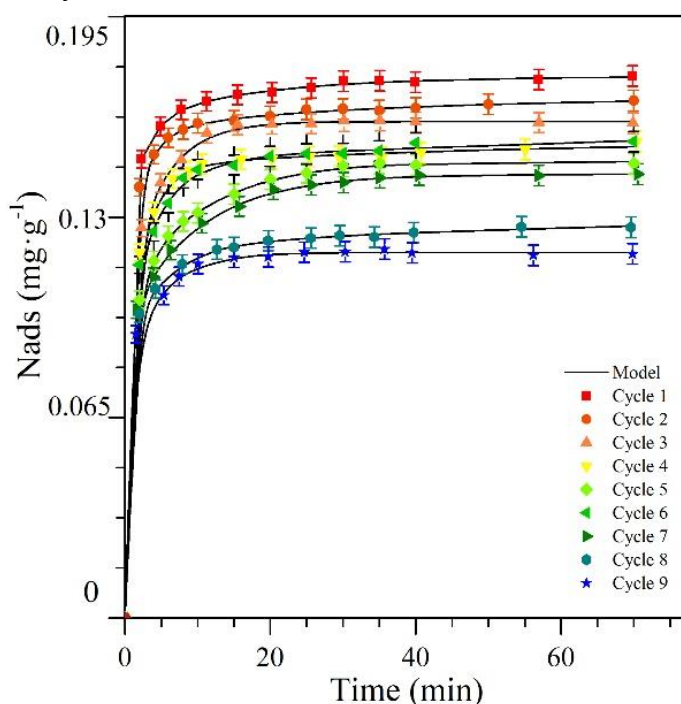


**Figure 1.** Asphaltene adsorption kinetics on CeNi<sub>0.89</sub>Pd<sub>1.1</sub> nanoparticles through several catalytic regeneration cycles of adsorption and subsequent catalytic steam gasification. Adsorption kinetics were constructed for a fixed initial concentration of  $n\text{-C}_7$  asphaltene of 10  $\text{mg}\cdot\text{L}^{-1}$ . The symbols are experimental data, and the continuous lines are from the double exponential model.

Table 1 presents the parameters of the double exponential model and the associated error obtained for the materials as a function of the initial concentration of  $n\text{-C}_7$  asphaltenes and the regeneration cycles of nanoparticles. The double exponential model correlates well with the experimental results, as the estimated related errors show. A proportional relationship is generally not observed between the  $D_i$  parameter and the amount adsorbed through the cycles.

**Table 1.** Estimated values of the parameters of the double exponential model of *n*-C<sub>7</sub> asphaltene adsorption kinetics on CeNi<sub>0.89</sub>Pd<sub>1.1</sub> nanoparticles through catalyst regeneration cycles of adsorption and subsequent catalytic steam gasification. The parameters are the amount adsorbed ( $N_{ads,m,cal}$ ), the adsorption ( $D_f$ ), and mass transfer ( $k_f$ ) coefficients for the fast stage and the adsorption ( $D_s$ ) and mass transfer ( $k_s$ ) coefficients for the slow stage, respectively. Adsorption kinetics were obtained for an initial *n*-C<sub>7</sub> asphaltene concentration of 10 mg·L<sup>-1</sup>.

Cycle	$N_{ads,m,exp} \pm 0.01$ (mg·g <sup>-1</sup> )	$N_{ads,m,cal} \pm 0.01$ (mg·g <sup>-1</sup> )	$D_f \pm 0.02$ (mg·L <sup>-1</sup> )	$k_f \pm 0.01$ (min <sup>-1</sup> )	$D_s \pm 0.02$ (mg·L <sup>-1</sup> )	$k_s \pm 0.01$ (min <sup>-1</sup> )	% <i>RMS</i>
1	0.17	0.17	0.98	0.41	0.45	0.06	0.12
2	0.16	0.17	0.76	0.38	0.34	0.03	0.11
3	0.15	0.15	0.69	0.21	0.65	0.00	0.29
4	0.15	0.15	0.70	0.36	0.20	0.02	0.28
5	0.15	0.15	0.84	0.63	0.47	0.10	0.14
6	0.14	0.14	0.59	0.24	0.97	0.01	0.17
7	0.14	0.13	0.79	0.34	0.73	0.10	0.13
8	0.12	0.12	0.83	0.22	0.12	0.02	0.07
9	0.12	0.12	0.65	0.20	0.53	0.00	0.28

The amount adsorbed can be explained by materials that, due to their high affinity for *n*-C<sub>7</sub> asphaltene, saturate quickly. This is because, with the passage of catalytic regeneration cycles, there was a loss of accessible active sites that allowed greater adsorption of the aggregates on its surface. Also, due to the low values of  $k_s$  and  $D_s$ , it is concluded that the adsorptive process of *n*-C<sub>7</sub> asphaltene on CeNi<sub>0.89</sub>Pd<sub>1.1</sub> nanoparticles was essentially governed by one stage [75].

#### 4.3. Adsorption Isotherms

Figures 2a–c show the *n*-C<sub>7</sub> asphaltene adsorption isotherms at 25, 55, and 75°C on CeNi<sub>0.89</sub>Pd<sub>1.1</sub> nanoparticles through several cycles. It was observed that these nanoparticles have a high amount of adsorbed *n*-C<sub>7</sub> asphaltene, and this feature is maintained in subsequent cycles. For all cases, type Ib isotherms were obtained according to the IUPAC classification. The effect of temperature, the experimental results, and the parameter  $N_{max}$  of the SLE model show that with increasing temperatures, the adsorbed amount of *n*-C<sub>7</sub> asphaltene decreases [74]. On the other hand, Figure 2 shows that the adsorption isotherms obtained throughout the cycles remain as type Ib, which means that the high affinity of the *n*-C<sub>7</sub> asphaltene towards the nanoparticles is maintained. In addition, at low

concentrations ( $C_0 < 500 \text{ mg}\cdot\text{L}^{-1}$ ), the amount adsorbed does not change significantly in any of the cycles evaluated. However, the values of the maximum possible adsorbed amounts were reduced from  $27.03 \times 10^{-2} \text{ g}\cdot\text{g}^{-1}$ ,  $28.86 \times 10^{-2} \text{ g}\cdot\text{g}^{-1}$ , and  $29.68 \times 10^{-2} \text{ g}\cdot\text{g}^{-1}$  for cycle 1 to  $22.37 \times 10^{-2} \text{ g}\cdot\text{g}^{-1}$ ,  $24.03 \times 10^{-2} \text{ g}\cdot\text{g}^{-1}$ , and  $25.36 \times 10^{-2} \text{ g}\cdot\text{g}^{-1}$  for cycle 9 at 25, 55, and 75°C, respectively.

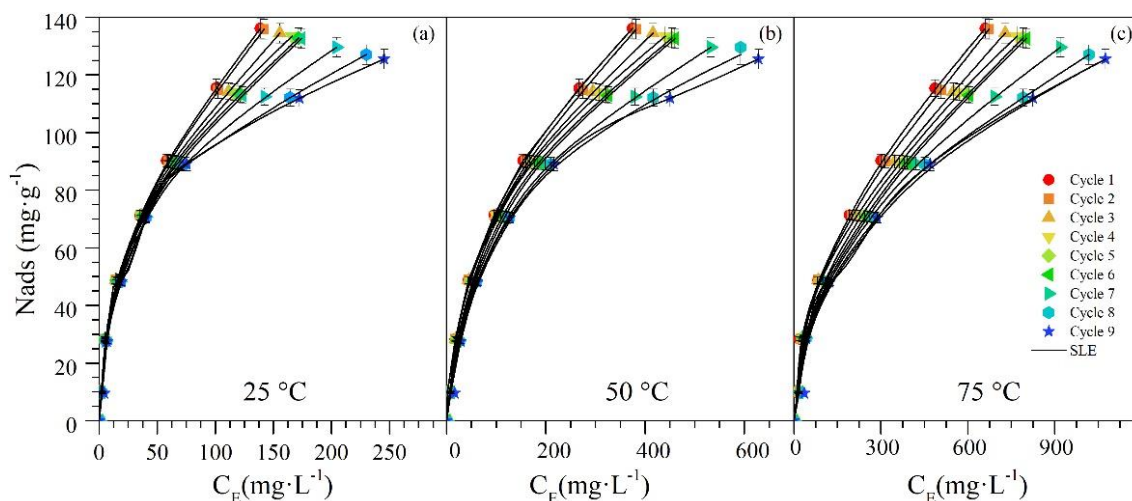


**Figure 2.** Adsorption isotherms of  $n\text{-C}_7$  asphaltenes onto  $\text{CeNi}_{0.89}\text{Pd}_{1.1}$  nanoparticles evaluated at (a) 25, (b) 55, and (c) 75°C through catalyst regeneration cycles of adsorption and subsequent catalytic steam gasification. Adsorption isotherms were constructed for different  $n\text{-C}_7$  asphaltene concentrations from  $100 \text{ mg}\cdot\text{L}^{-1}$  to  $1500 \text{ mg}\cdot\text{L}^{-1}$ . The symbols are experimental data, and the solid lines are from the SLE model.

Table 2 presents the parameters of the SLE model for the  $n\text{-C}_7$  asphaltenes adsorbed on nanoparticles. No significant change of  $K_{\text{a}}$  is observed as the cycles occur. This value increased by approximately 21, 26, and 31% for 25, 55, and 75°C, respectively, from cycle 1 to cycle 9, meaning that the adsorption affinity is strongly affected by the regeneration cycles. On the other hand, the  $K$  parameter did not exhibit great changes (from  $1.15 \times 10^{-2}$  to  $1.17 \times 10^{-2}$ ), which means that the degree of self-association of  $n\text{-C}_7$  asphaltenes tends to stay constant with the passage of the regeneration cycles.

**Table 2.** Estimated values of the solid–liquid equilibrium (SLE model parameters Henry's law constant ( $K_H$ ), the degree of self-association ( $K$ ) and maximum amount adsorbed ( $N_{max}$ ) for  $n$ -C<sub>7</sub> asphaltene adsorption isotherms onto CeNi<sub>0.89</sub>Pd<sub>1.1</sub> nanoparticles, evaluated at 25°C, 55°C, and 75°C through catalyst regeneration of adsorption and subsequent catalytic steam gasification.

Cycle	Temperature	$K_H \pm 0.02$	$K \pm 0.08$	$N_{max} \pm 0.01$	% RMS
		[mg·g <sup>-1</sup> ] × 10 <sup>-2</sup>	[g·g <sup>-1</sup> ] × 10 <sup>-2</sup>	[g·g <sup>-1</sup> ] × 10 <sup>-2</sup>	
1	25	2.64	1.15	27.03	0.004
	55	8.45	3.35	28.86	0.014
	75	15.98	3.45	29.68	0.023
2	25	2.65	1.15	27.02	0.004
	55	8.46	3.36	28.57	0.013
	75	16.03	3.46	29.43	0.020
3	25	2.65	1.16	25.78	0.004
	55	8.49	3.37	27.19	0.010
	75	15.84	3.48	29.43	0.012
4	25	2.76	1.16	25.46	0.002
	55	9.54	3.37	27.13	0.003
	75	19.44	3.48	29.43	0.007
5	25	2.86	1.16	25.35	0.001
	55	9.88	3.37	27.02	0.002
	75	20.12	3.49	29.33	0.022
6	25	3.09	1.16	25.31	0.000
	55	10.63	3.36	27.01	0.003
	75	21.57	3.48	29.09	0.026
7	25	3.15	1.17	24.00	0.000
	55	10.75	3.42	25.91	0.005
	75	21.76	3.49	27.49	0.039
8	25	3.20	1.17	22.81	0.001
	55	10.90	3.45	24.50	0.010
	75	22.03	3.49	25.88	0.063
9	25	3.35	1.17	22.37	0.006
	55	11.41	3.44	24.03	0.036
	75	23.03	3.54	25.36	0.119

#### 4.4. Thermodynamic Studies

Table 3 summarizes the estimated thermodynamic parameters of  $n$ -C<sub>7</sub> asphaltene adsorption onto CeNi<sub>0.89</sub>Pd<sub>1.1</sub> nanoparticles.

**Table 3.** Thermodynamic parameters for the adsorption of *n*-C<sub>7</sub> asphaltene onto CeNi<sub>0.89</sub>Pd<sub>1.1</sub> nanoparticles through different catalyst regeneration cycles of adsorption and subsequent catalytic steam gasification. The change in entropy is expressed by  $\Delta S_{ads}^{\circ}$ , the change in enthalpy is  $-\Delta H_{ads}^{\circ}$  and the change in Gibbs free energy is  $-\Delta G_{ads}^{\circ}$ .

Cycle	Temperature (°C)	$\Delta S_{ads}^{\circ} \pm 0.02 \times 10^{-2}$ [J·(mol·K) <sup>-1</sup> ]	$-\Delta H_{ads}^{\circ} \pm 0.01$ [kJ·mol <sup>-1</sup> ]	$-\Delta G_{ads}^{\circ} \pm 0.01$ [J·mol <sup>-1</sup> ]
1	25	6.03	29.08	6.04
	55			9.58
	75			10.25
2	25	6.05	29.13	6.04
	55			9.58
	75			9.90
3	25	6.07	29.18	6.03
	55			9.57
	75			9.68
4	25	6.08	29.23	6.02
	55			9.56
	75			9.67
5	25	6.14	29.32	6.02
	55			9.56
	75			9.66
6	25	6.22	29.36	6.02
	55			9.55
	75			9.63
7	25	6.30	29.43	6.02
	55			9.54
	75			9.60
8	25	6.35	29.66	6.02
	55			9.53
	75			9.60
9	25	6.65	29.87	6.01
	55			9.28
	75			9.58

In all cases, the negative value of  $\Delta G_{ads}^{\circ}$  was maintained throughout the nine cycles, indicating that no additional energy was necessary to generate the interactions between the asphaltene molecules and the nanoparticles. This suggests that the process was thermodynamically favorable. In addition,  $\Delta G_{ads}^{\circ}$  decreased only from cycle 1 to cycle 9 by 0.5, 3.1, and 6.5% for 25, 55, and 75°C, respectively, suggesting that the reaction did not lose spontaneity. Contrarily, the values  $\Delta S_{ads}^{\circ}$  were positive in all cases and did not significantly increase with each regeneration cycle. Therefore, the randomness at the interface of the

adsorbent/adsorbate did not change. It is important to note here that its value only increased by 9.3% in cycle 9 concerning adsorption cycle 1. This slight increase in  $\Delta S_{ads}^{\circ}$  could be because once the asphaltene is adsorbed on the nanoparticle, the self-association over the active sites is promoted. The values of  $\Delta H_{ads}^{\circ}$  were negative for all cycles evaluated, suggesting the exothermic nature of the interactions between the *n*-C<sub>7</sub> asphaltenes and the surface. This value increased only 2.6% from cycle 1 to cycle 9. The evaluated thermodynamic parameters agreed with Franco et al. [76] and Nassar et al. [67].

#### 4.5. Polanyi's Adsorption Potential

The characteristic curves for the *n*-C<sub>7</sub> asphaltene adsorption over the surface of the nanoparticles are illustrated in Figure 3. At this point, it is important to mention that low values of Polanyi's potential imply the need for a lower energy demand to carry out the adsorptive phenomenon. As observed, the adsorption potential slightly decreases as more cycles occur. However, it did not decrease considerably from cycle 1 to cycle 9 due to the conserved adsorptive capacity of the nanoparticles, and the adsorption remains strong during all cycles evaluated. In other words, the work required to transfer an asphaltene molecule from the surface to a given distance from the surface did not vary significantly, decreasing by only 2.6% for the same amount adsorbed from the first cycle to the ninth. This behavior also suggests that the adsorbate–adsorbent interactions in the case of CeNi<sub>0.89</sub>Pd<sub>1.1</sub> nanoparticles are stronger for the first cycle than for the remaining. The adsorption potential corresponds, therefore, to an increase in free energy experienced by the adsorbate during adsorption at equilibrium. This result indicates that the adsorbate–adsorbent interactions stay strong and the rate at which *n*-C<sub>7</sub> asphaltenes were adsorbed did not change. These results were in agreement with those found by Cortés et al. [68], Betancur et al. [69] and Wu et al. [77], who observed that a stronger affinity between the adsorbate–adsorbent pair generates a higher potential value, i.e., the adsorbate is more likely to migrate to the surface of the nanoparticle instead than remaining in the bulk phase.

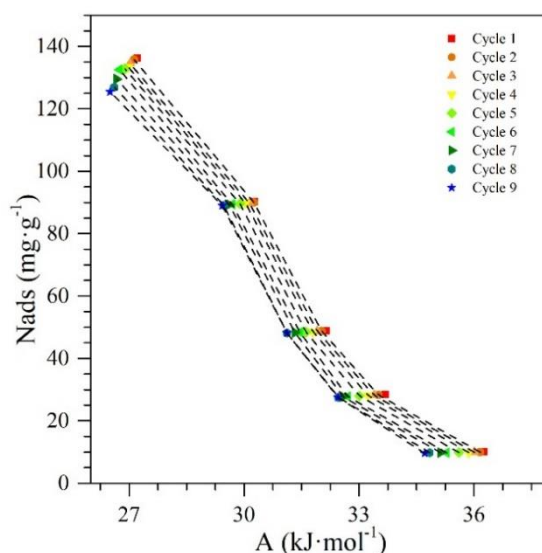


**Figure 3.** Polanyi's adsorption potential ( $A$ ) as a function of the adsorbed amount ( $N_{\text{ads}}$ ) for  $n\text{-C}_7$  asphaltene adsorption on  $\text{CeNi}_{0.89}\text{Pd}_{1.1}$  nanoparticles through several catalyst regenerations of adsorption and subsequent steam gasification

#### 4.6. Thermogravimetric Analysis of $n\text{-C}_7$ Asphaltenes

##### 4.6.1. Mass Loss Analysis

The decomposition-gasification of  $n\text{-C}_7$  asphaltenes adsorbed on the nanoparticle  $\text{CeNi}_{0.89}\text{Pd}_{1.1}$  was evaluated by heating the samples from 100 to 600 °C at a heating rate of 20 °C·min<sup>-1</sup> under a water-saturated N<sub>2</sub> atmosphere. Figure 4 shows the complete TGA profile as a function of the temperature for  $n\text{-C}_7$  asphaltenes in the absence and presence of raw and regenerated  $\text{CeNi}_{0.89}\text{Pd}_{1.1}$  nanoparticles. The temperature range evaluated was divided into three main regions of low (LTR), medium (MTR), and high (HTR) temperature, as suggested in the literature [78]. The first region ends at about 250 °C, the MTR region will then range between 251 and 450 °C, and finally, the HTR region has temperature values between 451 to 600 °C.

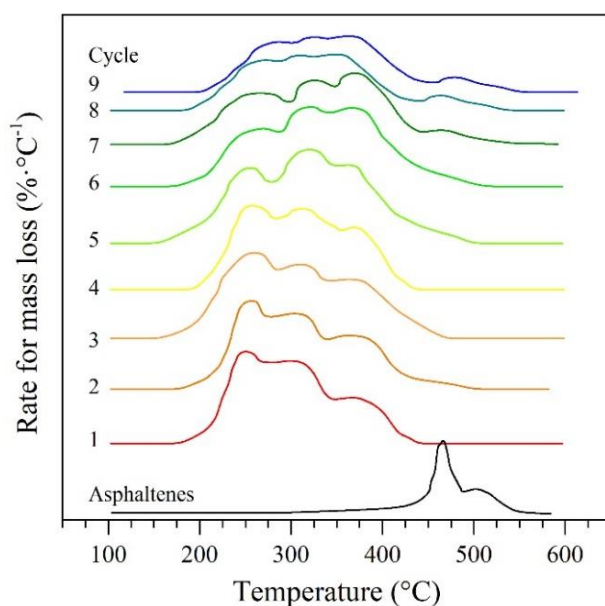


**Figure 4.** The rate for mass loss as a function of the temperature for catalytic steam decomposition of *n*-C<sub>7</sub> asphaltenes in the absence and presence of CeNi<sub>0.89</sub>Pd<sub>1.1</sub> nanoparticles for several catalyst regeneration cycles of adsorption and subsequent catalytic steam gasification. Nitrogen flow rate = 100 mL·min<sup>-1</sup>, H<sub>2</sub>O<sub>(g)</sub> flow rate = 6.30 mL·min<sup>-1</sup>, heating rate = 20°C·min<sup>-1</sup>, and asphaltene load of 0.02 mg·m<sup>-2</sup>.

The decomposition of *n*-C<sub>7</sub> asphaltenes in the absence of nanoparticles was carried out in the HTR region at 455 °C. The presence of the CeNi<sub>0.89</sub>Pd<sub>1.1</sub> nanoparticles decreases this value to 210 °C in the LTR, continuing the decomposition in the MTR between 280 and 370 °C. This is due to the different interactions between NiO, PdO, and the support (NiO/CeO<sub>2+δ</sub>, PdO/CeO<sub>2+δ</sub>, NiO-PdO/CeO<sub>2+δ</sub>), decomposing the asphaltenes in various stages. Also, a possible variation in the size of the asphaltene molecules can affect the decomposition. It is worth remembering that, as a fraction, asphaltene does not consider only one kind of molecule. Instead, a wide distribution of asphaltene molecules with diverse molecular weights can be found in crude oil, containing aliphatic chains, polycyclic aromatic hydrocarbons (PAH), heteroatoms, and metals. This trend was maintained during all the catalytic cycles evaluated, with the difference that the intensities in the first peak decrease as the nanoparticles are regenerated and the intensities of the other two peaks increase, evidencing the suppression of the addition reactions of the *n*-C<sub>7</sub> asphaltenes due to the stabilization of free radicals by hydrogen molecules in hydrogenation reactions [79-81].



Additionally, cycles 8 and 9 exhibited a mass loss in the HTR region at 455°C. This behavior reflects a small loss of the catalytic capacity of the nanoparticles to break down the heavier hydrocarbon into lower molecular weight compounds. This also leads to an increase in heteroatoms, like oxygen, and metals, such as iron, on the nanoparticle's surface by 9.2 and 6.3%, respectively (see XPS analyses below). The concentration of these elements could increase the probability of generating coordinated bonds (HA-TE), which require greater energy to break. Additionally, as explained in Section 4.7 below, CeNi<sub>0.89</sub>Pd<sub>1.1</sub> nanoparticles lose catalytic capacity by decreasing 28.6% of Ce<sup>3+</sup> ions on the surface.

#### 4.6.2. Isothermal Conversion

Panels a–c in Figure 5 shows the fraction of conversion ( $\alpha$ ) for *n*-C<sub>7</sub> asphaltenes adsorbed on CeNi<sub>0.89</sub>Pd<sub>1.1</sub> nanoparticles as a function of time at 230, 240, and 250 °C. Figure 5 shows that the degree of reaction ( $\alpha$ ) of the *n*-C<sub>7</sub> asphaltenes in the presence of the nanoparticles, changes with temperature. With the increase of this temperature, the reaction rate increases, and therefore, the transformation of the *n*-C<sub>7</sub> asphaltene molecules into lighter hydrocarbons and consequent gas generation occurs in a shorter time. This agrees with the results reported by Nassar et al. [70] and Cardona et al. [40]. Also, the catalytic effect of the nanoparticles is evidenced throughout all cycles evaluated, as CeNi<sub>0.89</sub>Pd<sub>1.1</sub> nanoparticles can decompose 100% of *n*-C<sub>7</sub> asphaltenes adsorbed. However, the time required to decompose the asphaltenes increased between cycle 1 and 9 by 30, 25, and 12.5% when samples are treated at 230, 240, and 250°C, respectively. This behavior is corroborated by the activation energy values obtained, which increased from 10.7 kJ·mol<sup>-1</sup> to 59.8 kJ·mol<sup>-1</sup>. The total conversion of *n*-C<sub>7</sub> asphaltenes was related, among many factors, to the role played by the hydrogen (H<sub>2</sub>) produced by the asphaltene-nanoparticle interactions [79]. The CeO<sub>2+δ</sub> nanoparticle and the transition element oxides cracked the heavier molecules into lighter molecules. Through hydrogen production, nanoparticles also stabilize the free radicals, which facilitates the complete decomposition of the heavy molecules. Stabilizing the free radicals also inhibited the self-association of *n*-C<sub>7</sub> asphaltenes, generating a residual of 0% [41,80,81]. The variation in the time required to convert 100% of *n*-C<sub>7</sub> asphaltenes was mainly due to a loss of available active sites on the surface of the support due to the retention of heteroatoms and metals that require a longer time to decompose.

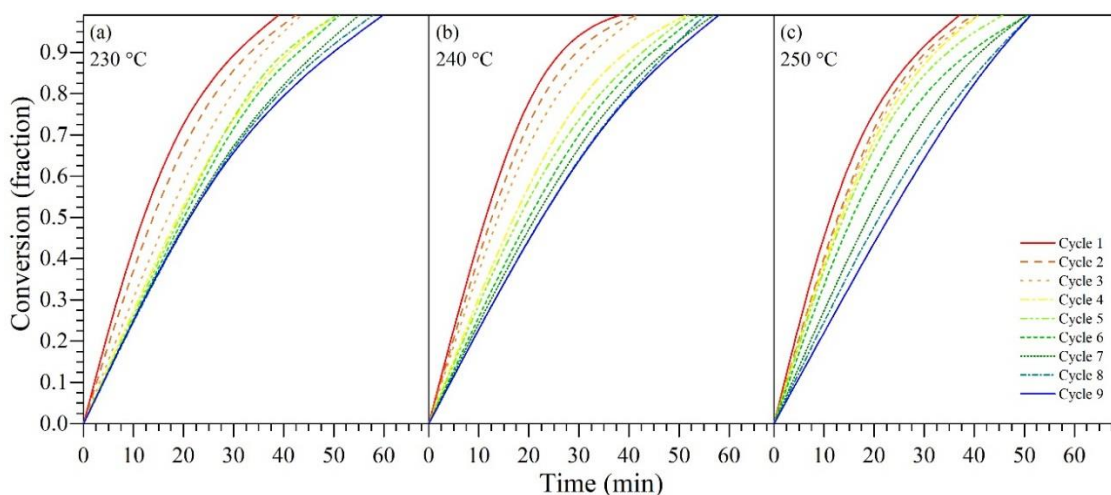


**Figure 5.** Isothermal conversion as a function of time at (a) 230, (b) 240, and (c) 250 °C for *n*-C<sub>7</sub> asphaltenes in the absence and presence of CeNi<sub>0.89</sub>Pd<sub>1.1</sub> through several catalyst regeneration cycles of adsorption and subsequent catalytic steam gasification. Nitrogen flow rate = 100 mL·min<sup>-1</sup>, H<sub>2</sub>O<sub>(g)</sub> flow rate = 6.30 mL·min<sup>-1</sup>, heating rate = 20°C·min<sup>-1</sup>, and asphaltene load of 0.2 mg·m<sup>-2</sup>.

#### 4.6.3. Effective Activation Energy of *n*-C<sub>7</sub> Asphaltene Thermo-Decomposition in the Presence and Absence of Nanoparticles

The effective activation energy was calculated following the isothermal method [70]. For this,  $\ln(t_{a,i})$  vs  $1/T_i^{-1}$  plots were constructed (Figure 6), and the value of the activation energy for each cycle was calculated. Figure 7 shows the activation energy values for the gasification of virgin *n*-C<sub>7</sub> asphaltenes and their gasification after adsorption on the CeNi<sub>0.89</sub>Pd<sub>1.1</sub> nanoparticles in each regeneration cycle. The estimated value for the activation energy of the *n*-C<sub>7</sub> asphaltene decomposition reactions on nanoparticles in cycle 1 was 10.7 kJ·mol<sup>-1</sup>, which decreased by approximately 95% over the value reported in the absence of nanoparticles (211.52 kJ·mol<sup>-1</sup>). As the nanoparticle was regenerated, the activation energy increased from cycle 1 to 9 by 49.1 kJ·mol<sup>-1</sup>. Up to the seventh cycle, the activation energy values are lower than those reported for the CeO<sub>2±δ</sub> support without TEO impregnation, which is 44 kJ·mol<sup>-1</sup> [41]. This means that, although the nanoparticle requires more energy after regeneration for asphaltene gasification, they still present an excellent catalytic yield. The main advantage of the NiO- and PdO-doped ceria nanoparticles lies in the temperature reduction for asphaltene decomposition. Also, the ability of the nanoparticles to change its oxidation state from Ce<sup>3+</sup> to Ce<sup>4+</sup> allows a greater number of interactions with the steam molecules and therefore, with the asphaltenes, increasing their reaction

capacity and catalytic activity. Finally, the change in the activation energy shows that the gasification reaction was affected by the redox cycle  $\text{Ce}^{3+}/\text{Ce}^{4+}$  since the concentration of  $\text{Ce}^{3+}$  ions on the nanoparticle surface decreases. Further, considering that these ions are mainly responsible for the catalytic performance of the support, it can be said that the effective activation energy increases as the capacity of the redox cycle is hindered.

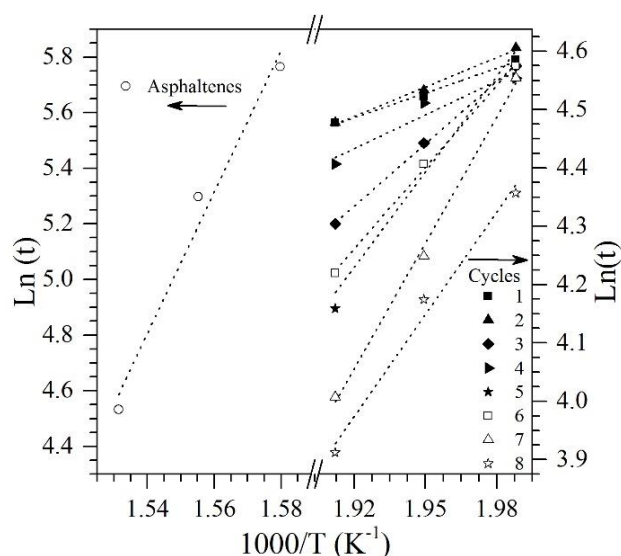


**Figure 6.** Arrhenius plot for the isothermal model of decomposition-gasification of  $n\text{-C}_7$  asphaltenes in the presence and absence of nanoparticles  $\text{CeNi}_{0.89}\text{Pd}_{1.1}$  through regeneration cycles of adsorption and subsequent catalytic steam gasification.

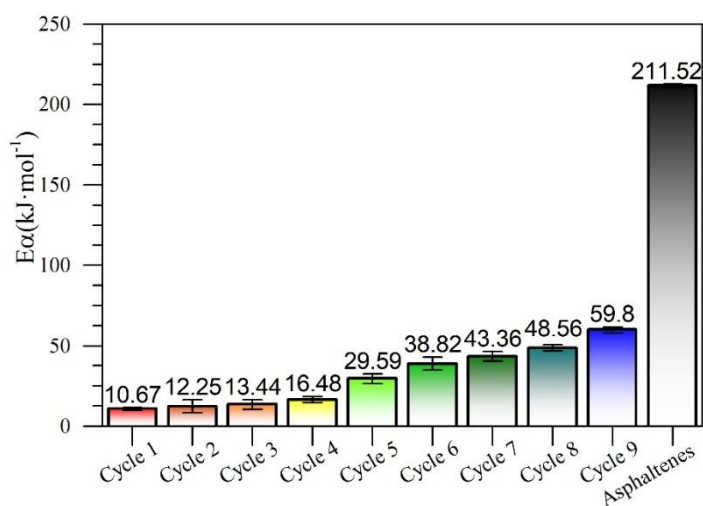


**Figure 7.** Estimated values of activation energy for isothermal model of catalytic steam decomposition of  $n\text{-C}_7$  asphaltenes using  $\text{CeNi}_{0.89}\text{Pd}_{1.1}$  nanoparticles through catalytic regeneration cycles of adsorption and subsequent catalytic steam gasification.

#### 4.7. XPS Analysis of CeNi<sub>0.89</sub>Pd<sub>1.1</sub> Nanoparticles through Catalytic Regeneration Cycles

Figure 8 shows the survey spectra for the catalysts after the fourth regeneration cycle. The high-resolution spectra for the main elements at the catalyst's surface are also shown. As expected, the catalyst surface was composed mainly of oxygen from the ceria and the transition elements oxides, palladium, and nickel. Furthermore, iron was found after the first cycle of regeneration. Depending on their origins, this element proceeds from the asphaltene molecules, which could contain some transition elements, such as Fe, Ni, and V [82]. Carbon from the sample support tape (graphite tape) was analyzed and used as a binding energy reference of 284.8 eV for all samples. According to the binding energies, after the calcination process of regeneration, all the transition elements are mainly found as oxides. The high-resolution O<sub>1s</sub> spectra were decomposed, and around 2% of the superficial oxygen was found as hydroxide. It is well known that Ce compounds were basic and could react with water to form cerium hydroxides [83]. Also, Ni and Fe held the same possibility [84,85]. Ni, Fe, and Pd were exhibited on the catalyst surface as NiO, Fe<sub>2</sub>O<sub>3</sub>, and PdO, respectively. For Pd, a signal at 335.5 eV was present, showing that a fraction of the element was present at the surface in its metallic state (Pd<sup>0</sup>) [86]. The thermal decomposition of the PdO can explain this phenomenon to form Pd<sup>0</sup> and gaseous oxygen [87].

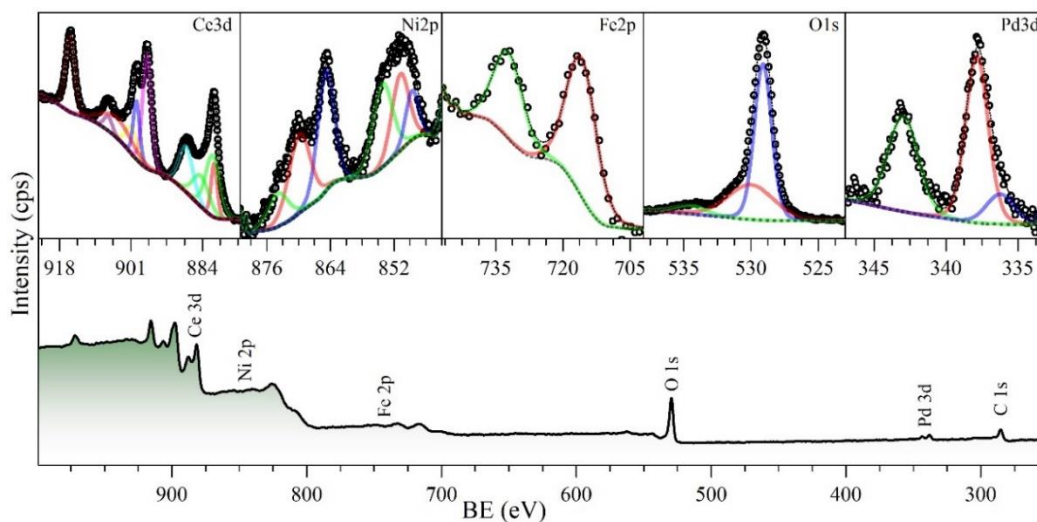


**Figure 8.** X-ray photoelectron spectroscopy (XPS) spectra of the nanoparticles CeNi<sub>0.89</sub>Pd<sub>1.1</sub> after cycle 4 of regeneration in the *n*-C<sub>7</sub> asphaltene adsorption/decomposition through catalytic steam gasification for the main elements present at the surface Ce<sub>3d</sub>, Ni<sub>2p</sub>, Fe<sub>2p</sub>, O<sub>1s</sub>, and Pd<sub>3d</sub>.

Using the XPS spectra survey at high resolution, the different concentrations and atomic ratios at the surface of the catalyst CeNi<sub>0.89</sub>Pd<sub>1.1</sub> were calculated. These results are shown in Figure 9 as a function of the regeneration cycles (1, 2, 4, y 9). In Figure 9a, the concentrations of the most relevant elements are shown. The surface of the nanoparticles is mainly composed of oxygen, increasing its concentration in each regeneration cycle. Conversely, the concentration of ceria on the nanoparticles' surface decreased with cycles, indicating that the active sites composed of ceria are covered by heteroatoms such as oxygen and iron.

The high-resolution Ce<sub>3d</sub> spectrum was decomposed to calculate the percentage of Ce<sup>3+</sup> and Ce<sup>4+</sup> (Figure 9b) [88]. Ceria signals present quite complex characteristics due to hybridization with bound orbitals and the fractional occupation of valence orbitals 4f [89,90]. The Ce<sub>3d</sub> XPS spectrum of a Ce<sup>4+</sup> compound can be deconvoluted into six signals (*u*, *v*, *u''*, *v''* and *u'''*, *v'''*); if some Ce<sup>3+</sup> species are also present, four more signals must be added (*v'*, *u<sup>0</sup>*, *v<sup>0</sup>* and *u'*,) [90]. From these peaks, it can be observed that the oxidation state Ce<sup>4+</sup> is predominant while the Ce<sup>3+</sup> peaks are weak. The percentages of Ce<sup>3+</sup> and Ce<sup>4+</sup> were calculated using Equations (16) and (17) [91-97].

$$Ce^{3+} = U^0 + U' + V^0 + V' \quad (16)$$

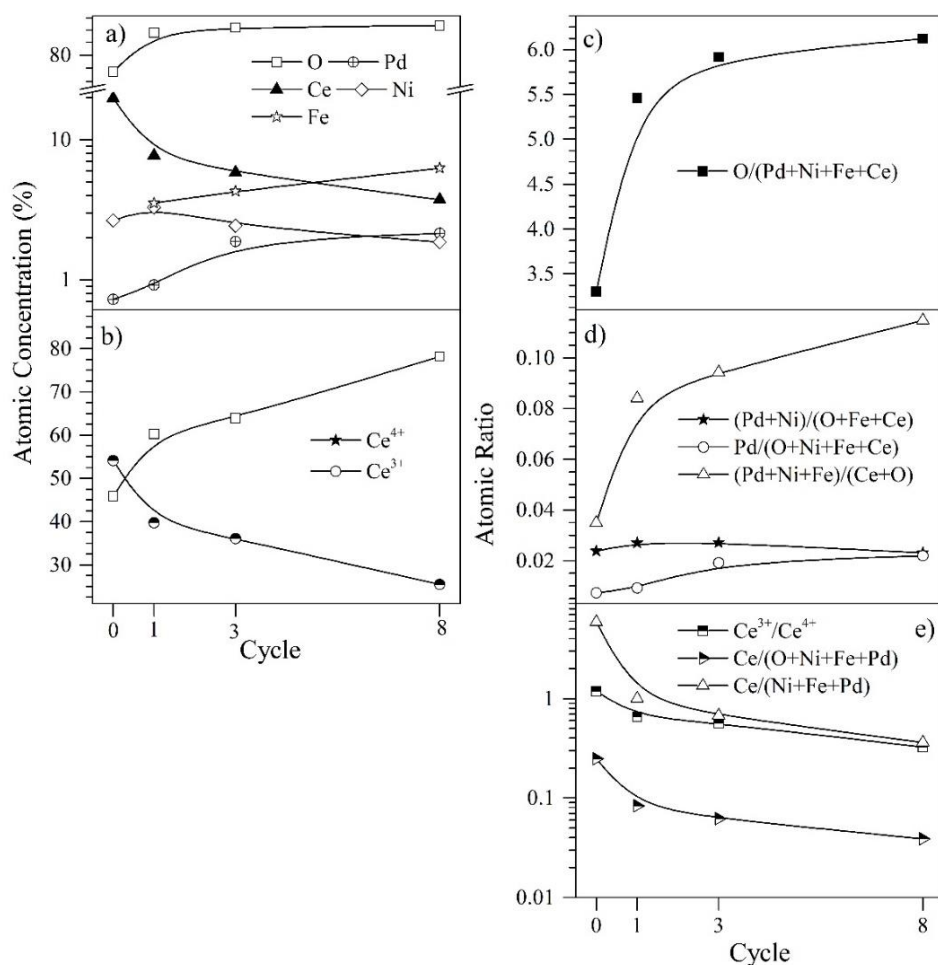
$$Ce^{4+} = U''' + U'' + U + V''' + V'' + V \quad (17)$$

As the cycles occur, the component corresponding Ce<sup>4+</sup> increase concerning the Ce<sup>3+</sup>. This is because the electrons are easily transferred from Ce<sup>3+</sup> to oxygen or other species. The Ce<sup>3+</sup>/Ce<sup>4+</sup> ratio on the surface of the sample is affected by nanoparticle regeneration. The ratio is strongly influenced by the absolute binding energy positions characteristic of Ce<sub>3d</sub>. As mentioned above, the CeO<sub>2δ</sub> also has autocatalytic properties that can reverse the oxidation state from Ce<sup>4+</sup> to Ce<sup>3+</sup>, allowing it to return to its initial state. However, through the regeneration cycles, the percentage of Ce<sup>3+</sup> ions on the nanoparticle's surface decreases, affecting the support's catalytic activity. In addition, the concentration ratio of Ce<sup>4+</sup>/Ce<sup>3+</sup> ions in the ceria nanoparticles also decreases with the passage of the cycles. Therefore, the number of oxygen vacancies on the surface increased, which was reflected in the behavior shown in Figure 9d-e. Consequently, the reaction capacity decreases to the extent that the nanoparticle loses part of its catalytic activity due to the interruption in its redox cycle. The concentration ratio of Ce<sup>4+</sup>/Ce<sup>3+</sup> ions in the ceria nanoparticles is important for the number of oxygen

vacancies on the surface, which determine reaction capacity. The mechanism had been described by Equations (18)–(20) [56]:



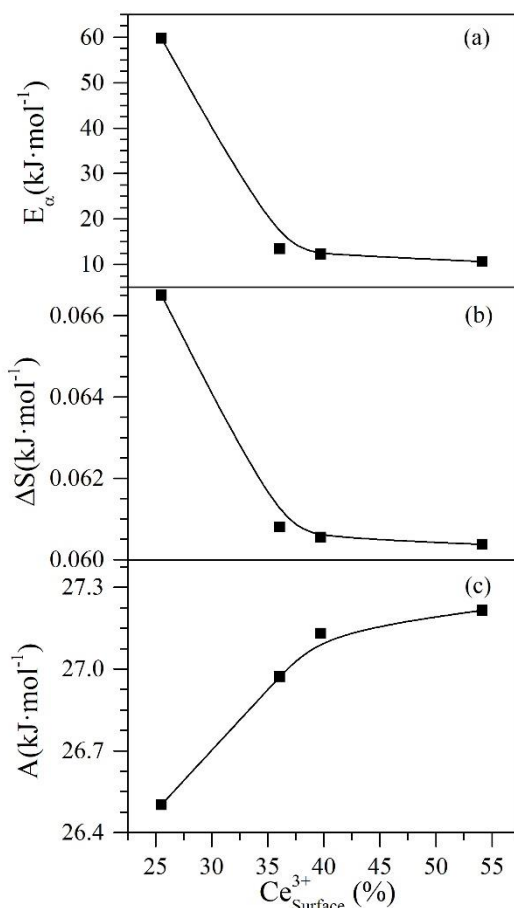
Figure 9c shows the variation of the transition elements (TE, Ni + Fe + Pd) regarding the cerium and oxygen on the surface. It is possible to observe that TE increases during the regeneration cycles, which implies that the cerium atoms are less accessible for the chemical reactions and involved in the redox cycle ( $Ce^{4+}/Ce^{3+}$ ) as shown by the decrease in  $Ce^{3+}$  concentration in atomic ratio to the  $Ce^{4+}$ . All these facts imply a decrease in active sites and, therefore, a reduction of the catalytic activity of the nanomaterial. The deposition of the iron over the catalyst's surface, which increases the TE content, can block the active catalytic sites of the ceria, implying a loss of catalytic activity. Also, the Ni concentration on the nanoparticle surface possibly decreases due to a coating of the ceria on the active site of the metal, decreasing its exposed surface area.



**Figure 9.** Surface atomic concentration and ratios of the different analyzed elements through XPS of the CeNi<sub>0.89</sub>Pd<sub>1.1</sub> nanoparticles in the *n*-C<sub>7</sub> asphaltene adsorption/decomposition in catalytic steam gasification for the regeneration cycles 1, 2, 4, and 9. (a) Atomic concentration of the all analyzed elements, (b) atomic Ce<sup>3+</sup> and Ce<sup>4+</sup> concentrations, (c-d) atomic ratios and (e) cerium ratios and concentrations according to oxidation state.

#### 4.7.1. Catalytic Effect of Ce<sup>4+</sup>/Ce<sup>3+</sup> Redox Couple on the Thermodynamic and Adsorption Properties of CeNi<sub>0.89</sub>Pd<sub>1.1</sub> Nanoparticles

As the chemical nature of the CeO<sub>2±δ</sub> nanoparticles can change depending on the amount of Ce<sup>3+</sup> and Ce<sup>4+</sup> species present in the system, it is essential to analyze how various properties change with the increase or decrease of species content. Figure 10 shows the behavior of entropy, Polanyi's potential, and activation energy regarding the concentration of Ce<sup>3+</sup> ions on the nanoparticle surface through different catalytic regeneration cycles.



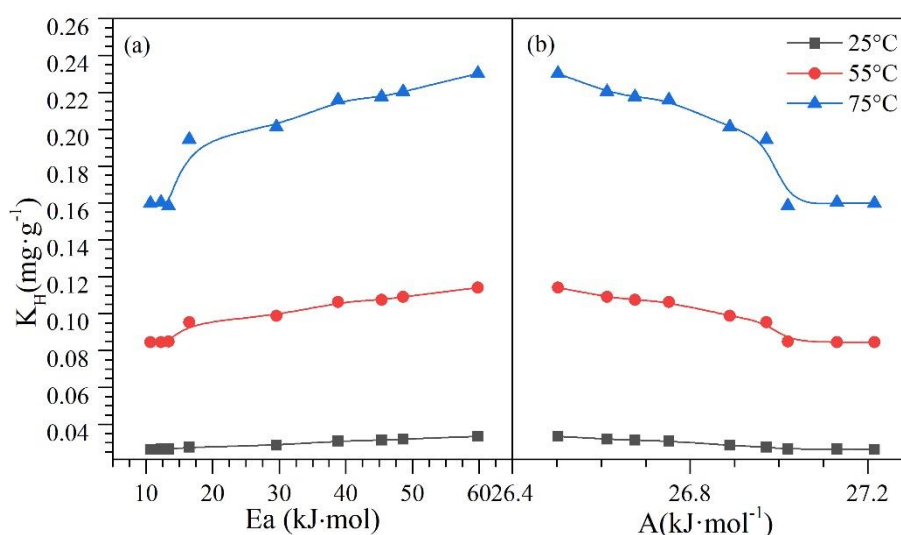
**Figure 10.** Catalytic effect of  $Ce^{3+}$  ions on (a) activation energy, (b) entropy, and (c) Polanyi's adsorption potential for  $n-C_7$  asphaltene adsorption onto CeNi<sub>0.89</sub>Pd<sub>1.1</sub> nanoparticles catalytic steam decomposition through regeneration catalytic cycles 1, 2, 4 and 9.

Figure 10a-b shows that activation energy and entropy increase with the rising concentration of  $Ce^{3+}$  ions on the surface of the nanoparticles. This is possible because these ions are responsible for the catalytic activity of the cerium oxide. The decrease in the presence of ions causes a reduction of this activity. Consequently, nanoparticles will require more energy for the thermal gasification reactions that decompose heavy-absorbed fractions. On the contrary, and as expected, the Polanyi potential decreases with the reduction in  $Ce^{3+}$  ions. If the nanoparticle loses catalytic activity, it may be due to a reduction in its adsorptive capacity and affinity to adsorb asphaltenes. As explained in Section 4.5, the potential to bring the asphaltene from the bulk phase to the nanoparticle's surface becomes lower when there is a reduced affinity between the adsorbed-adsorbent pair.



#### 4.7.2. Effective Activation Energy and Kinetics of the Catalytic Steam Gasification of Asphaltenes in the Presence and Absence of Nanoparticles

Figure 11 shows the Henry constant as a function of (a) Polanyi's potential and (b) activation energy. There is a direct relationship between the adsorptive and catalytic properties of the evaluated nanoparticles. From panel a of Figure 11, a slight increase in the values of Henry's law constant can be seen as Polanyi's potential decreases. This behavior is mainly due to the lower affinity between the adsorbate–adsorbent pair, so the potential decreases. Also, this trend is independent of the temperature. Conversely, if this affinity decreases, the energy needed to decompose the asphaltene molecules thermally increases. This behavior can be observed in panel b of Figure 11.



**Figure 11.** The relationship between Henry's law constant and (a) Polanyi's adsorption potential and (b) effective activation energy for  $n$ -C<sub>7</sub> asphaltene adsorption onto CeNi<sub>0.89</sub>Pd<sub>1.1</sub> nanoparticles and subsequent catalytic steam decomposition through catalytic regeneration cycles.

Finally, Figure 12 shows the behavior of Polanyi's potential ( $A$ ) as a function of the activation energy and the change in the system's entropy. From Figure 12, it is possible to see a decrease in the  $A$  values from 27.2 kJ·mol<sup>-1</sup> to 26.5 kJ·mol<sup>-1</sup> as the activation energy and entropy increase. With the decrease in Ce<sup>3+</sup>, the reduction in redox capability, and the increase of the TE on the surface of the nanoparticles with the passage of catalytic regeneration cycles, the catalytic capacity begins to decrease. Consequently, nanomaterials require more energy to promote gasification reactions. The increase in the entropy change as the

adsorption potential decreases is due to the loss of affinity between the adsorbate–adsorbent. Hence, asphaltenes present weaker interactions with nanoparticles and interact more easily with other asphaltene molecules due to their self-assembling capacity. All these tendencies show how the synergetic interaction between TE (Pd and Ni) and the support ( $\text{CeO}_{2\pm\delta}$  in this case) are important and crucial for catalytic performance concerning activation energy and resistance to regeneration through the oxidation cycles. Also, as shown in these results, the  $\text{Ce}^{3+}/\text{Ce}^{4+}$  redox couple and their interaction with the TE are quite important.

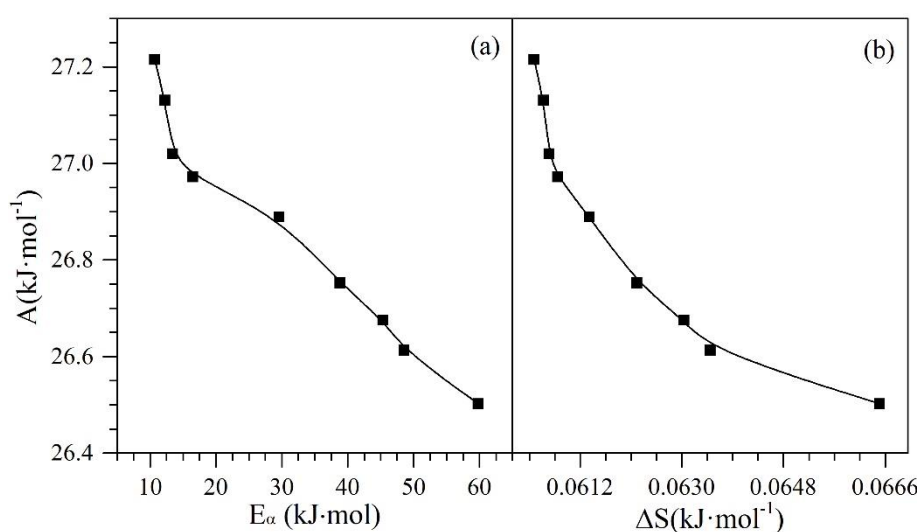


**Figure 12.** The relationship between Polanyi's adsorption potential and (a) effective activation energy and (b) entropy for  $n\text{-C}_7$  asphaltene adsorption onto  $\text{CeNi}_{0.89}\text{Pd}_{1.1}$  nanoparticles and subsequent catalytic steam decomposition through catalytic regeneration cycles.

## 5. Conclusions

This study provides information on the  $n\text{-C}_7$  asphaltene on  $\text{CeNi}_{0.89}\text{Pd}_{1.1}$  nanoparticles through several adsorption/decomposition cycles. The adsorption properties of the nanoparticles do not change significantly as the cycles advance, thus confirming their regenerative capacity. That is to say, the autocatalytic properties of  $\text{CeO}_{2\pm\delta}$  that allow it to reverse the oxidation state also give rise to a new cycle of  $n\text{-C}_7$  asphaltene adsorption/decomposition. This is reflected in the adsorption kinetics, where for a fixed concentration of  $n\text{-C}_7$  asphaltenes, the amount adsorbed, and the time needed to reach equilibrium remain approximately constant. Likewise, the asphaltene adsorption isotherm

nanoparticles showed a high affinity between both systems during all the cycles. The slight increase in the Polanyi adsorption potential showed that the work required for an adsorbate molecule to transfer to the surface of the adsorbent does not vary significantly between cycles, which conserves the adsorption properties of nanoparticles.

On the other hand, with the thermodynamic parameters calculated using the SLE model, it was shown that the process is spontaneous and thermodynamically favorable; that is, it does not need additional energy; it also has exothermic nature and randomness in the adsorbent/adsorbate interface.

On the other hand, the nanoparticles could completely decompose the *n*-C<sub>7</sub> asphaltenes during all cycles, causing a decrease in the activation energy necessary to carry out the asphaltene partial oxidation and gasification reactions. This serves as further proof that the catalytic property is not lost with the passage of the adsorption and decomposition cycles.

Finally, with this study, it was possible to demonstrate that functionalized CeO<sub>2±δ</sub> nanoparticles may improve the oil recovery process when applied to steam injection processes, allowing greater *n*-C<sub>7</sub> asphaltene decomposition without losing their catalytic and adsorption properties.

## References

1. Shah, A.; Fishwick, R.; Wood, J.; Leeke, G.; Rigby, S.; Greaves, M. A review of novel techniques for heavy oil and bitumen extraction and upgrading. *Energy & Environmental Science* **2010**, *3*, 700-714.
2. Agency, I.E. *World Energy Outlook 2017*; Agency, I.E., Ed. 2017.
3. Santos, R.; Loh, W.; Bannwart, A.; Trevisan, O. An overview of heavy oil properties and its recovery and transportation methods. *Brazilian Journal of Chemical Engineering* **2014**, *31*, 571-590.
4. Guo, K.; Li, H.; Yu, Z. In-situ heavy and extra-heavy oil recovery: A review. *Fuel* **2016**, *185*, 886-902.
5. Curtis, C.; Kopper, R.; Decoster, E.; Guzmán-García, A.; Huggins, C.; Knauer, L.; Minner, M.; Kupsch, N.; Linares, L.M.; Rough, H. Heavy-oil reservoirs. *Oilfield Review* **2002**, *14*, 30-51.

6. Rahimi, P.M.; Gentzis, T. The chemistry of bitumen and heavy oil processing. In *Practical advances in petroleum processing*, Springer: 2006; pp. 597-634.
7. Hamed Shokrlu, Y.; Babadagli, T. Kinetics of the in-situ upgrading of heavy oil by nickel nanoparticle catalysts and its effect on cyclic-steam-stimulation recovery factor. *SPE Reservoir Evaluation & Engineering* **2014**, *17*, 355-364.
8. Nassar, N.N.; Hassan, A.; Pereira-Almao, P. Metal oxide nanoparticles for asphaltene adsorption and oxidation. *Energy & Fuels* **2011**, *25*, 1017-1023.
9. Buckley, J.S.; Liu, Y.; Xie, X.; Morrow, N.R. Asphaltenes and crude oil wetting-the effect of oil composition. *SPE journal* **1997**, *2*, 107-119.
10. Terry, R.E. Enhanced oil recovery. *Encyclopedia of physical science and technology* **2001**, *18*, 503-518.
11. Alvarado, V.; Manrique, E. Enhanced oil recovery: an update review. *Energies* **2010**, *3*, 1529-1575.
12. Thomas, S. Enhanced oil recovery-an overview. *Oil & Gas Science and Technology-Revue de l'IFP* **2008**, *63*, 9-19.
13. Cardona, L.; Arias-Madrid, D.; Cortés, F.; Lopera, S.; Franco, C. Heavy oil upgrading and enhanced recovery in a steam injection process assisted by NiO-and PdO-Functionalized SiO<sub>2</sub> nanoparticulated catalysts. *Catalysts* **2018**, *8*, 132.
14. Wang, Y.; Ren, S.; Zhang, L.; Peng, X.; Pei, S.; Cui, G.; Liu, Y. Numerical study of air assisted cyclic steam stimulation process for heavy oil reservoirs: Recovery performance and energy efficiency analysis. *Fuel* **2018**, *211*, 471-483.
15. Chaar, M.; Venetos, M.; Dargin, J.; Palmer, D. Economics of Steam Generation for Thermal Enhanced Oil Recovery. *Oil and Gas Facilities* **2015**, *4*, 42-50.
16. Ali, S.; Thomas, S. The promise and problems of enhanced oil recovery methods. *Journal of Canadian Petroleum Technology* **1996**, *35*.
17. Karacan, C.Ö.; Okandan, E. Change of physical and thermal decomposition properties of in situ heavy oil with steam temperature. *Petroleum science and technology* **1997**, *15*, 429-443.

18. Kowalewski, I.; Fiedler, C.; Parra, T.; Adam, P.; Albrecht, P. Preliminary results on the formation of organosulfur compounds in sulfate-rich petroleum reservoirs submitted to steam injection. *Organic Geochemistry* **2008**, *39*, 1130-1136.
19. Kar, T.; Ovalles, C.; Rogel, E.; Vien, J.; Hascakir, B. The residual oil saturation determination for Steam Assisted Gravity Drainage (SAGD) and Solvent-SAGD. *Fuel* **2016**, *172*, 187-195.
20. Cardona, L.; Arias-Madrid, D.; Cortés, F.B.; Lopera, S.H.; Franco, C.A. Heavy Oil Upgrading and Enhanced Recovery in a Steam Injection Process Assisted by NiO-and PdO-Functionalized SiO<sub>2</sub> Nanoparticulated Catalysts. *Catalysts* **2018**, *8*, 132.
21. Nassar, N.N.; Franco, C.A.; Montoya, T.; Cortés, F.B.; Hassan, A. Effect of oxide support on Ni–Pd bimetallic nanocatalysts for steam gasification of n-C7 asphaltenes. *Fuel* **2015**, *156*, 110-120.
22. Nassar, N.N.; Hassan, A.; Pereira-Almao, P. Application of nanotechnology for heavy oil upgrading: Catalytic steam gasification/cracking of asphaltenes. *Energy & Fuels* **2011**, *25*, 1566-1570.
23. Sun, X.; Zhang, Y.; Chen, G.; Gai, Z. Application of nanoparticles in enhanced oil recovery: a critical review of recent progress. *Energies* **2017**, *10*, 345.
24. Agista, M.N.; Guo, K.; Yu, Z. A State-of-the-Art Review of Nanoparticles Application in Petroleum with a Focus on Enhanced Oil Recovery. *Applied Sciences* **2018**, *8*, 871.
25. Hashemi, R.; Nassar, N.N.; Almao, P.P. Nanoparticle technology for heavy oil in-situ upgrading and recovery enhancement: Opportunities and challenges. *Applied Energy* **2014**, *133*, 374-387.
26. Cheraghian, G.; Hendraningrat, L. A review on applications of nanotechnology in the enhanced oil recovery part B: effects of nanoparticles on flooding. *International Nano Letters* **2016**, *6*, 1-10.
27. Franco, C.A.; Montoya, T.; Nassar, N.N.; Pereira-Almao, P.; Cortés, F.B. Adsorption and subsequent oxidation of colombian asphaltenes onto nickel and/or palladium oxide supported on fumed silica nanoparticles. *Energy & Fuels* **2013**, *27*, 7336-7347.

28. López, D.; Giraldo, L.J.; Salazar, J.P.; Zapata, D.M.; Ortega, D.C.; Franco, C.A.; Cortés, F.B. Metal Oxide Nanoparticles Supported on Macro-Mesoporous Aluminosilicates for Catalytic Steam Gasification of Heavy Oil Fractions for On-Site Upgrading. *Catalysts* **2017**, *7*, 319.
29. Hosseinpour, N.; Mortazavi, Y.; Bahramian, A.; Khodatars, L.; Khodadadi, A.A. Enhanced pyrolysis and oxidation of asphaltenes adsorbed onto transition metal oxides nanoparticles towards advanced in-situ combustion EOR processes by nanotechnology. *Applied Catalysis A: General* **2014**, *477*, 159-171.
30. Nassar, N.N.; Hassan, A.; Pereira-Almao, P. Comparative oxidation of adsorbed asphaltenes onto transition metal oxide nanoparticles. *Colloids and surfaces A: Physicochemical and Engineering aspects* **2011**, *384*, 145-149.
31. Nassar, N.N.; Hassan, A.; Carbognani, L.; Lopez-Linares, F.; Pereira-Almao, P. Iron oxide nanoparticles for rapid adsorption and enhanced catalytic oxidation of thermally cracked asphaltenes. *Fuel* **2012**, *95*, 257-262.
32. Nassar, N.N.; Hassan, A.; Pereira-Almao, P. Effect of the particle size on asphaltene adsorption and catalytic oxidation onto alumina particles. *Energy & Fuels* **2011**, *25*, 3961-3965.
33. Druetta, P.; Raffa, P.; Picchioni, F. Plenty of Room at the Bottom: Nanotechnology as Solution to an Old Issue in Enhanced Oil Recovery. *Applied Sciences* **2018**, *8*, 2596.
34. Hassan, A.; Lopez-Linares, F.; Nassar, N.N.; Carbognani-Arambarri, L.; Pereira-Almao, P. Development of a support for a NiO catalyst for selective adsorption and post-adsorption catalytic steam gasification of thermally converted asphaltenes. *Catalysis today* **2013**, *207*, 112-118.
35. Sehested, J.; Gelten, J.A.; Remediakis, I.N.; Bengaard, H.; Nørskov, J.K. Sintering of nickel steam-reforming catalysts: effects of temperature and steam and hydrogen pressures. *Journal of Catalysis* **2004**, *223*, 432-443.
36. Nezhad, S.S.K.; Cheraghian, G. Mechanisms behind injecting the combination of nano-clay particles and polymer solution for enhanced oil recovery. *Applied Nanoscience* **2016**, *6*, 923-931.

37. Cheraghian, G.; Nezhad, S.S.K.; Kamari, M.; Hemmati, M.; Masihi, M.; Bazgir, S. Adsorption polymer on reservoir rock and role of the nanoparticles, clay and SiO<sub>2</sub>. *International Nano Letters* **2014**, *4*, 114.
38. Cheraghian, G. Synthesis and properties of polyacrylamide by nanoparticles, effect nanoclay on stability polyacrylamide solution. *Micro & Nano Letters* **2017**, *12*, 40-44.
39. Cheraghian, G. Evaluation of clay and fumed silica nanoparticles on adsorption of surfactant polymer during enhanced oil recovery. *Journal of the Japan Petroleum Institute* **2017**, *60*, 85-94.
40. Cardona Rojas, L. Efecto de nanopartículas en procesos con inyección de vapor a diferentes calidades. M.Sc. Thesis, Universidad Nacional de Colombia-Sede Medellín, March 2018.
41. Medina, O.E.; Gallego, J.; Arias-Madrid, D.; Cortés, F.B.; Franco, C.A. Optimization of the Load of Transition Metal Oxides (Fe<sub>2</sub>O<sub>3</sub>, Co<sub>3</sub>O<sub>4</sub>, NiO and/or PdO) onto CeO<sub>2</sub> Nanoparticles in Catalytic Steam Decomposition of n-C<sub>7</sub> Asphaltenes at Low Temperatures. *Nanomaterials* **2019**, *9*, 401.
42. Atta, A.; Al-Lohedan, H.; Al-Hussain, S. Functionalization of magnetite nanoparticles as oil spill collector. *International journal of molecular sciences* **2015**, *16*, 6911-6931.
43. Guo, K.; Zhang, Y.; Shi, Q.; Yu, Z. The effect of carbon-supported nickel nanoparticles in the reduction of carboxylic acids for in situ upgrading of heavy crude oil. *Energy & Fuels* **2017**, *31*, 6045-6055.
44. Hosseinpour, M.; Fatemi, S.; Ahmadi, S.J. Catalytic cracking of petroleum vacuum residue in supercritical water media: impact of  $\alpha$ -Fe<sub>2</sub>O<sub>3</sub> in the form of free nanoparticles and silica-supported granules. *Fuel* **2015**, *159*, 538-549.
45. Hosseinpour, N.; Khodadadi, A.A.; Bahramian, A.; Mortazavi, Y. Asphaltene adsorption onto acidic/basic metal oxide nanoparticles toward in situ upgrading of reservoir oils by nanotechnology. *Langmuir* **2013**, *29*, 14135-14146.
46. Kazemzadeh, Y.; Eshraghi, S.E.; Kazemi, K.; Sourani, S.; Mehrabi, M.; Ahmadi, Y. Behavior of asphaltene adsorption onto the metal oxide

- nanoparticle surface and its effect on heavy oil recovery. *Industrial & Engineering Chemistry Research* **2015**, *54*, 233-239.
47. Li, L.; Zhan, Y.; Zheng, Q.; Zheng, Y.; Lin, X.; Li, D.; Zhu, J. Water–Gas Shift Reaction Over Aluminum Promoted Cu/CeO<sub>2</sub> Nanocatalysts Characterized by XRD, BET, TPR and Cyclic Voltammetry (CV). *Catalysis Letters* **2007**, *118*, 91-97.
  48. Nematollahi, B.; Rezaei, M.; Lay, E.N. Preparation of highly active and stable NiO–CeO<sub>2</sub> nanocatalysts for CO selective methanation. *International Journal of Hydrogen Energy* **2015**, *40*, 8539-8547.
  49. Khajenoori, M.; Rezaei, M.; Nematollahi, B. Preparation of noble metal nanocatalysts and their applications in catalytic partial oxidation of methane. *Journal of Industrial and Engineering Chemistry* **2013**, *19*, 981-986.
  50. Estifae, P.; Haghighi, M.; Mohammadi, N.; Rahmani, F. CO oxidation over sonochemically synthesized Pd–Cu/Al<sub>2</sub>O<sub>3</sub> nanocatalyst used in hydrogen purification: Effect of Pd loading and ultrasound irradiation time. *Ultrasonics sonochemistry* **2014**, *21*, 1155-1165.
  51. De Lasa, H.; Salices, E.; Mazumder, J.; Lucky, R. Catalytic steam gasification of biomass: catalysts, thermodynamics and kinetics. *Chemical reviews* **2011**, *111*, 5404-5433.
  52. Koh, A.C.; Leong, W.K.; Chen, L.; Ang, T.P.; Lin, J.; Johnson, B.F.; Khimyak, T. Highly efficient ruthenium and ruthenium–platinum cluster-derived nanocatalysts for hydrogen production via ethanol steam reforming. *Catalysis Communications* **2008**, *9*, 170-175.
  53. Vidal, H.; Kašpar, J.; Pijolat, M.; Colon, G.; Bernal, S.; Córdón, A.; Perrichon, V.; Fally, F. Redox behavior of CeO<sub>2</sub>–ZrO<sub>2</sub> mixed oxides: I. Influence of redox treatments on high surface area catalysts. *Applied Catalysis B: Environmental* **2000**, *27*, 49-63.
  54. Wang, R.; Xu, H.; Liu, X.; Ge, Q.; Li, W. Role of redox couples of Rh<sup>0</sup>/Rh<sup>δ+</sup> and Ce<sup>4+</sup>/Ce<sup>3+</sup> in CH<sub>4</sub>/CO<sub>2</sub> reforming over Rh–CeO<sub>2</sub>/Al<sub>2</sub>O<sub>3</sub> catalyst. *Applied Catalysis A: General* **2006**, *305*, 204-210.
  55. Celardo, I.; Traversa, E.; Ghibelli, L. Cerium oxide nanoparticles: a promise for applications in therapy. *J Exp Ther Oncol* **2011**, *9*, 47-51.



56. Das, M.; Patil, S.; Bhargava, N.; Kang, J.-F.; Riedel, L.M.; Seal, S.; Hickman, J.J. Auto-catalytic ceria nanoparticles offer neuroprotection to adult rat spinal cord neurons. *Biomaterials* **2007**, *28*, 1918-1925.
57. Hayek, K.; Kramer, R.; Paál, Z. Metal-support boundary sites in catalysis. *Applied Catalysis A: General* **1997**, *162*, 1-15.
58. Alamolhoda, S.; Vitale, G.; Hassan, A.; Nassar, N.N.; Almaso, P.P. Synergetic effects of cerium and nickel in Ce-Ni-MFI catalysts on low-temperature water-gas shift reaction. *Fuel* **2019**, *237*, 361-372.
59. Munnik, P.; de Jongh, P.E.; de Jong, K.P. Recent developments in the synthesis of supported catalysts. *Chemical reviews* **2015**, *115*, 6687-6718.
60. Lensveld, D.J.; Mesu, J.G.; van Dillen, A.J.; de Jong, K.P. The application of well-dispersed nickel nanoparticles inside the mesopores of MCM-41 by use of a nickel citrate chelate as precursor. In *Studies in Surface Science and Catalysis*, Elsevier: 2000; Vol. 143, pp. 647-657.
61. Mansfield, E.; Tyner, K.M.; Poling, C.M.; Blacklock, J.L. Determination of nanoparticle surface coatings and nanoparticle purity using microscale thermogravimetric analysis. *Analytical chemistry* **2014**, *86*, 1478-1484.
62. Qiu, H.; Lv, L.; Pan, B.-c.; Zhang, Q.-j.; Zhang, W.-m.; Zhang, Q.-x. Critical review in adsorption kinetic models. *Journal of Zhejiang University-Science A* **2009**, *10*, 716-724.
63. Chiron, N.; Guilet, R.; Deydier, E. Adsorption of Cu (II) and Pb (II) onto a grafted silica: isotherms and kinetic models. *Water Research* **2003**, *37*, 3079-3086.
64. Wilczak, A.; Keinath, T.M. Kinetics of sorption and desorption of copper (II) and lead (II) on activated carbon. *Water Environment Research* **1993**, *65*, 238-244.
65. Talu, O.; Meunier, F. Adsorption of associating molecules in micropores and application to water on carbon. *AIChE journal* **1996**, *42*, 809-819.
66. Montoya, T.; Coral, D.; Franco, C.A.; Nassar, N.N.; Cortés, F.B. A novel solid-liquid equilibrium model for describing the adsorption of associating asphaltene molecules onto solid surfaces based on the "chemical theory". *Energy & Fuels* **2014**, *28*, 4963-4975.

67. Nassar, N.N. Asphaltene adsorption onto alumina nanoparticles: kinetics and thermodynamic studies. *Energy & Fuels* **2010**, *24*, 4116-4122.
68. Cortés, F.B.; Montoya, T.; Acevedo, S.; Nassar, N.N.; Franco, C.A. Adsorption-desorption of n-c7 asphaltenes over micro-and nanoparticles of silica and its impact on wettability alteration. *CT&F-Ciencia, Tecnología y Futuro* **2016**, *6*, 89-106.
69. Betancur, S.; Carrasco-Marín, F.; Franco, C.A.; Cortés, F.B. Development of Composite Materials Based on the Interaction between Nanoparticles and Surfactants for Application on Chemical Enhanced Oil Recovery. *Industrial & Engineering Chemistry Research* **2018**.
70. Nassar, N.N.; Hassan, A.; Luna, G.; Pereira-Almao, P. Kinetics of the catalytic thermo-oxidation of asphaltenes at isothermal conditions on different metal oxide nanoparticle surfaces. *Catalysis today* **2013**, *207*, 127-132.
71. Vyazovkin, S.; Burnham, A.K.; Criado, J.M.; Pérez-Maqueda, L.A.; Popescu, C.; Sbirrazzuoli, N. ICTAC Kinetics Committee recommendations for performing kinetic computations on thermal analysis data. *Thermochimica acta* **2011**, *520*, 1-19.
72. Scheffe, H. The simplex-centroid design for experiments with mixtures. *Journal of the Royal Statistical Society. Series B (Methodological)* **1963**, 235-263.
73. Murugan, P.; Mahinpey, N.; Mani, T. Thermal cracking and combustion kinetics of asphaltenes derived from Fosterton oil. *Fuel Processing Technology* **2009**, *90*, 1286-1291.
74. Mullins, O.C.; Sabbah, H.; Eyssautier, J.; Pomerantz, A.E.; Barré, L.; Andrews, A.B.; Ruiz-Morales, Y.; Mostowfi, F.; McFarlane, R.; Goual, L. Advances in asphaltene science and the Yen–Mullins model. *Energy & Fuels* **2012**, *26*, 3986-4003.
75. Nassar, N.N.; Betancur, S.; Acevedo, S.c.; Franco, C.A.; Cortés, F.B. Development of a population balance model to describe the influence of shear and nanoparticles on the aggregation and fragmentation of asphaltene aggregates. *Industrial & Engineering Chemistry Research* **2015**, *54*, 8201-8211.

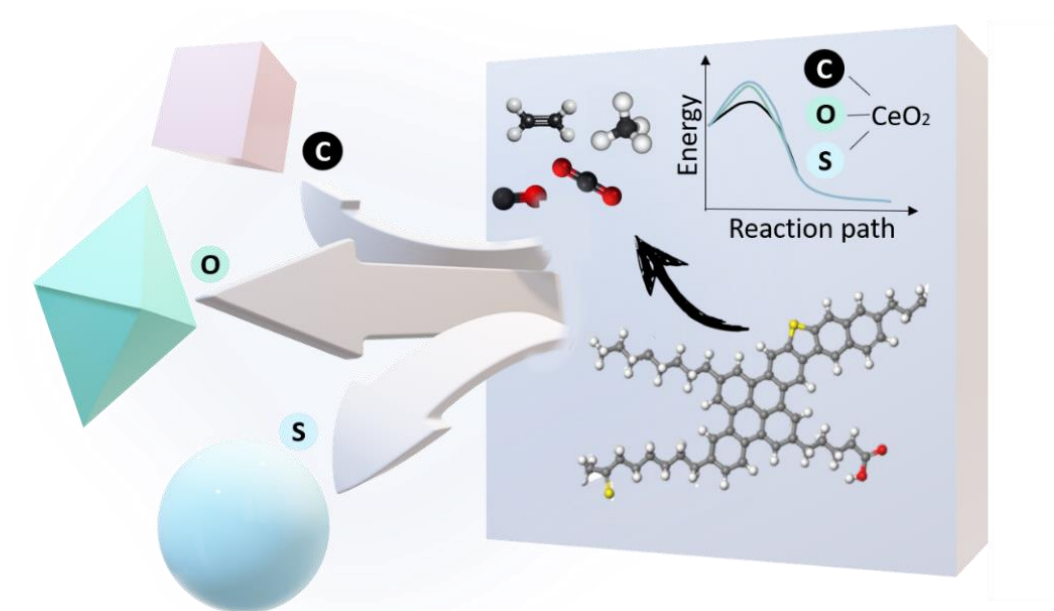
76. Franco, C.; Patiño, E.; Benjumea, P.; Ruiz, M.A.; Cortés, F.B. Kinetic and thermodynamic equilibrium of asphaltenes sorption onto nanoparticles of nickel oxide supported on nanoparticulated alumina. *Fuel* **2013**, *105*, 408-414.
77. Wu, S.; Tang, D.; Li, S.; Chen, H.; Wu, H. Coalbed methane adsorption behavior and its energy variation features under supercritical pressure and temperature conditions. *Journal of Petroleum Science and Engineering* **2016**, *146*, 726-734.
78. Franco, C.A.; Nassar, N.N.; Montoya, T.; Ruíz, M.A.; Cortés, F.B. Influence of asphaltene aggregation on the adsorption and catalytic behavior of nanoparticles. *Energy & Fuels* **2015**, *29*, 1610-1621.
79. Ternan, M. Catalytic hydrogenation and asphaltene conversion of Athabasca bitumen. *The Canadian Journal of Chemical Engineering* **1983**, *61*, 689-696.
80. Jacobs, G.; Ricote, S.; Graham, U.M.; Patterson, P.M.; Davis, B.H. Low temperature water gas shift: Type and loading of metal impacts forward decomposition of pseudo-stabilized formate over metal/ceria catalysts. *Catalysis today* **2005**, *106*, 259-264.
81. Vignatti, C.I.; Avila, M.S.; Apesteguia, C.R.; Garetto, T.F. Study of the water-gas shift reaction over Pt supported on CeO<sub>2</sub>-ZrO<sub>2</sub> mixed oxides. *Catalysis Today* **2011**, *171*, 297-303.
82. Speight, J. Petroleum Asphaltene-Part 1: Asphaltene, resins and the structure of petroleum. *Oil & gas science and technology* **2004**, *59*, 467-477.
83. Fu, Q.; Deng, W.; Saltsburg, H.; Flytzani-Stephanopoulos, M. Activity and stability of low-content gold-cerium oxide catalysts for the water-gas shift reaction. *Applied Catalysis B: Environmental* **2005**, *56*, 57-68.
84. Hilaire, S.; Wang, X.; Luo, T.; Gorte, R.; Wagner, J. A comparative study of water-gas-shift reaction over ceria supported metallic catalysts. *Applied Catalysis A: General* **2001**, *215*, 271-278.
85. Mierczynski, P.; Maniukiewicz, W.; Maniecki, T. Comparative studies of Pd, Ru, Ni, Cu/ZnAl<sub>2</sub>O<sub>4</sub> catalysts for the water gas shift reaction. *Open Chemistry* **2013**, *11*, 912-919.

86. Peuckert, M. XPS study on surface and bulk palladium oxide, its thermal stability, and a comparison with other noble metal oxides. *The Journal of Physical Chemistry* **1985**, *89*, 2481-2486.
87. Basile, F.; Fornasari, G.; Gazzano, M.; Vaccari, A. Thermal evolution and catalytic activity of Pd/Mg/Al mixed oxides obtained from a hydrotalcite-type precursor. *Applied clay science* **2001**, *18*, 51-57.
88. Pinc, W.; Yu, P.; O'Keefe, M.; Fahrenholtz, W. Effect of gelatin additions on the corrosion resistance of cerium based conversion coatings spray deposited on Al 2024-T3. *Surface & Coatings Technology* **2009**, *23*, 3533-3540.
89. Shyu, J.; Weber, W.; Gandhi, H. Surface characterization of alumina-supported ceria. *The Journal of Physical Chemistry* **1988**, *92*, 4964-4970.
90. Abi-aad, E.; Bechara, R.; Grimblot, J.; Aboukais, A. Preparation and characterization of ceria under an oxidizing atmosphere. Thermal analysis, XPS, and EPR study. *Chemistry of Materials* **1993**, *5*, 793-797.
91. Matta, J.; Courcot, D.; Abi-Aad, E.; Aboukais, A. Thermal analysis, EPR and XPS study of vanadyl (IV) oxalate behavior on the ceria surface. *Journal of thermal analysis and calorimetry* **2001**, *66*, 717-727.
92. Qiu, L.; Liu, F.; Zhao, L.; Ma, Y.; Yao, J. Comparative XPS study of surface reduction for nanocrystalline and microcrystalline ceria powder. *Applied Surface Science* **2006**, *252*, 4931-4935.
93. Sim, K.S.; Hilaire, L.; Le Normand, F.; Touroude, R.; Paul-Boncour, V.; Percheron-Guegan, A. Catalysis by palladium-rare-earth-metal (REPd 3) intermetallic compounds: hydrogenation of but-1-ene, buta-1, 3-diene and but-1-yne. *Journal of the Chemical Society, Faraday Transactions* **1991**, *87*, 1453-1460.
94. Kotani, A.; Jo, T.; Parlebas, J. Many-body effects in core-level spectroscopy of rare-earth compounds. *Advances in Physics* **1988**, *37*, 37-85.
95. Laachir, A.; Perrichon, V.; Badri, A.; Lamotte, J.; Catherine, E.; Lavalley, J.C.; El Fallah, J.; Hilaire, L.; Le Normand, F.; Quéméré, E. Reduction of CeO<sub>2</sub> by hydrogen. Magnetic susceptibility and Fourier-transform infrared, ultraviolet and X-ray photoelectron spectroscopy measurements. *Journal of the Chemical Society, Faraday Transactions* **1991**, *87*, 1601-1609.

96. Nagai, Y.; Hirabayashi, T.; Dohmae, K.; Takagi, N.; Minami, T.; Shinjoh, H.; Matsumoto, S.i. Sintering inhibition mechanism of platinum supported on ceria-based oxide and Pt-oxide–support interaction. *Journal of Catalysis* **2006**, *242*, 103-109.
97. Xu, J.; Harmer, J.; Li, G.; Chapman, T.; Collier, P.; Longworth, S.; Tsang, S.C. Size dependent oxygen buffering capacity of ceria nanocrystals. *Chemical communications* **2010**, *46*, 1887-1889.

Chapter 9.

# Insights into the Morphology Effect of Ceria on Catalytic Performance of NiO-PdO/CeO<sub>2</sub> Nanoparticles for Thermo-Oxidation of *n*-C<sub>7</sub> Asphaltenes under Isothermal Heating at Different Pressures



Published article in *Energy & Fuels*: [10.1021/acs.energyfuels.1c01424](https://doi.org/10.1021/acs.energyfuels.1c01424)

Impact factor: 4.654

# Insights into the Morphology Effect of Ceria on Catalytic Performance of NiO-PdO/CeO<sub>2</sub> Nanoparticles for Thermo-Oxidation of *n*-C<sub>7</sub> Asphaltenes under Isothermal Heating at Different Pressures

## Abstract

The overall objective of this study is to evaluate the effect of morphologies (C, cubic; O, orthorhombic; and S, spherical) of ceria in the catalytic activity for *n*-C<sub>7</sub> asphaltene thermo-oxidation. In this way, cubic (C-CeO<sub>2</sub>), orthorhombic (O-CeO<sub>2</sub>), and spherical (S-CeO<sub>2</sub>) ceria nanoparticles were synthesized using the hydrothermal method and doped with 1.0% in mass fraction of Ni and Pd oxides by the incipient wetness impregnation. The catalytic activity of the systems was evaluated through non-isothermal and isothermal thermogravimetric analyses at different pressures. The non-isothermal thermogravimetric results evidenced an increase in the *n*-C<sub>7</sub> asphaltene mass as the temperature increases between 100 and 230 °C for all systems and operating conditions. At 3.0 MPa, *n*-C<sub>7</sub> asphaltene gains 3.6, 5.8, and 3.2% for O-CeO<sub>2</sub>, C-CeO<sub>2</sub>, and S-CeO<sub>2</sub>, respectively, while at 6.0 MPa there is an increase 7.3, 10.4, and 5.9%, for the same systems, respectively. The Ni and Pd phases increase the amount of oxygen chemisorbed in all systems in the order S-NiPdCe < O-NiPdCe < C-NiPdCe, and reduce the temperature required for the total *n*-C<sub>7</sub> asphaltene decomposition at temperatures lower than 200 °C at 6.0 MPa in the same order. Also, isothermal thermogravimetric analysis demonstrates that the asphaltene conversion increased with ceria-based nanocatalysts in the increasing order S- CeO<sub>2</sub> < O- CeO<sub>2</sub> < C- CeO<sub>2</sub>. Cubic CeO<sub>2</sub> doped with Ni and Pd presents the highest yield, reaching 100% conversion at 170°C and 6.0 MPa at 60 min. The data confirms that the presence of Ni and Pd facilitate the transference oxygen vacancies between the bulk and surface of the nanocatalyst, and therefore, the catalytic activity is enhanced. The catalytic activity, in turn, is improved by the presence of {110}, {100}, and {111}, oxygen vacancies, and Ce<sup>3+</sup> and NiO-Ce species. This work reveals the benefits of structured cubic ceria nanocatalysts as promising support for nickel- and palladium-containing materials for *n*-C<sub>7</sub> asphaltene decomposition.

## 1. Introduction

Asphaltenes are the heaviest fraction of crude oil.<sup>1</sup> Because they are highly polar and present high molecular weights, their proper removal is of significance to enhance crude oil production technologies.<sup>2, 3</sup> The injection of air or oxygen-rich gases has been worldwide used for producing heavy and extra heavy crude oils, where the content of asphaltenes ranges between 2 and 30% in a mass fraction.<sup>4, 5</sup> Nevertheless, limited by the combustion front stability and the efficiency of combustion, pyrolysis, and oxidation reactions, asphaltenes convert mainly into coke. Hence, advanced strategies are needed to circumvent the problem.<sup>5-7</sup> The catalytic oxidation of asphaltenes using nanoparticles is attractive, but the synthesized materials tested were far from perfect. The major shortcoming is the reduction of the oxidative asphaltene decomposition temperature.<sup>8-15</sup> In most cases, it occurs at temperatures greater than 300 °C.<sup>13, 16-20</sup> The importance of reducing the oxidative decomposition temperature of asphaltenes lies in the subsequent improvement in the crude oil quality. Different thermal experiments carried out in atmospheres of air, steam, and inert, have shown that reducing the content of asphaltenes in the crude oil matrix leads to a reduction in the crude oil viscoelastic network and density, and therefore, higher mobility to reservoir and surface conditions.<sup>21-23</sup>

With excellent catalytic properties, including oxygen storage capacity (OSC), modified acid-base chemistry, potential redox property, and self-regeneration ability,<sup>24</sup> ceria have been evaluated in our previous studies for decomposing asphaltenes.<sup>25-28</sup> In the first study, we evaluated three different couples of element oxides (Ni-Pd, Co-Pd, and Fe-Pd) supported on amorphous CeO<sub>2</sub> for asphaltene decomposition under a steam atmosphere.<sup>26</sup> The Ni-Pd/CeO<sub>2</sub> showed the best results, reducing the asphaltene decomposition temperature from 450 °C to 220 °C. A second study showed that, as a result of the Ce<sup>4+</sup>/Ce<sup>3+</sup> redox cycle, there was helpful asphaltene selectivity and conversion over Ni-Pd/CeO<sub>2</sub> nanoparticles.<sup>25</sup> Further, this was identified as the main route for the self-regeneration of the material. Both works were done at atmospheric pressure. Recently, we developed multifunctional nanocatalysts composed of bimetallic phases of Au and Pd doped over Ce<sub>0.68</sub>Zr<sub>0.32</sub>O<sub>2</sub> amorphous mixed oxide.<sup>29</sup> The system with a 0.2 mg·m<sup>-2</sup> asphaltene adsorbed amount was tested under non-isothermal thermogravimetric experiments using an oxygen partial pressure of



6.0 MPa and a heating rate of  $10\text{ }^{\circ}\text{C}\cdot\text{min}^{-1}$  from 100 to 600  $^{\circ}\text{C}$ . Under these conditions, the oxidative asphaltene decomposition temperature was reduced from 450 to 190  $^{\circ}\text{C}$  for the  $\text{Ce}_{0.68}\text{Zr}_{0.32}\text{O}_2$  doped with a 10:1 Au:Pd molar ratio. Despite the satisfactory results, there are still limitations and challenges to overcome during these processes because there is no complete understanding of the oxidative thermo-catalytic reactions of asphaltenes at a high pressure. In this sense, it is essential to determine the controlling catalytic factors of  $\text{CeO}_2$  nanoparticles in asphaltene decomposition. Shape control is considered a knob for handling the chemical, textural, and catalytic properties of materials.<sup>30, 31</sup> Interestingly, this is a particular topic analyzed in the application of  $\text{CeO}_2$  as a catalyst for  $\text{H}_2\text{S}$  selective oxidation,<sup>31</sup> low-temperature CO oxidation,<sup>30</sup> oxidative steam reforming of methanol,<sup>32</sup> and ethanol,<sup>33</sup> and oil reforming.<sup>34</sup> It was reported that well-defined crystal planes in  $\text{CeO}_2$  display an improvement in catalytic performance due to synergistic interactions with transition elements and, therefore, the strong metal-support interaction (SMSI), surface energy, and atom arrangement,<sup>35-38</sup> as well as the surface chemistry and variations in coordinative unsaturation and  $\text{Ce}^{3+}$ - and  $\text{O}^{2-}$ -modified catalytic properties.<sup>31</sup> In this context, it becomes imperative to take advantage of the enhanced chemical properties through the modification of the  $\text{CeO}_2$  morphology in asphaltene adsorption and subsequent decomposition. Hence, the shape dependence of  $\text{CeO}_2$  based on catalytic performance for decomposing  $n\text{-C}_7$  asphaltenes is the main objective of this work. Further, this research studies exciting topics, including the effect of pressure on non-isothermal and isothermal heating of  $n\text{-C}_7$  asphaltenes and their respective kinetic study. Until now, the design of these systems for the application has not been explored.

In this research, three different ceria nanocatalysts with orthorhombic, cubic, and spherical morphologies were successfully synthesized for a simple hydrothermal method and tested in  $n\text{-C}_7$  asphaltene adsorption and oxidation. We investigated the impact of the redox cycle, oxygen vacancies, crystal size, and surface chemistry on the catalytic properties of ceria for asphaltene oxidative decomposition. Also, the effect of SMSI was assessed by doping the different  $\text{CeO}_2$  with the couple Ni-Pd in 1% of the mass fraction. To the best of our knowledge, this is the first attempt to systematically understand the effect of the  $\text{CeO}_2$  shapes on  $n\text{-C}_7$  asphaltene oxidation at different pressures. Findings are expected to guide enhancing the catalytic performance in  $n\text{-C}_7$  asphaltene decomposition.

## 2. Experimental

### 2.1. Materials

*n*-C<sub>7</sub> Asphaltenes were isolated from an extra-heavy crude oil based on the ASTM standard.<sup>39</sup> The crude oil composition in terms of saturates, aromatics, resins and asphaltenes was determined through a combined process of micro de-asphalting and the IP 469 method using a LATROSCAN MK6 TLC-FID/FPD equipment.<sup>40</sup> The viscosity was measured in a rheometer Kinexus Pro+ (Malvern Instruments, Worcestershire, UK) at 25 °C and the American Petroleum Institute (API) gravity was estimated using an Anton Paar Stabinger SVM 3000 (Madrid, Spain). The contents of carbon, hydrogen, nitrogen, sulfur and oxygen of the isolated asphaltenes were characterized by Thermo Flash elemental analyzer EA 1112 (Thermo Finnigan, Milan, Italy), using the conventional combustion procedure following the ASTM D5291 standard.<sup>41</sup> The average molecular weight for asphaltene samples was calculated by vapor pressure osmometry (VPO) using a Knauer osmometer (Knauer, Berlin-Heidelberg, West Germany) calibrated with benzyl. The properties of the EHO and *n*-C<sub>7</sub> asphaltenes are summarized in Table 1.

**Table 1.** Basic properties estimated for the extra-heavy crude oil and isolated *n*-C<sub>7</sub> asphaltenes.

Extra Heavy Crude Oil				<i>n</i> -C <sub>7</sub> asphaltenes				
S	Ar	R	A	C	H	N	S	O
13.0	16.9	49.9	20.2	81.7	7.8	0.3	6.6	3.6
Viscosity (cP) @25 °C			6 × 10 <sup>6</sup>	Molecular Weight (g·mol <sup>-1</sup> )				645.1
API °			6.7	H/C				1.15

Ce(NO<sub>3</sub>)<sub>3</sub>·6H<sub>2</sub>O, polyvinyl pyrrolidone (PVP, K29-32), ethanol (99.8%), and KOH all provided by Sigma-Aldrich (St. Louis, MO, USA) were used for the synthesis of morphological cerium nanoparticles. All the above chemicals were analytical reagents.

### 2.2. Synthesis of nanocatalysts

Three different routes were selected for the synthesis of nanoparticles and thus obtained three shapes, which were used to clear the controlling factors of adsorption capacity and catalytic activity of CeO<sub>2</sub> for *n*-C<sub>7</sub> asphaltene uptake and oxidative decomposition, respectively. First, spherical CeO<sub>2</sub> (S-CeO<sub>2</sub>) was

obtained by the hydrothermal method. Then, some variations of the operating conditions reported in the literature were executed to obtain nanometric particles.<sup>42</sup> Initially, 4 mmol of  $\text{Ce}(\text{NO}_3)_3 \cdot 6\text{H}_2\text{O}$  and PVP were diluted in 40 mL of deionized water. The solution was stirred for 4 h and transferred to a 50 mL Teflon-lined stainless-steel autoclave heated at 200 °C for 4 h. Next, orthorhombic  $\text{CeO}_2$  (O- $\text{CeO}_2$ ) was synthesized by a modified version of the previous method. For this, 8 mmol of the precursor cerium salt with 10 mmol of PVP were dissolved in an ethanol and deionized water solution (1:3 volume ratio) and stirred for 30 min. The autoclave was heated at 200 °C for 24 h. Finally, cubic  $\text{CeO}_2$  (C- $\text{CeO}_2$ ) was obtained by dissolving 1 mmol of  $\text{Ce}(\text{NO}_3)_3 \cdot 6\text{H}_2\text{O}$  in 35 mL of water. Once the solution was homogeneous, 0.35 mL of water containing 0.1 mol·L<sup>-1</sup> of KOH was added dropwise. The system was introduced in the autoclave and heated at 230 °C for 36 h. All the samples were slowly cooled at room temperature and washed several times with ethanol and water.

### 2.3. Nanocatalysts Characterization

$\text{N}_2$  adsorption-desorption at -196 °C was done using a Micromeritic ASAP2020 (Micromeritics, Norcross, GA, USA) to determine the specific surface area ( $S_{\text{BET}}$ ). BET equation was used for the calculation.<sup>43</sup> The morphology of the nanoparticles was analyzed by high-resolution transmission electron microscopy (HR-TEM) in an FEI Titan G2 microscope (HR-TEM) (Eindhoven, The Netherlands) and by scanning electron microscopy in an FEI microscope model Quanta 400 (SEM) (Eindhoven, The Netherlands) equipped for energy-dispersive X-ray analysis to obtain the Ce and O semiquantitative content. Inductively Coupled Plasma Mass Spectrometry (ICP-MS) was used to estimate the final metal loading of Ni and Pd.

The crystal size and lattice parameter were calculated from the Debye-Scherrer and Bragg equations, respectively,<sup>44</sup> using the data obtained from X-ray diffraction analysis on a Bruker D8 Venture X-ray diffractometer (BRUKER, Rivas-Vaciamadrid, Spain). The radiation was  $\text{Cu K}\alpha$  in the range of  $10^\circ < 2\theta < 80^\circ$ . The data was processed from Rietveld refinement. Raman spectroscopy was realized on a Renishaw spectrometer at ambient conditions using  $\lambda = 532$  nm. X-ray photoelectron spectroscopy was executed to analyze the surface chemistry of the samples. The experimental procedure was done in a Kratos Axis Ultra-DLD spectrometer (Manchester, UK). A monochromatic  $\text{Al K}\alpha$  source with step energy of 90 eV (1 eV step) and 20 eV (0.1 eV step) for general high-resolution spectra ( $\text{O}_{1s}$ ,  $\text{Ce}_{3d5/2}$ ,  $\text{Ni}_{2p}$ ,  $\text{Pd}_{3d}$ ). Calibration of the adventitious C=C peak was

performed at 284.8 eV. All patterns were analyzed using the XPSpeak4.1 software. Shirley-type background correction was used for baseline correction, whereas different Gaussian–Lorentzian ratios were employed to fit the deconvoluted peaks.

H<sub>2</sub> titration was performed for measuring metal dispersion and the average size of the nanocrystal in supported nanoparticles. The tests were performed in a Chembet 3000 (Quantachrome Instruments, Boynton Beach, FL, USA) following the previous work procedure.<sup>26</sup>

#### 2.4. Adsorption test

The adsorption capacity of the nanoparticles for *n*-C<sub>7</sub> asphaltenes was studied by batch experiments using a colorimetric method.<sup>45-47</sup> Different model solutions containing *n*-C<sub>7</sub> asphaltenes in toluene were done between 100 and 1500 mg·L<sup>-1</sup>. Then, nanoparticles were added in a 10:1 ratio of adsorbent mass (mg) to solution volume (mL). The ultraviolet-visible (UV-vis) spectrophotometer Genesys 10S UV-VIS (Thermo Scientific, Waltham, MA, USA) was used to determine the change in asphaltene concentration in the supernatant. First, a calibration curve of the UV-vis absorbance versus asphaltenes concentration was constructed in which the linearity can be ensured at 298 nm wavelength. Then, nanoparticles-asphaltene mixtures are stirred for 24 h at 25 °C. Finally, the remaining solid was separated through centrifugation at 4500 rpm. The residual concentration was obtained by the absorbance measurements.<sup>26</sup> The amount of adsorbed asphaltenes *q* (mg·m<sup>-2</sup>) was determined by mass balance (Equation 1):

$$q = \frac{C_o - C_E}{A} V \quad (1)$$

where *C<sub>E</sub>* (mg·L<sup>-1</sup>) is the equilibrium concentration of asphaltenes in the supernatant, *C<sub>o</sub>* (mg·L<sup>-1</sup>) is the initial concentration of *n*-C<sub>7</sub> asphaltenes in solution, *A* (m<sup>2</sup>·g<sup>-1</sup>) is the dry surface area of nanoparticles, and *V* (L) is the solution volume. The adsorption isotherms were adjusted to the SLE model described elsewhere.

#### 2.5. Non-isothermal experiments

Non-isothermal oxidation under an air atmosphere was investigated by differential scanning calorimetry (DSC) and high-pressure thermogravimetric analysis (HP-TGA). DSC runs were done in a Q2000 DSC (TA. Instruments, Inc., New Castel, DE, USA) at a heating rate of 10 °C·min<sup>-1</sup> from 100 °C to 700 °C in an

alumina crucible. The catalyzed and non-catalyzed experiments were executed with 5 mg of sample. The gas flow rate was 100 mL·min<sup>-1</sup>.

HP-TGA runs were carried out in HP-TGA 750 (TA instruments Inc., Hüllhorst, Germany) under the following procedure. Initially, a high vacuum was done at  $2.5 \times 10^{-4}$  MPa for 10 min for cleaning the surface sample. Then, the equipment adjusts the selected pressure (0.084 MPa, 3.0 MPa, and 6.0 MPa). Once the pressure is reached, the heating starts at a rate of 10 °C·min<sup>-1</sup> between 100 °C and 700 °C under an airflow of 80 mL·min<sup>-1</sup> in an alumina crucible. The sample weight was 1 mg. The run is done by two times, for the crucible with the sample and one more empty due to buoyancy correction. All the experiments were performed at least twice for repeatability.

## 2.6. Isothermal experiments

Isothermal experiments were done by high-pressure thermogravimetric analysis aligned to a mass spectrometer (Shimadzu GC-MS, Tokyo, Japan). The samples were heated at a fixed temperature (170, 200, and 230 °C) for 300 min to ensure the asphaltene conversion quantification. The runs were performed at 0.084, 3.0, and 6.0 MPa. The evolved gases were analyzed using a linear scan rate of ion trap mass analyzer of  $m/z$  0.03 from  $m/z$  0 up to 200. Repeatability was ensured by performing each test in triplicate.

## 2.7. Kinetic analysis

Insights about the kinetic of *n*-C<sub>7</sub> asphaltene catalytic oxidation were realized on the basis on fitting a *n*-order kinetic model.<sup>48, 49</sup> The instantaneous reactivity *r* of the fraction is described by Equations (2) and (3):<sup>50</sup>

$$r = \frac{d\theta}{dt} = f(\theta) \cdot P_{O_2}^n \cdot k \quad (2)$$

$$\frac{d\theta}{dt} \frac{1}{f(\theta)} = k_o \exp\left(-\frac{E_a}{RT}\right) \cdot P_{O_2}^n \quad (3)$$

where  $P_{O_2}^n$  (bar) represents the partial pressure of the reactant gas (O<sub>2</sub>), *k* is the velocity constant,  $\theta$  is associated with the conversion of asphaltene at any time *t*, *n* the order of reaction, *R* (J·mol<sup>-1</sup>K<sup>-1</sup>) the universal gas constant, *E<sub>a</sub>* (kJ·mol<sup>-1</sup>) the effective activation energy, *k<sub>o</sub>* (s<sup>-1</sup>·bar<sup>-*n*</sup>) the pre-exponential factor and *f*( $\theta$ ) considers the asphaltene conversion degree during the test. Variable separation and integration was done to Equation 3, obtaining the Equation (4):<sup>48, 49</sup>

$$F(\theta) = \int_0^\theta \frac{d\theta}{f(\theta)} = \int_0^t k_o \exp\left(\frac{-E_a}{R_{gas}T}\right) P_{O_2}^n dt \quad (4)$$

Considering the activation energy values constant and applying natural logarithm in both sides, Equation (5) is obtained.

$$\ln(t_{a,i}) = \ln\left[\frac{F(\theta)}{P_{O_2}^n T}\right] + \frac{E_a}{RT_i} \quad (5)$$

where,  $t_{a,i}$  is the time for the reaction to reach a defined conversion degree ( $\theta$ ) at a given temperature ( $i$ ). Considering the volumetric model for the radial consumption of the particle Equation (6) is written as follows:

$$\ln(t_{a,i}) = \ln\left[\frac{-\ln(1-\theta)}{P_{O_2}^n T}\right] + \frac{E_a}{RT_i} \quad (6)$$

Finally, effective activation energy and pre-exponential factor are obtained from the slope and intercept through the plot  $\ln(t_{a,i})$  against  $\frac{1}{T_i}$  when the 100% of *n*-C<sub>7</sub> asphaltene consumption is reached.

### 3. Results and discussion

#### 3.1. Characterization of non-doped nanocatalysts.

The  $S_{BET}$  of the prepared X-CeO<sub>2</sub> (X = S, C, and O) are summarized in Table 2. The surface area increases in the order S-CeO<sub>2</sub> < C-CeO<sub>2</sub> < O-CeO<sub>2</sub>. Their morphology and size were studied by SEM-EDX and HR-TEM and shown in Figures 1 and 2, respectively. The diameter of the S-CeO<sub>2</sub> (Fig 1a) was observed as 40 nm with a rough surface. Figure 1b shows that C-CeO<sub>2</sub> presents cubes with a smooth surface and average size between 40 nm and 60 nm. Finally, O-CeO<sub>2</sub> morphology was validated in panel c of Figure. 1. Orthorhombic shapes are observed with an average side size of 20 nm. Also, the structures are highly agglomerated. The EDX spectra for the samples are presented in panels b, d, and f of Figure 1. From them, we can corroborate the presence of Ce and O in the bulk phase of nanomaterials. These spectra have not been used for the quantitative calculation of each element. Furthermore, the ICP-MS analysis summarized in Table 2 shows that the bulk content of Ce was similar for all the synthesized

systems. The Ce content was slightly lower for the S-CeO<sub>2</sub>, and the oxygen content follows the opposite way.

**Table 2.** Estimated lattice parameter, crystallinity, compositional and textural properties of synthesized S-CeO<sub>2</sub>, C-CeO<sub>2</sub>, and O-CeO<sub>2</sub>

Sample	S <sub>BET</sub> (m <sup>2</sup> g <sup>-1</sup> )	Ce <sup>c</sup> (%)	O <sup>c</sup> (%)	Crystallite size <sup>a</sup> (nm)	Lattice Parameter <sup>b</sup> (nm) x 10 <sup>-2</sup>
S-CeO <sub>2</sub>	22.2	44.6	55.4	12	54.09
C-CeO <sub>2</sub>	32.1	43.7	56.3	15	54.12
O-CeO <sub>2</sub>	38.0	43.8	56.2	19	54.10

<sup>a</sup>Crystallite size was calculated based on the Scherrer equation; <sup>b</sup>Lattice parameters were calculated based on the Bragg equation  $2d \sin(\theta) = n\lambda$ ; <sup>c</sup>Atomic percentual fraction determined through ICP-MS.

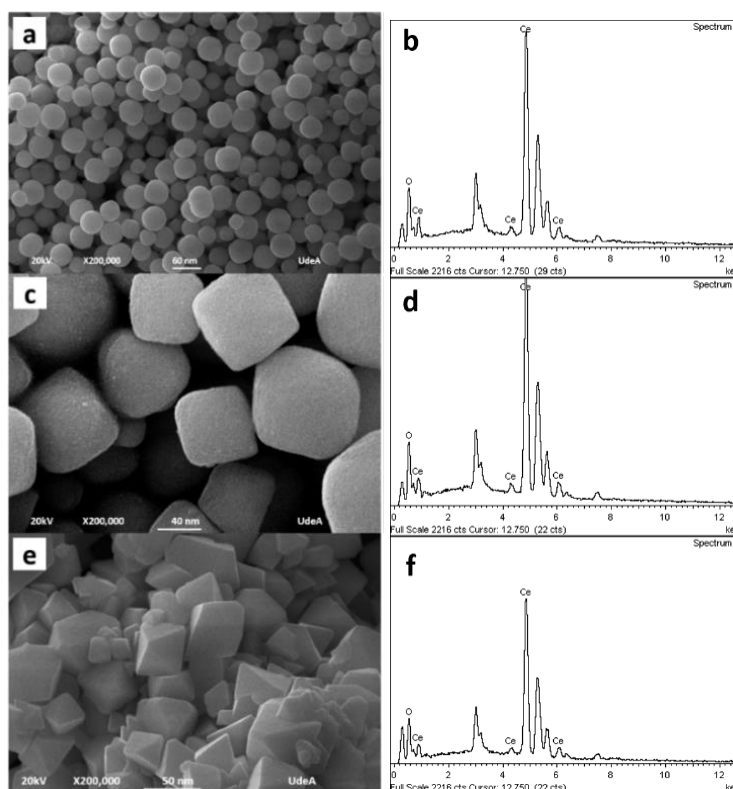


**Figure 1.** Scanning electron microscopy images and Energy-dispersive X-ray analysis of S-CeO<sub>2</sub> (a-b), C-CeO<sub>2</sub> (c-d) and O-CeO<sub>2</sub> (e-f).

Panels a, d, and g of Figure 2 corroborated the spherical-like morphology of S-CeO<sub>2</sub> with the presence of (024) facets. Also, HR-TEM images in panels b, e, and h confirm the cubic shape of C-CeO<sub>2</sub>. The HR-TEM image reveals that the {111} crystal face dominates the surface of C-CeO<sub>2</sub> with an interplanar space of 0.32 nm. The {111} crystal face is the thermodynamically most stable crystal facet. The orthorhombic CeO<sub>2</sub> (panels c, f, and i of Figure 2) is enclosed by {200} and {220} with an interplanar spacing of 0.27 nm and 0.19 nm, respectively.

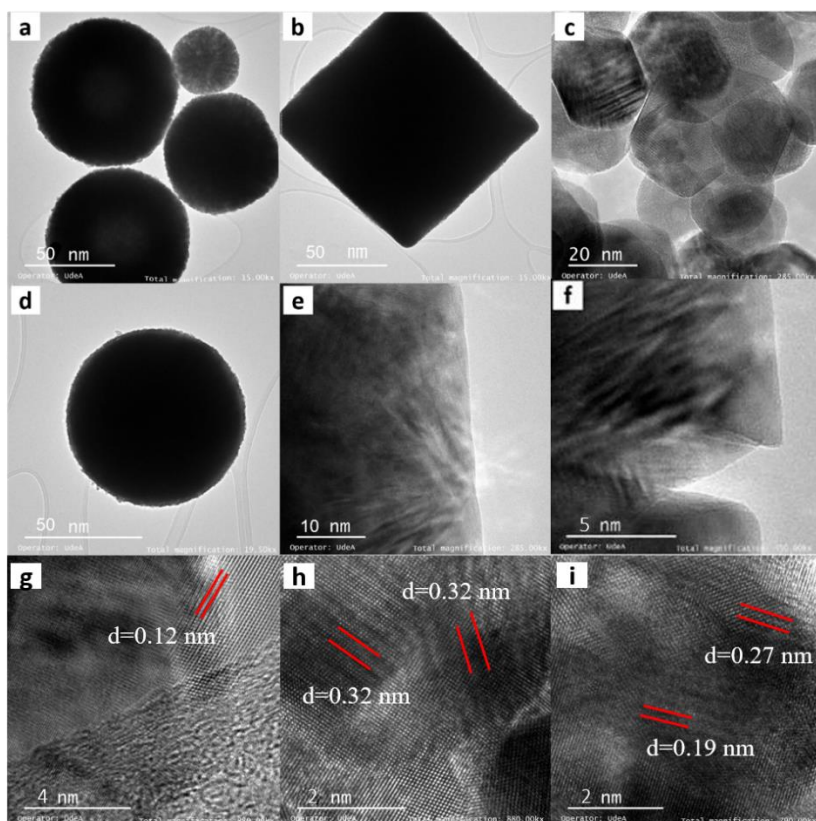
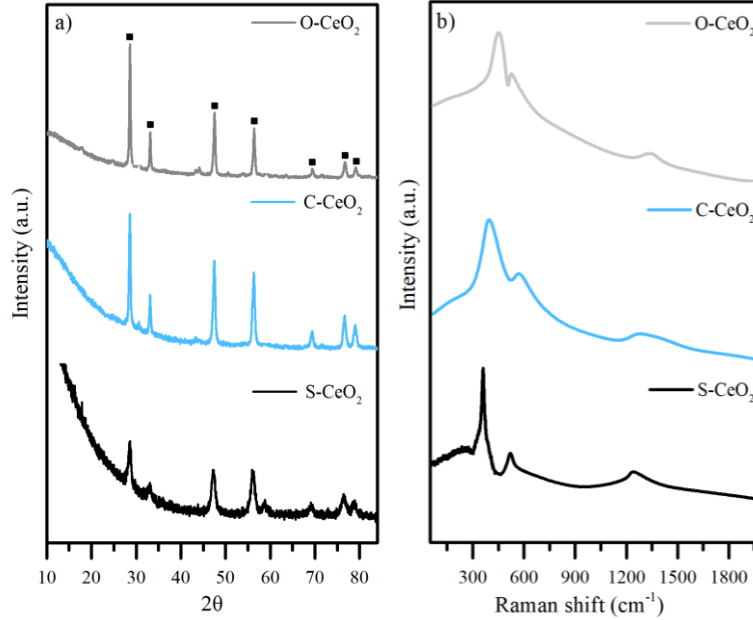


**Figure 2.** High-resolution transmission electron microscopy images of S-CeO<sub>2</sub> (a-b), C-CeO<sub>2</sub> (c-d) and O-CeO<sub>2</sub> (e-f).

XRD analysis was done for analyzing the phase structures of the samples. XRD patterns are shown in Figure 3. According to Joint Committee on Powder Diffraction Standards (JCPDS) 34-0394 and peaks of Figure 3, the materials present diffraction peaks characteristic of a face-centred cubic (fcc) fluorite structure (space group 225,  $Fm\bar{3}m$ ) of CeO<sub>2</sub> crystals, i.e.,  $2\theta = 28.7^\circ$  (111),  $33.2^\circ$  (200),  $47.4^\circ$  (220),  $56.4^\circ$  (311),  $59.2^\circ$  (222),  $69.3^\circ$  (400),  $76.5^\circ$  (331), and  $79.1^\circ$  (420). As seen, the intensities of the peaks at (111), (220), and (200) are more intensive for the samples C-CeO<sub>2</sub> and O-CeO<sub>2</sub> than S-CeO<sub>2</sub>, which agrees with HR-TEM analysis. Also, the intensities of each peak vary in each system; therefore, the full width at half maximum (fwhm) and lattice parameters change. The crystallite

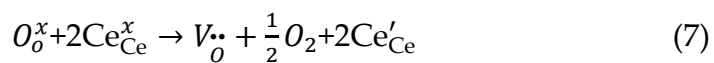


size and lattice parameter are shown in Table 2. It is observed that, with the change in CeO<sub>2</sub> shape, the lattice parameter is slightly affected, being higher for cubic nanoparticles. The crystallite (trough [111] direction) size increases in the order S-CeO<sub>2</sub> < C-CeO<sub>2</sub> < O-CeO<sub>2</sub>; therefore, crystallinity follows the opposite trend.



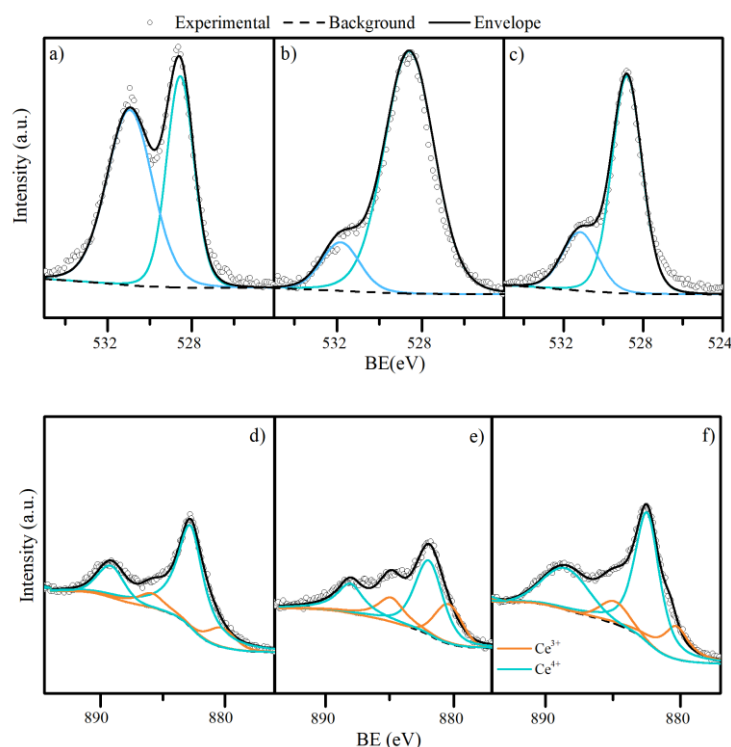
**Figure 3.** (a) XRD patterns where (■) refers to the CeO<sub>2</sub> crystals and (b) Raman spectra for S-CeO<sub>2</sub>, C-CeO<sub>2</sub>, and O-CeO<sub>2</sub>.

Figure 3b shows Raman spectra for the different CeO<sub>2</sub> materials. According to the results, all materials exhibit a strong peak at 458 cm<sup>-1</sup> ascribed to the F<sub>2g</sub> vibrational mode of fluorite-type structure because of symmetric breathing of O<sup>x-</sup> around Ce<sup>x+</sup>. Furthermore, there are three peaks at 255 cm<sup>-1</sup> (second-order transverse acoustic), 598 cm<sup>-1</sup> (defect induced (D)- Equation 7), and 1172 cm<sup>-1</sup> (longitudinal optical). The vibration of the D occurs close to 140 cm<sup>-1</sup> more than F<sub>2g</sub>, suggesting the presence of oxygen vacancies formed from intrinsic defects (Ce<sup>4+</sup> → Ce<sup>3+</sup>). The concentrations of oxygen vacancies were calculated in terms of the  $I_{(598+1172)}/I_{458}$  ratio, which increases in the order S-CeO<sub>2</sub> (0.10) < O-CeO<sub>2</sub> (0.19) < C-CeO<sub>2</sub> (0.23).



XPS patterns for O<sub>1s</sub> and Ce<sub>3d5/2</sub> are shown in Figure 4. From O<sub>1s</sub> profiles, two main peaks at 529.0 eV ± 0.5 eV and 531.5 eV ± 0.5 eV envelope the experimental

points. The peaks are assignable to lattice oxygen ( $O_{\text{latt}}$ ) and ascribed to the surface ( $O_{\text{ads}}$ ), respectively.<sup>51</sup> Commonly, the  $O_{\text{ads}}/O_{\text{latt}}$  ratio describes the concentration of oxygen vacancies, and the results are summarized in Table 3. It is noted that the ratio increases in the order  $S\text{-CeO}_2 < O\text{-CeO}_2 < C\text{-CeO}_2$ . Several authors reported that a high oxygen vacancies content promotes disordered oxygen in the ceria lattice, increasing the oxygen diffusion between the bulk and the surface.<sup>31, 32, 34, 51</sup>



**Figure 4.**  $O_{1s}$  and  $Ce_{3d_{5/2}}$  spectra of (a-d)  $S\text{-CeO}_2$ , (b-e)  $C\text{-CeO}_2$ , and (c-f)  $O\text{-CeO}_2$ , respectively.

**Table 3.** Atomic content and relationships calculated from the  $O_{1s}$  and  $Ce_{3d_{5/2}}$  spectra.

Sample	O (%)	Ce (%)	$Ce^{3+}$ (%)	$O_{\text{ads}}$ (%)	$O_{\text{latt}}$ (%)	$O_{\text{ads}}/O_{\text{latt}}$
$S\text{-CeO}_2$	57.44	42.56	18.39	41.86	58.14	0.71
$C\text{-CeO}_2$	51.19	48.81	32.60	88.03	11.97	7.35
$O\text{-CeO}_2$	55.70	44.30	26.91	75.94	24.06	3.15

Panels d-f of Figure 4 show the  $Ce_{3d_{5/2}}$  spectra of the synthesized materials. According to the literature, the  $Ce_{3d_{5/2}}$  region can be resolved into four signals. The peaks for  $Ce_{3d_{5/2}}$  that appear at  $881.2 \text{ eV} \pm 0.4 \text{ eV}$  and  $885.3 \text{ eV} \pm 0.4 \text{ eV}$  are ascribed to the  $Ce^{3+}$ . The peaks at  $882.7 \text{ eV} \pm 0.4 \text{ eV}$  and  $889.7 \text{ eV} \pm 0.4 \text{ eV}$  are used

to obtain the Ce<sup>4+</sup> content. The proportion of each component is enlisted in Table 3. The content of Ce<sup>3+</sup> increases in the sequence S-CeO<sub>2</sub> < O-CeO<sub>2</sub> < C-CeO<sub>2</sub>, which is in line with the O<sub>ads</sub>/O<sub>latt</sub> ratio. The presence of Ce<sup>3+</sup> is a consequence of the oxygen vacancies formation, and it promotes the activation of the oxygen on the bulk and the surface of the nanocatalysts.

### 3.2. Characterization of doped nanocatalysts.

The doped materials with Ni and Pd were characterized through ICP-MS for verifying the total metal content. In all cases, the metal percentage was between 0.99 % - 1.02 % in A mass fraction of Ni and Pd, corroborating the theoretically calculated. Table 4 shows BET surface area and Ni and Pd size and dispersion over CeO<sub>2</sub> nanocatalysts with different morphologies. S-CeNiPd presents the smallest BET surface area and, therefore, the largest nickel and palladium particle size. S<sub>BET</sub> increases in the same order as the supports, which declares that Ni and Pd impregnation do not affect structural characteristics. Also, a decrease in the surface area was detected, indicating the support's porosity. The mean crystal size for the active phases increases oppositely, leading to the C-NiPdCe sample with the lowest crystal sizes (Ni, 4.3 nm; Pd, 3.2 nm). Given this fact, it has been reported that the structural characteristics of ceria can determine the particle size of transition element oxides and the agglomeration tendency upon the surface. Interestingly, the dispersion follows the decreasing order S-NiPdCe < O-NiPdCe < C-NiPdCe, verifying the present findings.

**Table 4.** BET surface area estimated lattice parameter, crystallinity, and compositional properties of synthesized S-NiPdCe, C-NiPdCe, and O-NiPdCe.

Sample	S <sub>BET</sub> (m <sup>2</sup> ·g <sup>-1</sup> )	Ni size (nm)	Pd size (nm)	Ni dispersion (%)	Pd dispersion (%)	Ce Crystallite size <sup>a</sup> (nm)	Lattice Parameter <sup>b</sup> (nm) x 10 <sup>-2</sup>
S-NiPdCe	18.9	3.9	5.3	35.6	28.4	11.6	53.08
C-NiPdCe	25.5	4.3	3.2	31.0	40.1	12.4	54.01
O-NiPdCe	28.1	4.1	3.8	29.3	37.2	13.5	53.55

<sup>a</sup>Crystallite size was calculated based on the Scherrer equation; <sup>b</sup>Lattice parameters were calculated based on the Bragg equation  $2d \sin(\theta) = n\lambda$ .

The cerium crystallite size and lattice parameter are estimated from XRD patterns. The results are summarized in Table 4, while the XRD in Figure 5. Initially, the characteristic peaks of NiO (JCPDS 01-075-0269, gray circles), PdO (JPCDS 06-0515 black squares), and Pd (JCPDS 05-0681, orange circles) are observed. The figure noted a slight shift in the angle position of the (111) diffraction line of the support. This shift may be due to the replacement of Ce by Ni and Pd ions or the network contraction by the doped ions. Based on the Scherrer equation, the crystallite size of S-NiPdCe, C-NiPdCe, and O-NiPdCe was reduced because of the decrease in the lattice parameters regarding the non-doped systems. The reduction of the lattice parameter can be attributed to a portion of Ni, and Pd ions may substitute  $Ce^{4+}$  in the  $CeO_2$  lattice, altering the support unit cell parameters because a relatively smaller radius is found for  $Ni^{2+}$  (0.63 Å) and  $Pd^{2+}$  (0.86 Å) than  $Ce^{4+}$  (0.97 Å).

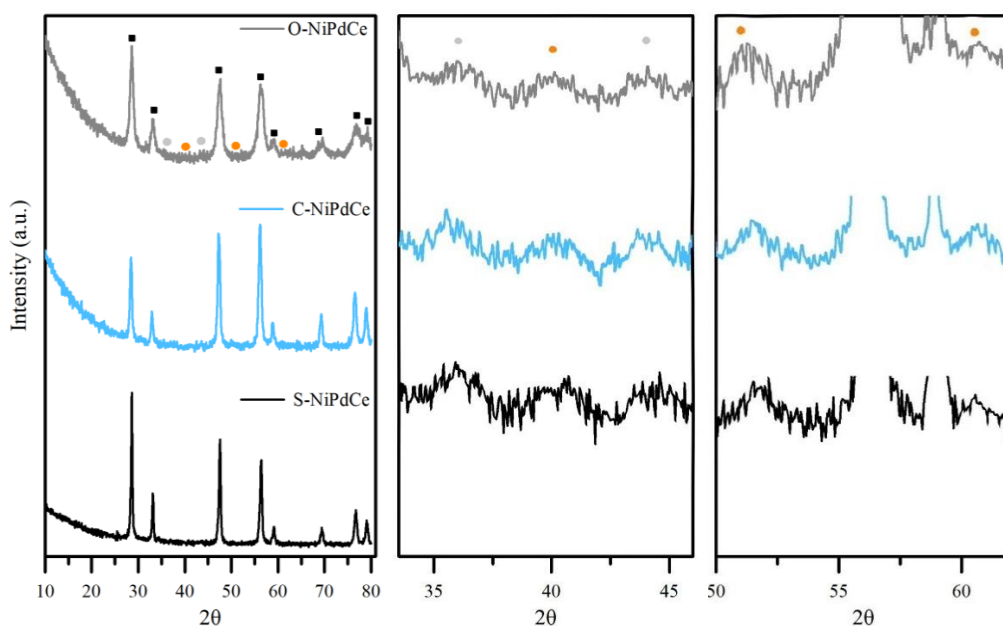


**Figure 5.** XRD patterns where (■) refers to the  $CeO_2$  crystals (●) refers to NiO crystals, and (●) (b) Raman spectra for S-NiPd, C-NiPd, and O-NiPd.

The Raman spectra (see Figure 6) of the doped samples show the  $F_{2g}$  at  $462\text{ cm}^{-1}$ . The doping of nickel and palladium ions into the fluorite structure of  $CeO_2$  changes the position and intensity of the  $F_{2g}$ . The intensity was decreased after the functionalization. The reduction of the crystallite size increases the oxygen vacancies formation in the  $CeO_2$  lattice after Ni and Pd entered the lattice.

The profiles also observed two addition features near 598 and 620  $\text{cm}^{-1}$  attributed to the defect sites, including  $\text{O}^{2-}$  and induced by ceria, nickel, and palladium cations. Finally, the concentrations of oxygen vacancies were calculated using the  $I_{(598+1172)}/I_{458}$  ratio. The ratio follows the increasing order  $\text{SNiPd}$  (0.18) <  $\text{ONiPd}$  (0.23) <  $\text{CNiPd}$  (0.25). As it is noted, in all cases, the  $I_{(598+1172)}/I_{458}$  ratio increased regarding the supports, confirming the above statements.

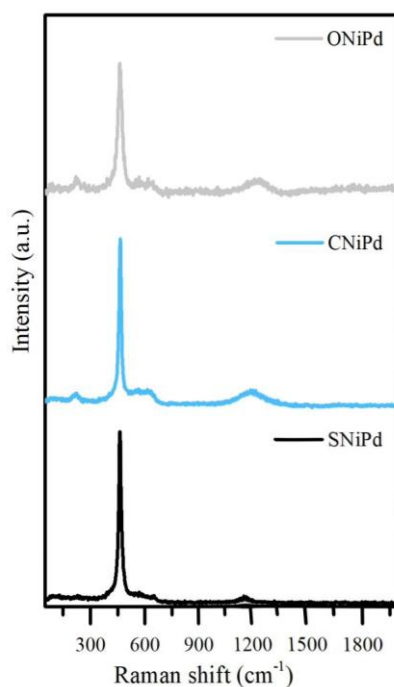


**Figure 6.** Raman spectra for  $\text{SNiPdCe}$ ,  $\text{CNiPdCe}$ , and  $\text{ONiPdCe}$ .

Panels a and b of Figure 7 exhibit  $\text{Pd}_{3d}$  and  $\text{Ni}_{2p}$  XPS spectra, respectively, for doped nanocatalysts. Four main peaks describe the  $\text{Pd}_{3d}$  spectra. The peaks on the right are ascribed to  $\text{Pd}_{3d_{5/2}}$ , while the other two are associated with  $\text{Pd}_{3d_{3/2}}$ . The binding energy at  $337.2 \text{ eV} \pm 0.3 \text{ eV}$  ( $\text{Pd } 3d_{5/2}$ ) and  $342.5 \text{ eV} \pm 0.3 \text{ eV}$  ( $\text{Pd } 3d_{3/2}$ ) refers to  $\text{Pd}^{2+}$  in bulk  $\text{PdO}$ , which can act as a reservoir for oxygen anchorage or more unstable oxide species such as  $\text{PdO}_2$ . The content of oxidized palladium regarding the total Pd is summarized in Table 5.

**Table 5.** Atomic content and relationships calculated from the O<sub>1s</sub>, Ni<sub>2p</sub>, Pd<sub>3d</sub>, and Ce<sub>3d5/2</sub> XP spectra and ICP-MS.

Sample	Ce (%) <sup>a</sup>	O (%) <sup>a</sup>	Ce <sup>3+</sup> (%)	O <sub>ads</sub> (%)	O <sub>latt</sub> (%)	O <sub>ads</sub> /O <sub>latt</sub>	Ni <sup>2+</sup> (NiO) (%)	Ni <sup>2+</sup> (Ni-Ce) (%)	Pd <sup>2+</sup> (%)
S-NiPdCe	43.7	54.3	33.5	40.9	59.1	0.7	26.1	24.5	53.4
C-NiPdCe	44.9	53.1	52.4	84.8	15.2	5.6	33.5	23.6	62.3
O-NiPdCe	44.5	53.5	39.5	73.7	26.3	2.8	30.9	24.3	55.9

<sup>a</sup>Atomic percentual fraction determined through ICP-MS.

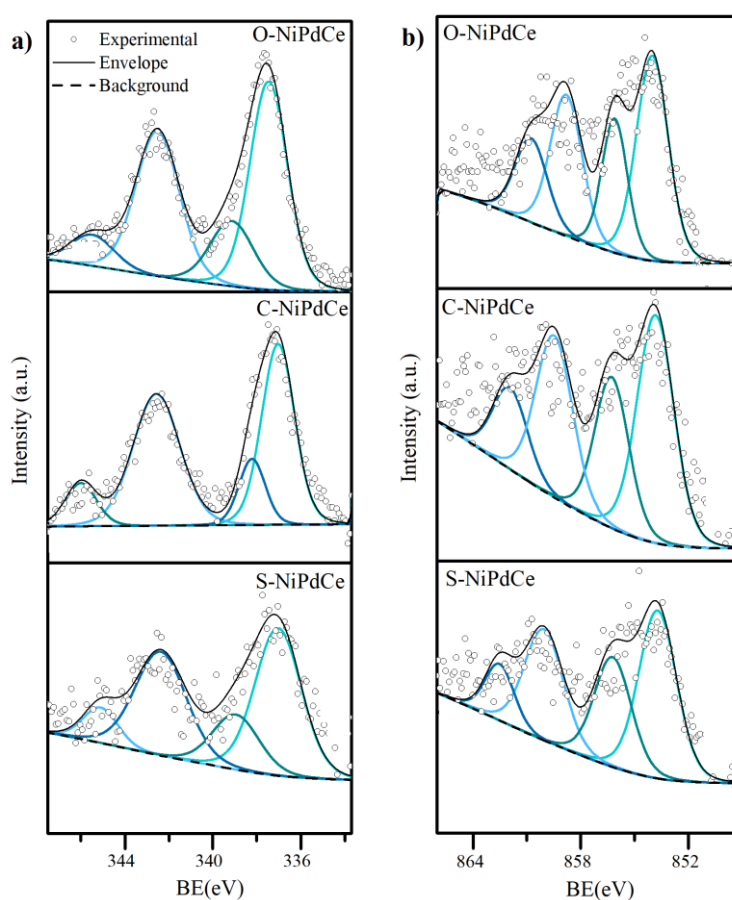


**Figure 7.** a) Pd<sub>3d</sub> spectra and b) Ni<sub>2p</sub> spectra of S-NiPdCe, C- NiPdCe, and O-NiPdCe, respectively.

From the high-resolution spectra for nickel spectra is observed four peaks. The Ni<sub>2p3/2</sub> spectral region shows the main band in the range between 851 eV and 859 eV. The satellite structures are observed at higher binding energies (860 eV-866 eV). The prominent peaks centered at 853.1 eV ± 0.3 eV, and 855.6 eV ± 0.4 eV are associated with Ni<sup>2+</sup> species in the NiO and NiO-Ce, respectively.<sup>25, 51</sup>

Considering the proportion of each active peak, different Ni-Ce interactions may occur. The S-NiPdCe presents the highest amount of NiO and, thus, the least proportion of NiO-Ce. In the case of C-NiPdCe, the greatest connection between ceria and Ni phases is obtained. This result agrees with the higher dispersion of Ni in the catalysts. The content of Ni-species is found in Table 5.

From the high-resolution spectra  $O_{1s}$  and  $Ce_{3d5/2}$ , similar information obtained for the supports was found, and the information is depicted in Table 5. Interestingly, the atomic  $Ce^{3+}$  content was enhanced after Ni and Pd functionalization in all samples. The increased  $Ce^{3+}$  proportion, ranked as S-NiPdCe < O-NiPdCe < C-NiPdCe, might infer the surface modification of oxygen vacancies after metal loading. The  $O_{1s}$  results corroborate the hypothesis. The content of lattice oxygen and ascribed to the surface was modified. In all samples, the lattice oxygen increased in the same increasing order for  $Ce^{3+}$ .

### 3.3. Adsorption isotherms

Figure 8a shows the experimental adsorption profiles and SLE fittings for *n*-C<sub>7</sub> asphaltenes over the different nanoparticles. Based on the International Union of Pure and Applied Chemistry standard, the adsorption occurs following a type Ib isotherm for all systems. The type Ib isotherms present a very steep slope at low concentrations, typical of high-affinity systems. This behavior is similar to the obtained for the amorphous CeO<sub>2</sub> and doped CeO<sub>2</sub> with Ni and Pd.<sup>26</sup> It is worth mentioning that both works have been carried out with the same type of asphaltenes so that the results are comparable.

For a fixed *n*-C<sub>7</sub> asphaltene concentration, the adsorbed amount increases in the trend: O-CeO<sub>2</sub> < S-CeO<sub>2</sub> < C-CeO<sub>2</sub> < O-NiPdCe < S-NiPdCe < C-NiPdCe. It has been reported that the systems with Pd<sup>2+</sup> improve the capability and interaction forces with the asphaltenes.<sup>29</sup> It could explain the higher adsorption amount of spherical-like systems than the orthorhombic. Also, the content of Ni<sup>2+</sup> was the highest for cubic-like systems, resulting in a higher yield for asphaltene adsorption.<sup>25</sup>

Between the supports and the doped nanoparticles, the adsorption was consistently higher for the latter. Thus, the presence of Ni and Pd could increase the interactions between doped nanoparticles and asphaltenes. Panel b shows the proposed mechanisms for *n*-C<sub>7</sub> asphaltene adsorption on synthesized nanoparticles considering slow variations in the asphaltene molecule model proposed to identify the main differences between the interactions doped nanocatalysts-asphaltenes and non-doped nanocatalysts-asphaltenes.

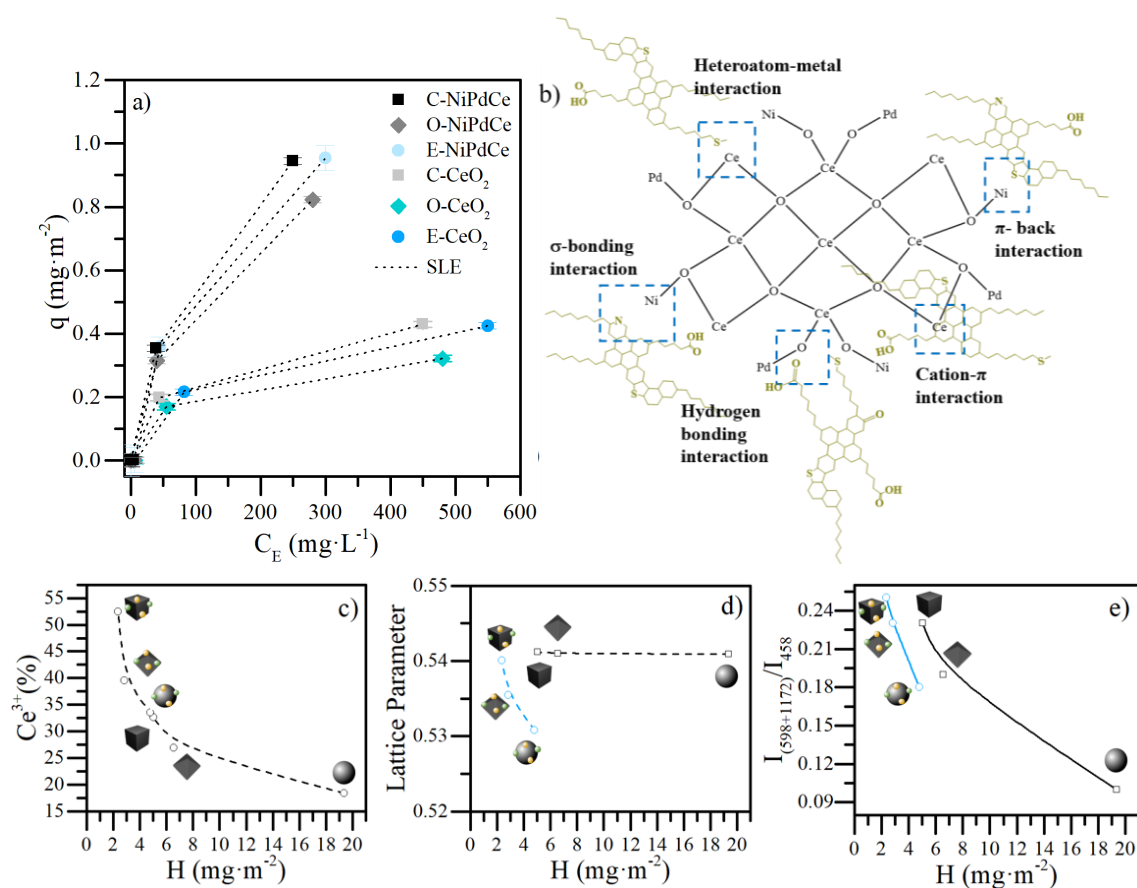


**Figure 8.** (a) experimental adsorption of *n*-C<sub>7</sub> asphaltene over CeO<sub>2</sub> nanoparticles with different morphologies (cubic, orthorhombic, and spherical), and doped with Ni and Pd in a mass fraction of 1 % (dotted lines represent the SLE fitting); and effect of a) Ce<sup>3+</sup>, b) lattice parameter, and c)  $I_{(598+1172)}/I_{(458)}$  on  $H$  values.

The main mechanisms for asphaltene uptake in non-doped systems (i.e., S-CeO<sub>2</sub>, C-CeO<sub>2</sub>, and O-CeO<sub>2</sub>) are hydrogen bonding and cation- $\pi$  interactions. Hydrogen atoms existing in intimate contact with heteroatoms (O, N, and S) in asphaltene structure present a high tendency to interact with oxygen atoms of CeO<sub>2</sub> nanoparticles. Furthermore, the non-covalent cation- $\pi$  interaction occurs between the face of an electron-rich pi system (i.e., benzene ring of asphaltene aromatic structure) with an adjacent cation (Ce<sup>3+</sup>). The presence of Ni and Pd phases intensifies the interactions with asphaltenes, promoting diverse adsorption mechanisms, including heteroatoms (like O, N, S) -metal interactions,  $\sigma$ -bonding and  $\pi$ -back interactions. First, the Ni and Pd atoms can act as Lewis acids; meanwhile, asphaltene heteroatoms act as Lewis's base sites, generating numerous interactions with the Ni and Pd species. Functional groups in the asphaltene structure, like pyridine and thiophenes, function as primary sites for



intermolecular interactions by  $\sigma$  and  $\pi$  bonding with active metal sites. Asphaltene adsorption mechanisms are illustrated in Figure 8b.

Finally, the estimated parameters of the SLE model for adsorption isotherms are summarized in Table S1 of supplementary material. The results agree with the experimental values and the discussion presented. Henry's law constant describes the inverse of the affinity between the adsorbate and adsorbent. As higher the values, the lower the affinity.  $H$  increases in the order C-NiPdCe < O-NiPdCe < S-NiPdCe < C-CeO<sub>2</sub> < O-CeO<sub>2</sub> < S-CeO<sub>2</sub>, that is, the C-NiPd system is the one with the highest affinity towards asphaltenes. Unlike the amount adsorbed, the affinity was greater for orthorhombic than spherical nanocatalysts. According to the amount of Ce<sub>EDX</sub> and Ce<sup>3+</sup> ions by XPS, both parameters follow the same trend: the higher the amount of bulk Ce and Ce<sup>3+</sup>, the higher the affinity for asphaltenes due to the reduction of the Polanyi's adsorption potential.<sup>25</sup> Also, the lattice parameter and oxygen vacancies ( $I_{(598+1172)}/I_{458}$ ) follow the similar trend between doped and supports materials. As the index of oxygen vacancies and the lattice parameter of the nanocatalysts increase, the values of  $H$  decreases, obtaining higher affinities. This result suggests the presence of vacancy -  $n$ -C<sub>7</sub> asphaltene interactions, which in turn promote higher asphaltene adsorption capability. All these results are summarized in panels c-e of Figure 8.

Similarly, the  $K$  parameter decreases oppositely, indicating that the degree of association of asphaltenes on the surface of the nanoparticles is higher for the non-doped systems. Even though there is a direct trend in both properties, comparing with the values reported for amorphous CeO<sub>2</sub> ( $H = 0.101 \text{ mg}\cdot\text{g}^{-1}$ ,  $K = 0.21 \text{ g}\cdot\text{g}^{-1}$ ), both variables are improved in all systems evaluated in this study. This suggests that the nanoparticles' shape influences the asphaltene adsorption mechanism since there is a change in their crystallographic exposed planes and chemical properties. Finally, all these facts are summarized in the values of  $q_m$ , which increases in the same inverse way regarding the  $H$  trend.

### 3.4. Catalytic experiments

#### 3.4.1. Differential scanning calorimetry

Before analyzing the catalyst potential of ceria-based nanocatalysts, becomes important the description of the  $n$ -C<sub>7</sub> asphaltene oxidation behavior. Figure 9 shows the DSC curves of the  $n$ -C<sub>7</sub> asphaltenes at atmospheric pressure. Two distinct exothermic peaks are noted from DSC profiles and named as first (FC) and second combustion (SC). It is commonly accepted that the main reaction

pathways in FC stage are oxygen-adding reactions to produce hydroperoxides and the subsequent isomerization/decomposition into ketones, alcohols, carboxylic acids, and in a lower degree CO<sub>2</sub>, CO, and H<sub>2</sub>O. This interval seems to end before the 400 °C for the virgin *n*-C<sub>7</sub> asphaltenes. Then, during the transition from FC to SC, the coke is formed, and in SC, its combustion occurs until 570 °C. Figure 9 also portrays the heat flow profiles under an oxidizing atmosphere of *n*-C<sub>7</sub> asphaltene adsorbed on the different nanoparticles synthesized (supports-panel a, doped-panel b). According to both panels, all the reaction intervals were shifted into lower temperature ranges with the addition of a ceria-based nanocatalyst. In non-doped nanoparticles, the catalysts' shape influences the oxygen consumption and asphaltenes' heat flow profile. The temperature ranges for FC and SC were shifted to lower temperatures in the order: S-CeO<sub>2</sub> < O-CeO<sub>2</sub> < C-CeO<sub>2</sub>. The first combustion ends at 300, 330, and 350 °C; meanwhile, SC ends at 450, 455, and 465 °C for C-CeO<sub>2</sub> < O-CeO<sub>2</sub> < S-CeO<sub>2</sub>, respectively. The shifting of reaction intervals into lower temperature ranges means that the CeO<sub>2</sub> nanoparticles promote oxidation reactions and make them easier and faster.

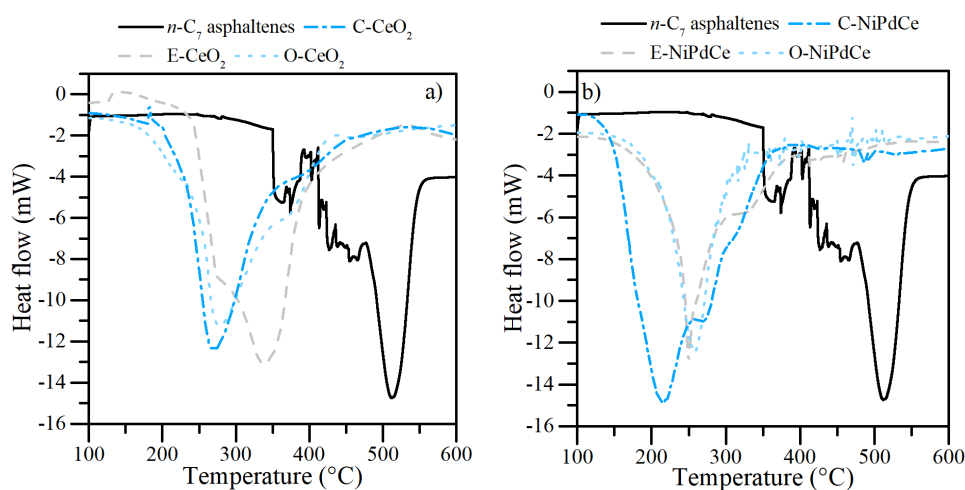


**Figure 9.** Heat flow profiles of *n*-C<sub>7</sub> asphaltenes in the absence and presence of a) CeO<sub>2</sub> nanoparticles with different morphologies (cubic, orthorhombic, and spherical), and b) doped with Ni and Pd in a mass fraction of 1 %. Heating rate: 10 °C·min<sup>-1</sup>, air flow: 100 ml·min<sup>-1</sup>, and sample mass 5 mg.

Simultaneously, it was observed that both intervals end in a narrower temperature range, releasing higher heat per unit mass in the presence of doped nanoparticles than non-doped systems. Interestingly, 220, 190, and 180 °C reductions of the end SC temperature were obtained for the C-NiPdCe, O-

NiPdCe, and S-NiPdCe, respectively. These results indicate that the active phases of nickel and palladium significantly improved ceria nanoparticles' combustion efficiency. Also, according to its morphology, there could be variations in the SMSI.

Based on this analysis, it can be inferred that ceria-based nanocatalysts had a remarkable catalytic effect on improving the *n*-C<sub>7</sub> asphaltene consumption, especially in the SC region. The possible catalytic mechanism will be discussed in the following sections.

#### 3.4.2. Non-isothermal thermogravimetric analysis

Figures 10, 11 and 12 presented the *n*-C<sub>7</sub> asphaltene oxidation, the catalytic performance of the prepared CeO<sub>2</sub> nanocatalysts with different morphologies as non-doped and doped, respectively, for *n*-C<sub>7</sub> asphaltene oxidation in the temperature range of 100-800 °C. Figure 10 shows that *n*-C<sub>7</sub> asphaltenes without nanocatalysts decompose entirely up to 500 °C at 0.084 MPa. When the pressure rises, different changes are evident in the mass change and mass change rate profiles. First, an increase in mass at low temperatures ( $T < 250$  °C), which is attributed to the oxygen chemisorption in the asphaltene molecular structure. Then there is a decline in the sample's mass, mainly associated with desorption and changes in the oxygenated systems formed. Finally, the asphaltenes finish their decomposition at lower temperatures (460 °C at 3.0 MPa and 450 °C at 6.0 MPa). Based on the analysis, the rate for mass change was fitted by two and four conventional Voigt functions, at low (0.084 MPa) and high pressure (3.0 and 6.0 MPa), respectively. The regions were named: oxygen chemisorption (OC), decomposition of chemisorbed oxygen (DCO), first combustion (FC), and second combustion (SC). At atmospheric pressure, only the FC and SC stages occur. These results indicate that *n*-C<sub>7</sub> asphaltene oxidation depends on the pressure system. Details about the effect of pressure on non-catalyzed asphaltenes are reported in our previous studies.<sup>52, 53</sup>

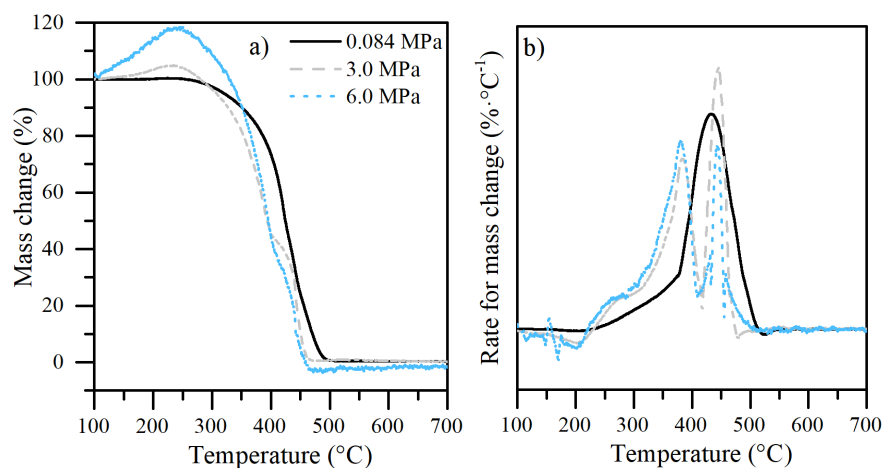


**Figure 10.** (a) Mass change and (b) rate for mass change profiles for *n*-C<sub>7</sub> asphaltene oxidation at 0.084 MPa, 3.0 MPa, and 6.0 MPa. Heating rate: 10 °C·min<sup>-1</sup>, air flow: 100 ml·min<sup>-1</sup>, and sample mass 1 mg.

The results for *n*-C<sub>7</sub> asphaltene oxidation catalyzed by CeO<sub>2</sub> nanoparticles with different shapes at different pressures are shown in Figure 11. Overall, the low- and high-pressure results are like those reported for non-catalyzed asphaltene. The low-pressure profiles are described by FC and SC, whereas the high-pressure are described by OC, DCO, FC, and SC. The presence of catalysts does not alter the reaction stages, regardless of the pressure and catalyst shape used. Also, the catalytic effect of the materials is noted in the reduction of the decomposition temperature of asphaltene. The shape of the catalyst appears to have an essential contribution to the oxidation of asphaltene. Minor but representative changes are observed when the different materials catalyze the reaction. In the first instance, changes in the OC region are identified. The mass that asphaltene gains vary as the shape of the catalyst changes. At 3.0 MPa, asphaltene gains 3.6, 5.8, and 3.2% for O-CeO<sub>2</sub>, C-CeO<sub>2</sub>, and S-CeO<sub>2</sub>, respectively, while at 6.0 MPa there is an increase of 7.3%, 10.4% and 5.9%, for the same systems, respectively. The Raman, TEM and XPS analyses demonstrate that C-CeO<sub>2</sub> nanocatalyst endowed with {111} crystal planes present the largest amount of oxygen vacancies, which promote an effective oxygen diffusion from the gas phase or catalyst bulk phase to the surface of the asphaltene. Therefore, it is the catalyst with more active oxygen for improving the ceria reactivity.

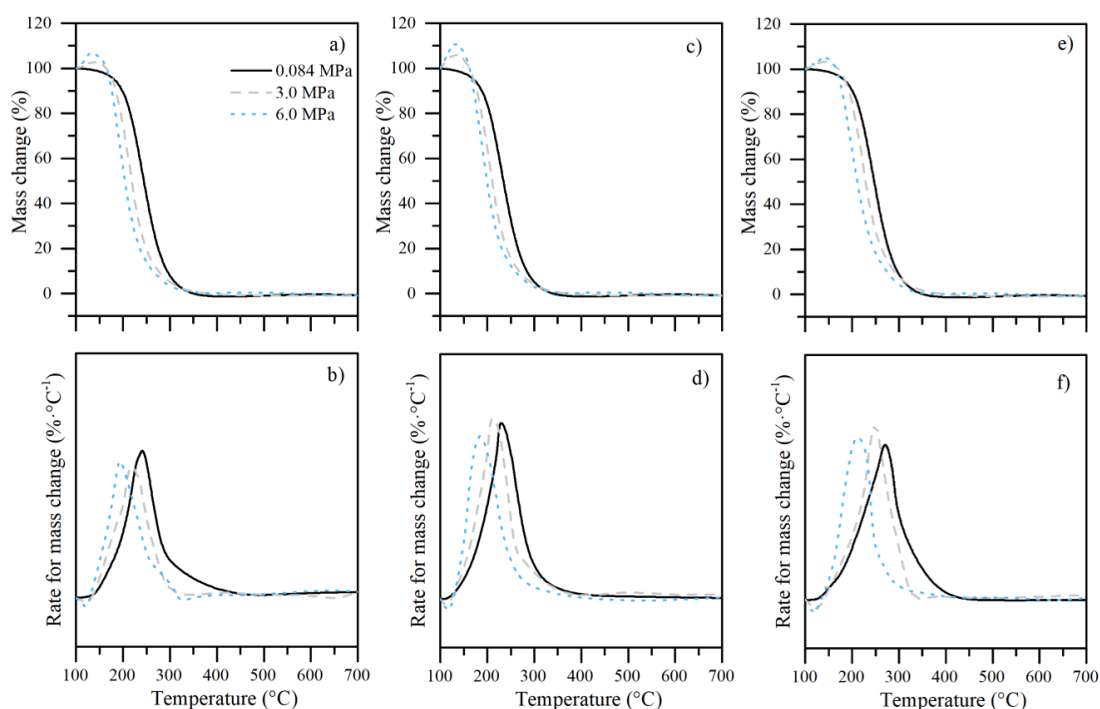


**Figure 11.** Mass change and rate for mass change profiles of *n*-C<sub>7</sub> asphaltenes in oxidation adsorbed on a-b) O-CeO<sub>2</sub>, c-d) C-CeO<sub>2</sub>, e-f) S-CeO<sub>2</sub>. Heating rate: 10 °C·min<sup>-1</sup>, air flow: 100 ml·min<sup>-1</sup>, and sample mass 1 mg.

As displayed in panels a, c, and e, the asphaltene decomposition over the three X-CeO<sub>2</sub> gradually increases and eventually reaches 100 %. The C-CeO<sub>2</sub> nanocatalyst is the most active decomposing of the sample up to 320 °C at 0.084 MPa, 300 °C at 3.0 MPa, and 290 °C at 6.0 MPa. Over O-CeO<sub>2</sub> the asphaltene decomposition ends at similar temperatures (around 10 °C later), whereas S-CeO<sub>2</sub> decomposition reaches 100 % between 320 °C and 350 °C for all pressures. The main decomposition temperature peak (panels b, d, and f) is observed during the DCO region for C-CeO<sub>2</sub> and O-CeO<sub>2</sub> at all pressures evaluated. The S-CeO<sub>2</sub> system exhibits the peak during FC at 0.084 MPa, and in DCO at 3.0 and 6.0 MPa. This result represents an important advantage for using cubic and orthorhombic ceria shapes for asphaltene decomposition. This ensures a lower tendency for coking during SC and, therefore, the longer useful life of the catalysts (no deactivation).

In this context, it is concluded that the catalytic activity follows the increasing order S-CeO<sub>2</sub> < O-CeO<sub>2</sub> < C-CeO<sub>2</sub>. This result highlights the influence of exposed ceria crystal planes on asphaltene oxidation and conversion. The Raman and TEM results show that the presence of {100} facets enhance the catalyst's reactivity. Also, each system presents a distinct concentration of oxygen vacancies, which are active sites for molecular oxygen adsorption. In the

same context, the surface chemistry of the sample influences its reactivity. Oxygen can be found ascribed by a physical process, chemically activated and lattice oxygen. The chemically adsorbed oxygen was higher for the system with an abundant amount of vacancies. Overall, the total amounts of  $O_{\text{ads}}$  species and  $O_{\text{ads}}/O_{\text{latt}}$  across the three nanocatalysts show an increasing order of S-CeO<sub>2</sub> < O-CeO<sub>2</sub> < C-CeO<sub>2</sub>. It is consistent with the variation trend of asphaltene catalyzed oxidation.

It is well recognized the redox property of CeO<sub>2</sub> also influences catalytic activity. The relationship between the redox cycle and the catalytic activity was observed by correlating XPS and TGA results. It is found that the relative abundance of Ce<sup>3+</sup> (%) increases in the order S-CeO<sub>2</sub> < O-CeO<sub>2</sub> < C-CeO<sub>2</sub>, which suggests the participation of Ce<sup>3+</sup> in asphaltene oxidation. Also, the consumption of lattice oxygen during asphaltene decomposition was observed due to the increased  $O_{\text{ads}}/O_{\text{latt}}$  ratio in the same order. Based on the above results, the catalytic activity of ceria catalysts in *n*-C<sub>7</sub> asphaltene oxidation strongly depends on the ceria nanocrystals' shape.

Figure 12 exhibits the results for doped nanoparticles. It is noted that similar profiles are obtained. The catalytic activity follows the same shape trend (spherical < orthorhombic < cubic). It is found that the mass gained in OC increases with the doping of Ni and Pd and that the decomposition of asphaltenes ends at temperatures close to 200 °C in all cases, obtaining the best results for the cube-shaped catalyst (C-NiPdCe). Other variables can affect their catalytic performance for doped nanocatalysts, including the interaction strength between the active phases and the support, the dispersion of the active phases and the change in the number of vacancies of the support after doping. As shown in section 4.2, Ni<sup>2+</sup> and Pd<sup>2+</sup> ions substituted in a higher degree Ce<sup>4+</sup> in the ceria lattice to increase the defect concentration. Hence, all catalysts improved their oxygen vacancy density and oxygen mobility. Between the systems, the oxidation of asphaltenes was enhanced by the C-NiPdCe, which agrees with its higher capacity to improve the active oxygen generation due to the improved Ni-Ce contact regarding the other samples (see XPS results).

Similarly, it is deduced that the strong interaction of NiO and PdO species with the cubic-shaped catalyst promotes the existence of Ni and Pd stable species. In summary, the strength of the interactions between active phases and CeO<sub>2</sub> and its surface chemistry are important factors for determining the activity of the nanocatalyst.

Regarding pressure, the trend is clear. For all the systems evaluated, the increase in pressure increases the number of oxygenated structures formed in the asphaltene and reduces the termination temperature of the asphaltene decomposition.

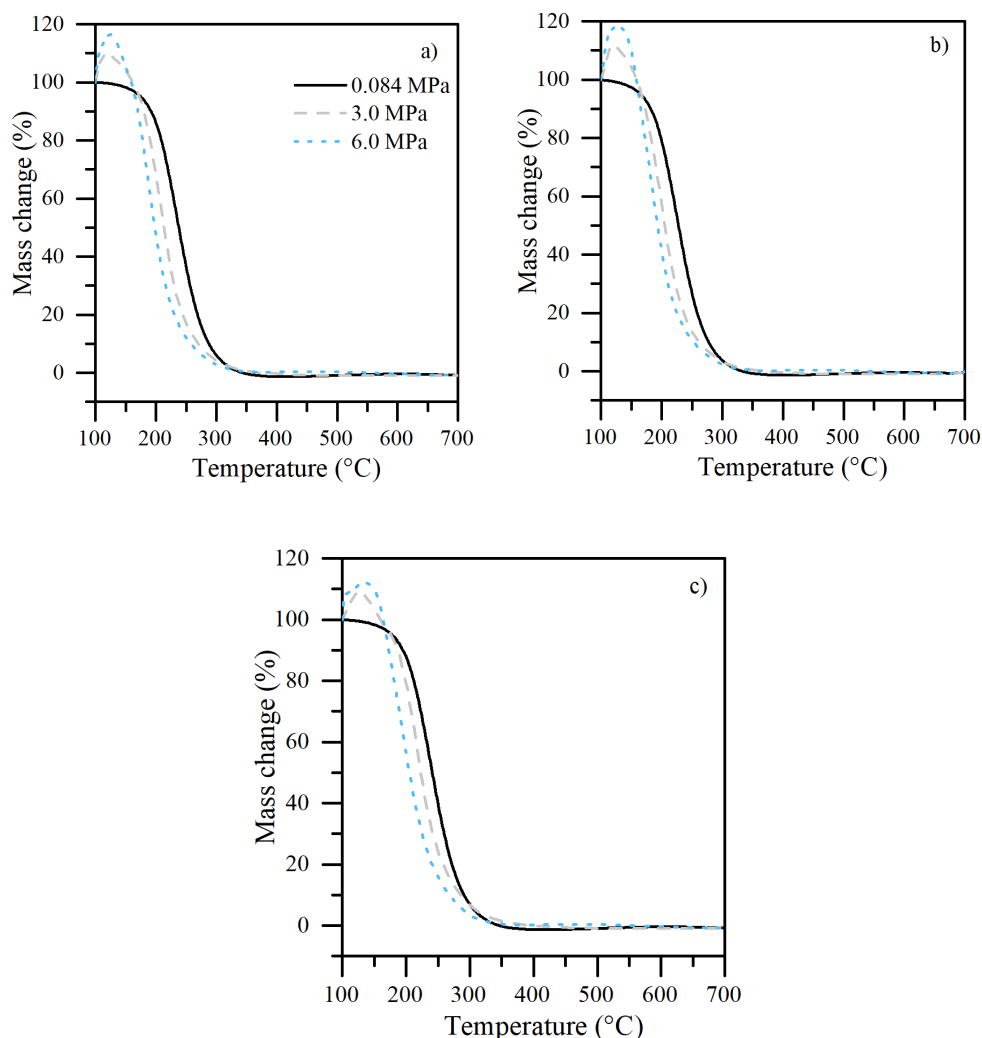


**Figure 12.** Mass change profiles of *n*-C<sub>7</sub> asphaltenes in oxidation adsorbed on a) O-NiPdCe, b) C-NiPdCe, c) S-NiPdCe. Heating rate: 10 °C·min<sup>-1</sup>, air flow: 100 ml·min<sup>-1</sup>, and sample mass 1 mg.

### 3.4.3. Isothermal thermogravimetric analysis

Figure 13 shows the extent of reaction ( $\alpha$ ) of *n*-C<sub>7</sub> asphaltenes as a function of time at isothermal heating of 300, 340, and 380 °C at different pressures. With increasing temperature,  $\alpha$  increases as a response to the increment in reaction rate. This result is similar to those obtained by several authors at low pressure conditions.<sup>25, 26</sup> Pressure also increases the reaction rate. Therefore, at 6.0 MPa, the asphaltenes convert the same mass in less time than at 3.0 MPa, less than at 0.084

MPa. From 0.084 to 6.0 MPa, the conversion increased about 50% at all evaluated temperatures. However, even though the increase in temperature and pressure increased the conversion rate, a total conversion of 40% of the sample is obtained in 350 min of heating in the best of cases. This result suggests that during the ISC processes, most of the asphaltene ends up converted into coke and therefore, its efficiency is reduced.

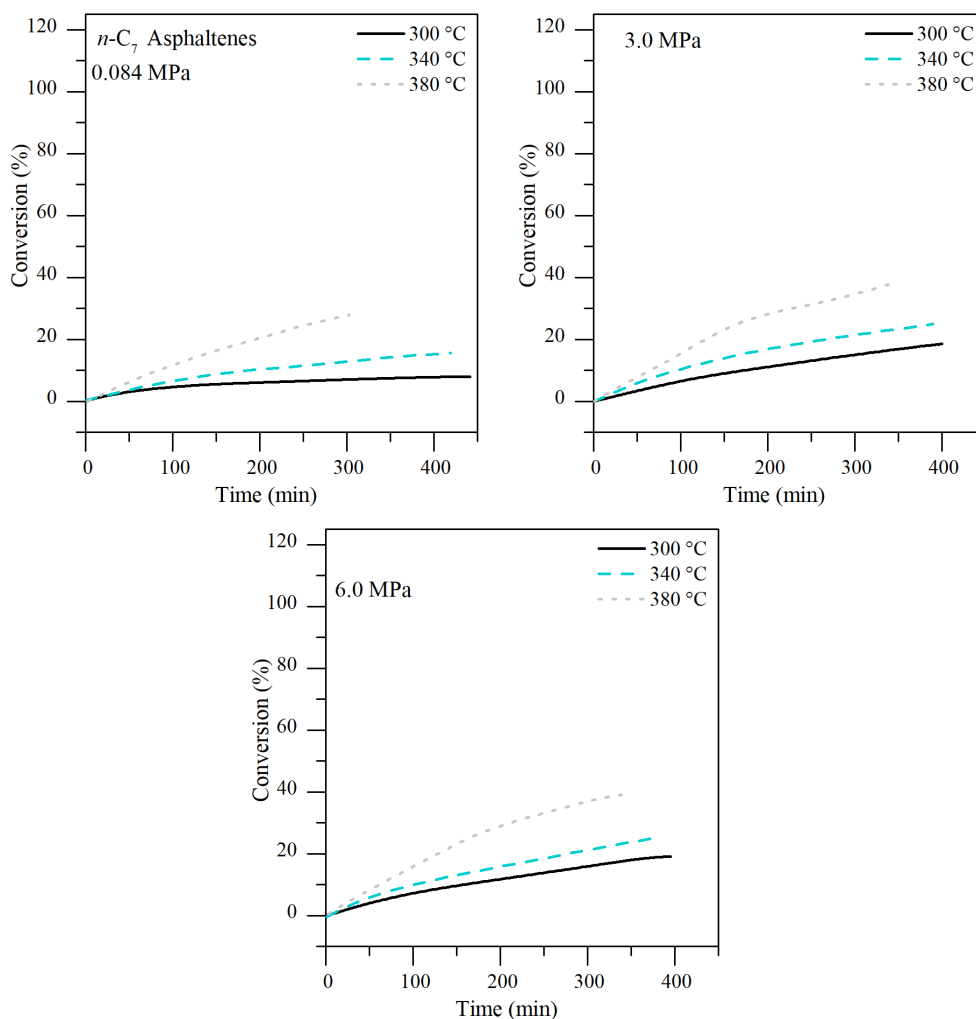


**Figure 13.** Isothermal conversion of *n*-C<sub>7</sub> asphaltenes oxidation at 0.084 MPa, 3.0 MPa, and 6.0 MPa. Air flow: 100 ml·min<sup>-1</sup>, and sample mass 1 mg.

Based on the results of the rate for mass change in the previous section, the conversion of *n*-C<sub>7</sub> asphaltenes was evaluated in the presence of the supports with different morphology (Figure 14) and doped with Ni and Pd (Figure 15) at 170 °C, 200 °C, and 230 °C. The results obtained show the high potential of the synthesized catalysts to improve the efficiency of the ISC processes to the extent that a complete conversion of asphaltene is achieved under the experimental conditions used. Like results without catalysts, *n*-C<sub>7</sub> asphaltene conversion



gradually increases and eventually reaches 100%, and the time is reduced as temperature and pressure increase. Considering the nanocatalysts, the time required to complete the conversion increased in the order S-CeO<sub>2</sub> < O-CeO<sub>2</sub> < C-CeO<sub>2</sub> < S-NiPdCe < O-NiPdCe < C-NiPdCe. The cubic nanoparticles are the most active, followed by orthorhombic and spherical. Over C-CeO<sub>2</sub> and C-NiPdCe, asphaltene conversion reaches 100% at 170 °C and 6.0 MPa at 110 min and 60 min. The system that required the longest time was S-CeO<sub>2</sub>, which at 0.084 MPa and 170 °C, took 150 min to convert 100% of the adsorbed sample.

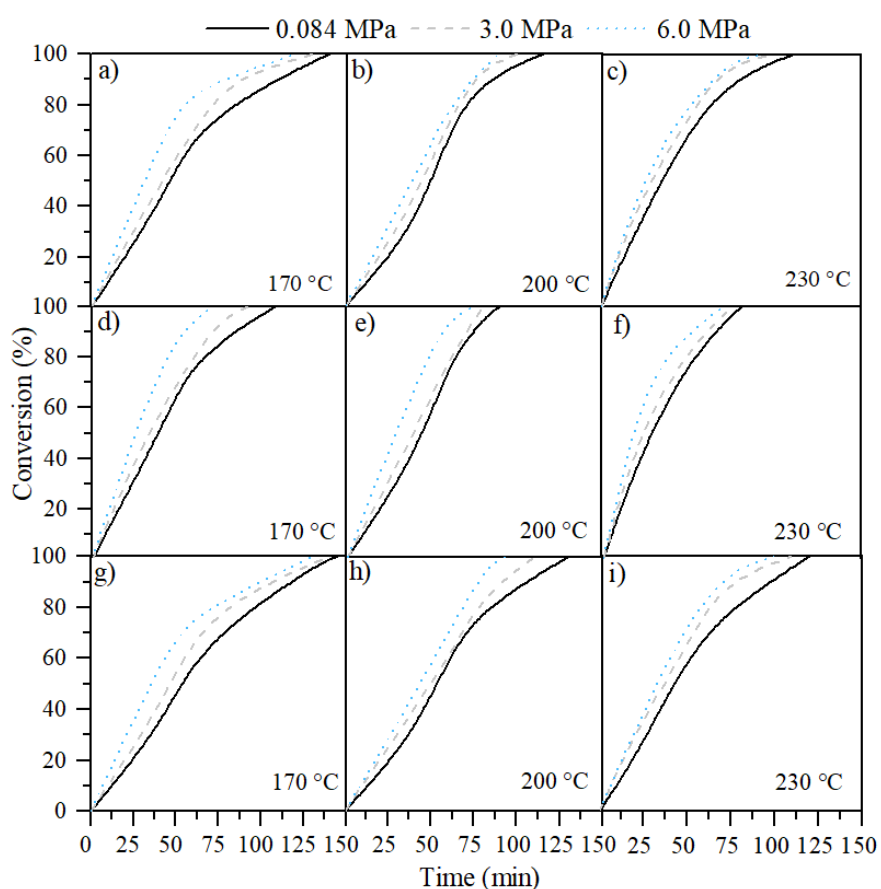


**Figure 14.** Isothermal conversion of *n*-C<sub>7</sub> asphaltenes oxidation adsorbed on a-c) O-CeO<sub>2</sub>, d-f) C-CeO<sub>2</sub>, g-h) S-CeO<sub>2</sub>. Air flow: 100 ml·min<sup>-1</sup>, and sample mass 1 mg.

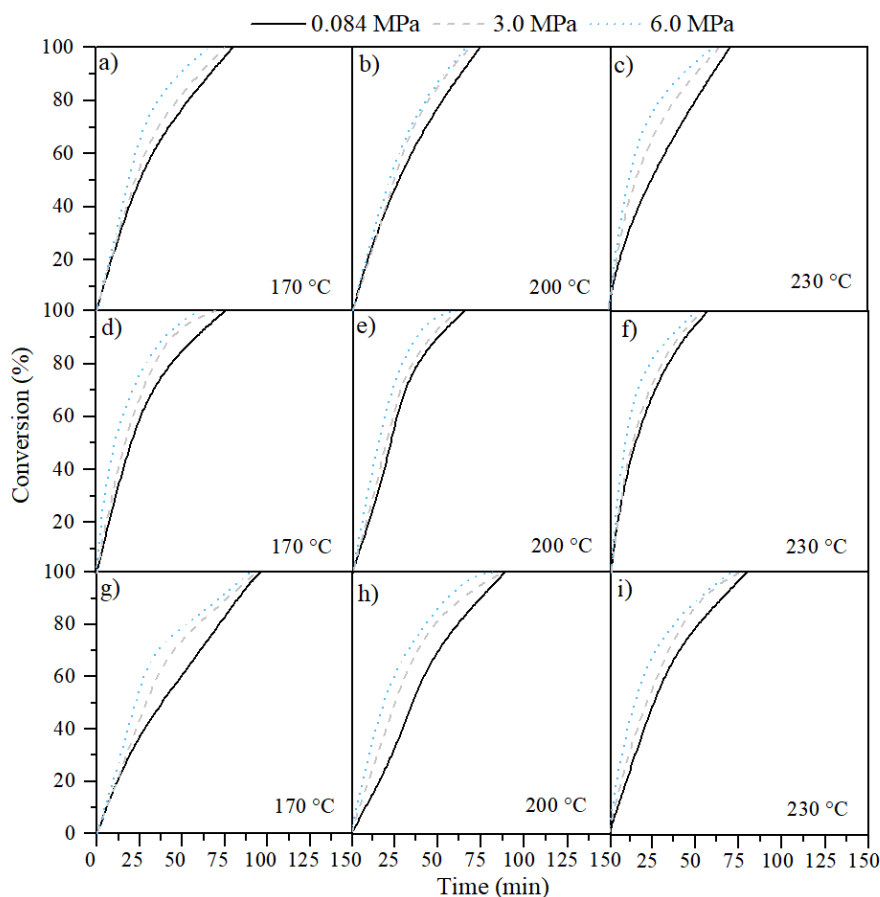


**Figure 15.** Isothermal conversion of  $n$ -C<sub>7</sub> asphaltenes oxidation adsorbed on a-c) O-NiPdCe, d-f) O-NiPdCe, g-h) S- NiPdCe. Air flow: 100 ml·min<sup>-1</sup>, and sample mass 1 mg.

To explain the enhanced activity of the doped CeO<sub>2</sub>-nanocatalysts, two factors are considered. First, the formation and stabilization of high catalytic active sites of nickel and palladium may depend on the ceria facets crystallographic orientation. One of the most significant factors in ceria catalysis is the oxygen vacancy creation, which was demonstrated in the previous section that plays an essential role in  $n$ -C<sub>7</sub> asphaltene oxidation. It is well known that the energy required for forming anion vacancies for different CeO<sub>2</sub> surfaces is low in {111} facets. Vacancies are essential to stabilize other transition element compounds, such as oxides. This means that cubic morphological nanocatalysts stabilize the Ni and Pd phases easier than orthorhombic and spherical. Ce-NiPdCe sample presents better supports for anchoring and dispersing nickel and palladium clusters, leading to a higher oxidative/reducibility activity for  $n$ -C<sub>7</sub> asphaltene decomposition.

The second aspect to describe the results of the doped materials is the increase in the oxygen diffusion rates. The data confirms that the presence of Ni

and Pd lead to further activation of CeO<sub>2</sub> nanoparticles, which may facilitate the migration of O-vacancies from the bulk to the ceria surface. This, in turn, is improved by the presence of {110}, {100}, and {111} planes. Finally, the crystallite size, which is intrinsically related to the first mechanism explained, is considered a key parameter determining the synergistic redox interplay between transition elements and CeO<sub>2</sub> reactions, including *n*-C<sub>7</sub> asphaltene oxidation, supporting the best performance of C-CeNiPd. This indicates that the catalyst's shape continues to have a significant effect on the oxidation of asphaltenes in non-doped and metal-doped materials.

This work confirms that, by exposing more reactive surfaces of the surface support, it is possible to design improved ceria-based Ni-Pd catalysts with enhanced catalytic characteristics for asphaltene decomposition.

#### 3.4.4. Activation energy estimation

Effective activation energy was estimated for analyzing the catalytic activity of the synthesized materials. The results are shown in Figure 16a. The activation energy was obtained when 20% and 100 % of the conversion were reached in the absence and presence of nanocatalysts. It is found that the E<sub>a</sub> values increase in the following order: C-NiPdCe < O-NiPdCe < S-NiPdCe < C-CeO<sub>2</sub> < O-CeO<sub>2</sub> < S-CeO<sub>2</sub> < *n*-C<sub>7</sub> asphaltenes, which is in complete accord with the catalytic activity results. C-NiPdCe is the most active among the 6 ceria-based catalysts presenting the lowest activation energy values at all pressures. For both groups of materials (doped and non-doped), the activation energy was reduced when the nanocatalyst presented a cubic shape, followed by the orthorhombic and the spherical samples. Besides, the presence of Ni and Pd phases reduces the E<sub>a</sub> values. The results already mentioned are independent of the pressure used. However, with the increase of pressure, the E<sub>a</sub> is also reduced.

The results highlight the apparent effect of exposed CeO<sub>2</sub> crystal planes, the redox cycle (Ce<sup>3+</sup>/Ce<sup>4+</sup>), the content of oxygen vacancies and the strongest interactions between the Ni and Pd species and support on *n*-C<sub>7</sub> asphaltene oxidation. Figure 16b-e shows the relationship between the Ce<sup>3+</sup>, lattice parameter, O<sub>ads</sub>/O<sub>latt</sub>, and I<sub>(598+1172)</sub>/I<sub>(458)</sub> with the increase in activation energy. The results are depicted for E<sub>a</sub> values at 6.0 MPa. As expected, a nanocatalyst with a high content of Ce<sup>3+</sup> and a high ratio of O<sub>ads</sub>/O<sub>lat</sub> requires lower energy for developing asphaltene decomposition. On the other hand, in doped nanocatalysts, the effect of the lattice parameter becomes more significant so that a higher value of this parameter makes it easier for the nanocatalyst to

decompose the asphaltenes. Finally, the vacancies have a similar effect, obtaining lower  $E_a$  for systems with higher  $I_{(598+1172)}/I_{(458)}$ .

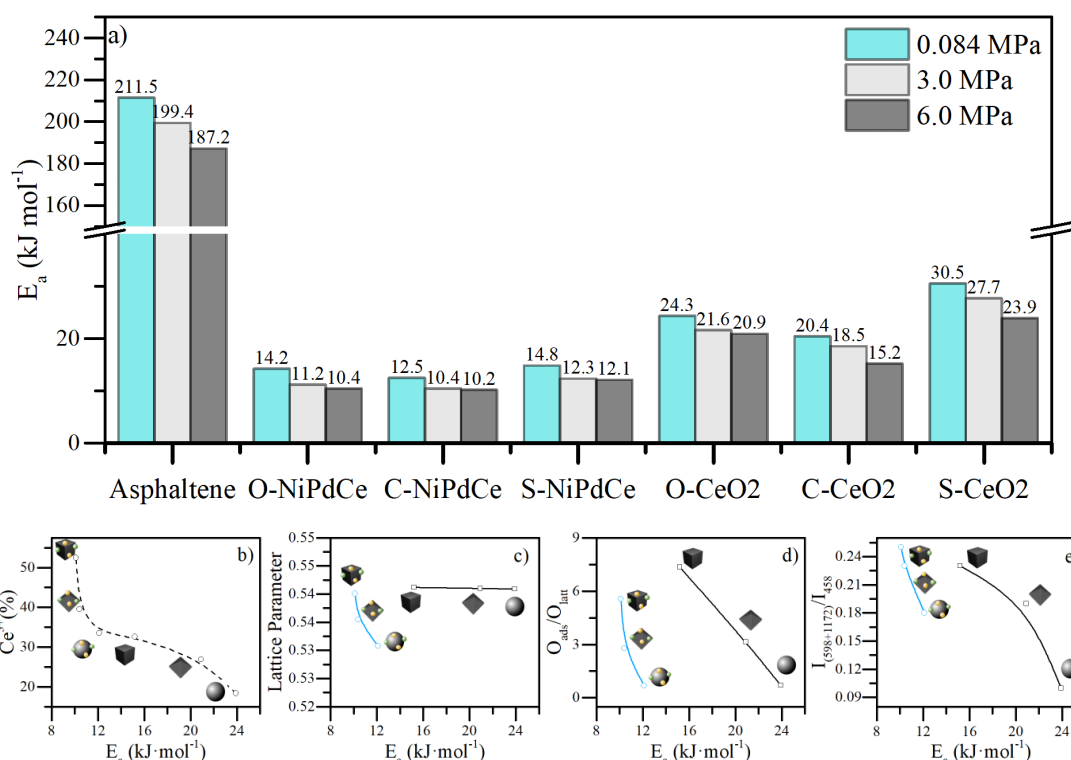


**Figure 16.** a) Estimated activation energy for isothermal oxidation of virgin  $n$ -C<sub>7</sub> asphaltene and adsorbed on CeO<sub>2</sub> nanocatalysts with different morphologies and doped with 1.0% in mass fraction of Ni and Pd. Pressure range: 0.084 MPa-6.0 MPa; and effect of b)  $Ce^{3+}$ , c) lattice parameter, d)  $O_{ads}/O_{latt}$ , and e)  $I_{(598+1172)}/I_{(458)}$  on effective activation energy at 6.0 MPa.

## 4. Conclusions

This work demonstrates the high redox performance of structured CeO<sub>2</sub> nanocatalysts and doped with low amounts of Ni/Pd as a new and promising proposal for  $n$ -C<sub>7</sub> asphaltene adsorption and subsequent decomposition. The interactions between CeO<sub>2</sub> and asphaltenes were dominated by hydrogen bonding and cation- $\pi$  interactions. The Ni and Pd phases promote diverse asphaltene adsorption mechanisms, including heteroatom-metal interactions,  $\sigma$ -bonding, and  $\pi$ -back interactions. Catalytic results show that cubic nanoparticles present the highest efficiency decomposing asphaltenes under all the evaluated conditions. The cubic doped catalyst reaches 100 % of  $\alpha$  at 170 °C and 6.0 MPa at 60 min (50 min less than the non-doped cubic catalyst). Similar results were

obtained for the spherical and orthorhombic nanocatalyst. The data confirms that the presence of Ni and Pd increases the catalytic activity of CeO<sub>2</sub>, reducing the E<sub>a</sub> values in all the evaluated scenarios for *n*-C<sub>7</sub> asphaltene decomposition.

## References

1. Acevedo, S.; Gutierrez, L. B.; Negrin, G.; Pereira, J. C.; Mendez, B.; Delolme, F.; Dessalces, G.; Broseta, D., Molecular weight of petroleum asphaltenes: A comparison between mass spectrometry and vapor pressure osmometry. *Energy & fuels* **2005**, 19, (4), 1548-1560.
2. Adams, J. J., Asphaltene adsorption, a literature review. *Energy & Fuels* **2014**, 28, (5), 2831-2856.
3. Medina, O. E.; Olmos, C.; Lopera, S. H.; Cortés, F. B.; Franco, C. A., Nanotechnology Applied to Thermal Enhanced Oil Recovery Processes: A Review. *Energies* **2019**, 12, (24), 4671.
4. Freitag, N. P., Chemical-reaction mechanisms that govern oxidation rates during in-situ combustion and high-pressure air injection. *SPE Reservoir Evaluation & Engineering* **2016**, 19, (04), 645-654.
5. Dabbous, M. K.; Fulton, P. F., Low-temperature-oxidation reaction kinetics and effects on the in-situ combustion process. *Society of Petroleum Engineers Journal* **1974**, 14, (03), 253-262.
6. Liu, D.; Hou, J.; Luan, H.; Pan, J.; Song, Q.; Zheng, R., Coke yield prediction model for pyrolysis and oxidation processes of low-asphaltene heavy oil. *Energy & Fuels* **2019**, 33, (7), 6205-6214.
7. Zhao, S.; Pu, W.; Sun, B.; Gu, F.; Wang, L., Comparative evaluation on the thermal behaviors and kinetics of combustion of heavy crude oil and its SARA fractions. *Fuel* **2019**, 239, 117-125.
8. Nassar, N. N.; Hassan, A.; Pereira-Almao, P., Effect of surface acidity and basicity of aluminas on asphaltene adsorption and oxidation. *Journal of colloid and interface science* **2011**, 360, (1), 233-238.
9. Marei, N. N.; Nassar, N. N.; Vitale, G.; Hassan, A.; Zurita, M. J. P., Effects of the size of NiO nanoparticles on the catalytic oxidation of Quinolin-65 as an asphaltene model compound. *Fuel* **2017**, 207, 423-437.
10. Franco, C. A.; Montoya, T.; Nassar, N. N.; Pereira-Almao, P.; Cortés, F. B., Adsorption and subsequent oxidation of colombian asphaltenes onto nickel and/or palladium oxide supported on fumed silica nanoparticles. *Energy & Fuels* **2013**, 27, (12), 7336-7347.

11. Nassar, N. N.; Hassan, A.; Pereira-Almao, P., Clarifying the catalytic role of NiO nanoparticles in the oxidation of asphaltenes. *Applied Catalysis A: General* **2013**, *462*, 116-120.
12. Lozano, M. M.; Franco, C. A.; Acevedo, S. A.; Nassar, N. N.; Cortés, F. B., Effects of resin I on the catalytic oxidation of n-C 7 asphaltenes in the presence of silica-based nanoparticles. *RSC advances* **2016**, *6*, (78), 74630-74642.
13. Nassar, N. N.; Hassan, A.; Pereira-Almao, P., Comparative oxidation of adsorbed asphaltenes onto transition metal oxide nanoparticles. *Colloids and surfaces A: Physicochemical and Engineering aspects* **2011**, *384*, (1-3), 145-149.
14. Mateus, L.; Moreno-Castilla, C.; López-Ramón, M. V.; Cortés, F. B.; Álvarez, M. Á.; Medina, O. E.; Franco, C. A.; Yebra-Rodríguez, Á., Physicochemical characteristics of calcined MnFe<sub>2</sub>O<sub>4</sub> solid nanospheres and their catalytic activity to oxidize para-nitrophenol with peroxymonosulfate and n-C7 asphaltenes with air. *Journal of Environmental Management* **2021**, *281*, 111871.
15. Arias-Madrid, D.; Medina, O. E.; Gallego, J.; Acevedo, S.; Correa-Espinal, A. A.; Cortés, F. B.; Franco, C. A., NiO, Fe<sub>2</sub>O<sub>3</sub>, and MoO<sub>3</sub> Supported over SiO<sub>2</sub> Nanocatalysts for Asphaltene Adsorption and Catalytic Decomposition: Optimization through a Simplex–Centroid Mixture Design of Experiments. *Catalysts* **2020**, *10*, (5), 569.
16. Nassar, N. N.; Hassan, A.; Carbognani, L.; Lopez-Linares, F.; Pereira-Almao, P., Iron oxide nanoparticles for rapid adsorption and enhanced catalytic oxidation of thermally cracked asphaltenes. *Fuel* **2012**, *95*, 257-262.
17. Tarboush, B. J. A.; Husein, M. M., Oxidation of asphaltenes adsorbed onto NiO nanoparticles. *Applied Catalysis A: General* **2012**, *445*, 166-171.
18. Amin, F., A Study on the Adsorption and Catalytic Oxidation of Asphaltene onto Nanoparticles. *Journal of Petroleum Science and Technology* **2017**, *7*, (2), 21-29.
19. Acosta, L. G.-C., D.; Medina, O.E.; Cortés, F.B.; Franco, C.A. , Nano-Intermediate of Magnetite Nanoparticles Supported on Activated Carbon from Spent Coffee Grounds for Treatment of Wastewater from Oil Industry and Energy Production. *Processes* **2021**, *9*, 63.
20. Medina, O. E.; Galeano-Caro, D.; Castelo-Quibén, J.; Ocampo-Pérez, R.; Perez-Cadenas, A. F.; Carrasco-Marín, F.; Franco, C. A.; Cortés, F. B., Monolithic carbon xerogels-metal composites for crude oil removal from oil in-saltwater emulsions and subsequent regeneration through oxidation process: Composites synthesis, adsorption studies, and oil decomposition experiments. *Microporous and Mesoporous Materials* **2021**, 111039.

21. Cardona, L.; Arias-Madrid, D.; Cortés, F. B.; Lopera, S. H.; Franco, C. A., Heavy oil upgrading and enhanced recovery in a steam injection process assisted by NiO-and PdO-Functionalized SiO<sub>2</sub> nanoparticulated catalysts. *Catalysts* **2018**, 8, (4), 132.
22. Afzal, S.; Nikookar, M.; Ehsani, M. R.; Roayaei, E., An experimental investigation of the catalytic effect of Fe<sub>2</sub>O<sub>3</sub> nanoparticle on steam injection process of an Iranian reservoir. *Iranian Journal of Oil & Gas Science and Technology* **2014**, 3, (2), 27-36.
23. Hamedi Shokrlu, Y.; Babadagli, T., In-situ upgrading of heavy oil/bitumen during steam injection by use of metal nanoparticles: A study on in-situ catalysis and catalyst transportation. *Spe Reservoir Evaluation & Engineering* **2013**, 16, (03), 333-344.
24. Aneggi, E.; Boaro, M.; de Leitenburg, C.; Dolcetti, G.; Trovarelli, A., Insights into the redox properties of ceria-based oxides and their implications in catalysis. *Journal of Alloys and Compounds* **2006**, 408, 1096-1102.
25. Medina, O. E.; Gallego, J.; Restrepo, L. G.; Cortés, F. B.; Franco, C. A., Influence of the Ce<sup>4+</sup>/Ce<sup>3+</sup> Redox-couple on the cyclic regeneration for adsorptive and catalytic performance of NiO-PdO/CeO<sub>2</sub>± $\delta$  nanoparticles for n-C<sub>7</sub> asphaltene steam gasification. *Nanomaterials* **2019**, 9, (5), 734.
26. Medina, O. E.; Gallego, J.; Arias-Madrid, D.; Cortés, F. B.; Franco, C. A., Optimization of the load of transition metal oxides (Fe<sub>2</sub>O<sub>3</sub>, Co<sub>3</sub>O<sub>4</sub>, NiO and/or PdO) onto CeO<sub>2</sub> nanoparticles in catalytic steam decomposition of n-C<sub>7</sub> asphaltenes at low temperatures. *Nanomaterials* **2019**, 9, (3), 401.
27. Medina, O. E.; Hurtado, Y.; Caro-Velez, C.; Cortés, F. B.; Riazi, M.; Lopera, S. H.; Franco, C. A., Improvement of Steam Injection Processes Through Nanotechnology: An Approach through in Situ Upgrading and Foam Injection. *Energies* **2019**, 12, (24), 4633.
28. Medina, O. E.; Caro-Vélez, C.; Gallego, J.; Cortés, F. B.; Lopera, S. H.; Franco, C. A., Upgrading of Extra-Heavy Crude Oils by Dispersed Injection of NiO-PdO/CeO<sub>2</sub>± $\delta$  Nanocatalyst-Based Nanofluids in the Steam. *Nanomaterials* **2019**, 9, (12), 1755.
29. Medina, O. E.; Gallego, J.; Olmos, C. M.; Chen, X.; Cortés, F. B.; Franco, C. A., Effect of Multifunctional Nanocatalysts on n-C<sub>7</sub> Asphaltene Adsorption and Subsequent Oxidation under High-Pressure Conditions. *Energy & Fuels* **2020**, 34(5), 6261-6278.
30. Huang, X.-S.; Sun, H.; Wang, L.-C.; Liu, Y.-M.; Fan, K.-N.; Cao, Y., Morphology effects of nanoscale ceria on the activity of Au/CeO<sub>2</sub> catalysts for

low-temperature CO oxidation. *Applied Catalysis B: Environmental* **2009**, 90, (1-2), 224-232.

31. Zheng, X.; Li, Y.; Zhang, L.; Shen, L.; Xiao, Y.; Zhang, Y.; Au, C.; Jiang, L., Insight into the effect of morphology on catalytic performance of porous CeO<sub>2</sub> nanocrystals for H<sub>2</sub>S selective oxidation. *Applied Catalysis B: Environmental* **2019**, 252, 98-110.

32. Soykal, I. I.; Bayram, B.; Sohn, H.; Gawade, P.; Miller, J. T.; Ozkan, U. S., Ethanol steam reforming over Co/CeO<sub>2</sub> catalysts: Investigation of the effect of ceria morphology. *Applied Catalysis A: General* **2012**, 449, 47-58.

33. Yang, S.; Zhou, F.; Liu, Y.; Zhang, L.; Chen, Y.; Wang, H.; Tian, Y.; Zhang, C.; Liu, D., Morphology effect of ceria on the performance of CuO/CeO<sub>2</sub> catalysts for hydrogen production by methanol steam reforming. *International Journal of Hydrogen Energy* **2019**, 44, (14), 7252-7261.

34. Dave, C. D.; Pant, K., Renewable hydrogen generation by steam reforming of glycerol over zirconia promoted ceria supported catalyst. *Renewable energy* **2011**, 36, (11), 3195-3202.

35. Chen, J. Z.; Talpade, A.; Canning, G. A.; Probus, P. R.; Ribeiro, F. H.; Datye, A. K.; Miller, J. T., Strong metal-support interaction (SMSI) of Pt/CeO<sub>2</sub> and its effect on propane dehydrogenation. *Catalysis Today* **2020**.

36. Figueiredo, W. T.; Della Mea, G. B.; Segala, M.; Baptista, D. L.; Escudero, C.; Pérez-Dieste, V.; Bernardi, F., Understanding the Strong Metal-Support Interaction (SMSI) Effect in Cu<sub>x</sub>Ni<sub>1-x</sub>/CeO<sub>2</sub> (0 < x < 1) Nanoparticles for Enhanced Catalysis. *ACS Applied Nano Materials* **2019**, 2, (4), 2559-2573.

37. Wang, Z.; Fu, H.; Tian, Z.; Han, D.; Gu, F., Strong metal-support interaction in novel core-shell Au-CeO<sub>2</sub> nanostructures induced by different pretreatment atmospheres and its influence on CO oxidation. *Nanoscale* **2016**, 8, (11), 5865-5872.

38. Jiang, Z.; Jing, M.; Feng, X.; Xiong, J.; He, C.; Douthwaite, M.; Zheng, L.; Song, W.; Liu, J.; Qu, Z., Stabilizing platinum atoms on CeO<sub>2</sub> oxygen vacancies by metal-support interaction induced interface distortion: Mechanism and application. *Applied Catalysis B: Environmental* **2020**, 278, 119304.

39. Barre, L.; Espinat, D.; Rosenberg, E.; Scarsella, M., Colloidal structure of heavy crudes and asphaltene solutions. *Revue de l'Institut Français du Pétrole* **1997**, 52, (2), 161-175.

40. Cardona, L.; Arias-Madrid, D.; Cortés, F.; Lopera, S.; Franco, C., Heavy oil upgrading and enhanced recovery in a steam injection process assisted by NiO-

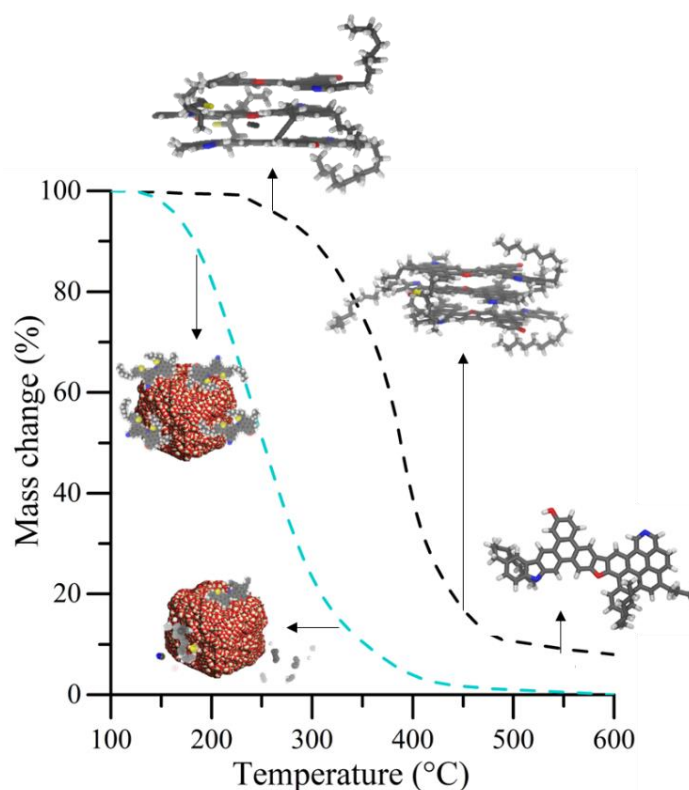


- and PdO-Functionalized SiO<sub>2</sub> nanoparticulated catalysts. *Catalysts* **2018**, 8, (4), 132.
41. Lopes, S. M.; Geng, P., Estimation of elemental composition of diesel fuel containing biodiesel. *SAE International Journal of Fuels and Lubricants* **2013**, 6, (3), 668-676.
42. Zhang, B.; Huyan, Y.; Wang, J.; Wang, W.; Zhang, Q.; Zhang, H., Synthesis of CeO<sub>2</sub> nanoparticles with different morphologies and their properties as peroxidase mimic. *Journal of the American Ceramic Society* **2019**, 102, (4), 2218-2227.
43. Naderi, M., Surface Area: Brunauer–Emmett–Teller (BET). In *Progress in filtration and separation*, Elsevier: 2015; pp 585-608.
44. Kroon, R., Nanoscience and the Scherrer equation versus the 'Scherrer-Gottingen equation'. *South African Journal of Science* **2013**, 109, (5-6), 01-02.
45. Mullins, O. C. S., E. Y., Eds.; Plenum Press: , Optical interrogation of aromatic moieties in crude oil sand asphaltenes. In *Structures and dynamics of asphaltenes*; **New York, 1998**.
46. Goncalves, S.; Castillo, J.; Fernandez, A.; Hung, J., Absorbance and fluorescence spectroscopy on the aggregation behavior of asphaltene–toluene solutions. *Fuel* **2004**, 83, (13), 1823-1828.
47. Acevedo, S.; Escobar, G.; Gutiérrez, L. B.; Rivas, H.; Gutiérrez, X., Interfacial rheological studies of extra-heavy crude oils and asphaltenes: role of the dispersion effect of resins in the adsorption of asphaltenes at the interface of water-in-crude oil emulsions. *Colloids and Surfaces A: Physicochemical and Engineering Aspects* **1993**, 71, (1), 65-71.
48. Senneca, O.; Vorobiev, N.; Wütscher, A.; Cerciello, F.; Heuer, S.; Wedler, C.; Span, R.; Schiemann, M.; Muhler, M.; Scherer, V., Assessment of combustion rates of coal chars for oxy-combustion applications. *Fuel* **2019**, 238, 173-185.
49. Niksa, S.; Liu, G.-S.; Hurt, R. H., Coal conversion submodels for design applications at elevated pressures. Part I. devolatilization and char oxidation. *Progress in Energy and Combustion Science* **2003**, 29, (5), 425-477.
50. Liu, G.-S.; Niksa, S., Coal conversion submodels for design applications at elevated pressures. Part II. Char gasification. *Progress in energy and combustion science* **2004**, 30, (6), 679-717.
51. Sellers-Antón, B.; Bailón-García, E.; Cardenas-Arenas, A.; Davó-Quiñonero, A.; Lozano-Castelló, D.; Bueno-López, A., Enhancement of the Generation and Transfer of Active Oxygen in Ni/CeO<sub>2</sub> Catalysts for Soot Combustion by Controlling the Ni–Ceria Contact and the Three-Dimensional Structure. *Environmental Science & Technology* **2020**, 54, (4), 2439-2447.

52. Medina, O. E.; Gallego, J.; Rodríguez, E.; Franco, C. A.; Cortés, F. B., Effect of pressure on the oxidation kinetics of Asphaltenes. *Energy & Fuels* **2019**, *33*, (11), 10734-10744.
53. Medina, O. E.; Gallego, J.; Nassar, N. N.; Acevedo, S. A.; Cortés, F. B.; Franco, C. A., Thermo-Oxidative Decomposition Behaviors of Different Sources of n-C7 Asphaltenes at High-Pressure Conditions. *Energy & Fuels* **2020**, *4*(7), 8740-8758.



# Molecular Dynamic Simulation and Experimental Study on $n$ -C<sub>7</sub> Asphaltene Pyrolysis under High-Pressure Conditions using Ceria-Based Nanocatalysts



Submitted to ACS Applied Nano Materials

Impact factor: 6.14

# Molecular Dynamic Simulation and Experimental Study on *n*-C<sub>7</sub> Asphaltene Pyrolysis under High-Pressure Conditions using Ceria-Based Nanocatalysts.

## Abstract

This work aims to widen our knowledge about the pyrolysis, and catalytic pyrolysis of asphaltenes at low and high pressure through experimental and simulation approaches. Experimentally, asphaltenes were subjected to high-pressure thermogravimetric analysis obtaining a pressure-dependent behavior. As pressure increases, asphaltene reactivity is reduced by the retardation in the thermal cracking temperature and increment of the coke amount deposition. The coke deposited follows the order 0.084 MPa (8.0%) < 3.0 MPa (10.0%) < 6.0 MPa (11.0%). When ceria-based nanoparticles were used for the catalytic thermal cracking of asphaltenes, it was obtained that during the low-temperature range (< 250 °C), the amount of mass lost was 60%, 45%, and 38% at 0.084 MPa, 3.0 MPa, and 6.0 MPa, respectively. The rest of the asphaltenes are cracked in the high-temperature region (HTR), which means that coke is not produced in the catalytic reaction regardless of the system pressure. The merit of the nanoparticles is established when the effective activation energy calculation. At 6.0 MPa, the activation energy was reduced from 332 kJ mol<sup>-1</sup> to 228 kJ mol<sup>-1</sup> to complete the reactions during HTR. Moreover, the obtained thermodynamic data showed a decrease in the enthalpy and entropy of activation of asphaltene pyrolysis in the presence of ceria-based nanoparticles. Molecular dynamic calculations were done based on the ReaxFF potential to provide an atomistic description of asphaltene pyrolysis at 0.084 MPa. The theoretical results were compared with those obtained experimentally, achieving successful reproducibility. During the LTR region, the asphaltene aggregate integrity remains without significant changes, whereas most structural changes in the HTR were obtained. The number of species increases with the rising temperature, getting 32, 1515, and 4065 species at 300, 450, and 550 °C, respectively. The species are mainly found in the form of reactive radicals such as CHO<sub>2</sub> (carboxyl radical), OH (hydroxyl radical), and CHO (aldehyde radical), and molecules of CO<sub>2</sub>, H<sub>2</sub>O, CH<sub>2</sub>O, and CO are observed as major O-containing gas products that account for most of the gas-phase.

## 1. Introduction

Conventional reserves are slowly depleting, and heavy oil (HO) and bitumen resources may be able to mitigate this concern.<sup>1</sup> Canada and Venezuela have an estimated 8 trillion barrels of heavy oil and bitumen. However, their physical and chemical properties limit primary production in HO reservoirs.<sup>2</sup> The poor quality is associated with its high density and high levels of S, N, O, and heavy metals like Ni, V, and Fe. These unfavorable properties constitute an excessive viscosity, which significantly limits the production flow rates of production wells.<sup>3</sup>

Several techniques were implemented to increase the amount of crude oil extracted from an oil field, and it is strongly believed that Thermal Enhanced Oil Recovery (TEOR) technology can accommodate future energy demand. Hot-fluid injection (HFI), *in-situ* combustion (ISC), steam (CSS and CSI), and thermal stimulation are well-known conventional methods of enhanced oil recovery.<sup>4</sup> In these techniques, heat or steam is injected into the hydrocarbon reservoirs, which decreases oil viscosity, increasing the recovery factor.<sup>5</sup>

Notwithstanding, heavy oil contains a significant amount of asphaltenes. Asphaltenes are macromolecular compounds consisting of sheets of condensed polynuclear and heterocyclic aromatic systems with alkyl side chains and naphthenic rings. Because of the complexity of asphaltenes, they are considered the main responsible for coke.<sup>6</sup> Coke is formed during the heavy oil thermal conversion process. The atmosphere in which heavy oil coking occurs may be inert or oxidizing (ISC).<sup>7</sup> The heavy oil coking mechanism significantly differs between these two atmospheres. In an inert atmosphere, heavy oil thermal cracking reactions occur at approximately 400 °C. The free radicals formed by cracking partially polymerize into polycyclic aromatic hydrocarbons, which act as the coke precursor. Coke is formed after further polymerization and cracking of these coke precursors. However, heavy oil converts into coke in an oxidizing atmosphere through a low-temperature oxidation (LTO) pathway.<sup>8</sup> Hence, to optimize the usage and conversion of heavy oil, it is necessary to understand the structure of the asphaltene and its processability. Our research group has made big efforts to describe the asphaltene response to oxidation at high pressure and high-temperature conditions; however, its pyrolysis is still missing.<sup>9-13</sup>

In the last decade, using nanoparticles to decompose asphaltenes and avoid coke production has gained significant interest.<sup>14, 15</sup> Nassar et al.<sup>16</sup> demonstrate that metal oxide nanoparticles (NiO, Co<sub>3</sub>O<sub>4</sub>, Fe<sub>3</sub>O<sub>4</sub>) can significantly enhance the thermal decomposition of heavy hydrocarbons like asphaltenes. Montoya et al.<sup>17</sup> investigated the post-adsorption catalytic thermal cracking of asphaltenes on Ni-Pd nanocatalysts supported on fumed silica nanoparticles. The authors confirmed by the lowest effective activation energy trend and lowest values of reaction temperature that the asphaltene pyrolysis reaction pathway can be improved by nanoparticles.<sup>17</sup> Also, Iron-based catalysts proposed by Khelkhal et al.<sup>18</sup> demonstrated being effective in the reduction of the activation energy of heavy oil pyrolysis as well as decreasing the enthalpy and entropy of activation of the reaction. Unfortunately, most previous studies on asphaltene pyrolysis neglected the pressure on the kinetic reaction.<sup>19</sup> We presented the influence of this variable on the oxidation of asphaltenes as well as the oxidation and pyrolysis of individual SAR and mixtures of them.<sup>3, 11</sup> During those studies, it was identified that pressure plays an important role in the oxidative kinetics of the crude oil fractions. However, the pyrolysis and catalytic pyrolysis of asphaltenes is still missing.

A deterministic tool for gaining a physical understanding of the connection between macroscopic behaviors and structural and compositional characteristics is the molecular dynamics (MD) simulation. Bhoi et al.<sup>20</sup> studied the combustion and pyrolysis of brown coal using reactive molecular dynamic (MD) simulation using the ReaxFF potential. The analysis of coal combustion revealed that coal combustion began with thermal decomposition to create smaller fragments. After that, the fragments underwent oxidation, and some of the hydrogen radicals engaged in an oxygen-hydrogen reaction to form H<sub>2</sub>O molecules. The temperature rose due to the production of major gaseous components like CO, CO<sub>2</sub>, and intermediates like HCHO. Goncalves et al.<sup>21</sup> presented the simulation of the pyrolysis and combustion of alternative jet fuels by reactive force field molecular dynamics methods. A comparison has been made between saturated hydrocarbon farnesane and two unsaturated compounds. Significant differences have been observed among the compound reactions during the decompositions. The study showed noticeably higher potential reactivity of unsaturated hydrocarbons compared to saturated hydrocarbons. On another study, Zhan et al.<sup>22</sup> investigated the mechanism of initial thermal decomposition associated with the pyrolysis of subbituminous coal through a series of molecular dynamics simulations using the ReaxFF. The processes by which typical pyrolysis products

are formed were investigated. For instance, the first step in the formation of carbon monoxide (CO) is the decarbonylation of a carbonyl or carboxyl group. In contrast, the main steps in the production of carbon dioxide (CO<sub>2</sub>) are hydrogen transfer and decarboxylation of carboxyl groups. The main way that CH<sub>4</sub> can be created is when a hydrogen atom from the hydroxyl group is abstracted by a CH<sub>3</sub> free radical. Two hydrogen atoms from one or more groups bond to form H<sub>2</sub>, increasing the residue fragments' stability. Additionally, unsaturated bonds or free radicals containing oxygen can react with hydrogen. Despite the literature's valuable contributions, we still do not fully comprehend the reaction pathway of asphaltene pyrolysis.

In this context, this work employs experimental and molecular dynamic simulation tools to describe asphaltene reactivity. Experimentally, the pressure effect on the pyrolysis of asphaltenes in the presence and absence of nanoparticles is evaluated. This study selected a previously designed cubic ceria nanoparticle doped with 1 wt.% of Ni and Pd element oxides.<sup>15</sup> The presence of oxygen vacancies which cause the co-existence and expedient exchange of Ce<sup>4+</sup> and Ce<sup>3+</sup> in its lattice structure, is thought to be one of the main reasons for its catalytic activity. Also, control over some factors like the strong metal support interactions (SMSI) with transition and noble elements as well as the morphology and size parameters, demonstrated to influence the catalytic performance. The specific nanoparticles were previously tested on asphaltene oxidation experiments obtaining excellent adsorptive and catalytic results at low and high-pressure conditions.<sup>9</sup>

In this context, this study presents for the first time a novel approach to understanding the pyrolysis and catalytic pyrolysis of asphaltenes at low and high pressure considering experimental and simulation tools.

## 2. Experimental

### 2.1. Materials

Asphaltenes isolated from Colombian extra-heavy crude oil were used in this study. These asphaltenes have been widely used in our studies, where there is a detailed description of their chemical properties, such as elemental analysis, X-ray photoelectron spectrometry, X-ray diffraction, nuclear magnetic resonance, and the construction of the model molecule. According to the mass fraction results, was including 81.7, 7.8, 6.6, 3.6, and 0.3% of carbon, hydrogen, nitrogen, sulfur, and oxygen, respectively. The molecular weight was 1051.6 g·mol<sup>-1</sup>, the



H/C ratio was 1.14, and the Double bond equivalent (DBE) was 44.5.<sup>23</sup> Pure nitrogen gas (NTC 2561, CRYOGAS, Colombia) was used to perform high-pressure thermogravimetric experiments. Also, doped cubic ceria nanoparticles with 1.0 wt.% of Ni and Pd (C-NiPdCe) were considered in this study for assessing asphaltene reactivity. Nanoparticles were prepared and fully characterized in our previous study.<sup>9</sup> Tables 1 and 2 summarize the textural and chemical properties of the nanoparticles.

**Table 1.** Textural properties estimated of synthesized C-NiPdCe nanoparticles.

Sample	$S_{BET}$ ( $m^2 \cdot g^{-1}$ )	Wo(CO <sub>2</sub> )	Lo(CO <sub>2</sub> )	Wo(N <sub>2</sub> )	Lo(N <sub>2</sub> )	V <sub>0.95</sub>	V <sub>meso(BJH)</sub>
C-NiPdCe	25.5	0.19	0.61	0.15	0.77	0.31	0.053

**Table 2.** Chemical properties estimated of synthesized and C-NiPdCe nanoparticles.

Sample	Crystallite size <sup>a</sup> (nm)	Lattice Parameter <sup>b</sup> (nm) x 10 <sup>-2</sup>	Ce <sup>3+</sup> (%)	O <sub>ads</sub> (%)	O <sub>latt</sub> (%)	Ni <sup>2+</sup> (NiO ) (%)	Pd <sup>2</sup> + (%)	$I_{(598+1172)}$ / $I_{458}$
C-NiPdCe	12.4	54.01	52.4	84.8	15.2	33.5	62.3	0.25

### 2.3. Thermogravimetric analysis

High-pressure thermogravimetric analysis of asphaltenes in the absence and presence of nanoparticles was executed under an inert atmosphere to elucidate pyrolysis reactivity. For this aim, 100 ml·min<sup>-1</sup> nitrogen flow was introduced into the equipment. Asphaltene reactivity was evaluated using 1 mg of the powder sample, whereas catalytic pyrolysis was executed using 0.2 mg·m<sup>-2</sup> adsorbed asphaltene per surface area of nanoparticles. Detailed descriptions of the equipment tools are widely described in our previous studies.<sup>10</sup>

### 2.4. Kinetic analysis

To describe the pyrolysis and catalytic pyrolysis of the *n*-C<sub>7</sub> asphaltene a, a single power-law model derived from the experimental results were used. In this model, the instantaneous reactivity (r) of the adsorbed material was considered between for the different pressures and temperatures.<sup>24</sup> The equation to determine the kinetic parameters is shown below (Equation 1)

$$\ln \ln \left[ \frac{\beta F(\theta)}{P_{N_2}^n T^2} \right] = \ln \left( \frac{k_0 R}{E_a} \right) - \frac{E_a}{RT} \quad (1)$$

where  $k_0$  ( $s^{-1} \cdot \text{bar}^{-n}$ ) and  $E_a$  ( $\text{kJ} \cdot \text{mol}^{-1}$ ) are the kinetic parameters of pre-exponential factor and apparent activation energy, respectively. The partial pressure (bar) of the  $N_2$  gas, the ideal gas constant ( $\text{J} \cdot \text{mol}^{-1} \cdot \text{K}^{-1}$ ), and the order of the reaction were shown as  $P$ ,  $R$ , and  $n$ , in order. The expression  $F(\theta)$  can be solved based on the volumetric model (Equation 2)

$$F(\theta) = \int \frac{d\theta}{f(\theta)} = -\ln(1-x) \quad (2)$$

According to the slope and intercept of Equation (1), the activation energy ( $E_a$ ) and pre-exponential factor ( $k_0$ ) will be obtained.

## 2.5. Thermodynamic analysis

To calculate thermodynamic parameters for the pyrolysis reaction, the Eyring equation was used (Equation 3)

$$k(T) = \frac{k_B T}{h} \exp \left( -\frac{\Delta^\ddagger G^0}{RT} \right) \quad (3)$$

where  $K_B$  and  $h$  are the Boltzmann and Planck constants and  $\Delta^\ddagger G^0$  is the standard Gibbs energy of activation complex formation.

The sophisticated Eyring equation is useful for giving insight into the nature of any transition state. The following equations could be useful for relating the thermodynamic and kinetic parameters obtained by the Arrhenius equation if we consider pyrolysis as a one-step process at each conversion degree.

$$\Delta^\ddagger H^0 = E_a - RT_{st} \quad (4)$$

$$\Delta^\ddagger S^0 = \left( \ln \frac{hk_o}{k_B T_{st}} - 1 \right) \quad (5)$$

$$\Delta^\ddagger G^0 = \Delta^\ddagger H^0 - T_{st} \Delta^\ddagger S^0 \quad (6)$$

where  $\Delta^\ddagger H^0$  and  $\Delta^\ddagger S^0$  are the standard enthalpy and entropy of activation complex formation, and  $T_{st}$  is a standard temperature which was defined as the peak temperature at each pressure. According to Equations (3) and (4), the activation energy is related to the energy difference between reactants and the transition state.

### 3. Molecular dynamic simulation

With the aim of providing a first theoretical approximation on asphaltene pyrolysis and identifying key aspects associated with its thermal conversion in non-reactive atmospheres, a molecular dynamic (MD) simulation was performed. To do this, the molecular structure reported by Medina et al.<sup>12</sup> for asphaltene-B was used (which is the same asphaltene experimentally evaluated in this study) to describe the pyrolysis process at 0.084 MPa. Asphaltene thermo-oxidative process was described by MD simulations in a prior study,<sup>25</sup> which served as the foundation for the theoretical pyrolysis approach. Simulations using REAX-FF MD and classical methods were used to accomplish this objective following the next procedure.

To start, conventional MD simulations were run to describe the formation of the asphaltene aggregate and the nitrogen density. Using an NVT ensemble (constant number of molecules  $N$ , volume  $V$ , and temperature  $T$ ), 27 asphaltene molecules were located in a  $120 \times 120 \times 120 \text{ \AA}^3$  box simulation to create the asphaltene aggregate. Separately, an NPT ensemble (constant number of molecules  $N$ , pressure  $P$ , and temperature  $T$ ) was used to determine the equilibrium density of nitrogen ( $N_2$ ) at 0.084 MPa and 100 °C. Then, both final configurations were merged to describe the pyrolysis process using 1683  $N_2$  atoms and the reactive force field (REAX-FF). Since REAX-FF can describe the formation and breaking of bonds using the relationship between bond distances, bond orders, and bond energies, all bonds, angles, and dihedrals were removed to properly dissociate atoms that were spaced far apart, that is, not forming a bond. Using geometric information derived from quantum chemistry calculations, this potential has been widely used to describe the chemical reactions of hydrocarbons.<sup>26</sup>

## 4. Results and discussion

### 4.1. Asphaltene pyrolysis at different pressures

Asphaltene pyrolysis at low, medium, and high-pressure conditions is shown in Figure 1. The results were executed at 0.084, 3.0, and 6.0 MPa to compare the results with the oxidative experiments reported previously.<sup>9</sup> For the three pressures evaluated, the thermal profile is divided into two main regions based on the mass change and rate for mass change profiles (Panels a and b). The events are recognized in the literature as low-temperature and high-temperature regions. The temperature region in LTR and HTR is similar for the three pressures. LTR is observed between 200 and 350 °C and HTR between 351 and 600 °C. The first event is characterized by physical evaporation, cracking of lower molecular weight hydrocarbons, isomerization, and polymerization reactions.<sup>27</sup><sup>28</sup> The amount of mass lost at the end of LTR was 25%, 11%, and 9% at 0.084 MPa, 3.0 MPa, and 6.0 MPa, respectively. This result means that the pressure increase affects the reactivity of asphaltenes pyrolysis. Previously, we evaluated the effect of the pyrolysis of resins and high-molecular-weight aromatics, founding the same trend as asphaltenes. Both fractions present a higher mass loss during low-temperature regions at lower pressures. The main difference is that the resins decompose a higher amount of their structure than aromatics because of the short-chain aliphatic chains and aliphatic heteroatoms. Probably the aromatic nuclei are the least reactive under an inert atmosphere and therefore the higher the aromaticity of the structure, the lower the mass loss in LTR. The asphaltenes studied in this work have an aromaticity of 0.69, higher than the resins (0.42) and the aromatics (0.40),<sup>11</sup> therefore, a lower mass loss is observed in the three pressures evaluated. During the second stage, a more marked difference in the thermal profile is observed at 0.084 MPa concerning the other two pressures. The rate for mass change increased at lower temperatures, obtaining at 400 °C a mass loss of 30%, much higher than 3.0 MPa (9%) and 6.0 MPa (7%). Interestingly, the asphaltene is not decomposed 100% at the evaluated temperature range for all pressures.

However, the amount of the remaining solid after pyrolysis at each pressure was different and increased in the order of 0.084 MPa (8.0%) < 3.0 MPa (10.0%) < 6.0 MPa (11.0%). The difference between the lowest mass loss at 0.084 MPa and the highest one at 6.0 MPa is 3%. These findings suggest that pressure influences the LTR and HTR of asphaltenes. In literature, it is believed that coke is produced by pyrolysis of non-volatile hydrocarbons, which means that at higher pressure,

the coke amount of these systems increases. The polymerization reactions during LTR probably result in more condensed and aromatic structures as pressure rises.<sup>29</sup> Consistently, Boytosova et al.<sup>30</sup> reported that higher pressure results in higher coke deposition during asphaltene gasification.

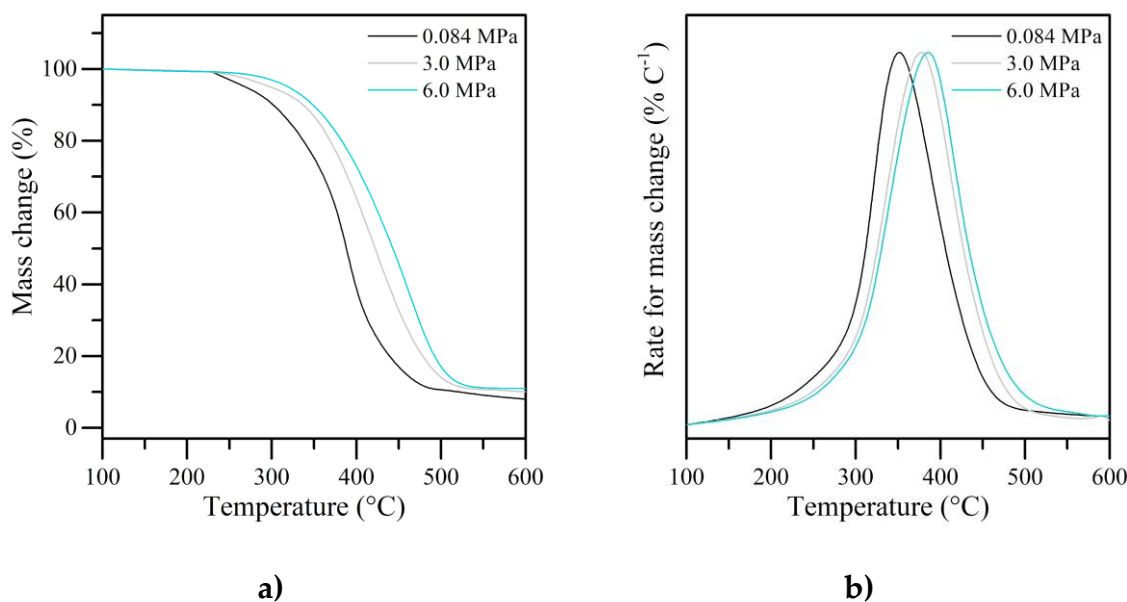


**Figure 1.** (a) Mass percentage and (b) rate for mass change for the pyrolysis of asphaltenes at different pressures. Sample mass: 1 mg, heating rate: 10 °C·min<sup>-1</sup>, and nitrogen flow: 80 mL·min<sup>-1</sup>.

#### 4.2. Asphaltene catalytic pyrolysis at different pressures

Figure 2 shows the mass change and rate for mass change profiles for asphaltene pyrolysis adsorbed on C-CeNiPd. In the first instance, the reduction in asphaltene decomposition temperature is observed by the presence of nanoparticles, which is evidence of their catalytic effect. Asphaltenes lose mass at 150 °C, and the complete decomposition is achieved close to 350 °C for pressures lower than 3.0 MPa, and around 400 °C at 6.0 MPa. Based on this result, it is evidenced that the pressure follows the same trend on asphaltene catalytic pyrolysis, that is, as higher pressure as lower the amount of asphaltene converted. During LTR (< 250 °C), the amount of mass lost was 60%, 45%, and 38% at 0.084 MPa, 3.0 MPa, and 6.0 MPa, respectively. The rest of the asphaltenes are cracked in the HTR region. The last means that coke is not produced when the pyrolysis is assisted by CeO<sub>2</sub> catalysts regardless of the system pressure. Deka et al.<sup>31</sup> stated that CeO<sub>2</sub> nanoparticles improved the pyrolysis process of carbon structures by enhancing the C-C bond scission reactions.

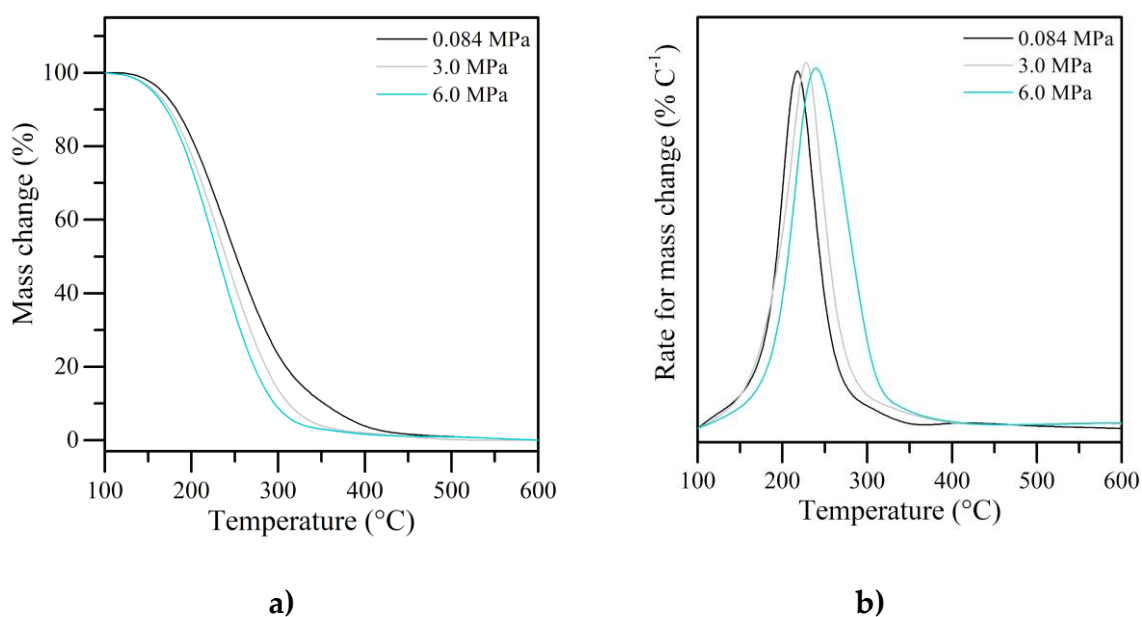


**Figure 2.** (a) Mass percentage and (b) rate for mass change for the catalytic pyrolysis of asphaltenes at different pressures. Sample mass: 1 mg, heating rate:  $10\text{ }^{\circ}\text{C}\cdot\text{min}^{-1}$ , and nitrogen flow:  $80\text{ mL}\cdot\text{min}^{-1}$ .

There are several possible reactions and mechanisms following the pyrolysis of asphaltenes. These reactions might include condensation with ester formation, polymerization or isomerization, dehydrogenation, aromatization, and dealkylation. The bond scission occurs at certain definite locations in catalytic reactions but randomly occurs in thermal reactions. Thermal cracking tends to yield molecules possessing three or four carbon atoms, whereas catalytic cracking produces compounds with one- and two-carbon atoms. This again establishes the merit of the nanoparticles in catalyzing the degradation process of asphaltenes.

#### 4.3. Kinetic calculations.

The obtained curves indicate the two defined regions, LTR and HTR, during pyrolysis. The adequate behavior for both catalytic and non-catalytic pyrolysis allows the kinetic calculation. The data was obtained based on the assumption of first-order whose fits were acceptable (correlation coefficients between 0.982-0.991). Effective activation is shown in Figure 3, discretized on LTR and HTR for the different considered scenarios. From the obtained data, we observe lower effective activation energy values for LTR and HTR for pyrolysis and catalytic pyrolysis of asphaltenes. Consistently with the results described by TGA, it is

expected that during LTR, the destruction of intermolecular associations and weaker chemical bonds, e.g., sulfur bridges, as well as the degradation of the weak aliphatic side chains ( $\alpha$ -methyl and  $\alpha$ -methine structures) occurs. Aliphatic side chains are easy to break, so the energy required is low compared with the required for complex structures.

After that, during HTR, effective activation energy increases to a level at which the decomposition of the heavy fractions is initiated. During this region, in addition to the increased volatilization rate due to the progressive evaporation of bigger molecules, the production of volatile fragments via cracking of these molecules and the formation of coke may take place. It is expected that the aforementioned processes result in higher  $E_a$ . The influence of pressure on the activation energy is clearly noted. Effective activation energy increases as pressure increase for both stages: from 214 kJ mol<sup>-1</sup> at 0.084 MPa to 230 kJ mol<sup>-1</sup> at 6.0 MPa during LTR and from 294 kJ mol<sup>-1</sup> at 0.084 MPa to 332 kJ mol<sup>-1</sup> at 6.0 MPa during HTR. This indicates that the whole reaction pathway of asphaltene pyrolysis is affected by pressure. The different reactions become hard as pressure increases, which can be assigned to the occurrence of faster rates of heat transfer at different pressures.

When nanoparticles assist pyrolysis, the effective activation energy is reduced, again establishing their merit in catalyzing the reactions. Pressure still affects the reactivity of asphaltenes, resulting in higher values at higher pressures. However, the complete transformation of coke indicates the capacity of nanoparticles to produce smaller fractions from high molecular weight structures characterized by low activation energy. It is worth mentioning that the wide variations in activation energies are attributed to the complex decomposition mechanism of the asphaltene molecule.

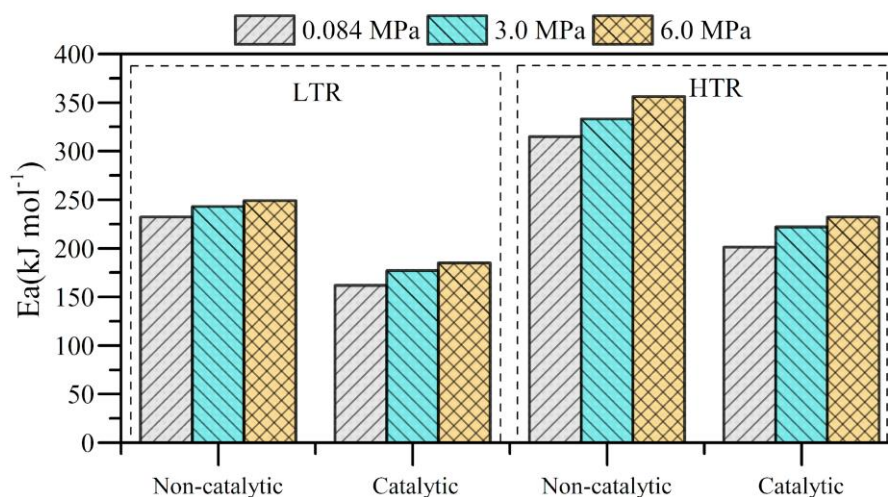


**Figure 3.** Estimated effective activation energy for non-catalytic and catalytic pyrolysis of asphaltenes at 0.084 MPa, 3.0 MPa, and 6.0 MPa, discretized on low temperature (LTR) and high-temperature region (HTR).

#### 4.4. Thermodynamic functions of asphaltene pyrolysis

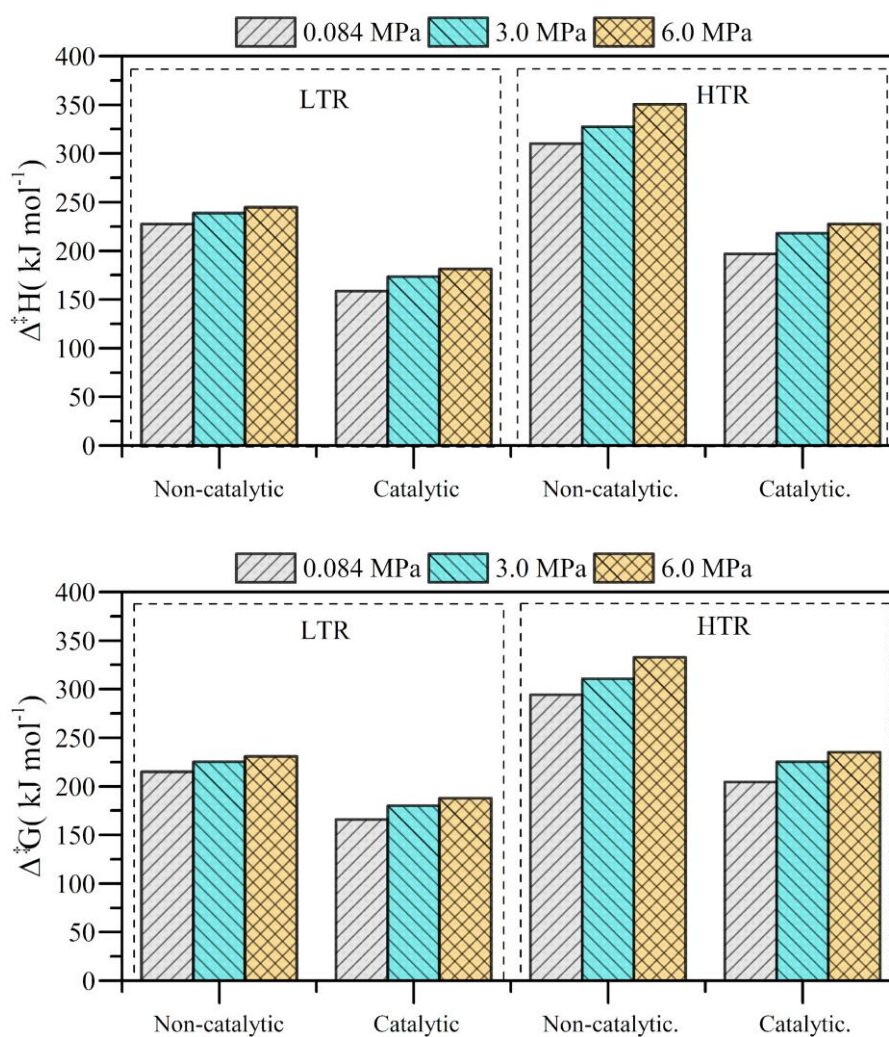
On the basis of thermodynamic calculations, the structure transformation and intermolecular interactions of asphaltenes were studied in the LTR and HTR stages, considering the free energy, enthalpy, and entropy. The thermodynamic properties of the transition state function for the thermal cracking of asphaltenes in the presence and absence of nanoparticles were studied following the procedure described in section 2.4. and are presented in Figure 4. Panel a shows the results for  $\Delta^\ddagger H^0$ , which is responsible for the strength of hydrocarbon molecules during pyrolysis. In both cases (catalytic and non-catalytic pyrolysis)  $\Delta^\ddagger H^0 > 0$ , which means that the reaction is endothermic for all samples (heat release).<sup>30</sup> The strength of the molecular bond of asphaltenes is lower in the presence of nanoparticles because of  $\Delta^\ddagger H^0_{\text{noncatalytic}} > \Delta^\ddagger H^0_{\text{catalytic}}$ ; this result agrees well with effective activation energy values, demonstrating the effect of the nanoparticles to reduce the energy consumption and avoid a significant increase in the activation enthalpy.

Additionally, as pressure increases, there is an increment in activation enthalpy, so it can be assumed that the reaction remains endothermic.<sup>18</sup> The reason for the increment tendency of  $\Delta^\ddagger H^0$  with the pressure implies the formation of complex structures with strong molecular bonds, which is in accordance with the coke production. Similarly, Boytsova et al.<sup>32</sup> stated that the inner strength of high-density particles becomes higher when compared to



asphaltenes and their vacuum residue. On the other hand, the Gibbs free energy followed the same trends as the enthalpy, corroborating the results.

According to the  $\Delta^\ddagger S^0$  (panel c), positive and negative values are obtained for the non-catalytic and catalytic reactions. From this result, it can be inferred that the entropy of the activated state is lower than that of the initial state when nanoparticles assist the pyrolysis reaction. Besides, considering the entropy as a measure of the changes in the location of the molecules (the ordering of components in the oil system),<sup>32</sup> it can be concluded that the asphaltenes present ordered structures with straightened macromolecules during pyrolysis, which increases with the increase in pressure. However, at the same time, when using the catalyst, the activation entropy is significantly reduced, which indicates a greater degree of arrangement of the transition state.<sup>18</sup>



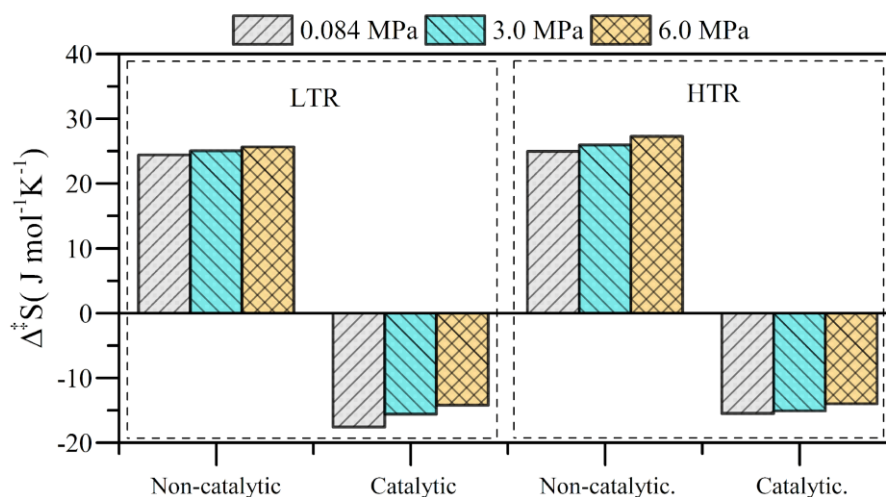


**Figure 4.** Thermodynamic parameters for non-catalytic and catalytic pyrolysis of asphaltenes at 0.084 MPa, 3.0 MPa, and 6.0 MPa, discretized on low temperature (LTR) and high-temperature region (HTR).

#### 4.5. Molecular dynamics

N<sub>2</sub> density results at 100 °C and 0.084 MPa are shown in Figure 5, yielding an average equilibrium density of 0.74 kg·m<sup>-3</sup> that is consistent with the experimental value (0.758 kg·m<sup>-3</sup>).<sup>33</sup> To describe the first stage of the reaction, between 25 – 100 °C, the atoms which compose the asphaltene molecules remain motionless, i.e., only N<sub>2</sub> atoms are integrated into the motion equation, since at low temperatures, the motion of the asphaltene aggregate (solid phase) is negligible compared to the motion of the gas phase (nitrogen).<sup>34</sup> Then, all atoms are integrated into the motion equation to represent the pyrolysis processes.

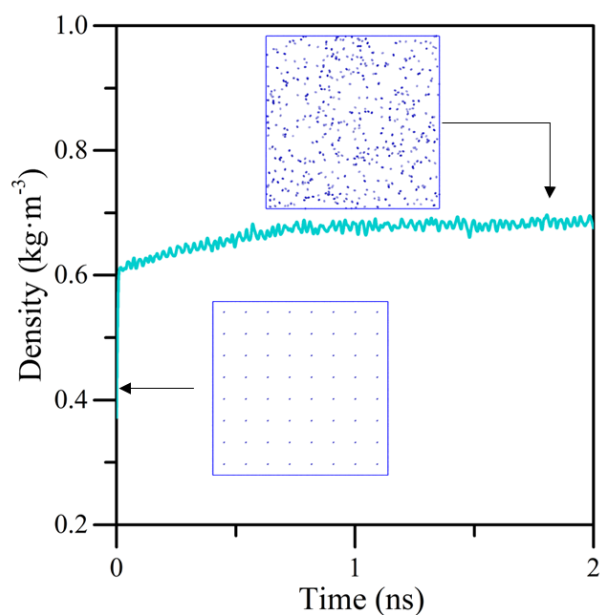


**Figure 5.** Nitrogen density equilibration at 0.084 MPa and 100 °C. Nitrogen atoms are shown in blue.

Figure 6 shows the results of the mass conversion obtained from the reactive MD simulations. It should be noted that the mass conversion was estimated from the molecular weights of each species formed, considering the boiling point to determine the mass loss at each temperature.<sup>34</sup> Conventionally, high temperatures are used to break the bonds (pyrolysis). Then, the Arrhenius equation is implemented to scale the temperatures of the simulations in orders that are testable with the experimental temperature data. However, the approach used in this study, allows describing the mass loss without the need for temperature correction. It is worth remembering that the reactive MD simulations adequately capture the experimental tendency.

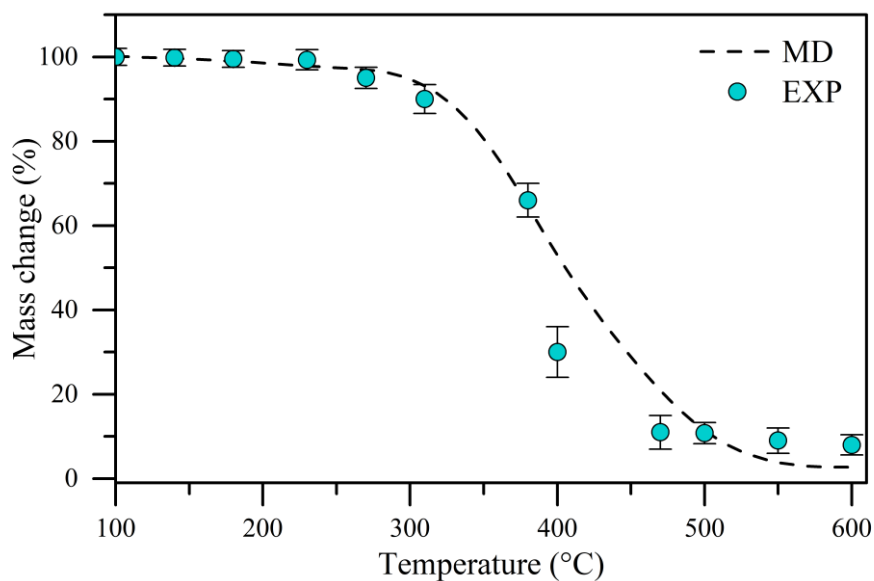


**Figure 6.** Mass conversion profile of pyrolysis at 0.084 MPa obtained from molecular dynamics (MD) simulations and comparative concerning experimental measurements (EXP).

Figure 7 shows the molecular configurations at different temperatures between 100 and 600 °C, illustrating the changes in asphaltene aggregates during the pyrolysis process. The snapshots show the complete decomposition of the aggregates. As a first instance, it can be observed that in the LTR region, the asphaltene aggregate integrity remains without significant changes, whereas, in the HTR, the most structural changes were obtained. Table 4 lists the molecular structures of some typical compounds observed during the simulation period at 300, 450, and 550 °C. As shown in the table, the number of the species increases with the rising temperature, obtaining 32, 1515, and 4065 species at 300, 450, and 550 °C, respectively. The variety of the molecules was found to be higher at 450 °C due to the breaking of a large amount of complex hydrocarbons.

The species are mainly found in the form of reactive radicals such as  $\text{CHO}_2$  (carboxyl radical),  $\text{OH}$  (hydroxyl radical), and  $\text{CHO}$  (aldehyde radical), and molecules of  $\text{CO}_2$ ,  $\text{H}_2\text{O}$ ,  $\text{CH}_2\text{O}$ , and  $\text{CO}$  are observed as major O-containing gas products that account for most of the gas-phase. Interestingly, at 450 °C, a high level of hydrogen production was found, however, its content decreases to zero at the end of heating, indicating that it has been used to stabilize previously cracked free radicals.

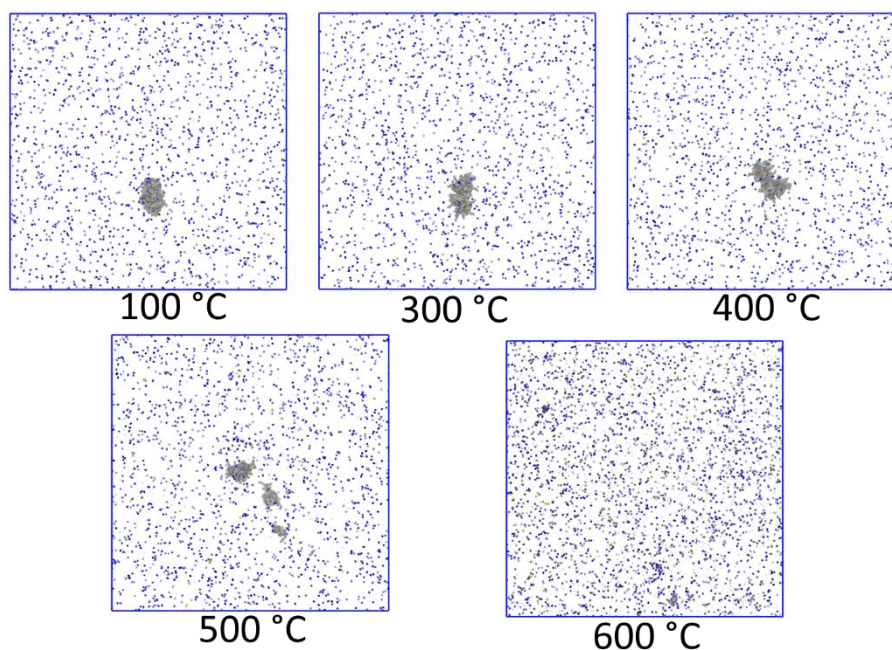


**Figure 7.** Snapshot of the molecular configuration of the reactive MD simulations between 100 and 600 °C.

**Table 3.** Summary of amount of gas products and remained structures from heat-up ReaxFF MD simulation of asphaltene pyrolysis between 300 and 550 °C at 0.084 MPa.

300 °C		450 °C		550 °C	
Specie	amount	Specie	amount	Specie	amount
C <sub>6</sub> H <sub>10</sub> S	1	CN	39	CN	1754
H <sub>2</sub>	5	HN	16	CHN	95
C <sub>3</sub> H <sub>7</sub>	1	CHN	6	C <sub>2</sub>	77
C <sub>6</sub> H <sub>11</sub>	1	C <sub>2</sub>	290	CH <sub>3</sub>	421
C <sub>9</sub> H <sub>19</sub> N	1	CH <sub>3</sub>	17	C <sub>2</sub> H <sub>4</sub>	62
H <sub>2</sub> S	1	C <sub>2</sub>	112	H	24
H <sub>2</sub> C <sub>2</sub> O	1	C <sub>2</sub> H <sub>4</sub>	24	C <sub>2</sub> H	999
HN	5	H	604	HS	27
H <sub>2</sub> N	1	C <sub>2</sub> H	51	C <sub>5</sub> H <sub>12</sub>	118
C <sub>4</sub> H <sub>9</sub>	1	H <sub>2</sub> SN	1	C <sub>2</sub> H <sub>2</sub>	1
CH <sub>2</sub>	1	HS	10	C	136
C <sub>2</sub> H <sub>5</sub>	1	C <sub>5</sub> H <sub>12</sub>	1	CH	24
HS	1	C <sub>7</sub> H <sub>15</sub>	1	CHO	36
CH <sub>2</sub> N	1	C	83	H <sub>2</sub>	1
C <sub>5</sub> H <sub>11</sub> SC	1	C <sub>3</sub> H <sub>4</sub>	2	C <sub>10</sub> H <sub>21</sub>	186
C <sub>134</sub> H <sub>136</sub> O <sub>6</sub> N <sub>2</sub> S <sub>2</sub>	1	CH	19	CO	27
C <sub>71</sub> H <sub>65</sub> O <sub>3</sub> N <sub>2</sub> S	1	CHO	3	C <sub>4</sub> H <sub>8</sub>	45
C <sub>72</sub> H <sub>69</sub> O <sub>3</sub> NS	1	C <sub>6</sub> H <sub>10</sub> S	1	HO	4
C <sub>72</sub> H <sub>70</sub> O <sub>3</sub> N <sub>3</sub>	1	C <sub>10</sub> H <sub>21</sub>	1	C <sub>7</sub> H <sub>15</sub> N	3
C <sub>144</sub> H <sub>138</sub> O <sub>6</sub> N <sub>3</sub> S <sub>2</sub>	1	H <sub>2</sub>	92	C <sub>2</sub> H <sub>5</sub>	1
C <sub>70</sub> H <sub>62</sub> O <sub>3</sub> N <sub>2</sub>	1	CO	41	CH <sub>2</sub>	5
C <sub>72</sub> H <sub>67</sub> O <sub>3</sub> NS	1	C <sub>2</sub> H <sub>2</sub>	4	C <sub>3</sub> H <sub>6</sub>	6

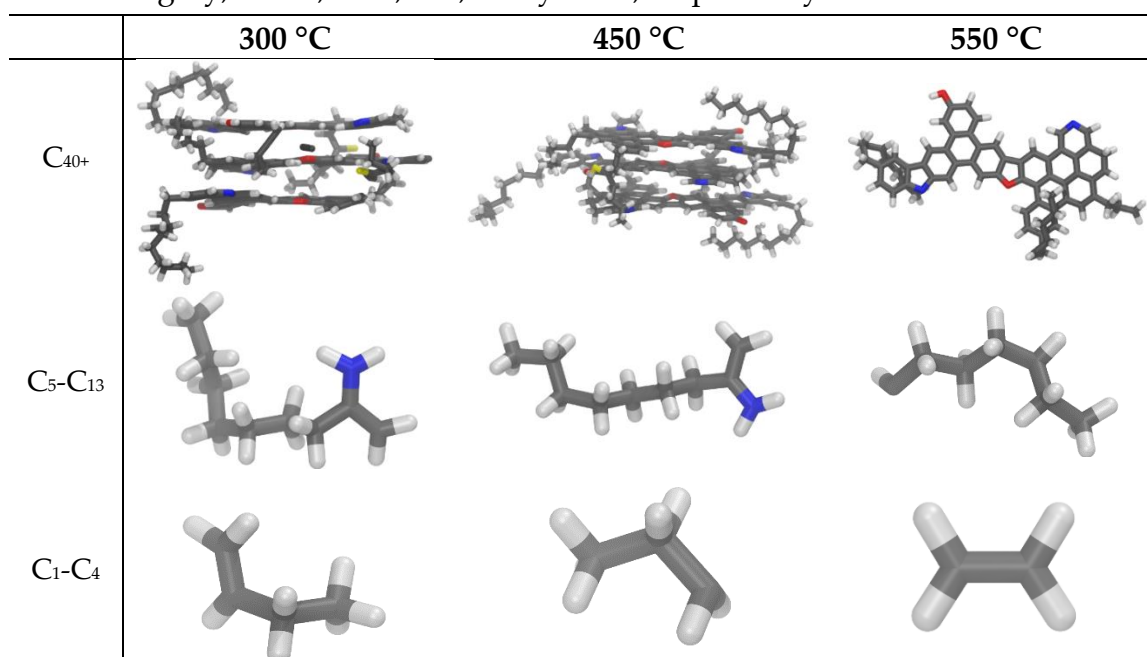
C <sub>336</sub> H <sub>294</sub> O <sub>14</sub> N <sub>8</sub> S <sub>3</sub>	1	CH	20	S	1
C <sub>135</sub> H <sub>115</sub> O <sub>6</sub> N <sub>4</sub> S	1	HO	4	C <sub>3</sub> H <sub>7</sub>	1
		C <sub>4</sub> H <sub>9</sub>	1	CH <sub>4</sub>	1
		O	5	H <sub>2</sub> O	1
		C <sub>7</sub> H <sub>15</sub> N	1	C <sub>6</sub> H <sub>12</sub>	2
		CHS	2	CHS	1
		CH <sub>2</sub>	11	CH <sub>2</sub> N	1
		C <sub>3</sub> H <sub>6</sub>	3	O	1
		HN <sub>2</sub>	3	C <sub>5</sub> H <sub>12</sub> N	1
		C <sub>2</sub> H <sub>3</sub> S	1	C <sub>9</sub> H <sub>19</sub>	1
		C <sub>3</sub> H <sub>7</sub>	3	C <sub>2</sub> H <sub>3</sub>	1
		C <sub>5</sub> H <sub>11</sub>	1	C <sub>58</sub> H <sub>38</sub> O <sub>2</sub> N <sub>2</sub>	1
		C <sub>2</sub> H <sub>5</sub>	6		
		C <sub>6</sub> H <sub>11</sub>	1		
		H <sub>2</sub> O	1		
		C <sub>2</sub> H <sub>3</sub>	1		
		CH <sub>2</sub> N	4		
		C <sub>9</sub> H <sub>19</sub> N	1		
		H <sub>2</sub> N	1		
		C <sub>4</sub>	1		
		S	10		
		C <sub>2</sub> H <sub>2</sub> O	1		
		C <sub>3</sub>	2		
		C <sub>4</sub> H <sub>9</sub> N	1		
		CH <sub>2</sub>	1		
		C <sub>9</sub> H <sub>19</sub>	1		
		C <sub>4</sub> H <sub>4</sub>	1		
		C <sub>5</sub> H <sub>11</sub> N	1		
		C <sub>72</sub> H <sub>65</sub> O <sub>3</sub> N <sub>2</sub> S	1		
		C <sub>68</sub> H <sub>58</sub> O <sub>3</sub> N <sub>2</sub>	1		
		C <sub>72</sub> H <sub>68</sub> O <sub>3</sub> N <sub>2</sub>	1		
		C <sub>66</sub> H <sub>57</sub> O <sub>2</sub> N	1		
		C <sub>124</sub> H <sub>90</sub> O <sub>6</sub> N <sub>3</sub> S	1		
		C <sub>63</sub> H <sub>48</sub> O <sub>3</sub> N	1		
		C <sub>71</sub> H <sub>57</sub> O <sub>3</sub> N <sub>2</sub>	1		
		C <sub>67</sub> H <sub>54</sub> O <sub>3</sub> N <sub>2</sub>	1		

Table 4 illustrates representative compounds observed at 300, 450, and 550 °C via ReaxFF MD classified in C<sub>1</sub>-C<sub>4</sub>, C<sub>5</sub>-C<sub>13</sub>, and C<sub>40+</sub>. Compounds between C<sub>14</sub>-C<sub>40</sub> were not found at these temperatures. These structures may be considered as the representative pyrolysis product cursors of asphaltene's structure based on the constructed model in this paper.

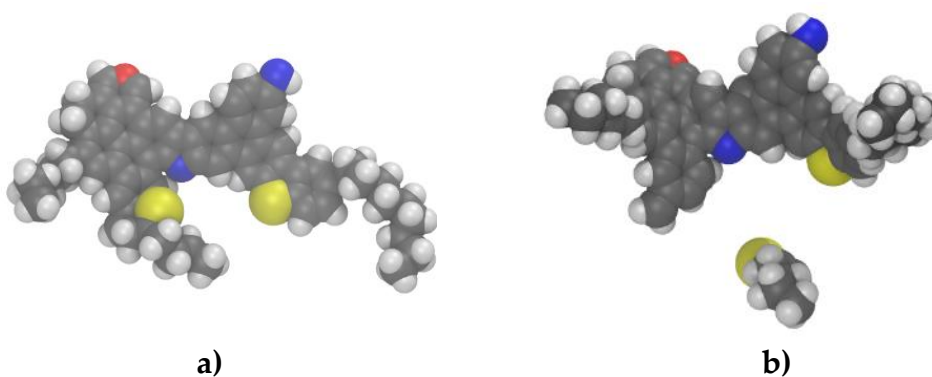
The structure presented at 450 °C (C<sub>124</sub>H<sub>90</sub>O<sub>6</sub>N<sub>3</sub>S) represents the coke generated under the experimental conditions. The molecule is characterized by a higher aromaticity and condensation degree than the asphaltene molecule. The molecular weight was found in 1760 g mol<sup>-1</sup>, the H/C ratio at 0.55, and the DBE at 81.5.



**Table 4.** Molecular structures of products during pyrolysis simulations via ReaxFF MD at 300, 450, and 550 °C and 0.084 MPa. C, H, N, O, and S atoms are shown in gray, white, blue, red, and yellow, respectively.



Finally, to elucidate asphaltene thermal cracking, a simple molecule was selected to show. The pyrolysis reaction pathway followed by the B-asphaltene during pyrolysis is shown in Figure 8. Panel a shows the asphaltene molecule at the beginning of heating. A small aliphatic chain containing a thioether functional group is initially cleaved from the asphaltene. Subsequently, in panels c and d, the breakage of longer aliphatic chains is generated, producing light hydrocarbons such as C<sub>2</sub>H<sub>4</sub> and C<sub>2</sub>H<sub>6</sub>. In panel e, the aromatic nucleus with N, O, and S heteroatoms is observed. Subsequently, the aromatic nucleus and aromatic oxygen species breakdown occur, releasing gases such as CO. Finally, the opening of the aromatic nucleus takes place in the reaction, releasing the aromatic group of nitrogen, to finally break the entire aliphatic chain and generating sulfur and nitrogen gases.



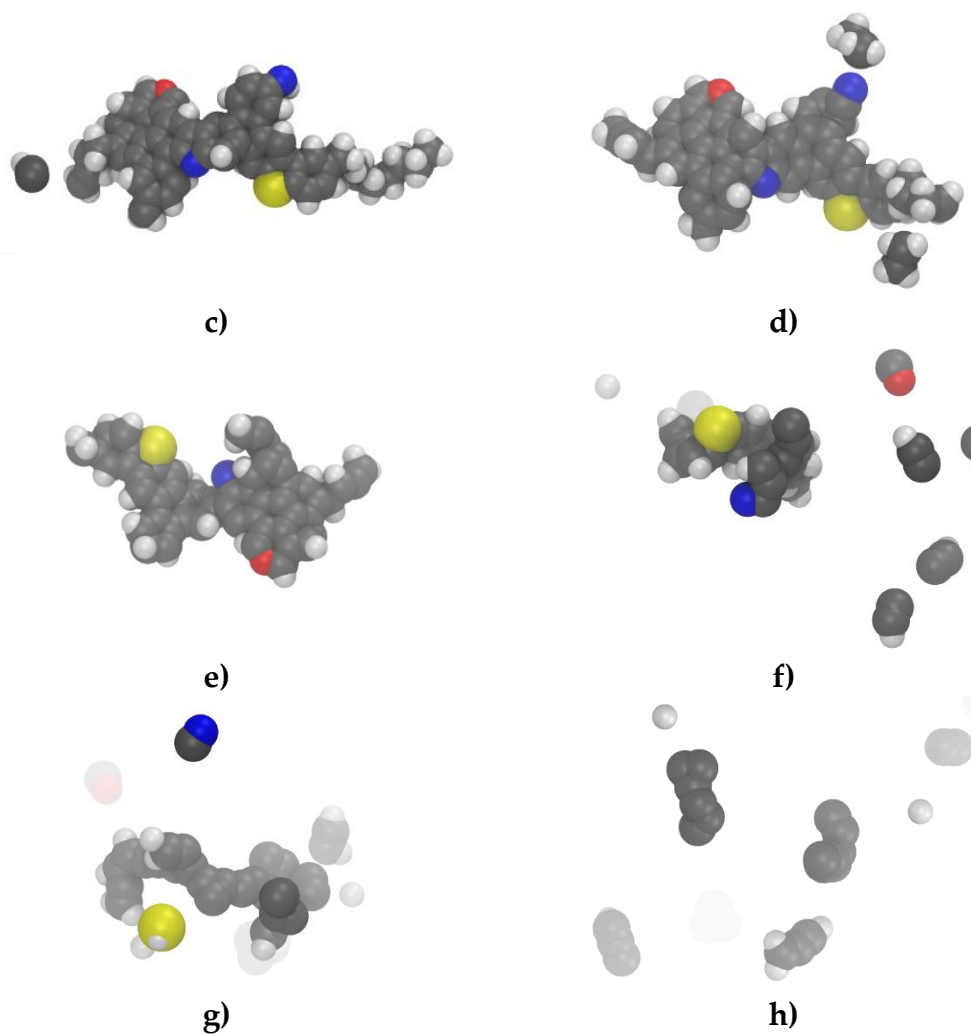


**Figure 8.** Reaction pathway of the B-asphaltene molecule during pyrolysis simulations via ReaxFF. C, H, N, O, and S atoms are shown in gray, white, blue, red, and yellow, respectively.

## 5. Conclusions.

This work provides the first experimental and theoretical insights on asphaltene pyrolysis at low and high pressure catalyzed by ceria nanoparticles. Experimentally, it was discovered that asphaltene decomposition under a non-reactive atmosphere is reduced by pressure rises. Similarly, the amount of coke generated increases with pressure obtaining the following values: 8.0% at 0.084 MPa, 10% at 3.0 MPa, and 11.0% at 6.0 MPa. In the presence of CeO<sub>2</sub> nanoparticles, the thermal cracking of asphaltenes occurred at lower temperatures, decomposing more than 38% during the LTR at 6.0 MPa and 60%



at 0.084 MPa. The effective activation energy was reduced from 332 KJ mol<sup>-1</sup> to 228 KJ mol<sup>-1</sup> at 6.0 MPa when nanoparticles assisted the pyrolysis. Moreover, the obtained thermodynamic data showed a decrease in the enthalpy and entropy of activation of asphaltene pyrolysis in the presence of ceria-based nanoparticles. Molecular dynamic calculations successfully reproduced the experimental results, obtaining that the asphaltene aggregate integrity remains unchanged during the LTR, and the most pronounced differences occur in the HTR.

## References.

- (1) Liu, D.; Hou, J.; Luan, H.; Pan, J.; Song, Q.; Zheng, R. Coke yield prediction model for pyrolysis and oxidation processes of low-asphaltene heavy oil. *Energy Fuels* **2019**, *33* (7), 6205.
- (2) Salehzadeh, M.; Husein, M. M.; Ghotbi, C.; Dabir, B.; Taghikhani, V. In-depth characterization of light, medium and heavy oil asphaltenes as well as asphaltenes subfractions. *Fuel* **2022**, *324*, 124525.
- (3) Medina, O. E.; Gallego, J.; Cespedes, S.; Nassar, N. N.; Montoya, T.; Cortés, F. B.; Franco, C. A. Effect of pressure on thermo-oxidative reactions of saturates, aromatics, and resins (S-Ar-R) from extra-heavy crude oil. *Fuel* **2021**, 122596.
- (4) Bueno, N.; Mejía, J. M. Numerical verification of in-situ heavy oil upgrading experiments and thermal processes for enhanced recovery. *Fuel* **2022**, *313*, 122730.
- (5) Wang, X.; Sun, X.; Luo, C.; Zhang, F.; Xu, B. Large-scale triaxial experimental investigation of geomechanical dilation start-up for SAGD dual horizontal wells in shallow heavy oil reservoirs. *Journal of Petroleum Science and Engineering* **2021**, *203*, 108687.
- (6) Jennings, J.; Growney, D.; Brice, H.; Mykhaylyk, O.; Armes, S. Application of scattering and diffraction techniques for the morphological characterization of asphaltenes. *Fuel* **2022**, *327*, 125042.
- (7) Zhao, S.; Pu, W.-F.; Su, L.; Shang, C.; Song, Y.; Li, W.; He, H.-Z.; Liu, Y.-G.; Liu, Z.-Z. Properties, combustion behavior, and kinetic triplets of coke produced by low-temperature oxidation and pyrolysis: Implications for heavy oil in-situ combustion. *Petroleum Science* **2021**, *18* (5), 1483-1491.
- (8) Trejo, F.; Rana, M. S.; Ancheyta, J. Thermogravimetric determination of coke from asphaltenes, resins and sediments and coking kinetics of heavy crude asphaltenes. *Catalysis Today* **2010**, *150* (3-4), 272-278.
- (9) Medina, O. E.; Gallego, J.; Pérez-Cadenas, A. F.; Carrasco-Marín, F.; Cortés, F. B.; Franco, C. A. Insights into the Morphology Effect of Ceria on the Catalytic

Performance of NiO–PdO/CeO<sub>2</sub> Nanoparticles for Thermo-oxidation of n-C<sub>7</sub> Asphaltenes under Isothermal Heating at Different Pressures. *Energy & Fuels* **2021**.

(10) Medina, O. E.; Gallego, J.; Olmos, C. M.; Chen, X.; Cortés, F. B.; Franco, C. A. Effect of multifunctional nanocatalysts on n-C<sub>7</sub> asphaltene adsorption and subsequent oxidation under high-pressure conditions. *Energy & Fuels* **2020**, *34* (5), 6261-6278.

(11) Medina, O. E.; Gallego, J.; Redondo, J. D.; Cortés, F. B.; Franco, C. A. Effect of pressure on the thermo-oxidative behavior of saturates, aromatics, and resins (S-Ar-R) mixtures. *Fuel* **2021**, 122787.

(12) Medina, O. E.; Gallego, J.; Nassar, N. N.; Acevedo, S. c. A.; Cortés, F. B.; Franco, C. A. Thermo-Oxidative Decomposition Behaviors of Different Sources of n-C<sub>7</sub> Asphaltenes under High-Pressure Conditions. *Energy & Fuels* **2020**, *34* (7), 8740-8758.

(13) Medina, O. E.; Gallego, J.; Rodríguez, E.; Franco, C. A.; Cortés, F. B. Effect of pressure on the oxidation kinetics of Asphaltenes. *Energy & Fuels* **2019**, *33* (11), 10734-10744. Medina, O. E.; Moncayo-Riascos, I.; Pérez-Cadenas, A. F.; Carrasco-Marín, F.; Franco, C. A.; Cortés, F. B. Experimental and theoretical study of the influence of solvent on asphaltene-aggregates thermo-oxidation through high-pressure thermogravimetric analysis. *Fuel* **2023**, *333*, 126491.

(14) Varfolomeev, M. A.; Yuan, C.; Bolotov, A. V.; Minkhanov, I. F.; Mehrabi-Kalajahi, S.; Saifullin, E. R.; Marvanov, M. M.; Baygildin, E. R.; Sabiryanov, R. M.; Rojas, A. Effect of copper stearate as catalysts on the performance of in-situ combustion process for heavy oil recovery and upgrading. *Journal of Petroleum Science and Engineering* **2021**, *207*, 109125. Medina, O. E.; Hurtado, Y.; Caro-Velez, C.; Cortés, F. B.; Riazi, M.; Lopera, S. H.; Franco, C. A. Improvement of steam injection processes through nanotechnology: An approach through in situ upgrading and foam injection. *Energies* **2019**, *12* (24), 4633. Medina, O. E.; Caro-Vélez, C.; Gallego, J.; Cortés, F. B.; Lopera, S. H.; Franco, C. A. Upgrading of extra-heavy crude oils by dispersed injection of NiO–PdO/CeO<sub>2</sub>±δ nanocatalyst-based nanofluids in the steam. *Nanomaterials* **2019**, *9* (12), 1755. Giraldo, L. J.; Medina, O. E.; Ortiz-Pérez, V.; Franco, C. A.; Cortés, F. B. Enhanced Carbon Storage Process from Flue Gas Streams Using Rice Husk Silica Nanoparticles: An Approach in Shallow Coal Bed Methane Reservoirs. *Energy & Fuels* **2023**, *37* (4), 2945-2959.

(15) Medina, O. E.; Galeano-Caro, D.; Brattekkås, B.; Pérez-Cadenas, A. F.; Carrasco-Marín, F.; Cortés, F. B.; Franco, C. A. Simultaneous CO<sub>2</sub> adsorption and

conversion over Ni-Pd supported CeO<sub>2</sub> nanoparticles during catalytic n-C<sub>7</sub> asphaltene gasification. *Fuel* **2023**, *342*, 127733.

(16) Nassar, N. N.; Hassan, A.; Pereira-Almao, P. Thermogravimetric studies on catalytic effect of metal oxide nanoparticles on asphaltene pyrolysis under inert conditions. *Journal of thermal analysis and calorimetry* **2012**, *110* (3), 1327-1332.

(17) Montoya, T.; Argel, B. L.; Nassar, N. N.; Franco, C. A.; Cortés, F. B. Kinetics and mechanisms of the catalytic thermal cracking of asphaltenes adsorbed on supported nanoparticles. *Petroleum Science* **2016**, *13* (3), 561-571.

(18) Khelkhal, M. A.; Lapuk, S. E.; Buzyurov, A. V.; Ignashev, N. E.; Shmeleva, E. I.; Mukhamatdinov, I. I.; Vakhin, A. V. Thermal Behavior of Heavy Oil Catalytic Pyrolysis and Aquathermolysis. *Catalysts* **2022**, *12* (4), 449.

(19) Medina, O. E.; Céspedes, S.; Zabala, R. D.; Franco, C. A.; Pérez-Cadenas, A. F.; Carrasco-Marín, F.; Lopera, S. H.; Cortés, F. B.; Franco, C. A. A Theoretical and Experimental Approach to the Analysis of Hydrogen Generation and Thermodynamic Behavior in an In Situ Heavy Oil Upgrading Process Using Oil-Based Nanofluids. *Catalysts* **2022**, *12* (11), 1349.

(20) Bhoi, S.; Banerjee, T.; Mohanty, K. Molecular dynamic simulation of spontaneous combustion and pyrolysis of brown coal using ReaxFF. *Fuel* **2014**, *136*, 326-333.

(21) Goncalves, R. F.; Iha, B. K.; Rocco, J. A.; Kuznetsov, A. E. Reactive molecular dynamics of pyrolysis and combustion of alternative jet fuels: A ReaxFF study. *Fuel* **2022**, *310*, 122157.

(22) Zhan, J.-H.; Wu, R.; Liu, X.; Gao, S.; Xu, G. Preliminary understanding of initial reaction process for subbituminous coal pyrolysis with molecular dynamics simulation. *Fuel* **2014**, *134*, 283-292.

(23) Franco, C. A.; Nassar, N. N.; Ruiz, M. A.; Pereira-Almao, P.; Cortés, F. B. Nanoparticles for inhibition of asphaltenes damage: adsorption study and displacement test on porous media. *Energy & Fuels* **2013**, *27* (6), 2899-2907.

(24) Senneca, O.; Vorobiev, N.; Wütscher, A.; Cerciello, F.; Heuer, S.; Wedler, C.; Span, R.; Schiemann, M.; Muhler, M.; Scherer, V. Assessment of combustion rates of coal chars for oxy-combustion applications. *Fuel* **2019**, *238*, 173-185. Niksa, S.; Liu, G.-S.; Hurt, R. H. Coal conversion submodels for design applications at elevated pressures. Part I. devolatilization and char oxidation. *Progress in Energy and Combustion Science* **2003**, *29* (5), 425-477.

(25) Ramírez, L.; Moncayo-Riascos, I.; Cortés, F. B.; Franco, C. A.; Ribadeneira, R. Molecular Dynamics Study of the Aggregation Behavior of Polycyclic Aromatic

Hydrocarbon Molecules in n-Heptane–Toluene Mixtures: Assessing the Heteroatom Content Effect. *Energy & Fuels* **2021**, *35* (4), 3119-3129.

(26) Hu, D.; Gu, X.; Cui, B.; Pei, J.; Zhang, Q. Modeling the oxidative aging kinetics and pathways of asphalt: A ReaxFF molecular dynamics study. *Energy & Fuels* **2020**, *34* (3), 3601-3613.

(27) Zhao, S.; Pu, W.; Sun, B.; Gu, F.; Wang, L. Comparative evaluation on the thermal behaviors and kinetics of combustion of heavy crude oil and its SARA fractions. *Fuel* **2019**, *239*, 117-125.

(28) Yuan, C.; Varfolomeev, M. A.; Emelianov, D. A.; Eskin, A. A.; Nagrimanov, R. N.; Kok, M. V.; Afanasiev, I. S.; Fedorchenko, G. D.; Kopylova, E. V. Oxidation behavior of light crude oil and its SARA fractions characterized by TG and DSC techniques: differences and connections. *Energy & fuels* **2018**, *32* (1), 801-808. Kok, M. V.; Gul, K. G. Thermal characteristics and kinetics of crude oils and SARA fractions. *Thermochimica acta* **2013**, *569*, 66-70.

(29) Yuan, C.; Emelianov, D. A.; Varfolomeev, M. A. Oxidation behavior and kinetics of light, medium, and heavy crude oils characterized by thermogravimetry coupled with fourier transform infrared spectroscopy. *Energy & fuels* **2018**, *32* (4), 5571-5580. Hao, J.; Che, Y.; Tian, Y.; Li, D.; Zhang, J.; Qiao, Y. Thermal cracking characteristics and kinetics of oil sand bitumen and its SARA fractions by TG–FTIR. *Energy & Fuels* **2017**, *31* (2), 1295-1309.

(30) Boytsova, A.; Kondrasheva, N.; Ancheyta, J. Pyrolysis kinetics of heavy oil asphaltenes under steam atmosphere at different pressures. *Energy & Fuels* **2018**, *32* (2), 1132-1138.

(31) Deka, K.; Nath, N.; Saikia, B. K.; Deb, P. Kinetic analysis of ceria nanoparticle catalysed efficient biomass pyrolysis for obtaining high-quality bio-oil. *Journal of Thermal Analysis and Calorimetry* **2017**, *130* (3), 1875-1883.

(32) Boytsova, A.; Kondrasheva, N.; Ancheyta, J. Thermogravimetric determination and pyrolysis thermodynamic parameters of heavy oils and asphaltenes. *Energy & Fuels* **2017**, *31* (10), 10566-10575.

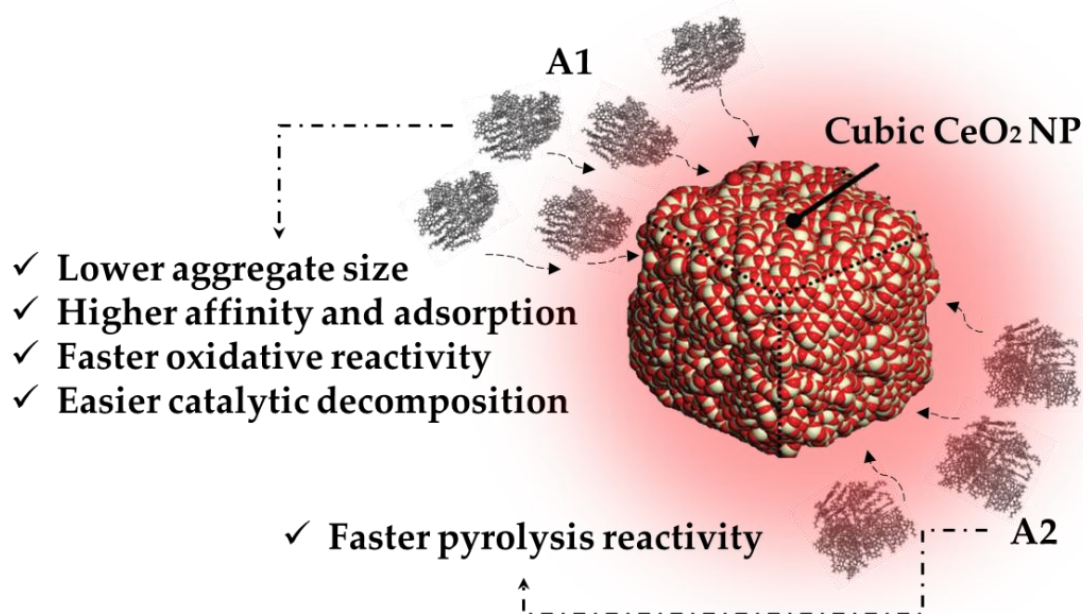
(33) Friend, D.; Huber, M. Thermophysical property standard reference data from NIST. *International journal of thermophysics* **1994**, *15*, 1279-1288. Huber, M. L.; Lemmon, E. W.; Bell, I. H.; McLinden, M. O. The NIST REFPROP database for highly accurate properties of industrially important fluids. *Industrial & Engineering Chemistry Research* **2022**, *61* (42), 15449-15472.

(34) Moncayo-Riascos, I.; Medina, O. E.; Cortés, F. B.; Franco, C. A. Structural-Compositional Effect of Polycyclic Aromatic Hydrocarbons on Thermal-

Oxidative Decomposition at High-Pressure: A Molecular Dynamics and Machine Learning Approach. *Energy & Fuels* **2023**, 37 (4), 2702-2712.

Chapter 11.

# Theoretical and Experimental Study of Adsorption and Catalytic Reactivity of Asphaltene Fractions A1 and A2 over Cubic NiO–PdO/CeO<sub>2</sub> Nanoparticles



Submitted to Journal of Petroleum Science and Engineering: PETROL33238

Impact factor: 5.168

# Theoretical and Experimental Study of Adsorption and Catalytic Reactivity of Asphaltene Fractions A1 and A2 over Cubic NiO–PdO/CeO<sub>2</sub> Nanoparticles

## Abstract

This study focuses on analyzing the aggregation state of A1 and A2 asphaltene subfractions and how it influences the adsorptive and reactivity of ceria-based nanoparticles. To this aim, a molecular dynamics (MD) model was proposed to determine the effect of the asphaltene concentration and structure type (A1 and A2) on the aggregation behavior. Then, batch adsorption experiments were conducted using toluene as a referent solvent and varying asphaltene concentrations between 100 and 1500 mg·L<sup>-1</sup>. Non-catalytic and catalytic experiments were executed at low (0.084 MPa) and high (6.0 MPa) pressure under air and nitrogen atmosphere to analyze their oxidative and pyrolytic responses. MD simulations reveal that the aggregate size increases in the order A1 < A2 which is explained by the higher density of A1. The adsorption affinity of A1-CeO<sub>2</sub> nanoparticles was greater than that of A2-CeO<sub>2</sub> nanoparticles, resulting in a greater amount of A1 asphaltenes adsorbed. Oxidative experiments show that oxygen chemisorption occurs on asphaltenes due to the A1 subfraction; no oxygen chemisorption was observed in A2. This means that the activation energy for A1 decomposition was lower for both catalytic and non-catalytic oxidation. Finally, the non-catalytic pyrolysis of A2 exhibited better thermogravimetric characteristics, including higher mass lost at lower temperatures and less coke at the conclusion of heating because of the different densities between A1 and A2 aggregates. The altered aggregation states of the samples on toluene for adsorption experiments lead to the opposite result when nanoparticles catalyze the reaction. To create catalysts that can enhance the reaction pathway of asphaltene aggregates, it is essential to analyze the adsorptive and catalytic behavior of nanoparticles with both fractions.

## 1. Introduction

Asphaltenes, the most polar and heaviest components of crude oil, tend to aggregate, causing severe and costly problems in production operations, transportation lines, and refining facilities (Akbarzadeh et al., 2007). Characterizing these macromolecular aromatics is challenging because of their incongruity and complex molecular structure. Over the years, various models and mechanisms have been presented to examine asphaltene aggregation and relate it to its chemical cartography (Ignasiak et al., 1977; Semple et al., 1990; Speight, 1994; Strausz, 1989). Some research has been done on the structure of asphaltene, emphasizing matching structural agents with confined experimental data (Abutaqiya et al., 2019; Miller et al., 1998; Murgich et al., 1999; Payzant et al., 1991; Strausz et al., 1999). For this purpose, asphaltenes have been isolated from crude oil, and some of their properties, including spectroscopic properties, molecular mass, and elemental composition, have been investigated. After determining these features, hypothetical structures were proposed according to the experimental data. In addition, many chemical methods were proposed to describe these structures (Ignasiak et al., 1977; Payzant et al., 1991; Strausz, 1989).

Two antagonistic mechanisms known to investigate the aggregation of asphaltenes are Yen Mullins as the colloidal model (Mullins, 2010; Mullins et al., 2007; Mullins et al., 2012) and Gray et al. (2011) as the supramolecular model. In the first model (Yen-Mullins model), it is assumed that asphaltenes first form agglomerates of 6 molecules on a nanoscale and then form clusters of 8 molecules through  $\pi$ -stacking, dipole/dipole, and van der Waals interactions among aromatic cores (Pacheco-Sánchez et al., 2004). However, this model was criticized by Gray et al. (2011), who believed that this model could not analyze all the intricacy of the physical-chemical interactions of asphaltenes. Therefore, they introduced a complex model that relates asphaltene aggregation to  $\pi$ -stacking, van der Waals, Coulomb-centered, and hydrogen bonding interactions.

Based on Saturates, Aromatics, Resins, and Asphaltene (SARA) analysis, asphaltene is soluble in aromatic solvents such as toluene and insoluble in *n*-alkanes such as *n*-heptane (Fan and Buckley, 2002; Qiao et al., 2017). Recently, Acevedo et al. (2007) divided asphaltenes into two different fractions: A1 and A2 based on the *p*-nitrophenol (PNP) method (Acevedo et al., 2007; Acevedo et al., 2004; Gutiérrez et al., 2001). To describe the difference in solubility of these two



groups, they did not emphasize different  $^{13}\text{C}$  NMR aromaticity, molecular mass (Acevedo et al., 2007), or heteroatom quantity (Acevedo et al., 2004; Gutiérrez et al., 2001). Their hypothesis was based on the existence of molecules with rigid and flexible cores in A1 and A2 structures, respectively. The difference between A1 and A2 could be attributed to how the polycyclic units (PCU) are joined. A2 is a stabilizing factor that causes the colloidal behavior of asphaltene, and by being placed in the nuclei composed of A1 molecules, it inhibits the growth of asphaltene aggregates. So far, several researches have been done on asphaltene subgroups and it has been found that although both categories have almost similar molecular mass and chemical composition, their main difference is in the H/C ratio and the double bond equivalent (DBE) in their structures (Gutiérrez et al., 2001; Villegas et al., 2020).

Molecular dynamics simulations are a powerful tool that contributes physical insights about the effect of this structural characteristic (HC ratio and DBE) on aggregation behavior. Santos-Silva et al.(2016) studied the effect of the location of the sulfur atom (S) on asphaltene aggregation. The authors found that the aggregation path is significantly different if the sulfur is in the aromatic core or in the lateral chains. Ramírez et al.(2021) determined the effect of the heteroatom content using the PA3-type asphaltene determined by Schuler et al.(2015) by atomic force microscopy (AFM), in a model solution using toluene, *n*-heptane and heptol (mixture of *n*-heptane and toluene in a mass fraction of 50%). The authors identified that the heteroatom content increases the aggregation size and that PA3-type with sulfur promotes bigger and more stable aggregates compared to those with nitrogen or oxygen. MD simulations have been also conducted to study A1 and A2 subfractions, Villegas et al. (2020) determined the heteroatom content in A1 and A2 subfraction on the aggregation behavior, finding that the oxygen present as hydroxyl or carboxylic acid allows forming larger aggregates. Recently, Villegas et al.(2023) evaluated the aggregation behavior of A1 and A2 subfractions in heptane, toluene, and tetrahydrofuran (THF) by MD simulations. The results indicated that the aggregation behavior is strongly related to the aromaticity of the solution in heptane and toluene, whereas smaller aggregates were obtained for solutions in THF. Acevedo et al.(2023) simulated the aggregation of A1 and A2 subfraction in toluene and THF. The results obtained from the simulations were contrasted with respect to experimental measurements, obtaining reasonable approximations of the hydrodynamic radii and the asphaltene size distributions and their corresponding subfractions A1 and subfraction A2. The authors found that the

highly aromatic island A30 molecular model and the continental type A40 molecular model form open-type (A40) colloids and A30 compact-type colloids. Additionally, adsorptive behaviors of the evaluated species on various surfaces were determined, identifying the tendency of asphaltenes to adsorb in aggregate form and not independently.

Most of the reported studies in the literature are focused on identifying textural and chemical differences of both subfractions, but remains, to our knowledge, their reactivity is still unaddressed (Villegas et al., 2020). The reactivity of asphaltenes is a fundamental property because, during Thermal Enhanced Oil Recovery (TEOR) processes, a large part of this fraction can be transformed into coke, reducing the effectiveness of the technologies. Asphaltenes commonly decompose at temperatures between 400 and 500 °C, which is why many authors have proposed using nanocatalysts, reducing the asphaltene decomposition temperature (Gates et al., 2008; Montoya et al., 2014; Snow, 2011). Nanoparticles (NPs) can act as excellent candidates for asphaltene adsorption (Weissman et al., 1996) while benefiting from a high surface area/volume ratio (Medina et al., 2019g) and high affinity for asphaltene adsorption (Medina et al., 2019a; Solaimany Nazar and Amin, 2017). Besides, they can act as a catalyst to decompose asphaltenes with their extraordinary catalytic activities, resulting in high oil recovery (Marei et al., 2017a; Medina et al., 2019c). NPs` affinity for asphaltenes is improved by functionalizing them with metal oxides, resulting in better adsorption quantity and energy (Hashemi et al., 2012; Nassar, 2010). To enhance the catalytic capacity of NPs, supports were functionalized with element oxides (Hashemi et al., 2012). Until now, several modified and nonmodified NPs like CeO<sub>2</sub> (Medina et al., 2019a; Medina et al., 2019c; Medina et al., 2019d; Medina et al., 2019f), TiO<sub>2</sub> (Nassar et al., 2015), SiO<sub>2</sub> (Franco et al., 2016; Franco et al., 2014), Al<sub>2</sub>O<sub>3</sub> (Nassar et al., 2015) and various nanocrystals (active phases) (Franco et al., 2016; Franco et al., 2014; Nassar et al., 2015) such as NiO, PdO, Fe<sub>2</sub>O<sub>3</sub>, Co<sub>3</sub>O<sub>4</sub>, and CuO, have been examined. Some authors used the functionalized supports with metal oxides to improve thermal-enhanced oil recovery (TEOR) processes (Amrollahi Biyouki et al., 2018; Kosari et al., 2017; Marei et al., 2017b; Zhang et al., 2018; Zhang et al., 2019). For example, although nickel oxide (NiO) NPs reduce the oxidation temperature of asphaltenes from 450 to almost 325 °C (Nassar et al., 2011), silica (Si) NPs act as a support in the low concentrations of NiO and serve a catalytic role, decomposing asphaltenes at 300 °C (Franco et al., 2013a). Some researchers concluded that the high content of metal oxides like those of iron could increase the adsorbed

asphaltenes (Carbognani, 2000; Carbognani et al., 1999), and some others showed that high concentrations of *n*-heptane in the nanosolutions increase the adsorption of asphaltene (Kazemzadeh et al., 2015). Madrid et al. (Arias-Madrid et al., 2020) used Si NPs and functionalized them with iron, nickel, and molybdenum oxides to investigate the impact of NPs' surface area, adsorbed asphaltene, and subsequent asphaltene oxidation in the presence of NPs. They optimized the quantity of each metal and supported it in such a way that they achieved the maximum and minimum amount of asphaltene adsorption and activation energy, respectively (Arias-Madrid et al., 2020). Among all investigated NPs, CeO<sub>2</sub>-based nanocatalysts have proved a decent catalytic performance (Medina et al., 2019b; Medina et al., 2019c), which is attributed to the easy Ce<sup>4+</sup>/Ce<sup>3+</sup> exchange (Kašpar et al., 1999; Martínez-Arias et al., 2000). The redox properties of the support increase the interaction with steam/air molecules and asphaltene heteroatoms and consequently the reaction capacity of CeO<sub>2</sub>-based nanocatalysts (Medina et al., 2019c), while the strong support metal interactions (SSMI) which provide transition and noble elements are the reason for its good catalytic performance (Medina et al., 2019c; Razeghi et al., 2010). Although various couples of element oxides like cobalt- palladium (Co-Pd), nickel-palladium (Ni-Pd), and iron-palladium (Fe-Pd) have been supported on CeO<sub>2</sub> to decompose asphaltene, our results showed that Ni and Pd are more successful in transferring oxygen vacancies between the bulk and the surface of nanocatalysts, increasing the catalytic activity (Medina et al., 2021b). Besides, our experiments illustrated that *n*-C<sub>7</sub> asphaltene decomposition depends on the morphology of CeO<sub>2</sub> and cubic ones were more successful than orthorhombic and spherical (Medina et al., 2021b). Therefore, in this study, cubic ceria NPs were considered as a promising support for Ni-Pd element oxides in *n*-C<sub>7</sub> asphaltene decomposition.

Despite the strong research and applications of NPs in TEOR processes, all studies have investigated thermal degradation and oxidation of a complete structure of asphaltene molecule. No research has been done on A1 and A2 subgroups. Analyzing the adsorptive and catalytic behavior of nanoparticles with both fractions is of vital help to developing catalysts that can improve the reaction pathway of asphaltene aggregates. This study tried for the first time to investigate the adsorption and catalytic reaction of *n*-C<sub>7</sub> asphaltenes with emphasis on the A1 and A2 subgroups using cubic CeO<sub>2</sub>-based nanoparticles under low (0.084 MPa) and high-pressure conditions (6.0 MPa). For this purpose, the chemical structures presented by Villegas et al. were considered (Villegas et

al., 2020). The main difference between these structures is the side chain (*n*-octyl) in A2 and two alkyl cycles in A1. In this way, the chemical properties of the asphaltene molecules were related to the proposed subgroups (A1 and A2), and a better understanding of the asphaltene absorption and oxidation/pyrolysis process was obtained.

## 2. Methodology

### 2.1. Materials

Asphaltenes were isolated from Hamaca crude oil of 9.0° API, 13.7% asphaltene content, 38% A1 content, 58% A2 content, and 3% trapped compounds (TC). Asphaltene separation was done considering the ASTM D6560-17 standard, widely reported in the literature (Acevedo and Castillo, 2023; Franco et al., 2013b). *n*-Heptane 99% (Sigma-Aldrich, St. Louis, MO) and Toluene 99.5% (Merk KgaA, Darmstadt, Germany) were purchased to perform asphaltene extraction and adsorption tests, respectively.

Pure nitrogen gas (NTC 2561, CRYOGAS, Colombia) was used to perform high-pressure thermogravimetric experiments.

Also, doped cubic ceria nanoparticles with 1.0 wt.% of Ni and Pd (C-NiPdCe) were considered in this study for assessing asphaltene adsorption and reactivity. Nanoparticles were prepared and fully characterized in our previous study (Medina et al., 2021c). Tables 1 and 2 summarize the textural and chemical properties of the nanoparticles.

**Table 1.** Textural properties estimated of synthesized C-NiPdCe nanoparticles. Data taken from (Medina et al., 2021c). Copyright ASC (2021).

Sample	$S_{BET}$ ( $m^2 \cdot g^{-1}$ )	Wo(CO <sub>2</sub> )	Lo(CO <sub>2</sub> )	Wo(N <sub>2</sub> )	Lo(N <sub>2</sub> )	V <sub>0.95</sub>	V <sub>meso(BJH)</sub>
C-NiPdCe	25.5	0.19	0.61	0.15	0.77	0.31	0.053

**Table 2.** Chemical properties estimated of synthesized and C-NiPdCe nanoparticles. Data taken from (Medina et al., 2021c). Copyright ASC (2021).

Sample	Crystallite size <sup>a</sup> (nm)	Lattice Parameter <sup>b</sup> (nm) x 10 <sup>-2</sup>	Ce <sup>3+</sup> (%)	O <sub>ads</sub> (%)	O <sub>latt</sub> (%)	Ni <sup>2+</sup> (NiO) (%)	Pd <sup>2+</sup> (%)	I <sub>(598+1172)</sub> /I <sub>458</sub>
C-NiPdCe	12.4	54.01	52.4	84.8	15.2	33.5	62.3	0.25

I<sub>(598+1172)</sub>/I<sub>458</sub> refers to the oxygen vacancies content.

## 2.2. Asphaltene fractionation

After being dissolved in PNP-saturated cumene, the asphaltenes were refluxed for six hours. Subfraction A1 precipitates as an insoluble asphaltene-PNP complex over the course of the 8-day resting period at room temperature, while subfractions A2 and TC persist in solution. The solid subfractions were obtained following the filtration steps, cumene reduced pressure distillation, and subsequent washing with n-heptane. By repeatedly washing with a 5% aqueous NaOH solution, the PNP was eliminated until colorless washing was achieved.

The average composition and characteristics of the A1 and A2 subfractions are identical (Gutiérrez et al., 2001), with the most significant differences being the H/C ratio, which is 1.023 for A1 and 1.116 for A2, and the Double Bond Equivalent (DBE), which is 22 for A1 and 20 for A2 .

## 2.3. Structural models of asphaltenes

One of the most contentious issues in petroleum chemistry is asphaltene structure. A single aromatic core or island versus multiple aromatic cores or an archipelago is how the aromatic cores of the asphaltene molecule are organized, and this is the subject of contention. The A1 and A2 subfractions are represented by the structures of the considered asphaltene molecular models. The key structural differences between A1 and A2 subfractions include a lower H/C ratio and a double bond equivalent (DBE) for A1. As a result, molecules from the A1 subfraction are stiffer than those from the A2 subfraction. Two asphaltene representative structures that fit the aforementioned criteria were proposed by Acevedo et al.(2018). In this study, we took into account the models used in an earlier study (Villegas et al., 2020) and the molecules were optimized based on the Clar's theory of the sextet. Figure 1 shows the molecular structures of the HC skeletons.

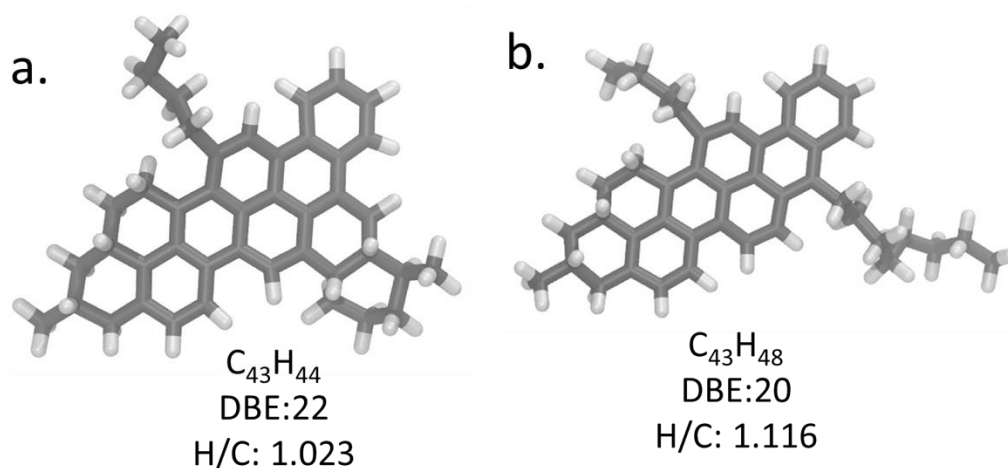


**Figure 1.** Molecular structures of the species evaluated in MD simulations for the subfraction a)A1 and b)A2. Reproduced from (Villegas et al., 2020). Copyright (2020).

#### 2.4. Molecular dynamics

To fully understand asphaltene adsorption and reactivity on nanoparticles, it is essential to examine how asphaltene aggregates behave in the experiment-related solvent. The MD model focused on analyzing the effect of the molecular characteristics of the A1 and A2 fractions on the aggregation behavior. In total, four model solutions were built using the A1 and A2 fractions (shown in Figure 1) separately, dissolved in toluene at two different concentrations (1 and 7 wt.%).

The well-known potential Optimized Potentials for Liquid Simulations (OPLS) forcefield, which has been extensively used to study the aggregation behavior of asphaltenes in model solutions, was used to describe asphaltenes and toluene. A Lennard-Jones 12-6 model was used to describe interactions of the Van der Waals type. The Coulomb model was used to represent electrostatic interactions. Harmonic models were used to represent the bonds and angles, and the Watkins and Jorgensen model was applied to explain the dihedral angle interactions. As shown in Table 3, 27 asphaltene molecules were taken into account for each system, because prior research suggested that this system size allows for an accurate description of the behavior of asphaltene aggregation. Three steps led to the systems being balanced. In order to relax the initial configuration and prevent the system from remaining in a local minimum of energy, all systems were initially initialized at a density of  $0.4 \cdot \text{cm}^{-3}$  using an NVT (constant number of molecules, volume, and temperature) at 298 K during 2 ns with a timestep of 1 fs. Secondly, an NPT (constant number of molecules, volume, and pressure) at 1 atm, over 3 ns with a timestep of 1 fs was used to calculate the

density of equilibrium. Finally, another NVT ensemble was used to fully equilibrated each system during 25 ns with a timestep of 1.5 fs.

**Table 3.** Setup of the MD model of A1 and A2 solution in toluene.

Asphaltene type	Number of solvent molecules	Asphaltene concentration (wt%)	Box of simulation dimension (Å <sup>3</sup> )
A1	16443	1	142.8 x 142.8 x 142.8
A2	16443		74 x 74 x 74
A1	2187	7	142.8 x 142.8 x 142.8
A2	2187		74.1 x 74.1 x 74.1

Five evaluation and comparison parameters were used to assess the changes in the aggregation state of each system. The first is determined by dividing the total number of asphaltene molecules (27) by the total number of aggregates, and it relates to the average size of aggregates. It was defined that two asphaltene molecules aggregate when the distance between the carbons of the aromatic nucleus is less than or equal to 4.5 Å. Therefore, the number of aggregates the number of aggregates was tracked throughout the simulation. In order to estimate the volume of the aggregates formed, the average radius of gyration of the aggregates was calculated as a second evaluation parameter. Equation (1) was used to calculate the gyration radii, where  $N$  is the total number of asphaltene aggregates,  $r_i$ , and  $r_{cm}$  are the position of a defined atom and the position of the center of mass of the asphaltene aggregate, respectively.

$$R_g^2 = \frac{1}{N} \sum_i m_i (r_i - r_{cm})^2 \quad (1)$$

The coordination number between the mass centers of the asphaltene molecules—which was derived from the radial distribution function—is the third evaluation parameter. The fourth parameter included calculations for the non-bonding interaction energies of asphaltene-asphaltene and asphaltene-toluene. The average non-bonding interaction energies between the specified groups of atoms (asphaltenes and toluene) were used to calculate the interaction energies. Finally, the fourth parameter for evaluation and comparison is the solubility parameter of Hildebrand (Equation 2) and Hasen (Equation 3) (Belmares et al., 2004; Sha et al., 2021), which characterizes the solubility behavior of the asphaltene fractions evaluated (A1 and A2). It should be mentioned that the molecular potential used in this study has no implicit representation of

hydrogen bond formation, only dispersion and polar contribution, so the results are an approximation to understand the aggregation phenomenon, since it has been shown that the hydrogen bonds are very important and affect the aggregation and solubility. As a result, this contribution was calculated by subtracting the total solubility parameter (Hildebrand) from the sum of the dispersion and polar contributions.

$$\delta_i = \sqrt{\frac{E_{coh}}{v_m}} = \sqrt{\frac{\Delta H_v - RT}{v_m}} \quad (2)$$

$$\delta_t^2 = \delta_D^2 + \delta_P^2 + \delta_H^2 \quad (3)$$

All simulations were run using the free software LAMMPS, and VMD was used to visualize the simulation images as well as calculate the radial distribution functions and coordination numbers. Geometric mixing rules were used to determine the cross-interaction parameters between atoms of different species. The cutoff radius was set to 16 Å for both electrostatic and van der Waals interactions. Long-range electrostatic interactions were calculated using the particle-particle-particle-mesh method. The temperature and pressure were controlled by the Nosé-Hoover thermostat and barostat, respectively.

## 2.5. Asphaltene adsorption

Adsorption experiments were accomplished in a batch medium based on the method described in previous works (López et al., 2020; Medina et al., 2020) for concentrations of asphaltene between 100 and 1500 mg·L<sup>-1</sup>. Since both A<sub>1</sub> and A<sub>2</sub> fractions are soluble in toluene, the adsorption experiments were performed in toluene. The ratio of the dry mass of NPs to the volume of the solution was 10 g·L<sup>-1</sup> (Medina et al., 2020).

To calculate the adsorbed amount of *n*-C<sub>7</sub> asphaltene (*q*, mg·m<sup>-2</sup>), the mass balance equation (Equation 4) was used.

$$q = \frac{(C_0 - C_e)}{A.M} \quad (4)$$

where C<sub>0</sub> (mg·L<sup>-1</sup>) and C<sub>e</sub> (mg·L<sup>-1</sup>) show the concentration of *n*-C<sub>7</sub> asphaltene in the beginning and after adsorption, respectively. The volume of the solution (L) and the measured surface area per mass of NPs (m<sup>2</sup>·g<sup>-1</sup>) were denoted as M



and  $A$ , respectively. To analyze the adsorption isotherms, a temperature-dependent model including three independent variables ( $H$ ,  $K$ , and  $q_m$ ) was used. In this solid-liquid equilibrium model,  $H$  ( $\text{mg}\cdot\text{g}^{-1}$ ),  $K$  ( $\text{g}\cdot\text{g}^{-1}$ ), and  $q_m$  ( $\text{mg}\cdot\text{m}^{-2}$ ) illustrated the adsorption affinity of asphaltenes on the surface of NPs, the rapid association of asphaltenes after occupying the primary sites, and the maximum capacity of adsorption, respectively (Montoya et al., 2014). There is more information about phase equilibrium and  $i$ -mer formation in the published paper by Montoya et al (2014).

## 2.6. Asphaltene catalytic oxidation

This part has been examined from two points of view (i) the role of asphaltene fraction (A1 and A2) on the oxidative response of asphaltene at high pressure (6.0 MPa) and (ii) catalytic oxidation of asphaltene fractions adsorbed on the surface of the functionalized NPs (C-NiPdCe) under high-pressure conditions.

Thermogravimetric analyses (TGA) were accomplished using a high-pressure TGA device (TGA 750 Instruments, Inc, Hullhorst, Germany) to investigate the oxidation/decomposition of  $n\text{-C}_7$  asphaltenes and asphaltene adsorbed on the surface of the functionalized NPs under high-pressure conditions. The samples were heated from 100 to 800 °C with a constant heat flux ( $10\text{ °C}\cdot\text{min}^{-1}$ ) under a specific flow rate of air gas ( $100\text{ ml}\cdot\text{min}^{-1}$ ). For catalytic experiments, it was tried to use NPs with the same ratio of adsorbed asphaltene to surface area ( $0.2\text{ mg}\cdot\text{m}^{-2}$ ). A detailed description of the routine is found in our previous work (Medina et al., 2020).

## 2.7. Asphaltene catalytic pyrolysis

Asphaltene pyrolysis was measured at high-pressure using a similar set-up of the previous section. Here, the non-adsorbed asphaltene and adsorbed asphaltene on Ce-NiPdCe were heated from 100 to 800 °C with a constant heat flux ( $10\text{ °C}\cdot\text{min}^{-1}$ ) under a specific flow rate of nitrogen gas ( $100\text{ ml}\cdot\text{min}^{-1}$ ).

## 2.8. Activation energy analysis

A single power-law model derived from the experimental results was used to describe the decomposition of the  $n\text{-C}_7$  asphaltene and investigate the catalytic effect of NPs. In this model, the instantaneous reactivity  $\mathbb{R}$  of the adsorbed material was considered between 100 and 800 °C at 6.0 MPa (Niksa et al., 2003; Senneca et al., 2019).

Equation 5 shows the conversion of the *n*-C<sub>7</sub> asphaltene.

$$\theta = \frac{m_0 - m(t)}{m_0 - m_\infty} \quad (5)$$

where  $m_0$ ,  $m_t$ , and  $m_\infty$  are the asphaltene mass at the beginning, time  $t$ , and the end of each region.

The instantaneous reactivity of asphaltenes during the pyrolysis/oxidation process can be described as Equation 6 (Liu and Niksa, 2004).

$$r = \frac{d\theta}{dt} = \frac{1}{f(\theta)} = k_0 \exp\left(\frac{-E_a}{R_{gas}T}\right) P_{O_2}^n \quad (6)$$

where  $f(\theta)$  is a function expressing the evolution of the conversion degree of the asphaltenes.  $K_0$  ( $s^{-1} \cdot bar^{-n}$ ) and  $E_a$  ( $Kj \cdot mol^{-1}$ ) are the kinetic parameters of pre-exponential factor and apparent activation energy, respectively. The partial pressure (bar) of the O<sub>2</sub>/N<sub>2</sub> gas, the ideal gas constant ( $J \cdot mol^{-1} \cdot K^{-1}$ ), and the order of the reaction were shown as  $P$ ,  $R$ , and  $n$ , in order

To integral  $f(\theta)$  in the non-isothermal thermogravimetric equation (Equation 6), Ozawa-Wall-Flynn estimation was used, and  $\beta$  ( $^{\circ}C \cdot min^{-1}$ ), the heating rate was considered equal to  $Dt/dt$  (Niksa et al., 2003) (Equation 7).

$$\ln \left[ \frac{\beta F(\theta)}{P_{O_2}^n T^2} \right] = \ln \left( \frac{k_0 R}{E_a} \right) - \frac{E_a}{RT} \quad (7)$$

Based on the volumetric model, Equation (8) is obtained:

$$F(\theta) = \int \frac{d\theta}{f(\theta)} = -\ln(1 - x) \quad (8)$$

According to the slope and intercept of the Equation (8), the activation energy ( $E_a$ ) and pre-exponential factor ( $k_0$ ) will be obtained.

### 3. Results and discussion

#### 3.1. Molecular dynamics

Figure 2 depicts the results of the solubility parameter evaluations performed to characterize the solubility behavior of asphaltenes A1 and A2. A2

has a higher dispersion (dD) and polar (dP) contribution than A1, while A1 has a higher H-bonding (dH) contribution than A2. It should be noted that dH was calculated using the total solubility parameter (dT, Equation 1), dD, and dP (directly determined from the MD simulations).

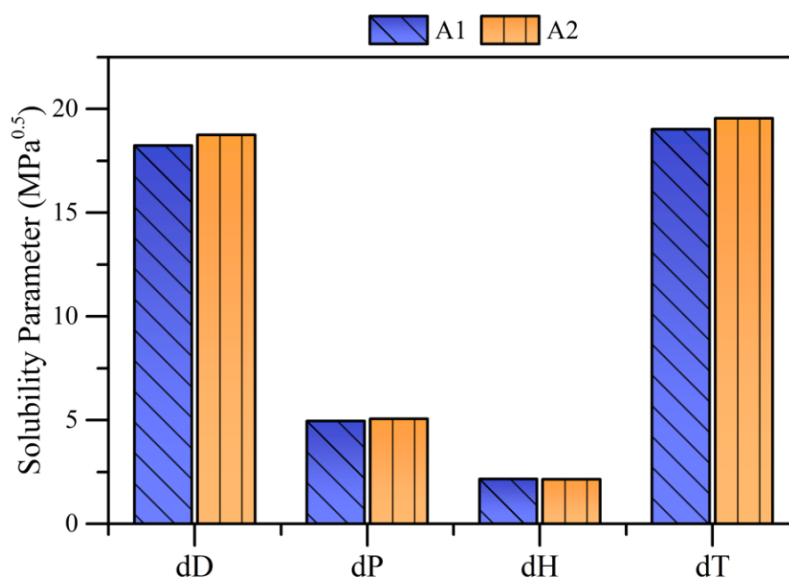
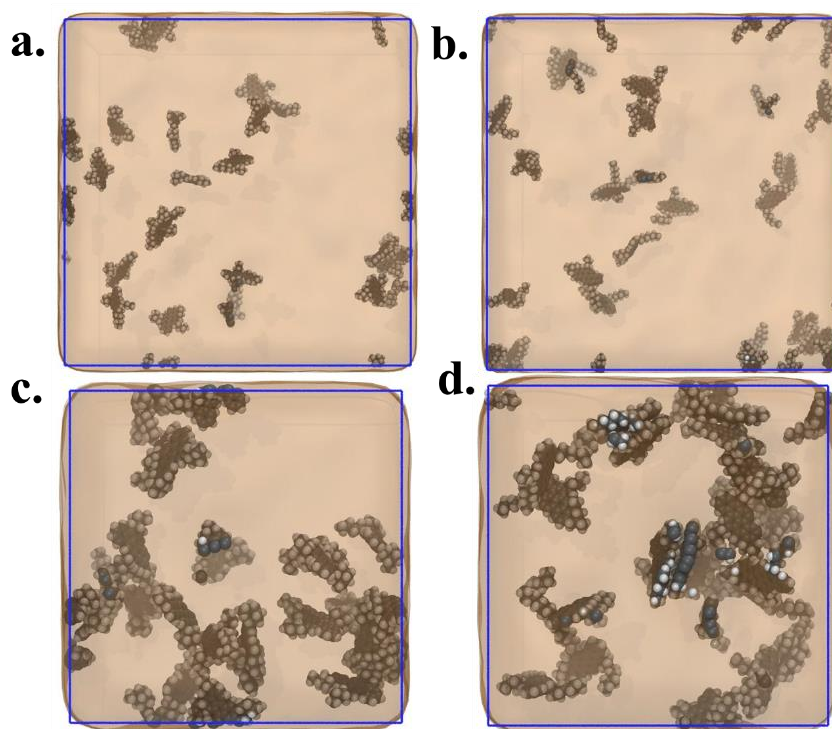


**Figure 2.** Solubility parameters results obtained from MD simulations for subfractions A1 and A2.

Though the DBE of A2 (20) was lower than that of A1 (22) it is interesting to note that the dT was higher for A2 than A1. On the basis of the formulation of the Hassen solubility parameter found in Equation (3), the radius distance (Ra) is typically used to calculate the solvent capacity. Therefore, as lesser is Ra more soluble would be the solute in a specific solvent, in this case toluene. Despite the dT seems similar for A1 and A2, their Ra values are significantly different, being 58.7 % higher for A2 (5.7) compared to A1 (3.6). Therefore, it can be concluded that A2 would be less soluble in toluene than A1 due to their molecular structure characteristics.

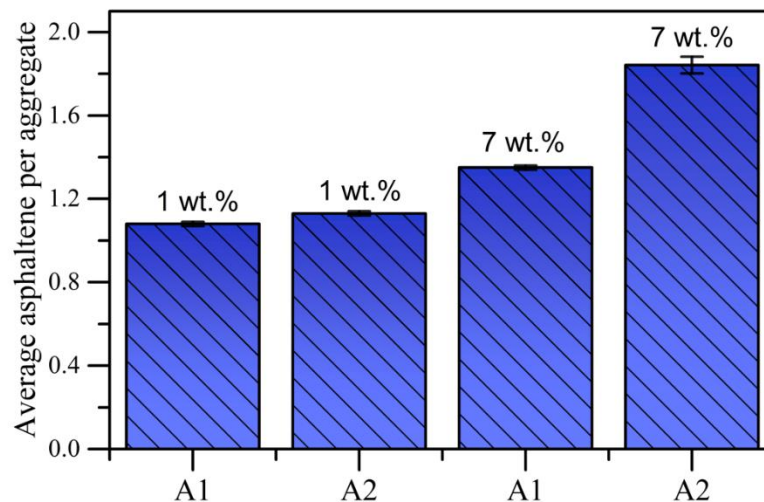
Figure 3 depicts the equilibrium configuration for each asphaltene structure that was tested at both concentrations. When asphaltenes are present in low concentrations (1 wt.%), it is possible to see that the molecules tend to remain dispersed in both scenarios, whereas when asphaltenes are present in higher concentrations (7 wt.%), the molecules tend to locate closer between them. This is because there are more solvent molecules per asphaltene at low concentrations, approximately 609 toluene molecules per asphaltene (Table 3), increasing the solvent dispersion ability. At high asphaltene concentration (7 wt.%), a ratio of

81 toluene molecules per asphaltene is evaluated (Table 3), resulting in a low dispersion ability and higher aggregation states.



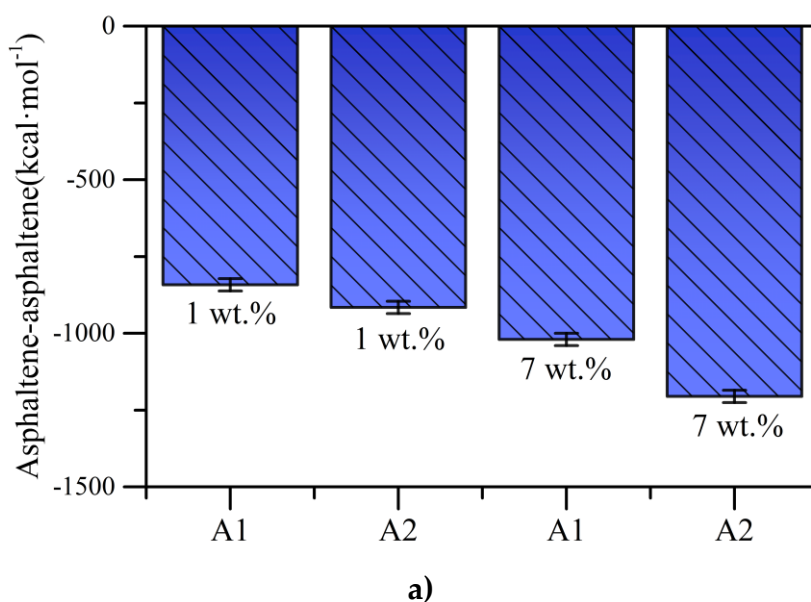
**Figure 3.** Snapshot of the final configuration of equilibrium for A1 and A2 solutions in toluene, (a) A1 at 1 wt.%, (b) A2 at 1 wt.%, (c) A1 at 7 wt.%, and (d) A2 at 7 wt.%. Carbon atoms are shown in gray and hydrogen in white. Toluene is shown in a solvent representation in orange.

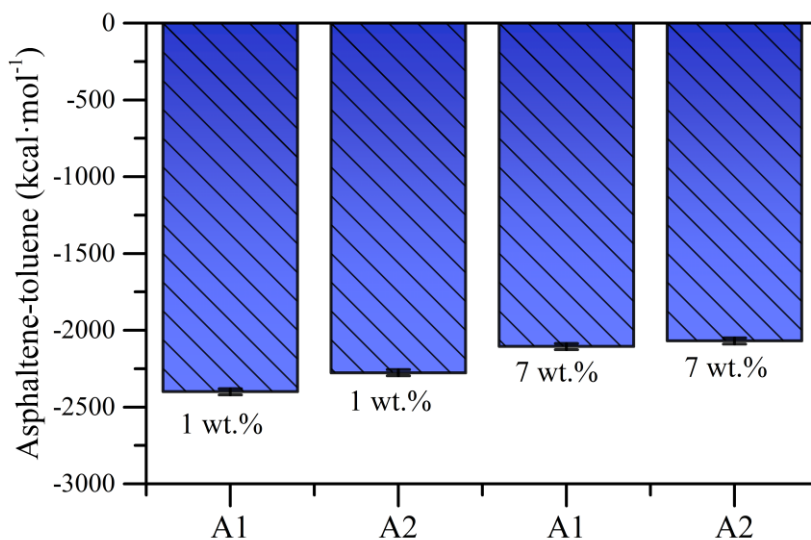
To validate the behavior depicted in Figure 3, the number of clusters was calculated. Figure 4 depicts the obtained results, which show a 40% increase in aggregation size as the asphaltene concentration increases from 1 wt.% to 7 wt.%. Furthermore, it was discovered that A2 forms larger aggregates than A1.



**Figure 4.** Average number of asphaltenes (A1 or A2) per aggregate at each asphaltene concentration evaluated by MD simulations.

Figure 5 depicts the outcomes of the interaction energy calculations. Figure 5-a shows that the interaction energy between the asphaltenes is greater (more negative values) for A2 than for A1, and that the interaction energy increases with asphaltene concentration. Figure 5-b shows that the opposite trend was obtained for asphaltene-toluene interaction energies, as the asphaltene-toluene interaction energy is lower at higher aggregation states, and higher in A1 than A2.

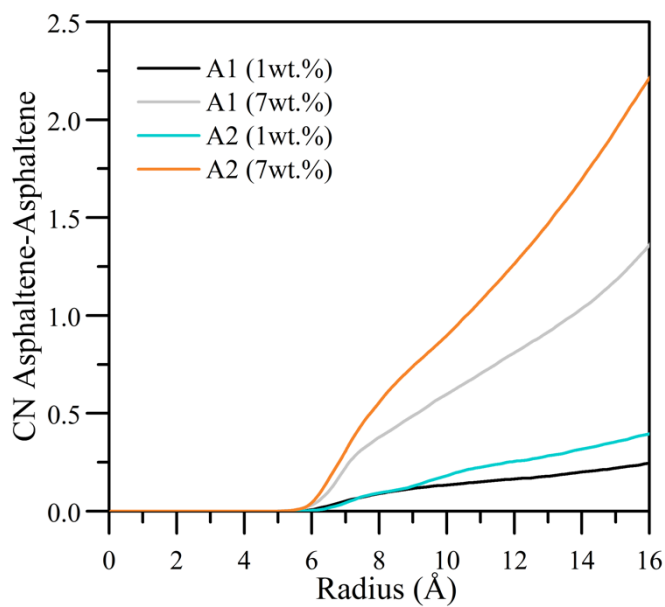




**b)**

**Figure 5.** Interaction energy results for (a) asphaltene-asphaltene (asph-asph) and (b) asphaltene-toluene (asph-tol).

Finally, the coordination number (CN) was calculated to characterize the internal structure of each asphaltene solution. Figure 6-a shows that A2 has higher number of near neighbors than A1, and this number rises as asphaltene concentrations do as well.



**a)**

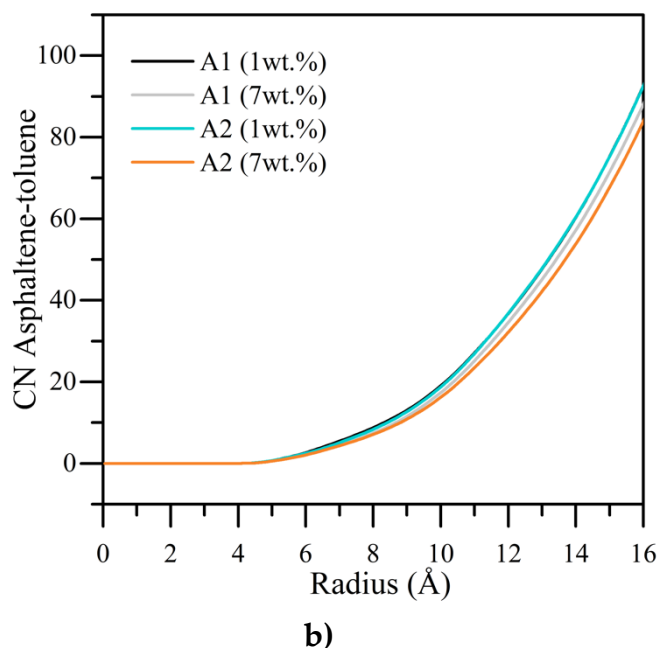


**Figure 6.** Coordination number (CN) results for (a) asphaltene-asphaltene and (b) asphaltene-toluene

The results of the asphaltene-toluene CN are shown in Figure 6-b, where the differences are not as obvious as they are between the asphaltene-asphaltene CN results. At 1 wt%, the CN curves for A1 and A2 overlap, but at a higher asphaltene concentration (7 wt%), A1 was found to have a higher number of near neighbors than A2. Therefore, a high aggregation state is determined for A2 at 7 wt%, followed by A1 at 7 wt%, A2 at 1 wt%, and A1 at 1wt% in that order. MD results indicate that A1 promotes smaller aggregation size, i.e., with higher surface area that increases the ability to chemisorb oxygen during thermal experiments. This result is associated with the fact that the aggregates of A1 are denser and more numerous than those of A2. This indicates that there is greater aggregation in A1 than in A2. At the same time, it is expected that a higher amount of this fraction is adsorbed on nanoparticles considering the described relationship between the asphaltene aggregate size and the adsorption capacity (Moncayo-Riascos et al., 2021).

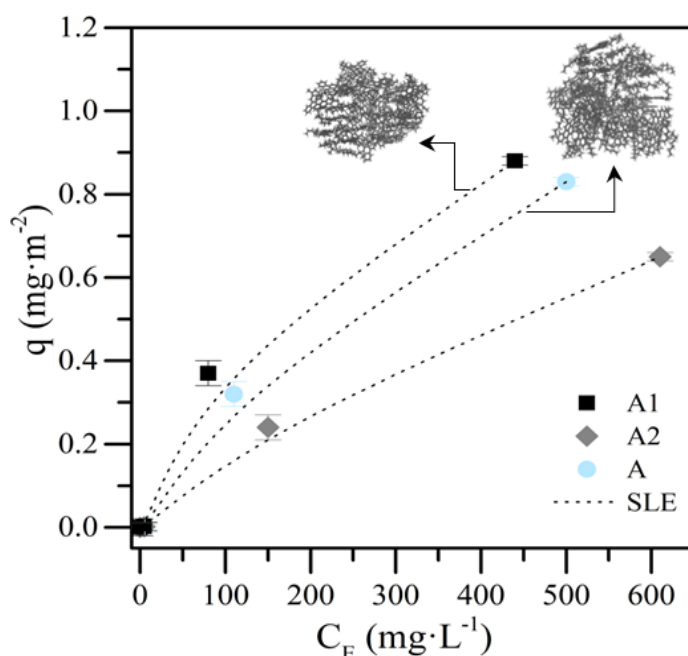
### 3.2. Asphaltene adsorption

Figure 7 shows the constructed asphaltene adsorption isotherms over C-NiPdCe and the SLE fittings (dotted lines). The profiles follow a type Ib isotherm in which the slope at low concentrations ( $C_E$ ) is high and tends to decrease as the  $C_E$  increases. Adsorbate-adsorbent systems with this type of isotherm are considered high-affinity systems. For a fixed concentration, the adsorption

amount increases in the order  $A2 < A < A1$ , which is related to the differences in the chemical structures of the three samples.

C-NiPdCe nanoparticles can interact with asphaltenes through cation- $\pi$ , hydrogen bonding, heteroatom-metal,  $\sigma$ -bonding, and  $\pi$ -back interactions. Many of these interactions occur primarily at the aromatic nucleus and heteroatoms in aromatic structures. Therefore, the A1 fraction interacts to a greater degree with the nanoparticles, and hence there is higher adsorption in the C-NiPdCe - A1 system. The A1 aggregates are denser than those of A2, so more A1 aggregates can be accommodated in nanoparticle's surface, which would make the adsorptive capacity greater in adsorbed mass. To verify these hypotheses, the fit parameters of the SLE model are calculated and shown in Table S1 of the supporting information material. Henry's law constant agreed with the experimental values and the discussion presented.  $H$  increased in the order  $A1 < A < A2$ , indicating that C-NiPdCe presents a higher affinity for A1.

On the other hand, the  $K$  parameter decreased oppositely; that is, the degree of self-association of A1 on the nanoparticles' surface is reduced to a higher degree than in A and A2 samples. The adsorbed capacity of the nanoparticles is highly defined by the aggregate size of the asphaltenes, as lower the aggregate size (described in MD simulations), the higher the asphaltene adsorbed amount.



**Figure 7.** Experimental *n*-C<sub>7</sub> asphaltene adsorption isotherms over C-NiPdCe nanoparticles. The dotted lines represent the SLE fitting.



### 3.3. Asphaltene reactivity under oxidative atmosphere without and with nanoparticles

Figure 8 shows the mass change profiles for the oxidation of asphaltene and asphaltene fractions A1 and A2 at 6.0 MPa, and Table 4 presents its thermogravimetric characteristics. The profile observed for sample A follows the trend identified for high-pressure oxidation of asphaltenes. This profile consists of four important regions discretized through decomposing the mass loss rate profile into Voigt functions. These temperature ranges are known as oxygen chemisorption (OC), desorption of oxygenated structures (DCO), first combustion (FC), and second combustion (SC). In the scientific literature, particular emphasis is placed on the OC region, where oxygen interacts with the molecular structure of asphaltene. Depending on the amount and type of structures formed in this region, the reactivity of the asphaltene increases; that is, it is wholly consumed at lower temperatures. In the asphaltene mass change profile, OC is observed between 100 and 250 °C, with an increase in mass of 7.5%. From this temperature, the DCO region appears where the asphaltene begins to lose mass due to the cracking of its functional groups, mainly more reactive oxygen structures, aliphatic chains, or low molecular weight functional groups, for example, sulfur as thioether. The DCO region is found between 250 and 350 °C. The change in curvature of the mass change indicates that the first combustion region has taken place. From this temperature (380 °C), the mass loss as a function of temperature decreases because higher molecular weight structures begin to decompose. Some specific reactions are expected to occur in this region, such as opening aromatic rings, cracking of oxygen-bridged thiophenes, and breaking of the aromatic nucleus, among others. This region ends at approximately 420 °C. Subsequently, the SC region between 420 °C and 500 °C promotes the total transformation of the asphaltene structure on lighter hydrocarbons. Based on the graph, coke is not produced at the evaluated conditions. In the same panel, interesting changes in thermal profiles for A1 and A2 fractions are observed. The A1 is described by the four mentioned regions (OC, DCO, FC, and SC). The OC region occurs in the temperature interval in A and A1, and the mass gained is also 7.5%. Based on this result, it is understood that fraction A1 is responsible for oxygen chemisorption in asphaltenes. From this point on, the amount of mass lost in the DCO, FC, and SC regions differs between A1 and A. Sample A loses less mass in DCO and FC regions; therefore, fraction A1 is consumed at lower temperatures. Notably, during DCO, A loses 40% of the mass, and A1 loses about 50%.

In contrast, during SC, the mass lost in A1 is less than in A. In addition, the SC region ends 50 °C earlier in A1 than in A. To fully understand the differences between both profiles, the A2 fraction is considered. The mass change profile for this fraction is characterized by two regions only (FC and SC). An increase in the mass (OC neglected) is not observed; therefore, the DCO region does not appear either. The latter corroborates the hypothesis that the A1 fraction promotes oxygen chemisorption in asphaltene while the A2 fraction delays reactivity. Acevedo et al.(2010) demonstrated that the affinity between A1 and A2 is high ( $R = 0.5$ ), and no interface is expected between them. The proposed models predict that the A2 fraction is in a peripheral position surrounding the A1 fraction. In this sense, when asphaltene undergoes oxidation, the most reactive fraction (A1) requires that part of the A2 fraction crack before reacting with oxygen. Thus, the profile of A ends at higher temperatures than A1. The A1 fraction, when not surrounded by the A2 fraction, can react directly with oxygen, and is decomposed at lower temperatures.

The results agree with those reported in our previous study, where oxidative experiments of the aggregates showed that the oxygen chemisorption decreased as the asphaltene aggregate size increased, reducing their reactivity. The MD simulation corroborates the obtained results, in which, asphaltene aggregate size increased in the order  $A1 < A2$ .

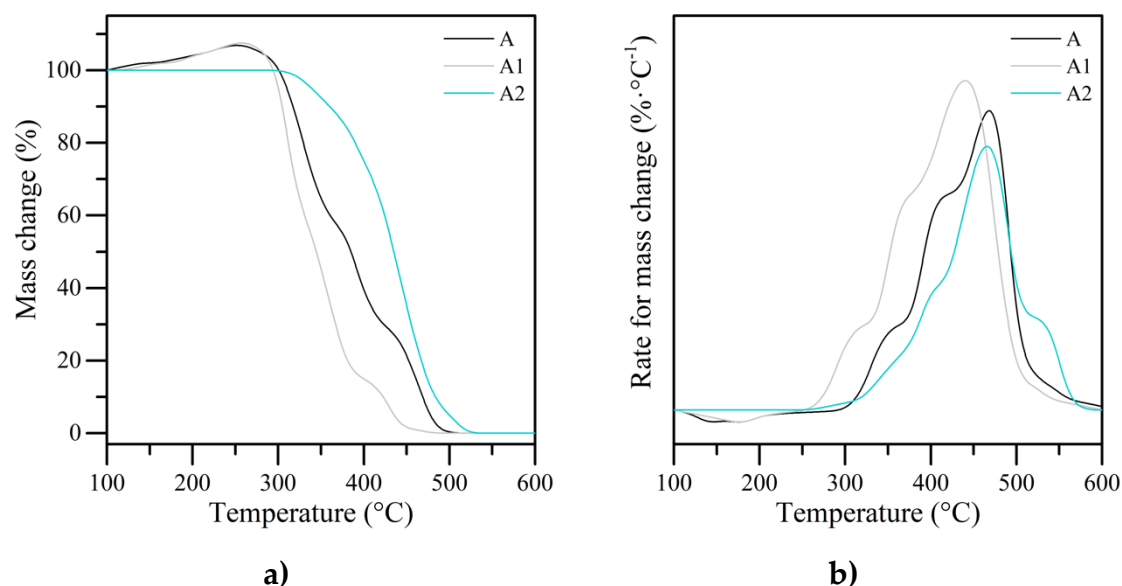


**Figure 8.** Mass percentage (a) and (c) rate for mass change for the oxidation of asphaltene fractions A2 and A1 at 6.0 MPa. Sample mass: 1 mg, heating rate: 10 °C·min<sup>-1</sup>, and airflow: 80 mL·min<sup>-1</sup>.

Figure 9 depicts the catalytic oxidation profiles for the three systems (A, A1, and A2) and Table 4 presents its thermogravimetric characteristics. Each fraction follows a similar behavior when its oxidation is catalyzed by the C-NiPdCe nanoparticles. Systems A and A1 experience all four regions, while A2 is only described by FC and SC. Some of the important features observed include i) the reduction of the required temperature to decompose the asphaltenes, ii) the effective diffusion of the oxygen to A1 and A samples during OC, and iii) the decomposing order of the fractions ( $A1 < A < A2$ ). The capacity of nanoparticles to reduce asphaltene decomposition temperature in different atmospheres has been widely studied. Our previous study demonstrated that C-NiPdCe nanoparticles have a better performance catalyzing asphaltene oxidation reactions compared to a wide variety of nanoparticles synthesized in the literature. The C-NiPdCe presents important textural and chemical characteristics, including a high concentration of  $Ce^{3+}$ ,  $Ni^{2+}$ ,  $Pd^{2+}$  and oxygen vacancies, is endowed by (111) facets, present a high surface area, and high micro and mesoporous volumes, as well as high dispersion of the NiO and PdO crystals. In this sense, the nanoparticles can decompose A1 and A2 fractions.

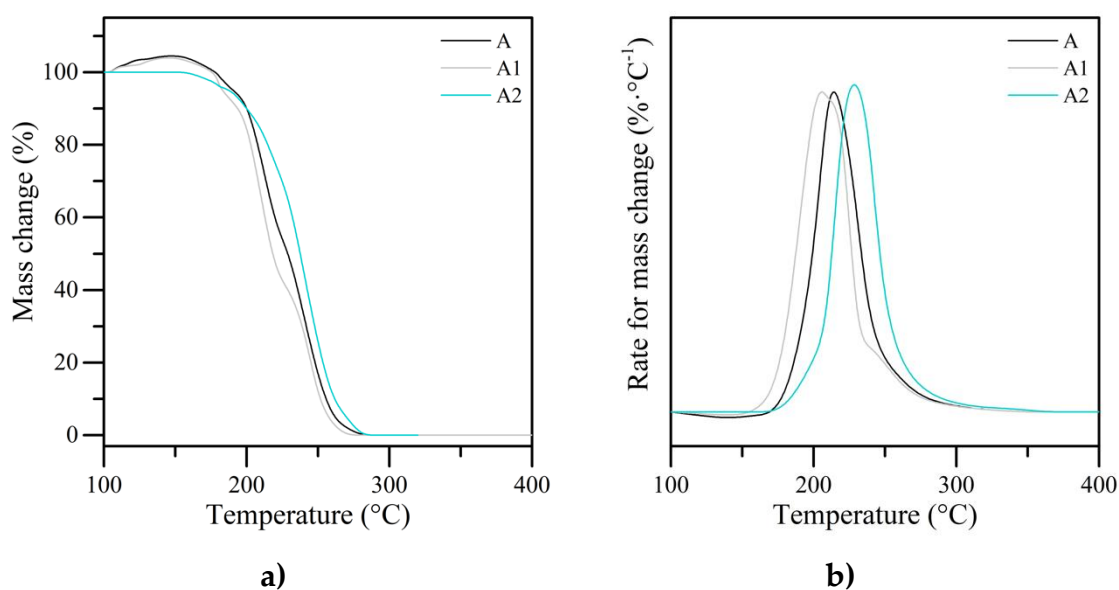


**Figure 9.** Mass percentage (a) and (c) rate for mass change for the catalytic oxidation of asphaltene fractions A2 and A1 at 6.0 MPa. Sample mass: 1 mg, heating rate:  $10\text{ °C}\cdot\text{min}^{-1}$ , and airflow:  $80\text{ mL}\cdot\text{min}^{-1}$ .

Secondly, the amount of oxygen chemisorbed on the asphaltenes was reduced by around 37.3% in the presence of nanoparticles. It demonstrates the effective diffusion of oxygen from the gas phase or catalyst bulk phase to the

asphaltene chemical structure. The fact that C-CeNiPd is endowed with (111) crystalline planes and contains a high concentration of oxygen vacancies facilitates oxygen transport and asphaltene oxidation.

Finally, the temperature required to decompose each fraction depends on its molecular structure. Despite A2 having the presence of long aliphatic open chains by opening some aliphatic rings, its catalytic decomposition finished at higher temperatures than A and A1. The chemisorbed fractions probably make asphaltene decomposition easier. Details of the thermogravimetric characteristics of the thermal profiles are summarized in Table 4.

**Table 4.** Thermogravimetric characteristics for the oxidation of asphaltene discretized A1 and A2 fractions in the different regions: *i*) oxygen chemisorption (OC) *ii*) decomposition of the chemisorbed oxygen (DCO) region, *iii*) first combustion (FC) region and *iv*) second combustion (SC) region at 6.0 MPa.

Sample	OC Region		DCO Region		FC Region		SC Region	
	Temperature range (°C)	Mass gain (mass fraction in %)	Temperature range (°C)	Mass loss (mass fraction in %)	Temperature range (°C)	Mass loss (mass fraction in %)	Temperature range (°C)	Mass loss (mass fraction in %)
A	100-250	7.5	251-380	47.5	381-420	28.0	421-500	32.0
A1	100-250	7.5	251-381	57.5	381-420	30.0	420-450	20.0
A2	-	-	-	-	100-420	30.0	420-530	70.0
A-NPs	100-150	4.7	151-220	44.7	221-250	40.0	251-275	20.0
A1-NPs	100-150	4.7	151-220	54.7	221-250	32.0	251-270	18.0
A2-NPs	-	-	-	-	100-250	60.0	250-280	40.0

### 3.3. Asphaltene reactivity under pyrolysis atmosphere without and with nanoparticles

Figure 10 shows the mass change results for non-isothermal TGA of asphaltenes at 6.0 MPa. As expected, any noticeable change can be detected from the initial temperature (100 °C) to 350 °C for all samples; that is, the asphaltene structure remains almost unbroken. Also, all the profiles can be fitted to two distinctive Voigt functions, representing the well-known low-temperature (LTR) and high-temperature region (HTR). Once the decomposition started, specific differences were detected in each system. The A profile is in the middle of the A1 and A2 profiles, and the A2 is the system that loses more mass at lower temperatures. This trend is opposite to the one found during oxidative experiments. During pyrolysis, no reacting atmosphere can improve the reactivity of the asphaltenes at lower temperatures; therefore, their cracking is a function of the initial molecular structure. As described above, the A2 fraction

has a higher H/C and higher content of long aliphatic chains in the peripheries. Hauser et al.(2008) reported that for temperatures lower than 370 °C, thermal decomposition of asphaltenes occurs by eliminating groups on peripheral sites. Therefore, the A2 fraction during LTO lost high mass than A1.

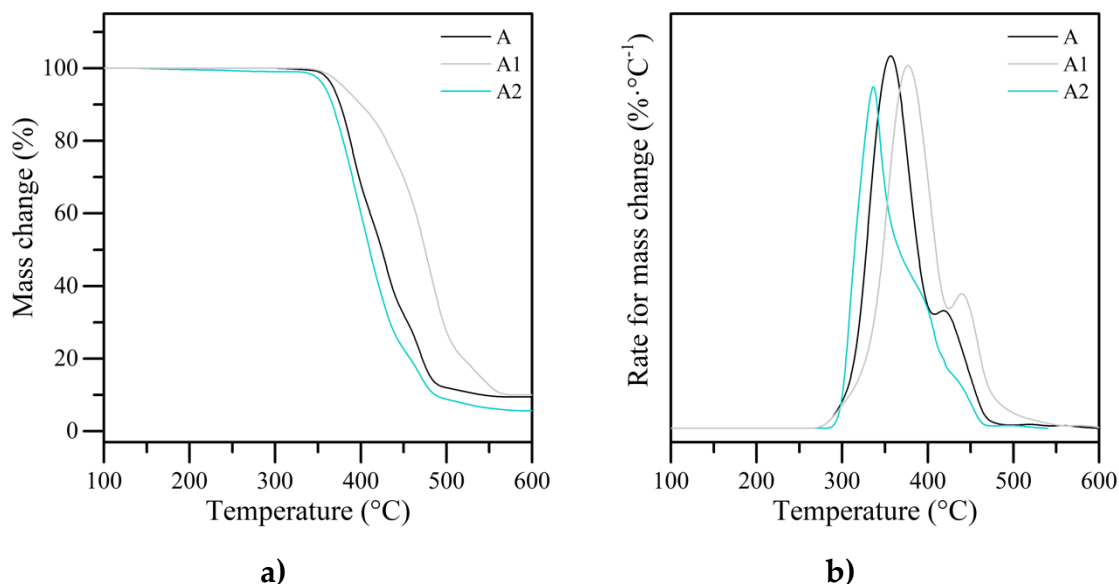


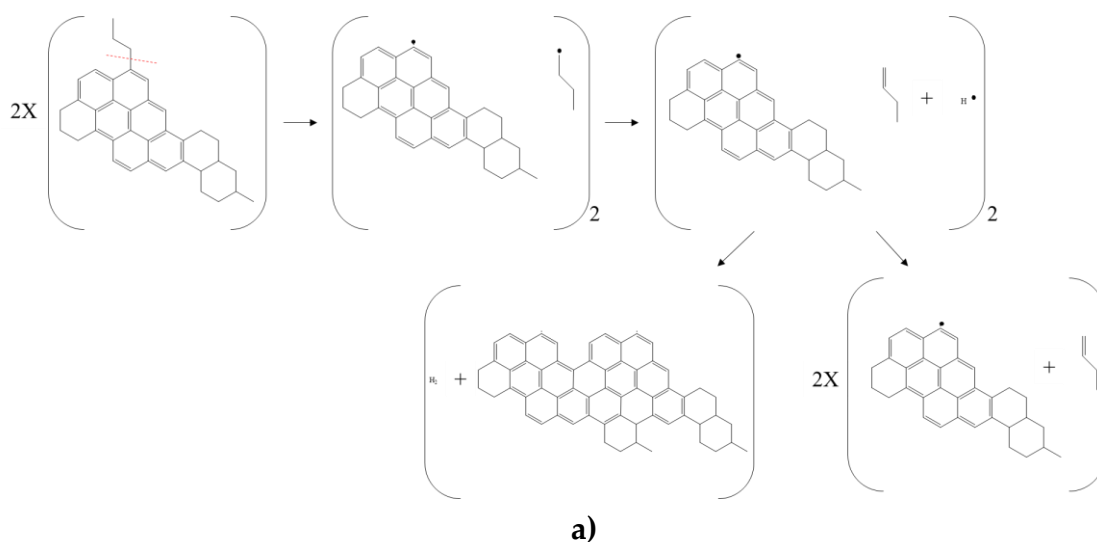
**Figure 10.** Mass percentage (a) and (c-d) rate for mass change for the pyrolysis of asphaltene fractions A2 and A1 at 6.0 MPa. Sample mass: 1 mg, heating rate: 10 °C·min<sup>-1</sup>, and nitrogen flow: 80 mL·min<sup>-1</sup>.

Subsequently, during the second region (HTR), it is noted that almost 8% of A2 and 11% of A and A1 is not cracked, implying coke formation. Cracking reaction and polymerization reaction are two parallel reactions that are found in the HTR during asphaltene conversion. Asphaltene would condense into larger polycyclic aromatic hydrocarbons and coke at higher temperatures. Hence, the fraction with a higher content of heteroatoms-containing aromatic structures, polycyclic aromatic hydrocarbons, and big nuclei cores produces a higher amount of coke; that is, the increasing order found is A2 < A < A1.

**Table 5.** Thermogravimetric characteristics for the pyrolysis of asphaltene discretized A1 and A2 fractions in the different regions: *i*) low-temperature region (LTR) and *ii*) high-temperature region (HTR) at 6.0 MPa.

Sample	LT Region		HT Region	
	Temperature range (°C)	Mass gain (mass fraction in %)	Temperature range (°C)	Mass loss (mass fraction in %)
A	100-455	73.4	456-560	16.6
A1	100-500	72.2	501-560	16.8
A2	100-440	77.1	441-560	14.9
A	100-330	76.3	331-540	23.7
A1-NPs	100-300	78.7	301-540	21.3
A2-NPs	100-365	56.6	366-540	43.4

Figure 11 shows a representative mechanism for the polycondensation and cracking of A2 and A1 asphaltenes during pyrolysis. In panel a, the mechanism begins with the cracking of an aliphatic chain of A1, which leaves two free radicals, one in the aromatic nucleus and one in the aliphatic chain. If, during the process, the free radical manages to be stabilized by H molecules, the aromatic nucleus and the aliphatic chain can be stabilized; otherwise, the aromatic nucleus could join another similar fraction and generate, through polycondensation, a much more complex structure with higher molecular weight. In the case of fraction A2 (panel b), the molecule is similar to the previous one. Two aromatic rings have been opened in this case, generating a longer aliphatic chain. The aromatic nucleus and two aliphatic chains with free radicals are obtained during the first cracking. Given the event that the free radicals are not stabilized, the generated polycondensated structure is of lower molecular weight and smaller than that formed by the A1 fraction.



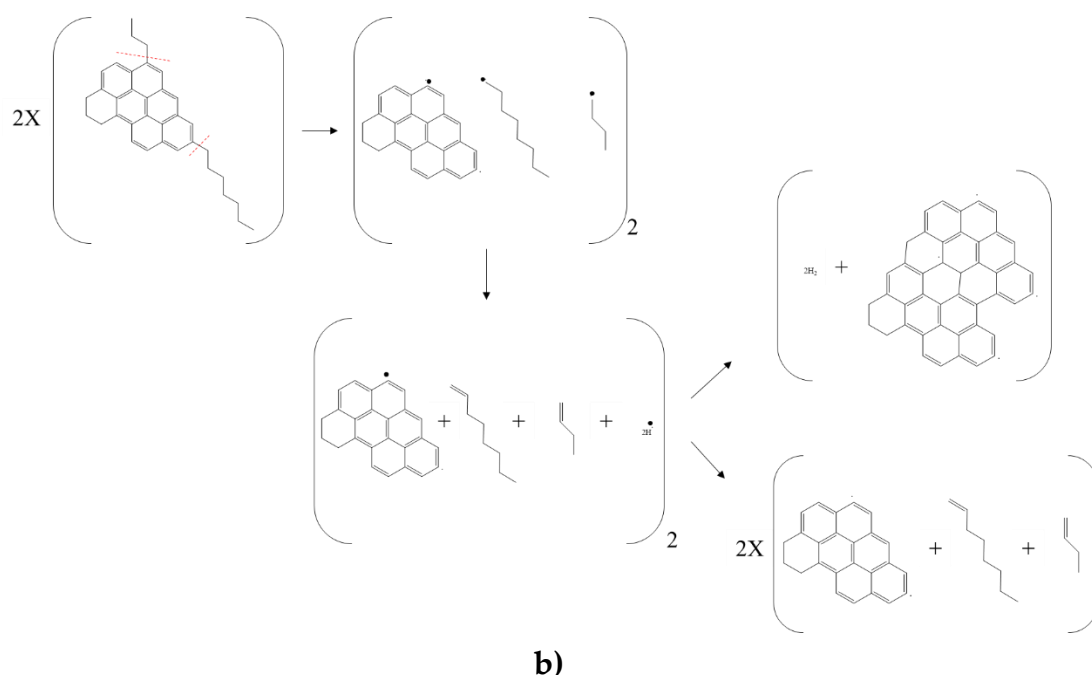


**Figure 11.** Tentative mechanism for a) A1 and b) A2 thermal conversion.

Figure 12 shows the results of the catalytic pyrolysis of asphaltenes A1, A and A2. Some interesting results were found. Contrary to the non-catalytic experiments, the profiles obtained show the highest reactivity of A1 followed by A and A2, in that order. Because asphaltene distribution in toluene is necessary for adsorption experiments, the state of aggregation changes, resulting in smaller aggregates in A1 asphaltenes. The self-association degree is inhibited to a greater extent in A1 asphaltenes when they are adsorbed on nanoparticles, which also contributes to the reactivity of the samples. Accordingly, for the catalytic pyrolysis of A1 and A2, the mass loss during the LTR region was 78.7 and 56.6%, respectively. This finding suggests that an important factor in catalytic experimentation is the aggregation state. Another significant finding is that both fractions completely decompose, which prevents the formation of coke due to the exceptional properties of the nanoparticle.

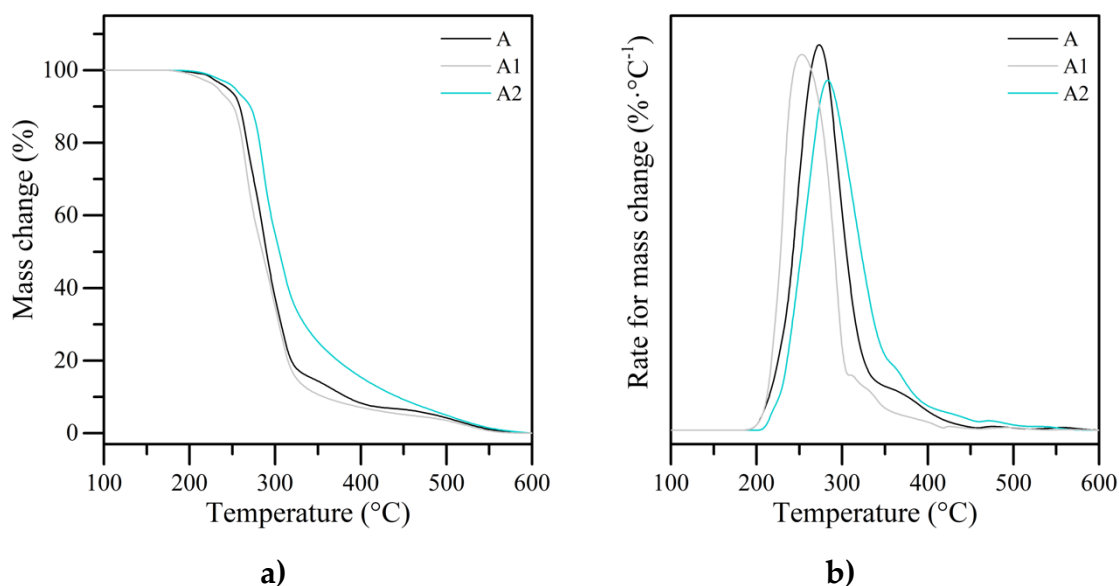


**Figure 12.** Mass percentage (a) and (b) rate for mass change for catalytic pyrolysis of asphaltene fractions A2 and A1 at 6.0 MPa. Sample mass: 1 mg, heating rate:  $10\text{ }^{\circ}\text{C}\cdot\text{min}^{-1}$ , and nitrogen flow:  $80\text{ mL}\cdot\text{min}^{-1}$ .

### 3.4. Kinetic analysis

Kinetic parameters were estimated based on the multi-step reaction followed by the asphaltenes, i.e., OC, DCO, FC, and SC regions. The slope and the intercept were obtained by fitting the thermal profiles with the line  $\ln[\beta(-\ln(1-x))/P_{O_2}T^2]$  against  $1/T_i^{-1}$  and used to determine the effective activation energy and the pre-exponential factor, respectively. The fractions and the asphaltene followed a first-order reaction with  $R^2 > 0.99$  in all cases, which agrees well with literature studies about oxygen and pyrolysis of SARA fractions at high pressure (Medina et al., 2021a; Medina et al., 2021d; Niksa et al., 2003; Senneca et al., 2019). Tables 6 and 7 show the results for oxidation/catalytic oxidation and pyrolysis/catalytic pyrolysis of asphaltenes, respectively. As the first result, it was observed that the effective activation energy in OC was very similar for A1 than A with and without nanoparticles, with values close to  $13\text{ kJ}\cdot\text{mol}^{-1}$ . On the other hand, DCO activation energy was higher for A1 than A because of the higher amount of structures lost during this event in A1. During FC, the trend was very similar to the one in DCO. The A1 requires more energy to carry out the FC reactions, whereas SC region follows the opposite behavior. Because of most of the asphaltene A1 is consumed between DCO and FC, the SC region requires less energy to be completed. Analyzing the A2 fraction, combustion regions presented higher values than A1 and A. The mentioned



trend is expected because A2 does not exhibit oxygen chemisorption, which is an essential factor in reducing effective activation energy.

Additionally, the catalytic oxidation followed the same trends. However, the required effective activation energy decreased in all cases. In previous work, we identified that some variables, including the content of  $Ce^{3+}$ , high  $O_{ads}/O_{lat}$  ratio, and high amount of oxygen vacancies, make easier asphaltene oxidation. Also, Ni and Pd species enhance the overall reaction pathway by strong-metal support interactions (SMSI) with ceria.

The pre-exponential factor results showed a dependence on the asphaltene fractions. Lower values are found during OC than in the other regions because of the lower entropy change produced during oxygen chemisorption (Medina et al., 2019e). Then, the regions controlled by cracking, polycondensation, and oxidation (DCO, FC, and SC), exhibit increasing order values for  $k_o$ . The entropy change increased by the collision frequency, therefore,  $k_o$  is increased. Comparing the fractions and the asphaltene A, the  $k_o$  found was always higher for the A sample. Understanding that within A, it can find structures A1 and A2, the entropy during their decomposition can be much higher than in the isolated fractions.

Table 7 summarizes the estimated kinetic parameters for the pyrolysis reaction pathway discretized in LTR and HTR. The LTR presents lower values than HTR for activation energy and pre-exponential factor. These results can be explained due to LTR being endowed by the volatilization of light hydrocarbons and the cracking of lighter structures which require less energy to be completed. The HTO region in which polycondensation of A1 and A2 fractions occurs is characterized by higher  $E_a$  and  $k_o$ . The A system presents the highest values for both parameters. Cracking the A1-A2 complex structures probably requires higher energy expenditure and generates a higher entropy in the system.

**Table 6.** Estimated kinetic parameters for the oxidation of the asphaltenes A1 and A2 discretized in the different regions: *i*) oxygen chemisorption (OC), *ii*) decomposition of the chemisorbed oxygen (DCO) region, *iii*) first combustion (FC) region, and *iv*) second combustion (SC) region.

Sample	Treatment	Thermal event					
		$E_a$ (kJ·mol <sup>-1</sup> )	$k_o$ (min <sup>-1</sup> ·MPa <sup>-1</sup> )	R <sup>2</sup>	$E_a$ (kJ·mol <sup>-1</sup> )	$k_o$ (min <sup>-1</sup> ·MPa <sup>-1</sup> )	R <sup>2</sup>
A1		OC Region			DCO Region		
	Without NPs	12.81	7.03 × 10 <sup>-6</sup>	0.999	28.75	3.17 × 10 <sup>2</sup>	0.998
	With NPs	9.23	1.03 × 10 <sup>11</sup>	0.998	32.33	3.56 × 10 <sup>5</sup>	0.999
		FC Region			SC Region		
	Without NPs	44.32	5.42 × 10 <sup>5</sup>	0.992	51.23	4.30 × 10 <sup>4</sup>	0.997
	With NPs	33.12	8.01 × 10 <sup>5</sup>	0.997	11.24	6.11 × 10 <sup>3</sup>	0.999
A		OC Region			DCO Region		
	Without NPs	12.78	6.20 × 10 <sup>-6</sup>	0.997	22.43	1.44 × 10 <sup>3</sup>	0.999
	With NPs	9.08	1.01 × 10 <sup>11</sup>	0.999	30.03	5.55 × 10 <sup>4</sup>	0.999
		FC Region			SC Region		
	Without NPs	40.21	7.21 × 10 <sup>6</sup>	0.999	30.21	3.08 × 10 <sup>5</sup>	0.998
	With NPs	44.74	8.44 × 10 <sup>6</sup>	0.998	10.32	1.26 × 10 <sup>3</sup>	0.999
A2		OC Region			DCO Region		
	Without NPs	-	-	-	-	-	-
	With NPs	-	-	-	-	-	-
		FC Region			SC Region		
	Without NPs	61.02	8.21 × 10 <sup>6</sup>	0.998	55.20	6.58 × 10 <sup>6</sup>	0.998
	With NPs	67.92	9.43 × 10 <sup>7</sup>	0.999	33.08	4.71 × 10 <sup>4</sup>	0.998

**Table 7.** Estimated kinetic parameters for the pyrolysis of the asphaltenes A1 and A2 discretized in the different regions: *i*) high-temperature region (HTR) and *ii*) low-temperature region (LTO).

Sample	Treatment	Thermal event					
		$E_a$ (kJ·mol <sup>-1</sup> )	$k_o$ (min <sup>-1</sup> ·MPa <sup>-1</sup> )	R <sup>2</sup>	$E_a$ (kJ·mol <sup>-1</sup> )	$k_o$ (min <sup>-1</sup> ·MPa <sup>-1</sup> )	R <sup>2</sup>
A1		LTR			HTR		
	Without NPs	107.21	2.54 × 10 <sup>9</sup>	0.999	114.31	5.39 × 10 <sup>11</sup>	0.999
	With NPs	38.51	1.23 × 10 <sup>5</sup>	0.995	44.31	2.11 × 10 <sup>6</sup>	0.995
A	Without NPs	123.87	7.23 × 10 <sup>11</sup>	0.999	128.52	2.34 × 10 <sup>12</sup>	0.999
	With NPs	57.76	7.05 × 10 <sup>9</sup>	0.999	59.21	9.32 × 10 <sup>10</sup>	0.999
A2	Without NPs	67.99	3.47 × 10 <sup>8</sup>	0.996	78.21	7.81 × 10 <sup>9</sup>	0.996
	With NPs	3.45 × 10 <sup>6</sup>	0.998	66.44	8.31 × 10 <sup>8</sup>	0.998	3.45 × 10 <sup>6</sup>

On the other hand, the catalytic activity of nanoparticles is elucidated in the reduction of the activation energy for carrying out both regions in all samples. The reaction pathway is favored regardless of the asphaltene fraction, obtaining reductions in asphaltene activation energy between 40 and 60%.

#### **4. Conclusions.**

This work highlights the use of CeO<sub>2</sub>-based nanoparticles on asphaltene adsorption and decomposition with emphasis on the A1 and A2 subgroups. MD simulations show that a difference of only two hydrogen atoms in the representative A1 and A2 molecular structures promotes significantly changes in the aggregation behavior in toluene at two different asphaltene concentrations. It was determined that A2 tend to form larger aggregates than A1 subfraction, at low and high asphaltene concentrations since the H/C ratio is higher increasing the cohesive energy and thus its Hansen solubility parameter distance regarding the solvent toluene. Adsorption experiments show that for a fixed concentration, the adsorption amount increases in the order A2 < A < A1, which is related to the differences in the chemical structures of the three samples and the density of the aggregates. The profiles follow a type Ib isotherm in which the slope at low concentrations ( $C_E$ ) is high and tends to decrease as the  $C_E$  increases. During oxidation, systems A and A1 experience all four regions, while A2 is only described by FC and SC. Some of the important features observed include i) the reduction of the required temperature to decompose the asphaltenes, ii) the effective diffusion of the oxygen to A1 and A samples during OC, and iii) the decomposing order of the fractions (A1 < A < A2). During pyrolysis, the A profile is in the middle of the A1 and A2 profiles, and the A2 is the system that loses more mass at lower temperatures. This trend is opposite to the one found during oxidative experiments. During pyrolysis, no reacting atmosphere can improve the reactivity of the asphaltenes at lower temperatures; therefore, their cracking is a function of the initial molecular structure. Some interesting results were found. Contrary to the non-catalytic experiments, the profiles obtained show the highest reactivity of A1 followed by A and A2, in that order.

#### **References**

Abutaqiya, M.I., Sisco, C.J., Wang, J. and Vargas, F.M., 2019. Systematic investigation of asphaltene deposition in the wellbore and near-wellbore

- region of a deepwater oil reservoir under gas injection. Part 1: thermodynamic modeling of the phase behavior of polydisperse asphaltenes. *Energy & Fuels*, 33(5): 3632-3644.
- Acevedo, S. and Castillo, J., 2023. Asphaltenes: Aggregates in Terms of A1 and A2 or Island and Archipelago Structures. *ACS omega*.
- Acevedo, S. et al., 2018. Suppression of phase separation as a hypothesis to account for nuclei or nanoaggregate formation by asphaltenes in Toluene. *Energy & fuels*, 32(6): 6669-6677.
- Acevedo, S. et al., 2007. Relations between asphaltene structures and their physical and chemical properties: The rosary-type structure. *Energy & fuels*, 21(4): 2165-2175.
- Acevedo, S., Castro, A., Vásquez, E., Marcano, F. and Ranaudo, M.a.A., 2010. Investigation of physical chemistry properties of asphaltenes using solubility parameters of asphaltenes and their fractions A1 and A2. *Energy & fuels*, 24(11): 5921-5933.
- Acevedo, S., Escobar, O., Echevarria, L., Gutiérrez, L.B. and Méndez, B., 2004. Structural analysis of soluble and insoluble fractions of asphaltenes isolated using the PNP method. Relation between asphaltene structure and solubility. *Energy & fuels*, 18(2): 305-311.
- Akbarzadeh, K. et al., 2007. Los asfaltenos: Problemáticos pero ricos en potencial. *Oilfield review*, 19: 25.
- Amrollahi Biyouki, A., Hosseinpour, N. and Nassar, N.N., 2018. Pyrolysis and oxidation of asphaltene-born coke-like residue formed onto in situ prepared NiO nanoparticles toward advanced in situ combustion enhanced oil recovery processes. *Energy & fuels*, 32(4): 5033-5044.
- Arias-Madrid, D. et al., 2020. NiO, Fe<sub>2</sub>O<sub>3</sub>, and MoO<sub>3</sub> supported over SiO<sub>2</sub> nanocatalysts for asphaltene adsorption and catalytic decomposition: optimization through a simplex-centroid mixture design of experiments. *Catalysts*, 10(5): 569.
- Belmares, M. et al., 2004. Hildebrand and Hansen solubility parameters from molecular dynamics with applications to electronic nose polymer sensors. *Journal of computational chemistry*, 25(15): 1814-1826.
- Carbognani, L., 2000. Effects of iron compounds on the retention of oil polar hydrocarbons over solid sorbents. *Petroleum science and technology*, 18(3-4): 335-360.
- Carbognani, L., Orea, M. and Fonseca, M., 1999. Complex nature of separated solid phases from crude oils. *Energy & fuels*, 13(2): 351-358.

- Fan, T. and Buckley, J.S., 2002. Rapid and accurate SARA analysis of medium gravity crude oils. *Energy & Fuels*, 16(6): 1571-1575.
- Franco, C., Cardona, L., Lopera, S., Mejía, J. and Cortés, F., 2016. Heavy oil upgrading and enhanced recovery in a continuous steam injection process assisted by nanoparticulated catalysts, SPE improved oil recovery conference. OnePetro.
- Franco, C.A., Montoya, T., Nassar, N.N. and Cortés, F.B., 2014. NiO and PdO supported on fumed silica nanoparticles for adsorption and catalytic steam gasification of colombian asphaltenes. *Handbook on Oil Production Research*; Nova Science Publishers: Hauppauge, NY, USA: 101-145.
- Franco, C.A., Montoya, T., Nassar, N.N., Pereira-Almao, P. and Cortés, F.B., 2013a. Adsorption and subsequent oxidation of colombian asphaltenes onto nickel and/or palladium oxide supported on fumed silica nanoparticles. *Energy & Fuels*, 27(12): 7336-7347.
- Franco, C.A., Nassar, N.N., Ruiz, M.A., Pereira-Almao, P. and Cortés, F.B., 2013b. Nanoparticles for inhibition of asphaltenes damage: adsorption study and displacement test on porous media. *Energy & Fuels*, 27(6): 2899-2907.
- Gates, I. et al., 2008. In situ upgrading of Llançanelo heavy oil using in situ combustion and a downhole catalyst bed. *Journal of Canadian Petroleum Technology*, 47(09).
- Gray, M.R., Tykwinski, R.R., Stryker, J.M. and Tan, X., 2011. Supramolecular assembly model for aggregation of petroleum asphaltenes. *Energy & Fuels*, 25(7): 3125-3134.
- Gutiérrez, L.B., Ranaudo, M.A., Méndez, B. and Acevedo, S., 2001. Fractionation of asphaltene by complex formation with p-nitrophenol. A method for structural studies and stability of asphaltene colloids. *Energy & Fuels*, 15(3): 624-628.
- Hashemi, R., Nassar, N.N. and Pereira-Almao, P., 2012. Transport behavior of multimetallic ultradispersed nanoparticles in an oil-sands-packed bed column at a high temperature and pressure. *Energy & Fuels*, 26(3): 1645-1655.
- Hauser, A., Bahzad, D., Stanislaus, A. and Behbahani, M., 2008. Thermogravimetric analysis studies on the thermal stability of asphaltenes: pyrolysis behavior of heavy oil asphaltenes. *Energy & Fuels*, 22(1): 449-454.

- Ignasiak, T., Kemp-Jones, A. and Strausz, O., 1977. The molecular structure of Athabasca asphaltene. Cleavage of the carbon-sulfur bonds by radical ion electron transfer reactions. *The Journal of organic chemistry*, 42(2): 312-320.
- Kašpar, J., Fornasiero, P. and Graziani, M., 1999. Use of CeO<sub>2</sub>-based oxides in the three-way catalysis. *Catalysis Today*, 50(2): 285-298.
- Kazemzadeh, Y. et al., 2015. Behavior of asphaltene adsorption onto the metal oxide nanoparticle surface and its effect on heavy oil recovery. *Industrial & Engineering Chemistry Research*, 54(1): 233-239.
- Kosari, M., Golmohammadi, M., Ahmadi, S.J., Towfighi, J. and Chenari, A.H., 2017. On the catalysis capability of transition metal oxide nanoparticles in upgrading of heavy petroleum residue by supercritical water. *The Journal of Supercritical Fluids*, 126: 14-24.
- Liu, G.-S. and Niksa, S., 2004. Coal conversion submodels for design applications at elevated pressures. Part II. Char gasification. *Progress in energy and combustion science*, 30(6): 679-717.
- López, D. et al., 2020. Cardanol/SiO<sub>2</sub> Nanocomposites for Inhibition of Formation Damage by Asphaltene Precipitation/Deposition in Light Crude Oil Reservoirs. Part II: Nanocomposite Evaluation and Coreflooding Test. *ACS omega*, 5(43): 27800-27810.
- Marei, N.N. et al., 2017a. Nanosize effects of NiO nanosorbents on adsorption and catalytic thermo-oxidative decomposition of vacuum residue asphaltenes. *The Canadian Journal of Chemical Engineering*, 95(10): 1864-1874.
- Marei, N.N., Nassar, N.N., Vitale, G., Hassan, A. and Zurita, M.J.P., 2017b. Effects of the size of NiO nanoparticles on the catalytic oxidation of Quinolin-65 as an asphaltene model compound. *Fuel*, 207: 423-437.
- Martínez-Arias, A., Fernández-García, M., Belver, C., Conesa, J. and Soria, J., 2000. EPR study on oxygen handling properties of ceria, zirconia and Zr-Ce (1: 1) mixed oxide samples. *Catalysis letters*, 65(4): 197-204.
- Medina, O.E. et al., 2019a. Upgrading of extra-heavy crude oils by dispersed injection of NiO-PdO/CeO<sub>2+δ</sub> nanocatalyst-based nanofluids in the steam. *Nanomaterials*, 9(12): 1755.
- Medina, O.E., Gallego, J., Arias-Madrid, D., Cortés, F.B. and Franco, C.A., 2019b. Optimization of the load of transition metal oxides (Fe<sub>2</sub>O<sub>3</sub>, Co<sub>3</sub>O<sub>4</sub>, NiO and/or PdO) onto CeO<sub>2</sub> nanoparticles in catalytic steam decomposition of n-C<sub>7</sub> asphaltenes at low temperatures. *Nanomaterials*, 9(3): 401.

- Medina, O.E. et al., 2021a. Effect of pressure on thermo-oxidative reactions of saturates, aromatics, and resins (S-Ar-R) from extra-heavy crude oil. *Fuel*: 122596.
- Medina, O.E. et al., 2020. Effect of multifunctional nanocatalysts on n-C7 asphaltene adsorption and subsequent oxidation under high-pressure conditions. *Energy & Fuels*, 34(5): 6261-6278.
- Medina, O.E. et al., 2021b. Insights into the Morphology Effect of Ceria on the Catalytic Performance of NiO–PdO/CeO<sub>2</sub> Nanoparticles for Thermo-oxidation of n-C7 Asphaltenes under Isothermal Heating at Different Pressures. *Energy & Fuels*, 35(22): 18170-18184.
- Medina, O.E. et al., 2021c. Insights into the Morphology Effect of Ceria on the Catalytic Performance of NiO–PdO/CeO<sub>2</sub> Nanoparticles for Thermo-oxidation of n-C7 Asphaltenes under Isothermal Heating at Different Pressures. *Energy & Fuels*.
- Medina, O.E., Gallego, J., Redondo, J.D., Cortés, F.B. and Franco, C.A., 2021d. Effect of pressure on the thermo-oxidative behavior of saturates, aromatics, and resins (S-Ar-R) mixtures. *Fuel*: 122787.
- Medina, O.E., Gallego, J., Restrepo, L.G., Cortés, F.B. and Franco, C.A., 2019c. Influence of the Ce<sup>4+</sup>/Ce<sup>3+</sup> Redox-couple on the cyclic regeneration for adsorptive and catalytic performance of NiO-PdO/CeO<sub>2</sub>± $\delta$  nanoparticles for n-C7 asphaltene steam gasification. *Nanomaterials*, 9(5): 734.
- Medina, O.E., Gallego, J., Rodríguez, E., Franco, C.A. and Cortés, F.B., 2019d. Effect of pressure on the oxidation kinetics of Asphaltenes. *Energy Fuels*, 33(11): 10734.
- Medina, O.E., Gallego, J., Rodríguez, E., Franco, C.A. and Cortés, F.B., 2019e. Effect of pressure on the oxidation kinetics of Asphaltenes. *Energy & Fuels*, 33(11): 10734-10744.
- Medina, O.E. et al., 2019f. Improvement of steam injection processes through nanotechnology: An approach through in situ upgrading and foam injection. *Energies*, 12(24): 4633.
- Medina, O.E., Olmos, C., Lopera, S.H., Cortés, F.B. and Franco, C.A., 2019g. Nanotechnology applied to thermal enhanced oil recovery processes: a review. *Energies*, 12(24): 4671.
- Miller, J., Fisher, R., Thiyagarajan, P., Winans, R. and Hunt, J., 1998. Subfractionation and characterization of Mayan asphaltene. *Energy & Fuels*, 12(6): 1290-1298.

- Moncayo-Riascos, I. et al., 2021. Physical Insights about Viscosity Differences of Asphaltene Dissolved in Benzene and Xylene Isomers: Theoretical–Experimental Approaches. *Energy & Fuels*, 35(22): 18574-18582.
- Montoya, T., Coral, D., Franco, C.A., Nassar, N.N. and Cortés, F.B., 2014. A novel solid–liquid equilibrium model for describing the adsorption of associating asphaltene molecules onto solid surfaces based on the “chemical theory”. *Energy & Fuels*, 28(8): 4963-4975.
- Mullins, O.C., 2010. The modified Yen model. *Energy & Fuels*, 24(4): 2179-2207.
- Mullins, O.C. et al., 2007. The colloidal structure of crude oil and the structure of oil reservoirs. *Energy & Fuels*, 21(5): 2785-2794.
- Mullins, O.C. et al., 2012. Advances in asphaltene science and the Yen–Mullins model. *Energy & Fuels*, 26(7): 3986-4003.
- Murgich, J., Abanero, J.A. and Strausz, O.P., 1999. Molecular recognition in aggregates formed by asphaltene and resin molecules from the Athabasca oil sand. *Energy & Fuels*, 13(2): 278-286.
- Nassar, N.N., 2010. Asphaltene adsorption onto alumina nanoparticles: kinetics and thermodynamic studies. *Energy & Fuels*, 24(8): 4116-4122.
- Nassar, N.N., Franco, C.A., Montoya, T., Cortés, F.B. and Hassan, A., 2015. Effect of oxide support on Ni–Pd bimetallic nanocatalysts for steam gasification of n-C7 asphaltenes. *Fuel*, 156: 110-120.
- Nassar, N.N., Hassan, A. and Pereira-Almao, P., 2011. Comparative oxidation of adsorbed asphaltenes onto transition metal oxide nanoparticles. *Colloids and surfaces A: Physicochemical and Engineering aspects*, 384(1-3): 145-149.
- Niksa, S., Liu, G.-S. and Hurt, R.H., 2003. Coal conversion submodels for design applications at elevated pressures. Part I. devolatilization and char oxidation. *Progress in Energy and Combustion Science*, 29(5): 425-477.
- Pacheco-Sánchez, J., Alvarez-Ramirez, F. and Martínez-Magadán, J., 2004. Morphology of aggregated asphaltene structural models. *Energy & Fuels*, 18(6): 1676-1686.
- Payzant, J., Lown, E. and Strausz, O., 1991. Structural units of Athabasca asphaltene: the aromatics with a linear carbon framework. *Energy & fuels*, 5(3): 445-453.
- Qiao, P. et al., 2017. Fractionation of asphaltenes in understanding their role in petroleum emulsion stability and fouling. *Energy & Fuels*, 31(4): 3330-3337.



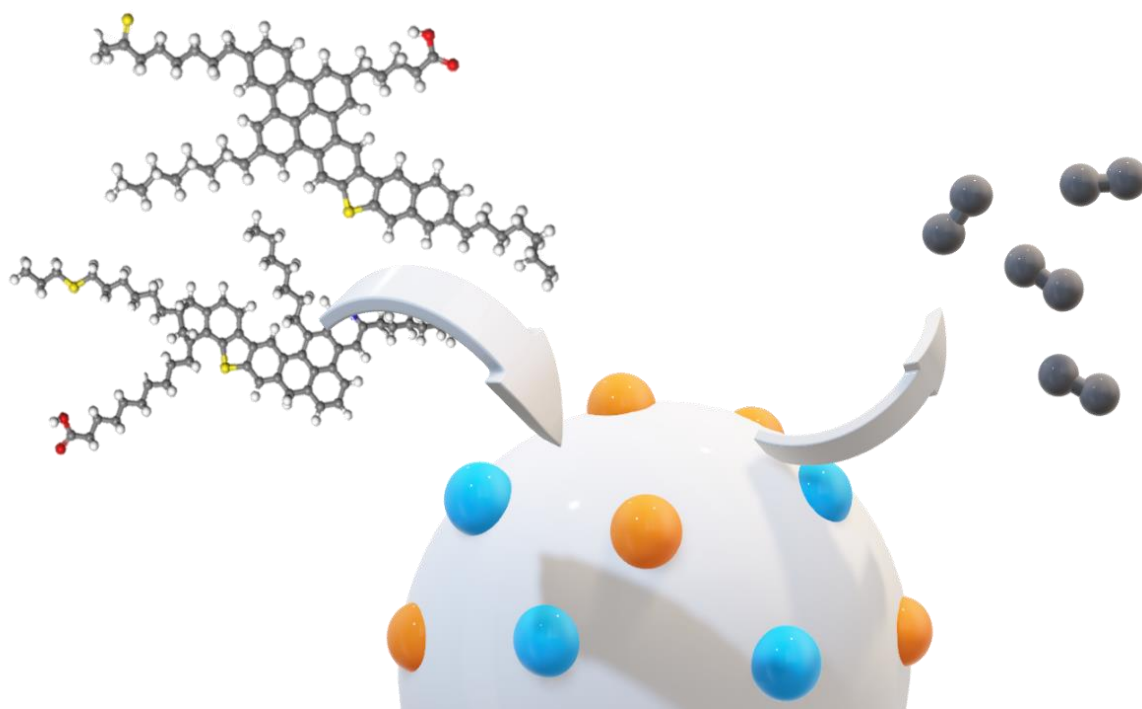
- Ramírez, L., Moncayo-Riascos, I., Cortés, F.B., Franco, C.A. and Ribadeneira, R., 2021. Molecular Dynamics Study of the Aggregation Behavior of Polycyclic Aromatic Hydrocarbon Molecules in n-Heptane–Toluene Mixtures: Assessing the Heteroatom Content Effect. *Energy & Fuels*, 35(4): 3119-3129.
- Razeghi, A., Khodadadi, A., Ziaei-Azad, H. and Mortazavi, Y., 2010. Activity enhancement of Cu-doped ceria by reductive regeneration of CuO–CeO<sub>2</sub> catalyst for preferential oxidation of CO in H<sub>2</sub>-rich streams. *Chemical Engineering Journal*, 164(1): 214-220.
- Schuler, B., Meyer, G., Peña, D., Mullins, O.C. and Gross, L., 2015. Unraveling the molecular structures of asphaltenes by atomic force microscopy. *Journal of the American Chemical Society*, 137(31): 9870-9876.
- Semple, K.M., Cyr, N., Fedorak, P.M. and Westlake, D.W., 1990. Characterization of asphaltenes from Cold Lake heavy oil: variations in chemical structure and composition with molecular size. *Canadian journal of chemistry*, 68(7): 1092-1099.
- Senneca, O. et al., 2019. Assessment of combustion rates of coal chars for oxy-combustion applications. *Fuel*, 238: 173-185.
- Sha, J. et al., 2021. Solubility determination, model evaluation, Hansen solubility parameter, molecular simulation and thermodynamic properties of benflumetol in four binary solvent mixtures from 278.15 K to 323.15 K. *Journal of Molecular Liquids*, 333: 115867.
- Snow, R.H., 2011. In-situ upgrading of bitumen and shale oil by RF electrical heating, SPE heavy oil conference and exhibition. OnePetro.
- Sodero, A.C. et al., 2016. Investigation of the effect of sulfur heteroatom on asphaltene aggregation. *Energy & Fuels*, 30(6): 4758-4766.
- Solaimany Nazar, A. and Amin, F., 2017. A study on the adsorption and catalytic oxidation of Asphaltene onto nanoparticles. *Journal of Petroleum Science and Technology*, 7(2): 21-29.
- Speight, J., 1994. The molecular nature of petroleum asphaltenes. *Arabian Journal for Science and Engineering*, 19(2 B): 335-353.
- Strausz, O., 1989. Structural features of Athabasca bitumen related to upgrading performance. American Chemical Society, Division of Petroleum Chemistry, Preprints;(USA), 34(CONF-8904131-).
- Strausz, O.P., Mojelsky, T.W., Lown, E.M., Kowalewski, I. and Behar, F., 1999. Structural features of Boscan and Duri asphaltenes. *Energy & Fuels*, 13(2): 228-247.

- Villegas, O. et al., 2023. Aggregation of Asphaltene Subfractions A1 and A2 in Different Solvents from the Perspective of Molecular Dynamics Simulations. *Energy & Fuels*.
- Villegas, O. et al., 2020. Molecular cartography of A1 and A2 asphaltene subfractions from classical molecular dynamics simulations. *Energy & Fuels*, 34(11): 13954-13965.
- Weissman, J. et al., 1996. Down-hole catalytic upgrading of heavy crude oil. *Energy & fuels*, 10(4): 883-889.
- Zhang, E. et al., 2018. Numerical simulation for erosion effects of three-phase flow containing sulfur particles on elbows in high sour gas fields. *Petroleum*, 4(2): 158-167.
- Zhang, X., Liu, Q. and Fan, Z., 2019. Enhanced in situ combustion of heavy crude oil by nickel oxide nanoparticles. *International Journal of Energy Research*, 43(8): 3399-3412.



## Chapter 12

# Conversion of *n*-C<sub>7</sub> Asphaltenes and Resins II into Hydrogen Using CeO<sub>2</sub>-Based Nanocatalysts



Published article in *Nanomaterials*: [doi.org/10.3390/nano11051301](https://doi.org/10.3390/nano11051301)

Impact factor: 5.719

## Conversion of *n*-C<sub>7</sub> Asphaltenes and Resins II into Hydrogen Using CeO<sub>2</sub>-Based Nanocatalysts

### Abstract

This study focuses on evaluating the volumetric hydrogen content in the gaseous mixture released from the steam catalytic gasification of *n*-C<sub>7</sub> asphaltenes and resins II at low temperatures (<230 °C). For this purpose, four nanocatalysts were selected: CeO<sub>2</sub>, CeO<sub>2</sub> functionalized with Ni-Pd, Fe-Pd, and Co-Pd. The catalytic capacity was measured by non-isothermal (from 100 to 600 °C) and isothermal (220 °C) thermogravimetric analyses. The samples show the main decomposition peak between 200 and 230 °C for bi-elemental nanocatalysts and 300 °C for the CeO<sub>2</sub> support, leading to reductions up to 50% compared with the samples in the absence of nanoparticles. At 220 °C, the conversion of both fractions increases in the order CeO<sub>2</sub> < Fe-Pd < Co-Pd < Ni-Pd. Hydrogen release was quantified for the isothermal tests. The hydrogen production agrees with the catalytic activity of each material for decomposing both fractions at the evaluated conditions. CeNi1Pd1 showed the highest performance among the other three samples, leading to the most increased hydrogen production in the effluent gas with values of ~44 vol%. When the samples were heated at higher temperatures (i.e., 230 °C), H<sub>2</sub> production increased up to 55 vol% during catalyzed *n*-C<sub>7</sub> asphaltene and resin conversion, indicating an increase of up to 70% compared with the non-catalyzed systems at the same temperature conditions.

## 1. Introduction

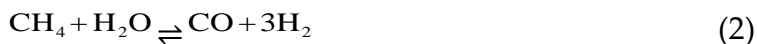
Global warming and energy supply challenges have attracted increasing attention worldwide [1]. Hydrogen is renewable and clean energy; its application only generates water as a by-product. However, fossil fuels are currently the most used sources of energy consumption [2]. Generally, there is a desire to generate an energy transition from fossil fuels to a cleaner energy source, including hydrogen [3]. During the energy transition, the co-production of fossil fuels and hydrogen could be an exciting strategy to supply several issues.

As hydrocarbons are hydrogen-rich compounds, they can be used to produce hydrogen by applying different methods, such as gasification with air and oxygen and steam reforming [4]. The first two methods have been extensively studied in coal gasification processes and natural gas reforming [5,6]; however, hydrogen production from crude oils emerges as a novel research topic with many challenges and opportunities. Crude oils are classified into light (LO), medium (MO), heavy (HO), and extra heavy (EHO) oils [7]. HO and EHO represent about 70% of the worldwide oil reserves. They are characterized by high viscosities and low American Petroleum Institute (API) gravity values, mainly associated with the high content of asphaltenes and resins [8-12]. Asphaltenes and resins are complex molecules composed of polyaromatic hydrocarbon cores surrounded by aliphatic chains [13-16]. Resins have fewer aromatic species but longer aliphatic chains; therefore, they have a higher H/C ratio and lower polarity than asphaltenes [17,18]. Commonly, to improve the mobility of HO and EHO, thermal processes like steam injection [19,20], steam-assisted gravity drainage (SAGD) [7,21], and in situ combustion [22] are used. However, in most cases, these techniques produce less than 50% in situ crude oil and low calorific gaseous products, including greenhouse gases like CO<sub>2</sub> [23-28].

Other nanoparticles and nanofluid-based technologies have been used to increase the efficiency of the thermal process. Some studies report that nanocatalysts have great potential to improve thermal methods efficiency by decomposing asphaltenes and upgrading crude oil [29-32]. CeO<sub>2</sub> has been widely used for assisting several reactions and processes [33,34] as this catalyst has a fluorite cubic structure, and its cations migrate easily at low temperatures [35]. The cerium ion circulates between Ce<sup>4+</sup> and Ce<sup>3+</sup> through a redox cycle; therefore, the material surface can store oxygen [36]. To improve the adsorptive and

catalytic performance of nanocatalysts, some authors proposed using functionalized and/or composite nanomaterials [29,37-40]. Therefore, nanocrystals of transition (NOT) and noble element oxides (NON) supported over different nanocatalysts, including CeO<sub>2</sub> have been proposed in the literature, obtaining satisfactory results.

Previously, we developed a study to evaluate the effect of three bi-elemental systems composed of 1.0% in mass fraction of Ni-Pd, Co-Pd, and Fe-Pd supported for the steam catalytic gasification of *n*-C<sub>7</sub> asphaltenes [38]. The systems were named CeNi1Pd1, CeCo1Pd1, and CeFe1Pd1, respectively. The results demonstrate higher *n*-C<sub>7</sub> asphaltene adsorption for CeNi1Pd1 nanocatalysts, followed by CeCo1Pd1, CeFe1Pd1, and CeO<sub>2</sub> [38]. During the thermal experiments, it was observed that two of the primary gaseous products (i.e., CO and CH<sub>4</sub>) were released. CO can be used to develop water-gas shift (WGS) reactions (Equation (1)) as well as CH<sub>4</sub> for steam reforming (Equation (2)). It is worth mentioning that steam as a gasifying agent is necessary to convert the gas products into hydrogen-enriched synthesis gas and applied WGS. However, the release of hydrogen was not analysed in this work.



Due to the potential application of this type of nanocatalysts, it is expected that they can be used in the reservoir to co-produce upgraded crude oils and hydrogen through steam catalytic gasification [2]. To date, there are no works reported in the literature evaluating this technology. Since crude oil is a complex mixture of different fractions, it is important to consider the hydrogen production from the steam catalytic gasification of *n*-C<sub>7</sub> asphaltenes, resins II, and their combinations. Therefore, this work aims to evaluate for the first time the hydrogen production efficiency of different CeO<sub>2</sub> based- nanocatalysts containing different ratios between three NOT (i.e., Ni, Co, and Fe) and a NON-element oxide (Pd) through the steam catalytic gasification of the crude oil heaviest fractions (i.e., resins II and *n*-C<sub>7</sub> asphaltenes). The adsorption of both fractions and a mixture of them in the nanocatalysts is evaluated to meet this objective. Then, the hydrogen release was calculated during the isothermal gasification process. Some variables such as temperature, resins:asphaltenes (R:A) ratio, and nanocatalyst nature were analyzed. This study is expected to

broaden the use of fossil fuels for producing a hydrogen-rich gas with low content of CO<sub>2</sub> (<5%vol) from the gasification of the most complex fractions of crude oil.

## 2. Experimental

### 2.1. Materials

CeNi1Pd1, CeFe1Pd1, and CeCo1Pd1 were previously synthesized through the incipient wetness technique [41] using commercial cerium oxide nanocatalysts (Nanostructured & Amorphous Materials, Houston, TX, USA) with an average particle size of 21.6 nm. Salt precursors (FeCl<sub>3</sub>·6H<sub>2</sub>O, NiCl<sub>2</sub>·6H<sub>2</sub>O, CoCl<sub>2</sub>·6H<sub>2</sub>O, and Pd(NO<sub>3</sub>)<sub>2</sub>·2H<sub>2</sub>O) were supplied by Merck KGaA, Darmstadt, Germany. Each system was named considering the initials of the support, the elements with which the doping was made, and the percentage of impregnation. For example, CeNi1Pd1 is a system supported on CeO<sub>2</sub>, with Ni and Pd at 1.0% (*w/w*). Details of nanoparticle characterization are found in our previous work [38]. Table 1 shows some properties of the employed nanocatalysts.

**Table 1.** Estimated basic properties of synthesized CeO<sub>2</sub> nanocatalysts [38].

Sample	S <sub>BET</sub> ± 0.1 m <sup>2</sup> ·g <sup>-1</sup>	dp (nm ± 0.2 nm)				Dispersion (%)	
		NiO	Co <sub>3</sub> O <sub>4</sub>	Fe <sub>2</sub> O <sub>3</sub>	PdO	Ni/Co/Fe	Pd
CeO <sub>2</sub>	67.0	-	-	-	-	-	-
CeNi1Pd1	63.8	6.4	-	-	3.9	12.7	38.6
CeFe1Pd1	64.1	-	-	5.4	6.9	11.2	12.8
CeCo1Pd1	64.4	-	1.9	-	6.1	18.1	20.4

The molar fraction for the couples Ni:Pd, Fe:Pd, and Co:Pd, are 0.4:0.7, 0.9:0.7, and 1.4:0.9, respectively. Considering the metal dispersion results, the nominal molar ratio affects the structure of nanocrystals of transition element (NOT)- Pd, causing a lower possibility of sintering processes for higher Pd/NOE molar value, (1.75 Pd/Ni, 0.78 Pd/Fe, and 0.64 Pd/Co).

X-ray photoelectron spectroscopy analysis was done to characterize the nanocatalysts' surface chemistry following the protocol described in previous work [42]. The atomic content and relationships from O<sub>1s</sub>, Ce<sub>3d</sub>, and Pd<sub>3d</sub> profiles are shown in Table 2. The O<sub>1s</sub> pattern was deconvoluted in two main peaks at 529.0 eV and 531.5 eV ascribed to lattice oxygen (O<sub>latt</sub>) and ascribed to the surface (O<sub>ads</sub>) [43]. Between the functionalized nanocatalysts, the amount of O<sub>ads</sub> follows



the increasing order CeCo1Pd1 < CeFe1Pd1 < CeNi1Pd1; therefore,  $O_{ads}/O_{latt}$  follows the same order.

**Table 2.** Atomic content and relationships calculated from the  $O_{1s}$ ,  $Ce_{3d}$ , and  $Pd_{3d}$  spectra.

Sample	O (%)	Ce (%)	Pd (%)	Ce <sup>3+</sup> (%)	O <sub>ads</sub> (%)	O <sub>latt</sub> (%)	O <sub>ads</sub> /O <sub>latt</sub>	Pd <sup>2+</sup> (%)	Pd <sup>0</sup> (%)
CeO <sub>2</sub>	62.11	37.89	-	18.11	39.44	60.56	0.65	-	-
CeNi1Pd1	58.21	39.79	0.99	32.92	38.21	61.79	0.61	51.22	48.78
CeFe1Pd1	59.29	38.71	0.99	31.11	35.56	64.44	0.55	43.21	56.79
CeCo1Pd1	59.71	38.29	0.99	29.43	31.43	68.57	0.45	38.55	61.45

The peaks for  $Ce_{3d_{5/2}}$  and  $Ce_{3d_{3/2}}$  at 881.6 eV, 885.3 eV, 899.8 eV, and 903.0 eV are associated with Ce<sup>3+</sup> species. Ce<sup>4+</sup> is found at 882.7 eV, 889.7 eV, 898.6 eV, 901.3 eV, 907.6 eV, and 919.3 eV [44]. The increasing sequence for Ce<sup>3+</sup> is CeCo1Pd1 < CeFe1Pd1 < CeNi1Pd1, which agrees with the sequences of  $O_{ads}$  and  $O_{ads}/O_{latt}$ . The formation of Ce<sup>3+</sup> is intrinsically related to the oxygen vacancies formation, promoting the activation of surface oxygen.

From  $Pd_{3d}$  pattern, four main peaks are found. The binding energy at 337.2 eV ( $Pd_{3d_{5/2}}$ ) and 344.5 eV ( $Pd_{3d_{3/2}}$ ) refers to Pd<sup>2+</sup> in bulk PdO [45]. The content of Pd<sup>2+</sup> increases in the same order as Ce<sup>3+</sup>,  $O_{ads}$ , and  $O_{ads}/O_{latt}$ , demonstrating the correlation between the three species. In the case of Pd<sup>2+</sup>, they can function as a reservoir for oxygen adsorption. The other peak at 335.2 eV and its respective satellite refers to the metallic palladium, which follows the opposite behavior of Pd<sup>2+</sup>.

A Colombian extra-heavy crude oil (EHO) of 6.4°API and a viscosity of 3.1 × 10<sup>6</sup> cP at 25 °C was used for the isolation of *n*-C<sub>7</sub> asphaltenes (A) and resins II (R). The content of asphaltenes and total resins were 12.64 and 51.98 wt%, respectively. *n*-Heptane (99%, Sigma-Aldrich, St. Louis, MO, USA) was used to isolate the asphaltenes from the EHO, and chromatographic silica (Sigma-Aldrich, St. Louis, MO, USA) was added to the de-asphalted crude oil to separate the resins from the solution. Both fractions were isolated following the protocols described elsewhere [46,47]. Finally, toluene (99% Sigma-Aldrich, St. Louis, MO, USA) was used as a solvent for the adsorption experiments.

## 2.2. Methods

### 2.2.1. Asphaltenes and Resins Characterization

The characterization of individual *n*-C<sub>7</sub> asphaltenes and resins II was carried out through elemental analysis (C, H, N, S, and O) following the ASTM

D5291 standard method [48] using an elemental analyzer (Perkin-Elmer, Waltham, MA, USA). Average molecular weight ( $M_w$ ) was obtained by vapor pressure osmometry (VPO) using a Knauer osmometer (Knauer, Berlin-Heidelberg, West Germany).  $^1\text{H}$  NMR and  $^{13}\text{C}$  NMR were carried out in a Bruker AMX 300 spectrometer (Karlsruhe, Germany). X-ray photoelectron spectrometry analysis was obtained in a PHOIBOS 150 1D-DLD analyzer (SPECS, Berlin, Germany). The procedures are described elsewhere [49]. Based on these results, average representative molecules for both fractions were constructed and optimized by density functional theory applying Becke's three-parameter and Lee-Yang-Parr functions. Material Studio (BIOVIA, San Diego, CA, USA) was used for this purpose.

### 2.2.2. Adsorption Experiments

Adsorption isotherms were constructed at 25 °C by making stock solutions of 2.2 mmol·L<sup>-1</sup> of resins II and/or *n*-C<sub>7</sub> asphaltenes in toluene and 100 mg of nanocatalysts per 10 mL of volume solution. Initial concentrations of resins II were varied between 0.1 mmol·L<sup>-1</sup> and 2.2 mmol·L<sup>-1</sup>, and asphaltenes between 0.1 mmol·L<sup>-1</sup> and 1.5 mmol·L<sup>-1</sup>. The instrument and protocol employed for the adsorption isotherms construction were like those described in the previous studies [23,43,50,51].

In the first stage, the individual components' adsorption was performed in the three bielemental systems (i.e., CeNi1Pd1, CeCo1Pd1, and CeFe1Pd1) and the support CeO<sub>2</sub>. The system with higher adsorption was then selected to evaluate the competitive adsorption in different R:A mass ratios of 8:2, 1:1, and 2:8. The amount adsorbed of each component was obtained by combining softening point (SP) and thermogravimetric (TGA) experiments following the ASTM E28-12 standard methods [50]. Figure 1 shows the calibration curve of SP against *n*-C<sub>7</sub> asphaltenes percentage where an R<sup>2</sup> value close to the unity was obtained.

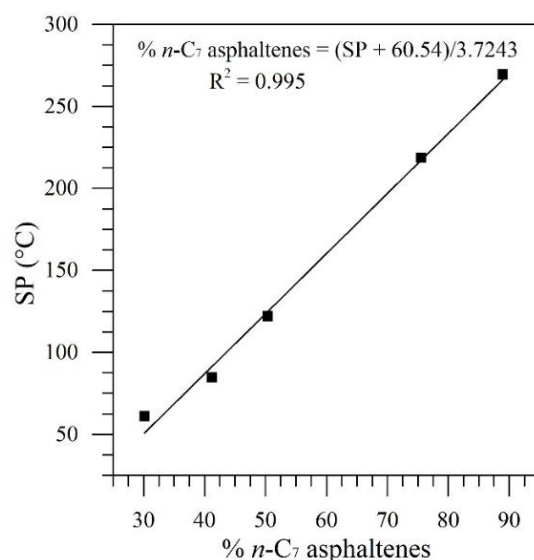


**Figure 1.** Softening point calibration curve.

Finally, this work uses the Solid–Liquid Equilibrium (SLE) model to describe the adsorption isotherms based on the theory of adsorption and the association of molecules on microporous surfaces [51].

### 2.2.3. Steam Catalytic Gasification of Resins II and n-C<sub>7</sub> Asphaltenes.

The steam catalytic gasification of virgin and adsorbed compounds on nanocatalysts was performed using a Q50 thermogravimetric analyzer (TA Instruments, Inc., New Castel, DE, USA). Two different processes were executed. The first one, under non-isothermal heating between 100–600 °C, at a heating rate of 20 °C·min<sup>-1</sup>. The samples were subjected to isothermal heating at three different temperatures in the second one. Samples in the absence of nanocatalysts were heated at 370 °C, while the asphaltenes/resins-containing nanocatalysts were at 220 °C. The steam atmosphere was simulated by introducing 100 mL·min<sup>-1</sup> of N<sub>2</sub> and 6.30 mL·min<sup>-1</sup> of H<sub>2</sub>O<sub>(g)</sub> using a gas saturator controlled by a thermostatic bath at atmospheric pressure [37].

Nanocatalysts with the highest catalytic activity were selected to evaluate the isothermal conversion of different R:A ratios. Catalytic experiments were developed for an adsorbed asphaltene and/or resin II amount of 0.0002 mmol·m<sup>-2</sup> ± 0.00002 mmol·m<sup>-2</sup> [52]. The experimental results were used to calculate the activation energy according to the isothermal procedure [53].

Gas monitoring during the experiments was done in a mass spectrometer (Shimadzu GC-MS, Tokyo, Japan) coupled with the TGA. The equipment was adjusted at an ion trap linear scan rate of 0.03 m/z between 0 and 200 m/z and an electron impact mode of 100 eV to obtain detailed information on the sample's

gasification. The gases were analyzed following the protocols described elsewhere [24,49,54,55]. The evolved gases during steam catalytic gasification were evaluated at three different temperatures (210 °C, 220 °C, and 230 °C). Each run was repeated at least twice to ensure the reproducibility of the experiments.

### 3. Results and discussion

#### 3.1. Resins II and *n*-C<sub>7</sub> asphaltenes characterization

The estimated elemental composition of *n*-C<sub>7</sub> asphaltenes and resins II is shown in Table 3. The resins I data was also reported in Table 3 taken from our previous work for comparative purposes only [56]. The content of heteroatoms differs for each fraction. Nitrogen was lower than 0.5% for *n*-C<sub>7</sub> asphaltenes and resins II, while sulfur content was similar for resin II and *n*-C<sub>7</sub> asphaltene. As expected, the most significant difference between the two resins is the oxygen content, which was higher for resins II than for resins I. Due to the strong aromaticity of *n*-C<sub>7</sub> asphaltenes and their degree of unsaturation, resins II and I have a higher H/C ratio. The average molecular weight follows the increasing order resin I < *n*-C<sub>7</sub> asphaltenes < resin II. This result shows that resin II isolated from the EHO employed in this study is heavier than asphaltenes.

**Table 3.** Elemental composition percentage of *n*-C<sub>7</sub> asphaltenes, resins I, and resins II isolated from a Colombian EHO.

Fraction	Mw (g mmol <sup>-1</sup> )	H/C	Elemental Mass Fraction Concentration (%)				
			C	H	O*	N	S
<i>n</i> -C <sub>7</sub> Asphaltene	907.3	1.14	81.7	7.8	3.6	<0.5	6.6
Resin I	509.0	1.61	82.1	11.0	<0.5	<0.5	6.1
Resin II	957.0	1.36	80.0	9.1	3.2	1.1	6.6

\* Obtained by difference.

Tables 4 and 5 show the XPS and NMR results for both fractions, respectively. The survey spectra for both fractions indicate X-ray-induced Auger transitions of oxygen, nitrogen, carbon, and sulfur. Analyzing the high-resolution spectra, the following results were obtained: Oxygen was present as single bonds (C–O–C, C–O) (532.4 eV) or carboxyl (533.5 eV) in both fractions. Carboxyl groups were in a higher percentage in resins II than *n*-C<sub>7</sub> asphaltenes. The C<sub>1s</sub> was divided into single bonds (C–C, C–H) (284.6 eV), C=O (287.9 eV), and COO– (289.4 eV) species. As expected, C–C and C–H predominate for both

samples, while C=O was higher for n-C<sub>7</sub> asphaltenes and COO<sup>-</sup> for resins II. Although nitrogen was present in low concentration for n-C<sub>7</sub> asphaltenes (elemental analysis), it was slightly detected by XPS. The spectra were deconvoluted in three peaks (i.e., pyridinic (398.8 eV), pyrrolic (399.9), and amines (400.7 eV)) for both fractions. The pyridinic content was the highest for both and the lowest for amines. Finally, sulfur high-resolution spectra show the presence of thioethers (163.4 eV), thiophenes (164.4 eV), and sulfones (167.7 eV). For asphaltenes, the sulfur form percentage increases in the order of sulfones (1.8%) < thioethers < (23.4%) < thiophenes (74.8%). In resins, the trend changes as follows: thiophenes (25.2%) < sulfones (25.3%) < thioethers (49.5%).

**Table 4.** Atomic concentrations (%) of a) oxygen forms, b) nitrogen forms, c) carbon forms, and d) sulfur forms obtained by the fitting results of the O<sub>1s</sub>, N<sub>1s</sub>, C<sub>1s</sub>, and S<sub>2p</sub> spectra, respectively, for n-C<sub>7</sub> asphaltenes and resins II.

Sample	Peak							
	C <sub>1s</sub>		O <sub>1s</sub>		S <sub>2p</sub>		N <sub>1s</sub>	
	Assignment	%	Assignment	%	Assignment	%	Assignment	%
n-C <sub>7</sub> Asphaltene	C-C, C-H	77.4	C-O-C, C-O	76.4	Thioether	23.4	Pyridines	40.3
	C=O	18.0	COO <sup>-</sup>	23.6	Thiophene	74.8	Pyrrolic	32.5
	COO <sup>-</sup>	4.6			Sulfones	1.8	Amines	27.3
Resin II	C-C, C-H	76.3	C-O-C, C-O	73.2	Thioether	49.5	Pyridines	63.1
	C=O	8.6	COO <sup>-</sup>	26.8	Thiophene	25.2	Pyrrolic	22.6
	COO <sup>-</sup>	15.1			Sulfones	25.3	Amines	14.3

Results from NMR show that hydrogen was found in four different forms: Aromatic hydrogen (H<sub>a</sub>), and aliphatic hydrogens α, β, and γ linked to aromatic rings (H<sub>α</sub>, H<sub>β</sub>, and H<sub>γ</sub>, respectively). H<sub>a</sub> content was higher for n-C<sub>7</sub> asphaltenes than resins II. For both fractions, the H<sub>β</sub> species were in higher proportion than H<sub>α</sub> and H<sub>γ</sub>. This result indicates the predominant presence of paraffinic/naphthenic β-hydrogens in aliphatic and aromatic structures, respectively. Resins II present a higher content of long aliphatic chains in γ-position (H<sub>γ</sub>) than n-C<sub>7</sub> asphaltenes [57]. From the <sup>13</sup>C NMR spectra, carbon was found in aromatic (C<sub>ar</sub>) and aliphatic (C<sub>al</sub>) forms. As expected, resins II present a predominant C<sub>al</sub> content (60.96%) and asphaltenes a higher proportion of C<sub>ar</sub> (64.48%).

**Table 5.** Hydrogen and carbon types present in *n*-C<sub>7</sub> asphaltenes and resins II fractions obtained by <sup>1</sup>H NMR and <sup>13</sup>C NMR analyses, respectively.

Sample	<sup>1</sup> H-NMR			<sup>13</sup> C NMR		
	H <sub>α</sub>	H <sub>β</sub>	H <sub>γ</sub>	H <sub>a</sub>	C <sub>al</sub>	C <sub>ar</sub>
<i>n</i> -C <sub>7</sub> Asphaltene	4.79	62.72	8.98	23.49	35.51	64.48
Resin II	18.09	53.86	17.36	10.69	60.96	39.04

Average structure molecules were proposed based on the general properties obtained from elemental analysis, molecular mass, nuclear magnetic resonance, and X-ray photoelectron spectroscopy. Figure 2 shows the *n*-C<sub>7</sub> asphaltene and resin II molecules. The samples show the continental type of model widely accepted for both fractions. *n*-C<sub>7</sub> asphaltene molecular formula proposed is C<sub>62</sub>H<sub>70</sub>S<sub>2</sub>O<sub>2</sub>, the theoretical molecular weight of 911.36 g·mol<sup>-1</sup> and deviation of 0.4%. The resin II molecular formula proposed is C<sub>63</sub>H<sub>85</sub>NS<sub>2</sub>O<sub>2</sub>, molecular weight estimated at 952.5 g·mol<sup>-1</sup> and a deviation of 0.5%.

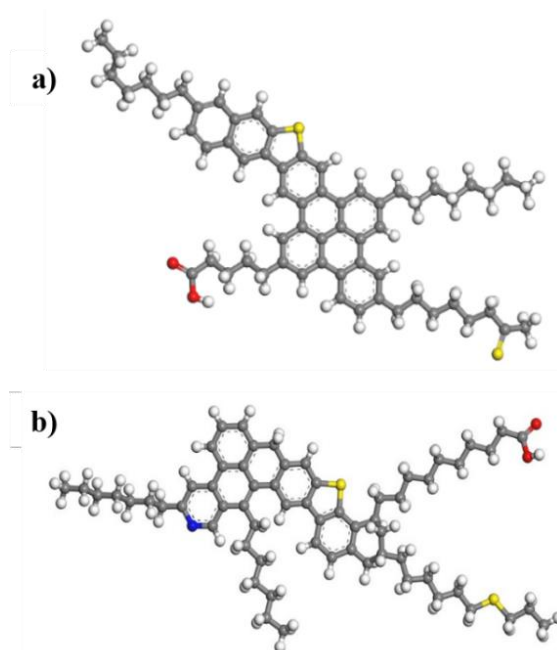


**Figure 2.** Average (a) *n*-C<sub>7</sub> asphaltene and (b) resins II molecule model constructed from DFT analysis. The carbon, hydrogen, oxygen, nitrogen, and sulfur are represented by the green, white, red, blue, and yellow atoms, respectively.

### 3.2. Adsorption Isotherms

Figure 3 shows the adsorption isotherms of *n*-C<sub>7</sub> asphaltenes (panel a) and resins II (panel b) onto CeNi1Pd1, CeCo1Pd1, CeFe1Pd1, and CeO<sub>2</sub> nanocatalysts. A high affinity observed between the different nanocatalysts and the *n*-C<sub>7</sub> asphaltenes is related to the type Ib isotherms following the International Union of Pure and Applied Chemistry (IUPAC) [58].

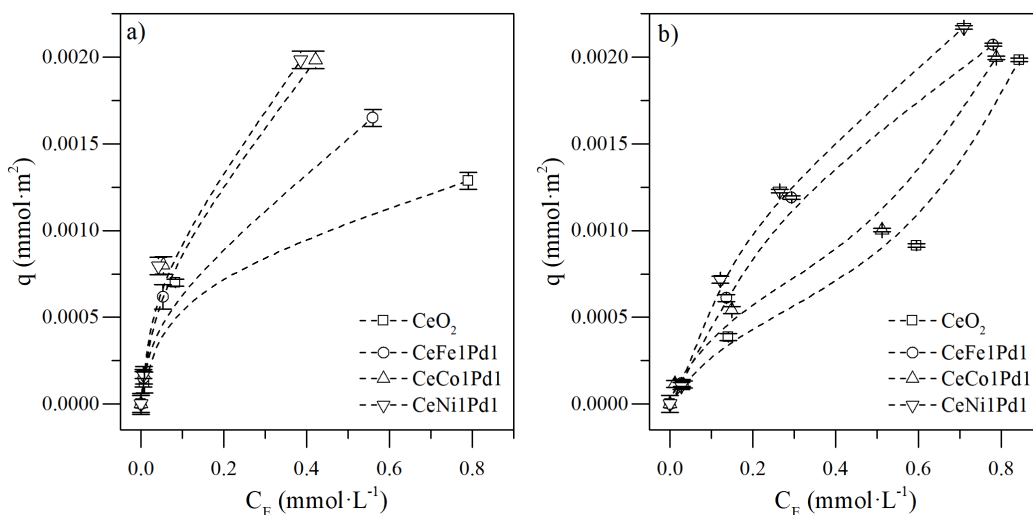


**Figure 3.** Adsorption isotherms of (a) *n*-C<sub>7</sub> asphaltenes and (b) resins II onto CeNi1Pd1, CeFe1Pd1, CeCo1Pd1, and CeO<sub>2</sub> nanocatalysts evaluated at 25 °C. The solid lines represent the prediction of the SLE model, and the symbols are experimental data. Panel (a) was taken from previous work [38].

Adsorption capacity at any concentration decreases in the order CeNi1Pd1 > CeCo1Pd1 > CeFe1Pd1 > CeO<sub>2</sub> for *n*-C<sub>7</sub> asphaltenes, whereas, for resins II uptakes, the order increases as CeNi1Pd1 > CeFe1Pd1 > CeCo1Pd1 > CeO<sub>2</sub>. This result indicates an increase in the adsorptive capacity by NOT impregnation following the order Fe < Co < Ni for asphaltene adsorption since the effective nuclear charge increases in the same order changing Lewis acidity [59], hence, facilitating the formation of coordinated bonds between heteroatoms (Lewis bases) and metals of heavy hydrocarbons, and the active site of NOTs in the different nanocatalysts [60]. On the other hand, the resins II chemical structure changes regarding asphaltenes increase their selectivity for Fe crystals more than Co.

A high affinity is observed according to the slope in Henry's region for the adsorption isotherms curves of resins II on CeNi1Pd1 and CeFe1Pd1 nanocatalysts. The isotherms obtained follow the IUPAC standard

corresponding to type Ib isotherm [58], indicating that resins II have greater selectivity for the Ni and Fe functional groups [61]. Some authors explain that the content of aromatic nitrogen and sulfur species has a high affinity for iron and nickel nanocatalysts [62]. Resins II adsorption on non-functionalized support and bielemental CeCo1Pd1 nanocatalyst shows an isotherm type II. At low concentrations, adsorption at the active sites accessible for resins II is high, indicating a high slope in Henry's region; however, as the concentration of resins II increases, the formation of aggregates Increases, generating adsorption multilayer and taking a profile of type II isotherms [63].

Comparing the adsorptive capacity of different samples, for a fixed concentration of resins, the adsorption amount increases in the following order  $\text{CeO}_2 < \text{CeCo1Pd1} < \text{CeFe1Pd1} < \text{CeNi1Pd1}$ . Unlike the adsorption of *n*-C<sub>7</sub> asphaltenes, the adsorption of resins II is greater for the Fe-Pd couple than for the Co-Pd couple. Based on the results, the competitive adsorption in R:A systems was evaluated in CeNi1Pd1 nanocatalysts, and Figure 4 shows the obtained results.

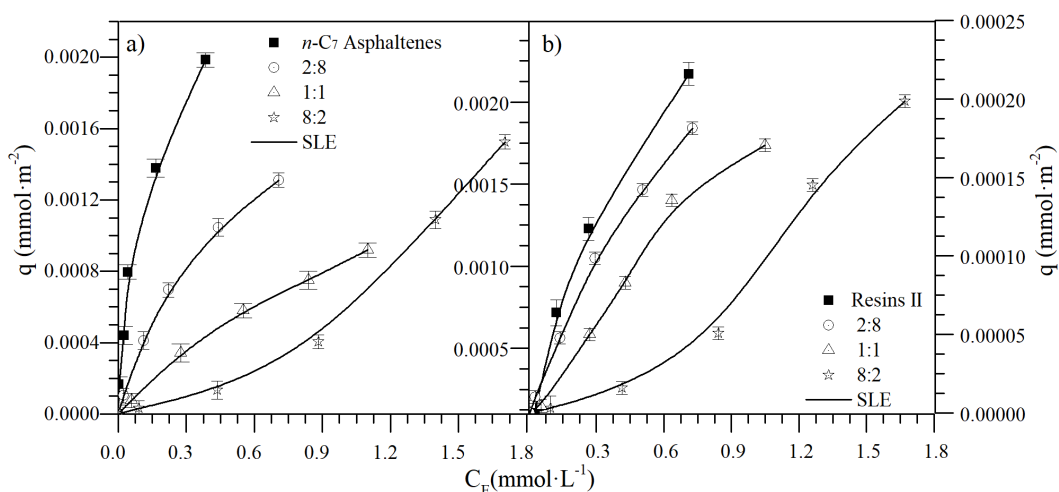


**Figure 4.** Adsorption isotherms constructed for (a) *n*-C<sub>7</sub> asphaltenes and (b) resins II on CeNi1Pd1 nanoparticles for different R:A ratios. The dotted lines are from the SLE model, and the symbols are experimental data.

Figure 4a shows that *n*-C<sub>7</sub> asphaltene adsorption capacity on CeNi1Pd1 nanocatalysts decreases with resin II content. For 2:8 and 1:1 ratios, the isotherms obtained are classified as type I, while the isotherm for 2:8 system behaves type III according to the IUPAC [58]. The change in the asphaltene adsorption mechanism can be associated with a change in their colloidal structure or competitive adsorption between the two polar fractions. As the amount of resins II increases in the system, the active surface sites are reduced for *n*-C<sub>7</sub> asphaltene



adsorption. For example, at fixed  $C_E = 0.33 \text{ mmol}\cdot\text{L}^{-1}$ , the asphaltene adsorption amount was  $0.002 \text{ mmol}\cdot\text{m}^{-2}$ ,  $0.0018 \text{ mmol}\cdot\text{m}^{-2}$ ,  $0.0011 \text{ mmol}\cdot\text{m}^{-2}$ , and  $0.0008 \text{ mmol}\cdot\text{m}^{-2}$  for *n*-C<sub>7</sub> asphaltene, 2:8; 1:1, and 8:2 systems, respectively.

Structurally, given the similarity between both fractions, it is likely that strong and stable interactions will occur between them. As shown in Table 1, asphaltenes and resins contain similar percentages of N-, S-, and O- heteroatoms. Because asphaltenes could interact with traces of resins containing oxygen and/or nitrogen, the primary interaction is likely of the attractive type. In this sense, resins tend to interact more with asphaltenes, as shown in Figure 5 below.

When the amount of resins in the system is high enough, a solvation phenomenon could be generated, which reduces the asphaltene–nanoparticle interactions by blocking important active sites, such as aromatic, naphthenic rings, and heteroatoms.

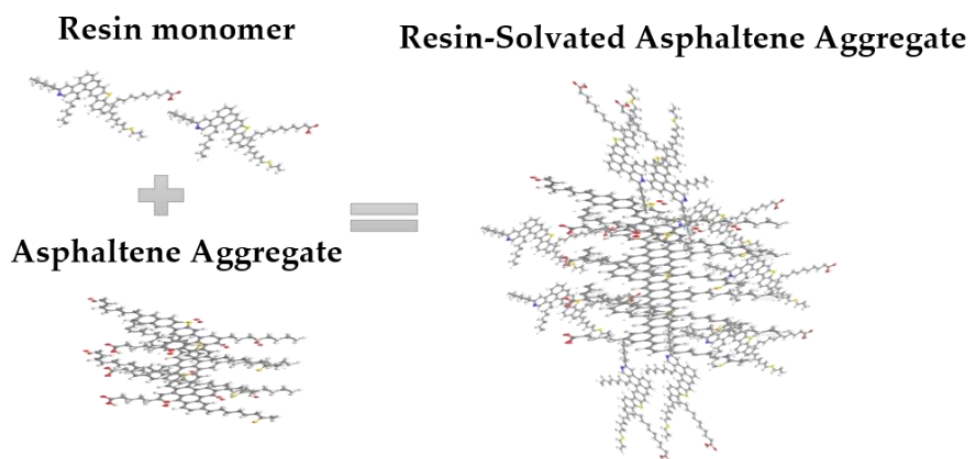


**Figure 5.** Interactions between resins and asphaltene aggregates. Own source.

Figure 4b shows the adsorption isotherms for resins II at different R:A ratios. The results show that type I isotherms for 8:2 and 1:1 ratio. However, in 2:8 system, the isotherm obtained is changed to type III. Results suggest that resins II adsorption is affected by *n*-C<sub>7</sub> asphaltene content. The multilayer behavior of 2:8 ratio shows that the resin-asphaltene interactions prevail over resin–resin interactions [64]. The adsorption amount of resins at  $C_E = 0.33 \text{ mmol}\cdot\text{L}^{-1}$  were  $0.0013 \text{ mmol}\cdot\text{m}^{-2}$ ,  $0.0011 \text{ mmol}\cdot\text{m}^{-2}$ ,  $0.0007 \text{ mmol}\cdot\text{m}^{-2}$ , and  $0.0005 \text{ mmol}\cdot\text{m}^{-2}$  for individual resins, 2:8; 1:1, and 8:2 systems, respectively.

Table 6 summarizes  $H$ ,  $K$ , and  $Q_m$  values of the SLE model for each system evaluated. The experimental data adjustment through the SLE model shows the highest affinity of both resin II and *n*-C<sub>7</sub> asphaltene fractions for CeNi1Pd1

nanocatalysts according to the low  $H$  values. Resins II presented lower  $K$  values than  $n\text{-C}_7$  asphaltenes, which could result from the lower amount of  $C_{ar}$  on their structure. It is reported that the aggregation mechanism of both fractions occurs through  $\pi\text{-}\pi$  stacking interactions between the aromatic cores. Hence, the lower  $C_{ar}$  the lower the self-association degree on the nanocatalysts surface. On the contrary, the  $H$  values were higher for  $n\text{-C}_7$  asphaltenes than those for resins II due to the higher content of carboxyl, thiophene, and pyrrolic functional groups. It is worth mentioning that resins presented a higher value for Fe-Pd couples due to the high content of pyridines, which offer a high affinity for this NOT.

Concerning the self-association degree of  $n\text{-C}_7$  asphaltenes and resins, each fraction's parameter decreases as the content of the other fraction increases. This result suggests that asphaltene–asphaltene and resins–resins interactions are affected by stronger resin-asphaltene interactions [64,65]. In this case, multilayer adsorption of  $n\text{-C}_7$  asphaltenes on CeNi1Pd1 nanocatalysts is favored for higher R:A ratios.

To understand the adsorption mechanism of  $n\text{-C}_7$  asphaltenes in resins II presence on nanoparticles, the adsorbed and desorbed amount of asphaltenes was predicted. If the colloidal state of  $n\text{-C}_7$  asphaltenes is affected by resin II, the predicted and the experimental adsorbed amount will differ. The predicted adsorbed amount in R:A systems is calculated as a fraction of the individual adsorbed amount of each component. For example, in 8:2 system the predicted adsorbed amount of  $n\text{-C}_7$  asphaltenes are assumed as 20.0% of the individual mass fraction adsorbed. A linear graph  $q_{predicted}$  against  $q_{experimental}$  with a slope  $m = 1$ , intersection  $b = 0$ , and  $R^2 = 1.0$  is associated with a good prediction. Table 7 shows the results for the predicted adsorbed amount of  $n\text{-C}_7$  asphaltenes on CeNi1Pd1 nanoparticles in R:A systems. The results show a good fit between the predicted and experimental values. The values of  $m$  were close to 1 in all cases and  $b$  were close to the origin. These results give a clear idea about the influence of resins II on the phenomenon evaluated, indicating that the adsorption of  $n\text{-C}_7$  asphaltenes are mainly controlled by their concentration in the systems and by the affinity of the nanoparticle for resins II. In this way, the colloidal state of the asphaltenes is not affected by the presence of resins II. These results are in good agreement with the reported results in previous works [18,66].

**Table 6.** Estimated SLE model parameters for adsorption isotherms of *n*-C<sub>7</sub> asphaltenes and/or resins II on different nanocatalysts and different Resins-Asphaltene (R:A ratios). *H* represents Henry's law constant, *K* gives an idea about the self-association degree of asphaltenes over nanoparticle surface, and *q<sub>m</sub>* is the maximum amount adsorbed.

Sample	<i>n</i> -C <sub>7</sub> asphaltenes					Resins II			
	R:A	<i>H</i> (mmol· g <sup>-1</sup> ) x10 <sup>-3</sup>	<i>K</i> (mmol ·g <sup>-1</sup> ) x10 <sup>-3</sup>	<i>q<sub>m</sub></i> (mmol· m <sup>-2</sup> ) x10 <sup>-3</sup>	% RS M	<i>H</i> (mmol· g <sup>-1</sup> ) x10 <sup>-2</sup>	<i>K</i> (mmol· g <sup>-1</sup> ) x10 <sup>-2</sup>	<i>q<sub>m</sub></i> (mmol· m <sup>-2</sup> )	% RS M
CeNi1Pd1	Individual	6.97	4.36	0.21	0.01	7.60	0.61	0.19	0.01
CeFe1Pd1	Individual	7.25	4.39	0.19	0.01	8.05	0.21	0.18	0.05
CeCo1Pd1	Individual	6.99	6.36	0.21	0.01	9.17	1.66	22.51	0.02
CeO <sub>2</sub>	Individual	11.15	22.81	0.13	0.01	11.50	7.96	19.40	0.01
	2:8	8.38	5.75	0.20	0.01	171.68	9.06	23.47	0.02
CeNi1Pd1	1:1	13.90	6.24	0.15	0.01	0.18	8.53	31.57	0.01
	8:2	117.05	6.91	28.18	0.01	4.42	3.35	0.25	0.02

**Table 7.** Estimated slope and intercept of the linear plots of *q<sub>predicted</sub>* as a function of *q<sub>experimental</sub>* for the adsorption and desorption of *n*-C<sub>7</sub> asphaltenes in absence and presence of resins II in the systems at different R:A ratios.

R:A Ratio	<i>m</i>	<i>b</i> (x10 <sup>-3</sup> )	<i>R</i> <sup>2</sup>
<i>n</i> -C <sub>7</sub> Asphaltenes	1.0	0.0	1.0
2:8	1.03	-1.11	0.99
1:1	1.05	-2.80	0.98
8:2	1.04	-3.21	0.99

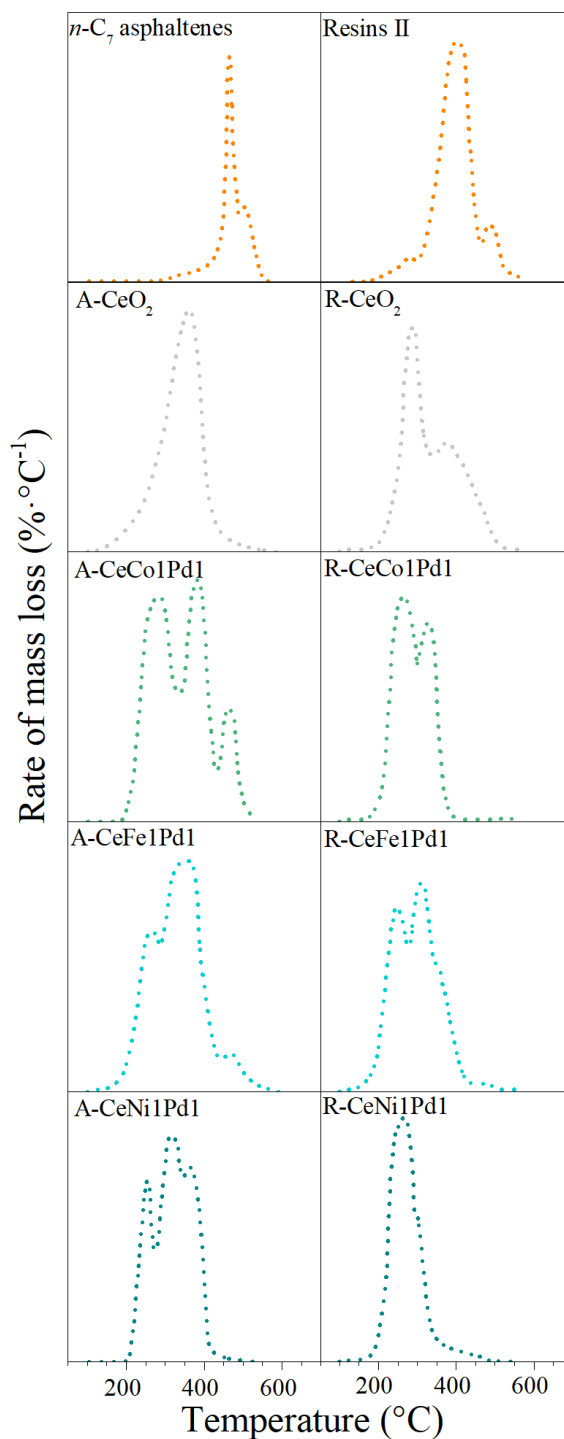
### 3.3. Thermogravimetric Experiments.

Figure 6 shows the rate for mass loss for the steam catalytic gasification of *n*-C<sub>7</sub> asphaltenes and resins II, respectively. Results reveal that pure resins II and *n*-C<sub>7</sub> asphaltenes decompose around 420 °C and 450 °C, respectively (rate for mass loss peak). However, with nanocatalysts, the decomposition temperature reduces, and decomposition begins at approximately 200 °C in all systems.

Bielemental and support systems reduce the *n*-C<sub>7</sub> asphaltenes decomposition temperature from 450 °C, to 220 °C, 230 °C, 250 °C, and 370 °C for CeNi1Pd1, CeCo1Pd1, CeCo1Pd1, and CeO<sub>2</sub>, respectively. On the other hand, the three bielemental and CeO<sub>2</sub> nanocatalysts decompose resins II at 220 °C and 300 °C, respectively. The conversion of both fractions continues at high temperatures, around 350 °C, due to the distribution of high, medium, and low molecular weight hydrocarbons [29].

The decomposition temperature peaks of resins II suggest a high content of lower molecular weight hydrocarbons (aliphatic structures) than those present

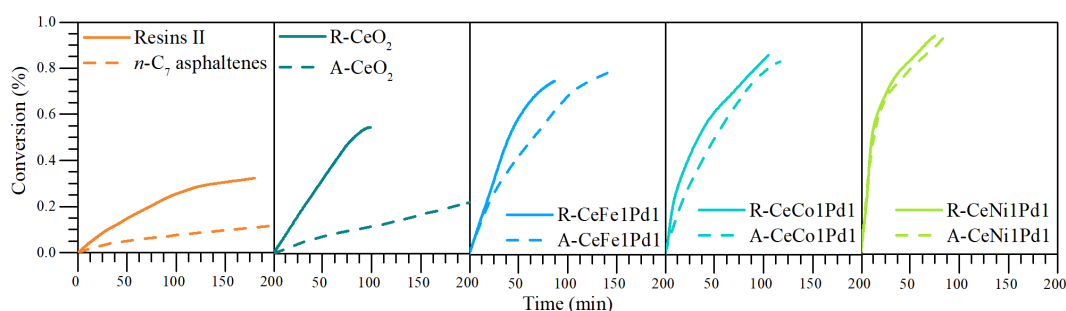
in the asphaltenes' molecular structure. This agrees with  $^{13}\text{C}$ -NMR results. In both cases, nanocatalysts' catalytic activity was improved with the addition of NOT in the order of  $\text{Fe} < \text{Co} < \text{Ni}$ . The highest performance for the couple Ni-Pd is due to the support's ability to interact with Ni and Pd nanocrystals to promote cracking and isomerization reactions [45,67-69]. The strong metal-support interaction between  $\text{Ce}^{3+}$  ions and Ni nanocrystals may promote water gas shift reactions at low temperatures [67]. During this process, the support conducts a redox cycle, which generates oxygen anion vacancies ( $V_o^{2*}$ ). These are active sites for the adsorption of steam molecules and, therefore, have greater interaction with the adsorbed heavy oil fractions [45,68].



**Figure 6.** Rate of mass loss for  $n\text{-C}_7$  asphaltenes and resins II steam gasification in the absence and presence of  $\text{CeO}_2$ ,  $\text{CeNi1Pd1}$ ,  $\text{CeCo1Pd1}$ , and  $\text{CeFe1Pd1}$  nanocatalysts.  $\text{N}_2$  flow rate =  $100 \text{ mL}\cdot\text{min}^{-1}$ ,  $\text{H}_2\text{O}_{(\text{g})}$  flow rate =  $6.30 \text{ mL}\cdot\text{min}^{-1}$ , heating rate =  $20 \text{ }^\circ\text{C}\cdot\text{min}^{-1}$ , asphaltene load =  $0.0002 \text{ mmol}\cdot\text{m}^{-2}$ , resins load =  $0.0002 \text{ mmol}\cdot\text{g}\cdot\text{m}^{-2}$ . Thermograms for  $n\text{-C}_7$  asphaltenes were taken from Medina et al. [38].

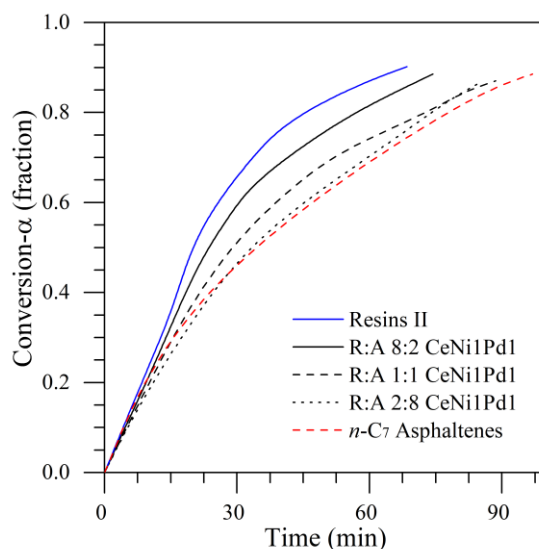
Figure 7 shows the isothermal conversion at 220 °C for *n*-C<sub>7</sub> asphaltenes and resins II adsorbed on the bielemental systems and the support. It is appreciated that the conversion degree increases in the order of CeO<sub>2</sub> < CeFe1Pd1 < CeCo1Pd1 < CeNi1Pd1 in both fractions.

Between the support and the best bielemental nanoparticle (Ni-Pd), to convert 20% of resins II and *n*-C<sub>7</sub> asphaltenes, the time decreases by approximately 70 min and 155 min, respectively. Among many factors, this is due to the role played by the Ni-Pd couple. NiO nanocrystals can inhibit PdO nanocrystals growth [38]; therefore, they acquire a higher dispersion than Co-Pd and Fe-Pd bielemental systems, generating many HA-PdO interactions. This implies increased hydrogen and light gas production capable of stabilizing the cracked heavy oil fractions' free radicals [7].



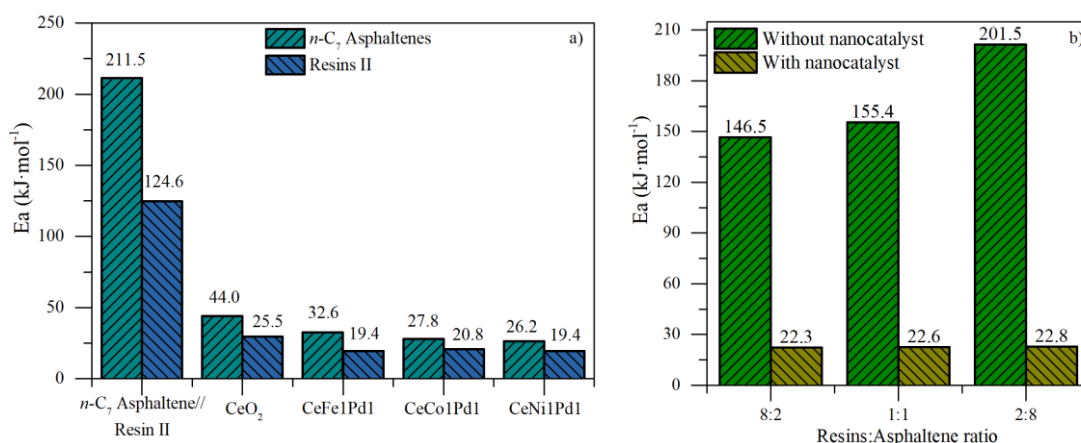
**Figure 7.** Isothermal conversion for *n*-C<sub>7</sub> asphaltenes and resins II in the absence (370 °C) and presence of CeNi1Pd1, CeFe1Pd1, CeCo1Pd1, and CeO<sub>2</sub> nanocatalysts (220 °C). N<sub>2</sub> flow rate = 100 mL·min<sup>-1</sup>, H<sub>2</sub>O<sub>(g)</sub> flow rate = 6.30 mL·min<sup>-1</sup>, asphaltene load = 0.0002 mmol·m<sup>-2</sup>, resin load = 0.0002 mmol·m<sup>-2</sup>. Isothermal conversions of *n*-C<sub>7</sub> asphaltenes were taken from Medina et al. [38].

Figure 8 shows the isothermal conversions at 220 °C for R:A ratios of 8:2, 1:1, and 2:8 on CeNi1Pd1 nanocatalysts. The conversion degree increases in the order A < 2:8 < 1:1 < 8:2 < R at any time. It was reported that resins are composed of a higher degree of aliphatic carbon structures. This composition influences the interactions generated in R:A systems between asphaltenes and resins and, therefore, on catalysis [56]. Decomposing structures by R–R bonds is less complicated than breaking R-A structures [56]. Additionally, with a higher asphaltene content, thiophenes and pyrroles prevail; therefore, more time is required for their cracking [49]. In addition, the first cracked products can polymerize and form coke.



**Figure 8.** Isothermal conversion for different R:A ratios adsorbed on CeNi1Pd1 nanocatalysts at 220 °C. N<sub>2</sub> flow rate = 100 mL·min<sup>-1</sup>, H<sub>2</sub>O<sub>(g)</sub> flow rate = 6.30 mL·min<sup>-1</sup>, asphaltene/resin load = 0.0002 mmol·m<sup>-2</sup>.

The effective activation energy was used to estimate the energy requirements needed for the chemical reaction. Figure 9a shows the results of effective activation energy ( $E_a$ ) for *n*-C<sub>7</sub> asphaltenes and resins II with and without bielemental nanocatalysts and support.  $E_a$  decreases considerably by adding nanocatalysts in the order of CeO<sub>2</sub> < CeFe1Pd1 < CeCo1Pd1 < CeNi1Pd1. NOTs impregnation modifies the decomposition mechanism of the heavy oil fractions, indicating that the catalyst's chemical nature influences gasification reactions. On the other hand, the energy required for thermo-gasification and thermo-catalytic gasification is lower for resins II than for asphaltenes. In addition, the estimated activation energy values for the R:A systems above CeNi1Pd1 nanocatalysts are shown in panel b. It is observed that  $E_a$  increases in the order of 8:2 < 1:1 < 2:8 for virgin and adsorbed fractions. CeNi1Pd1 nanocatalysts reduced the activation energy from 146.5, 155.4, and 201.5 kJ·mol<sup>-1</sup> to 22.3, 22.6, and 22.8 kJ·mol<sup>-1</sup> for 8:2, 1:1, and 2:8 systems, respectively.



**Figure 9.** Estimated effective activation energy for isothermal gasification of (a)  $n-C_7$  asphaltenes and resins II with  $\text{CeO}_2$ , CeFe1Pd1, CeCo1Pd1 and CeNi1Pd1 nanocatalysts, and (b) R:A systems with and without CeNi1Pd1 nanocatalysts.

### 3.4. Analysis of Gaseous Profiles during Steam Gasification

#### 3.4.1. Effect of Nanocatalyst Chemical Nature

The effect of the nanocatalyst's chemical nature on evolved gases during the steam gasification of  $n-C_7$  asphaltenes and resins II was analyzed under isothermal heating at  $220\text{ }^\circ\text{C}$ . The results are shown in Figure 10 as a function of time. It is observed the release of  $\text{CO}_2$ ,  $\text{CH}_4$ ,  $\text{CO}$ , a mixture of light hydrocarbons (LHC), and  $\text{H}_2$ . Some traces of other gases were evidenced in different time intervals, but their contribution was less than 0.1%; thus, they were neglected.

It is worth mentioning that non-catalyzed systems were evaluated at  $370\text{ }^\circ\text{C}$  due to their complex structure. The gasification results for the non-catalyzed systems show considerable  $\text{CO}$  and  $\text{CO}_2$  production during the conversion of the samples. The higher production of  $\text{CO}$  is associated with the reverse Boudouard reaction. As the reaction is endothermic, the production of  $\text{CO}$  becomes meaningful over time. On the other hand, the LHC mixture was composed mainly of  $\text{C}_2\text{H}_2$ ,  $\text{C}_2\text{H}_4$ , and  $\text{C}_6\text{H}_6$ . Its production was markedly at the beginning of the warm-up. This is because the aliphatic chains break down at low temperatures and promote the production of these gases. However, over time, asphaltenes and resins produce a higher proportion of  $\text{CO}_2$  and  $\text{CO}$  and do not promote intermediate reactions that give rise to LHC.

On the other hand, methane and hydrogen were produced in low quantities all the time evaluated. It should be noted that these fractions decompose less than 20% of their mass at  $370\text{ }^\circ\text{C}$  during the time analyzed. It is noted that asphaltenes produce a higher amount of  $\text{CO}_2$  and a lower amount of  $\text{H}_2$  than resins II in all the time evaluated. This result agrees with the higher content of aromatic carbon



in asphaltenes. During thermal heating, the aromatic core is susceptible to the formation of ketones and finally released as CO<sub>2</sub>. The higher the content of hydrogens  $\alpha$  and  $\gamma$  linked to aromatic rings, the higher the hydrogen release.

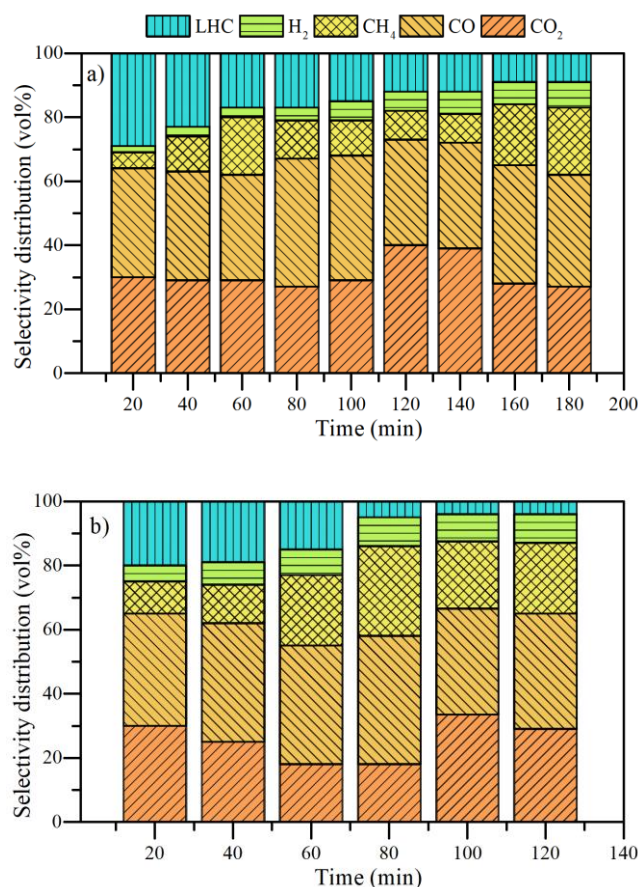


**Figure 10.** Selectivity distribution of light gases produced from the isothermal conversion of (a) *n*-C<sub>7</sub> asphaltenes and (b) resins at 370 °C. N<sub>2</sub> flow rate = 100 mL·min<sup>-1</sup>, H<sub>2</sub>O<sub>(g)</sub> flow rate = 6.30 mL·min<sup>-1</sup>.

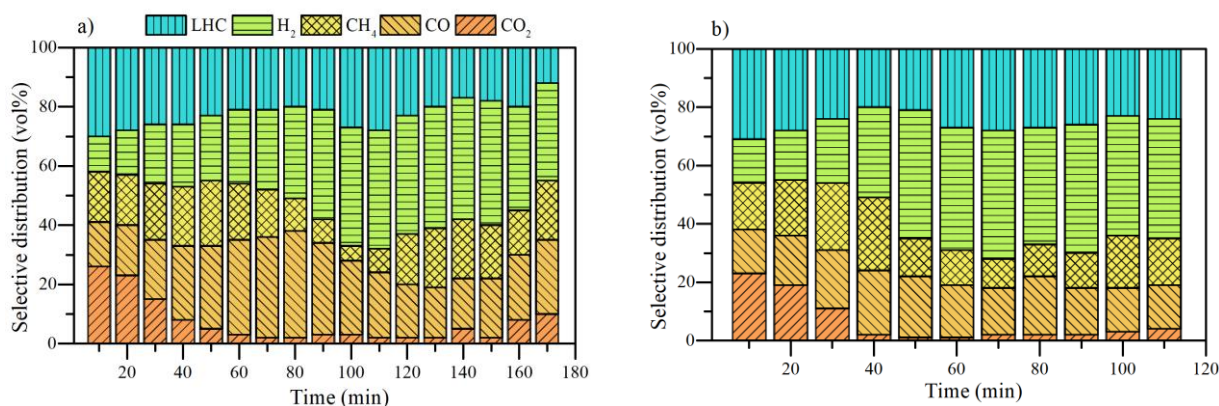
Figures 11 and 12 show the selectivity distribution of light gases for *n*-C<sub>7</sub> asphaltenes and resins adsorbed on different nanocatalysts, respectively. The results reveal an increase in LHC, CH<sub>4</sub>, and H<sub>2</sub> at all times at 220 °C for both fractions. The asphaltenes begin their decomposition with a CO<sub>2</sub> production between 20% and 30% (vol) for all nanocatalysts. Unlike the virgin fractions, there is a higher production of H<sub>2</sub> and LHC from the first 10 min of heating. Subsequently, CO<sub>2</sub> production falls to a greater degree for asphaltenes adsorbed on CeNi1Pd1 than in the rest of the systems. In turn, the production of CO, CH<sub>4</sub>, and H<sub>2</sub> increases. When reacting with CO<sub>2</sub>, carbon produces CO, while CH<sub>2</sub> is produced by breaking short aliphatic chains (methyl, methylene, etc.). Hydrogen,

in the first instance, can be produced by the reaction of C in asphaltenes and  $\text{H}_2\text{O}_{(g)}$  molecules.

During thermal gasification, there is a drop in  $\text{CH}_4$  production in all cases. For  $\text{CeO}_2$ , it occurs at 50 min, for  $\text{CeFe1Pd1}$  at 40 min, and for  $\text{CeCo1Pd1}$  and  $\text{CeNi1Pd1}$  at 30 min. In turn, the production of  $\text{H}_2$  increases. This may suggest the development of steam-reforming reactions assisted by different nanocatalysts [69]. The difference in the time it occurs is a response to each system's catalytic activity. Therefore, the most catalytic system ( $\text{CeNi1Pd1}$ ) generates this change in less time and with more outstanding vol% production of  $\text{H}_2$ . Likewise, the drop in  $\text{CO}$  and a slight increase in  $\text{CO}_2$  and  $\text{H}_2$  indicate the WGS reaction development [69]. These changes in the selective distribution of gaseous products were first observed in the system ( $\text{CeNi1Pd1}$ ) between 40 and 50 min.

Moreover, the increase in  $\text{CO}_2$  was minimal.  $\text{CeO}_2$  (90–100 min) was the system that took the longest. Regarding several studies on the catalytic gasification of carbon, all the materials in this study produced a lower content of  $\text{CO}_2$  in the entire time interval analyzed [5,70-72].

Finally, the mixture of light hydrocarbons was mainly composed of  $\text{C}_2\text{H}_2$ , obtaining a total gas mixture with an average calorific value of  $82.45 \text{ kcal}\cdot\text{kg}^{-1}$  for  $\text{CeO}_2$ ,  $102.51 \text{ kcal}\cdot\text{kg}^{-1}$  for  $\text{CeFe1Pd}$ ,  $124.23 \text{ kcal}\cdot\text{kg}^{-1}$  for  $\text{CeCo1Pd1}$ , and  $139.14 \text{ kcal}\cdot\text{kg}^{-1}$  for  $\text{CeNi1Pd1}$  on time evaluated. It is observed that the dispersion and average crystallite size of Pd in functionalized systems follows the same order as the increase in  $\text{H}_2$  release and the average calorific values of the release gas mixture. As higher the dispersion and lower the average crystal size, the higher the calorific values and the content of  $\text{H}_2$  produced.



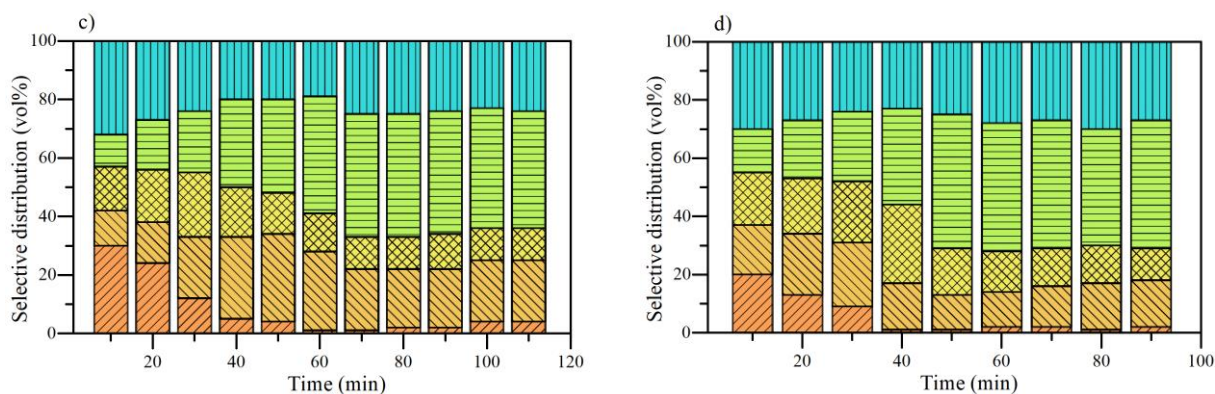


**Figure 11.** Selectivity distribution of light gases produced from the isothermal conversion of *n*-C<sub>7</sub> asphaltenes at 220 °C in the presence of (a) CeO<sub>2</sub>, (b) CeCo1Pd1, (c) CeFe1Pd1, and (d) CeNi1Pd1 nanocatalysts. N<sub>2</sub> flow rate = 100 mL·min<sup>-1</sup>, H<sub>2</sub>O<sub>(g)</sub> flow rate = 6.30 mL·min<sup>-1</sup>, asphaltene load = 0.0002 mmol·m<sup>-2</sup>.

Figure 12 depicts the results for resins II. The resins followed the same trend as *n*-C<sub>7</sub> asphaltenes. The main differences lie in how the nanocatalysts generate significant changes in the selective distribution of gases and their volumetric proportion.

The maximum production of CO<sub>2</sub> in all cases is observed at 10 min, which follows the incremental order of CeNi1Pd1 < CeFe1Pd1 < CeCo1Pd1 < CeO<sub>2</sub>. The order in which the LHCs were produced in this interval follows the opposite order. This indicates that in the presence of the CeNi1Pd1 catalyst, the resins decompose a high content of their aliphatic structure. The production of CO<sub>2</sub> tends to decrease, being more noticeable in the catalyst CeNi1Pd1. In other words, the catalyst promotes C-CO<sub>2</sub> interactions, increasing the release of CO [69]. Methane reforming reactions appear to occur between 30 and 40 minutes for functionalized catalysts and between 60 and 70 minutes for CeO<sub>2</sub> support. On the other hand, the production of H<sub>2</sub> intensified with CO reduction; this gas participates in WGS reactions. This reaction occurs at higher temperatures, between 40 and 60 min for CeNi1Pd1, 60 and 80 min for CeCo1Pd1 and CeFe1Pd1, and 90 and 100 min for CeO<sub>2</sub>.

The future trend in hydrogen production is increasing toward Fe < Co < Ni for both fractions. Many researchers cite the oxygen storage/reduction of cerium-based materials and nanocrystals' catalytic activity on the supports' surface as a key component of the WGS and methane reforming activity of catalysts [67,69,73-75].

Studies have also shown that the addition of dopants or a combination of multiple metals as active phases creates defects in the structure and oxygen

vacancies in which pure, highly dispersed metal catalysts are located [62,67]. This allows the adsorption of reactants and facilitates the WGS and methane reforming reactions. The hydrogen production trend also agreed with each material's catalytic activity for decomposing both fractions at the evaluated conditions. CeNi1Pd1 showed a higher performance than the other three samples, leading to a higher hydrogen vol% in the effluent gas.

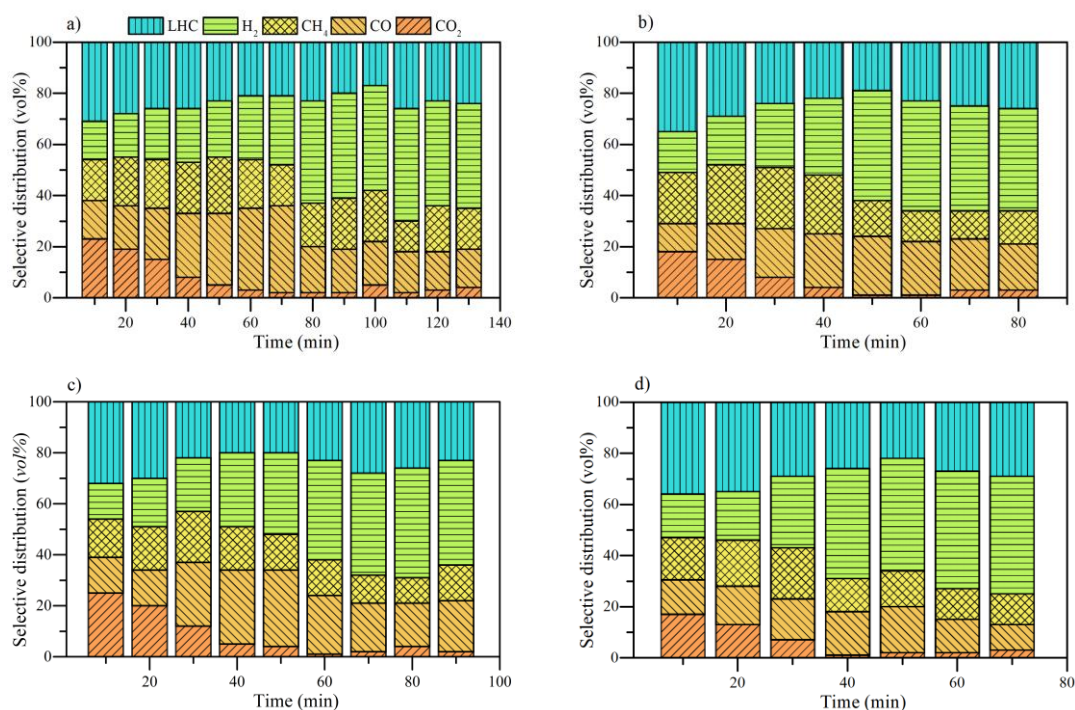


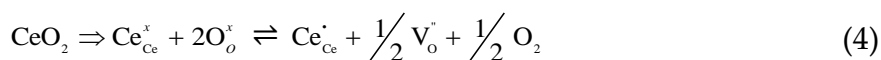
**Figure 12.** Selectivity distribution of light gases produced from the isothermal conversion of resins II at 220 °C in the presence of (a) CeO<sub>2</sub>, (b) CeCo1Pd1, (c) CeFe1Pd1, and (d) CeNi1Pd1 nanocatalysts. N<sub>2</sub> flow rate = 100 mL·min<sup>-1</sup>, H<sub>2</sub>O(g) flow rate = 6.30 mL·min<sup>-1</sup>, resin load = 0.0002 mmol·m<sup>-2</sup>.

Cerium nanoparticles as active support facilitate the production of low molecular weight compounds due to (a) the positive effect of the NOT- and NON-elements and ceria interactions and (b) the activity of redox couple Ce<sup>3+</sup>/Ce<sup>4+</sup>. There is evidence that oxygen atoms migrate from the support (CeO<sub>2</sub>) to transition element particles at higher temperatures during spillover phenomena. This oxygen can be used to oxidize CO to CO<sub>2</sub>, and subsequently, the partially reduced ceria can be re-oxidized by water, completing the catalytic cycle. Moreover, the gases can be used to produce H<sub>2</sub> during the WGS reaction. In this sense, the surface of the support will be composed of Ce<sup>3+</sup> and Ce<sup>4+</sup> ions. Ce<sup>3+</sup> ions formed after reducing Pd-based catalysts play an essential role in activating CO and CO<sub>2</sub> molecules at the ceria-transition element interface.



The heterogeneous surface of the material promotes different types of reactions. For example, the Ni/CeO<sub>2</sub> active sites first generate the total combustion of CH<sub>4</sub> followed by H<sub>2</sub>O and CO reforming. For Pd/CeO<sub>2</sub>, the reaction follows a direct mechanism with H<sub>2</sub>, CO, CO<sub>2</sub>, and H<sub>2</sub>O's simultaneous formation. These differences are explained due to the transfer of electrons between the element's particles and the support. In a steam atmosphere, the CO oxidation is enhanced by OH· and O<sub>2</sub> species' reaction to the support's basic sites, following the gasification mechanisms, increasing CO<sub>2</sub> and H<sub>2</sub> production. Methane activation occurs through the active surface of oxygen. The high electronic affinity with the coordinated surface of unsaturated oxygen (cus) generates a strong interaction with methane and light hydrocarbon molecules, activating C-H bonds at low temperatures and their subsequent breakdown, finally desorbing as CO<sub>2</sub> and H<sub>2</sub>O.

The surface chemistry of the nanocatalysts was correlated with the results of selective distribution in hydrogen released from asphaltene and resin decomposition. The results are shown in Figure 13. As described, hydrogen release increases in the order CeFe1Pd1 < CeCo1Pd1 < CeNi1Pd1, which agrees with the tendencies for Pd<sup>2+</sup>, Ce<sup>3+</sup>, and O<sub>ads</sub>/O<sub>lat</sub> in the surface chemistry of the nanocatalysts. It is well-recognized the redox property of CeO<sub>2</sub> influences catalytic activity. The relative abundance of Ce<sup>3+</sup> and O<sub>ads</sub>/O<sub>lat</sub> suggests their participation in hydrogen formation. First, the redox cycle allows oxygen adsorption under oxidation conditions and its release under reduced conditions, as is shown in Equations (3) and (4):



Furthermore, hydroxyl groups (OH) formed by the reaction between H<sub>2</sub>O and partially reduced ceria oxygen vacancies react with CO to form methanoate species of the bridge [76]. Above 170 °C, these species are transformed into bidentate formates to decompose into final products of CO<sub>2</sub> and H<sub>2</sub> [76]. Similarly, the higher the content of Pd<sup>2+</sup> species, the higher the selective distribution for hydrogen production in the catalytic decomposition of both fractions. These ions could substitute Ce<sup>4+</sup> in the ceria lattice to increase the defect concentration. Hence, the catalysts improved their oxygen vacancy density and oxygen mobility as increases Pd<sup>2+</sup> on their surface. In complete agreement, it is

reported that the strong interactions between Ni and Pd species with Ce support lead to more thermal stable metal species [38], which contributed to the synergistic effect of both phases for crude oil fractions decomposition and hydrogen production.

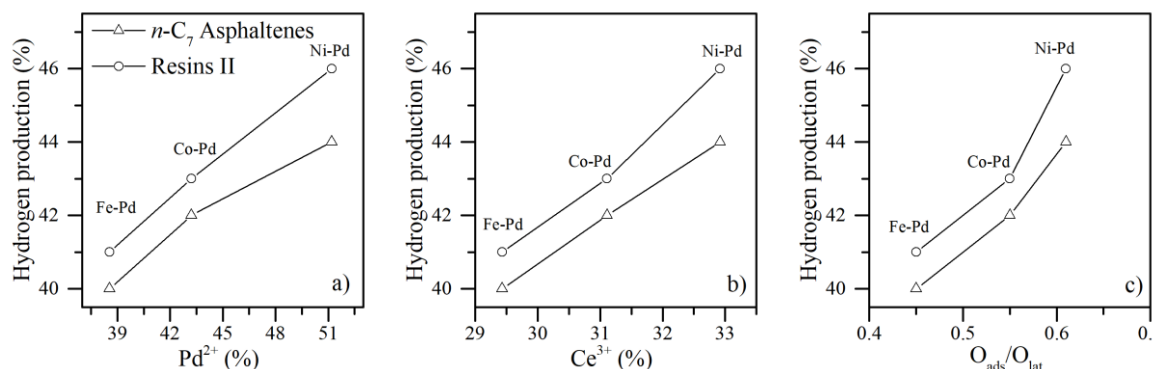


**Figure 13.** Hydrogen percentage produced from the isothermal conversion of  $n$ -C<sub>7</sub> asphaltenes and resins II at 220 °C in the presence of functionalized nanocatalysts CeFe1Pd1, CeCo1Pd1, and CeNi1Pd1 as a function of the (a) Pd<sup>2+</sup>, (b) Ce<sup>3+</sup> and (c) O<sub>ads</sub>/O<sub>lat</sub> content. Hydrogen release at 90 min and 70 min was taken for constructing asphaltene and resins graphs.

### 3.4.2. Effect of R:A Ratio

The CeNi1Pd1 was selected to evaluate the effect of R:A ratio on hydrogen release from its isothermal steam catalytic gasification at 220 °C. The results are shown as a function of the conversion degree ( $\alpha$ ) in Figure 14. It is found that the R:A ratio influences the H<sub>2</sub> content in the effluent gas. At low conversions ( $\alpha < 0.2$ ) the H<sub>2</sub> content is very similar in all systems. Between 0.4 and 0.7, the trend is evident. For the same transformation, the production of H<sub>2</sub> increases in the order of R < 8:2 < 1:1 < 2:8 < A. As shown in the previous section, different reactions contribute to the generation of H<sub>2</sub> in the presence of the CeNi1Pd1 catalyst. However, depending on the chemical nature of the adsorbed fraction, H<sub>2</sub> release can vary. The high content of short aliphatic chains promotes methane production in greater quantity, and as previously shown, asphaltenes have a higher range of H <sub>$\alpha$</sub>  species. In this sense, methane reforming may have a greater contribution as the content of asphaltenes increases in R:A mixtures.

On the other hand, the systems show a production peak generated at lower conversions when the asphaltene content is lower. These data coincide with the slight increase in the production of CO<sub>2</sub> in samples A and R, an indicator of WGS reactions. For conversions greater than 0.8, H<sub>2</sub> production is fluctuating.

However, it does not fall below 40.0 vol%. These results indicate the nanocatalyst's potential to produce a hydrogen-rich gas from the steam catalytic gasification of asphaltenes and resins adsorbed individually and in mixtures. All the results demonstrate the potential of the technology to release a hydrogen-rich gaseous mixture.

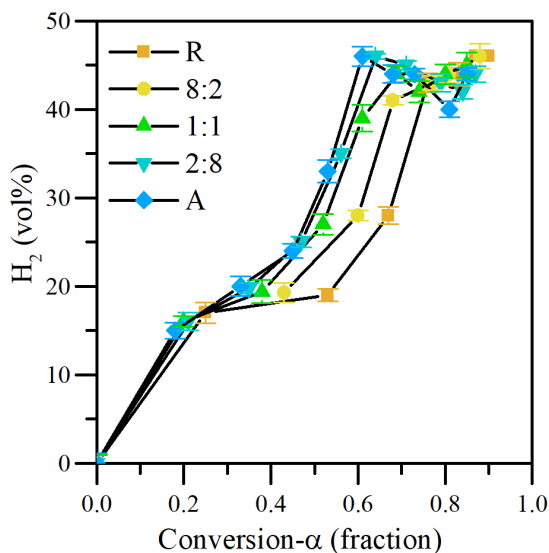


**Figure 14.** H<sub>2</sub> production as a function of conversion degree of different R:A ratios adsorbed on CeNi1Pd1 nanocatalysts at 220 °C. N<sub>2</sub> flow rate = 100 mL·min<sup>-1</sup>, H<sub>2</sub>O<sub>(g)</sub> flow rate = 6.30 mL·min<sup>-1</sup>, asphaltene/resin load = 0.0002 mmol·m<sup>-2</sup>.

### 3.4.3. Effect of Temperature

Operation temperature was varied between 210 and 230 °C to analyze its effect on H<sub>2</sub> generation from the steam catalytic gasification of *n*-C<sub>7</sub> asphaltenes. Figure 15 shows the results obtained. Higher H<sub>2</sub> concentration was observed as the temperature increased. This indicates that at 230 °C, the most favorable conditions for steam reforming and WGS reactions are received. This trend follows the degree of conversion of each fraction. In the same figure, it is observed that asphaltenes convert greater mass at 230 °C. Therefore, it produces a greater quantity of H<sub>2</sub> catalyzed by CeNi1Pd1. The higher the temperature, the higher the H<sub>2</sub>O<sub>(g)</sub> and CO<sub>2</sub> gasification reaction rates, obtaining a higher release of H<sub>2</sub> at 230 °C than the other two temperatures evaluated.

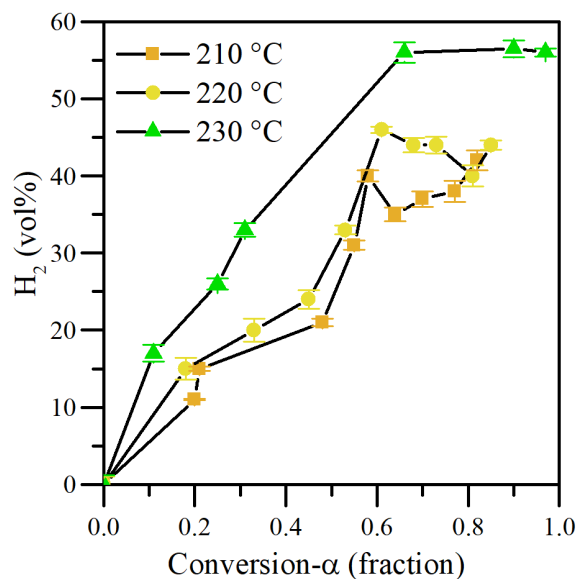


**Figure 15.** H<sub>2</sub> production as a function of conversion degree of *n*-C<sub>7</sub> asphaltenes adsorbed on CeNi1Pd1 nanocatalysts at 220 °C. N<sub>2</sub> flow rate = 100 mL·min<sup>-1</sup>, H<sub>2</sub>O<sub>(g)</sub> flow rate = 6.30 mL·min<sup>-1</sup>, asphaltene/resin load = 0.0002 mmol·m<sup>-2</sup>.

#### 4. Conclusions

For the first time, the present study shows the effect of resin II in the adsorption and catalytic steam gasification of *n*-C<sub>7</sub> asphaltene on hydrogen production using functionalized CeO<sub>2</sub> nanocatalysts with different pairs of transition element oxides. The individual resin II adsorption follows the Co < Fe < Ni order. For competitive adsorption, the simultaneous presence of two fractions influences the individual adsorption of *n*-C<sub>7</sub> asphaltene and resin II correspondingly because when the amount of resin II increases in the system, the adsorption of *n*-C<sub>7</sub> asphaltenes decreases. Additionally, resin II decomposition temperature dropped from 420 to 220 °C for bielemental nanocatalysts and 300 °C for the support of CeO<sub>2</sub>, whereas *n*-C<sub>7</sub> asphaltenes decompose at about 220 °C for bielemental nanocatalysts and 350 °C when the support catalyzes them. For the R:A systems, the conversion increases in the order of (R:A) 8:2 < 1:1 < 2:8, because asphaltenes have a greater content of heavy molecular weight components that require higher time for their decomposition. CeNi1Pd1 nanocatalysts decrease the effective activation energy in all R:A and individual systems, evidencing the positive thermal effect against the steam injection processes.

Hydrogen release was successfully quantified. The results depict an increasing H<sub>2</sub> production order of CeO<sub>2</sub> < CeFe1Pd1 < CeCo1Pd1 < CeNi1Pd1



under isothermal heating at 220 °C during asphaltene and resin conversion. The CeNi1Pd1 catalyst produces a gas effluent of more than 40 vol% of H<sub>2</sub>, decomposing both fractions. When the samples were heated at 230 °C, H<sub>2</sub> production was increased by close to 55 vol% during *n*-C<sub>7</sub> asphaltene conversion.

It was noted that asphaltenes produce a higher amount of CO<sub>2</sub> and a lower amount of H<sub>2</sub> than resins II in all the time evaluated. This result agrees with the higher content of aromatic carbon in asphaltenes. During thermal heating, the aromatic core is susceptible to the formation of ketones and finally released as CO<sub>2</sub>. The higher the content of hydrogens  $\alpha$  and  $\gamma$  linked to aromatic rings, the higher the hydrogen release. In the presence of CeNi1Pd1, a high efficiency to produce H<sub>2</sub> was obtained regardless of the nature of the fraction and the R:A systems. The decomposition of the R:A mixtures also generated gas contents similar to the individual fractions.

Likewise, CO<sub>2</sub> production was minimal in all the cases evaluated, highlighting the use of the nanocatalysts studied. A gas average mixture with a content < 4% vol CO<sub>2</sub> was produced with CeNi1Pd1, a relatively low result and similar to those reported for biomass and natural gas gasification.

## References

1. Holladay, J.D.; Hu, J.; King, D.L.; Wang, Y. An overview of hydrogen production technologies. *Catalysis today* **2009**, *139*, 244-260.
2. Navarro, R.M.; Pena, M.; Fierro, J. Hydrogen production reactions from carbon feedstocks: fossil fuels and biomass. *Chemical reviews* **2007**, *107*, 3952-3991.
3. Ni, M.; Leung, D.Y.; Leung, M.K.; Sumathy, K. An overview of hydrogen production from biomass. *Fuel processing technology* **2006**, *87*, 461-472.
4. Muradov, N. How to produce hydrogen from fossil fuels without CO<sub>2</sub> emission. *International Journal of Hydrogen Energy* **1993**, *18*, 211-215.
5. Seyitoglu, S.; Dincer, I.; Kilicarslan, A. Energy and exergy analyses of hydrogen production by coal gasification. *International Journal of Hydrogen Energy* **2017**, *42*, 2592-2600.
6. Blok, K.; Williams, R.; Katofsky, R.; Hendriks, C.A. Hydrogen production from natural gas, sequestration of recovered CO<sub>2</sub> in depleted gas wells and enhanced natural gas recovery. *Energy* **1997**, *22*, 161-168.

7. Medina, O.E.; Olmos, C.; Lopera, S.H.; Cortés, F.B.; Franco, C.A. Nanotechnology Applied to Thermal Enhanced Oil Recovery Processes: A Review. *Energies* **2019**, *12*, 4671.
8. Santos, R.; Loh, W.; Bannwart, A.; Trevisan, O. An overview of heavy oil properties and its recovery and transportation methods. *Brazilian Journal of Chemical Engineering* **2014**, *31*, 571-590.
9. Guo, K.; Li, H.; Yu, Z. In-situ heavy and extra-heavy oil recovery: A review. *Fuel* **2016**, *185*, 886-902.
10. Curtis, C.; Kopper, R.; Decoster, E.; Guzmán-García, A.; Huggins, C.; Knauer, L.; Minner, M.; Kupsch, N.; Linares, L.M.; Rough, H. Heavy-oil reservoirs. *Oilfield Review* **2002**, *14*, 30-51.
11. Rahimi, P.M.; Gentzis, T. The chemistry of bitumen and heavy oil processing. In *Practical advances in petroleum processing*, Springer: 2006; pp. 597-634.
12. Hamedi Shokrlu, Y.; Babadagli, T. Kinetics of the in-situ upgrading of heavy oil by nickel nanoparticle catalysts and its effect on cyclic-steam-stimulation recovery factor. *SPE Reservoir Evaluation & Engineering* **2014**, *17*, 355-364.
13. Terry, R.E. Enhanced oil recovery. *Encyclopedia of physical science and technology* **2001**, *18*, 503-518.
14. Alvarado, V.; Manrique, E. Enhanced oil recovery: an update review. *Energies* **2010**, *3*, 1529-1575.
15. Thomas, S. Enhanced oil recovery-an overview. *Oil & Gas Science and Technology-Revue de l'IFP* **2008**, *63*, 9-19.
16. Zhang, T.; Davidson, D.; Bryant, S.L.; Huh, C. Nanoparticle-stabilized emulsions for applications in enhanced oil recovery. In Proceedings of SPE improved oil recovery symposium.
17. Speight, J. Petroleum Asphaltenes-Part 1: Asphaltenes, resins and the structure of petroleum. *Oil & gas science and technology* **2004**, *59*, 467-477.
18. Franco, C.A.; Lozano, M.M.; Acevedo, S.; Nassar, N.N.; Cortés, F.B. Effects of resin I on asphaltene adsorption onto nanoparticles: a novel method for obtaining asphaltenes/resin isotherms. *Energy & Fuels* **2015**, *30*, 264-272.
19. Ali, S. Current status of steam injection as a heavy oil recovery method. *Journal of Canadian Petroleum Technology* **1974**, *13*.
20. Medina, O.E.; Hurtado, Y.; Caro-Velez, C.; Cortés, F.B.; Riazi, M.; Lopera, S.H.; Franco, C.A. Improvement of Steam Injection Processes Through

- Nanotechnology: An Approach through in Situ Upgrading and Foam Injection. *Energies* **2019**, *12*, 4633.
21. Shin, H.; Polikar, M. Review of reservoir parameters to optimize SAGD and Fast-SAGD operating conditions. *Journal of Canadian Petroleum Technology* **2007**, *46*.
  22. Melcon, S. Oil recovery by in situ combustion. Google Patents: 1965.
  23. Sun, X.; Zhang, Y.; Chen, G.; Gai, Z. Application of nanoparticles in enhanced oil recovery: a critical review of recent progress. *Energies* **2017**, *10*, 345.
  24. Nassar, N.N.; Hassan, A.; Pereira-Almao, P. Application of nanotechnology for heavy oil upgrading: Catalytic steam gasification/cracking of asphaltenes. *Energy & Fuels* **2011**, *25*, 1566-1570.
  25. Ogolo, N.; Olafuyi, O.; Onyekonwu, M. Enhanced oil recovery using nanoparticles. In Proceedings of SPE Saudi Arabia section technical symposium and exhibition.
  26. Agista, M.N.; Guo, K.; Yu, Z. A State-of-the-Art Review of Nanoparticles Application in Petroleum with a Focus on Enhanced Oil Recovery. *Applied Sciences* **2018**, *8*, 871.
  27. Hashemi, R.; Nassar, N.N.; Almao, P.P. Nanoparticle technology for heavy oil in-situ upgrading and recovery enhancement: Opportunities and challenges. *Applied Energy* **2014**, *133*, 374-387.
  28. Cheraghian, G.; Hendraningrat, L. A review on applications of nanotechnology in the enhanced oil recovery part B: effects of nanoparticles on flooding. *International Nano Letters* **2016**, *6*, 1-10.
  29. Ariza, F.; Andrés, C. Synthesis and application of supported metallic and multi-metallic oxides nanoparticles for in-situ upgrading and inhibition of formation damage. Universidad Nacional de Colombia-Sede Medellín.
  30. Nassar, N.N.; Hassan, A.; Pereira-Almao, P. Metal oxide nanoparticles for asphaltene adsorption and oxidation. *Energy & Fuels* **2011**, *25*, 1017-1023.
  31. Hosseinpour, N.; Khodadadi, A.A.; Bahramian, A.; Mortazavi, Y. Asphaltene adsorption onto acidic/basic metal oxide nanoparticles toward in situ upgrading of reservoir oils by nanotechnology. *Langmuir* **2013**, *29*, 14135-14146.
  32. Kazemzadeh, Y.; Eshraghi, S.E.; Kazemi, K.; Sourani, S.; Mehrabi, M.; Ahmadi, Y. Behavior of asphaltene adsorption onto the metal oxide nanoparticle surface and its effect on heavy oil recovery. *Industrial & Engineering Chemistry Research* **2015**, *54*, 233-239.

33. Zheng, X.; Li, Y.; Zhang, L.; Shen, L.; Xiao, Y.; Zhang, Y.; Au, C.; Jiang, L. Insight into the effect of morphology on catalytic performance of porous CeO<sub>2</sub> nanocrystals for H<sub>2</sub>S selective oxidation. *Applied Catalysis B: Environmental* **2019**, *252*, 98-110.
34. Maciel, C.G.; de Freitas Silva, T.; Hirooka, M.I.; Belgacem, M.N.; Assaf, J.M. Effect of nature of ceria support in CuO/CeO<sub>2</sub> catalyst for PROX-CO reaction. *Fuel* **2012**, *97*, 245-252.
35. Eaimsumang, S.; Wongkasemjit, S.; Pongstabodee, S.; Smith, S.M.; Ratanawilai, S.; Chollacoop, N.; Luengnaruemitchai, A. Effect of synthesis time on morphology of CeO<sub>2</sub> nanoparticles and Au/CeO<sub>2</sub> and their activity in oxidative steam reforming of methanol. *Journal of Rare Earths* **2019**, *37*, 819-828.
36. Razeghi, A.; Khodadadi, A.; Ziaei-Azad, H.; Mortazavi, Y. Activity enhancement of Cu-doped ceria by reductive regeneration of CuO–CeO<sub>2</sub> catalyst for preferential oxidation of CO in H<sub>2</sub>-rich streams. *Chemical Engineering Journal* **2010**, *164*, 214-220.
37. Franco, C.A.; Montoya, T.; Nassar, N.N.; Cortés, F.B. NIOAND PDO SUPPORTED ON FUMED SILICA NANOPARTICLES FOR ADSORPTION AND CATALYTIC STEAM GASIFICATION OF COLOMBIAN C7ASPHALTENES. **2014**.
38. Medina, O.E.; Gallego, J.; Arias-Madrid, D.; Cortés, F.B.; Franco, C.A. Optimization of the Load of Transition Metal Oxides (Fe<sub>2</sub>O<sub>3</sub>, Co<sub>3</sub>O<sub>4</sub>, NiO and/or PdO) onto CeO<sub>2</sub> Nanoparticles in Catalytic Steam Decomposition of n-C<sub>7</sub> Asphaltenes at Low Temperatures. *Nanomaterials* **2019**, *9*, 401.
39. Cardona Rojas, L. Efecto de nanopartículas en procesos con inyección de vapor a diferentes calidades. M.Sc. Thesis, Universidad Nacional de Colombia-Sede Medellín, March 2018.
40. Cardona, L.; Arias-Madrid, D.; Cortés, F.; Lopera, S.; Franco, C. Heavy oil upgrading and enhanced recovery in a steam injection process assisted by NiO-and PdO-Functionalized SiO<sub>2</sub> nanoparticulated catalysts. *Catalysts* **2018**, *8*, 132.
41. Delannoy, L.; El Hassan, N.; Musi, A.; Le To, N.N.; Krafft, J.-M.; Louis, C. Preparation of supported gold nanoparticles by a modified incipient wetness impregnation method. *The Journal of Physical Chemistry B* **2006**, *110*, 22471-22478.
42. Medina, O.E.; Gallego, J.; Restrepo, L.G.; Cortés, F.B.; Franco, C.A. Influence of the Ce<sup>4+</sup>/Ce<sup>3+</sup> Redox-couple on the cyclic regeneration for

- adsorptive and catalytic performance of NiO-PdO/CeO<sub>2</sub>+ $\delta$  nanoparticles for n-C7 asphaltene steam gasification. *Nanomaterials* **2019**, *9*, 734.
43. Sellers-Antón, B.; Bailón-García, E.; Cardenas-Arenas, A.; Davó-Quiñonero, A.; Lozano-Castelló, D.; Bueno-López, A. Enhancement of the Generation and Transfer of Active Oxygen in Ni/CeO<sub>2</sub> Catalysts for Soot Combustion by Controlling the Ni–Ceria Contact and the Three-Dimensional Structure. *Environmental Science & Technology* **2020**, *54*, 2439-2447.
  44. Wrobel, G.; Sohier, M.; D'Huysser, A.; Bonnelle, J.; Marcq, J. Hydrogenation catalysts based on nickel and rare earth oxides: Part II: XRD, electron microscopy and XPS studies of the cerium-nickel-oxygen-hydrogen system. *Applied Catalysis A: General* **1993**, *101*, 73-93.
  45. Wang, X.; Chen, J.; Zeng, J.; Wang, Q.; Li, Z.; Qin, R.; Wu, C.; Xie, Z.; Zheng, L. The synergy between atomically dispersed Pd and cerium oxide for enhanced catalytic properties. *Nanoscale* **2017**, *9*, 6643-6648.
  46. Ancheyta, J.; Centeno, G.; Trejo, F.; Marroquin, G.; Garcia, J.; Tenorio, E.; Torres, A. Extraction and characterization of asphaltenes from different crude oils and solvents. *Energy & Fuels* **2002**, *16*, 1121-1127.
  47. López, D.; Giraldo, L.J.; Salazar, J.P.; Zapata, D.M.; Ortega, D.C.; Franco, C.A.; Cortés, F.B. Metal Oxide Nanoparticles Supported on Macro-Mesoporous Aluminosilicates for Catalytic Steam Gasification of Heavy Oil Fractions for On-Site Upgrading. *Catalysts* **2017**, *7*, 319.
  48. Nadkarni, R.; Nadkarni, R. *Guide to ASTM test methods for the analysis of petroleum products and lubricants*; ASTM International West Conshohocken: 2007.
  49. Medina, O.E.; Gallego, J.; Nassar, N.N.; Acevedo, S.A.; Cortés, F.B.; Franco, C.A. Thermo-Oxidative Decomposition Behaviors of Different Sources of n-C7 Asphaltenes at High-Pressure Conditions. *Energy & Fuels* **2020**.
  50. D36, A. Standard Test Method for Softening Point of Bitumen (Ring-and-Ball Apparatus). *Annual Book of Standards* **2006**.
  51. Talu, O.; Meunier, F. Adsorption of associating molecules in micropores and application to water on carbon. *AIChE journal* **1996**, *42*, 809-819.
  52. Franco, C.A.; Zabala, R.D.; Zapata, J.; Mora, E.; Botero, O.; Candela, C.; Castillo, A. Inhibited gas stimulation to mitigate condensate banking and maximize recovery in cupiagua field. *SPE Production & Operations* **2013**, *28*, 154-167.

53. Nassar, N.N.; Hassan, A.; Luna, G.; Pereira-Almao, P. Kinetics of the catalytic thermo-oxidation of asphaltenes at isothermal conditions on different metal oxide nanoparticle surfaces. *Catalysis today* **2013**, *207*, 127-132.
54. Medina Erao, O.E.; Gallego, J.; Olmos, C.M.; Chen, X.; Cortés, F.B.; Franco, C.A. Effect of Multifunctional Nanocatalysts on n-C7 Asphaltene Adsorption and Subsequent Oxidation under High Pressure Conditions. *Energy & Fuels* **2020**.
55. Moghtaderi, B. Effects of controlling parameters on production of hydrogen by catalytic steam gasification of biomass at low temperatures. *Fuel* **2007**, *86*, 2422-2430.
56. Lozano, M.M.; Franco, C.A.; Acevedo, S.A.; Nassar, N.N.; Cortés, F.B. Effects of resin I on the catalytic oxidation of n-C 7 asphaltenes in the presence of silica-based nanoparticles. *RSC advances* **2016**, *6*, 74630-74642.
57. Rakhmatullin, I.; Efimov, S.; Tyurin, V.; Al-Muntaser, A.; Klimovitskii, A.; Varfolomeev, M.; Klochkov, V. Application of high resolution NMR (<sup>1</sup>H and <sup>13</sup>C) and FTIR spectroscopy for characterization of light and heavy crude oils. *Journal of Petroleum Science and Engineering* **2018**, *168*, 256-262.
58. Schneider, P. Adsorption isotherms of microporous-mesoporous solids revisited. *Applied Catalysis A: General* **1995**, *129*, 157-165.
59. Bates, M.K.; Jia, Q.; Doan, H.; Liang, W.; Mukerjee, S. Charge-transfer effects in Ni-Fe and Ni-Fe-Co mixed-metal oxides for the alkaline oxygen evolution reaction. *ACS Catalysis* **2015**, *6*, 155-161.
60. Dong, Y.-B.; Jin, G.-X.; Smith, M.D.; Huang, R.-Q.; Tang, B.; zur Loye, H.-C. [Ag<sub>2</sub> (C<sub>33</sub>H<sub>26</sub>N<sub>2</sub>O<sub>2</sub>)(H<sub>2</sub>O)<sub>2</sub> (SO<sub>3</sub>CF<sub>3</sub>)<sub>2</sub>]<sup>⊖</sup> 0.5 C<sub>6</sub>H<sub>6</sub>: A Luminescent Supramolecular Silver (I) Complex Based on Metal- Carbon and Metal-Heteroatom Interactions. *Inorganic chemistry* **2002**, *41*, 4909-4914.
61. Ignasiak, T.; Kemp-Jones, A.; Strausz, O. The molecular structure of Athabasca asphaltene. Cleavage of the carbon-sulfur bonds by radical ion electron transfer reactions. *The Journal of organic chemistry* **1977**, *42*, 312-320.
62. Arias-Madrid, D.; Medina, O.E.; Gallego, J.; Acevedo, S.; Correa-Espinal, A.A.; Cortés, F.B.; Franco, C.A. NiO, Fe<sub>2</sub>O<sub>3</sub>, and MoO<sub>3</sub> Supported over SiO<sub>2</sub> Nanocatalysts for Asphaltene Adsorption and Catalytic Decomposition: Optimization through a Simplex-Centroid Mixture Design of Experiments. *Catalysts* **2020**, *10*, 569.

63. Leon, O.; Rogel, E.; Espidel, J.; Torres, G. Asphaltenes: structural characterization, self-association, and stability behavior. *Energy & Fuels* **2000**, *14*, 6-10.
64. Alvarez-Ramirez, F.; Ramirez-Jaramillo, E.; Ruiz-Morales, Y. Calculation of the interaction potential curve between asphaltene– asphaltene, asphaltene– resin, and resin– resin systems using density functional theory. *Energy & fuels* **2006**, *20*, 195-204.
65. Merino-Garcia, D.; Andersen, S.I. Thermodynamic characterization of asphaltene– resin interaction by microcalorimetry. *Langmuir* **2004**, *20*, 4559-4565.
66. Medina, O.E.; Caro-Vélez, C.; Gallego, J.; Cortés, F.B.; Lopera, S.H.; Franco, C.A. Upgrading of Extra-Heavy Crude Oils by Dispersed Injection of NiO–PdO/CeO<sub>2</sub>± $\delta$  Nanocatalyst-Based Nanofluids in the Steam. *Nanomaterials* **2019**, *9*, 1755.
67. Alamolhoda, S.; Vitale, G.; Hassan, A.; Nassar, N.N.; Almao, P.P. Synergetic effects of cerium and nickel in Ce-Ni-MFI catalysts on low-temperature water-gas shift reaction. *Fuel* **2019**, *237*, 361-372.
68. Luo, M.-F.; Hou, Z.-Y.; Yuan, X.-X.; Zheng, X.-M. Characterization study of CeO<sub>2</sub> supported Pd catalyst for low-temperature carbon monoxide oxidation. *Catalysis letters* **1998**, *50*, 205-209.
69. Gradisher, L.; Dutcher, B.; Fan, M. Catalytic hydrogen production from fossil fuels via the water gas shift reaction. *Applied Energy* **2015**, *139*, 335-349.
70. Coughlin, R.W.; Farooque, M. Hydrogen production from coal, water and electrons. *Nature* **1979**, *279*, 301-303.
71. Li, S.; Cheng, Y. Catalytic gasification of gas-coal char in CO<sub>2</sub>. *Fuel* **1995**, *74*, 456-458.
72. Hauserman, W.B. High-yield hydrogen production by catalytic gasification of coal or biomass. *International journal of hydrogen energy* **1994**, *19*, 413-419.
73. Alamolhoda, S.; Vitale, G.; Hassan, A.; Nassar, N.N.; Pereira Almao, P. Development and characterization of novel combinations of Ce-Ni-MFI solids for water gas shift reaction. *The Canadian Journal of Chemical Engineering* **2019**, *97*, 140-151.
74. Vignatti, C.I.; Avila, M.S.; Apestequia, C.R.; Garetto, T.F. Study of the water-gas shift reaction over Pt supported on CeO<sub>2</sub>–ZrO<sub>2</sub> mixed oxides. *Catalysis Today* **2011**, *171*, 297-303.

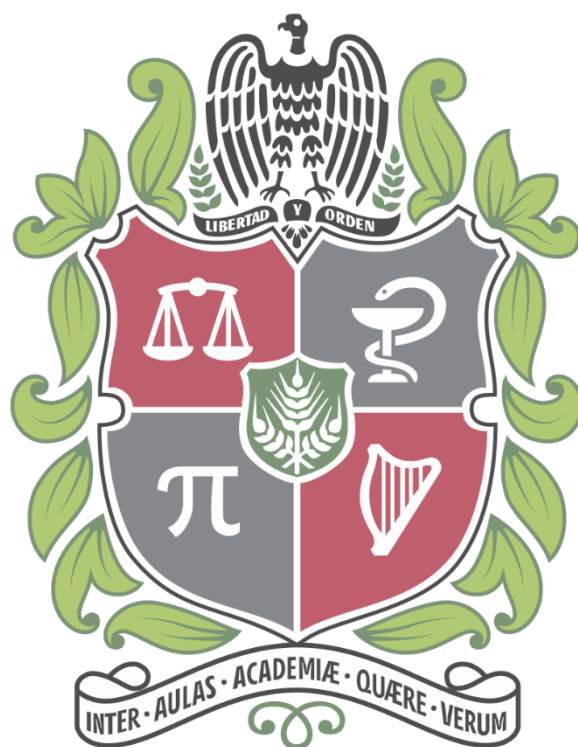
75. de Oliveira Rocha, K.; Marques, C.M.P.; Bueno, J.M.C. Effect of Au doping of Ni/Al<sub>2</sub>O<sub>3</sub> catalysts used in steam reforming of methane: Mechanism, apparent activation energy, and compensation effect. *Chemical Engineering Science* **2019**, *207*, 844-852.
76. Shido, T.; Iwasawa, Y. Reactant-promoted reaction mechanism for water-gas shift reaction on Rh-doped CeO<sub>2</sub>. *Journal of Catalysis* **1993**, *141*, 71-81.







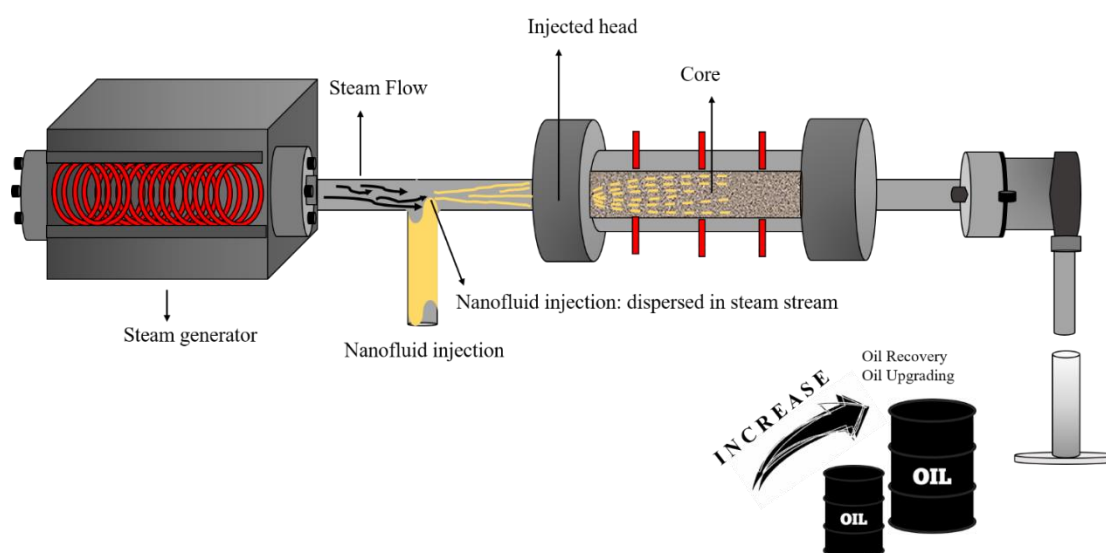
## Apartado 5.





## Chapter 13

# Upgrading of Extra-Heavy Crude Oils by Dispersed Injection of NiO– PdO/CeO<sub>2±δ</sub> Nanocatalyst-Based Nanofluids in the Steam



Published article in *Nanomaterials*: [doi.org/10.3390/nano9121755](https://doi.org/10.3390/nano9121755)

Impact factor: 5.719

# Upgrading of Extra-Heavy Crude Oils by Dispersed Injection of NiO–PdO/CeO<sub>2±δ</sub> Nanocatalyst-Based Nanofluids in the Steam

## Abstract

The main objective of this study is to evaluate the injection of a dispersed nanocatalyst-based nanofluid in a steam stream for in situ upgrading and oil recovery during a steam injection process. The nanocatalyst was selected through adsorption and thermogravimetric experiments. Two nanoparticles were proposed, ceria nanoparticles (CeO<sub>2±δ</sub>), with and without nickel and palladium oxides (CeNi<sub>0.89</sub>Pd<sub>1.1</sub>). Each one was employed for static tests of adsorption and subsequent decomposition using a model solution composed of *n*-C<sub>7</sub> asphaltenes (A) and resins II (R) separately and for different R:A ratios of 2:8, 1:1, and 8:2. Then, a displacement test consisting of three main stages were successfully developed. In the beginning, steam was injected into the porous media at a temperature of 210 °C, the pore and overburden pressure were fixed at 150 and 800 psi, respectively, and the steam quality was 70%. This was followed by CeNi<sub>0.89</sub>Pd<sub>1.1</sub> dispersed injection in the steam stream. Finally, the treatment was allowed to soak for 12 h, and the steam flooding was carried out again until no more oil production was observed. Among the most relevant results, doped nanoparticles achieved higher adsorption of both fractions and a lower decomposition temperature. The resins did not affect the amount of asphaltene adsorption over the evaluated materials. The catalytic activity suggests that the increase in resin content promotes a higher conversion in a shorter period. Also, for the different steps of the dynamic test, increases of 25 and 42% in oil recovery were obtained for the dispersed injection of the nanofluid in the steam stream and after a soaking time of 12 h, compared with the base curve with only steam injection, respectively. The upgraded crude oil reached an API gravity level of 15.9°, i.e., an increase of 9.0° units in comparison with the untreated extra-heavy crude oil, which represents an increase of 130%. Also, reductions of up to 71 and 85% in the asphaltene content and viscosity were observed.

## 1. Introduction

Steam injection has been the main thermal enhanced oil recovery (TEOR) technique for the exploitation of heavy (HO) and extra-heavy crude oil (EHO) reservoirs in recent decades [1,2]. Nevertheless, high costs [3], steam channeling [4], and no appreciable change in crude oil quality [5] are the difficulties that conventional steam injection has. To increase the efficiency of the steam injection technology and overcome the problems associated with the transport and refining operations because of the low quality of the crude oils [6], non-condensable gases [7] and chemical agents [8] are injected into the reservoir in parallel or in sequence with steam, showing excellent results in some field cases related mainly to the increase in oil production. In this order, the injection of chemicals for in situ upgrading has emerged as a promising solution to produce an oil of higher quality after its interaction with catalysts in the reservoir [9]. This occurs through the transformation of the heaviest oil components into lighter molecules employing different reactions such as water–gas shift, steam reforming, methanation, and aquathermolysis, among others [10]. During these reactions, an increase in the American Petroleum Institute (API) gravity can be obtained [11][12].

The implementation of catalysts also helps to control the heat front temperature [13], enhance the recovery performance [9,14], and promote steam quality maintenance [15]. As an important frontier technology, the development of catalysts at the nanoscale has been proposed by several authors as a TEOR additive to improve the efficiency of the processes [16,17]. Different nanoparticles of SiO<sub>2</sub> [18], Al<sub>2</sub>O<sub>3</sub> [15], TiO<sub>2</sub> [19], or rare earth oxides [16,17] have been assessed to increase the rate of gasification reactions under steam injection conditions [20]. These nanoparticles have been used as support nanocatalysts for transition element oxides (TEOS) such as Pd [9,21], Pt [22], Co [16], Ni [23,24], and Fe [25] to improve the adsorption and catalytic decomposition of the oil heavy fractions such as asphaltenes and resins [16,26]. The injection of the nanoparticles into the porous medium has been carried out mainly through batch injection of the nanofluid containing the nanocatalysts [18] or utilizing a pre-treatment of the heavy crude oil sample under static conditions [24]. Hashemi et al. [27] reported the implementation of Ni–W–Mo ultra-dispersed nanocatalysts for in situ upgrading of Athabasca bitumen between 320 and 340 °C under a hydrogen flow

rate, obtaining increases in API gravity and decreases in the sulfur and nitrogen content favored by the hydrogenation reactions and subsequent coke formation inhibition. As for the batch injection of nanofluid, Cardona et al. [18] used silica nanoparticles with 1.0 wt.% of nickel and palladium oxides at 220 °C for the steam injection test. The authors found an increase from untreated crude oil to upgraded oil in API gravity from 7.2° to 12.1° and reductions in the asphaltene content of 40%. Although the injection of nanofluid in batch-mode showed a good result, the nanofluid injection into the reservoir must be considerably improved to achieve a deeper penetration in the reservoir and a better distribution within the porous spaces, generating a greater interaction with heavy crude oil molecules.

In this way, recently, a novel technique for well stimulation and fluid injection known as gas stimulation (GaStim) was proposed by Franco et al. [28] and Restrepo et al. [29]. The method consists of the dispersion of a liquid treatment on the gas stream, achieving high injection rates and liquid droplets with a smaller size and increasing the invasion radius of the liquid around the injector well [29]. Restrepo et al. [29] reported positive results in the first pilot test in Colombia to overcome the formation damage because of the combined effect of condensate banking and asphaltene precipitation. The injection of the treatment by means of the GaStim method led to an increase of 40% in oil rate production and a decrease of 30% in the gas–oil ratio. However, to our knowledge, no studies have reported the dispersed injection of nanofluids for EOR or TEOR applications. With the development of this work, a new approach for the application of nanofluids dispersed in the steam stream and, in general, for future applications in enhanced thermal oil recovery processes is expected.

## 2. Experimental

### 2.1. Materials

An extra-heavy crude oil from a field in the center of Colombia was employed for asphaltene and resin extraction and displacement tests. The selected EHO has an API gravity of 6.4°, resin and asphaltene contents of 52.0 wt.% and 28.7 wt.%, respectively, and a viscosity of  $6 \times 10^6$  cP at 25 °C. *n*-Heptane (99%, Sigma-Aldrich, St. Louis, MO, USA) was used to isolate the asphaltenes from the EHO, and chromatographic silica (Sigma-Aldrich, St. Louis, MO, USA) was added to the deasphalted crude oil to separate the resins from the solution. The extraction procedure has been explained in previous studies [30]. The

compositions of the isolated asphaltenes and resins are shown in Table 1. The concentrations of heteroatoms in the organic fractions were obtained by elemental analysis using the ASTM D 5291 standard employing an elemental analyzer Flash EA 1112 (Thermo Finnigan, Milan, Italy). The difference calculated the oxygen content. Besides, *n*-C<sub>7</sub> asphaltene has a lower H/C ratio (1.15) compared with resin II (1.32) because of the strong aromaticity of the former and its unsaturation degree.

The nanocatalyst was synthesized through the impregnation of salt precursors NiCl<sub>2</sub>·6H<sub>2</sub>O (Merck, KGaA, Darmstadt, Germany) and Pd(NO<sub>3</sub>)<sub>2</sub>·2H<sub>2</sub>O (Merck, KGaA, Darmstadt, Germany) following the incipient wetness method [31] over a CeO<sub>2</sub> nanoparticulated support (Nanostructures & Amorphous Materials, Houston, TX, USA). The average particle size and surface area of the support were 21 nm and 65 m<sup>2</sup>·g<sup>-1</sup>. The nanocatalyst was designed for final loads of Ni and Pd of 0.89 and 1.1 wt.%, respectively, and is labeled as CeNi0.89Pd1.1 following a previous study focused on material optimization [16,17]. The catalyst presents a crystal size of 5.53–3.61 nm with 25% and 36% dispersions for Ni and Pd crystals.

The nanofluid was prepared using 2000 mg·L<sup>-1</sup> of the CeNi0.89Pd1.1 nanocatalyst, 0.3 wt.% of Tween 80 surfactant (Panreac, Barcelona, Spain), and 0.2 wt.% of NaCl. The porous medium was composed of Ottawa-silica sand (Minercol S.A., Bogotá, Colombia). The cleaning was done using methanol (99.8%, Panreac, Barcelona, Spain), hydrochloric acid (HCl, 37%, Panreac, Barcelona, Spain), and toluene (99.8% Panreac, Barcelona, Spain), following the procedure detailed in a previous study [32].

**Table 1.** Elemental composition of *n*-C<sub>7</sub> asphaltenes and resin II of Colombian extra-heavy crude oil.

Fraction	Elemental Mass Fraction Concentration (%)				
	Carbon	Hydrogen	Nitrogen	Oxygen	Sulphur
Resin II	82.10	9.00	0.54	2.26	6.10
<i>n</i> -C <sub>7</sub> Asphaltenes	81.70	7.80	0.33	3.57	6.60

## 2.2. Methods

### 2.2.1. Adsorption Experiments

Oil model solutions of resin II and/or *n*-C<sub>7</sub> asphaltenes in toluene were prepared at different concentrations between 100 and 2000 mg·L<sup>-1</sup>. The adsorption isotherms were constructed at 25 °C using 100 mg of doped and non-doped nanoparticles per 10 mL solution. The mixtures were left under magnetic



stirring at 300 rpm for 24 h until the system reached the adsorption equilibrium [33]. The nanoparticles with resin II and/or *n*-C<sub>7</sub> asphaltene molecules adsorbed were separated by centrifugation at 4500 rpm for 45 min. The precipitate was analyzed using a Q50 thermogravimetric analyzer (TA Instruments, Inc., New Castel, DE, USA) and corroborated through UV-vis measurements [34,35].

For the best system in terms of the adsorption and catalysis of the heavy oil fractions, adsorption isotherms for a solution model were constructed for the different resin-to-asphaltene ratios (R:A) of 8:2, 1:1, and 2:8. Regarding the quantity of *n*-C<sub>7</sub> asphaltenes and resin II adsorbed on the nanoparticle for the composite systems, and it was measured by combining the tests of the softening point (SP) and thermogravimetric analysis (TGA) based on our previous work [36]. Following the ASTM E28-12 standard [37], experiments to determine the SP were developed. The amount of resin II or *n*-C<sub>7</sub> asphaltenes adsorbed individually or in the mixture systems was calculated following the protocol detailed by Lozano et al. [36].

### 2.2.2. Thermogravimetric Analyses

The catalytic steam gasification of adsorbed compounds on the nanoparticles was carried out using a Q50 thermogravimetric analyzer (TA Instruments, Inc., New Castel, DE, USA). The N<sub>2</sub> flow was fixed at 100 mL·min<sup>-1</sup> and the H<sub>2</sub>O<sub>(g)</sub> at 6.30 mL·min<sup>-1</sup> was introduced using a gas saturator filled with distilled water and controlled by a thermostatic bath with a flow rate of 6.30 mL·min<sup>-1</sup> [38]. Finally, the amount of adsorbed asphaltenes and/or resins was set at 0.2 ± 0.02 mg·m<sup>-2</sup> for all samples [28]. The samples were subjected to non-isothermal and isothermal procedures. Under non-isothermal conditions, the samples were subjected to temperatures between 100 and 600 °C at a heating rate of 20 °C·min<sup>-1</sup>. For the test under isothermal conditions, the samples were heated at 210, 220, and 230 °C for *n*-C<sub>7</sub> asphaltenes and resins II adsorbed over nanoparticles and 360, 370, and 380 °C for the heavy fractions in the absence of nanoparticles.

### 2.2.3. Nanofluid formulation for *In-Situ* upgrading

The formulation of the nanofluid for the *in-situ* upgrading of the employed EHO was carried out using a Tween 80 surfactant and CeNi<sub>0.89</sub>Pd<sub>1.1</sub> nanoparticles in a NaCl-based brine solution. To obtain the best formulation of surfactant and nanoparticles, a sweep of concentrations of each component was made between 0.1 % and 0.5 % in mass fraction. The best nanoparticle

concentration was determined based on its catalytic activity to decompose heavy oil compounds in a steam atmosphere [59]. The nanoparticles were mixed with the EHO and the solutions were stirred magnetically for 24 hours at 80 °C. By centrifugation, filtering and washing with *n*-heptane, the nanoparticles are separated with the adsorbed fractions from the solutions. Nanoparticles are dried at 100 °C to remove solvent residues and finally the catalytic steam gasification of the samples was carried out using a thermogravimetric analyzer Q50 (TA Instruments, Inc., New Castel, DE, USA) at a heating rate of 20 °C·min<sup>-1</sup> from 100 to 600 °C under an airflow of 100 mL·min<sup>-1</sup> and a H<sub>2</sub>O<sub>(g)</sub> flow of 6.30 mL·min<sup>-1</sup> [35].

On the other hand, the appropriate surfactant concentration was determined based on nanofluid stability. For this, the nanoparticles concentration was fixed, the nanofluids were subjected to an ultrasound bath for 4 h, and then the zeta potential was measured during 8 days with a Nanoplus-3 (Micromeritics, GA, USA) [60].

The nanofluid was characterized by viscosity at 25 °C using a Kinexus Pro+ (Malvern Instruments, Worcestershire, UK) rheometer, and the density as measured using an Anton Paar Stabinger SVM 3000 (Madrid, Spain).

#### 2.2.4. Oil Recovery

The displacement test was divided into four main stages to recreate the injection conditions of the steam stimulation processes and evaluate the effect of the CeNi<sub>0.89</sub>Pd<sub>1.1</sub> nanocatalyst in oil recovery and in situ upgrading. Table 2 shows the properties of the porous medium employed. Figure 1 shows a schematic representation of the experimental setup. The system consists of two positive displacement pumps (DB Robinson Group, Edmonton, AB, Canada), one to control the injection of oil and water and another to control the injection of water to the steam generator and nanofluid to the porous medium. The system also includes four cylinders (Max Servicios, S.A.S., Medellín, Colombia) containing EHO, synthetic brine, deionized water, and nanofluid; a steam generator (Thermo Scientific Waltham, MA, USA), thermocouples (Termocuplas, S.A.S., Medellín, Colombia); valves (Swagelok, Cleveland, OH, USA); manometers (Rosemount, Emerson, Chesterfield, MO, USA); fraction collectors; a pressure transducer (Rosemount, Emerson, Chesterfield, MO, USA); a hydraulic pump (Enercap, Actuant Corporation, Milwaukee, WI, USA); and a pressure multiplier. A leak test was performed by pressuring the core holder with N<sub>2</sub> up to 1000 psi, where a change in 1% pressure per hour was considered the maximum pressure reduction allowed.

**Table 2.** Properties of porous media employed for the oil recovery experiments.

Property	Value
Mineralogy	99% Silica
Length	67 cm
Diameter	3.8 cm
Porosity	26.5%
Porous Volume	194 cm <sup>3</sup>
Initial oil saturation state	77.4%
Initial water saturation state	22.6%

Before the steam injection, measurements of the absolute permeability ( $K$ ) and the effective permeabilities of water ( $k_w$ ) and oil ( $k_o$ ) were performed. For this, 10 VP of each phase was injected in the order water–oil–water until a constant pressure drop was observed during each injection.  $K$ ,  $k_w$ , and  $k_o$  values were calculated using the Darcy equation [39]. For this scenario, the system temperature was maintained at 80 °C, and the pore and overburden pressure were fixed at 150 and 800 psi, respectively.

To construct initial oil recovery by steam injection, 7 porous volumes of water equivalent (PVWE) were injected at 210 °C. Steam was injected between 3 and 5 mL·min<sup>-1</sup> to prevent condensation into the coil line and porous medium. Under these conditions, steam was injected at 70% quality, with a massive flow of vapor and liquid water. The steam quality was ensured through numerical simulation by calculating the mass balance between the steam generator and the entrance of the porous medium. Considering the steam injection conditions ( $T = 210$  °C,  $x = 70\%$ ), the properties of the line connecting the points for the material balance (length = 0.63 m, thermal conductivity = 16.3 W·m<sup>-1</sup>·K<sup>-1</sup>, internal radius = 0.0046 m, and external radius = 0.00635 m) and using the Antoine correlation, heat losses, and the pressure at each node necessary to ensure the quality of steam at the entrance of the porous medium were calculated. Radial heat persistence was not considered because of the liquid–vapor equilibrium conditions of the system. The heat transfer coefficient was very high; therefore, the resistance value could be neglected [40].

The injection of the nanocatalyst-based nanofluid was performed through the continuous nanofluid addition to the steam current for approximately 7 PVWE. The nanofluid was injected into the steam generator outlet at a rate between 0.5 and 1 mL·min<sup>-1</sup> before entering the porous medium. The pressure profile of the system was monitored throughout the displacement test to ensure the nanofluid transport in the steam stream. The oil recovery was obtained until

no more oil was produced. Then, the porous media was left to stand for 12 h, and steam in the absence of the nanofluid was injected again until there was no oil production.

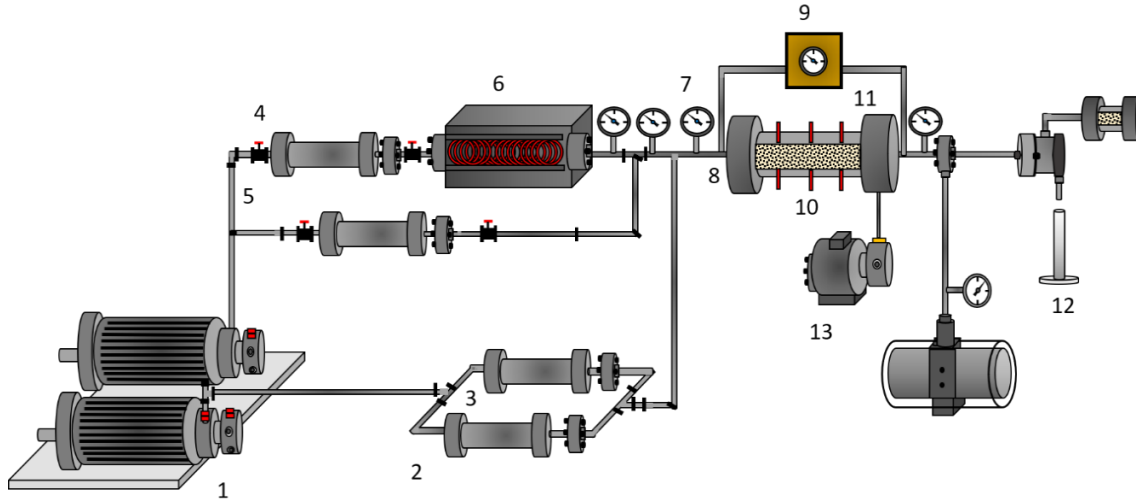


**Figure 1.** Experimental setup: (1) positive displacement pumps, (2,3,4,5) oil, brine water, and nanofluid-containing cylinders, respectively, (6) steam generator, (7) manometers, (8) thermocouple, (9) pressure transducer, (10) core holder, (11) sand packed bed, (12) sample output and (13) hydraulic pump.

### 2.2.5. Oil Characterization before and after Upgrading

The effectiveness of the CeNi<sub>0.89</sub>Pd<sub>1.1</sub> nanoparticles in changing the physicochemical properties of the EHO was evaluated through API gravity, oil viscosity, and *n*-C<sub>7</sub> asphaltene content. The API gravity measurements were performed using an Anton Paar Stabinger SVM 3000 (Madrid, Spain). The asphaltene content was calculated by micro deasphalting, following the protocol described in previous works [18,41]. The rheological behavior of the crude oil after each stage was evaluated through a Kinexus Pro (Malvern Instruments, Worcestershire, UK) rheometer, using a parallel plate-plate geometry and 0.3 mm of GAP at 25 °C and varying the shear rate from 0 to 100 s<sup>-1</sup>. The degree of viscosity reduction (DVR) was calculated using the viscosity of the untreated EHO ( $\mu_{v,EHO}$ ) and upgraded crude oil ( $\mu_{treated}$ ) after the three stages, using the following expression:

$$DVR = \frac{(\mu_{v,EHO} - \mu_{treated})}{\mu_{v,EHO}} \times 100 \quad (1)$$

### 3. Modeling

#### 3.1. Adsorption Model

The solid-liquid equilibrium (SLE) model [32,42] describes the adsorption isotherms of the asphaltenes and/or resins II over the nanocatalysts employed in this study, from the theory of adsorption and association of molecules in microporous surfaces, according to the following equations (Equations 2-4):

$$C_E = \frac{\psi H}{1 + K\psi} e^{\left(\frac{\psi}{q_m \cdot SA}\right)} \quad (2)$$

$$K = \frac{K_r RT}{A} \quad (3)$$

$$\psi = \frac{-1 + \sqrt{1 + 4K\xi}}{2K} \quad (4)$$

where  $C_E$  ( $\text{mg}\cdot\text{g}^{-1}$ ) is the concentration of asphaltenes and/or resins in the equilibrium,  $H$  ( $\text{mg}\cdot\text{g}^{-1}$ ) refers to the affinity that the adsorbate presents for the adsorbent,  $K$  ( $\text{g}\cdot\text{g}^{-1}$ ) is a parameter that indicates the self-association of  $n\text{-C}_7$  asphaltenes and/or resin II molecules on the surface of the nanoparticles, and  $q_m$  ( $\text{g}\cdot\text{g}^{-1}$ ) is the maximum adsorption capacity of the nanocatalysts [42]. Finally,  $SA$  is the surface area of the catalyst,  $\psi$  and  $\xi$  are defined as the adjustment parameters [42].

#### 3.2. Effective Activation Energy Estimation

The activation energy was calculated from the following equation (Equation 5) [43]:

$$\frac{d\alpha}{dt} = K_\alpha \exp\left(-\frac{E_a}{RT}\right) f(\alpha) \quad (5)$$

where  $K_\alpha$  ( $\text{s}^{-1}$ ) is a pre-exponential factor,  $R$  ( $\text{J}\cdot\text{mol}^{-1}\cdot\text{K}^{-1}$ ) is the ideal gas constant, and  $E_a$  ( $\text{kJ}\cdot\text{mol}^{-1}$ ) is the activation energy. On the other hand,  $d\alpha/dt$  refers to the change in the conversion ( $\alpha$ ) of asphaltenes and/or resin II at a determined time during the decomposition reactions. According to the isothermal conditions of operation, the integration of Equation (5) leads to the following:

$$g(\alpha) = K_{\alpha} \exp\left(-\frac{E_{\alpha}}{RT}\right) t \quad (6)$$

Applying the natural logarithm on both sides of Equation (6), this can be written in linear terms as:

$$\ln(t_{a,i}) = \ln\left(\frac{g(\alpha)}{K_{\alpha}}\right) + \frac{E_{\alpha}}{RT_i} \quad (7)$$

Finally, by graphing  $\ln(t_{a,i})$  vs.  $1/T_i$  and obtaining the value of the slope, the effective activation energy can be obtained.

### 3.3. Rheological Model

To describe the EHO rheological behavior in the different stages, the Cross model was employed:

$$\mu = \mu_{\infty,\gamma} \frac{\mu_{0,\gamma} - \mu_{\infty,\gamma}}{1 + (\alpha_c \gamma)^m} \quad (8)$$

where  $\mu$  (cP) is the fluid viscosity,  $m$  is a constant that represents the trend of a fluid to have a Newtonian behavior,  $\alpha_c$  (s) is the relaxation time, and  $\mu_{0,\gamma}$  and  $\mu_{\infty,\gamma}$  (cP) are the viscosities at zero shear rate and infinite shear rate, respectively.

## 4. Results and discussion

### 4.1. Adsorption Isotherms

The adsorption isotherms of resin II and *n*-C<sub>7</sub> asphaltenes at 25 °C for the CeNi<sub>0.89</sub>Pd<sub>1.1</sub> and CeO<sub>2</sub> nanoparticles together with the SLE model fitting are shown in Figure 2. A high affinity between the *n*-C<sub>7</sub> asphaltenes and the different nanoparticles used can be observed. The shape of the adsorption isotherms in the two systems is Type Ib, according to the International Union of Pure and Applied Chemistry (IUPAC) [44]. This type of isotherm indicates a strong affinity between the adsorbate and the adsorbent. This property is always higher for the CeNi<sub>0.89</sub>Pd<sub>1.1</sub> than for the CeO<sub>2</sub> nanoparticles, showing an increase in the adsorptive capacity of the nanomaterial with the addition of the transition element oxides (TEO) on its surface [45] through the formation of coordinated

bonds between the heteroatoms and the functional groups of the transition elements [46].

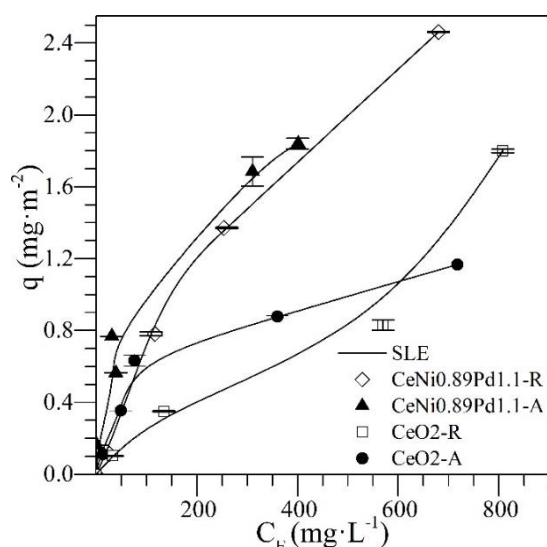


**Figure 2.** Adsorption isotherms of *n*-C<sub>7</sub> asphaltenes (A) and resin II (R) onto CeNi<sub>0.89</sub>Pd<sub>1.1</sub> and CeO<sub>2</sub> nanoparticles evaluated at 25 °C. The solid lines are from the solid–liquid equilibrium (SLE) model and the symbols are experimental data.

Regarding the adsorption isotherms of resin II onto CeNi<sub>0.89</sub>Pd<sub>1.1</sub> nanoparticles, a high affinity is observed over the range of concentrations evaluated. According to the International Union of Pure and Applied Chemistry (IUPAC), this behavior corresponds to a Type I isotherm [44]. This result is due to the interactions formed by the functional groups of NiO and PdO on the nanoparticle surface with the active bonds and heteroatoms in the chemical structures of the resins [47]. Regarding the adsorption of resin II on the non-doped support, a type II isotherm is obtained [44]. When the concentration of resin II increases, molecules with a larger size have reduced diffusion through the material surface, leading to a high self-association around the nanoparticles' active sites [48]. This indicates that, although the resin–resin interactions are low in the bulk phase, once adsorbed on the nanoparticle surface, self-association occurs through coordinated bonds and bonds between carbon-based molecules and heteroatoms (C–C, C–N, C–O) because of their polar character [49,50]. In this sense, for both resins and asphaltenes, the adsorption is higher for CeNi<sub>0.89</sub>Pd<sub>1.1</sub> nanoparticles than for the support without TEOs. Because of the presence of transition elements, the adsorption of polar molecules on the nanoparticles is controlled to a high degree by the Lewis acidity [51], which favors the adsorption

on the doped nanoparticles compared to the support. The nanoparticle that showed the best performance by adsorbing resin II and *n*-C<sub>7</sub> asphaltenes was CeNi<sub>0.89</sub>Pd<sub>1.1</sub>. Therefore, the competitive adsorption between *n*-C<sub>7</sub> asphaltenes and resin II for different R:A ratios was evaluated with this sample, and the results are shown in Figure 3a,b, together with the SLE model fitting.

Figure 3a shows that the adsorption affinity between *n*-C<sub>7</sub> asphaltenes and CeNi<sub>0.89</sub>Pd<sub>1.1</sub> nanoparticles decreases as the amount of resin II in the system increases. For the R:A ratios of 2:8 and 1:1, the adsorption isotherms are also Type I, and for the 8:2 system, the isotherm obtained behaves as type III according to the IUPAC [44]. The change in the adsorbate–adsorbent affinity may be related to an interruption or change in the colloidal structure of *n*-C<sub>7</sub> asphaltenes because of resins that prevent asphaltene–asphaltene interactions, thus avoiding self-association [52,53]. Also, because of the high selectivity that CeNi<sub>0.89</sub>Pd<sub>1.1</sub> nanoparticles present for resin II, competitive adsorption between the two polar fractions may be generated. In this way, there is a reduction in the active sites on the surface of the nanoparticles occupied by resin. These results are consistent with those published by Lozano et al. [36] and Franco et al. [26], where the adsorption of asphaltenes on nanoparticles of different chemical natures is affected to a small extent by the presence of resin I in the system.

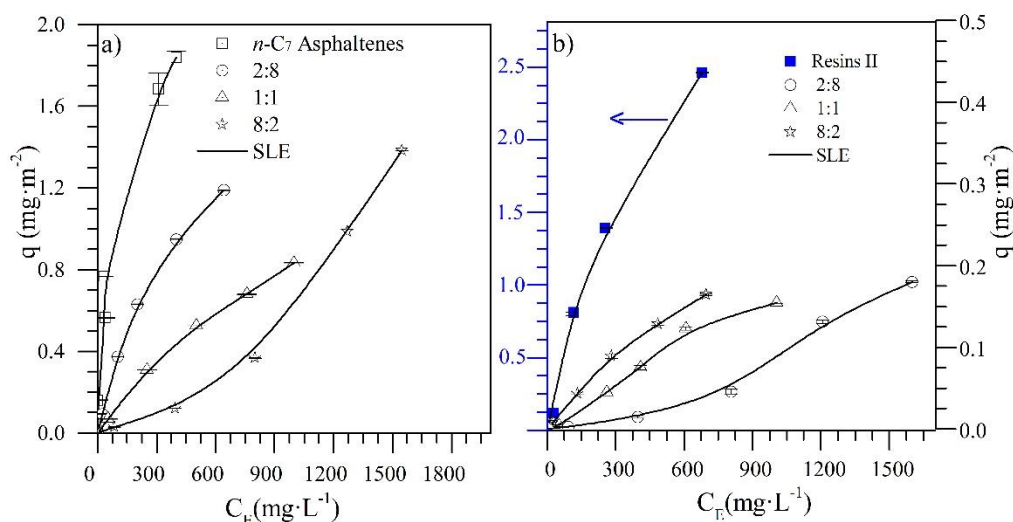


**Figure 3.** Adsorption isotherms of (a) *n*-C<sub>7</sub> asphaltenes (A) and (b) resins II (R) on CeNi<sub>0.89</sub>Pd<sub>1.1</sub> nanoparticles evaluated at 25 °C and from different ratios of R:A of 8:2, 1:1, and 2:8. The solid lines are from the SLE model, and the symbols are experimental data.

Figure 3b shows the adsorption isotherms for resin II in the presence of *n*-C<sub>7</sub> asphaltenes at different R:A ratios. In general, the adsorption isotherms keep



their type I behavior for the ratios 8:2 and 1:1. However, for the 2:8 system, a high presence of *n*-C<sub>7</sub> asphaltenes generates a change in the type of isotherm to Type III. In both cases, it is indicated that the presence of *n*-C<sub>7</sub> asphaltenes also influences the adsorption of resin II. The adsorption of resins II over the nanoparticles increases as the amount of *n*-C<sub>7</sub> asphaltenes in the system decreases following the order 2:8 < 1:1 < 8:2. The interactions between the functional groups of the metal oxides and the heteroatoms in the molecular structure of resins II are stronger than the resin–resin and resin–asphaltene interactions because of the presence of acidic and basic sites that the TEO and CeO<sub>2</sub> generate [54]. The multilayer behavior of the 2:8 ratio could be due to the resin–asphaltene interactions being more significant than the resin–resin interaction [55].

Table 3 shows the *H*, *K*, *y*, and *Q<sub>m</sub>* parameters of the SLE model for the adsorption of asphaltenes and resin II in different R:A ratios over the doped and CeO<sub>2</sub> nanoparticles.

**Table 3.** Estimated SLE model parameters of *n*-C<sub>7</sub> asphaltenes and/or resin II adsorption onto different nanoparticles for different resin–asphaltene ratios (R:A ratios).

Sample	R:A	<i>n</i> -C <sub>7</sub> Asphaltenes				Resin II			
		<i>H</i> (mg·g <sup>-1</sup> ) × 10 <sup>-2</sup>	<i>K</i> (g·g <sup>-1</sup> ) × 10 <sup>-2</sup>	<i>q<sub>m</sub></i> (mg·m <sup>-2</sup> )	% RSM	<i>H</i> (mg·g <sup>-1</sup> ) × 10 <sup>-2</sup>	<i>K</i> (g·g <sup>-1</sup> ) × 10 <sup>-2</sup>	<i>q<sub>m</sub></i> (mg·m <sup>-2</sup> )	% RSM
CeNi0.89Pd1.1	Individual	6.02	3.91	0.22	0.01	3.26	0.48	0.19	0.1
CeO <sub>2</sub>	Individual	10.12	20.7	0.12	0.02	4.03	7.62	18.57	0.1
CeNi0.89Pd1.1	2:8	6.70	4.32	0.16	0.01	1552	8.81	25.66	0.2
	1:1	10.61	4.66	0.11	0.02	985.1	7.66	0.22	0.1
	8:2	1343	5.77	27.17	0.01	3.33	2.33	0.25	0.2

According to the *H* parameter, there is a greater affinity for CeNi0.89Pd1.1 material with the resin II and *n*-C<sub>7</sub> asphaltenes as individual components. For the adsorption isotherms of *n*-C<sub>7</sub> asphaltene in the presence of resin II, the *H* parameter increased as the amount of resin II in the system increased because of the high selectivity that CeNi0.89Pd1.1 nanoparticles presented for resin II. In this way, resin II reduces the preference of *n*-C<sub>7</sub> asphaltenes to be present in the adsorbed phase. Concerning the degree of self-association of *n*-C<sub>7</sub> asphaltenes on the surface of the nanoparticles, the *K* parameter follows the R:A trend of 2:8 <

1:1 < 8:2, which indicates that the asphaltene–asphaltene interactions are reduced because of the presence of stronger asphaltene–resin interactions [55,56]. Also, the value of  $H$  for the adsorption of resin II decreases as the amount of  $n\text{-C}_7$  asphaltene increases, and the  $K$  parameter behaves similarly to the self-association of  $n\text{-C}_7$  asphaltenes. This is also because resin–resin interactions are affected by asphaltene–resin interactions [57].

#### 4.2. Prediction of the Adsorbed Amount of $n\text{-C}_7$ Asphaltenes

To better understand the influence of resin II on the adsorption phenomenon of  $n\text{-C}_7$  asphaltenes over the  $\text{CeNi}_{0.89}\text{Pd}_{1.1}$  nanoparticles, the adsorbed amount of asphaltenes was predicted as individual systems for the different R:A ratios employed. If the behavior of  $n\text{-C}_7$  asphaltenes were affected by the amount of resin II in the systems, there would be a difference between the predicted and the experimental adsorbed amounts. On the other hand, if the resin did not affect the asphaltene adsorption, the adsorption of the latter would depend only on its concentration and the occupation of the active sites of the nanoparticle by resin II. For the prediction of the adsorbed amount of  $n\text{-C}_7$  asphaltenes ( $q_{\text{predicted}}$ ), it was assumed that for a fixed R:A system, the amount adsorbed would correspond to a fraction of the individual asphaltenes adsorbed. For a 1:1 system, the amount of adsorbed  $n\text{-C}_7$  asphaltenes corresponds to 50% of the mass fraction initially adsorbed. A linear plot  $q_{\text{predicted}}$  against  $q_{\text{experimental}}$  that represents a good prediction would imply a slope of  $m = 1$  and an intercept of  $b = 0$  associated with  $R^2 = 1.0$ , indicating that asphaltene adsorption depends mainly on the amount of asphaltenes present in the system.

Figure 4 shows the prediction plot of the adsorbed amount of  $n\text{-C}_7$  asphaltenes in the  $\text{CeNi}_{0.89}\text{Pd}_{1.1}$  nanoparticles in the absence and presence of resin II. In addition, Table 4 shows the values of the slope and the intercept of the equation associated with the linear fit and the respective errors. According to Figure 4 and the data in Table 4, a very accurate prediction was observed for the adsorbed amount of  $n\text{-C}_7$  asphaltenes on  $\text{CeNi}_{0.89}\text{Pd}_{1.1}$  nanoparticles in the presence of resin II for the R:A systems evaluated. The values of the slopes in all cases were close to 1, and the intercepts were close to the origin with  $R^2 > 0.98$ . These results indicate that the adsorption of  $n\text{-C}_7$  asphaltenes is controlled mainly by the concentration of these in the system and the affinity that the nanoparticle presents for resin II. These results agree with those Franco et al. reported [26].

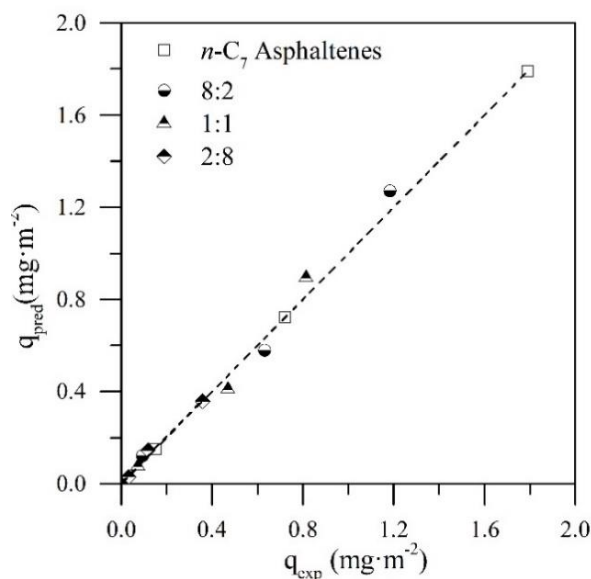


**Figure 4.** Linear plots of  $q_{\text{predicted}}$  as a function of  $q_{\text{experimental}}$  for the adsorption of  $n\text{-C}_7$  asphaltenes (A) over CeNi<sub>0.89</sub>Pd<sub>1.1</sub> nanoparticles in the presence of resin II (R) in the systems at different R:A ratios of 2:8, 1:1, and 8:2.

**Table 4.** Estimated slopes and intercepts of the linear plots of  $q_{\text{predicted}}$  as a function of  $q_{\text{experimental}}$  for the adsorption of  $n\text{-C}_7$  asphaltenes (A) over CeNi<sub>0.89</sub>Pd<sub>1.1</sub> nanoparticles in the presence of resin II (R) in the systems at different R:A ratios.

R:A Ratio	Slope	Intercept	$R^2$
2:8	1.04	0.007	0.99
1:1	1.06	-0.002	0.98
8:2	1.04	-0.007	0.99

#### 4.3. Thermogravimetric Experiments

The nanoparticles evaluated in this work were tested in an N<sub>2</sub> atmosphere saturated with H<sub>2</sub>O<sub>(g)</sub> for the catalytic steam gasification of  $n\text{-C}_7$  asphaltenes and resin II. Figure 5 shows the rate of mass loss for  $n\text{-C}_7$  asphaltenes and resins II in panels a and b, respectively. It can be observed from Figure 5 that for virgin resin II and  $n\text{-C}_7$  asphaltenes, i.e., before adsorption onto nanoparticles, the decomposition occurs at 420 and 450 °C, respectively. Nevertheless, their decomposition occurs at lower temperatures when they are adsorbed on the nanoparticles.

Doped and non-doped nanoparticles reduce the main decomposition peak from 400 to 220 and 270 °C for resin II and from 450 to 220 and 370 °C for  $n\text{-C}_7$  asphaltenes, respectively. However, the heavy oil fractions do not decompose entirely at these temperatures; therefore, the conversion continues at higher temperatures. This result suggests the presence of high, medium, and low

molecular weight sizes that vary from alkyl chains that decompose at low temperatures (<250 °C) to polycyclic aromatic hydrocarbons (PAH), whose decomposition is achieved at average temperatures of around 450 °C.

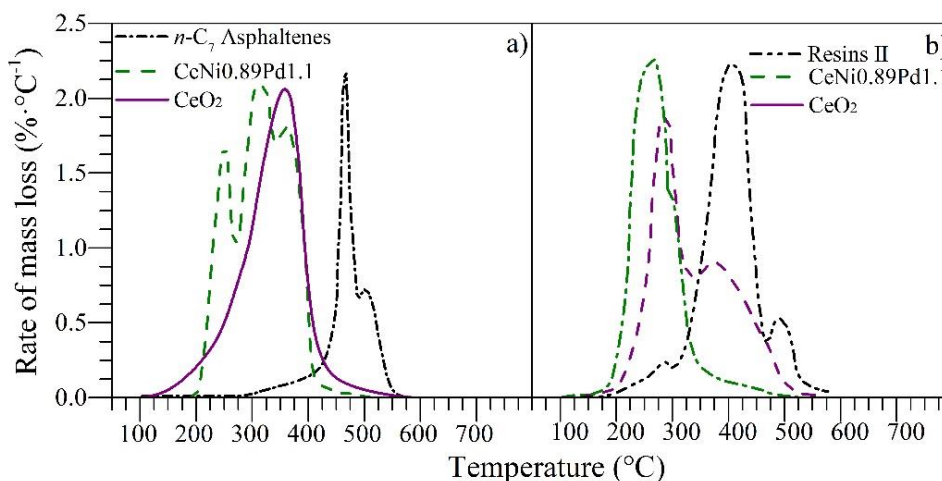
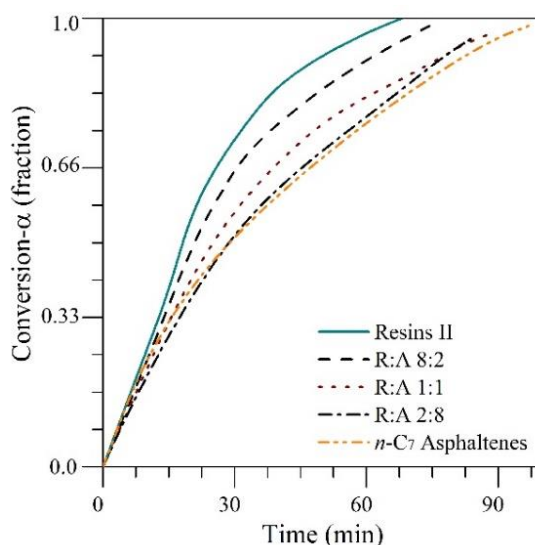


**Figure 5.** Rate of mass loss as a function of temperature for steam gasification of (a) *n*-C<sub>7</sub> asphaltenes and (b) resin II in the absence and presence of CeO<sub>2</sub> and CeNi<sub>0.89</sub>Pd<sub>1.1</sub> nanoparticles. Panel (a) was adapted from Medina et al. [16].

Besides, the doped nanoparticle manages to reduce the resin II decomposition temperature to 220 °C, which inhibits the development of additional reactions of resin II after its initial cracking, showing a single peak of decomposition [16]. The catalytic effect was improved by adding oxides of transition elements on the CeO<sub>2</sub> surface for *n*-C<sub>7</sub> asphaltene and resin II decomposition. The good performance of the doped nanoparticles is due to the ability of the support to interact with the nanocrystals to produce and promote cracking and isomerization reactions [58]. The Ce–Ni interactions can stimulate the production of the water–gas shift reaction through vacancies of oxygen anions provided by the CeO<sub>2</sub> [20]. Meanwhile, the interactions of the support with noble elements like Pd [22] promote the production of hydrogen and oxygen, which controls the stability of highly polar molecules. Hence, further experiments under isothermal conditions were performed with the doped nanoparticles and for different R:A ratios.

Figure 6 shows the isothermal conversions at 220 °C for different R:A ratios of 8:2, 1:1, and 2:8 and for the individual components. The transformation of resin II at any time is always greater than the conversion of asphaltenes. In addition, the conversion of R:A systems decrease as the amount of *n*-C<sub>7</sub> asphaltenes in the

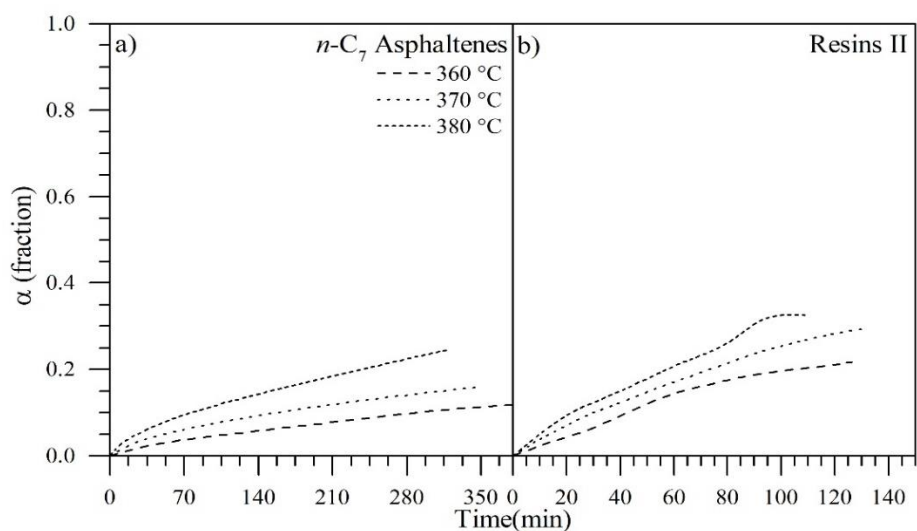
mixture increases because of the high presence of heteroatoms and metals and the high refractory behavior of  $n\text{-C}_7$  asphaltenes.



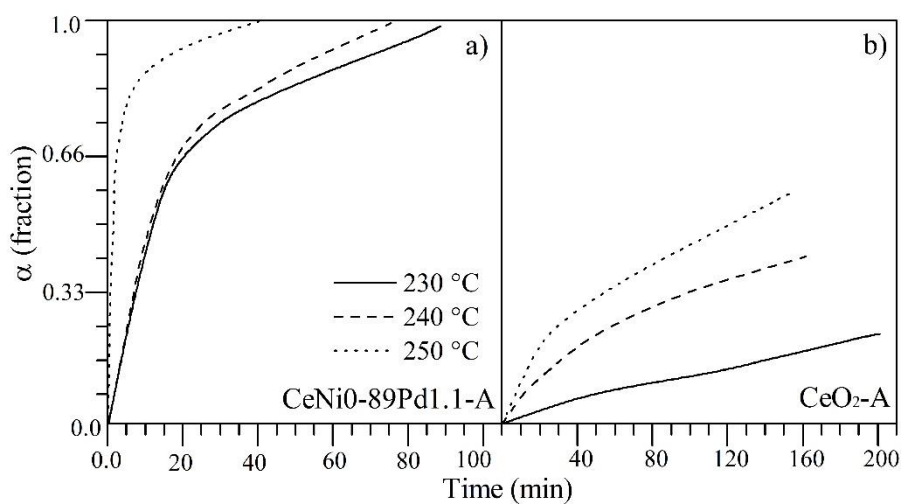
**Figure 6.** Isothermal conversion times at different R:A ratios of 8:2, 1:1, and 2:8 in the presence of  $\text{CeNi}_{0.89}\text{Pd}_{1.1}$  nanoparticles at  $220\text{ }^\circ\text{C}$ .

#### 4.4. Effective Activation Energy

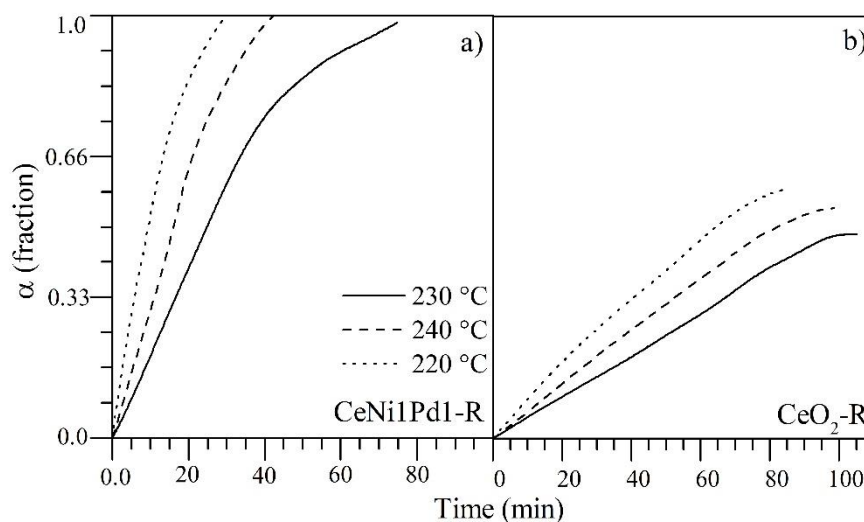
For the effective activation energy estimation, a plot of  $\ln(t_{a,i})$  vs.  $1/T_i$  was obtained using the conversion of each fraction at three different temperatures. The value of the activation energy was obtained from the slope. The isothermal conversions of resin II and  $n\text{-C}_7$  asphaltenes in the presence of nanoparticles were made at  $210$ ,  $220$ , and  $230\text{ }^\circ\text{C}$ . For the fraction in the absence of nanoparticles, the employed temperatures were  $360$ ,  $370$ , and  $380\text{ }^\circ\text{C}$ . These curves are shown in Figures 7-9.



**Figure 7.** Isothermal conversion times at different temperatures for (a) virgin resins II and (b) virgin  $n\text{-C}_7$  asphaltenes at 360 °C, 370 °C, and 380 °C.



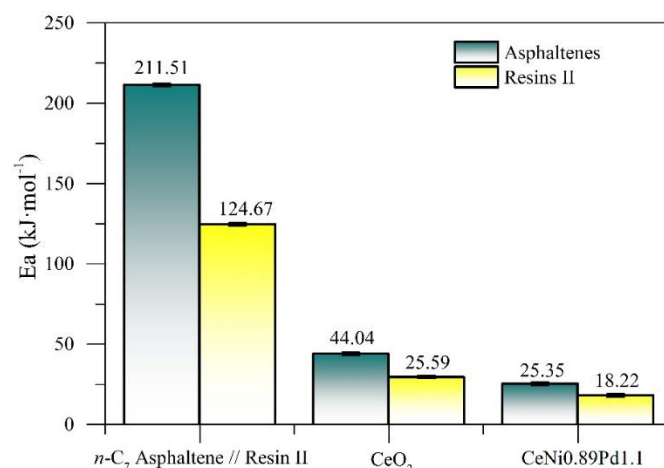
**Figure 8.** Isothermal conversion times at different temperatures for  $n\text{-C}_7$  asphaltenes adsorbed onto (a) CeNi<sub>0.89</sub>Pd<sub>1.1</sub> and (b) CeO<sub>2</sub>, at 230 °C, 240 °C, and 250 °C.



**Figure 9.** Isothermal conversion times at different temperatures for resins II adsorbed onto (a) CeNi<sub>0.89</sub>Pd<sub>1.1</sub> and (b) CeO<sub>2</sub>, at 230 °C, 240 °C, and 250 °C.

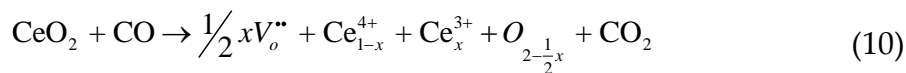
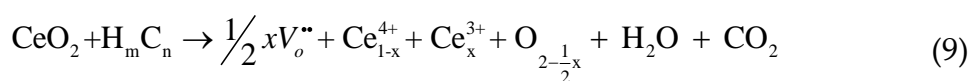
Figure 10 shows the activation energy values for the resin II and *n*-C<sub>7</sub> asphaltene decomposition in the presence and absence of the doped nanoparticles and the CeO<sub>2</sub> support. There is a significant decrease in the activation energy values for resin II adsorbed on the different nanoparticles, with the CeNi<sub>0.89</sub>Pd<sub>1.1</sub> system generating the biggest decrease in  $E_a$ . The presence of oxides on the surface of the nanoparticle causes a change in the decomposition mechanism of the heavy oil fractions, and their performance depends, to a considerable extent, on the chemical nature of the nanoparticle. In addition, the activation energy values are lower for the decomposition of resin II than for *n*-C<sub>7</sub> asphaltenes.

The activation energy values for the R:A systems in the presence and absence of CeNi<sub>0.89</sub>Pd<sub>1.1</sub> nanoparticles were calculated by following the same procedure, and the results are shown in Figure 11. The required activation energy increases as the amount of asphaltenes in the system increases, both in the presence and absence of the CeNi<sub>0.89</sub>Pd<sub>1.1</sub> nanoparticles. Nevertheless, the nanoparticles reduce the activation energy values necessary to carry out the decomposition reactions of the systems to  $21.51 \pm 1.05$  kJ·mol<sup>-1</sup> independently of the amount of asphaltenes in the system.



**Figure 10.** Estimated effective activation energy ( $E_a$ ) for isothermal gasification of resin II with CeO<sub>2</sub> and CeNi<sub>0.89</sub>Pd<sub>1.1</sub> nanoparticles for temperatures between 230 and 250 °C and without nanoparticles for temperatures between 360 and 380 °C.

Cerium oxide nanoparticles can regenerate their Ce<sup>4+</sup> atoms through a redox mechanism, maintaining the catalytic power of the support. This is achieved by carrying out processes of adsorption of reagents (H<sub>2</sub>O and heavy oil fractions), decomposition and chemical change of adsorbed molecules, desorption of reaction products between the support and reagents (CO<sub>2</sub>, CH<sub>4</sub>, LHD, CO, among others), and the interactions between the products and the active sites of the nanocatalyst. Here, the chemical reactions between the hydrocarbons Equation (9) and carbon monoxide Equation (10) with CeO<sub>2</sub> to produce Ce<sup>3+</sup> ions are shown, where  $V_o^{\square}$  is the oxygen vacancy produced from the redox cycle Ce<sup>4+</sup>/Ce<sup>3+</sup>:





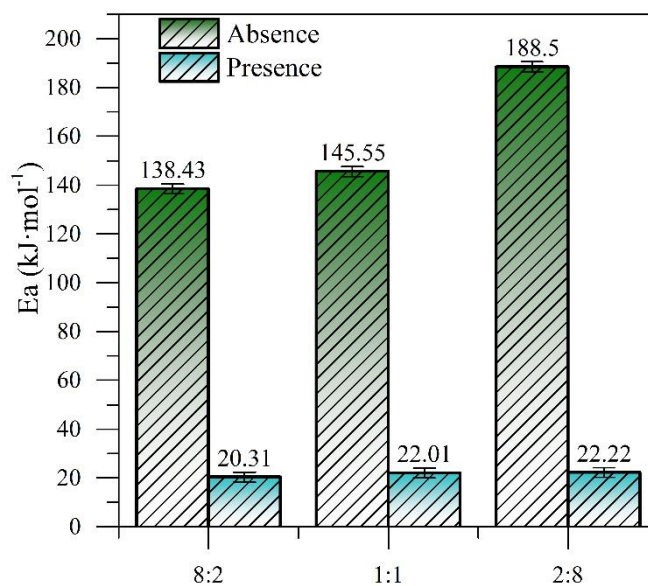


**Figure 11.** The estimated effective activation energy for isothermal catalytic gasification of the R:A systems in the absence and presence of CeNi<sub>0.89</sub>Pd<sub>1.1</sub> nanoparticles for temperatures between 230 and 250 °C and without nanoparticles for temperatures between 360 and 380 °C.

In this way, reducing Ce<sup>4+</sup> to Ce<sup>3+</sup> produces water vapor molecules and CO<sub>2</sub>. Then, through a redox cycle, the initial oxidation state is recovered, and the decomposition of asphaltenes and resins continues. However, the high performance of this catalyst is also associated with the active phases formed by the TEO on the surface of the support. The resulting species –O and –OH from the dissociative adsorption of water by the lower valence state of cerium may be transferred to nickel and palladium and react with surface carbonaceous species. Besides, through the movement of oxygen vacancies formed by the change in the oxidation state of the CeO<sub>2±δ</sub> species and the destabilization of the same, the reagents are transferred to the active sites of the transition element oxides, as schematized in Figure 12.

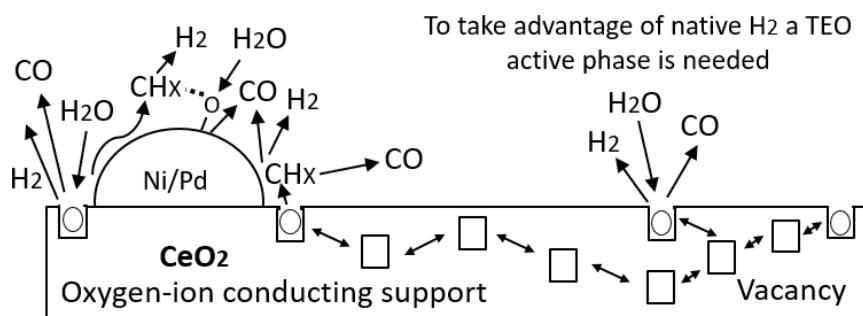


**Figure 12** Graphical representation of oxygen ion vacancy conducting support to active sites of transition element oxides of Ni and Pd for hydrogen, methane, dioxide carbon, and monoxide carbon production.

#### 4.5. Design of nanofluid for *In-Situ* upgrading

Figure 13 shows the tests carried out for the formulation of the nanofluid to select the best concentration of CeNi<sub>0.89</sub>Pd<sub>1.1</sub> nanoparticles and Tween 80 surfactant through a) thermogravimetric and b) zeta potential analysis, respectively. The nanoparticles and surfactant concentrations evaluated were 0.1, 0.2, 0.3, and 0.5% in a mass fraction. From the panel a) of Figure 13, it is possible to observe that the dosage of the treatment has a significant effect on the decomposition of the extra-heavy oil compounds, which is reflected in the intensities and temperature peaks for each sample. For the particular case of 0.1% of CeNi<sub>0.89</sub>Pd<sub>1.1</sub> nanoparticles, the peaks around 470 and 540 °C are predominant, indicating that with this amount of nanoparticles, the decomposition temperature of the heaviest hydrocarbons occurs in this region and that a higher amount of nanoparticles is needed [68,69] as a consequence of the high content of heavy compounds in the crude oil. For concentrations of 0.2, 0.3, and 0.5% in a fraction mass of the nanoparticles, an increase the intensities of the peaks located around 210 and 280 °C is observed. This means that the catalytic effect of the nanoparticles starts to be significant regarding the amount of heavy compounds in the system from the dosage of 0.2%. At this concentration, the intensities of the peaks at low temperatures (< 250 °C) are higher than for the other concentrations employed. Also, at high temperatures (> 450 °C) the intensity of the peak for a concentration of 0.2% is the lowest in comparison with the other concentrations evaluated. These results could be due to concentrations higher than 0.2% lead to a higher nanoparticle aggregation and a reduction of the available surface area [59]. Hence, a nanoparticle dosage of 0.2% was selected for injection into the porous medium.

From Panel b in Figure 13 it can be observed that the surfactant concentration changes the nanofluid stability for a fixed concentration of CeNi<sub>0.89</sub>Pd<sub>1.1</sub> nanoparticles of 0.2%. For surfactant concentrations  $\leq 0.2\%$ , the Z potential ( $\zeta$ ) of the system has fluctuations in both the stability zone ( $> 20\text{mV}$  and  $< -20\text{ mV}$ ) and the non-stability zone ( $-20 - 20\text{mV}$ ) [70]. On the other hand, the concentrations of 0.3 and 0.5 % maintain the value constant of the  $\zeta$  up to day 6 at 25 and -5 mV, respectively. The nanoparticles absorb surfactant and consequently, there are variations in the  $\zeta$ . Probably for concentrations below 0.02% the adsorption equilibrium is never reached, so the z potential is not stable. In this order, a dosage of 0.3% of Tween 80 surfactant was selected for nanofluid preparation. It is worth to mention here, according to previous studies, Tween 80 was selected as it has null influence on the heavy oil recovery and the main mechanisms are controlled by the nanoparticles [33,71,72]. The density and viscosity of the selected nanofluid were 1.12 cP and  $0.998\text{ g}\cdot\text{cm}^{-3}$  at 25 °C.

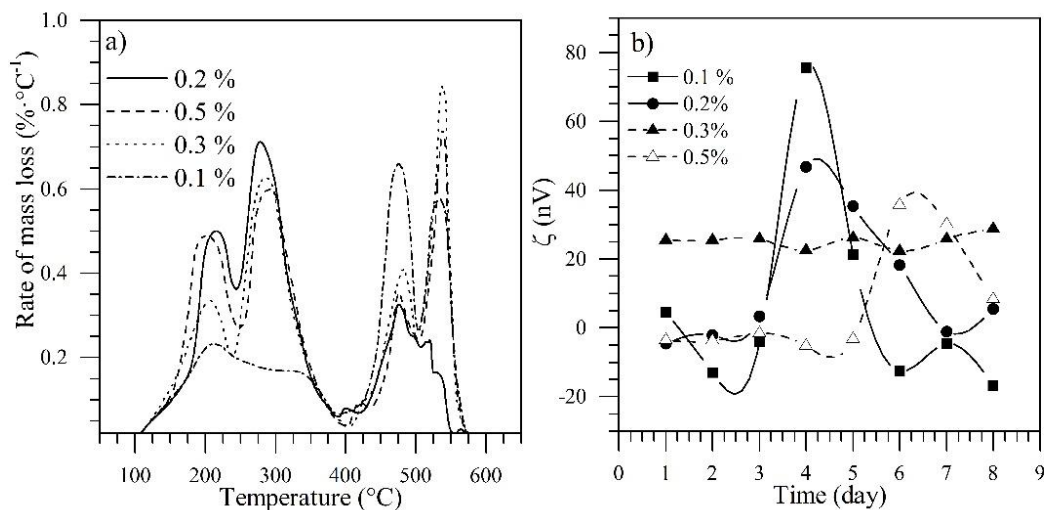


**Figure 13.** Thermogravimetric analysis and zeta potential measurements to select the best formulation of CeNi<sub>0.89</sub>Pd<sub>1.1</sub> nanoparticles and Tween 80 surfactant varying its concentration from a fraction mass of 0.1 to 0.5% of each one.

#### 4.6. Dynamic Tests of Oil Recovery

The oil recovery curve for the dispersed injection of CeNi<sub>0.89</sub>Pd<sub>1.1</sub>-based nanofluid in the steam stream to assist the steam injection technology is shown in Figure 14. In addition, the saturation states of both fluids, water, and oil, are shown in Table 5. For these tests, the effective permeabilities of water ( $k_w$ ) and oil ( $k_o$ ) were estimated to be 3744 and 2264 mD, respectively, which agrees with the properties of an HO reservoir. After the injection of 7 PVWE, an oil recovery

of 51% was obtained because of the transfer of heat to the rock and fluids, promoting its thermal expansion. In addition, other related mechanisms are the possible gravitational segregation of fluids, the volatilization of the lightest hydrocarbons, and the disaggregation of the viscoelastic network of the oil. After the dispersed injection of the nanofluid in the steam, an increment of 25% in the oil recovered was obtained. This is, to a great extent, due to the small size of the liquid droplets as a steam stream carries them to achieve higher penetration. Finally, after soaking the porous medium for 12 h, steam was injected again, and an ultimate oil recovery of 93% was reached. The technology is compared with the results obtained by those obtained when the nanofluid is injected in a liquid batch. The results are shown in Figure 1 of the Appendix C. In this scenario, 72% of the OOIP was produced, indicating that nanofluid injection dispersed in the steam stream provides better conditions for oil mobility and recovery.

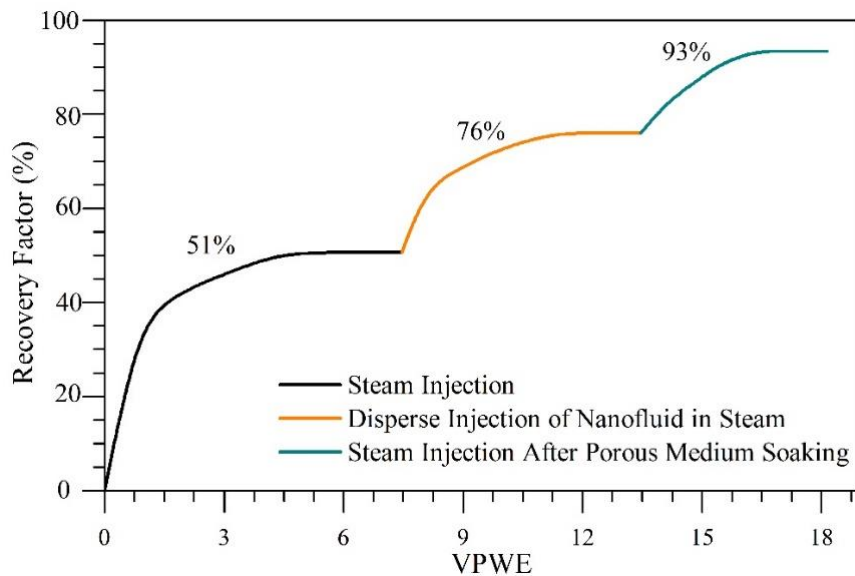


**Figure 14.** Oil recovery curve for steam injection assisted by CeNi<sub>0.89</sub>Pd<sub>1.1</sub> nanocatalyst dispersed in the steam stream during the stages: (1) continuous steam injection, (2) dispersed injection of nanofluid in steam, and (3) steam injection after porous medium soaking.

**Table 5.** Oil ( $S_{or}$ ) and water ( $S_{wr}$ ) residual saturation states in steam injection processes assisted by CeNi<sub>0.89</sub>Pd<sub>1.1</sub> nanocatalyst dispersed in the steam stream.

Stage	$S_{wr}$ (%)	$S_{or}$ (%)
Steam Injection	62.3	24.0
Steam injection assisted by ND	81.5	14.0
Steam injection after ND injection	94.6	7.0

The good performance obtained in the test carried out through nanofluid injection dispersed by the steam stream compared with the batch injection reported in previous studies [9,18] is related to the rapid interaction between the water vapor and the active sites of the CeNi<sub>0.89</sub>Pd<sub>1.1</sub> nanocatalyst [59]. Moreover, the C–C bond cleavage rate was improved in the catalytic cracking of heavy oil fractions, and higher amounts of H<sub>2</sub> and O<sub>2</sub> species could be produced from the splitting of steam molecules to react with the asphaltenes and resins over the catalyst surfaces [59]. At the same time, the increase in asphaltene–CeO<sub>2</sub> interactions enabled the enhanced adsorption and release of oxygen through the Ce<sup>4+</sup>/Ce<sup>3+</sup> redox cycle [60]. Thus, the vacancies of oxygen anions on the surface of the nanocatalyst became unstable [21,61], cracking the heavy oil fractions via partial oxidation through the oxygen production promoted by the CeNi<sub>0.89</sub>Pd<sub>1.1</sub> nanocatalyst or water via the redox reaction [59]. In addition, the redox reaction mechanism between the nanocatalyst, the heavy hydrocarbons, and the H<sub>2</sub>O<sub>(g)</sub> results in the formation of hydrogen as a byproduct, which could participate in stabilizing the previously cracked free radicals [62].

#### 4.7. Crude Oil Characterization before and after Nanofluid Injection

Panels a and b in Figure 15 show the values of API gravity and asphaltene content, respectively, for the untreated EHO, crude oil after steam injection, crude oil recovered by the dispersed injection of the nanofluid, and after a soaking time of 12 h. As observed, the API gravity increased, and the asphaltene content reduced after the steam injection with the CeNi<sub>0.89</sub>Pd<sub>1.1</sub> nanocatalyst. The results showed increases in API of 114.8% and 130% before and after the soaking treatment, confirming that the reaction time between adsorbed heavy fractions and nanocatalysts occurs immediately in the presence of steam. Furthermore, the asphaltene content was reduced by 72% in the presence of nanoparticles.

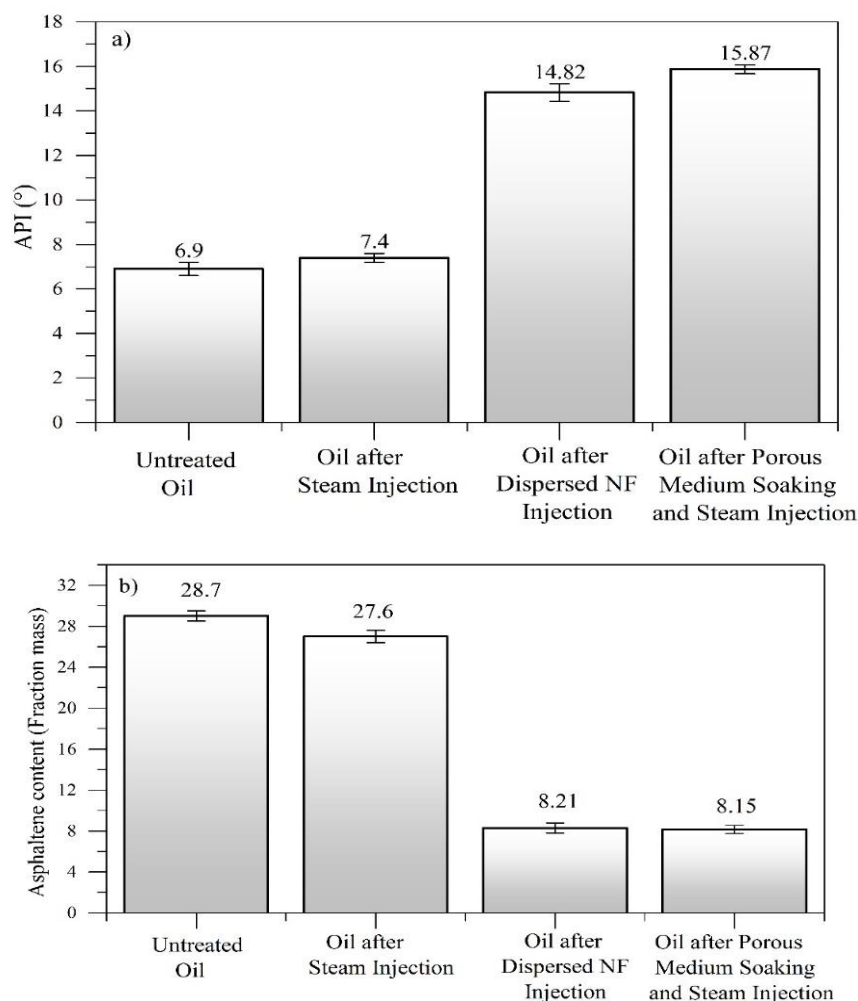


**Figure 15.** (a) API gravity and (b) asphaltene content in wt.% for untreated extra heavy oil and crude oil recovered after the steam injection, during the injection of CeNi<sub>0.89</sub>Pd<sub>1.1</sub> nanocatalyst-based nanofluid dispersed in a steam stream, and after soaking for 12 h.

Rheological behavior experiments were conducted at 25 °C for oil samples taken after each step of the displacement test. Figure 16 shows the viscosity of the samples as a function of the shear rate together with the fit of the Cross model. Also, Table 6 summarizes the estimated rheological parameters from the regression analysis. In Figure 16, it is observed for all samples that with the increase in shear rate, the viscosity of the crude oil decreases because of the breakdown of the internal structure of the crude oil, typical of shear-thinning pseudo-plastic fluids. With the injection of the steam without nanoparticles, a decrease in the heavy oil viscosity is appreciable. This could be related to the reduction in the cohesive forces on the molecular structures of combined asphaltene–resin compounds. For the scenarios assisted by nanotechnology, there were more pronounced reductions in viscosity, showing a higher decrease

for the crude oil obtained after soaking for 12 h. The viscosity reduction mechanisms associated with the presence of the nanoparticles are the fragmentation and subsequent redistribution of the  $n$ -C<sub>7</sub> aggregate asphaltenes [63], breaking the bonds and hindering the further formation of the heaviest compounds through the hydrogenation of free radicals and the asphaltene decomposition into lighter components. These results agree with Franco et al. [9] and Cardona et al. [18].

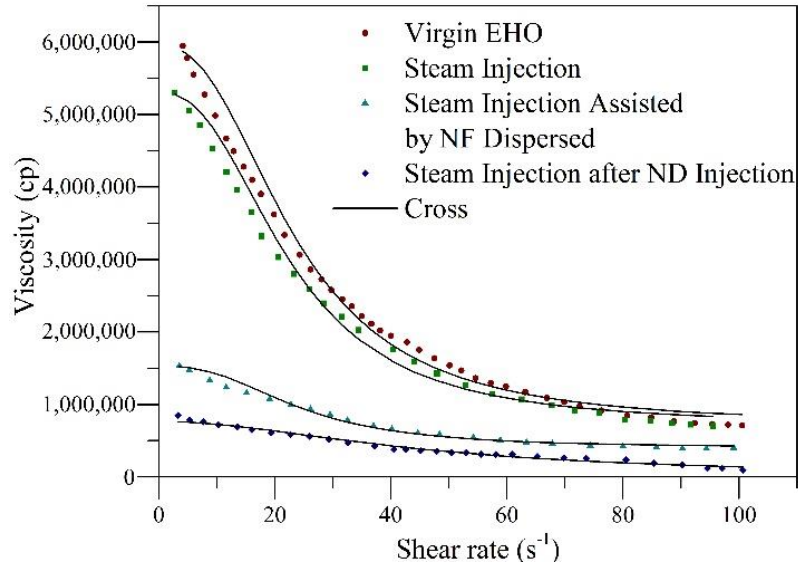


**Figure 16.** Rheological behavior at 25 °C and a shear rate from 0 to 100 s<sup>-1</sup> for untreated extra heavy oil (EHO) and crude oil recovered after the steam injection without and with Ni<sub>0.89</sub>Pd<sub>1.1</sub> nanocatalyst-based nanofluid.

The fitting of the Cross model presents an RMSE% < 1.0. The viscosity at zero ( $\mu_{0,\gamma}$ ) and infinity shear rate ( $\mu_{\infty,\gamma}$ ) are consistent with the experimental data, following the order crude oil after steam injection after porous media soaking < crude oil during nanofluid dispersed injection in steam stream < crude oil after steam injection < EHO. Considering the values of  $m \approx 1$ , the non-Newtonian behavior of the untreated oil is corroborated. These results agree with those obtained by Franco et al. [9]. Finally, the degree of viscosity reduction (DVR) was calculated at a shear rate of 10 s<sup>-1</sup> using Equation (1). The results indicate viscosity reductions of 85%, 75%, and 10% for the crude oil recovered after the steam injection post-soaking time during the nanocatalyst-based nanofluid injection by the steam stream and steam injection without nanoparticles, respectively. This reduction in viscosity could lead to a reduction in the costs associated with transport and refining operations, mitigation of the

environmental impact through the naphtha consumption reduction, and an increase in the sale price for crude oil produced.

**Table 6.** Estimated rheological parameters by the Cross Model for virgin extra heavy oil (EHO) and crude oil recovered after the steam injection, during the injection of CeNi<sub>0.89</sub>Pd<sub>1.1</sub> nanocatalyst-based nanofluid in the steam stream, and after soaking for 12 h.

Parameters	Virgin EHO	EHO after Steam Injection	EHO during Nanofluid Dispersed Injection	EHO Post Nanofluid Dispersed Injection
$\mu_{o,\gamma} \times 10^6$	5.95	5.31	0.55	0.27
$\mu_{\infty,\gamma} \times 10^6$	7.10	7.04	1.60	0.98
$\alpha_c \times 10^{-2}$	4.48	4.44	4.32	4.01
$m$	0.87	0.83	0.45	0.38
%RMSE	0.34	0.29	0.21	0.33
DVR (%)	-	10	75	85

## 5. Conclusions

The present study shows, for the first time, the effect of resin II on adsorption and catalytic steam gasification of *n*-C<sub>7</sub> asphaltene on doped and non-doped ceria nanoparticles. Among the most important results, doped nanoparticles achieved higher adsorption of both fractions as well as a higher decomposition temperature. The resin did not affect the amount of asphaltene adsorption over the material. In addition, the increase in the resin content promoted a higher conversion in a shorter time.

The dispersed injection of nanocatalyst-based nanofluid has been presented as a promising technique for assisting steam injection processes. In this case, the steam stream dragged the liquid drops, reaching a greater penetration depth in the porous medium; thus, a higher quantity of extra-heavy crude oil can be contacted, and nanoparticles can be better distributed in the pore throats. An increase in oil recovery from 51% to 93% at the end of the displacement test was obtained. Also, crude oil quality was improved considerably in terms of API gravity, asphaltene content, and viscosity. The API gravity increased from 6.9° to 15.87°. The asphaltene content was reduced from 28.7 to 8.15 wt.%, and the final viscosity of the sample was reduced by 85%.



## References

1. Patzek, T.; Koinis, M. Kern River steam-foam pilots. *J. Petrol. Technol.* **1990**, *42*, 496–503.
2. Yang, C.-z.; Han, D.-k. Present status of EOR in the Chinese petroleum industry and its future. *J. Petrol. Sci. Eng.* **1991**, *6*, 175–189.
3. Thomas, S. Enhanced oil recovery-an overview. *Oil Gas Sci. Technol.* **2008**, *63*, 9–19.
4. Lu, C.; Liu, H.; Zhao, W. Visualized study of displacement mechanisms by injecting viscosity reducer and non-condensable gas to assist steam injection. *J. Energy Inst.* **2017**, *90*, 73–81.
5. Dong, X.; Liu, H.; Chen, Z.; Wu, K.; Lu, N.; Zhang, Q. Enhanced oil recovery techniques for heavy oil and oilsands reservoirs after steam injection. *Appl. Energy* **2019**, *239*, 1190–1211.
6. Rana, M.S.; Sámano, V.; Ancheyta, J.; Diaz, J. A review of recent advances on process technologies for upgrading of heavy oils and residua. *Fuel* **2007**, *86*, 1216–1231.
7. Metwally, M. Effect of gaseous additives on steam processes for Lindbergh field, Alberta. *J. Can. Petrol. Technol.* **1990**, *29*, 26-30.
8. Saboorian-Jooybari, H.; Dejam, M.; Chen, Z. Heavy oil polymer flooding from laboratory core floods to pilot tests and field applications: Half-century studies. *J. Petrol. Sci. Eng.* **2016**, *142*, 85–100.
9. Franco, C.; Cardona, L.; Lopera, S.; Mejía, J.; Cortés, F. Heavy oil upgrading and enhanced recovery in a continuous steam injection process assisted by nanoparticulated catalysts. In Proceedings of the SPE Improved Oil Recovery Conference, Tulsa, OK, USA, 11–13 April 2016.
10. Abdrafikova, I.; Kayukova, G.; Petrov, S.; Ramazanov, A.; Musin, R.; Morozov, V. Conversion of extra-heavy Ashal'chinskoe oil in hydrothermal catalytic system. *Pet. Chem.* **2015**, *55*, 104–111.
11. Demirbas, A.; Alidrisi, H.; Balubaid, M. API gravity, sulfur content, and desulfurization of crude oil. *Petrol. Sci. Technol.* **2015**, *33*, 93–101.
12. Hashemi, R.; Nassar, N.N.; Almao, P.P. Nanoparticle technology for heavy oil in-situ upgrading and recovery enhancement: Opportunities and challenges. *Appl. Energy* **2014**, *133*, 374–387.
13. Wang, T.; Yang, W.; Wang, J.; Kalitaani, S.; Deng, Z. Low temperature oxidation of crude oil: Reaction progress and catalytic mechanism of metallic salts. *Fuel* **2018**, *225*, 336–342.

14. Hashemi, R.; Nassar, N.N.; Pereira Almaso, P. Enhanced heavy oil recovery by in situ prepared ultradispersed multimetallic nanoparticles: A study of hot fluid flooding for Athabasca bitumen recovery. *Energy Fuels* **2013**, *27*, 2194–2201.
15. Cardona Rojas, L. Efecto de Nanopartículas en Procesos con Inyección de Vapor a Diferentes Calidades. Master Thesis, Universidad Nacional de Colombia-Sede Medellín, Medellín, Colombia, March 2018.
16. Medina, O.E.; Gallego, J.; Arias-Madrid, D.; Cortés, F.B.; Franco, C.A. Optimization of the load of transition metal oxides (Fe<sub>2</sub>O<sub>3</sub>, Co<sub>3</sub>O<sub>4</sub>, NiO and/or PdO) onto CeO<sub>2</sub> nanoparticles in catalytic steam decomposition of n-C<sub>7</sub> asphaltenes at low temperatures. *Nanomaterials* **2019**, *9*, 401.
17. Medina, O.E.; Gallego, J.; Restrepo, L.G.; Cortés, F.B.; Franco, C.A. Influence of the Ce<sup>4+</sup>/Ce<sup>3+</sup> Redox-couple on the cyclic regeneration for adsorptive and catalytic performance of NiO-PdO/CeO<sub>2</sub>±δ nanoparticles for n-C<sub>7</sub> asphaltene steam gasification. *Nanomaterials* **2019**, *9*, 734.
18. Cardona, L.; Arias-Madrid, D.; Cortés, F.; Lopera, S.; Franco, C. Heavy oil upgrading and enhanced recovery in a steam injection process assisted by NiO-and PdO-Functionalized SiO<sub>2</sub> nanoparticulated catalysts. *Catalysts* **2018**, *8*, 132.
19. Nassar, N.N.; Franco, C.A.; Montoya, T.; Cortés, F.B.; Hassan, A. Effect of oxide support on Ni–Pd bimetallic nanocatalysts for steam gasification of n-C<sub>7</sub> asphaltenes. *Fuel* **2015**, *156*, 110–120.
20. Alamolhoda, S.; Vitale, G.; Hassan, A.; Nassar, N.N.; Almaso, P.P. Synergetic effects of cerium and nickel in Ce-Ni-MFI catalysts on low-temperature water-gas shift reaction. *Fuel* **2019**, *237*, 361–372.
21. Wang, X.; Chen, J.; Zeng, J.; Wang, Q.; Li, Z.; Qin, R.; Wu, C.; Xie, Z.; Zheng, L. The synergy between atomically dispersed Pd and cerium oxide for enhanced catalytic properties. *Nanoscale* **2017**, *9*, 6643–6648.
22. Vignatti, C.I.; Avila, M.S.; Apesteguía, C.R.; Garetto, T.F. Study of the water-gas shift reaction over Pt supported on CeO<sub>2</sub>–ZrO<sub>2</sub> mixed oxides. *Catal. Today* **2011**, *171*, 297–303.
23. Franco, C.A.; Montoya, T.; Nassar, N.N.; Pereira-Almaso, P.; Cortés, F.B. Adsorption and subsequent oxidation of colombian asphaltenes onto nickel and/or palladium oxide supported on fumed silica nanoparticles. *Energy Fuels* **2013**, *27*, 7336–7347.

24. Yi, S.; Babadagli, T.; Li, H.A. Use of nickel nanoparticles for promoting aquathermolysis reaction during cyclic steam stimulation. *SPE J.* **2018**, *23*, 145–156.
25. Afzal, S.; Nikookar, M.; Ehsani, M.R.; Roayaei, E. An experimental investigation of the catalytic effect of Fe<sub>2</sub>O<sub>3</sub> nanoparticle on steam injection process of an Iranian reservoir. *Iran. J. Oil Gas Sci. Technol.* **2014**, *3*, 27–36.
26. Franco, C.A.; Lozano, M.M.; Acevedo, S.; Nassar, N.N.; Cortés, F.B. Effects of resin I on asphaltene adsorption onto nanoparticles: A novel method for obtaining asphaltenes/resin isotherms. *Energy Fuels* **2015**, *30*, 264–272.
27. Hashemi, R.; Nassar, N.N.; Pereira Almaso, P. In situ upgrading of Athabasca bitumen using multimetallic ultradispersed nanocatalysts in an oil sands packed-bed column: Part 1. Produced liquid quality enhancement. *Energy Fuels* **2013**, *28*, 1338–1350.
28. Franco, C.A.; Zabala, R.D.; Zapata, J.; Mora, E.; Botero, O.; Candela, C.; Castillo, A. Inhibited gas stimulation to mitigate condensate banking and maximize recovery in cupiagua field. *SPE Prod. Oper.* **2013**, *28*, 154–167.
29. Restrepo, A.; Ocampo, A.; Lopera Castro, S.H.; Diaz, M.P.; Clavijo, J.; Marin, J. GaStim concept—A novel technique for well stimulation. Part I: Understanding the Physics. In Proceedings of the SPE Latin America and Caribbean Petroleum Engineering Conference, Mexico City, Mexico, 16–18 April 2012; doi:10.2118/152309-ms.
30. Medina, O.E.; Gallego, J.; Rodriguez, E.; Franco, C.A.; Cortés, F.B. Effect of pressure on the oxidation kinetics of Asphaltenes. *Energy Fuels* **2019**, *33* (11), 10734–10744.
31. Delannoy, L.; El Hassan, N.; Musi, A.; Le To, N.N.; Krafft, J.-M.; Louis, C. Preparation of supported gold nanoparticles by a modified incipient wetness impregnation method. *J. Phys. Chem. B* **2006**, *110*, 22471–22478.
32. Nassar, N.N.; Montoya, T.; Franco, C.A.; Cortés, F.B.; Pereira-Almaso, P. A new model for describing the adsorption of asphaltenes on porous media at a high pressure and temperature under flow conditions. *Energy Fuels* **2015**, *29*, 4210–4221.
33. Cortés, F.B.; Montoya, T.; Acevedo, S.; Nassar, N.N.; Franco, C.A. Adsorption-desorption of n-c7 asphaltenes over micro-and nanoparticles of silica and its impact on wettability alteration. *CT&F-Ciencia, Tecnología y Futuro* **2016**, *6*, 89–106.
34. Hurtado, Y.; Beltrán, C.; Zabala, R.D.; Lopera, S.H.; Franco, C.A.; Nassar, N.N.; Cortés, F.B. Effects of surface acidity and polarity of SiO<sub>2</sub> nanoparticles

- on the foam stabilization applied to natural gas flooding in tight gas-condensate reservoirs. *Energy Fuels* **2018**, *32*, 5824–5833.
35. Betancur, S.a.; Carrasco-Marín, F.; Franco, C.A.; Cortés, F.B. Development of composite materials based on the interaction between nanoparticles and surfactants for application in chemical enhanced oil recovery. *Ind. Eng. Chem. Res.* **2018**, *57*, 12367–12377.
  36. Lozano, M.M.; Franco, C.A.; Acevedo, S.A.; Nassar, N.N.; Cortés, F.B. Effects of resin I on the catalytic oxidation of n-C 7 asphaltenes in the presence of silica-based nanoparticles. *RSC Adv.* **2016**, *6*, 74630–74642.
  37. ASTM D36. *Standard Test Method for Softening Point of Bitumen (Ring-and-Ball Apparatus)*; Annual Book of ASTM Standards; ASTM International, West Conshohocken, PA, USA, **2006**.
  38. Franco, C.A.; Montoya, T.; Nassar, N.N.; Cortés, F.B. NiO and PdO Supported on fumed silica nanoparticles for adsorption and catalytic steam gasification of colombian n-C7 asphaltenes. In *Handbook on Oil Production Research*; Nova Science Publishers: Hauppauge, NY, USA, 2014; pp. 101–145.
  39. Whitaker, S. Flow in porous media I: A theoretical derivation of Darcy's law. *Transp. Porous Med.* **1986**, *1*, 3–25.
  40. Incropera, F.P.; Lavine, A.S.; Bergman, T.L.; DeWitt, D.P. *Fundamentals of Heat and Mass Transfer*; Wiley: Hoboken, NJ, USA, 2007.
  41. Bansal, V.; Krishna, G.; Chopra, A.; Sarpal, A. Detailed hydrocarbon characterization of RFCC feed stocks by NMR spectroscopic techniques. *Energy Fuels* **2007**, *21*, 1024–1029.
  42. Montoya, T.; Coral, D.; Franco, C.A.; Nassar, N.N.; Cortés, F.B. A novel solid–liquid equilibrium model for describing the adsorption of associating asphaltene molecules onto solid surfaces based on the “chemical theory”. *Energy Fuels* **2014**, *28*, 4963–4975.
  43. Nassar, N.N.; Hassan, A.; Luna, G.; Pereira-Almao, P. Kinetics of the catalytic thermo-oxidation of asphaltenes at isothermal conditions on different metal oxide nanoparticle surfaces. *Catal. Today* **2013**, *207*, 127–132.
  44. Schneider, P. Adsorption isotherms of microporous-mesoporous solids revisited. *Appl. Catal. A* **1995**, *129*, 157–165.
  45. Bates, M.K.; Jia, Q.; Doan, H.; Liang, W.; Mukerjee, S. Charge-transfer effects in Ni–Fe and Ni–Fe–Co mixed-metal oxides for the alkaline oxygen evolution reaction. *ACS Catal.* **2015**, *6*, 155–161.
  46. Dong, Y.-B.; Jin, G.-X.; Smith, M.D.; Huang, R.-Q.; Tang, B.; zur Loye, H.-C. [Ag<sub>2</sub> (C<sub>33</sub>H<sub>26</sub>N<sub>2</sub>O<sub>2</sub>)(H<sub>2</sub>O) <sub>2</sub> (SO<sub>3</sub>CF<sub>3</sub>) <sub>2</sub>]⊙ 0.5 C<sub>6</sub>H<sub>6</sub>: A Luminescent

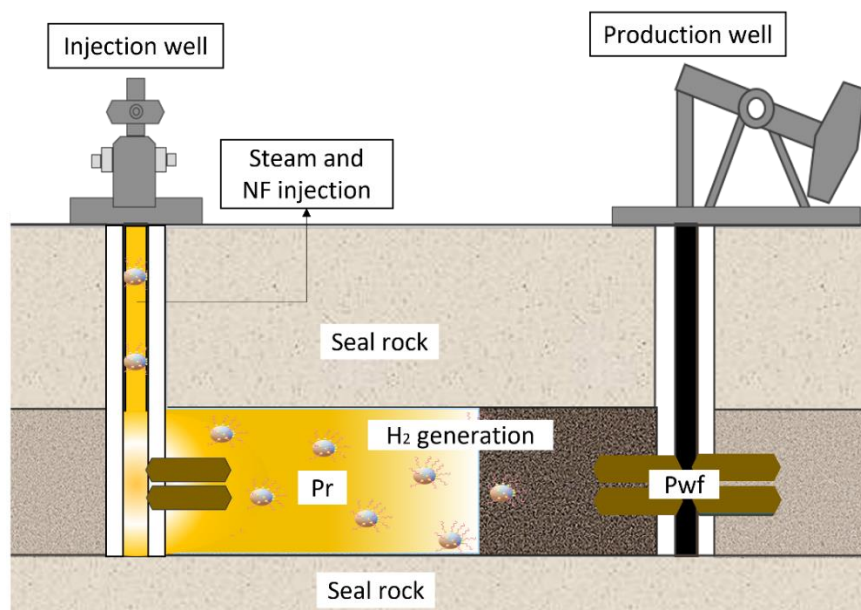
- Supramolecular Silver (I) Complex Based on Metal–Carbon and Metal–Heteroatom Interactions. *Inorg. Chem.* **2002**, *41*, 4909–4914.
47. Ignasiak, T.; Kemp-Jones, A.; Strausz, O. The molecular structure of Athabasca asphaltene. Cleavage of the carbon-sulfur bonds by radical ion electron transfer reactions. *J. Org. Chem.* **1977**, *42*, 312–320.
  48. Leon, O.; Rogel, E.; Espidel, J.; Torres, G. Asphaltenes: Structural characterization, self-association, and stability behavior. *Energy Fuels* **2000**, *14*, 6–10.
  49. Praharaj, S.; Nath, S.; Ghosh, S.K.; Kundu, S.; Pal, T. Immobilization and recovery of Au nanoparticles from anion exchange resin: Resin-bound nanoparticle matrix as a catalyst for the reduction of 4-nitrophenol. *Langmuir* **2004**, *20*, 9889–9892.
  50. Aguilera-Mercado, B.; Herdes, C.; Murgich, J.; Müller, E. Mesoscopic simulation of aggregation of asphaltene and resin molecules in crude oils. *Energy Fuels* **2006**, *20*, 327–338.
  51. Brewer, L.; Wengert, P.R. Erratum to: Transition metal alloys of extraordinary stability; An example of generalized Lewis-acid-base interactions in metallic systems. *Metall. Trans.* **1973**, *4*, 83–104.
  52. Murgich, J.; Rodríguez, J.; Aray, Y. Molecular recognition and molecular mechanics of micelles of some model asphaltenes and resins. *Energy Fuels* **1996**, *10*, 68–76.
  53. León, O.; Contreras, E.; Rogel, E.; Dambakli, G.; Acevedo, S.; Carbognani, L.; Espidel, J. Adsorption of native resins on asphaltene particles: A correlation between adsorption and activity. *Langmuir* **2002**, *18*, 5106–5112.
  54. Jacobs, G.; Ricote, S.; Graham, U.M.; Patterson, P.M.; Davis, B.H. Low temperature water gas shift: Type and loading of metal impacts forward decomposition of pseudo-stabilized formate over metal/ceria catalysts. *Catal. Today* **2005**, *106*, 259–264.
  55. Alvarez-Ramirez, F.; Ramirez-Jaramillo, E.; Ruiz-Morales, Y. Calculation of the interaction potential curve between asphaltene-asphaltene, asphaltene-resin, and resin-resin systems using density functional theory. *Energy Fuels* **2006**, *20*, 195–204.
  56. Merino-Garcia, D.; Andersen, S.I. Thermodynamic characterization of asphaltene-resin interaction by microcalorimetry. *Langmuir* **2004**, *20*, 4559–4565.
  57. Acevedo, S.; Zuloaga, C.; Rodríguez, P. Aggregation-dissociation studies of asphaltene solutions in resins performed using the combined freeze fracture-

- transmission electron microscopy technique. *Energy Fuels* **2008**, *22*, 2332–2340.
58. Kuang, W.; Rives, A.; Tayeb, B.O.B.; Fournier, M.; Hubaut, R. Isomerization of n-Hexane over silica-supported heteropoly acids promoted by the reduced Ce-Ni oxides. *J. Colloid Interf. Sci.* **2002**, *248*, 123–129.
  59. Hosseinpour, M.; Fatemi, S.; Ahmadi, S.J. Catalytic cracking of petroleum vacuum residue in supercritical water media: Impact of  $\alpha$ -Fe<sub>2</sub>O<sub>3</sub> in the form of free nanoparticles and silica-supported granules. *Fuel* **2015**, *159*, 538–549.
  60. Lamonier, C.; Ponchel, A.; D’huysser, A.; Jalowiecki-Duhamel, L. Studies of the cerium-metal-oxygen-hydrogen system (metal= Cu, Ni). *Catal. Today* **1999**, *50*, 247–259.
  61. Pinc, W.; Yu, P.; O’Keefe, M.; Fahrenholtz, W. Effect of gelatin additions on the corrosion resistance of cerium based conversion coatings spray deposited on Al 2024-T3. *Surf. Coat. Technol.* **2009**, *23*, 3533–3540.
  62. Yamaguchi, T.; Ikeda, N.; Hattori, H.; Tanabe, K. Surface and catalytic properties of cerium oxide. *J. Catal.* **1981**, *67*, 324–330.
  63. Tabora, E.A.; Franco, C.A.; Lopera, S.H.; Alvarado, V.; Cortés, F.B. Effect of nanoparticles/nanofluids on the rheology of heavy crude oil and its mobility on porous media at reservoir conditions. *Fuel* **2016**, *184*, 222–232.



Chapter 14.

# A Theoretical and Experimental Approach to the Analysis of Hydrogen Generation and Thermodynamic Behavior in an In Situ Heavy Oil Upgrading Process Using Oil-Based Nanofluids



Published article in Catalysts: [doi.org/10.3390/catal12111349](https://doi.org/10.3390/catal12111349)

Impact factor: 4.501



# **A Theoretical and Experimental Approach to the Analysis of Hydrogen Generation and Thermodynamic Behavior in an In Situ Heavy Oil Upgrading Process Using Oil-Based Nanofluids**

## **Abstract**

This study aims to show a theoretical and experimental approach to the analysis of hydrogen generation and its thermodynamic behavior in an in situ upgrading process of heavy crude oil using nanotechnology. Two nanoparticles of different chemical natures (ceria and alumina) were evaluated in asphaltene adsorption/decomposition under a steam atmosphere. Then, a nanofluid containing  $500 \text{ mg}\cdot\text{L}^{-1}$  of the best-performing nanoparticles on a light hydrocarbon was formulated and injected in a dispersed form in the steam stream during steam injection recovery tests of two Colombian heavy crude oils (HO1 and HO2). The nanoparticles increased the oil recovery by 27% and 39% for HO1 and HO2 regarding the steam injection. The oil recovery at the end of the displacement test was 85% and 91% for HO1 and HO2, respectively. The recovered crude oil showed an increment in API° gravity from 12.4° and 12.1° to 18.5° and 29.2° for HO1 and HO2, respectively. Other properties, such as viscosity and content of asphaltenes and resins with high molecular weight, were positively modified in both crude oils. The fugacity of  $\text{H}_2$  was determined between the reservoir and overburden pressure and different temperatures, which were determined by the thermal profiles in the displacement test. The fugacity was calculated using the application of virial equations of state with mixing rules based on the possible intermolecular interactions between the components. Hydrogen acquired a higher chemical potential via nanoparticle presence. However, the difference in  $\text{H}_2$  fugacity between both points is much higher with nanoparticles, which means that hydrogen presents a lower tendency to migrate by diffusion to the high-pressure point. The difference between HO1 and HO2 lies mainly in the fact that the pressure difference between the reservoir and the overburden pressure is greater in HO2; therefore, the difference in fugacity is greater when the pressure differential is greater.

## 1. Introduction

In recent years, the challenges of energy supply and global warming have drawn increasing attention from humanity [1]. The world is facing a severe problem known as the greenhouse effect. The consequences of this phenomenon are an increase in the Earth's average temperature of 0.2 °C per decade and an increase in the concentration of CO<sub>2</sub> in the atmosphere, which can cause disastrous and irreversible changes to our planet's ecosystem [2].

Hydrogen is an essential energy vector for decarbonization, which allows the development of a clean, sustainable energy source with a low carbon footprint. In addition, hydrogen has important implications for other factors, such as reducing greenhouse gas emissions at the end-use point, enhancing the security of energy supply, and improving economic competitiveness, among others, and it is also considered a potential fuel for the transport sector [3]. However, most of the technologies used to produce gray and blue hydrogen involve releasing large quantities of CO<sub>2</sub> [4]. Moreover, these processes use large additional amounts of fossil fuels as an energy source and are highly endothermic. On the other hand, hydrogen production from renewable sources is still disadvantageous economically [5].

Nowadays, there is a need to promote technologies that help us transition from fossil fuels to sustainable energy systems such as hydrogen. Therefore, during the energy transition, it is important to establish processes that help conventional technologies to improve their energy efficiency by minimizing the amount of CO<sub>2</sub> emitted into the atmosphere and the environmental impacts [6]. An exciting strategy to foster energy transition is the co-production of hydrogen and fossil fuels with a low carbon footprint [7]. Some processes, including steam and air gasification, have been widely applied in coal, natural gas, and light hydrocarbons [8,9]. However, the use of heavy (HO) and extra heavy crude (EHO) oils for this purpose appears as a novel research topic accompanied by several challenges and considerations [10-14].

Around 70% of the worldwide reserves are from HO and EHO, representing significant economic value [15]. There are substantial difficulties associated with the high viscosity and content of asphaltenes and resins of high molecular weights [10,16-18].

Commonly, to improve the mobility and production of HO and EHO, thermal treatments are used in situ [18–30]. Most conventional processes inject steam in different ways, such as continuous steam injection [19,20], cyclic steam injection [20,21], and steam-assisted gravity drainage (SAGD) [18,22]. However, these techniques are limited by different mechanisms, including high operation costs [23], steam condensation [24], and temporal oil viscosity reduction with no change in crude oil quality [25], obtaining recovery factors close to 50% and low calorific gaseous products, including greenhouse gases (GHG) such as CO<sub>2</sub> [26–31].

The efficiency of the steam injection could be enhanced by adding chemical additives and solvent-based chemicals, mainly light to medium hydrocarbons, which can reduce steam requirement, heat losses, and GHG emissions, and increase HO productivity [32]. According to the Canadian Energy Research Institute, steam injection and SAGD generate 60.4 kgCO<sub>2</sub>eq/bbl, which can be reduced between 15–20% using steam solvent and 10–15% with steam-chemical additives [33]. However, several limitations, such as low thermal stability, high costs, and low possibility to upgrade the HO, are associated with chemical additive usage.

Consequently, nanoparticles have been extensively explored in the field of heavy oil recovery, assisting conventional thermal treatments such as steam injection. A clear understanding of how nanoparticles interact with crude oil is an area of extensive research. Authors have made tremendous efforts to understand parameters such as the rheology of heavy oil, as well as compositional changes to obtain insights on how crude oil upgrading can be achieved [18,34–38]. As mentioned before, heavy oils are laden with asphaltenes in the bulk, which imparts them with their semi-solid structure. Breaking—more technically referred to as ‘cracking’—of the asphaltene structure is the first step in making the oil more accessible for further treatment [35–37]. Catalytic cracking also distributes the asphaltene aromatic structure into lighter fractions, which increases the value of the oil. Involving nanotechnology in the field of heavy oil recovery is a way of exploring efficient ways to implement the same process but with improved results [39].

Although so far, many nanomaterials have been developed to improve HO recovery, there is still work to be done to improve the quality of products obtained during the cracking of heavy oil fractions. Well-designed nanoparticles can achieve this goal, which should present a high affinity for heavy oil fractions (asphaltenes), that subsequently can be decomposed into lower molecular weight

hydrocarbons and high calorific gases (such as hydrogen and others) by the interactions between steam and the catalytic active sites of nanoparticles [19,27,40-49].

In this context, this study looks for an alternative to implement energy transition strategies. It is well known that renewable energy sources should incorporate traditional energy sources to be more sustainable [7]. Hence, the application of tailor-made nanofluids for the revaluation and production of HO and EHO, in parallel, will entail obtaining H<sub>2</sub> as a transitory and complementary source of energy that will help the implementation of this fuel on a large scale until it achieves the development of 100% “eco” technologies that allow a sufficient supply of green H<sub>2</sub>. However, the particular properties of hydrogen, such as the small size of the molecule, provide it with great transport capacity in a porous medium, even with almost impermeable properties [50]. Thus, it is imperative to analyze the thermodynamic characteristics of the H<sub>2</sub> produced in the reservoir during the implementation of nanotechnology-assisted steam injection.

To this end, this study considers both experimental and theoretical components. The experimental section includes the static and dynamic evaluation of nanoparticles during steam injection, considering two representative Colombian oil fields. For static experiments, two nanoparticles were considered. NP1: commercial Al<sub>2</sub>O<sub>3</sub> nanoparticles (Petrora S.A.S, Medellín, Colombia) doped with 1.0% in mass fraction of Ni and Pd; and NP2: commercial CeO<sub>2</sub> nanoparticles (Nanostructured & Amorphous Materials, Houston, TX, USA) doped with 1.0% in mass fraction of Ni and Pd. The best one was selected to design the nanofluid and perform the dynamic tests. Some of the analyzed characteristics include crude oil recovery, crude oil upgrading, and perdurability of the oil quality and produced gases. Next, a thermodynamic analysis of the fugacity of hydrogen was performed to obtain a clearer landscape of its in-situ behavior. Based on this analysis, it was possible to determine the tendency of hydrogen to be trapped in the reservoir and its dissipation into the porous media.

## 2. Experimental

### 2.1. Materials

Asphaltenes and resins were extracted based on ASTM D2892 and ASTM D5236 standards [51,52] from two different HO. *n*-Heptane (99% Sigma-Aldrich,

St. Louis, MO, USA) was used as the precipitating agent. Static tests were executed with two different nanoparticles. NP1: commercial Al<sub>2</sub>O<sub>3</sub> nanoparticles (Petroraza S.A.S, Medellín, Colombia) doped with 1.0% in mass fraction of Ni and Pd; and NP2: commercial CeO<sub>2</sub> nanoparticles (Nanostructured & Amorphous Materials, Houston, TX, USA) doped with 1.0% in mass fraction of Ni and Pd. Nickel and palladium were doped through the incipient wetness technique [53]. The doped amount of Ni and Pd was ensured by Energy Dispersive X-ray spectroscopy (EDX) using a Field Electron and Ion (FEI) microscope model Quanta 400 (SEM) (Eindhoven, The Netherlands) coupled with the EDX source.

Both materials have been extensively characterized and reported by Cardona et al. [54] and Medina et al. [55]. The most important properties are shown in Table 1.

**Table 1.** Basic characteristic of nanoparticles

Properties	NP1	NP2
Hydrodynamic diameter (nm)	76.0	20.2
BET surface area (m <sup>2</sup> ·g <sup>-1</sup> )	223.4	65.4
Ni crystal size (nm)	2.2	6.4
Pd crystal size (nm)	4.1	3.9
Ni dispersion (%)	5.4	12.7
Pd dispersion (%)	9.9	38.6
Point of zero charge	7.8	7.5

Displacement tests were performed using the reservoir fluids of two different Colombian fields, consisting of two heavy crude oils and two synthetic brines. The basic properties of the crude oils are shown in Table 2. Brines were composed of 22,000 (brine 1) and 18,000 ppm (brine 2) NaCl eq (Sigma-Aldrich, St. Louis, MO, USA). Deionized water with 3 μS·cm<sup>-1</sup> conductivity was used to generate the steam.

**Table 2.** Basic characteristic of heavy crude oil for the steam injection test.

Properties	HO1	HO2
API °	12.4	12.1
Viscosity 25°C	4000	3500
SARA content	Saturates (%)	18.98
	Aromatic (%)	48.24
	Resins (%)	31.04
	Asphaltenes (%)	1.76

Sand samples were provided by Ecopetrol S.A. to construct the porous media. The constructed porous media for the two Colombian fields were cleaned with a mixture of methanol (99.8%), toluene (99.8%), and HCl (37%), all provided by Merk KGaA (Darmstadt, Germany) following the tests reported in previous studies [24,25].

The nanoparticle with the best performance in the static tests is selected to formulate the nanofluid. The carrier fluid consists of an oil-based fluid provided by Petroraza S.A.S (Medellín, Colombia). Fourier Transform–Infrared Spectra corroborated the oil-based chemical nature [56-58], and this is shown in Figure 1. Figure S6 shows the presence of characteristic bands of the hydroxyl functional groups (O-H) associated with the presence of alcohols at  $3391\text{ cm}^{-1}$  wavelengths [56]. The vibration corresponding to the  $-\text{CH}$  bonds are also found at  $2900\text{ cm}^{-1}$ , related to the presence of olefins, and finally, bands with  $\text{C}=\text{C}$ ,  $\text{C}=\text{O}$ ,  $\text{C}-\text{N}$ ,  $\text{C}-\text{C}$ ,  $\text{C}-\text{O}$ , and  $\text{C}-\text{O}-\text{C}$  bonds are recognized ( $1500 - 1700\text{ cm}^{-1}$ ) [57]. The carrier comprises aliphatic hydrocarbons, with carboxylic acids, ester groups, amines, amides, and nitrogen groups [58]. The nanofluid (Al-NF) consists of  $500\text{ mg}\cdot\text{L}^{-1}$  nanoparticles dispersed in the commercial carrier. Some properties of the carrier and the nanofluid are shown in Table 3.

**Table 3.** Basic characteristic of carrier and nanofluid

Properties	Carrier	Nanofluid
Density ( $\text{g}\cdot\text{mL}^{-1}$ )	0.96	0.96
Viscosity (cP)	2.13	3.05
Surface tension ( $\text{mN}\cdot\text{m}^{-1}$ )	24.23	23.01
Conductivity ( $\text{mS}\cdot\text{cm}^{-1}$ )	4.9	5.7
Thermal conductivity ( $\text{W}\cdot\text{mK}^{-1}$ )	0.1502	0.1562
Thermal resistivity ( $^{\circ}\text{C cm}\cdot\text{W}^{-1}$ )	660	640

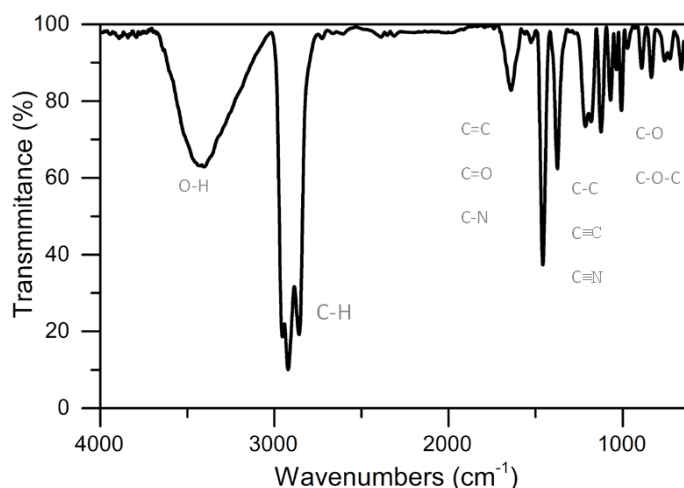


**Figure 1.** IR spectra for carrier used in the nanofluid for steam injection displacement.

## 2.2. Static Tests for Nanoparticle Selection through Adsorption Isotherms and Thermogravimetric Analysis

The asphaltene/resin adsorption capacity of the nanoparticles was measured through the construction of adsorption isotherms preparing oil model solutions consisting of different concentrations of asphaltenes/resins ( $100 \text{ mg}\cdot\text{L}^{-1}$ – $2000 \text{ mg}\cdot\text{L}^{-1}$ ) diluted in toluene. The instrument and protocol employed for the adsorption isotherms construction were described in previous studies [39,55,59].

A high-pressure thermogravimetric analyzer evaluated the subsequent catalytic decomposition of asphaltenes/resins adsorbed on nanoparticles (HP-TGA 750, TA instruments Inc., Hüllhorst, Germany). The tests were carried out at 700 and 400 psi for the asphaltenes isolated from HO1 and HO2 based on the pressure of the respective oil field.

Initially, the surface of the samples was cleaned by subjecting them to a vacuum at 0.036 psi for 10 min. After that, the equipment reached pressure and flow conditions before warming up. The experiments were carried out at isothermal steam injection conditions ( $250 \text{ }^\circ\text{C}$ ) for 300 min. The experiments were executed for an asphaltene/resin adsorbed amount of  $0.2 \text{ mg}\cdot\text{m}^{-2} \pm 0.02 \text{ mg}\cdot\text{m}^{-2}$  [60]. The steam atmosphere was simulated by introducing  $100 \text{ mL}\cdot\text{min}^{-1}$  of  $\text{N}_2$  and  $6.30 \text{ mL}\cdot\text{min}^{-1}$  of  $\text{H}_2\text{O}_{(\text{g})}$  using a gas saturator controlled by a thermostatic bath [61].

## 2.3. Oil recovery and Upgrading Evaluation

For dynamic tests, two different porous media were used. Table 4 summarizes the absolute and oil-effective permeability for both systems.

**Table 4.** Properties of porous media for the steam recovery processes

System	Porous medium 1	Porous medium 2
Mineralogy	Silica (99%)	Silica (99%)
Porosity (%)	22.0	21.0
Absolute permeability	4331	2103
Oil effective permeability	3558	1887

Displacement tests were executed in three stages to recreate steam injection at field conditions. Steam was injected at 80% quality at 250 °C. The steam quality was ensured through numerical simulation using the protocol described in our previous works [39,54]. The first stage includes the steam injection between 3 mL·min<sup>-1</sup> and 5 mL·min<sup>-1</sup>. During this stage, the steam was injected until no more crude oil was produced. Then, during the second stage, the incremental crude oil produced by nanofluid injection dispersed into the steam stream was estimated. The nanofluid was injected between 0.5 mL·min<sup>-1</sup> and 1 mL·min<sup>-1</sup>. The third stage started when no increment in oil production was observed. Here, the porous media were left to stand for 12 h, and then the steam was injected again until there was no oil production. The pressure profile was monitored during the complete process to ensure the nanofluid transport in the steam stream.

The overburden pressure was fixed at 1582 psi and 1992 psi for HO1 and HO2, respectively. The pore pressure was 150 psi in both cases. The instrumental details of the configuration system are reported in previous works [21,39,54].

Finally, the gas outlet line was coupled with a mass spectrometer (Shimadzu MS, Tokyo, Japan). The scan rate of the linear ion trap mass analyzer was 0.03 *m/z* from 0 *m/z* to 200 *m/z*. The MS instrument was equipped with a hot capillary column heated at 150 °C to prevent gas condensation. The components targeted for analysis were obtained by using a 100-eV electron impact mode to achieve sufficiently strong signals for information on the HO transformation.

#### 2.4. Effluents Characterization

The crude oil recovered during the three stages of the displacement test was characterized by different techniques, including SARA distribution following the ASTM D6560 standard [62,63]. Additionally, API gravity and dynamic viscosity were measured using an Anton Paar Stabinger SVM 3000 (Madrid, Spain), following the protocols described elsewhere [21,54]. The perdurability of the treatment in the crude oil quality was evaluated in terms of API gravity and dynamic viscosity for four consecutive weeks.



## 2.5. Description of the Considered Scenario for In Situ Hydrogen Generated

With the aim of analyzing the behavior of hydrogen in the reservoir during in situ crude oil upgrading, a thermodynamic analysis based on its fugacity was performed. Figure 2 shows the schematic representation of the proposed system. The system considers a scenario where both the producing well and the injection well are closed, and gases have been generated during in situ crude oil upgrading. The  $\Delta P$  on the  $x$ -axis is neglected ( $P_{fw,injection} = P_r = P_{wf,production}$ ), whereas the  $\Delta P$  on the  $y$ -axis was calculated based on the overburden gradient and the reservoir pressure of each oil field. The overburden gradient is obtained considering the density of the rock matrix for the two reservoirs at  $2.55 \text{ g}\cdot\text{cm}^{-3}$  (sand rock) and the depth of the reservoirs (HO1 = 1600 ft, HO2 = 2000 ft). The overburden pressures for HO1 and HO2 were 1582 and 1992 psi, respectively. Additionally, the system considers a caprock below the reservoir, so hydrogen diffusion could only occur upwards.

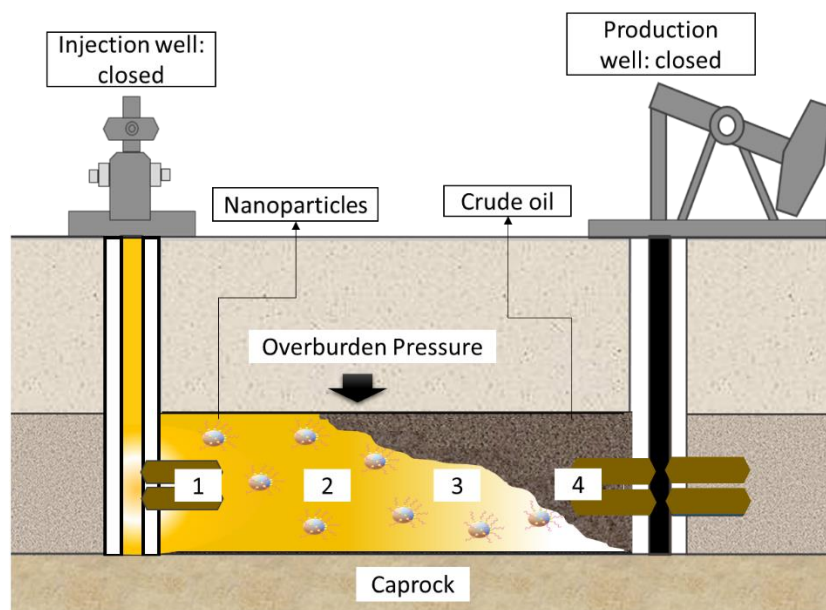


**Figure 2.** Schematic representation of considered scenario for hydrogen fugacity analysis. The system considers the following assumptions: injection and production well are closed (the  $\Delta P$  on the  $x$ -axis is neglected); the overburden pressures for HO1 and HO2 were 1582 and 1992 psi, respectively; the density of the rock matrix for the two reservoirs was  $2.55 \text{ g}\cdot\text{cm}^{-3}$  (sand rock); the depths of the reservoirs were HO1 = 1600 ft, HO2 = 2000 ft; white boxes assume different temperatures based on displacement tests; and presence of caprock below the reservoir.

This section contemplates different analyses as follows:

1. Hydrogen fugacity analysis at steam injection temperature (first box of Figure 2) for the gaseous mixture produced without nanoparticles on the HO1 sample.
2. Hydrogen fugacity analysis at steam injection temperature (first box of Figure 2) for the gaseous mixture produced from the nanotechnology-assisted steam injection on the HO1 sample.
3. Hydrogen fugacity analysis as a function of temperature (second, third, and fourth boxes of Figure 2). The temperature was fixed based on the thermal profiles obtained in the experimental setup using four thermocouples at the beginning, inside, and exit of the porous medium. The analysis was performed for steam injection assisted by nanoparticles on HO1.
4. Hydrogen fugacity analysis for HO2 considering the variation in temperature and comparison with HO1.2

## 2.6. Thermodynamic Analysis of In situ Hydrogen Generated

Fugacity is a thermodynamic property that measures the chemical potential of species and can be used in phase equilibrium calculations. The use of fugacity allows the identification of the phase in which a component is likely to remain [64]. Its analysis can be conducted through cubic [65,66] or virial [67,68] equations of state in a mixture of gases or through correlations obtained from experimental information [69,70]. For this research, the fugacity of the gas mixture released during the displacement test of HO1 and HO2 by steam injection assisted by nanotechnology was calculated. The gas mixture contains hydrogen ( $H_2$ ), ethylene ( $C_2H_4$ ), methane ( $CH_4$ ), carbon dioxide ( $CO_2$ ), carbon monoxide ( $CO$ ), and hydrogen sulfide ( $H_2S$ ). The application of virial equations of state truncated in the second term with mixing rules was considered to represent the possible intermolecular interactions between pairs of components. The truncation to the second term occurs because the interaction between pairs of molecules in gases is more likely than between triples or higher-order interactions [64,71]. The mixing rules allow us to calculate the properties of pseudo components that represent the interaction between pairs of molecules. The mixing properties considered were the acentric factor ( $\omega$ ), critical temperature ( $T_c$ ), critical compressibility factor ( $Z_c$ ), critical molar volume ( $v_c$ ), and critical pressure ( $P_c$ ). The mixing rules are applied to the critical conditions because they are characteristic of each compound and allow the evaluation of the deviation from ideality from the concept of reduced property, which is explained by the theorem of corresponding states [72].

The equations used to calculate the fugacity of gases using the virial equations of state truncated in the second term are shown below. First, the mixing rules are shown, then the calculation of the virial coefficients of the pure substances, as well as the coefficients of the interactions.

Next, we provide the mixing rules used to calculate the mixing properties of gases for the application of the truncated virial equation of state in the second term (Equations (1)–(5)).

$$\omega_{ij} = \frac{\omega_i + \omega_j}{2} \quad (1)$$

$$T_{cij} = (T_{ci}T_{cj})^{1/2} \quad (2)$$

$$Z_{cij} = \frac{Z_{ci} + Z_{cj}}{2} \quad (3)$$

$$v_{cij} = \left( \frac{(v_{ci})^{1/3} + (v_{cj})^{1/3}}{2} \right)^3 \quad (4)$$

$$P_{cij} = \frac{Z_{cij}RT_{cij}}{v_{cij}} \quad (5)$$

where the subscript  $ij$  indicates a property of the mixture and the subscripts  $i$  and  $j$  indicate the component  $i$  and component  $j$ , respectively.

Thus, Equation (6) was used to calculate the second virial coefficient for the component mixture.

$$B_{ij} = \frac{RT_{cij}\hat{B}_{ij}}{P_{cij}} \quad (6)$$

where  $\hat{B}_{ij}$  is the reduced second virial coefficient. To calculate the reduced virial coefficient, it must be considered that this is only a function of temperature [64]. A good approximation to this property is the following equation (Equation (7)):

$$\hat{B}_{ij} = B_{ij}^0 + \omega_{ij}B_{ij}^1 \quad (7)$$

where  $B_m^0$  and  $B_m^1$  are only a function of temperature. These values can be calculated through the following equations (Equations (8) and (9)):

$$B_{ij}^0 = 0.083 - \frac{0.422}{T_{rij}^{1.6}} \quad (8)$$

$$B_{ij}^1 = 0.139 - \frac{0.172}{T_{rij}^{4.2}} \quad (9)$$

where  $T_{rij}$  refers to the reduced temperature of the mixture and is calculated as the ratio of the system temperature  $T$  to the critical temperature of the mixture  $T_{cij}$  (Equation (10)).

$$T_{rij} = \frac{T}{T_{cij}} \quad (10)$$

For the second virial coefficient calculation, the reduced properties were considered. To carry out the calculations previously explained, it is necessary to consider the properties of each species in the gas mixture. For this purpose, the following table (Table 5) shows the properties of interest for each of the components considered.

**Table 5.** Thermodynamic properties of gas mixture components produced during the steam gasification of HO1 and HO2 with and without nanoparticles.

Component	Critical Temperature (K)	Critical Pressure (bar)	Critical Molar Volume (cm <sup>3</sup> ·mol <sup>-1</sup> )	Critical Compressibility Factor	Acentric Factor
H <sub>2</sub>	33.19	13.13	64.1	0.305	-0.216
C <sub>2</sub> H <sub>4</sub>	282.3	50.4	131	0.281	0.087
CH <sub>4</sub>	190.6	45.99	98.6	0.286	0.012
CO <sub>2</sub>	304.2	73.83	94	0.274	0.224
CO	132.9	34.99	93.4	0.299	0.048
H <sub>2</sub> S	373.5	89.63	98.5	0.284	0.094

The second virial coefficient is a function of composition and temperature in a gas mixture. A composition dependence equation at moderate pressures is as follows (Equation (11)) [64]:

$$B = \sum_i \sum_j y_i y_j B_{ij} \quad (11)$$

To obtain a mathematical expression for calculating the fugacity, it is necessary to develop the expression from the virial equation of state (Equation (12)).

$$Z = 1 + \frac{BP}{RT} \quad (12)$$

Equation (12) can be rewritten for a mixture of  $n$  moles as Equation (13):

$$Zn = n + \frac{BPn}{RT} \quad (13)$$

In this way, considering an expression for the coefficient of fugacity of component  $k$  ( $\hat{\phi}_k$ ) in the mixture (Equation (14)), an expression for the activity coefficient of component  $k$  in the gas mixture is obtained from the virial equation of state (Equation (15)):

$$\ln \hat{\phi}_k = \int_0^P \left( \frac{\bar{Z}_k}{P} - 1 \right) \frac{dP}{P} \quad (14)$$

$$\ln \hat{\phi}_k = \frac{P}{RT} \left[ B_{kk} + \frac{1}{2} \sum_i \sum_j y_i y_j (2\delta_{ik} - \delta_{ij}) \right] \quad (15)$$

where subscripts  $i$  and  $j$  represent all species and  $\delta_{ij}$  are calculated as shown below (Equations (16) and (17)):

$$\delta_{ik} = 2B_{ik} - B_{ii} - B_{kk} \quad (16)$$

$$\delta_{ij} = 2B_{ij} - B_{ii} - B_{jj} \quad (17)$$

The calculations were carried out using the Matlab® software (Version R2021a, Mathworks Inc., USA). The purpose of the calculations made here is to show how the chemical potential of hydrogen is affected by the presence of nanoparticles, modifying its behavior.

### 3. Results and discussion

#### 3.1. Nanoparticle Selection through Adsorption Isotherms and Thermogravimetric Analysis

Adsorption isotherms constructed for the  $n$ -C<sub>7</sub> asphaltenes isolated from HO1 and HO2 over NP1 y NP2 are shown in Figure 3. According to the International Union of Pure and Applied Chemistry (IUPAC), the adsorption isotherms profiles correspond to a type Ib, which agreed well with results reported previously [48], where the adsorption of asphaltenes on nanometric solid surfaces is described. In general, the asphaltene adsorption of heavy oil 1 (HO1) was slightly higher in nanoparticle 1 (NP1) and very similar to that obtained by nanoparticle 2 (NP2). The same train was found for the heavy oil 2 (HO2) asphaltenes. These results indicate a high affinity for both asphaltenes for the metallic phases of Ni and Pd and slightly higher for species based on alumina than on ceria.

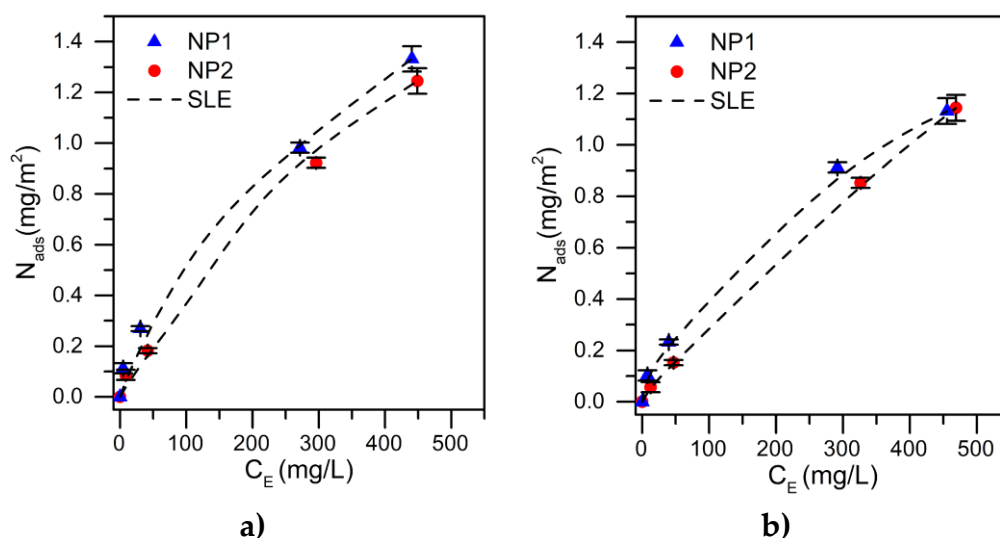


**Figure 3.** Experimental adsorption of  $n$ -C<sub>7</sub> asphaltene isolated from a) HO1 and b) HO2 over NP1 and NP2 (dotted lines represent the SLE fitting).

The non-isothermal thermogravimetric analysis at high pressure for asphaltenes adsorbed and non-adsorbed over NP1 and NP2 is shown in Figures 4a,b. The results of asphaltenes isolated from HO1 are shown in panel a. Asphaltenes have a main decomposition peak at 510 °C and a final decomposition peak at 590 °C. When asphaltenes are adsorbed on nanoparticles, gasification appears to occur at much lower temperatures. The results show that

the temperature of asphaltene decomposition is reduced from 510 °C to 200-250 °C.

The rate of mass change profiles, on the other hand, have different peaks associated with the different molecular weights of adsorbed asphaltenes and the chemical nature of nanoparticles (alumina and ceria). The decomposition of alumina nanoparticles is completed around 30 °C earlier than that of ceria nanoparticles. Asphaltenes isolated from HO2 decompose at 500 °C in the absence of nanoparticles and at around 210 °C and 220 °C when adsorbed over NP1 and NP2, respectively. Finally, Figure 5 shows the isothermal conversion for both asphaltenes. NP1 decomposes 100% of both adsorbed asphaltenes at a lower time than NP2. Using NP1, asphaltenes from HO1 and HO2 are completely decomposed at 88 and 95 min, respectively.

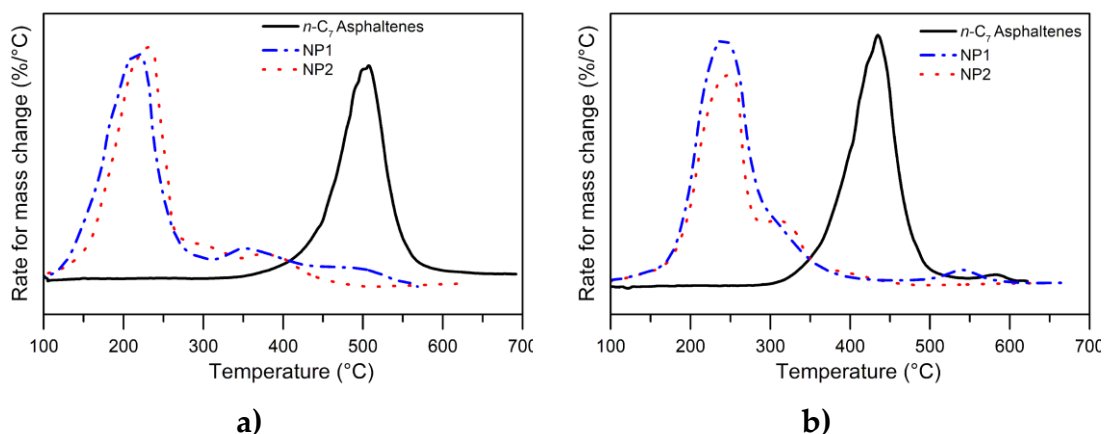


**Figure 4.** Rate for mass change profiles for steam gasification of  $n\text{-C}_7$  asphaltenes isolated from a)HO1 and b)HO2, with and without NP1 and NP2. Heating rate:  $10\text{ °C}\cdot\text{min}^{-1}$ ,  $\text{N}_2$  flow:  $100\text{ ml}\cdot\text{min}^{-1}$ ,  $\text{H}_2\text{O}_{(\text{g})}$  flow:  $6.7\text{ ml}\cdot\text{min}^{-1}$  and sample mass 1 mg.

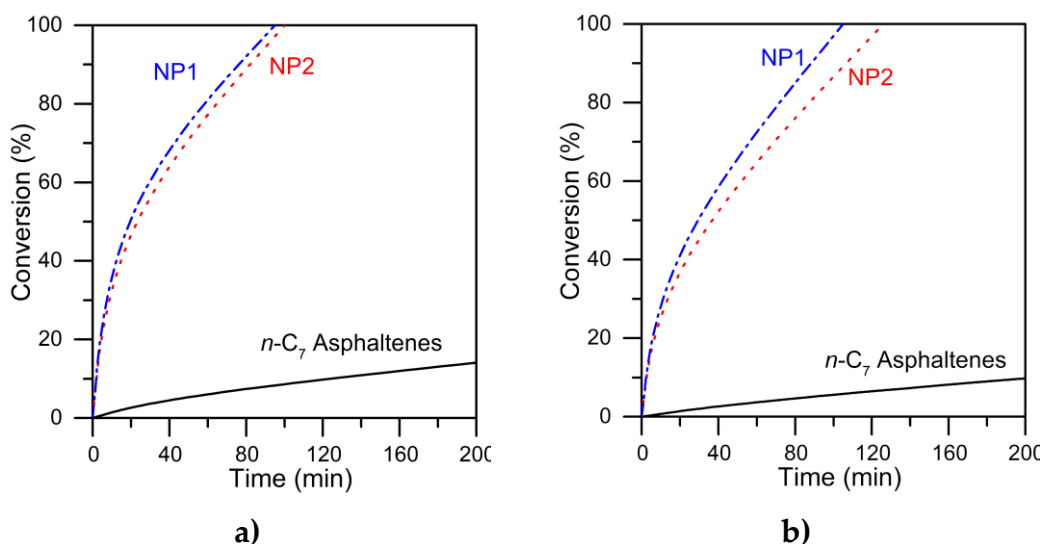


**Figure 5.** Isothermal conversion for steam gasification of *n*-C<sub>7</sub> asphaltenes isolated from a)HO1 and b)HO2 with and without NP1 and NP2. Heating rate: 10 °C·min<sup>-1</sup>, N<sub>2</sub> flow: 100 ml·min<sup>-1</sup>, H<sub>2</sub>O<sub>(g)</sub> flow: 6.7 ml·min<sup>-1</sup> and sample mass 1 mg.

On the other hand, Figure 6 shows resin adsorption isotherms for both crude oils (Panels a and b). The nanoparticles exhibit a type Ib adsorption isotherm for resins adsorption. For HO1 and HO2, NP1 uptake was higher than NP2. The difference in resins adsorption between NP1 and NP2 is around 0.23 (resins from HO1) and 0.25 mg m<sup>-2</sup> (resins from HO2), respectively. Compared with asphaltene adsorption, nanoparticles adsorb a similar amount of resins, which indicates good selectivity for both heavy compounds. Figure 7 shows the conversion of resins evaluated at isothermal conditions. The profiles show that resins conversion achieves 100% when nanoparticles catalyze the reaction; otherwise, just 30% of resins can be converted at the evaluated conditions. The time to decompose 100% of adsorbed resins increases in the order NP2 < NP1 for both samples, following the same trend of asphaltenes. All these results highlight the NP1 capacity to absorb and decompose asphaltene and resins over NP2.



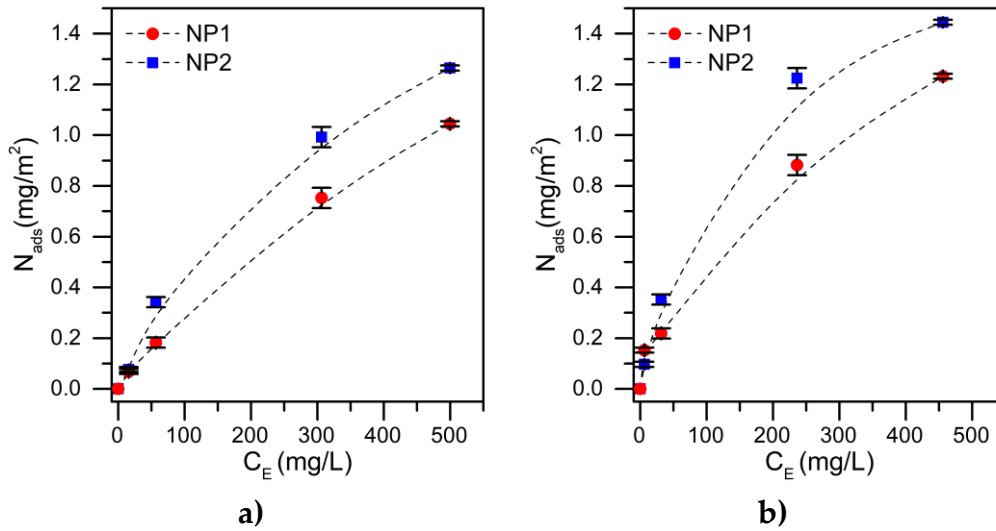


**Figure 6.** Experimental adsorption of resins isolated from a) HO1 and b) HO2 over NP1 and NP2 (dotted lines represent the SLE fitting).

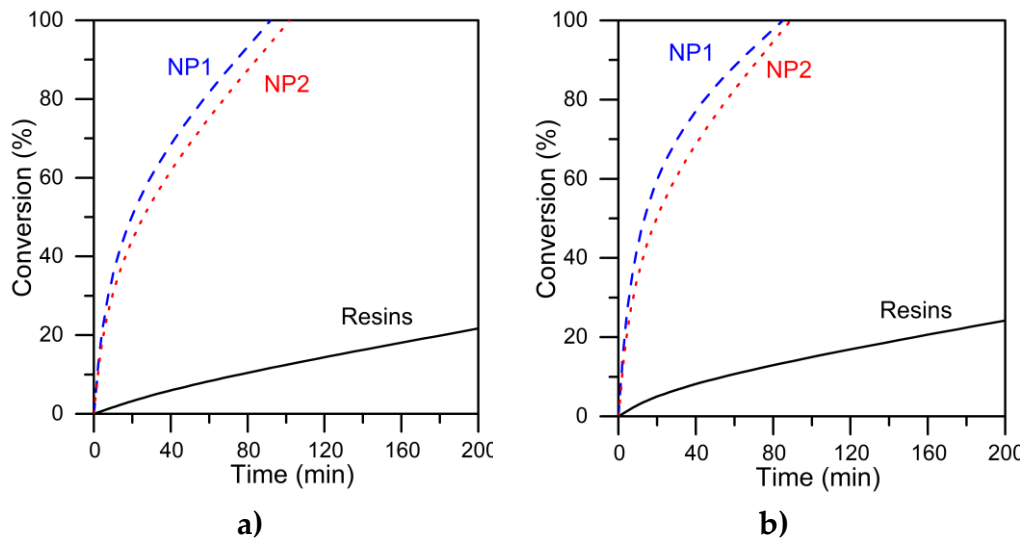
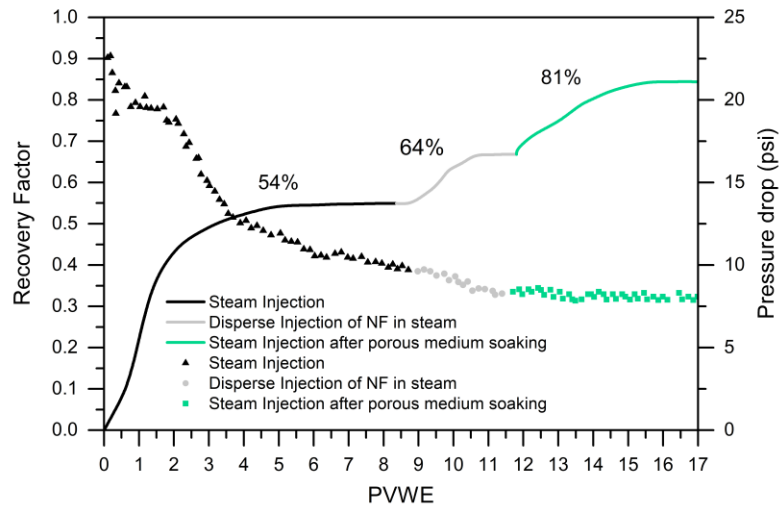


**Figure 7.** Isothermal conversion for steam gasification of resins isolated from a)HO1 and b)HO2 with and without NP1 and NP2. Heating rate:  $10\text{ }^{\circ}\text{C}\cdot\text{min}^{-1}$ ,  $\text{N}_2$  flow:  $100\text{ ml}\cdot\text{min}^{-1}$ ,  $\text{H}_2\text{O}_{(\text{g})}$  flow:  $6.7\text{ ml}\cdot\text{min}^{-1}$  and sample mass  $1\text{ mg}$ .

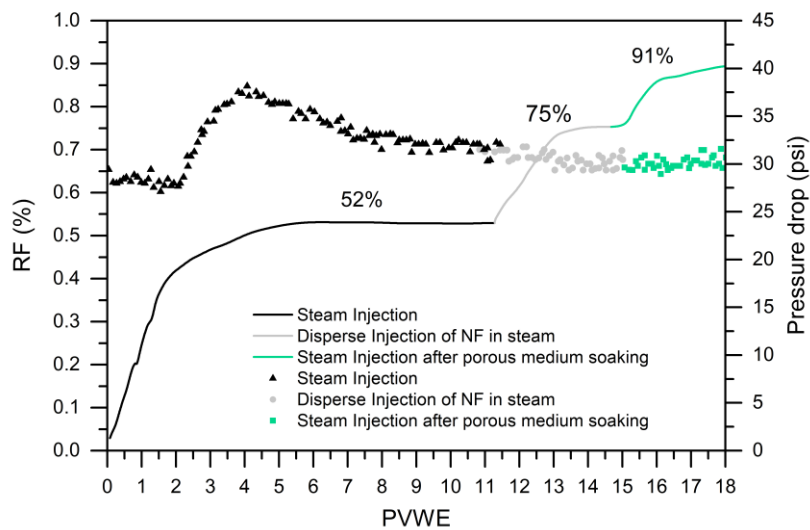
### 3.2. Crude Oil Recovery

Based on static results, the nanofluid was formulated with NP1. The crude oil recovery curves for the dispersed nanofluid injection in the steam stream in HO1 and HO2 are shown in Figure 8a,b. The absolute permeability was estimated at  $4331\text{ mD}$  and  $2103\text{ mD}$  for HO1 and HO2 systems. Additionally, the oil effective permeability was  $3558$  and  $1887$  for the same systems. For the HO1,

after the injection of 11 PVWE, an oil recovery of 54% was obtained. Some mechanisms are associated with the steam effect on crude oil production, including heat transfer to the rock and reservoir fluids, thermal expansion, volatilization of lighter hydrocarbons, and the disintegration of the viscoelastic network of crude oil. The dispersed injection of the nanofluid into the steam resulted in a 10% increase in recovered oil. This is primarily because the tiny liquid droplets dispersed in the steam stream have a larger contact area. Finally, an oil recovery of 81% was achieved after the final steam injection



(a)



(b)

**Figure 8.** Oil recovery curve for steam injection assisted by Al-NF dispersed in the steam stream during the stages: (1) continuous steam injection, (2) dispersed injection of nanofluid in steam, and (3) steam injection after porous medium soaking in (a) HO1, and (b) HO2. Steam injection temperature: 270 °C for both

cases. Pore pressure = 150 psi for both cases. Overburden pressure 1528 and 1992 psi for HO1 and HO2, respectively.

From Panel b in Figure 8, the crude oil recovery curve for HO2 is observed. During the first stage (steam injection without nanofluid), an oil recovery of 56% was obtained. Then, during the injection of nanofluid dispersed in the steam stream, the crude oil produced increased by 23%. Finally, 91% of the original oil in place (OOIP) was recovered at the end of the third stage. The missing 9% is considered residual oil saturation, which could not be displaced by the number of pore volumes of water equivalent injected (PVWE) and with similar characteristics to the untreated crude oil.

Instantaneous oil production was observed once the nanofluid was injected into the steam stream. This result potentiates the conventional steam injection technology and helps obtain better yields than in the scenarios assisted by injection with a liquid batch of nanofluid [19,63]. Some properties that can influence this process are the interactions between steam and the Al-, Ni-, and Pd- active sites of the nanoparticles [73]. During the second stage, both crude oils exhibit this behavior. It is expected that once the nanoparticles contact the crude oil matrix, heavy fraction adsorption and catalysis will occur quickly, improving the crude oil's mobility. This result is consistent with previous evaluations, which obtained an immediate recovery of an extra-heavy crude oil during the injection of a CeO<sub>2</sub>-based nanofluid dispersed in the steam stream [39].

### 3.3. Effluent Analysis

Panels a and b of Figure 9 show the API gravity values for untreated crude oil, crude oil after steam injection, crude oil recovered by nanofluid injection dispersed in the steam stream, and crude oil after a soaking time of 12 h for HO1 and HO2, respectively. For HO1, the API gravity increased after steam injection without the nanoparticles from 12.4° to 12.6°. The results showed increases in the API up to 18° and 18.5° before and after the soaking treatment (Panel a). Similarly, for HO2, API gravity remained constant after steam injection without NF (Panel b). Then, during the nanofluid injection, the API gravity increased to 29° and after the soaking stage, it increased to 29.2°. To understand the difference in API gravity changes, it is essential to analyze the compositional changes in the content of the SARA fractions. These results are shown in Panels c and d for HO1 and HO2, respectively. No appreciable or significant change in asphaltene content is observed during the first steam injection. The distribution of the rest of

the SAR components is similar in both crude oils. This result agrees well with the unchanged API values described above. Likewise, several works in the literature report that steam does not modify the chemical composition of crude oil [15,30].

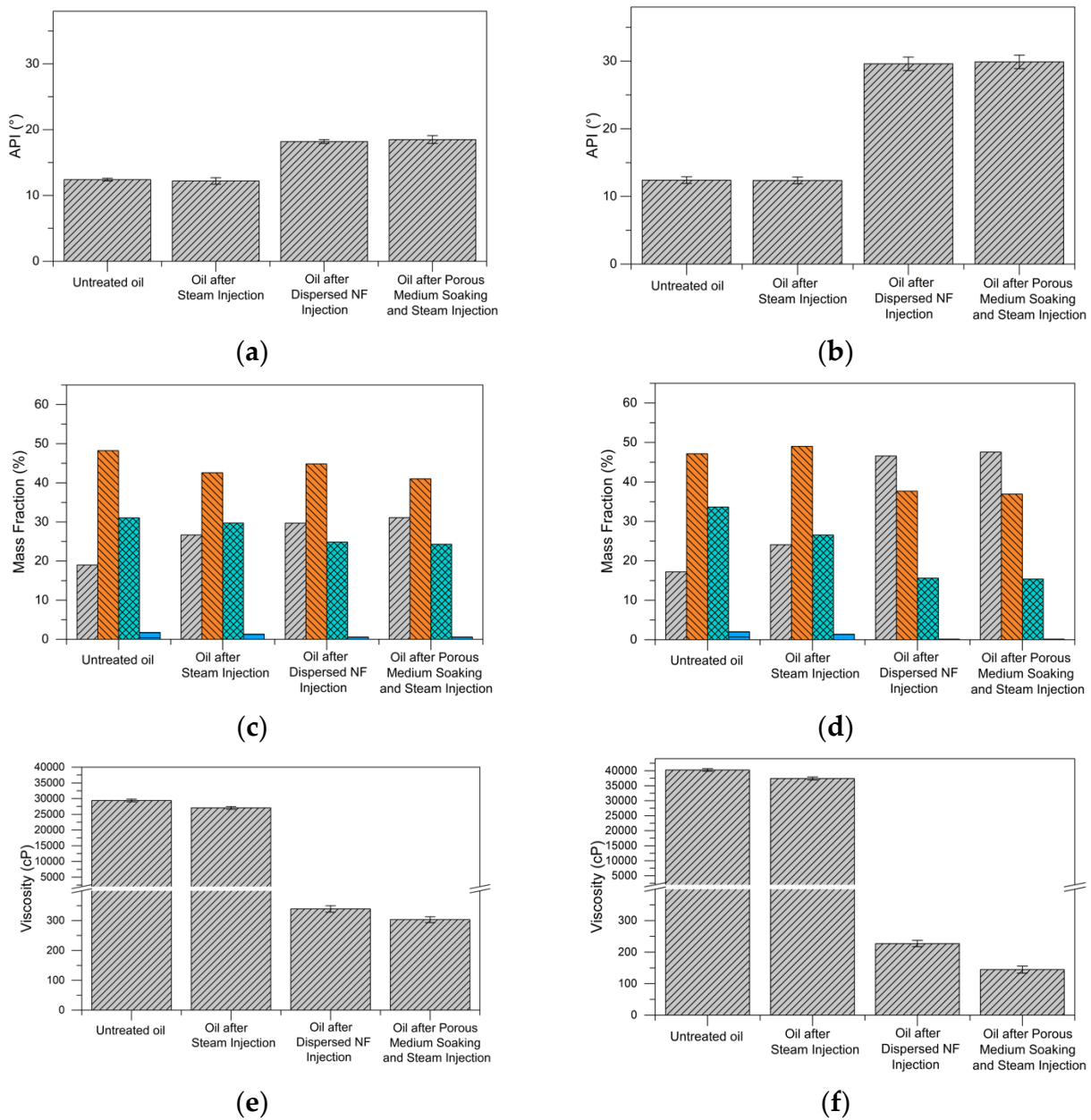


**Figure 9.** (a,b) API gravity and (c,d) SARA content distribution in wt.% (gray is saturates, orange is aromatics, green is resins and blue is aromatics) and (e,f) crude oil viscosity for untreated extra-heavy oil and crude oil recovered after the steam injection, during the injection of Al-NF dispersed in a steam stream, and after soaking for (a,c,e) HO1 and (b,d,f) HO2.

The presence of the NF generates a decrease from 1.76% to 0.7% and 0.2% of the asphaltene content in the HO1 for the respective stage after steam injection with nanofluid dispersed in its stream and subsequent steam injection after the

12 h soaking of the nanofluid with the porous medium, demonstrating the high catalytic activity of the catalyst. In the case of the HO2, the asphaltene content was reduced from 2.01% to 0.3% and 0.1% in a mass fraction in the same stages. Both crude oils had a very low final asphaltene content. However, the saturates and resins distribution change to a greater extent between both samples. In the HO1, saturates increased from 19% (stage 1) to 26% (stage 3) in mass fraction, whereas in HO2, they increased from 17% (stage 1) to 46% (stage 3) in mass fraction. Finally, resin content was reduced by 22% (untreated crude oil) and 50% (crude oil recovered after soaking of NF and steam injection) for HO1 and HO2, respectively. According to these results, the injected NP1 attack both asphaltenes and high molecular weight resins, increasing the content of lighter hydrocarbons such as saturates. In this way, better quality is obtained in the HO2. Many factors can explain the good performance of NP1. First, the combined selectivities and reactivities of Ni and Pd toward the asphaltene and resin molecules result in a decrease in the content of both fractions. Additionally, because of strong metal support interactions (SMSI) alumina nanoparticles avoid metal sintering after the doping process, which leads to an increase in the number of active sites available for gasification reactions. Finally, the species  $-O$  and  $-OH$  resulting from the dissociative adsorption of steam by the alumina lower valence state, can be transferred to nickel and palladium and react with surface carbonaceous species [46]. Besides, through the movement of oxygen vacancies formed by the change in the oxidation state of the alumina species and the destabilization of the same, the reagents are transferred to the active sites of the transition element oxides. Finally, Panels e and f depict the viscosity values at a shear rate of  $10\text{ s}^{-1}$  and  $25\text{ }^{\circ}\text{C}$  of the HO1 and HO2, respectively. During the first stage, oil viscosity was slightly reduced for both samples due to the reduction in cohesive intermolecular forces between asphaltenes and resins.

For the nanotechnology-assisted scenarios (second and third stage), a significant reduction in oil viscosity was noted, which was higher for the effluent recovered after 12 h of soaking. The oil viscosity for HO1 and HO2 recovered in the third stage was 300 and 104 cP, respectively. The main mechanism that explains the reduction in oil viscosity is the cracking/redistribution of asphaltene–resin systems and their subsequent stabilization through free radical hydrogenation to prevent the formation of heavier compounds.

Interestingly, crude oil upgrading was more noticeable in HO2 than in HO1. The catalytic activity of the material promoted higher API values and lower viscosities in the HO2 sample, probably due to interactions with its heaviest

fractions. The chemical nature of the asphaltenes and resins of each crude oil greatly influences the response in gasification reactions for oil upgrading. In this sense, it is to be expected that the HO2 fractions are energetically easier to transform into lighter compounds.

On the other hand, Figure 10 shows the results of API and dynamic viscosity of the HO1 and HO2 recovered after the 12 h soaking of the nanofluid in the porous medium during days 1, 8, 15, and 30 after its recovery. In both systems, it is observed that API gravity and oil viscosity remain constant during the first 30 days evaluated, indicating the potential of the nanofluid to generate a permanent crude oil upgrading.

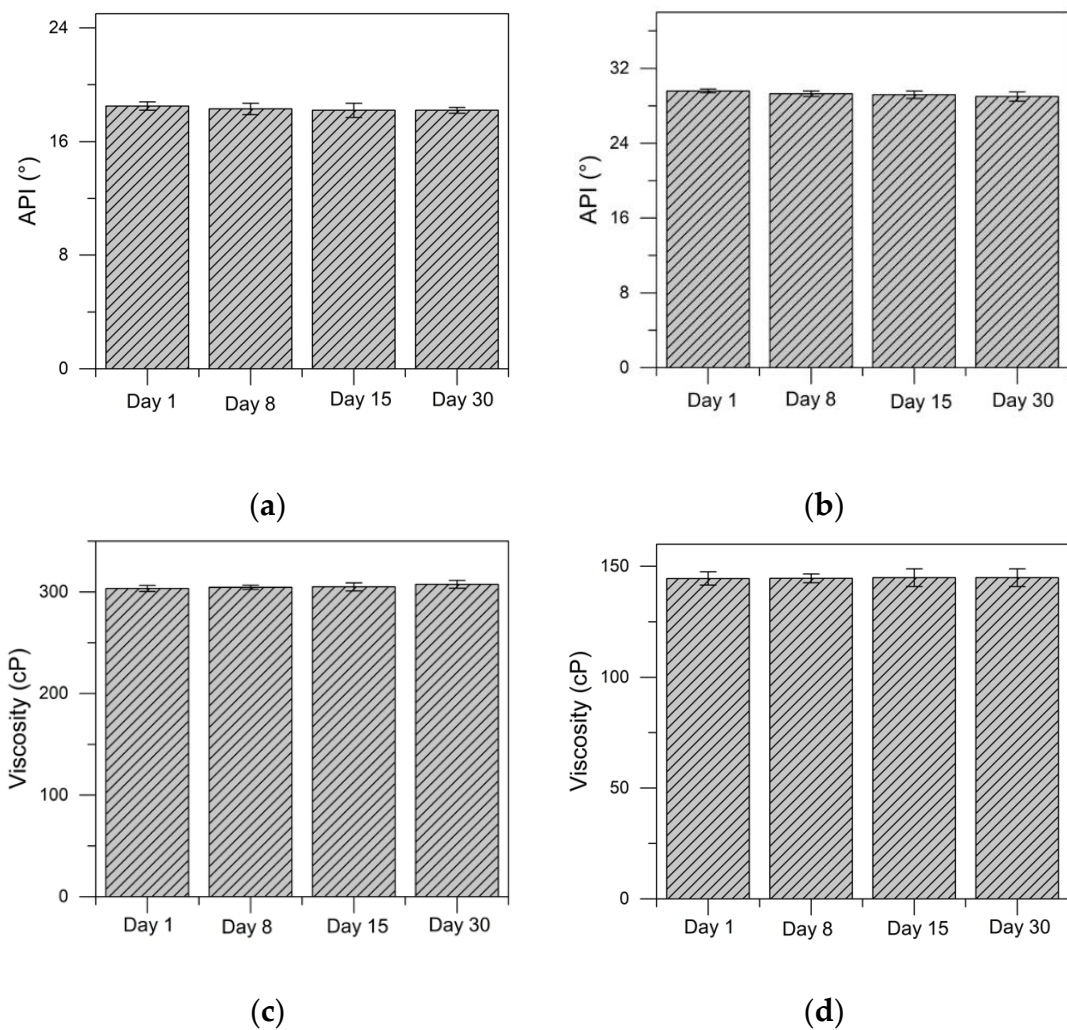
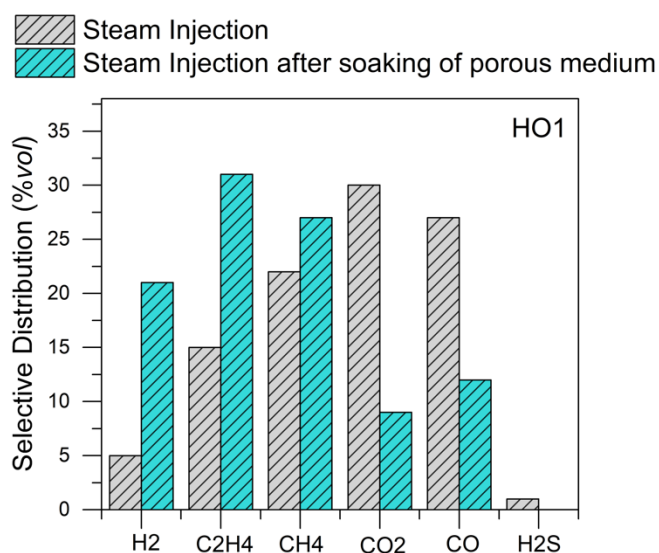


**Figure 10.** Perdurability of crude oil for (a,c) for HO1 and (b,d) for HO2, for the effluents recovered after the 12 h soaking of the nanofluid in the porous medium.

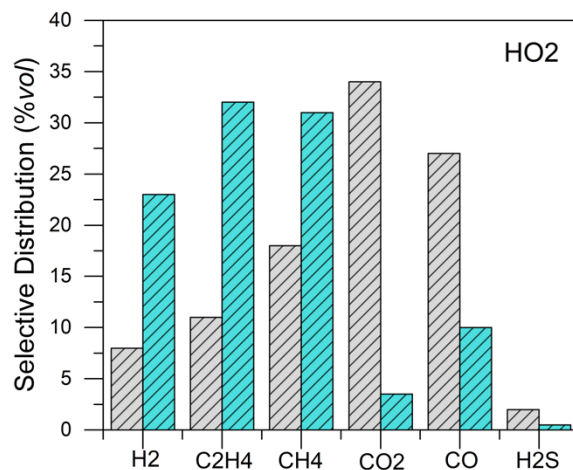
### 3.4. Gaseous Products

The gas produced during the dynamic test was collected in hermetically sealed aluminum containers for subsequent analysis in a mass spectrometer. The gases were analyzed during the first and third stages (i.e., steam injection and after NF soaking). The gaseous products released were  $H_2$ ,  $CO$ ,  $CH_4$ ,  $CO_2$ ,  $C_2H_4$ , and a small amount of  $H_2S$ . The volume fraction indicates the content of the components in the gaseous product, and the results are shown in Figure 11. Panel a in Figure 11 shows the results obtained for HO1. As the main result, it can be observed that the content of light hydrocarbons ( $C_2H_4$  and  $CH_4$ ) increases considerably after the injection of the nanofluid in the porous medium, accompanied by the reduction in  $CO_2$  (<7% vol),  $CO$  (<12% vol) and  $H_2S$  (<1% vol). Additionally, the nanofluid generates  $H_2$  during the catalytic cracking of the crude oil fractions, obtaining a gas with approximately 5% vol and 22% vol hydrogen during the first and third stages, respectively. The results obtained for HO2 are shown in Panel b of Figure 11. Similar components to HO1 are observed. The content of light hydrocarbons ( $C_2H_4$  and  $CH_4$ ) and hydrogen increased in the stage after the injection of the nanofluid. Hydrogen released was around 23% vol and 7% vol for the third and first stages, respectively. Oppositely, the gases  $CO_2$ ,  $H_2S$ , and  $CO$  decrease during the steam injection after the nanofluid soaking.



(a)





(b)

**Figure 11.** Selectivity distribution of light gases produced from steam gasification of (a) HO1 and (b) HO2 at reservoir conditions in the presence and absence of nanofluid.

The benefit of nanoparticles in heavy oil gasification is elucidated when hydrogen production is increased, and CO<sub>2</sub> release is reduced after the catalytic process. Hydrogen is a typical product of free radical reactions of the heavier molecules in crude oil. Therefore, the nanoparticles are expected to promote these reactions under the conditions evaluated, increasing the amount produced. A previous study demonstrated that hydrogen could be produced from the catalytic steam gasification of asphaltenes and resins [34]. First, the reaction between H<sub>2</sub>O and C atoms in both fractions releases hydrogen as a direct byproduct [73]. Other reactions, including water–gas shift and steam reforming, were also evidenced by the authors [73]. Nanoparticles could facilitate the production of H<sub>2</sub> from H<sub>2</sub>O-CH<sub>4</sub> and H<sub>2</sub>O-CO through steam reforming and water–gas shift reactions, respectively [74,75].

Moreover, the presence of Ni and Pd phases and their interactions with Al<sub>2</sub>O<sub>3</sub> support benefit the production of H<sub>2</sub>. For example, H<sub>2</sub> can be produced by Ni/Al<sub>2</sub>O<sub>3</sub> phases through the complete combustion of CH<sub>4</sub>, H<sub>2</sub>O, and CO reforming. On the other hand, the Pd/Al<sub>2</sub>O<sub>3</sub> can simultaneously produce different species such as H<sub>2</sub> and CO. Both systems follow different reaction pathways because of the further transfer of electrons between the active phase to the support [76,77].

Comparing crude oil upgrading results, the production of hydrogen and light hydrocarbons (C<sub>2</sub>H<sub>4</sub> and CH<sub>4</sub>) is correlated with heavy oil upgrading



results. The higher the API gravity of the recovered crude oil during the displacement test, the higher the selective distribution of H<sub>2</sub>, C<sub>2</sub>H<sub>4</sub>, and CH<sub>4</sub> during the conversion process. The opposite was found for the viscosity. It means that HO2 produced a higher amount of H<sub>2</sub> and light hydrocarbons than HO1 because the nanoparticles presented the best performance in the in situ upgrading of HO2. Both trends highlight the relationship between oil upgrading and the release of a gas mixture with high calorific power.

### 3.5. Thermodynamic Analysis of Produced Hydrogen

#### 3.5.1. Hydrogen Fugacity on HO1 during Steam Injection Assisted by Nanoparticles

The analysis of hydrogen fugacity was performed using the molar composition of the released gas mixture presented in Table 6.

**Table 6.** Molar composition of the gas mixture released during steam injection test of HO1 during the first steam injection (without nanoparticles) and the steam injection after nanofluid soaking with porous medium (with nanoparticles).

Component	Without Nanoparticles	With Nanoparticles
H <sub>2</sub>	0.05	0.22
C <sub>2</sub> H <sub>4</sub>	0.15	0.33
CH <sub>4</sub>	0.22	0.27
CO <sub>2</sub>	0.30	0.07
CO	0.27	0.11
H <sub>2</sub> S	0.01	0.00

The fugacity of each component was calculated for both scenarios with and without the assistance of nanoparticles using the thermodynamic properties shown in the Methods section and the molar composition (Table 6) of the gas mixture. The pressure range for HO1 was 600-1600 psi, as determined by reservoir pressure and overburden gradient. Figure 12 depicts the results at the temperature of the steam injection (270 °C). Hydrogen fugacity was measured at 36.12 and 158 psi without and with nanoparticles, indicating that the presence of nanoparticles increased hydrogen's chemical potential. For the same scenarios, the hydrogen fugacity near 1600 psi was 85.0 psi and 370.5 psi. The hydrogen produced in the above-mentioned pressure range has a higher fugacity near the reservoir limits, so it will move forward to areas with a lower fugacity (far from the reservoir limit with the overburden pressure). The smallest difference in fugacity between scenarios with and without nanoparticles suggests that at reservoir pressure, hydrogen has a lower tendency to migrate to the low-pressure

point via diffusion. Therefore, hydrogen can be lost in the stratigraphic columns above the reservoir. The results agree with those reported by Chen et al. [69]. The authors show the separation of CH<sub>4</sub> and H<sub>2</sub> with fugacity measurements, where high pressures allow the purification of the components using a membrane-like technology. In this way, they show the fugacity of each component as a tool to evaluate the separation and purification of components.

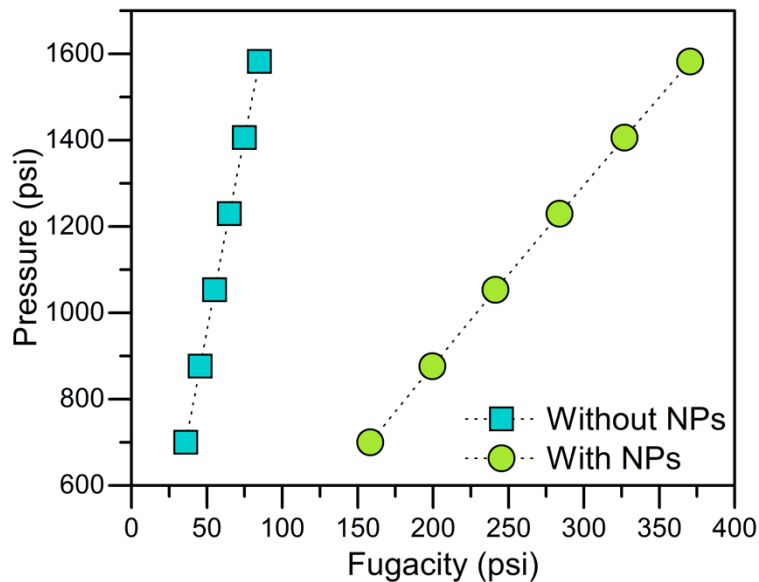


**Figure 12.** Fugacity of H<sub>2</sub> generated during the steam injection in the presence and absence of nanoparticles on HO1 between reservoir pressure (700 psi) and overburden pressure (1600 psi) at the steam injection temperature (270 °C).

### 3.5.2. Hydrogen Fugacity on HO1 at Different Temperatures Assisted by Nanoparticles

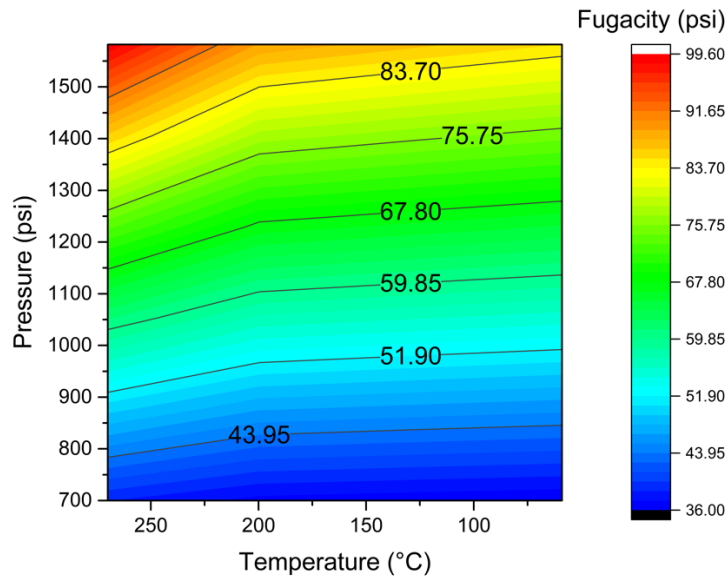
The temperature variation was selected according to the thermal gradient observed on the porous media of the displacement tests. Table 7 summarized the temperature of the coordinates. The pressure range was 700–1600 psi, as in the previous section.

**Table 7.** Temperature of coordinates of HO1 during the first steam injection (without nanoparticles) and the steam injection after nanofluid soaking with porous medium (with nanoparticles).

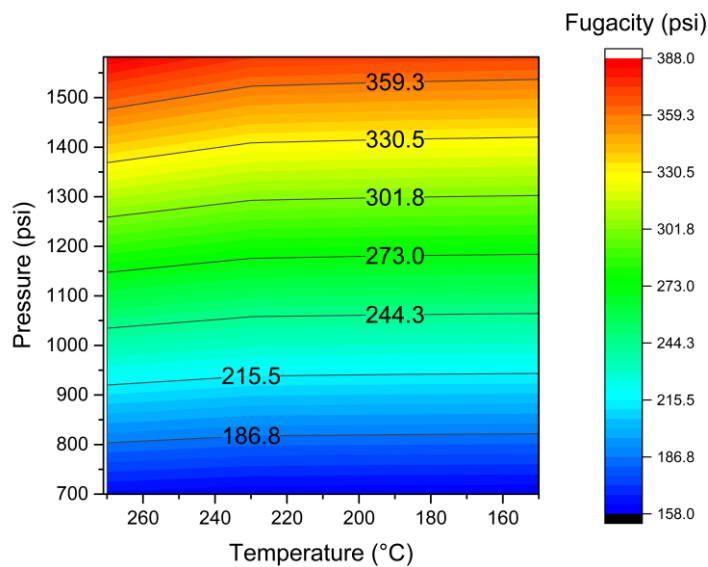
Component	Temperature (°C)	
	Without Nanoparticles	With Nanoparticles
1	270	270
2	212	255
3	168	234
4	59	150

Figure 13 shows the fugacity contour as a function of pressure and temperature for hydrogen produced during the steam injection non-assisted and assisted by nanoparticles. With the increase in temperature, fugacity decreased in both scenarios. When nanoparticles were used, fugacity increased from 158 psi to 161 psi between 1 and 4 coordinates at reservoir pressure. In the absence of nanoparticles, fugacity also increased by 3 psi in the same conditions. As pressure increased (close to the overburden pressure), the nanoparticles-assisted step increased fugacity at a higher degree when the temperature lowered from coordinate 1 to 4. In this way, when comparing both scenarios, nanoparticles increase the gap between the fugacities that the hydrogen acquires in the external points evaluated. This leads to reduced displacement of the gas out of the reservoir. Similar behavior of hydrogen within a gas mixture was shown by Redlich et al. [78].

It is worth mentioning that at low pressure, fugacity acquires lower values (reservoir pressure) regardless of the temperature and scenario evaluated (with or without nanoparticles). This result could be explained because the fugacity is a correction to the relative pressure of the component in the mixture, and at higher pressures, there are more significant deviations due to the intermolecular interactions between the components of the gas mixture [64,67]. In this way, the effect of nanoparticles on hydrogen fugacity holds more importance at higher system pressures. All these results highlight the use of nanoparticles to assist a steam injection process where it is possible to produce hydrogen during heavy crude oil production.



(a)



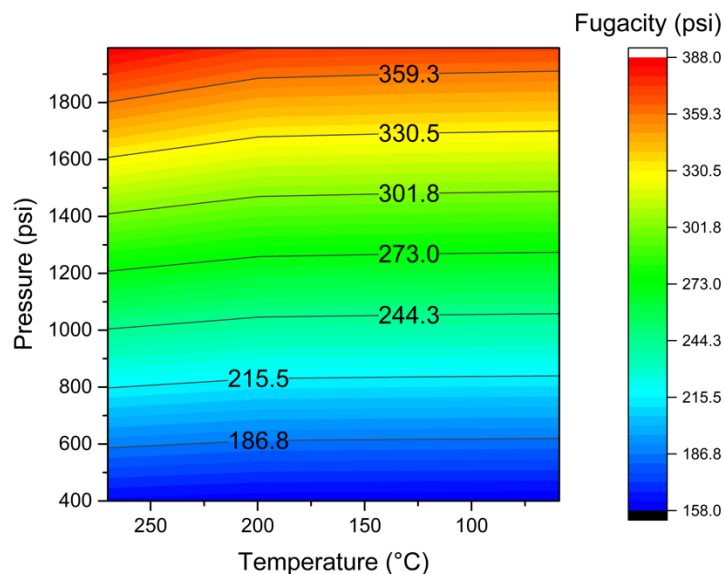
(b)

**Figure 13.** Fugacity contour of H<sub>2</sub> generated during the steam injection in the (a) absence and (b) presence of nanoparticles on HO1 between reservoir pressure (700 psi) and overburden pressure (1600 psi) as a function of temperature decline.

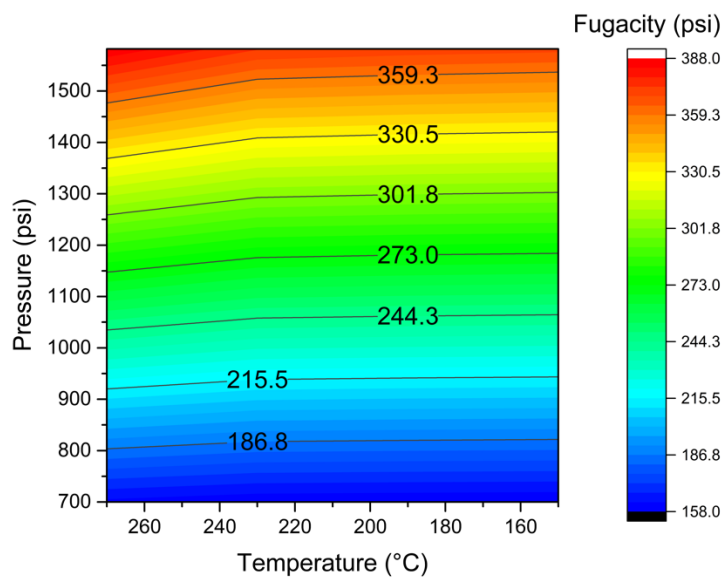
### 3.5.3. Hydrogen Fugacity on HO2 at Different Temperatures in the Presence and Absence of Nanoparticles and Comparison with HO1

This section describes the estimated results of fugacity for HO2, considering the reservoir pressure (400 psi) and the overburden pressure (1992 psi) at the same temperature range evaluated in HO1. Figure 14 shows the contour areas for

H<sub>2</sub> generated during the steam injection. The H<sub>2</sub> fugacity at reservoir pressure was 32.5 psi and 93.3 psi when H<sub>2</sub> was produced in the absence and presence of nanoparticles at 270 °C. Regarding overburden pressure, the fugacity of H<sub>2</sub> was around 173 and 210 psi for the same scenarios, respectively. Based on these results, it is expected that the hydrogen produced in zones closer to the overburden pressure will migrate more easily toward zones of lower pressure (i.e., around 400 psi). The difference in fugacity between the unassisted and nanoparticle-assisted scenarios is 141 and 400 psi. This means that the H<sub>2</sub> produced in the stage without nanoparticles tends to migrate more easily through the porous medium out of the reservoir concerning the hydrogen obtained when there are nanoparticles. The results agree with those obtained for HO1. The difference between both systems lies mainly in the fact that the pressure difference between the reservoir and the overburden pressure is greater in HO2. The difference in fugacity found is greater when the pressure differential is greater.



(a)



(b)

**Figure 14.** Fugacity contour of H<sub>2</sub> generated during the steam injection in (a) absence and (b) presence of nanoparticles on HO<sub>2</sub> between reservoir pressure (400 psi) and overburden pressure (1990 psi) as a function of temperature decline.

#### 4. Conclusions

The present work evidence, for the first time, the positive thermal effect of nanoparticles in assisting a steam injection process in terms of upgraded crude oil and hydrogen co-production. The fugacity of H<sub>2</sub> was determined between the reservoir and overburden pressure and different temperatures, which were determined by the thermal profiles in the displacement test. The fugacity was calculated using the application of virial equations of state with mixing rules based on the possible intermolecular interactions between the components. Hydrogen acquired a higher chemical potential due to the nanoparticles' presence. However, the difference in H<sub>2</sub> fugacity between both points is much higher with nanoparticles, which means that hydrogen presents a lower tendency to migrate by diffusion to the high-pressure point. The difference between HO<sub>1</sub> and HO<sub>2</sub> lies mainly in the fact that the pressure difference between the reservoir and the overburden pressure is greater in HO<sub>2</sub>; therefore, the difference in fugacity is greater when the pressure differential is greater. By considering the fugacity of each species as a measure of the chemical potential, the development of this work allows us to elucidate the effect of nanoparticles on

the fugacity of the hydrogen formed in the reservoir due to thermal treatments, providing a clearer landscape of in situ hydrogen behavior, as well as the possibility of having a gaseous mixture rich in H<sub>2</sub> on the surface with upgraded crude oil.

## References

1. Holladay, J.D.; Hu, J.; King, D.L.; Wang, Y. An overview of hydrogen production technologies. *Catal. Today* **2009**, *139*, 244–260.
2. Hansen, J.; Sato, M.; Ruedy, R.; Lo, K.; Lea, D.W.; Medina-Elizade, M. Global temperature change. *Proc. Natl. Acad. Sci. USA* **2006**, *103*, 14288–14293.
3. Guilbert, D.; Vitale, G. Hydrogen as a Clean and Sustainable Energy Vector for Global Transition from Fossil-Based to Zero-Carbon. *Clean Technol.* **2021**, *3*, 881–909.
4. Navarro, R.M.; Pena, M.; Fierro, J. Hydrogen production reactions from carbon feedstocks: Fossil fuels and biomass. *Chem. Rev.* **2007**, *107*, 3952–3991.
5. Shibata, Y. Economic analysis of hydrogen production from variable renewables. *IEEJ Energy J.* **2015**, *10*, 26–46.
6. Ni, M.; Leung, D.Y.; Leung, M.K.; Sumathy, K. An overview of hydrogen production from biomass. *Fuel Process. Technol.* **2006**, *87*, 461–472.
7. Muradov, N. How to produce hydrogen from fossil fuels without CO<sub>2</sub> emission. *Int. J. Hydrogen Energy* **1993**, *18*, 211–215.
8. Seyitoglu, S.; Dincer, I.; Kilicarslan, A. Energy and exergy analyses of hydrogen production by coal gasification. *Int. J. Hydrogen Energy* **2017**, *42*, 2592–2600.
9. Blok, K.; Williams, R.; Katofsky, R.; Hendriks, C.A. Hydrogen production from natural gas, sequestration of recovered CO<sub>2</sub> in depleted gas wells and enhanced natural gas recovery. *Energy* **1997**, *22*, 161–168.
10. Santos, R.; Loh, W.; Bannwart, A.; Trevisan, O. An overview of heavy oil properties and its recovery and transportation methods. *Braz. J. Chem. Eng.* **2014**, *31*, 571–590.
11. Guo, K.; Li, H.; Yu, Z. In-situ heavy and extra-heavy oil recovery: A review. *Fuel* **2016**, *185*, 886–902.

12. Curtis, C.; Kopper, R.; Decoster, E.; Guzmán-García, A.; Huggins, C.; Knauer, L.; Minner, M.; Kupsch, N.; Linares, L.M.; Rough, H. Heavy-oil reservoirs. *Oilfield Rev.* **2002**, *14*, 30–51.
13. Rahimi, P.M.; Gentzis, T. The chemistry of bitumen and heavy oil processing. In *Practical Advances in Petroleum Processing*; Springer: Berlin/Heidelberg, Germany, 2006; pp. 597–634.
14. Hamed Shokrlu, Y.; Babadagli, T. Kinetics of the in-situ upgrading of heavy oil by nickel nanoparticle catalysts and its effect on cyclic-steam-stimulation recovery factor. *SPE Reserv. Eval. Eng.* **2014**, *17*, 355–364.
15. Elahi, S.M.; Scott, C.E.; Chen, Z.; Pereira-Almao, P. In-situ upgrading and enhanced recovery of heavy oil from carbonate reservoirs using nanocatalysts: Upgrading reactions analysis. *Fuel* **2019**, *252*, 262–271.
16. Dorian, J.P.; Franssen, H.T.; Simbeck, D.R. Global challenges in energy. *Energy Policy* **2006**, *34*, 1984–1991.
17. Owen, N.A.; Inderwildi, O.R.; King, D.A. The status of conventional world oil reserves—Hype or cause for concern? *Energy Policy* **2010**, *38*, 4743–4749.
18. Medina, O.E.; Olmos, C.; Lopera, S.H.; Cortés, F.B.; Franco, C.A. Nanotechnology applied to thermal enhanced oil recovery processes: A review. *Energies* **2019**, *12*, 4671.
19. Franco, C.; Cardona, L.; Lopera, S.; Mejía, J.; Cortés, F. Heavy oil upgrading and enhanced recovery in a continuous steam injection process assisted by nanoparticulated catalysts. In Proceedings of the SPE Improved Oil Recovery Conference, Tulsa, OK, USA, 11–13 April 2016.
20. Ali, S. Current status of steam injection as a heavy oil recovery method. *J. Can. Pet. Technol.* **1974**, *13*. <https://doi.org/10.2118/74-01-06>.
21. Medina, O.E.; Hurtado, Y.; Caro-Velez, C.; Cortés, F.B.; Riazi, M.; Lopera, S.H.; Franco, C.A. Improvement of steam injection processes through nanotechnology: An approach through in situ upgrading and foam injection. *Energies* **2019**, *12*, 4633.
22. Shin, H.; Polikar, M. Review of reservoir parameters to optimize SAGD and Fast-SAGD operating conditions. *J. Can. Pet. Technol.* **2007**, *46*. [doi.org/10.2118/07-01-04](https://doi.org/10.2118/07-01-04)
23. Thomas, S. Enhanced oil recovery-an overview. *Oil Gas Sci. Technol. -Rev. De L'ifp* **2008**, *63*, 9–19.
24. Lu, C.; Liu, H.; Zhao, W. Visualized study of displacement mechanisms by injecting viscosity reducer and non-condensable gas to assist steam injection. *J. Energy Inst.* **2017**, *90*, 73–81.



25. Dong, X.; Liu, H.; Chen, Z.; Wu, K.; Lu, N.; Zhang, Q. Enhanced oil recovery techniques for heavy oil and oilsands reservoirs after steam injection. *Appl. Energy* **2019**, *239*, 1190–1211.
26. Sun, X.; Zhang, Y.; Chen, G.; Gai, Z. Application of nanoparticles in enhanced oil recovery: A critical review of recent progress. *Energies* **2017**, *10*, 345.
27. Nassar, N.N.; Hassan, A.; Pereira-Almao, P. Application of nanotechnology for heavy oil upgrading: Catalytic steam gasification/cracking of asphaltenes. *Energy Fuels* **2011**, *25*, 1566–1570.
28. Ogolo, N.; Olafuyi, O.; Onyekonwu, M. Enhanced oil recovery using nanoparticles. In Proceedings of the SPE Saudi Arabia Section Technical Symposium and Exhibition, Al Khobar, Saudi Arabia, 8–11 April 2012.
29. Agista, M.N.; Guo, K.; Yu, Z. A State-of-the-Art Review of Nanoparticles Application in Petroleum with a Focus on Enhanced Oil Recovery. *Appl. Sci.* **2018**, *8*, 871.
30. Hashemi, R.; Nassar, N.N.; Almao, P.P. Nanoparticle technology for heavy oil in-situ upgrading and recovery enhancement: Opportunities and challenges. *Appl. Energy* **2014**, *133*, 374–387.
31. Cheraghian, G.; Hendraningrat, L. A review on applications of nanotechnology in the enhanced oil recovery part B: Effects of nanoparticles on flooding. *Int. Nano Lett.* **2016**, *6*, 1–10.
32. Saboorian-Jooybari, H.; Dejam, M.; Chen, Z. Heavy oil polymer flooding from laboratory core floods to pilot tests and field applications: Half-century studies. *J. Pet. Sci. Eng.* **2016**, *142*, 85–100.
33. Rampa, R.; Agogué, M. Developing radical innovation capabilities: Exploring the effects of training employees for creativity and innovation. *Creat. Innov. Manag.* **2021**, *30*, 211–227.
34. Medina, O.E.; Gallego, J.; Acevedo, S.; Riazi, M.; Ocampo-Pérez, R.; Cortés, F.B.; Franco, C.A. Catalytic Conversion of n-C7 Asphaltenes and Resins II into Hydrogen Using CeO<sub>2</sub>-Based Nanocatalysts. *Nanomaterials* **2021**, *11*, 1301.
35. Ariza, F.; Andrés, C. *Synthesis and Application of Supported Metallic and Multi-Metallic Oxides Nanoparticles for In-Situ Upgrading and Inhibition of Formation Damage*; Universidad Nacional de Colombia-Sede Medellín: Medellín, Colombia, 2015.
36. Nassar, N.N.; Hassan, A.; Pereira-Almao, P. Metal oxide nanoparticles for asphaltene adsorption and oxidation. *Energy Fuels* **2011**, *25*, 1017–1023.

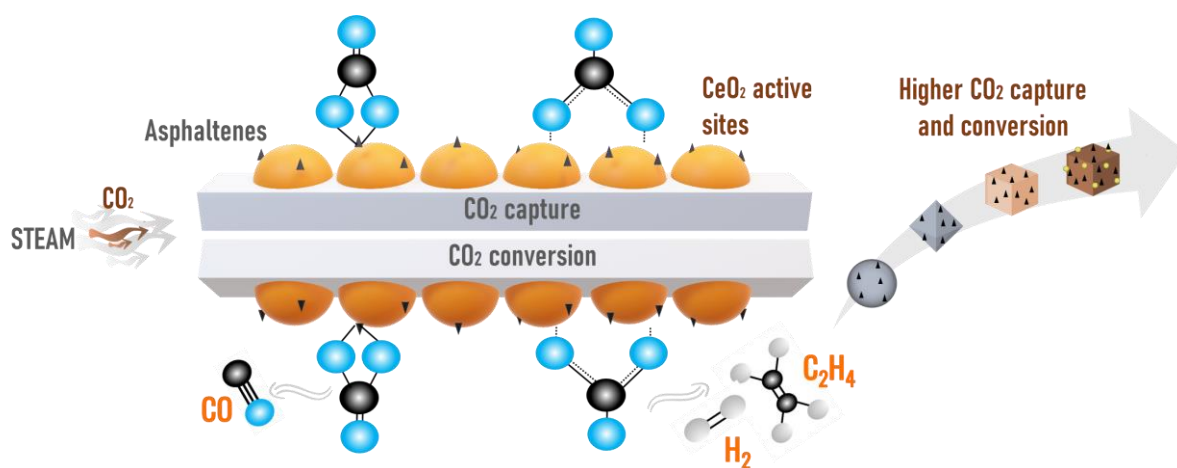
37. Hosseinpour, N.; Khodadadi, A.A.; Bahramian, A.; Mortazavi, Y. Asphaltene adsorption onto acidic/basic metal oxide nanoparticles toward in situ upgrading of reservoir oils by nanotechnology. *Langmuir* **2013**, *29*, 14135–14146.
38. Kazemzadeh, Y.; Eshraghi, S.E.; Kazemi, K.; Sourani, S.; Mehrabi, M.; Ahmadi, Y. Behavior of asphaltene adsorption onto the metal oxide nanoparticle surface and its effect on heavy oil recovery. *Ind. Eng. Chem. Res.* **2015**, *54*, 233–239.
39. Medina, O.E.; Caro-Vélez, C.; Gallego, J.; Cortés, F.B.; Lopera, S.H.; Franco, C.A. Upgrading of extra-heavy crude oils by dispersed injection of NiO–PdO/CeO<sub>2</sub>± $\delta$  nanocatalyst-based nanofluids in the steam. *Nanomaterials* **2019**, *9*, 1755.
40. Nassar, N.N. Asphaltene adsorption onto alumina nanoparticles: Kinetics and thermodynamic studies. *Energy Fuels* **2010**, *24*, 4116–4122.
41. Franco, C.A.; Nassar, N.N.; Ruiz, M.A.; Pereira-Almao, P.; Cortés, F.B. Nanoparticles for inhibition of asphaltene damage: Adsorption study and displacement test on porous media. *Energy Fuels* **2013**, *27*, 2899–2907.
42. Vargas, V.; Castillo, J.; Ocampo-Torres, R.; Lienemann, C.-P.; Bouyssiere, B. Surface modification of SiO<sub>2</sub> nanoparticles to increase asphaltene adsorption. *Pet. Sci. Technol.* **2018**, *36*, 618–624.
43. Setoodeh, N.; Darvishi, P.; Esmailzadeh, F. Adsorption of asphaltene from crude oil by applying polythiophene coating on Fe<sub>3</sub>O<sub>4</sub> nanoparticles. *J. Dispers. Sci. Technol.* **2018**, *39*, 578–588.
44. Madhi, M.; Bemani, A.; Daryasafar, A.; Khosravi Nikou, M.R. Experimental and modeling studies of the effects of different nanoparticles on asphaltene adsorption. *Pet. Sci. Technol.* **2017**, *35*, 242–248.
45. Cortés, F.B.; Montoya, T.; Acevedo, S.; Nassar, N.N.; Franco, C.A. Adsorption-desorption of n-C<sub>7</sub> asphaltenes over micro- and nanoparticles of silica and its impact on wettability alteration. *CTF-Cienc. Tecnol. Futuro* **2016**, *6*, 89–106.
46. Nassar, N.N.; Franco, C.A.; Montoya, T.; Cortés, F.B.; Hassan, A. Effect of oxide support on Ni–Pd bimetallic nanocatalysts for steam gasification of n-C<sub>7</sub> asphaltenes. *Fuel* **2015**, *156*, 110–120.
47. Lei, Y.; Bin, Y.; Tao, Z. Gasification of n-C<sub>7</sub> asphaltenes using Ni-based catalysis. *Pet. Sci. Technol.* **2017**, *35*, 2283–2286.
48. Medina, O.E.; Gallego, J.; Arias-Madrid, D.; Cortés, F.B.; Franco, C.A. Optimization of the Load of Transition Metal Oxides (Fe<sub>2</sub>O<sub>3</sub>, Co<sub>3</sub>O<sub>4</sub>, NiO

- and/or PdO) onto CeO<sub>2</sub> Nanoparticles in Catalytic Steam Decomposition of n-C<sub>7</sub> Asphaltenes at Low Temperatures. *Nanomaterials* **2019**, *9*, 401.
49. Hassan, A.; Lopez-Linares, F.; Nassar, N.N.; Carbognani-Arambarri, L.; Pereira-Almao, P. Development of a support for a NiO catalyst for selective adsorption and post-adsorption catalytic steam gasification of thermally converted asphaltenes. *Catal. Today* **2013**, *207*, 112–118.
  50. Oladyshkin, S.; Panfilov, M. Hydrogen penetration in water through porous medium: Application to a radioactive waste storage site. *Environ. Earth Sci.* **2011**, *64*, 989–999.
  51. Cardona, L.; Arias-Madrid, D.; Cortés, F.; Lopera, S.; Franco, C. Heavy oil upgrading and enhanced recovery in a steam injection process assisted by NiO- and PdO-Functionalized SiO<sub>2</sub> nanoparticulated catalysts. *Catalysts* **2018**, *8*, 132.
  52. Hosseinpour, M.; Fatemi, S.; Ahmadi, S.J. Catalytic cracking of petroleum vacuum residue in supercritical water media: Impact of  $\alpha$ -Fe<sub>2</sub>O<sub>3</sub> in the form of free nanoparticles and silica-supported granules. *Fuel* **2015**, *159*, 538–549.
  53. Pinc, W.; Yu, P.; O'Keefe, M.; Fahrenholtz, W. Effect of gelatin additions on the corrosion resistance of cerium based conversion coatings spray deposited on Al 2024-T3. *Surf. Coat. Technol.* **2009**, *23*, 3533–3540.
  54. Wang, X.; Chen, J.; Zeng, J.; Wang, Q.; Li, Z.; Qin, R.; Wu, C.; Xie, Z.; Zheng, L. The synergy between atomically dispersed Pd and cerium oxide for enhanced catalytic properties. *Nanoscale* **2017**, *9*, 6643–6648.
  55. Lamonier, C.; Ponchel, A.; D'huysser, A.; Jalowiecki-Duhamel, L. Studies of the cerium-metal–oxygen–hydrogen system (metal= Cu, Ni). *Catal. Today* **1999**, *50*, 247–259.
  56. Yamaguchi, T.; Ikeda, N.; Hattori, H.; Tanabe, K. Surface and catalytic properties of cerium oxide. *J. Catal.* **1981**, *67*, 324–330.
  57. Chen, H.; Sholl, D.S. Predictions of selectivity and flux for CH<sub>4</sub>/H<sub>2</sub> separations using single walled carbon nanotubes as membranes. *J. Membr. Sci.* **2006**, *269*, 152–160.
  58. Redlich, O.; Kwong, J.N. On the thermodynamics of solutions. V. An equation of state. Fugacities of gaseous solutions. *Chem. Rev.* **1949**, *44*, 233–244.
  59. Spycher, N.F.; Reed, M.H. Fugacity coefficients of H<sub>2</sub>, CO<sub>2</sub>, CH<sub>4</sub>, H<sub>2</sub>O and of H<sub>2</sub>O-CO<sub>2</sub>-CH<sub>4</sub> mixtures: A virial equation treatment for moderate

- pressures and temperatures applicable to calculations of hydrothermal boiling. *Geochim. Et Cosmochim. Acta* **1988**, *52*, 739–749.
60. Smith, J.; Van Ness, H.; Abbot, M. *Introduction to Thermodynamics in Chemical Engineering*; 2005, McGraw-Hill, España.
  61. Ancheyta, J.; Centeno, G.; Trejo, F.; Marroquin, G.; Garcia, J.; Tenorio, E.; Torres, A. Extraction and characterization of asphaltenes from different crude oils and solvents. *Energy Fuels* **2002**, *16*, 1121–1127.
  62. López, D.; Giraldo, L.J.; Salazar, J.P.; Zapata, D.M.; Ortega, D.C.; Franco, C.A.; Cortés, F.B. Metal Oxide Nanoparticles Supported on Macro-Mesoporous Aluminosilicates for Catalytic Steam Gasification of Heavy Oil Fractions for On-Site Upgrading. *Catalysts* **2017**, *7*, 319.
  63. Delannoy, L.; El Hassan, N.; Musi, A.; Le To, N.N.; Krafft, J.-M.; Louis, C. Preparation of supported gold nanoparticles by a modified incipient wetness impregnation method. *J. Phys. Chem. B* **2006**, *110*, 22471–22478.
  64. Cardona, L.; Medina, O.E.; Céspedes, S.; Lopera, S.H.; Cortés, F.B.; Franco, C.A. Effect of Steam Quality on Extra-Heavy Crude Oil Upgrading and Oil Recovery Assisted with PdO and NiO-Functionalized Al<sub>2</sub>O<sub>3</sub> Nanoparticles. *Processes* **2021**, *9*, 1009.
  65. Medina, O.E.; Gallego, J.; Restrepo, L.G.; Cortés, F.B.; Franco, C.A. Influence of the Ce<sup>4+</sup>/Ce<sup>3+</sup> Redox-couple on the cyclic regeneration for adsorptive and catalytic performance of NiO-PdO/CeO<sub>2</sub>± $\delta$  nanoparticles for n-C7 asphaltene steam gasification. *Nanomaterials* **2019**, *9*, 734.
  66. Pérez-Robles, S.; Cortés, F.B.; Franco, C.A. Effect of the nanoparticles in the stability of hydrolyzed polyacrylamide/resorcinol/formaldehyde gel systems for water shut-off/conformance control applications. *J. Appl. Polym. Sci.* **2019**, *136*, 47568.
  67. Socrates, G. *Infrared and Raman Characteristic Group Frequencies: Tables and Charts*; John Wiley & Sons: Hoboken, NJ, USA, 2004.
  68. Taborda-Acevedo, E.A.; Jurado, W.J.; Cortés, F.B. Efecto de la temperatura en el proceso de adsorción de agua en Carbón sub-bituminoso colombiano. *Bol. Cienc. Tierra* **2016**, *39*, 57–64.
  69. Medina, O.E.; Gallego, J.; Olmos, C.M.; Chen, X.; Cortés, F.B.; Franco, C.A. Effect of Multifunctional Nanocatalysts on n-C7 Asphaltene Adsorption and Subsequent Oxidation under High-Pressure Conditions. *Energy Fuels* **2020**, *34*, 6261–6278. <https://doi.org/10.1021/acs.energyfuels.0c00653>.

70. Franco, C.A.; Zabala, R.D.; Zapata, J.; Mora, E.; Botero, O.; Candela, C.; Castillo, A. Inhibited gas stimulation to mitigate condensate banking and maximize recovery in cupiagua field. *SPE Prod. Oper.* **2013**, *28*, 154–167.
71. Franco, C.A.; Montoya, T.; Nassar, N.N.; Cortés, F.B. *Nioand pdo Supported on Fumed Silica Nanoparticles for Adsorption and Catalytic Steam Gasification of Colombian C7asphaltenes*; Nova Science Publishers: Hauppauge, NY, USA, 2014.
72. Bansal, V.; Krishna, G.; Chopra, A.; Sarpal, A. Detailed hydrocarbon characterization of RFCC feed stocks by NMR spectroscopic techniques. *Energy Fuels* **2007**, *21*, 1024–1029.
73. Holland, T.; Powell, R. A Compensated-Redlich-Kwong (CORK) equation for volumes and fugacities of CO<sub>2</sub> and H<sub>2</sub>O in the range 1 bar to 50 kbar and 100–1600 C. *Contrib. Mineral. Petrol.* **1991**, *109*, 265–273.
74. Grevel, K.-D.; Chatterjee, N.D. A modified Redlich-Kwong equation of state for H<sub>2</sub>-H<sub>2</sub>O fluid mixtures at high pressures and at temperatures above 400 C. *Eur. J. Mineral.* **1992**, *4*, 1303–1310.
75. Hagelstein, P.L. Equation of State and Fugacity Models for H<sub>2</sub> and for D<sub>2</sub>. *J. Condens. Matter Nucl. Sci.* **2015**, *16*, 23–45.
76. Chiodini, G.; Marini, L. Hydrothermal gas equilibria: The H<sub>2</sub>O-H<sub>2</sub>-CO<sub>2</sub>-CO-CH<sub>4</sub> system. *Geochim. Cosmochim. Acta* **1998**, *62*, 2673–2687.
77. Cengel, Y.A.; Boles, M.A.; Kanoğlu, M. *Thermodynamics: An Engineering Approach*; McGraw-hill: New York, NY, USA, 2011; Volume 5.
78. Rice, S.A. On the Theorem of Corresponding States and Its Application to Mixtures. *J. Chem. Phys.* **1958**, *29*, 141–147.

# Simultaneous CO<sub>2</sub> Adsorption and Conversion over Ni-Pd Supported CeO<sub>2</sub> Nanoparticles During Catalytic *n*-C<sub>7</sub> Asphaltene Gasification



Published manuscript in Fuel: doi.org/10.1016/j.fuel.2023.127733

Impact factor: 8.035

# Simultaneous CO<sub>2</sub> Adsorption and Conversion over Ni-Pd Supported CeO<sub>2</sub> Nanoparticles During Catalytic *n*-C<sub>7</sub> Asphaltene Gasification

## Abstract

Shallow heavy oil reservoirs are suitable for the geo-sequestration of CO<sub>2</sub> based on its adsorption and conversion during thermal-enhanced oil recovery processes. This study aims to evaluate multifunctional nanomaterials for CO<sub>2</sub> adsorption and its subsequent transformation into valuable sub-products during the catalytic decomposition of asphaltenes in a steam gasification atmosphere. Three ceria nanoparticles with cubic (C-CeO<sub>2</sub>), orthorhombic (O-CeO<sub>2</sub>), and spherical (S-CeO<sub>2</sub>) shapes were tested in four stages, including *i*) CO<sub>2</sub> adsorption at 30, 50, 100, and 200 °C between 0.084 and 3.0 MPa, *ii*) dynamic *in-situ* CO<sub>2</sub> adsorption in the presence of steam between 170 and 230 °C at 3.0 MPa, *iii*) dynamic *in-situ* CO<sub>2</sub> adsorption in the presence of steam with adsorbed asphaltenes between 170 and 230 °C at 3.0 MPa and *iv*) CO<sub>2</sub> conversion at the same conditions. The best nanoparticle morphology was doped with 1 wt.% of Ni and Pd (C-CeNiPd) and was tested in the same experiments. Among the most important results, CO<sub>2</sub> adsorption increased in the order S-CeO<sub>2</sub> < O-CeO<sub>2</sub> < C-CeO<sub>2</sub> < C-CeNiPd, regardless of the temperature. When steam was injected, CO<sub>2</sub> adsorption is reduced in all the systems. At 200 °C adsorption decreased by 3.0, 2.7, 2.5, and 2.0% in processes assisted by S-CeO<sub>2</sub>, O-CeO<sub>2</sub>, C-CeO<sub>2</sub>, and C-CeNiPd, respectively. Nanoparticles with adsorbed asphaltenes presented a high tendency for CO<sub>2</sub> adsorption as well. The nanoparticle with the best morphology (C-CeO<sub>2</sub>) adsorbed about 24.3% (3.92 mmol) of CO<sub>2</sub> at 200 °C, and the yield increased after doping with Ni and Pd, obtaining CO<sub>2</sub> adsorption of 34 %. Finally, for CO<sub>2</sub> conversion, a mixture of gases composed of CO, CH<sub>4</sub>, H<sub>2</sub>, and light hydrocarbons (LHC) is obtained. The hydrogen production content follows a trend that agrees well with each material's adsorptive capacity and catalytic activity. The maximum %*vol* of H<sub>2</sub> produced at 200 °C during asphaltene gasification was 31, 29, 24, and 23% for C-CeNiPd, C-CeO<sub>2</sub>, O-CeO<sub>2</sub>, and S-CeO<sub>2</sub>, respectively.

## 1. Introduction

The anthropogenic emission of the greenhouse gas CO<sub>2</sub> is considered a driver for continued climate change [1, 2]. In the last century, the concentration of CO<sub>2</sub> in the atmosphere increased to over 400 ppm, and the global surface temperature simultaneously increased by around 0.8°C [3]. It is expected that at the end of this century, the atmospheric CO<sub>2</sub> level will reach 700 ppm, implying an increase in the global surface temperature of up to 5 °C [3]. Therefore, effective measures for controlling CO<sub>2</sub> emissions need to be urgently established. Carbon capture, utilization, and sequestration (CCUS) technologies capture CO<sub>2</sub> for further usage [4-6], which can lead to significant reductions in greenhouse gas emissions [7, 8]. Nowadays, most studies on CCUS technologies focus on evaluating CO<sub>2</sub> capture/adsorption and utilization in separate steps [9]. However, the large-scale application of technologies to capture and utilize (transform) CO<sub>2</sub> is limited by the heat transfer required to conduct CO<sub>2</sub> adsorption (commonly at temperatures lower than 60 °C) and convert CO<sub>2</sub> at high temperatures [10]. Hence, implementing multifunctional materials that both act as sorbents and catalysts appears as an alternative for CO<sub>2</sub> capture and utilization in an integrated process [11-14]. These applications seek the design of reactors where both methods can be carried out [15, 16]. Different reactors currently functioning for adsorption or conversion of CO<sub>2</sub> are coal-fired power plants [17], mixed electron and carbonate ion conductor (MECC) membranes [18], dual-phase membranes [18], and electrochemical reactors [19], among others. The main limitation is that the dual process (adsorption/conversion) is not possible in the same system.

The feasibility of using geological petroleum formations as reactors: where both the adsorption and conversion of CO<sub>2</sub>, as well as the production of other high-quality subproducts occurs, is investigated in this paper. Currently, many oilfields use high-temperature technologies (350 °C) that include steam injection under different mechanisms (cyclic, continuous, etc.), mainly focused on the production of heavy and extra-heavy crude oils [20-23]. Steam is injected into a wide range of reservoir depths from 60 m, which are considered shallow reservoirs. In these reservoirs, the pressure reaches up to 3.0 MPa, the reservoir temperature between 40 - 60 °C, and the steam injection temperature up to 350 °C [24-26], which can be suitable for geo-sequestration of CO<sub>2</sub> based on



adsorption phenomena and conversion during steam injection processes [24-30]. Under these conditions, gaseous CO<sub>2</sub> can be injected with the steam stream for mobility improvement of the crude oil with simultaneous geo-storage of adsorbed CO<sub>2</sub> on the rock surface. Adsorption capacity is generally lower than 0.0013 mmol·g<sup>-1</sup> and can limit CO<sub>2</sub> storage in shallow reservoirs [31]. Hence, improving CO<sub>2</sub> adsorption phenomena in shallow reservoirs may also promote CO<sub>2</sub> geo-sequestration [31-33]. Using combined CO<sub>2</sub> and steam injection technologies assisted by nanocatalysts can result in a potential path to increase the volume of crude oil produced, its quality based on the *in-situ* upgrading, and at the same time, improve CO<sub>2</sub> sequestration and its conversion [34-37].

Several nanotechnology-based solutions have been proposed to improve, in a different way, the CO<sub>2</sub> storage in shallow reservoirs [31, 38, 39] and the enhancement of steam injection processes [40-44]. In the case of geological CO<sub>2</sub> capture, different nanoparticles, including carbon [33], metal oxides [45], and inorganic nanoparticles [46], have been employed, obtaining adsorption capacities between 3 and 5 mmol g<sup>-1</sup> at 3.0 MPa [33, 38, 47]. Rodriguez et al. [31, 33] previously developed innovative nanomaterials for carbon capture with high selectivity from flue gas streams, obtaining incremental factors of 922 and 730 at 25 °C and 50 °C, respectively, for the sandstone adsorption capacity using 20 wt.% of nanoparticles.

Nanoparticles based on transition element oxides and lanthanides have also been proposed to improve steam injection processes [48-55], mainly through the conversion of crude oil-heavy fractions such as asphaltenes into lighter compounds while increasing the thermal conductivity of the reservoir. The transformation of asphaltenes means an improvement in crude oil quality asphaltenes are mainly responsible for high viscosities and low densities [56, 57]. Intelligent nanomaterials could additionally result in a selective asphaltene conversion into H<sub>2</sub> and other high-quality subproducts [58-60].

During thermal enhance oil recovery (TEOR) assisted by nanotechnology, the interactions of the nanomaterials with heavy fractions of the crude oil and reactants are of primary importance to describe the system. In this case, the CO<sub>2</sub>-nanoparticles-asphaltene interactions should be first considered to understand the CO<sub>2</sub> capture and conversion during steam injection. To our knowledge, there are currently no studies in specialized literature that report the use of nanoparticles for simultaneous CO<sub>2</sub> adsorption and conversion during the catalytic *n*-C<sub>7</sub> asphaltene gasification in shallow reservoirs. In this sense, the main objective of this study is to develop a nanoparticle-based technology that allows

the sequestration of CO<sub>2</sub>, with the simultaneous conversion of this compound and *n*-C<sub>7</sub> asphaltenes into high-quality subproducts. For this, three ceria nanoparticles with different morphologies were tested in four stages including *i*) CO<sub>2</sub> adsorption at 30, 50, 100, and 200 °C between 0.084 and 3.0 MPa, *ii*) dynamic *in-situ* CO<sub>2</sub> adsorption between 170 and 230 °C at 3.0 MPa, *iii*) dynamic *in-situ* CO<sub>2</sub> adsorption in the presence of steam between 170 and 230 °C at 3.0 MPa and *iv*) dynamic *in-situ* CO<sub>2</sub> adsorption in the presence of steam with adsorbed asphaltenes between 170 and 230 °C at 3.0 MPa. Through the development of this study, a new panorama of TEOR methods during energy transition is proposed through the capture and use of CO<sub>2</sub>, improving the efficiency of the operation of the oil and gas industry, and reducing greenhouse gas emissions.

## 2. Experimental

### 2.1. Materials

Asphaltenes were isolated from Colombian extra-heavy crude oil using *n*-heptane purchased by Sigma-Aldrich (St. Louis, MO, USA) with 99% purity following the ASTM standard [61]. Asphaltenes have a C, H, N, S, and O content of 81.7, 7.8, 0.3, 6.6, and 3.6 wt.%, respectively. Asphaltene molecular weight is 645.1 g·mol<sup>-1</sup>. Details of the properties of crude oil and asphaltenes are reported in our previous study [50].

Cubic (C-CeO<sub>2</sub>), orthorhombic (O-CeO<sub>2</sub>), and spherical (S-CeO<sub>2</sub>) ceria nanoparticles were used to evaluate asphaltene adsorption/conversion and CO<sub>2</sub> adsorption/conversion. Doped C-CeO<sub>2</sub> with 1.0 wt.% of Ni and Pd (C-CeNiPd) was considered in this study. The morphology and size were corroborated by Scanning Electron Microscopy and shown in our previous study. The diameter of the S-CeO<sub>2</sub> was observed as 40 nm with a rough surface. C-CeO<sub>2</sub> presents cubes with a smooth surface and average size between 40 and 60 nm. Finally, orthorhombic shapes are observed with an average side size of 20 nm in O-CeO<sub>2</sub>. Textural properties of nanoparticles were characterized by N<sub>2</sub> adsorption/desorption at -196 °C to determine the surface area ( $S_{\text{BET}}$ ), and CO<sub>2</sub> adsorption at 0 °C to estimate the micropore volume ( $W_0$ ), mesopore volume ( $V_{\text{meso}}$ ) and micropore size ( $L_0$ ). Nanoparticle chemical properties were characterized by X-ray diffraction to estimate the crystallite size and lattice parameter, X-ray photoelectron spectroscopy for surface functional groups identification, and Raman spectroscopy for oxygen vacancies calculation. Table 1 and 2 summarizes the main properties of the employed nanomaterials. Details

of the synthesis process, as well as details of the chemical and textural properties of employed nanoparticles, are reported in a previous study [62].

**Table 1.** Textural properties estimated of synthesized S-CeO<sub>2</sub>, C-CeO<sub>2</sub>, O-CeO<sub>2</sub>, and C-CeNiPd.

Sample	S <sub>BET</sub> (m <sup>2</sup> ·g <sup>-1</sup> )	Wo(CO <sub>2</sub> )	Lo(CO <sub>2</sub> )	Wo(N <sub>2</sub> )	Lo(N <sub>2</sub> )	V <sub>0.95</sub>	V <sub>meso(BJH)</sub>
S-CeO <sub>2</sub>	22.2	0.17	0.55	0.14	0.75	0.26	0.045
C-CeO <sub>2</sub>	32.1	0.22	0.58	0.17	0.79	0.33	0.056
O-CeO <sub>2</sub>	28.0	0.21	0.58	0.15	0.78	0.32	0.044
C-CeNiPd	25.5	0.19	0.61	0.15	0.77	0.31	0.053

**Table 2.** Chemical properties estimated of synthesized S-CeO<sub>2</sub>, C-CeO<sub>2</sub>, O-CeO<sub>2</sub>, and C-CeNiPd.

Sample	Crystallite size <sup>a</sup> (nm)	Lattice Parameter <sup>b</sup> (nm) x 10 <sup>-2</sup>	Ce <sup>3+</sup> (%)	O <sub>ads</sub> (%)	O <sub>latt</sub> (%)	Ni <sup>2+</sup> (NiO) (%)	Pd <sup>2+</sup> (%)	I <sub>(598+1172)</sub> /I
S-CeO <sub>2</sub>	12.0	54.09	18.39	41.86	58.14	-	-	0.10
C-CeO <sub>2</sub>	15.0	54.12	32.60	88.03	11.97	-	-	0.23
O-CeO <sub>2</sub>	19.0	54.10	26.91	75.94	24.06	-	-	0.19
C-CeNiPd	12.4	54.01	52.4	84.8	15.2	33.5	62.3	0.25

## 2.2. CO<sub>2</sub> adsorption at high pressure

Figure 1 summarizes the experimental road map used in this study to measure CO<sub>2</sub> adsorption and conversion over ceria-based nanoparticles.

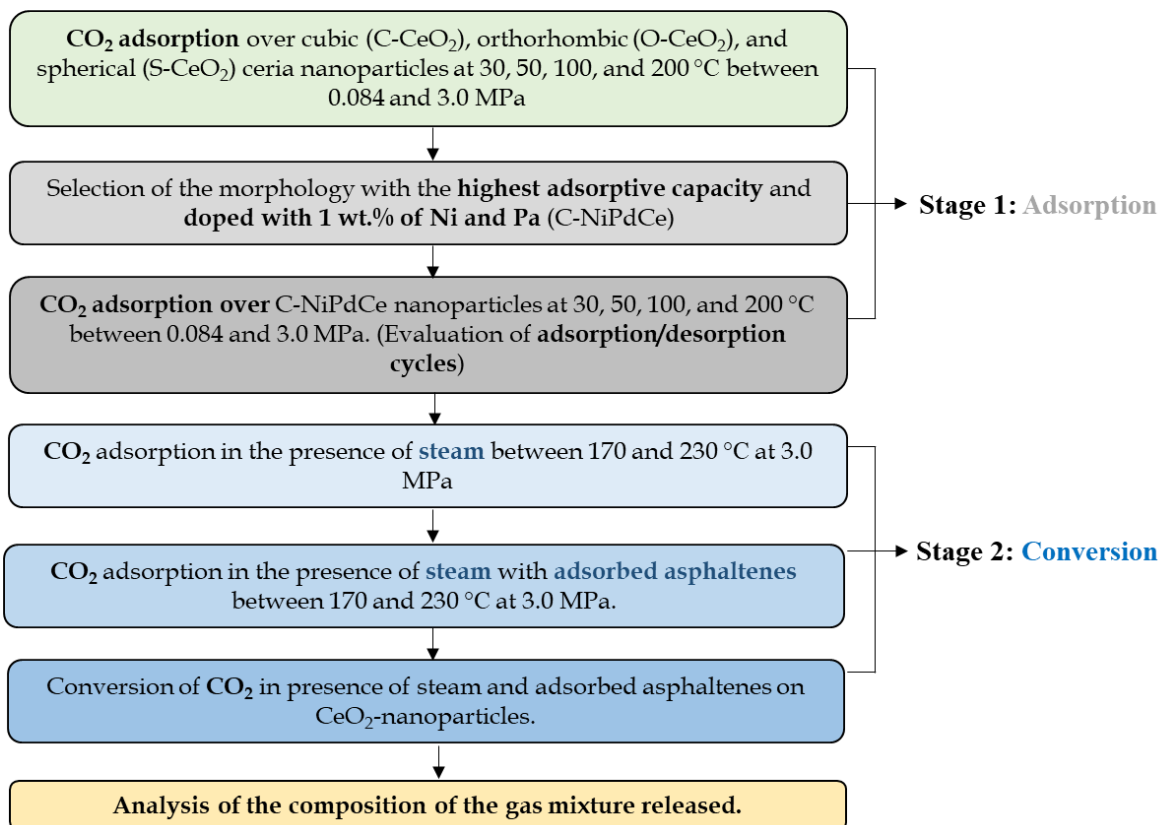


**Figure 1.** Experimental flowline to study CO<sub>2</sub> adsorption and conversion over CeO<sub>2</sub>-based nanoparticles.

An HP-TGA 750 analyzer (Hullhorst, Germany) was used to evaluate the CO<sub>2</sub> adsorption capacity of CeO<sub>2</sub>-based nanoparticles at temperatures of 30, 50, 100, and 200 °C and pressures ranging between 0.084 MPa and 3.0 MPa based on a magnetic levitation technique [63]. The magnetic system provided a monotone electromagnetic field capable of levitating a magnet set on the suspension shaft and sample maintainer. The device was calibrated based on temperature and weight. However, changing the heat conductivity of the gas by pressure and temperature makes temperature calibration at high-pressure conditions very challenging. Therefore, it is essential to measure the Curie temperature in the entire pressure range of the device. The CO<sub>2</sub> flow used was 60 mL·min<sup>-1</sup> in the experiments. The sample mass was adjusted to 30 mg to avoid the impacts of mass/heat transfer and provide enough total surface area for adsorption [33].

To perform the CO<sub>2</sub> adsorption tests, first, a vacuum condition (0.00025 MPa and 120 °C) was used to clean the solid surfaces of the samples for 12 h. The subsequent pressure, temperature, and gas flow rate were adjusted to the initial conditions. To correct the buoyancy effect of the gas flow, two different runs were made with empty and solid-filled sample containers. Then, the obtained mass profile for each sample was removed from the mass profile of the empty sample

container. The best morphology and doped material for CO<sub>2</sub> adsorption were evaluated in several consecutive cycles using the TGA-HP at 3.0 MPa. CO<sub>2</sub> desorption was performed by subjecting the sample to a vacuum for 12 hours. After that, a new adsorption cycle was completed. The procedure was repeated 20 times.

The adsorption isotherms were fitted with the Sips model [64], which considers multilayer adsorption of CO<sub>2</sub> over nanoparticles' surfaces. The Sips model is described by Equation (1). Here,  $b$  represents the adsorption equilibrium constant,  $n$  represents the heterogeneity of the system,  $N_{ads}$  (mmol·g<sup>-1</sup>) and  $N_m$  (mmol·g<sup>-1</sup>) represent the adsorbed amount and maximum adsorption capacity at an equilibrium pressure  $P$  (kPa).

$$N_{ads} = N_m \frac{(bP)^{1/n}}{1 + (bP)^{1/n}} \quad (1)$$

### 2.3. CO<sub>2</sub> adsorption during asphaltene catalytic gasification

Asphaltene adsorption over nanoparticles was tested by batch experiments based on a colorimetric method [57, 65, 66]. Nanoparticles containing 0.02 mg·m<sup>-2</sup> of adsorbed asphaltenes were subjected to CO<sub>2</sub> and *in-situ* CO<sub>2</sub> adsorption measures. The HP-TGA 750 analyzer was equipped with a mass spectrometer (GC-MS, Shimadzu GC, Japan) to study CO<sub>2</sub> adsorption during asphaltene catalytic gasification. The experiments were performed in two main stages. First, CO<sub>2</sub> adsorption in the presence of steam was analyzed (without asphaltenes). H<sub>2</sub>O<sub>(g)</sub> flow was fixed at 6.30 mL min<sup>-1</sup>, and CO<sub>2</sub> flow at 60 mL·min<sup>-1</sup> (i.e., 0.269 mmol min<sup>-1</sup>). The gasifying atmosphere was controlled using a gas saturator and thermostatic bath at atmospheric pressure. Then, nanoparticles containing 0.02 mg·m<sup>-2</sup> of adsorbed asphaltenes were subjected to similar conditions to determine CO<sub>2</sub> adsorption during asphaltene catalytic gasification. The tests were executed at 170, 200, and 230 °C.

The adsorbed amount of CO<sub>2</sub> was found using the equipped TGA device with an online MS spectrometer through a hot capillary column heated to 150 °C to prevent gas condensation. The scan rate of the linear ion trap mass analyzer was 0.03 M/Z from M/Z 0 up to 200. The equipment operates with an electron impact mode of 100 eV to have sufficiently intense signals for the released gas information. The MS profiles are deconvoluted and the percentage of each gas is obtained. CO<sub>2</sub> adsorption percentage was calculated using Equation (2), where CO<sub>2<sub>entry,t</sub></sub> and CO<sub>2<sub>exit,t</sub></sub> refer to the moles of CO<sub>2</sub> at the entry and exit of the TGA

device at a determined time  $t$ . Also, the  $\sum X_{i_{exit,t}}$  refers to the moles of other gases (i) produced at a determined time  $t$ .

$$\text{CO}_2 \text{ Capture}(\%) = \frac{\text{CO}_{2_{\text{entry},t}} - (\text{CO}_{2_{\text{exit},t}} + \sum X_{i_{\text{exit},t}})}{\text{CO}_{2_{\text{entry},t}}} \times 100 \quad (2)$$

Each experiment was repeated three times to ensure the accuracy of the results, obtaining uncertainties of 0.001 mg and  $\pm 0.01$  °C.

### 3. Results and discussion

#### 3.1. CO<sub>2</sub> adsorption over CeO<sub>2</sub> nanoparticles

##### 3.1.1. Effect of ceria morphology

Figure 2.a shows the experimental adsorption profiles and Sips fits for CO<sub>2</sub> in the materials C-CeO<sub>2</sub>, O-CeO<sub>2</sub>, and S-CeO<sub>2</sub> at a fixed temperature of 30 °C. According to the IUPAC (International Union of Pure and Applied Chemistry) classification, the adsorption of CO<sub>2</sub> on all materials follows a type Ib isotherm. These isotherms are typical of materials with a high affinity for adsorbate molecules (CO<sub>2</sub>) and are characterized by a high slope at pressures below 1.5 MPa. At higher pressures, between 2.5 and 3.0 MPa, a tendency towards stabilization in the amount of CO<sub>2</sub> adsorbed is evident, similar to the reports by Rodriguez et al. [31]. The shape of the isotherms indicates that the saturation of the active sites of the nanomaterial is reached between 2.5 and 3.0 MPa, regardless of the temperature evaluated [67]. The isotherms have a typical behavior of the adsorption monolayer that increases the amount adsorbed as the pressure increases until reaching endpoint saturation (filled pore volume) [31]. CeO<sub>2</sub>-based materials have high oxygen vacancies (Table 2), which promote the physisorption of CO<sub>2</sub> by interactions with the Ce<sup>3+</sup> present on the surface of the adsorbent [68, 69]. The adsorptive capacity of CO<sub>2</sub> decreases in the direction C-CeO<sub>2</sub> > O-CeO<sub>2</sub> > S-CeO<sub>2</sub> for a fixed pressure. Some chemical and textural properties could influence the capability of each material to adsorb CO<sub>2</sub>. From Table 1 it is recognized that the micro and mesoporous volume of ceria-nanoparticles follows the order S-CeO<sub>2</sub> < O-CeO<sub>2</sub> < C-CeO<sub>2</sub>. Interestingly, other properties like the size of the mesopore and surface area follow the same order; suggesting that the textural properties of C-CeO<sub>2</sub> are more suitable for CO<sub>2</sub> adsorption as it contributes to greater diffusion of CO<sub>2</sub> in the pore space [31].

Additionally, density functional theory analysis demonstrated that CO<sub>2</sub> is adsorbed on CeO<sub>2</sub> as three types of CO<sub>2</sub> adsorbed species including *i*) monodentate configuration forming carbonate species with two oxygen atoms on its surface, *ii*) bidentate configurations with one oxygen atom on its surface, and *iii*) polydentate carbonate species [70-72]. The mechanism is favored by the positive surface charges of the ceria that allow interactions between C (from CO<sub>2</sub>) and oxygen (from CeO<sub>2</sub>). Figure 2.b shows a schematical representation of bidentate and polydentate configurations [70-72]. The bidentate species are considered less stable, whereas monodentate configurations are the most stable with binding energies of -0.31 eV and preferably formed in (111) crystal facets [73]. The strongest interaction of CO<sub>2</sub> with CeO<sub>2</sub> (111) occurs when it adsorbs as a polydentate/tridentate species, forming one Ce–O and two O<sub>surf</sub>–C interactions [33, 70, 73]. In this way, the higher capacity of the C-CeO<sub>2</sub> material to adsorb CO<sub>2</sub> is explained by the abundant presence of highly reactive crystallographic planes such as {111}, which was determined by TEM analysis in our previous work [62]. Similarly, the lattice parameter (see Table 2) of ceria could improve the adsorption mechanism. Increasing the lattice parameter increases the oxygen vacancies and, therefore, the vacancies-CO<sub>2</sub> interactions. The tendency is shown in Figure 2.c.

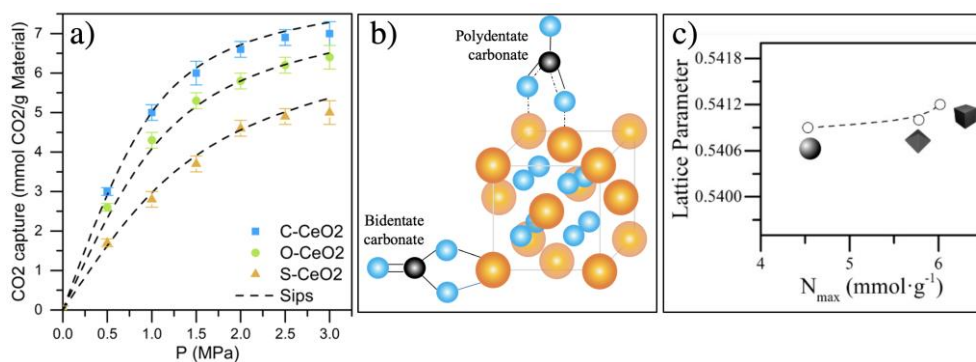


**Figure 2.** a) High-pressure CO<sub>2</sub> adsorption isotherms for materials C-CeO<sub>2</sub> (blue), O-CeO<sub>2</sub> (green), and S-CeO<sub>2</sub> (orange) at 30 °C. The Sips model [64] used for modeling the isotherms is represented as black dotted lines in all cases. b) Interactions CO<sub>2</sub>/CeO<sub>2</sub>-base materials. Ce, O, and C molecules are represented by orange, blue, and black spheres, respectively. c) Relationship between the amount adsorbed and the Lattice parameter for the materials C-CeO<sub>2</sub> (cubic), S-CeO<sub>2</sub> (orthorhombic), and O-CeO<sub>2</sub> (spherical).

The estimated parameters of the Sips model are summarized in Table 3. It is observed that  $b$  increases in the direction S-CeO<sub>2</sub>→O-CeO<sub>2</sub>→C-CeO<sub>2</sub>, indicating that the system affinity is higher in C-CeO<sub>2</sub>. In addition, the parameter  $n$  (related to the system's heterogeneity) increases in the opposite direction, indicating that the homogeneity of cubic nanoparticles enhances the adsorptive capacity of ceria [62]. A good fit of the model is observed with an  $R^2 \sim 1$  and %RSME < 0.3.

**Table 3.** Estimated Sips model [64] parameters for high-pressure CO<sub>2</sub> adsorption isotherms on C-CeO<sub>2</sub> (cubic), O-CeO<sub>2</sub> (orthorhombic), and S-CeO<sub>2</sub> (spherical) materials at 30 °C.

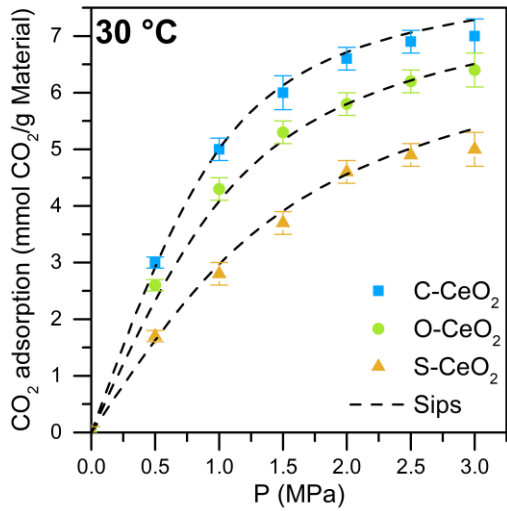
Sample	$b$	$n$	$N_m$ (mmol·g <sup>-1</sup> )	$R^2$	%RSME
C-CeO <sub>2</sub>	1.48	0.64	8.00	1.00	0.35
O-CeO <sub>2</sub>	1.15	0.73	7.70	1.00	0.17
S-CeO <sub>2</sub>	0.78	0.79	7.20	1.00	0.25

### 3.1.2. Effect of temperature

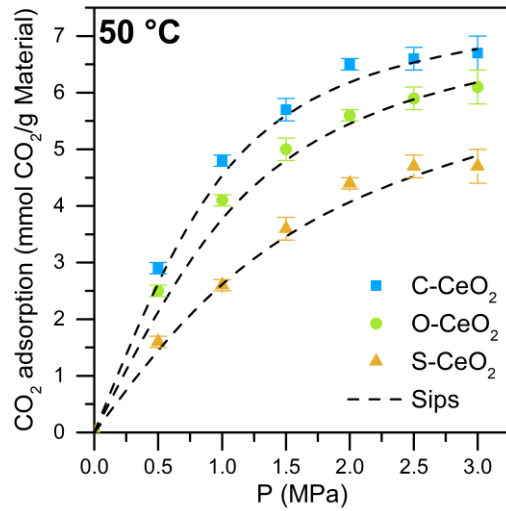
The effect of temperature on the adsorption of CO<sub>2</sub> in the materials S-CeO<sub>2</sub>, C-CeO<sub>2</sub> and O-CeO<sub>2</sub> was evaluated through adsorption isotherms at 30, 50, 100, and 200 °C in Figure 3. The amount of CO<sub>2</sub> adsorbed decreases with increasing temperature due to the highly exothermic nature of the CO<sub>2</sub>/CeO<sub>2</sub> interactions. At fixed conditions of 1.0 MPa and 30 °C, adsorption reductions of 50.0%, 53.5%, and 35.7% are observed for C-CeO<sub>2</sub>, O-CeO<sub>2</sub>, and S-CeO<sub>2</sub>, respectively. These results are in agreement with reports by Ghalandari et al. [74], and Melouki et al. [75]. The exothermicity of the system provides high energy to the molecules in the vapor phase with increased temperature. Therefore, adsorption sites will have a lower capacity to interact with CO<sub>2</sub> particles due to their high diffusion rate [67]. Melouki et al. [75] also indicate that the adsorption process is reversible, for which the captured CO<sub>2</sub> can be desorbed and subsequently transformed to generate products with higher energetic value.

The results suggest that the nanoparticles present a high adsorption capacity at shallow reservoir conditions ( $T < 100$  °C,  $P < 3.0$  MPa), and at steam injection conditions on HO shallow reservoirs ( $T < 200$  °C,  $P < 3.0$  MPa) [33].

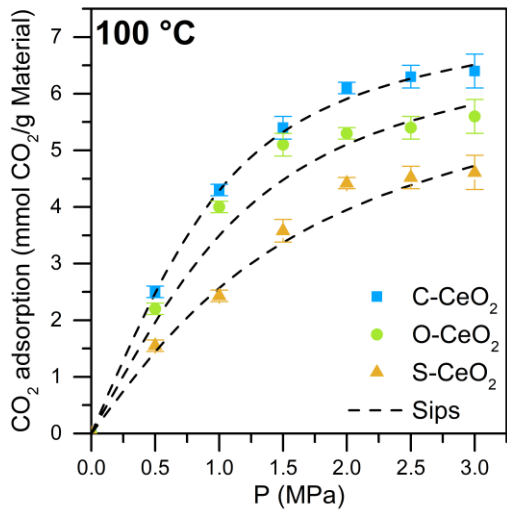




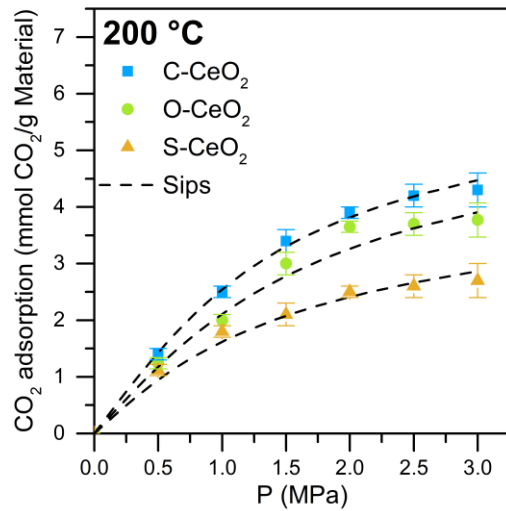
a)



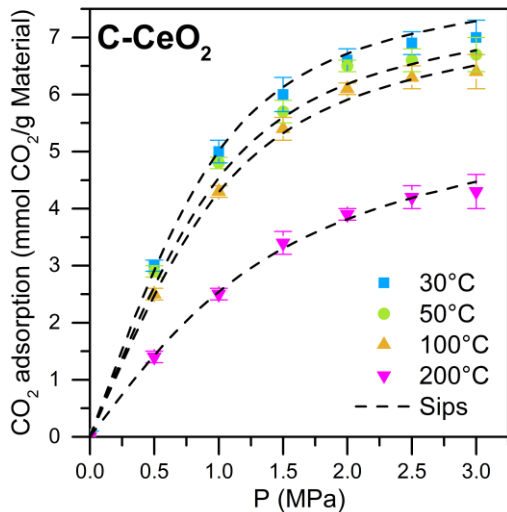
b)



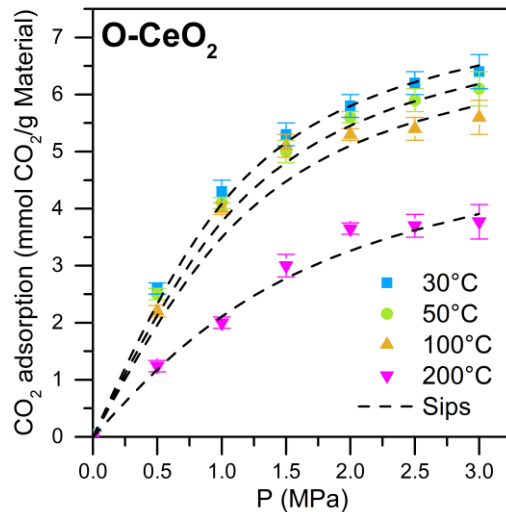
c)



d)



e)



f)

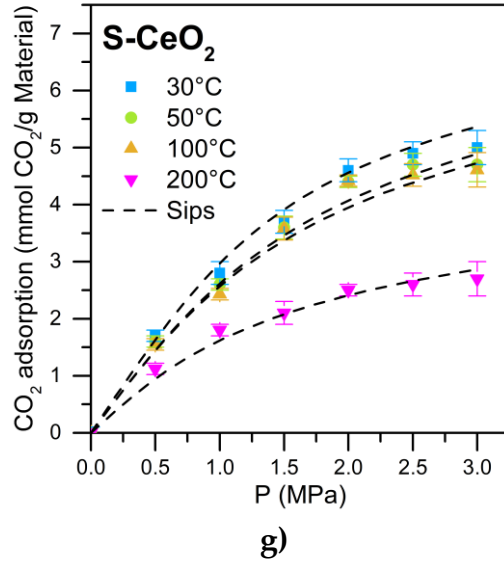


**Figure 3.** High-pressure CO<sub>2</sub> adsorption isotherms for materials C-CeO<sub>2</sub>, O-CeO<sub>2</sub>, and S-CeO<sub>2</sub> at temperatures of a) 30 °C, b), 50 °C, c) 100 °C and d) 200 °C. Temperature tendency for e) C-CeO<sub>2</sub>, f) O-CeO<sub>2</sub>, and g) S-CeO<sub>2</sub>. The Sips model [64] used for modeling the isotherms is represented as black dotted lines in all cases.

The estimated parameters of the Sips model are shown in Table 4. *b* increases in the direction of 200 °C → 100 °C → 50 °C → 30 °C showing that the higher the temperature, the lower the affinity and adsorptive capacity of the materials toward the adsorbate CO<sub>2</sub>, due to the increase in the internal energy of the molecules of the vapor phase. These results agree with reports by Sreńscek-Nazzal and co-workers [39]. A good model fit is achieved with an  $R^2 > 0.98$  and %RSME < 0.5.

**Table 4.** Adjustment parameters of the Sips model [64] for high-pressure CO<sub>2</sub> adsorption isotherms on C-CeO<sub>2</sub> (cubic), S-CeO<sub>2</sub> (orthorhombic), and O-CeO<sub>2</sub> (spherical) materials at 50, 100 and 200 °C.

Sample	Temperature (°C)	<i>b</i>	<i>n</i>	$N_m$ (mmol·g <sup>-1</sup> )	$R^2$	%RSME
C-CeO <sub>2</sub>	50	1.38	0.67	7.60	1.00	0.25
	100	1.32	0.69	7.40	1.00	0.42
	200	0.80	0.83	6.02	1.00	0.35
O-CeO <sub>2</sub>	50	1.06	0.74	7.50	1.00	0.17
	100	1.01	0.75	7.15	0.98	0.02
	200	0.64	0.87	5.78	0.98	0.01
S-CeO <sub>2</sub>	50	0.64	0.86	7.20	0.99	0.33
	100	0.63	0.89	7.05	0.99	0.24
	200	0.57	1.00	4.53	0.98	0.55

### 3.1.3. Effect of doped material

The previous results showed that the C-CeO<sub>2</sub> material has the highest performance in CO<sub>2</sub> adsorption under high-pressure and high-temperature conditions. Hence, this material was used further in this study. C-CeO<sub>2</sub> was doped with nickel and palladium as metallic phases (C-CeNiPd) using the incipient wet technique and was tested under low temperature (30 °C) and high temperature (200 °C) conditions using pressure ranging from 0 to 3.0 MPa. The results obtained are shown in Figure 4. The doped C-CeO<sub>2</sub> material has a higher adsorptive capacity than the non-doped C-CeO<sub>2</sub> material. This is because the Ni and Pd metallic phases provide more significant CO<sub>2</sub>/CeO<sub>2</sub> interaction due to Ni<sup>2+</sup> and Pd<sup>2+</sup> cations, which facilitate the formation of oxygen vacancies between the surface and the mass of the base material [76].

Interestingly, a relationship between the maximum adsorptive capacity with  $I_{(598+1172)}/I_{458}$  and the percentage of Ce<sup>3+</sup> was observed. The increment in both properties (regardless of non-doped nanoparticles) improved the adsorption capacity of the nanoparticle. Different defects including O<sup>2-</sup> are induced by ceria, nickel, and palladium cations, increasing the values of  $I_{(598+1172)}/I_{458}$  and therefore, increasing the proportion of Ce<sup>3+</sup>.

Similar to the non-doped ceria nanoparticles, a reduction of the adsorptive capacity is observed with increasing temperature. At a fixed pressure (3.0 MPa) a 35% reduction of CO<sub>2</sub> adsorbed was found when the temperature increased from 30 to 200 °C.

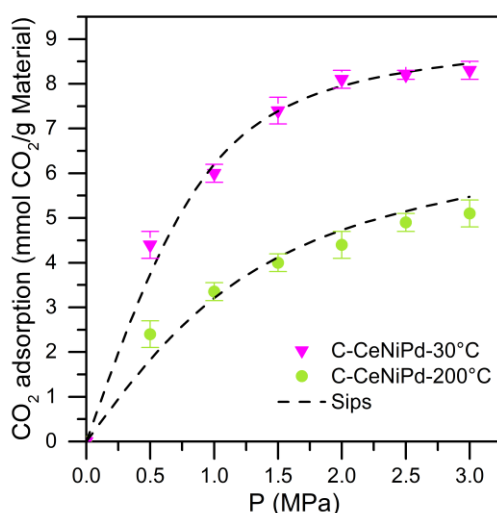


**Figure 4.** High-pressure CO<sub>2</sub> adsorption isotherms on C-CeNiPd at 30 °C and 200 °C. The Sips model used for modeling the isotherms is represented as black dotted lines in all cases.

Table 5 presents the Sips model parameters for CO<sub>2</sub> adsorption isotherms at high pressure. The results indicate a good fit of the model and the experimental data with an  $R^2 > 0.97$ . The Sips constant is higher for the functionalized material ( $b_{C-CeNiPd} > b_{C-CeO_2}$ ), while the parameter  $n$  follows an opposite trend ( $n_{C-CeNiPd} < n_{C-CeO_2}$ ). This is explained by the higher affinity of the material in the presence of the metallic phase due to the increase in the amount of Ce<sup>3+</sup> cations, lattice parameter, the oxygen vacancy index, and active sites for adsorbate/adsorbent interaction.

A representative mechanism for CO<sub>2</sub> capture on C-CeNiPd is depicted in Figure 5. As mentioned, the {111} is the most abundant terminating facet on the cubic-ceria support; therefore, CO<sub>2</sub> can be adsorbed as monodentate, bidentate, and polydentate species. When CO<sub>2</sub> is planarly positioned above the surface, the geometric and electronic structures are not perturbed noticeably, and a very weak interaction (irrespective of the surface) results, which is merely physisorption [77].

CO<sub>2</sub> can bind in a monodentate fashion in the tilted orientation atop the Ce atom and in a bidentate fashion through Ce–O and O<sub>surf</sub>–C bonds with physisorption, thus effectively forming a carbonate species with one free (dangling) oxygen. The strongest interaction of CO<sub>2</sub> with CeO<sub>2</sub>(111) occurs when it adsorbs as a polydentate/tridentate species forming one Ce–O and two O<sub>surf</sub>–C interactions [77].

The presence of Ni and Pd becomes sites for CO<sub>2</sub> adsorption. Ni interacts with CO<sub>2</sub> by four stable structures with binding modes B-C1O1, B-C2O2, H-C2O2, and H-C3O2 (see Figure 5). DFT studies confirmed that CO<sub>2</sub>/Ni in the B-C1O1 binding mode is the most stable structure (i.e., bridge site with one oxygen bonding, one carbon bonding, with two surface nickel atoms). On the Pd atoms, three stable structures are recognized to bind with CO<sub>2</sub>: B-C1O1, B-C2, and T-C1.

For the B-C1O1 binding mode, one C-Pd bond and one O-Pd bond are formed. For the B-C2 binding mode, two C-Pd bonds are formed, and for the T-C1 binding mode, one C-Pd bond is formed (see Figure 5). These analyses offer insights about CO<sub>2</sub> adsorption on the synthesized materials and agree well with their characteristics.

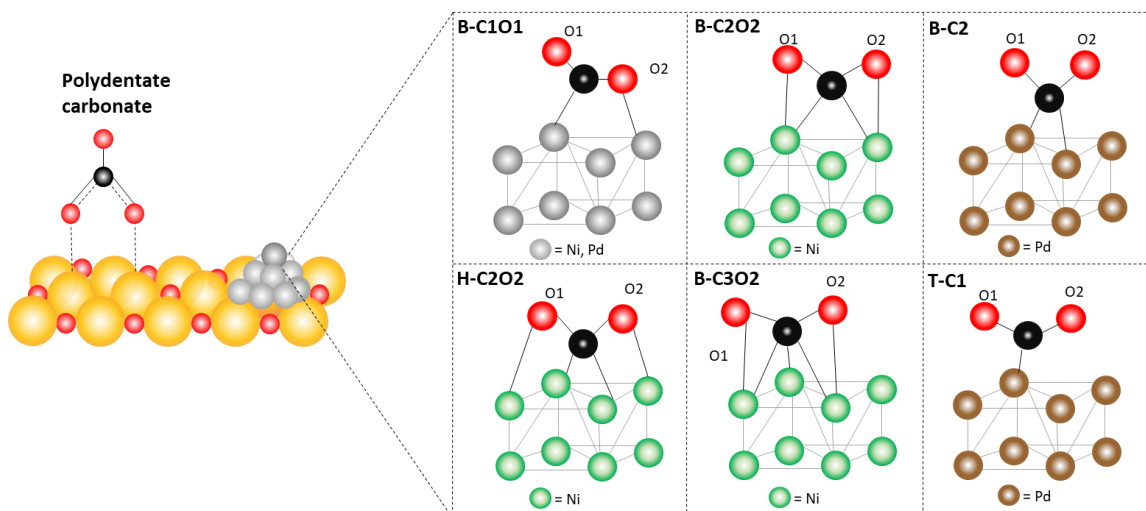


**Figure 5.** Representative mechanism for CO<sub>2</sub> adsorption on C-CeNiPd. CO<sub>2</sub> as polydentate species on CeO<sub>2</sub>. CO<sub>2</sub> adsorbed as: B-C1O1, B-C2O2, H-C2O2, and H-C3O2 on nickel and B-C1O1, B-C2, and T-C1 on palladium. Orange, red, green, brown, and black spheres refer to ceria, oxygen, nickel, palladium, and carbon atoms, respectively.

**Table 5.** Adjustment parameters of Sips model [64] for high-pressure CO<sub>2</sub> adsorption isotherms on C-CeNiPd (Doped cubic ceria nanoparticle with 1wt.% of Ni and Pd).

Sample	Temperature (°C)	<i>b</i>	<i>n</i>	<i>N<sub>m</sub></i> (mmol·g <sup>-1</sup> )	<i>R</i> <sup>2</sup>	%RSME
C-CeNiPd	30	1.74	0.61	9.02	0.97	0.02
	200	0.87	0.82	7.18	0.99	0.14

Finally, the C-CeO<sub>2</sub> (support) and C-CeNiPd (doped) materials were evaluated during twenty CO<sub>2</sub>-adsorption/desorption cycles at 200 °C for a fixed pressure (3.0 MPa) (Figure 6). There is no significant decrease in the amount of CO<sub>2</sub> adsorbed during the cycles evaluated for both materials (less than 8%). The high stability of the CeO<sub>2</sub> particles is due to the high Tamman temperature, which prevents the sintering process during the formation of carbonate configurations during several CO<sub>2</sub> adsorption cycles [78, 79]. In addition, the reduction in CO<sub>2</sub> adsorbed was lower in the C-CeNiPd because Ni and Pd increase the reducibility of ceria chemical species (from Ce<sup>4+</sup> to Ce<sup>3+</sup>). The catalytic activity of the material increases significantly, allowing total desorption of CO<sub>2</sub> at lower temperatures. In this way, rapid regeneration translates into greater stability of the chemical structure of the support (CeO<sub>2</sub>). The results agree with Hu et al. [78] and Shen et al. [80].

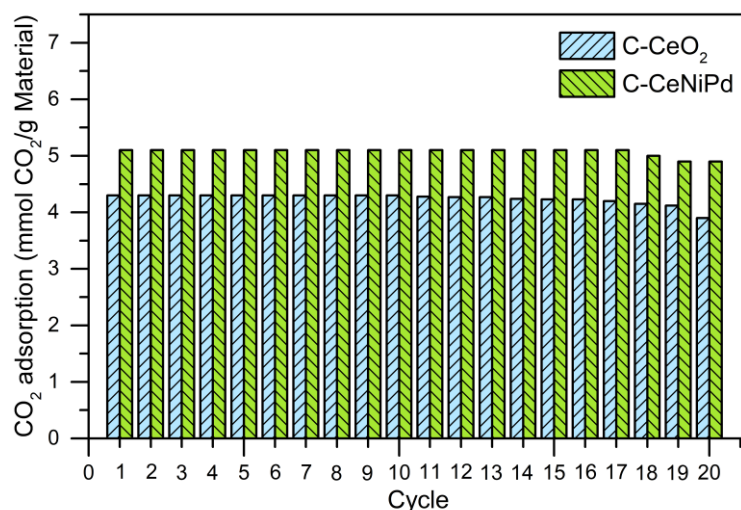


**Figure 6.** CO<sub>2</sub> adsorption in C-CeO<sub>2</sub> (cubic) and C-CeNiPd (Ni/Pd- doped cubic nanoparticle) through 20 CO<sub>2</sub>-adsorption/desorption cycles at 200 °C and 3.0 MPa.

### 3.2. In-situ CO<sub>2</sub> Adsorption during n-C<sub>7</sub> Asphaltene Gasification over CeO<sub>2</sub> – based Nanoparticles

TGA tests were used to analyze and obtain: i) CO<sub>2</sub> adsorption, which refers to the moles of CO<sub>2</sub> adsorbed on the nanoparticles and depends on the moles of CO<sub>2</sub> at the entry and exit of the TGA device at a determined time  $t$ , and ii) CO<sub>2</sub> conversion, which was defined as the moles of other gases (i) produced at a determined time  $t$  ( $\sum X_{i_{exit,t}}$ ).

#### 3.2.1. In-situ CO<sub>2</sub> adsorption with steam

CO<sub>2</sub> adsorption without steam was verified in the previous sections. Once steam was injected CO<sub>2</sub> adsorption was slightly reduced. Without steam, CO<sub>2</sub> adsorption was 4.53 mmol, 5.78 mmol, 6.01 mmol, and 7.18 mmol (see Table 2 and 3) in S-CeO<sub>2</sub>, O-CeO<sub>2</sub>, C-CeO<sub>2</sub>, and C-CeNiPd, respectively (at 200 °C). At the same temperature, with steam presence, CO<sub>2</sub> adsorption was 24.1%, 26.3%, 32.1%, and 33.0% when the process was assisted by S-CeO<sub>2</sub>, O-CeO<sub>2</sub>, C-CeO<sub>2</sub>, and C-CeNiPd, respectively (see Figure 7). Considering the molar flow of CO<sub>2</sub> (0.296 mmol·min<sup>-1</sup>), during 60 min, around 16.15 mmol of CO<sub>2</sub> was injected. Hence, around 3.97 mmol, 4.32 mmol, 5.29 mmol, 5.44 mmol of CO<sub>2</sub> were adsorbed by S-CeO<sub>2</sub>, O-CeO<sub>2</sub>, C-CeO<sub>2</sub>, and C-CeNiPd, respectively. The %vol of  $\sum X_{i_{exit,t}}$  for S-CeO<sub>2</sub>, O-CeO<sub>2</sub>, C-CeO<sub>2</sub>, and C-CeNiPd was 2.62%, 2.70%, 2.80%, and 2.85%, respectively. It means that, 0.43 mmol, 0.44 mmol, 0.46 mmol, and 0.47 mmol of CO<sub>2</sub> were converted by the same systems. The C-CeNiPd, therefore, stands out

as the material with both the highest CO<sub>2</sub> adsorption and conversion. Between the supports with different morphologies, both variables increase in the order: S-CeO<sub>2</sub> < O-CeO<sub>2</sub> < C-CeO<sub>2</sub>.

The CO<sub>2</sub> conversion under steam presence could be a result of the interactions between both molecules and the nanoparticles. It is reported that the adsorption of CO<sub>2</sub> is strongly affected by the overwhelming competitive adsorption of steam on CO<sub>2</sub> adsorbents which can react at high temperatures [81]. Under these conditions, it is confirmed that the nanoparticles can adsorb CO<sub>2</sub> in the presence of steam molecules.

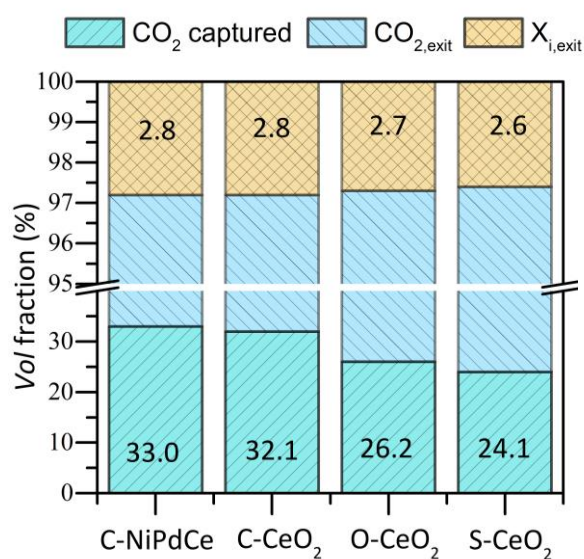


**Figure 7.** Volume fraction (%) of *in-situ* CO<sub>2</sub> adsorbed, CO<sub>2</sub> at the exit of TGA device, and CO<sub>2</sub> conversion ( $\sum X_{i,exit}$ ) in CeO<sub>2</sub> and doped CeO<sub>2</sub> nanoparticles with steam at 200 °C.

### 3.2.2. Effect of ceria morphology on *in-situ* CO<sub>2</sub> Adsorption during *n*-C<sub>7</sub> Asphaltene Gasification

This section focuses on evaluating CO<sub>2</sub> adsorption based on a scenario of CO<sub>2</sub> injection into a steam stream, in which CO<sub>2</sub> will contact the asphaltene-containing nanocatalyst where CO<sub>2</sub> adsorption and conversion are expected to occur. During this process, nanocatalysts also convert the adsorbed asphaltenes, generating different types of by-products through different reactions that can be assisted by the adsorbed CO<sub>2</sub>. The asphaltene conversion on the different nanoparticles is shown in Figure 8

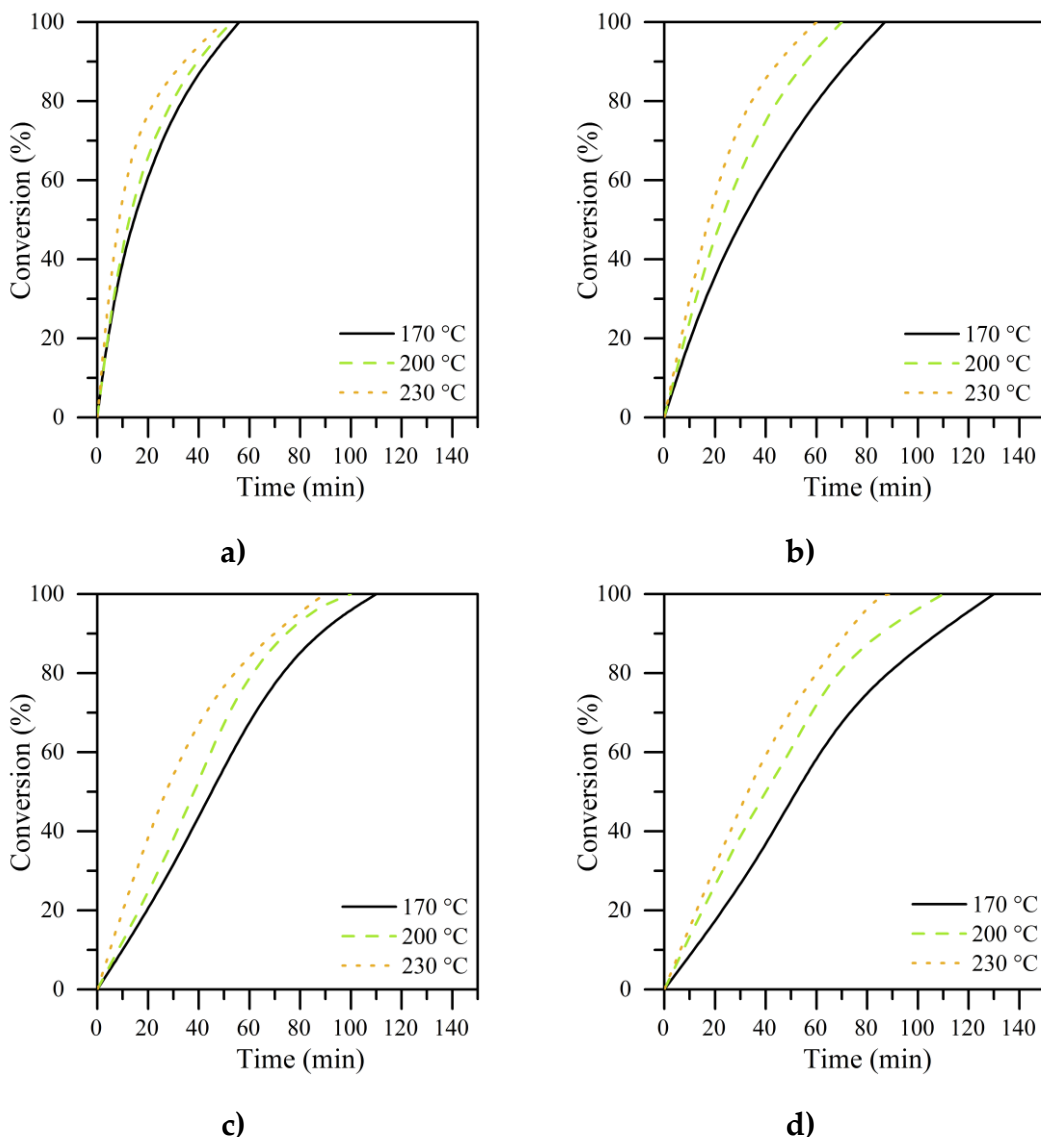


**Figure 8.** Isothermal conversion of  $n\text{-C}_7$  asphaltenes steam gasification adsorbed on a) C-CeNiPd, b) C-CeO<sub>2</sub>, c) O-CeO<sub>2</sub>, d) S-CeO<sub>2</sub>. Nitrogen flow: 100 ml·min<sup>-1</sup>, steam flow: 6.7 ml·min<sup>-1</sup>, and sample mass 5 mg.

Figure 9 shows the results of *in-situ* CO<sub>2</sub> adsorption in asphaltenes-containing C-CeO<sub>2</sub> at 200 °C and 3.0 MPa. With increasing time, the CO<sub>2</sub> adsorbed % increased because of the increment in asphaltene conversion. Once the asphaltenes are transformed, the availability of active sites for CO<sub>2</sub> anchoring increases. The results suggest that asphaltenes block CO<sub>2</sub>-CeO<sub>2</sub> interactions. Because ceria is a Lewis base, it is thermodynamically desirable for asphaltene and CO<sub>2</sub> adsorption. However, the adsorbed asphaltenes limit CO<sub>2</sub>-CeO<sub>2</sub> interactions because they are insoluble in CO<sub>2</sub>, and the asphaltene-CO<sub>2</sub> interactions are not expected [82]. Similarly, CO<sub>2</sub> conversion ( $\sum X_{i,exit,t}$ ) is time-dependent and increases with increasing asphaltene conversion (increasing



time). Based on the assumption that the activation of the C=O bond of the CO<sub>2</sub> molecule needs to introduce a reductant carrying H and/or C atoms, such as H<sub>2</sub> (from steam) and hydrocarbons (like asphaltenes) [83-85], nanomaterials are expected to take advantage of both sources to achieve a correct conversion of CO<sub>2</sub>. At 60 min, 16.15 mmol of CO<sub>2</sub> was injected into the TGA device. The C-CeO<sub>2</sub> nanoparticle adsorbed around 24.3% and converts 15.2%, that is, 3.92 mmol and 2.45 mmol of CO<sub>2</sub> are adsorbed and converted at 200 °C during the 60 min analysis.

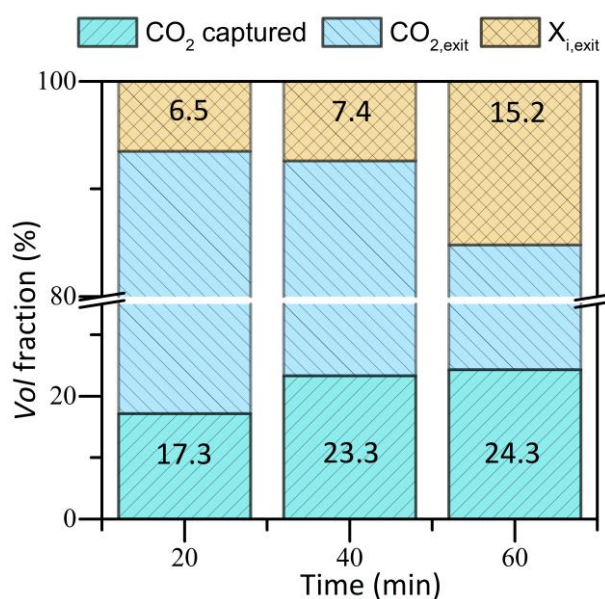


**Figure 9.** Volume fraction (%) of *in-situ* CO<sub>2</sub> adsorbed, CO<sub>2</sub> at the exit of TGA device, and CO<sub>2</sub> conversion ( $\sum X_{i,exit,j}$ ) during *n*-C<sub>7</sub> asphaltene catalytic gasification using C-CeO<sub>2</sub> at 200 °C.

To analyze the effect of ceria morphology on *in-situ* CO<sub>2</sub> adsorption, a fixed temperature of 200 °C was selected and results for orthorhombic and spherical nanoparticles are shown in Figure 10. Based on the information in Figures 9 and 10, CO<sub>2</sub> adsorption during asphaltene consumption follows the increasing order: S-CeO<sub>2</sub> < O-CeO<sub>2</sub> < C-CeO<sub>2</sub>. According to the conversion results (Figure 8), the spherical nanoparticles have a large part of the active sites occupied by asphaltene molecules during the analyzed time (lower conversion degree), which are progressively decomposed into light hydrocarbons and gaseous products that are desorbed from the catalyst surface, leaving active sites available to interact with CO<sub>2</sub>. In this sense, the greatest adsorption of CO<sub>2</sub> occurs when most of the asphaltene has been converted and desorbed from the catalyst surface.

*In-situ* CO<sub>2</sub> adsorption (%) was 18.6% (3.00 mmol), 23.7% (3.82 mmol), and 24.3% (3.92 mmol) in S-CeO<sub>2</sub>, O-CeO<sub>2</sub>, and C-CeO<sub>2</sub>, respectively, at 60 min of isothermal heating at 200 °C. The change in the morphology of the CeO<sub>2</sub> systems presented different yields in the *in-situ* CO<sub>2</sub> uptake because of their different chemical and textural properties. According to the literature, the exposure of the more reactive (100), (100), and (111) crystal facets facilitate the formation of oxygen vacancies on the ceria surface. We verified that cubic nanoparticle exposes more reactive facets than orthorhombic and spherical nanoparticles [62]. Hence, it is speculated that the surface defects on the CeO<sub>2</sub> contributed to the oxygen storage capacity and consequently in the *in-situ* CO<sub>2</sub> adsorption. Liu and co-workers report similar results [86]. Also, Li and co-workers [87] found that CO<sub>2</sub> adsorption is performed in bidentate carbonate and bridge carbonate over (111) planes exhibited in C-CeO<sub>2</sub>. These systems are characterized by the stability of the bridge carbonate on the catalyst's surface.

In addition, CeO<sub>2</sub> with abundantly exposed oxygen vacancies is a potent surface for gas adsorption [86], and therefore, cubic nanoparticles have advantages over others because the formation of oxygen vacancies in the high energy facets enhances the OSC capacity [88]. The  $I_{(598+1172)}/I_{458}$  ratio increases in the order S-CeO<sub>2</sub> (0.10) < O-CeO<sub>2</sub> (0.19) < C-CeO<sub>2</sub> (0.23).

In the same way, Ce<sup>3+</sup> ions concentration enhances CO<sub>2</sub> adsorption. This property goes hand in hand with oxygen vacancies. The formation of an oxygen vacancy requires the formation of two Ce<sup>3+</sup> by the reduction of Ce<sup>4+</sup> [87]. During the reduction of Ce<sup>4+</sup>, a small polaron is formed by the distortion of the surrounding oxygen shell to screen the charge when the Ce<sub>4f</sub> state is occupied. Both properties (oxygen vacancies position and ceria polarons) influence the energy required for the formation of crystalline defects, and this in turn has a critical impact on interactions with CO<sub>2</sub> [89]. In this way, CO<sub>2</sub> molecules easily interact with Ce<sup>3+</sup> arranged on the CeO<sub>2</sub> surface. As the cubic nanoparticle has a higher content of Ce<sup>3+</sup> (48.81%) than orthorhombic (44.3%) and spherical (42.56%), the adsorption increases. Likewise, the conversion of asphaltenes is greater at shorter times in the same system, and therefore many active sites are vacated faster for *in-situ* CO<sub>2</sub> adsorption.

CO<sub>2</sub> conversion ( $\sum X_{i, exit}$ ) increased in the order S-CeO<sub>2</sub> < O-CeO<sub>2</sub> < C-CeO<sub>2</sub>. Around 15.2% (2.45 mmol), 14.7% (2.37 mmol), and 12.2% (1.97 mmol) of the injected CO<sub>2</sub> was converted by C-CeO<sub>2</sub>, O-CeO<sub>2</sub>, and S-CeO<sub>2</sub>, respectively. It is corroborated that, the capacity of the materials to convert CO<sub>2</sub> is influenced by the morphology which in turn modifies the oxygen storage capacity, textural

properties, redox cycling, and therefore its participation as a three-way catalyst in many chemical reactions [90-92]. In this case, the cubic nanoparticle presents the best yield in CO<sub>2</sub> conversion as a result of the higher Ce<sup>3+</sup> exposure on its surface [86, 93]. In addition, cubic material showed the highest performance in asphaltene conversion (Figure 8).

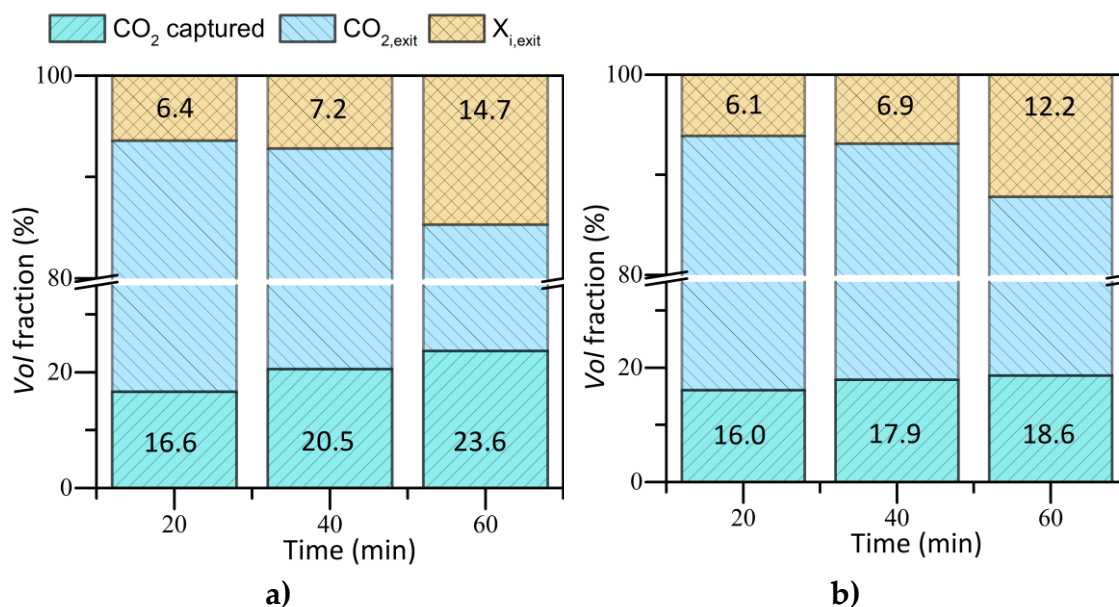


**Figure 10.** Volume fraction (%) of *in-situ* CO<sub>2</sub> adsorbed CO<sub>2</sub> at the exit of TGA device, and CO<sub>2</sub> conversion ( $\sum X_{i,exit,j}$ ) during *n*-C<sub>7</sub> asphaltene catalytic gasification using a) O-CeO<sub>2</sub> and b) S-CeO<sub>2</sub> at 200 °C.

Figure 11 shows *in-situ* CO<sub>2</sub> adsorption at 170 and 230 °C for the three CeO<sub>2</sub> nanoparticles. In agreement with the thermodynamic characteristics of CO<sub>2</sub> adsorption by CeO<sub>2</sub> described in the previous section, the CO<sub>2</sub> adsorption % decreased with temperature and reached the maximum at 170 °C. The S-CeO<sub>2</sub>, O-CeO<sub>2</sub>, and C-CeO<sub>2</sub> adsorbed around 19.5, 25.0, and 26.3%, equivalent to 3.10, 4.03, and 4.24 mmol of CO<sub>2</sub>, respectively. Oppositely, the %vol of  $\sum X_{i,exit,j}$  increased with the increase in temperature, obtaining the maximum at 230 °C. It means that at higher temperatures CO<sub>2</sub> conversion increased, reaching values of 13.4% (2.16 mmol), 15.8% (2.55 mmol), and 16.4% (2.64 mmol), respectively.

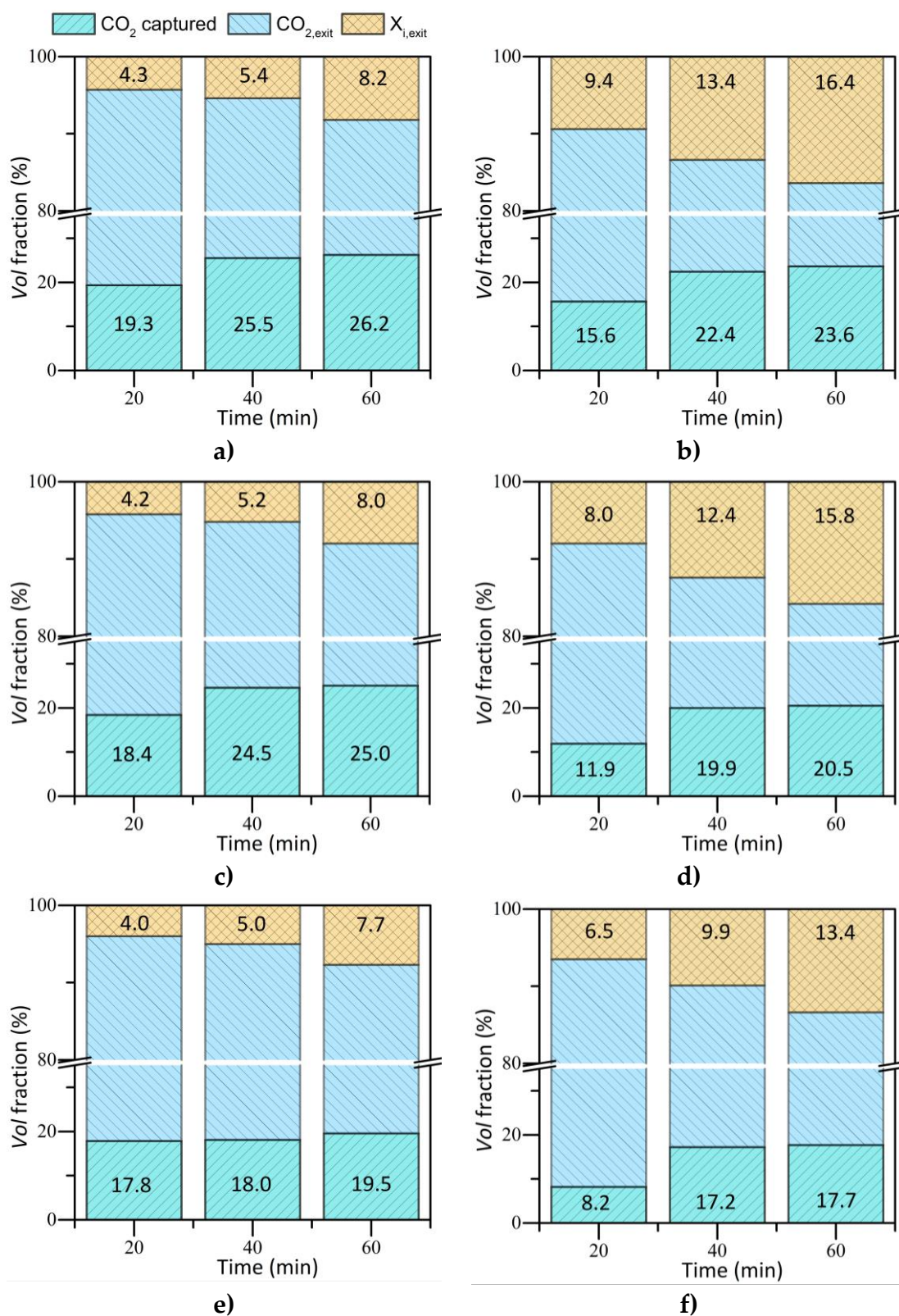


**Figure 11.** Volume fraction (%) of *in-situ*  $\text{CO}_2$  adsorbed,  $\text{CO}_2$  at the exit of TGA device, and  $\text{CO}_2$  conversion ( $\sum X_{i,\text{exit}}$ ) during *n*-C<sub>7</sub> asphaltene catalytic gasification using a-b) C-CeO<sub>2</sub>, c-d) O-CeO<sub>2</sub> and e-f) S-CeO<sub>2</sub>. The figures on the right were tested at 230 °C and those on the left at 170 °C.

### 3.2.3. Effect of doped material

Figure 12 shows the volume fraction (%) of *in-situ* CO<sub>2</sub> adsorbed, CO<sub>2</sub> at the exit of the TGA device, and CO<sub>2</sub> conversion ( $\sum X_{i_{exit,t}}$ ) during *n*-C<sub>7</sub> asphaltene catalytic gasification for doped cubic ceria nanoparticles (C-CeNiPd) as a function of time at different temperatures (170, 200, and 230 °C). The *in-situ* adsorption of CO<sub>2</sub> and %*vol* of  $\sum X_{i_{exit,t}}$  on the doped material follow a similar behavior to non-doped systems but was significantly more efficient. At the end of the analyzed time (60 min), the CO<sub>2</sub> adsorption (%) was close to 37, 34, and 26%, at 170, 200, and 230 °C, respectively, that is, 11.6, 11.8, and 1.6% more than C-CeO<sub>2</sub> at the same temperatures. Similarly, for a fixed temperature (200 °C) at 60 min, the C-CeNiPd adsorbed 15.4% (2.48 mmol) and 17.3% (2.79 mmol) more than O-CeO<sub>2</sub> and S-CeO<sub>2</sub>, respectively.

The highest yield for the doped material is related to an increase in Ce<sup>3+</sup> phases (52.4%). This stoichiometric phase generally occurs in small oxygen-deficient nanoparticles concentrated in low-coordination Ce, so the concentration of Ce<sup>3+</sup> is proportional to the dispersion of NiO and PdO. Also, the oxygen vacancies increase in the CeO<sub>2</sub> lattice ( $I_{(598+1172)}/I_{458}$  ratio = 0.25) after Ni and Pd entered the lattice due to the reduction of the Ce crystallite size (C-CeNiPd: 12.4 nm, C-CeO<sub>2</sub>: 15 nm). This result is further evidenced by the increase in the lattice oxygen by adding Ni and Pd (C-CeNiPd: 15.2% and C-CeO<sub>2</sub>: 11.9%). It has been noted that the high-mobility lattice oxygen on CeO<sub>2</sub> is highly active to bond with CO<sub>2</sub>.

The % *vol* of  $\sum X_{i_{exit,t}}$  during the analyzed time (60 min) at 170, 200, and 230°C was 14.3 (2.30 mmol), 16.9 (2.72 mmol), and 17.2% (2.77 mmol), respectively. Regarding non-doped materials, the C-CeNiPd presents a higher percentage of CO<sub>2</sub> converted at all temperatures because of the catalytic activity of the active phases of Ni and Pd and the Support-Metal Strong Interactions (SMSI). Compared with C-CeO<sub>2</sub> (support with the highest efficiency in *in-situ* CO<sub>2</sub> adsorption), the C-CeNiPd shows a higher overall CO<sub>2</sub> uptake. Indeed, the Ni and Pd phases promoted the CO<sub>2</sub> affinity of CeO<sub>2</sub>, thereby accelerating the CO<sub>2</sub> diffusion rate, which is confirmed by the higher adsorption at earlier times in the CeO<sub>2</sub>-modified system.

Our results reveal that adding Ni and Pd would enhance the CO<sub>2</sub> affinity of CeO<sub>2</sub> during asphaltene catalytic steam gasification, hence underlining the importance of CeO<sub>2</sub> modification to bifunctional material for the successful



implementation of the isothermal asphaltene steam gasification and CO<sub>2</sub> adsorption.

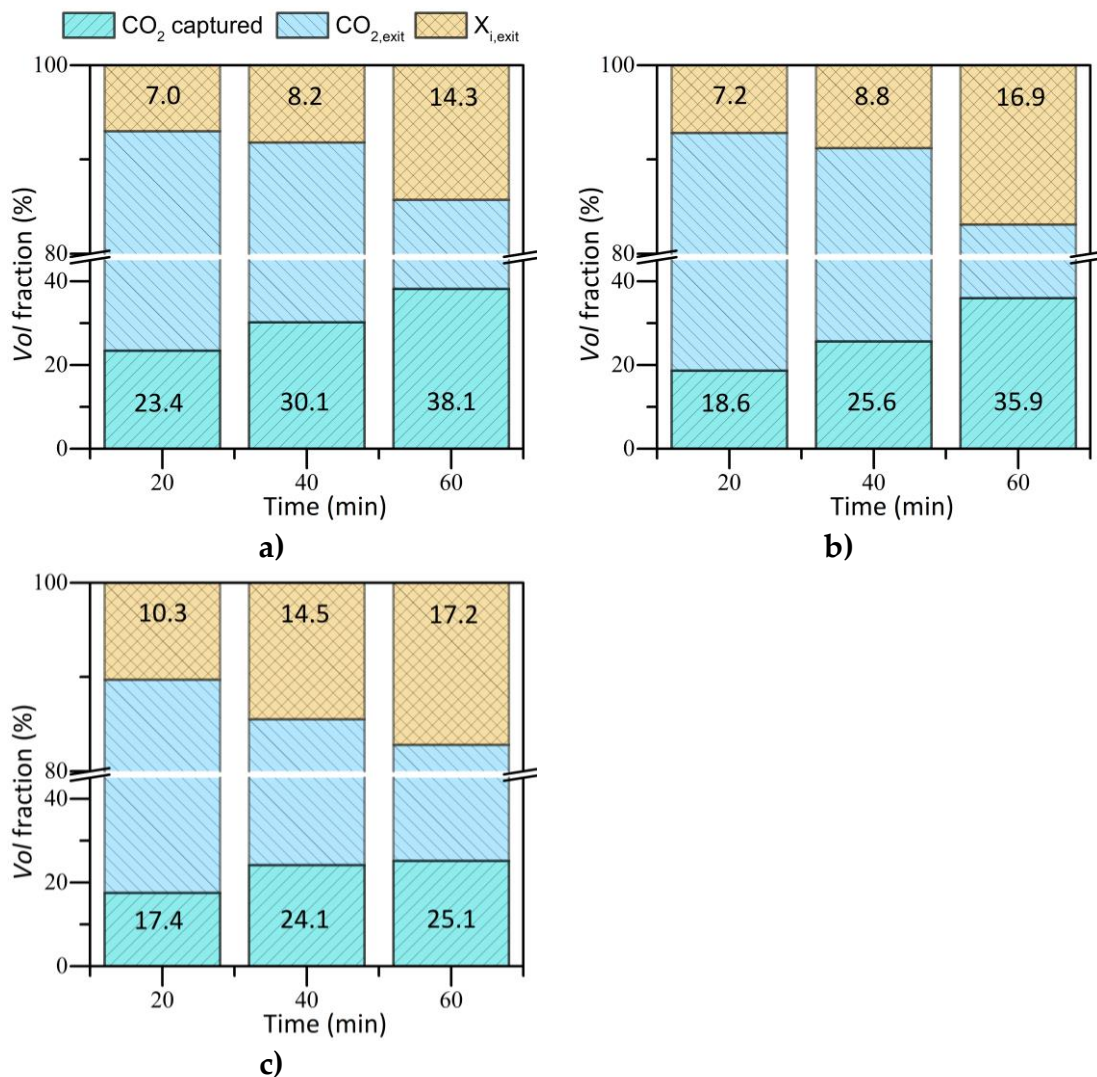


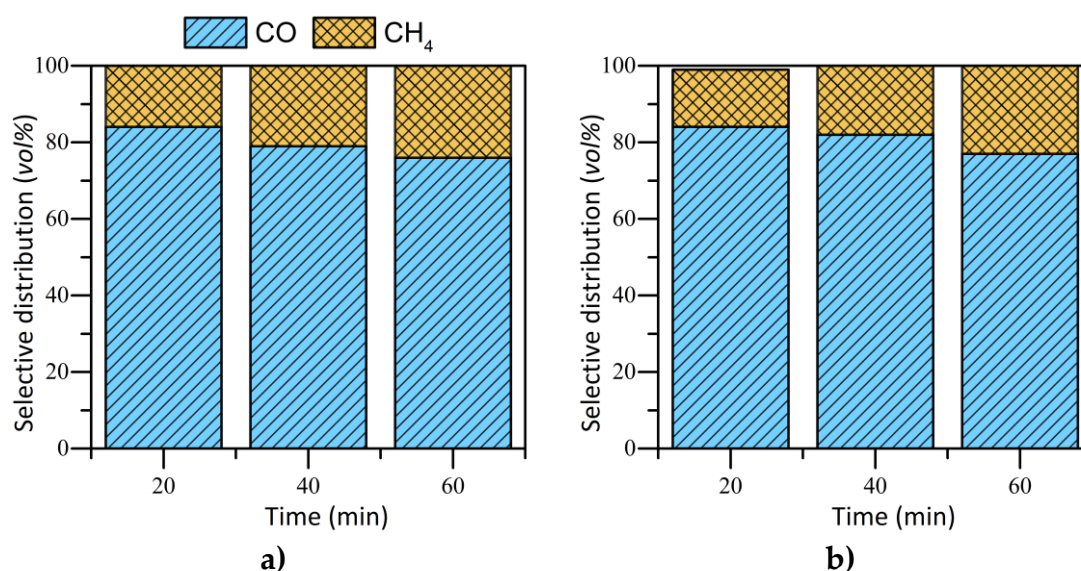
**Figure 12.** Volume fraction (%) of *in-situ* CO<sub>2</sub> adsorbed, CO<sub>2</sub> at the exit of TGA device, and CO<sub>2</sub> conversion ( $\sum X_{i,exit}$ ) during *n*-C<sub>7</sub> asphaltene catalytic gasification using C-CeNiPd at a) 170, b) 200, and c) 230°C.

### 3.3. Conversion of CO<sub>2</sub>

This section evaluates the selective distribution of produced gases from CO<sub>2</sub> conversion in different scenarios including i) conversion of CO<sub>2</sub> in ceria nanoparticles with steam, and ii) conversion of CO<sub>2</sub> during *n*-C<sub>7</sub> asphaltene steam gasification assisted by ceria nanoparticles.

### 3.3.1. Conversion of CO<sub>2</sub> in the presence of steam

The released gases (selective distribution of  $\sum X_{i_{exit,j}}$ ) during in-situ CO<sub>2</sub> adsorption were analyzed at a fixed temperature (200 °C). The released mixture was composed of non-adsorbed CO<sub>2</sub>, CH<sub>4</sub> and CO. In this part, 24%, 26%, 32%, and 33 %vol for S-CeO<sub>2</sub>, O-CeO<sub>2</sub>, C-CeO<sub>2</sub>, and C-CeNiPd, respectively, correspond to a mixture of CH<sub>4</sub> and CO. Based on these percentages, Figure 13 shows the selective distribution between CO and CH<sub>4</sub> %vol released at 200 °C. It is noted that CH<sub>4</sub> %vol released increased in the order S-CeO<sub>2</sub> < O-CeO<sub>2</sub> < C-CeO<sub>2</sub> < C-CeNiPd. For example, at 20 min of heating, CH<sub>4</sub> %vol was 16.0, 15.8, 15.4, and 13.0%vol for C-CeNiPd, C-CeO<sub>2</sub>, O-CeO<sub>2</sub>, and S-CeO<sub>2</sub>, respectively. Congruently with the higher values of  $I_{(598+1172)}/I_{458}$ , in C-CeNiPd, the introduction of Ni and Pd promoted the disorder of the CeO<sub>2</sub> supports to form more surface defect, which also indicated the existence of interaction between the metal and support. Similarly, the concentrations of Ce<sup>3+</sup> in the spent catalysts indicate the relative equilibrium of oxygen vacancies during the reaction process. Moreover, the presence of Ni<sup>0</sup> and NiO-CeO<sub>2</sub> species are considered as collaborative active sites for the activation of C-O bonds, during which CO<sub>2</sub> was dissociated on the Ni<sup>2+</sup>-CeO<sub>2</sub> interface while H<sub>2</sub> was dissociated on Ni<sup>0</sup>. The results suggest that the presence of steam molecules manages to activate reactions on the CeO<sub>2</sub> surface to simulate reactions that result in the generation of CH<sub>4</sub>.



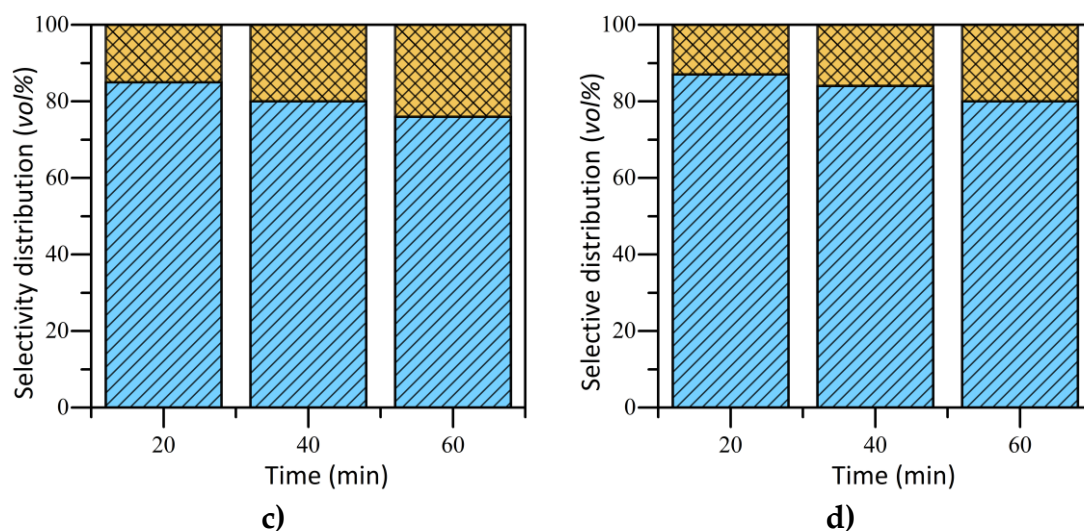


**Figure 13.** Selectivity distribution of light gases by CO<sub>2</sub> conversion in presence of steam over a) C-CeNiPd, b) C-CeO<sub>2</sub>, c) O-CeO<sub>2</sub>, and d) S-CeO<sub>2</sub> at 2000 °C. CO<sub>2</sub> flow rate = 60 mL·min<sup>-1</sup>, H<sub>2</sub>O<sub>(g)</sub> flow rate = 6.30 mL·min<sup>-1</sup>. Each gas is represented by the following colors: CO (blue) and CH<sub>4</sub> (yellow).

### 3.3.2. Conversion of CO<sub>2</sub> during asphaltene gasification

The effect of ceria morphology and Ni/Pd doping on evolved gases released from CO<sub>2</sub> conversion during *n*-C<sub>7</sub> asphaltene gasification at 200 °C was analyzed (Figure 14). The injection stream was mainly composed of CO<sub>2</sub> and CO<sub>2</sub> was not considered in the resulting gaseous mixture. The selectivity distribution in Figure 14 presents the produced gas mixture. Interestingly, the main produced gases were CO, CH<sub>4</sub>, H<sub>2</sub>, and light hydrocarbons (LHC). The remaining gases were neglected because their contribution was less than 0.05%*vol*. During the first 40 minutes of isothermal heating, a considerable production of CO was noted for all systems, being higher for C-CeNiPd and decreasing in the order C-CeO<sub>2</sub> > O-CeO<sub>2</sub> > S-CeO<sub>2</sub>. The CO can be produced from the direct interactions between CO<sub>2</sub> and carbon-based systems (like asphaltenes) or the Boudouard reaction by asphaltenes-H<sub>2</sub>O<sub>(g)</sub> interactions. The Boudouard reaction is exothermically enhancing the CO release with time. However, between 40-60 minutes, the CO %*vol* decreased, redistributing the produced gas mix and CO content was lowest for C-CeNiPd and highest for S-CeO<sub>2</sub>. This behavior could promote water-gas shift reactions, where CO is mainly transformed into H<sub>2</sub>. This agrees with the H<sub>2</sub> profiles, i.e., hydrogen production increases at the end of heating. The content of CH<sub>4</sub> follows a similar trend as CO. First, an increasing output during the first 40 min, and then decreasing. The S-CeO<sub>2</sub> nanoparticle presents the higher CH<sub>4</sub>



release between 1-60 min. CH<sub>4</sub> can be produced by breaking methyl, methylene, and other short aliphatic chains. Then, methane can produce H<sub>2</sub> by steam reforming reactions, which are assisted more easily in the cubic and cubic catalyst with Ni and Pd, which generate a more outstanding hydrogen production [94].

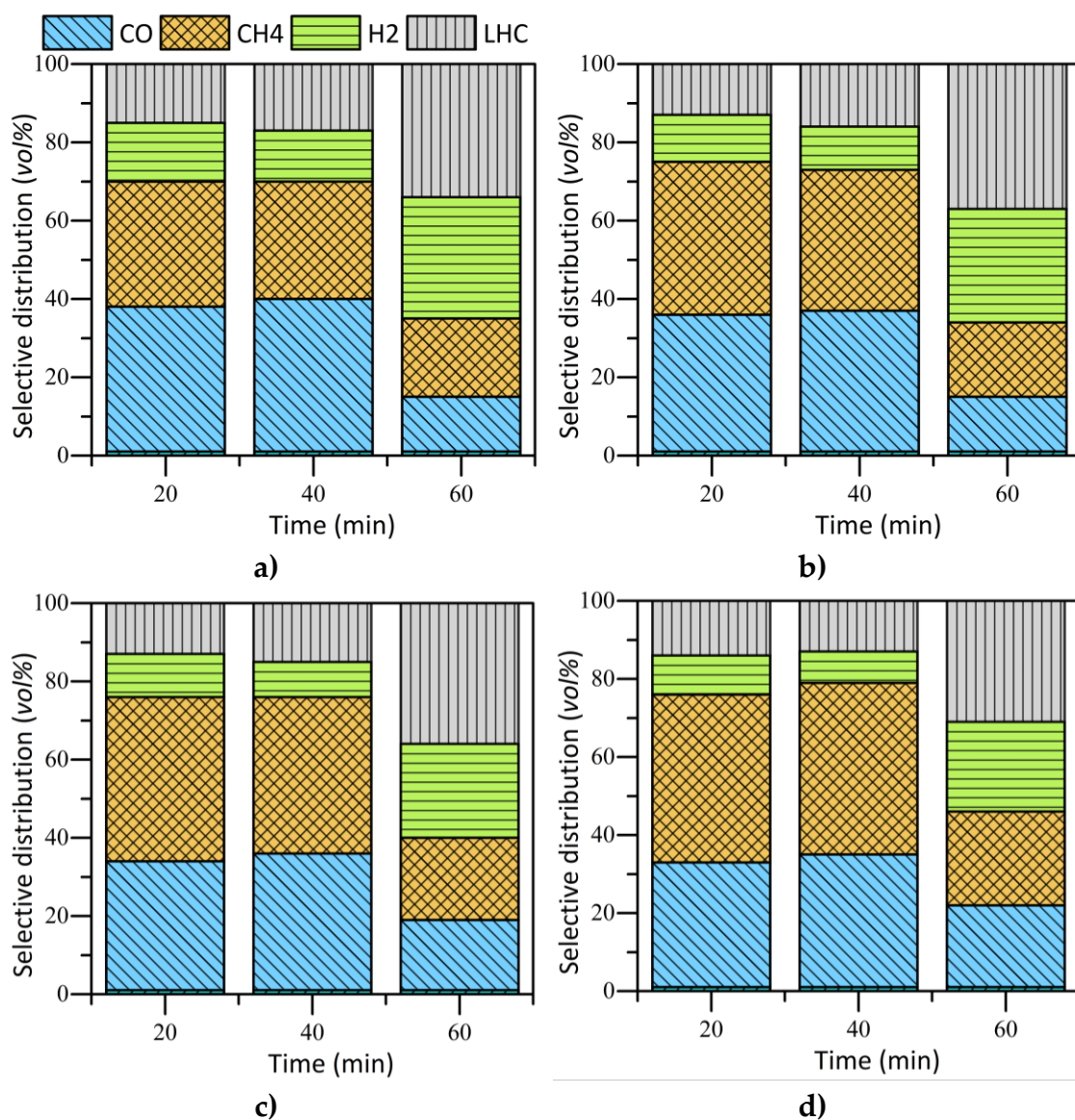
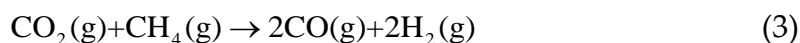


**Figure 14.** Selectivity distribution of light gases by CO<sub>2</sub> conversion during isothermal gasification of *n*-C<sub>7</sub> asphaltenes over a) C-CeNiPd, b) C-CeO<sub>2</sub>, c) O-CeO<sub>2</sub>, and d) S-CeO<sub>2</sub> at 200 °C. CO<sub>2</sub> flow rate = 60 mL·min<sup>-1</sup>, H<sub>2</sub>O<sub>(g)</sub> flow rate = 6.30 mL·min<sup>-1</sup>. Each gas is represented by the following colors: CO (blue), CH<sub>4</sub> (yellow), H<sub>2</sub> (green), and LHC (gray).

A mixture of LHC, composed mainly of C<sub>2</sub>H<sub>2</sub>, C<sub>2</sub>H<sub>4</sub>, and C<sub>6</sub>H<sub>6</sub>, was also observed in the three samples. The LHC released contains 50, 47, 45, and 34% of

C<sub>2</sub>H<sub>2</sub> when CO<sub>2</sub> and asphaltene conversion is developed by C-CeNiPd, C-CeO<sub>2</sub>, O-CeO<sub>2</sub>, and S-CeO<sub>2</sub>, respectively. The gas mixture presents an average calorific value of 87.22 kcal·kg<sup>-1</sup> for S-CeO<sub>2</sub>, 104.31 kcal·kg<sup>-1</sup> for O-CeO<sub>2</sub>, 121.26 kcal·kg<sup>-1</sup> for C-CeO<sub>2</sub>, and 142.94 kcal·kg<sup>-1</sup> for C-Ni1PdCe. LHC is produced mainly by the asphaltene breaking, and the different concentrations obtained are a response to each material's catalytic activity. As previously mentioned, hydrogen was produced by all materials within the measured time. The %*vol* released increased over time, reaching its maximum at 60 min. As a first instance, H<sub>2</sub> can be produced by the reaction of C in asphaltenes and H<sub>2</sub>O<sub>(g)</sub> molecules. Also, H<sub>2</sub> can be produced by CO<sub>2</sub> and CH<sub>4</sub> reactions, as shown in Equation (3). Methane and carbon monoxide content reduction while H<sub>2</sub> release increased indicates that steam reforming and water-gas shift reactions are probably taking place. The hydrogen production content follows a trend that agrees well with each material's adsorptive capacity and catalytic activity for *in-situ* CO<sub>2</sub> adsorption during asphaltene gasification at these conditions. The maximum H<sub>2</sub>%*vol* was 31%, 29%, 24%, and 23% for C-CeNiPd, C-CeO<sub>2</sub>, O-CeO<sub>2</sub>, and S-CeO<sub>2</sub>, respectively. These results suggest the participation of Ce<sup>3+</sup> in intermediate reactions that promotes hydrogen production.



#### 4. Conclusions

Three ceria nanoparticles with cubic (C-CeO<sub>2</sub>), orthorhombic (O-CeO<sub>2</sub>), and spherical (S-CeO<sub>2</sub>) were tested in CO<sub>2</sub> adsorption and conversion during *n*-C<sub>7</sub> asphaltene steam gasification. The best nanoparticle was doped with 1 wt.% of Ni and Pd (C-CeNiPd). First, asphaltene conversion was evaluated in all systems obtaining 100% conversion at 170, 200, and 230°C. The time required to obtain 100% conversion increased in the order: C-CeNiPd < C-CeO<sub>2</sub> < O-CeO<sub>2</sub> < S-CeO<sub>2</sub>. During the second experiment, CO<sub>2</sub> uptake was tested at different pressures. The adsorptive capacity of CO<sub>2</sub> increased in the direction S-CeO<sub>2</sub> < O-CeO<sub>2</sub> < C-CeO<sub>2</sub> < C-CeNiPd. The functionalization with the metallic phases significantly increases the adsorptive capacity of ceria support, obtaining a high CO<sub>2</sub> adsorption capacity during the 20 adsorption/desorption cycles. Then, CO<sub>2</sub> adsorption was evaluated during *n*-C<sub>7</sub> asphaltene decomposition. The results reveal that *in-situ* CO<sub>2</sub> adsorption (%) was 19.5, 23.3, and 26.2% in S-CeO<sub>2</sub>, O-

CeO<sub>2</sub>, and C-CeO<sub>2</sub>, respectively, at 170 °C. The adsorption rate decreased with temperature and reached the minimum at 230 °C. Interestingly, oxygen vacancies concentration and Ce<sup>3+</sup> content was found to follow the same trend that CO<sub>2</sub> adsorption, suggesting that both properties enhance the interactions between CO<sub>2</sub> and CeO<sub>2</sub>. Moreover, the presence of Ni and Pd also increases the interactions with CO<sub>2</sub> due to the increase in Lewis basic sites on the catalyst. Finally, for CO<sub>2</sub> conversion, a mixture of gases composed of CO, CH<sub>4</sub>, H<sub>2</sub>, and light hydrocarbons (LHC) was obtained. The hydrogen production content follows a trend that agrees well with the adsorptive capacity and catalytic activity of each material for *in-situ* CO<sub>2</sub> adsorption during asphaltene gasification. The maximum H<sub>2</sub>%vol at 200 °C was 31, 29, 24, and 23% for C-CeNiPd, C-CeO<sub>2</sub>, O-CeO<sub>2</sub>, and S-CeO<sub>2</sub>, respectively. These results suggest the participation of Ce<sup>3+</sup> in intermediate reactions that promotes hydrogen production.

Under the results of this work, it was possible to see the TEOR methods from another point of view, not as polluting and harmful methods for the environment, but as a solution that contributes to the energy transition through CCUS technologies. The development and implementation of nanotechnology in these processes would reduce their carbon footprint, increase oil productivity, improve the quality of crude oil through the decomposition of the heaviest oil fractions, and capture and use CO<sub>2</sub>

## References

- [1] Prentice IC, Farquhar G, Fasham M, Goulden M, Heimann M, Jaramillo V, et al. The carbon cycle and atmospheric carbon dioxide. 2001.
- [2] Wuebbles DJ, Jain AK. Concerns about climate change and the role of fossil fuel use. *Fuel processing technology* 2001;71(1-3):99-119.
- [3] Jardine CN. Calculating the environmental impact of aviation emissions. Environmental Change Institute, Oxford University Centre for Environment 2005.
- [4] Al-Mamoori A, Krishnamurthy A, Rownaghi AA, Rezaei F. Carbon capture and utilization update. *Energy Technology* 2017;5(6):834-49.
- [5] Kätelhön A, Meys R, Deutz S, Suh S, Bardow A. Climate change mitigation potential of carbon capture and utilization in the chemical industry. *Proceedings of the National Academy of Sciences* 2019;116(23):11187-94.

- [6] Ho H-J, Iizuka A, Shibata E. Carbon capture and utilization technology without carbon dioxide purification and pressurization: a review on its necessity and available technologies. *Industrial & Engineering Chemistry Research* 2019;58(21):8941-54.
- [7] Mohsin I, Al-Attas TA, Sumon KZ, Bergerson J, McCoy S, Kibria MG. Economic and environmental assessment of integrated carbon capture and utilization. *Cell Reports Physical Science* 2020;1(7):100104.
- [8] Patricio J, Angelis-Dimakis A, Castillo-Castillo A, Kalmykova Y, Rosado L. Region prioritization for the development of carbon capture and utilization technologies. *Journal of CO2 Utilization* 2017;17:50-9.
- [9] Gao W, Liang S, Wang R, Jiang Q, Zhang Y, Zheng Q, et al. Industrial carbon dioxide capture and utilization: state of the art and future challenges. *Chemical Society Reviews* 2020;49(23):8584-686.
- [10] Wang J, Huang L, Yang R, Zhang Z, Wu J, Gao Y, et al. Recent advances in solid sorbents for CO<sub>2</sub> capture and new development trends. *Energy & Environmental Science* 2014;7(11):3478-518.
- [11] Sun H, Wang J, Zhao J, Shen B, Shi J, Huang J, et al. Dual functional catalytic materials of Ni over Ce-modified CaO sorbents for integrated CO<sub>2</sub> capture and conversion. *Applied Catalysis B: Environmental* 2019;244:63-75.
- [12] Arellano-Trevino MA, Kanani N, Jeong-Potter CW, Farrauto RJ. Bimetallic catalysts for CO<sub>2</sub> capture and hydrogenation at simulated flue gas conditions. *Chemical Engineering Journal* 2019;375:121953.
- [13] Duyar MS, Trevino MAA, Farrauto RJ. Dual function materials for CO<sub>2</sub> capture and conversion using renewable H<sub>2</sub>. *Applied Catalysis B: Environmental* 2015;168:370-6.
- [14] Shao B, Hu G, Alkebsi KA, Ye G, Lin X, Du W, et al. Heterojunction-redox catalysts of Fe<sub>x</sub>Co<sub>y</sub>Mg<sub>10</sub>CaO for high-temperature CO<sub>2</sub> capture and in situ conversion in the context of green manufacturing. *Energy & Environmental Science* 2021;14(4):2291-301.
- [15] Kim SM, Abdala PM, Broda M, Hosseini D, Copéret C, Müller C. Integrated CO<sub>2</sub> capture and conversion as an efficient process for fuels from greenhouse gases. *ACS Catalysis* 2018;8(4):2815-23.

- [16] Hu J, Hongmanorom P, Galvita VV, Li Z, Kawi S. Bifunctional Ni-Ca based material for integrated CO<sub>2</sub> capture and conversion via calcium-looping dry reforming. *Applied Catalysis B: Environmental* 2021;284:119734.
- [17] Miguel C, Soria M, Mendes A, Madeira L. A sorptive reactor for CO<sub>2</sub> capture and conversion to renewable methane. *Chemical Engineering Journal* 2017;322:590-602.
- [18] Fang J, Jin X, Huang K. Life cycle analysis of a combined CO<sub>2</sub> capture and conversion membrane reactor. *Journal of Membrane Science* 2018;549:142-50.
- [19] Lin R, Guo J, Li X, Patel P, Seifitokaldani A. Electrochemical reactors for CO<sub>2</sub> conversion. *Catalysts* 2020;10(5):473.
- [20] Adams R, Khan A. Cyclic steam injection project performance analysis and some results of a continuous steam displacement pilot. *Journal of Petroleum Technology* 1969;21(01):95-100.
- [21] Lombard MS, Lee R, Manini P, Slusher MS. New Advances and a Historical Review of Insulated Steam-Injection Tubing. *SPE Western Regional and Pacific Section AAPG Joint Meeting*. OnePetro; 2008.
- [22] Bao Y, Wang J, Gates ID. On the physics of cyclic steam stimulation. *Energy* 2016;115:969-85.
- [23] Giacchetta G, Leporini M, Marchetti B. Economic and environmental analysis of a Steam Assisted Gravity Drainage (SAGD) facility for oil recovery from Canadian oil sands. *Applied Energy* 2015;142:1-9.
- [24] Kim D-S, Kwon Y-K, Chang C-D. Geological Characteristics of Extra Heavy Oil Reservoirs in Venezuela. *Economic and Environmental Geology* 2011;44(1):83-94.
- [25] Mohanty KK. Development of Shallow Viscous Oil Reserves in North Slope. University of Houston (US); 2004.
- [26] Santos R, Loh W, Bannwart A, Trevisan O. An overview of heavy oil properties and its recovery and transportation methods. *Brazilian Journal of Chemical Engineering* 2014;31(3):571-90.
- [27] Zan C, Ma D, Wang H, Li X, Guo J, Li M, et al. Experimental and simulation studies of steam flooding process in shallow, thin extra-heavy

- oil reservoirs. *International Oil and Gas Conference and Exhibition in China*. OnePetro; 2010.
- [28] Huang X, Wang P, Tian J, Qi Z, Yan W, Qian Y, et al. A novel method to assess steam injection rate in the steam-flooding process of shallow heavy oil reservoirs. *Energy Sources, Part A: Recovery, Utilization, and Environmental Effects* 2020;1-17.
- [29] Wang X, Sun X, Luo C, Zhang F, Xu B. Large-scale triaxial experimental investigation of geomechanical dilation start-up for SAGD dual horizontal wells in shallow heavy oil reservoirs. *Journal of Petroleum Science and Engineering* 2021;203:108687.
- [30] Dunn-Norman S, Gupta A, Summers DA, Koederitz L, Numbere DT. Recovery methods for heavy oil in ultra-shallow reservoirs. *SPE Western Regional/AAPG Pacific Section Joint Meeting*. OnePetro; 2002.
- [31] Rodriguez Acevedo E, Franco CA, Carrasco-Marín F, Pérez-Cadenas AF, Cortés FB. Biomass-Derived Carbon Molecular Sieves Applied to an Enhanced Carbon Capture and Storage Process (e-CCS) for Flue Gas Streams in Shallow Reservoirs. *Nanomaterials* 2020;10(5):980.
- [32] Lee J, Baik S, Cho SK, Cha JE, Lee JI. Issues in performance measurement of CO<sub>2</sub> compressor near the critical point. *Applied Thermal Engineering* 2016;94:111-21.
- [33] Rodriguez Acevedo E, Cortés FB, Franco CA, Carrasco-Marín F, Pérez-Cadenas AF, Fierro V, et al. An enhanced carbon capture and storage Process (e-CCS) applied to shallow reservoirs using nanofluids based on nitrogen-rich carbon Nanospheres. *Materials* 2019;12(13):2088.
- [34] Wang C, Liu P, Wang F, Atadurdyev B, Ovluyagulyyev M. Experimental study on effects of CO<sub>2</sub> and improving oil recovery for CO<sub>2</sub> assisted SAGD in super-heavy-oil reservoirs. *Journal of Petroleum Science and Engineering* 2018;165:1073-80.
- [35] Hamdi Z, Foo FK. Cold CO<sub>2</sub> and Steam Injection for Heavy Oil Recovery. *International Petroleum Technology Conference*. OnePetro; 2020.
- [36] Sun F, Yao Y, Li X. Effect of gaseous CO<sub>2</sub> on superheated steam flow in wells. *Engineering Science and Technology, an International Journal* 2017;20(6):1579-85.

- [37] Bagci A, Gumrah F. Effects of CO<sub>2</sub> and CH<sub>4</sub> addition to steam on recovery of West Kozluca heavy oil. *SPE international thermal operations and heavy oil symposium and western regional meeting*. OnePetro; 2004.
- [38] Ashley M, Magiera C, Ramidi P, Blackburn G, Scott TG, Gupta R, et al. Nanomaterials and processes for carbon capture and conversion into useful by-products for a sustainable energy future. *Greenhouse gases: science and technology* 2012;2(6):419-44.
- [39] Sreńscek-Nazzal J, Narkiewicz U, Morawski A, Wróbel R, Gęsikiewicz-Puchalska A, Michalkiewicz B. Modification of Commercial Activated Carbons for CO<sub>2</sub> Adsorption. *Acta Physica Polonica, A* 2016;129(3).
- [40] Amin F. A Study on the Adsorption and Catalytic Oxidation of Asphaltene onto Nanoparticles. *J Pet Sci Technol* 2017;7(2):21.
- [41] Cardona L, Arias-Madrid D, Cortés FB, Lopera SH, Franco CA. Heavy oil upgrading and enhanced recovery in a steam injection process assisted by NiO- and PdO-Functionalized SiO<sub>2</sub> nanoparticulated catalysts. *Catalysts* 2018;8(4):132.
- [42] Medina OE, Caro-Vélez C, Gallego J, Cortés FB, Lopera SH, Franco CA. Upgrading of extra-heavy crude oils by dispersed injection of NiO–PdO/CeO<sub>2±δ</sub> nanocatalyst-based nanofluids in the steam. *Nanomaterials* 2019;9(12):1755.
- [43] Medina OE, Hurtado Y, Caro-Velez C, Cortés FB, Riazi M, Lopera SH, et al. Improvement of steam injection processes through nanotechnology: An approach through in situ upgrading and foam injection. *Energies* 2019;12(24):4633.
- [44] Hamedi Shokrlu Y, Babadagli T. In-situ upgrading of heavy oil/bitumen during steam injection by use of metal nanoparticles: A study on in-situ catalysis and catalyst transportation. *SPE Reservoir Eval Eng* 2013;16(03):333.
- [45] Rathnaweera T, Ranjith P. Nano-modified CO<sub>2</sub> for enhanced deep saline CO<sub>2</sub> sequestration: A review and perspective study. *Earth-Science Reviews* 2020;200:103035.
- [46] Al-Yaseri A, Ali M, Abbasi GR, Abid HR, Jha NK. Enhancing CO<sub>2</sub> storage capacity and containment security of basaltic formation using silica

- nanofluids. *International Journal of Greenhouse Gas Control* 2021;112:103516.
- [47] Roy KS, Naik AK. Recent Development of Novel Composite Materials for Carbon Capture: A Green Technology. *Green Innovation, Sustainable Development, and Circular Economy* 2020:3-16.
- [48] Nassar NN, Hassan A, Pereira-Almao P. Clarifying the catalytic role of NiO nanoparticles in the oxidation of asphaltenes. *Appl Catal, A* 2013;462:116.
- [49] Afzal S, Nikookar M, Ehsani MR, Roayaei E. An experimental investigation of the catalytic effect of Fe<sub>2</sub>O<sub>3</sub> nanoparticle on steam injection process of an Iranian reservoir. *Iran J Oil Gas Sci Technol* 2014;3(2):27.
- [50] Medina OE, Gallego J, Acevedo S, Riazi M, Ocampo-Pérez R, Cortés FB, et al. Catalytic Conversion of n-C<sub>7</sub> Asphaltenes and Resins II into Hydrogen Using CeO<sub>2</sub>-Based Nanocatalysts. *Nanomaterials* 2021;11(5):1301.
- [51] Marei NN, Nassar NN, Vitale G, Hassan A, Pérez Zurita MJ. Effects of the size of NiO nanoparticles on the catalytic oxidation of Quinolin-65 as an asphaltene model compound. *Fuel* 2017;207:423.
- [52] Lozano MM, Franco CA, Acevedo SA, Nassar NN, Cortés FB. Effects of resin I on the catalytic oxidation of n-C<sub>7</sub> asphaltenes in the presence of silica-based nanoparticles. *RSC Adv* 2016;6(78):74630.
- [53] Nassar NN, Hassan A, Carbognani L, Lopez-Linares F, Pereira-Almao P. Iron oxide nanoparticles for rapid adsorption and enhanced catalytic oxidation of thermally cracked asphaltenes. *Fuel* 2012;95:257.
- [54] Arias-Madrid D, Medina OE, Gallego J, Acevedo S, Correa-Espinal AA, Cortés FB, et al. NiO, Fe<sub>2</sub>O<sub>3</sub>, and MoO<sub>3</sub> Supported over SiO<sub>2</sub> Nanocatalysts for Asphaltene Adsorption and Catalytic Decomposition: Optimization through a Simplex–Centroid Mixture Design of Experiments. *Catalysts* 2020;10(5):569.
- [55] Mateus L, Moreno-Castilla C, López-Ramón MV, Cortés FB, Álvarez MÁ, Medina OE, et al. Physicochemical characteristics of calcined MnFe<sub>2</sub>O<sub>4</sub> solid nanospheres and their catalytic activity to oxidize para-nitrophenol



- with peroxymonosulfate and n-C7 asphaltenes with air. *Journal of Environmental Management* 2021;281:111871.
- [56] Acevedo S, Ranaudo MaA, García C, Castillo J, Fernández A, Caetano M, et al. Importance of asphaltene aggregation in solution in determining the adsorption of this sample on mineral surfaces. *Colloids and Surfaces A: Physicochemical and Engineering Aspects* 2000;166(1-3):145-52.
- [57] Acevedo S, Escobar G, Gutiérrez LB, Rivas H, Gutiérrez X. Interfacial rheological studies of extra-heavy crude oils and asphaltenes: role of the dispersion effect of resins in the adsorption of asphaltenes at the interface of water-in-crude oil emulsions. *Colloids and Surfaces A: Physicochemical and Engineering Aspects* 1993;71(1):65-71.
- [58] Ayala M, Hernandez-Lopez EL, Perezgasga L, Vazquez-Duhalt R. Reduced coke formation and aromaticity due to chloroperoxidase-catalyzed transformation of asphaltenes from Maya crude oil. *Fuel* 2012;92(1):245-9.
- [59] Li N, Yan B, Xiao X-M. Kinetic and reaction pathway of upgrading asphaltene in supercritical water. *Chemical Engineering Science* 2015;134:230-7.
- [60] Trejo F, Rana MS, Ancheyta J. Thermogravimetric determination of coke from asphaltenes, resins and sediments and coking kinetics of heavy crude asphaltenes. *Catalysis Today* 2010;150(3-4):272-8.
- [61] Barre L, Espinat D, Rosenberg E, Scarsella M. Colloidal structure of heavy crudes and asphaltene solutions. *Revue de l'Institut Français du Pétrole* 1997;52(2):161-75.
- [62] Medina OE, Gallego J, Pérez-Cadenas AF, Carrasco-Marín F, Cortés FB, Franco CA. Insights into the Morphology Effect of Ceria on the Catalytic Performance of NiO–PdO/CeO<sub>2</sub> Nanoparticles for Thermo-oxidation of n-C7 Asphaltenes under Isothermal Heating at Different Pressures. *Energy & Fuels* 2021;35(22):18170-84.
- [63] Medina OE, Gallego J, Rodríguez E, Franco CA, Cortés FB. Effect of pressure on the oxidation kinetics of Asphaltenes. *Energy & Fuels* 2019;33(11):10734-44.

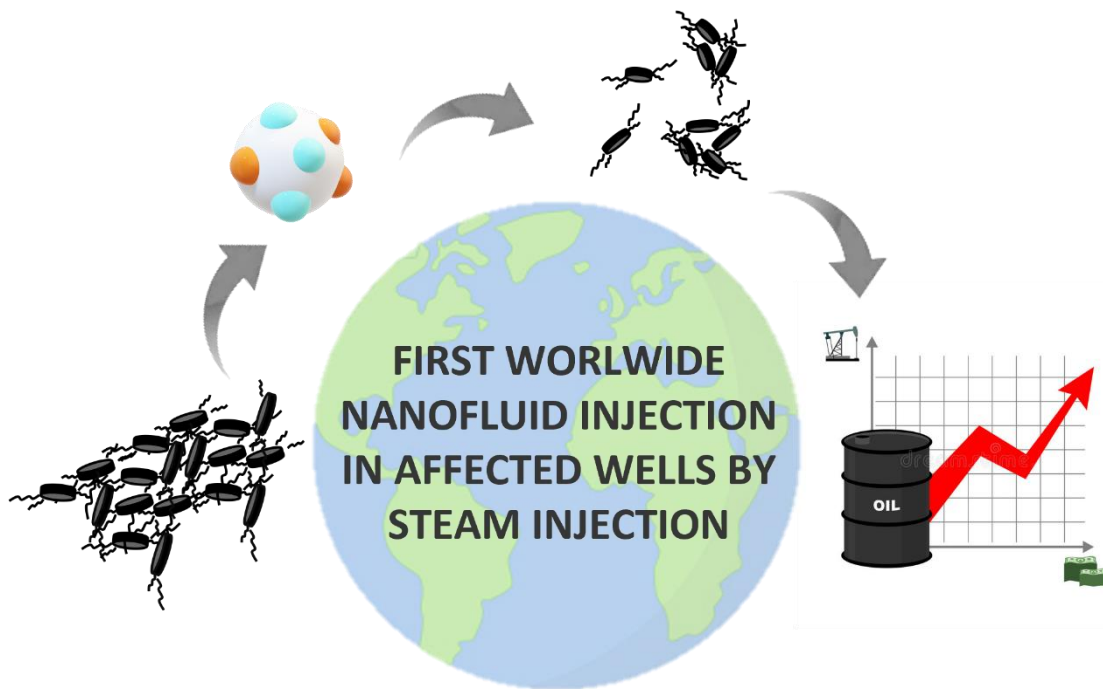
- [64] Carvajal-Bernal AM, Gomez-Granados F, Giraldo L, Moreno-Pirajan JC. Application of the Sips model to the calculation of maximum adsorption capacity and immersion enthalpy of phenol aqueous solutions on activated carbons. *European Journal of Chemistry* 2017;8(2):112-8.
- [65] Mullins OCS, E. Y., Eds.; Plenum Press: . Optical interrogation of aromatic moieties in crude oil sand asphaltenes. In *Structures and dynamics of asphaltenes*; New York, 1998.
- [66] Goncalves S, Castillo J, Fernandez A, Hung J. Absorbance and fluorescence spectroscopy on the aggregation behavior of asphaltene-toluene solutions. *Fuel* 2004;83(13):1823-8.
- [67] Sarker AI, Aroonwilas A, Veawab A. Equilibrium and kinetic behaviour of CO<sub>2</sub> adsorption onto zeolites, carbon molecular sieve and activated carbons. *Energy Procedia* 2017;114:2450-9.
- [68] Ojelade OA, Zaman SF, Daous MA, Al-Zahrani AA, Malik AS, Driss H, et al. Optimizing Pd: Zn molar ratio in PdZn/CeO<sub>2</sub> for CO<sub>2</sub> hydrogenation to methanol. *Applied Catalysis A: General* 2019;584:117185.
- [69] Karelovic A, Galdames G, Medina JC, Yévenes C, Barra Y, Jiménez R. Mechanism and structure sensitivity of methanol synthesis from CO<sub>2</sub> over SiO<sub>2</sub>-supported Cu nanoparticles. *Journal of Catalysis* 2019;369:415-26.
- [70] Albrecht PM, Jiang D-e, Mullins DR. CO<sub>2</sub> adsorption as a flat-lying, tridentate carbonate on CeO<sub>2</sub> (100). *The Journal of Physical Chemistry C* 2014;118(17):9042-50.
- [71] Yoshikawa K, Sato H, Kaneeda M, Kondo JN. Synthesis and analysis of CO<sub>2</sub> adsorbents based on cerium oxide. *Journal of CO<sub>2</sub> Utilization* 2014;8:34-8.
- [72] Yoshikawa K, Kaneeda M, Nakamura H. Development of Novel CeO<sub>2</sub>-based CO<sub>2</sub> adsorbent and analysis on its CO<sub>2</sub> adsorption and desorption mechanism. *Energy Procedia* 2017;114:2481-7.
- [73] Hahn KR, Iannuzzi M, Seitsonen AP, Hutter Jr. Coverage effect of the CO<sub>2</sub> adsorption mechanisms on CeO<sub>2</sub> (111) by first principles analysis. *The Journal of Physical Chemistry C* 2013;117(4):1701-11.
- [74] Ghalandari V, Hashemipour H, Bagheri H. Experimental and modeling investigation of adsorption equilibrium of CH<sub>4</sub>, CO<sub>2</sub>, and N<sub>2</sub> on activated

- carbon and prediction of multi-component adsorption equilibrium. *Fluid Phase Equilibria* 2020;508:112433.
- [75] Melouki R, Ouadah A, Llewellyn PL. The CO<sub>2</sub> adsorption behavior study on activated carbon synthesized from olive waste. *Journal of CO<sub>2</sub> Utilization* 2020;42:101292.
- [76] Huygh S, Bogaerts A, Neyts EC. How oxygen vacancies activate CO<sub>2</sub> dissociation on TiO<sub>2</sub> anatase (001). *The Journal of Physical Chemistry C* 2016;120(38):21659-69.
- [77] Lorber K, Zavasnik J, Arčon I, Huš M, Terzan J, Likozar B, et al. CO<sub>2</sub> activation over nanoshaped CeO<sub>2</sub> decorated with nickel for low-temperature methane dry reforming. *ACS Applied Materials & Interfaces* 2022;14(28):31862-78.
- [78] Hu J, Hongmanorom P, Chirawatkul P, Kawi S. Efficient integration of CO<sub>2</sub> capture and conversion over a Ni supported CeO<sub>2</sub>-modified CaO microsphere at moderate temperature. *Chemical Engineering Journal* 2021:130864.
- [79] Ratchahat S, Sudoh M, Suzuki Y, Kawasaki W, Watanabe R, Fukuhara C. Development of a powerful CO<sub>2</sub> methanation process using a structured Ni/CeO<sub>2</sub> catalyst. *Journal of CO<sub>2</sub> Utilization* 2018;24:210-9.
- [80] Shen W-J, Ichihashi Y, Ando H, Matsumura Y, Okumura M, Haruta M. Effect of reduction temperature on structural properties and CO/CO<sub>2</sub> hydrogenation characteristics of a Pd-CeO<sub>2</sub> catalyst. *Applied Catalysis A: General* 2001;217(1-2):231-9.
- [81] Li G, Xiao P, Webley PA, Zhang J, Singh R. Competition of CO<sub>2</sub>/H<sub>2</sub>O in adsorption based CO<sub>2</sub> capture. *Energy Procedia* 2009;1(1):1123-30.
- [82] Gonzalez DL, Vargas FM, Hirasaki GJ, Chapman WG. Modeling study of CO<sub>2</sub>-induced asphaltene precipitation. *Energy & Fuels* 2008;22(2):757-62.
- [83] Martens JA, Bogaerts A, De Kimpe N, Jacobs PA, Marin GB, Rabaey K, et al. The chemical route to a carbon dioxide neutral world. *ChemSusChem* 2017;10(6):1039-55.
- [84] Shi L, Yang G, Tao K, Yoneyama Y, Tan Y, Tsubaki N. An introduction of CO<sub>2</sub> conversion by dry reforming with methane and new route of low-

- temperature methanol synthesis. *Accounts of chemical research* 2013;46(8):1838-47.
- [85] Das S, Pérez-Ramírez J, Gong J, Dewangan N, Hidajat K, Gates BC, et al. Core-shell structured catalysts for thermocatalytic, photocatalytic, and electrocatalytic conversion of CO<sub>2</sub>. *Chemical Society Reviews* 2020;49(10):2937-3004.
- [86] Liu X, Zhou K, Wang L, Wang B, Li Y. Oxygen vacancy clusters promoting reducibility and activity of ceria nanorods. *Journal of the American Chemical Society* 2009;131(9):3140-1.
- [87] Li C, Liu X, Lu G, Wang Y. Redox properties and CO<sub>2</sub> capture ability of CeO<sub>2</sub> prepared by a glycol solvothermal method. *Chinese Journal of Catalysis* 2014;35(8):1364-75.
- [88] Pérez-Bailac P, Lustemberg PG, Ganduglia-Pirovano MV. Facet-dependent stability of near-surface oxygen vacancies and excess charge localization at CeO<sub>2</sub> surfaces. *Journal of Physics: Condensed Matter* 2021;33(50):504003.
- [89] Baumann N, Lan J, Iannuzzi M. CO<sub>2</sub> adsorption on the pristine and reduced CeO<sub>2</sub> (111) surface: Geometries and vibrational spectra by first principles simulations. *The Journal of Chemical Physics* 2021;154(9):094702.
- [90] Kašpar J, Fornasiero P, Graziani M. Use of CeO<sub>2</sub>-based oxides in the three-way catalysis. *Catalysis Today* 1999;50(2):285-98.
- [91] Li P, Chen X, Li Y, Schwank JW. A review on oxygen storage capacity of CeO<sub>2</sub>-based materials: Influence factors, measurement techniques, and applications in reactions related to catalytic automotive emissions control. *Catalysis Today* 2019;327:90-115.
- [92] Trovarelli A. Structural and oxygen storage/release properties of CeO<sub>2</sub>-based solid solutions. *Comments on Inorganic Chemistry* 1999;20(4-6):263-84.
- [93] López JM, Gilbank AL, García T, Solsona B, Agouram S, Torrente-Murciano L. The prevalence of surface oxygen vacancies over the mobility of bulk oxygen in nanostructured ceria for the total toluene oxidation. *Applied Catalysis B: Environmental* 2015;174:403-12.

- [94] Gradisher L, Dutcher B, Fan M. Catalytic hydrogen production from fossil fuels via the water gas shift reaction. *Applied Energy* 2015;139:335-49.

# Upscaling Process for Nanofluids Deployment in Wells Affected by Steam Injection Processes: Experimental Design and Field Trial Application.



# **Upscaling Process for Nanofluids Deployment in Wells Affected by Steam Injection Processes: Experimental Design and Field Trial Application.**

## **Abstract.**

The increasing demand for fossil fuels and the depletion of light crude oil in the following years generates the need to exploit heavy crude oils. To face this challenge, the oil and gas industry has implemented new technologies capable of improving the efficiency of the enhanced recovery oil (EOR) processes. In this context, incorporating nanotechnology by developing nanoparticles and nanofluids to increase the productivity of heavy and extra-heavy crude oils has become important. However, its implementation in field applications at upstream conditions is still underexplored. Thus, the primary objective of this study is to expose the methodology applied for carrying out an upscaling from a technology readiness level (TRL) of 3 up to a TRL-8 for the nanotechnology implementation at a field application in wells affected by steam injection processes, going through the experimental design and the initial field trial results. Nanofluids were designed to enhance the productivity of a heavy oil reservoir under cold injection (without steam) and with steam injection. The static tests showed the capability of the nanofluids to reduce the viscosity of the crude oil, the high affinity of the nanoparticles for the adsorption of heavy oil molecules as well as altering the wettability of the system to a strong water-wet state. Accordingly, displacement tests were conducted for both cold and hot scenarios, showing an improvement in oil mobility and recovery in the presence of the nanofluids compared to the system in the absence of nanotechnology.

Finally, a field trial application was performed in four wells in a Colombian field of interest. Two wells consisted of a cold nanofluid injection, and two included steam injection alongside the nanofluids. The main target of the field trial was to achieve an increase in oil mobility and reduce the amount of combustion gas required to develop the field. According to the field trial results, the benefits are mainly associated with the incremental production after the execution of the first 2 tests with nanofluids, one with steam and one cold (wells A and B) between June and July 2022. The incremental production perceived during 2022

corresponds to 8603 bbls related to 3231 bbl (well A) and 5372 bbl (well B). Similarly, with the execution of 2 additional tests, one with steam and one cold (wells C and D), between November and December 2022, benefits associated with technological implementation are reported in 430 bbl (well C) for the cold processes, and 980 bbl (well D) in the case of steam injection in the presence of nanofluids.



## 1. Introduction

The complexity of heavy (HO) and extra-heavy oils (EHO) is attributed to their high content of heavy fractions like asphaltenes and resins, reducing API gravity and increasing oil viscosity.<sup>1-5</sup> These properties affect the productivity of HO reservoirs and the cost-effectiveness of transport and refining operations.<sup>5,6</sup> Steam injection has been the main thermal enhanced oil recovery (TEOR) technique for exploiting HO and EHO reservoirs.<sup>7, 8</sup> Nevertheless, different problems, such as steam channeling,<sup>9</sup> loss of energy,<sup>10</sup> low thermal conductivity, and steam condensation, are associated with this process, reducing the efficiency and making the operation economically expensive.<sup>11</sup> Last but not least, the decomposition temperature of the heaviest fractions ranges around 550 °C, while in a steam injection operation, it is possible to reach temperatures between 250 - 300 °C.<sup>12, 13</sup>

In this context, nanometric-scale materials have been proposed to assist the steam injection processes. The small size of the nanoparticles (1-100 nm) favors their injection in the porous medium with a low risk of blockage. The properties of nanoparticles, such as high thermal conductivity,<sup>14</sup> excellent thermal stability,<sup>15</sup> high catalytic activity,<sup>16</sup> and selectivity towards heavy hydrocarbons,<sup>17</sup> can increase the efficiency of steam injection processes. One approach is related to using nanoparticles to increase the mobility of HO and EHO through the adsorption of asphaltenes, and the disruption of the viscoelastic network of crude oil.<sup>18, 19</sup> Different functionalized and non-functionalized nanoparticles have been widely studied for this purpose. The functionalized materials involve supporting nanoparticles such as SiO<sub>2</sub>,<sup>20</sup> Al<sub>2</sub>O<sub>3</sub>,<sup>21</sup> TiO<sub>2</sub>,<sup>22</sup> CeO<sub>2</sub>,<sup>23</sup> that are generally responsible for the high affinity for heavy hydrocarbons. The supports are doped with smaller nanoparticles/nanocrystals on their surface, commonly of metal oxides such as NiO, PdO, Fe<sub>3</sub>O<sub>4</sub>, and Co<sub>3</sub>O<sub>4</sub>,<sup>20, 23-28</sup> which act as an active phase to increase the adsorptive capacity and catalytic activity. It has been demonstrated that these nanoparticles can decompose the heaviest fraction of crude oil at temperatures that can be found in a steam injection process (< 250 °C).<sup>23, 29</sup> Although important advances were made in the application of nanotechnology to assist steam injection processes, the maturity of the technique was a technological readiness level of 3 (TRL-3).

The evaluation of nanoparticles under dynamic conditions will guarantee the success of their application under field conditions. The injection of the nanoparticles into the porous medium has been carried out mainly through batch injection of the nanofluid containing the nanocatalysts<sup>24</sup> or a pre-treatment of the heavy crude oil sample under static conditions.<sup>30</sup> Yuan et al.<sup>30</sup> employed nickel nanoparticles to promote aqua-thermolysis reactions during CSS processes.<sup>30</sup> The authors evaluated the effect of Ni nanoparticles' presence, concentration, and penetration depth at low temperatures between 150 and 220 °C.<sup>30</sup> They found that the highest recovery factor was generated with a mass fraction of 0.02 % of nickel nanoparticles at 220 °C, associated with the breakdown of C-S bonds.<sup>30</sup> However, the effect of nanoparticles tends to decrease significantly with the passage of cycles.

Similarly, Cardona et al.<sup>24</sup> used silica nanoparticles with 1.0 wt.% of nickel and palladium oxides at 220 °C for the steam injection test. The authors found an increase from untreated crude oil to upgraded oil in API gravity from 7.2° to 12.1° and reductions in the asphaltene content of 40%. Although the injection of nanofluid in batch mode showed promising results, the nanofluid injection into the reservoir must be considerably improved to achieve deeper penetration and a better distribution within the porous spaces to generate more interaction with the heavy crude oil.

In this way, recently, a novel technique for well stimulation and fluid injection known as gas stimulation (GaStim) was proposed by Franco et al.<sup>31</sup> and Restrepo et al.<sup>32</sup> The method consists of the dispersion of a liquid treatment on the gas stream, achieving high injection rates and liquid droplets with a smaller size, and increasing the invasion radius of the liquid around the injector well.<sup>32</sup> Medina et al.<sup>33</sup> reported positive results in injecting nanofluid dispersed in the steam stream. The oil recovery increased by 25 and 42% for the dispersed injection of the nanofluid in the steam stream and after a soaking time of 12 h.<sup>23,</sup>

<sup>34</sup>

With these studies, it was achieved nearly a TRL-4. However, a robust study that compiles these advances to achieve a TRL-8 (field test) was still missing.

From the last, it was concluded that relevant advances were needed to reach the upscaling from a TRL-3 to a TRL-8. Therefore, the main objective of the present study was to compile the experimental proof of concept necessary to apply the nanofluids at an upstream operation alongside the missing methodological steps which would guide the technique maturity up to a TRL-8. Thus, this text presents the experimental design and the first worldwide field trial

application of nanofluids implementation in wells affected by steam injection processes.

## 2. Experimental

### 2.1. Materials

Petroraza S.A.S. (Medellín, Colombia) provided commercial silica and alumina nanoparticles for laboratory experimentation. The nanoparticles consist of 4.5 nm silica-based nanoparticles and 76 nm alumina-based nanoparticles, which were applied for cold and steam injection operations, respectively. Two carrier fluids (CF) for nanofluids design were also provided by Petroraza S.A.S. CF1 and NF1 were the fluids used in the cold evaluation, whereas CF2 and NF2 were used to assist the steam injection. The general properties of the carrier fluids and the designed nanofluids are shown in Table 1. It is worth mentioning that the carrier fluids are oil-based.

**Table 1.** Basic characteristic of the carrier fluids and nanofluids.

Properties	CF1	NF1	CF2	NF2
Density (g mL <sup>-1</sup> )	0.86	0.86	0.96	0.96
Viscosity (cP)	3.11	3.08	2.13	3.05
Surface tension (mN m <sup>-1</sup> )	25.71	24.75	24.23	23.01
Conductivity (mS cm <sup>-1</sup> )	6.6	7.2	4.9	5.7
Thermal conductivity (W mK <sup>-1</sup> )	0.1112	0.1123	0.1502	0.1562
Thermal resistivity (°C cm W <sup>-1</sup> )	786	784	660	640

The reservoir fluids (heavy oil and brine) were used in different steps of the experimental work. The characteristics of the crude oils are summarized in Table 2. API gravity measurement followed the ASTM D-1250 standard, while SARA analysis followed the IP 469 standard using a TLC-FID/FPD Iatronscan MK6 (Iatron Labs Inc, Tokyo, Japan). The brine was formulated to resemble the composition of the in-situ brine. It included the salts NaCl, CaCl<sub>2</sub>.2H<sub>2</sub>O, MgCl<sub>2</sub>.6H<sub>2</sub>O, BaCl<sub>2</sub>.2H<sub>2</sub>O, and KCl, all provided by Sigma Aldrich (St. Louis, MO, USA). Asphaltenes and resins were isolated from the crude oil following the ASTM D2892 and ASTM D5236 standards.<sup>3, 35</sup>

**Table 2.** Basic characteristics of heavy crude oil for the steam injection test.

Properties	HO1	HO2
API °	12.1	11.6
Viscosity 25°C (cP)	6400	4500
SARA content	Saturates (%)	25.9
	Aromatic (%)	48.28
	Resins (%)	24.04
	Asphaltenes (%)	1.78
Oil effective permeability	541	1887

Dynamic tests were executed using the reservoir fluids. Sand samples (Ecopetrol S.A.) from the oil fields were used for porous media assembly based on the procedure described elsewhere.<sup>36</sup> Methanol 99.8%, toluene 99.8%, and HCl 37%, all provided by Merck KGaA (Darmstadt, Germany), were used for porous media cleaning.<sup>36, 37</sup> The porosity of the porous media was obtained by a saturation method,<sup>36, 37</sup> and the permeability using Darcy's law equation. The porous volume for the cold process was found at 18.1 mL, and the porosity at 23.0%. In the case of steam injection, the pore volume and porosity were 202 mL and 26.0%, respectively. Steam was generated using deionized water (3  $\mu\text{S}\cdot\text{cm}^{-1}$  conductivity).

## 2.2. Methods

### 2.2.1. Nanoparticles characterization

The surface area of the nanoparticles was obtained by nitrogen adsorption/desorption hysteresis at -196 °C using a Micromeritic ASAP2020 (Micromeritics, Norcross, GA, U.S.A.). Brunauer-Emmett-Teller (BET) equation was used to determine the specific surface area ( $S_{\text{BET}}$ ). To characterize the active phases on  $\text{Al}_2\text{O}_3$  nanoparticles the following techniques were applied. Inductively coupled plasma mass spectrometry (ICP-MS) was used to estimate the final metal loading of Ni and Pd on  $\text{Al}_2\text{O}_3$  nanoparticles based on the procedure described in the previous work.<sup>38</sup> Metal dispersion and the average size of the nanocrystals of Ni and Pd were determined by hydrogen titration in a Chembet 3000 (Quantachrome Instruments, Boynton Beach, FL, USA.). XRD analysis was performed on a Bruker D8 Venture X-ray diffractometer (Bruker, Rivas-Vaciamadrid, Spain) using a Cu-K $\alpha$  target (wavelength  $\lambda = 1.5405 \text{ \AA}$ ). The samples were analyzed in the  $2\theta$  range of 1–70°. The valence states of the elements in the samples were characterized using XPS (VG-Microtech Multilab 3000). A monochromatic Al K $\alpha$  source with step energy of 90 eV (1 eV step) and 20 eV (0.1 eV step) was used for general high-resolution spectra ( $\text{O}_{1s}$ ,  $\text{Al}_{3d}$ ,  $\text{Ni}_{2p}$ ,

and Pd<sub>3d</sub>). Calibration of the adventitious C=C peak was performed at 284.8 eV. All patterns were analyzed using the XPSpeak4.1 software.

### 2.2.2. Nanoparticle evaluation.

Nanoparticles were evaluated by asphaltene and resin adsorption and thermogravimetric analysis. Adsorption isotherms were constructed using a colorimetric method in a UV-vis spectrophotometer Genesys 10S UV-VIS (Thermo Scientific, Waltham, MA, USA) following the protocols described elsewhere.<sup>39, 40</sup> Concentrations between 100 mg L<sup>-1</sup> and 2000 mg L<sup>-1</sup> of asphaltenes or resins were used and diluted in toluene.<sup>13</sup> The amount of *n*-C<sub>7</sub> asphaltenes adsorbed "Nads" in units of mg m<sup>-2</sup> was obtained from the mass balance  $Nads = (C_0 - C_E) \cdot M / A$ , where  $C_E$  (mg L<sup>-1</sup>) and  $C_0$  (mg L<sup>-1</sup>) denote the hydrocarbon concentration after adsorption, and initial concentration,  $M$  (L g<sup>-1</sup>) is the ratio of the solution volume to the dry mass of the nanoparticles (0.1) and  $A$  (m<sup>2</sup> g<sup>-1</sup>) is the measured surface area per unit mass of the nanoparticles.

The catalytic activity of nanoparticles to increase the asphaltene/resin conversion at low temperatures was measured by high-pressure thermogravimetric analysis using a HP-TGA 750 (TA instruments Inc., Hüllhorst, Germany). Isothermal runs were done at 250 °C and 900 psi, considering the steam injection temperature and the pressure of the heavy oil field, respectively. The experiments were executed for an asphaltene/resin adsorbed amount of 0.2 mg m<sup>-2</sup> ± 0.02 mg m<sup>-2</sup>. Details of the equipment tools and protocols can be found in our previous studies.<sup>31</sup>

### 2.2.3. Nanofluid design.

#### 2.2.3.1. Cold process

Nanofluids were evaluated as viscosity reducers through steady shear analysis using a Kinexus Pro rotational rheometer (Malvern Instruments, Worcestershire – UK) at 25 °C in a shear rate range between 1 and 100 s<sup>-1</sup>. Measurements were done with a plate-plate geometry of 20 mm diameter and 3.0 μm gap. To analyze the change in viscosity induced by the addition of nanofluids, the HO1 was mixed with 4% v/v of nanofluid containing several concentrations of silica-based nanoparticles, namely 0, 100, 300, and 500 mg L<sup>-1</sup>, dispersed in CF1.

It was estimated how the nanofluids would affect wettability. To achieve this, a sandstone outcrop sample was sliced, cleaned, dried, and then aged using the technique suggested in the earlier research. In a nutshell, the samples were

aged for 200 hours at 65 °C in a 40:60 mixture of HO1 and *n*-heptane.<sup>41</sup> An imbibition test and contact angle measurement were performed after that. The sandstone outcrops were submerged in the nanofluids containing 0, 100, 300, and 500 mg L<sup>-1</sup> of silica nanoparticles in CF1 at 70 °C for 12 hours and then removed from the corresponding nanofluid and dried at 70 °C for 24 h. The Attention Theta optical tensiometer (Biolin Scientific, Finland) was used to measure the contact angle of aged and restored samples using the sessile drop technique under reservoir pressure and temperature. With the help of the Young-Laplace model and the Attention Theta software (Biolin Scientific, ver. 4.1.0), static contact angles for oil/water/sandstone systems were calculated.<sup>42</sup> Additionally, spontaneous imbibition tests were evaluated using the synthetic brine in the aged core samples at reservoir temperature. The wettability of the rock surface has a significant impact on the water imbibition test, which involves the water uptake without applying pressure and driving the phase into the rock pores. Once the rock is submerged in an aqueous solution, the weight of the samples is recorded as a function of time. The test's initial and final weight values are used to normalize the weight data, yielding a normalized water weight fraction plotted as a time function. A high water-wet character can be seen in rock samples showing a high water imbibition rate. The rock surface is more oil-wet when the rate of water imbibition is low. In this sense, the ratio of the desired weight ( $W_t$ ) to the maximum sample weight ( $M_w$ ) at the point at which the fluids saturate the medium is recorded. According to each measurement, the standard deviation for spontaneous imbibition tests and contact angle measurements ranged between  $\pm 0.07$  and  $\pm 2.6^\circ$ , respectively.

Finally, using a spinning drop tensiometer (SDT; Kruss GmbH, Germany), the interfacial tension (IFT) value between the reservoir's fluids in the presence of the proposed nanofluids was measured by adding a drop of the oil phase to brine solutions at 70 °C. For measurements, crude oil and nanofluid are combined in the oil phase at a 20:80 ratio. The IFT value was measured using Vonnegut's equation.<sup>43</sup>

#### 2.2.3.2. Steam injection process.

The dosage of nanoparticles was determined through HO2 upgrading tests. To this aim, the CF2 was mixed with different concentrations of AlNiPd, including 0, 500, 1000, and 2000 mg L<sup>-1</sup>. During these tests, mixtures of HO2 and 5 wt.% CF2 were made. These systems are mechanically stirred to ensure the complete dilution of the CF2 in the HO2. The defined amount of nanoparticles is

then added and stirred manually until the nanoparticles are dispersed (10 minutes of mixing). The systems are deposited in the reactor programmed to set a temperature of 250 °C, like the conditions of the steam injection test. The systems are heated for 5 hours and are subsequently dried under an ice bath at 2 °C to ensure condensation of the light compounds in the system. Next, they are characterized by API gravity and dynamic viscosity following the procedures described in section 2.3.5.

#### 2.2.3.3. Nanofluids stability.

The suspension stability of the nanofluid was investigated using a UV-Vis spectrophotometer. Initially, the sample is subjected to an ultrasound bath for 4 hours to be transferred to a UV-Vis spectrophotometer. The stability is determined by the absorbance ratio ( $A/A_0$ ). The initial absorbance ( $A_0$ ) is the absorbance value of the reference fluid (carrier fluid). The final absorbance ( $A$ ) is the absorbance value of the nanofluid. This condition will reflect the constant absorbance value over time and is perfectly stable for suspended particles without settling occurring during the settling period.

#### 2.2.4. Dynamic test

##### 2.2.4.1. Cold process

The impact of nanoparticles on oil mobility at reservoir pressure and temperature conditions is assessed by analyzing relative permeability curves and oil recovery before and after the treatment. The "base system test" sought to ascertain the relative permeabilities of water and oil in the absence of nanoparticles. The wettability of a reservoir can change throughout the reservoir's producing life, regardless of the origin and mineralogical makeup of the porous media. For this reason, the "base system test" involved aging the porous media for wettability restoration. HO1 is continuously injected for 15 days to achieve this. Once the system is assumed to have become more oil-wet, oil ( $k_o$ ) and water ( $k_w$ ), which stand for the end-point effective permeabilities of the oil and water phases, are measured. To do this, 20 pore volumes (PV) of water must first be injected at conditions of oil residual saturation ( $S_{or}$ ), and then 20 PV of oil must be injected at conditions of water residual saturation ( $S_{wr}$ ). In order to prepare the core for nanofluid injection, the sample is once more saturated with oil in a secondary drainage process. The "post nanoparticles injection" is obtained by injecting 1 PV in production direction, which is left to

soak for 12 hours. Following the process mentioned above, values for the  $k_o$ ,  $k_w$ ,  $k_{rw}$ ,  $k_{ro}$ , and recovery curves are then obtained.

#### 2.2.4.2. Steam injection.

Crude oil recovery was analyzed through displacement tests simulating a steam injection operation. Steam quality was fixed at 80% at the entry of the porous medium.<sup>33, 36</sup> The test was divided into three main stages, including i) oil recovery estimation by steam injection, ii) nanofluid injection dispersed in the steam stream and nanofluid soaking (12 h), and iii) oil recovery estimation by steam injection after nanofluid soaking. During the tests, the steam was injected between 3 and 5 mL min<sup>-1</sup>, and nanofluid was dispersed in the steam at 0.5-1 mL min<sup>-1</sup>. The first and third stages end when no more oil production is obtained. The pressure profile was monitored during the complete process to ensure the nanofluid transport in the steam stream. The overburden and pore pressure were fixed at 900 psi and 150 psi, respectively. The experimental assembly used for steam injection tests can be found in our previous work.<sup>33</sup>

#### 2.2.4.3. Effluents characterization.

The crude oil samples recovered from steam injection tests were characterized by API gravity, rheology measurements, and content of saturates, aromatics, resins, and asphaltenes, following the protocols described elsewhere.<sup>36, 44</sup> The perdurability of the treatment was monitored by API gravity and dynamic viscosity as a function of time for four consecutive weeks.

#### 2.2.5. Upscaling and field test.

The upscaling process for the candidates' selection was based on four steps: 1) determining the criteria for the technology application in terms of limitations, required facilities, production rate, and reserves requirements, 2) steady-state and relevant environment experimentation and upscaling results, 3) surface facilities management and 4) candidate selection. The numerical simulation required in step 2 is reported by Bueno et al.<sup>45</sup> The authors introduce a benchmark case to compare thermal results and numerical verification of our recent upgrading experiment.<sup>33</sup> With the calibrated parameters, the model can reproduce experimental measurements during the steam and nanoparticles injection, such as the enhanced oil recovery and the improvement of thermodynamic properties such as density (or API gravity) and viscosity. The model also provides additional insights into important time-dependent



processes, such as local kinetic reactions, nanoparticle retention on the porous rock, or species distribution, that cannot be measured in the laboratory.

Critical variables considered in the first step include the petrophysical properties, accumulated oil, decline index, water cur, reserves, and well integrity. In the third step, other variables associated with the EOR process were considered. Some variables were the production method, the well-completion conditions, the type of steam injection technique, and, based on the last, the number of cycles. Different analyses compared the candidate's performance regarding other indexes and/or variables. Then, scatter plots are used, and the graphs are divided into quadrants. This qualitative analysis provides practical information on the candidates to classify and rank them. In this sense, the candidates were chosen based on their reserves versus production rate analysis.

The chosen well for nanofluid injection under cold conditions (without steam) was previously affected by cyclic steam stimulation. Before the nanofluid intervention, the well was producing about 19 BOPD, and it was anticipated that production would quickly fall below 5 BOPD. Figure 1 depicts the protocol followed for nanofluid stimulation without steam. In the first step, 26 bbl of NF1 were injected in a liquid batch through the well tubing. Second, three injections of KCL-inhibited brine were performed. In the first injection, 14 bbls of brine inhibited with  $250 \text{ mg L}^{-1}$  of KCl were injected through the tubing to displace the remaining nanofluid. Next, 63 bbl of the same brine was injected through the annulus to fill the well. Finally, 133 bbl of inhibited brine containing  $10000 \text{ mg L}^{-1}$  of KCl is injected to displace the nanofluid in the reservoir. Nanofluid was left to soak for 1 week, and then the well was opened to production.

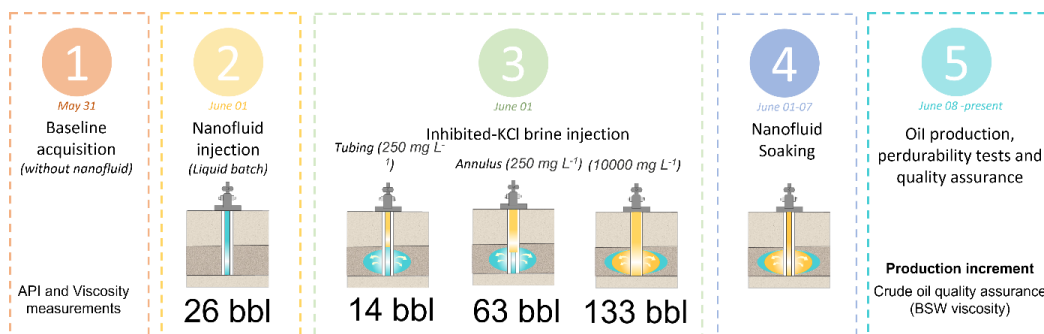


**Figure 1.** Scheme describing the field trial application process for nanofluid injection in a cold process.

The selected candidate for nanofluids injection in the steam injection is counted with a cyclic steam stimulation. The system configurations include 1100

psi injection pressure, 80% generator outlet steam quality, 70% estimated downhole steam quality, 5–10-day injection time, 3-5 days steam soaking, 4 to 8 months production time, and volume of steam injected around 56-68 Bcwe/ft-net/cycle. The well was producing about 25 BOPD before stimulation, and under the forecast scenario, in five months, production will decline below 5 BOPD. These characteristics make the selected well an attractive candidate for the field trial application.

The field trial process is schematized in Figure 2. The process consisted of injecting 204 bbl of NF2 in a liquid batch. Subsequently, the conventional procedure of CSS was done. Steam was injected for 12 days, which in turn displaces the nanofluid and increases its penetration radius. Steam and nanofluid soaking was done for five days, and the production stage started.

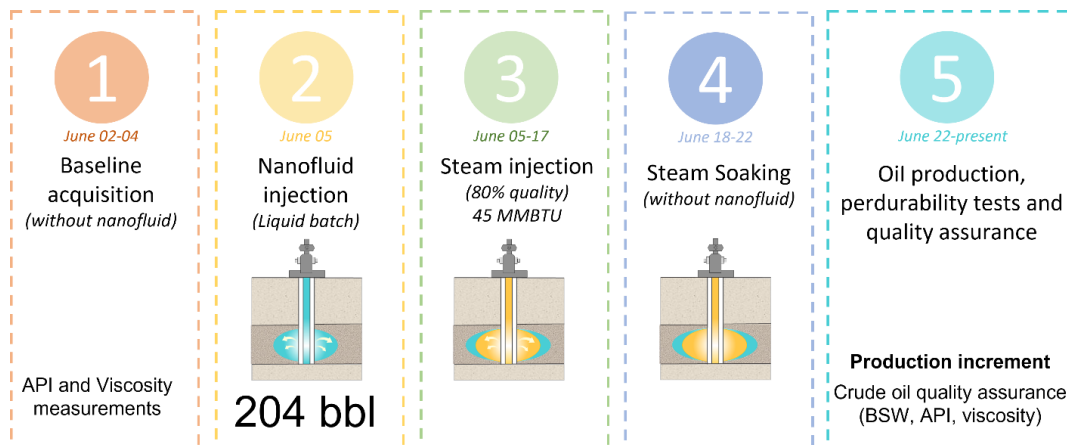


**Figure 2.** Scheme describing the field trial application process for nanofluid injection in steam injection process.

### 3. Results and discussion

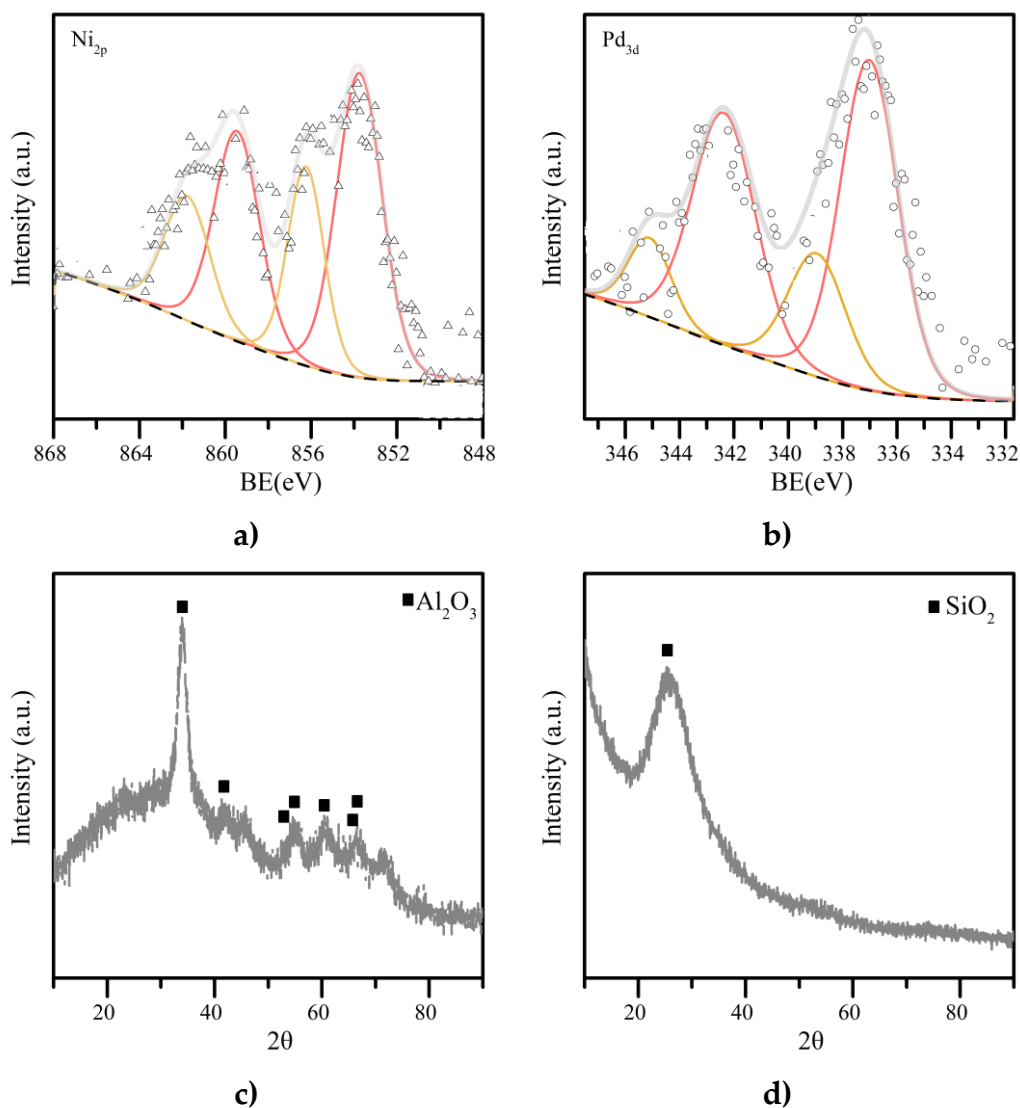
#### 3.1. Nanoparticles characterization

Table 3 summarizes some general properties of the nanoparticles, including surface area ( $220.4 \text{ m}^2 \text{ g}^{-1}$ ), hydrodynamic diameter (76.0 nm), and final doped amount of Ni and Pd (close to 1 wt.%). Based on XPS analysis, the core level binding energies of alumina exhibit two remarked peaks at 117.21 eV and 74.19 eV, ascribed to  $\text{Al}_{1s}$  and  $\text{Al}_{2p}$  species, respectively. The peak at the highest binding energy corresponds to Al-metal bonds, whereas the other peak refers to Al-O.  $\text{N}_{2p_{3/2}}$  and  $\text{Pd}_{3d_{5/2}}$  spectra are shown in Figure 3 (panels a and b). The  $\text{N}_{2p_{3/2}}$  spectral region shows predominant peaks at  $852.9 \pm 0.3$  and  $856.0 \pm 0.4$  eV ascribed to  $\text{Ni}^{2+}$  species in NiO (28%) and NiO–Al (24%), respectively. The other two peaks at

higher binding energies refer to satellite structures. 4 peaks described the Pd<sub>3d5/2</sub>. Pd<sup>2+</sup> is found as PdO at 336.9 ± 0.3 eV and PdO<sub>2</sub> at 342.5 ± 0.3 eV.

**Table 3.** Basic properties of the nanoparticle.

Sample	Doped amount (%)		S <sub>BET</sub> ± 0.1 m <sup>2</sup> ·g <sup>-1</sup>	Hydrodynamic diameter	dp (nm ± 0.2 nm)		Dispersion (%)	
	Ni	Pd			NiO	PdO	NiO	PdO
AlNiPd	1.12	0.98	220.4	76.0	5.4	3.2	22	30
SiO <sub>2</sub>	-	-	379.0	4.5	-	-	-	-



**Figure 3.** (a) Ni<sub>2p</sub> spectra, (b) Pd<sub>3d</sub> spectra, and XRD pattern of (c) AlNiPd and (d) SiO<sub>2</sub>.

Panel c of Figure 3 shows the diffraction peaks of crystalline AlNiPd. The peaks observed at 2θ = 25.54, 35.10, 37.73, 43.34, 52.51, 57.50, 61.33, 66.44, and

68.18° correspond to the (012), (104), (110), (113), (024), (116), (018), (214) and (300) reflections of the Al<sub>2</sub>O<sub>3</sub> nanoparticles (JCPDS 001–1243). The average crystallite size of Al<sub>2</sub>O<sub>3</sub>, NiO, and PdO, the Debye-Scherrer approximation, was used. To this aim, the diffraction peaks with the highest intensities of each specie were considered. The average crystalline size of the samples was determined in 5.2, 3.2, and 28 nm for NiO, PdO, and Al<sub>2</sub>O<sub>3</sub>, respectively. Finally, the spectrum for SiO<sub>2</sub> exhibits one broad peak at 22°, attributed to amorphous silica.<sup>46</sup>

### 3.2. Asphaltene adsorption isotherms and conversion

The adsorption isotherms profiles obtained for resins and asphaltenes over AlNiPd are shown in Figure 4a. The adsorption phenomenon of both fractions over alumina-based nanoparticles has been widely explained in the literature. Briefly, our results agree with the type IB adsorption isotherm of both fractions.<sup>23</sup> This result could indicate that AlNiPd presents a high affinity for the adsorption of both fractions. Due to the adsorption amount, nanoparticles adsorb more asphaltenes than resins because of their stronger molecular interactions.<sup>47</sup>

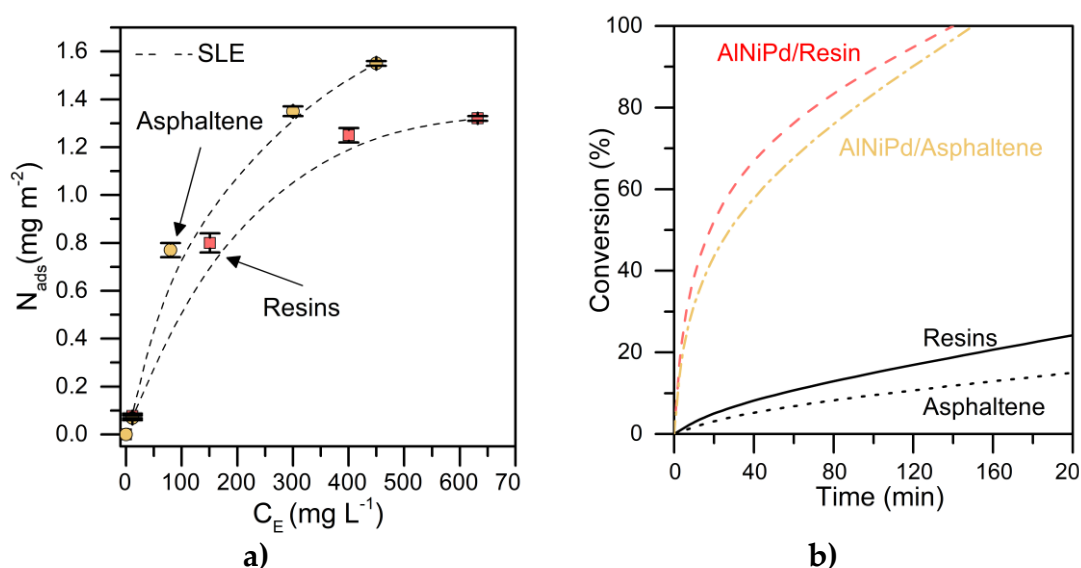


**Figure 4.** a) Experimental adsorption of asphaltenes and resins isolated from a Colombian HO over AlNiPd (dotted lines represent the SLE fitting), b) Isothermal conversion for steam gasification of both fractions at 900 psi, with and without AlNiPd. Temperature was fixed at 250 °C. Both experiments were done using an N<sub>2</sub> flow: 100 ml min<sup>-1</sup>, H<sub>2</sub>O<sub>(g)</sub> flow: 6.7 ml min<sup>-1</sup> and sample mass of 1 mg.

Based on the AlNiPd structure, some mechanisms exist for asphaltene and resin adsorption. The first mechanism corresponds to hydrogen bonding between oxygen atoms of Al<sub>2</sub>O<sub>3</sub>, NiO, and PdO with H-O, H-N, and H-S

functional groups of asphaltene and resins molecules. As asphaltenes present a higher content of heteroatom species, this factor could explain well why asphaltenes molecules are adsorbed in a higher quantity than resins over AlNiPd. The second mechanism is a result of Lewis acid/base interactions. The Al atoms located on the Al<sub>2</sub>O<sub>3</sub> structure act as Lewis acid, which can interact with N, O, and S atoms in the structure of the asphaltenes and resins, playing a Lewis base role. Again, this factor intensifies the asphaltene adsorption over resin adsorption on AlNiPd. Other mechanism results because resonance structures on alumina core facilitate generating  $\pi$ - $\pi$  interactions with aromatic rings presented in asphaltene and resins. The stronger aromaticity of asphaltenes can increase their adsorption on AlNiPd over resins. Finally, metal bonds (Ni and Pd) with asphaltene/resins heteroatoms can take place, facilitating the adsorption phenomenon.

Figure 3b shows the isothermal conversion of both fractions with and without nanoparticles. Asphaltenes and resins convert less than 25% at the temperature evaluated during the experiment. However, when they are adsorbed over AlNiPd, the 100% conversion is achieved at 132 and 145 min for resins and asphaltenes, respectively.

### 3.3. Design of nanofluids

#### 3.3.1. Selection of nanoparticle concentration for nanofluid injection in cold process.

Figure 4 depicts the viscosity reduction produced by adding nanofluids in the HO1. It was found that all the designed nanofluids reduce oil viscosity. Taborda et al. explained that SiO<sub>2</sub> nanoparticles generate strong interactions between heavy molecules such as *n*-C<sub>7</sub> asphaltenes, producing fragmentation of high molecular weight aggregates. Due to this fragmentation, a redistribution of *n*-C<sub>7</sub> aggregates asphaltenes remaining in the liquid medium to be smaller, breaking the bonds forming the large viscoelastic network and hindering further formation.

Comparing the nanofluids, oil viscosity increased in the order 300 < 100 < 500 < 0 mg L<sup>-1</sup>, indicating an optimum point at 300 mg L<sup>-1</sup>, where a maximum degree of viscosity reduction (DVR) is obtained. Regardless of untreated crude oil, a viscosity reduction of 57% at 25 °C was achieved with the nanofluid containing 300 mg L<sup>-1</sup>. Probably, the stability of the nanoparticles in the CF1 decreases at a concentration of 500 mg L<sup>-1</sup>, reducing the number of active sites

due to aggregation phenomena and, therefore, decreasing their efficiency in reducing oil viscosity.

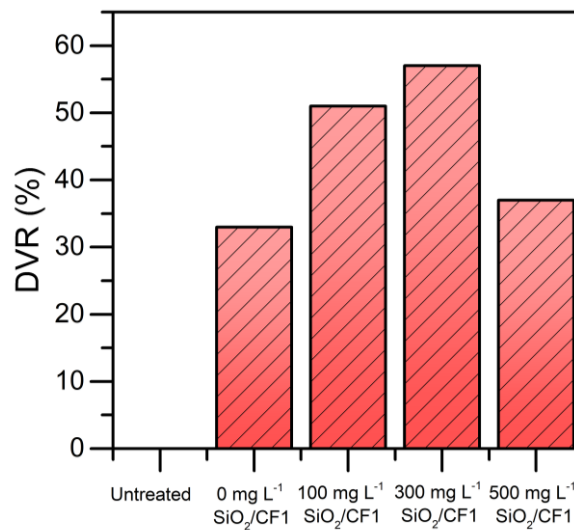


**Figure 4.** Viscosity of crude oil in absence and presence of nanofluid with different concentrations of nanoparticles at 25 °C and a shear rate of 10 s<sup>-1</sup>.

Figure 5a shows the water imbibition test of treated and untreated samples. The imbibed water fraction growth is increased by nanoparticles, following the order 300 < 100 < 500 mg L<sup>-1</sup>, obtaining the worst scenario using 500 mg L<sup>-1</sup> of nanoparticles. This result can be explained by increased hydrophobic functional groups deposited in the rock surface, making the imbibition process harder. Contact angle photographs of water drop in sandstone samples are shown in Figure 5b. The contact angle value trend obtained for the treated cores supports the results of the imbibition test. With the increase of nanoparticle dosage, a more oil-wet surface is obtained. In terms of the wettability alteration potential, based on the obtained results, it is advised that to avoid adverse effects on rock wettability, low nanoparticle concentration must be used.

Finally, the IFT measurements as a function of the concentration of the nanoparticles in CF1 are shown in Figure 5c. It is observed a minimum IFT value at a nanoparticle dosage of 300 mg L<sup>-1</sup>, with a reduction of 38.01% compared to the base system. Based on these experiments, a concentration of 300 mg L<sup>-1</sup> of SiO<sub>2</sub> was selected for the nanofluid cold injection.

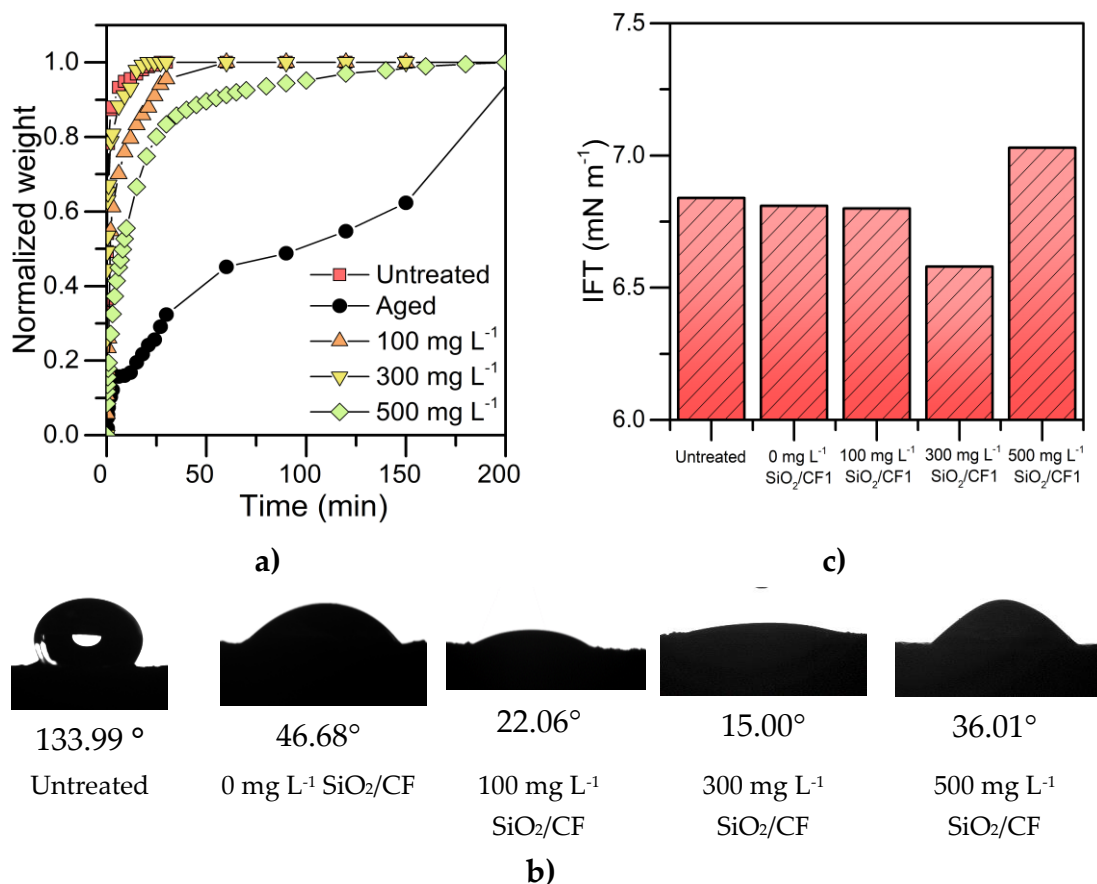


**Figure 5.** a) Water imbibition test into air-saturated sandstone samples, b) Contact angle photographs of water drop on sandstone samples untreated and treated with nanofluids containing different concentrations of nanoparticles, and c) Measured IFT data for crude oil and nanofluid containing different concentrations of nanoparticles /Brine systems.

### 3.3.2. Selection of nanoparticle concentration for nanofluid injection in steam process.

Figure 6 shows the results of API gravity and dynamic viscosity of the HO2 effluents obtained from the reactor test with different concentrations of AlNiPd. The first system analyzed was crude oil at steam injection temperature. In this scenario, it was found that the resulting crude oil after the thermal treatment has an approximate viscosity of 3500 cP and an API of 11.6°. In other words, the crude oil recovered its initial properties after the thermal treatment. In the following scenario, the crude oil is mixed with 5 wt.% of the carrier fluid without nanoparticles. In this system, a reduction of more than 50% in the viscosity of the crude oil and a slight increase in the API gravity (12.6°) are obtained. The

dissolution of crude oil reduces viscosity on the carrier fluid; however, the SARA distribution is not modified; therefore, API gravity is not affected.

The other systems consist of crude oil with 5 wt.% CF2 and different concentrations of nanoparticles. API was highly increased in all cases, following the decreasing order of  $1000 \text{ mg L}^{-1}$  ( $13.7^\circ$ ) <  $2000 \text{ mg L}^{-1}$  ( $14.6^\circ$ ) <  $500 \text{ mg L}^{-1}$  ( $15^\circ$ ). The viscosity was improved in the same order. In other words, the best crude oil quality conditions are obtained for a concentration of  $500 \text{ mg L}^{-1}$  of nanoparticle in 5 wt.% of the carrier fluid (API of  $15^\circ$  and oil viscosity of 330 cP). Therefore,  $500 \text{ mg L}^{-1}$  of AlNiPd was selected for the nanofluid formulation to assist the steam injection process. As previously discussed, AlNiPd can adsorb and decompose asphaltenes and resins at the evaluated temperature. It is expected that the SARA distribution is slightly changed by the nanofluid effect, which generates an improvement in oil quality.

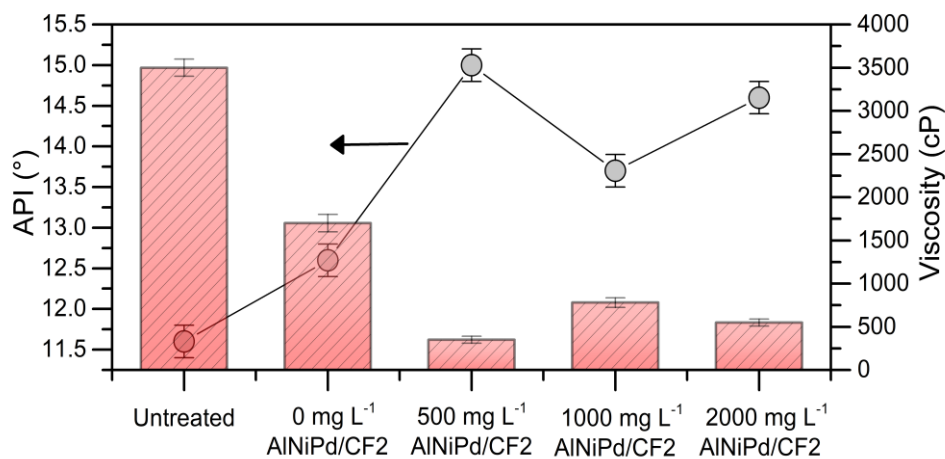


**Figure 6.** API gravity and dynamic viscosity measurements of HO2 treated with CF2 and nanofluid containing different concentrations of nanoparticles 500, 1000, and  $2000 \text{ mg L}^{-1}$ .

### 3.3.3. Nanofluids stability

The nanofluid stability for the best concentration of each nanoparticle is shown in Figure 7. The stability was analyzed based on the absorbance ratio. The closer the value of  $A/A_0$ , which varies with sedimentation time, to one, the greater the stability condition of the sample. The  $A/A_0$  ratio is reduced by around 5% during the first 24 h. Therefore, the dispersed nanoparticles are considered stable and suitable for injection in reservoir rock.



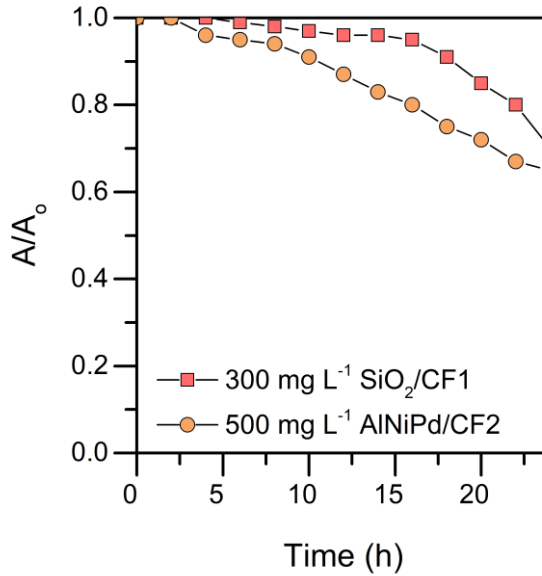


**Figure 7.** Absorbance ratio of mixtures of nanoparticles and CF1 or CF2 with sedimentation time.

### 3.4. Dynamic experiments

#### 3.4.1. Coreflooding test – Cold scenario

The relative permeability curves constructed using the analytical mode created by Buckley and Leverett and expanded by Johnson, Bossler, and Naumann (JBN technique)<sup>48</sup> are shown in Figure 8a.  $K_o$  values were found in 664 and 704 mD for the base and after the nanofluid injection scenario, respectively, indicating that the nanofluid successfully raises oil's relative permeability. Viscosity and relative permeability, both influenced by the system's wettability, are the main variables determining how mobile crude oil is.<sup>49, 50</sup> Since the nanofluid inclusion reduced the oil viscosity during the static tests, the oil mobility in the porous medium was consequently increased. Additionally, wettability changes are noticeable because residual water and oil saturations show a change in the system's wetting state following the injection of the nanofluid. Additionally, the crossover point shifts from 76 to 82%  $S_w$ , which according to Craig's rules of thumb,<sup>51</sup> a modification in the system's wetting condition occurred.

The volume of oil recovered over time as the crude oil is displaced by water is used to create oil recovery curves. Figure 8b shows that 89 and 92% of the original oil in place is recovered by the base and after nanofluid injection, respectively, i.e., the system increases its oil production capacity by 3%. This illustrates the significance and impact of the proposed technology as an optimizer agent mobility heavy oil.

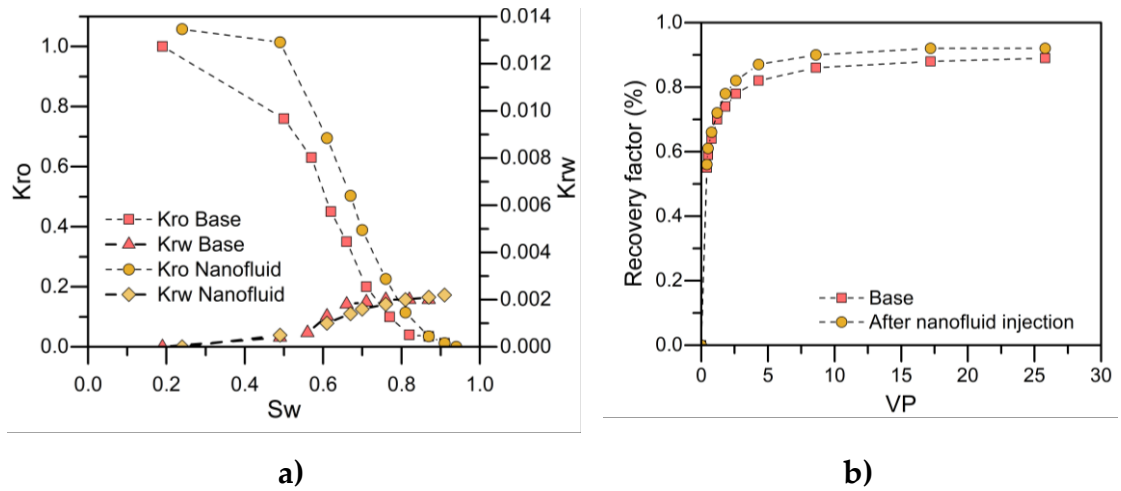


**Figure 8.** a) Relative permeability and b) oil recovery curves before after the injection of the nanofluid containing  $300 \text{ mg L}^{-1}$  of  $\text{SiO}_2$  in CF1.

### 3.4.2. Coreflooding test - Steam injection scenario

Figure 9 depicts the oil recovery profiles obtained during the displacement test. During the first steam injection, 56% of the original oil in place was produced. The oil recovery mechanisms ascribed to steam injection include oil viscosity reduction by heat transfer, thermal expansion, gravitational segregation, light hydrocarbon volatilization, and fluids and rock expansion.<sup>24, 52-</sup>

55

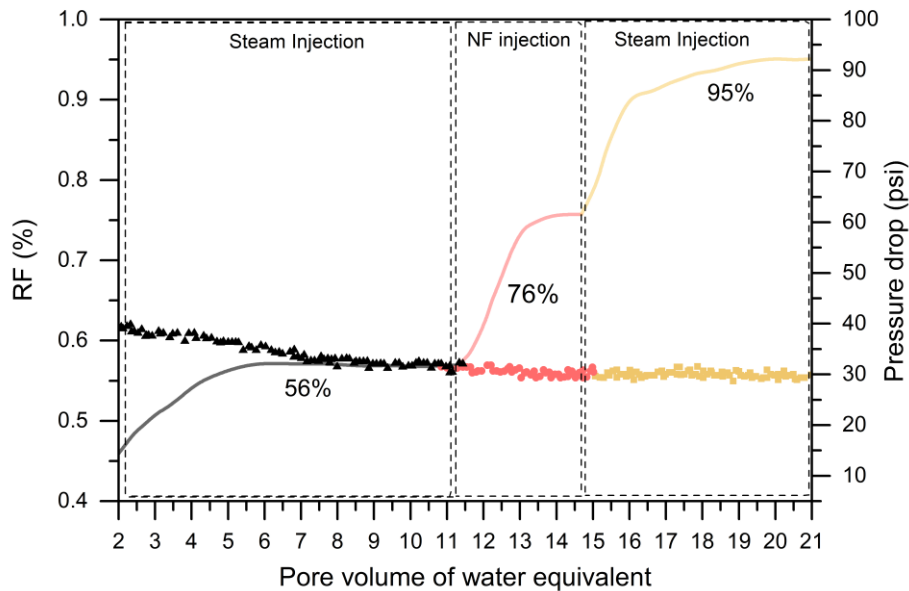


**Figure 9.** Oil recovery curve of steam injection discretized in three main stages, including (1) continuous steam injection, (2) dispersed injection of nanofluid in steam, and (3) steam injection after porous medium soaking with nanofluid containing  $500 \text{ mg L}^{-1}$  of  $\text{AlNiPd}$  in CF2.

When the nanofluid was injected and dispersed in the steam stream, the oil recovery increased to 76%. Alumina is characterized as having high thermal conductivity and allowing the heat to spread faster and further, decreasing the oil viscosity, one of the main mechanisms for oil production, as mentioned. During the last stage, when steam is injected after 12 h nanofluid soaking, the recovery increased by 19% regarding the previous stage. These results indicate that the residual oil saturation (Sor) at the end of the stimulation operation was 5%. Compared with the Sor after steam injection (44%), the benefits of the designed nanofluid on oil recovery are evidenced. The slight pressure drop observed during the experimental test ensures the nanofluid transport in the porous media.

#### 3.4.3. Effluent analysis from steam injection test.

Panels a of Figure 10a show the API gravity values for untreated HO2, crude oil after steam injection, and crude oil recovered by nanofluid injection dispersed in the steam stream and after a soaking time of 12 h. After the steam injection without nanoparticles, the API gravity increased from 11.6° to 12.1°. Then, this property was increased up to 28.7 and 29.2° in the effluents obtained during nanofluid injection in the steam stream and after nanofluid soaking. On the other hand, panel b of Figure 10 depicts the viscosity values at a shear rate of 10 s<sup>-1</sup> and 25 °C of the effluents. During the first stage, oil viscosity was slightly reduced due to the reduction of cohesive intermolecular forces between asphaltenes and resins. For the nanotechnology-assisted scenarios (2<sup>nd</sup> and 3<sup>rd</sup> stage), a significant decrease in oil viscosity was noted, being higher for the effluent recovered after 12 h of soaking. The oil recovered in the third stage was 104 cP. The main mechanism that explains the reduction in oil viscosity is the cracking/redistribution of asphaltene-resin systems and their subsequent stabilization through free radical hydrogenation to prevent the formation of heavier compounds.

On the other hand, Figure 10c-d shows the results of API and dynamic viscosity of the HO2 recovered after the 12-hour soaking of the containing 500 mg L<sup>-1</sup> of AlNiPd in CF2 in the porous medium during days 1, 8, 15, and 30 after its recovery. Interestingly, the API gravity and oil viscosity remain constant during the first 30 days evaluated, indicating the potential of the nanofluid to generate permanent crude oil upgrading.

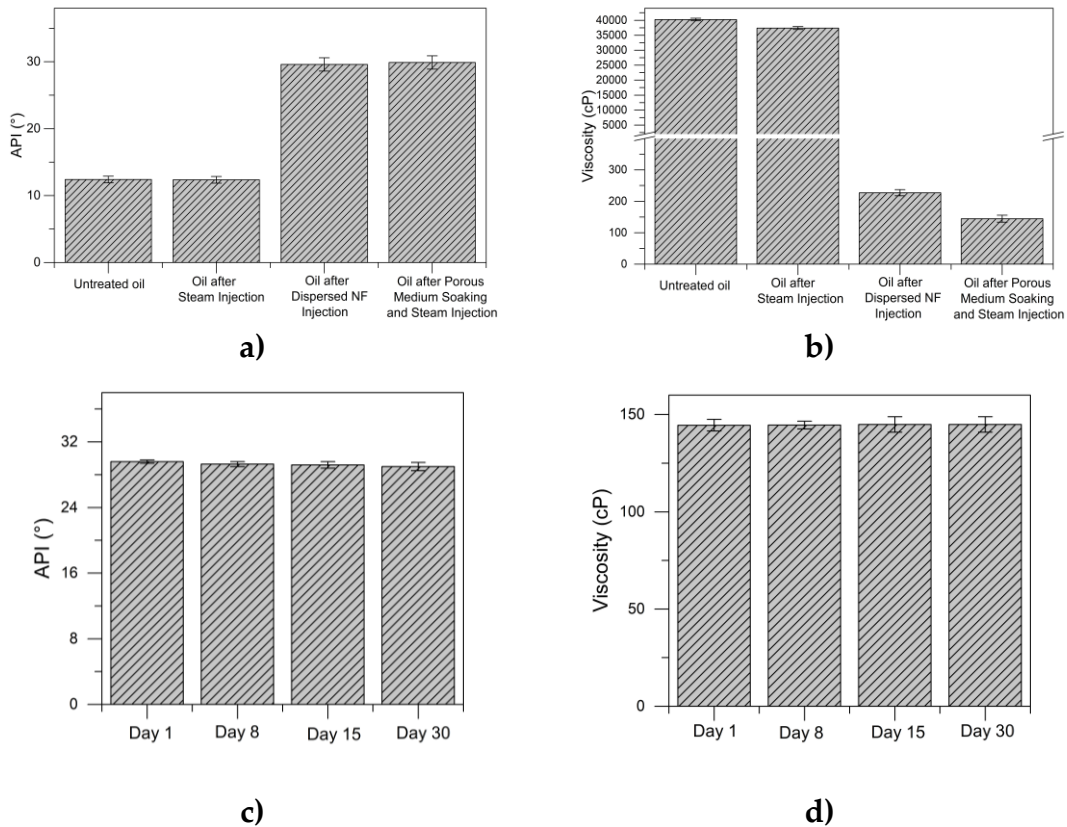


**Figure 10.** a) API gravity and b) crude oil viscosity for untreated extra-heavy oil and crude oil recovered after the steam injection, during the injection of nanofluid containing  $500 \text{ mg L}^{-1}$  of AlNiPd in CF2. dispersed in a steam stream, and after soaking of 12 h. Perdurability of crude oil quality by c) API and d) oil viscosity of the effluents recovered after the 12-hour soaking of the nanofluid in the porous medium.

### 3.5. Field test

Based on the previous results, academy-industry joint work decided to carry out the first worldwide field trial application of this technology in two wells affected by steam injection from a Colombian field. One well consisted of a cold nanofluid injection (Well A), and one included a steam injection (Well B) alongside the nanofluids. The main target of the field trial was to achieve an increase in oil mobility and reduce the amount of combustion gas required for the development of the field. NF1 consisted of  $300 \text{ mg L}^{-1}$  of  $\text{SiO}_2$  nanoparticles dispersed in CF1 and NF2 in  $500 \text{ mg L}^{-1}$  of AlNiPd in CF2, which were injected following the described processes in Section 2.2.5. According to the field trial results, the benefits are mainly associated with the incremental production after the execution of the first 2 tests with nanofluids, one with steam and one cold (wells A and B) between the months of June and July 2022. The incremental

production perceived during 2022 corresponds to 8603 bbls related to 3231 bbl (well A) and 5372 bbl (well B). Based on these results, two more wells were stimulated with the technology, one cold and one with steam (wells C and D), between the months of November and December 2022, benefits associated with technological implementation are reported in 430 bbl (well C) for the cold processes, and 980 bbl (well D) in the case of steam injection in the presence of nanofluids.

### 3.5.1. Fluid Quality Assurance.

Fluids on-site monitoring was done by measuring crude oil viscosity. Figure 11a-b shows the rheological profiles obtained for different samples from both wells between June and December. It is observed that the viscosity of the untreated crude oil decreases as the shear rate increases. Fluids that display this behavior are known as pseudoplastic materials or shear-thinning, which is a behavior for heavy crude oil that is frequently reported. However, the effluents obtained after the intervention of nanofluids show a slight deviation toward a Newtonian fluid. The findings show that viscosity decreased every month from June to December. As previously mentioned, nanoparticles can disrupt the bonds that keep the viscoelastic network stable and redistribute asphaltene aggregates, preventing further formation.

Fluids exhibiting this behavior are called pseudoplastic materials or shear-thinning, a widely reported behavior for heavy crude oil. However, a slight deviation to a Newtonian fluid is observed for the effluents obtained after nanofluids intervention. The results reveal a decrease in viscosity during all the months between June and December. As we previously explained, nanoparticles can fragment and redistribute asphaltene aggregates, breaking bonds that stabilize the viscoelastic network and hinder further formation.

In the case of the steam-stimulated Well B, a higher reduction in viscosity is obtained over time, which is consistent with the catalytic activity of nanoparticles to decompose heavy oil fractions under steam injection conditions and thus perform *in-situ* oil upgrading. In both cases, the reduction in oil viscosity was demonstrated, showing that the treatment maintains the samples' quality, which may reduce transportation and refining operations costs. With the field test design, application, and validation, a TRL of 8 was obtained. In this phase, the systems are integrated, and the technology has been tested in its final form under assumed conditions, thus demonstrating its commercial potential. It is expected to continue with the validation of the technology and the monitoring of the

production and quality of effluents. Likewise, economic proof of the technology is expected to be carried out to massify the technology and reach a TRL-9.

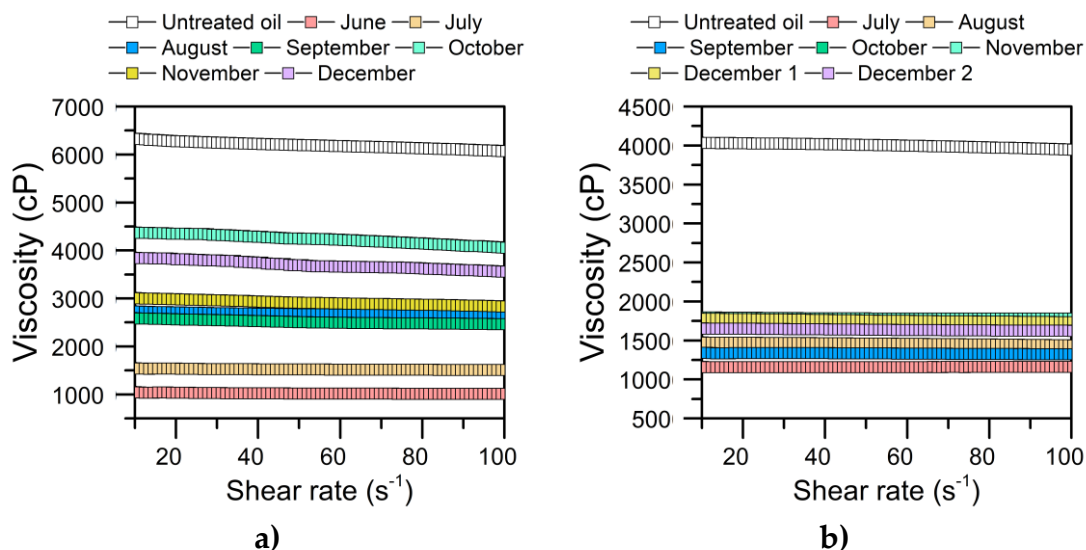


**Figure 11.** Viscosity as a function of shear rate for untreated crude oil and effluents obtained in a) well A and b) well B after the intervention with nanofluids. Temperature: 25 °C.

#### 4. Conclusions

This paper exposed an upscaling from a TRL-3 to a TRL-8 of implementation at a field application in wells affected by steam injection processes. In the first place, the experimental design was disclosed, including the treatment evaluation under steady-state conditions and in a relevant environment. Secondly, the methodology used for the candidate selection was explained, and finally, the field tests and validation were accounted. The steady-state experiments concluded that using 300 mg L<sup>-1</sup> of SiO<sub>2</sub> nanoparticles in CF1 reduces oil viscosity, and other properties like wettability and IFT are enhanced. Therefore, this nanofluid was selected for the cold process. On the other hand, Al<sub>2</sub>O<sub>3</sub> nanoparticles function well when doped with transition and noble element oxides for asphaltene adsorption and conversion. A concentration of 500 mg·L<sup>-1</sup> in CF2 was the best concentration to increase API gravity and reduce oil viscosity. Dynamic flow experiments evidenced both nanofluids to improve the recovery factor and oil mobility under cold and steam injection.

According to the field trial results, the benefits are mainly associated with the incremental production after the execution of the first 2 tests with nanofluids, one with steam and one cold (wells A and B) between June and July 2022. The

incremental production perceived during 2022 corresponds to 8603 bbls related to 3231 bbl (well A) and 5372 bbl (well B). Additionally, during the fluids on-site monitoring, the viscosity was reduced in both wells, obtaining a quality perdurability between June and December. This study is expected to exhibit the high performance of the nanotechnology-based techniques for enhancing enhanced oil recovery operations and praise a broader landscape for its application in field processes.

## References

1. Acevedo, S.; Zuloaga, C.; Rodríguez, P., Aggregation– dissociation studies of asphaltene solutions in resins performed using the combined freeze fracture–transmission electron microscopy technique. *Energy & Fuels* **2008**, *22*, (4), 2332-2340.
2. Acevedo, S.; Méndez, B.; Rojas, A.; Layrissé, I.; Rivas, H., Asphaltenes and resins from the Orinoco basin. *Fuel* **1985**, *64*, (12), 1741-1747.
3. Ancheyta, J.; Centeno, G.; Trejo, F.; Marroquin, G.; Garcia, J.; Tenorio, E.; Torres, A., Extraction and characterization of asphaltenes from different crude oils and solvents. *Energy & Fuels* **2002**, *16*, (5), 1121-1127.
4. Andersen, S. I.; Speight, J. G., Petroleum resins: separation, character, and role in petroleum. *Petroleum science and technology* **2001**, *19*, (1-2), 1-34.
5. Boduszynski, M. M., Composition of heavy petroleums. 2. Molecular characterization. *Energy & Fuels* **1988**, *2*, (5), 597-613.
6. Calemma, V.; Iwanski, P.; Nali, M.; Scotti, R.; Montanari, L., Structural characterization of asphaltenes of different origins. *Energy & Fuels* **1995**, *9*, (2), 225-230.
7. Patzek, T.; Koinis, M., Kern River steam-foam pilots. *Journal of Petroleum Technology* **1990**, *42*, (04), 496-503.
8. Yang, C.-z.; Han, D.-k., Present status of EOR in the Chinese petroleum industry and its future. *Journal of Petroleum Science and Engineering* **1991**, *6*, (2), 175-189.
9. Sandiford, B. B., Gel and method for reducing steam channeling. In Google Patents: 1987.
10. Aljundi, I. H., Energy and exergy analysis of a steam power plant in Jordan. *Applied thermal engineering* **2009**, *29*, (2-3), 324-328.

11. Herranz, L. E.; Anderson, M. H.; Corradini, M. L., A diffusion layer model for steam condensation within the AP600 containment. *Nuclear Engineering and Design* **1998**, 183, (1-2), 133-150.
12. Dong, X.; Liu, H.; Chen, Z.; Wu, K.; Lu, N.; Zhang, Q., Enhanced oil recovery techniques for heavy oil and oilsands reservoirs after steam injection. *Applied energy* **2019**, 239, 1190-1211.
13. Nassar, N. N.; Hassan, A.; Pereira-Almao, P., Application of nanotechnology for heavy oil upgrading: Catalytic steam gasification/cracking of asphaltenes. *Energy & Fuels* **2011**, 25, (4), 1566-1570.
14. Choi, S. U.; Eastman, J. A. *Enhancing thermal conductivity of fluids with nanoparticles*; Argonne National Lab., IL (United States): 1995.
15. Li, W.; Ni, C.; Lin, H.; Huang, C.; Shah, S. I., Size dependence of thermal stability of TiO<sub>2</sub> nanoparticles. *Journal of Applied Physics* **2004**, 96, (11), 6663-6668.
16. Hwang, Y.-j.; Lee, J.; Lee, C.; Jung, Y.; Cheong, S.; Lee, C.; Ku, B.; Jang, S., Stability and thermal conductivity characteristics of nanofluids. *Thermochimica Acta* **2007**, 455, (1-2), 70-74.
17. Adams, J. J., Asphaltene adsorption, a literature review. *Energy & Fuels* **2014**, 28, (5), 2831-2856.
18. Bera, A.; Babadagli, T., Status of electromagnetic heating for enhanced heavy oil/bitumen recovery and future prospects: A review. *Applied Energy* **2015**, 151, 206-226.
19. Shah, A.; Fishwick, R.; Wood, J.; Leeke, G.; Rigby, S.; Greaves, M., A review of novel techniques for heavy oil and bitumen extraction and upgrading. *Energy & Environmental Science* **2010**, 3, (6), 700-714.
20. Franco, C. A.; Montoya, T.; Nassar, N. N.; Cortés, F. B., NIOAND PDO SUPPORTED ON FUMED SILICA NANOPARTICLES FOR ADSORPTION AND CATALYTIC STEAM GASIFICATION OF COLOMBIAN C7ASPHALTENES. **2014**.
21. Cardona Rojas, L. Efecto de nanopartículas en procesos con inyección de vapor a diferentes calidades. M.Sc. Thesis, Universidad Nacional de Colombia-Sede Medellín, March 2018.
22. Nassar, N. N.; Franco, C. A.; Montoya, T.; Cortés, F. B.; Hassan, A., Effect of oxide support on Ni-Pd bimetallic nanocatalysts for steam gasification of n-C<sub>7</sub> asphaltenes. *Fuel* **2015**, 156, 110-120.
23. Medina, O. E.; Gallego, J.; Arias-Madrid, D.; Cortés, F. B.; Franco, C. A., Optimization of the Load of Transition Metal Oxides (Fe<sub>2</sub>O<sub>3</sub>, Co<sub>3</sub>O<sub>4</sub>, NiO and/or



- PdO) onto CeO<sub>2</sub> Nanoparticles in Catalytic Steam Decomposition of n-C<sub>7</sub> Asphaltenes at Low Temperatures. *Nanomaterials* **2019**, 9, (3), 401.
24. Cardona, L.; Arias-Madrid, D.; Cortés, F.; Lopera, S.; Franco, C., Heavy oil upgrading and enhanced recovery in a steam injection process assisted by NiO- and PdO-Functionalized SiO<sub>2</sub> nanoparticulated catalysts. *Catalysts* **2018**, 8, (4), 132.
25. Badoga, S.; Sharma, R. V.; Dalai, A. K.; Adjaye, J., Hydrotreating of Heavy Gas Oil on Mesoporous Mixed Metal Oxides (M–Al<sub>2</sub>O<sub>3</sub>, M= TiO<sub>2</sub>, ZrO<sub>2</sub>, SnO<sub>2</sub>) Supported NiMo Catalysts: Influence of Surface Acidity. *Industrial & Engineering Chemistry Research* **2014**, 53, (49), 18729-18739.
26. Gao, Y.; Ghorbanian, B.; Gargari, H. N.; Gao, W., Steam reforming of gaseous by-products from bitumen oil using various supported Ni-based catalysts. *Petroleum Science and Technology* **2018**, 36, (1), 34-39.
27. Guo, K.; Zhang, Y.; Shi, Q.; Yu, Z., The effect of carbon-supported nickel nanoparticles in the reduction of carboxylic acids for in situ upgrading of heavy crude oil. *Energy & Fuels* **2017**, 31, (6), 6045-6055.
28. Vignatti, C. I.; Avila, M. S.; Apesteguía, C. R.; Garetto, T. F., Study of the water-gas shift reaction over Pt supported on CeO<sub>2</sub>–ZrO<sub>2</sub> mixed oxides. *Catalysis Today* **2011**, 171, (1), 297-303.
29. Franco, C.; Cardona, L.; Lopera, S.; Mejía, J.; Cortés, F. In *Heavy oil upgrading and enhanced recovery in a continuous steam injection process assisted by nanoparticulated catalysts*, SPE improved oil recovery conference, 2016; Society of Petroleum Engineers: 2016.
30. Yi, S.; Babadagli, T.; Li, H. A., Use of nickel nanoparticles for promoting aquathermolysis reaction during cyclic steam stimulation. *SPE Journal* **2018**, 23, (01), 145-156.
31. Franco, C. A.; Zabala, R. D.; Zapata, J.; Mora, E.; Botero, O.; Candela, C.; Castillo, A., Inhibited gas stimulation to mitigate condensate banking and maximize recovery in cupiagua field. *SPE Production & Operations* **2013**, 28, (02), 154-167.
32. Restrepo, A.; Ocampo, A.; Lopera Castro, S. H.; Diaz, M. P.; Clavijo, J.; Marin, J., GaStim Concept - A Novel Technique for Well Stimulation. Part I: Understanding the Physics. **2012**.
33. Medina, O. E.; Caro-Vélez, C.; Gallego, J.; Cortés, F. B.; Lopera, S. H.; Franco, C. A., Upgrading of extra-heavy crude oils by dispersed injection of NiO–PdO/CeO<sub>2±δ</sub> nanocatalyst-based nanofluids in the steam. *Nanomaterials* **2019**, 9, (12), 1755.

34. Medina, O. E.; Gallego, J.; Restrepo, L. G.; Cortés, F. B.; Franco, C. A., Influence of the Ce<sup>4+</sup>/Ce<sup>3+</sup> Redox-couple on the cyclic regeneration for adsorptive and catalytic performance of NiO-PdO/CeO<sub>2</sub>± $\delta$  nanoparticles for n-C<sub>7</sub> asphaltene steam gasification. *Nanomaterials* **2019**, 9, (5), 734.
35. López, D.; Giraldo, L. J.; Salazar, J. P.; Zapata, D. M.; Ortega, D. C.; Franco, C. A.; Cortés, F. B., Metal Oxide Nanoparticles Supported on Macro-Mesoporous Aluminosilicates for Catalytic Steam Gasification of Heavy Oil Fractions for On-Site Upgrading. *Catalysts* **2017**, 7, (11), 319.
36. Cardona, L.; Medina, O. E.; Céspedes, S.; Lopera, S. H.; Cortés, F. B.; Franco, C. A., Effect of Steam Quality on Extra-Heavy Crude Oil Upgrading and Oil Recovery Assisted with PdO and NiO-Functionalized Al<sub>2</sub>O<sub>3</sub> Nanoparticles. *Processes* **2021**, 9, (6), 1009.
37. Cardona, L.; Arias-Madrid, D.; Cortés, F. B.; Lopera, S. H.; Franco, C. A., Heavy oil upgrading and enhanced recovery in a steam injection process assisted by NiO- and PdO-Functionalized SiO<sub>2</sub> nanoparticulated catalysts. *Catalysts* **2018**, 8, (4), 132.
38. Medina, O. E.; Gallego, J.; Pérez-Cadenas, A. F.; Carrasco-Marín, F.; Cortés, F. B.; Franco, C. A., Insights into the Morphology Effect of Ceria on the Catalytic Performance of NiO-PdO/CeO<sub>2</sub> Nanoparticles for Thermo-oxidation of n-C<sub>7</sub> Asphaltenes under Isothermal Heating at Different Pressures. *Energy & Fuels* **2021**.
39. Mullins, O. C. S., E. Y., Eds.; Plenum Press: , Optical interrogation of aromatic moieties in crude oil sand asphaltenes. In Structures and dynamics of asphaltenes;. **New York, 1998**.
40. Goncalves, S.; Castillo, J.; Fernandez, A.; Hung, J., Absorbance and fluorescence spectroscopy on the aggregation behavior of asphaltene-toluene solutions. *Fuel* **2004**, 83, (13), 1823-1828.
41. López, D.; Jaramillo, J. E.; Lucas, E. F.; Riazi, M.; Lopera, S. H.; Franco, C. A.; Cortés, F. B., Cardanol/SiO<sub>2</sub> Nanocomposites for Inhibition of Formation Damage by Asphaltene Precipitation/Deposition in Light Crude Oil Reservoirs. Part II: Nanocomposite Evaluation and Coreflooding Test. *ACS omega* **2020**, 5, (43), 27800-27810.
42. Mo, J.; Sha, J.; Li, D.; Li, Z.; Chen, Y., Fluid release pressure for nanochannels: the Young-Laplace equation using the effective contact angle. *Nanoscale* **2019**, 11, (17), 8408-8415.
43. Lin, S.-Y.; Hwang, H.-F., Measurement of low interfacial tension by pendant drop digitization. *Langmuir* **1994**, 10, (12), 4703-4709.

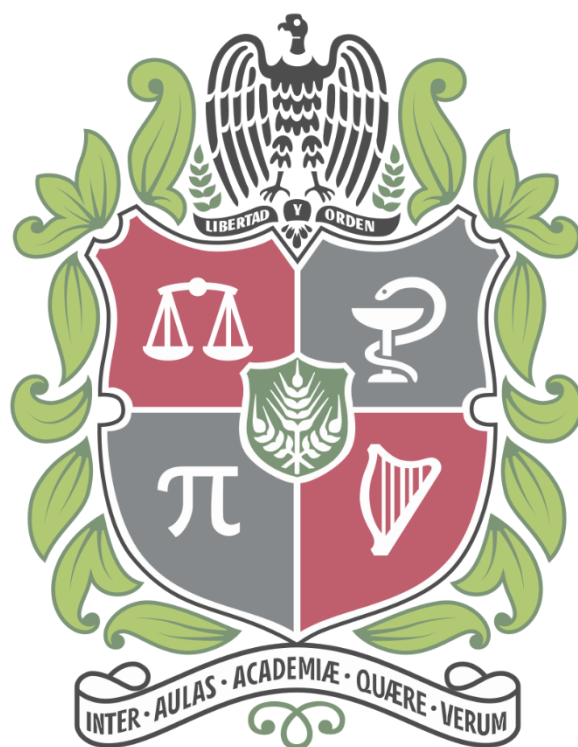
44. Medina, O. E.; Hurtado, Y.; Caro-Velez, C.; Cortés, F. B.; Riazi, M.; Lopera, S. H.; Franco, C. A., Improvement of steam injection processes through nanotechnology: An approach through in situ upgrading and foam injection. *Energies* **2019**, *12*, (24), 4633.
45. Bueno, N.; Mejía, J. M., Numerical verification of in-situ heavy oil upgrading experiments and thermal processes for enhanced recovery. *Fuel* **2022**, *313*, 122730.
46. Tang, B.; Qiu, M.; Zhang, S., Thermal conductivity enhancement of PEG/SiO<sub>2</sub> composite PCM by in situ Cu doping. *Solar energy materials and solar cells* **2012**, *105*, 242-248.
47. Franco, C. A.; Montoya, T.; Nassar, N. N.; Pereira-Almao, P.; Cortés, F. B., Adsorption and subsequent oxidation of colombian asphaltenes onto nickel and/or palladium oxide supported on fumed silica nanoparticles. *Energy Fuels* **2013**, *27*, (12), 7336.
48. Almutairi, A.; Othman, F.; Ge, J.; Le-Hussain, F., Modified Johnson–Bossler–Naumann method to incorporate capillary pressure boundary conditions in drainage relative permeability estimation. *Journal of Petroleum Science and Engineering* **2022**, *210*, 110064.
49. Anderson, W. G., Wettability literature survey part 5: the effects of wettability on relative permeability. *Journal of Petroleum Technology* **1987**, *39*, (11), 1453-1468.
50. Heaviside, J.; Black, C. In *Fundamentals of relative permeability: experimental and theoretical considerations*, SPE annual technical conference and exhibition, 1983; OnePetro: 1983.
51. Mirzaei-Paiaman, A., New methods for qualitative and quantitative determination of wettability from relative permeability curves: Revisiting Craig's rules of thumb and introducing Lak wettability index. *Fuel* **2021**, *288*, 119623.
52. Tang, F.-S.; Lin, R.-B.; Lin, R.-G.; Zhao, J. C.-G.; Chen, B., Separation of C<sub>2</sub> hydrocarbons from methane in a microporous metal-organic framework. *Journal of Solid State Chemistry* **2018**, *258*, 346-350.
53. Ji, D.; Zhong, H.; Dong, M.; Chen, Z., Study of heat transfer by thermal expansion of connate water ahead of a steam chamber edge in the steam-assisted-gravity-drainage process. *Fuel* **2015**, *150*, 592-601.
54. Huang, S.; Cao, M.; Cheng, L., Experimental study on aquathermolysis of different viscosity heavy oil with superheated steam. *Energy & fuels* **2018**, *32*, (4), 4850-4858.

55. Ageeb, A. A.; Al-siddig, M. H.; Nor-aldeen, M. R.; Soliman, M. S.; Ibrahim, I. H. The Influence of Steam Injection Volume on Sand and Oil Production in Cyclic Steam Stimulation (CSS) Wells. Sudan University of Science and Technology, 2017.



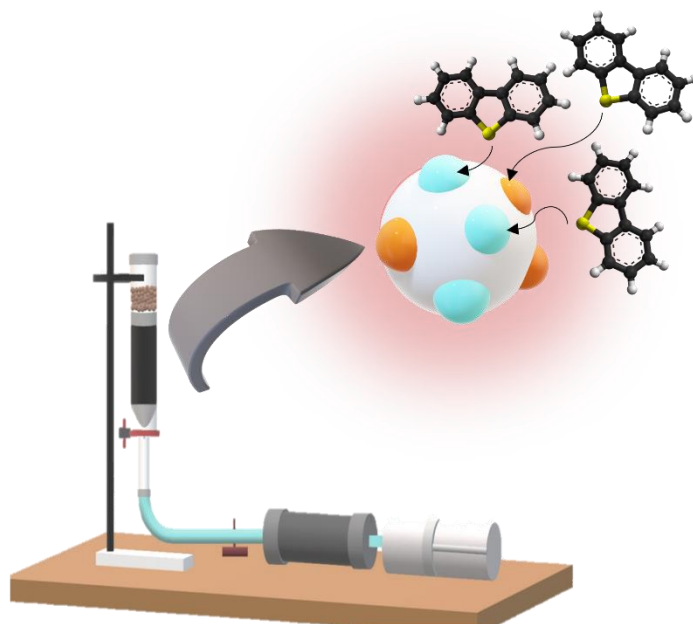


## Apartado 6.





# Sulfur Removal from Heavy Crude Oils based on the Adsorption Process using Nanomaterials: Experimental and Theoretical Study





# Sulfur Removal from Heavy Crude Oils based on the Adsorption Process using Nanomaterials: Experimental and Theoretical Study

## Abstract

This work aims to develop a highly-affinity nanomaterial for sulfur removal from heavy crude oils consisting of silica-support doped with active metal phases and the subsequent validation through experimental and simulation tools. First, different transition element oxide nanoparticles of  $\text{Fe}_3\text{O}_4$ ,  $\text{NiO}$ ,  $\text{ZnO}$ ,  $\text{MoO}_3$ ,  $\text{CuO}$ , and  $\text{AgO}$  were synthesized and tested for sulfur adsorption in batch mode at different adsorbent:crude oil ratios, and then used to modify the surface of the silica-support. The  $\text{AgO}$  and  $\text{CuO}$  have a higher yield, removing 24 and 21% sulfur with 2 g per 40 g of crude oil, respectively. To reduce and optimize the Ag and Cu charge, seven nanomaterials were prepared using silica support doped with various loads of  $\text{CuO}$  and  $\text{AgO}$ , including  $\text{SiCu}_2$ ,  $\text{SiAg}_2$ ,  $\text{SiCu}_4$ ,  $\text{SiCu}_4$ ,  $\text{SiAg}_2\text{Cu}_2$ ,  $\text{SiAg}_{1.32}\text{Cu}_{1.32}$ , and  $\text{SiAg}_{1.5}\text{Cu}_{1.4}$  via incipient wetness impregnation. The efficiency of the nanomaterials' adsorption process is validated by estimating their adsorption capacity/removal and affinity for sulfur species using batch and continuous adsorption experiments. The sulfur adsorption amount/removal on the non-doped material ( $\text{SiO}_2$ ) was  $\sim 80 \text{ mg S}\cdot\text{g}^{-1}$ , using 2 g per 40 g of crude oil. However, when it is doped with 2 mmol of Cu and Ag ( $\text{SiCu}_2$  and  $\text{SiAg}_2$ ), the adsorbed amount increases to  $\sim 115$  and  $\sim 195 \text{ mg S}\cdot\text{g}^{-1}$ , respectively, and in turn, increases with increasing the active phase doses ( $\text{SiAg}_2\text{Cu}_2$ ). The bi-elemental systems (i.e., containing Cu and Ag) present higher yields considering mono-elemental systems in the order  $\text{SiAg}_{1.32}\text{Cu}_{1.32} < \text{SiAg}_2\text{Cu}_2 < \text{SiAg}_{1.5}\text{Cu}_{1.4}$ . Adsorption isotherms were constructed for the best material evaluated ( $\text{SiAg}_{1.5}\text{Cu}_{1.4}$ ) at 25, 35, and 55 °C, obtaining a high affinity between the nanomaterial and the sulfur compounds present in the crude oil. The dynamic adsorption process was evaluated in the  $\text{SiAg}_{1.5}\text{Cu}_{1.4}$  system due to its higher adsorption capacity, which took more than 350 minutes to reach the adsorbent's target point, demonstrating that the  $\text{SiAg}_{1.5}\text{Cu}_{1.4}$  system worked efficiently for dynamic sulfur adsorption. At 425 minutes, the adsorbent loses its capacity for sulfur adsorption. The Aspen Adsorption software was used to

simulate the sulfur adsorption process of crude oil. For this, the continuity equations were solved in conjunction with adsorption isotherm models (Freundlich isotherm). The parameters required to solve the set of equations were obtained through experimentation. The built model was validated using laboratory adsorption tests, yielding a maximum relative error of 5.0%. Furthermore, this model was used to determine the sensitivity of the crude injection flow in the packed bed varying the dimensions. The results showed that 3280 barrels of oil were successfully treated in 57 hours using a bed with a 5 m height and 1.24 m diameter.

## 1. Introduction

Sulfur is the foremost important heteroelement primarily found in heavy crude oil and has the most significant effect on refining. It poisons catalysts, corrodes refining equipment, and the combustion of sulfur products leads to environmental pollution (Ismagilov et al., 2011). Due to the significant content of sulfur compounds in crude oil, several desulphurization processes during crude oil refining are required to meet the sulfur transportation standards established by the Environmental Protection Agency (EPA), which states that gasoline and diesel must be less than 10 and 15 ppm, respectively (Lee and Valla, 2019). In Colombia, the maximum sulfur concentration allowed for 2021 is between 10-15 ppm and 50 ppm for diesel and gasoline, respectively (Minambiente, 2019). In this context, the oil and gas industry commonly uses three strategies to reduce the sulfur content from heavy oils, mainly in the refining processes (Javadli and De Klerk, 2012). The first desulfurization process is to chemically remove the sulfur by hydrodesulfurization (HDS) (Javadli and De Klerk, 2012). In this method, sulfur is hydrotreated and removed as hydrogen sulfide. However, during HDS, high pressures, high temperatures, and operating costs are needed (Gao et al., 2019). The second strategy is to remove sulfur during the carbon rejection process (coking). Thermal cracking is used in coking to allow free radicals to disproportionate between lighter hydrogen-enriched fragments and heavier carbon-enriched coke (Al-Haj-Ibrahim and Morsi, 1992). Aromatic sulfur is difficult to remove by HDS, but some of it can be removed as part of the coke (Al-Haj-Ibrahim and Morsi, 1992). The third desulfurization strategy is to physically remove the sulfur with the heaviest material via solvent deasphalting, which can be used as a pre-refining process. However, the deasphalting technique is not very selective when it comes to sulfur removal. The processes mentioned above have been used in refineries for many years, but their shortcomings, primarily the cost associated with the process, necessitate the development of better technologies in this field (Babich and Moulijn, 2003).

Adsorptive desulfurization (ADS) has recently gained popularity for sulfur removal due to its adaptability to various fuels and process simplicity (Lee and Valla, 2019). During ADS, the sulfur compounds are transferred from the fuel, followed by the attachment of the compound to the sorbent materials through chemical interactions. A wide range of adsorbents have been reported for

desulphurization, including activated carbon (Jha et al., 2019), silica gel (Kwon et al., 2008), zeolites (Dehghan and Anbia, 2017), molecular sieve carbon (Saleh et al., 2016), activated alumina (Hussain and Tatarchuk, 2014), polymers (Li et al., 2012), and nanocomposites/nanomaterials (Saleh et al., 2016; Li et al., 2016). Each of these materials has distinct physical and chemical characteristics, such as pore size and structure, porosity, and nature of the adsorbing surface (Saleh et al., 2016; Li et al., 2016).

Due to the benefits of nanomaterials, including high surface area (Xiao et al., 2018), malleable surface chemistry (Medina et al., 2020; Medina et al., 2021b; Cardona et al., 2021), excellent textural properties (Acosta, 2021; Díez et al., 2020), high adsorption capacity for different hydrocarbon compounds (Medina et al., 2021a; Arias-Madrid et al., 2020; Medina et al., 2019a), and high catalytic activity to assist different chemical reaction and facilitate the regeneration of the adsorbent (Mateus et al., 2021; Medina et al., 2019b; Medina et al., 2019c), their use has been shown excellent results for crude oil desulfurization. Zirconia is mostly used as catalyst support in desulfurization (Kumar et al., 2011; Peterson et al., 2011; Li and Gonzalez, 1997), according to the existing literature. However, the optimal regeneration of the material occurs up to 800 °C (Saleh et al., 2016), which can difficult its application due to the associated cost. Meanwhile, activated alumina-based nanomaterials also present good adsorption yields for sulfur compounds, although it is revealed that they are not highly selective (Saleh et al., 2016). On the contrary, silica-nanomaterials have a high affinity for sulfur compounds and high regeneration potential (Kwon et al., 2008; Mendiratta and Ali, 2020). Also, doping adsorbents with metals and metal oxides enhances the sulfur species' selectivity, reactivity, and adsorption capacity. Most adsorbents adsorb at ambient conditions, and the desulfurization efficiency depends on the amount of metals and the type of sorbents used (Saleh et al., 2016). Some studies report high efficiencies for CuO (Khan et al., 2017), NiO (Ju et al., 2019), Fe<sub>2</sub>O<sub>3</sub> (Li et al., 2016), MoO<sub>3</sub> (Li et al., 2020), AgO (Hernández-Maldonado and Yang, 2003), among others. However, we have noticed that very complex materials must be developed to obtain high efficiencies, including more than two supporting and active phases (Khan et al., 2017; Watanabe et al., 2020; Ju et al., 2019; XU et al., 2016).

On the other hand, due to the interest presented in the last decade in applying these technologies at different scales, modeling, and simulation have been handy tools. The modeling of these processes has focused on adsorption and absorption technologies, such as ionic liquids (Gao et al., 2019; Jha et al., 2016)

and activated carbon-type adsorbents applied to diesel fuel desulfurization (Jha et al., 2019).

Regarding the absorption processes, in the research developed by Gao et al. (2019), the simulation of a desulfurization-extraction of 37-component diesel fuel with  $[C_{1}pyr] H_2PO_4$  was carried out on an industrial scale to make a sensitivity analysis of different parameters, including mass ratio ionic liquid-oil, temperature, and pressure. The model demonstrates that the coupled process can bring the diesel to the necessary conditions in the industry ( $S < 10$  ppm). Also, Jha et al. (Jha et al., 2016) studied the effect of ionic liquids on the desulfurization of an oil solution model consisting of 250 ppm of dibenzothiophene in *n*-heptane. It was done experimentally by adsorption batch experiments and then simulated the continuous extraction process. In this research, the effect of extraction time (15, 30, 60, and 90 min), temperature (25, 30, and 35 °C), the mass ratio between ionic liquid (trihexyl tetradecyl phosphonium chloride ionic liquid), and the model diesel fuel (1:8, 1:5, 1:4 and 1:3) were studied. The maximum sulfur removal was obtained at 60 min, 30°C, and a mass ratio between the ionic liquid and the model diesel fuel model of 1:3, which was 81.4%. Also, it was demonstrated that the ionic liquid could be used for five cycles. In this research, from the simulation of the batch process, it was obtained correlations between the interaction parameters of the components. Through the simulation of the continuous process, the validation of the application of the process was done, getting a good agreement between experimental and simulation data. Few works have focused on the simulation of crude oil adsorptive desulfurization in the literature. Jha et al. (2019) used a carbon-based adsorbent to model the diesel desulfurization of 500 ppm dibenzothiophene in *n*-heptane. This work used modeling to understand the sulfur adsorption equilibrium using Aspen Plus®, obtaining the interaction parameters of different isotherms (Langmuir, Dual Site Langmuir, and Sips models) with the best fit of Sips for PMAC 1/3 and dual site for PMAC 1. Another research involving activated carbon (Chemviron Carbon SOLCARB) was conducted by Muzic et al. (2011), which studied diesel desulfurization through the simulation of bed adsorption varying parameters such as feed flows (1, 5, 10, and 15  $cm^3 \cdot min^{-1}$ ), bed depths (9.6, 18.8 and 28.4 cm) and temperature (50 and 70 °C). For this, activated carbon with a particle size between 0.4-0.8 mm and a surface area of 936  $m^2 \cdot g^{-1}$  was used with a diesel fuel model (sulfur content equivalent to 27  $mg \cdot kg^{-1}$ ). The results showed that the best scenario is obtained with the lowest feed flow (1  $cm^3 \cdot min^{-1}$ ) at temperatures of 50 °C and a bed depth of 28.4 cm, where effluents with concentrations less than 0.7

mg·kg<sup>-1</sup> of sulfur content are achieved. With this scenario, numerical simulations were done to predict the dimension of an adsorptive column for industrial application, showing a column with a height of 17.32 m and an adsorbent load of 93.5 tons.

Also, most of the reported studies evaluate sulfur adsorption from model solutions, light crude oils, or diesel (Kwon et al., 2008; Watanabe et al., 2020; Tian et al., 2010; Li et al., 2020; Li et al., 2016). This work proposes for the first time a desulfurization process from a heavy crude oil matrix using nanomaterials to improve the selectivity of the sulfur compounds and their regeneration process based on experimental and simulation tools. This represents a challenge given the presence of macromolecules and other metallic compounds that hinder the adsorptive-selective process. In this sense, this work aims to develop a simple-highly adsorbent nanomaterial for sulfur removal from virgin heavy crude oils consisting of silica-support doped active metal phases and the subsequent validation through experimental y simulation tools. For this, our work is composed of 5 main steps, including i) synthesis and evaluation of different transition element oxides nanoparticles in sulfur adsorption, ii) doping, evaluation, and statistical analysis of SiO<sub>2</sub> with transition element oxides, iii) construction of adsorption isotherms for the best-in-class system, iv) displacement tests and v) validation through numerical simulation and subsequent upscaling of the technology.

The efficiency of reactive 704dsorptionn of the nanomaterial is validated by estimating the adsorption capacity, its affinity for sulfur species, and its thermal and mechanical stability. To the best of our knowledge, this is the first work that attempts a combined evaluation of sulfur removal through experimental and simulation studies using a heavy crude oil-like sulfur source.

## 2. Experimental

### 2.1. Materials

The heavy crude oil employed for this study was obtained from Hocol S.A., Colombia. The basic properties of crude oil are given in Table 1. Salt precursors of Fe(NO<sub>3</sub>)<sub>3</sub>, Ni(NO<sub>3</sub>)<sub>2</sub>, (NH<sub>4</sub>)<sub>6</sub>Mo<sub>7</sub>O<sub>24</sub>, Ag(NO<sub>3</sub>), CuCl<sub>2</sub>·2H<sub>2</sub>O, and Zn(NO<sub>3</sub>)<sub>2</sub> (Merck KGaA, Darmstadt, Germany), and distilled water were used for the hydrothermal synthesis of transition element oxides nanoparticles. Commercial silica microparticles with a particle size of 3.0 μm (Sigma-Aldrich, USA) were

used to support and doped with  $\text{Ag}(\text{NO}_3)$  and  $\text{CuCl}_2 \cdot 2\text{H}_2\text{O}$ . After impregnation, samples were calcined at  $450^\circ\text{C}$ .

**Table 1.** Basic properties estimated for the heavy crude oil.

Liquid density ( $\text{g}\cdot\text{ml}^{-1}$ )	API 60 $^\circ\text{F}$	Sulfur content (ppm)	SARA content (%)			
			Saturates	Aromatics	Resins	Asphaltenes
0.96	14.4	35867	17.19	15.36	61.25	6.20

## 2.2. Methods

Figure 1 shows the proposed workflow to develop and evaluate a highly sulfur-selective nanomaterial to carry out heavy crude oil desulfurization. The process starts with the nanoparticle synthesis of different transition element oxides nanoparticles and their evaluation in batch type for sulfur adsorption. From these results, the two TEO nanoparticles with the higher sulfur removal were selected and used as active phases for doping  $\text{SiO}_2$  microparticles. In this sense, seven nanomaterials were synthesized, and the metal loads were selected following simplex-centroid mixture experiments to optimize the metal load on the  $\text{SiO}_2$  surface. Once the optimized nanomaterial was obtained, adsorption isotherms were constructed at different temperatures, including 25, 35, and  $55^\circ\text{C}$ , along with a thermodynamic analysis of the adsorptive phenomenon. Next, the dynamic adsorption of the same material was evaluated at atmospheric conditions. The dynamic system was validated through numerical simulation in Aspen Adsorption V10. Also, the simulation tool was used to perform sensitivity analysis on parameters such as feed flow ( $1, 10, 50 \text{ ml}\cdot\text{min}^{-1}$ ) in the laboratory-scale process and assess the performance of the desulfurization process at different scales.

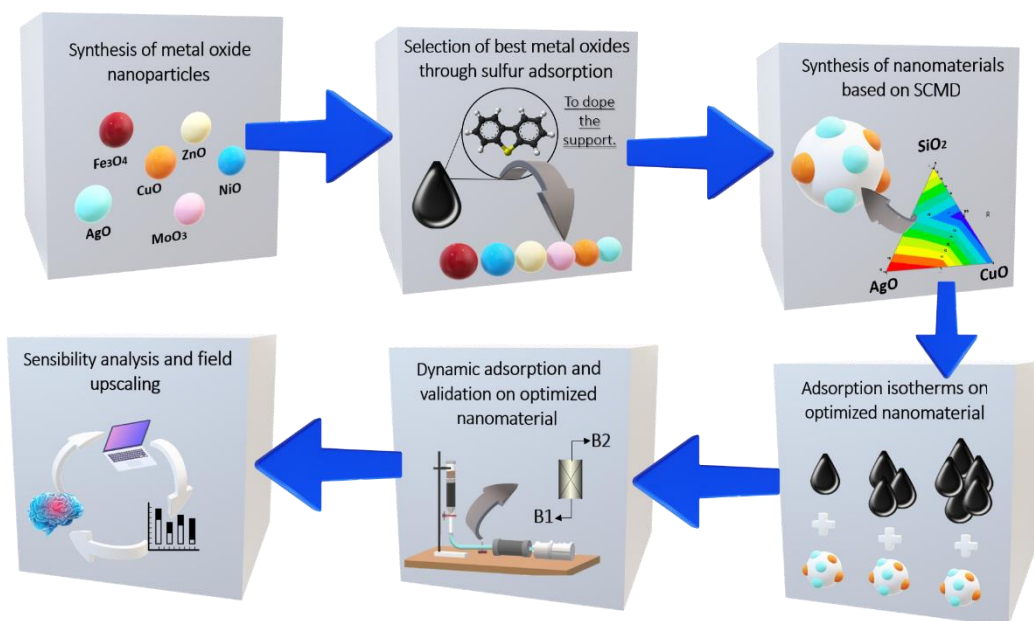


**Figure 1.** Workflow conducted in this investigation.

### 2.2.1. Characterization of nanomaterials

The silica gel used as support was provided by (Evonik, Essen, Germany) and doped with  $\text{Ag}(\text{NO}_3)$  and  $\text{CuCl}_2 \cdot 2\text{H}_2\text{O}$  (Merck KGaA, Darmstadt, Germany). The doped nanomaterials were robustly characterized. Seven nanomaterials, including  $\text{SiCu}_2$ ,  $\text{SiAg}_2$ ,  $\text{SiCu}_4$ ,  $\text{SiAg}_4$ ,  $\text{SiAg}_2\text{Cu}_2$ ,  $\text{SiAg}_{1.32}\text{Cu}_{1.32}$ ,  $\text{SiAg}_{1.5}\text{Cu}_{1.4}$ , were prepared through incipient wetness impregnation. The samples were labeled using the first two letters of the support (Si), the periodic symbol of the active phase (Ag or Cu), and the mmol of the TEO (2, 4, 1.32, 1.5, and 1.4).

The morphology and structure of the nanoparticles were characterized by transmission electron microscopy using an FEI Titan G2 microscope (HRTEM) (Eindhoven, The Netherlands). with an accelerating voltage of 200 Kv. Also, the particle size was estimated through dynamic light scattering (DLS) using a Nanoplus-3, Micromeritics (GA, USA), following the protocol described in the literature (Montes et al., 2020). The textural properties of the nanomaterials were measured on a micrometric ASAP 2020 (Micromeritics, Norcross, GA, USA) through  $\text{N}_2$  adsorption-desorption at  $-196^\circ\text{C}$ . The samples were degassed before measurement at  $300^\circ\text{C}$  for four h to remove impurities. The surface area of the composites was calculated by the BET method (Naderi, 2015), and the Dubinin-Radushkevich method was used for the estimation of the micropore volume ( $W_0$ ) and micropore means ( $L_0$ ) (Nguyen and Do, 2001). X-ray powder diffraction (XRD) was conducted to characterize the crystal phase of the samples. The diffraction patterns were recorded on a Bruker-D8 Venture X-ray diffractometer



(BRUKER, Rivas-Vaciamadrid, Spain) using Cu K $\alpha$  radiation source ( $\lambda=1.54 \text{ \AA}$ ). Scanning angles for all samples were set in the  $2\theta$  range of  $0-90^\circ$  (scan rate  $0.02^\circ 2\theta \text{ s}^{-1}$ ) (Kroon, 2013). X-ray photoelectron spectroscopy (XPS) was performed on a Kratos Axis Ultra-DLD spectrometer (Manchester, UK) equipped with a hemispherical electron analyzer connected to a detector DLD (delay-line detector). The dispersion of the metals was obtained through H<sub>2</sub> titration following the protocol described in the literature (Medina et al., 2019a).

### 2.2.2. Batch adsorption experiments

The crude oil containing  $35867 \text{ mg}\cdot\text{L}^{-1}$  of sulfur was used for batch adsorption experiments. The TEO nanoparticles were selected by evaluating three adsorption points of 1:2, 1:10, and 1:20 adsorbent mass: crude oil mass ratio. The sulfur adsorption of the doped nanomaterials was assessed in the same ratio. Then, adsorption isotherms were constructed for the optimized system resulting in the simplex-centroid mixture design varying the amount of the crude oil (40, 30, 20, 10 g, 4, and 2g, that is, 1:20, 2:30, 1:10, 1:5, 1:2, and 1:1 adsorbent mass: crude oil mass ratio, respectively). The mixtures were magnetically stirred at three temperatures (25, 35, and  $55^\circ\text{C}$ ) until equilibrium was achieved. Then, aliquot samples were collected using a syringe filter (hydrophobic polytetrafluoroethylene). After adsorption, the concentration of sulfur was determined through X-ray fluorescence spectrometry (XRF) in a Philips model 1400 wavelength-dispersive spectrometer. The instrumental conditions were fixed as 100 s irradiation time, operating at 100 mA and set at 15 kV. A Germanium crystal and a proportional flow counter were used to measure the K alpha lines of sulfur and the background next to the peaks. Sulfur standards were prepared from *n*-dibutyl sulfide diluted with mineral spirits. A fivefold dilution of the waste oil samples with mineral spirits prepared samples for the XRF measurements. The diluted samples were introduced into the spectrometer in 31 mm diameter plastic cups with polypropylene windows (Chemplex). Initially, the cups were filled to within 4 mm of the top. The analyte adsorption ( $N_{ads}$ ,  $\text{mg S}\cdot\text{g}^{-1}$ ) at equilibrium was calculated using the Equation (1):

$$N_{ads} = (C_o - C_E) \frac{V}{W} \quad (1)$$

where  $C_0$  and  $C_E$  ( $\text{mg}\cdot\text{L}^{-1}$ ) are the initial and equilibrium concentrations of sulfur compounds in crude oil, respectively,  $V$  (L) is the volume of the crude oil, and  $W$  (g) represents the weight of the adsorbents.

The adsorption isotherms were fitted by the solid-liquid equilibrium (SLE) model proposed by Montoya et al. (2014). The model describes the concentration of sulfur at the equilibrium  $C$  ( $\text{mg}\cdot\text{L}^{-1}$ ) by the Equation (2):

$$C = \frac{\psi H}{1 + K\psi} e^{\left(\frac{\psi}{N_m}\right)} \quad (2)$$

where  $H$  ( $\text{mg}\cdot\text{g}^{-1}$ ) is known as the Henry's Law constant,  $K$  ( $\text{g}\cdot\text{g}^{-1}$ ) is an indicator of the association of surfactant molecules once the primary sites are filled, and  $N_m$  ( $\text{g}\cdot\text{g}^{-1}$ ) parameter refers to the maximum adsorption capacity. Details of the model are found elsewhere (Montoya et al., 2014; Nassar et al., 2015; Medina et al., 2019b; Medina et al., 2020). The thermodynamic properties ( $\Delta H_{ads}^0$  - enthalpy,  $\Delta S_{ads}^0$  - entropy,  $\Delta G_{ads}^0$  - Gibbs free energy) of the adsorption phenomenon were determined based on the five-parameter SLE model (Montoya et al., 2014).

Also, for simulation purposes, the Freundlich model fitted the adsorption isotherms, which is part of the Aspen Adsorption program (AspenTech, 10.1, Bedford, EE. UU.) interface, where the numerical simulation and scaling of the system was done (Proctor and Toro-Vazquez, 1996). The model is shown in Equation (3):

$$w_i = K_1 c_i^{1/n} \quad (3)$$

where  $w_i$  is the loading of an  $i$ -adsorbate in the adsorbent ( $\text{mg}\cdot\text{g}^{-1}$ ),  $K_1$  is a constant related to the adsorption capacity of the adsorbent ( $\text{kg}\cdot\text{g}^{-1}$ ),  $c_i$  is the equilibrium concentration of the adsorbate in solution ( $\text{mg}\cdot\text{kg}^{-1}$ ), and  $n$  is a constant indicative of the adsorption intensity.

### 2.2.3. Dynamic adsorption and validation through simulation

Dynamic adsorption tests were performed on a fixed-bed column based on the experimental setup shown in Figure 2. It consists of a positive displacement pump, a crude oil-containing cylinder containing two regulating valves, and an

open packed-bed system with 0.3 porosity. The adsorbent was packed inside the column (2 cm diameter - 50 cm height). Next, the crude oil was injected with a controlled flow rate of 2.0 ml·min<sup>-1</sup> at room pressure (0.1 MPa) and temperature (25 °C). The desulfurization products were collected periodically in a beaker to analyze sulfur content by XRF. The test provides information about the adsorption capacity and speed of saturation of the packed bed.

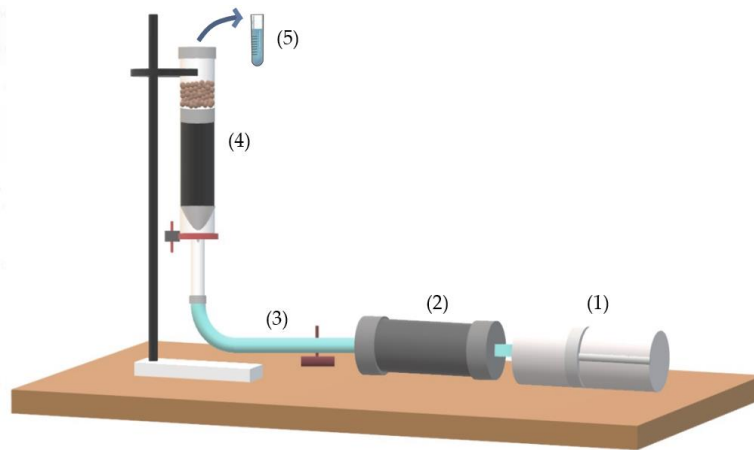


**Figure 2.** Experimental setup for dynamic adsorption tests consisting of (1) positive displacement pump, (2) crude oil containing cylinder, (3) regulating valves, (4) open packed-bed system, and (5) effluent collection. Adapted from Acosta et al. (2021).

Sulfur adsorption simulation was done in the Aspen Adsorption program (AspenTech, 10.1, Bedford, EE. UU.). Sulfur was represented by dibenzothiophene for dynamic adsorption simulation on a fixed-bed column backed with SiAg1.5Cu1.4. Some assumptions were considered for modeling the process. The mass balance was determined considering only convection, a constant mass transfer coefficient, and an isothermal process (heat transfer is neglected). The kinetics of mass transfer is described by the linear driving force model (LDF). Finally, the adsorption isotherm is defined by the Freundlich isotherm model.

The model applied by Aspen Adsorption contemplates the following conservation of mass equation (Equation (4)):

$$\varepsilon_i \frac{\partial \rho_p}{\partial t} + \frac{\partial}{\partial z} (v_i \rho_p) + \rho_s \sum_{i=1}^N \left( M_i \frac{\partial w_i}{\partial t} \right) = 0 \quad (4)$$

where  $\varepsilon_i$  is the porosity,  $\rho_{lp}$  is the liquid phase mass density,  $v_l$  is the liquid phase superficial velocity,  $\rho_s$  is the adsorbent bulk density,  $M_i$  is the molecular weight of  $i$ -components, and  $w_i$  is the molar loading of an  $i$ -adsorbate in the adsorbent. Conservation of the mass equation for component  $i$  is given by Equation (5), shown below.

$$-\varepsilon_i E_z \frac{\partial^2 c_i}{\partial z^2} + \frac{\partial}{\partial z} (v_l c_i) + \varepsilon_i \frac{\partial c_i}{\partial t} + \rho_s \frac{\partial \bar{w}_i}{\partial t} = 0 \quad (5)$$

where  $E_z$  is the axial dispersion coefficient, and  $c_i$  is the molar concentration of the  $i$ -component.

To complement the mass balance, momentum transport through the bed is considered. This equation is used to relate internal superficial velocities to local pressure gradients. For this purpose, the darcy equation represented by Equation (6) is used

$$\frac{\partial P}{\partial z} = -K_p v_L \quad (6)$$

where  $K_p$  is a proportionality constant and  $v_L$  superficial velocity of the liquid phase.

To describe the adsorption kinetics, the Linear Lumped Resistance model was used (Felinger and Guiochon, 2004), where the mass transfer driving force for component  $i$  is expressed as a linear function of the solid phase load (Equation (7)):

$$\frac{\partial w_i}{\partial t} = MTC_{si} (w_i^* - w_i) \quad (7)$$

where  $MTC_{si}$  is the solid film mass transfer coefficient. The crude oil described in section 2.1 was considered.

The boundary conditions considered for the solution of the system are: *i*) The concentration of the sulfur component at the inlet is constant, *ii*) fluid velocity at the inlet is constant, and *iii*) the Linear Lumped Resistance gives the mass transfer on the adsorbent surface.

Figure 2 shows the representation of the adsorption system. Also, the simulation parameters for the described model are shown in Table 2.

**Table 2.** Simulation parameters estimated from the experimental data.

Parameter	Value
Solid density $\rho_s$ , (kg·m <sup>-3</sup> )	2650
Porosity $\varepsilon_i$	0.15
Isotherm parameter $K_1$ , (kg·g <sup>-1</sup> ) @ 25°C	2.62x10 <sup>-5</sup>
Isotherm parameter $n$ @ 25°C	0.63

In the first stage, the model was validated from experimental data (Case 1), followed by an analysis of the system to changes in the feed flow to evaluate the model's ability to capture this trend (cases 2, 3, 4). Subsequently, the process is carried out on a larger scale with feed flows like those obtained in an oil field; in this stage, a dimensioning of the column is carried out, preserving an aspect ratio of 4 (cases 5, 6, 7, 8, and 9). Finally, variations in case 8 from 25 °C to 35 °C and 55 °C are evaluated (Cases 10 and 11). Table 3 shows the cases analyzed and the characteristics of each simulation. Finally, Table 4 shows the convergence criteria used for the simulations of the cases raised.

**Table 3.** simulated case characteristics.

Case	Height (m)	Diameter (m)	Feed flow (ml·min <sup>-1</sup> )	Temperature (°C)
Case 1	0.5	0.02	3	25
Case 2	0.3	0.02	1	25
Case 3	0.3	0.02	10	25
Case 4	0.3	0.02	50	25
Case 5	1.0	0.25	151800	25
Case 6	1.5	0.37	151800	25
Case 7	2.0	0.50	151800	25
Case 8	3.0	0.75	151800	25
Case 9	5.0	1.25	151800	25
Case 10	3.0	0.75	151800	35
Case 11	3.0	0.75	151800	55

**Table 4.** Convergence criterion for simulations.

Method	Mixed Newton
Convergence criterion	Residual
Maximum number of iterations	500
Integration Method	Implicit Euler
Absolute tolerance	1x10 <sup>-7</sup>
Relative tolerance	1x10 <sup>-7</sup>
Nodes	20
Initialization	Hybrid

### 3. Optimization of a load of active phases through Simplex-Centroid Mixture Design

To increase the adsorption amount of sulfur in the adsorbent, an optimization of the load of the transition element oxides of Cu and Ag over the SiO<sub>2</sub> support was done. A simplex-centroid mixture design (SCMD) was developed using STATGRAPHICS Centurion XVI software (XVI version, StatPoint Technologies Inc., Addison, TX, USA). The model is detailed below:

Three components were considered, including the support (SiO<sub>2</sub>) and the active phases of the TEO Ag and Cu, varying their concentrations (Ag and Cu between 0 and 4.0% in mass fraction) to obtain seven different systems. The samples were mixed with the crude oil in a 1:10 adsorbent mass: crude oil mass ratio. The concentrations of each component must satisfy the following restriction (Equation (8)) (Cornell, 2011):

$$\sum_i^q x_i = x_1 + x_2 + x_3 + \dots + x_q = 1, x_i \geq 0 \quad (8)$$

where  $q$  refers to the number of components varying in the mixture (i.e., 3). The selected range of concentrations for each element consists of the following (Equations 9-11):

$$0.96 \leq SiO_2 \leq 1.00 \quad (9)$$

$$0 \leq Ag \leq 0.04 \quad (10)$$

$$0 \leq Cu \leq 0.04 \quad (11)$$

The simplex-centroid mixture design was resolved by considering a cubic model to evaluate the maximum and minimum concentration of each component and intermedium points (Humberto and de la Vara, 2003). Illustratively, the limits of the compounds used for the statistical design of the Si-Ag-Cu system are shown in Figure 3. Finally, the regression model was established using a special cubic regression fitting.

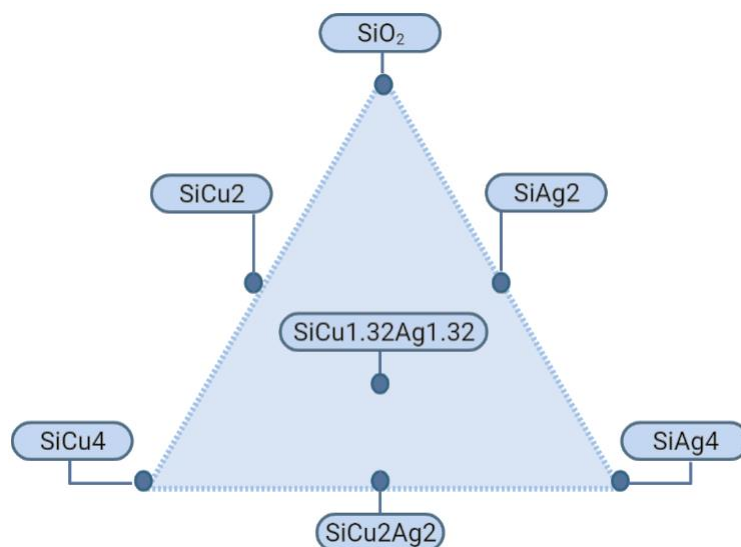


**Figure 3.** Three components simplex-centroid mixture design proposed to optimize the load of transition element oxides of Cu and Ag over SiO<sub>2</sub> for increasing the sulfur adsorption amount. The mass fraction varied between 0 and 4% for the TEO.

## 4. Results and discussion

### 4.1. Adsorbent characterization

Representative TEM images of the SiO<sub>2</sub> support and doped adsorbents are shown in Figure 4. Results show some variability in the shape and size of the doped phases and slight signs of aggregation. The shaded parts in each sample may be associated with Ag and Cu in the SiO<sub>2</sub> support. Most of the crystals formed do not have a defined morphology. On the other hand, the hydrodynamic size of the doped adsorbents did not change concerning the size of the SiO<sub>2</sub> support (3.0 μm).

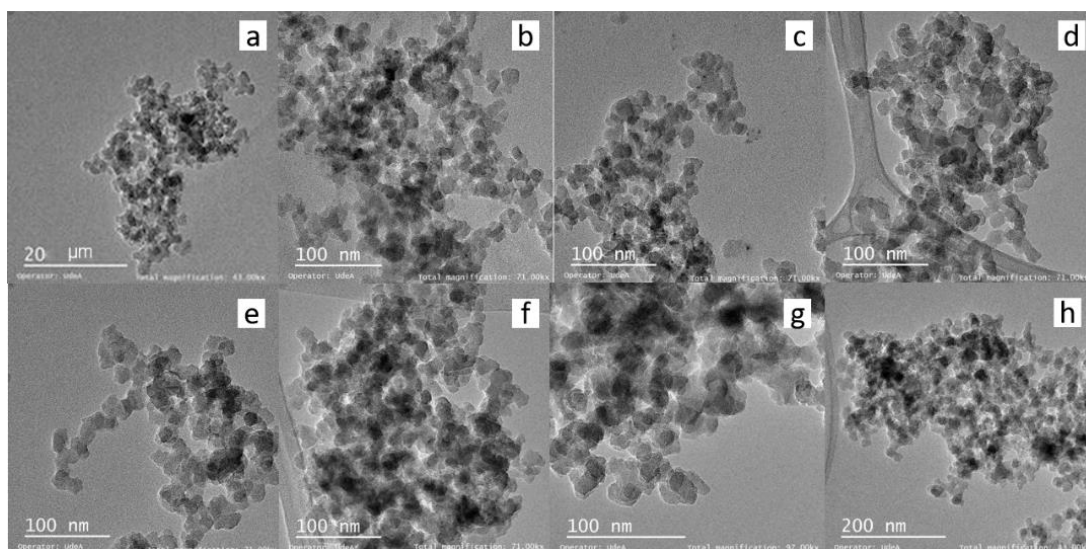


**Figure 4.** TEM images of a) SiO<sub>2</sub>, b) SiCu<sub>2</sub>, c) SiCu<sub>4</sub>, d) SiAg<sub>2</sub>, e) SiAg<sub>4</sub>, f) SiAg<sub>1.32</sub>Cu<sub>1.32</sub>, g) SiAg<sub>2</sub>Cu<sub>2</sub>, and h) SiAg<sub>1.5</sub>Cu<sub>1.4</sub>.

The XRD pattern of the doped adsorbents and support is depicted in Figure 5. The spectrum for SiO<sub>2</sub> exhibits one broad peak at 22°, attributed to amorphous silica (Tang et al., 2012). The XRD patterns of SiCu<sub>2</sub> and SiCu<sub>4</sub> showed slight reflection patterns of silicon at 2θ values 46.3° (220), 57.5° (311), and 67.4° (400) and (331) that correspond to crystalline planes of silicon (Kiran et al., 2020).

The main characteristic diffraction peaks of the SiCu<sub>2</sub> and SiCu<sub>4</sub> samples are consistent, and the corresponding 2θ is also consistent, indicating that the two samples have the same phases. According to the peaks of the cuprite standard (JCPDS 48-1548), at 36.6°, the (111) facet is observable (Zhu et al., 2018). The other peaks at 41.3°, 51.0°, and 72.8° result from a Cu<sup>0</sup> presence (He et al., 2011). No diffraction peaks for copper oxide could be observed, indicating that copper was highly dispersed in the porous silica support (He et al., 2011). On the contrary, copper exhibits different phases in doped systems with Ag and Cu. Following the JCPDS 48-1548, the peaks at 32.6, 35.7, 38.9, 49.0, 53.6, 61.7, and 68.4°, are ascribed to (110), (002), (111), (202), (020), (113), and (220) (Zhu et al., 2018). Also, the characteristic diffraction peak of Cu<sub>2</sub>O (JCPDS 034-1354) at 2θ of 42.4° appeared in the three samples (He et al., 2011).

The XRD pattern of SiAg<sub>1.32</sub>Cu<sub>1.32</sub>, SiAg<sub>2</sub>Cu<sub>2</sub>, and SiAg<sub>1.5</sub>Cu<sub>1.4</sub> exhibit reflection peaks at 2θ = 32.2, 38.2, 44.6, 64.4, and 77.4°, which correspond to (112), (111), (200), (220) and (311) face-centered cubic (fcc) crystalline structure of Ag particles (Muthuchamy et al., 2015). Similarly, the samples SiAg<sub>2</sub> and SiAg<sub>4</sub> exhibit the same peaks (except for 32.2°), and also another peak at 81.0° that



corresponds to the (222) facet of silver in face centers cubic structure (ICDD 04-0783) (Kiran et al., 2020). Also, diffraction peaks at  $46.3^\circ$ ,  $54.9^\circ$ , and  $67.4^\circ$  can be indexed to (211), (220), and (222) planes of face-center cubic silver, respectively. These peaks agree with the standard  $\text{Ag}_2\text{O}$  (JCPDS 76-1393) (Dhoondia and Chakraborty, 2012). It is worth mentioning that the patterns obtained for Ag- and Cu- doped nanomaterials show no displacement in the peaks regarding the mono elemental systems, indicating no Ag doping on the Cu sites or vice versa.

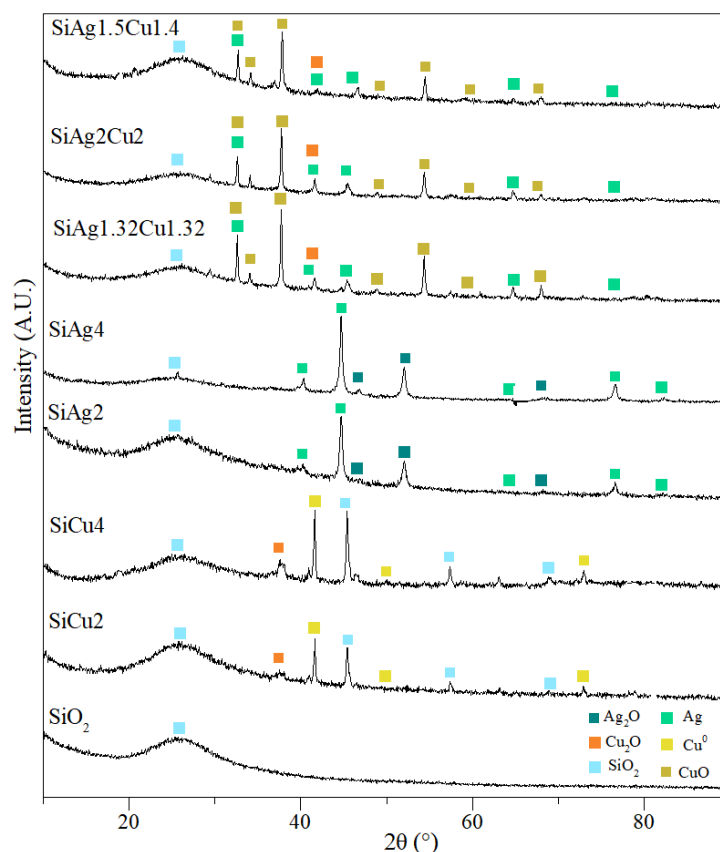


**Figure 5.** XRD patterns of the adsorbents composed of  $\text{SiO}_2$  support doped with different loads of Ag and Cu.

The average crystallite size of metal phases was calculated from the XRD data using the Debye- Scherrer equation (Kroon, 2013), and the results are summarized in Table 5.  $\text{CuO}$  crystal size decreases in the order  $\text{SiCu}_2 < \text{SiCu}_4 < \text{SiAg1.32Cu1.32} < \text{SiAg2Cu}_2 < \text{SiAg1.5Cu1.4}$ . In the case of Ag crystal size, it follows the decreasing order  $\text{SiAg}_2 < \text{SiAg}_4 < \text{SiAg1.32Cu1.32} < \text{SiAg2Cu}_2 < \text{SiAg1.5Cu1.4}$ . Both trends indicate that Ag- and Cu-doped systems have smaller Ag and  $\text{CuO}$  crystal sizes. It means that the presence of another phase in  $\text{SiO}_2$  surface avoids sintering processes, generating a more homogeneous surface,

which agrees with the dispersions of Ag and Cu, lower for mono-elemental systems than bi-elemental systems.

**Table 5.** Average crystal size of silica doped with different loads of Ag and Cu.

Sample	Ag dispersion (%)	Cu dispersion (%)	Ag <sub>2</sub> O size <sub>DRX</sub> (%)	Ag size <sub>DRX</sub> (%)	CuO size <sub>DRX</sub> (%)	Cu size <sub>DRX</sub> (%)
SiO <sub>2</sub>	-	-	-	-	-	-
SiAg2	25	-	20.4	28.2	-	-
SiAg4	19	-	32.6	24.4	-	-
SiCu2	-	29	-	-	9.6	22.0
SiCu4	-	21	-	-	7.1	26.8
SiAg1.32Cu1.32	33	40	nd	16.1	4.4	nd
SiAg2Cu2	37	41	nd	11.2	4.2	nd
SiAg1.5Cu1.4	39	42	nd	10.3	3.2	nd

The textural properties of the catalysts were estimated, and the results are shown in Table 6. The area BET of the support was determined in 172.4 m<sup>2</sup>·g<sup>-1</sup>. After the doping process, the area was reduced due to the porosity and deposition of the Cu and Ag metals in the porous space. This was also corroborated by the slight reduction of the pore volume from 9.23 cm<sup>3</sup>·g<sup>-1</sup> to 5.51 cm<sup>3</sup>·g<sup>-1</sup> - 7.45 cm<sup>3</sup>·g<sup>-1</sup>. Finally, the average pore size was not affected by the doping process obtaining a pore size between 2.13-2.14 nm in all systems.

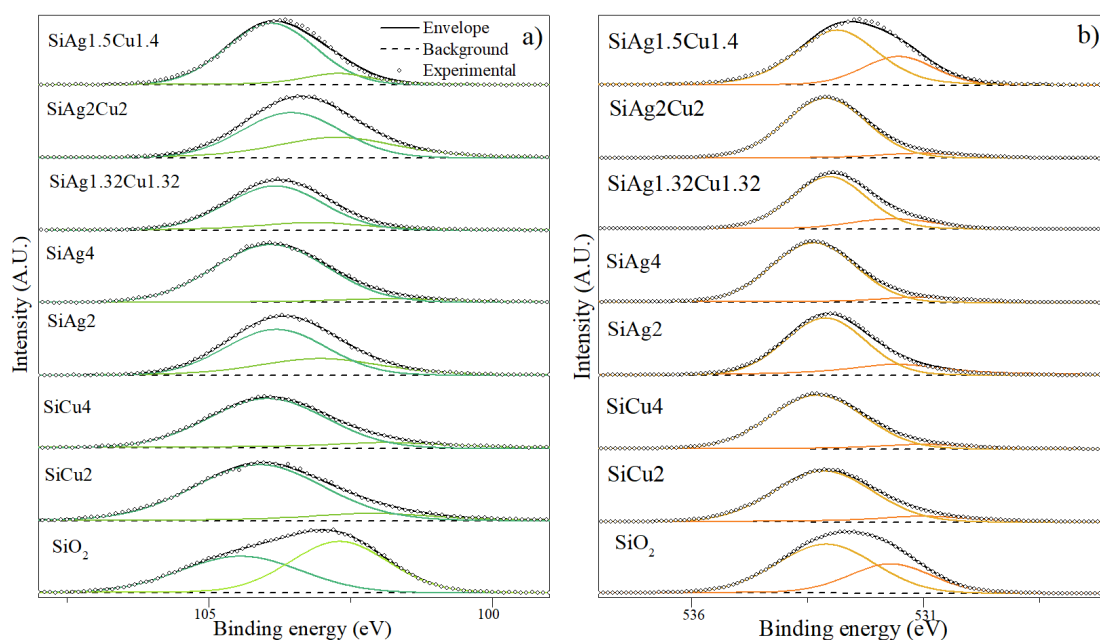
**Table 6.** Estimated porous textural characteristics of the doped SiO<sub>2</sub> microparticles with different loads of Ag and Cu obtained from N<sub>2</sub> adsorption-desorption and CO<sub>2</sub> adsorption.

Sample	S <sub>BET</sub> m <sup>2</sup> ·g <sup>-1</sup>	W <sub>0</sub> (N <sub>2</sub> ) x 10 <sup>-2</sup> cm <sup>3</sup> ·g <sup>-1</sup>	L <sub>0</sub> (N <sub>2</sub> ) nm
SiO <sub>2</sub>	172.4	9.23	2.14
SiAg2	135.3	6.66	2.13
SiAg4	127.1	5.51	2.13
SiCu2	139.5	7.45	2.14
SiCu4	124.5	6.10	2.13
SiAg1.32Cu1.32	128.5	6.87	2.13
SiAg2Cu2	124.3	6.64	2.14
SiAg1.5Cu1.4	124.3	6.63	2.13

XPS was used to investigate the oxidation state and coordination number of the metal ions on the outermost surface of the doped adsorbents. Figure 6a-d

depicts the XP spectra of Si<sub>2p</sub>, O<sub>1s</sub>, Ag<sub>3d</sub>, and Cu<sub>2p<sub>3/2</sub></sub> core-level regions. A pair of Si<sub>2p</sub> peaks (Figure 6a) is located at 102.3 and 103.5 eV, which corresponds to the Si-O-Si and Si-OH signals of silicon oxide (Post et al., 2018). From the O<sub>1s</sub> spectra (Figure 6b), the deconvoluted spectrum at 533.2 eV is from the SiO<sub>2</sub>, and the spectrum at 531.8 eV, which is minor, is due to the Ag<sub>2</sub>O and CuO species (Mo et al., 2018). In the same sense, panel c of Figure 6 shows the high-resolution spectra of Ag<sub>3d</sub>, which offers a doublet structure with the typical binding energy of 368.5 eV with a doublet splitting of 6 eV. The peaks in the 3d<sub>5/2</sub> region at 368.2 eV and 367.8 eV indicate the presence of pure silver - Ag<sup>0</sup> state and silver (II) oxide, respectively (Urán et al., 2020). The Cu<sub>2p<sub>3/2</sub></sub> of the adsorbents (Figure 6d) showed two peaks at 932.4 and 933.4 eV assigned to Cu<sup>+</sup> and Cu<sup>2+</sup>, respectively (López-Ramón et al., 2018).

The atomic concentration of the species was calculated and summarized in Table 7. The concentration of Cu<sup>+</sup> species follows the increasing order SiCu<sub>2</sub> < SiCu<sub>4</sub> < SiAg<sub>1.32</sub>Cu<sub>1.32</sub> < SiAg<sub>2</sub>Cu<sub>2</sub> < SiAg<sub>1.5</sub>Cu<sub>1.4</sub>, which agrees with the intensity signals of the XRD peaks for CuO facets. Interestingly, the bi-elemental samples (with Ag and Cu) present the highest content of Ag<sup>0</sup> and the lowest of Cu<sup>2+</sup> and Ag<sup>2+</sup>. Finally, the oxygen anchored to metal species was higher in the SiAg<sub>1.5</sub>Cu<sub>1.4</sub> system, while the range of Si-O-Si was slightly lower regarding the support.



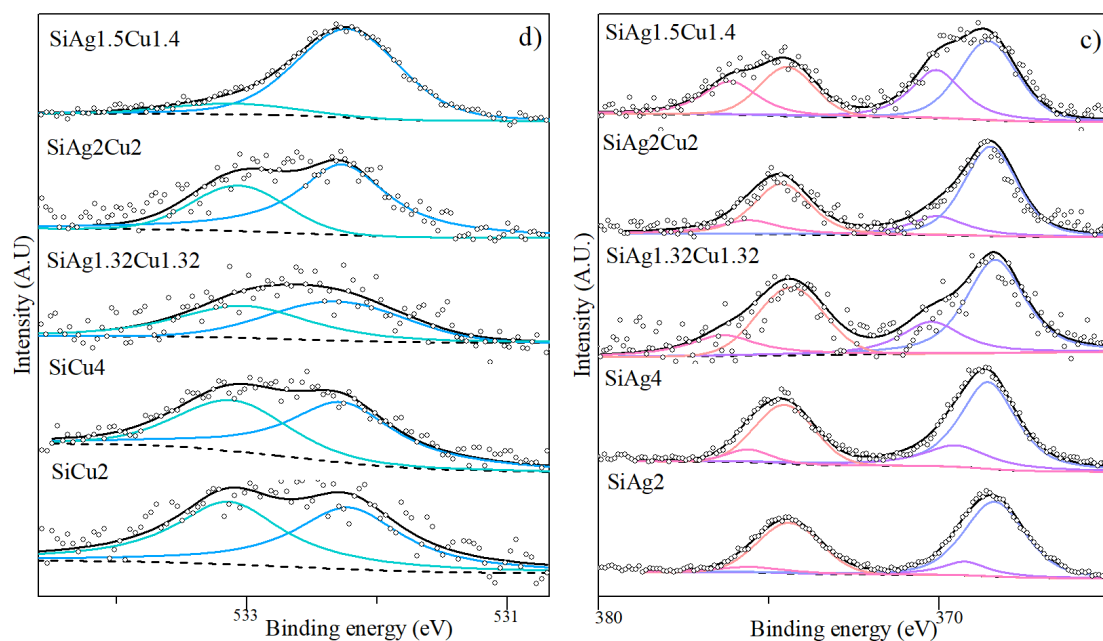


**Figure 6.** High-resolution XPS spectra of a) Si<sub>2p</sub>, b) O<sub>1s</sub>, c) Ag<sub>3d</sub>, and d) Cu<sub>2p<sub>5/2</sub></sub> of silica doped with different loads of Ag and Cu.

**Table 7.** Chemical surface composition of silica doped with different loads of Ag and Cu determined by XPS.

Sample	Si <sub>x</sub> <sup>XPS</sup> (%)	O <sub>x</sub> <sup>XPS</sup> (%)	Ag <sub>x</sub> <sup>XPS</sup> (%)	Cu <sub>x</sub> <sup>XPS</sup> (%)	Si-OH (%)	Si-O-Si (%)	O-Metal (%)	Cu <sup>+</sup> (%)	Cu <sup>2+</sup> (%)	Ag <sup>0</sup> (%)	Ag <sup>2+</sup> (%)
SiO <sub>2</sub>	31.4	68.6	-	-	60.5	39.5	-	-	-	-	-
SiAg <sub>2</sub>	29.8	68.3	1.9	-	62.4	37.6	15.0	-	-	20.7	79.3
SiAg <sub>4</sub>	27.3	68.7	4.0	-	62.8	37.2	16.9	-	-	26.5	73.5
SiCu <sub>2</sub>	28.5	69.7	-	1.8	62.0	38.0	15.6	47.6	52.4	-	-
SiCu <sub>4</sub>	27.0	69.1	-	3.9	62.6	37.4	16.3	50.3	49.7	-	-
SiAg <sub>1.32</sub> Cu <sub>1.32</sub> 2	29.6	67.7	1.3	1.4	63.2	36.8	27.8	76.8	23.2	30.6	69.4
SiAg <sub>2</sub> Cu <sub>2</sub>	26.5	69.6	1.9	2.0	63.5	36.5	26.5	80.2	19.8	33.2	66.8
SiAg <sub>1.5</sub> Cu <sub>1.4</sub>	26.5	70.6	1.5	1.4	63.4	36.6	30.4	85.7	14.3	47.2	52.8

## 4.2. Batch adsorption experiments

### 4.2.1. Active phase selection

Six different nanoparticles of different transition element oxides were evaluated to select the active phases for constructing the doped nanomaterial based on the affinity and the adsorbed amount of sulfur compounds. The results

are depicted in Figure 7, which assessed different ratios, including 1:2, 1:10, and 1:20 mass:mass at 25 °C. It is noted that the chemical nature of the adsorbent influences the adsorption amount of sulfur compounds following the increasing order  $\text{Fe}_3\text{O}_4 < \text{NiO} < \text{ZnO} < \text{MoO}_3 < \text{CuO} < \text{AgO}$  for all the ratios. Different sulfur removal percentages are obtained due to the adsorbents' different chemical and textural properties, which promote other interactions with the sulfur-based compounds (Khan et al., 2017; Watanabe et al., 2020; Zhang et al., 2019; Ju et al., 2019; Li et al., 2016). Selective adsorption is reported to occur in site-specific interactions between sulfur species and metals in organometallic complexes (Ju et al., 2019). The possible adsorption configurations of thiophene compounds on metal oxides result from the coordination geometries that thiophene exerts upon contact with organometallic complexes (Khan et al., 2017). On the other hand, aromatic sulfur and non-sulfur aromatic forms can interact with metal species by  $\pi$ -electrons (Saleh et al., 2016), so the probable coordination geometries will better explain the interaction of the sulfur atom of thiophene compounds with the adsorbent are:  $\eta^1\text{S}$  (sulfur atom of thiophenes and a metal relation) and  $\text{S}-\mu_3$  (sulfur atom of thiophenes and two metal species) (Saleh et al., 2016). In this section,  $\eta^1\text{S}$  structures are the most likely found in the adsorption process.

Also, adsorption by chemical complexation ( $\pi$ -complexation) explains the selectivity of sulfur compounds for different transition element oxides (Hernández-Maldonado and Yang, 2003). Cations, including  $\text{Ag}^+$  and  $\text{Cu}^+$  form  $\pi$ -complexes between the metals and thiophene, benzodithiophene, and dibenzothiophene (Hernández-Maldonado and Yang, 2003). The cations form  $\sigma$ -bonds with free s-orbitals, and the d-orbitals will back-donate electron density to the antibonding  $\pi$ -orbitals in the sulfur-containing ring of thiophenes (Hussain and Tatarchuk, 2014). Bonds formed due to this interaction are stronger and easily broken by alternating the temperature or pressure, enhancing the capacity and selectivity of sulfur compounds. In this order, the AgO and CuO nanoparticles achieve higher sulfur removal efficiency and, consequently, are selected as active phases for the  $\text{SiO}_2$  support. The systems are used in a statistical experimental design for optimizing their load on the surface of the  $\text{SiO}_2$  support.

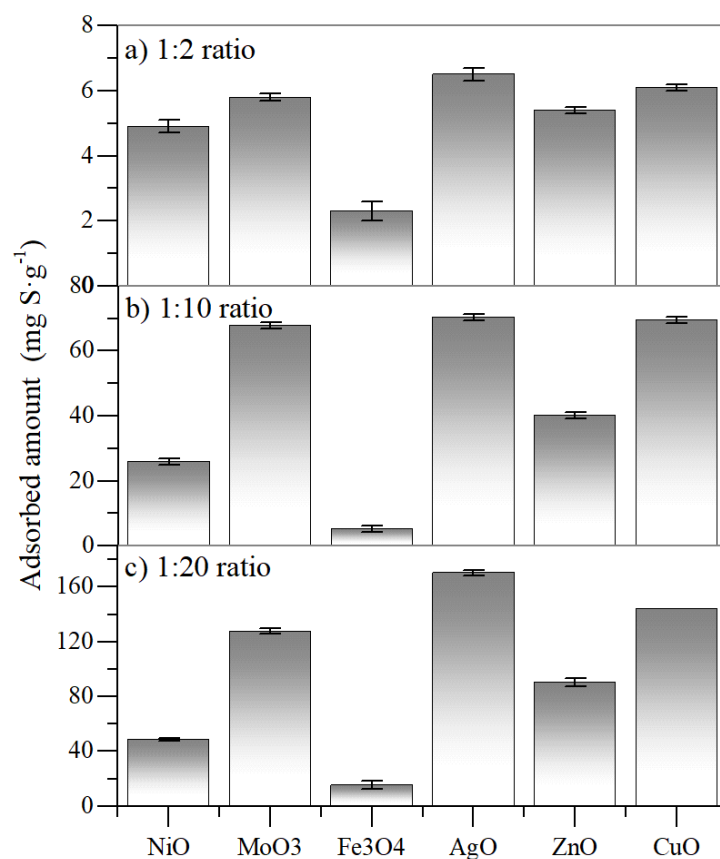


**Figure 7.** Sulfur removal adsorbed amount over different transition element oxides-based nanoparticles for different adsorbent mass (g): crude oil mass ratio(g) of a) 1:2, b) 1:10, and c) 1:20, Temperature: 25 °C.

#### 4.2.2. Optimization of the load of TEO

To investigate the effect of the incorporated metal on the adsorbent performance, SiO<sub>2</sub> was loaded with different mass fractions of Cu, Ag, and Cu-Ag, between 0 and 4 mmol per 2 gr of support, selected previously. The performance of these nanomaterials was evaluated under the same experimental conditions used for the TEO-based nanoparticles, and the results are depicted in Figure 8. The sulfur adsorption amount on the SiO<sub>2</sub> was  $\sim 80 \text{ mg S}\cdot\text{g}^{-1} \pm 0.1 \text{ mg S}\cdot\text{g}^{-1}$ . However, when it is doped with 2 mmol of Cu and Ag, the adsorbed amount increases to  $\sim 115 \pm 0.1 \text{ mg S}\cdot\text{g}^{-1}$  and  $\sim 195 \pm 0.1 \text{ mg S}\cdot\text{g}^{-1}$ , respectively, and in turn, increases with increasing the active phase doses. In SiCu<sub>4</sub>, the adsorption amount increases by 173.9% regarding SiCu<sub>2</sub>, whereas SiAg<sub>4</sub> increases by 104.3% regarding SiAg<sub>2</sub>. The higher yield of these samples than the unloaded SiO<sub>2</sub> can be explained by applying hard and soft acids and the bases principle that soft acids prefer to interact with weak bases.

In contrast, hard acids prefer to interact with hard bases (Hernández-Maldonado and Yang, 2003). The Cu<sup>+</sup> and Ag<sup>2+</sup> are considered borderline acids, increasing

the local soft acid of the SiO<sub>2</sub> surface (Hernández-Maldonado and Yang, 2003). As a result, loading the surface of SiO<sub>2</sub> with these ions may increase its interaction with the sulfur compound (soft base) and ultimately enhance its adsorptive performance.

The bi-elemental systems (i.e., containing Cu and Ag) present higher yields considering the mono-elementals in the order: SiAg1.32Cu1.32 < SiAg2Cu2. These results are reasonable since the number of active sites increases with the TEO dosage and varies their chemical natures, which leads to better adsorption performance. Also, for both systems, it is most probable the S-μ3 structures contain thiophene sulfur atoms and two metal species, as well as η<sup>1</sup>S structures (Saleh et al., 2016). Considering all these results, the simplex centroid–mixture design was resolved to obtain an optimal point consisting of 1.5 mmol of Ag and 1.4 mmol of Cu per 2 g of SiO<sub>2</sub>. The system was evaluated, and an adsorption amount of ~390 ± 0.1 mg S·g<sup>-1</sup> was obtained. The system presents an increase of 387.5% and 18.2% concerning SiO<sub>2</sub> and SiAg2Cu2, respectively. This result corroborates the successful development of the statistical analysis, in which the amount of sulfur uptake was increased by evaluating the system with the optimal load of both TEOs. It is worth mentioning that the total load of TEOs was reduced (2.9 mmol) considering the SiAg2Cu2 (4.0 mmol).

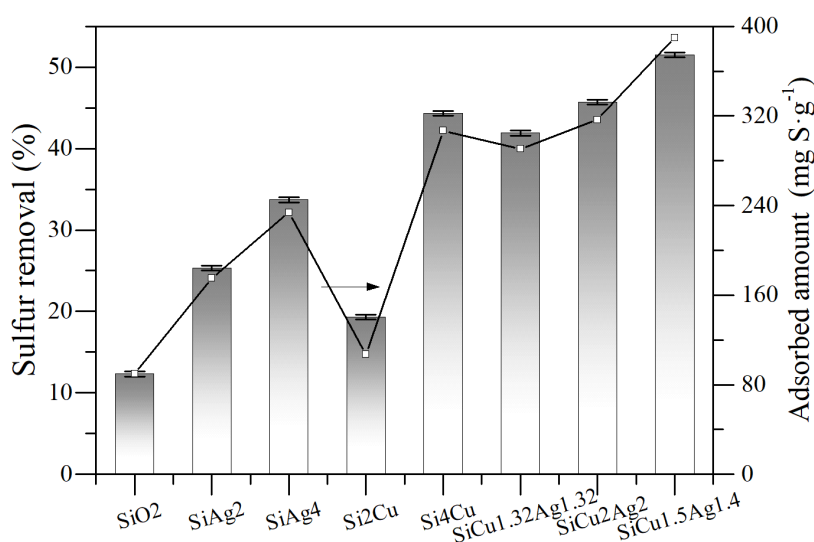


**Figure 8.** Sulfur removal (%) and sulfur adsorbed amount over different nanomaterials containing SiO<sub>2</sub> microparticles with different loads of Ag and Cu between 0 and 4 mmol. Adsorbent mass (g): crude oil mass ratio(g) 1:20, Temperature: 25 °C.

Figure 9 shows the nanomaterial's chemical and structural properties influence sulfur removal from crude oil. A clear correlation between the crystal size of CuO and Ag with the ability of the nanomaterial to remove sulfur compounds is observed. The sulfur adsorption is enhanced by reducing the crystal size of CuO and Ag, further related to the higher degree of dispersion of both species. However, it is commonly accepted that the attraction forces between both species primarily drive the adsorption process. Thereby, the effect of the atomic content of Cu<sup>+</sup> and Ag<sup>0</sup> species in sulfur removal is analyzed and reported in panels c and d, respectively. A direct relationship is established between the increment of the exposed Cu<sup>+</sup> and Ag<sup>0</sup> species and the increased adsorption capacity of the adsorbents. The nanomaterial obtains the adsorptive desulfurization by  $\pi$ -complexation between Cu<sup>+</sup> and sulfur compounds. Through the  $\pi$ -complexation mechanism, the Cu<sup>+</sup> can form the usual  $\sigma$  bonds with their empty s-orbitals and, in addition, their d-orbitals can back-donate electron density to the antibonding  $\pi$ -orbitals ( $\pi^*$ ) of the sulfur rings (Tian et al., 2010). Thus, a  $\pi$ -complex is produced between adsorbate and adsorbent, and desulfurization by adsorption is realized (Tian et al., 2010). These results agree with those obtained for sulfur adsorption on copper nanoparticles with a predominant content of Cu<sup>+</sup> species (Tian et al., 2010).



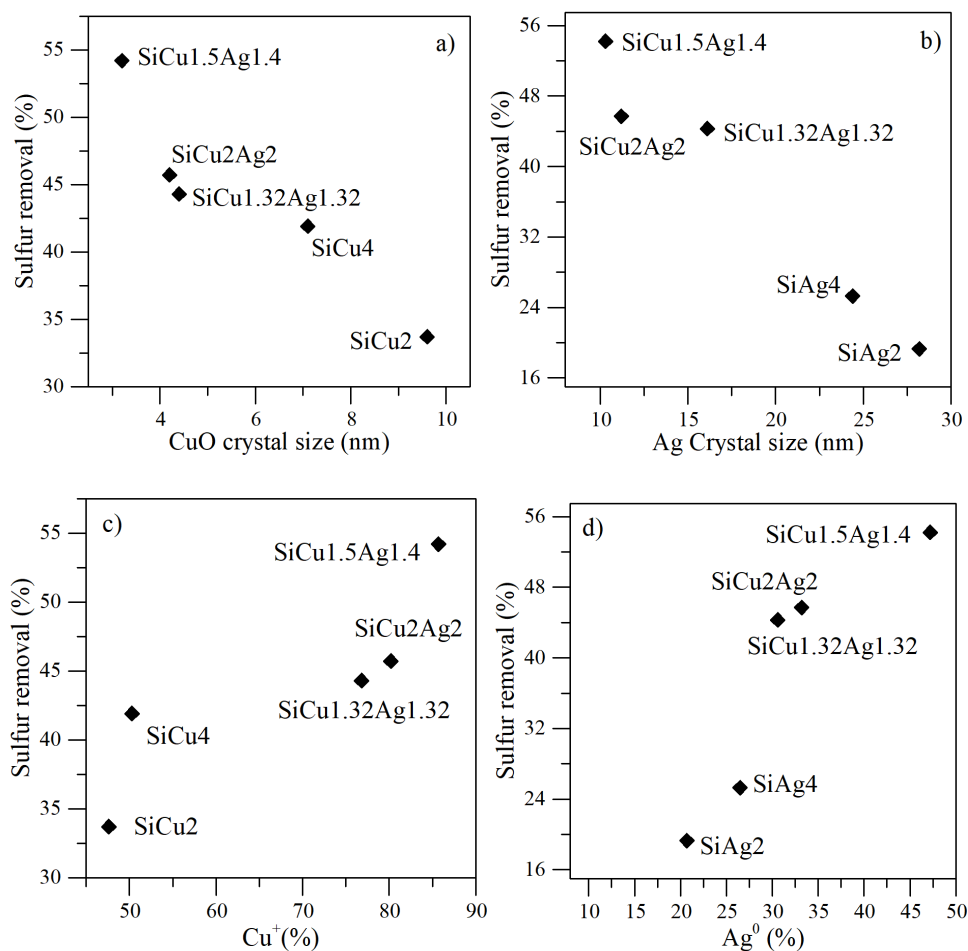


**Figure 9.** Influence of the nanomaterial's chemical and structural properties on sulfur removal from crude oil: a) CuO crystal size, b) Ag crystal size, c) atomic content of Cu<sup>+</sup>, and d) atomic content of Ag<sup>0</sup>.

#### 4.2.3. Adsorption isotherms and thermodynamic analysis

The interactions between sulfur compounds and SiAg1.5Cu1.4 were evaluated through adsorption isotherms at three different temperatures, including 25 °C, 35 °C, and 55 °C, which were described using the Solid-Liquid Equilibrium and Freundlich models. The results are summarized in Figure 10. Based on the International Union of Pure and Applied Chemistry (IUPAC) classification (Ravikovitch and Neimark, 2001), a type III adsorption behavior describes the sulfur adsorption on the optimized system. The obtained behavior is particular to systems with multilayer adsorption represented by low slopes in Henry's region (low C<sub>E</sub>). In other words, the adsorption capacity increased with increasing initial sulfur concentration, which showed that favorable adsorption of sulfur on SiAg1.5Cu1.4 could be obtained at a high concentration.

On the other hand, due to the temperature increase, the adsorbent's desulfurization capacity is reduced. The temperature could cause a change in the

aggregation state of sulfur on the surface of the nanomaterial, affecting the interaction forces and decreasing the adsorption amount (Díez et al., 2020; López et al., 2017).

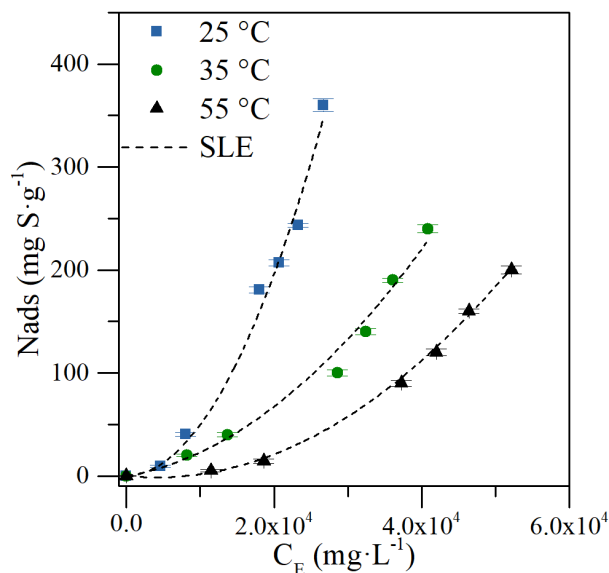


**Figure 10.** Sulfur adsorption isotherms on SiAg1.5Cu1.4 estimated at 25, 35, and 55 °C using 1:20, 2:30, 1:10, 1:5, 1:2, and 1:1 adsorbent mass: crude oil mass ratios. The dotted lines refer to the SLE model.

The adsorption data fitted the SLE model, with a correlation coefficient of 0.999, and the Freundlich model, with a correlation coefficient of 0.988. The results are summarized in Table 8. The maximum adsorption amount from SLE model was 60186.57, 60186.77, and 60187.97  $\text{g}\cdot\text{g}^{-1}$  at 25, 35, and 55°C, respectively. It corroborated the effect of temperature on reducing the efficiency of the adsorbent at higher temperatures. In addition, it is noted that increasing temperatures increase Henry's law constant and the self-association (K) parameter. In effect, the temperature decreases the adsorbent's affinity for sulfur compounds and the inhibition capacity to form aggregates on its surface. Using the five-parameter SLE model, it was proved that the adsorption process was exothermic ( $\Delta H_{\text{ads}}^0 = -0.11 \text{ kJ}\cdot\text{mol}^{-1}$ ) and spontaneous ( $\Delta G_{\text{ads}}^0 = -4.35 \text{ J}\cdot\text{mol}^{-1}$  at 25°C,  $-4.64 \text{ J}\cdot\text{mol}^{-1}$  at 35°C, and  $-10.10 \text{ J}\cdot\text{mol}^{-1}$  at 45 °C). Thus, 25 °C was in favor of adsorptive desulfurization. Besides,  $\Delta S_{\text{ads}}^0$  was  $29.79 \text{ J}\cdot(\text{mol}\cdot\text{K})^{-1}$ , confirming the system's randomness and disorder increment at the adsorbate-adsorbent interface. The positive value of  $\Delta S_{\text{ads}}^0$  also corresponds to an increase in the degree of freedom of the adsorbed species. These results cause the sulfur molecules to remain in the solid phase instead of the liquid phase, indicating a high affinity

for nanoparticles. On the other hand, Freundlich isotherm constants show a decrease in adsorptive capacity when the temperature increases ( $K_1 = 2.62 \times 10^{-5} \text{ kg}\cdot\text{g}^{-1}$  at  $25^\circ\text{C}$ ,  $2.40 \times 10^{-5} \text{ kg}\cdot\text{g}^{-1}$  at  $35^\circ\text{C}$ , and  $2.24 \times 10^{-5} \text{ kg}\cdot\text{g}^{-1}$  at  $55^\circ\text{C}$ ). This is expected due to the increase in the Gibbs free energy of the process, as mentioned previously, making the process less spontaneous due to the reduction in the interaction forces (Kumar and Sivanesan, 2005; Chattha et al., 2007; Montanher et al., 2005). Also, unlike temperatures of  $25^\circ\text{C}$  and  $35^\circ\text{C}$ , when the process temperature is  $55^\circ\text{C}$ , the adsorption intensity decreases drastically ( $n = 0.63$  at  $25^\circ\text{C}$ ,  $0.64$  at  $35^\circ\text{C}$ , and  $0.47$  at  $55^\circ\text{C}$ ), showing a more significant impact on adsorption intensity at high temperatures, as expected (HUANG and CHO, 1989; Darwish et al., 2019). These results agree with Chen et al. (2013), who evaluated adsorption systems for industrial waters, and with Uslu and Tanyol et al. (2006), who evaluated ion bio-adsorption systems, where temperature significantly affects the Freundlich isotherm constants, specifically  $n$ .

**Table 8.** Estimated SLE model and Freundlich parameters for adsorption isotherms of sulfur compounds on SiAg1.5Cu1.4.  $H$  represents Henry's law constant,  $K$  gives an idea about the self-association degree of sulfur over the adsorbent surface,  $N_m$  is the maximum adsorbed amount,  $K_1$  and  $n$  represents the adsorbent's adsorption capacity and the adsorption intensity, respectively.

Model	Temperature (°C)	$H$ (mg·g <sup>-1</sup> )	$K$ (g·g <sup>-1</sup> )	$N_m$ (g·g <sup>-1</sup> )	R <sup>2</sup>
SLE	25	303.31	5.78	60186.57	0.99
	35	541.61	5.46	60186.77	0.98
	55	2436.28	32.70	60188.97	0.99
		$K_1$ (kg·g <sup>-1</sup> )	$n$ (adimensional)	R <sup>2</sup>	
Freundlich	25	$2.62 \times 10^{-5}$	0.63	0.98	
	35	$2.40 \times 10^{-5}$	0.64	0.97	
	55	$2.24 \times 10^{-5}$	0.47	0.96	

#### 4.2.4. Dynamic adsorption simulation

Further study was conducted into the fixed bed system to evaluate the dynamic adsorption performance of SiAg1.5Cu1.4. As depicted in Figure 1, the fixed bed, laboratory-scale reactor comprised a low-flow liquid positive displacement pump, a feed tank, a valve, a custom-made column backed with the sample, and the collecting system. During continuous liquid desulfurization, the crude oil can pass through the fixed bed in an up-flow direction. The sulfur removal plots (%) against cumulative time gave the breakthrough curve shown in Figure 11. At the early stage of adsorption, the sulfur content was above 0 ppm

(i.e., 100% of sulfur removal), and it remains at 0 ppm after up to approximately 100 min of adsorption. More than 350 min were required to reach the adsorbent's target point, demonstrating that the SiAg<sub>1.5</sub>Cu<sub>1.4</sub> worked efficiently for dynamic sulfur adsorption. The adsorbent loses its capacity for sulfur adsorption at 425 min. This scene in the experimental test obeys Case 1, which is presented in Table 3. The experimental conditions of Case 1 are simulated, and the breakthrough curves are compared (Figure 11). As shown in Figure 11, the simulation captures the trend of the experimental process, delivering a maximum relative error of 5.0%. This result demonstrates the capacity of process modeling to describe adsorption dynamics. In the adsorption model, there are deviations in the first breakthrough point, where the dibenzothiophene (representative sulfur component) concentration increased in the effluent at 140 minutes. On the other hand, in the breakthrough curve, it can be identified that the model follows the growth trend in the experimental setup's sulfur concentration. This indicates the capacity of the model to describe the increased velocity in sulfur concentration in the effluent. At the end of the curve, the model is above the experimental data, showing a change in the adsorption rate. The behavior shown at the beginning and end of the breakthrough curve can be explained by how the material is distributed inside the custom-made column-packed device. In the end, the material can be distributed differently from how it is found in the interior, affecting the mass transfer. Despite this, the model shows a good match with the experimental part between 140 min and 425 min (area of interest). After this validation from the breakthrough curve, the response of the model to changes in the feed flow is shown to evaluate the ability of the process modeling to capture expected trends in variables of importance.

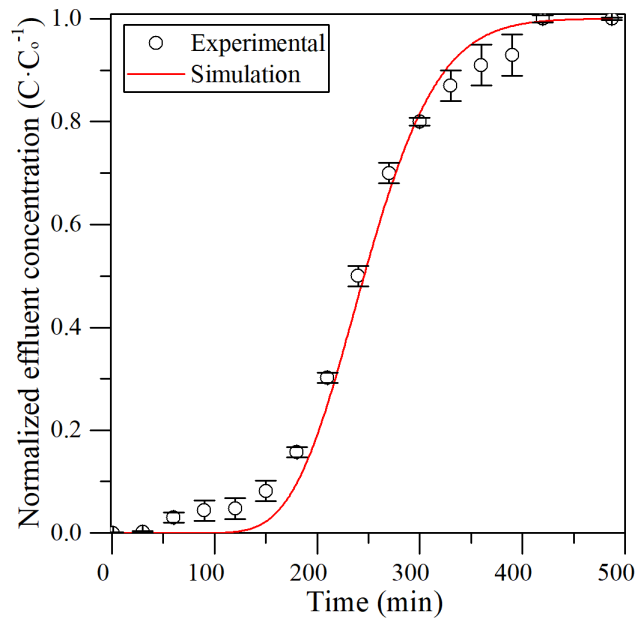


**Figure 11.** Breakthrough curves comparison between experimental and numerical simulation for total sulfur content using SiAg1.5Cu1.4 at 25 °C and atmospheric pressure.

#### 4.2.4.1. Evaluation of the modification in the feed flow in adsorption column modeling

This section shows the model's response to changes in the feed flow (see Table 3). the evaluated flows are 1, 10, and 50 ml·min<sup>-1</sup> of feed flow. Figure 12 shows the breakthrough curve for the cases assessed.

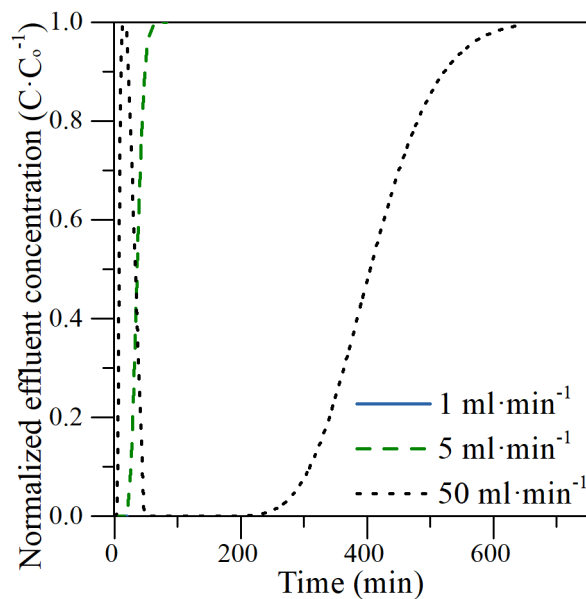


**Figure 12.** Breakthrough curves simulation at different feed flows for total sulfur content using SiAg1.5Cu1.4 at 25 °C and atmospheric pressure.

From the results shown in Figure 12, it is possible to observe the capacity of the modeling proposed for the process to represent the changes in the feed flow. In this sense, it can be observed that at higher feed flows, the times to reach the breakthrough point are shorter, as expected. Breakthrough times are 10, 1.1, and 0.23 h for 1, 10, and 50 ml·min<sup>-1</sup>, respectively. In addition, this type of sensitivity analysis makes it possible to elucidate the capacity of the model to evaluate different scenarios. This will be shown in the next section, where with a fixed feed flow (151800 mL·min<sup>-1</sup>), different dimensions of the packed bed will be evaluated. Additionally, this analysis will allow observing the behavior of the system at the field scale, giving a first step to implementing the technology.

#### 4.2.4.2. Adsorption process scaling

In this section, cases 5, 6, 7, 8, and 9 (See Table 3) analyze the performance of the desulfurization process at different scales, maintaining an aspect ratio of 4. Figure 13 shows the breakthrough curves obtained for the simulation of cases 5, 6, 7, 8, and 9.

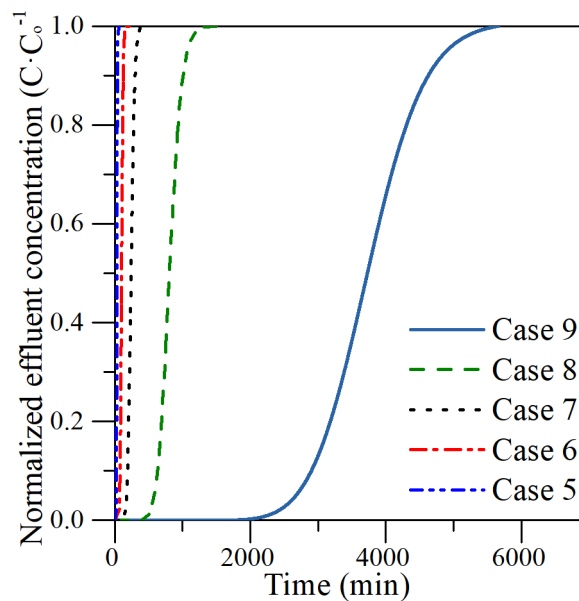


**Figure 13.** Breakthrough curves simulation at different feed flows for total sulfur content using SiAg<sub>1.5</sub>Cu<sub>1.4</sub> at 25 °C and atmospheric pressure.

The cases evaluated range from heights from 1 to 5 meters, with diameters between 0.25 and 1.25 m. All with flows like those obtained in oil fields. From the results, the greater the volume of the fixed column, the breakthrough times take longer. The trends of the breakthrough point explain this, this decreases as the height of the bed falls and the fluid flow through the bed increases (Treybal,

1980). For example, if the effluent is required in the desulfurization process with  $C/C_0$  less than 0.34, the following crude oil production results would be obtained (Table 9).

**Table 9.** Oil treatment results in a fixed-bed adsorption column.

Case	Time to reach requirement limit (min)	Barrels of treated crude that meet the requirement (bbl)
5	25	26
6	91	86
7	222	210
8	748	710
9	3458	3280

Based on the results shown in Table 9, if the technology proposed in Case 9 is going to be implemented in an oil field, the process would work under the necessary conditions for 2.4 days. After this time, the regeneration of the bed is required.

#### 4.2.4.3. Effect of temperature on process scaling

In this section, the sulfur adsorption phenomenon of Case 8 was evaluated at 35 °C and 55 °C. Figure 14 shows the breakthrough curves for the different temperatures.

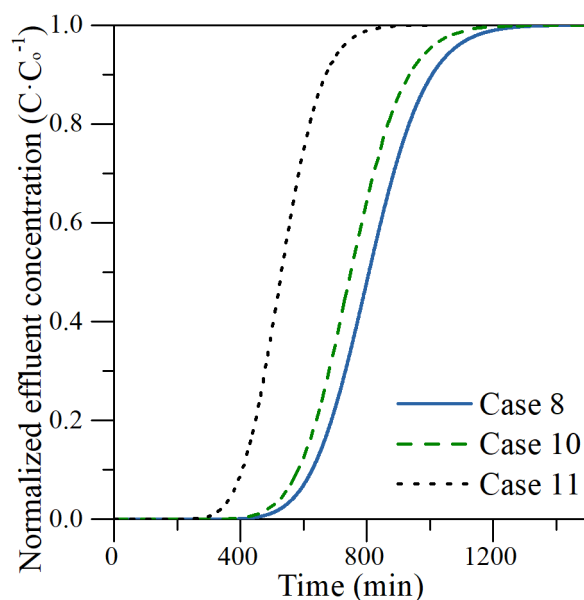


**Figure 14.** Breakthrough curves simulation at different temperatures (25°C, 35°C, and 55°C) for total sulfur content using SiAg1.5Cu1.4 at atmospheric pressure.

The system proposed in Figure 14 evaluates Case 8 at different temperatures, and Table 10 summarizes the parameters assessed. When the temperature increases, the adsorptive capacity decreases, reaching the saturation point in the order 55 < 35 < 25 °C. It was described in the previous section that the interaction between the sulfur component and the fluid matrix is strongly affected by the temperature of the system (Claudino et al., 2004; Alalwan et al., 2018; Siahpoosh et al., 2009).

Although mass transfer is favored at high temperatures, the interaction between the sulfur component and the adsorbent decreases due to the decrease in the affinity between both components (Brea et al., 2017). In this sense, at 55 °C, the breakthrough occurs faster than at other evaluated temperatures. In this way, the number of barrels that meet the desired condition ( $C/C_0 < 0.34$ ) is lower at high temperatures. Furthermore, it is recommended to carry out the process to lower temperatures.

**Table 10.** Oil treatment results in a fixed-bed adsorption column.

Temperature	Time to reach requirement limit (min)	Barrels of treated crude that meet requirement (bbl)
25 °C	748	710
35 °C	694	658
55 °C	488	462

## 5. Conclusions

The efficiency of the adsorption process of the nanomaterials was validated by estimating the adsorption capacity/removal and its affinity for sulfur species through batch and continuous adsorption experiments. The sulfur adsorption amount/removal on the non-doped material ( $\text{SiO}_2$ ) was  $\sim 80 \text{ mg S}\cdot\text{g}^{-1}$ . However, when it is doped with 2 mmol of Cu and Ag, the adsorbed amount increases to  $\sim 115$  and  $\sim 195 \text{ mg S}\cdot\text{g}^{-1}$ , respectively, and in turn, increases with increasing the active phase doses. The bi-elemental systems (i.e., containing Cu and Ag) present higher yields considering the mono-elementals in the order  $\text{SiAg1.32Cu1.32} < \text{SiAg2Cu2} < \text{SiAg1.5Cu1.4}$ . The sulfur adsorption is enhanced by reducing the crystal size of Cu and Ag, which is further related to the higher degree of dispersion of both species. Also, it is established a direct relationship between the increment of the exposed  $\text{Cu}^+$  and  $\text{Ag}^0$  species and the increased adsorption capacity of the adsorbents. Adsorption isotherms were constructed for the  $\text{SiAg1.5Cu1.4}$  at 25, 35, and 55 °C, obtaining a high affinity between the



nanomaterial and the sulfur compounds. The dynamic adsorption process was evaluated in the SiAg<sub>1.5</sub>Cu<sub>1.4</sub> system due to higher adsorption capacity, which required more than 350 min to reach the adsorbent's saturation point, demonstrating that the SiAg<sub>1.5</sub>Cu<sub>1.4</sub> worked efficiently for dynamic sulfur adsorption. The modeling and numerical simulation of the adsorption process were carried out in the Aspen Adsorption software, this model was validated based on experimental data, and its sensitivity to modifications in the feed flow was evaluated, delivering a maximum relative error of 5.0%. This model was used to obtain performance values of the technology on larger scales than the experimental ones, specifically on a field scale. Additionally, the effect of temperature in the fluid treatment process was evaluated, obtaining that the target point is reached faster for higher temperatures.

## References

- Acosta LG-C, D.; Medina, O.E.; Cortés, F.B.; Franco, C.A. (2021) Nano-Intermediate of Magnetite Nanoparticles Supported on Activated Carbon from Spent Coffee Grounds for Treatment of Wastewater from Oil Industry and Energy Production. *Processes* 9: 63.
- Al-Haj-Ibrahim H and Morsi BI (1992) Desulfurization of petroleum coke: a review. *Industrial & engineering chemistry research* 31(8): 1835-1840.
- Alalwan HA, Abbas MN, Abudi ZN, et al. (2018) Adsorption of thallium ion (Tl<sup>3+</sup>) from aqueous solutions by rice husk in a fixed-bed column: Experiment and prediction of breakthrough curves. *Environmental Technology & Innovation* 12: 1-13.
- Arias-Madrid D, Medina OE, Gallego J, et al. (2020) NiO, Fe<sub>2</sub>O<sub>3</sub>, and MoO<sub>3</sub> Supported over SiO<sub>2</sub> Nanocatalysts for Asphaltene Adsorption and Catalytic Decomposition: Optimization through a Simplex–Centroid Mixture Design of Experiments. *Catalysts* 10(5): 569.
- Babich I and Moulijn J (2003) Science and technology of novel processes for deep desulfurization of oil refinery streams: a review☆. *Fuel* 82(6): 607-631.
- Brea P, Delgado J, Águeda V, et al. (2017) Modeling of breakthrough curves of N<sub>2</sub>, CH<sub>4</sub>, CO, CO<sub>2</sub> and a SMR type off-gas mixture on a fixed bed of BPL activated carbon. *Separation and Purification Technology* 179: 61-71.
- Cardona L, Medina OE, Céspedes S, et al. (2021) Effect of Steam Quality on Extra-Heavy Crude Oil Upgrading and Oil Recovery Assisted with PdO and NiO-Functionalized Al<sub>2</sub>O<sub>3</sub> Nanoparticles. *Processes* 9(6): 1009.

- Claudino A, Soares J, Moreira R, et al. (2004) Adsorption equilibrium and breakthrough analysis for NO adsorption on activated carbons at low temperatures. *Carbon* 42(8-9): 1483-1490.
- Cornell JA (2011) *Experiments with mixtures: designs, models, and the analysis of mixture data*. John Wiley & Sons.
- Chattha T, Yousaf M and Javeed S (2007) Phosphorus adsorption as described by Freundlich adsorption isotherms under rainfed conditions of Pakistan. *Pakistan Journal of Agriculture Science* 44(4): 27.
- Chen C (2013) Evaluation of equilibrium sorption isotherm equations. *The Open Chemical Engineering Journal* 7(1).
- Darwish A, Rashad M and AL-Aoh HA (2019) Methyl orange adsorption comparison on nanoparticles: isotherm, kinetics, and thermodynamic studies. *Dyes and Pigments* 160: 563-571.
- Dehghan R and Anbia M (2017) Zeolites for adsorptive desulfurization from fuels: A review. *Fuel processing technology* 167: 99-116.
- Dhoondia ZH and Chakraborty H (2012) Lactobacillus mediated synthesis of silver oxide nanoparticles. *Nanomaterials and nanotechnology* 2: 15.
- Díez R, Medina OE, Giraldo LJ, et al. (2020) Development of Nanofluids for the Inhibition of Formation Damage Caused by Fines Migration: Effect of the interaction of Quaternary Amine (CTAB) and MgO Nanoparticles. *Nanomaterials* 10(5): 928.
- Felinger A and Guiochon G (2004) Comparison of the kinetic models of linear chromatography. *Chromatographia* 60(1): S175-S180.
- Gao S, Chen X, Xi X, et al. (2019) Coupled oxidation-extraction desulfurization: a novel evaluation for diesel fuel. *ACS Sustainable Chemistry* 7(6): 5660-5668.
- He Z, Lin H, He P, et al. (2011) Effect of boric oxide doping on the stability and activity of a Cu-SiO<sub>2</sub> catalyst for vapor-phase hydrogenation of dimethyl oxalate to ethylene glycol. *Journal of Catalysis* 277(1): 54-63.
- Hernández-Maldonado AJ and Yang RT (2003) Desulfurization of liquid fuels by adsorption via  $\pi$  complexation with Cu (I)- Y and Ag- Y zeolites. *Industrial & engineering chemistry research* 42(1): 123-129.
- HUANG T-C and CHO L-T (1989) Relationships between constants of the Freundlich equation and temperature for gaseous adsorption. *Chemical Engineering Communications* 75(1): 181-194.
- Humberto GP and de la Vara SR (2003) Análisis y diseño de experimentos. *Mc Graw Hill. Ubicación 1: G9846a*.

- Hussain AS and Tatarchuk BJ (2014) Mechanism of hydrocarbon fuel desulfurization using Ag/TiO<sub>2</sub>-Al<sub>2</sub>O<sub>3</sub> adsorbent. *Fuel processing technology* 126: 233-242.
- Ismagilov Z, Yashnik S, Kerzhentsev M, et al. (2011) Oxidative desulfurization of hydrocarbon fuels. *Catalysis Reviews* 53(3): 199-255.
- Javadli R and De Klerk A (2012) Desulfurization of heavy oil. *Applied Petrochemical Research* 1(1-4): 3-19.
- Jha D, Haider MB, Kumar R, et al. (2016) Extractive desulfurization of dibenzothiophene using phosphonium-based ionic liquid: Modeling of batch extraction experimental data and simulation of continuous extraction process. *Chemical Engineering Research and Design* 111: 218-222.
- Jha D, Haider MB, Kumar R, et al. (2019) Enhanced adsorptive desulfurization using Mongolian anthracite-based activated carbon. *ACS omega* 4(24): 20844-20853.
- Ju F, Wang M, Wu T, et al. (2019) The role of NiO in reactive adsorption desulfurization over NiO/ZnO-Al<sub>2</sub>O<sub>3</sub>-SiO<sub>2</sub> adsorbent. *Catalysts* 9(1): 79.
- Khan NA, Kim CM and Jhung SH (2017) Adsorptive desulfurization using Cu-Ce/metal-organic framework: Improved performance based on synergy between Cu and Ce. *Chemical Engineering Journal* 311: 20-27.
- Kiran JU, Roners JP and Mathew S (2020) XPS and thermal studies of silver doped SiO<sub>2</sub> matrices for plasmonic applications. *Materials Today: Proceedings* 33: 1263-1267.
- Kroon R (2013) Nanoscience and the Scherrer equation versus the 'Scherrer-Gottingen equation'. *South African Journal of Science* 109(5-6): 01-02.
- Kumar KV and Sivanesan S (2005) Prediction of optimum sorption isotherm: Comparison of linear and non-linear method. *Journal of hazardous materials* 126(1-3): 198-201.
- Kumar S, Srivastava VC and Badoni R (2011) Studies on adsorptive desulfurization by zirconia based adsorbents. *Fuel* 90(11): 3209-3216.
- Kwon JM, Moon JH, Bae YS, et al. (2008) Adsorptive desulfurization and denitrogenation of refinery fuels using mesoporous silica adsorbents. *ChemSusChem: Chemistry & Sustainability Energy & Materials* 1(4): 307-309.
- Lee KX and Valla JA (2019) Adsorptive desulfurization of liquid hydrocarbons using zeolite-based sorbents: a comprehensive review. *Reaction Chemistry & Engineering* 4(8): 1357-1386.
- Li B and Gonzalez RD (1997) TGA/FT-IR studies of the deactivation of sulfated zirconia catalysts. *Applied Catalysis A: General* 165(1-2): 291-300.

- Li B, Yu S, Jiang Z, et al. (2012) Efficient desulfurization by polymer–inorganic nanocomposite membranes fabricated in reverse microemulsion. *Journal of hazardous materials* 211: 296-303.
- Li S-W, Wang W and Zhao J-S (2020) Catalytic oxidation of DBT for ultra-deep desulfurization under MoO<sub>3</sub> modified magnetic catalyst: The comparison influence on various morphologies of MoO<sub>3</sub>. *Applied Catalysis A: General* 602: 117671.
- Li Y, Yi H, Tang X, et al. (2016) Study on the performance of simultaneous desulfurization and denitrification of Fe<sub>3</sub>O<sub>4</sub>-TiO<sub>2</sub> composites. *Chemical Engineering Journal* 304: 89-97.
- López-Ramón MV, Álvarez MA, Moreno-Castilla C, et al. (2018) Effect of calcination temperature of a copper ferrite synthesized by a sol-gel method on its structural characteristics and performance as Fenton catalyst to remove gallic acid from water. *Journal of colloid and interface science* 511: 193-202.
- López D, Giraldo LJ, Salazar JP, et al. (2017) Metal Oxide Nanoparticles Supported on Macro-Mesoporous Aluminosilicates for Catalytic Steam Gasification of Heavy Oil Fractions for On-Site Upgrading. *Catalysts* 7(11): 319.
- Mateus L, Moreno-Castilla C, López-Ramón MV, et al. (2021) Physicochemical characteristics of calcined MnFe<sub>2</sub>O<sub>4</sub> solid nanospheres and their catalytic activity to oxidize para-nitrophenol with peroxymonosulfate and n-C<sub>7</sub> asphaltenes with air. *Journal of Environmental Management* 281: 111871.
- Medina OE, Galeano-Caro D, Castelo-Quibén J, et al. (2021a) Monolithic carbon xerogels-metal composites for crude oil removal from oil in-saltwater emulsions and subsequent regeneration through oxidation process: Composites synthesis, adsorption studies, and oil decomposition experiments. *Microporous and Mesoporous Materials*. 111039.
- Medina OE, Gallego J, Acevedo S, et al. (2021b) Catalytic Conversion of n-C<sub>7</sub> Asphaltenes and Resins II into Hydrogen Using CeO<sub>2</sub>-Based Nanocatalysts. *Nanomaterials* 11(5): 1301.
- Medina OE, Gallego J, Arias-Madrid D, et al. (2019a) Optimization of the load of transition metal oxides (Fe<sub>2</sub>O<sub>3</sub>, Co<sub>3</sub>O<sub>4</sub>, NiO and/or PdO) onto CeO<sub>2</sub> nanoparticles in catalytic steam decomposition of n-C<sub>7</sub> asphaltenes at low temperatures. *Nanomaterials* 9(3): 401.

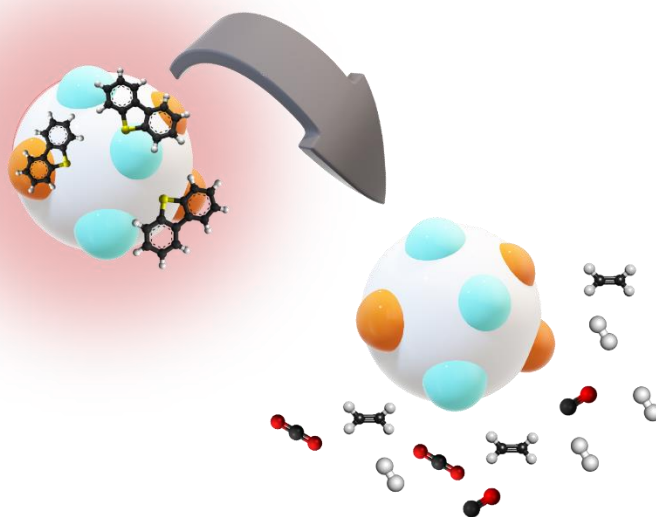
- Medina OE, Gallego J, Olmos CM, et al. (2020) Effect of multifunctional nanocatalysts on n-C7 asphaltene adsorption and subsequent oxidation under high-pressure conditions. *Energy & Fuels* 34(5): 6261-6278.
- Medina OE, Gallego J, Restrepo LG, et al. (2019b) Influence of the Ce<sup>4+</sup>/Ce<sup>3+</sup> Redox-couple on the cyclic regeneration for adsorptive and catalytic performance of NiO-PdO/CeO<sub>2</sub>± $\delta$  nanoparticles for n-C7 asphaltene steam gasification. *Nanomaterials* 9(5): 734.
- Medina OE, Hurtado Y, Caro-Velez C, et al. (2019c) Improvement of Steam Injection Processes Through Nanotechnology: An Approach through in Situ Upgrading and Foam Injection. *Energies* 12(24): 4633.
- Mendiratta S and Ali AAA (2020) Recent Advances in Functionalized Mesoporous Silica Frameworks for Efficient Desulfurization of Fuels. *Nanomaterials* 10(6): 1116.
- Minambiente (2019) NORMA NACIONAL DE CALIDAD DE COMBUSTIBLES DIESEL Y BIODIESEL.
- Mo L, Saw E-T, Kathiraser Y, et al. (2018) Preparation of highly dispersed Cu/SiO<sub>2</sub> doped with CeO<sub>2</sub> and its application for high temperature water gas shift reaction. *International Journal of Hydrogen Energy* 43(33): 15891-15897.
- Montanher S, Oliveira E and Rollemberg M (2005) Removal of metal ions from aqueous solutions by sorption onto rice bran. *Journal of hazardous materials* 117(2-3): 207-211.
- Montes D, Henao J, Taborda EA, et al. (2020) Effect of Textural Properties and Surface Chemical Nature of Silica Nanoparticles from Different Silicon Sources on the Viscosity Reduction of Heavy Crude Oil. *ACS omega* 5(10): 5085-5097.
- Montoya T, Coral D, Franco CA, et al. (2014) A novel solid–liquid equilibrium model for describing the adsorption of associating asphaltene molecules onto solid surfaces based on the "chemical theory". *Energy & fuels* 28(8): 4963-4975.
- Muthuchamy N, Gopalan A and Lee K-P (2015) A new facile strategy for higher loading of silver nanoparticles onto silica for efficient catalytic reduction of 4-nitrophenol. *RSC Advances* 5(93): 76170-76181.
- Muzic M, Sertic-Bionda K and Adzamic T (2011) Desulfurization of diesel fuel in a fixed bed adsorption column: experimental study and simulation. *Petroleum Science and Technology* 29(22): 2361-2371.

- Naderi M (2015) Surface Area: Brunauer–Emmett–Teller (BET). *Progress in filtration and separation*. Elsevier, pp.585-608.
- Nassar NN, Franco CA, Montoya T, et al. (2015) Effect of oxide support on Ni–Pd bimetallic nanocatalysts for steam gasification of n-C7 asphaltenes. *Fuel* 156: 110-120.
- Nguyen C and Do D (2001) The Dubinin–Radushkevich equation and the underlying microscopic adsorption description. *Carbon* 39(9): 1327-1336.
- Peterson GW, Rossin JA, Karwacki CJ, et al. (2011) Surface chemistry and morphology of zirconia polymorphs and the influence on sulfur dioxide removal. *The Journal of Physical Chemistry C* 115(19): 9644-9650.
- Post P, Wurlitzer L, Maus-Friedrichs W, et al. (2018) Characterization and applications of nanoparticles modified in-flight with silica or silica-organic coatings. *Nanomaterials* 8(7): 530.
- Proctor A and Toro-Vazquez J (1996) The Freundlich isotherm in studying adsorption in oil processing. *Journal of the American Oil Chemists' Society* 73(12): 1627-1633.
- Ravikovitch PI and Neimark AV (2001) Characterization of nanoporous materials from adsorption and desorption isotherms. *Colloids and surfaces A: Physicochemical and Engineering aspects* 187: 11-21.
- Saleh TA, Danmaliki GI and Shuaib TD (2016) Nanocomposites and hybrid materials for adsorptive desulfurization. *Applying Nanotechnology to the Desulfurization Process in Petroleum Engineering*. IGI Global, pp.129-153.
- Siahpoosh M, Fatemi S and Vatani A (2009) Mathematical modeling of single and multi-component adsorption fixed beds to rigorously predict the mass transfer zone and breakthrough curves. *Iranian Journal of Chemistry and Chemical Engineering (IJCCE)* 28(3): 25-44.
- Tang B, Qiu M and Zhang S (2012) Thermal conductivity enhancement of PEG/SiO<sub>2</sub> composite PCM by in situ Cu doping. *Solar energy materials and solar cells* 105: 242-248.
- Tian W-H, Sun L-B, Song X-L, et al. (2010) Adsorptive desulfurization by copper species within confined space. *Langmuir* 26(22): 17398-17404.
- Treybal RE (1980) Mass transfer operations. *New York* 466.
- Urán L, Gallego J, Bailón-García E, et al. (2020) Isotopic study of the La<sub>0.7</sub>Ag<sub>0.3</sub>MnO<sub>δ</sub>±3 perovskite-catalyzed soot oxidation in presence of NO. *Applied Catalysis A: General* 599: 117611.
- Uslu G and Tanyol M (2006) Equilibrium and thermodynamic parameters of single and binary mixture biosorption of lead (II) and copper (II) ions onto

- Pseudomonas putida*: effect of temperature. *Journal of hazardous materials* 135(1-3): 87-93.
- Watanabe S, Ma X and Song C (2020) Adsorptive desulfurization of jet fuels over TiO<sub>2</sub>-CeO<sub>2</sub> mixed oxides: Role of surface Ti and Ce cations. *Catalysis Today*.
- Xiao R, Luo Z, Wei Z, et al. (2018) Activation of peroxymonosulfate/persulfate by nanomaterials for sulfate radical-based advanced oxidation technologies. *Current opinion in chemical engineering* 19: 51-58.
- XU C-z, ZHENG M-q, Keng C, et al. (2016) CeO<sub>x</sub> doping on a TiO<sub>2</sub>-SiO<sub>2</sub> supporter enhances Ag based adsorptive desulfurization for diesel. *Journal of Fuel Chemistry and Technology* 44(8): 943-953.
- Zhang M, Liu J, Yang J, et al. (2019) Molybdenum-containing dendritic mesoporous silica spheres for fast oxidative desulfurization in fuel. *Inorganic Chemistry Frontiers* 6(2): 451-458.
- Zhu D, Wang L, Yu W, et al. (2018) Intriguingly high thermal conductivity increment for CuO nanowires contained nanofluids with low viscosity. *scientific reports* 8(1): 1-12.

## Chapter 18.

# Sulfur removal using nanomaterials as a potential upgrading mechanism of heavy-crude oils: Cyclic reuse and thermal regeneration.





## **Sulfur removal using nanomaterials as a potential upgrading mechanism of heavy-crude oils: Cyclic reuse and thermal regeneration.**

### **Abstract**

This work aims to continue previous research focused on developing and evaluating a nanomaterial for sulfur removal from heavy crude oil consisting of silica-support doped with 1.5 mmol of Ag and 1.4 mmol of Cu. This part focused on discovering the influence of the regeneration atmosphere on sulfur adsorption, sulfur conversion, and hydrogen production. Sulfur adsorption was determined through batch adsorption experiments using different adsorbent mass:crude oil ratios. After ten reuses using a 1:20 ratio, the sulfur removal yield decreased by 1.1, 2.5, and 5.1%, during oxidation, gasification, and pyrolysis, respectively. Sulfur conversion and the gas mixture released were evaluated through isothermal heating at 230 °C using a thermogravimetric analysis coupled to a mass spectrometer. The time required to convert 100% of the adsorbed fraction increased by only 6 and 10 minutes under an oxidative and gasification atmosphere. By contrast, during pyrolysis treatment, after the 5<sup>th</sup> cycle, the conversion was reduced to 80% in cycle 10. Finally, hydrogen production during each treatment was considered, where the importance of the presence of different oxidation states of Cu and Ag was found. In the case of Cu<sup>+</sup> and Ag<sup>0</sup>, they preserve a high capture of sulfur. During oxidative regeneration, they allow the formation of highly catalytic phases such as Cu<sup>2+</sup> and Ag<sup>2+</sup> that help increase hydrogen production. In gasification, the Cu<sup>2+</sup> and Ag<sup>2+</sup> species corroborate that their high content increases hydrogen production during heat treatment. In the case of pyrolysis, it was identified that the presence of Cu<sub>2</sub>S and Ag<sub>2</sub>S drastically affects the effect of metallic oxides, poisoning the catalyst and reducing hydrogen production. In this sense, the oxidation and gasification atmospheres are proposed as promising alternatives for the regeneration of the material.

## 1. Introduction

There is a consensus in the legislation of many countries for improving the environmental quality of fuels in terms of sulfur content (< 10 ppm for gasoline and 15 ppm for diesel) [1]. To address the challenge of crude oil desulfurization, research in academia and industry is devoting more attention. Some of the most common strategies used include hydrodesulfurization (HDS) [2], carbon rejection processes [3], solvent deasphalting [4], and adsorptive desulfurization (ADS) [5,6]. ADS has received great attention due to its simplicity, adaptability, and effectiveness. The ADS technology is accompanied by the development of adsorbents such as activated carbon [7], aluminosilicates [6], polymers [8], and nanocomposites/nanomaterials [9,10]. Recently, we have developed a series of silica-based nanomaterials doped with different loads of Ag and Cu. This research was concluded by synthesizing optimized materials containing 1.5 mmol of Ag and 1.4 mmol of Cu (SiAg1.5Cu1.4) for increasing the sulfur removal percentage from a Colombian heavy crude oil with 35867 ppm of sulfur. The system had a 51.5% sulfur removal yield during the first use for an adsorbent mass (g):crude oil mass ratio (g) of 1:20 at static conditions. Similarly, dynamic adsorption reveals that the system required more than 350 min to reach the saturation point. Despite the promising results found, adsorbent deactivation and regeneration must be addressed during development of an industrially viable material. Some of the most common methods used includes physic (using a solvent for washing for backflow) and chemical (reactions) processes [11,12]. The use of solvents is considered an economically unviable process due to the large quantity of volumes of solvent required [4].

On the other hand, chemical reactions though thermal applications assisted with adsorbents with tailor made catalytic properties could facilitate the regeneration of the catalyst, the final disposal of the adsorbed sulfur compounds and the co-production of highly calorific gases using low energy costs [2,13-16].

Currently, HDS assisted by nanomaterials has shown promising results for crude oil removal [2,17,18]. Most HDS catalysts are composed of cobalt or nickel-promoted MoS<sub>2</sub> nanoparticles dispersed on  $\gamma$ -alumina [19]. The promoter is believed to be located at the edges of the MoS<sub>2</sub> particles as described in the CoMoS model and serves as active sites during HDS reactions [20]. More recently, several binary mixed oxides such as Al<sub>2</sub>O<sub>3</sub>-Ga<sub>2</sub>O<sub>3</sub> [21], Al<sub>2</sub>O<sub>3</sub>-TiO<sub>2</sub> [22],

ZrO<sub>2</sub>-TiO<sub>2</sub> [23], and Al<sub>2</sub>O<sub>3</sub>-ZrO<sub>2</sub> [24] have been studied, showing high adsorptive capacity.

Similarly, catalytic oxidative desulfurization has been studied slightly [25,26]. During this method, sulfur compounds can be oxidized by the electrophilic addition of oxygen atoms to the sulfur to form sulfoxides (1-oxides) and sulfones (1,1-dioxides) [27]. The use of transition-metal (Ti, Mo, Fe, V, W, Re, Ru) complexes as active catalysts for the selective oxidation of sulfur compounds in homogeneous conditions has also been reported [28-30]. In other work, Etemadi and Yen indicate that organic sulfone compounds, which are slightly more polar than organic sulfur compounds, can be selectively removed by solid adsorption on alumina oxide at low temperatures and atmospheric pressure via pyrolysis [31]. Similarly, Murata et al. [32] achieved nearly 100% removal of oxidized sulfur compounds by alumina oxide adsorption and subsequent pyrolysis application. Although each thermal treatment presents several advantages, the selectivity of the adsorbent for sulfur depends on the surface chemical changes generated in the different atmospheres.

Therefore, this study aims to continue with the previous research, mainly addressing the optimized (SiAg1.5Cu1.4) nanomaterial regenerating capacity during several sulfur adsorption/decomposition cycles under different atmospheres. This work focuses on evaluating the surface chemical changes of the nanomaterial under atmospheres of oxidation, gasification, and pyrolysis. This study, for the first time, makes a detailed analysis of the atmosphere that would enhance the chemical properties of a nanomaterial to extend its useful half-life with high selectivity, adsorptive and catalytic capacity. This generates valuable information on adsorbent reuse processes while removing sulfur compounds from heavy crude oils.

## 2. Experimental

### 2.1. Materials

A Colombian heavy crude oil containing mass fractions of 17.19, 15.36, 61.25, and 6.20% of saturates, aromatics, resins, and asphaltenes. The crude oil has a sulfur content of 35867 ppm and 14.4 °API. Salt precursors of Ag(NO<sub>3</sub>) (Merck KGaA, Darmstadt, Germany), and distilled water, CuCl<sub>2</sub>·2H<sub>2</sub>O (Merck KGaA, Darmstadt, Germany), and distilled water were used for the doping process. The support is commercial silica (3.0 μm, Sigma-Aldrich, USA). The oxidation atmosphere was simulated by injecting synthetic air NTC 2561

(CRYOGAS, Bogotá, Colombia) composed of 20.93% balanced O<sub>2</sub> with high purity. The reacting gas for pyrolysis consists of N<sub>2</sub> (CRYOGAS, Bogotá, Colombia) with high purity (99.5% N<sub>2</sub> and 0.5% O<sub>2</sub> content). The gasification process was simulated by introducing N<sub>2</sub> and H<sub>2</sub>O<sub>(g)</sub> using a gas saturator controlled by a thermostatic bath at atmospheric pressure.

## 2.2. Methods

### 2.2.1. Sulfur adsorption and subsequent decomposition

Sulfur adsorption tests were done by batch experiments over the optimized system (SiAg1.5Cu1.4) using three adsorbent mass (g): crude oil mass (g) ratios of 1:2, 1:10, and 1:20. The systems were magnetically stirred at 25 °C until the adsorption equilibrium. The sulfur adsorbed amount was estimated through X-ray fluorescence spectrometry (XRF) in a Philips model 1400 wavelength-dispersive spectrometer following the protocol described in the previous work.

The system with 1:2 adsorbent mass (g) crude oil mass (g) ratio was selected for thermogravimetric experiments using a TGA Q50 (TA Instruments, Inc., New Castle, DE) coupled to a mass spectrometer (Shimadzu MS, Tokyo, Japan). Sulfur decomposition was evaluated under isothermal heating at 230 °C under an oxidative, gasifying, and pyrolysis atmosphere. Air and nitrogen flow were fixed at 100 mL min<sup>-1</sup>, whereas H<sub>2</sub>O<sub>(g)</sub> was injected at 6.20 mL min<sup>-1</sup> during an N<sub>2</sub> flow of 100 mL min<sup>-1</sup>. The gases released were analyzed through mass spectrometry using a linear scan rate of 0.03 *m/z* between 0 – 200 *m/z*.

### 2.2.2. Nanomaterial regeneration

The regeneration of the nanomaterials was done through the catalytic decomposition of the adsorbed sulfur. The samples were placed in a pyrotubular furnace at 230 °C for 4 hours to guarantee complete regeneration.

### 2.2.3. Chemical changes in the reused nanomaterial.

During each cycle, a sample was examined through X-ray photoelectron spectroscopy (XPS), x-ray diffraction, point of zero charge (pH<sub>pzc</sub>), and N<sub>2</sub> adsorption/desorption. The XPS analysis was performed in a Specs-NAP-XPS X-ray photoelectronic spectrometer (Germany) with a monochromatic source Al-K $\alpha$  (1486.7 eV, 13 kV, 100 W). The XRD was assessed in Bruker-D8 Venture X-ray diffractometer (BRUKER, Rivas-Vaciamadrid, Spain) using Cu K $\alpha$  radiation source ( $\lambda=1.54$  Å) between  $2\theta = 0$  and  $90^\circ$  [33]. Finally, N<sub>2</sub> adsorption-desorption at  $-196$  °C was conducted in a micrometric ASAP 2020 (Micromeritics, Norcross, GA, USA). The surface area was calculated using the BET method [34], and the

micropore volume ( $W_0$ ) and micropore means ( $L_0$ ) were estimated using the Dubinin-Radushkevich method [35]. Considering this analysis, chemical and textural changes are analyzed as a function of three atmospheres.

### 3. Results and discussion.

#### 3.1. Sulfur adsorption capacity of the reused nanomaterial

The reusability of adsorbents is required to reduce the operational cost and realize their successful application in crude oil cleanup. Therefore, multicycle desulfurization experiments have been conducted to evaluate the recyclability of the SiAg<sub>1.5</sub>Cu<sub>1.4</sub>. Figure 1 shows the sulfur adsorbed amount on the SiAg<sub>1.5</sub>Cu<sub>1.4</sub> regenerated under different atmospheres. First, it is observed that the sulfur adsorption increases as the adsorbent mass (g): crude oil mass (g) ratio order 1:2 < 1:10 < 1:20. Considering that the system has not been completely saturated in any of the three systems, it can be primarily associated to the higher quantity of sulfur compounds in the 1:20 scenario. Further, the textural properties of the SiAg<sub>1.5</sub>Cu<sub>1.4</sub> material provide an efficient and easy diffusion of sulfur compounds within the material's channels.

The obtained increase in the adsorbed amount as the adsorbate content increases is explained by [36]. The authors established that the higher amount of adsorbate promotes more adsorbate-adsorbent interactions, which increases the contact area between the adsorbent and adsorbate, increasing the adsorption amount.

Another important fact is reducing the sulfur adsorbed amount as the SiAg<sub>1.5</sub>Cu<sub>1.4</sub> is regenerated in the different atmospheres. During the first evaluation, the sulfur removal percentage was estimated at 53.4% for a 1:20 ratio. After ten reuses, for the same adsorbent mass:crude oil ratio, the sulfur removal yield decreased by 1.1%, 2.5%, and 5.1% during oxidation, gasification, and pyrolysis, respectively. Interestingly, depending on the regenerative atmosphere employed, some organic compounds remained on the surface of the nanomaterial. The organic fraction could affect the block pores and the catalytic sites, decreasing the regeneration performance in increasing order: oxidation < gasification < pyrolysis. The results suggest that the adsorptive sites on the SiAg<sub>1.5</sub>Cu<sub>1.4</sub> were fully regenerable under oxidative conditions, which agrees with results reported by Dong et al. [37] who observed the complete regeneration of silica gel-supported TiO<sub>2</sub> is possible under an oxidative atmosphere instead an N<sub>2</sub> treatment.

The previous study demonstrated that the  $\text{Cu}^+$  and  $\text{Ag}^{2+}$  ions increase the interactions between the  $\text{SiO}_2$  support and the sulfur species due to the acid-base interactions. During thermal regeneration, the surface chemistry can be modified in different forms according to the employed atmosphere. In this context, it is possible that in an atmosphere of oxidation, the chemical species on the surface are not detrimentally affected, while in pyrolysis processes, the opposite occurs.

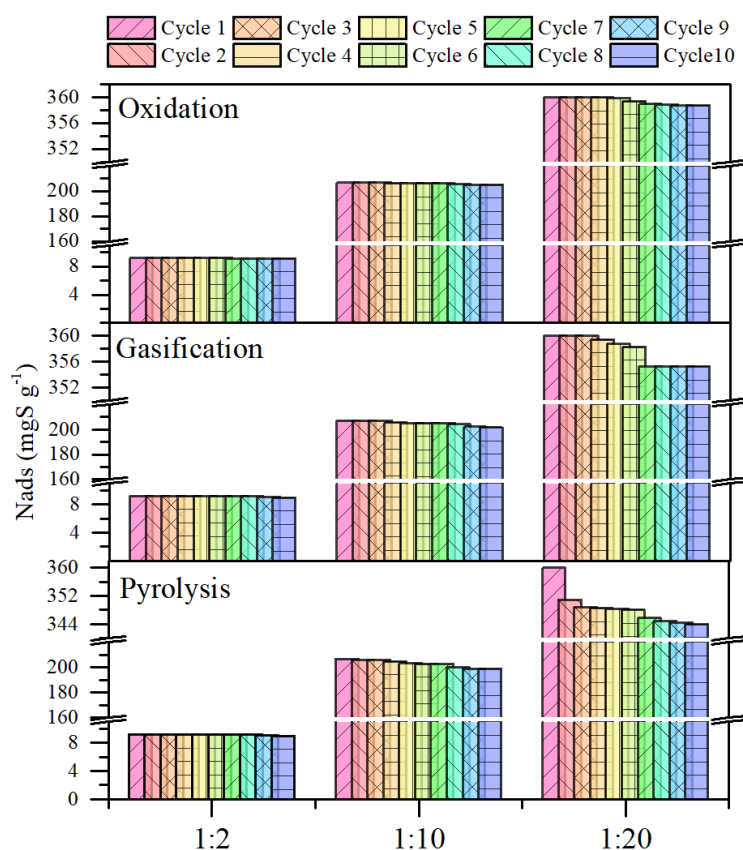


**Figure 1.** Sulfur removal adsorbed amount over  $\text{SiAg}_{1.5}\text{Cu}_{1.4}$  nanoparticles at 10 reuse cycles for different adsorbent mass (g):crude oil mass ratio(g) of 1:2, 1:10, and 1:20. The material was regenerated during oxidation, gasification, and pyrolysis processes at 230 °C.

### 3.2. Catalytic activity of the reused nanomaterial

The capacity of the  $\text{SiAg}_{1.5}\text{Cu}_{1.4}$  nanoparticles to decompose the sulfur adsorbed under different atmospheres was evaluated, and the results are shown in Figures 2-5. Initially, the oxidative atmosphere was tested to regenerate the nanomaterials and assess the degree of conversion of sulfur adsorbed under isothermal heating at 230 °C. The results for ten reuses are summarized in Figure 2. As the nanomaterial is reused, the time required to convert the adsorbed sulfur species increases slightly. At the same time, the conversion degree is somewhat

reduced. The most remarkable change was observed at minute 40, where the conversion for cycle 1 was greater by 7% compared to the last cycle evaluated. However, the conversion profiles are very similar throughout the estimated time and tend to coalesce at the end of heating. Among all the existing chemical bonds in hydrocarbon molecules, the C-S bond has the smallest bond-dissociation energy. The fact that the nanomaterial manages to decompose 100% of the adsorbed sulfur during the evaluated cycles indicates that support poisoning is not occurring, and the active sites of Ag and Cu are not being blocked either. This suggests that the oxidizing atmosphere is efficient enough to take advantage of the catalytic activity of the nanomaterial and decompose sulfur compounds. On the other hand, the surface chemistry of the SiAg<sub>1.5</sub>Cu<sub>1.4</sub> nanomaterial had previously been investigated, and it was found that the highly active surface chemical groups for sulfur capture were Cu<sup>+</sup> and Ag<sup>0</sup>. It could be expected that under the evaluated atmosphere, the surface chemistry of the material is not negatively affected, obtaining a good performance in all the evaluated cycles. The highly catalytic systems are expected to be composed mainly of a high group of Cu<sup>2+</sup> and Ag<sup>2+</sup>. In this way, the presence of the Ag<sup>0</sup> and Cu<sup>+</sup> groups is very valuable in an initial state since they oxidize in contact with oxygen, forming a larger group of highly catalytic species.

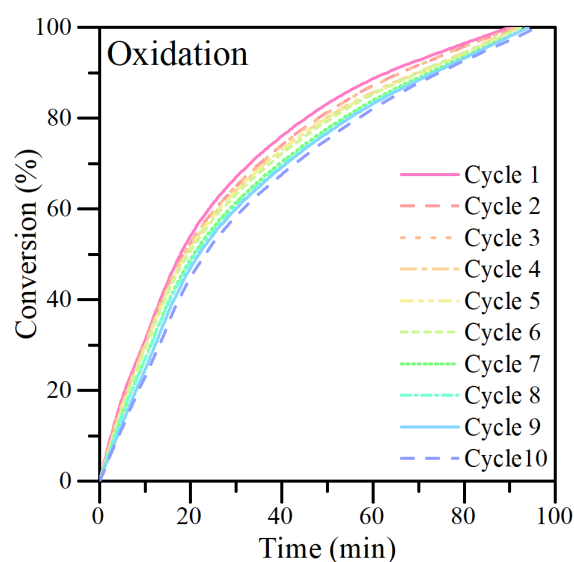


**Figure 2.** Isothermal sulfur decomposition over SiAg<sub>1.5</sub>Cu<sub>1.4</sub> nanoparticles at 10 reuse cycles for an adsorbent mass (g):crude oil mass ratio(g) of 1:2. The material was regenerated through oxidation at 230 °C.

The second selected atmosphere for the catalytic regeneration of SiAg<sub>1.5</sub>Cu<sub>1.4</sub> nanoparticles was gasification. The results are depicted in Figure

3. The regeneration protocol using  $\text{H}_2\text{O}_{(\text{g})}$  can successfully remove sulfur from the nanomaterial at  $230\text{ }^\circ\text{C}$ , and it can recover a significant amount of its activity. During the 10 reuse cycles, the nanomaterial decomposes 100% of the sulfur adsorbed indicating a high regeneration efficiency. Among all the existing chemical bonds in hydrocarbon molecules, the C-S bond has the smallest bond-dissociation energy. The nanomaterial performs well in breaking the C-S and transforming the sulfur-rich compounds into simpler hydrocarbons, which is analyzed in the next section.

However, as the material is regenerated, the time required to decompose 100% of adsorbed species increases 10 min. Also, the time to achieve a determined degree of conversion was always lower during oxidation than during gasification with  $\text{H}_2\text{O}_{(\text{g})}$ . This suggests that the nanomaterial displays better activity in activating the C-S bond of sulfur species in contact with  $\text{O}_2$  molecules than  $\text{H}_2\text{O}$ , which might be ascribed to the oxidation of  $\text{Cu}^+$  and  $\text{Ag}^0$  facets and their higher intrinsic activity. More interestingly, the conversion is almost similar when the heating time is lower than 40 min, suggesting that for  $\text{SiAg}_{1.5}\text{Cu}_{1.4}$  nanomaterial, further change in the regeneration atmosphere does not result in considerable activity enhancement at the beginning of heating. Since Ag and Cu nanoparticles exhibit different temperature-activity trends, it could be speculated that the catalytic reactions for the two systems might follow different reaction pathways. However, these changes are more pronounced above 40 min in both atmospheres.

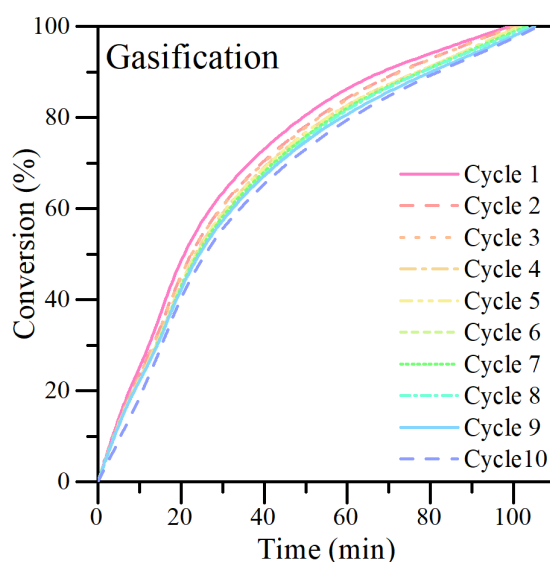


**Figure 3.** Isothermal sulfur decomposition over  $\text{SiAg}_{1.5}\text{Cu}_{1.4}$  nanoparticles at 10 reuse cycles for an adsorbent mass (g): crude oil mass ratio(g) of 1:2. The material was regenerated through gasification at  $230\text{ }^\circ\text{C}$ .



Nitrogen injection was used to simulate the pyrolysis atmosphere, the third checked in this study. The results are summarized in Figure 4. The conversion degree under the pyrolysis atmosphere shows very marked changes, unlike the atmospheres of gasification with steam and oxidation with air. In the first instance, under a non-reactive atmosphere, 100% of the adsorbed fraction is decomposed in the first cycle, and this catalytic activity is maintained until cycle 5 of reuse. However, in these cycles, the time required to reach 100% conversion increases by more than 15 minutes, greater than the time increased in all the cycles evaluated in the other two atmospheres. From cycle 5, the nanomaterial achieves conversion degrees below 100%, obtaining 84% conversion in cycle 10. The results indicate that a portion of the sulfur may remain in the nanomaterial, causing its poisoning. It is generally admitted that there are three causes of catalyst deactivation, the main one being, by far, coke formation. The second cause may be the damage of active phase structure and dispersion, while the third one is contamination by various chemicals that adsorb on the active sites.

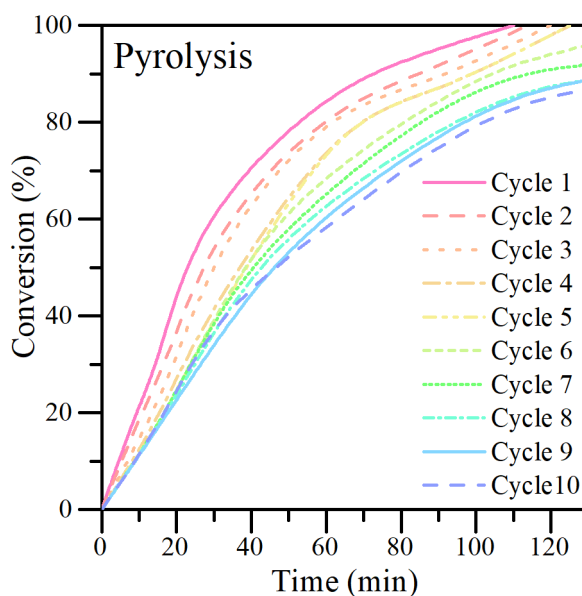


**Figure 4.** Isothermal sulfur decomposition over SiAg<sub>1.5</sub>Cu<sub>1.4</sub> nanoparticles at 10 reuse cycles for an adsorbent mass (g): crude oil mass ratio(g) of 1:2. The material was regenerated through pyrolysis at 230 °C.

### 3.3. Analysis of gaseous products during nanomaterial regeneration

The gas mixture released during the thermal decomposition process of the fraction adsorbed on the nanomaterial was analyzed. The results for the gases generated during the oxidation process are shown in Figure 5. The mass spectra profiles of H<sub>2</sub>, CO, CO<sub>2</sub>, CH<sub>4</sub>, C<sub>2</sub>H<sub>4</sub>, C<sub>2</sub>H<sub>6</sub>, and SO<sub>x</sub> (SO<sub>2</sub>, SO<sub>3</sub><sup>+</sup>) are considered in

this study. The untreated heavy oil (HO) exhibits a gas mixture composed by 1.5%vol H<sub>2</sub>, > 25% vol of CO and CO<sub>2</sub>, >15% vol of SO<sub>x</sub> and <15%vol of light hydrocarbons including CH<sub>4</sub>, C<sub>2</sub>H<sub>4</sub>, C<sub>2</sub>H<sub>6</sub>. This is a gaseous mixture with a low calorific value, and a fairly high content of polluting gases. However, when the sulfur fraction of the heavy crude is adsorbed by the material and is cracked, the gas mixture changes to a great extent in all the cycles evaluated. First, SO<sub>x</sub> production was less than 1% vol in the 10 cycles evaluated. It is expected that during the oxidation SO<sub>x</sub> compounds are produced, however, the catalyst can take advantage of these molecules to carry out other reactions and generate other gaseous products. In this order of ideas, the increase of CH<sub>4</sub>, C<sub>2</sub>H<sub>4</sub>, and C<sub>2</sub>H<sub>6</sub> was identified in all cycles compared to virgin crude. In addition, the production of CO and CO<sub>2</sub> fell below 10% vol in the 10 cycles. Finally, the hydrogen production was close to 15% vol. One of the most accepted pathways for H<sub>2</sub> productions during oxidation of hydrocarbons consists in the production of methane during hydrocarbon cracking and subsequent interactions with O<sub>2(g)</sub> to produce H<sub>2</sub>O<sub>(g)</sub>. This reaction is exothermic ( $\Delta H = -802 \text{ kJ}\cdot\text{mol}^{-1}$ ). Then, the steam molecules can react with carbon<sub>(s)</sub> ( $\Delta H = 172 \text{ kJ}\cdot\text{mol}^{-1}$ ), CO<sub>(g)</sub> ( $\Delta H = -41 \text{ kJ}\cdot\text{mol}^{-1}$ ), CH<sub>4(g)</sub> ( $\Delta H = 206 \text{ kJ}\cdot\text{mol}^{-1}$ ) to produce H<sub>2(g)</sub>.

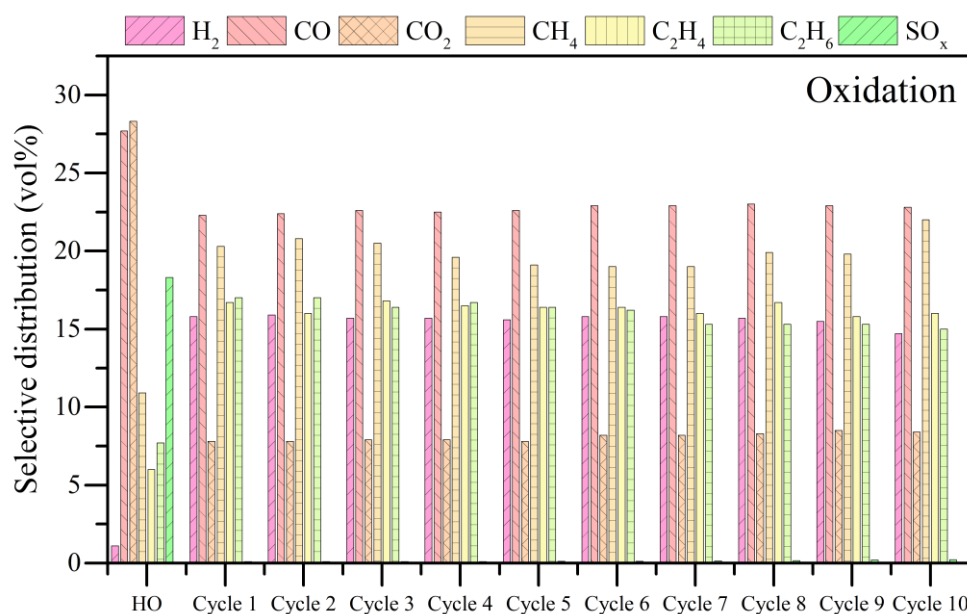


**Figure 5.** Selective gas distribution released from the catalytic sulfur decomposition on SiAg1.5Cu1.4 nanoparticles during 10 reuse cycles in an oxidative atmosphere.

On the other hand, the gas mixture released during steam gasification of nanomaterials regeneration is shown in Figure 6. Like oxidation, the mass spectra

profiles of H<sub>2</sub>, CO, CO<sub>2</sub>, CH<sub>4</sub>, C<sub>2</sub>H<sub>4</sub>, C<sub>2</sub>H<sub>6</sub>, were considered, but adding the analysis of H<sub>2</sub>S. The gaseous mixture produced for the untreated crude oil consists mainly of CO (26% *vol*) and CO<sub>2</sub> (27% *vol*), followed by CH<sub>4</sub> (11% *vol*), and to a lesser degree light hydrocarbons (<10% *vol*) and hydrogen (<1% *vol*). The nanomaterial on the other hand reduces the release of polluting gases such as CO<sub>2</sub> and CO. Interestingly, the production of H<sub>2</sub>S is also reduced, probably because the catalytic mechanisms of the material lead to a different pathway that inhibits the production of this gas. In addition, the production of light hydrocarbons was favored in all the cycles evaluated and in the same way the production of hydrogen (> 20% *vol*). Hydrogen could be produced by several mechanisms that involves cleave of C-C bonds, as well as C-H and/or O-H bonds to form adsorbed species on the nanomaterial surface.

In previous investigations, we demonstrated that during the catalytic decomposition of heavy hydrocarbons, the water gas shift (WGS) and steam/methane reforming reactions take place. Both reactions release hydrogen as a main product. Also, the high release of hydrogen during all cycles analyzed may be associated to the presence of binary Ag-Cu, which have been widely used in literature to improve the resistance to deactivation of catalysts [38].

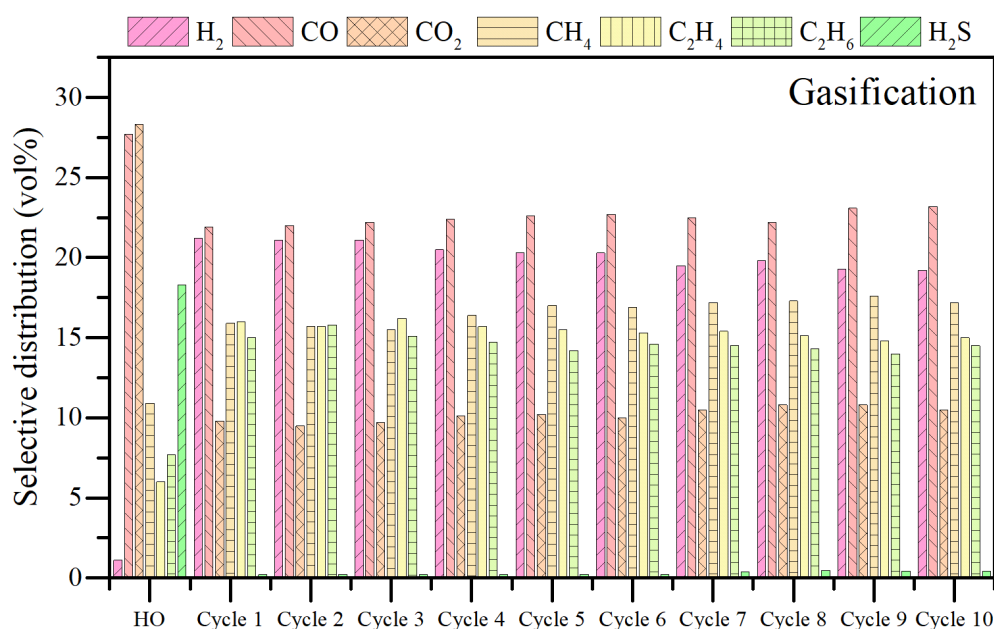


**Figure 6.** Selective gas distribution released from the catalytic sulfur decomposition on SiAg<sub>1.5</sub>Cu<sub>1.4</sub> nanoparticles during 10 reuse cycles in a gasifying atmosphere.

Finally, Figure 7 shows the released mixture during pyrolysis treatment in the 10 cycles. The Figure shows that the nanomaterials released a gas mixture mainly composed by CO (>25%vol) in all cycles. Besides, CO<sub>2</sub> was higher than 15%vol and its distribution increases as the nanomaterial is reused. The production of light hydrocarbons was similar to CO<sub>2</sub>, but they decrease the total production around 10%vol from cycle 1 to cycle 10. Hydrogen release was negatively affected obtaining 10%vol in the first cycle and reduced to 7%vol to the tenth cycle.

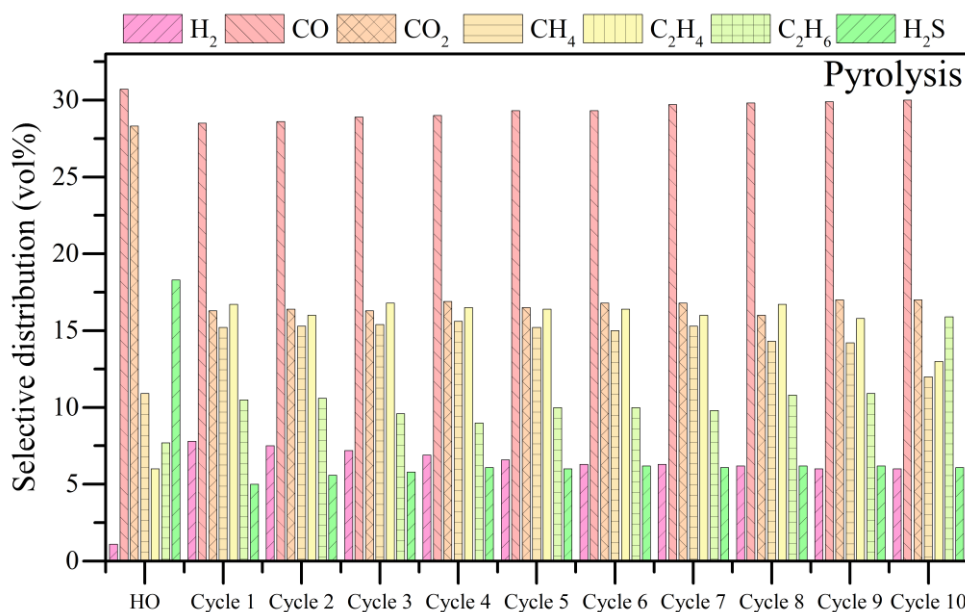
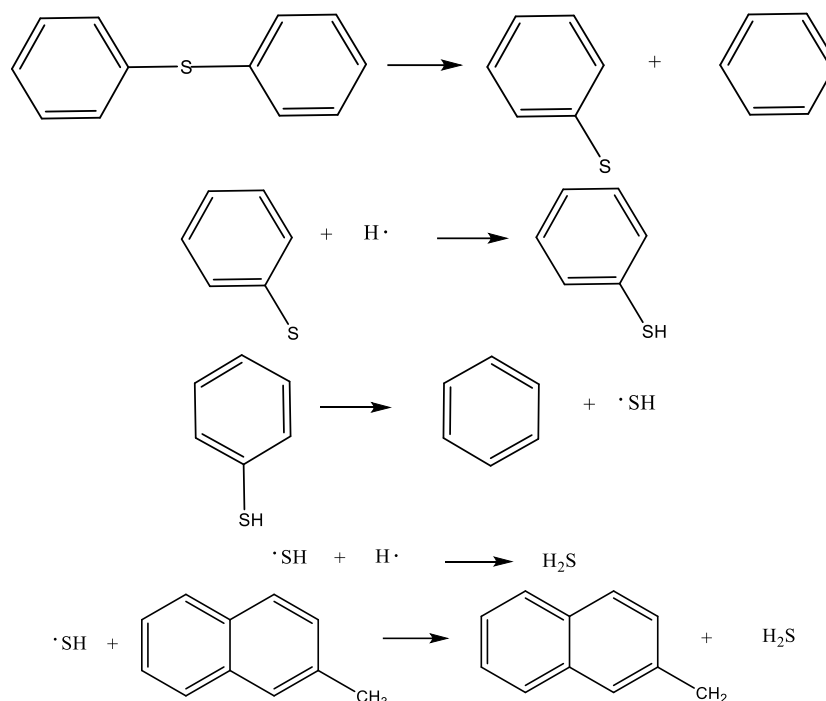


**Figure 7.** Selective gas distribution released from the catalytic sulfur decomposition on SiAg<sub>1.5</sub>Cu<sub>1.4</sub> nanoparticles during 10 reuse cycles in an inert atmosphere.

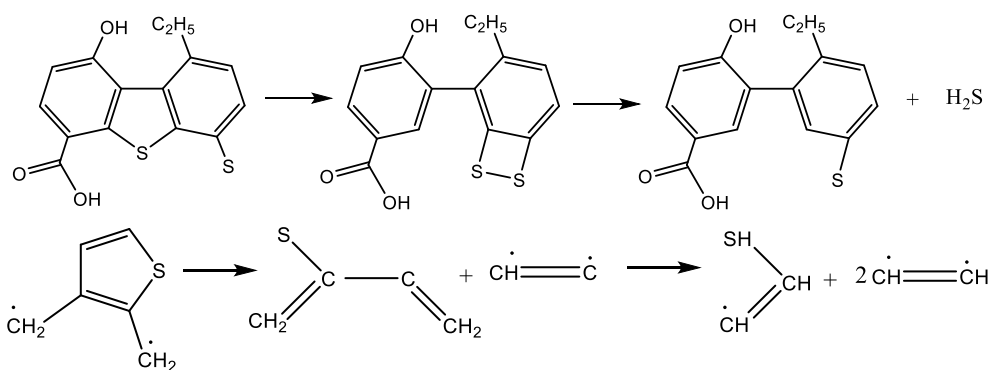
Particularly, H<sub>2</sub>S production was observed in all the cycles evaluated. This could be associated to the nanomaterial poisoning and the subsequent decrease in catalytic and adsorption capacity. Wang et al. [39] proposed a mechanism for H<sub>2</sub>S generation from mercaptan, sulfide and thiophene through molecular dynamic simulation during pyrolysis. It is worth mentioning that these are common structures in fossil fuels and some fractions, particularly asphaltenes and resins. Figure 8 shows the proposed pathways.

It was observed that mercaptan and sulfide are easy to be decomposed into H<sub>2</sub>S and unsaturated compounds during pyrolysis process. Because the ring opening reaction must happen before H<sub>2</sub>S generation, the thiophene sulfur is relatively difficult to remove. However, in both ways, H<sub>2</sub>S is produced.

As displayed in Fig. 8, the generation of H<sub>2</sub>S starts with the breakage of C-S bond. This is coincident with the viewpoint of Attar [40] who considers the breakage of C-S bond is the decisive step of desulfurization in hydropyrolysis.



a) Mercaptan and sulfide decomposition



b) Thiophene decomposition.

**Figure 8.** H<sub>2</sub>S generation from mercaptan, sulfide and thiophene from molecular dynamic simulation. Taken with permission from [39].

### 3.4. Chemical composition of re-used nanomaterial

X-ray photoelectron spectroscopy was done to analyze the surface chemistry changes as the SiAg<sub>1.5</sub>Cu<sub>1.4</sub> is reused. Table 1 shows the results obtained for oxidation treatment. It was identified the Si<sub>2p</sub>, O<sub>1s</sub>, Ag<sub>3d<sub>5/2</sub></sub>, and Cu<sub>2p<sub>3/2</sub></sub> core-level regions during the 10 cycles evaluated. The Si<sub>2p</sub> spectrum was

deconvoluted by two main peaks at 102.3 eV for Si-O-Si and 103.5 eV for Si-OH signals [41]. During sample regeneration, the peak percentage for Si-O-Si was slightly increased from 37% (cycle 1) to 45% (cycle 10). Simultaneously, an oxygen peak O–Metal has grown at the outer surface at 531.8 eV (binding energy of O– Ag, O-Cu) [42]. The greater increase in these species is probably since transition elements are more susceptible to interacting with oxygen molecules. The  $Ag_{3d5/2}$  binding energies of 368.2 eV f and 367.8 eV for the first cycle are close to the value reported for metallic Ag and silver (II) oxide, respectively [43]. Silver exhibits a yet-to-be-explained shift to lower binding energy because of the oxidation of Ag during the reuse. According to the literature, the shift is usually between 0.3–0.4 eV for  $Ag_2O$  and between 0.8-1.0 eV for AgO. The direction and magnitude of the  $Ag_{3d}$  peak shift in our case suggests the formation of  $Ag_2O$  [44,45]. Its content increased around 6% from cycle 1 to cycle 10. Finally, the  $Cu_{2p3/2}$  spectrum exhibits two marked peaks at 932.4 eV associated to  $Cu^+$  and 933.3 eV ascribed to  $Cu^{2+}$  [46]. After the reuse cycles, the  $Cu^+$  species were oxidized to  $Cu^{2+}$ , as confirmed by the shift of the  $Cu_{2p3/2}$  XPS peak. The percentage of  $Cu^{2+}$  increased 8% during 10 cycles. In the first part of this study, we identified the presence of {100} and {111} facets. According to the literature, the {100} can be easily oxidized during the subjected process, while the {111} resists the surface oxidation [47]. In this order, it is demonstrated the higher stability of  $Cu_2O(111)$  over  $Cu_2O(100)$ , which is in line with the literature reporting [48].

**Table 1.** Peak percentage of silica, oxygen, silver, and copper components obtained by the fitting results of the  $Si_{2p}$ ,  $O_{1s}$ ,  $Ag_{3d5/2}$ , and  $Cu_{2p3/2}$  spectra, respectively, for SiAg1.5Cu1.4 regenerated by air oxidation during 10 reuses.

Cycle	Peak							
	$Si_{2p}$		$O_{1s}$		$Ag_{3d5/2}$		$Cu_{2p3/2}$	
	Assignment	%	Assignment	%	Assignment	%	Assignment	%
1	Si-OH	63	O-Metal	30	$Ag^0_{5/2}$	47	$Cu^+_{3/2}$	85
	Si-O-Si	37			$Ag^{2+}_{5/2}$	53	$Cu^{2+}_{3/2}$	15
3	Si-OH	62	O-Metal	32	$Ag^0_{5/2}$	47	$Cu^+_{3/2}$	84
	Si-O-Si	38			$Ag^{2+}_{5/2}$	53	$Cu^{2+}_{3/2}$	16
5	Si-OH	59	O-Metal	33	$Ag^0_{5/2}$	45	$Cu^+_{3/2}$	81
	Si-O-Si	41			$Ag^{2+}_{5/2}$	55	$Cu^{2+}_{3/2}$	19
7	Si-OH	56	O-Metal	36	$Ag^0_{5/2}$	42	$Cu^+_{3/2}$	80
	Si-O-Si	44			$Ag^{2+}_{5/2}$	58	$Cu^{2+}_{3/2}$	20
10	Si-OH	55	O-Metal	37	$Ag^0_{5/2}$	41	$Cu^+_{3/2}$	77
	Si-O-Si	45			$Ag^{2+}_{5/2}$	59	$Cu^{2+}_{3/2}$	23

Table 2 shows the peak percentage of the high-resolution spectra of the different components in the SiAg1.5Cu1.4 nanomaterial during the different reuses. Minor changes were found in the Si<sub>2p</sub> and O<sub>1s</sub> spectra. The concentration of the Si-OH species was slightly increased (3%) from cycle 1 to cycle 10. Similarly, the peak assigned to O-Metal increased around 2%. Ag species mainly exist as Ag<sup>2+</sup>, while as the material is reused, Ag<sup>0</sup> species increase remarkably. It is likely that at the first cycles, some of the silver oxide is reduced by the SiO<sub>2</sub> and steam, a similar effect has been reported on Ag<sub>2</sub>O-doped TiO<sub>2</sub> and CeO<sub>2</sub> nanoparticles [49,50].

For the latest cycle, most of the silver present in the catalysts remains as metallic Ag (54%). Based on literature reports involving silver oxides, it can be concluded that some electrons may transfer from SiO<sub>2</sub> to the Ag dopant and there is strong interaction between the Ag species and the SiO<sub>2</sub> support. On the other hand, the Cu species also changed during the material regeneration. The Cu<sup>+</sup> percentage was increased in a low degree from 85% to 87%, due to the probable interactions with SiO<sub>2</sub> through the Cu–O bonds [51]. Similarly, the atmosphere evaluated has a notable effect on the surface chemistry of the catalyst. Despite the opposite trend to that found when the material was subjected to oxidation, the adsorptive and catalytic results of the material continued to be good in both atmospheres. Apparently, the OH species deposited by the H<sub>2</sub>O protect the surface of the nanomaterial from the H<sub>2</sub>S poisoning and dissociation to complete the surface sulphidation.

**Table 2.** Peak percentage of silica, oxygen, silver, and copper components obtained by the fitting results of the Si<sub>2p</sub>, O<sub>1s</sub>, Ag<sub>3d5/2</sub>, and Cu<sub>2p3/2</sub> spectra, respectively, for SiAg1.5Cu1.4 regenerated by steam gasification during 10 reuses.

Cycle	Peak							
	Si <sub>2p</sub>		O <sub>1s</sub>		Ag <sub>3d5/2</sub>		Cu <sub>2p3/2</sub>	
	Assignment	%	Assignment	%	Assignment	%	Assignment	%
1	Si-OH	63	O-Metal	30	Ag <sup>0</sup> <sub>5/2</sub>	47	Cu <sup>+</sup> <sub>3/2</sub>	85
	Si-O-Si	37			Ag <sup>2+</sup> <sub>5/2</sub>	53	Cu <sup>2+</sup> <sub>3/2</sub>	15
3	Si-OH	63	O-Metal	30	Ag <sup>0</sup> <sub>5/2</sub>	49	Cu <sup>+</sup> <sub>3/2</sub>	85
	Si-O-Si	37			Ag <sup>2+</sup> <sub>5/2</sub>	51	Cu <sup>2+</sup> <sub>3/2</sub>	15
5	Si-OH	64	O-Metal	31	Ag <sup>0</sup> <sub>5/2</sub>	51	Cu <sup>+</sup> <sub>3/2</sub>	86
	Si-O-Si	36			Ag <sup>2+</sup> <sub>5/2</sub>	49	Cu <sup>2+</sup> <sub>3/2</sub>	14
7	Si-OH	65	O-Metal	31	Ag <sup>0</sup> <sub>5/2</sub>	53	Cu <sup>+</sup> <sub>3/2</sub>	86
	Si-O-Si	35			Ag <sup>2+</sup> <sub>5/2</sub>	47	Cu <sup>2+</sup> <sub>3/2</sub>	14
10	Si-OH	66	O-Metal	32	Ag <sup>0</sup> <sub>5/2</sub>	54	Cu <sup>+</sup> <sub>3/2</sub>	87
	Si-O-Si	34			Ag <sup>2+</sup> <sub>5/2</sub>	46	Cu <sup>2+</sup> <sub>3/2</sub>	13

Finally, the peak percentage of the different species in SiAg1.5Cu1.4 regenerated by pyrolysis is shown in Table 3.

**Table 3.** Peak percentage of silica, oxygen, silver, and copper components obtained by the fitting results of the Si<sub>2p</sub>, O<sub>1s</sub>, Ag<sub>3d5/2</sub>, and Cu<sub>2p3/2</sub> spectra, respectively, for SiAg1.5Cu1.4 regenerated by nitrogen injection during 10 reuses.

Cycle	Peak									
	Si <sub>2p</sub>		O <sub>1s</sub>		Ag <sub>3d5/2</sub>		Cu <sub>2p3/2</sub>		S <sub>2p</sub>	
	Assignment	%	Assignment	%	Assignment	%	Assignment	%	Assignment	%
1	Si-OH	63	O-Metal	30	Ag <sup>0</sup> <sub>5/2</sub>	47	Cu <sup>+</sup> <sub>3/2</sub>	85	S <sup>2-</sup>	-
	Si-O-Si	37			Ag <sup>2+</sup> <sub>5/2</sub>	53	Cu <sup>2+</sup> <sub>3/2</sub>	15	HS <sup>-</sup>	-
					Ag <sub>2</sub> S <sub>5/2</sub>	-	Cu <sub>2</sub> S <sub>3/2</sub>	-		
3	Si-OH	63	O-Metal	30	Ag <sup>0</sup> <sub>5/2</sub>	47	Cu <sup>+</sup> <sub>3/2</sub>	85	S <sup>2-</sup>	-
	Si-O-Si	37			Ag <sup>2+</sup> <sub>5/2</sub>	53	Cu <sup>2+</sup> <sub>3/2</sub>	15	HS <sup>-</sup>	-
					Ag <sub>2</sub> S <sub>5/2</sub>	-	Cu <sub>2</sub> S <sub>3/2</sub>	-		
5	Si-OH	63	O-Metal	30	Ag <sup>0</sup> <sub>5/2</sub>	46	Cu <sup>+</sup> <sub>3/2</sub>	85	S <sup>2-</sup>	-
	Si-O-Si	37			Ag <sup>2+</sup> <sub>5/2</sub>	54	Cu <sup>2+</sup> <sub>3/2</sub>	15	HS <sup>-</sup>	-
					Ag <sub>2</sub> S <sub>5/2</sub>	-	Cu <sub>2</sub> S <sub>3/2</sub>	-		
7	Si-OH	64	O-Metal	30	Ag <sup>0</sup> <sub>5/2</sub>	44	Cu <sup>+</sup> <sub>3/2</sub>	84	S <sup>2-</sup>	1
	Si-O-Si	36			Ag <sup>2+</sup> <sub>5/2</sub>	54	Cu <sup>2+</sup> <sub>3/2</sub>	14	HS <sup>-</sup>	1
					Ag <sub>2</sub> S <sub>5/2</sub>	2	Cu <sub>2</sub> S <sub>3/2</sub>	2		
10	Si-OH	65	O-Metal	31	Ag <sup>0</sup> <sub>5/2</sub>	44	Cu <sup>+</sup> <sub>3/2</sub>	84	S <sup>2-</sup>	2
	Si-O-Si	36			Ag <sup>2+</sup> <sub>5/2</sub>	52	Cu <sup>2+</sup> <sub>3/2</sub>	13	HS <sup>-</sup>	3
					Ag <sub>2</sub> S <sub>5/2</sub>	4	Cu <sub>2</sub> S <sub>3/2</sub>	3		

The Si<sub>2p</sub> and O<sub>1s</sub> spectra were deconvoluted similarly to the previous sections. The content of the silica-base and oxygen-base species were not modified during the nanomaterial regeneration. Unlike the other two atmospheres, when the SiAg1.5Cu1.4 was treated under pyrolysis it was identified the presence of S<sub>2p</sub> core-level spectra for successive H<sub>2</sub>S exposures. The peak at 161.9 eV is associated to sulphide species, indicating that H<sub>2</sub>S is dissociated on the surface within the regeneration conditions. Also, the presence of HS<sup>-</sup> surface species at 163.5 eV is identified. Both species increased 1% (sulphide) and 2% (HS<sup>-</sup>) from cycle 1 to cycle 10. During the first 5 cycles, the Cu<sub>2p3/2</sub> core level do not change, so the Cu<sup>+</sup> and Cu<sup>2+</sup> samples are not changed into Cu<sub>2</sub>S. However, the evolution of the cycles indicates that for the exposures of H<sub>2</sub>S, the Cu<sup>2+</sup> reduced to Cu<sup>+</sup>. From cycle 6, it was detected a signal peak at 162 eV that corresponds well with a Cu<sub>2</sub>S-type sulphide or to S species adsorbed in an S<sup>2-</sup>-like state on Cu [52,53]. Similarly, Ag<sub>3d5/2</sub> spectra exhibits two main peaks associated to Ag<sup>0</sup> and Ag<sup>2+</sup> species at 368.2 eV and 367.8 eV, respectively. The distribution percentage of both components were not drastically changed until



the sixth cycle, where it was noted the presence of a peak at a binding energy of 367.8 eV. This indicates that some selective sputtering of sulfur occurs, generating Ag<sub>2</sub>S species by the H<sub>2</sub>S exposure [54-56].

### 3.5. Textural properties of re-used nanomaterial

The textural properties of the SiAg1.5Cu1.4 though its regeneration under different atmosphere were estimated, and results are shown in Table 4. In the first cycle, the area BET of the sample was estimated in 124.3 m<sup>2</sup>·g<sup>-1</sup>, the pore volume (W<sub>0</sub>) in 6.63 cm<sup>3</sup>·g<sup>-1</sup> and the pore size (L<sub>0</sub>) in 2.13 nm. Then, during oxidative treatment for sample regeneration, the textural properties remain very similar. The surface area decreases 0.6 m<sup>2</sup>·g<sup>-1</sup>, while the W<sub>0</sub> and L<sub>0</sub> are not decreased by more than 1%. Similarly, the steam gasification treatment does not affect the textural properties of the material. These tendencies support the high performance obtained by the material when it is regenerated by both atmospheres in terms of sulfur adsorption and subsequent decomposition. Conversely, when the material is regenerated by pyrolysis, the surface area decreases to 110.2 m<sup>2</sup>·g<sup>-1</sup>, probably associated with the blocking of active sites and pores by H<sub>2</sub>S and metallic sulfur molecules, as demonstrated by XPS. In addition, the W<sub>0</sub> is greatly affected after the 5th cycle. Its value decreases more than 15%, indicating the possible formation of coke within the pore space, which may be related to the decay in its adsorptive and catalytic capacity.

**Table 4.** Estimated porous textural characteristics of the doped SiO<sub>2</sub> microparticles with different loads of Ag and Cu obtained from N<sub>2</sub> adsorption-desorption and CO<sub>2</sub> adsorption.

Cycle	Oxidation			Gasification					
	S <sub>BET</sub> m <sup>2</sup> ·g <sup>-1</sup>	W <sub>0</sub> (N <sub>2</sub> ) x 10 <sup>-2</sup> cm <sup>3</sup> ·g <sup>-1</sup>	L <sub>0</sub> (N <sub>2</sub> ) nm	S <sub>BET</sub> m <sup>2</sup> ·g <sup>-1</sup>	W <sub>0</sub> (N <sub>2</sub> ) x 10 <sup>-2</sup> cm <sup>3</sup> ·g <sup>-1</sup>	L <sub>0</sub> (N <sub>2</sub> ) nm	S <sub>BET</sub> m <sup>2</sup> ·g <sup>-1</sup>	W <sub>0</sub> (N <sub>2</sub> ) x 10 <sup>-2</sup> cm <sup>3</sup> ·g <sup>-1</sup>	L <sub>0</sub> (N <sub>2</sub> ) nm
1	124.3	6.63	2.13	124.3	6.63	2.13	124.3	6.63	2.13
3	124.3	6.63	2.13	124.2	6.63	2.13	124.1	6.23	2.13
5	124.2	6.63	2.12	124.0	6.62	2.12	120.0	6.10	2.12
7	123.9	6.62	2.12	123.7	6.62	2.12	113.4	5.54	2.01
10	123.7	6.62	2.12	123.5	6.61	2.12	110.2	5.42	2.01

### 3.6. Influence of chemical and textural properties on adsorptive and catalytic activity of SiAg1.5Cu1.4

Considering the results in changes of surface chemistry and textural properties, it was identified which parameters particularly control hydrogen production during each regeneration treatment of the SiAg1.5Cu1.4 sample.

Results for oxidation, gasification, and pyrolysis are summarized in Figure 9. As the material was regenerated through oxidative experiments, a direct relationship between the selective distribution of  $H_2(\%)$  released during the decomposition of adsorbed compounds and the atomic content of  $Ag^0$  and  $Cu^+$ .

Apparently, both species participate in the reaction pathway favoring the hydrogen release from the thermal heating. Previously, we reported the interactions between  $Cu^+$  and  $Ag^0$  species and sulfur compounds, dominated by the  $\pi$ -complexation by the formation of  $\sigma$  bonds with the empty s-orbitals and, the d-orbitals can back-donate electron density to the antibonding  $\pi$ -orbitals ( $\pi^*$ ) of the sulfur rings [57]. These interactions are expected to play an important role in the catalytic activity of the material. A high content of  $Cu^+$  and  $Ag^0$  ions leads to greater sulfur capture, and during oxidation to  $Cu^{2+}$  and  $Ag^+$ , highly catalytic active sites are produced that allow the generation of high calorific value products such as hydrogen.

Analyzing the results from the regeneration by steam gasification it was identified that  $H_2(\%)$  production was enhanced with the increase in  $Ag^{2+}$  and  $Cu^{2+}$  species. As the material regenerates, both ions are transformed into  $Ag^0$  and  $Cu^+$  ions, whereby the production of  $H_2$  decreases. However, the coexistence of both Ag and Cu oxidation states is necessary to ensure good sulfur capture and high regeneration efficiency. In this scenario, hydrogen production decreased only 2% in the 10 cycles evaluated, presenting an excellent scenario in terms of generating a gas with high calorific power. In the last scenario, during the pyrolysis treatment, it was identified that the effect of the oxidation states of Cu and Ag is affected by the presence of  $Cu_2S$  and  $Ag_2S$  species. Poisoning the active sites of metallic oxides reduces the release of hydrogen during the decomposition of adsorbed sulfur. As previously identified (section 3.5), it is possible that during this treatment, not only the catalyst is being poisoned, but also that coke is being retained in the pore space and therefore the reduction in its pore volume. In this order of ideas, as the atomic content of  $Cu_2S$  and  $Ag_2S$  increases, the production of hydrogen decreases.

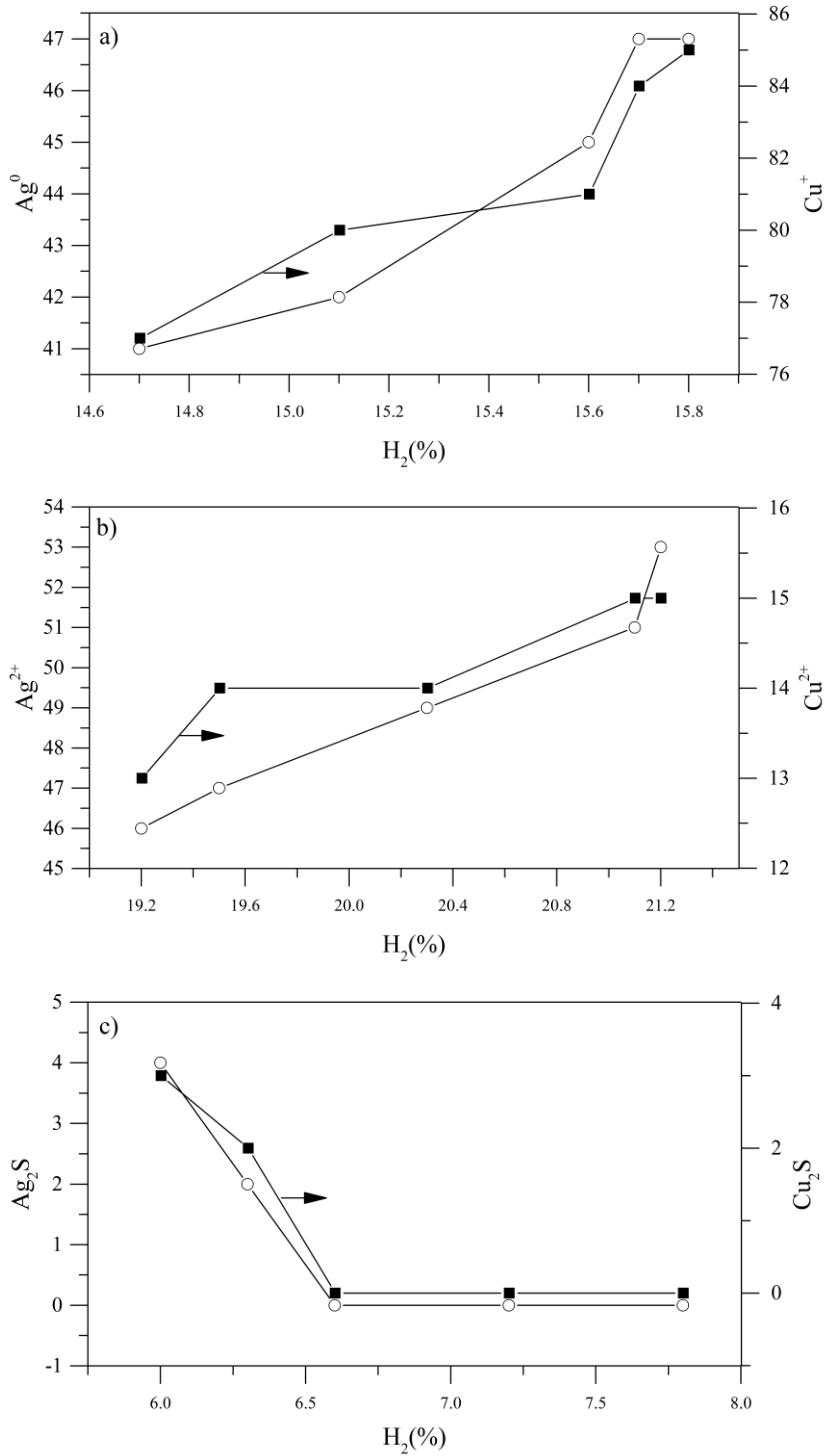


**Figure 9.** Influence of the nanomaterial's chemical properties on hydrogen release from catalytic decomposition of sulfur adsorbed on SiAg1.5Cu1.4 under different thermal treatments including a) oxidation, b) gasification, and c) pyrolysis.

## 4. Conclusions.

Among all the existing chemical bonds in hydrocarbon molecules, C-S bond is found to have the smallest bond-dissociation energy. The breaking of C-S bond contributes greatly to the viscosity reduction and crude oil quality upgrading. Furthermore, desulfurization of crude oil in the oil refineries is becoming an increasingly important task due to the stringent environmental and clean-fuel legislations. This work aims to discover the best scenario to regenerate a silicon-based nanomaterial supported with Ag and Cu metal phases. Three regeneration atmospheres were considered, including: oxidation, gasification, and pyrolysis. In terms of adsorption and sulfur capture, it was determined that in oxidation the best performance was obtained during ten evaluated cycles, while the atmosphere of pyrolysis presented the lowest performance. On the other hand, the isothermal conversion of the adsorbed compounds at 230 °C was also evaluated, obtaining a conversion of or 100% in the 10 cycles evaluated both for the system treated by oxidation and gasification, while in pyrolysis, the conversion was reduced close to 80% for the last cycle. Finally, the production of hydrogen during each treatment was considered, where the importance of the presence of different oxidation states of Cu and Ag was found. In the case of Cu<sup>+</sup> and Ag<sup>0</sup>, they preserve a high capture of sulfur, and during the treatment of oxidation, allow the formation of highly catalytic phases such as Cu<sup>2+</sup> and Ag<sup>2+</sup> that help increase hydrogen production. On the other hand, in gasification, the Cu<sup>2+</sup> and Ag<sup>2+</sup> species corroborate that their high content increases hydrogen production during heat treatment. In the case of pyrolysis, it was identified that the presence of Cu<sub>2</sub>S and Ag<sub>2</sub>S drastically affects the effect of metallic oxides, poisoning the catalyst and reducing hydrogen production. In this sense, the oxidation and gasification atmospheres are proposed as good alternatives for the regeneration of the material. The combined evaluation of both atmospheres is suggested to develop a more efficient scenario.

## References

1. Lee, K.X.; Valla, J.A. Adsorptive desulfurization of liquid hydrocarbons using zeolite-based sorbents: a comprehensive review. *Reaction Chemistry & Engineering* **2019**, *4*, 1357-1386, doi:10.1039/c9re00036d.

2. Prins, R.; De Beer, V.; Somorjai, G. Structure and function of the catalyst and the promoter in Co–Mo hydrodesulfurization catalysts. *Catalysis Reviews—Science and Engineering* **1989**, *31*, 1-41.
3. Aguilar, R.A.; Ancheyta, J.; Trejo, F. Simulation and planning of a petroleum refinery based on carbon rejection processes. *Fuel* **2012**, *100*, 80-90.
4. Sattarin, M.; Modarresi, H.; Talachi, H.; Teymori, M. Solvent deasphalting of vacuum residue in a bench-scale unit. *Petroleum & Coal* **2006**, *48*, 14-19.
5. Srivastav, A.; Srivastava, V.C. Adsorptive desulfurization by activated alumina. *Journal of hazardous materials* **2009**, *170*, 1133-1140.
6. Kwon, J.M.; Moon, J.H.; Bae, Y.S.; Lee, D.G.; Sohn, H.C.; Lee, C.H. Adsorptive desulfurization and denitrogenation of refinery fuels using mesoporous silica adsorbents. *ChemSusChem: Chemistry & Sustainability Energy & Materials* **2008**, *1*, 307-309.
7. Jha, D.; Haider, M.B.; Kumar, R.; Byamba-Ochir, N.; Shim, W.G.; Marriyappan Sivagnanam, B.; Moon, H. Enhanced adsorptive desulfurization using Mongolian anthracite-based activated carbon. *ACS omega* **2019**, *4*, 20844-20853.
8. Li, B.; Yu, S.; Jiang, Z.; Liu, W.; Cao, R.; Wu, H. Efficient desulfurization by polymer–inorganic nanocomposite membranes fabricated in reverse microemulsion. *Journal of hazardous materials* **2012**, *211*, 296-303.
9. Saleh, T.A.; Danmaliki, G.I.; Shuaib, T.D. Nanocomposites and hybrid materials for adsorptive desulfurization. In *Applying Nanotechnology to the Desulfurization Process in Petroleum Engineering*, IGI Global: 2016; pp. 129-153.
10. Li, Y.; Yi, H.; Tang, X.; Liu, X.; Wang, Y.; Cui, B.; Zhao, S. Study on the performance of simultaneous desulfurization and denitrification of Fe<sub>3</sub>O<sub>4</sub>-TiO<sub>2</sub> composites. *Chemical Engineering Journal* **2016**, *304*, 89-97.
11. Zannikos, F.; Lois, E.; Stournas, S. Desulfurization of petroleum fractions by oxidation and solvent extraction. *Fuel processing technology* **1995**, *42*, 35-45.
12. Ramirez-Verduzco, L.; Torres-Garcia, E.; Gomez-Quintana, R.; Gonzalez-Pena, V.; Murrieta-Guevara, F. Desulfurization of diesel by oxidation/extraction scheme: influence of the extraction solvent. *Catalysis Today* **2004**, *98*, 289-294.
13. Medina, O.E.; Gallego, J.; Restrepo, L.G.; Cortés, F.B.; Franco, C.A. Influence of the Ce<sup>4+</sup>/Ce<sup>3+</sup> Redox-couple on the cyclic regeneration for

- adsorptive and catalytic performance of NiO-PdO/CeO<sub>2</sub>+ $\delta$  nanoparticles for n-C7 asphaltene steam gasification. *Nanomaterials* **2019**, *9*, 734.
14. Medina, O.E.; Gallego, J.; Arias-Madrid, D.; Cortés, F.B.; Franco, C.A. Optimization of the load of transition metal oxides (Fe<sub>2</sub>O<sub>3</sub>, Co<sub>3</sub>O<sub>4</sub>, NiO and/or PdO) onto CeO<sub>2</sub> nanoparticles in catalytic steam decomposition of n-C7 asphaltenes at low temperatures. *Nanomaterials* **2019**, *9*, 401.
  15. Medina, O.E.; Hurtado, Y.; Caro-Velez, C.; Cortés, F.B.; Riazi, M.; Lopera, S.H.; Franco, C.A. Improvement of steam injection processes through nanotechnology: An approach through in situ upgrading and foam injection. *Energies* **2019**, *12*, 4633.
  16. Razeghi, A.; Khodadadi, A.; Ziaei-Azad, H.; Mortazavi, Y. Activity enhancement of Cu-doped ceria by reductive regeneration of CuO–CeO<sub>2</sub> catalyst for preferential oxidation of CO in H<sub>2</sub>-rich streams. *Chemical Engineering Journal* **2010**, *164*, 214-220.
  17. Tanimu, A.; Alhooshani, K. Advanced hydrodesulfurization catalysts: a review of design and synthesis. *Energy & Fuels* **2019**, *33*, 2810-2838.
  18. Saleh, T.A. Carbon nanotube-incorporated alumina as a support for MoNi catalysts for the efficient hydrodesulfurization of thiophenes. *Chemical Engineering Journal* **2021**, *404*, 126987.
  19. Varakin, A.; Mozhaev, A.; Pimerzin, A.; Nikulshin, P. Comparable investigation of unsupported MoS<sub>2</sub> hydrodesulfurization catalysts prepared by different techniques: Advantages of support leaching method. *Applied Catalysis B: Environmental* **2018**, *238*, 498-508.
  20. Bai, X.; Li, Q.; Shi, L.; Ling, C.; Wang, J. Edge promotion and basal plane activation of MoS<sub>2</sub> catalyst by isolated Co atoms for hydrodesulfurization and hydrodenitrogenation. *Catalysis Today* **2020**, *350*, 56-63.
  21. Puello-Polo, E.; Pájaro, Y.; Márquez, E. Effect of the Gallium and Vanadium on the Dibenzothiophene Hydrodesulfurization and Naphthalene Hydrogenation Activities Using Sulfided NiMo-V<sub>2</sub>O<sub>5</sub>/Al<sub>2</sub>O<sub>3</sub>-Ga<sub>2</sub>O<sub>3</sub>. *Catalysts* **2020**, *10*, 894.
  22. Vázquez-Garrido, I.; López-Benítez, A.; Berhault, G.; Guevara-Lara, A. Effect of support on the acidity of NiMo/Al<sub>2</sub>O<sub>3</sub>-MgO and NiMo/TiO<sub>2</sub>-Al<sub>2</sub>O<sub>3</sub> catalysts and on the resulting competitive hydrodesulfurization/hydrodenitrogenation reactions. *Fuel* **2019**, *236*, 55-64.
  23. Pozos, J.A.T.; Esquivel, G.C.; Arista, I.C.; de los Reyes Heredia, J.A.; Toriello, V.A.S. Co-processing of hydrodeoxygenation and

- hydrodesulfurization of phenol and dibenzothiophene with NiMo/Al<sub>2</sub>O<sub>3</sub>-ZrO<sub>2</sub> and NiMo/TiO<sub>2</sub>-ZrO<sub>2</sub> catalysts. *International Journal of Chemical Reactor Engineering* **2021**.
24. Díaz-García, L.; Santes, V.; Viveros-García, T.; Sánchez-Trujillo, A.; Ramírez-Salgado, J.; Ornelas, C.; Rodríguez-Castellón, E. Electronic binding of sulfur sites into Al<sub>2</sub>O<sub>3</sub>-ZrO<sub>2</sub> supports for NiMoS configuration and their application for hydrodesulfurization. *Catalysis Today* **2017**, *282*, 230-239.
  25. Javadli, R.; de Klerk, A. Desulfurization of heavy oil-oxidative desulfurization (ODS) as potential upgrading pathway for oil sands derived bitumen. *Energy & fuels* **2012**, *26*, 594-602.
  26. Zhang, M.; Liu, J.; Yang, J.; Chen, X.; Wang, M.; Li, H.; Zhu, W.; Li, H. Molybdenum-containing dendritic mesoporous silica spheres for fast oxidative desulfurization in fuel. *Inorganic Chemistry Frontiers* **2019**, *6*, 451-458.
  27. Ismagilov, Z.; Yashnik, S.; Kerzhentsev, M.; Parmon, V.; Bourane, A.; Al-Shahrani, F.; Hajji, A.; Koseoglu, O. Oxidative desulfurization of hydrocarbon fuels. *Catalysis Reviews* **2011**, *53*, 199-255.
  28. Di Furia, F.; Modena, G.; Curci, R.; Bachofer, S.J.; Edwards, J.O.; Pomerantz, M. Evidence concerning peroxovanadate structures in solution and their role in catalytic oxidation process. *Journal of Molecular Catalysis* **1982**, *14*, 219-229.
  29. Campestrini, S.; Conte, V.; Di Furia, F.; Modena, G.; Bortolini, O. Metal catalysis in oxidation by peroxides. 30. Electrophilic oxygen transfer from anionic, coordinatively saturated molybdenum peroxo complexes. *The Journal of Organic Chemistry* **1988**, *53*, 5721-5724.
  30. Chica, A.; Corma, A.; Dómine, M.E. Catalytic oxidative desulfurization (ODS) of diesel fuel on a continuous fixed-bed reactor. *Journal of Catalysis* **2006**, *242*, 299-308.
  31. Etemadi, O.; Yen, T.F. Surface characterization of adsorbents in ultrasound-assisted oxidative desulfurization process of fossil fuels. *Journal of colloid and interface science* **2007**, *313*, 18-25.
  32. Chen, T.-C.; Shen, Y.-H.; Lee, W.-J.; Lin, C.-C.; Wan, M.-W. The study of ultrasound-assisted oxidative desulfurization process applied to the utilization of pyrolysis oil from waste tires. *Journal of Cleaner Production* **2010**, *18*, 1850-1858.

33. Kroon, R. Nanoscience and the Scherrer equation versus the 'Scherrer-Gottingen equation'. *South African Journal of Science* **2013**, *109*, 01-02.
34. Naderi, M. Surface Area: Brunauer–Emmett–Teller (BET). In *Progress in filtration and separation*, Elsevier: 2015; pp. 585-608.
35. Nguyen, C.; Do, D. The Dubinin–Radushkevich equation and the underlying microscopic adsorption description. *Carbon* **2001**, *39*, 1327-1336.
36. Guzmán, J.D.; Betancur, S.; Carrasco-Marín, F.; Franco, C.A.; Nassar, N.N.; Cortés, F.B. Importance of the adsorption method used for obtaining the nanoparticle dosage for asphaltene-related treatments. *Energy & Fuels* **2016**, *30*, 2052-2059.
37. Dong, L.; Miao, G.; Ren, X.; Liao, N.; Anjum, A.W.; Li, Z.; Xiao, J. Desulfurization kinetics and regeneration of silica gel-supported TiO<sub>2</sub> extrudates for reactive adsorptive desulfurization of real diesel. *Industrial & Engineering Chemistry Research* **2020**, *59*, 10130-10141.
38. Levin, D.B.; Chahine, R. Challenges for renewable hydrogen production from biomass. *International Journal of Hydrogen Energy* **2010**, *35*, 4962-4969.
39. Wang, H.; Feng, Y.; Zhang, X.; Lin, W.; Zhao, Y. Study of coal hydrolysis and desulfurization by ReaxFF molecular dynamics simulation. *Fuel* **2015**, *145*, 241-248.
40. Attar, A. Chemistry, thermodynamics and kinetics of reactions of sulphur in coal-gas reactions: A review. *Fuel* **1978**, *57*, 201-212.
41. Post, P.; Wurlitzer, L.; Maus-Friedrichs, W.; Weber, A.P. Characterization and applications of nanoparticles modified in-flight with silica or silica-organic coatings. *Nanomaterials* **2018**, *8*, 530.
42. Mo, L.; Saw, E.-T.; Kathiraser, Y.; Ang, M.L.; Kawi, S. Preparation of highly dispersed Cu/SiO<sub>2</sub> doped with CeO<sub>2</sub> and its application for high temperature water gas shift reaction. *International Journal of Hydrogen Energy* **2018**, *43*, 15891-15897.
43. Urán, L.; Gallego, J.; Bailón-García, E.; Bueno-López, A.; Santamaría, A. Isotopic study of the La<sub>0.7</sub>Ag<sub>0.3</sub>MnO<sub>3</sub> perovskite-catalyzed soot oxidation in presence of NO. *Applied Catalysis A: General* **2020**, *599*, 117611.
44. Waterhouse, G.; Bowmaker, G.; Metson, J. Oxidation of a polycrystalline silver foil by reaction with ozone. *Applied Surface Science* **2001**, *183*, 191-204.
45. Biemann, M.; Schwaller, P.; Ruffieux, P.; Gröning, O.; Schlapbach, L.; Gröning, P. AgO investigated by photoelectron spectroscopy: evidence for mixed valence. *Physical Review B* **2002**, *65*, 235431.



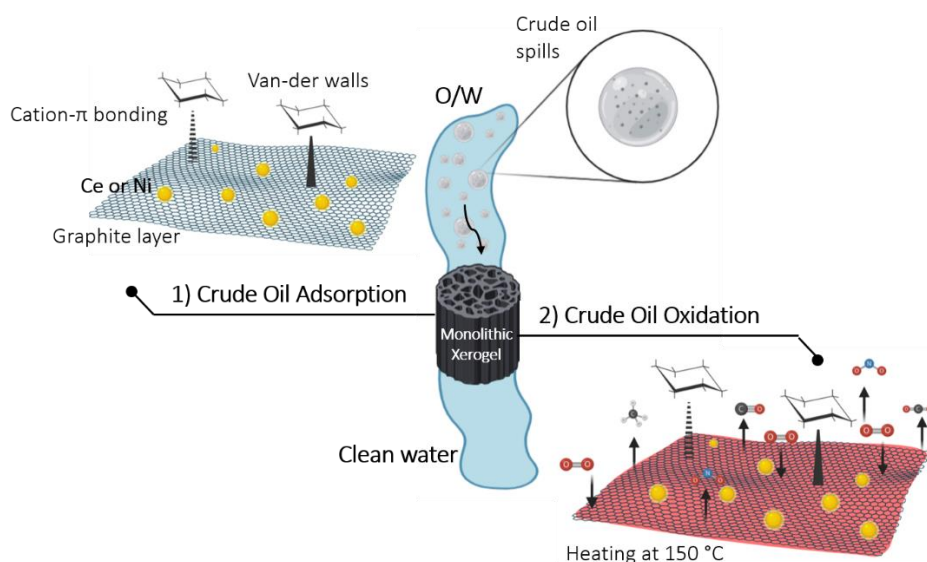
46. López-Ramón, M.V.; Álvarez, M.A.; Moreno-Castilla, C.; Fontecha-Cámara, M.A.; Yebra-Rodríguez, Á.; Bailón-García, E. Effect of calcination temperature of a copper ferrite synthesized by a sol-gel method on its structural characteristics and performance as Fenton catalyst to remove gallic acid from water. *Journal of colloid and interface science* **2018**, *511*, 193-202.
47. Bao, H.; Zhang, W.; Hua, Q.; Jiang, Z.; Yang, J.; Huang, W. Crystal-Plane-Controlled Surface Restructuring and Catalytic Performance of Oxide Nanocrystals. *Angewandte Chemie* **2011**, *123*, 12502-12506.
48. Ferrer, M.M.; Fabris, G.S.; de Faria, B.V.; Martins, J.B.; Moreira, M.L.; Sambrano, J.R. Quantitative evaluation of the surface stability and morphological changes of Cu<sub>2</sub>O particles. *Heliyon* **2019**, *5*, e02500.
49. Sadanandam, G.; Valluri, D.K.; Scurrrell, M.S. Highly stabilized Ag<sub>2</sub>O-loaded nano TiO<sub>2</sub> for hydrogen production from glycerol: water mixtures under solar light irradiation. *International Journal of Hydrogen Energy* **2017**, *42*, 807-820.
50. Ivanova, T.V.; Homola, T.; Bryukvin, A.; Cameron, D.C. Catalytic performance of Ag<sub>2</sub>O and Ag doped CeO<sub>2</sub> prepared by atomic layer deposition for diesel soot oxidation. *Coatings* **2018**, *8*, 237.
51. Yang, S.; Zhou, F.; Liu, Y.; Zhang, L.; Chen, Y.; Wang, H.; Tian, Y.; Zhang, C.; Liu, D. Morphology effect of ceria on the performance of CuO/CeO<sub>2</sub> catalysts for hydrogen production by methanol steam reforming. *Int. J. Hydrogen Energy* **2019**, *44*, 7252.
52. Galtayries, A.; Bonnelle, J.P. XPS and ISS studies on the interaction of H<sub>2</sub>S with polycrystalline Cu, Cu<sub>2</sub>O and CuO surfaces. *Surface and interface analysis* **1995**, *23*, 171-179.
53. Chen, J.; Shen, S.; Guo, P.; Wang, M.; Wu, P.; Wang, X.; Guo, L. In-situ reduction synthesis of nano-sized Cu<sub>2</sub>O particles modifying g-C<sub>3</sub>N<sub>4</sub> for enhanced photocatalytic hydrogen production. *Applied Catalysis B: Environmental* **2014**, *152*, 335-341.
54. Graedel, T.; Franey, J.; Gualtieri, G.; Kammlott, G.; Malm, D. On the mechanism of silver and copper sulfidation by atmospheric H<sub>2</sub>S and OCS. *Corrosion Science* **1985**, *25*, 1163-1180.
55. Gabitto, J.F.; Tsouris, C. Sulfur poisoning of metal membranes for hydrogen separation. *International Review of Chemical Engineering* **2009**, *1*, 394-411.

56. McMahon, M.; Lopez, R.; Meyer, H.; Feldman, L.; Haglund, R. Rapid tarnishing of silver nanoparticles in ambient laboratory air. *Applied Physics B* **2005**, *80*, 915-921.
57. Tian, W.-H.; Sun, L.-B.; Song, X.-L.; Liu, X.-Q.; Yin, Y.; He, G.-S. Adsorptive desulfurization by copper species within confined space. *Langmuir* **2010**, *26*, 17398-17404.



Chapter 19.

# Monolithic Carbon Xerogels-Metal Composites for Crude Oil Removal from Oil in-Saltwater Emulsions and Subsequent Regeneration Through Oxidation Process: Composites Synthesis, Adsorption Studies, and Oil Decomposition Experiments.



Published manuscript in *Microporous and Mesoporous Materials*:

[doi.org/10.1016/j.micromeso.2021.111039](https://doi.org/10.1016/j.micromeso.2021.111039)

Impact factor: 5.455

# **Monolithic Carbon Xerogels-Metal Composites for Crude Oil Removal from Oil in-Saltwater Emulsions and Subsequent Regeneration Through Oxidation Process: Composites Synthesis, Adsorption Studies, and Oil Decomposition Experiments.**

## **Abstract**

This work is focused on the development of monolithic carbon xerogels-metal composites for oil removal through adsorption and regeneration processes from oil-in-saltwater emulsions. In this way, three carbon materials with and without metal content (Ni and/or Ce) were prepared by a sol-gel method, namely XCe (carbon xerogel with 18 wt.% of cerium), XCeNi (carbon xerogel with 18 and 4 wt.% of cerium and nickel, respectively), and X (free metal-carbon xerogel). Crude oil adsorption was tested by batch adsorption experiments, varying different operational conditions, including pH (2, 7, and 11), temperature (25, 35, and 45°C), amount of monolithic composite (0.01, 0.1 and 0.3M) and its nature. Regeneration studies were done through oxidation method using air in a thermogravimetric analyzer under isothermal (150, 200, and 250°C) and non-isothermal conditions (100-600°C). From N<sub>2</sub> adsorption isotherms it was found that all materials presented a type Ib behavior distinctive of microporous materials. Adsorption results show that crude oil removal increased with the increase of metal content in the composite for all experimental setups. Also, crude oil decomposition was successfully assessed, obtaining the main decomposition peak at 150°C during non-isothermal runs. For isothermal experiments, the three monolithic carbon xerogels achieved 100% conversion of the crude oil adsorbed for all temperatures, whereas raw crude oil only decomposed 60%. The catalytic activity of three monolithic carbon xerogels was corroborated with effective activation energy calculations, which was reduced by 24.9, 32.5, and 52.4% from virgin crude oil decomposition to decomposition adsorbed on the samples X, XCe, and XCeNi, respectively.

## 1. Introduction

In the oil and gas industry, water is one of the main by-products, which is generally contaminated with hydrocarbons as oil-in-water (O/W) emulsions [1, 2], which must be removed before disposal or reinjection in compliance with environmental regulations standards (National Association of Corrosion Engineers – NACE) [3, 4]. Nowadays, the oil industry has several technologies for water treatment based on different mechanisms, including flotation [5], coagulation [6], filtration [7], reverse osmosis [8], and adsorption [9]. The latter is the most used mechanism due to its simplicity, effectiveness, and the positive cost-benefit ratio [7]. During these processes, walnut shell granular filter beds are used [10]; however, other systems such as organoclay [11], zeolites [12], resins [13], and nanomaterials [9, 14] have also been studied for their application. However, some materials have brittle mechanical properties and complicated preparation methods [15]. As an alternative, carbon-based materials with superhydrophobic properties have been analyzed in the literature [16]. The low density, high surface area, good chemical, and thermal stability, large pore volume, and environmental friendliness make carbon materials excellent candidates to assist oil removal treatments [16]. A broad range of carbon materials have been studied, including carbon nanotubes [17], graphene foams [18], sponges [19], activated carbon [16], multiwalled nanotubes [20], nanofibers [21], and gels [22, 23], obtaining high efficiencies for oil removal, oil/water separation, and wastewater treatments.

Carbon gels (i.e., aerogels, cryogels, and xerogels) can be produced by the carbonization of organic gels throughout the sol-gel polycondensation method using organic monomers such as resorcinol<sup>®</sup> and formaldehyde (F) [24]. Their porosity and structure can be custom designed at the nanoscale by varying experimental conditions like gelation, curing, drying, the composition of the RF and other reagents mixture, reaction temperature, and carbonization/activation [25-28]. In this order, different morphologies can be obtained, from films to monoliths, and hence, surface area, pore-size distribution, and volume change [24]. The advantage of monolithic carbon xerogels is the possibility of generating high macro- and mesopore volumes, which is essential to ensure an excellent intraparticle diffusion of crude oil into the material [29-31]. Further, they can be synthesized as composites or doped with metal oxides [32]. Despite the porosity

properties of carbon gels being a crucial factor in oil removal, surface, and bulk chemistry also determine adsorption affinity and hence, the success of their application. Moreover, the large surface area and pore size distribution of carbon materials allow materials to decrease the total metal content favoring more significant dispersion of the metal phase throughout the carbon matrix. This implies small metal particle size, higher contact metal-support as well as higher active surface exposed to the contaminant in addition to the cost-effective production [16].

Nevertheless, despite the satisfactory results in the removal step by adsorption, there are still limitations to the regeneration/desorption and ultimate removal of the contaminants from sorbent materials [14]. In this sense, it is worth mentioning that the removal step, as well as the regeneration of the materials step, are crucial. Therefore, looking for cost-effective alternatives to regenerate and reuse the material is imperative.

Some research has evaluated the regeneration of crude oil removal materials for reuse in a new cycle [33, 34]. One of the most featured processes for regenerating the adsorbent/catalyst is the thermal process. The materials are regenerated depending on their catalytic activity to decompose the crude oil adsorbed [14].

Therefore, this work proposes for the first time the development of novel carbon xerogels – metal composites prepared in monolith form using cerium and nickel as promising materials for crude oil adsorption and subsequent oxidation as a final stage for water disposal. Three carbon materials were prepared: Xce (carbon xerogel with 18 wt.% of cerium), XceNi (carbon xerogel with 18 wt.% of cerium, and 4 wt.% of nickel), and X (free metal-carbon xerogel). To the best of our knowledge, monolithic carbon xerogels-metal composites with cerium and nickel have never been used for oil removal from oil-in-saltwater emulsions, and this is the first application of crude oil oxidation as a final treatment stage for the reuse of the materials.

## 2. Experimental

### 2.1. Materials

#### 2.1.1. Monolithic carbon xerogels

Resorcinol (R), formaldehyde (F), and cesium carbonate ( $\text{CsCO}_3$ ) were provided from Sigma-Aldrich (St. Louis, MO, USA) and were used for carbon

xerogels synthesis. Active phases of cerium and nickel were formed using  $\text{Ce}(\text{NO}_3)_3 \cdot 6\text{H}_2\text{O}$  and  $\text{Ni}(\text{C}_2\text{H}_3\text{O}_2)_2 \cdot 4\text{H}_2\text{O}$ , respectively.

The synthesis of the monolithic carbon xerogels was done by sol-gel polymerization of R with F in water (W), following a modification of Pekala's method [27] using  $\text{CsCO}_3$  as polymerization catalyst (C). The molar ratios were  $F/R=2$ ,  $W/R=20$ , and  $R/C=500$ . The mixture was stirred and cast into glass molds to prevent the evaporation of the solvent. The mixture was cured as follows: 24 hours at 20 °C, then 24 h at 50 °C, and ends heating at 80 °C for 120 h. Once obtained the organic gel, monoliths were cut into 5-cm length 2-mm diameter pellets, removed from the glass molds, and immersed into acetone for five days for a solvent exchange, refreshing the acetone daily. Afterward, the organic gel was dried by microwave heating using a Saivod MS-287W microwave oven (Spain), through argon injection for periods of 1 minute at 20 Watts until a constant weight was achieved. Finally, the organic gel was carbonized under pure nitrogen flow at 900 °C with a heating rate of 2 °C  $\text{min}^{-1}$  for a soft removal of the pyrolysis gases and a dwell time of 2 h at the target temperature. The sample obtained was labeled as X.

The monolithic carbon xerogels-metal composites were obtained by following the same procedure with the exception of the precursors mixing step, where the corresponding amount of  $\text{Ce}(\text{NO}_3)_3 \cdot 6\text{H}_2\text{O}$  and  $\text{Ni}(\text{C}_2\text{H}_3\text{O}_2)_2 \cdot 4\text{H}_2\text{O}$  were added into the R/F/W mixture. The amount of the metal precursor, to obtain a Ce and Ni content of 20 and 5 wt.%, respectively, was calculated assuming a mass loss of 50.0% during the carbonization, which was corroborated posteriorly by Inductively Coupled Plasma Mass-Spectrometry (ICP-MS). Monolithic carbon xerogels are designated XCe (carbon xerogel with 18 wt.% of cerium), XCeNi (carbon xerogel with 18 wt.% of cerium and 4 wt.% of nickel). These values are computed theoretically and experimentally.

### 2.1.2. O/W Emulsions

A Colombian light crude oil and a synthetic brine were used for the synthetic oil- in-saltwater emulsion (O/W) formulation. The crude oil has an *API* gravity of 38.2°, a viscosity of 3.48 cP at 25 °C and 10  $\text{s}^{-1}$ , and a content of saturates, aromatics, resins, and asphaltenes (SARA) components of 65.6, 18.4, 15.9, and 0.1 wt.%, respectively. Synthetic brine is representative of the Colombian field where was taken the crude oil, and this was prepared with deionized water and 244.28  $\text{mg L}^{-1}$  of  $\text{BaCl}_2 \cdot 2\text{H}_2\text{O}$ , 147.23  $\text{mg L}^{-1}$   $\text{CaCl}_2 \cdot 2\text{H}_2\text{O}$ , 58.44  $\text{mg L}^{-1}$   $\text{NaCl}$ , 74.56  $\text{mg L}^{-1}$   $\text{KCl}$ , 270.32  $\text{mg L}^{-1}$   $\text{FeCl}_3 \cdot 6\text{H}_2\text{O}$ , 84.07  $\text{mg L}^{-1}$   $\text{NaHCO}_3$ , 203.30  $\text{mg L}^{-1}$   $\text{MgCl}_2 \cdot 6\text{H}_2\text{O}$ , 120.37



mg L<sup>-1</sup> MgSO<sub>4</sub>, and 142.04 mg L<sup>-1</sup> Na<sub>2</sub>SO<sub>4</sub>, all provided by Panreac AppliChem (Barcelona, Spain). The employed brine has a conductivity of 26.15 μS m<sup>-1</sup>, a density of 1.04 mg L<sup>-1</sup>, and a pH of 6.9. O/W emulsions were stabilized using polyethylene sorbitan monooleate “Tween 80” surfactant (Panreac, Barcelona, Spain). HCl (37%, Sigma Aldrich, St. Louis, MO, USA) and NaOH (80%, Sigma Aldrich, St. Louis, MO, USA) were used for pH adjustments.

## 2.2. Methods

### 2.2.1. Textural and chemical characterization

The porous texture was analyzed by N<sub>2</sub> adsorption-desorption and CO<sub>2</sub> adsorption at -196 °C and 0 °C, respectively, using a Micromeritic ASAP2020 instrument (Micromeritics, Norcross, GA, USA). First, samples were outgassed overnight at 110 °C under a high vacuum (10<sup>-6</sup> mbar), and then the gas adsorption isotherms were constructed. To obtain the specific surface area ( $S_{\text{BET}}$ ) through the N<sub>2</sub> adsorption data, the BET equation was used [35]; meanwhile, the micropore volume ( $W_0$ ) and micropore means ( $L_0$ ) were estimated by the Dubinin-Radushkevich (DR) equation [36]. Total pore volume ( $V_{0.95}$ ) is obtained from the N<sub>2</sub> adsorption isotherms at 0.95 relative pressure. Finally, the mesopore volume ( $V_{\text{MESO}}$ ) is calculated using the BJH method. Thermal stability was assessed by heating samples from 50 to 800 °C, using a heating ramp of 10 °C min<sup>-1</sup>, and an air flow of 100 mL min<sup>-1</sup> in a thermogravimetric analyzer Q50 (TA Instruments, Inc., New Castel, DE, USA).

The point of zero charges ( $\text{pH}_{\text{pzc}}$ ) was estimated based on the solid addition method [37], using a Nanoplus-3, Micromeritics (GA, USA). The final amount of cerium and nickel was estimated by Inductively Coupled Plasma Mass Spectrometry (ICP-MS).

The texture and morphology of samples were analyzed by scanning electron microscopy (SEM) and high-resolution transition electron microscopy (HR-TEM) using an FEI microscope model Quanta 400 (SEM) (Eindhoven, The Netherlands) and an FEI Titan G2 microscope (HR-TEM) (Eindhoven, The Netherlands).

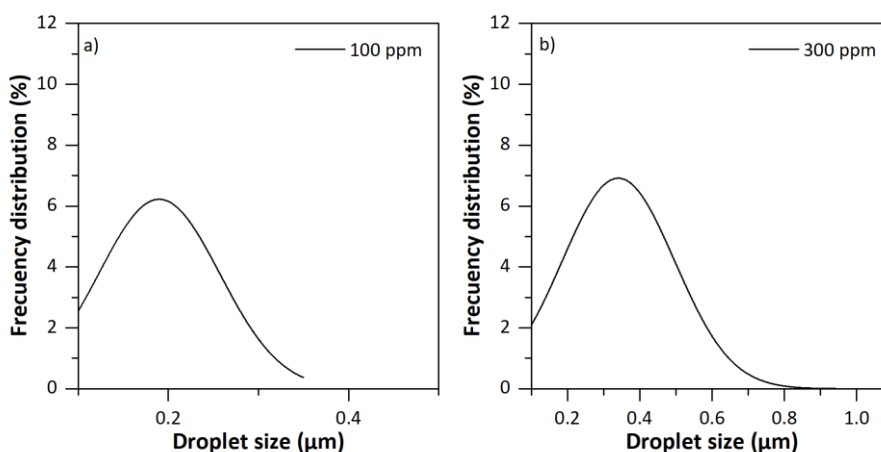
The crystalline phases of the obtained materials were analyzed by X-ray diffraction using a Bruker D8 Venture X-ray diffractometer (BRUKER, Rivas-Vaciamadrid, Spain) with Cu K $\alpha$  radiation. The XRD patterns were recorded in the 2-theta ( $2\theta$ ) range from 6° to 77°. The Debye-Scherrer equation was used for estimating the average crystal size [38].}The surface chemistry was studied by X-ray photoelectron spectroscopy (XPS) by using a Kratos Axis Ultra-DLD

spectrometer (Manchester, UK) equipped with a hemispherical electron analyzer connected to a detector DLD (delay-line detector). Finally, Raman spectra were recorded using a Micro-Raman JASCO NRS-5100 (JASCO, Tokyo, Japan) dispersive spectrophotometer with a 532 nm laser line.

Finally, the samples' wettability was estimated through contact angle measurements in crude oil/monolithic carbon xerogels/air systems using the sessile drop method. For this test, an optical tensiometer (Attention Theta, Biolin Scientific, Finland) was employed. The setup included an automatic pump, a contact angle platform, a light source, and software (Attention Theta, Biolin Scientific, Ver 4.1.0) analyzer. The oil droplets were placed into the monolithic carbon surface using the automatic pump using 0.5  $\mu\text{L}$  of fluid, and the photographs were taken with a high-definition camera.

### 2.2.2. Preparation and characterization of oil-in-saltwater (O/W) emulsions

An oil-in-saltwater stock emulsion containing 5000  $\text{mg L}^{-1}$  of crude oil, 0.5 wt.% of Tween 80 (which is used for stabilizing the emulsion), and brine was prepared by stirring at 10000 rpm for 5 h. The proposed final crude oil concentrations were 100, 300, 500, and 1000  $\text{mg L}^{-1}$ . The emulsion stability was monitored during 120 h by measuring oil drop sizes using a 20 X of magnification in an optical microscope Motic BA310 (Motic, Stockholm, Sweden), following the protocol described by Lopez et al. [39]. The absorbance changes were also measured in a Genesys 10S spectrophotometer (Thermo Scientific, Waltham, USA). Finally, emulsion stability was established based on the emulsion creaming index (*CI*) [40]. According to the analysis of the data, i.e., droplet size distribution (see Figure 1) and the *CI* values ( $>0.99$ ), it is concluded that all emulsions present a high stability degree.



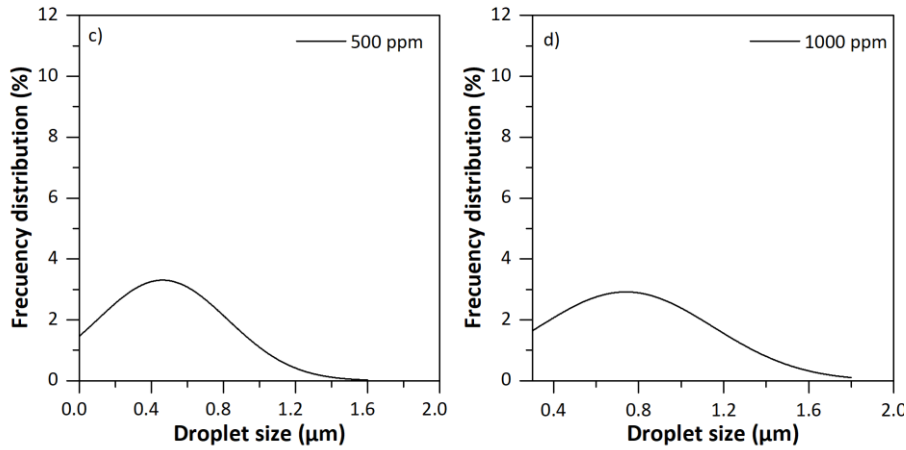


**Figure 1.** Droplet size distribution (DSD) of the obtained O/W emulsions at oil contents of 100, 300, 500, and 1000 mg L<sup>-1</sup>.

### 2.2.3. Batch adsorption experiments

Emulsions containing 100 mg L<sup>-1</sup>, 300 mg L<sup>-1</sup>, 500 mg L<sup>-1</sup>, and 1000 mg L<sup>-1</sup> of crude oil as a dispersed phase were employed for batch adsorption studies. Monolithic carbon xerogels were added into the glass beaker with the O/W emulsions and stirred for 24 h to ensure adsorption equilibrium. Next, each system was centrifuged at 4500 rpm for 45 min. The supernatant was removed, and the precipitate was dried at room temperature. The adsorbed amount of the crude oil ( $N_{ads}$ ) was determined by thermogravimetric analysis in an air atmosphere and using the mass balance described by the Equation (1)

$$N_{ads} = \frac{m_i - m_f}{m_a} \quad (1)$$

where,  $m_i$ ,  $m_f$ , and  $m_a$  are the initial, final and dry mass of the adsorbent. Different variables were analyzed during this test. Initially, different ratios of the solution volume to the dry mass of the xerogels ( $M$ ) were evaluated (0.03, 0.1, and 0.3 g L<sup>-1</sup>) at a fixed temperature of 25 °C and pH of 7.0.  $M$  were selected according to the ratios found in the literature [42, 43]. Then, the effect of temperature was assessed measuring crude oil adsorption at 25, 55, and 75 °C at a fixed  $M$ . Finally, pH was varied fixing the rest of the variables. To understand the adsorption mechanisms and the thermodynamics of the adsorptive phenomenon of crude oil on carbon xerogels, the solid-liquid equilibrium (SLE) and the five parameters models were used, respectively [44]. The SLE model is described by Equations (2)–(4):

$$C = \frac{\psi H}{1 + K\psi} \exp\left(\frac{\psi}{N_m}\right) \quad (2)$$

$$\psi = \frac{-1 + \sqrt{1 + 4K\xi}}{2K} \quad (3)$$

$$\xi = \frac{N_m N}{(N_m - N)}, \quad (4)$$

where  $C$  ( $\text{mg g}^{-1}$ ), represents the crude oil concentration at the equilibrium and  $H$  ( $\text{mg g}^{-1}$ ) is the affinity of the adsorbate for the surface of the solid. A low value implies greater affinity, i.e., greater accessibility (or ease of access) of the crude oil to the active sites.

Likewise,  $K$  ( $\text{g g}^{-1}$ ) refers to the self-association degree of crude oil on the adsorbent's surface,  $N_m$  ( $\text{mg g}^{-1}$ ) is the maximum adsorbed amount and the amount adsorbed is expressed as  $N$  ( $\text{g g}^{-1}$ ). Finally,  $\xi$  is a relation that depends on the maximum adsorption capacity ( $N_m$ ) and amount adsorbed ( $N$ ).

The five parameters model predicts thermodynamic parameters such as  $\Delta G_{ads}^o$ ,  $\Delta S_{ads}^o$ , and  $\Delta H_{ads}^o$ , from SLE fittings.  $H$  and  $K$  are expressed by Equations (5) and (6):

$$H = e^{\left(\frac{H_0 + H_1}{T}\right)} \quad (5)$$

$$K = e^{\left(\frac{K_0 + K_1}{T}\right)}, \quad (6)$$

where  $K_0$  and  $H_0$  are related to the entropy of reaction and  $K_1$  and  $H_1$  are related to the enthalpy. It is possible to find the three thermodynamic parameters through Equations (7)-(9) shown below.

$$\Delta S_{ads}^o = K_0 R \quad (7)$$

$$\Delta H_{ads}^o = K_1 R \quad (8)$$

$$\Delta G_{ads}^o = -RT \ln K \quad (9)$$

Details of each model are shown in the literature [45-48].

#### 2.2.4. Oxidation process experiments

The catalytic power of synthesized monolithic carbon xerogels for decomposing crude oil adsorbed by thermo-oxidation reactions was evaluated in

a thermogravimetric analyzer Q50 (TA Instruments, Inc., New Castel, DE, USA) coupled to a mass spectrometer (Shimadzu MS, Tokyo, Japan). Air flow was fixed at 100 mL min<sup>-1</sup> and mass sample at 10 mg. Adsorbed and free crude oil was subjected to different processes. First, non-isothermal experiments were conducted using a heating ramp of 20 °C min<sup>-1</sup> from to 600 °C to obtain the rate for mass loss of crude oil on xerogel's surface. Then, the samples were heated under isothermal conditions at three different temperatures (180, 200, and 210 °C). Each run was done for a fixed adsorbed amount of crude oil of 0.2 mg m<sup>-2</sup> and repeatability was ensure by performed each test by triplicate, obtaining uncertainties of 0.001 mg and ± 0.01 °C. Gaseous products were analyzed for isothermal runs performed at 200 °C using a linear scan rate of 0.03 m/z between 0 – 200 m/z. The kinetic analysis of crude oil oxidation was made by measuring the effective activation energy  $E_a$  (kJ·mol<sup>-1</sup>) using an isothermal kinetic model [49]. The calculation of the activation energy was carried out with the following model given by the ICTAC Kinetics committee. Equation (10) provides a basis for differential kinetic methods and applies to any temperature [49, 50].

$$\frac{d\alpha}{dt} = K_a \exp\left(-\frac{E_a}{RT}\right) f(\alpha) \quad (10)$$

where the effective activation energy is expressed by  $E_a$  (kJ mol<sup>-1</sup>), while  $\alpha$  is the degree of conversion that depends on the initial mass of the sample, the current mass at time t and, the final mass [51, 52].

Likewise,  $K_a$  (s<sup>-1</sup>) is the pre-exponential factor and  $T$  (K) is reaction temperature. The reaction mechanism is given by  $f(\alpha)$ , and  $d\alpha/dt$  is the reaction rate. With the analysis of isothermal conditions and integration by separation of variables, the integral reaction model given by Equation (11) is obtained:

$$g(\alpha) = K_a e^{\left(\frac{-E_a}{RT}\right)} \quad (11)$$

Taking constant the energy of activation and applying natural logarithm to both sides, Equation (12) is obtained,

$$\ln(t_{a,i}) = \ln\left(\frac{g(\alpha)}{K_a}\right) + \frac{E_a}{RT_i} \quad (12)$$

From the plot of  $\ln(t_{a,i})$  vs.  $1/T_i$ , it is possible to obtain the value of the activation energy from the slope.

### 3. Results and discussion

#### 3.1. Textural and chemical characterization

Table 1 shows the results of the total and surface metal content of materials modified with Ce and Ni through ICP-MS and XPS techniques. As it is observed, the metal percentage has varied compared to the theoretically calculated one (20 wt.% Ce and 5 wt.% Ni). The thermal stability of monolithic carbon xerogels under air injection are presented in Figure 2. The curves show that the materials are thermally stable up to temperatures above 500 °C. The chemistry modification reduces the thermal stability of materials. In particular, the material contains Ce and Ni exhibited lower thermal stability.

**Table 1.** Total and surface metal content estimated by Inductively Coupled Plasma Mass Spectrometry (ICP-MS) and X-ray photoelectron spectroscopy, respectively.

Sample	Metal <sub>ICP-MS</sub> (%)		Metal <sub>xps</sub> (%)	
	Ce	Ni	Ce	Ni
X	-	-	-	-
XCe	18.0	-	4.80	-
XCeNi	18.0	4.0	9.60	0.60

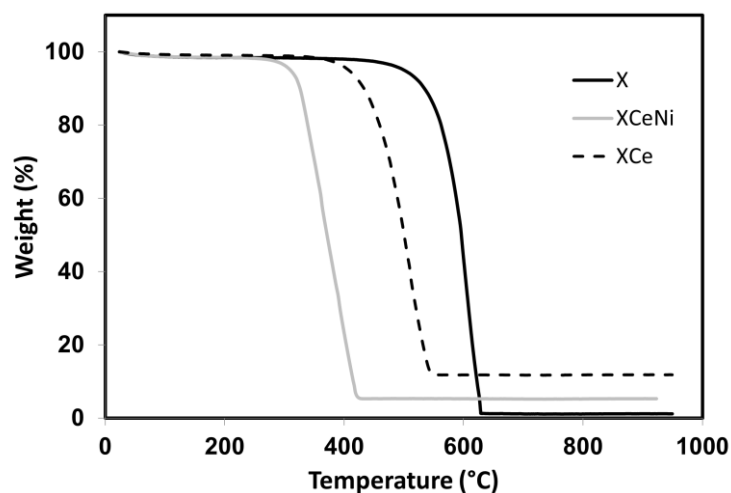


**Figure 2.** Thermogravimetric analysis of monolithic carbon xerogels under air atmosphere.

Figure 3 depicts the N<sub>2</sub> adsorption-desorption isotherms and Table 2 presents the porous characteristics of the materials obtained from the BET and Dubinin-Radushkevich equations. Following the IUPAC classification, it is observed that the materials exhibit a quasi-type I isotherms. This behavior

indicates that materials are mainly composed of microporous. However, the presence of small hysteresis loops suggests the presence of some mesoporosity.

In all cases, the volume of micropore obtained by CO<sub>2</sub> adsorption ( $W_{0CO_2}$ ) is higher than the volume of micropore obtained by nitrogen adsorption ( $W_{0N_2}$ ). This result can be attributed to the presence of constrictions at the entrance of the micropore that prevents the access of nitrogen. However, in CO<sub>2</sub> isotherms the kinetic barrier is overcome since they are carried out at 273 °C (instead of 70 K with N<sub>2</sub>), which allows the gas to enter the narrowest micropores. Likewise, the micropore size obtained by CO<sub>2</sub> is smaller than that obtained by N<sub>2</sub>, supporting the fact that nitrogen encounters a diffusion barrier, and it cannot access the narrower micropores. In addition to microporosity, the slight increase of nitrogen adsorption at higher  $P/P_0$  after the microporous filling (XCe and XCeNi samples) and the presence of hysteresis cycle can verify a certain amount of mesopores.

Compared to the X sample, the presence of Ce produces a certain porous blockage, decreasing the surface area of the material. This result is in agreement with the reported by Orge et al. [81]. However, the presence of cerium modifies the porous network since, once the monolayer ( $P/P_0 = 0.1$ ) is reached, it continues to adsorb nitrogen at high relative pressures. In addition, in this case, there is an H2-type hysteresis cycle that is associated with the blocking of pores or the presence of bottleneck type pores where desorption occurs by cavitation. The cavitation is related with the spontaneous nucleation of a bubble in the pore causes the emptying of the pore inner while the neck of the pore remains filled.

Ni catalyzes the gelation of the organic xerogel where mesopores are generated, and, during the carbonization process. Likewise, the presence of Ni in the materials favors the elimination of a greater number of functional groups causing a considerable increase in the microporosity. In this way, the presence of nickel increases both the micro and the mesoporosity and therefore the BET area 20%. With regards to the mesoporous type, the XCeNi material and the reference carbon shown an H4-type hysteresis cycle characteristic of opened mesoporosity. The results obtained are like the reported by in literature for xerogels with metal phases [81, 82].

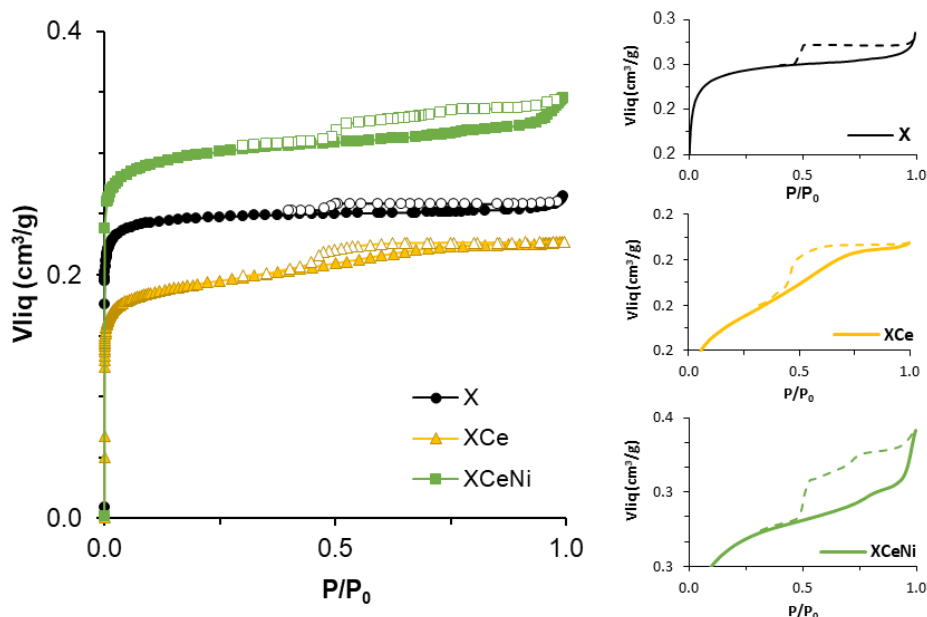


**Figure 3.** N<sub>2</sub> adsorption-desorption isotherms (a). Detail of the hysteresis cycle (b) for monolithic carbon xerogels-metal composites.

**Table 2.** Estimated porous textural characteristics of the carbon-metal composites obtained from N<sub>2</sub> adsorption-desorption and CO<sub>2</sub> adsorption.

Sample	S <sub>BET</sub> m <sup>2</sup> g <sup>-1</sup>	W <sub>0</sub> (N <sub>2</sub> ) cm <sup>3</sup> g <sup>-1</sup>	W <sub>0</sub> (CO <sub>2</sub> ) cm <sup>3</sup> g <sup>-1</sup>	L <sub>0</sub> (N <sub>2</sub> ) nm	L <sub>0</sub> (CO <sub>2</sub> ) nm	V <sub>0.95</sub> cm <sup>3</sup> g <sup>-1</sup>	V <sub>meso</sub> (BJH) cm <sup>3</sup> g <sup>-1</sup>	pH <sub>pzc</sub>
X	628	0.25	0.29	0.92	0.60	0.26	0.014	8.3
XCe	475	0.18	0.24	0.97	0.65	0.23	0.042	4.2
XCeNi	742	0.29	0.31	0.72	0.58	0.32	0.054	3.8

The pH values at which the total charge on the surface of the adsorbents is neutral (pH<sub>pzc</sub>) were obtained. Sample X presents a basic pH<sub>pzc</sub> of 8.3, whereas samples XCe and XCeNi show an acidic character with pH<sub>pzc</sub> equal to 3.8 and 4.2, respectively. Because of carbonization eliminates oxide groups [22], pure carbon structures results from this process, and therefore, high pH<sub>pzc</sub> are obtained. When the xerogel contains Ce and Ni, pH<sub>pzc</sub> decreases due to the formation of oxygen-based functional groups on bulk and surface structure, providing negative charges.

Figure 4 shows the SEM images of the monolithic carbon xerogels. Based on the reported in the literature, carbon xerogels are synthesized from interconnected primary particles where the microporosity is located inside these primary particles, while the mesopores are developed from the interparticle voids [83]. The images clearly show the typical morphology of R-F xerogels, like a carbon network formed by nearly spherical particles with different degrees of fusion [30, 84, 85]. However, significant differences are observed for each sample,



especially thus relating to the macroporosity. For X sample, a well-developed macroporous structure and nanometric particles interconnected with a homogeneous particle size around 80-90 nm are observed. XCeNi, shows similar characteristics to the X sample, whereas XCe changes completely its microstructure. Specifically, cerium has catalyzed the gelification process in the XCeN material promoting “holes” with a micrometric diameter as shown in Figure 5. This observation could be attributed to the faster time of gelling in XCe that avoids forming the structure of semi-fused spheres. By contrast, XCeNi materials form such structure. The textural properties have also been affected leading to materials with a more opened porosity, especially in the case of XCeNi which presents the highest level of mesoporosity concerning the total surface area.

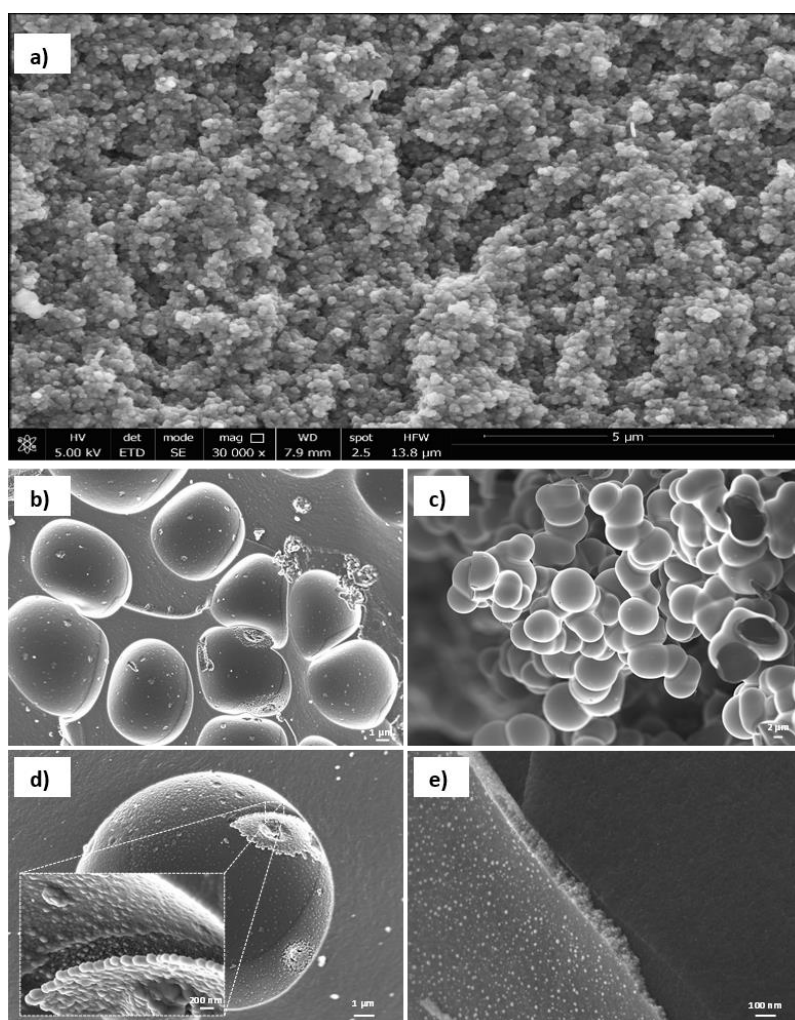


**Figure 4.** Scanning electron microscopy images of X (a), XCe (b, d) and XCeNi (c,e).

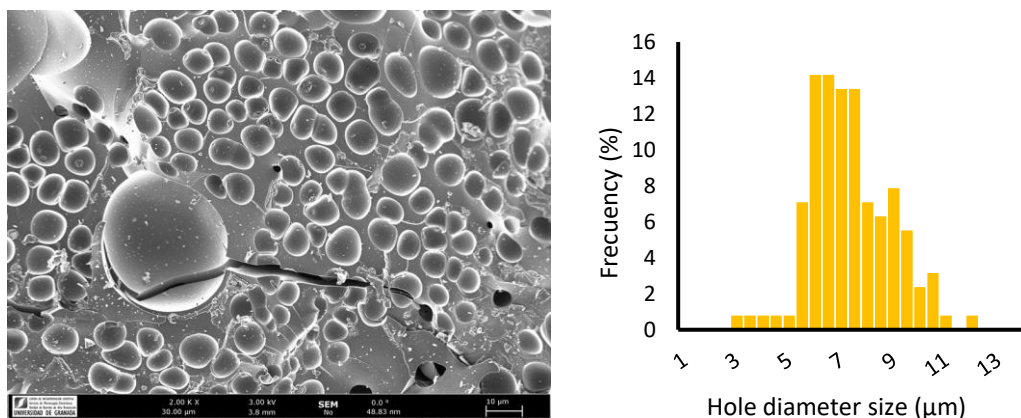
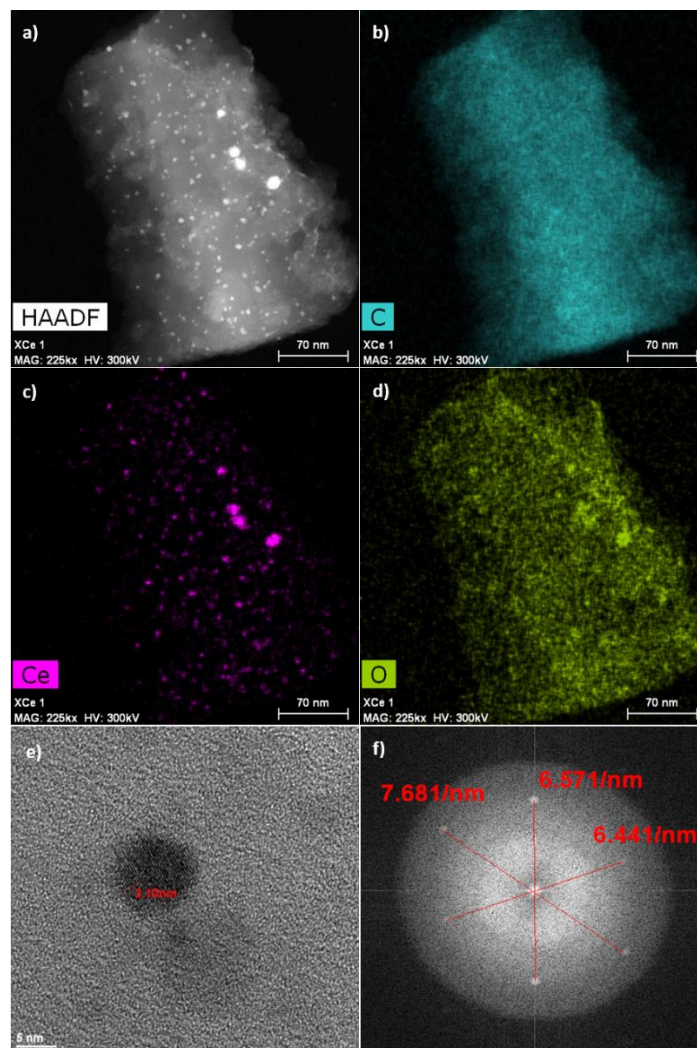


**Figure 5.** SEM picture of XCe with the *hole* size distribution.

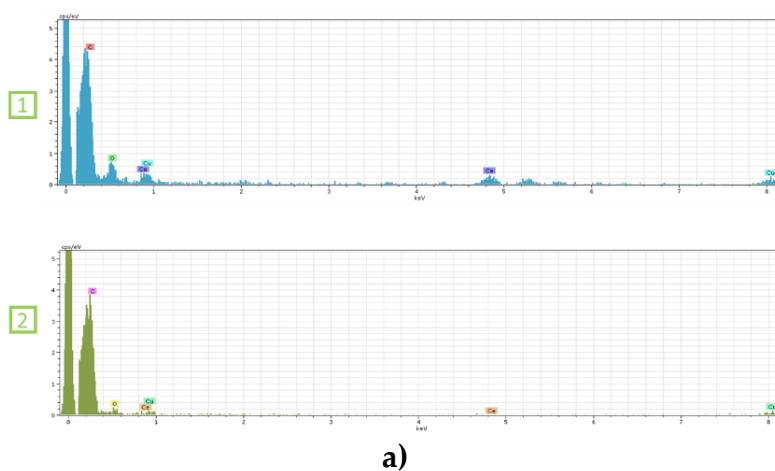
The results of the structural characterization for the materials containing nickel and cerium show that both phases are located mainly embedded within the carbon matrix, as confirmed by XPS and ICP results (Table 1). It is well known that XPS technic analyzes the surface of the material. Thus, the lower metal<sub>xps</sub> content concerning the ICP-MS data demonstrates that the metal phase is located within the matrix. This observation is also supported by TEM images (Figures 6-9), where highly dispersed metal nanoparticles are appreciated. Furthermore, the small size of these particles facilitates their location inner the micro-mesopores, and XPS is blind at this depth. As it was mentioned, it is noted a homogeneous distribution of both elements throughout the carbon matrix.

Figures 6 and 8 show the elements mapping analysis and the distribution of each element present in the XCe and XCeNi samples, respectively. It can be noted the presence of oxygen in the metal particles, denoting the presence of the metal oxide. This behavior is more noticeable in the bigger particles. The biggest particles are located mainly on the surface, suggesting its potentially oxidizable.

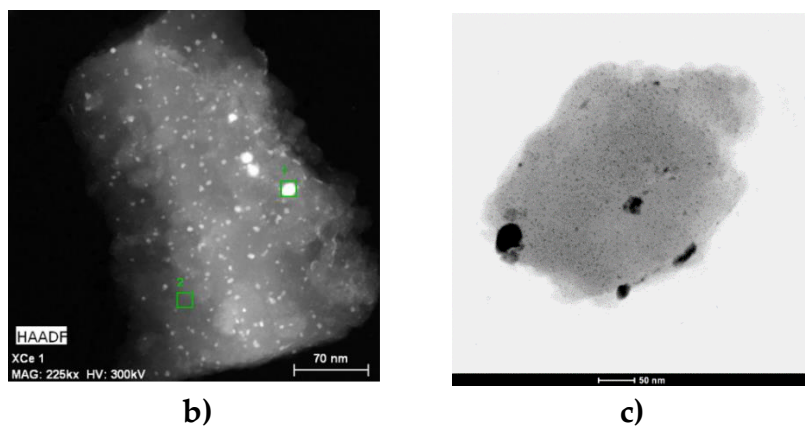
Figure 10 shows the particle size distribution of particles of CE and Ni in XCe and XCeNi materials. The size of ceria particles in XCe and XCeNi ranges from 1-20 nm and 1-50 nm, respectively. However, the particle size de ceria in XCeNi is lower than that for XCe. From the HR-TEM picture and FFT analysis (Figure 6e and 6f) can be observed the multiple d-spacing that corresponds to the different crystal planes. Specifically, Figure 6e shows a cerium-based nanoparticle with interplanar spacing equal to 0.310 nm, which corresponds to 111 planes. FFT analysis show d-spacing values of 0.260, 0.304, and 0.310 corresponded to 002, 110, and 111 planes, respectively.



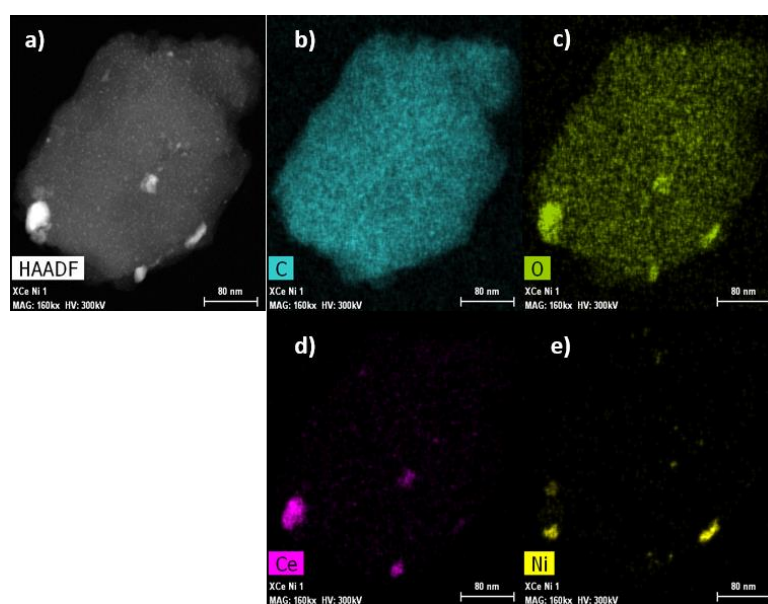
**Figure 6.** Transmission electron microscopy images. a) STEM- HAADF image; b), c) and d) TEM mapping; e) CeO<sub>2</sub> particle HRTEM image; f) FFT analysis of XCe.



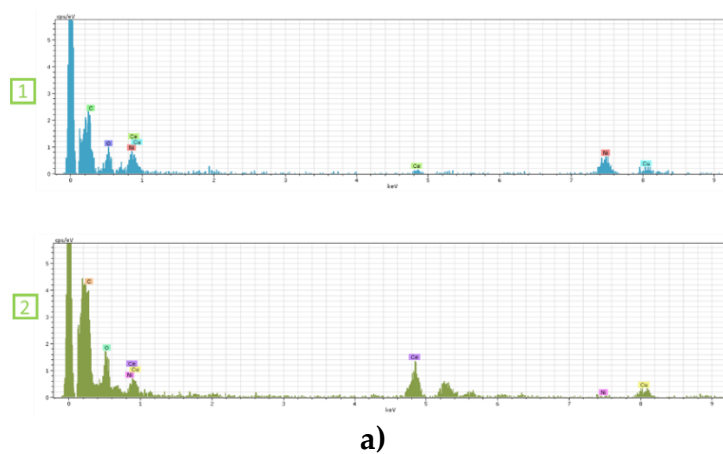
**a)**



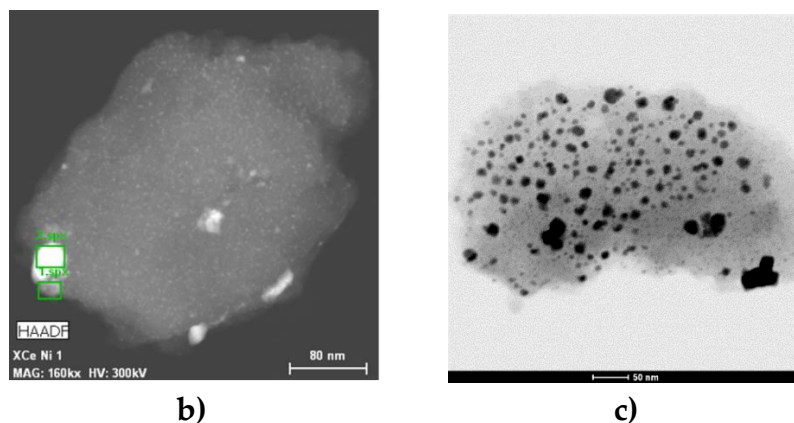
**Figure 7.** Transmission electron microscopy images. a) HAADF-STEM image; b) EDX and c) TEM of XCe sample.



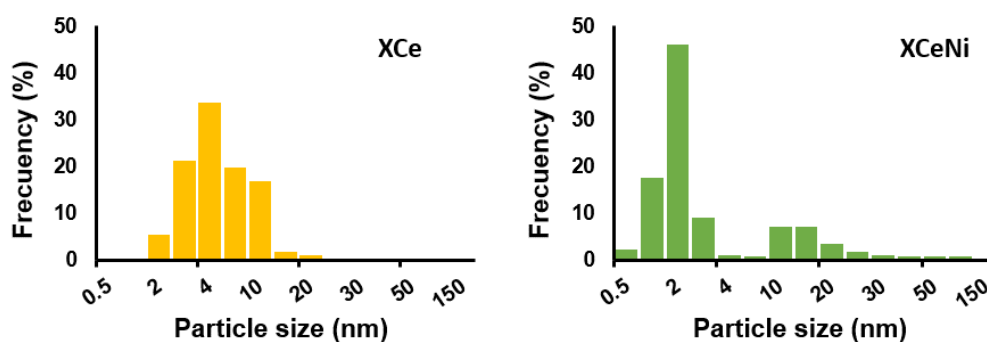
**Figure 8.** Transmission electron microscopy images. a) HAADF-STEM image; b), c), d) and e) TEM mapping for XCeNi sample.



**a)**



**Figure 9.** Transmission electron microscopy images. a) HAADF-STEM image; b) EDX and c) TEM of XCeNi sample.



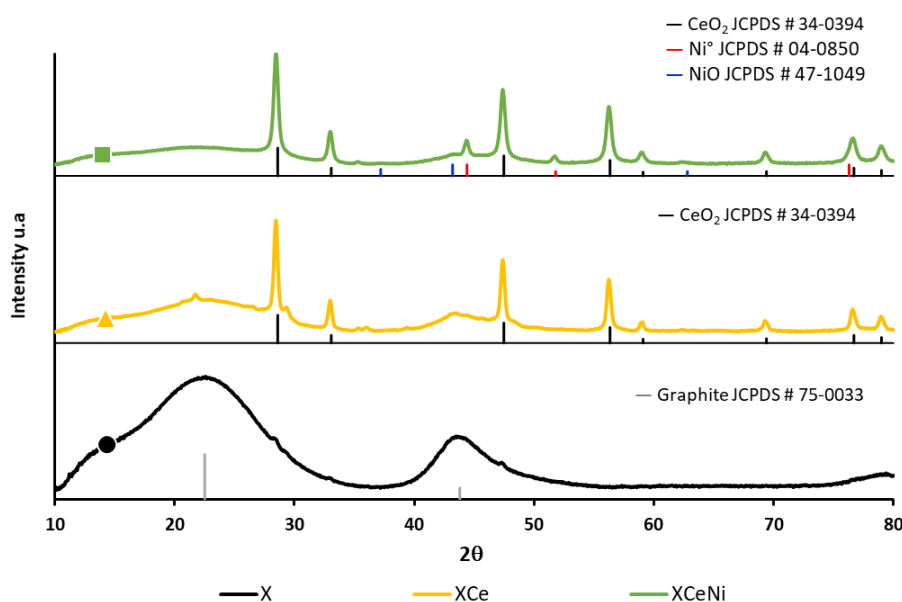
**Figure 10.** CeO<sub>2</sub> particle size distribution obtained from TEM analysis of XCe and XCeNi samples.

Figure 11 presents the XRD patterns for the synthesized monolithic carbon xerogels (X, XCe, and XCeNi). All materials exhibit two broad diffraction peaks around  $2\theta = 26^\circ$  (110) and  $44^\circ$  (220) with different intensities. Both peaks are related to the graphite structure in monolithic carbon xerogels [82]. Likewise, several strong peaks were observed at different  $2\theta$ , which correspond to the metallic and lanthanide phases in the XCe and XCeNi materials [86, 87].

The broad diffraction peaks regarding the presence of CeO<sub>2</sub> phases were found very narrow and confirmed by the JCPDS-34-0394 card. For XCe and XCeNi were found eight characteristic peaks corresponded to CeO<sub>2</sub> at  $2\theta = 28.46, 33.02, 47.38, 56.26, 58.98, 69.24, 76.52, \text{ and } 78.96^\circ$ , associated to the (111), (200), (220), (311), (222), (400), (331), and (420) lattice planes, respectively [86]. The diffraction peaks could be assigned to cubic fluorite CeO<sub>2</sub> [88]. These results corroborate the FFT analysis presented in Figure 6. Furthermore, three peaks at  $2\theta = 44.3^\circ$  (111),  $51.7^\circ$  (200), and  $76.2^\circ$  (220) are due to the face-centered cubic



(fcc) of metallic nickel ( $\text{Ni}^0$ ) [89]. On the other hand, the intensity and sharpness of the peaks confirm the well crystalline nature of monolithic xerogels. Also, three small humps were observed at  $2\theta = 37, 43,$  and  $62^\circ$  corresponding to (111), (200), and (220) crystal planes in the bulk  $\text{NiO}$ , respectively. The peaks detected are in concordance with the standards data (JCPDS 04-0850 and 47-1049) [87]. The XCeNi XRD pattern shows that there is no displacement in the peaks, indicating that there is no Ni doping on the ceria. However, the intensity of the peaks increases revealing a slight expansion of the cell because of the carbon. These results suggest that no Ni/Ce alloys were formed in the XCeNi.



**Figure 11.** XRD patterns of the catalysts and the corresponding JCPDS cards assignment.

Table 3 shows the average crystal size of the graphitic (Lc) and metal phases of the materials. Graphitic crystal size decreases in the order  $X > \text{XCe} > \text{XCeNi}$ . Meanwhile,  $\text{CeO}_2$  crystal size exhibits the same behavior ( $\text{XCe} > \text{XCeNi}$ ). The reduction in the size of the ceria crystal could be related to the formation of a solid solution between lanthanides and transition metal oxides, where  $\text{Ni}^{2+}$  ions with a small ionic ratio can occupy the position of the largest  $\text{Ce}^{4+}$  (ionic radius =  $0.97 \text{ \AA}$ ) [87]. On the other hand, metallic nickel shows an average crystal size of 12.62 nm.

**Table 3.** Average crystal size of the graphitic and metal phases.

Sample	$D_{XRD}$ (nm)			
	Lc	CeO <sub>2</sub>	Ni	NiO
X	0.71	-	-	-
XCe	0.67	19.06	-	-
XCeNi	0.54	16.73	12.62	nd

XPS was further performed to determine the surface composition and oxidation states of carbon and metal phases. Table 4 and Figures 12-14 present the results obtained from the spectra deconvolution for all samples.

**Table 4.** Configuration and atomic content obtained from the deconvolution of the XP Spectra of synthesized monolithic carbon xerogels.

Sample	C <sub>1s</sub>	Assignment	FWHM	%Peak	O <sub>1s</sub>	Assignment	%Peak	%O	O <sub>ads</sub> /O <sub>latt</sub>	
X	284.5	C=C	0.86	48	532.4	O=C	49	4.7		
	285.4	C-C		30	533.8	O-C	51			
	286.6	C-O		11						
	287.5	C=O		3						
	289.2	COO-		6						
	290.5	$\pi$ - $\pi^*$		2						
XCe	284.6	C=C	1.10	71	529.9	O <sub>latt</sub>	9	6.9	1.35	
	285.5	C-C		13	531.4	O <sub>ads</sub>	13			
	286.5	C-O		7	532.4	O=C	41			
	287.7	C=O		3	533.8	O-C	37			
	289.3	COO-		4						
	291.0	$\pi$ - $\pi^*$		2						
XCeNi	284.6	C=C	1.03	69	529.7	O <sub>latt</sub>	44	3.5	0.33	
	285.6	C-C		13	530.7	O <sub>ads</sub>	14			
	286.5	C-O		8	531.8	O=C	25			
	287.6	C=O		3	533.1	O-C	17			
	289.3	COO-		4						
	291.0	$\pi$ - $\pi^*$		3						
Sample	Ce <sub>3d</sub>	Assignment	%Peak	%Ce	Ce <sup>3+</sup>	Ce <sup>4+</sup>	Ni <sub>2p</sub>	Assignment	%Peak	%Ni
XCe	881.5	Ce <sup>3+</sup> <sub>5/2</sub>	6.6	4.8	36.7	63.3				
	882.9	Ce <sup>4+</sup> <sub>5/2</sub>	10.2							
	885.2	Ce <sup>3+</sup> <sub>5/2</sub>	16.5							
	889.4	Ce <sup>4+</sup> <sub>5/2</sub>	13.2							
	898.8	Ce <sup>4+</sup> <sub>5/2</sub>	12.4							
	899.1	Ce <sup>3+</sup> <sub>3/2</sub>	4.1							
	901.3	Ce <sup>4+</sup> <sub>3/2</sub>	8.4							
	903.7	Ce <sup>3+</sup> <sub>3/2</sub>	9.5							
	907.8	Ce <sup>4+</sup> <sub>3/2</sub>	8.1							
	917.2	Ce <sup>4+</sup> <sub>3/2</sub>	11.0							
XCeNi	881.8	Ce <sup>3+</sup> <sub>5/2</sub>	6.0				854.1	Ni <sup>0</sup> <sub>3/2</sub>	34	0.6
	882.6	Ce <sup>4+</sup> <sub>5/2</sub>	10.0				855.7	Ni <sup>2+</sup> <sub>3/2</sub>	39	
	885.5	Ce <sup>3+</sup> <sub>5/2</sub>	14.0				857.5	sat	18	
	889.9	Ce <sup>4+</sup> <sub>5/2</sub>	15.0				861.1	sat	65	
	898.4	Ce <sup>4+</sup> <sub>5/2</sub>	14.0				871.4	Ni <sup>0</sup> <sub>1/2</sub>	12	
	899.7	Ce <sup>3+</sup> <sub>3/2</sub>	5.0				873.0	Ni <sup>2+</sup> <sub>1/2</sub>	15	
	901.2	Ce <sup>4+</sup> <sub>3/2</sub>	6.0				875.5	sat	5	
	903.5	Ce <sup>3+</sup> <sub>3/2</sub>	10.0							
	907.4	Ce <sup>4+</sup> <sub>3/2</sub>	10.0							
	917.1	Ce <sup>4+</sup> <sub>3/2</sub>	11.0							

All materials exhibit six peaks after deconvolution of XPS patterns for C<sub>1s</sub> region, including C=C bonds, whose contribution was predominant (peak at 284.6 ± 0.1 eV), C-C non-functional structures (285.5 ± 0.1 eV), C-O from carbon as phenols, ethers, and alcohols (286.5 ± 0.1 eV), C=O due to carbon in the form of carbonyl quinone (287.6 ± 0.2 eV), COO<sup>-</sup> (289.3 ± 0.1 eV) and π-π\* transition interbond peak (290.5 ± 0.5 eV) [90]. The lower functional groups contribution was associated with carbonyl, carboxyl, and plasmon peak for all xerogels. Based on the results of Table 4, cerium and nickel impregnation has a significant effect on carbon chemistry, as C=C increases around 50% from X to XCe and XCeNi.

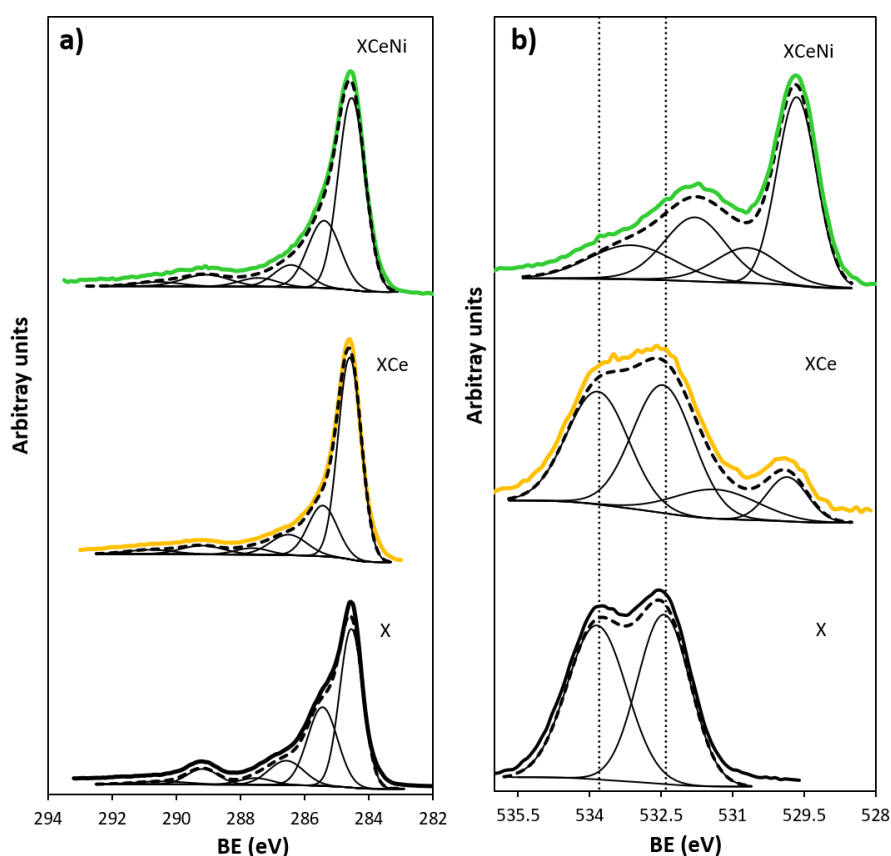
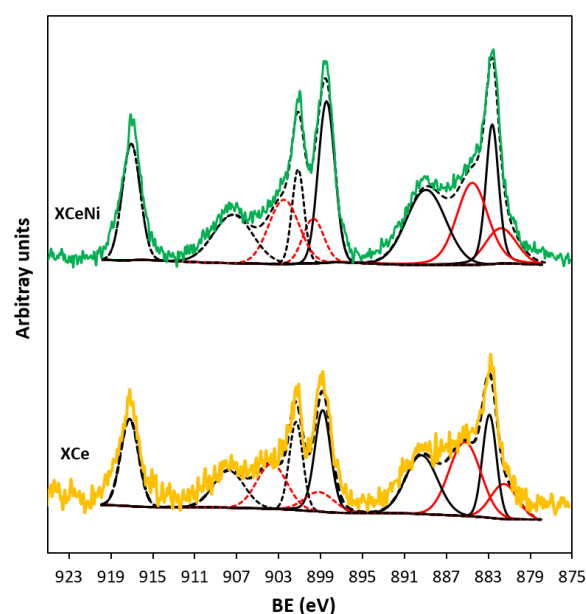


**Figure 12.** High-resolution spectra of XPS analysis of monolithic carbon xerogels for a) C<sub>1s</sub> and b) O<sub>1s</sub>.

Figure 12b and Table are summarized the information associated with the high-resolution spectra of the O<sub>1s</sub>, and their deconvolution. The X sample was deconvoluted as follows: (i) O=C, coming presumably from carbonyl oxygen in lactones, esters, or anhydrides (532.5 ± 0.2 eV), and (ii) O-C from esters and/or anhydrides groups (533.5 ± 0.4 eV) [90]. The samples XCe and XCeNi exhibited the same contributions for the X material. However, these materials shows two additional peaks related to lattice oxygen (O<sub>latt</sub>) and ascribed to the surface O



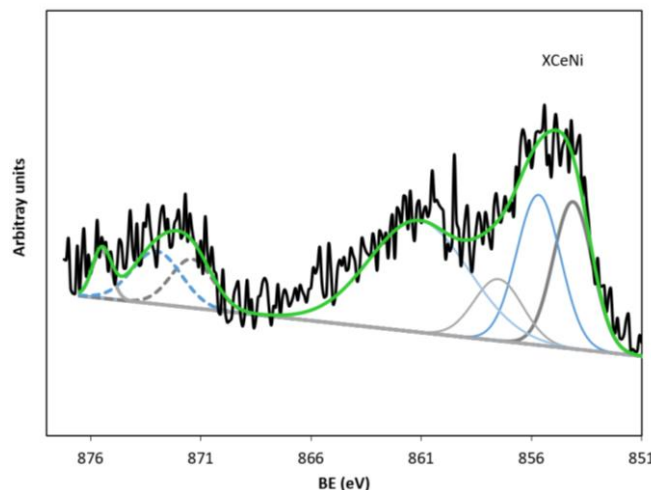
( $O_{\text{ads}}$ , e.g.,  $O^-$ ,  $O_2^{2-}$ ,  $O_2^-$ ) at  $529.8 \pm 0.1$  eV and  $531.0 \pm 0.4$  eV, respectively [91]. Due to  $O_{\text{ads}}$  are usually found as oxygen vacancies, the high content of  $O_{\text{ads}}$  suggests a large amount of oxygen vacancies [92, 93].  $O_{\text{ads}}/O_{\text{latt}}$  ratios of the monolithic xerogels are summarized in Table 4. The trends obtained for  $O_{\text{ads}}$  and  $O_{\text{ads}}/O_{\text{latt}}$  ratios was opposite, where XCeNi has a greater content than  $O_{\text{ads}}$  and a lower  $O_{\text{ads}}/O_{\text{latt}}$  ratio. This property is important due to the surface oxygen content plays an important role in the catalytic activity for  $\text{CeO}_2$ -based materials. Figure 13 presents the high-resolution spectra of cerium 3d for XCe and XCeNi. Dotted lines correspond to the  $3d_{3/2}$  region while the solid ones represent the  $3d_{5/2}$  region. As it is shown, ten peaks are necessary for deconvoluting the  $\text{Ce}_{3d}$  region.  $\text{Ce}^{4+}$  ions were calculated trough the peaks at  $882.7 \pm 0.2$  eV,  $889.7 \pm 0.3$  eV,  $898.6 \pm 0.2$  eV,  $901.3 \pm 0.1$  eV,  $907.6 \pm 0.2$  eV, and  $917.26 \pm 0.2$  eV, whereas the peaks at  $881.6 \pm 0.2$  eV,  $884.9 \pm 0.4$  eV,  $899.4 \pm 0.3$  eV, and  $903.0 \pm 0.3$  eV were assigned to  $\text{Ce}^{3+}$  [36, 91]. The atomic concentration of  $\text{Ce}^{3+}$  was higher for XCe (36.7%) than XCeNi (34.6%). This behavior is related to the surface reducibility in absence of Ni. In both systems,  $\text{Ce}^{4+}$  were predominant on xerogel's surfaces, because electrons in  $\text{Ce}^{3+}$  are easily transferred to oxygen or other elements



**Figure 13.** High-resolution spectra of XPS analysis of monolithic carbon xerogels for  $\text{Ce}_{3d}$ .

Figure 14 presents the high-resolution spectra for nickel. The  $\text{Ni}_{2p_{1/2}}$  spectral region shows the main bands at 854.1 and 871.4 eV corresponding to metallic Ni and  $\text{Ni}^{2+}$  species, respectively.  $\text{Ni}_{2p_{3/2}}$  presents the binding energies at 855.7 and

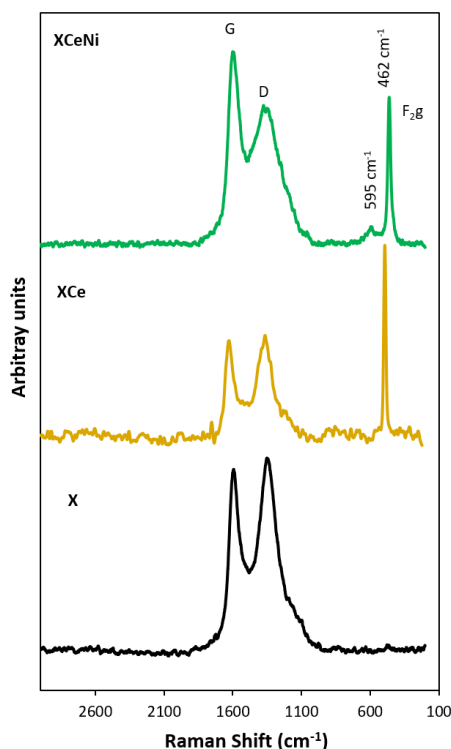
873.0 eV of the Ni<sup>0</sup> and Ni<sup>2+</sup> species in the materials structure [37, 92]. Ni<sup>2+</sup> also can be found in contact with cerium (NiO-Ce) according to the BE at 855.7 eV [92]. Satellite structures are identified at 857.5, 861.1, and 875.5 eV, corresponding to the Ni in the form of oxide and hydroperoxide phases.



**Figure 14.** High-resolution spectra of XPS analysis of monolithic carbon xerogels for Ni<sub>2p</sub>.

The Raman spectra for X, XCe, and XCeNi samples are shown in Figure 15. Graphitization degree can be evaluated considering the wavenumber, width of the G peak, and the D/G peak intensity ratio [30]. Taking into account the intensity of D peak at 1350 cm<sup>-1</sup> and G peak at 1590 cm<sup>-1</sup> the quantitative index  $I_D/I_G$  is determined [30]. The X sample presents an  $I_D/I_G$  of 1.05, whereas XCe and XCeNi exhibit lower values (1.02 and 0.91, respectively). It was also observed that the smallest ratio of the  $I_D/I_G$  intensities indicating that the nickel catalyzes the graphitization of carbon. This observation is in independence of the graphitized carbon.

XCe and XCeNi spectra show the main F<sub>2g</sub> peak at 462 cm<sup>-1</sup> assigned to the symmetric stretching of the Ce-O bonds [95]. The signal at 595 cm<sup>-1</sup> appears in both materials and it is more noticeable in the XCeNi sample. The D1 peak can be assigned to Frenkel-type defects, generated by the displacement of an oxygen atom to an interstitial position [93]. These vacancies are formed in greater proportion in the sample with Ni, due to the Ni has increased the degree of graphitization and the carbon is more reduced. The result are in concordance with O<sub>adds</sub> content obtained by XPS.



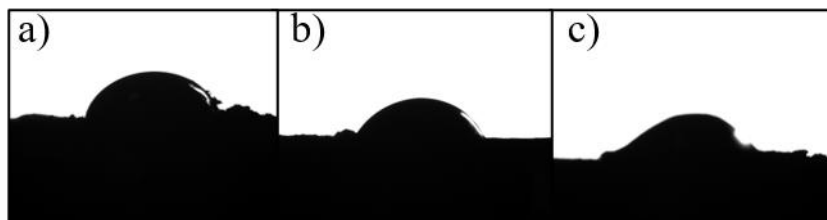
**Figure 15.** Raman spectra of monolithic carbon xerogels.

Figure 16 presents the photomicrographs of crude oil contact angles on monolithic carbon xerogels. It is observed that the crude oil contact angles with X, XCe and XCeNi are 60.9, 46.8, and 27.3°, respectively, suggesting that the materials are oil wet. On the other hand, the non-polar component of surface energy was determined as a function of the crude oil's surface tension at 25 °C (29.6 mN m<sup>-1</sup>) and the crude oil contact angle for the synthesized materials. Based on the results obtained from oil contact angle and Young's equation [96], the solid surface non-polar energy was calculated as follows:

$$\sigma_{solid}^{np} = \sigma_{crude-oil} \left( \frac{1 - \cos(\theta_{crude-oil})}{2} \right)^2 \quad (13)$$

The results showed that the non-polar component of surface energy is 16.4, 20.9, and 26.4 mN m<sup>-1</sup>, for X, XCe and XCeNi, respectively. These results indicate that the systems are highly oleophilic and that the oil selectivity improves in the order X > XCe > XCeNi. which agrees with the results obtained in the adsorption stage. Compared to the X sample, the presence of Ce<sup>3+</sup> and Ni<sup>2+</sup> species in XCe and XCeNi, reduces the oil contact angle. This observation could be attributed to the higher content of active sites exposed on their surface for interacting with

crude oil molecules. This result is in agreement with the reported by Galeano et al. [96], who demonstrate that higher surface energy led to a reduction in lipophilicity of the system associated with the increment of attraction forces between the solid and the oil-based fluid.



**Figure 16.** Contact angle photographs in crude oil/ monolithic carbon xerogels/air systems for (a) X, (b) XCe, and (c) XCeNi.

### 3.2. Crude oil removal based on adsorption process.

#### 3.2.1. Effect of treatment

First, batch adsorption experiments were used to assess each monolithic carbon xerogel's capacity to remove crude oil from oil-in-saltwater emulsions while controlling the temperature, pH, and M ratio. Adsorption isotherms for X, XCe, and XCeNi samples at 25 °C, pH = 7, and M = 0.1 are shown in Figure 17 along with the fitting of the SLE model. Taking into account the International Union of Pure and Applied Chemistry's (IUPAC) definition of isotherms [96], the obtained isotherms behave like type Ib, which agrees with the reported in the literature [76, 97-101]. All samples exhibit good results when compared to other synthesized materials. Adsorption capacity increased in the order  $X < XCe < XCeNi$  [4, 11, 102]. Asphaltenes, the most polar and metal-containing crude oil fractions, as well as various paraffin, aromatic, and saturates fractions, have all been found to be easily removed using carbon-based materials [102, 103]. Additionally, the xerogels' non-polar nature produces hydrophobic attraction toward aromatic hydrocarbons [24]. The three xerogels have high levels of doubly bonded carbon (C=C) atoms, which are typical of graphite carbon layers (X = 48%, XCe = 71.0%, and XCeNi = 69%). This characteristic establishes London dispersion forces with crude oil matrix's polycyclic aromatic hydrocarbons (PAH) [81]. The adsorption activity of the materials is further increased by the addition of metal to the xerogel matrix. A greater heterogeneous selectivity for the functional groups presents in the aliphatic and aromatic structures of the crude oil is provided by the different active sites present in XCe and XCeNi. According to reports,  $Ce^{3+}$  ions are crucial in the adsorption of hydrocarbons

because they serve as significant active sites for the anchoring of asphaltene and resins as well as the activation of C-C and C-H bonds [80].

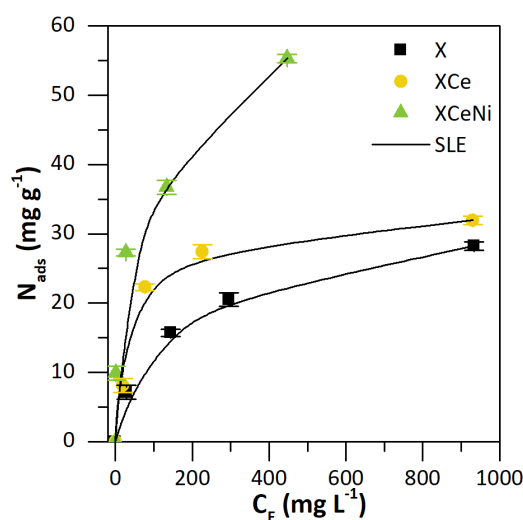


**Figure 17.** Adsorption isotherms of crude oil on monolithic carbon xerogels-metal composites with Ce and Ni. Temperature = 25 °C, pH = 7.0, and  $M = 0.1$ . Adsorption isotherms were constructed for crude oil initial concentrations between 100 mg·L<sup>-1</sup> and 1000 mg·L<sup>-1</sup> in oil-in-saltwater emulsions.

Additionally, the SLE model's fitting parameters serve to validate the adsorption results. Table 5 provides a summary of the results. It was discovered that crude oil had a higher affinity for XCeNi, increasing  $H$  in the following trend XCeNi < XCe < X. The transition element oxides (NiO) were discovered to have the ability to interact with carbonaceous molecules and activate various chemical bonds in a previous study [80]. Ceria addition has the potential to enhance this activity. Additionally,  $K$  parameter exhibits a similar pattern of behavior, demonstrating the capacity of XCe and XCeNi samples to lower the degree of self-association of crude oil compounds on their surfaces. The maximum adsorption capacity ( $N_{ads}$ ), which rises in the order X < XCe < XCeNi, supports the experimental findings.

**Table 5.** Estimated values of the SLE model parameters for the adsorption isotherms of crude oil on X, XCe, and XCeNi at different temperatures, pH, and  $M$  ratios.

Material	Temperature (°C)	$M$	pH	$H \pm 0.02$ (mg g <sup>-1</sup> ) × 10 <sup>-2</sup>	$K \pm 0.08$ (g g <sup>-1</sup> ) × 10 <sup>-1</sup>	$N_m \pm 0.01$ (g g <sup>-1</sup> )	RSM (%)
X	25	0.10	2	7.9	0.04	0.03	0.02
		0.10	7	4.68	0.03	0.04	0.01
		0.10	11	5.7	0.02	0.06	0.01
		0.03	7	3.63	0.2	0.05	0.04
		0.30	7	6.7	0.2	0.03	0.01
	35	0.10	7	5.65	0.2	0.04	0.04
	45	0.10	7	7.39	0.22	0.03	0.02
XCe	25	0.10	2	1.86	0.04	0.07	0.03
		0.10	7	0.52	0.02	0.05	0.01
		0.10	11	0.1	0.01	0.07	0.02
		0.03	7	1.59	0.04	0.08	0.01
		0.30	7	2.74	0.04	0.04	0.02
	35	0.10	7	1.66	0.04	0.06	0.01
	45	0.10	7	1.07	0.04	0.05	0.01
XCeNi	25	0.10	2	1.72	0.02	0.09	0.04
		0.10	7	0.2	0.02	0.08	0.02
		0.10	11	0.02	0.01	0.10	0.03
		0.03	7	1.23	0.03	0.14	0.01
		0.30	7	2.31	0.02	0.04	0.03
	35	0.10	7	1.39	0.02	0.09	0.01
	45	0.10	7	1.04	0.03	0.08	0.01

### 3.2.2. Effect of solution volume xerogel mass ratio

When designing adsorbents to remove crude oil from O/W emulsions, the ratio of the solution volume (mL) to the dry mass (mg) of the xerogels ( $M$ ) is crucial [104]. The outcomes for the monolithic carbon xerogels-metal composites (XCeNi, XCe, and X) for  $M$  values of 0.03, 0.1, and 0.3 are shown in Figure 18. The xerogel mass was fixed, and different volumes of O/W emulsion were added to create these experimental conditions. Results indicate that as  $M$  decreases, crude oil uptake increases. Since it appears that none of the three systems have completely saturated the monolith, adsorption is controlled by the amount of crude oil in the emulsion, which is largely the cause of this behavior in the system of  $M = 0.03$  compared to the others. Additionally, the macro- and mesoporous qualities of these materials enable effective crude oil diffusion within the xerogel channels. Additionally, this behavior is permitted by its high surface areas and surface chemistry, which is consistent with other research [105]. According to Guzman et al. [105], an increase in adsorbent promotes adsorbate-adsorbate

interaction, which reduces the surface area of contact between the two and lowers the system's adsorptive capacity. This decrease could also be explained by a reduction in the amount of mesoporous spaces available for emulsion diffusion through the material.

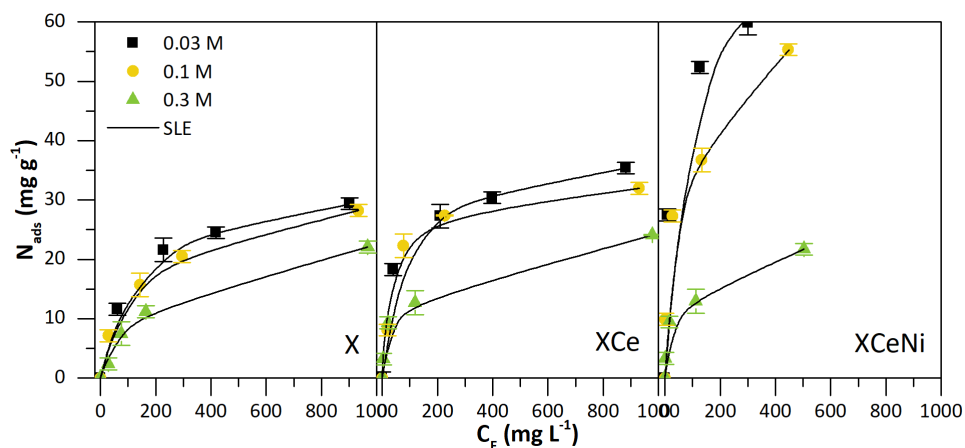


**Figure 18.** Adsorption isotherms of crude oil on monolithic carbon xerogel-metal composites with Ce and Ni at different solution volume/xerogel mass ratios of 0.03, 0.1, and 0.3. Temperature = 25 °C and pH = 7.0. Adsorption isotherms were constructed for crude oil initial concentrations between 100 mg L<sup>-1</sup> and 1000 mg L<sup>-1</sup> in oil-in-saltwater emulsions.

### 3.2.3. Effect of temperature

To comprehend the thermodynamic insights about the adsorptive phenomenon, the impact of temperature on crude oil adsorption onto monolithic carbon xerogels was evaluated. Batch tests were conducted at 25, 35, and 45 °C with a fixed pH of 7 and  $M$  of 0.1. Figure 19 displays the outcomes, and Table 5 lists the SLE model's fitting parameters ( $H$ ,  $K$ , and  $N_{ads}$ ). First, all temperatures considered yielded type Ib isotherms, which are indicative of porous materials with a strong affinity for the adsorptive couple [106]. For all samples, the adsorbed amount decreases with rising temperature at a fixed crude oil equilibrium concentration. For instance, at a  $C_e$  of 300 mg L<sup>-1</sup>, the amount of X that is adsorbed drops from 21.1 mg g<sup>-1</sup> at 25 °C to 18.3 mg g<sup>-1</sup> and 16.7 mg g<sup>-1</sup>, respectively, at 35 °C and 45 °C. At the same temperatures, XCe decreases from 28.8 mg g<sup>-1</sup> at 25 °C to 25.9 mg g<sup>-1</sup> at 45 °C, and XCeNi decreases from 45.6 mg g<sup>-1</sup> to 39.2 mg g<sup>-1</sup>. These findings demonstrate that the temperature affects the interaction forces between adsorbate and adsorbent [107]. This behavior agrees with reported in previous works [36, 108]. Additionally, SLE fitting results that showed a decrease in Henry's law constant, an increase in self-association degree,

and a decrease in maximum adsorption amount with temperature increase support the experimental findings. These findings led to the estimation of the thermodynamics parameters for crude oil adsorption over X, XCe, and XCeNi, which are listed in Table 6.

**Table 6.** Thermodynamic parameters change in entropy ( $\Delta S_{ads}^{\circ}$ ), change in enthalpy ( $\Delta H_{ads}^{\circ}$ ), and change in Gibbs free energy ( $\Delta G_{ads}^{\circ}$ ) for crude oil adsorption on monolithic carbon xerogels-metal composites, from O/W emulsions at pH of 7 and  $M$  of 0.1.

Material	Temperature (°C)	$\Delta S_{ads}^{\circ} \pm 0.02$ [J (mol K) <sup>-1</sup> ]	$-\Delta H_{ads}^{\circ} \pm 0.01$ [kJ mol <sup>-1</sup> ]	$-\Delta G_{ads}^{\circ} \pm 0.01$ [J mol <sup>-1</sup> ]
X	25	0.22	74.81	8.69
	35			4.12
	45			4.26
XCe	25	0.06	27.33	9.70
	35			8.25
	45			8.51
XCeNi	25	0.02	15.98	9.69
	35			10.02
	45			9.28

The positive values of entropy for all systems confirm the randomness and molecular disorder on monolithic carbon surface, where crude oil adsorption takes place. This variable increases in the order  $X < XCe < XCeNi$ , indicating that crude oil molecules are more prone to remain in solid phase of XCeNi instead of the liquid one (emulsion). Adsorption affinity was also corroborated by  $-\Delta H_{ads}^{\circ}$  and  $-\Delta G_{ads}^{\circ}$  parameters.  $\Delta H_{ads}^{\circ} < 0$  was evidenced for all samples, indicating the exothermic nature of the crude oil-xerogel interactions, whereas  $\Delta G_{ads}^{\circ}$  was positive. In addition, increasing the temperature from 25 °C to 45 °C, reduced  $-\Delta G_{ads}^{\circ}$  values in 14.96% and 4.35% for XCe and XCeNi, respectively. All these facts suggest the exothermic and spontaneous nature of adsorption phenomenon.

Considering all the results, crude oil adsorption on XCeNi is thermodynamically more favorable (highest value of  $-\Delta G_{ads}^{\circ}$  and lowest value of  $-\Delta H_{ads}^{\circ}$ ) than in XCe and X. The values and trends of the thermodynamic properties agree with reported by Medina et al. [45], Nassar et al. [48], and Franco et al. [71] for adsorption of hydrocarbons on solid surfaces.



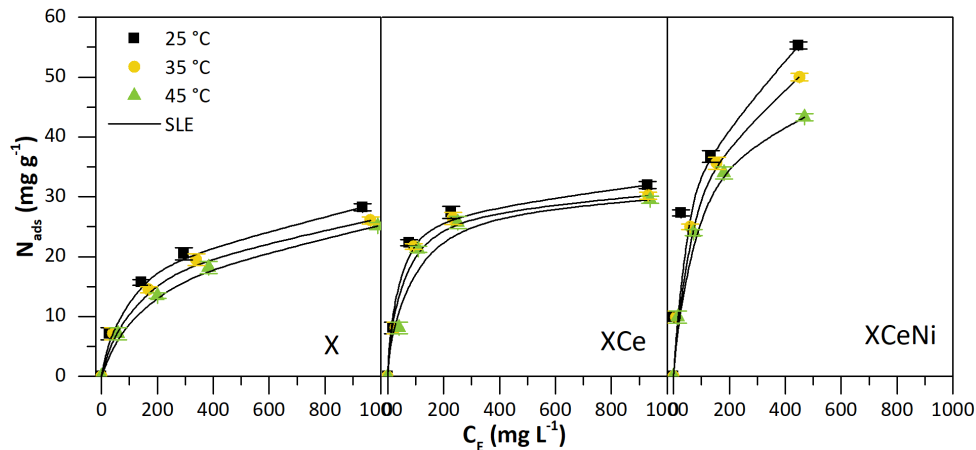


**Figure 19.** Adsorption isotherms of crude oil on monolithic carbon xerogels-metal composites with Ce and Ni at different temperatures of 25 °C, 35 °C, and 45 °C. pH = 7.0 and  $M = 0.1$ . Adsorption isotherms were constructed for crude oil initial concentrations between 100 mg L<sup>-1</sup> and 1000 mg L<sup>-1</sup> in oil-in-saltwater emulsions.

### 3.2.4. Effect of pH

The physico-chemical characteristics of the adsorbent and adsorbate can be altered by a pH change, which may result in a decrease or increase in the system's adsorptive capacity. At 25 °C, the impact of pH on basic (pH = 11.0), neutral (pH = 7.0), and acidic (pH = 2.0) O/W emulsions was examined. The obtained adsorption isotherms are shown in Figure 20. First, it is noted that the presence of more acidic functional groups on the standard crude oil sample as a result of the solution's pH change favors the crude oil adsorption in all samples for the acidic emulsión [1, 22]. This results from the various functional groups found in crude oils, including nitrogen-based functional groups, carboxyls, benzothiophenes, and ketones, among others, which can go through structural changes during the pH modification and, as a result, modify their interactions with carbon xerogels [109-111].

Further, based on the previously reported point of zero charge (pHpzc) values ( $X = 8.3$ ,  $XCe = 4.2$ , and  $XCeNi = 3.8$ ), all the materials would have a predominately positive surface charge for a pH of 2. Materials XCe and XCeNi have a negative charge for the pH of 7, whereas material X has a positive charge. Finally, all samples have a negative surface charge at a pH of 11. It explains why crude oil adsorption significantly decreases as pH rises. Electrostatic forces between the electrons in the aromatic ring and the surface cations can stabilize aromatic hydrocarbons when positive charges predominate on carbon xerogels.

Additionally, some researchers explained this behavior as being caused by an increase in dispersion forces at pH values lower than  $pH_{pzc}$  and a decrease in repulsive forces at pH values higher than  $pH_{pzc}$  [1]. The affinity for crude oil could therefore rise for a pH of 2, where all materials have a preferably positive surface charge, as a result of the presence of more pyrrolic ( $pK_a(16) > pH$ ) and pyridine ( $pK_a(5.2) > pH$ ) protonated compounds [112]. Pyrrole and pyridine lose their aromaticity when they are protonated, transforming into decile bases that can interact with the acidic surfaces of materials. For all systems examined, the pyrrolic protonated groups remain present. Protonated pyridine components, on the other hand, are only present at  $pH = 2$ . As a result, the adsorption of crude oil will be greater for the surface (XCeNi) with the highest concentration of negative charges and will decrease as the solution's pH rises [1, 113]. The modification of the materials'  $pH_{pzc}$  due to the functionalization effect influenced crude oil adsorption positively. As a result of the more cationic behavior of the materials in a system with pH greater than  $pH_{pzc}$ , the affinity and adsorbed quantity decreased. The presence of ions (saltwater) facilitated the interaction by lowering the attractive electrostatic forces between the crude oil and the material [102]. These findings show that the synthesized monolithic carbon xerogels can be used to remove crude oil from a variety of produced waters

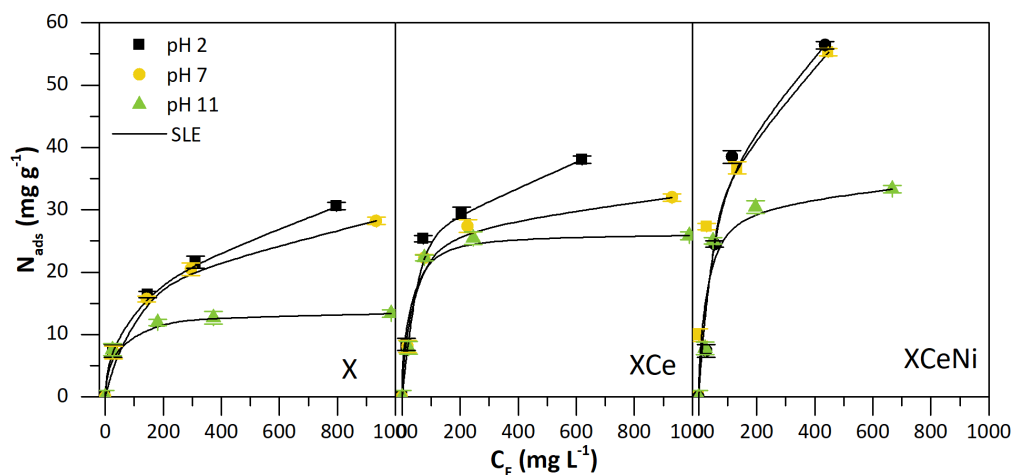


**Figure 20.** Adsorption isotherms of crude oil on monolithic carbon xerogels-metal composites with Ce and Ni at different pH of 2, 7, and 11. Temperature = 25 °C and  $M = 0.1$ . Adsorption isotherms were constructed for crude oil initial concentrations between 100 mg L<sup>-1</sup> and 1000 mg L<sup>-1</sup> in oil-in-saltwater emulsions.

The efficiency of the crude oil adsorption process was determined using the initial crude oil concentrations tested, which were 100, 300, 500, and 1000 mg L<sup>-1</sup>. The final concentration was determined by using the equilibrium concentration

obtained after the adsorption process in each of the systems. The efficiency values obtained show that the efficiencies were greater than 33.3% at 1000 mg L<sup>-1</sup> for the system with the highest adsorption capacity (XCeNi). The efficiency was greater than 98.0, 90.0, and 80.0% for crude oil initial concentrations of 100, 300, and 500 mg L<sup>-1</sup>, respectively. This result suggests that the process is more efficient when the initial concentration is lower, i.e., when there is a preliminary removal process due to the free surface adsorbing the adsorbate molecules before performing the removal with the synthesized xerogels.

Evaluating the different scenarios, the results demonstrates that the effect chemical nature of the treatment is better in the following order  $X < XCe < XCeNi$  for a pH of 7 and 0.1  $M$ . The lower values of  $M$ , improves the adsorption phenomenon obtaining the highest efficiencies at 0.03  $M$ . Concerning temperature, an increase in this parameter disadvantages the adsorption of crude oil due to that the process is exothermic and spontaneous. Therefore, the efficiency behaves in the direction  $25 > 30 > 45^{\circ}C$ . Finally, for an acid pH (pH = 2), the system is much more efficient in all the cases evaluated.

### 3.3. Crude oil oxidation

#### 3.3.1. Rate for mass loss analysis

The monolithic carbon xerogels were tested in an air atmosphere for crude oil oxidation removal from O/W emulsions at various pH levels. Figure 21 shows the mass loss rate of crude oil with and without X, XCe, and XCeNi. For crude oil, mass loss began at the start of heating and the main decomposition peak was observed at 250 °C. The crude oil sample exhibits a mass loss peak due to vaporization during this first interval, which is attributed to the high content of saturates [110]. At higher temperatures, between 400 and 500 °C, there is a distinct low mass loss peak. Many studies have found that asphaltenes and resins decompose during the time when deposited solid fuel is cracked [37, 114-116]. Thermal cracking and oxidation/combustion reactions in an air atmosphere are the primary reaction pathways for the heaviest fractions in this region; thus, evaporation is ignored [114, 116].

The lack of a strong peak at higher temperatures indicates that not enough fuel was deposited, and crude oil reacted almost completely at the first temperature intervals [117]. The results are consistent with the standard sample's low content of both fractions.

The mass loss profile rate of crude oil oxidation in the presence of monolithic carbon xerogels was shifted to lower temperatures when compared

to virgin crude oil. For three materials, the main temperature peak was observed at similar temperatures. As the temperature rises, distinct differences emerge, with the XCeNi sample exhibiting the highest catalytic activity and the X sample exhibiting the lowest yield. This can be seen in the fact that sample X continues to exhibit strong decomposition intensities up to temperatures of about 300 °C, whereas XCeNi and XCe completely decompose the adsorbed sample before 250 °C. The two monolithic carbon xerogels-metal composites differ in that the decomposition of the XCeNi sample is more intense at low temperatures while that of the XCe sample continues at higher temperatures. This finding suggests that the heaviest fractions were more thoroughly converted by the XCeNi sample into lower molecular weight hydrocarbons during oxidation, which encouraged the breaking of weaker bonds like the C-S, C-N, and C-O and stronger bonds like the C-C and C-H bonds. The differences between each system are associated with their different chemical composition [40, 118, 119]. As a first instance, carbon presents an elevated content of active sites, constituted by graphitic hexagonal crystallites with defects and unsaturated valences at the edges [81]. As the metal particle size decreases and the porosity and surface area rise, the number of these active sites also rises. The catalytic activity then increases in composites containing Ce [81]. This supports the additive ceria's positive effects. High metal dispersions, small crystal and particle sizes, heterogeneous selectivity, and increased oxygen mobility on the sample surface are just a few benefits of the XCe system. Due to the well-developed porosity and surface area of xerogels, as seen in STEM-HAADF images, XCe has a significant metal dispersion. In addition to increasing catalytic activity, CeO<sub>2</sub> also plays important roles in enhancing the reusability of the sample, due to its regeneration capacity produced by a redox cycle (Ce<sup>4+</sup>/Ce<sup>3+</sup>) [120]. It is an oxidation-reduction reaction in which the O<sup>2-</sup> ion is oxidized to molecular oxygen, yielding electrons, which are captured by the Ce<sup>4+</sup> cation and then reduced to Ce<sup>3+</sup>. CeO<sub>2-x</sub> maintains the fluorite structure but with oxygen vacancies [121]. When an O<sub>2</sub> molecule is released, two Ce<sup>3+</sup> cations appear on the material's surface for every oxygen vacancy that is created. While Ce<sup>3+</sup> prefers to live in low-coordinated positions on surfaces, partially oxidized Ce<sup>4+</sup> tends to occupy highly coordinated surface positions. Therefore, the ratio of Ce<sup>4+</sup>/Ce<sup>3+</sup> affects the material's surface reactivity.

According to reports, ceria-based materials demonstrated excellent decomposition abilities for crude oil fractions in a variety of atmospheres [36, 79, 80]. In earlier research, we show that airflow-driven ceria catalysts can break down hydrocarbons at temperatures lower than 250 °C [116]. The best outcomes

were produced by catalysts with a higher  $\text{Ce}^{3+}$  content. This work follows the same trend ( $\text{XCe} < \text{XCeNi}$ ) when looking at the relative content of  $\text{Ce}^{3+}$  in comparison to the total superficial Ce in monolithic carbon xerogels.

This process is influenced by various factors. The XCeNi sample therefore displayed better yields. The energy needed to reduce  $\text{CeO}_2$  generally decreased as particle size decreased, and as HR-TEM demonstrated, XCeNi has smaller ceria particles. Since there are a lot of active sites, surface area also encourages better catalytic yields. Oxygen vacancies are also a crucial component in this process [120].  $\text{O}_{\text{adds}}$  and Frenkel-type defects are present in high concentrations in XCeNi and XCe, as reported by XPS and Raman analysis. Both variables show an increase in oxygen mobility and a decrease in cerium. The incorporation of  $\text{O}_2$  into the lattice oxygen is made possible by the gas-phase  $\text{O}_2$  dissociation, which is facilitated by oxygen vacancies [91]. In addition to the fact that, according to XRD results, Ni metal does not physically block the ceria active sites, the presence of nickel may lower the temperature of  $\text{O}_2^-$  formation and thereby the generation of oxygen vacancies. Additionally, XCeNi offers a significant contribution linked to active Ni sites and the synergistic effect of  $\text{CeO}_2$ -NiO. Several researchers have reported that both materials together generate greater catalytic activity to intermediate oxidation reactions [91, 122]. This finding shows that surface chemistry, crystal size and dispersion, and surface area of monolithic carbon xerogels all play significant roles in the oxidation and decomposition of crude oil [41, 123].

Finally, it was discovered that pH has no effect on the catalytic performance of carbon xerogels. The findings are in line with those of Villegas et al. [11], who discovered that crude oil extracted from various O/W emulsions at various pH levels decomposes at the same temperatures for various catalysts.

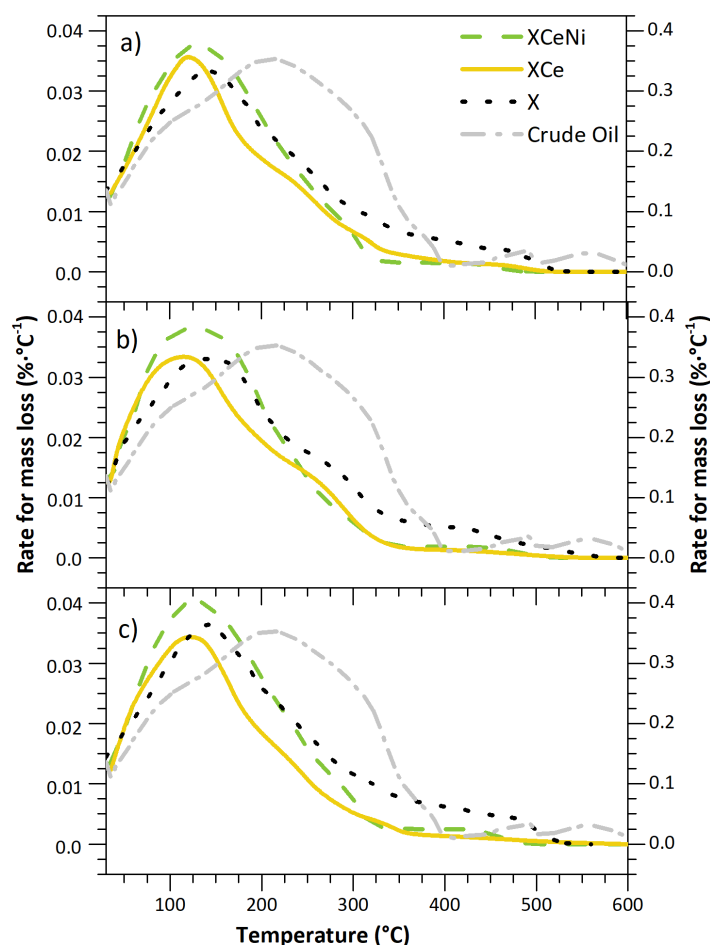


**Figure 21.** Rate for mass loss of crude oil in the presence and absence of monolithic carbon xerogels- metal composites with nickel and cerium oxides. Crude oil was adsorbed from O/W emulsions at pH of a) 2, b) 7, and c) 11. Airflow rate = 100 mL min<sup>-1</sup>, heating rate = 20 °C min<sup>-1</sup>, and crude oil load of 0.2 mg m<sup>-2</sup>.

### 3.3.2. Isothermal oxidation

Isothermal tests were performed at 150, 200, and 250 °C for samples with oil adsorbed from O/W emulsions at pH 7.0, according to the rate for mass loss analysis. Panels a-d in Figure 22 show the fraction of conversion ( $\alpha$ ) as a function of time for crude oil oxidation with and without monolithic carbon xerogels at three temperatures. As an example, the degree of reaction ( $\alpha$ ) of virgin crude oil changes with temperature, and the same behavior is observed when carbon xerogels are added. As the heating temperature rises, the reaction rate increases, resulting in faster crude oil conversion into lighter hydrocarbons and gas generation. This agrees with the results reported by several authors [77, 80]. Panel d shows that at 250 °C, crude oil has a conversion degree of up to 0.8%. However, in the oil and gas industry, surface facilities are extremely limited, and such high temperatures are rarely achieved. Furthermore, the remaining 20% is associated

with the heaviest fractions of crude oil, therefore, the management and control of which in water treatment equipment necessitates significant economic investments. Because X, XCe, and XCeNi can decompose 100% of the crude oil adsorbed, the catalytic effect of the synthesized material is visible at all temperatures. Significant differences were discovered in each material. For all temperatures and times, the conversion degree increases in the order  $X < XCe < XCeNi$ , indicating the composites' high potential for crude oil decomposition. Furthermore, the time required to achieve 100% conversion is less than 70 minutes, 80 minutes, and 100 minutes for XCeNi, XCe, and X at 150 °C, indicating that effective crude oil decomposition can be achieved using carbon xerogels at low temperatures. The interactions between crude oil and treatments are associated with the complete decomposition of hydrocarbons at lower times. The X sample performs well in this first experiment because, as revealed by XPS, it is composed of graphitic hexagonal crystallites with a high proportion of defects and unsaturated valences, which facilitates oxygen diffusion within xerogels channels and thus crude oil oxidation. However, because it lacks elements with redox properties for self-regeneration, its catalytic capacity may be harmed by reuse. The main goal of this investigation is to evaluate this property in detail.

In this regard, XCe and XCeNi samples received special consideration. The formation of coordinatively unsaturated oxygen (cus) by outgassing at high temperatures on the surface of light hydrocarbons, which can adsorb lattice oxygen anions, could be attributed to one of them as having the best performance for the XCeNi sample [120]. Because of the cus oxygen's high electron affinity, there is a stronger interaction between Ce and Ni and crude oil, which may result in the activation of the C-H bond at low temperatures, which then decomposes to surface carbonates and finally desorbs as CO<sub>2</sub> and CO.

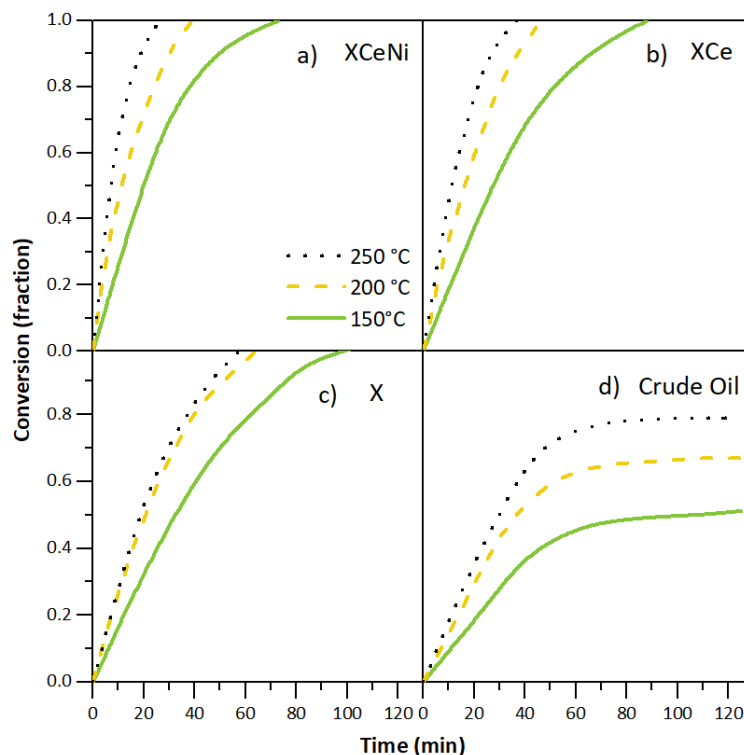


**Figure 22.** Isothermal conversion as a function of time at 150 °C, 200°C, and (c) 250°C for crude oil oxidation in the presence and absence of monolithic carbon xerogels. Oil adsorption from O/W emulsion at pH of 7. Airflow rate = 100 mL min<sup>-1</sup> and crude oil load of 0.2 mg m<sup>-2</sup>.

Gaseous analysis was done by coupling a mass spectrometer to the TGA instrument during isothermal heating at 200 °C in the presence and absence of monolithic carbon- Ce/Ni composite. Special attention was given to the thermal release profile of carbon monoxide (CO), carbon dioxide (CO<sub>2</sub>), light hydrocarbons (LHC), nitrogen oxides (NO<sub>x</sub>), and sulfur oxides (SO<sub>x</sub>). During crude oil oxidation, a series of reactions occur such as evaporation, distillation, partial oxidation reactions, thermal cracking reactions (pyrolysis), and combustion reactions. Results show that the main gases produced for crude oil oxidation were LHC (70.1%), CO<sub>2</sub> (13.5%), and CO (10.7%). However, once XCeNi is added to the system, the relative content of CO<sub>2</sub> and CO experience a small reduction around 7.5 and 3.2 %, respectively, suggesting a slight conversion of CO<sub>x</sub> class species. Interestingly, when crude oil is oxidized with XCeNi at 200 °C, both SO<sub>x</sub> and NO<sub>x</sub> species are markedly reduced from 3.2 to 0.6% and 2.5 to 0.3%, respectively, and consequently, the LHC becomes the most abundant species (83.7%).



Effective activation energy ( $E_{\alpha}$ ) was calculated to validate the catalytic behavior of monolithic carbon xerogel from the slope of the plot  $\ln(t_{a,i})$  against  $1/T_i$ . For decomposing 100% of adsorbed asphaltenes, the values of  $E_{\alpha}$  for X, XCe, and XCeNi were 18.89, 16.36, and 11.53 kJ mol<sup>-1</sup>, whereas the decomposition of 50 % of virgin crude oil requires 24.25 kJ mol<sup>-1</sup>. Results indicate higher efficiencies for XCe and XCeNi in crude oil oxidation/decomposition, which agrees with thermogravimetric results. Furthermore, adsorption and catalytic parameters show a direct correlation. The higher  $E_{\alpha}$ , the higher is Henry's law constant, that is, for higher affinities between treatments and crude oil, lower energy is required for their decomposition. Similarly, the self-association degree (represented by  $K$  parameter), is reduced in the same order that  $E_{\alpha}$  decreases. It indicates that the proximity of crude oil compounds to the catalytic active sites is lower for systems with multilayers. Also, heterogeneous surfaces, reduces energy expenditures, due to synergic effects between two or more phases can be obtained. These results agree well with those reported in the literature [73], in which the effective activation energy depended on the adsorption affinity, the degree of adsorbate self-association, and the chemical nature of the catalyst.

#### 4. Conclusions

Carbon xerogels-metal composites in a monolithic form containing Ni and/or Ce have been successfully synthesized by a sol-gel polycondensation method. The textural properties were affected by the addition of Ni and/or Ce to the material, leading to a more opened porosity, especially in the case of XCeNi which presents the highest level of mesoporosity. Also, Ni catalyzes the gelation of the organic xerogel where mesopores are generated and, during the carbonization process, the microporosity is increased. These materials show a high-performance adsorption capacity of light crude oil from aqueous solutions and excellent catalytic efficiency for its subsequence oxidation. The samples' adsorption potential increase in the order X < XCe < XCeNi, for all the conditions tested. The affinity of the three materials increases in basic media, but even under acidic pH they also have good yields. Therefore, the addition of Ce and Ni to the xerogel matrix-forming composites increases the adsorption activity of the pure carbon xerogel, not only due to the modification of the porous texture but for the different chemical nature developed. The adsorption efficiency values were higher than 98.0%, 90.0%, 80.0 %, and 33.3% for crude oil initial concentrations of

100, 300, 500, and 1000 mg L<sup>-1</sup>, respectively, for the system with the highest adsorption capacity (XCeNi).

On the other hand, the properties of these composites make possible the catalytic oxidation of crude oil. For isothermal experiments, the three monolithic carbon xerogels achieved 100% conversion of the crude oil adsorbed for all temperatures, whereas raw crude oil only decomposed 60%. Another significant result is that the main gases produced for crude oil oxidation were LHC (70.1%), CO<sub>2</sub> (13.5%), and CO (10.7%). However, once XCeNi is added to the system, the relative content of CO<sub>2</sub> and CO is reduced to 7.5 and 3.2 %, respectively. Interestingly, when crude oil is oxidized with XCeNi at 200 °C, both SO<sub>x</sub> and NO<sub>x</sub> species are markedly reduced from 3.2 to 0.6% and 2.5 to 0.3%, respectively, and the LHC becomes the most abundant species (83.7%). The catalytic activity of three monolithic carbon xerogels was corroborated with the effective activation energy, which was reduced by 24.9, 32.5, and 52.4% from non-catalyzed crude oil decomposition to the catalyzed decomposition by X, XCe, and XCeNi, respectively. Therefore, these results indicate that carbon xerogel – Ce/Ni composites in monolithic form have a great potential for oil removal from water solutions and its subsequent decomposition in oxidative atmospheres at low temperatures

## References

- [1] C.A. Franco, F.B. Cortés, N.N. Nassar, Adsorptive removal of oil spill from oil-in-fresh water emulsions by hydrophobic alumina nanoparticles functionalized with petroleum vacuum residue, *Journal of colloid and interface science*, 425 (2014) 168-177.
- [2] P. Sun, A. Elgowainy, M. Wang, J. Han, R.J. Henderson, Estimation of US refinery water consumption and allocation to refinery products, *Fuel*, 221 (2018) 542-557.
- [3] B. Goodale, J. La Du, S. Tilton, C. Sullivan, W. Bisson, K. Waters, R. Tanguay, Ligand-specific transcriptional mechanisms underlie aryl hydrocarbon receptor-mediated developmental toxicity of oxygenated PAHs, *Toxicological Sciences*, 147 (2015) 397-411.
- [4] K. Zapata Acosta, F. Carrasco-Marin, F.B. Cortés, C.A. Franco, S.H. Lopera, B.A. Rojano, Immobilization of *P. stutzeri* on activated carbons for degradation of hydrocarbons from oil-in-saltwater emulsions, *Nanomaterials*, 9 (2019) 500.

- [5] A. Ghaffari, M. Karimi, Numerical investigation on multiphase flow simulation in a centrifugal flotation cell, *International Journal of Coal Preparation and Utilization*, 32 (2012) 120-129.
- [6] A. Fakhru'l-Razi, A. Pendashteh, L.C. Abdullah, D.R.A. Biak, S.S. Madaeni, Z.Z. Abidin, Review of technologies for oil and gas produced water treatment, *Journal of hazardous materials*, 170 (2009) 530-551.
- [7] E.T. Igunnu, G.Z. Chen, Produced water treatment technologies, *International Journal of Low-Carbon Technologies*, 9 (2014) 157-177.
- [8] C. Murray-Gulde, J.E. Heatley, T. Karanfil, J.H. Rodgers Jr, J.E. Myers, Performance of a hybrid reverse osmosis-constructed wetland treatment system for brackish oil field produced water, *Water Research*, 37 (2003) 705-713.
- [9] S. Syed, M. Alhazaa, M. Asif, Treatment of oily water using hydrophobic nano-silica, *Chemical Engineering Journal*, 167 (2011) 99-103.
- [10] A. Srinivasan, T. Viraraghavan, Removal of oil by walnut shell media, *Bioresource technology*, 99 (2008) 8217-8220.
- [11] U.C. Ugochukwu, M.D. Jones, I.M. Head, D.A. Manning, C.I. Fialips, Biodegradation of crude oil saturated fraction supported on clays, *Biodegradation*, 25 (2014) 153-165.
- [12] Q. Wen, J. Di, L. Jiang, J. Yu, R. Xu, Zeolite-coated mesh film for efficient oil-water separation, *Chemical Science*, 4 (2013) 591-595.
- [13] R.T. Duraisamy, A.H. Beni, A. Henni, State of the art treatment of produced water, *Water Treatment*, (2013) 199-222.
- [14] J.P. Villegas, N. Arcila, D. Ortega, C.A. Franco, F.B. Cortés, Crude oil removal from production water using nano-intermediates of a SiO<sub>2</sub> support functionalized with magnetic nanoparticles, *Dyna*, 84 (2017) 65-74.
- [15] L.-Y. Meng, S.-J. Park, Superhydrophobic carbon-based materials: a review of synthesis, structure, and applications, *Carbon letters*, 15 (2014) 89-104.
- [16] S. Gupta, N.-H. Tai, Carbon materials as oil sorbents: a review on the synthesis and performance, *Journal of Materials Chemistry A*, 4 (2016) 1550-1565.
- [17] X. Gui, J. Wei, K. Wang, A. Cao, H. Zhu, Y. Jia, Q. Shu, D. Wu, Carbon nanotube sponges, *Advanced materials*, 22 (2010) 617-621.
- [18] H. Shi, D. Shi, L. Yin, Z. Yang, S. Luan, J. Gao, J. Zha, J. Yin, R.K. Li, Ultrasonication assisted preparation of carbonaceous nanoparticles modified polyurethane foam with good conductivity and high oil absorption properties, *Nanoscale*, 6 (2014) 13748-13753.

- [19] M.-Q. Zhao, J.-Q. Huang, Q. Zhang, W.-L. Luo, F. Wei, Improvement of oil adsorption performance by a sponge-like natural vermiculite-carbon nanotube hybrid, *Applied clay science*, 53 (2011) 1-7.
- [20] Z. Li, B. Wang, X. Qin, Y. Wang, C. Liu, Q. Shao, N. Wang, J. Zhang, Z. Wang, C. Shen, Superhydrophobic/superoleophilic polycarbonate/carbon nanotubes porous monolith for selective oil adsorption from water, *ACS Sustainable Chemistry & Engineering*, 6 (2018) 13747-13755.
- [21] N. Xiao, Y. Zhou, Z. Ling, J. Qiu, Synthesis of a carbon nanofiber/carbon foam composite from coal liquefaction residue for the separation of oil and water, *Carbon*, 59 (2013) 530-536.
- [22] B.S. Girgis, I.Y. El-Sherif, A.A. Attia, N.A. Fathy, Textural and adsorption characteristics of carbon xerogel adsorbents for removal of Cu (II) ions from aqueous solution, *Journal of non-crystalline solids*, 358 (2012) 741-747.
- [23] K. Zapata, F. Carrasco-Marín, J.P. Arias, J. Castelo-Quibén, C.A. Franco, B. Rojano, F.B. Cortés, Novel biomaterial design based on *Pseudomonas stutzeri*-carbon xerogel microspheres for hydrocarbon removal from oil-in-saltwater emulsions: A new proposed treatment of produced water in oilfields, *Journal of Water Process Engineering*, 35 (2020) 101222.
- [24] S. Morales-Torres, F.J. Maldonado-Hódar, A.F. Pérez-Cadenas, F. Carrasco-Marín, Structural characterization of carbon xerogels: From film to monolith, *Microporous and mesoporous materials*, 153 (2012) 24-29.
- [25] R.W. Pekala, C.T. Alviso, Carbon aerogels and xerogels, *MRS Online Proceedings Library Archive*, 270 (1992).
- [26] M. Perez-Cadenas, C. Moreno-Castilla, F. Carrasco-Marin, A.F. Perez-Cadenas, Surface chemistry, porous texture, and morphology of N-doped carbon xerogels, *Langmuir*, 25 (2009) 466-470.
- [27] S. Morales-Torres, F.J. Maldonado-Hódar, A.F. Pérez-Cadenas, F. Carrasco-Marín, Textural and mechanical characteristics of carbon aerogels synthesized by polymerization of resorcinol and formaldehyde using alkali carbonates as basification agents, *Physical Chemistry Chemical Physics*, 12 (2010) 10365-10372.
- [28] E. Gallegos-Suárez, A.F. Pérez-Cadenas, F.J. Maldonado-Hódar, F. Carrasco-Marín, On the micro-and mesoporosity of carbon aerogels and xerogels. The role of the drying conditions during the synthesis processes, *Chemical Engineering Journal*, 181 (2012) 851-855.
- [29] D. Fairén-Jiménez, F. Carrasco-Marín, C. Moreno-Castilla, Porosity and surface area of monolithic carbon aerogels prepared using alkaline carbonates and organic acids as polymerization catalysts, *Carbon*, 44 (2006) 2301-2307.

- [30] W. Kiciński, M. Norek, M. Bystrzejewski, Monolithic porous graphitic carbons obtained through catalytic graphitization of carbon xerogels, *Journal of Physics and Chemistry of Solids*, 74 (2013) 101-109.
- [31] F. Maldonado-Hódar, C. Moreno-Castilla, A. Pérez-Cadenas, Surface morphology, metal dispersion, and pore texture of transition metal-doped monolithic carbon aerogels and steam-activated derivatives, *Microporous and mesoporous materials*, 69 (2004) 119-125.
- [32] A.F. Pérez-Cadenas, C.H. Ros, S. Morales-Torres, M. Pérez-Cadenas, P.J. Kooyman, C. Moreno-Castilla, F. Kapteijn, Metal-doped carbon xerogels for the electro-catalytic conversion of CO<sub>2</sub> to hydrocarbons, *Carbon*, 56 (2013) 324-331.
- [33] P. Lee, M.A. Rogers, Phase-selective sorbent xerogels as reclamation agents for oil spills, *Langmuir*, 29 (2013) 5617-5621.
- [34] P.B. Sarawade, J.-K. Kim, A. Hilonga, D.V. Quang, H.T. Kim, Synthesis of hydrophilic and hydrophobic xerogels with superior properties using sodium silicate, *Microporous and mesoporous materials*, 139 (2011) 138-147.
- [35] M. Naderi, Surface Area: Brunauer–Emmett–Teller (BET), *Progress in filtration and separation*, Elsevier2015, pp. 585-608.
- [36] C. Nguyen, D. Do, The Dubinin–Radushkevich equation and the underlying microscopic adsorption description, *Carbon*, 39 (2001) 1327-1336.
- [37] N.N. Nassar, Iron oxide nanoadsorbents for removal of various pollutants from wastewater: an overview, *Application of adsorbents for water pollution control*, (2012) 81-118.
- [38] R. Kroon, Nanoscience and the Scherrer equation versus the 'Scherrer-Gottingen equation', *South African Journal of Science*, 109 (2013) 01-02.
- [39] D. López, R.D. Zabala, C. Matute, S.H. Lopera, F.B. Cortés, C.A. Franco, Well injectivity loss during chemical gas stimulation process in gas-condensate tight reservoirs, *Fuel*, 283 118931.
- [40] H. Mirhosseini, C.P. Tan, N.S. Hamid, S. Yusof, Effect of Arabic gum, xanthan gum and orange oil contents on  $\zeta$ -potential, conductivity, stability, size index and pH of orange beverage emulsion, *Colloids and Surfaces A: Physicochemical and Engineering Aspects*, 315 (2008) 47-56.
- [41] O.E. Medina, D. Galeano-Caro, J. Castelo-Quibén, R. Ocampo-Pérez, A.F. Perez-Cadenas, F. Carrasco-Marín, C.A. Franco, F.B. Cortés, Monolithic carbon xerogels-metal composites for crude oil removal from oil in-saltwater emulsions and subsequent regeneration through oxidation process: Composites synthesis, adsorption studies, and oil decomposition experiments, *Microporous and Mesoporous Materials*, 319 (2021) 111039.

- [42] T. Pekdemir, M. Copur, K. Urum, Emulsification of crude oil–water systems using biosurfactants, *Process Safety and Environmental Protection*, 83 (2005) 38-46.
- [43] V. Rajaković-Ognjanović, G. Aleksić, L. Rajaković, Governing factors for motor oil removal from water with different sorption materials, *Journal of hazardous materials*, 154 (2008) 558-563.
- [44] T. Montoya, D. Coral, C.A. Franco, N.N. Nassar, F.B. Cortés, A novel solid–liquid equilibrium model for describing the adsorption of associating asphaltene molecules onto solid surfaces based on the “chemical theory”, *Energy & Fuels*, 28 (2014) 4963-4975.
- [45] O.E. Medina, J. Gallego, L.G. Restrepo, F.B. Cortés, C.A. Franco, Influence of the Ce<sup>4+</sup>/Ce<sup>3+</sup> Redox-couple on the cyclic regeneration for adsorptive and catalytic performance of NiO-PdO/CeO<sub>2±δ</sub> nanoparticles for n-C<sub>7</sub> asphaltene steam gasification, *Nanomaterials*, 9 (2019) 734.
- [46] C.A. Franco, N.N. Nassar, T. Montoya, M.A. Ruíz, F.B. Cortés, Influence of asphaltene aggregation on the adsorption and catalytic behavior of nanoparticles, *Energy & Fuels*, 29 (2015) 1610-1621.
- [47] D. López, L.J. Giraldo, J.P. Salazar, D.M. Zapata, D.C. Ortega, C.A. Franco, F.B. Cortés, Metal Oxide Nanoparticles Supported on Macro-Mesoporous Aluminosilicates for Catalytic Steam Gasification of Heavy Oil Fractions for On-Site Upgrading, *Catalysts*, 7 (2017) 319.
- [48] N.N. Nassar, Asphaltene adsorption onto alumina nanoparticles: kinetics and thermodynamic studies, *Energy & Fuels*, 24 (2010) 4116-4122.
- [49] N.N. Nassar, A. Hassan, G. Luna, P. Pereira-Almao, Kinetics of the catalytic thermo-oxidation of asphaltenes at isothermal conditions on different metal oxide nanoparticle surfaces, *Catalysis today*, 207 (2013) 127-132.
- [50] S. Vyazovkin, A.K. Burnham, J.M. Criado, L.A. Pérez-Maqueda, C. Popescu, N. Sbirrazzuoli, ICTAC Kinetics Committee recommendations for performing kinetic computations on thermal analysis data, *Thermochimica acta*, 520 (2011) 1-19.
- [51] O.E. Medina, C. Caro-Vélez, J. Gallego, F.B. Cortés, S.H. Lopera, C.A. Franco, Upgrading of extra-heavy crude oils by dispersed injection of NiO–PdO/CeO<sub>2±δ</sub> nanocatalyst-based nanofluids in the steam, *Nanomaterials*, 9 (2019) 1755.
- [52] O.E. Medina, J. Gallego, D. Arias-Madrid, F.B. Cortés, C.A. Franco, Optimization of the load of transition metal oxides (Fe<sub>2</sub>O<sub>3</sub>, Co<sub>3</sub>O<sub>4</sub>, NiO and/or PdO) onto CeO<sub>2</sub> nanoparticles in catalytic steam decomposition of n-C<sub>7</sub> asphaltenes at low temperatures, *Nanomaterials*, 9 (2019) 401.

- [53] C. Orge, J. Órfão, M. Pereira, Carbon xerogels and ceria-carbon xerogel materials as catalysts in the ozonation of organic pollutants, *Applied Catalysis B: Environmental*, 126 (2012) 22-28.
- [54] Z. Liu, C. Lv, X. Tan, One-pot synthesis of Fe, Co and Ni-doped carbon xerogels and their magnetic properties, *Journal of Physics and Chemistry of Solids*, 74 (2013) 1275-1280.
- [55] J. Castelo-Quibén, E. Bailón-García, F.J. Pérez-Fernández, F. Carrasco-Marín, A.F. Pérez-Cadenas, Mesoporous carbon nanospheres with improved conductivity for electro-catalytic reduction of O<sub>2</sub> and CO<sub>2</sub>, *Carbon*, 155 (2019) 88-99.
- [56] J. Castelo-Quibén, A. Abdelwahab, M. Pérez-Cadenas, S. Morales-Torres, F.J. Maldonado-Hódar, F. Carrasco-Marín, A.F. Pérez-Cadenas, Carbon-iron electro-catalysts for CO<sub>2</sub> reduction. The role of the iron particle size, *Journal of CO<sub>2</sub> Utilization*, 24 (2018) 240-249.
- [57] A. Abdelwahab, J. Castelo-Quibén, M. Pérez-Cadenas, A. Elmouwahidi, F.J. Maldonado-Hódar, F. Carrasco-Marín, A.F. Pérez-Cadenas, Cobalt-doped carbon gels as electro-catalysts for the reduction of CO<sub>2</sub> to hydrocarbons, *Catalysts*, 7 (2017) 25.
- [58] L. Yue, X.-M. Zhang, Structural characterization and photocatalytic behaviors of doped CeO<sub>2</sub> nanoparticles, *Journal of Alloys and Compounds*, 475 (2009) 702-705.
- [59] N.A. Fathy, S.M. El-Khouly, N.A. Hassan, R.M. Awad, Free-and Ni-doped carbon xerogels catalysts for wet peroxide oxidation of methyl orange, *Journal of water process engineering*, 16 (2017) 21-27.
- [60] R. Saravanan, S. Joicy, V. Gupta, V. Narayanan, A. Stephen, Visible light induced degradation of methylene blue using CeO<sub>2</sub>/V<sub>2</sub>O<sub>5</sub> and CeO<sub>2</sub>/CuO catalysts, *Materials Science and Engineering: C*, 33 (2013) 4725-4731.
- [61] J.M. Skowroński, M. Osińska, Effect of nickel catalyst on physicochemical properties of carbon xerogels as electrode materials for supercapacitor, *Current Applied Physics*, 12 (2012) 911-918.
- [62] C. Alegre, D. Sebastián, M.J. Lázaro, Carbon xerogels electrochemical oxidation and correlation with their physico-chemical properties, *Carbon*, 144 (2019) 382-394.
- [63] B. Sellers-Antón, E. Bailón-García, A. Cardenas-Arenas, A. Davó-Quiñonero, D. Lozano-Castelló, A. Bueno-López, Enhancement of the Generation and Transfer of Active Oxygen in Ni/CeO<sub>2</sub> Catalysts for Soot Combustion by

Controlling the Ni–Ceria Contact and the Three-Dimensional Structure, *Environmental Science & Technology*, 54 (2020) 2439-2447.

[64] F. Liang, Y. Yu, W. Zhou, X. Xu, Z. Zhu, Highly defective CeO<sub>2</sub> as a promoter for efficient and stable water oxidation, *Journal of Materials Chemistry A*, 3 (2015) 634-640.

[65] V. Santos, M. Pereira, J. Órfão, J. Figueiredo, The role of lattice oxygen on the activity of manganese oxides towards the oxidation of volatile organic compounds, *Applied Catalysis B: Environmental*, 99 (2010) 353-363.

[66] Z. Wu, M. Li, J. Howe, H.M. Meyer III, S.H. Overbury, Probing defect sites on CeO<sub>2</sub> nanocrystals with well-defined surface planes by Raman spectroscopy and O<sub>2</sub> adsorption, *Langmuir*, 26 (2010) 16595-16606.

[67] D. Galeano-Caro, J.P. Villegas, J.H. Sánchez, F.B. Cortés, S.H. Lopera, C.A. Franco, Injection of Nanofluids with Fluorosurfactant-Modified Nanoparticles Dispersed in a Flue Gas Stream at Very Low Concentration for Enhanced Oil Recovery (EOR) in Tight Gas–Condensate Reservoirs, *Energy & Fuels*, 34 (2020) 12517-12526.

[68] P.I. Ravikovitch, A.V. Neimark, Characterization of nanoporous materials from adsorption and desorption isotherms, *Colloids and Surfaces A: Physicochemical and Engineering Aspects*, 187 (2001) 11-21.

[69] C. Franco, E. Patiño, P. Benjumea, M.A. Ruiz, F.B. Cortés, Kinetic and thermodynamic equilibrium of asphaltenes sorption onto nanoparticles of nickel oxide supported on nanoparticulated alumina, *Fuel*, 105 (2013) 408-414.

[70] F.B. Cortés, J.M. Mejía, M.A. Ruiz, P. Benjumea, D.B. Riffel, Sorption of asphaltenes onto nanoparticles of nickel oxide supported on nanoparticulated silica gel, *Energy & Fuels*, 26 (2012) 1725-1730.

[71] C.A. Franco, T. Montoya, N.N. Nassar, P. Pereira-Almao, F.B. Cortés, Adsorption and subsequent oxidation of colombian asphaltenes onto nickel and/or palladium oxide supported on fumed silica nanoparticles, *Energy & Fuels*, 27 (2013) 7336-7347.

[72] L. Cardona, D. Arias-Madrid, F.B. Cortés, S.H. Lopera, C.A. Franco, Heavy oil upgrading and enhanced recovery in a steam injection process assisted by NiO- and PdO-Functionalized SiO<sub>2</sub> nanoparticulated catalysts, *Catalysts*, 8 (2018) 132.

[73] N.N. Nassar, C.A. Franco, T. Montoya, F.B. Cortés, A. Hassan, Effect of oxide support on Ni–Pd bimetallic nanocatalysts for steam gasification of n-C<sub>7</sub> asphaltenes, *Fuel*, 156 (2015) 110-120.



- [74] C.A. Franco, N.N. Nassar, F.B. Cortés, Removal of oil from oil-in-saltwater emulsions by adsorption onto nano-alumina functionalized with petroleum vacuum residue, *Journal of colloid and interface science*, 433 (2014) 58-67.
- [75] S. Yapar, V. Özbudak, A. Dias, A. Lopes, Effect of adsorbent concentration to the adsorption of phenol on hexadecyl trimethyl ammonium-bentonite, *Journal of hazardous materials*, 121 (2005) 135-139.
- [76] J.D. Guzmán, S. Betancur, F. Carrasco-Marín, C.A. Franco, N.N. Nassar, F.B. Cortés, Importance of the adsorption method used for obtaining the nanoparticle dosage for asphaltene-related treatments, *Energy & Fuels*, 30 (2016) 2052-2059.
- [77] M. Muttakin, S. Mitra, K. Thu, K. Ito, B.B. Saha, Theoretical framework to evaluate minimum desorption temperature for IUPAC classified adsorption isotherms, *International Journal of Heat and Mass Transfer*, 122 (2018) 795-805.
- [78] Y. Feng, F. Yang, Y. Wang, L. Ma, Y. Wu, P.G. Kerr, L. Yang, Basic dye adsorption onto an agro-based waste material–Sesame hull (*Sesamum indicum* L.), *Bioresource Technology*, 102 (2011) 10280-10285.
- [79] R. Díez, O.E. Medina, L.J. Giraldo, F.B. Cortés, Development of Nanofluids for the Inhibition of Formation Damage Caused by Fines Migration: Effect of the interaction of Quaternary Amine (CTAB) and MgO Nanoparticles, *Nanomaterials*, 10 (2020) 928.
- [80] X. Qi, D. Wang, H. Xue, L. Jin, B. Su, H. Xin, Oxidation and self-reaction of carboxyl groups during coal spontaneous combustion, *Spectroscopy Letters*, 48 (2015) 173-178.
- [81] L. Yang, J.J. Sheng, Experimental study on the oxidation behaviors of Wolfcamp light crude oil and its saturate, aromatic and resin fractions using accelerated rate calorimetry tests, *Fuel*, 276 (2020) 117927.
- [82] I. Rakhmatullin, S. Efimov, V. Tyurin, A. Al-Muntaser, A. Klimovitskii, M. Varfolomeev, V. Klochkov, Application of high resolution NMR (<sup>1</sup>H and <sup>13</sup>C) and FTIR spectroscopy for characterization of light and heavy crude oils, *Journal of Petroleum Science and Engineering*, 168 (2018) 256-262.
- [83] E. Clark, S. Hecker, G. Jarvinen, M. Neu, *Kirk-Othmer Encyclopedia of Chemical Technology, Thorium and Thorium Compounds*, (2006).
- [84] W. Wainipee, D.J. Weiss, M.A. Sephton, B.J. Coles, C. Unsworth, R. Court, The effect of crude oil on arsenate adsorption on goethite, *Water Research*, 44 (2010) 5673-5683.
- [85] N.N. Nassar, A. Hassan, G. Vitale, Comparing kinetics and mechanism of adsorption and thermo-oxidative decomposition of Athabasca asphaltenes onto

TiO<sub>2</sub>, ZrO<sub>2</sub>, and CeO<sub>2</sub> nanoparticles, *Applied Catalysis A: General*, 484 (2014) 161-171.

[86] N.N. Marei, N.N. Nassar, G. Vitale, A. Hassan, M.J.P. Zurita, Effects of the size of NiO nanoparticles on the catalytic oxidation of Quinolin-65 as an asphaltene model compound, *Fuel*, 207 (2017) 423-437.

[87] M.M. Lozano, C.A. Franco, S.A. Acevedo, N.N. Nassar, F.B. Cortés, Effects of resin I on the catalytic oxidation of n-C 7 asphaltenes in the presence of silica-based nanoparticles, *RSC advances*, 6 (2016) 74630-74642.

[88] O.E. Medina Erao, J. Gallego, C.M. Olmos, X. Chen, F.B. Cortés, C.A. Franco, Effect of Multifunctional Nanocatalysts on n-C7 Asphaltene Adsorption and Subsequent Oxidation under High Pressure Conditions, *Energy & Fuels*, (2020).

[89] O.E. Medina, J. Gallego, N.N. Nassar, S.A. Acevedo, F.B. Cortés, C.A. Franco, Thermo-Oxidative Decomposition Behaviors of Different Sources of n-C7 Asphaltenes at High-Pressure Conditions, *Energy & Fuels*, (2020).

[90] T. Montoya, B.L. Argel, N.N. Nassar, C.A. Franco, F.B. Cortés, Kinetics and mechanisms of the catalytic thermal cracking of asphaltenes adsorbed on supported nanoparticles, *Petroleum Science*, 13 (2016) 561-571.

[91] O.E. Medina, J. Gallego, E. Rodríguez, C.A. Franco, F.B. Cortés, Effect of pressure on the oxidation kinetics of Asphaltenes, *Energy & Fuels*, 33 (2019) 10734-10744.

[92] O.E. Medina, Y. Hurtado, C. Caro-Velez, F.B. Cortés, M. Riazi, S.H. Lopera, C.A. Franco, Improvement of steam injection processes through nanotechnology: An approach through in situ upgrading and foam injection, *Energies*, 12 (2019) 4633.

[93] E. Aneggi, M. Boaro, C. de Leitenburg, G. Dolcetti, A. Trovarelli, Insights into the redox properties of ceria-based oxides and their implications in catalysis, *Journal of Alloys and Compounds*, 408 (2006) 1096-1102.

[94] A. Razeghi, A. Khodadadi, H. Ziaei-Azad, Y. Mortazavi, Activity enhancement of Cu-doped ceria by reductive regeneration of CuO–CeO<sub>2</sub> catalyst for preferential oxidation of CO in H<sub>2</sub>-rich streams, *Chemical Engineering Journal*, 164 (2010) 214-220.

[95] S. Alamolhoda, G. Vitale, A. Hassan, N.N. Nassar, P. Pereira Almaso, Development and characterization of novel combinations of Ce-Ni-MFI solids for water gas shift reaction, *The Canadian Journal of Chemical Engineering*, 97 (2019) 140-151.

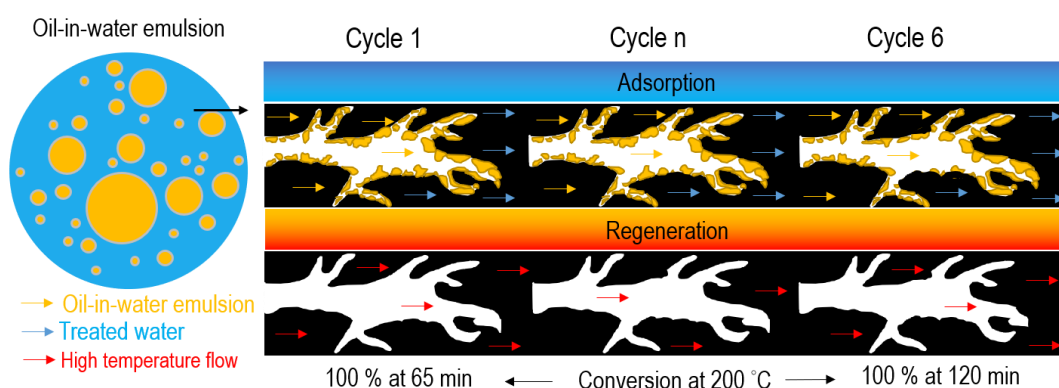
[96] L.G.-C. Acosta, D.; Medina, O.E.; Cortés, F.B.; Franco, C.A. , Nano-Intermediate of Magnetite Nanoparticles Supported on Activated Carbon from

Spent Coffee Grounds for Treatment of Wastewater from Oil Industry and Energy Production, *Processes*, 9 (2021) 63.

[97] L. Mateus, C. Moreno-Castilla, M.V. López-Ramón, F.B. Cortés, M.Á. Álvarez, O.E. Medina, C.A. Franco, Á. Yebra-Rodríguez, Physicochemical characteristics of calcined  $\text{MnFe}_2\text{O}_4$  solid nanospheres and their catalytic activity to oxidize para-nitrophenol with peroxymonosulfate and n-C7 asphaltenes with air, *Journal of Environmental Management*, 281 (2021) 111871.

Chapter 20.

# Development of a Monolithic Carbon Xerogel-Metal Composite for Crude Oil Removal from Oil in-Saltwater Emulsions: Evaluation of Reuse Cycles



Published manuscript in *Microporous and Mesoporous Materials*:

[doi.org/10.1016/j.micromeso.2021.111424](https://doi.org/10.1016/j.micromeso.2021.111424)

Impact factor: 5.455

# Development of a Monolithic Carbon Xerogel-Metal Composite for Crude Oil Removal from Oil in-Saltwater Emulsions: Evaluation of Reuse Cycles

## Abstract

This study aims to evaluate the reuse capacity of carbon xerogels-Ce/Ni composite (XCeNi) during crude oil adsorption from O/W emulsions and subsequent regeneration through the oxidation process using air as an oxidant agent for six cycles. For the six cycles of evaluation, batch adsorption experiments were done at different temperatures and modeled using the solid-equilibrium model (SLE). In contrast, catalytic tests were performed under *non*-isothermal and isothermal heating. To estimate the change in the sample's surface composition, X-ray photoelectron spectroscopy (XPS) analysis was carried out during each regeneration cycle. According to batch adsorption experiments and SLE fitting, the XCeNi sample presents a high affinity for hydrocarbons and a similar maximum adsorption capacity during six regeneration cycles. Crude oil was also successfully decomposed under non-isothermal heating (100 - 800 °C), reducing the main decomposition peak from 250 to 150 °C for all the evaluated cycles. Under isothermal heating at 150, 200, and 250 °C, conversions of 100 % were obtained for all cycles evaluated. At the first cycle the time required to decompose 100 % of adsorbed crude oil at 60 min, whereas, after the 6 cycles, it is achieved at 120 min. The gaseous analysis of the products involved in the oxidation of the crude oil in each cycle was considered, finding an increase in the production of light hydrocarbons, and reducing gas emissions such as CO<sub>2</sub>, NO<sub>x</sub>, and SO<sub>x</sub> during all reuses. The activation energy increases from 10.1 to 18.7 kJ mol<sup>-1</sup> during the six cycles due to the reduction of the content of Ce<sup>3+</sup>. The Ce<sup>3+</sup> concentration is reduced to 0 after each adsorption cycle. Apparently, the ability of the xerogel to decompose the adsorbed crude during all cycles may be associated with the increase in Ce<sup>3+</sup> during the adsorption process, and then during the oxidation treatment is transformed to Ce(OH)<sub>2</sub><sup>2+</sup>. Also, the influence of Ni<sup>2+</sup> on XCeNi is noted. Through the regeneration, the Ni<sup>2+</sup>/Ni<sup>3+</sup> ratio varies, which shows the continuous redox processes that have taken place in this sample.

## 1. Introduction

Crude oil is commonly found emulsified in produced water (O/W) during the extraction of oil or natural gas [1-3]. Economic and environmental problems arise through the incorrect disposal of produced waters, generating ecological changes and negative impacts on wildlife [4]. Consequently, the scientific community has focused on developing methods and materials for the optimal separation of crude oil from oil-in-water emulsions to accomplish the basic requirements for its shedding or reinjection [5]. Techniques such as separation with membranes [6, 7], degradation by heat or microorganisms [8-11], decantation [12], chemical dispersion [13], and adsorption with different materials have been used to remove crude oil from produced waters [14, 15]. The last one has been of great interest in the previous two decades since the adsorbent materials have shown significant advantages for oil removal due to their high cost/effective ratio [15, 16]. Most materials showed high efficiencies to remove free crude oil, but many of them require great economic expenses and very complex synthesis processes [17].

Some research has evaluated the regeneration of crude oil removal materials for reuse in a new cycle [18, 19]. It worth mention that an excellent approach to reuse could generate a cost-effective process for the Oil & Gas industry. One of the most featured processes for the regeneration of the adsorbent/catalyst is the thermal process. The materials are regenerated depending on their catalytic activity to decompose the crude oil adsorbed [20].

The implementation of nanoparticles with catalytic capacity has been widely studied. It has been proven that they can generate highly efficient reactions at lower temperatures, as can be seen in other industrial applications such as thermal EOR processes [21-27]. Recently, Acosta et al.[28] developed magnetite/activated carbon nano-intermediates from spent coffee grounds, where heat treatments were used to simulate pyrolysis reactions in the final desorption of crude oil, generating valuable products such as CH<sub>4</sub> and C<sub>2</sub>H<sub>6</sub> [28].

On the other hand, surface-modified materials with ceria have been shown to have autocatalytic and auto regenerative properties due to the redox behavior of CeO<sub>2</sub> nanoparticles [29-32]. Furthermore, due to strong metal-support interaction phenomena, the inclusion of transition metal oxides could optimize the autocatalytic process; NiO in particular has been used as an active phase in

synergy with CeO<sub>2</sub>, obtaining excellent results when decomposing hydrocarbons [23, 33].

In a previous study [34], the monolithic carbon xerogel-metal composites synthesis, adsorption studies, and oil decomposition experiments of oil from O/W emulsion were performed. Different composites were synthesized, namely, carbon xerogel without metals (X), carbon xerogel-Ce composite with 18.0 wt.% of cerium (XCe), and one synthesized with 18.0 wt.% and 4.0 wt.% of cerium and nickel, respectively (XCeNi). The adsorptive capacity of monolithic carbon xerogels was evaluated for different solution volume/xerogel mass ratios (0.03, 0.1, and 0.3 g L<sup>-1</sup>), different pH (2, 7, and 11), and different temperatures (25, 35, and 45 °C). It was found that the XCeNi material assessed the highest oil adsorption capacity in all the evaluated scenarios. The tests were done by different routes, including isothermal and non-isothermal conditions, by thermogravimetric analysis. The results showed that the XCeNi material presented the highest crude oil removal, obtaining conversions of 100% at a temperature of 150 °C in less than 50 minutes. Likewise, the activation energy for this material presented the most significant reduction, equal to 52.4%. Considering the typical conditions in real field cases for water treatment, the regeneration capacity of the XCeNi was done at a pH of 7, using an adsorbent/emulsion ratio of 0.1 *M* considering literature studies [16]. However, it worth mentioning that the regeneration process and the reuse of the materials were not evaluated.

Therefore, this study aims to continue with the previous research, mainly addressing the monolithic carbon xerogel's regenerating capacity during several crude oil adsorption/decomposition cycles. This generates valuable information on adsorbent reuse processes during removing emulsified crude oil from hydrocarbon production waters. For this proposal, a monolithic carbon composite with nickel and ceria at loads of 4 wt.% and 18 wt.%, respectively, will be used. For this, we have evaluated six adsorption steps (crude oil removal) based on the adsorption phenomena through batch adsorption experiments. The regeneration process from the oxidation reactions using non-isothermal and isothermal heating was evaluated during the same steps. There is no research about the regenerating capacity of the material through several regeneration cycles (crude oil removal and subsequent regeneration based on the oxidation process) to the best of our knowledge.

## 2. Experimental

### 2.1. Materials

For emulsion formulation, light crude oil and a brine characteristic of a Colombian oil field were used. Emulsions were stabilized by adding 5.0 wt.% of polyethylene sorbitan monooleate (Tween 80) supplied by Panreac (Barcelona, Spain). The droplet size and absorbance were followed for five days until the change in measurements was < 2% to ensure the emulsions' stability. The droplet size was found to be between 0.2-0.8 mm. Details about the preparation and characterization of oil-in-saltwater (O/W) emulsions are found in our previous study [34]. The main characteristics of the reservoir fluids were shown in Table 1.

**Table 1.** Main characteristics of crude oil and brine

<b>Crude oil</b>	
°API @15°C	38.2
Viscosity (cP) @25°C and 10s <sup>-1</sup>	3.48
Saturates (wt.%)	65.6
Aromatics (wt.%)	18.4
Resins (wt.%)	15.9
Asphaltenes (wt.%)	0.1
<b>Brine</b>	
pH	7.1
Density (mg L <sup>-1</sup> )	1.07
Conductivity (mS cm <sup>-1</sup> )	26.23

Materials supplied by Sigma-Aldrich (St. Louis, MO, USA), such as formaldehyde, resorcinol, and cesium carbonate, Ce(NO<sub>3</sub>)<sub>3</sub>·6H<sub>2</sub>O, and Ni(C<sub>2</sub>H<sub>3</sub>O<sub>2</sub>)<sub>2</sub>·4H<sub>2</sub>O were used for the synthesis of the monolithic carbon xerogel Ce/Ni metal composite constituted by 18 and 4 wt.% of cerium and nickel (XCeNi). The material was selected due to its high adsorptive and catalytic performance) showed previously [34].

### 2.2. Methods

#### 2.2.1. Characterization of XceNi

Table 2 shows the main properties of the XceNi. Briefly, the Inductively Couple Plasma – Mass Spectrometry (ICP-MS) was done to corroborate the metal content, obtaining final concentrations of Ce and Ni of 18.0 and 4.0 wt.%, respectively. The results of High-Resolution transmission electron microscopy (HR-TEM) and HAADF analysis demonstrated that the XceNi material consists



of a carbonaceous structure with a high dispersion of Ce and Ni (larger than 40 %) and average crystal sizes of 20 and 2 nm, respectively.

The adsorption curves of N<sub>2</sub> and CO<sub>2</sub> show that the material is mainly microporous and presents an H4-type hysteresis cycle characteristic of opened mesoporosity. The addition of Ni increases the surface area of the material by 20% ( $S_{\text{BET}} = 742 \text{ m}^2 \text{ g}^{-1}$ ). Besides, scanning electron microscopy images demonstrated that the material has a well-developed microporous structure with interconnected particles (80-90 nm). Finally, the surface composition and the oxidation states (carbon-metal) of the XceNi material were determined by X-ray emitted photoelectron spectroscopy (XPS). The results showed a predominant contribution of C=C bonds, whose content was increased around 50% with the addition of cerium and nickel. The atomic concentration of Ce<sup>3+</sup> was 34.6%. At the same time, bands associated with the Ni and Ni<sup>2+</sup> species were observed. Finally, the point of zero charge for the material was 3.8.

**Table 2.** Estimated textural and chemical characteristics of the carbon-metal composite with Ce and Ni of 18.0 and 4.0 wt.%, respectively

Ce <sub>ICP-MS</sub> (%)	Ni <sub>ICP-MS</sub> (%)	S <sub>BET</sub> (m <sup>2</sup> g <sup>-1</sup> )	Ce <sub>XRD</sub> (nm)	Ni <sub>XRD</sub> (nm)	Ce <sup>3+</sup> /Ce-Total XPS (%)	pH <sub>pzc</sub>
18.0	4.0	742	16.73	12.62	34.6	3.8

### 2.2.2. Crude oil Adsorption over XceNi: Removal step

A defined amount of XceNi was added to the different O/W emulsions prepared to evaluate the adsorptive capacity through reusing the synthesized material. The protocol is described in detail previously [34]. The Solid-Liquid Equilibrium (SLE) model was used to determine material affinity ( $H$ ), degree of self-association of adsorbed compounds ( $K$ ), and amount of crude oil adsorbed ( $N_{\text{ads}}$ ). Also, the adsorption curves were constructed at 25, 35, and 45 °C, and thermodynamic studies were done in terms of change in standard enthalpy ( $\Delta H_{\text{ads}}^\circ$ ), entropy ( $\Delta S_{\text{ads}}^\circ$ ), and Gibbs free energy ( $\Delta G_{\text{ads}}^\circ$ ), and mechanistic insights were analyzed based on the Polanyi's potential ( $A$ ) for each of the cycles [23, 35].

### 2.2.3. Thermogravimetric experiments

Crude oil decomposition was evaluated by thermogravimetric analysis in a thermogravimetric analyzer Q50 (TA Instruments, Inc., New Castle, DE) coupled to a mass spectrometer (Shimadzu MS, Tokyo, Japan). Catalytic experiments were developed under non-isothermal and isothermal conditions. For the first

tests, samples were heated from 30 to 600 °C using a heating rate of 20 °C min<sup>-1</sup>, whereas isothermal runs were done at 150, 200, and 250 °C under airflow injection of 100 mL min<sup>-1</sup>. Sample mass was 5 mg for avoiding thermal diffusive effects, and a load of crude oil was 0.2 mg m<sup>-2</sup> for all cases. Gaseous products were analyzed for isothermal runs performed at 200 °C during each catalytic cycle using a linear scan rate of 0.03 *m/z* between 0 – 200 *m/z*. The catalytic powder of monolithic carbon xerogel-metal composite (XCeNi) during all regeneration cycles evaluated was corroborated by measuring effective activation energy.

#### 2.2.4. XceNi Regeneration: Oxidation process

The regeneration process of the synthesized materials consists of the catalytic decomposition of the crude oil adsorbed. The materials with the adsorbed crude oil were subjected to an oxidizing atmosphere in a tubular furnace at 200 °C for 3 h, to ensure its complete regeneration. In each cycle, a sample was taken for examining the surface chemical composition by X-ray photoelectron spectroscopy (XPS) and point of zero charge (pH<sub>pzc</sub>). For this purpose, a Specs-NAP-XPS X-ray photoelectronic spectrometer (Germany) and a PHOIBOS 150-1D-DLD analyzer were used. A monochromatic source Al-K $\alpha$  (1486.7 eV, 13 kV, 100 W) was used under vacuum conditions. Energies of 100 and 20 eV were used to estimate the stoichiometry and the chemical state of the chemical elements present in the material [23]. Also, the point of zero charge in each cycle was analyzed using a Nanoplus-3, Micromeritics (GA, USA) according to the solid addition method [36].

### 3. Results and discussion

#### 3.1. Adsorption isotherms

Figure 1 displays the crude oil adsorption isotherms on the XCeNi composite at 25, 35, and 45 °C after six (6) adsorption/decomposition catalytic cycles. According to the IUPAC classification, the results reveal type I isotherms for all cycles [37]. It is common for systems with high adsorbate-adsorbent affinity to exhibit this type of isotherms, and the persistence of this behavior through various regeneration cycles suggests that affinity is maintained [38]. Additionally, it is noted that as the material regenerates from cycle 1 to cycle 6, the adsorbed amount for an oil equilibrium concentration (i.e., 100 mg L<sup>-1</sup>) decreases (9.5%) at 25 °C.

On the other hand, it was determined from the experimental data that as temperatures drop, the amount of crude oil adsorbed rises [23]. This is due to the fact that as the temperature rises, the activity or energy of the hydrocarbon molecules rises, the ability of the molecules around the high-energy sites to self-associate decreases, and the forces that bind the adsorbate to the adsorbent weaken [39]. Additionally, the nonpolar nature of the XCeNi material results in a hydrophobic attraction (also known as London dispersion forces) with polycyclic aromatic hydrocarbons [40, 41].

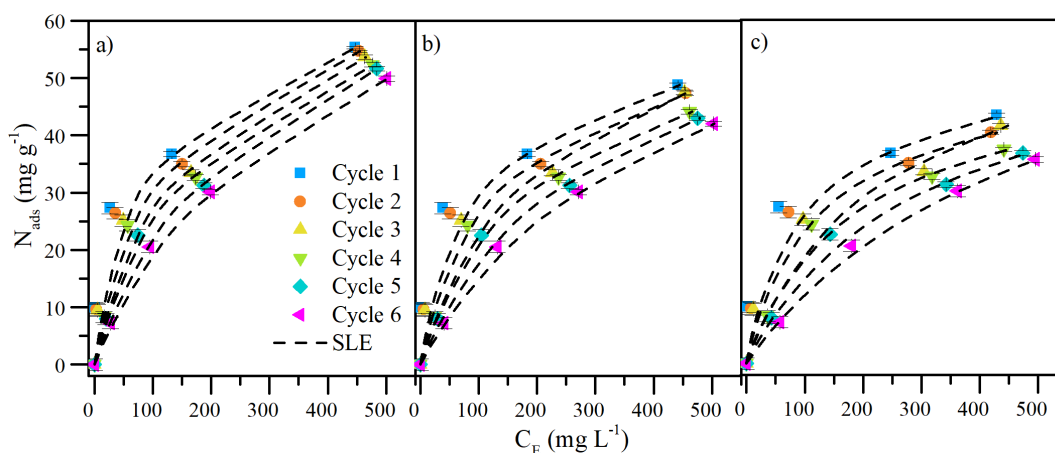


**Figure 1.** Crude oil adsorption isotherms on XCeNi material at a) 25 °C, b) 35 °C, and c) 45 °C through several reuses. The symbols represent the experimental data, and the dotted lines represent the Solid-Liquid Equilibrium model predictions.

Table 3 displays the SLE model's estimated fitting parameters. No significant changes in the self-association degree of the crude oil particles on the XCeNi surface, represented by the  $K$  parameter, were seen for the evaluated cycles. Similar to this, from cycle 2 to cycle 6, the maximum amount adsorbed ( $N_m$ ) remains constant, indicating a condition of complete saturation for its regeneration.

The  $H$  parameter, however, underwent significant changes, rising slightly from cycle 1 to cycle 6 from 1.20 to 1.77 mg g<sup>-1</sup> at 25 °C to 1.39 to 2.08 mg g<sup>-1</sup> at 35 °C to 1.44 to 2.19 mg g<sup>-1</sup> at 45 °C. This suggests that there have been modifications in the interactions between the crude oil molecules and the XCeNi, which may have affected the surface chemistry characteristics of the composite. As a result, the sample's active sites (which are characterized by the presence of Ce<sup>3+</sup> ions) offer good selectivity for cyclic and linear hydrocarbon structures; it is

remarkable that these sites also serve as anchoring sites for large molecules like resins and asphaltenes [42]. This ability is not diminished through cycles. Although  $H$  changed,  $K$  only slightly changed as the cycles progressed. This finding suggests that, despite changes in the interactions between the xerogel and the crude oil molecules, the presence of new elements like iron has no impact on the xerogel's ability to prevent the self-association of the crude oil on its surface. As a result, neither the minimum nor maximum amount adsorbed is impacted.

**Table 3.** Parameters  $H$ ,  $K$ ,  $N_m$  and % $RSME$  of the SLE model for crude oil adsorption on XCeNi during six reuses.

Cycle	Temperature (°C)	$H$ (mg g <sup>-1</sup> )	$K$ (g g <sup>-1</sup> ) × 10 <sup>-2</sup>	$N_m$ (mg g <sup>-1</sup> ) × 10 <sup>-1</sup>	% $RSME$
1	25	1.20	1.99	1.03	0.04
	35	1.39	2.45	0.99	0.06
	45	1.44	2.85	0.78	0.06
2	25	1.25	2.00	0.99	0.04
	35	1.44	2.45	0.88	0.06
	45	1.50	2.87	0.77	0.07
3	25	1.41	1.99	0.99	0.05
	35	1.61	2.46	0.88	0.08
	45	1.68	2.87	0.77	0.09
4	25	1.59	1.98	0.99	0.05
	35	1.86	2.45	0.88	0.07
	45	2.00	2.88	0.77	0.08
5	25	1.68	1.99	0.99	0.04
	35	1.94	2.46	0.88	0.05
	45	2.14	2.89	0.77	0.05
6	25	1.77	2.01	0.99	0.04
	35	2.08	2.45	0.88	0.05
	45	2.19	2.90	0.77	0.05

### 3.1.1. Thermodynamic study of crude oil adsorption

Table 4 displays the results of calculating the change in standard enthalpy ( $\Delta H_{ads}^\circ$ ), entropy ( $\Delta S_{ads}^\circ$ ) and change in Gibbs free energy ( $\Delta G_{ads}^\circ$ ) of the adsorptive phenomenon. The positive value of entropy ( $\Delta S_{ads}^\circ$ ) for each scenario under consideration denotes randomness at the XCeNi/crude oil interface. As XCeNi is reused, these values changed marginally, rising 13.12% from cycles 1 to 6. The adsorption mechanism of crude oil affects the molecular disorder on the

adsorbent's surface. The previous section demonstrated how the degree of self-association of the molecules in crude oil increases as the cycles go by. This finding implies that their ability to prevent crude oil associations is diminished, leading to a higher level of randomness in the system.

All cycles' enthalpy values were negative, which suggests that heat is released during adsorbent/adsorbate interactions. Only 4.55% more enthalpy was produced between cycles 1 and 6 overall. The findings corroborated Medina et al. [23] assessment of the regeneration capacity of Ce/Ni-based nanocatalysts for the adsorption and subsequent decomposition of heavy oil fractions and showed that the system's exothermic nature was maintained during the cycles evaluated. The researchers discovered that interactions between crude oil compounds, ceria, and nickel continue to be exothermic as the material is renewed. The change in XCeNi's adsorption capacity is what caused the slight increase in enthalpy during the six reuses.

Finally, the values of the Gibbs free energy variations are nearly constant throughout the evaluated adsorption/desorption cycles, with maximum variations at 25, 35, and 45 °C, of 0.01, 0.06, and 0.45%, respectively. These findings show that all the evaluated processes have favorable thermodynamic properties. The system maintained its spontaneity throughout the 6 cycles being evaluated, meaning no additional energy was needed to encourage adsorbate/adsorbent interactions. They are contrasted with research findings. The XCeNi material exhibits values of  $\Delta H_{ads}^{\circ}$ ,  $\Delta G_{ads}^{\circ}$ , and  $\Delta S_{ads}^{\circ}$  that are comparable to those of materials used for a single adsorption cycle, showing that it retains its better properties despite being reused.

**Table 4.** Thermodynamic parameters for the adsorption of crude oil on the XCeNi material during six reuses.

Cycle	$\Delta S_{ads}^{\circ} \pm 0.03 \times 10^{-2}$ (J (mol K) <sup>-1</sup> )	$-\Delta H_{ads}^{\circ} \pm 0.02$ (kJ mol <sup>-1</sup> )	$-\Delta G_{ads}^{\circ} \pm 0.01 \times 10^{-2}$ (kJ mol <sup>-1</sup> )
1	1.50	14.19	971.15
			950.19
			941.11
2	1.55	14.33	971.14
			949.98
			940.18
3	1.59	14.46	971.13
			949.87
			939.26

			971.11
4	1.64	14.60	949.67
			938.34
5	1.68	14.73	971.10
			949.64
			937.42
6	1.73	14.87	971.09
			949.63
			936.51

### 3.1.2. Polanyi's adsorption potential for crude oil adsorption

Crude oil over XCeNi adsorption potential curves are shown in Figure 2. It is acknowledged that the potential does not change significantly between cycles 1 and 6. The parameter decrease (from cycle 1 to cycle 6) does not exceed 0.46% when the amount of crude oil adsorbed is higher. The reduction is 21.6% in the worst-case scenario. The outcome is consistent with earlier predictions based on thermodynamic parameters and SLE modeling. Due to the minimal alteration of the adsorption potential for high adsorption uptakes, a similar maximum amount of material is adsorbed during the regeneration cycles.

The evaluation of the adsorption of crude oil on the surface of XCeNi revealed several interesting findings, including the following: *i)* the material has a high affinity and adsorptive capacity for crude oil molecules; *ii)* the material retains various adsorptive properties, indicating its high ability to remove crude oil from O/W emulsions during several regeneration catalytic cycles; and *iii)* adsorbate-adsorbent interactions are spontaneous and ex

The results found during the evaluation of the adsorption of crude oil on the surface of XCeNi suggest that *i)* the material has a high affinity and capacity for adsorbing molecules of crude oil.; *ii)* the xerogel still possesses a variety of adsorptive qualities, demonstrating a high capacity to remove crude oil from O/W emulsions over several regeneration catalytic cycles.; and *iii)* Adsorbent-adsorbate interactions are exothermic and spontaneous, with the potential for catalytic regeneration.

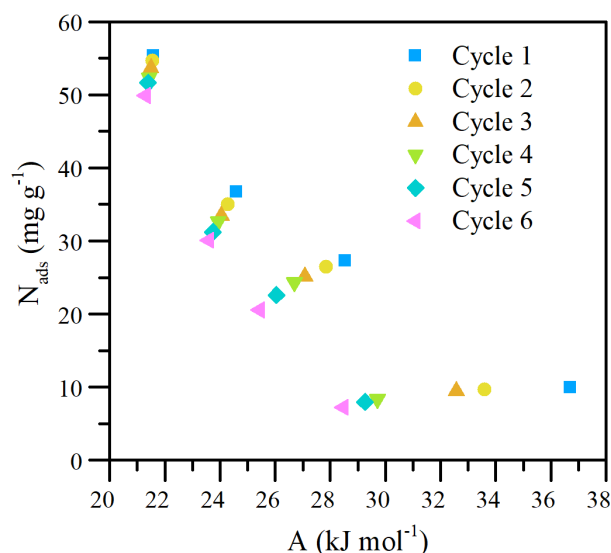


**Figure 2.** Polanyi adsorption potential ( $A$ ) as a function of the adsorbed amount ( $N_{ads}$ ) for the adsorption of crude oil on the XCeNi material through six reuses.

### 3.2. Mass loss analysis

The XCeNi sample's catalytic activity for oxidizing the crude oil adsorbed over the course of various cycles was tested during the regeneration assays. Figure 3 displays differential thermogravimetric curves, which illustrate the breakdown of crude oil at non-isothermal heating both in the absence and presence of XCeNi over the course of six catalytic regeneration cycles. From panel a, although the mass loss of the crude oil began at lower temperatures (roughly 100 °C), the main decomposition peak occurs at 250 °C. The lighter crude oil compounds evaporate at these temperatures, which results in mass loss. Then, reactions for oxygen addition, isomerization, and decomposition occur. Most crude oil reacts during this phase, known as Low-Temperature Oxidation (100 - 350 °C), corroborated with the obtained mass-loss rate profile [43, 44]. It is noticeable that the peak is weaker at higher temperatures, where the main pathway is caused by cracking reactions. Higher Temperature Oxidation (HTO) (>350 °C) is the name of this region. It oversees breaking down a solid residue left over from the transition between LTO and HTO when resins and asphaltenes are broken down.

Additionally, panel b demonstrates that the conversion degree for virgin crude oil was always lower than that catalyzed by XCeNi. Until cycle 4, when a larger shift in temperature is required to produce the same conversion degree due to changes in the catalyst's reaction mechanism because of changes in its surface chemistry properties, the conversion varies very little as the material is regenerated.

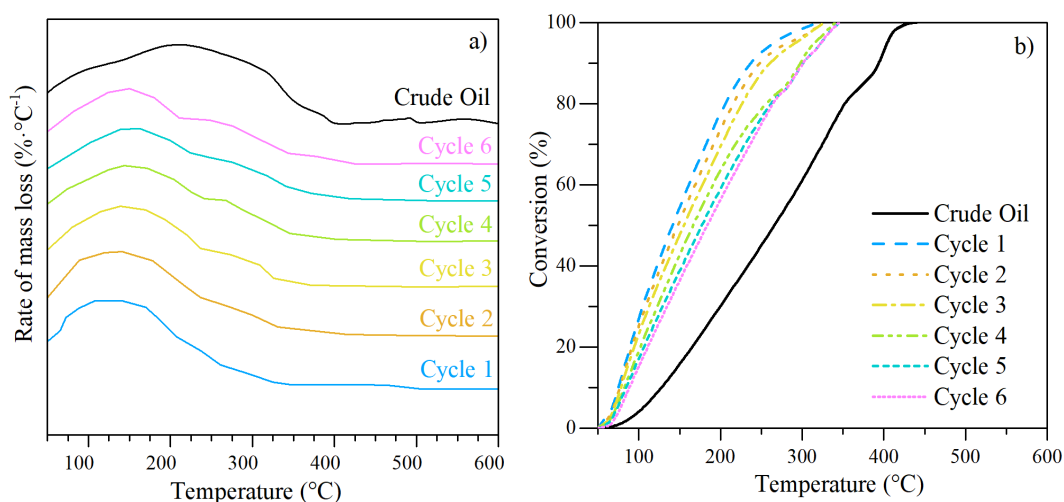


**Figure 3.** (a) Rate for mass loss and (b) conversion of crude oil in the presence and absence of monolithic carbon xerogels- metal composite with nickel and cerium oxides during 6 regeneration cycles. Airflow rate = 100 mL min<sup>-1</sup>, heating rate = 20 °C min<sup>-1</sup>, and crude oil load of 0.2 mg m<sup>-2</sup>.

Like this, the main decomposition peak in cycle 1 for the crude oil sample without the composite is reduced by the adsorbed crude oil on XCeNi. Since the total decomposition of the adsorbed crude oil ends around 300 °C, whereas virgin crude oil continues to decompose up to 550 °C, the catalytic effect of the xerogel is clearly visible. The material's chemical nature enables to decompose the heavier crude oil fractions with less energy than other materials.

The synthetic material's chemical makeup enables it to decompose the heavier crude oil fractions with less energy than other materials. First, the decomposition of aromatic compounds takes place at the carbonaceous active sites, which include defects, unsaturated valences at the edges, and hexagonal graphite crystals. Cerium oxide is a significant catalyst as well, and the ratio of Ce<sup>4+</sup> to Ce<sup>3+</sup> affects the material's reactivity. Additionally, oxygen vacancies are necessary for the dissociation of gaseous O<sub>2</sub> and the formation of lattice oxygen [45].

Nickel could lower the temperature at which O<sub>2</sub> is produced and thereby prevent the formation of oxygen vacancies. Oxygen mobility and CeO<sub>2</sub> reduction depend on the high proportion of O<sub>adds</sub> and Frenkel-type defects found in XCeNi, as demonstrated by XPS and Raman, respectively. Finally, it is reported that the combination of CeO<sub>2</sub>-NiO enhances intermediate oxidation reactions [45, 46]. All the catalytic cycles that were evaluated showed this behavior, with minor variations in the profiles from cycle to cycle that were primarily related to the strength of the first peak in LTO. The intensity of the first peak is weakly reduced



as the XCeNi material regenerates, and the total decomposition of the adsorbed crude oil appears to terminate at higher temperatures. Cycle 6's complete decomposition occurred at 350 °C, which is 20 °C hotter than cycle 1's temperature. This reflects a decline in the monolithic carbon xerogel-Ce/Ni composite's catalytic activity.

### 3.2.1. Isothermal conversion

At three different temperatures, including 150, 200, and 250 °C, isothermal experiments were conducted. The experiments were performed in an oxidizing environment. In Figure 4's panels a to c, the crude oil conversion degree ( $\alpha$ ) as a function of time is depicted. In the beginning, it is understood that a rise in temperature accelerates the reaction rate ( $\alpha$ ), resulting in a quicker breakdown of adsorbed crude oil into lighter gaseous hydrocarbons.

Additionally, a complete conversion of the crude oil adsorbed throughout all the assessed cycles is seen. The small Ni and Ce particle sizes, high dispersion of both elements, high surface area, the presence of active catalytic sites ( $\text{Ce}^{3+}$  and  $\text{Ni}^{2+}$ ), the abundance of sites for oxygen anchorage ( $\text{O}_{\text{ads}}$ , e.g.,  $\text{O}^-$ ,  $\text{O}_2^-$ ), the presence of lattice oxygen, and the presence of Frenkel-type defects all contribute to this result.

However, the time needed to decompose 100% of the adsorbed fractions increased by 55 min, 43 min, and 38 min, respectively, at 150 °C, 200 °C, and 250 °C. It is possible that the material's regeneration reduced the amount of active sites that could catalyze the conversion of crude oil into gaseous products, which would explain why it took longer for the material to convert crude oil completely. These findings imply that all cycles examined when considering crude oil conversion have a regeneration efficiency of 100%. It is important to note that, for all scenarios, the crude oil catalytic conversion curve was higher than the virgin crude oil conversion curve. Due to the presence of refractory substances like asphaltenes and high molecular weight resins, the virgin crude oil sample under the evaluated conditions cannot convert 100%. Due to the presence of free radicals, these compounds, after initially cracking, tend to aggregate through addition and isomerization reactions. This results in the production of compounds with heavier molecular weights and high energy requirements for their breakdown [2, 25, 47].

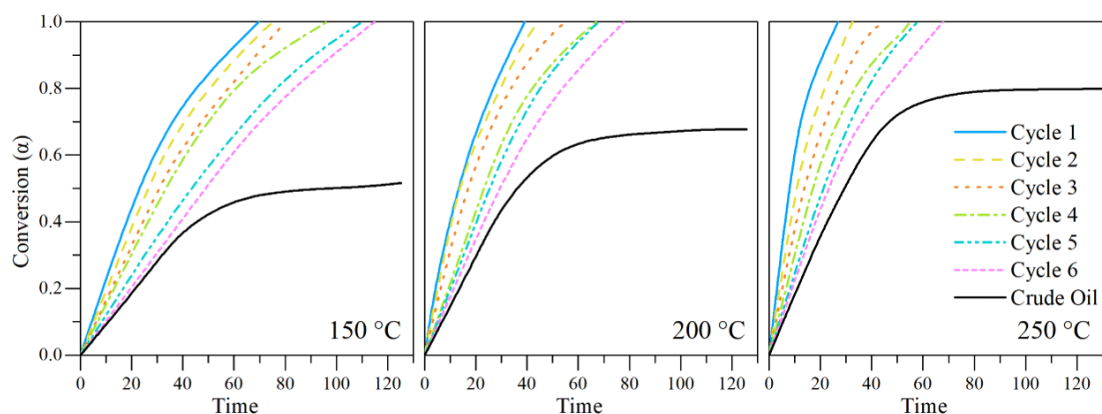


**Figure 4.** Isothermal conversion as a function of time at 150, 200, and 250 °C for crude oil oxidation in the presence and absence of monolithic carbon xerogel (XCeNi). Airflow rate = 100 mL min<sup>-1</sup> and crude oil load of 0.2 mg m<sup>-2</sup>.

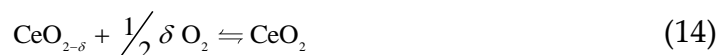
### 3.2.2. Gaseous products evolved during crude oil oxidation in the presence and absence of XCeNi under isothermal conditions.

By connecting a mass spectrometer to the TGA instrument, the gaseous analysis was carried out. In both the presence and absence of monolithic carbon-Ce/Ni composite during 6 catalytic regeneration cycles, the evolved gases during crude oil oxidation during isothermal heating at 200 °C are shown in Figure 5. Carbon monoxide (CO), carbon dioxide (CO<sub>2</sub>), light hydrocarbons (LHC), nitrogen oxides (NO<sub>x</sub>), and sulfur oxides (SO<sub>x</sub>) thermal release profiles received particular attention. Several reactions, including evaporation, distillation, partial oxidation, thermal cracking (pyrolysis), and combustion, take place during the oxidation of crude oil. Figure 5 demonstrates that LHC, CO<sub>2</sub>, and CO were the primary gases generated during the oxidation of crude oil. However, the relative content of CO<sub>2</sub> and CO decreases slightly with XCeNi. It is interesting to note that both SO<sub>x</sub> and NO<sub>x</sub> species are significantly reduced during the oxidation of crude oil with XCeNi at 200 °C, making the LHC the most prevalent species. This behavior was observed between 150 and 250 °C in all temperatures tested.

With a slight drop in LHC production from cycle 1 to cycle 6, this behavior is seen throughout all catalytic cycles. Polluting gas output, however, was never as high as crude oil's relative production. The catalytic effect of carbon, ceria, and active nickel sites result in the gases released. Due to their low bond dissociation energy, carbon-based materials may aid in activating and rupturing C-S bonds. Additionally, because of their large surface area, high degree of graphitization, and favorable surface chemistry, carbon xerogels can act as efficient catalysts for the oxidation of crude oil. As we recently reported, the surface of XCeNi contains

numerous carboxylic and unsaturated bond groups that serve as active sites for oxygen adding reactions, and the subsequent oxidation of adsorbed crude oil.

Like that, the redox cycle ( $\text{Ce}^{4+}/\text{Ce}^{3+}$ ) allows oxygen to be adsorb under oxidative conditions and released under reduced conditions, as illustrated in the following equations (2–3). This characteristic enables cerium particles to maintain a constant level of catalytic activity by utilizing atmospheric oxygen to break down the adsorbed fractions.



The oxygen-adding reactions produce TE=O, TE-O-TE, or TE-O support bonds over the supported transition element (TE), where TE is the supported transition element (Ni). The adsorbed crude oil fractions become more reactive because of the spillover phenomenon, which causes the  $\text{O}_2$  molecules to break at the metallic sites. This increases their reactivity and leads to their oxidation and subsequent decomposition into  $\text{CO}_2$  and  $\text{CO}_2$ . But light hydrocarbons are primarily released through the evaporation of low boiling point hydrocarbons and the dissolution of weak chemical bonds.  $\text{C}_2\text{H}_4$  is created when the  $\beta$  C-C bond in alkyl free radicals breaks or when aromatic or naphthenic ( $\text{C}_{\text{aromatic}}-\text{C}_\alpha$  or  $\text{C}_{\text{naphthenic}}-\text{C}_\alpha$ ) rings are opened or dealkylated. Meanwhile, the demethylation of methoxyl groups or the cracking of methyl and methylene can release methane [48-50]. Thus, it is concluded that the conversion of oil fractions, which the XCeNi can facilitate during successive regeneration cycles, is responsible for the oxidation of crude oil.

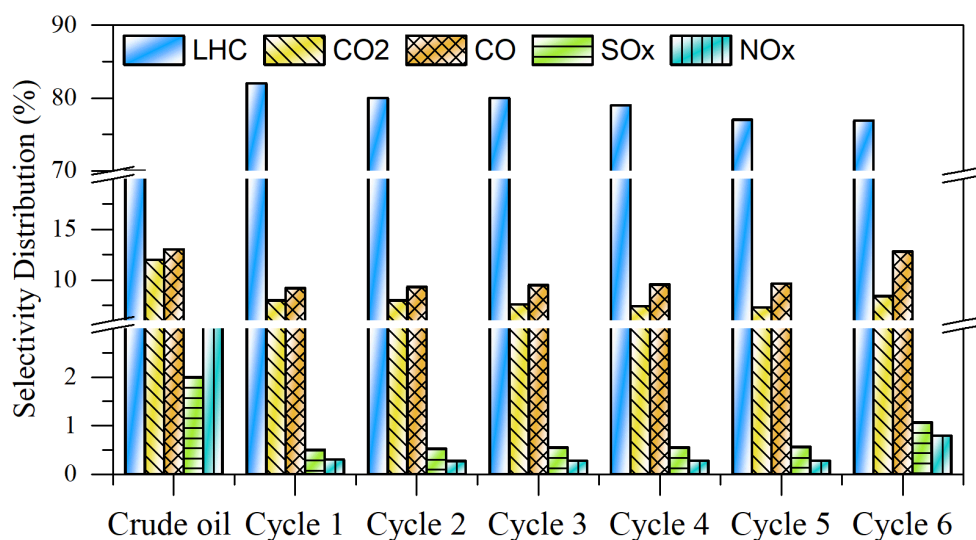


**Figure 5.** Selectivity distribution of gases released from crude oil oxidation in the absence and presence of the XCeNi throughout six reuses at 200 °C.

### 3.2.3. Effective activation energy estimation

For researching and verifying the catalytic effect of XCeNi to improve the oxidation behavior of crude oil under isothermal conditions, the effective activation energy ( $E_a$ ) was calculated. The process considers the plot  $\ln(t_{\alpha,i})$  against  $1/T_i$ , where  $t_{\alpha,i}$  denotes the time at a specified conversion ( $\alpha$ ) and temperature ( $i$ ), and the values of conversion of crude oil under isothermal heating at three different temperatures.  $E_a$  is calculated using the straight line's slope, and the results are displayed in Figure 6.

The kinetic reaction pathway for crude oil oxidation requires 27.4 kJ mol<sup>-1</sup>, whereas, when it is adsorbed on the XCeNi sample, it is reduced by 63.1%. The  $E_a$  values rise from 10.1 to 18.2 kJ mol<sup>-1</sup> as the monolithic carbon xerogel regenerates, which is 33.5% less than crude oil oxidation in the absence of XCeNi.

This means that even though the monolithic xerogel requires more energy for the reactions involved in the oxidation of crude oil as the system regenerates, it still performs well during the cycles that were evaluated because of Cerias's catalytic properties and its synergy with Ni. Additionally, because a decrease in the amount of Ce<sup>3+</sup> ions can lead to a decrease in the reaction rate, the change in activation energy provides insight into the impact of the redox cycle (Ce<sup>4+</sup>/Ce<sup>3+</sup>) on oxidation reactions.

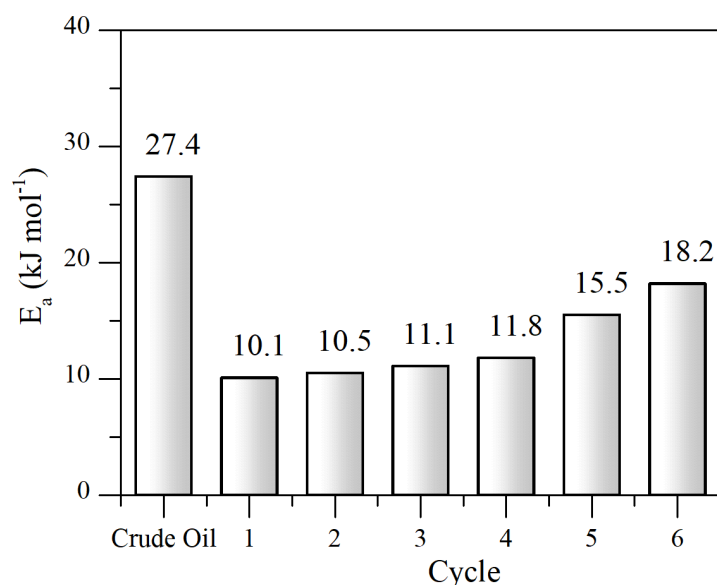


**Figure 6.** Estimated effective activation energy ( $E_a$ ) for isothermal catalytic oxidation of crude oil with XCeNi through six reuses.

### 3.3. Surface chemistry characterization

Through XPS analysis, changes in the XCeNi sample's surface chemistry during its regeneration were assessed. After their fourth reuse, the catalysts' high-resolution spectra are shown in Figure 7 and were examined using the freeware program XPSPEAK version 4.1. The XCeNi surface contained cerium ( $Ce_{3d}$ ), nickel ( $Ni_{2p}$ ), oxygen ( $O_{1s}$ ), and carbon ( $C_{1s}$ ), as was to be expected. Nevertheless, during sample regeneration, the concentration of the various species of each element changed.

Figure 7a-d displays the deconvoluted carbon, oxygen, cerium, and nickel species obtained from the high-resolution spectra. Table 5 provides a summary of the findings. The  $C_{1s}$  peak, which has a binding energy of 284.8 eV, served as the reference point for these measurements. In all cycles evaluated, the patterns for the  $C_{1s}$  region (Figure 7a) show four main peaks associated with the C=C bonds at 284.6 eV, the C-C bonds at 285.5 eV, the C=O bonds at 287.6 eV, and the  $CO_2$  at 290.5 eV [51]. These functional groups' contents varied a little bit from cycle to cycle. After the thermal treatment, the area of the C=C peak decreases. This outcome is consistent with Estrade-Szwarczkopf's findings, which showed that derived carbon thermal treatments reduced crystal defects and the FWHM C=C peak [52, 53]. As the material was recycled, the C=O band grew, indicating an oxygen chemisorption process during XCeNi regeneration in an oxidizing environment.

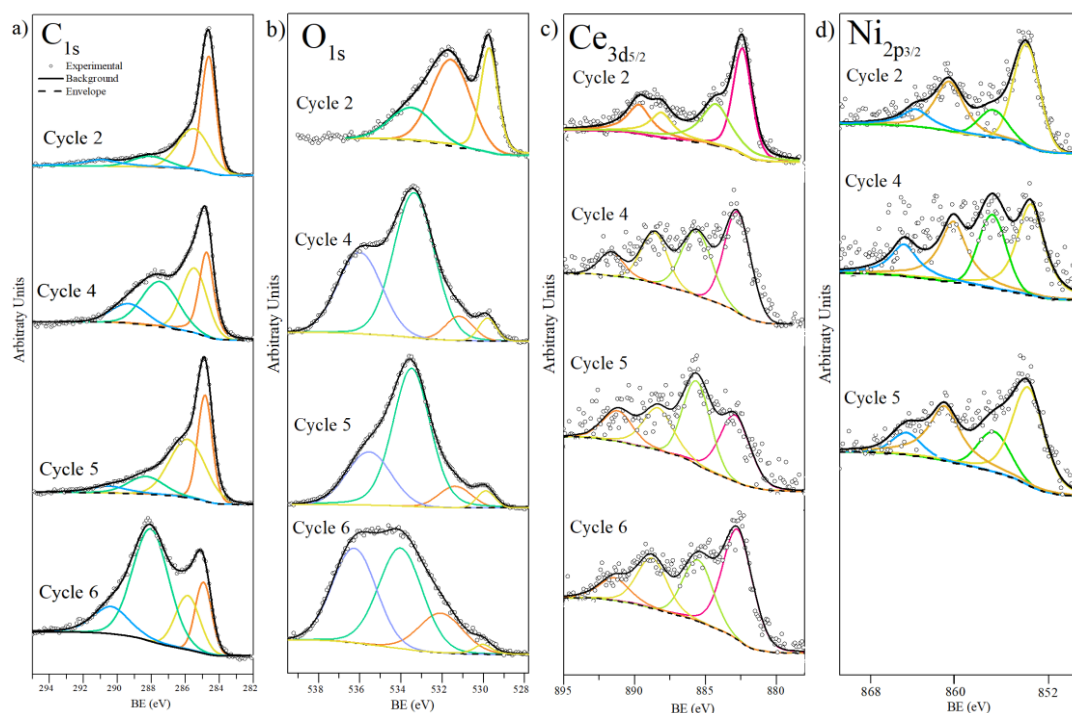


**Figure 7.** High-resolution XPS spectra of XCeNi after crude oil adsorption/decomposition regeneration cycles for the main elements present at the surface: a) carbon ( $C_{1s}$ ), b) oxygen ( $O_{1s}$ ), c) ceria ( $Ce_{3d\ 5/2}$ ), and d) nickel ( $Ni_{2p\ 3/2}$ ).

Up until the second cycle, three oxygen forms from metal oxides (O-Ce, O-Ni) (529.8 eV), O=C (531.5 eV), and O-C (533.5 eV) were used to describe the  $O_{1s}$  spectrum (Figure 7b) [54]. The oxygen content of metal oxides in relation to total oxygen one was higher (30.5%) in the second cycle. However, its content significantly decreased following the third cycle. The O-Ce and O-Ni species were present in 3.67, 3.32, and 2.05% of the cycles 4, 5, and 6, respectively. There is a broad peak at 535 eV in these (4-6) cycles. This component is most likely connected to the diffusion of oxygen atoms into the material's bulk at temperatures higher than 200 °C [55]. The percentage of this content ranged from 30.0% to 38.0%. In cycles 4 and 5, as well as cycle 6, the O=C species were reduced to below 10% and 20%, respectively.

The  $Ce_{3d_{5/2}}$  spectra are shown in Figure 7c. The  $Ce_{3d}^4f^1O_2p^5$  final state in the  $CeO_2$  results in a lower binding energy of 882.8 eV for  $Ce^{4+}_{5/2}$ . The  $Ce_{3d_{5/2}}$  spectra show a further peak at 885.5 eV. Shi et al. [56] reported that in the presence of oxygen,  $Ce^{3+}$  could completely transform into  $Ce(OH)_2^{2+}$  and obtain a band at higher binding energies than  $Ce^{4+}$  in the  $3d_{5/2}$  region. The  $Ce^{4+}$  concentration in relation to the total Ce one was 49.6, 45.4, 40.6, and 32.5% in

cycles 2, 4, 5, and 6, respectively, when the same proportions in the 3d<sub>3/2</sub> region were considered.

It is conceivable to imagine that Ce<sup>3+</sup> concentration rises during crude oil adsorption and after, Ce(OH)<sub>2</sub><sup>2+</sup> is produced during oxidation. This theory is consistent with the findings provided by Watanabe et al. [57]. The authors demonstrated that the reduction of Ce<sup>4+</sup> species during sulfur-based hydrocarbons adsorption could result in an increase in Ce<sup>3+</sup> concentration of approximately 50.0%. The XCeNi sample facility for decomposing crude oil adsorbed during its oxidation, can also be explained by this finding. Finally, the ligand (O2p) to metal (Ce4f) charge transfer is made easier, leading to the discovery of the respective satellites at 888.3 and 891.2 eV [45].

The deconvolution for the Ni2p<sub>3/2</sub> spectral region is displayed in Figure 7d. Ni<sup>2+</sup> species are responsible for the Ni2p<sub>3/2</sub> signal at 855.3 eV and the broad satellite peak centered at 860.5 eV [58]. The surface Ni<sup>3+</sup> responsible for the shoulder peak at 855 eV can be identified by comparing its binding energy to that of the Ni<sup>3+</sup> found in Ni<sub>2</sub>O<sub>3</sub> and NiOOH [58]. Finally, it is noted that the Ni<sup>2+</sup>/Ni<sup>3+</sup> ratio varies following each regeneration cycle, demonstrating the ongoing redox processes that have occurred in this sample.

**Table 5.** Peak percentage of carbon, oxygen, cerium, and nickel components obtained by the fitting results of the C<sub>1s</sub>, O<sub>1s</sub>, Ce<sub>3d5/2</sub> and Ni<sub>2p3/2</sub> spectra, respectively, for XCeNi till 6 crude oil adsorption/decomposition cycles.

Cycle	Peak							
	C <sub>1s</sub>		O <sub>1s</sub>		Ce <sub>3d5/2</sub>		Ni <sub>2p3/2</sub>	
	Assignment	%	Assignment	%	Assignment	%	Assignment	%
2	C=C	45	O-Ce, O-Ni	30	Ce <sup>4+ 5/2</sup>	49	Ni <sup>2+ 3/2</sup>	44
	C-C	35	O=C	49	Ce(OH) <sub>2</sub> <sup>2+</sup>	21	Ni <sup>3+ 3/2</sup>	14
	C=O	10	O-C	21	sat	14	sat	30
	CO <sub>2</sub>	10			sat	16	sat	12
4	C=C	27	O-Ce, O-Ni	4	Ce <sup>4+ 5/2</sup>	41	Ni <sup>2+ 3/2</sup>	37
	C-C	30	O=C	6	Ce(OH) <sub>2</sub> <sup>2+</sup>	30	Ni <sup>3+ 3/2</sup>	22
	C=O	30	O-C	58	sat	20	sat	27
	CO <sub>2</sub>	13	Obulk	32	sat	9	sat	15
5	C=C	34	O-Ce, O-Ni	3	Ce <sup>4+ 5/2</sup>	45	Ni <sup>2+ 3/2</sup>	43
	C-C	44	O=C	8	Ce(OH) <sub>2</sub> <sup>2+</sup>	24	Ni <sup>3+ 3/2</sup>	17
	C=O	15	O-C	63	sat	21	sat	30
	CO <sub>2</sub>	7	Obulk	26	sat	10	sat	10
6	C=C	15	O-Ce, O-Ni	3	Ce <sup>4+ 5/2</sup>	31		
	C-C	18	O=C	17	Ce(OH) <sub>2</sub> <sup>2+</sup>	33		
	C=O	53	O-C	42	sat	21		
	CO <sub>2</sub>	14	Obulk	38	sat	14		

Additionally, the point of zero charge ( $\text{pH}_{\text{pzc}}$ ) was examined for each time the XCeNi sample was used to remove crude oil from O/W emulsions, yielding a  $\text{pH}_{\text{pzc}}$  value of  $3.87 \pm 0.05$ , indicating that the sample exhibits an acidic  $\text{pH}_{\text{pzc}}$  over the course of its six times as a crude oil remover. The material's surface is primarily negatively charged due to the O/W emulsions' neutral pH. The metal phases of Ce, Ni, and Fe as well as oxygen-based functional groups are what give the substance its acidic nature. Some researchers link a sufficient adsorption capacity to a reduction in repulsive forces. There are more protonated compounds in crude oil, such as pyrrolic-pKa (16) and pyridine-pKa (5.2), which can interact with the materials' acidic surfaces. Consequently, a rise in  $\text{pH}_{\text{pzc}}$  reduces the interaction forces since fewer negative charges are on the XCeNi surface.

#### 4. Conclusions

The total regeneration capacity of the carbon-xerogel-Ce/Ni composite was done successfully. The adsorption capacity, catalytic activity and the surface chemistry properties of the composite were intensely studied to evaluate the regeneration efficiency. Adsorption capacity and catalytic activity remain high during the six cycles considered. However, the surface properties of the material were affected during the process. The  $\text{Ce}^{3+}$  concentration is reduced to 0 after each adsorption cycle. The xerogel's ability to decompose the adsorbed crude during all cycles may be associated with the increase in  $\text{Ce}^{3+}$  during the adsorption process. These facts generate changes in different parameters such as activation energy, adsorbate-adsorbate affinity, and thermodynamic properties ( $\Delta H_{\text{ads}}^{\circ}$ ,  $\Delta G_{\text{ads}}^{\circ}$ , and  $\Delta S_{\text{ads}}^{\circ}$ ). Also, the influence of  $\text{Ni}^{2+}/\text{Ni}^{3+}$  on XCeNi is noted. Through the regeneration, it is noted that the  $\text{Ni}^{2+}/\text{Ni}^{3+}$  ratio varies, which shows the continuous redox processes that have taken place in this sample. Finally, the gaseous products released in the oxidation process were analyzed, obtaining an increased production of light hydrocarbons during the decomposition of the crude oil in the presence of XCeNi, giving added value to the material and the proposed process.



## References

- [1] X. Dong, H. Liu, Z. Chen, K. Wu, N. Lu, Q. Zhang, Enhanced oil recovery techniques for heavy oil and oilsands reservoirs after steam injection, *Applied Energy*, 239 (2019) 1190-1211.
- [2] O.E. Medina, C. Olmos, S.H. Lopera, F.B. Cortés, C.A. Franco, Nanotechnology applied to thermal enhanced oil recovery processes: a review, *Energies*, 12 (2019) 4671.
- [3] H. Rezvani, D. Panahpoori, M. Riazi, R. Parsaei, M. Tabaei, F.B. Cortés, A novel foam formulation by Al<sub>2</sub>O<sub>3</sub>/SiO<sub>2</sub> nanoparticles for EOR applications: A mechanistic study, *Journal of Molecular Liquids*, 304 (2020) 112730.
- [4] M. Bijani, E. Khomehchi, Optimization and treatment of wastewater of crude oil desalting unit and prediction of scale formation, *Environmental Science and Pollution Research*, 26 (2019) 25621-25640.
- [5] A. Fakhru'l-Razi, A. Pendashteh, L.C. Abdullah, D.R.A. Biak, S.S. Madaeni, Z.Z. Abidin, Review of technologies for oil and gas produced water treatment, *Journal of hazardous materials*, 170 (2009) 530-551.
- [6] S. Kim, H. Wang, Y.M. Lee, 2D nanosheets and their composite membranes for water, gas, and ion separation, *Angewandte Chemie*, 131 (2019) 17674-17689.
- [7] B. Olufemi, L. Jimoda, N. Agbodike, Adsorption of crude oil using meshed corncobs, *Asian Journal of Applied Science and Engineering*, 3 (2014) 63-75.
- [8] T. He, H. Zhao, Y. Liu, C. Zhao, L. Wang, H. Wang, Y. Zhao, H. Wang, Facile fabrication of superhydrophobic Titanium dioxide-composited cotton fabrics to realize oil-water separation with efficiently photocatalytic degradation for water-soluble pollutants, *Colloids and Surfaces A: Physicochemical and Engineering Aspects*, 585 (2020) 124080.
- [9] B. Ge, X. Yang, H. Li, L. Zhao, G. Ren, X. Miao, X. Pu, W. Li, A durable superhydrophobic BiOBr/PFW cotton fabric for visible light response degradation and oil/water separation performance, *Colloids and Surfaces A: Physicochemical and Engineering Aspects*, 585 (2020) 124027.
- [10] X. Wei, S. Zhang, Y. Han, F.A. Wolfe, Treatment of petrochemical wastewater and produced water from oil and gas, *Water Environment Research*, 91 (2019) 1025-1033.
- [11] T.P.A. Bregnard, P. Höhener, A. Häner, J. Zeyer, Degradation of weathered diesel fuel by microorganisms from a contaminated aquifer in aerobic and anaerobic microcosms, *Environmental Toxicology and Chemistry: An International Journal*, 15 (1996) 299-307.

- [12] H. Gai, X. Zhang, S. Chen, C. Wang, M. Xiao, T. Huang, J. Wang, H. Song, An improved tar–water separation process of low–rank coal conversion wastewater for increasing the tar yield and reducing the oil content in wastewater, *Chemical Engineering Journal*, 383 (2020) 123229.
- [13] H. Chapman, K. Purnell, R.J. Law, M.F. Kirby, The use of chemical dispersants to combat oil spills at sea: A review of practice and research needs in Europe, *Marine Pollution Bulletin*, 54 (2007) 827-838.
- [14] I.F. Al-sharuee, F.H. Mohammed, Investigation study the ability of superhydrophobic silica to adsorb the Iraqi crude oil leaked in water, *IOP Conference Series: Materials Science and Engineering*, IOP Publishing 2019, pp. 012116.
- [15] K. Zapata, F. Carrasco-Marín, J.P. Arias, J. Castelo-Quibén, C.A. Franco, B. Rojano, F.B. Cortés, Novel biomaterial design based on *Pseudomonas stutzeri*–carbon xerogel microspheres for hydrocarbon removal from oil-in-saltwater emulsions: A new proposed treatment of produced water in oilfields, *Journal of Water Process Engineering*, 35 (2020) 101222.
- [16] C.A. Franco, F.B. Cortés, N.N. Nassar, Adsorptive removal of oil spill from oil-in-fresh water emulsions by hydrophobic alumina nanoparticles functionalized with petroleum vacuum residue, *Journal of colloid and interface science*, 425 (2014) 168-177.
- [17] Y.-C. Chiang, R.-S. Juang, Surface modifications of carbonaceous materials for carbon dioxide adsorption: A review, *Journal of the Taiwan Institute of Chemical Engineers*, 71 (2017) 214-234.
- [18] P. Lee, M.A. Rogers, Phase-selective sorbent xerogels as reclamation agents for oil spills, *Langmuir*, 29 (2013) 5617-5621.
- [19] P.B. Sarawade, J.-K. Kim, A. Hilonga, D.V. Quang, H.T. Kim, Synthesis of hydrophilic and hydrophobic xerogels with superior properties using sodium silicate, *Microporous and mesoporous materials*, 139 (2011) 138-147.
- [20] J.P. Villegas, N. Arcila, D. Ortega, C.A. Franco, F.B. Cortés, Crude oil removal from production water using nano-intermediates of a SiO<sub>2</sub> support functionalized with magnetic nanoparticles, *Dyna*, 84 (2017) 65-74.
- [21] I.V. Yentekakis, G. Goula, M. Hatzisymeon, I. Betsi-Argyropoulou, G. Botzolaki, K. Kousi, D.I. Kondarides, M.J. Taylor, C.M. Parlett, A. Osatiashtiani, Effect of support oxygen storage capacity on the catalytic performance of Rh nanoparticles for CO<sub>2</sub> reforming of methane, *Applied Catalysis B: Environmental*, 243 (2019) 490-501.

- [22] R. Linhardt, Q.M. Kainz, R.N. Grass, W.J. Stark, O. Reiser, Palladium nanoparticles supported on ionic liquid modified, magnetic nanobeads–recyclable, high-capacity catalysts for alkene hydrogenation, *RSC Advances*, 4 (2014) 8541-8549.
- [23] O.E. Medina, J. Gallego, L.G. Restrepo, F.B. Cortés, C.A. Franco, Influence of the Ce<sup>4+</sup>/Ce<sup>3+</sup> Redox-couple on the cyclic regeneration for adsorptive and catalytic performance of NiO-PdO/CeO<sub>2±δ</sub> nanoparticles for n-C<sub>7</sub> asphaltene steam gasification, *Nanomaterials*, 9 (2019) 734.
- [24] N.N. Nassar, A. Hassan, G. Vitale, Comparing kinetics and mechanism of adsorption and thermo-oxidative decomposition of Athabasca asphaltenes onto TiO<sub>2</sub>, ZrO<sub>2</sub>, and CeO<sub>2</sub> nanoparticles, *Applied Catalysis A: General*, 484 (2014) 161-171.
- [25] C.A. Franco, N.N. Nassar, T. Montoya, M.A. Ruíz, F.B. Cortés, Influence of asphaltene aggregation on the adsorption and catalytic behavior of nanoparticles, *Energy & Fuels*, 29 (2015) 1610-1621.
- [26] N.N. Nassar, Asphaltene adsorption onto alumina nanoparticles: kinetics and thermodynamic studies, *Energy & Fuels*, 24 (2010) 4116-4122.
- [27] T. Montoya, B.L. Argel, N.N. Nassar, C.A. Franco, F.B. Cortés, Kinetics and mechanisms of the catalytic thermal cracking of asphaltenes adsorbed on supported nanoparticles, *Petroleum Science*, 13 (2016) 561-571.
- [28] L.G.-C. Acosta, D.; Medina, O.E.; Cortés, F.B.; Franco, C.A. , Nano-Intermediate of Magnetite Nanoparticles Supported on Activated Carbon from Spent Coffee Grounds for Treatment of Wastewater from Oil Industry and Energy Production, *Processes*, 9 (2021) 63.
- [29] H. Vidal, J. Kašpar, M. Pijolat, G. Colon, S. Bernal, A. Cordón, V. Perrichon, F. Fally, Redox behavior of CeO<sub>2</sub>–ZrO<sub>2</sub> mixed oxides: I. Influence of redox treatments on high surface area catalysts, *Applied Catalysis B: Environmental*, 27 (2000) 49-63.
- [30] H. Vidal, J. Kašpar, M. Pijolat, G. Colon, S. Bernal, A. Cordón, V. Perrichon, F. Fally, Redox behavior of CeO<sub>2</sub>–ZrO<sub>2</sub> mixed oxides: II. Influence of redox treatments on low surface area catalysts, *Applied Catalysis B: Environmental*, 30 (2001) 75-85.
- [31] I. Celardo, E. Traversa, L. Ghibelli, Cerium oxide nanoparticles: a promise for applications in therapy, *J Exp Ther Oncol*, 9 (2011) 47-51.
- [32] R. Wang, H. Xu, X. Liu, Q. Ge, W. Li, Role of redox couples of Rh<sup>0</sup>/Rh<sup>δ+</sup> and Ce<sup>4+</sup>/Ce<sup>3+</sup> in CH<sub>4</sub>/CO<sub>2</sub> reforming over Rh–CeO<sub>2</sub>/Al<sub>2</sub>O<sub>3</sub> catalyst, *Applied Catalysis A: General*, 305 (2006) 204-210.

- [33] S. Alamolhoda, G. Vitale, A. Hassan, N.N. Nassar, P.P. Almao, Synergetic effects of cerium and nickel in Ce-Ni-MFI catalysts on low-temperature water-gas shift reaction, *Fuel*, 237 (2019) 361-372.
- [34] O.E. Medina, D. Galeano-Caro, J. Castelo-Quibén, R. Ocampo-Pérez, A.F. Perez-Cadenas, F. Carrasco-Marín, C.A. Franco, F.B. Cortés, Monolithic carbon xerogels-metal composites for crude oil removal from oil in-saltwater emulsions and subsequent regeneration through oxidation process: Composites synthesis, adsorption studies, and oil decomposition experiments, *Microporous and Mesoporous Materials*, (2021) 111039.
- [35] T. Montoya, D. Coral, C.A. Franco, N.N. Nassar, F.B. Cortés, A novel solid-liquid equilibrium model for describing the adsorption of associating asphaltene molecules onto solid surfaces based on the “chemical theory”, *Energy & Fuels*, 28 (2014) 4963-4975.
- [36] N.N. Nassar, Iron oxide nanoadsorbents for removal of various pollutants from wastewater: an overview, *Application of adsorbents for water pollution control*, (2012) 81-118.
- [37] M. Thommes, K. Kaneko, A.V. Neimark, J.P. Olivier, F. Rodriguez-Reinoso, J. Rouquerol, K.S. Sing, Physisorption of gases, with special reference to the evaluation of surface area and pore size distribution (IUPAC Technical Report), *Pure and Applied Chemistry*, 87 (2015) 1051-1069.
- [38] O.E. Medina, C. Caro-Vélez, J. Gallego, F.B. Cortés, S.H. Lopera, C.A. Franco, Upgrading of extra-heavy crude oils by dispersed injection of NiO-PdO/CeO<sub>2</sub>+ $\delta$  nanocatalyst-based nanofluids in the steam, *Nanomaterials*, 9 (2019) 1755.
- [39] X. Geng, P. Ren, G. Pi, R. Shi, Z. Yuan, C. Wang, High selective purification of flavonoids from natural plants based on polymeric adsorbent with hydrogen-bonding interaction, *Journal of Chromatography A*, 1216 (2009) 8331-8338.
- [40] R.W. Pekala, C.T. Alviso, Carbon aerogels and xerogels, *MRS Online Proceedings Library Archive*, 270 (1992).
- [41] C. Orge, J. Órfão, M. Pereira, Carbon xerogels and ceria-carbon xerogel materials as catalysts in the ozonation of organic pollutants, *Applied Catalysis B: Environmental*, 126 (2012) 22-28.
- [42] C.A. Franco, N.N. Nassar, F.B. Cortés, Removal of oil from oil-in-saltwater emulsions by adsorption onto nano-alumina functionalized with petroleum vacuum residue, *Journal of colloid and interface science*, 433 (2014) 58-67.
- [43] C.A. Franco, T. Montoya, N.N. Nassar, P. Pereira-Almao, F.B. Cortés, Adsorption and subsequent oxidation of colombian asphaltenes onto nickel

and/or palladium oxide supported on fumed silica nanoparticles, *Energy & Fuels*, 27 (2013) 7336-7347.

[44] M.K. Dabbous, P.F. Fulton, Low-temperature-oxidation reaction kinetics and effects on the in-situ combustion process, *Society of Petroleum Engineers Journal*, 14 (1974) 253-262.

[45] B. Sellers-Antón, E. Bailón-García, A. Cardenas-Arenas, A. Davó-Quiñonero, D. Lozano-Castelló, A. Bueno-López, Enhancement of the Generation and Transfer of Active Oxygen in Ni/CeO<sub>2</sub> Catalysts for Soot Combustion by Controlling the Ni–Ceria Contact and the Three-Dimensional Structure, *Environmental Science & Technology*, 54 (2020) 2439-2447.

[46] S. Alamolhoda, G. Vitale, A. Hassan, N.N. Nassar, P. Pereira Almas, Development and characterization of novel combinations of Ce-Ni-MFI solids for water gas shift reaction, *The Canadian Journal of Chemical Engineering*, 97 (2019) 140-151.

[47] N.N. Nassar, C.A. Franco, T. Montoya, F.B. Cortés, A. Hassan, Effect of oxide support on Ni–Pd bimetallic nanocatalysts for steam gasification of n-C<sub>7</sub> asphaltenes, *Fuel*, 156 (2015) 110-120.

[48] M. Rezaei, M. Schaffie, M. Ranjbar, Thermocatalytic in situ combustion: Influence of nanoparticles on crude oil pyrolysis and oxidation, *Fuel*, 113 (2013) 516-521.

[49] D. Liu, J. Hou, H. Luan, J. Pan, Q. Song, R. Zheng, Coke yield prediction model for pyrolysis and oxidation processes of low-asphaltene heavy oil, *Energy & Fuels*, 33 (2019) 6205-6214.

[50] A. Amrollahi Biyouki, N. Hosseinpour, N.N. Nassar, Pyrolysis and Oxidation of Asphaltene-Born Coke-like Residue Formed onto in Situ Prepared NiO Nanoparticles toward Advanced in Situ Combustion Enhanced Oil Recovery Processes, *Energy & fuels*, 32 (2018) 5033-5044.

[51] J. Castelo-Quibén, A. Abdelwahab, M. Pérez-Cadenas, S. Morales-Torres, F.J. Maldonado-Hódar, F. Carrasco-Marín, A.F. Pérez-Cadenas, Carbon-iron electrocatalysts for CO<sub>2</sub> reduction. The role of the iron particle size, *Journal of CO<sub>2</sub> Utilization*, 24 (2018) 240-249.

[52] A. Abdelwahab, J. Castelo-Quibén, M. Pérez-Cadenas, F.J. Maldonado-Hódar, F. Carrasco-Marín, A.F. Pérez-Cadenas, Insight of the effect of graphitic cluster in the performance of carbon aerogels doped with nickel as electrodes for supercapacitors, *Carbon*, 139 (2018) 888-895.

[53] H. Estrade-Szwarckopf, XPS photoemission in carbonaceous materials: A “defect” peak beside the graphitic asymmetric peak, *Carbon*, 42 (2004) 1713-1721.

- [54] C. Alegre, D. Sebastián, M.J. Lázaro, Carbon xerogels electrochemical oxidation and correlation with their physico-chemical properties, *Carbon*, 144 (2019) 382-394.
- [55] A. Boronin, S. Koscheev, G. Zhidomirov, XPS and UPS study of oxygen states on silver, *Journal of electron spectroscopy and related phenomena*, 96 (1998) 43-51.
- [56] H. Shi, F. Liu, E. Han, Corrosion behaviour of sol-gel coatings doped with cerium salts on 2024-T3 aluminum alloy, *Materials Chemistry and Physics*, 124 (2010) 291-297.
- [57] S. Watanabe, X. Ma, C. Song, Adsorptive desulfurization of jet fuels over TiO<sub>2</sub>-CeO<sub>2</sub> mixed oxides: Role of surface Ti and Ce cations, *Catalysis Today*, (2020).
- [58] X. Xu, L. Li, J. Huang, H. Jin, X. Fang, W. Liu, N. Zhang, H. Wang, X. Wang, Engineering Ni<sup>3+</sup> cations in NiO lattice at the atomic level by Li<sup>+</sup> doping: the roles of Ni<sup>3+</sup> and oxygen species for CO oxidation, *ACS Catalysis*, 8 (2018) 8033-8045.





## Conclusiones Generales





## Conclusiones generales

Los resultados recogidos en la presente tesis doctoral demostraron que el desarrollo de nanomateriales con propiedades catalíticas ajustadas a la medida permite la reevaluación y aprovechamiento de crudos pesados y extrapesados mediante su gasificación bajo diversas atmósferas y diferentes condiciones de presión y temperatura, a través de la descomposición de la fracción más pesada del petróleo crudo y la obtención de H<sub>2</sub> durante el mismo proceso.

Inicialmente se generó una amplia comprensión de la reactividad térmica de fracciones de petróleo crudo en ausencia y presencia de nanomateriales con el fin de proponer nanomateriales capaces de asistir reacciones químicas que potencialicen la producción de hidrogeno. En estos estudios se demostró que la reactividad de las fracciones SARA es dependiente de la presión y la atmosfera de reacción. Particularmente los asfáltenos presentaron una mayor reactividad a condiciones de alta presión en atmosferas reactivas, debido a la quimisorción de las moléculas de la atmosfera. Se identificaron diferentes factores que pueden influenciar dichas reacciones de quimisorción, entre las cuales destacan la aromaticidad, el grado de condensación, el tamaño de agregado, y el tipo de grupos funcionales formados.

Seguidamente se sintetizaron nanomateriales a base de CeO<sub>2</sub>, los cuales demostraron propiedades texturales y químicas adecuadas para generar altas eficiencias adsorptivas y catalíticas en la captura y descomposición térmica de las fracciones más pesadas del crudo, tales como los afaltenos y las resinas. Los nanomateriales sintetizados fueron capaces de craquear las fracciones mencionadas bajo diferentes condiciones de presión, temperatura, y atmosfera de reacción. Bajo atmosferas reactantes, permitieron la difusión de las moléculas de gas hacia la estructura química del asfalteno adsorbido, aumentando su reactividad. En el mismo orden, durante el proceso de adsorción fueron capaces de inhibir la formación de agregados de asfalteno, generando interacciones intermoleculares más fuertes que las interacciones asfalteno-asfalteno. Bajo estas mismas condiciones, también se demostró la selectividad de los nanomateriales para generar una mezcla gaseosa rica en hidrocarburos livianos e hidrogeno a bajas temperaturas, y disminuyendo el libramiento de CO<sub>2</sub>. Otra propiedad importante de los nanomateriales fue su capacidad para capturar CO<sub>2</sub> y usarlo

en reacciones de craqueo de asfaltenos, promoviendo una mayor liberación de hidrogeno.

Los nanomateriales fueron testeados bajo condiciones de flujo dinámico, simulando procesos de recobro térmico convencionales, como la inyección de vapor, obteniendo resultados favorables en términos de aumento del factor de recobro, mejoramiento de la calidad del crudo, y liberación de hidrogeno. Los crudos tratados con nanotecnología presentaron menores valores de viscosidad, menor contenido de asfaltenos, y mayor gravedad API. Además, estas propiedades se mantuvieron con el tiempo, indicando una perdurabilidad en la calidad mejorada del crudo.

En base a los desarrollos estáticos y dinámicos, se llevó a cabo la primera aplicación a nivel mundial de nanotecnología en pozos afectados por procesos de inyección de vapor. Los nanofluidos se diseñaron para mejorar la productividad de un yacimiento de petróleo pesado con inyección en frío (sin vapor) y con inyección de vapor. De acuerdo con los resultados de las pruebas de campo, los beneficios se asocian principalmente a la producción incremental luego de la ejecución de las 2 primeras pruebas con nanofluidos, una en frío y otra con vapor (pozos A y B) entre junio y julio de 2022. La producción incremental percibida durante 2022 corresponde a 8603 bbl relacionados con 3231 bbl (pozo A) y 5372 bbl (pozo B). De igual forma, con la ejecución de 2 pruebas adicionales, una en frío y otra con vapor (pozos C y D), entre noviembre y diciembre de 2022, se reportan beneficios asociados a la implementación tecnológica en 430 bbl (pozo C) para los procesos en frío, y 980 bbl (pozo D) en el caso de inyección de vapor en presencia de nanofluidos. Los resultados demuestran el desarrollo de una tecnología rentable y altamente eficiente para la producción de crudos pesados.

Finalmente se propusieron dos tecnologías que incluyen: *i*) el uso de heteroátomos presentes en las fracciones más pesadas del crudo, tales como el azufre, para el mejoramiento de la calidad del crudo y la co-producción de hidrogeno a través de procesos de adsorción/catálisis con nanomateriales diseñados a la medida, y *ii*) la remoción de aceite proveniente de emulsiones de crudo en agua para la producción de gases con alto poder calorífico a través de procesos de adsorción y catálisis. Para estas aplicaciones se sinterizaron nanomateriales de aluminosilicatos y xerogeles de carbono dopados con óxidos metálicos y óxidos lantánidos. En estos estudios se demostró que los nanomateriales son capaces de usar otras fuentes de hidrocarburo para producir hidrogeno e hidrocarburos livianos a través de su craqueo térmico.

## Recomendaciones y trabajos futuros

De acuerdo con los resultados obtenidos, se proponen las siguientes recomendaciones:

- Evaluar la reactividad a condiciones de baja y alta presión de mezclas asfalteno-SAR, y sistemas DAO bajo herramientas experimentales y de simulación molecular.
- Evaluar a través de dinámica molecular las interacciones nanopartícula-asfalteno bajo diferentes condiciones de presión y temperatura.
- Evaluar la descomposición del asfalteno en presencia de nanopartículas a través de dinámica molecular bajo diferentes atmosferas y condiciones de presión y temperatura.
- Analizar a escala de poro el comportamiento de hidrogeno en ausencia y presencia de nanopartículas en medios porosos a través de herramientas de microfluidica y simulación de yacimientos.
- Desarrollar una metodología para el escalamiento de la aplicación de nanopartículas en pozos afectados por procesos de combustión in-situ e inyección de agentes oxidantes.
- Realizar un análisis económico y social a partir de los resultados de producción de crudo durante la aplicación en campo de la tecnología.
- Realizar un análisis de ciclo de vida y huella de carbono a partir de los resultados de producción de crudo durante la aplicación en campo de la tecnología.

# Appendix A

## Thermogravimetric Analysis

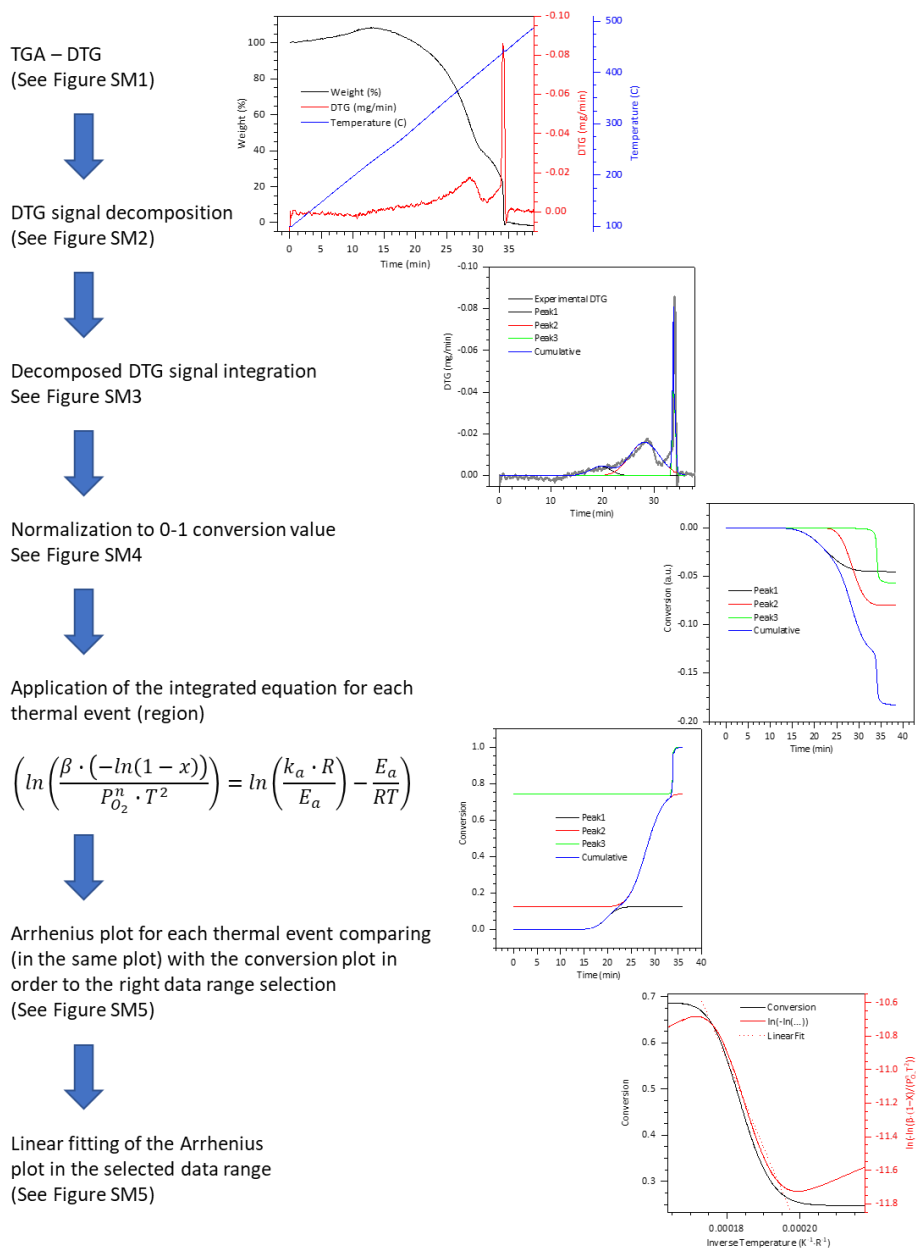


**Figure 1.** General scheme for the HP-TGA data treatment in order to individualize the different thermal events and calculate its apparent kinetic parameters,  $E_a$  and  $k_0$ . Example applied to n-C<sub>7</sub> asphaltenes oxidation in air at 70 bar.

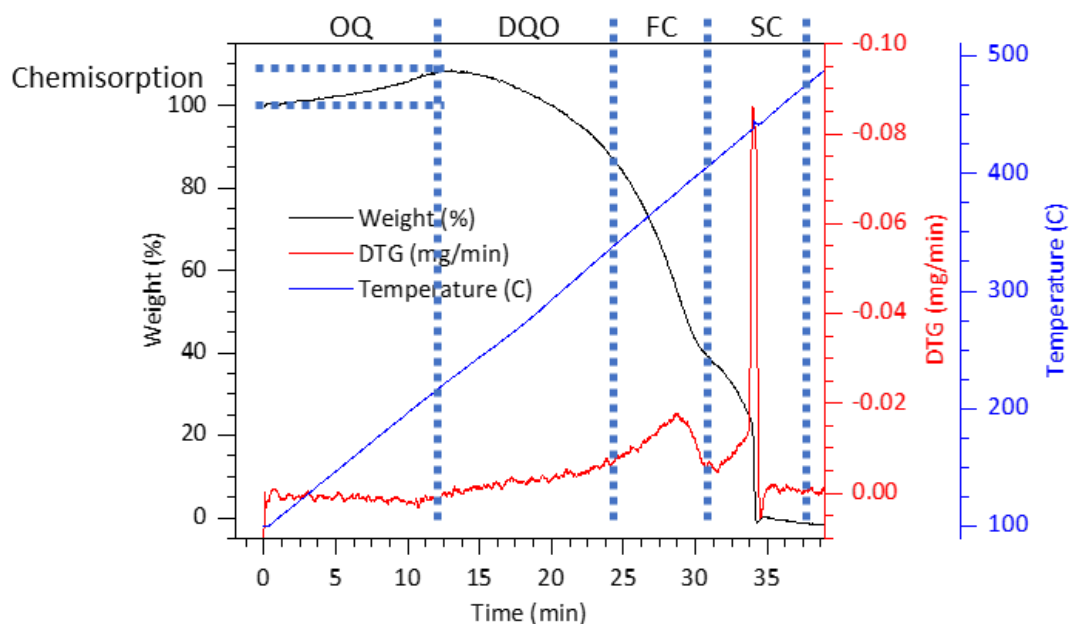


**Figure 2.** HP-TGA for *n*-C<sub>7</sub> asphaltene oxidation under air at 70 bar. Selection of different thermal events o regions. 1. Oxygen chemisorption, 2. Decomposition of the functional oxygenated groups, 3. First combustion event, and 4. Second combustion event.

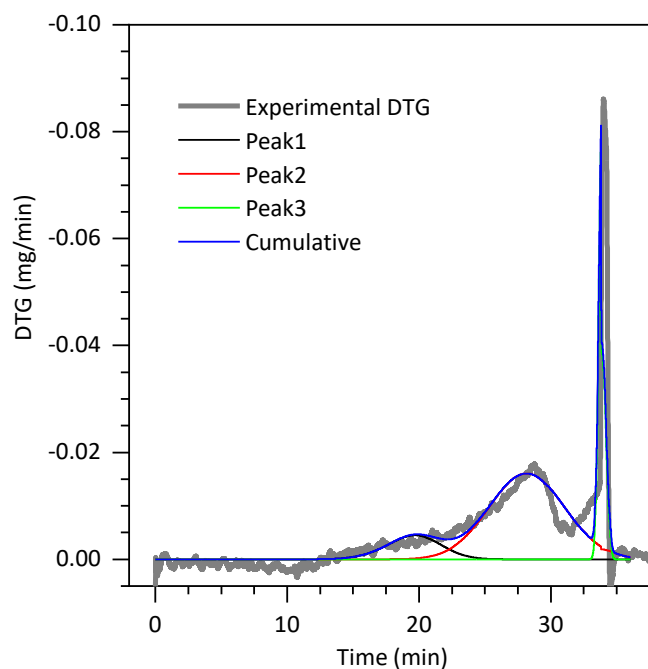


**Figure 3.** Example of the HP-DTG decomposition on mathematical functions (conventionally gaussian/Lorentzian) for each thermal selected event.

## Appendix B

### Viscosity determination

The viscosity of the *n*-C<sub>7</sub> asphaltene solutions was determined through steady shear analysis using a Kinexus Pro rotational rheometer (Malvern Instruments, Worcestershire – UK) at 25 °C in a shear rate range between 1 and 100 s<sup>-1</sup>. For samples with mass fractions of 0.1% and 1.0% of *n*-C<sub>7</sub> asphaltenes, concentric cylinder geometry was employed, whereas for solutions with 10.0 wt.%, a 20 mm cone-plate geometry was used with a gap of 0.3 mm. Measurements were done in triplicate to ensure repeatability.

The viscosity analysis is divided into three sections including *i*) rheological behavior analysis of the solutions, *ii*) relative viscosities determination at a fixed shear rate (10 s<sup>-1</sup>) ( $\mu_r = \mu_{solution} / \mu_{solvent}$ ), i.e., the viscosity of the *n*-C<sub>7</sub> asphaltene ( $\mu_{solution}$ ) solution divided by the solvent's viscosity ( $\mu_{solvent}$ ) and *iii*) intrinsic viscosity ( $\mu_{in}$ ) calculation. The intrinsic viscosity is a measure of the hydrodynamic volume occupied by macromolecules in solution and therefore a reflection of their size.<sup>1</sup> To this aim, Huggins and Kraemer equations (Equations 1 and 2, respectively) were used.<sup>2,3</sup>

$$\mu_{sp} / c = \mu_{in} + k_H \mu_{in}^2 c \quad (1)$$

$$\ln \mu_r / c = \mu_{in} + k_K \mu_{in}^2 c \quad (2)$$

where, *c* is the asphaltene concentration (mg·mL<sup>-1</sup>) in each solution,  $\mu_{sp}$  refers to the specific viscosity and  $k_H$  and  $k_K$  are Huggins and Kraemer's viscosity slope constant, respectively. The values of  $k_H$  and  $k_K$  are obtained by the slope of the curves  $\mu_{sp} / c$  against *c* and  $\ln \mu_r / c$  against *c*, respectively. Then, the  $\mu_{in}$  is obtained at the crossing point of both graphs.

Figure 1 shows the rheological profiles for asphaltenes dissolved in the three xylene isomers using concentrations between 0.1 and 10.0 wt.%. The solutions at low concentrations of *n*-C<sub>7</sub> asphaltenes (0.1 and 1.0 wt.%) demonstrated a Newtonian behavior. In contrast, at high concentrations of *n*-C<sub>7</sub> asphaltenes (10 wt.%), non-Newtonian behavior was observed, i.e.,

dependent on the shear rate.<sup>4</sup> The results are consistent with those reported in the literature.<sup>5-7</sup>

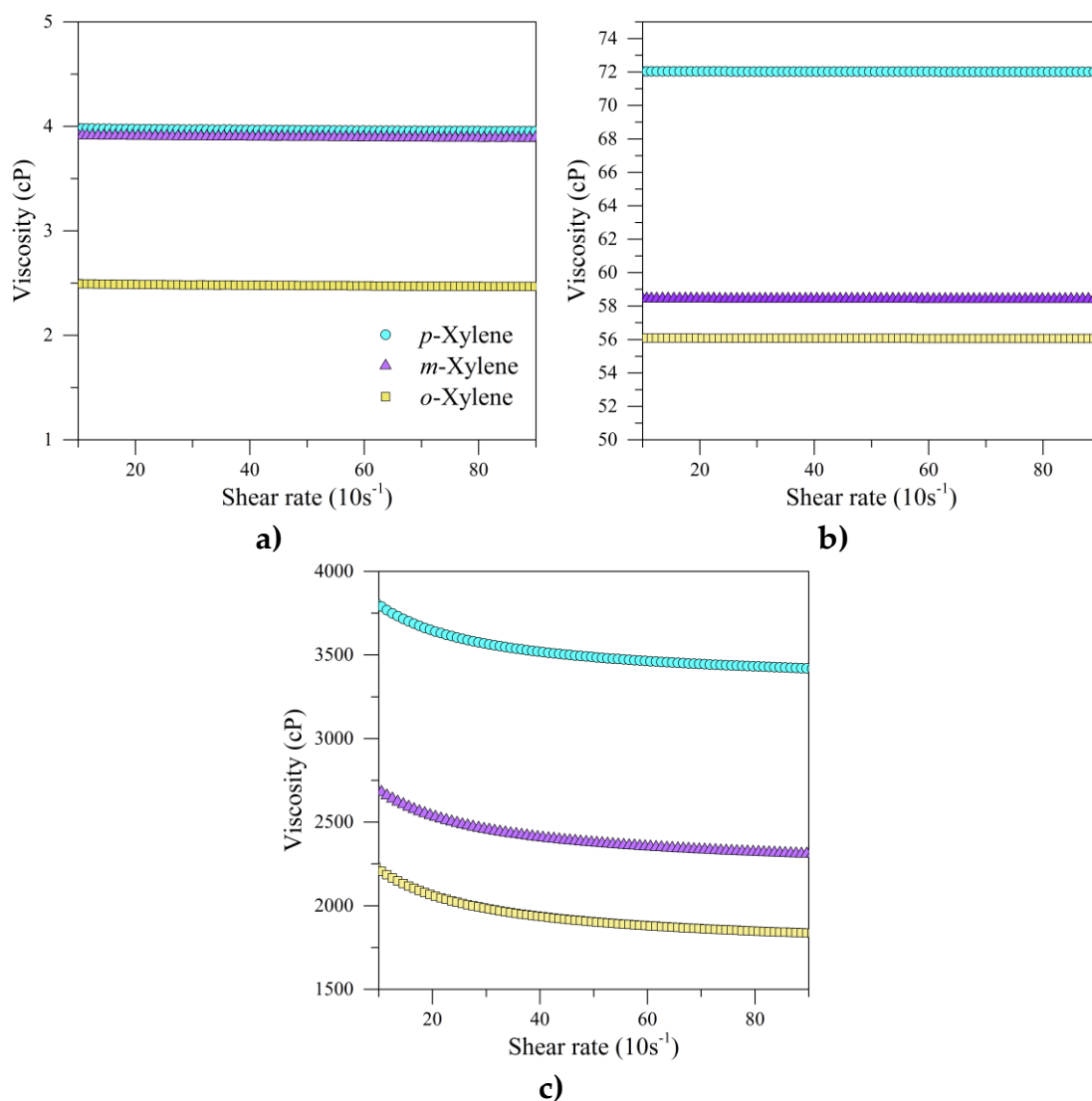


**Figure 1.** Experimental measurements of viscosities of asphaltenes dissolved in xylene isomers at a) 0.1 wt.%, 1.0 wt.%, and 10.0 wt.% asphaltene concentration.

Figure 2 shows the results from experimental relative viscosity ( $\mu_r$ ) for different asphaltene concentrations dissolved in *p*-, *m*-, and *o*- xylene. The relative viscosity was calculated at a shear rate of  $10\text{ s}^{-1}$  considering the rheological profiles (Figure 1). Similar trends were found for asphaltene aggregate size and relative viscosity for solution models. The increment of asphaltene concentration on the model solution, increases the asphaltene aggregate size and the viscosity. These results are associated with the

overlapping ability of asphaltenes, which increases the elasticity of the fluid.<sup>8</sup>

9

Interestingly, it was found a relationship between asphaltene aggregate size and viscosity. Both properties were found to be higher when the concentration of asphaltenes was higher. Therefore, the size of the asphaltene aggregate is expected to influence the viscosity of the solution. This result agrees with the trends reported in the literature.<sup>10, 11</sup>

Furthermore, viscosity is also affected by the diluent used. For both low and high asphaltene concentrations,  $\mu_r$  increases in the order *o*-xylene < *m*-xylene < *p*-xylene, indicating that the position of a methyl group affects the asphaltene size and viscosity of the model solution prepared.

Some differences were found in both variables as the concentration of the asphaltene changed. In the first instance, for a mass fraction of 0.1% of asphaltenes, the relative viscosity for all solutions was similar between 3 and 5 a.u. When asphaltene concentration increased up to 1.0% in mass fraction, viscosities vary from 69 a.u. (*o*-xylene) to 89 a.u. (*p*-xylene), correlated with a higher variation in asphaltene aggregate size (8.19 nm to 8.99 nm). For the systems with 10.0% in mass fraction of asphaltenes, the viscosity varies by more than 1700 u.a. between the system with the lowest viscosity (*o*-xylene) and the system with the highest viscosity (*p*-xylene). In particular, the aggregate size in systems at the concentration of 10.0% by mass fraction varies to a greater extent. This behavior is closely related to the asphaltene aggregate sizes, promoted by the heteroatom content (N, O, and S) in the chemical structure and the self-association behavior of asphaltenes. The aggregation mechanisms gain importance at high concentrations, increasing the interactions between the aromatic cores forming aggregates by full stacking.<sup>11, 12</sup> Hence, the results indicate that the asphaltene solution models behave as concentrated suspensions, considering that an increase in volumetric fraction promotes an increase in viscosity.<sup>11</sup>



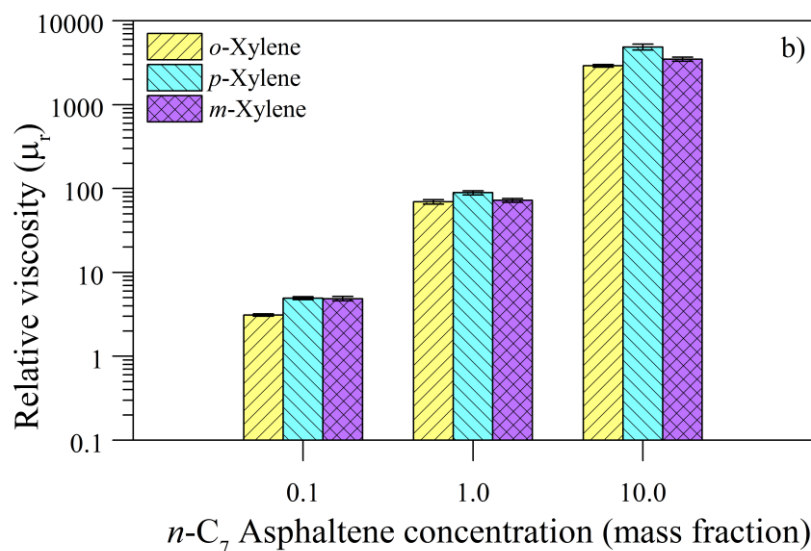


**Figure 2.** Relative viscosity ( $\mu_r = \mu_{\text{solution}} / \mu_{\text{solvent}}$ ) for asphaltene solution in different aromatic solvents. The viscosity was taken for a shear rate of  $10 \text{ s}^{-1}$ .

Based on the results of average length ( $L$ ) and relative viscosity, the intrinsic viscosity was calculated. Table S1 shows the results of viscosity at 5 asphaltene concentrations (0.1 wt.%, 0.5 wt.%, 1.0 wt.%, 5.0 wt.%, and 10.0 wt.%) which were used to determine the intrinsic viscosity. Figure 3 shows the plots of  $\mu_{sp} / c$  against  $c$  and  $\ln \mu_r / c$  against  $c$  for asphaltenes dissolved on *o*-, *m*-, and *p*-xylene. The intrinsic viscosity was found at  $0.019 \text{ mg}\cdot\text{mL}^{-1}$ ,  $0.027 \text{ mg}\cdot\text{mL}^{-1}$ , and  $0.031 \text{ mg}\cdot\text{mL}^{-1}$ , for *o*-xylene - asphaltene, *m*-xylene - asphaltene, and *p*-xylene - asphaltene systems, respectively. The values of the intrinsic viscosity are consistent with the average length of the asphaltene aggregates in the organic solvents (*o*- < *m*- < *p*-xylene). As the intrinsic viscosity is considered a measure of the macromolecule size, it is expected to be the observed trend. Based on these results, it is expected that its state of aggregation strongly influences the interaction energies between asphaltene molecules and therefore the viscosity of the solution. This evidence that the position of the  $-\text{CH}_3$  substituent in the xylene structure can modify the fluid's internal network from a volume entropic effect, as shown later in MD results.<sup>10, 11</sup>

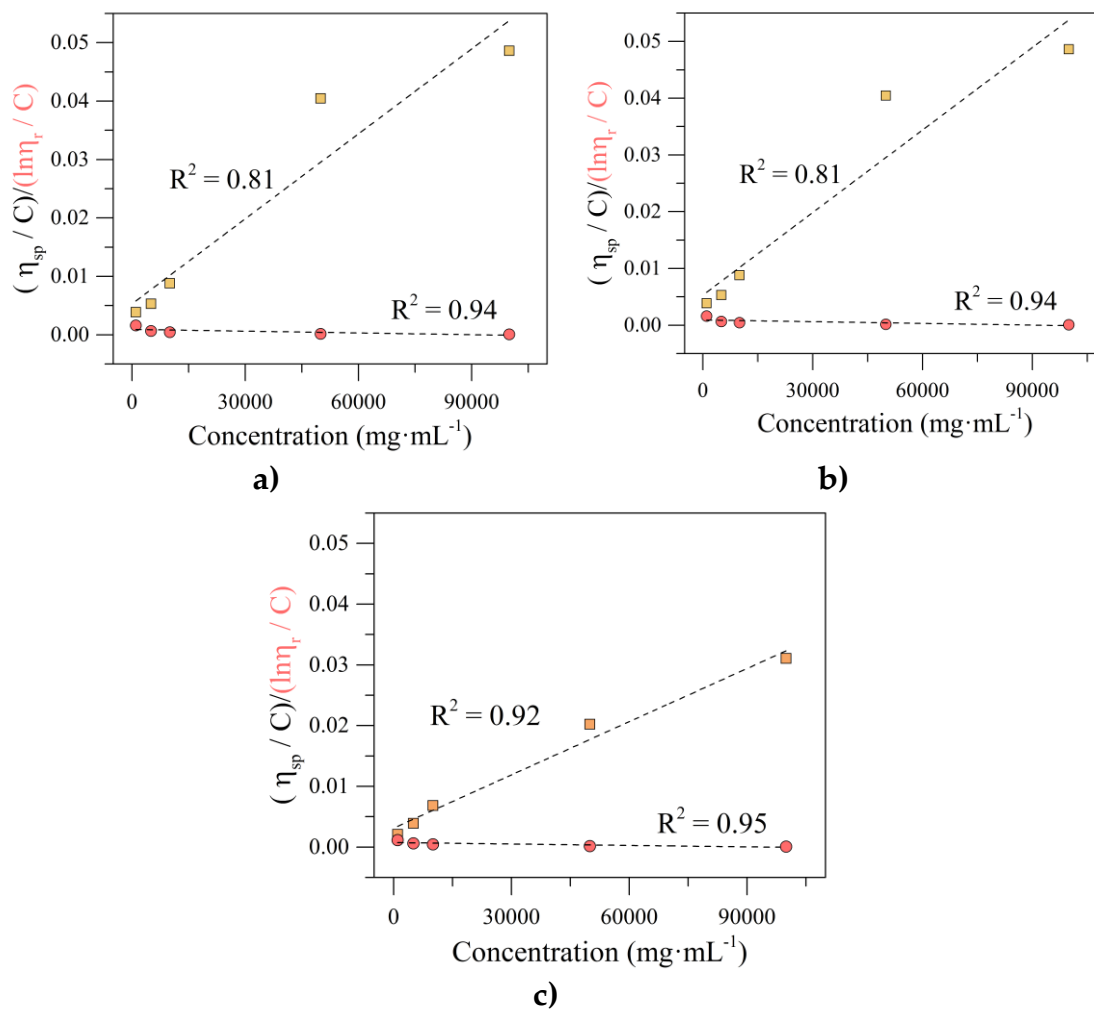


**Figure 3.** Plots  $(\mu_{sp}/c$  against  $c$ ) and  $(\ln\mu_r/c$  against  $c$ ) for asphaltenes dissolved on a) *p*-xylene, b) *m*-xylene, and c) *o*-xylene. Where  $c$  is the asphaltene concentration ( $\text{mg}\cdot\text{mL}^{-1}$ ) in each solution,  $\mu_{sp}$  and  $\mu_r$  refer to the specific and relative viscosity.

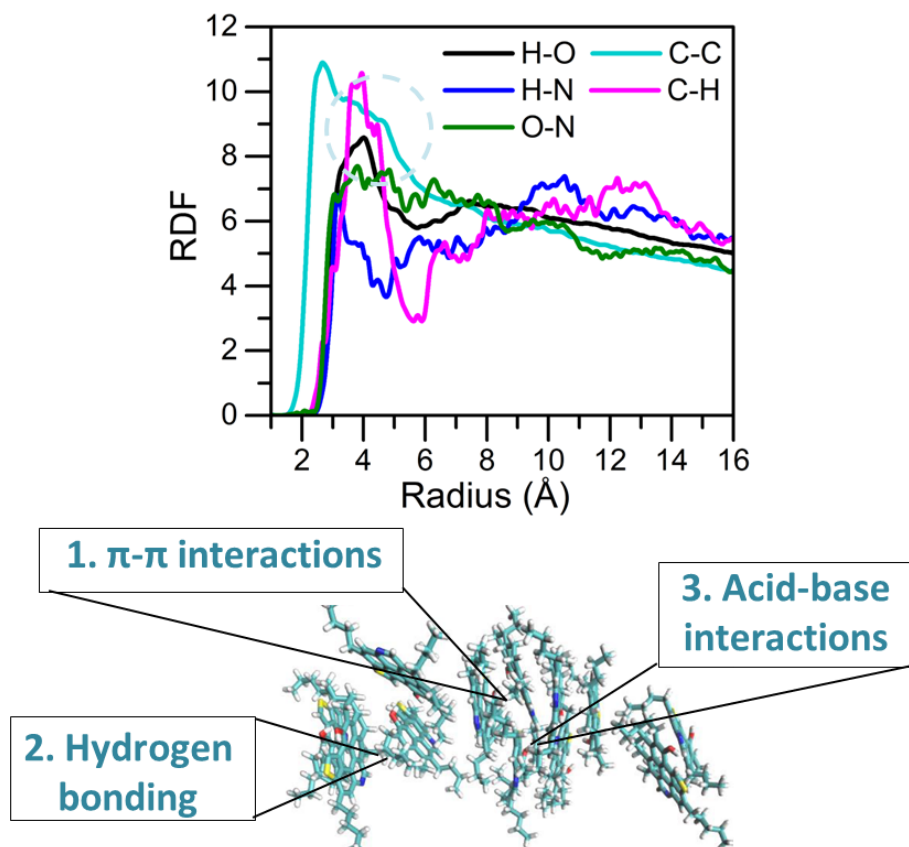


**Figure 4.** Radial function distribution between the heteroatoms of asphaltene molecules.

## References

1. Ako, K.; Elmarhoum, S.; Munialo, C. D., The determination of the lower critical concentration temperature and intrinsic viscosity: The syneresis reaction of polymeric gels. *Food Hydrocolloids* **2022**, 124, 107346.
2. Huggins, M. L., The viscosity of dilute solutions of long-chain molecules. IV. Dependence on concentration. *Journal of the American Chemical Society* **1942**, 64, (11), 2716-2718.
3. Kraemer, E. O., Molecular weights of celluloses and cellulose derivatives. *Industrial & Engineering Chemistry* **1938**, 30, (10), 1200-1203.
4. Al-Obaidi, S. In *Investigation of rheological properties of heavy oil deposits*, Conference of the Arabian Journal of Geosciences, 2022; Springer: 2022; pp 399-402.
5. Chanda, D.; Sarmah, A.; Borthakur, A.; Rao, K.; Subrahmanyam, B.; Das, H., Combined effect of asphaltenes and flow improvers on the rheological behaviour of Indian waxy crude oil. *Fuel* **1998**, 77, (11), 1163-1167.

6. D'Avila, F.; Silva, C.; Steckel, L.; Ramos, A.; Lucas, E., Influence of asphaltene aggregation state on the wax crystallization process and the efficiency of EVA as a wax crystal modifier: A study using model systems. *Energy & Fuels* **2020**, *34*, (4), 4095-4105.
7. Ramírez, L.; Moncayo-Riascos, I.; Cortés, F. B.; Franco, C. A.; Ribadeneira, R., Molecular Dynamics Study of the Aggregation Behavior of Polycyclic Aromatic Hydrocarbon Molecules in n-Heptane–Toluene Mixtures: Assessing the Heteroatom Content Effect. *Energy & Fuels* **2021**, *35*, (4), 3119-3129.
8. Taborda, E. A.; Alvarado, V.; Franco, C. A.; Cortés, F. B., Rheological demonstration of alteration in the heavy crude oil fluid structure upon addition of nanoparticles. *Fuel* **2017**, *189*, 322-333.
9. Moghaddam, R. K.; Yarranton, H.; Natale, G., Interfacial micro and macro rheology of fractionated asphaltenes. *Colloids and Surfaces A: Physicochemical and Engineering Aspects* **2022**, *651*, 129659.
10. Pierre, C.; Barré, L.; Pina, A.; Moan, M., Composition and heavy oil rheology. *Oil & Gas Science and Technology* **2004**, *59*, (5), 489-501.
11. Moncayo-Riascos, I.; Taborda, E.; Hoyos, B. A.; Franco, C. A.; Cortés, F. B., Theoretical-experimental evaluation of rheological behavior of asphaltene solutions in toluene and p-xylene: Effect of the additional methyl group. *Journal of Molecular Liquids* **2020**, *303*, 112664.
12. Oguamah, I. A. U.; Isehunwa, S.; Ndubisi, O.; Stephen, U.; Jude, O., Molecular Dynamics Study of Solvent Effect on the Structure and Characteristics of Asphaltene aggregates. **2022**.

# Appendix C

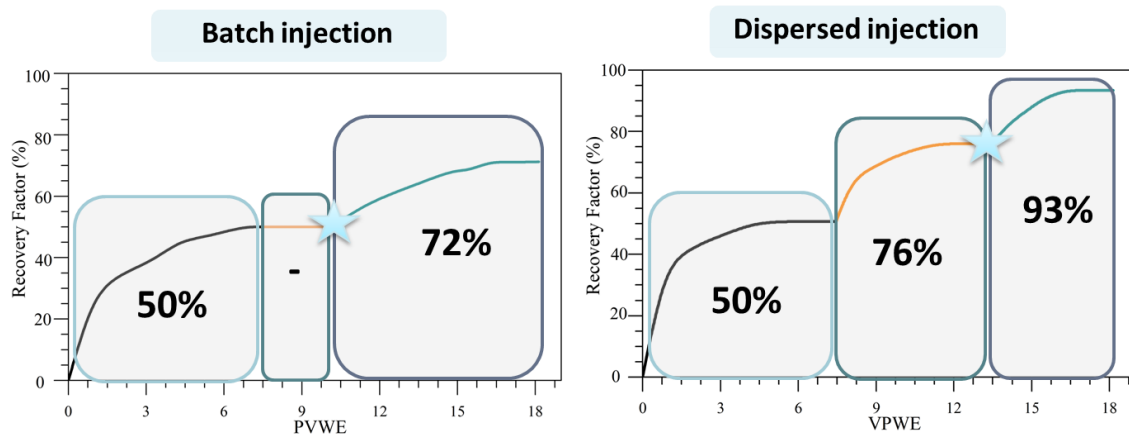


**Figure 1.** Crude oil recovery during steam injection assisted by nanotechnology. a) Nanofluid injected in liquid batch and b) dispersed in the steam stream.